

2000



Proceedings of the NINTH  
United States - Japan  
Conference  
on Composite Materials

— Edited by  
**Hiroshi Fukuda**, *Science University of Tokyo*  
**Takashi Ishikawa**, *National Aerospace Laboratory*  
**Yasuo Kogo**, *Science University of Tokyo*



July 3 and 4, 2000

Toray Human Resources Development Center,  
Mishima, Shizuoka, Japan

20000720 013

# REPORT DOCUMENTATION PAGE

Form Approved

OMB No. 0704-0188

The public reporting burden for this collection of information is estimated to average 1 hour per response, including the time for reviewing instructions, searching existing data sources, gathering and maintaining the data needed, and completing and reviewing the collection of information. Send comments regarding this burden estimate or any other aspect of this collection of information, including suggestions for reducing the burden, to Department of Defense, Washington Headquarters Services, Directorate for Information Operations and Reports (0704-0188), 1215 Jefferson Davis Highway, Suite 1204, Arlington, VA 22202-4302. Respondents should be aware that notwithstanding any other provision of law, no person shall be subject to any penalty for failing to comply with a collection of information if it does not display a currently valid OMB control number.

1. REPORT DATE (DD-MM-YYYY)

14-07-2000

2. REPORT TYPE

Conference Proceedings

3. DATES COVERED (From - To)

3-4 July 2000

4. TITLE AND SUBTITLE

The 9th US-Japan Conference on Composite Materials

5a. CONTRACT NUMBER

F6256299M9241

5b. GRANT NUMBER

5c. PROGRAM ELEMENT NUMBER

5d. PROJECT NUMBER

5e. TASK NUMBER

5f. WORK UNIT NUMBER

6. AUTHOR(S)

Conference Committee

7. PERFORMING ORGANIZATION NAME(S) AND ADDRESS(ES)

Science University of Tokyo  
2641 Yamazaki, Noda  
Chiba 278-8510  
Japan

8. PERFORMING ORGANIZATION  
REPORT NUMBER

N/A

9. SPONSORING/MONITORING AGENCY NAME(S) AND ADDRESS(ES)

AOARD  
UNIT 45002  
APO AP 96337-5002

10. SPONSOR/MONITOR'S ACRONYM(S)

AOARD

11. SPONSOR/MONITOR'S REPORT  
NUMBER(S)

CSP-991016

12. DISTRIBUTION/AVAILABILITY STATEMENT

Approved for public release; distribution is unlimited.

13. SUPPLEMENTARY NOTES

14. ABSTRACT

PROCEEDINGS FROM THIS CONFERENCE INCLUDE THE FOLLOWING CATEGORIES:  
PLENARY SESSION (Overview for Composites) (Low Cost Composite Structures) (Composites for Infrastructure) (Smart and Intelligent Composites).  
LOW COST COMPOSITE STRUCTURES, I AND II  
SMART AND INTELLIGENT COMPOSITES  
MMC, CMC & C/C  
FIBER AND REPAIR  
FRACTURE TOUGHNESS  
NEW CONCEPT COMPOSITES, I AND II  
COMPOSITE MECHANICS, I AND II  
DAMAGE TOLERANCE  
COMPOSITES FOR INFRASTRUCTURE, I AND II  
CREEP AND FATIGUE  
DAMAGE IDENTIFICATION; CRYOGENIC COMPOSITE TANK; AND BRAIDED AND FW COMPOSITES

15. SUBJECT TERMS

Composite Materials

16. SECURITY CLASSIFICATION OF:

a. REPORT

U

b. ABSTRACT

U

c. THIS PAGE

U

17. LIMITATION OF  
ABSTRACT

UU

18. NUMBER  
OF  
PAGES

889

19a. NAME OF RESPONSIBLE PERSON

Thomas D. Kim

19b. TELEPHONE NUMBER (Include area code)

+81-3-5410-4409

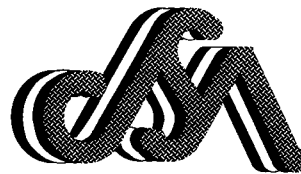
DMC QUALITY INSPECTED 4

Standard Form 298 (Rev. 8/98)  
Prescribed by ANSI Std. Z39.18





2000



# **Proceedings of the NINTH United States - Japan Conference on Composite Materials**

**Edited by**

**Hiroshi Fukuda**, *Science University of Tokyo*  
**Takashi Ishikawa**, *National Aerospace Laboratory*  
**Yasuo Kogo**, *Science University of Tokyo*

**July 3 and 4, 2000**

**Toray Human Resources Development Center,  
Mishima, Shizuoka, Japan**

**Co-Organized by**

*The Japan Society for Composite Materials*  
*The American Society for Composites*

**Sponsored by**

*Asian Office of Aerospace Research and Development / Air Force Office of Scientific  
Research (AOARD/AFOSR)*  
*Army Research Office - Far East (AROFE)*

**In cooperation with**

*The Japan Society for Aeronautical and Space Sciences,  
The Japan Society of Mechanical Engineers,  
The Society of Materials Science, Japan,  
The Japan Reinforced Plastics Society,  
SAMPE Japan,  
R&D Institute of Metals and Composites for Future Industries (RIMCOF),  
Japan Institute for Metals,  
Ceramic Society of Japan*

---

**Hiroshi Fukuda:** Professor, Science University of Tokyo  
**Takashi Ishikawa:** Section Head, National Aerospace Laboratory  
**Yasuo Kogo:** Associate Professor, Science University of Tokyo

**Proceedings of the NINTH United States - Japan Conference on  
Composite Materials**

Published by the Japan Society for Composite Materials  
c/o Business Center for Academic Societies Japan (BCASJ)  
BCASJ: C-21, 5-16-9 Honkomagome, Bunkyo-ku, Tokyo 113-8622, Japan

Copyright © 2000 by the Japan Society for Composite Materials  
All rights reserved

No part of this publication may be reproduced, stored in a retrieval system, or  
transmitted, in any form or by any means, electronic, mechanical, photocopying  
recording or otherwise, without the prior written permission of the publisher.

Printed in Japan

ISBN4-931136-03-6 C3053 ¥00000E

How to order this book

Order to the Japan Society for Composite Materials by Credit Card using a copy of this  
page.

c/o BCASJ (Mr. Nobuhiko Takeda)

By FAX: +81(Country Code of Japan) - 3-5814-5820

By Mail: BCASJ: C-21, 5-16-9 Honkomagome, Bunkyo-ku, Tokyo 113-8622, Japan

Post Conference Price: ¥20,000 with shipping per each set

By Credit Card: American Express, VISA, MasterCard

(Information of BCASJ: <http://www.bcasj.or.jp/index.html>)

Your Name (Print): \_\_\_\_\_

Your Address: \_\_\_\_\_

Date: \_\_\_\_\_ Your Credit Card: \_\_\_\_\_ Exp.Date

No.:

Signature: \_\_\_\_\_

# Table of Contents

---

*Preface*            xi

## **Plenary Session**

*(Overview for Composites)*

**Aerospace Force Research in Composite Materials..... 3**

R. L. Sierakowski

**Development of Carbon Fiber Industry - Past and Future.....15**

A. Takeo

**Status of Project on Advanced Composite Materials for Transportation in Japan.....23**

A. Sakamoto, M. Noda and Y. Yamaguchi

*(Low Cost Composite Structures)*

**Rationale & Approaches for Low-Cost Aerospace Composite Products.....29**

K. T. Kedward

**Low-Cost Fabrication of Advanced Polymeric Composites by Resin Infusion Process...31**

A. C. Loos

*(Composites for Infrastructure)*

**Composites in Marine Structures.....39**

Y. D. S. Rajapakse

**Composites in the Renewal of Civil Infrastructure – Materials, Manufacturing, Design and Durability.....41**

V. M. Karbhari

**Improvement of Shear and Ductility of Reinforced Concrete Columns by Wrapping of Continuous Fiber Reinforced Polymer Sheet.....49**

K. Maruyama, H. Nakai, F. Katsuki, and T. Shimomura

*(Smart and Intelligent Composites)*

**Manufactured Shapes of Piezoceramic-Composite Actuators.....57**

M. W. Hyer and A. B. Jilani

**Summary Report of Structural Health Monitoring Project for Smart Composite Structure Systems.....65**

N. Takeda

**Design of Intelligent Composite Structures.....75**

F. -K. Chang

**Health Monitoring of Composite Structure Using Optical Fiber Sensors.....77**

C. S. Hong, C. Y. Ryu and J. W. Park

---

## **Low Cost Composite Structures, I**

**Design and Manufacturing Considerations in the Raytheon Premier I Business Jet .....87**  
R. Abbott (Invited)

**Development Program and a Status of Advanced Composite Design and Manufacturing Technology for Future Supersonic Transport.....95**  
H. Tamura

**Low Cost Manufacturing Approach for Composite Outer Wing of SST .....97**  
H. Tamura, K. Kosugi, S. Maekawa, Y. Hirose, T. Sana and T. Hatakeyama.....97

**Study on Processability, Composite Properties and Fiber Placement Processing for High Temp. Composites.....105**  
Y. Yamaguchi, H. Mizuno, H. Horizono, Y. Sugiyama, Y. Ishimuro, K. Ishikiriama and H. Tamura

## **Low Cost Composite Structures, II**

**Property Characterization in On-Line Consolidation of Thermoplastic Composites.....115**  
C. Kuo, S. I. Guceri and C. Pistor

**A Study on the Induction Heating of Carbon Fiber Reinforced Thermoplastic Composites .....117**  
H. J. Kim, S. Yarlagadda, J. W. Gillespie, Jr., N. Shevchenko and B. K. Fink

**Needs for Predictable Damage Growth Design of Aircraft Composite Structures.....125**  
H. Kikukawa and H. Tamura

**Cost Reduction in Compression-after-Impact (CAI) Tests: Proposal of Half SACMA Specimen Size.....133**  
T. Ishikawa, M. Mastushima, E. Hara and G. Ben

## **Smart and Intelligent Composites**

**Delamination Monitoring of Graphite/epoxy Composites by Electric Resistance Change .....143**  
A. Todoroki, Y. Tanaka, Y. Shimamura and H. Kobayashi

**Internal Strain Measurement of FW FRP Pipe with Optical Fiber Sensors.....151**  
T. Kosaka, K. Osaka, M. Sando and T. Fukuda

**Strain Monitoring of IACC Yachts Using Fiber Optic Distributed Sensors.....159**  
H. Murayama, K. Kageyama, I. Kimpara, A. Shimada and H. Naruse

**Effects of Pressure on Measurement of Strains in EFPI Optical Fiber Sensors Embedded in FRP Laminates.....167**  
K. Osaka, T. Kosaka, Y. Kawasaki and T. Fukuda

**Application of Embedded FBG Sensors for Detection of Damages in CFRP Composites 175**  
Y. Okabe, S. Yashiro, T. Kosaka and N. Takeda

## **MMC**

<b>Fracture Behavior and Its Influence on Superconducting Property of Nb<sub>3</sub>Al Composite Wire.....</b>	<b>185</b>
S. Ochiai, T. Sawada, M. Ohno, M. Hojo and K. Watanabe	

<b>Fabrication and Mechanical Properties of Titanium Metal Matrix Composite Rings...</b>	<b>193</b>
N. Yunoki, T. Honda, K. Moriya, S. Nishide and M. Uyama	

<b>Mechanical Properties of Aluminum Borate Whisker Reinforced AZ91D Magnesium Alloy Composites by Semi-Solid Process.....</b>	<b>201</b>
M. Yoshida, S. Takeuchi, J. Pan, G. Sasaki, N. Fuyama, T. Fujii and H. Fukunaga	

<b>Effect of Whisker Surface Treatment on the Strength of Al<sub>18</sub>B<sub>4</sub>O<sub>33</sub>/Al Alloy Composites</b>	<b>209</b>
J. Pan, A. Okamoto, M. Yoshida, G. Sasaki, H. Fukunaga, N. Fuyama and T. Fujii	

## **CMC & C/C**

<b>Multiple Micro-cracking and Tensile Behavior of Orthogonal 3-D Woven Si-Ti-C-O Fiber/Si-Ti-C-O Matrix Composite.....</b>	<b>219</b>
T. Ogasawara, H. Ito, T. Ishikawa and N. Watanabe	

<b>Scanning Electrion Microscopy Study of Failure in Glass-Sealed SiC·SiC-based Composite (NUSK-CMC) Creep Tested at 1100 and 1200 ° C in Air.....</b>	<b>227</b>
I. J. Davies, T. Ogasawara, T. Ishikawa, and N. Suzuki	

<b>Strength Improvement by Densification of C/C Composites.....</b>	<b>235</b>
H. Hatta, Y. Kogo, Y. Hamada, T. Shigei, Y. Sawada, and S. Somiya	

<b>Suppression of Through-the-Thickness Cracking in SiC Coating Deposited on C/C Composites.....</b>	<b>243</b>
T. Aoki, H. Hatta, T. Hitomi, H. Fukuda, and I. Shiota	

<b>Development of Glass Fiber Reinforced Carbon Composite.....</b>	<b>251</b>
S. Somiya, and T. Nojiri	

## **Fiber and Repair**

<b>A Back Stress Constitutive Model for High Temperature Deformation of SiC Monofilaments.....</b>	<b>257</b>
C. E. Bakis, R. E. Tressler, and S. J. Strait	

<b>A Representative Diameter for the Evaluation of Brittle Monofilament Strength.....</b>	<b>265</b>
T. Morimoto	

<b>Crack Growth Analysis in Cracked Aluminum Panels Repaired with a Bonded Composite Patch.....</b>	<b>273</b>
Y. Shibuya, S. Fujimoto, M. Sato, H. Shirahata, H. Fukunaga, and H. Sekine	

<b>Experimental Study of Repair Efficiency for Single-Side Composite Patches Bonded to Aircraft Structural Panels.....</b>	<b>281</b>
M. Sato, A. T. Yokobori, Jr., Y. Ozawa, T. Kamiyama, T. Miyanaga, P. R. W. Beaumont and H. Sekine	

---

## **Fracture Toughness**

### **Mode II Interlaminar Properties under Static and Fatigue Loadings for CF/Epoxy Laminates with Different Fiber Surface Treatment.....291**

M. Hojo, S. Matsuda, S. Ochiai, N. Tsujioka, Y. Nakanishi, Z. Maekawa, and A. Murakami

### **Highly Accurate Mode-Separated Energy Release Rates for Delamination Cracks.....299**

H. -S. Oh

### **Propagation Behavior of Mixed-Mode Delamination Fatigue Cracks in Graphite/Epoxy and Graphite/Thermoplastic Laminates.....307**

H. Tanaka and K.Tanaka

### **Evaluating the Fracture Toughness of Glass Fiber/Epoxy Interface Using Slice Compression Test - Propagation Behavior of Interfacial Debonding.....315**

K. N. Tsay, K. Toge, and H. Kawada

### **Interlaminar Fracture Toughness of Composite Laminates with Whisker Reinforced Interlamination.....323**

W. X. Wang, Y. Takao, T. Matsubara, and H. -S. Kim

### **Delamination Growth Simulation of Composite Plates by Using Finite Element Method 331**

Y. Shimamura, A. Todoroki, H. Kobayashi and H. Nakamura

## **New Concept Composites, I**

### **Effects of Rolling on the Microstructure and the Mechanical Properties of Injection-Molded Sheets of PP/LCP Blend.....341**

M. Kawagoe, J. Qiu, W. Mizuno, and M. Morita

### **Mechanical Properties of PE Fiber Reinforced Thermoplastics Composites.....349**

T. Fukui, and H. Hamada

### **Effect of Thermal Cycling on Degradation of High-Temperature Polymer Composite Materials for the Next-Generation SST Structures.....355**

T. Shimokawa, H. Katoh, Y. Hamaguchi, S. Sanbongi, H.Mizuno, H.Nakamura, R. Asagumo, and H.Tamura

### **Novel Carbon Fiber Reinforced Composites with Newly Developed Silicon Containing Polymer MSP.....363**

T. Ogasawara, T. Ishikawa, M. Itoh, T. Abe, R. Yokota, and M. Ando

## **New Concept Composites, II**

### **Flexural and Compressive Properties of Polymer Matrix Composites Containing a Mixture of Carbon and Silicon Carbide Fibers: Part2-Compression.....373**

I. J. Davies, H. Hamada, and M. Shibuya

### **Development of Carbon Fiber Composites using Biodegradable Plastics and Their Mechanical Properties.....375**

J.Jiang, K.Okubo, and T. Fujii

### **Energy Absorption Properties of Pultruded Rectangular Pipes.....383**

H.Saito, R.Inai, K.Kameo, and H.Hamada

## **Composite Mechanics, I**

- Use of Glass Fibers in Tailoring Laminated Composites with Directionally Negative and Near-Zero Coefficients of Thermal Expansion.....393**  
K. Wakashima, T. Suganuma, and T. Ito

- Full-Field Singular Stresses in a Composite Laminate Weakened by a Cylindrical Cavity: Theory and Experiment.....401**  
E. V. Larve, and D. H. Mollenhauer

- Interaction of Shear Wave with Fiber Orientations in Composite Laminate: Model and Experiment.....409**  
D. K. Hsu and D. Fei

- Finite Element Analysis of Creep in Unidirectional Composites Based on Homogenization Theory.....417**  
K. Kondo and R. Takiguchi

- Correlation Between Acoustic Emission Waveform Parameters and the Damage and Failure Mechanisms in CFRP Materials.....425**  
O. Siron, H. Tsuda, and T. Hamada

## **Composite Mechanics, II**

- Characterization of Mechanical Behavior of CFRP Laminates Containing Matrix Cracks Using Damage Mechanics Analysis.....435**  
S. Kobayashi, S. Ogihara, and N. Takeda

- Bearing Failure Mechanisms of Carbon/Bismaleimide Composite in Mechanically Fastened Joints.....443**  
Y. Xiao and I. Susuki

- Mechanical Property Analysis of Matrix Hybrid Laminates.....451**  
T. Onita, T. Nishiwaki, and Z. Maekawa

## **Damage Tolerance**

- Damage and Failure in FRP Composite Laminates under Low-Velocity Impact.....461**  
K. Minnaar, J. Zhai, S. W. Park, and M. Zhou

- Damage Accumulation in Composite Laminates during Quasi-Static Transverse Loading.....469**  
Y. Aoki, H. Suemasu, and O. Majima

- Damage Progression of Composite Laminates under Low-Velocity Impact.....477**  
N. Uda, K. Kunoo, K. Ono, T. Nagayasu, T. Izumiya, and K. Machida

- Impact Perforation of Orthotropic and Quasi-isotropic CFRP Laminates by a Steel Ball Projectile.....485**  
H. Kasano

- Damage Tolerant Behaviors of a Biomimetic CFRP Laminate.....493**  
T. Tanimoto

## **Composites for Infrastructure, I**

- The Application of Composites for the Rehabilitation of Concrete Bridge Infrastructure.....503**  
A. S. Crasto, R. Y. Kim, and J. P. Mistretta (Invited)

<b>Composite Spoolable Tubulars.....</b>	<b>513</b>
O. Ochoa (Invited)	
<b>Ductility of Reinforced Concrete Beams Externally Retrofitted with Carbon Fiber Polymer Composites.....</b>	<b>521</b>
S. E. Mouring, O. Barton, Jr., and D. K. Simmons	
<b>MMA Resin Application for the Continuous Fiber Retrofitting Method.....</b>	<b>529</b>
M. Saito, and A. Kobayashi	
<b>Composites for Infrastructure, II</b>	
<b>Behavior of Concrete Columns Confined with Hybrid Composite Materials.....</b>	<b>539</b>
H. Toutanji and M. Saafi	
<b>Stress-Strain Behavior of Concrete Columns Confined with Advanced Fiber Composite Sheets.....</b>	<b>547</b>
H. Toutanji and Y. Deng	
<b>Durability of Steel Members Reinforced with FRP Sheets in Marine Environments.....</b>	<b>555</b>
K. Yamaguchi, I. Kimpara, K. Kageyama, and M. Takanashi	
<b>Mechanical Characterization of Unidirectional CFRP Thin Strip and CFRP Cables under Quasi-Static and Dynamic Tension.....</b>	<b>563</b>
H. Kimura, M. Itabashi, and K. Kawata	
<b>Creep and Fatigue</b>	
<b>Time-Temperature Dependence of Fatigue Strength of Unidirectional CFRP.....</b>	<b>573</b>
M. Nakada, Y. Miyano, and R. Muki	
<b>Fatigue of High Strength Fiber Caused by Repeated Axial Compression .....</b>	<b>581</b>
Y. Yamashita, S. Kawabata, and A. Kido	
<b>Study on Creep Behavior of Glass Fiber Reinforced Polycarbonate.....</b>	<b>589</b>
K. K. Biswas, M. Ikueda, and S. Somiya	
<b>Creep and Recovery of a Quasi-isotropic GFRP Laminate with Damage.....</b>	<b>597</b>
K. Ogi and P. A. Smith	
<b>Bearing Creep Behavior of a Carbon/Bismaleimide Composite Material for the Next-Generation Supersonic Transport.....</b>	<b>603</b>
H. Katoh, T. Shimokawa, H. Tsuda, A. Sakai, and R. Asagumo	
<b>Damage Identification</b>	
<b>Effective Use of Fracture Surface of DCB Specimen for Better Understanding of Interphase.....</b>	<b>613</b>
M. Maeda, Y. Ma, K. Inomata, K. Kitagawa, Y. Fujii, and H. Hamada	
<b>Damage Identification of Laminated Composite Structures Based on Dynamic Residual Forces.....</b>	<b>621</b>
H. Fukunaga, M. Kameyama, and Y. Ogi	



<b>Damage Detection of CFRP Pipes and Shells by Using Localized Flexibility Method.....</b>	<b>629</b>
Y. Aoki and O-IL Byon	
<b>Damage Detection of CFRP Laminates Using Vibration Analysis Data.....</b>	<b>637</b>
T. Inada, Y. Shimamura, A. Todoroki, H. Kobayashi, and H. Nakamura	
<b>Composite Structure and Tank</b>	
<b>Development of High Speed Composite Flywheel Rotors for Energy Storage Systems...</b>	<b>647</b>
K. Takahashi, S. Kitade, and H. Morita	
<b>Development of H-2A Launch Vehicle Composite Interstage Structure.....</b>	<b>655</b>
M. Kobayashi, S. Sakai, and R. Shimizu	
<b>Postbuckled Behavior of Composite Isogrid Stiffened Shell Structure.....</b>	<b>661</b>
T. D. Kim	
<b>Effect of Transverse Crack on Strength Degradation in Filament Wound Composites...</b>	<b>669</b>
A. Horide, A. Tanaka, S. Wakayama, Y. Shigenari, K. Miyagawa, and S. Suzuki	
<b>Edge Effect on the Damage Development of CFRP.....</b>	<b>677</b>
T. Yokozeki, Y. Hayashi, T. Ishikawa, and T. Aoki	
<b>Cryogenic Composite Tank</b>	
<b>Applicability of CFRP Materials to the Cryogenic Propellant Tank for Reusable Launch Vehicles.....</b>	<b>687</b>
Y. Morino, T. Shimoda, T. Morimoto, T. Ishikawa, and T. Aoki	
<b>Cryogenic Mechanical Properties of CF/Polymer Composites for Tanks of Reusable Rockets.....</b>	<b>697</b>
T. Aoki, T. Ishikawa, H. Kumazawa, and Y. Morino	
<b>Influence of Mechanical and Thermal Loads on Propellant Leak of CFRP Laminates for Tanks of Reusable Rockets.....</b>	<b>705</b>
H. Kumazawa, Y. Hayashi, T. Ishikawa, T. Aoki, and Y. Morino	
<b>Braided and FW Composites</b>	
<b>Mechanical Properties of Braided Composites with Traditional Braided Structures.....</b>	<b>715</b>
M. Tada, T. Osada, K. Kameo, A. Nakai, N. Takeda, and H. Hamada	
<b>Bending Properties of Square Braided Composites with Middle-end-fibers.....</b>	<b>723</b>
T. Ueda, H. Hamada, A. Nakai, and N. Takeda	
<b>Micro-fracture Behavior of Flat Braided Composites with a Circular Hole.....</b>	<b>729</b>
T. Ohki, A. Nakai, H. Hamada, and N. Takeda	
<b>Analysis of Filament-Wound Sandwich Pipe under Internal Pressure.....</b>	<b>737</b>
M. Xia, K. Kemmochi, and H. Takayanagi	
<b>Textile Composites</b>	
<b>In-Plane Strength of 3-D Orthogonal Interlocked Fabric Composite.....</b>	<b>745</b>
N. Watanabe and H. Mibayashi	
<b>Micro/Macro Analyses for Mechanical Properties of Textile Composites.....</b>	<b>753</b>
A. Nakai, H. Hamada, and N. Takeda	

<b>Open Hole Compression Fatigue Test of Stitched CFRP Laminates.....</b>	<b>761</b>
Y. Iwahori, T. Ishikawa and S. Murase	
<b>Delamination Toughness of New 3-D Orthogonal Interlocked Fabric Composite.....</b>	<b>769</b>
N. Watanabe and N. Nishii	
<b>Static and Dynamic Properties of Tri-axially Woven CFRP.....</b>	<b>777</b>
T. Ozawa and T. Ozaki	
 <b>Poster Session</b>	
<b>Bending Test for CFRP Skin/Foamed Core Sandwich Plates.....</b>	<b>785</b>
H. Fukuda, T. Kawasaki, A. Kataoka, and S. Tashiro	
<b>Effects of Stacking Sequences on Mechanically Fastened Joint Strength of Matrix Hybrid Laminates.....</b>	<b>793</b>
H. Hamada and K. Sugimoto	
<b>Comparison and Discussion about Compression after Impact (CAI) Properties Obtained by Several Test Methods.....</b>	<b>801</b>
E. Hara, T. Ishikawa, M. Matsushima, and G. Ben	
<b>Investigation of Fracture Mechanisms of Braided Pultrusion Composite Rods.....</b>	<b>809</b>
R. Inai, H. Saito, K. Kameo, T. Uozumi, M. Iwamoto, and H. Hamada	
<b>Structure and Mechanical Properties of Injection Molded CF/LCP Thin Plates.....</b>	<b>817</b>
A. Fujita, H. Ishida, E. Tanigaki, H. Hamada, and F. Baba	
<b>Fabrication and Mechanical properties of PP/PP Composites.....</b>	<b>825</b>
T. Kitayama, K. Ishikura, T. Fukui, and H. Hamada	
<b>Thermal Shock Induced Damage in Si-Ti-C-O Fiber Bonded Ceramics.....</b>	<b>831</b>
Y. Kogo, M. Kamiya, H. Hatta, and T. Ishikawa	
<b>Design of Musical Instrument Material Substitutes Using FRP Structures.....</b>	<b>839</b>
T. Matsubara, T. Nishiwaki, and Z. Maekawa	
<b>Effects of Matrix Characteristics on Mechanical Properties in Knitted Composites.....</b>	<b>847</b>
A. Nakai, T. Osada, M. Inoda, N. Takeda, and H. Hamada	
<b>Effect of Pre-tensioned Fiber on Mechanical Properties of Plain Woven Glass Fabric Composite Materials.....</b>	<b>855</b>
T.Ota, T.Matsuoka, and K.Sakaguchi	
<b>Eigenvalue Analysis Method for Honeycomb Sandwich Panels.....</b>	<b>863</b>
T.Shiomi, T.Nishiwaki, and Z.Maekawa	
<b>Development for CAE Predicting Stiffness of SMC Structure - Research on the Young's Modulus in Rib Part.....</b>	<b>871</b>
T. Katayama, M. Shinohara, M. Hakotani, and M. Toutani	
<b>Elastoplastic Shear-lag Monte Carlo Simulation for the Single Fiber Composite Test...</b>	<b>879</b>
T. Okabe, and N. Takeda	

# Preface

---

The Ninth U.S.-Japan Conference on Composite Materials (July 3-4, 2000, Mishima, Japan) is organized by the Organizing Committee within the Japan Society for Composite Materials in cooperation with the U.S. Organizing Committee and the American Society for Composites.

Since the first conference which was held in January 1981 in Japan (Professor Kozo Kawata and Professor Jack R. Vinson as co-chairs, Professor Minoru Taya and H. Fukuda as secretaries), this conference has been held every two or three years alternately in the United States and in Japan. This 9th conference was decided to be held in 2000, in Japan at the committee meeting during the 8th conference held at Baltimore in 1998. The 8th conference was dedicated to the late Professor Tsuyoshi Hayashi and we, as the Japanese organizing side, fully thank the U. S. Organizing Committee for their cooperation.

The subjects of the 9th conference cover all areas of composite materials research and development. In particular, we specially focus on (1) low cost composite structures, (2) composites for infrastructure, and (3) smart and intelligent composites because these subjects are of current interest and are expected to develop further in the 21st Century. A total of 111 papers including poster presentations with 21 presentations from the United States and one from Korea will be presented at the conference. General plenary talks by Dr. R. Sierakowski, Mr. A. Takeo, and Mr. Y. Yamaguchi as well as plenary lectures on low cost composite structures (Professor K. T. Kedward, Professor A. C. Loos), infrastructure (Dr. Y. Rajapakse, Professor V. Karbhari and Professor K. Maruyama), and smart composites (Professor M. W. Hyer, Professor N. Takeda, Professor F.-K. Chang and Professor C. S. Hong) will highlight this conference. Their contribution is hereby acknowledged as well as contribution by invited speakers, Dr. R. Abbott, Professor O. Ochoa and Professor A. S. Crasto.

On behalf of the Japanese Organizing Committee, we would like to express our sincere thanks to the U. S. Organizing Committee members, especially to Professor J. M. Whitney, U. S. side chair, and to Professor M. W. Hyer, U. S. representative, whose dedication was the key for the success of this conference. We extend our sincere thanks to all speakers and authors, session co-chairs, and participants for making the conference a success.

We also wish to thank the Asian Office of Aerospace Research and Development/ Air Force Office of Scientific Research (AOARD/AFOSR), Army Research Office-Far East (AROFE), and some foundations for their financial support. Generous assistance, both implicit and explicit, by Toray Co. LTD is also acknowledged.

---

We acknowledge finally Mr. Kenji Ito of Toray Co. LTD, Mr. Masamichi Matsushima and Ms. Yoko Shino of NAL for their contributions in supporting us for making the conference fruitful.

Hiroshi Fukuda  
Conference Co-Chair  
Science University of Tokyo

Takashi Ishikawa  
Conference Co-Chair  
National Aerospace  
Laboratory

Yasuo Kogo  
Conference Secretary  
Science University of Tokyo

# Conference Organizing Committee

---

## U.S. Organizing Committee:

D.Adams (University of Wyoming)  
C.W.Bert (University of Oklahoma)  
C.C.Chamis (NASA Lewis Research Center)  
J.Chang (Air Force Office of Scientific Research)  
D.Cohen (Hercules Aerospace, Inc.)  
A.K.Dhingra (EI Du Pont de Nemours Inc.)  
T.Dunyak (General Electric Corporation)  
M.Hyer (**U.S. Representative**, Virginia Polytechnic Institute and State University)  
B.Long (Babcock & Wilcox)  
Y.Rajapakse (Office of Naval Research)  
K.L.Reifsnider (Virginia Polytechnic Institute and State University)  
C.T.Sun (Purdue University)  
J.R.Vinson (University of Delaware)  
J.M.Whitney (**U.S. Chairman**, University of Dayton)

## Japanese Organizing Committee:

K.Amaoka (Fuji Heavy Industries Ltd.)	S.Ochiai (Kyoto University)
G.Ben(O.-II Byon) (Nihon University)	A.Sakamoto (R&D Institute of Metals and Composites for Future Industries)
T.Fujii (Doshisha University)	H.Sekine (Tohoku University)
H.Fukuda ( <b>Co-Chairman</b> , Science University of Tokyo)	T.Shimokawa (National Aerospace Laboratory)
T.Fukuda (Osaka City University)	S.Somiya (Keio University)
H.Fukunaga (Tohoku University)	H.Suemasu (Sophia University)
H.Hamada (Kyoto Institute of Technology)	I.Susuki (National Aerospace Laboratory)
H.Hatta (Institute of Space and Astronautical Science)	Y.Tada (The Foundation for Promotion of Japanese Aerospace Technology)
H.Hira (Kawasaki Heavy Industries, Ltd)	Y.Takao (Kyushu University)
M.Hojo (Kyoto University)	N.Takeda (The University of Tokyo)
T.Ishikawa ( <b>Co-Chairman</b> , National Aerospace Laboratory)	A.Takeo (Toray Industries, Inc)
K.Kabe (The Yokohama Rubber Co., Ltd.)	T.Tanimoto (Shonan Institute of Technology)
Y.Kagawa (The University of Tokyo)	M.Uemura (Nippon Steel Composite Co. Ltd.)
K.Kageyama (The University of Tokyo)	Y.Yamaguchi (Mitsubishi Heavy Industries Ltd.)
T.Katayama (Doshisha University)	E.Yasuda (Tokyo Institute of Technology)
HKawada (Waseda University)	M.Zako (Osaka University)
I.Kimpara (The University of Tokyo)	
Y.Kogo ( <b>Secretary</b> , Science University of Tokyo)	
H.Kosuda (Toho Composites Co., Ltd.)	
Z.Maekawa (Kyoto Institute of Technology)	
T.Matsuoka (Doshisha University)	
Y.Miyano (Kanazawa Institute of Technology)	
H.Morita (Ishikawajima-Harima Heavy Industries Co., Ltd.)	

## Plenary Session

---

*Proceedings of the 9th US-Japan Conference on Composite Materials*

## **Aerospace Force Research in Composite Materials**

Robert L. Sierakowski

---

Robert L. Sierakowski,  
Chief Scientist, Munitions Directorate, AFRL/MN  
101 West Eglin Boulevard, Eglin AFB FL 32542-6810 U.S.A.

## AIR FORCE RESEARCH LABORATORY



### AEROSPACE FORCE RESEARCH IN COMPOSITE MATERIALS

Ninth US – Japan Conference  
On Composite Materials  
3-4 July, 2000

Dr. R. L. Sierakowski  
Chief Scientist  
Munitions Directorate



## OUTLINE

- Aerospace Force Leadership / Heritage in Composite Materials
- Composite Materials Research
  - Organic Matrix Composites
  - Mechanics of Materials
  - Structural Mechanics

## Aerospace Force Leadership and Heritage in Advanced Composites

### Develop Fundamental Materials, Processes, Understanding...

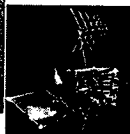
- 1963: USAF Project Forecast Identifies PMCs as Critical Technology. Creates First Composites Program

### Demonstrate Benefits (Performance - 1960s-1980s, Performance + Affordability 1990s)

- 1970s: Demonstrated First Advanced Composites


### Exploit Enabling Material Forms, Novel Processes...

- Advanced Composites  
Enable Supersonic  
Stealth



## ORGANIC MATRIX COMPOSITES

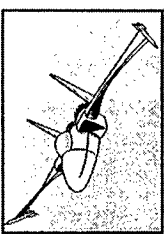
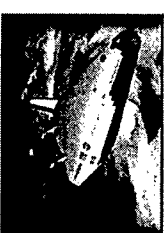





## Organic Matrix Composites

### Goal

- Provide the science and knowledge base that will lead to higher performance, more durable, more affordable composite structures for Air Force Applications



## Organic Matrix Composites


### Organic Matrix Composites Program

- Materials science
- Development and processing of improved materials
- Environmental effects
- Materials nondestructive evaluation

### Mechanics of Materials Program

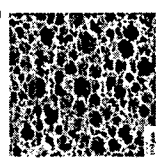
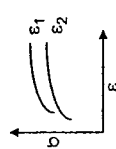

- Materials mechanics
- Constitutive models for design of advanced structures
- Health management
- Multifunctional performance

### Structural Mechanics Program



## Organic Matrix Composites

### Design for Performance and Cost

Design/Processing of Advanced Materials


Constitutive Information

Design/Manufacture of Advanced Structures




Organic Matrix Composite Program

Mechanics of Materials Program

Structural Mechanics Program




## Organic Matrix Composites Thrust Areas


### Durable High Temperature OMCs:


- Polymide resin degradation
- Processing cost
- Repair technology
- Auxiliary fabrication materials
- Oxidation protection






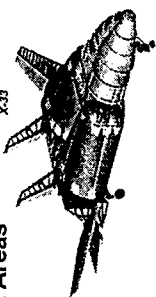
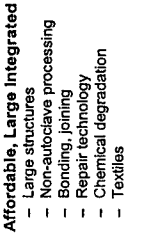

### Thermal Management:

- Lightweight thermally conductive structures
- Cost
- Data
- Assembly

 <p><b>Organic Matrix Composites</b></p>	<p><b>High Temperature Thrust</b></p> <ul style="list-style-type: none"> <li>• Future Applications Demand High Temp Lightweight Structure             <ul style="list-style-type: none"> <li>• Uninhabited Combat Air Vehicle (UCAV)</li> <li>• Turbine engine and exhaust washed structure</li> <li>• Hot space structure and vehicle substructure</li> </ul> </li> <li>• Currently Extreme Environments, Boundaries of Envelope             <ul style="list-style-type: none"> <li>• Point Design, Phenomenological, &amp; Static Properties</li> <li>• This is irrelevant for life prediction/materials selection</li> </ul> </li> <li>• What is needed:             <ul style="list-style-type: none"> <li>• Coupled Mechanism/Performance Approach</li> <li>• Service Life Predictive Capability</li> </ul> </li> </ul>
---	--

 <p><b>Organic Matrix Composites</b></p>	<p><b>Thrust Areas</b></p> <p><b>Expanding Capabilities Through Use of OMCs:</b></p> <ul style="list-style-type: none"> <li>– Revolutionary composites</li> <li>– Modeling, simulation</li> <li>– Fastenerless joining</li> <li>– Chemistry-mechanics integration</li> <li>– Novel material forms</li> <li>– Improved performance</li> </ul>
---	--

 <p><b>Organic Matrix Composites</b></p>	<p><b>High Temperature Hygrothermal Degradation</b></p> <ul style="list-style-type: none"> <li>• Goal: Characterize high temperature hygrothermal degradation of polyimide composite             <ul style="list-style-type: none"> <li>– Roles of holes in controlling moisture diffusion</li> <li>– Cycling effect on moisture retention</li> <li>– High temperature solid state reaction</li> </ul> </li> </ul>
---	--

 <p><b>Organic Matrix Composites</b></p>	<p><b>Thrust Areas</b></p> <div style="display: flex; justify-content: space-around;">   </div> <p><b>Affordable, Large Integrated Structures:</b></p> <ul style="list-style-type: none"> <li>– Large structures</li> <li>– Non-autoclave processing</li> <li>– Bonding, joining</li> <li>– Repair technology</li> <li>– Chemical degradation</li> <li>– Textiles</li> </ul> <div style="display: flex; justify-content: space-around;">   </div>
---	---



## Organic Matrix Composites

### Durability Prediction of Composites

- Goal: Develop mechanism based accelerated aging test methods and life prediction models for more reliable long term durability
  - Thermo-oxidative degradation - chemical
  - Solvent and moisture effects - chemical and physical
  - Damage initiation mechanisms
  - Incorporation of time dependant material changes into mechanical and life prediction models



## Mechanics Of Materials

### Background

Composites fail in regions where stress concentrations and gradients are high. In such regions, effective properties (constant moduli) are not valid. We need to calculate the severity of this assumption with regard to fiber diameter, spacing, and orientation under severe stress gradients. When is conventional 3-D elasticity valid and when is it not? We need to find out and make improvements where necessary.

Designers do not use realistic failure criteria or analysis tools. They rely heavily on empirical testing which is expensive, inefficient, and inconclusive.

Few technologists understand the nature of the problem. The same old tired methods will not lead to efficient design. Composites can be both penalized due to large safety factors or unsafe because of lack of understanding of micromechanical behavior.



## Mechanics Of Materials

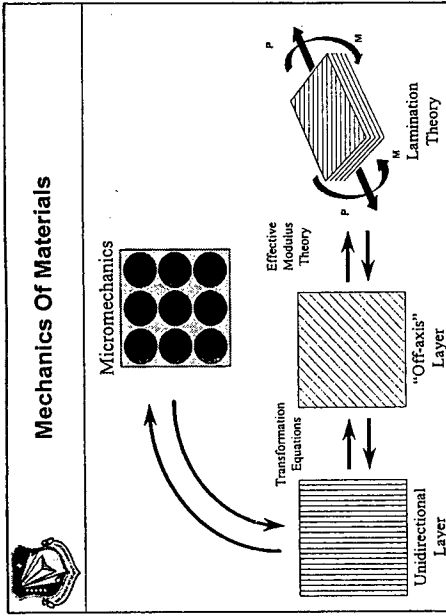
### Goals


Derive models for failure of composites at the micro (constituent material) level. This involves application of continuum mechanics at the micron scale.

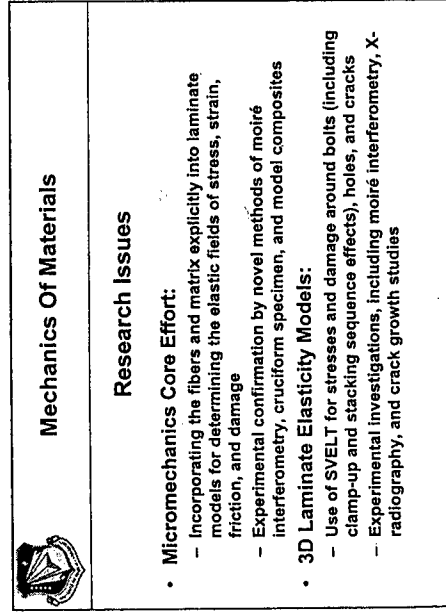
Develop macro-approaches to define the effects of stress concentrations in composite laminates that are consistent with the micromechanical response.


Validate by experiment all models, including the very fine details of the fracture process.

## MECHANICS OF MATERIALS



 <h2 style="text-align: center;">Mechanics Of Materials</h2>	<h3 style="text-align: center;">Research Issues</h3> <ul style="list-style-type: none"> <li>• Damage Tolerance: <ul style="list-style-type: none"> <li>– Modeling of transverse crack and delamination initiation and growth in laminates</li> <li>– High temperature and cryogenic cycling experiments</li> </ul> </li> <li>• E-Beam Effects on Composites: <ul style="list-style-type: none"> <li>– Micromechanical studies of sizing properties and thickness on composite performance</li> <li>– Studies of effect of resin mechanical properties</li> </ul> </li> </ul>
---	--



 <h2 style="text-align: center;">Mechanics Of Materials</h2>	<h3 style="text-align: center;">Research Issues</h3> <ul style="list-style-type: none"> <li>• Adhesive Joint Modeling: <ul style="list-style-type: none"> <li>– Stresses and fracture mechanics of adhesive joints, including the effect of adhesive reinforcement material</li> </ul> </li> <li>• Entropic Thermomechanics: <ul style="list-style-type: none"> <li>– Formulation of generalized constitutive laws for materials incorporating thermodynamics and finite deformation</li> <li>– Input to lead to a model to study environmental and processing effects on composites</li> </ul> </li> </ul>
---	---



## Mechanics Of Materials

### Research Issues

- Analysis of Fracture Test Specimens:
  - Precise elastic modeling of conventional composite fracture test specimens such as the double cantilever beam, end notched flexure, and pushout tests
- Variational Model of Textile Composites:
  - Accurate model for elastic response of textile-reinforced composites accounting for variable fiber orientations and curvature at the yarn bundle scale



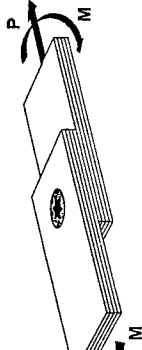
## Mechanics Of Materials

### SVELT (Spline Variational Elastic Laminate Theory)

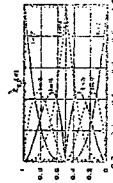
#### • 3D Laminate Stress Model:

- Stacking sequence effects
- Holes
- Elastic fasteners
- Clamp-up effects
- Cracks
- "Stiffness degradation"
- Explicit singularities

#### • Cubic Spline Basis Functions: Special Case-3D FEM



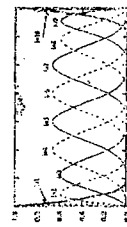
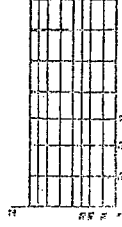
## Displacement Spline Approximation



$$u = \sum_{i=1}^N \frac{1}{N} \phi_i(x) \phi_i(x)$$

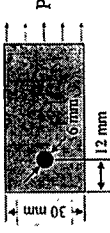
7 - number of splines in x-direction  
10 - number of splines in z-direction

$u$  - displacement at all points  
 $\phi_i$  - basis functions  
 $N$  - number of splines in x-direction  
 $M$  - dimension of  $z(x)$

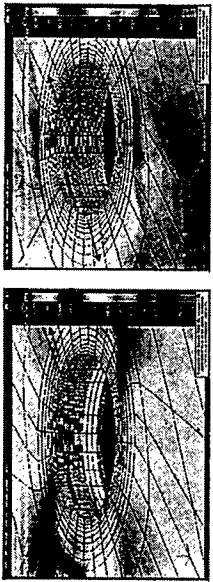


### Experimental Results

- Several papers with experimental results were examined
- Analytical results were compared with the experimental results obtained from:
  - Hamada, H., Haruna, K., and Maekawa, Z. "Effects of Stacking Sequences on Mechanically Fastened Joint Strength in Quasi-Isotropic Carbon-Epoxy Laminates," Journal of Composites Technology & Research, Vol. 17, No. 3, 1995.
- This paper reported experimental failure loads and damage in five different quasi-isotropic ply sequences and their bearing failure loads ( $\sigma_c = \pi p / b$ ):
  - specimen N:  $[0_2/45_2/90_2/45_2]$ ,  $\sigma_c = 318$  MPa
  - specimen A:  $[0_2/45_2/45_2/90_2]$ ,  $\sigma_c = 333$  MPa
  - specimen B:  $[0_2/90_2/45_2/45_2]$ ,  $\sigma_c = 333$  MPa
  - specimen C:  $[0_2/90_2/45_2/45_2]$ ,  $\sigma_c = 360$  MPa
  - specimen E:  $[0_2/90_2/45_2/45_2/45_2]$ ,  $\sigma_c = 433$  MPa
- Specimens were loaded in pin bearing and had the following dimensions:


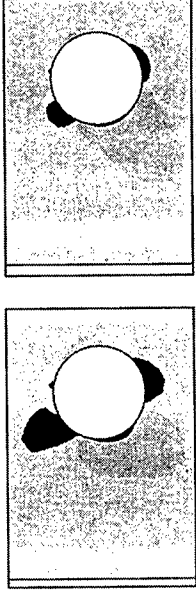


### Variation in Contact Regions



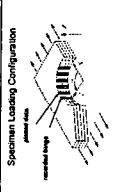
Bypass Loading: Far Field Stress = 20.8 Ksi

### Stacking Sequence Effects on In-plane Stress Components

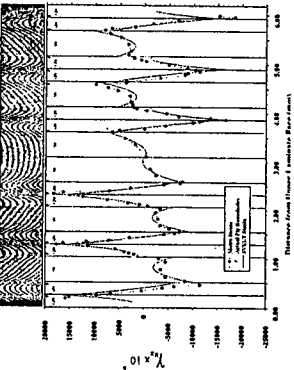



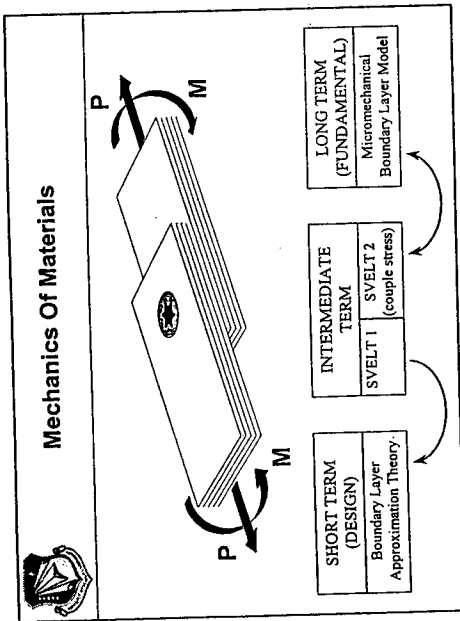
Maximum  $\sigma_{yz}$  criteria on the mid-plane in the  $-45^\circ$  ply group

### Experimental Validation

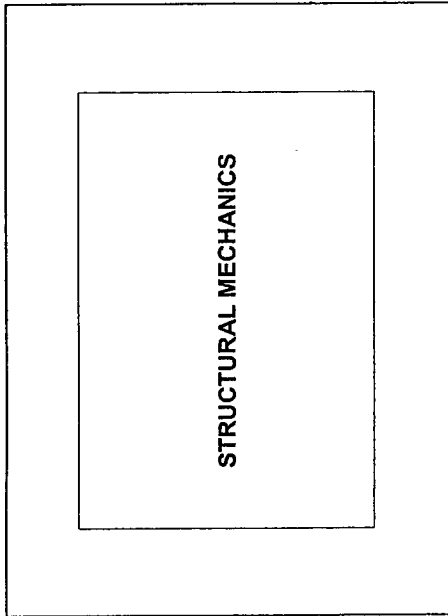


Three-Z Shear Strain Comparison at  $75^\circ$  for the  $(+30/-30/90)_s$  Laminate





	<b>Mechanics Of Materials</b>
<b>Contributions</b>	
<p>Exhaustive demonstration of feasibility of micromechanical fracture mechanics and its applicability to unidirectional composites.</p>	
<p>Theory of friction combines with adhesion and experimental confirmation up to and including failure.</p>	
<p>Comprehensive theory of steady state cracking mode in composite laminates. The whole ball of wax, including experimental characterization of all required properties, demonstration of the phenomenon, practical limitations, and key remaining issues.</p>	
<p>Development of laminate damage model.</p>	
<p>Theory for effect of damage on 3-D laminate moduli - an important issue in space structures.</p>	
<p>Accurate development of SVELT for holes and elastic fastener problems in laminates. Exact stress intensity factors for hole problems.</p>	
<p>Creative experiment designed and used to correlate with SVELT.</p>	

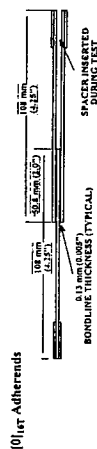
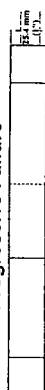


	<b>Structural Mechanics</b>
<b>Composite Bonded Joints/Repairs</b>	
<ul style="list-style-type: none"> <li>• Surface Preparation and Progressive Failure</li> </ul>	
<ul style="list-style-type: none"> <li>• Damage Modeling</li> </ul>	
<ul style="list-style-type: none"> <li>• Adhesive Reinforcement</li> </ul>	
<ul style="list-style-type: none"> <li>• Bonded Joints on Curved Surfaces</li> </ul>	
<ul style="list-style-type: none"> <li>• In-situ Bondline Monitoring</li> </ul>	

## Structural Mechanics



### Progressive Failure

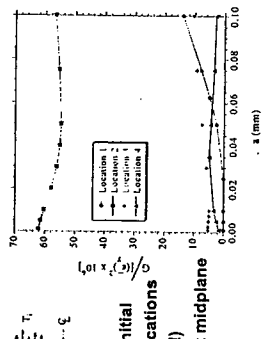


### 90% of Failure Load

## Damage Modeling: Failure Initiation Location



### Fracture Mechanics Criterion



- Independently analyzed Initial damage at each of four locations (Interface crack assumed!)
- Symmetric damage about midplane

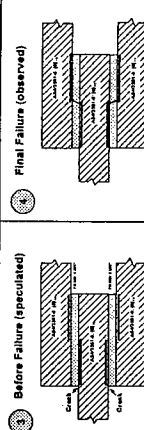
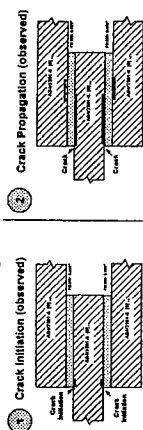
- Symmetric damage about midplane

**Failure Initiation**  **Lower Bondline at Location 2**

## Structural Mechanics

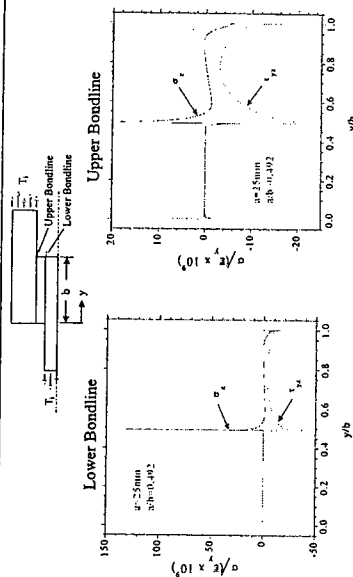


### Progressive Failure



Failure occurred within the adherends!

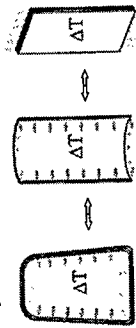
## Damage Modeling: Interlaminar Stresses





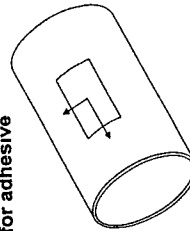
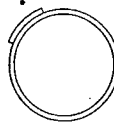
## Bonded Joints on Curved Surfaces

- Current analysis methods and empirical databases limited to flat geometries
- Flat joints are rarely used in the design of composite aerospace structures
- The effect of curvature on the performance/durability of bonded joints is unknown



## Bonded Joints on Curved Surfaces

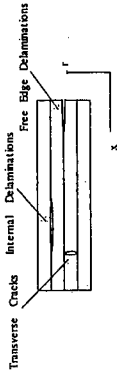
- Effect of curvature on critical interlaminar stresses due to thermo-mechanical loading will be determined
- Material non-linearity for adhesive



- 3-Dimensional FEM
- Experimental validation for composite cylinders with bonded patches

## Damage Modeling

### • 2-D Discrete Layer Generalized Plane Strain Model




- 3-D Discrete Layer Model Development Planned
  - Geometric and material non-linearity
  - Field equations for curved surfaces
  - Discrete damage modeling
  - Based on Spline Variational Technique


## Thermo-mechanical Ply Level Cracking


Thermal cycling and mechanical fatigue induce transverse ply cracks in laminated composites, changing the effective properties.




For stiffness critical structures, the structural design and functionality may depend on the 3-D effective properties.

	<b>Future Directions</b>
<b>Organic Matrix Composites</b> <ul style="list-style-type: none"><li>• Resin and composite systems designed for processing</li><li>• Toughening of high temperature composites</li><li>• Improved composite systems for space applications</li></ul>	

	<b>Future Directions</b>
<b>Structural Mechanics</b> <ul style="list-style-type: none"><li>• Multifunctional composites for smart structures</li><li>• Configuration effects for modeling</li><li>• Mechanics of processing for virtual manufacturing</li></ul>	

	<b>Future Directions</b>
<b>Mechanics of Materials</b> <ul style="list-style-type: none"><li>• Constitutive models for design</li><li>• Health management methods for durability</li><li>• Information systems for accelerated material development and utilization</li><li>• Nanocomposites for improved performance</li></ul>	

	<b>Acknowledgements</b>
<ul style="list-style-type: none"><li>★ Dr. H. Thomas Hahn</li><li>★ Dr. Greg Schoeppner</li><li>★ Dr. Nick Pagano</li><li>★ Dr. Steve Donaldson</li></ul>	

## **Development of Carbon Fiber Industry Past and Future**

A. Takeo

### **Abstract**

This paper describes the history of the commercialization of Carbon Fiber (CF) used as a structural material in view of the widely used Polyacrylonitrile (PAN) based CF and the future trend of the CF industry. The actual commercialization of PAN based CF started in the early 1970s, utilizing its superior properties of high strength, high modulus of elasticity, and lower density. It has been widely used as the reinforcement fiber for thermoset resin matrix. Although the current demand of PAN based CF exceeds 10,000 metric tons a year, there has been 3 important epochs along the way in the expansion of CF commercialization. The First Epoch was in the early 1970s, the Second Epoch was in the early 1980s, and the Third Epoch is the one we are about to enter. In order to achieve a greater expansion of the CF industry in the third epoch, it is necessary to produce more affordable CF for a wide variety of industrial applications, by which a large scale industrial utilization of CF will be firmly established. The past CF commercialization history, the future prospect, and issues associated with them are delineated in this paper.

### **1. Carbon Fiber Market Overview**

The commercialization of PAN based CF occurred in the early 1970's. Since then, a general upward trend trends of the PAN based CF market has been observed to this date as it is depicted in Figure 1.

The CF industry is believed to have experienced three important epochs in the course of its history. The First Epoch started in the early 1970s. Utilizing high mechanical

---

Akira Takeo, Toray Industries Inc., 2-1, Nihonbashi-Muromachi 2-chome, Chuo-ku, Tokyo103-8666, Japan

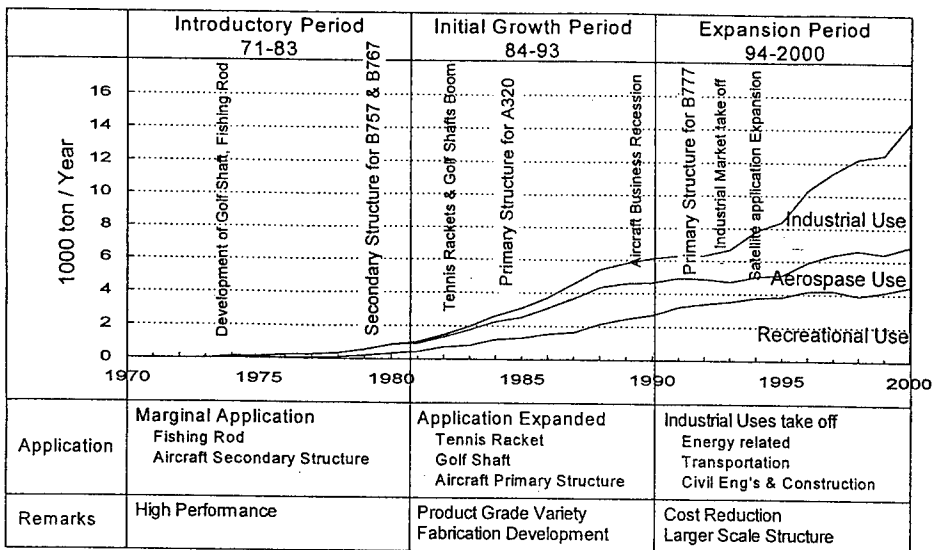


Figure 1 The trends of the PAN based CF market.

properties, which were not available in existing fibers, the commercialization of CF began with applications to sporting goods, such as the golf shaft, fishing rod, etc. The Second Epoch started in the early 1980s. Accumulation of production experience and firmly established confidence level has led the CF application to the aerospace industry. This period also saw the development of many CF types and material forms as well as a variety of new products using them.

With the coming of the year 2000, we are seeing the Third Epoch. With respect to the existing CF market, a comparatively steady market growth is predicted. On the other hand, there is a strong anticipation for a sizable market expansion in the areas of Energy, Transportation, Civil, Construction and General Industrial applications. In those markets, there is an increased demand on CF to become a utilitarian material, possessing a desired feature such as affordability and high quality. The past CF history and the anticipated future trend are delineated below.

## 2. The First Epoch Making Event: Growth of Sporting Goods Applications

The study on the application of CF to sporting goods started around 1972, and a sizable application started around 1975. This was believed to be the First Epoch for CF commercialization.

In Japan, the first application in the sporting goods market was for fishing rods.

In those days, the weight of fiberglass fishing rods ranged from 800 to 1000 grams. In comparison, the weight of CFRP (Carbon Fiber Reinforced Plastics) fishing rods developed in 1972 was a mere 580 grams. A drastic decrease in weight was achieved through the use of CF. Figure 2. shows the trend of weight and length of CFRP fishing rods (for Ayu or Sweetfish) with respect to the year in which they were developed. In order to achieve higher performance fishing rods, the following transitions have occurred over the years: Higher modulus CF (From 230GPa Class to 450GPa Class and higher); Higher prepreg fiber content (From  $W_f$  of 60% to 75% and higher); From fiberglass fabric to UD (Unidirectional) prepreg with 0/90 degree lay-up. Currently, fishing rods that are 10 meters in length and weighting less than 300 grams are being produced.

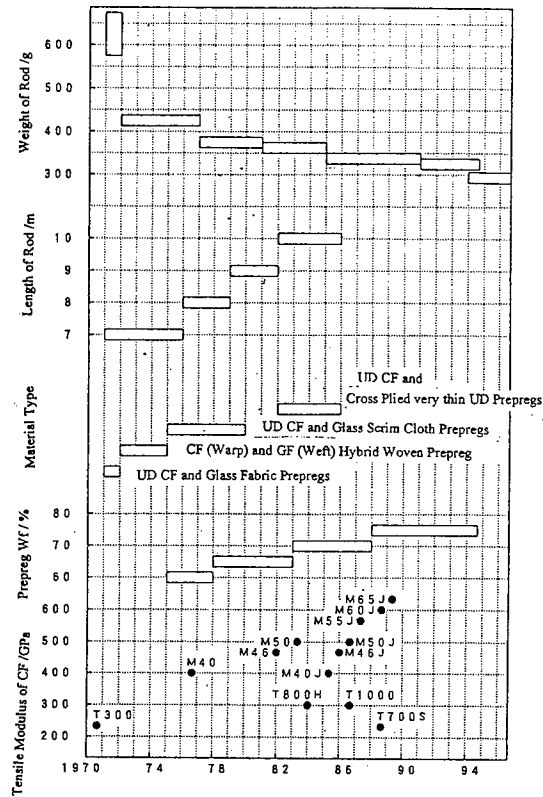


Figure 2 Trend of weight and length of CFRP fishing rods for Ayu (or Sweetfish)

Another sizable application of CFRP was to the golf shaft. The development of the CFRP golf shaft started about the same time as the fishing rod, around 1972. The CFRP golf shaft was the first product used as a vehicle toward the commercialization of CF. Just as it was with the fishing rod, the golf shaft development demanded high CFRP performance. With respect to materials, the following transitions occurred: Higher strength (From 3.5GPa Class to 5GPa Class and higher); Higher modulus (From 230GPa Class to 400GPa Class and higher); Higher prepreg fiber content (From  $W_f$  of 60% to 75% and higher). In the beginning

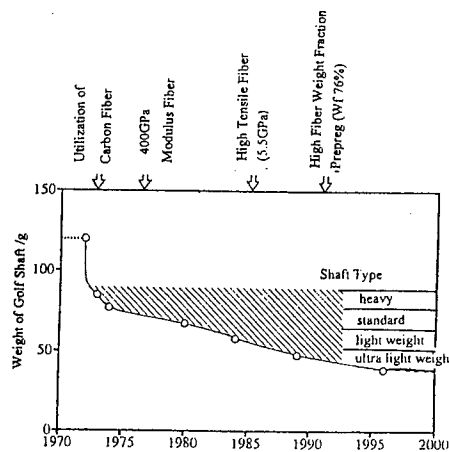


Figure 3 Weight Reduction History of Golf Shaft

the CFRP golf shaft weighed well over 100 grams, but now the lightest of them is around 30 grams (See Figure 3).

Responding to ever-higher CF performance requirements of sporting goods, Figure 4 shows Toray's history of the Torayca carbon fiber performance advancement. The performance advancement was achieved by an increased

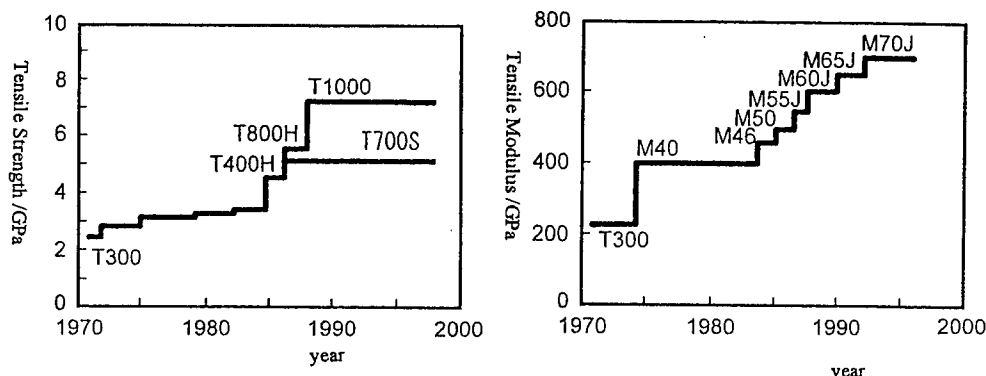


Figure 4 Torayca's history of Tensile Strength and Modulus of Elasticity Advancement

performance of precursor, uniformity of carbonization, clean process, and higher carbonization temperature.

### 3. The Second Epoch Making Event: Growth of Aerospace Applications

The demand for CF increased in the 1980s. In 1981 the production of CF exceeded 1000 metric tons. This was the Second Epoch. The increase in CF demand was mainly contributed by applications in the aerospace industry. The opportunity that made this possible was NASA's ACEE (Aircraft Energy Efficiency) research and development program started in 1975. In this program, lightweight composite components were developed to increase the energy efficiency of the aircraft.

A prepreg, which was the combination of a CF having the modulus of 230 GPa and the strength of 3.5 GPa and the 350F cure type high performance Narmco 5208 epoxy resin developed in 1973, was used for the aerospace applications. Figure 5 shows the aircraft components and their weight savings achieved under the ACEE program.

Weight performance and reliability were demonstrated through the ACEE program, which led to the application of CFRP to control surfaces and other secondary structures of large transport aircraft by Boeing, Lockheed, and McDonnell Douglas.

Boeing has continued its effort in expanding the application of CFRP.

Initially, Boeing made plans to use CFRP for the 100-passenger B-7J7 Horizontal Stabilizer. Subsequently, Boeing decided to apply CFRP to primary structures of the much larger B-777 transport aircraft, which made its maiden flight in 1994. Upon making the decision to use CFRP for the Horizontal Stabilizer, Vertical Stabilizer, and

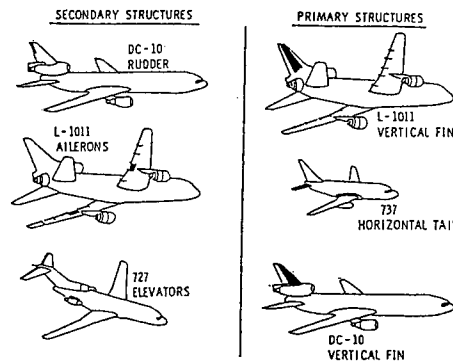


Figure 5 Composite Components being developed as parts of ACEE program.

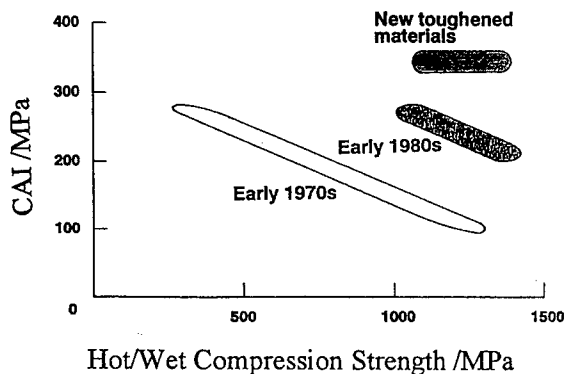


Figure 6 Relationship between CAI and Hot/Wet Compression Strength

Floor Beams, Boeing asked material suppliers for a new prepreg, which was referred to as the 3rd generation prepreg, having a much higher CAI (Compression After Impact) and Hot/Wet compression property. Simultaneously satisfying these two key properties was considered extremely difficult and it required a quantum leap as shown in the Figure 6. To simultaneously satisfy the tough requirements, Boeing selected

Toray's prepreg consisting of high

strength, intermediate modulus carbon fiber T800H (Strength 5.5GPa, Modulus 295GPa) and thermoplastic particle toughened 350F cure 3900-2 high toughness resin matrix. The total weight of composites used, including the selected Toray material, for each B-777 aircraft is 9,500kg.

On the European side, Airbus in 1979 used CFRP for control surfaces and other components during the development of the A310-200. Airbus started to use CFRP for primary structures earlier than Boeing. In 1985, Airbus began using the prepreg made from Toray's T300 CF and Ciba Geigy 250F cure 913 resin for the A310 Vertical Stabilizer. The total weight of composite materials used on the A340 aircraft is 8,000kg, which is more than 10% of the total structural weight of the aircraft. There is a plan to use even more CF on the A3XX aircraft to achieve further weight reduction by utilizing RTM and other advanced manufacturing processes.

#### 4. Expansion and Development of Carbon Fiber Industry

As is shown in Figure 1, the CF demand started to climb around 1975, and it became a sizable amount by the 1980s, reaching 1000 metric tons in 1981. The demand steadily grew during the 1980s; however, beginning in 1989 the demand for CF decreased mainly due to the recession in the commercial aircraft industry. Around 1995, the demand started to increase again due to an increase in usage of carbon fibers mainly for industrial uses.

Figure 7 shows trends of PAN based CF production capacity and a history of carbon fiber producers. With respect to the CF production capacity, a "plan ahead" strategy was taken. During the late 1970s and early 1980s, many companies entered the CF market thinking that there would be a great demand for CF. As a result, there was a steady increase in CF production capability. This increased production capability caused an over-supply situation. Consequently, in the late 1980s, starting with the acquisition of UCC carbon fiber unit by Amoco, several carbon fiber production units were sold. By the early 1990s, Grafil, Celanese, and others had withdrawn from the CF market because of a reduction in CF demand.

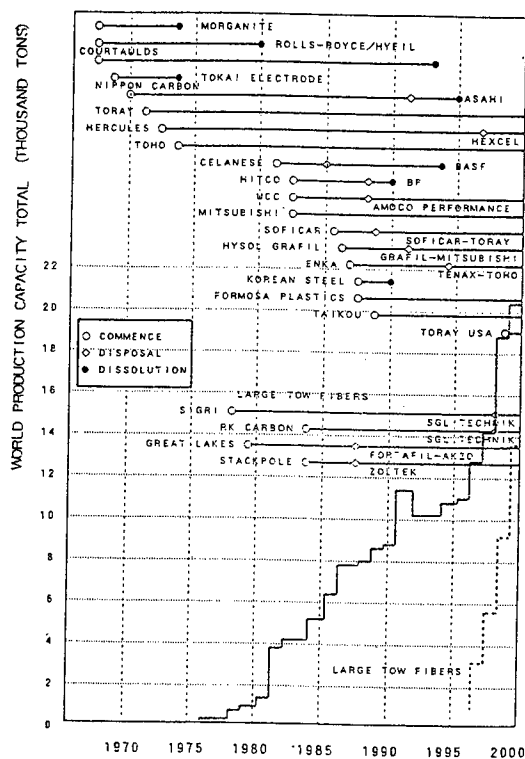


Figure 7. PAN based CF Production Capacity and a History of Carbon Fiber Producers.

Currently, the CF market is facing a supply-demand unbalance, which is causing a decline in price. This was caused by a combination of large tow (filament count of 50K and above) entering the traditional regular filament (filament count of 24K and less) market and the excessive CF supply as a result of increased production capacity due to the construction of new facilities and/or expansion of existing facilities by most of the CF suppliers.



## 5. Future Scope of Carbon Fiber Usage and Carbon Fiber Industry

Although we are facing to over-supply situation of CF, this will provide an opportunity to develop new applications and markets with respect to a long-term outlook. Therefore, this situation will in turn establish an even stronger CF industry in the future. With this point of view, it is believed that the CF industry is entering into the Third Epoch, where a new large scale industrial application is starting.

It is safe to state that the reliability and high performance of CF has been firmly established during the First and Second Epochs for filament yarn type CF. Consequently, the important theme for the Third Epoch is the achievement of "Affordability" in composites. The meaning of affordability is not only to reduce the material cost but also to attain an efficient manufacturing process.

With respect to application of CF to aerospace industry, cost reduction has been achieved through the effort of increasing the number of tow count of filament yarn CF and the development of advanced manufacturing processes. Wider usage of CF is expected at the time of a new aircraft launch, such as A3XX, by utilizing the know-how acquired from the affordability efforts on prior projects as well as currently considered advanced manufacturing processes such as RTM, Automatic Pre-plying, Fiber-Placement, EB curing, etc.

With respect to industrial applications, large scale applications of CF in the following areas are expected: SCBA, LNG Tank, and other pressure vessels using filament winding processes; Repair and Reinforcement of Buildings and Civil Structures; OA equipment utilizing electrical conductivity property of CF, Automobile; Windmill; Deep Sea Oil Drilling, etc.

In order to firmly capture the large scale CF market in the coming Third Epoch, it is essential for the CF suppliers to develop products that possess improved reliability, affordability. Only then, it is believed a large scale utilization of CF, with its core usage being the industrial applications, becomes a reality.

## **Status of Project on Advanced Composite Materials for Transportation in Japan**

A.Sakamoto, M.Noda and Y.Yamaguchi

### **Abstract**

The research and development project on advanced composite materials for transportation has been performed since September, 1998 as a 5-year project, being sponsored by the Ministry of International Trade and Industry.

This project aims to develop innovative design and manufacturing technologies simultaneously cost reduction and reliability improvement of polymer matrix composite structures for transportation. This paper introduces briefly the purpose and contents, and current activities of the program.

### **Introduction**

An increasing demand for carrying power of transportation and social factors such as a move towards energy and resource saving are growing the needs of times for reducing weight of the structures of vehicles to reduce fuel consumption. Composite materials, especially polymer matrix composites are the vital materials responding these demands.

The biggest cause to suppress the expanding applications of the materials is the disadvantage of cost competitiveness faced by composite materials compared with conventional metallic structures. Therefore, the biggest issue facing advanced composite materials is cost improvement, which imposes stringent demands on the weight reduction to cost aspect, underpinned by the need to reduce design and manufacturing costs and reduce maintenance costs, and technology development to achieve environmental harmony.

---

A.Sakamoto, M.Noda and Y.Yamaguchi, R&D Institute of Metals and Composites for Future Industries(RIMCOF), 3-25-2, Minato-ku, Tokyo 105-0001, Japan

Improvements in material performance constitute one form of breakthrough, but the technologies conducting to this breakthrough depend on the projection of conventional technologies, so that the development of creative design and manufacturing technologies are required.

The research and development project on advanced composite materials for transportation has been performed since September, 1998 as a 5-year project, being sponsored by the Ministry of International Trade and Industry. This project aims to develop innovative design and manufacturing technologies simultaneously enabling cost reduction and reliability improvement of polymer matrix composite materials and structures for transportation systems.

### Themes and Functional Organization of the Project

The program is divided into the following four themes.

- (1) Development of application technologies for high temperature composites to future aerospace transportation systems.
- (2) Development of high productive fabrication technologies of large structures for advanced high speed trains.
- (3) Development of joining technologies and improvement of flame-retardation of composite structures for advanced high speed trains.
- (4) Fundamental research on the damage-tolerant design of composite structures.

Figure 1 shows the functional organization of the project in which research activities are being conducted with close cooperation among industries, universities and governmental institutes. Themes (1), (2) and (3) have been carried out researches by industries and theme (4) has been studied by universities.

The steering committee is organized by the researchers of universities, governmental institutes and industries, in which the annual plans and results are checked and reviewed.

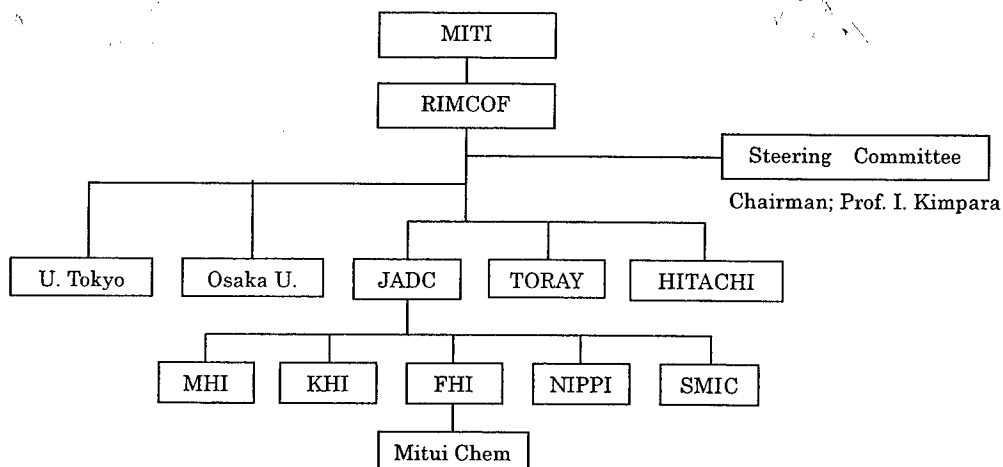


Figure 1 Functional Organization

## **Application Technologies for High Temperature Composites to Future Aerospace Transportation Systems**

This theme aims to elucidate the characteristics of high temperature composites and develop designing and manufacturing technologies enabling the production of composite airframe structures at low cost, applicable to future aerospace transportation systems such as the next-generation SST.

### **Material Development**

The next-generation SST will be designed for a cruising speed of Mach 2.0-2.4, so the maximum surface temperatures due to aerodynamic heating will be estimated to 110-180°C. Also, a structure weight reduction of about 30% will be necessary modeling from the Concorde level technologies.

The candidate material systems in this theme are carbon fiber reinforced polyimide matrix composites with long-term durability of over 180°C and a carbon fiber reinforced bismaleimide matrix composite with long-term durability of about 150°C. The former is classified into thermosetting polyimide(PETI-5) and thermoplastic polyimide(PIXA). The present studies are being conducted to improve the chemistry of thermoplastic polyimide(PIXA) for performance and processability of composites, and to acquire basic data of the materials processed in optimized conditions, relating to static strength characteristics, fatigue and heat-resisting characteristics. The durability characterization of the materials of the materials exposed to thermal cycles and thermal aging in the aircraft service environments is excluded in this program.

### **Low-cost Fabrication Technology**

In order to fabricate the airframes economically, the development of technologies to fabricate the composite structures at low cost is indispensable. Direct consolidation of the thermoplastic polyimide composite via tow-placement is to be developed., which is a non-autoclave process with the potential to reduce part cost and to improve product quality. And also, the process development for thermoset composites of polyimide and bismaleimide is being conducted. The resin transfer molding / resin film infusion (RTM / RFI) process development for bismaleimide composites is being conducted as a low cost non-autoclave process.

### **Development of Design Technology**

To use composites in the primary airframe structures, the development of damage-tolerant design and buckling allowance design will be indispensable. The

application of these design procedure cannot be evaded in order to improve the damage tolerant properties and to achieve a 30% weight reduction over the Concorde level technology.

#### Manufacture of Prototype Structures and Evaluation

In order to demonstrate and prove the technologies to be developed as mentioned above, the prototype structures are to be designed and manufactured in the final stage of the program. The structures are to be non-destructively inspected and to be tested to evaluate the performance and the quality. And also, the target weight reduction and cost saving are to be verified.

#### Typical Results of Research up to FY1999

Thermoplastic polyimide composite of PIXA family which could directly consolidated was improved to reduce micro-cracking by solvent. Curing mechanism of PETI-5 was analyzed and validity of current process condition was confirmed. And the state of material throughout the process in autoclave was analyzed and preliminary criteria of salvage on process were developed.

R&D Facilities of automated fiber/tow placement , composed of head, platform, some other equipment and software were introduced by the end of FY1999. Trial run of facilities was conducted and preliminary process concept has been created. Fabrication trials were made on both RTM and RFI of bismaleimide(5250-4-RTM) with cloth preform, to determine applicability to outer wing ribs. There was no apparent difference on the quality of each trial product. Trade off studies showed that RFI was much efficient to reduce cost for the case of the ribs which were relatively small in length and consist of more part counts, because a large number of parts could be processed in a batch utilizing existing autoclave. So, RFI was selected for the ribs.

Design development was carried out to apply damage tolerance and post buckling concept. More than one hundred of residual strength data of notched coupons and panels on tension and compression loading, have been obtained and evaluated from FY1998. It was confirmed that Mar-Lin model could predict residual strength accurately on both loading condition. Interlaminar fracture toughness was obtained and evaluated , and fracture criteria were determined. Shear buckling panel test was conducted, and post buckling behavior and failure strength were determined.

#### High Productive Technologies of Large Scale Composite Structures for Advanced High Speed Train

This theme aims to establish the high productive fabrication technologies of

large composite structures in order to reduce cost and weight and to enhance the applicability of polymer matrix composites to a wide use.

#### Material Development

The matrix resin with high flame-retardation suitable for high cycle liquid process is to be developed.

#### High Productive Fabrication Process

The high cycle liquid process including preformed materials and high efficient curing applicable to large scale composite structures is to be developed.

#### Evaluation and Inspection

The durability and fatigue characteristics of the large scale composite structures will be evaluated and the non-destructive inspection of the structures is to be established.

#### Typical Results of Research up to FY1999

The early stage of the program focused on a high cycle process fabrication of sandwich structure which is one of basic structural elements for large scale composite structures and screening of matrix resin systems which have high flame-retardation and meet processability criteria for large composite structures. Fabrication of a 5m length curved composite structure having a hybrid of flame-skin and sandwich structures was conducted by the RTM process, using resin flow media having very low flow resistance, developed in this project. The new RTM process can fabricate a large scale hybrid composite structure by controlling properly resin flow path, resin inlet and outlet ports

Heat resisting and flame-retarding properties and processability of several thermosetting resins were studied. As a result, phenolic resin and cyanate ester resin were chosen as candidate matrix resins for further study.

#### **Joining Technologies and Flame-Retardation of Composite Structures for Advanced High Speed Train**

This theme aims to establish the joining technologies of composite structures including composite/metal joints and flame-retardation of the structures for an advanced high speed train.

## Joining Techniques

Adhesive bonding process (joint design, adhesive, surface treatment) including combination with mechanical fastening is to be developed, and strength and durability of the joints are to be evaluated. And also, inspection method of the joints is to be established.

## Durability Characterization

The evaluation method of durability of the joints under service environments of the train including acceleration test is to be established.

## Flame-Retarded Structure

Flame-retarded composite structures are to be developed by studying matrix resins, fibers, core materials and so on.

## Typical Results of Research up to FY1999

Estimation methods of initiation and propagation behavior of delamination on adhesive joint structures were developed using stress singularity parameters. And these methods were applied to the estimation of temperature dependence of fatigue strength of FRP/metal adhesive joints. Using these results, the dependence of threshold intensity of stress singularity range on both temperature and thermal stress was clarified respectively.

Bending strength tests for some bolted joint structure models made by FRP-honeycomb were performed and failure mode of each joint structure models were clarified.

Temperature/moisture/light-combined environmental degradation test equipment was developed and thermal degradation characteristics of unidirectional CFRP were measured. Using these test results, the acceleration test method for thermal environment was developed based on the Arrhenius equation.

## Conclusion

The current status of the national project on advanced composite materials for transportation was outlined in order to introduce some aspects of activities on composite materials in Japan.

## **RATIONALE & APPROACHES FOR LOW-COST AEROSPACE COMPOSITE PRODUCTS**

Keith T. Kedward

The wider exploitation of composites for aerospace products can be inhibited by either, or both, the performance-drivers, as well as the economics-drivers. Items comprising both categories will form the introduction prior to discussing more specific issues and approaches related to economics for low cost product development that is constrained by the utilization of relatively high-cost material systems.

Various approaches that are available and under consideration, based on potential cost reductions, will be presented in this paper together with a rationale and some case studies as examples. Both composite aircraft and spacecraft products will be addressed by giving consideration to:

- (i) utilization of net-shape concepts facilitated by selected dry preforms reinforcement architectures that are now being considered for commercial aircraft wing structures,
- (ii) use of modular assemblies for spacecraft structures.

The presentation will include a discussion of the rationale, issues and potential concerns associated with the stitched/Resin Film Infusion (RFI) process as applied to large wing structures as a case study for the commercial category. Next, the modular approaches used for small satellite structures, such as the Pegasus-XL, will be described to illustrate the design considerations and manufacturing issues that are key to the attainment of cost and performance goals and requirements. Comparisons will be drawn between the modular approaches for novel composite concepts and both that of conventional composite concepts and aluminum alloy-based concepts.

Looking to the future, the final section of the paper will address potential further enhancement of inhibiting cost issues, including material costs, and some emerging opportunities for the exploitation of some of the approaches presented.

---

Keith T. Kedward, Professor, Department of Mechanical & Environmental Engineering  
University of California at Santa Barbara, Santa Barbara, California 93106-5070, USA



## **Low-Cost Fabrication of Advanced Polymeric Composites By Resin Infusion Processes**

Alfred C. Loos

### **Abstract**

The resin infusion processes RTM, RFI, and VARTM have been identified as cost-effective fabrication techniques for the manufacture of complex shape composite structures. Dry textile preforms are resin impregnated, consolidated, and cured in a single step process which eliminates costly prepreg tape manufacture and ply-by-ply layup. The principles of the three infusion processes are discussed along with the advantages of each technique compared to traditional composite fabrication methods such as prepreg tape layup and autoclave cure. The large number of processing variables and the complex material behavior during infiltration and cure make experimental optimization of the infusion processes inefficient. Three-dimensional computer models have been developed which can be used to simulate the resin infusion processes. The model formulation and solution procedures are presented, and the material property input data required for solution of the model are discussed. Potential benefits of the model include reduced manufacturing cost and risk.

### **Introduction**

Advanced composites offer performance characteristics that are superior to that of conventional materials. Although advanced composites have been attractive materials for high-performance aerospace applications due to their high strength and stiffness and light weight, use of these materials in commercial aircraft and other industries has been limited due to high manufacturing costs. Composite manufacturers recognize that new fabrication techniques that reduce material and assembly labor costs will lead to wider composite applications.

Resin transfer molding (RTM) and resin film infusion (RFI) have become popular cost-effective processing techniques for the manufacture of advanced composite structures [1]. The resin infusion processes lend themselves to the use of near net shape textile preforms manufactured through a variety of automated textile

---

A.C. Loos, Department of Engineering Science and Mechanics, Virginia Polytechnic Institute and State University, Blacksburg, VA 24061, USA

processes such as knitting and braiding [2]. Often, these advanced fiber architecture preforms have through-the-thickness stitching for improved damage tolerance and delamination resistance [3]. The challenge facing users of the resin infusion techniques is to design a robust process that will consistently ensure complete infiltration and cure of a geometrically complex shape preform with the high fiber volume fraction needed for structural applications.

One major disadvantage of the RTM and RFI processes is that they require expensive molds or tools that allow high-pressure resin infusion. In addition, long duration, high temperature cure cycles are required to fully cure the resin-saturated preforms. The vacuum assisted resin transfer molding (VARTM) and the patented SCRIMP (Seemann Composite Resin Infusion Molding Process) [4,5] processes have been developed as alternative low cost methods for the manufacture of composite structures.

This paper will review recent research and development activities related to advanced composite manufacture by the low-cost resin infusion processing techniques, RTM, RFI, and VARTM. Many of these programs are focusing on the development and verification of process simulation models to eliminate the costly trial and error procedures that are frequently used in tool design and cure cycle development. The development of computer simulation models of the resin infusion processes will be reviewed. The material property input data that must be measured for use in the model and the type of information that can be generated by the model will be discussed.

## Resin Infusion Processes

A schematic of the RTM process is shown in Figure 1. A dry, net shape, textile preform is placed into the lower cavity of a two part mold assembly. The mold assembly is closed which compacts the preform to the desired thickness and fiber volume fraction. A liquid thermosetting resin is injected into mold which flows into the preform. Once resin has completely filled the mold, injection is terminated and the part is cured either at room temperature or at elevated temperature. The exact cure temperature depends on the resin system. Upon completion of the cure, the composite part is removed from the mold. The major advantages of RTM over the traditional composite manufacturing techniques include:

- Near net shape molded parts
- Short cycle time
- Close dimensional tolerances
- Void-free, structural quality parts
- Low pressure and temperature process
- Closed mold process, reduced volatile emissions
- Smooth surface finish on both sides of part (Class A surface possible)
- Cores, ribs, and inserts can be encapsulated into part

Today, the RTM process is used to fabricate both primary and secondary structural parts for commercial and military aircraft industries. RTM is the dominant

composite manufacturing process for the F-22 Raptor. Three hundred and sixty individual parts are produced by RTM, which accounts for 45 percent by weight of all non-skin composites [6]. In addition, RTM is used extensively in the sports and recreation, marine, and transportation industries.

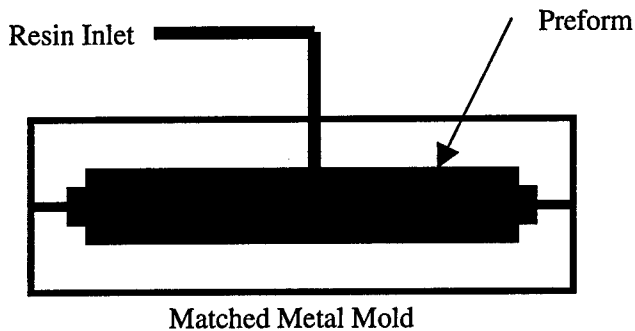


Figure 1 Schematic Diagram of the RTM Process

RTM requires the use of matched metal heated tools which must be properly designed to allow the resin to flow into and completely wet-out the compacted preform. Hence, the tooling material and fabrication costs can be prohibitive for large structural composites. In addition, the ability to completely saturate high fiber volume fraction complex shape preforms at low to moderate injection pressures, requires the use of low viscosity ( $<0.3 \text{ Pa}\cdot\text{s}$ ) resin systems. This limits the selection of resin systems to the lower performance polyesters, vinyl esters, and low  $T_g$  epoxies. Higher performance, low-viscosity resins are available, but the cost is quite high.

In order to address the disadvantages of RTM for the fabrication of large composite structures, the RFI process is being developed by the aerospace industry. The RFI process combines the advantages of RTM with the flexibility of traditional prepregging processing technology. An example of the RFI manufacturing technique for a two-blade stiffened panel is shown in Figure 2.

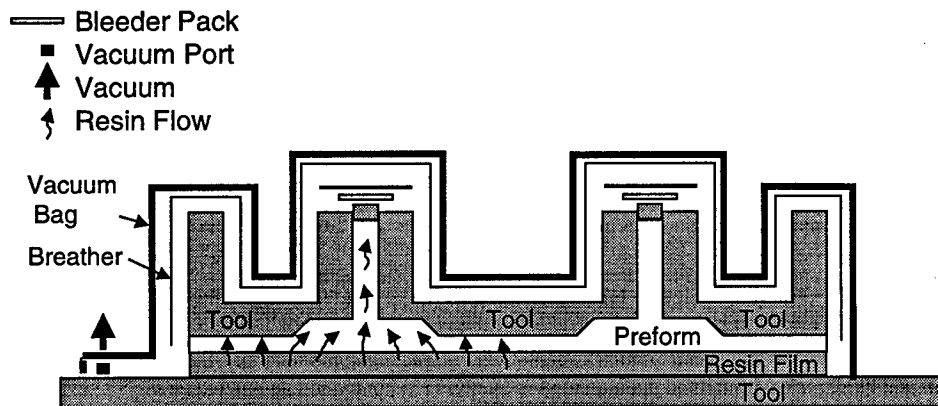


Figure 2 Schematic Diagram of the RFI Process

The RFI process is similar to the RTM process except that a hot-melt resin film is used to infiltrate the dry textile preform instead of a liquid resin. The hot-melt film is placed on the surface of the base plate. The thickness of the resin film depends on the mass of resin required to completely infiltrate and wet-out the preform. The dry preform is placed on the top of the resin film and the metallic tool blocks and bleeder packs are located in place. A vacuum bag is placed over the tool and the entire assembly is placed into an autoclave for infiltration and cure. At some point in the processing cycle, consolidation pressure is applied to the assembly. The pressure compacts the fabric preform to the specified fiber volume fraction and forces resin into the preform. The tool assembly is heated according to the prescribed temperature cycle, which decreases the resin viscosity, allowing for infusion and fiber wet-out, and cure of the resin saturated preform.

NASA and The Boeing Company have developed the RFI process to fabricate cost-effective wing structures for commercial transport aircraft [7,8]. A 13m long wing cover panel was fabricated by Boeing using the RFI process [9]. The preform was infiltrated with a reduced catalyst Hexcel 3501-6 resin system. The resin is similar to the well-characterized 3501-6 prepreg system except that the amount of catalyst is reduced to lengthen the flow time. The melt viscosity of the 3501-6 resin is much too high for traditional RTM process. However, in RFI, the resin flow into the preform is predominately in the through the thickness direction which shortens the resin travel distance and allows the use of higher viscosity resin systems.

In the VARTM process, the vacuum bag is used for one tool surface. Liquid resins are infused into the dry preform using only vacuum pressure. The key to successful resin infiltration of the preform is the design and placement of the resin distribution medium which allows complete wet-out of the preform and elimination of voids and dry spots. Since resin infiltration is in the through-the-thickness direction, race tracking and resin leakage around the preform are eliminated. An illustration of the VARTM process is shown in Figure 3.

- Resin Injection Port
- Resin Distribution Medium
- Vacuum Port
- ↑ Vacuum
- ↑ Resin Flow

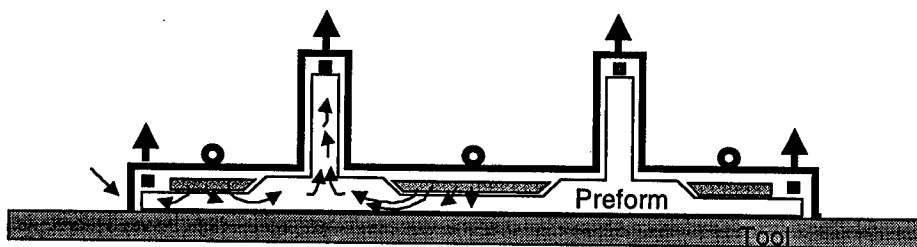


Figure 3 Schematic diagram of the VARTM Process

VARTM is ideal for the fabrication of very large composite structures since an autoclave or an oven is often not required. VARTM has been used to successfully fabricate marine composites for both military and commercial applications [10-12] and structural laminates for ground combat vehicles [13]. The ability of the VARTM processes to fabricate aircraft-quality stiffened composite structures still needs to be established. However, recently developed stitching and debulking methods are being used to produce near net shape preforms, which require no additional compaction during manufacture [7].

### Process Simulation Models

The large number of material properties and processing parameters that must be specified and controlled during resin infiltration and cure of textile composites make trial-and-error procedures of determining the processing cycle extremely inefficient. Analytical simulation models are clearly far superior alternatives for determination of a processing cycle that will result in complete resin infiltration and cure of the textile preform. Furthermore, process simulation models are useful in mold design and in specifying the location of resin injection and vacuum ports in the tool for the liquid resin molding processes.

Three-dimensional models have been developed to simulate the manufacture of complex shape composite structures by the resin infusion processes [14,15]. The models are comprehensive and include modules that describe resin flow, heat transfer, resin cure kinetics, preform compaction, and residual stress and warpage. For a specified compaction and temperature cure cycle, the model can be used to predict the following parameters during infiltration and cure:

- a) resin flow front position during infiltration and total infiltration time;
- b) temperature distributions in the preform and tooling components;
- c) resin viscosity and degree of cure of the resin saturated preform;
- d) final cured thickness and fiber volume fraction of the preform; and
- e) residual stresses and the final shape of the cured part.

A schematic diagram of the model construction is shown in Figure 4. The user provides the geometries of the preform and tooling and the time-temperature-processing cycle. The governing equations are solved numerically by the finite element technique. Input and output format for the model is generated using a solid modeling package such as PATRAN. Input to the code includes the finite element mesh, boundary conditions, choice of materials, and various control parameters. Two important material characterizations are required inputs into the model.

The first includes the flow characteristics of the preform materials. The textile preforms are deformable and anisotropic porous materials. Hence, the permeability depends both on the direction of flow and the degree of compaction of the preform. The compaction characteristics and the permeabilities in the principal material directions must be measured for each textile preform. Test methods that can be used to measure the compaction behavior and permeabilities of textile preforms have been developed [16]. Permeability test fixtures have been constructed and used to measure transverse and in-plane permeabilities by both the advancing front and steady-state

techniques. A cure kinetics model and resin viscosity model must be developed for each new resin system used in the process [14,15]. The cure kinetics model relates the cure rate to temperature and degree of cure. The data are obtained by differential scanning calorimetry (DSC). The procedure is to use the DSC to measure the heat evolved as a function of time at constant temperature (isothermal mode) and the heat evolved as a function of temperature at constant heating rate (dynamic mode). These measurements are made on small resin samples. From the scans, the cure rate, degree of cure, and heat of reaction are measured. The cure rate and degree of cure data are fit to a mathematical equation using a nonlinear regression analysis program. The resin viscosity model relates the temperature and cure of the resin to its viscosity. A series of isothermal viscosity tests are performed which give the viscosity as a function of time at temperature. Using the cure kinetics model, the viscosity as a function of degree of cure is determined and fit to a mathematical expression. Once the material properties are determined, the model calculations are performed and the desired output parameters are displayed as shown in Figure 4.

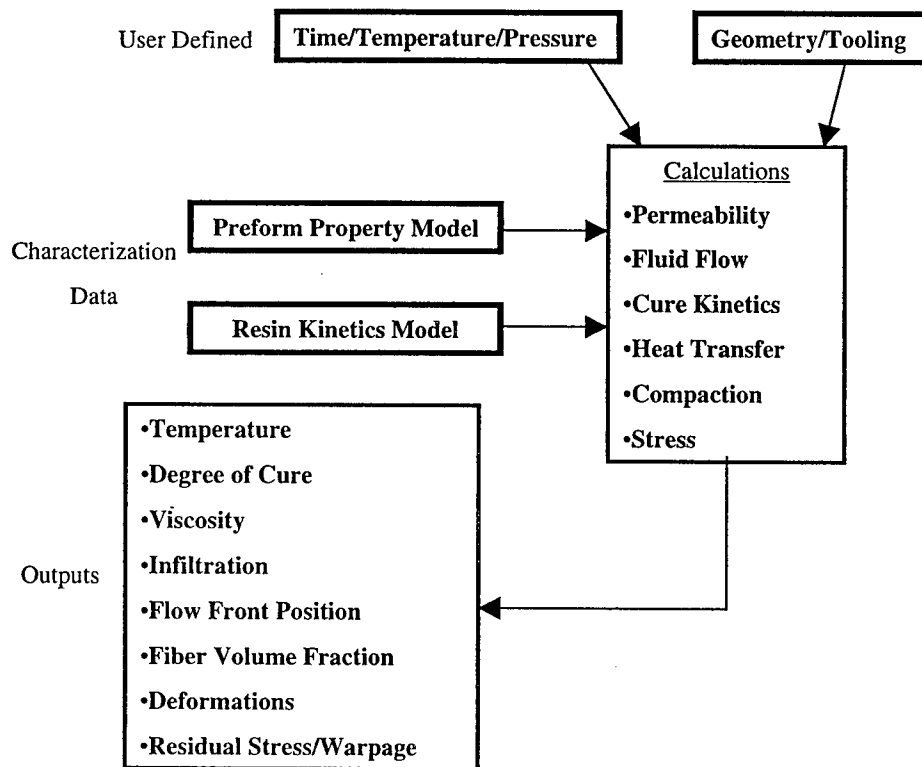


Figure 4 Computer Model Structure

A full three-dimensional computer simulation of the nonisothermal mold filling process coupled with preform compaction and residual stress calculations usually requires large amounts of computer memory. In addition, it can take many hours to run a complete process simulation on a high-end workstation. This limits the

size of the composite part that can be modeled. Further research must be performed to develop new algorithms, improvements in matrix assembly and storage processes, and parallel processing techniques that will result in significant reductions in memory and CPU requirements and computation time.

## Summary

The three resin infusion processes, RTM, RFI, and VARTM have become popular low-cost techniques for the manufacture of high quality composite structures. Dry fibrous preforms, produced by highly automated textile processes, are rapidly infused to produce void-free, near net-shape composite parts. Post-fabrication machining and assembly requirements are reduced compared to conventional composite fabrication methods.

Comprehensive three-dimensional computer models of the resin infusion processes have been developed. The physical processes modeled include the flow of resin through a three-dimensional anisotropic preform, heat transfer in the preform and tooling components, cure kinetics of the resin, and the residual stresses and final shape of the part. Process simulations have been used for mold and tool design and to optimize processing parameters to ensure proper infiltration and cure of the preform. The simulation model can be used to model manufacturing uncertainties and reduce manufacturing cost and risk.

## Acknowledgments

This work was supported by NASA Langley Research Center, Grant NAG1-1881. Mr. H. Benson Dexter was the grant monitor. The modeling work was also supported by the Boeing Company, Long Beach, CA. Dr. Thomas K. Tsotsis was the contract monitor.

## References

1. G. Hasko, H. B. Dexter, A. Loos and D. Kranbuehl, 1994. "Science Based RTM for Fabrication Primary Aircraft Structures." *39<sup>th</sup> International SAMPE Symposium*, pp. 779-792.
2. H. B. Dexter, 1996. "Innovative Textile Reinforced Composite Materials for Aircraft Structures." *28<sup>th</sup> International SAMPE Technical Conference*, pp. 404-416.
3. R. J. Palmer, M. B. Dow and D. L. Smith, 1991. "Development of Stitching Reinforcement for Transport Wing Panels." *Proceedings of the First ACT Conference*, NASA CP 3104, Part 2, pp. 621-646.
4. W. H. Seemann, U. S. Patent 4,902,215, 1990.
5. W. H. Seemann, U. S. Patent 5,316,462, 1994.

6. "SAMPE Update: F-22 Raptor." *High Performance Composites*, July/August 1998, p. 23.
7. H. B. Dexter, 1998. "Development of Textile Reinforced Composites for Aircraft Structures." *4<sup>th</sup> International Symposium for Textile Composites*, Kyoto Institute of Technology, Kyoto, Japan, October 12-14, 1998.
8. A. M. Markus, 1992. "Resin Transfer Molding for Composite Primary Wing and Fuselage Structures." *Proceedings of the Ninth DoD/NASA/FAA Conference on Fibrous Composites in Structural Design*, NASA CP 3154, pp. 141-167.
9. S. W. Beckwith and C. R. Hyland, 1998. "Resin Transfer Molding: A Decade of Technology Advances." *SAMPE Journal*, 34(6): 7-19.
10. S. M. Lewis and, J. C. Jakubowski, 1997. "Low Cost VARTM Process for Commercial and Military Applications." *42<sup>nd</sup> International SAMPE Symposium*, pp. 1173-1187.
11. L. B. Nguyen, T. Juska and S. J. Mayes, 1997. "Evaluation of Low Cost Manufacturing Technologies for Large Scale Composite Ship Structures," *Proceeding of the 38<sup>th</sup> AIAA/ASME/ASCE/AHS/ASC Structures, Structural Dynamics, and Materials Conference*, V.2, AIAA, New York, pp. 992-1001.
12. P. Lazarus, 1996. "Resin Infusion of Marine Composites." *41<sup>st</sup> International SAMPE Symposium*, pp. 1447-1458.
13. T. Pike, M. MacArthur, and D. Schade, 1996. "Vacuum Assisted Resin Transfer Molding of a Layered Structural Laminate for Application on Ground Combat Vehicles." *28<sup>th</sup> International SAMPE Technical Conference*, pp. 374-380.
14. A. C. Loos, J. D. MacRae, D. Hood, D. E. Kranbuehl and H. B. Dexter, 1996. "Resin Film Infusion (RFI) Process Simulation of Complex Shaped Composite Structures." *37th AIAA/ASME/ASCE/AHS/ASC Structures, Structural Dynamics and Materials Conference*, Paper No. AIAA-96-1533-CP, AIAA, Reston, VA, pp. 1828-1837.
15. A. C. Caba, D. Rattazzi, R. Batra, and A. C. Loos, 1999. "Verification of a Simulation Model for Resin Film Infusion of Complex Shaped Composite Structures." *Journal of Reinforced Plastics and Composites*, 18 (16): 1465- 1478.
16. J. C. Fingerson, "Verification of a Three-Dimensional Resin Transfer Molding Process Simulation Model." M. S. Thesis, Virginia Polytechnic Institute and State University, Blacksburg, VA, September, 1995.



## **Composites in Marine Structures**

Yapa D. S. Rajapakse

The use of composite materials in two broad classes of marine structures, offshore and ship structures, will be discussed. The advantages of using composites in these structures will be presented. Affordability is an important issue in the use of composites in the marine environment, narrowing the choice of composite material systems and processing/manufacturing techniques which provide for cost-effective, durable and reliable marine structures. Research issues and challenges in these structures will be discussed, together with examples of current research which address some of these issues. The effect of the severe marine environment, with continuous wave loading, and the presence of sea water, pose problems not encountered in aerospace or civil infrastructure applications. For submerged marine structures, hydrostatic pressure will be shown to have a significant effect on the mechanical response and failure modes. The importance of accounting for three-dimensional effects will be emphasized. Innovative experiments involving multi-axial loading will be described, with strategies for discriminating between a multitude of failure criteria. The dynamic response of composites will also be discussed. Real-time studies of dynamic failure under Mode II loading have revealed the existence of dynamic failure surfaces traveling at speeds approaching the dilatational wave speed. The advantages of the use of composite sandwich construction in certain types of marine structures will be discussed, and examples will be given of composite sandwich marine structures. Recently developed carbon fibers have been shown to provide exciting opportunities for designing advanced marine structures with new capabilities. The importance of collaborative research efforts between U.S. and Japanese researchers in composites will be reiterated.

---

Yapa D. S. Rajapakse, U.S. Office of Naval Research, Arlington, VA 22217, U.S.A.

## **Composites in the Renewal of Civil Infrastructure – Materials, Manufacturing, Design and Durability**

V.M. Karbhari

### **Abstract**

Fiber reinforced polymer matrix composites, once considered to have future untapped potential for large structural systems, are increasingly being used worldwide in civil infrastructure, in applications ranging from retrofit, rehabilitation, and repair, to use as replacement components and even full structural systems. This paper provides an overview of recent developments in testing, and field implementation, with special emphasis on the interactions between materials selection, processing method, and overall durability.

### **Introduction**

Fiber reinforced polymer (FRP) matrix composites are rapidly being accepted by the civil engineering and construction communities in applications ranging from replacement for steel components in applications such as rebar and cables, to use in repair and retrofit of concrete components, and even in new structural systems for bridges and industrial facilities. The unique and tailorable characteristics of composites provide significant impetus for their use in rehabilitation and restoration of historic structures without causing significant changes to the aesthetic features or geometric configurations of the original structures. Similarly, the performance attributes, in conjunction with their light-weight attributes, enable their use in strengthening of severely degraded structural elements, as well as in the modification of existing structures without egress on available head-room or open space. Further, when used in new structural systems they provide the designer with the ability to truly blend form and function. As applied to bridges they enable the construction of longer spans with significantly reduced cross sections, higher safety against seismic events, and faster overall construction. When applied to building systems they promise the potential for large clear spans with increased load carrying capacity, greater resistance to seismic events, faster construction, and ease of overall fabrication through the use of light prefabricated elements.

Despite the increasing use of FRP composites in civil infrastructure applications worldwide, there are a number of significant challenges that have still to be faced before this class of materials is widely accepted as belonging to the palette of construction materials. Chief among the challenges, are those related to (a) the verification and validation of long-term durability (75+ years), (b) the development of lower cost, but high quality, manufacturing processes, (c) the development of appropriate codes, standards, specifications and guidelines, and (d) the education of

civil engineers and designers in the intricacies of composites while simultaneously educating the composites community in the requirements and constraints of civil infrastructure.

A number of focussed programs have been initiated worldwide to address these concerns and to assist in the rapid implementation of composites technology in the civil sector. In the United States, programs funded and supported by the Federal Highway Administration (FHWA), State Departments of Transportation (DOTs), federal and local agencies, and industry have provided significant impetus in this area. In addition to these efforts, the Civil Engineering Research Foundation (CERF) is coordinating programs aimed at the development of test protocols, durability databases, and acceptance criteria for the use of composites in applications such as (a) dowel bars, (b) seismic retrofit of columns, (c) external strengthening of beams and slabs, and (d) bridge decks. This paper provides a brief overview of specific applications of FRP composites in the areas of renewal of structures as a means of highlighting durability and systems level aspects.

### **Seismic Retrofit of Columns**

The use of composite jackets has been shown to be extremely effective in retrofitting concrete columns that are deficient in flexural ductility, shear strength, bar buckling restraint, and/or lap splice clamping, and thereby enhancing their resistance to seismic events. The use of jackets/wraps around the columns induces lateral confining stresses in the concrete as it expands laterally in compression as a function of the high axial compressive strains, or in the tension zone as a function of dilation of lap splices, or through the development of diagonal shear cracks. The use of composites as jackets/wraps can be differentiated into five basic types based on the method of processing/installation, including: (a) the use of the wet lay-up process using fabric, tape or individual tow, (b) the use of prepreg in the form of tow, tape or fabric, (c) the use of prefabricated shells, (d) the use of resin infusion processes, and (e) the use of external composite cables or prefabricated strips [1]. Considerable testing at 40% and full-scale levels has been conducted on a number of these systems, and a comprehensive set of design equations has been developed and validated based on scale and full-scale testing [2]. A number of state departments of transportation in the US and various Japanese agencies have already published guidelines for determination of required thickness, and composite jackets are rapidly gaining widespread acceptance in the construction world.

However, there are still a number of issues, related to durability, design detailing, qualification of materials and processes, and even the accurate determination of required jacket thickness, that need further investigation. Although it can be considered that composite jackets are essentially unstressed till the occurrence of a seismic event, failure can still occur due to process-induced defects and stresses and even poor initial design or workmanship. The early failure of some jackets has been attributed to the development of overwrap stresses due to grout pressurization that exceeded the materials creep rupture strength providing an example of this in the field [3]. Because FRP composites provide ease of application and handling, there is a tendency to be lax on detailing practice and materials-

specific use restrictions. A common example is that related to the tight winding/wrapping of fibers/fabric around sharp corners of walls and prismatic columns. Corners need to be rounded in these application so as to both increase the effectiveness of confinement as well as to decrease the chance of fiber fracture due to stress concentration induced through the sharp edge. In large aspect ratio rectangular columns, significant challenges exist in achievement of proper levels of confinement. Composite sheets can be easily applied to large aspect ratio columns or pier walls. However, due to the long length between the corners, the composite does not in actuality confine the internal concrete structure if just applied to the surface. In fact, if used in this manner, reinforcing fibers are often loose and unable to provide confinement. In order to achieve confinement, the composite wrap needs to be constrained on both sides along the length through the use of dowels or bolts that anchor the composite in the column core, thereby creating shorter distances of confinement [4]. This is actually similar to the technique used in conventional reinforced concrete construction wherein the transverse reinforcement on the two side faces is tied together through the use of J-hooks. In the absence of the dowels/bolts/ties the jacket is not anchored and does not actually confine the material appropriately between the two shorter ends. Beyond the flexibility afforded by composites for the rapid and cost-effective retrofit of circular and rectangular columns/piers, composites are also invaluable for seismic retrofit of historical structures such as arch bridges with rectangular spandrel columns, which cannot be retrofit using steel jackets which would require the use of either circular or oval geometries with space between the original column and the jacket being taken by pouring/injection of new concrete/grout. Further location considerations also make the use of the steel option difficult in such cases, emphasizing the overall effectiveness of composites. In these cases, again, however, detailing is extremely important as incorrect details can cause less desirable failure modes than that seen in the unretrofitted columns. A recently completed study [5] highlights potential errors due to this aspect as related to the retrofit of spandrel columns with inclined interfaces between the column and the arch rib and the presence of a concrete pedestal located in the lap splice region.

A common concern related to the use of fiber reinforced composites for seismic retrofit is the accurate determination of composite properties under loading conditions that replicate the actual situation of a confined column. In cases of circular columns, the composite is reinforced predominantly in the hoop direction with fibers arranged in the circumferential direction around the concrete core. This entails the formation of a composite that is curved rather than flat, and by definition incorporates stresses resulting from that curvature. Although standard tensile tests such defined by ASTM D3039 could be used to determine performance levels as related to tensile strength, stiffness and strain-to-failure in the fiber direction these do not accurately reflect the state in the composite formed as a jacket. An efficient way to determine properties which simulate those in a field wrap is to conduct an NOL ring or "burst" test, wherein a 508 mm (20 in.) diameter ring with 25.4 mm (1 in.) height of the material in the configuration used in a jacket is placed in a constraining apparatus and then hydraulically pressurized internally to simulate confinement and impart only circumferential stresses to the ring. An added advantage to such a test,

beyond the determination of design properties, is the capability to test systems that are fabricated through the adhesive bonding of shell segments to form a jacket.

Whereas tensile, or other characterization level tests would not give a true indication of structural performance, and failure mode, the NOL ring test does, even replicating failure modes ranging from tensile failure of fibers in a well cured hoop dominated prepreg tow based system (Figure 1a) or due to incorrect cure of a prepreg system resulting in hoop splitting and unraveling (Figure 1b), to an adhesive joint failure in the case of prefabricated jackets which are field bonded (Figure 1c) and even the unraveling type failure which would be expected from a specimen fabricated using the wet layup process but without good interlayer adhesion due to either poor impregnation or premature gelation of the resin system prior to subsequent layers being placed during the lay up process (Figure 1d). This test provides ease of differentiation in overall response based on process related features, including defects, and overall effects of exposure on structural properties.

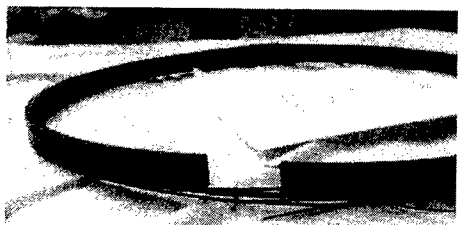


Figure 1a: Tensile Failure Showing Well-Consolidated and Cured Specimen



Figure 1b: Failure Through Hoop Splitting and Unraveling

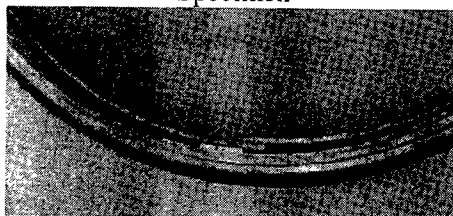


Figure 1c: Failure Initiated At Adhesive Level in a System Using Prefabricated Adhesively Bonded Sections

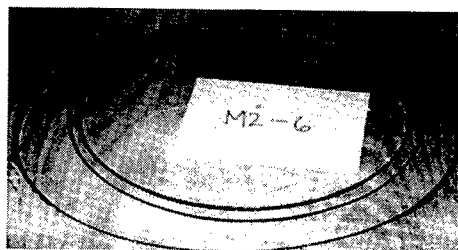


Figure 1d: Failure Through Layer Separation Due to Poor Wet-Out/Interply Bonding

The ring tests are currently being used as part of a base-line and durability test protocol in the United States as part of a FHWA (Federal Highway Administration) funded HITEC (Highway Innovation Technology Evaluation Center) program [6], wherein jackets are exposed to a variety of environments (immersion in water at 23 C, immersion in water at 64 C, immersion in alkaline solution at pH 9.5, immersion in concrete derived alkaline solution at pH 11.5, freeze, and freeze-thaw) in the laboratory and in the field over a period of time upto 18 months, and tested at periodic intervals to characterize changes in NOL-burst derived properties, short-beam-shear-strength, and glass transition temperature. These tests are ongoing and will serve as the basis for a durability database being developed by CERF. Further correlations are being drawn based on overall test

results and comparisons of laboratory exposure to actual field exposures and results will be published after the end of the 18-month test period.

### **Rehabilitation and Strengthening**

Degradation due to corrosion of steel reinforcement, extensive cracking of concrete due to carbonation and/or freeze-thaw action or other deterioration, and rapidly changing traffic needs (both in terms of intensity and load levels) have created a critical need for methods of strengthening of soffits of bridge decks. In the case of buildings, besides materials degradation, changing needs of building occupancy (e.g. residential to office) as well as upgrades to facilities (e.g. cutting of floor slabs to facilitate the construction of elevator shafts for the installation of elevators in older buildings), necessitates the strengthening of existing slabs and beams. Fiber reinforced polymer matrix composites provide a cost-effective, efficient, and rapid alternative to conventional methods of repair/strengthening, and can often facilitate renewal in cases where it would not have been possible through conventional means. Since the composite element is bonded onto the concrete substrate, the efficacy of the method depends on the combined action of the entire system with emphasis on the integrity of the bond and the interface layers. Thus the composite-adhesive/resin-concrete system has to be considered as a complete system, and materials aspects of each of the constituents, and interactions thereof between themselves and with the external environment could have a significant effect on overall efficiency, renewal capacity, and durability. The 'plate' (or external reinforcement) can itself be fabricated in three generic ways namely (a) adhesive bonding of prefabricated elements, (b) wet lay-up of fabric, and (c) resin infusion. Details related to each of these methods and aspects related to field detailing can be found in [4,7] and hence will not be repeated herein. In the following sections, two specific examples of application will be highlighted to emphasize aspects related to materials and field implementation.

#### **Application to Cut-Outs**

The use of externally bonded composite strips as a means of strengthening of existing concrete structural elements such as slabs is of special interest in enabling the modification of existing structures through the addition of elevators, escalators, service facilities through the cutting of holes in existing slabs. In order to provide these facilities, areas of existing slabs, including the steel reinforcement, are cut necessitating the use of additional columns and walls to support the weakened slab. FRP composite strips can, however be used around the cut-out to externally reinforce and slab and carry load locally, redistributing it back into the remaining structure, without the need for additional construction. This not only saves space that would otherwise have been needed for construction of additional supporting members around the cutout but also saves cost. In a recently completed series of tests, the response of unstrengthened and strengthened full-scale slabs, of size 6 m x 3.2 m with a central cut-out of size 1 m x 1.6 m, was investigated. The objective of the test was to externally strengthen the slab, after the cutout was made, using prefabricated

carbon/epoxy pultruded strips that were adhesively bonded to the tension face of the slab. Equivalent point loads were applied in the longitudinal and transverse directions on either side of the cut-out in two separate sets of tests (unstrengthened and strengthened) for transverse and longitudinal loading, to observe biaxial bending behavior as well as shear behavior in the slab. Strengthening schemes were based on determination of external reinforcement area required for rehabilitation through finite element analysis. Prefabricated (pultruded) FRP composite strips of 1-mm thickness and 100 mm and 50 mm width were used. For loading along the transverse direction a total of four 50 mm width strips of length 250 cm and two 100 mm width strips of length 350 cm were placed in the longitudinal direction centered on either side of the cutout, with one 50 mm width strip placed on either side of the cutout in the transverse direction over the width of the slab at 25.4 cm from the edge of the cutout. Figures 2a and b show a comparison of results between the unstrengthened and strengthened slabs, tested in the transverse and longitudinal directions, respectively.

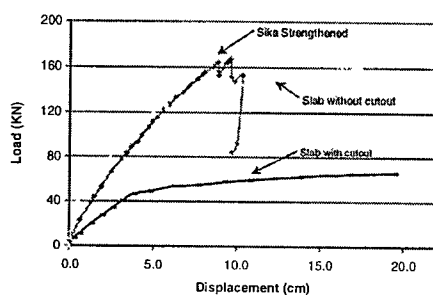


Figure 2a: Load-displacement Response under Transverse Loading

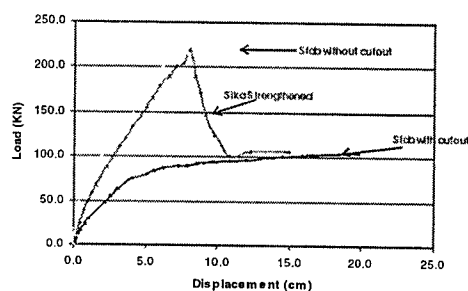


Figure 2b: Load-displacement Response under Longitudinal Loading

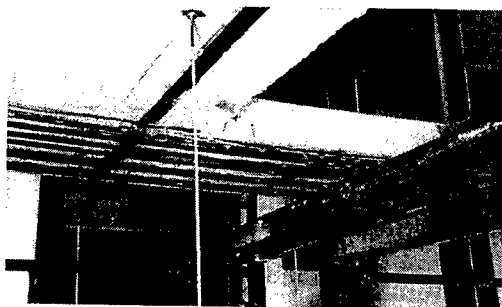


Figure 3a: Initial Debonding of Strips is at the Corner

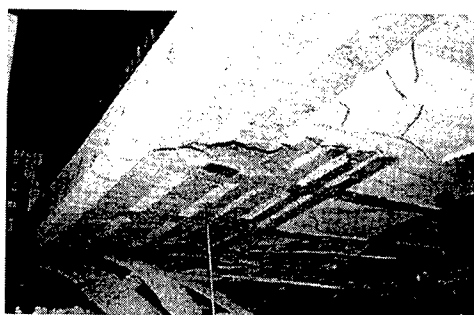


Figure 3b: Peeling and Debonding of Strips from the Concrete Substrate

As can be seen, the use of the FRP strips results in the slab regaining its initial capacity, albeit with less deformation capability. It is noted that in addition to enabling load distribution through the strips resulting in a recovered load capacity, the FRP composite also restrains crack growth especially in areas of local stress concentration formed through the construction of the cutout. Figures 3(a) and (b) depict configurations of the final failure mode of strip debonding with the horizontal crack being either within the cover concrete or within the FRP composite itself.

Although the initiation of failure is approached in fairly linear fashion, there is significant prior warning through local debonding and concrete cracking. It is also noted that after debonding of the FRP composite the slab response follows that of the original slab with the cutout, thereby emphasizing that if appropriately designed, failure would not be catastrophic.

#### Application to Rehabilitation of Punching Shear

In a number of cases bridge decks subjected to high traffic loads and having deficiency of reinforcement in the slabs in one direction show distress in the form of punching shear wherein for the case of deficiency in longitudinal reinforcement, transverse spanning decks first crack in longitudinal bending along the transverse soffit reinforcement since longitudinally very little flexural capacity exists and transverse cracks can open wide. Subsequently the effective width in the transverse direction is limited to the spacing between transverse cracks resulting in significant flexure and shear overloads. As a consequence, longitudinal cracks develop which spread along the entire deck length due to the moving nature of the wheel loads. Finally the local shear capacity is exceeded over a shear area limited by the existing flexural cracks in both directions. In a recent project, FRP composites were applied to the soffit of the deck slab of the Byron Road bridge, a 103 m long 5 span bridge in northern California built in 1964 as a cast-in-place reinforced concrete T-girder bridge that has longitudinal deck reinforcement that is only 57% that of the transverse reinforcement and has started showing advanced signs of distress as shown in Figures 4(a) and (b).



Figure 4(a): Distributed Crack Pattern in a Bay

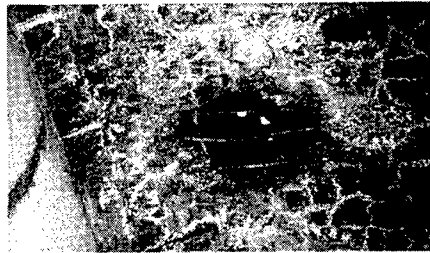


Figure 4(b): Local Punching Shear Failure

Failure assessment studies were performed using a slab demand model for deck cracking and rehabilitation criteria were established to ensure that further sequential crack opening was restricted through the addition of external FRP composite strips such that bottom soffit strains would be limited to less than 0.75%. to ensure sufficient aggregate interlock and a nominal concrete shear capacity of more than  $2(f_c')^{1/2}$ . To prevent punching shear cones from forming, clear spacing between the externally applied FRP strips was required to be less than the spacing for the observed punching shear diameter (300-mm). Rehabilitation was conducted in continuous fashion using both prefabricated strips, which were adhesively bonded to the deck soffit, and unidirectional fabric, which was placed using the wet lay-up process. Since the rehabilitation was conducted in winter months during which temperatures were generically lower than those required for appropriate cure of the



adhesive and resin, and since significant rainfall is seen in winter in the geographical vicinity of the bridge, work was carried out using rolling scaffolds that were enclosed using polyethylene sheets with hot air being blown in through an external heater in order to maintain a constant temperature in bays that were being rehabilitated.

## Challenges

As the use of FRP composites in civil infrastructure rehabilitation increases there is a need to optimize materials, that heretofore had been directly derived from commercial systems initially developed for other application areas such as aerospace, marine or automotive, for use in this new applications area. Chief amongst these aspects is the need for development of materials systems and product forms that lend themselves to use in a varying and harsh environment wherein quality control attributes cannot be expected to reach levels expected in the aerospace industry and where routine maintenance and inspection of the type used on FRP composites in the aerospace industry will be rare.

## References

1. V.M. Karbhari, 1998. "Rehabilitation of concrete Structures Using Fibre-Reinforced Composites." *Proceedings of the 2<sup>nd</sup> International RILEM Conference on Rehabilitation of Structures*, pp. 417-430.
2. F. Seible and V.M. Karbhari, 1997. "Seismic Retrofit of Bridge Columns Using Advanced Composite Materials," *Proceedings of the National Seminar on Advanced Composite Material Bridges*, Washington, D.C., 29 pp.
3. G.F. Hawkins, N.R. Patel, G.L. Steckel and M. Sultan, 1995. "Failure Analysis of Highway Bridge Column Composite Overwraps." *Proceedings of the National Seismic Conference on Bridges and Highways*, San Diego, CA, December, 10 pp.
4. V.M. Karbhari, 1998. "Materials and Design Considerations in FRP Rehabilitation of Concrete Structures." *Proceedings of FRAMCOS-3*, Gifu, Japan, Vol. 3, pp. 1805-1816
5. F. Seible, D. Innamorato, J. Baumgartner, V. Karbhari and L.H. Sheng, 1999. "Seismic Retrofit of Flexural Bridge Spandrel Columns Using Fiber Reinforced Polymer Composite Jackets." *ACI SP-188*, pp. 919-931.
6. D. Reynaud, V.M. Karbhari and F. Seible, 1999. "The HITEC Evaluation Program for Composite Column Wrap Systems for Seismic Retrofit." *International Composites Exposition '99*, Cincinnati, OH, pp. 4A/1-6.
7. V.M. Karbhari and L. Zhao, 1998. "Issues Related to Composite Plating and Environmental Exposure Effects on Composite-Concrete Interface in External Strengthening." *Composite Structures*, Vol. 40[3/4], pp. 293-304.

## **Improvement of Shear and Ductility of Reinforced Concrete Columns by Wrapping of Continuous Fiber Reinforced Polymer Sheet**

K. Maruyama, H. Nakai, F. Katsuki and T. Shimomura

### **Abstract**

Concrete Committee of Japan Society of Civil Engineers (JSCE) has set up a technical committee on retrofit of concrete structures by continuous fiber reinforced polymer sheet (CFRP sheet). The technical committee has been working to make a recommendation for one and half years, and has proposed the first draft. This paper describes some parts of the recommendation, in particular, on how to design the shear strengthening and the ductility improvement by use of CFRP sheet. In addition, discussion is extended to the proposed test methods on the tensile strength and the bond strength of CFRP sheet.

### **Introduction**

Continuous fiber reinforced polymers (CFRP's) have been developed for more than twenty years. The application of CFRP to the civil engineering structures was firstly considered as the substitutes for reinforcing steel bars because CFRP's are not corrosive materials. Extensive research works have been conducted widely and several design guidelines were published [1-7].

In comparison with ordinary steel reinforcing bars, CFRP bars are good in high tensile strength but a modulus of elasticity is relatively low. In addition, CFRP's are quite elastic up to failure and the ultimate strain capacity is 1 – 3 %. They do not have any yield phenomenon. These material properties of CFRP result in less effective as the substitutes for steel reinforcing bars in the seismic design of concrete structures. This is one of the reasons why CFRP bars have not been used so much for concrete structures in Japan.

On the other hand, CFRP sheets have become attractive for design engineers as retrofit or strengthening materials for the existing RC structures after the disaster by the Great Hanshin Earthquake in 1995. High strength, lightweight and easy handling of CFRP sheets become strongly beneficial for retrofit or strengthening of RC structures.

---

K. Maruyama and T. Shimomura, Department of Civil and Environmental Engineering, Nagaoka University of Technology, 1603-1 Nagaoka, Niigata 940-2188, Japan

H. Nakai, Sumitomo Corporation Ltd, 13-4 Araki, Shinjuku-ku, Tokyo 160-8577, Japan

F. Katsuki, Shibaura Institute of Technology, 3-9-14 Shiba, Minato-ku, Tokyo 108-8548, Japan

Authorities in Japan, such as Railway Technical Research Institute, Japan Highway Public Corporation as well as the Ministries of Construction and Transportation, have been studying the effectiveness of CFRP sheets for retrofit or strengthening of existing RC structures. With a lot of experimental works they have made their own design guidelines for their specific applications with specified type of fiber [1-5].

### JSCE Activity

With consideration on the situation of CFRP sheets applications in Japan, the Japan Society of Civil Engineers (JSCE) decided to establish the unified and more widely applicable design recommendations of CFRP sheets for retrofit or strengthening of the existing concrete structures as well as repair and enhancement of durability of concrete structures.

The research committee on CFRP sheets started in April 1998 with two years term. The missions of the committee are to make the recommendations for design and construction practice of CFRP sheets applied to existing RC structures for retrofit, strengthening and enhancement of durability, and to establish the standard test procedures for mechanical properties of CFRP sheets, such as tensile strength, bond strength, durability etc.

Different from the previous recommendations, the JSCE recommendations are formatted and described based on the performance of RC structures with CFRP sheets. It means that the descriptions in the design part are made as how to evaluate the contribution of CFRP sheets in terms of flexure, shear and ductility of RC members as well as enhancement of durability.

This paper discusses mainly the evaluations of shear and ductility contribution of CFRP sheets, and some aspects of test method.

### Contribution to Shear Capacity

In the previous guidelines, the contribution of CFRP sheet to the shear capacity of RC member is expressed by the truss model.

$$V_u = V_c + V_s + V_f \quad (1)$$

$$V_f = K \cdot A_f \cdot f_f \cdot z \cdot (\sin \alpha + \cos \alpha) / s_f \quad (2)$$

Where,  $V_u$ : ultimate shear capacity of RC members with CFRP sheet,  $V_c$ : concrete contribution,  $V_s$ : contribution of shear reinforcing bars,  $V_f$ : contribution of CFRP sheet,  $K$ : coefficient of effectiveness of CFRP sheet,  $A_f$ : cross sectional area of CFRP sheet,  $f_f$ : tensile strength of CFRP sheet,  $z$ : lever arm length,  $\alpha$ : angle of fiber to longitudinal direction,  $s_f$ : =1 or spacing of CFRP strip.

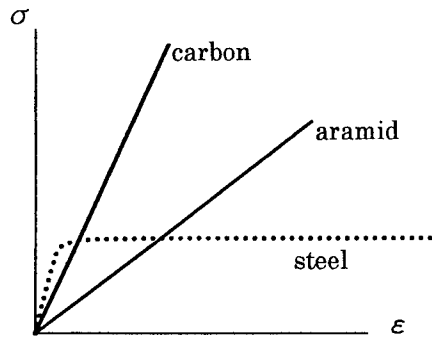


Figure 1 Stress-Strain Diagram of CFRP

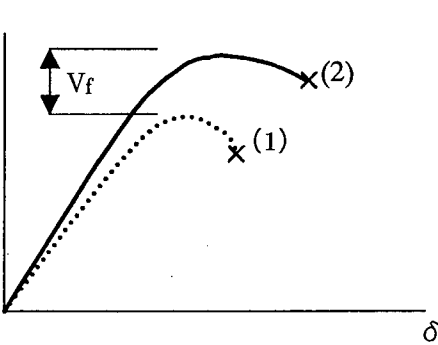
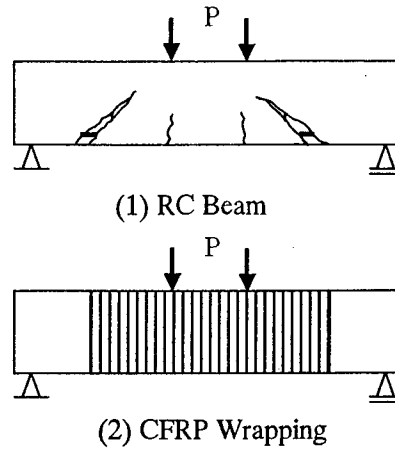


Figure 2 Contribution of CFRP Sheet to Shear Capacity

Comparing with steel reinforcement CFRP (both carbon fiber and aramid fiber) is quite elastic up to failure with less ultimate strain as shown in Fig.1. This property does not bring stress redistribution in the resistant mechanism, which is typical phenomenon of resistance with steel reinforcement due to yielding of steel. Therefore, the equation derived from the truss model should account for the non stress redistribution of CFRP using K factor. Otherwise, the contribution of CFRP sheet to the shear capacity can not be evaluated properly (Fig.2).

However, the problem of those guidelines lies in that the value of K is determined for a specific type of fiber regardless the mechanical properties of fiber, for example, 0.8 for carbon fiber sheet and 0.6 for aramid fiber sheet are recommended. Since there have been developed various types of carbon fiber sheet as well as aramid fiber sheet which have different tensile strength, modulus of elasticity and ultimate strain, those guidelines are limited to the specific fiber sheet.

The JSCE committee on CFRP sheet surveyed previous test results widely and reevaluated the contribution of the sheet using the tensile strength, the modulus of elasticity, the cross sectional area of CFRP sheet as well as the concrete strength. With a lot of parametric studies, the K factor is proposed in the following form.

$$0.4 \leq K = 1.0 - 0.3R \leq 0.8 \quad (3)$$

$$R = \frac{\sqrt{p_f} \cdot f_f}{\sqrt{f'_c} \cdot E_f} \quad (4)$$

Where,  $p_f = A_f / (b_w \cdot s_f)$ ,  $f'_c$ : concrete strength.  $E_f$ : modulus of elasticity of CFRP sheet.

The effectiveness of the equation is shown in Fig.3 having the factor of correlation being 0.76. The equation is still empirical and has a limit for application because the collected data are limited within the ranges of  $d = 200-540$  mm,  $a/d=1.1-3.6$ ,  $f'_c = 21-45$  MPa,  $f_t = 2480-4300$  MPa,  $E_f = 87 - 252$  GPa. Although the data for forming the equation are collected from the test results of column specimens (similar ones as shown in Fig.4), the equation could be applicable to beams shown in Fig.2.

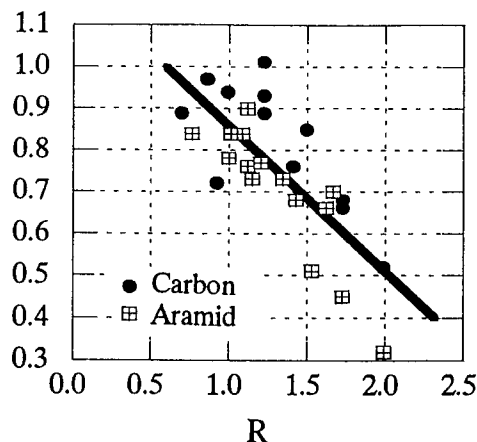


Figure 3 Correlation of K and R

### Contribution to Ductility

Mechanism on how CFRP sheet contributes to the ductility of RC members is much more complicate than that on how the sheet contributes to the shear capacity. Even for ordinary RC members, the ductility is still difficult to determine analytically. It is, however, observed in the experimental works that RC members with relatively higher shear capacity to flexural capacity exhibit large ductility. This fact is taken in the JSCE seismic design code for concrete structures expressing that the ductility ratio is a linear function of the ratio of shear capacity to flexural capacity.

The contribution of CFRP sheet to ductility can not be attributed only to the increase of shear capacity by sheet, but also to the confinement of cracked concrete by sheet wrapping (Fig.3). Conducting the parametric study of existing experimental data, the following equation is proposed.

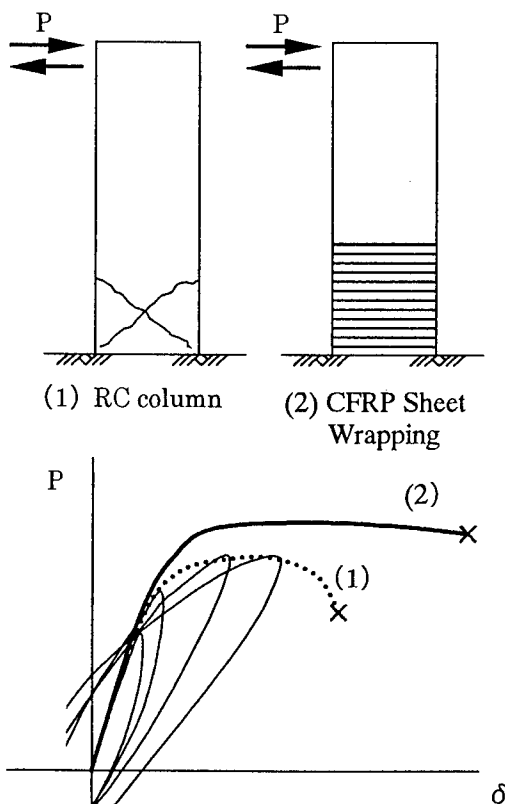


Figure 4 Contribution of Sheet to Ductility

$$\mu = 2.33 \cdot \frac{(0.5V_c + V_s)}{V_{mu}} \cdot \left( 1 + \alpha_o \cdot \frac{\varepsilon_f \cdot P_f}{V_{mu} / (B \cdot z)} \right) + 3.29 \quad (5)$$

Where,  $\mu$ : ductility ratio (ratio of yield deformation to ultimate deformation),  $V_{mu}$ : shear force at the ultimate flexural capacity,  $B$ : width,  $\alpha_o$ : coefficient (same value of Young's modulus of steel can be taken).

The equation is examined as shown in Fig.5 having the factor of correlation being 0.78. The equation has also a limit for application since the collected data are within the ranges of  $d=300-800$  mm,  $a/d = 4.0-5.7$ ,  $f'_c = 18-24$ MPa,  $f_t = 2050-3430$ MPa,  $E_t = 28-252$ Gpa, axial stress =  $3.2-5.9$ MPa.

Different from the contribution to shear capacity, the contribution of sheet to ductility depends upon the existing structural performance. As mentioned before, CFRP sheet wrapping increases both the shear capacity and the confinement effect of cracked concrete. These effects should provide the member a large deformation capacity.

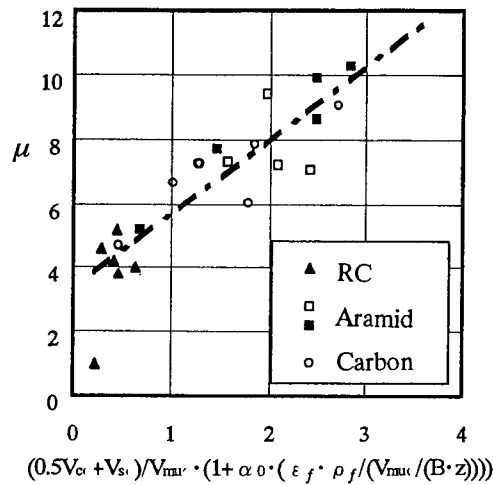


Figure 5 Correlation of  $\mu$

## Test Methods

The committee proposed 9 test methods to determine the mechanical and durable properties of CFRP sheet. Those are to determine (1) tensile strength of sheet, (2) anchorage strength between sheets, (3) bond strength between sheet and concrete, (4) bond strength between sheet and steel plate, (5) adhesive strength between sheet and concrete, (6) tensile fatigue strength of sheet, (7) accelerated exposure test, (8) freezing and thawing test, and (9) resistance against water, acid and alkali. Most of test methods are concerned with the property of sheet itself, but the bond test represents the interface strength among sheet, adhesive material and the surface condition of concrete. Since the bond strength between sheet and concrete is important to the contribution of sheet to the flexural and shear capacity of RC members, some aspect of the test method is discussed.

## Bond Strength Test

Test specimen is shown in Fig. 6. Two concrete blocks (100 x 100 x 300 mm)

are aligned to match the center of cross section. Each has a steel bar mounted at the center of cross section. After alignment of two blocks, two CFRP sheets (more than 50 mm width x 400mm length) are attached on the opposite sides. In order to obtain consistent data, sheets in one side should be anchored sufficiently. The left parts of sheets are measured. The load is applied by pulling a steel bar at the both ends. Strain gages should be attached on the both surfaces of sheet. Based on the strain distribution of sheet as shown in Fig. 7, the bond strength is determined.

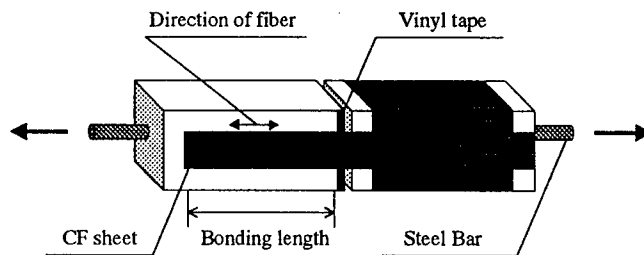


Figure 6 Test Specimen for Bond

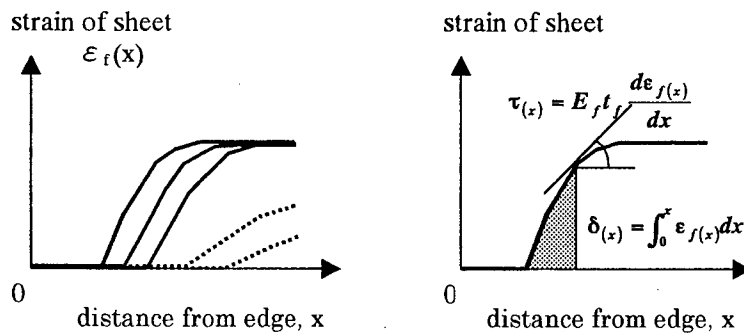


Figure 7 Strain Distribution of Sheet

### Concluding Remarks

Due to the deterioration of material or the changes of requirements for structures, upgrading of existing RC structures is becoming a more and more important issue. CFRP sheets have advantageous material properties, such as high strength, lightweight, high resistance to corrosion. Making the application of CFRP sheets to upgrading structures more effective, the contribution of the sheet should be evaluated sufficiently in the performance of structures as a whole. With further understandings on the mechanism and with computational invention, the evaluation could be improved by numerical analyses.

## References

1. Experimental Research Institute, The Japan Highway Public Corporation, 1995: *Design/Construction Guidelines on the Retrofitting of Reinforced Concrete Bridge Piers using Carbon Fiber (proposal)*, (in Japanese).
2. Railway Technical Research Institute (RTRI), 1996: *Design/Construction Guidelines on the Seismic Retrofitting of Railway Viaduct Columns using Carbon Fiber Sheet*, (in Japanese).
3. Railway Technical Research Institute (RTRI), 1996: *Design/Construction Guidelines on the Seismic Retrofitting of Railway Viaduct Columns using Aramid Fiber Sheet*, (in Japanese).
4. Railway Technical Research Institute (RTRI), 1997: *Design/Construction Guidelines on the Seismic Retrofitting of Subway RC Columns using Carbon Fiber Sheet*, (in Japanese).
5. The Hanshin Highway Public Corporation, 1997: *Design/Construction Guidelines on the Seismic Retrofitting of RC Bridge Piers using Carbon Fiber Sheet*, (in Japanese).
6. The Building Research Institute of Japan, 1998: *US-Japan Research Collaboration on the Hybrid Structures – The Retrofitting Design Guidelines on the Application of Continuous Fiber Sheets*.
7. ACI Committee 440, 1999: *Guidelines for the Selection, Design, and Installation of Fiber Reinforced Polymer (FRP) Systems for Externally Strengthening Concrete Structures*.



## **Manufactured Shapes of Piezoceramic-Composite Actuators**

M. W. Hyer and A. B. Jilani

### **Abstract**

An analysis is presented to predict the processed shapes of the piezoceramic actuator known as RAINBOW. Also considered is the case where a single  $0^\circ$  layer of fiber-reinforced composite material is applied to one side of the actuator.

### **Introduction**

Haertling [1] reported on using a reducing technique to produce a piezoceramic actuator with more displacement capability than the usual unimorph or bimorph bender device. A flat piezoceramic wafer is placed upon a carbon block and the temperature is raised to  $975^\circ\text{C}$  for a number of minutes. The result is the partial reduction of the material through the thickness of the wafer, thus producing a layered wafer. The material properties of the reduced layer are different than the material properties of the unreduced layer, resulting in a bimaterial wafer. Due to the internal stress state, the layered wafer deforms out-of-plane as the temperature is lowered to room temperature, much like the response of a bimetallic strip to a temperature change. This deformed wafer then acts as a bimorph when an electric field is passed through the unreduced layer. Furthermore, it is felt that the internal stress state enhances the piezoelectric effect through domain reorientation. The terminology RAINBOW (Reduced And Internally Biased Oxide Wafer) was adapted for this technology. Another step in the manufacturing can be considered. For a number of reasons it may be desirable to add one or more layers of a fiber-reinforced composite material to the wafer. This paper will focus on the development of a methodology to predict the shape of the wafers at room temperature with and without the addition of composite layers. Because the deformations are large relative to the flat state, geometric nonlinearities are included. To move forward with the problem, linear elastic temperature-independent material behavior is assumed. A Rayleigh-Ritz approach, whereby the functional forms of the possible cooled shapes are approximated, is used in conjunction with the total potential energy and variational methods to find the shape that results from cool down. In the next section the problem being studied is more clearly defined. The section after that outlines the analysis used to predict the cooled shape. Following that, numerical results are presented.

M. W. Hyer, Department of Engineering Science and Mechanics, Virginia Polytechnic Institute and State University, Blacksburg, Virginia 24061

A. B. Jilani, Hewlett-Packard Company, Research & Development Department, Inkjet Supplies Business, Corvallis, Oregon 97330

## Problem Definition

Consider a rectangular wafer situated in a Cartesian coordinate system, as shown in fig. 1, a greatly distorted view. The important geometric parameters are identified in the figure. The wafer is assumed to be flat at the elevated reducing temperature  $T_r$ . The original wafer, i.e., the RAINBOW wafer, is assumed to have  $N$  layers, though here  $N$  will be restricted to two, a reduced layer and an unreduced layer. The composite layers consist of layers  $N+1$  through  $N+M$  and they add thickness  $H_c$  to the wafer. In fig. 1 it is shown that layers  $N+1$  through  $N+M$  are all added to one side of the original RAINBOW wafer. Though that will be the case in the numerical example considered, it is not required for the analysis presented. It is shown that way in fig. 1 simply to emphasize that there is an accounting system for keeping track of all layers, as not all of them experience the same temperature change.

The wafer will be considered a small thin layered plate, so the assumptions of classical layered plate theory [2] will be valid. The displacements of the reference surface in the  $x$  and  $y$  directions are denoted by  $u^\circ$  and  $v^\circ$ , respectively, and out-of-plane displacements by  $w^\circ$ . Throughout, the notation  $^\circ$  is reserved for reference surface quantities. A key to the analysis is as follows: Consider a RAINBOW wafer consisting of just a reduced and an unreduced layer being cooled from the reducing temperature  $T_r$  to the cure temperature of the composite,  $T^*$ . The fiber-reinforced composite layers are added, the elastic and thermal expansion properties of the composite develop at that temperature, and then the combination composite-RAINBOW wafer is further cooled to room temperature. There are three key temperatures: the reducing temperature  $T_r$ , the cure temperature of the composite  $T^*$ , and then some arbitrary temperature,  $T$ , the interest here being in room temperature, 20 °C. There are, accordingly, two key temperature changes. At a temperature below the composite cure temperature the RAINBOW portion of the combination wafer experiences a temperature change  $\Delta T = T - T_r$ . The composite layers experience less of a temperature change, namely,  $\Delta T_c = T - T^*$ . Of course, the difference in reducing temperature and composite cure temperature is given by  $\Delta T^* = T^* - T_r$ .

## Development of the Analysis

Integrating through the thickness of the composite-RAINBOW combination, the total potential energy becomes

$$\begin{aligned} \Pi = & \frac{1}{2} \int_{-\frac{L_x}{2}}^{+\frac{L_x}{2}} \int_{-\frac{L_y}{2}}^{+\frac{L_y}{2}} \left\{ (N_x - \hat{N}_x^T \Delta T - N_x^*) \epsilon_x^\circ + (N_y - \hat{N}_y^T \Delta T - N_y^*) \epsilon_y^\circ \right. \\ & + (N_{xy} - N_{xy}^*) \gamma_{xy}^\circ + (M_x - \hat{M}_x^T \Delta T - M_x^*) \kappa_x^\circ \\ & \left. + (M_y - \hat{M}_y^T \Delta T - M_y^*) \kappa_y^\circ + (M_{xy} - M_{xy}^*) \kappa_{xy}^\circ \right\} dx dy \end{aligned} \quad (1)$$

Including geometrically nonlinear effects, the reference surface strains and curvatures are given by

$$\begin{aligned}
\epsilon_x^o &= \frac{\partial u^o}{\partial x} + \frac{1}{2} \left( \frac{\partial w^o}{\partial x} \right)^2 & \kappa_x^o &= -\frac{\partial^2 w^o}{\partial x^2} \\
\epsilon_y^o &= \frac{\partial v^o}{\partial y} + \frac{1}{2} \left( \frac{\partial w^o}{\partial y} \right)^2 & \kappa_y^o &= -\frac{\partial^2 w^o}{\partial y^2} \\
\gamma_{xy}^o &= \left( \frac{\partial u^o}{\partial y} + \frac{\partial v^o}{\partial x} \right) + \frac{\partial w^o}{\partial x} \frac{\partial w^o}{\partial y} & \kappa_{xy}^o &= -2 \frac{\partial^2 w^o}{\partial x \partial y}
\end{aligned} \quad (2)$$

Assuming orthotropic material behavior, the stress resultants are

$$\begin{aligned}
N_x &\equiv \int_0^{H+H_c} \sigma_x dz = A_{11} \epsilon_x^o + A_{12} \epsilon_y^o + B_{11} \kappa_x^o + B_{12} \kappa_y^o - \hat{N}_x^T \Delta T - N_x^* \\
N_y &\equiv \int_0^{H+H_c} \sigma_y dz = A_{12} \epsilon_x^o + A_{22} \epsilon_y^o + B_{12} \kappa_x^o + B_{22} \kappa_y^o - \hat{N}_y^T \Delta T - N_y^* \\
N_{xy} &\equiv \int_0^{H+H_c} \tau_{xy} dz = A_{66} \gamma_{xy}^o + B_{66} \kappa_{xy}^o - N_{xy}^* \\
M_x &\equiv \int_0^{H+H_c} z \sigma_x dz = B_{11} \epsilon_x^o + B_{12} \epsilon_y^o + D_{11} \kappa_x^o + D_{12} \kappa_y^o - \hat{M}_x^T \Delta T - M_x^* \\
M_y &\equiv \int_0^{H+H_c} z \sigma_y dz = B_{12} \epsilon_x^o + B_{22} \epsilon_y^o + D_{12} \kappa_x^o + D_{22} \kappa_y^o - \hat{M}_y^T \Delta T - M_y^* \\
M_{xy} &\equiv \int_0^{H+H_c} z \tau_{xy} dz = B_{66} \gamma_{xy}^o + D_{66} \kappa_{xy}^o - M_{xy}^*
\end{aligned} \quad (3)$$

and

$$\begin{aligned}
N_x^* &\equiv \int_H^{H+H_c} \sigma_x dz = A_{11}^* \epsilon_x^{o*} + A_{12}^* \epsilon_y^{o*} + B_{11}^* \kappa_x^{o*} + B_{12}^* \kappa_y^{o*} - \hat{N}_x^{T*} \Delta T^* \\
N_y^* &\equiv \int_H^{H+H_c} \sigma_y dz = A_{12}^* \epsilon_x^{o*} + A_{22}^* \epsilon_y^{o*} + B_{12}^* \kappa_x^{o*} + B_{22}^* \kappa_y^{o*} - \hat{N}_y^{T*} \Delta T^* \\
N_{xy}^* &\equiv \int_H^{H+H_c} \tau_{xy} dz = A_{66}^* \gamma_{xy}^{o*} + B_{66}^* \kappa_{xy}^{o*} \\
M_x^* &\equiv \int_H^{H+H_c} z \sigma_x dz = B_{11}^* \epsilon_x^{o*} + B_{12}^* \epsilon_y^{o*} + D_{11}^* \kappa_x^{o*} + D_{12}^* \kappa_y^{o*} - \hat{M}_x^{T*} \Delta T^* \\
M_y^* &\equiv \int_H^{H+H_c} z \sigma_y dz = B_{12}^* \epsilon_x^{o*} + B_{22}^* \epsilon_y^{o*} + D_{12}^* \kappa_x^{o*} + D_{22}^* \kappa_y^{o*} - \hat{M}_y^{T*} \Delta T^* \\
M_{xy}^* &\equiv \int_H^{H+H_c} z \tau_{xy} dz = B_{66}^* \gamma_{xy}^{o*} + D_{66}^* \kappa_{xy}^{o*}
\end{aligned} \quad (4)$$

The effective thermal stress resultants are defined as

$$\begin{aligned}
\hat{N}_x^T &\equiv \int_0^{H+H_c} (\bar{Q}_{11} \alpha_x + \bar{Q}_{12} \alpha_y) dz = \sum_{k=1}^{N+M} (\bar{Q}_{11} \alpha_x + \bar{Q}_{12} \alpha_y)_k (z_k - z_{k-1}) \\
\hat{N}_y^T &\equiv \int_0^{H+H_c} (\bar{Q}_{12} \alpha_x + \bar{Q}_{22} \alpha_y) dz = \sum_{k=1}^{N+M} (\bar{Q}_{12} \alpha_x + \bar{Q}_{22} \alpha_y)_k (z_k - z_{k-1}) \\
\hat{M}_x^T &\equiv \int_0^{H+H_c} (\bar{Q}_{11} \alpha_x + \bar{Q}_{12} \alpha_y) z dz = \frac{1}{2} \sum_{k=1}^{N+M} (\bar{Q}_{11} \alpha_x + \bar{Q}_{12} \alpha_y)_k (z_k^2 - z_{k-1}^2) \\
\hat{M}_y^T &\equiv \int_0^{H+H_c} (\bar{Q}_{12} \alpha_x + \bar{Q}_{22} \alpha_y) z dz = \frac{1}{2} \sum_{k=1}^{N+M} (\bar{Q}_{12} \alpha_x + \bar{Q}_{22} \alpha_y)_k (z_k^2 - z_{k-1}^2)
\end{aligned}$$

$$\begin{aligned}
\hat{N}_x^{T*} &\equiv \int_H^{H+H_c} (\bar{Q}_{11}\alpha_x + \bar{Q}_{12}\alpha_y) dz = \sum_{k=N}^{N+M} (\bar{Q}_{11}\alpha_x + \bar{Q}_{12}\alpha_y)_k (z_k - z_{k-1}) \quad (5) \\
\hat{N}_y^{T*} &\equiv \int_H^{H+H_c} (\bar{Q}_{12}\alpha_x + \bar{Q}_{22}\alpha_y) dz = \sum_{k=N}^{N+M} (\bar{Q}_{12}\alpha_x + \bar{Q}_{22}\alpha_y)_k (z_k - z_{k-1}) \\
\hat{M}_x^{T*} &\equiv \int_H^{H+H_c} (\bar{Q}_{11}\alpha_x + \bar{Q}_{12}\alpha_y) z dz = \frac{1}{2} \sum_{k=N}^{N+M} (\bar{Q}_{11}\alpha_x + \bar{Q}_{12}\alpha_y)_k (z_k^2 - z_{k-1}^2) \\
\hat{M}_y^{T*} &\equiv \int_H^{H+H_c} (\bar{Q}_{12}\alpha_x + \bar{Q}_{22}\alpha_y) z dz = \frac{1}{2} \sum_{k=N}^{N+M} (\bar{Q}_{12}\alpha_x + \bar{Q}_{22}\alpha_y)_k (z_k^2 - z_{k-1}^2)
\end{aligned}$$

In the above, the  $A$ s,  $B$ s,  $D$ s,  $A^*$ s,  $B^*$ s, and  $D^*$ s have the following definitions

$$\begin{aligned}
A_{ij} &= \sum_{k=1}^{N+M} (\bar{Q}_{ij})_k (z_k - z_{k-1}) & A_{ij}^* &= \sum_{k=N}^{N+M} (\bar{Q}_{ij})_k (z_k - z_{k-1}) \\
B_{ij} &= \frac{1}{2} \sum_{k=1}^{N+M} (\bar{Q}_{ij})_k (z_k^2 - z_{k-1}^2) & B_{ij}^* &= \frac{1}{2} \sum_{k=N}^{N+M} (\bar{Q}_{ij})_k (z_k^2 - z_{k-1}^2) \\
D_{ij} &= \frac{1}{3} \sum_{k=1}^{N+M} (\bar{Q}_{ij})_k (z_k^3 - z_{k-1}^3) & D_{ij}^* &= \frac{1}{3} \sum_{k=N}^{N+M} (\bar{Q}_{ij})_k (z_k^3 - z_{k-1}^3)
\end{aligned} \quad (6)$$

The out-of-plane displacement field,  $w^o(x, y)$ , can be approximated as

$$w^o(x, y) = \frac{1}{2}(ax^2 + by^2) \quad (7)$$

where  $a$  and  $b$  are to-be-determined constants and represent the curvatures of the cooled actuator in the  $x$  and  $y$  directions, respectively. The inplane displacements  $u^o(x, y)$  and  $v^o(x, y)$  are approximated as

$$u^o(x, y) = cx - \frac{a^2x^3}{6} - \frac{abxy^2}{4} \quad v^o(x, y) = dy - \frac{b^2y^3}{6} - \frac{abx^2y}{4} \quad (8)$$

Here  $c$  and  $d$  are additional to-be-determined constants. The four constants are determined by minimizing the total potential energy, specifically,

$$\delta\Pi = \frac{\partial\Pi}{\partial a}\delta a + \frac{\partial\Pi}{\partial b}\delta b + \frac{\partial\Pi}{\partial c}\delta c + \frac{\partial\Pi}{\partial d}\delta d = f_a\delta a + f_b\delta b + f_c\delta c + f_d\delta d = 0 \quad (9)$$

or

$$f_a = 0 \quad f_b = 0 \quad f_c = 0 \quad f_d = 0 \quad (10)$$

Stability is insured if the second variation is positive definite, i.e.,

$$\delta^2\Pi = \begin{bmatrix} \delta a & \delta b & \delta c & \delta d \end{bmatrix} \begin{bmatrix} C \end{bmatrix} \begin{bmatrix} \delta a \\ \delta b \\ \delta c \\ \delta d \end{bmatrix} > 0 \quad (11)$$

$$[C] = \begin{bmatrix} \partial f_a/\partial a & \partial f_a/\partial b & \partial f_a/\partial c & \partial f_a/\partial d \\ \partial f_b/\partial a & \partial f_b/\partial b & \partial f_b/\partial c & \partial f_b/\partial d \\ \partial f_c/\partial a & \partial f_c/\partial b & \partial f_c/\partial c & \partial f_c/\partial d \\ \partial f_d/\partial a & \partial f_d/\partial b & \partial f_d/\partial c & \partial f_d/\partial d \end{bmatrix} \quad (12)$$

Table 1: Material properties.

Property	Unreduced PZT	Reduced PZT	Composite
Thickness (mm)	0.248	0.1330	0.1270
$E_1$ (GPa)	44.4	29.9	155.0
$E_2$ (GPa)	44.4	29.9	12.10
$\nu_{12}$	0.377	0.381	0.248
$G_{12}$ (GPa)	16.12	10.83	4.00
$\alpha_1$ ( $10^{-6}/^\circ\text{C}$ )	2.13	8.41	-0.0180
$\alpha_2$ ( $10^{-6}/^\circ\text{C}$ )	2.13	8.41	24.3
$d$ ( $10^{-12}$ m/V)	-190.0	-	-

If all the eigenvalues of the four-by-four matrix  $[C]$  are positive, then the equilibrium solution is stable. Otherwise the equilibrium solution is unstable.

## Numerical Results

The material properties assumed for the various constituents in the problem are given in Table 1. Here results will be presented for the case of composite layers added to only one side of the RAINBOW actuator. Empirical data suggest that there is little difference between the coefficients of thermal expansion of the reduced and unreduced materials at temperatures greater than the Curie temperature of the unreduced material, 340 °C. Therefore, it will be assumed that the out-of-plane deformations of the original RAINBOW wafer do not begin until it is cooled to 340 °C.

### Room-temperature shapes of RAINBOW

It is important to first discuss the shape characteristics of the original RAINBOW. This will put the results with composite layers into context. One of the most instructive ways to discuss the shape characteristics of the wafers, both with and without the composite layer, is shown in fig. 2, where the curvatures  $a$  and  $b$  (nondimensionalized and scaled) vs. temperature of a square ( $L_y/L_x = 1$ ) and quite thin ( $L_x/H = 100$ ) wafer with a reduced thickness to total thickness ratio ( $H_r/H$ ) of 0.35 are illustrated. The reduced layer is the bottom layer in fig. 1. The Curie temperature of 340 °C is to the right (off the scale) and at that temperature the curvatures are zero. As the temperature of the RAINBOW wafer is decreased from the Curie temperature, both curvatures become negative, and they are equal. The existence of equal curvatures in both the  $x$ - and  $y$ -directions means the shape is a dome. With a rectangular geometry, this may be difficult to detect. If the wafer was round instead of rectangular, the dome shape would be quite evident. In the context of fig. 1, with negative values for  $a$  and  $b$  the edges of the wafer are displaced downward relative to the center. The development of the dome shape with the negative curvatures continues until the temperature is decreased to the point identified by point  $B$ , a temperature of about 190 °C. At point  $B$  the temperature-curvature relationships branch, specifically, trifur-

cate. Along branch  $BC$ , point  $C$  being room temperature, the curvature in the  $x$ -direction decreases with decreasing temperature and approaches a small negative value. On the otherhand, the curvature in the  $y$ -direction becomes more negative. This represents the case of the wafer changing from the dome shape of the branch from 340 °C to point  $B$  and assuming a shape where one curvature is more dominant. The terminology near-cylindrical is used to describe the shape. Branch  $BD$  also represents a near-cylindrical shape at room temperature, but with a large negative curvature in the  $x$ -direction. Branch  $BE$  is a continuation of the dome behavior of the branch from 340 °C to point  $B$ . Interestingly, a stability analysis of the shapes represented by the various branches shows that all branches correspond to stable shapes except branch  $BE$ . Thus, as the wafer is being cooled from 340 °C, it takes on a dome shape until point  $B$ . Below that point the dome shape is unstable and the shape makes a transition to one of the two near-cylindrical shapes.

#### Room-temperature shapes with a composite layer

The branches in fig. 2 which begin at 177 °C (the vertical dotted line) represent the effect of adding a single 0° layer of composite to the upper surface of the RAINBOW wafer. As the temperature is decreased below 177 °C, the temperature-curvature relation deviates significantly from branches  $BC$ ,  $BD$ , and  $BE$ . The temperature-curvature relation with the addition of the composite layer is identified by branches  $C^*C_1$ ,  $D^*D_1$ , and  $E^*E_1$ , all of which are stable and similar in character. At room temperature the curvatures in the  $y$ -direction of these three branches are small and almost the same, and the curvatures in the  $x$ -direction are each negative and have a magnitude of approximately two. The addition of the composite layer has taken some of the ambiguity out of the final shape of the wafer, but at the expense of the curvature magnitude. Interestingly, the addition of the composite layer has stabilized the unstable branch.

#### Summary

This brief presentation has shown that multiple near-cylindrical processed shapes of rectangular RAINBOW actuators are predicted. The addition of a composite layer significantly alters the predicted shapes. Expanded details of a similar analysis can be found in [3].

#### Acknowledgements

The work reported on in this paper was accomplished while the authors were supported by Grant NCC-1-304 from the NASA-Langley Research Center. The support of the grant is deeply appreciated by both authors.

## References

1. G. H. Haertling, 1994. RAINBOW Ceramics - A New Type of Ultra High Displacement Actuator, *American Ceramic Society Bulletin*, 73 (1), 93-6.
2. M. W. Hyer, 1998. *Stress Analysis of Fiber-Reinforced Composite Materials*, WCB McGraw-Hill, New York.
3. M. W. Hyer, and A. Jilani, 1998. Predicting the Deformation Characteristics of Rectangular Unsymmetrically Laminated Piezoelectric Materials, *Smart Materials and Structures* (7): 784-91.

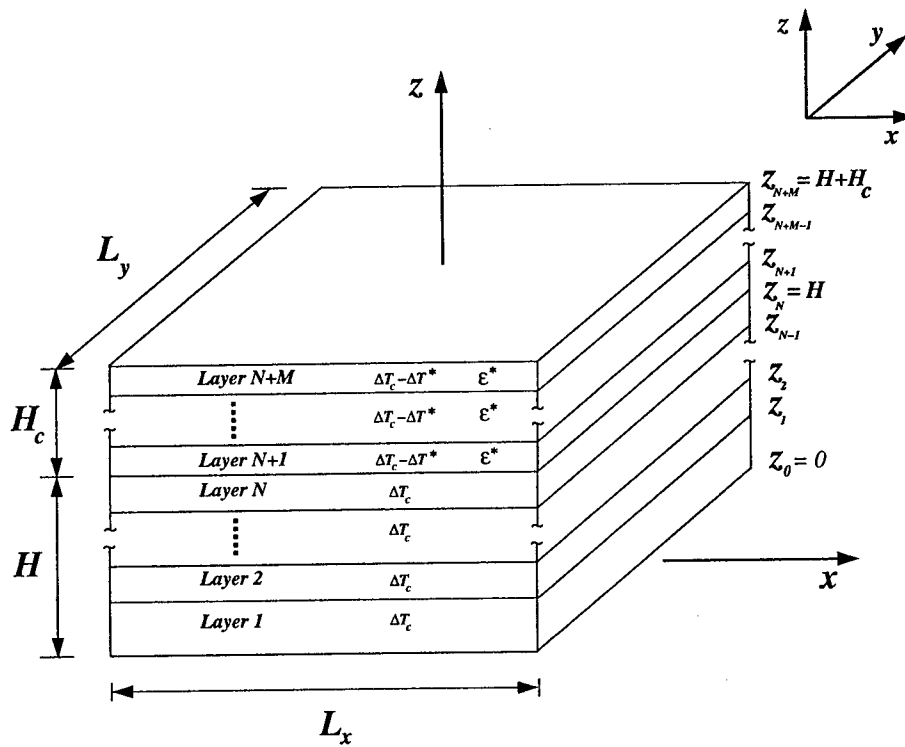


Fig. 1 Geometry, nomenclature, and coordinate system for analysis of actuator.

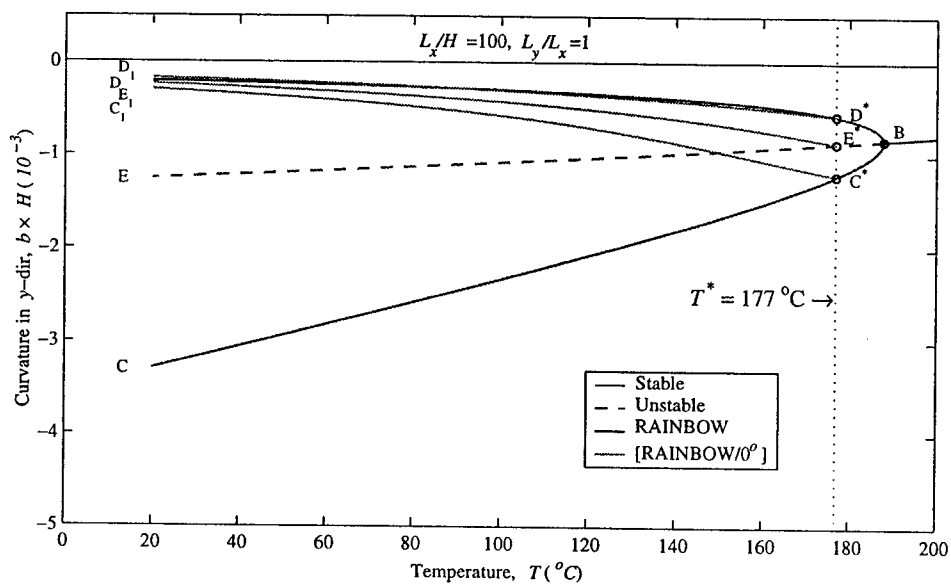
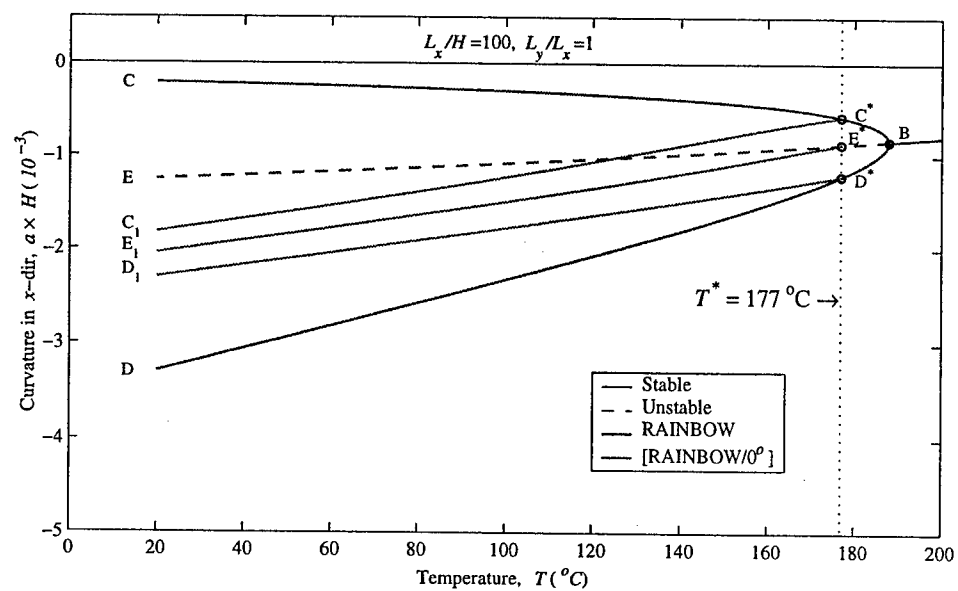


Fig. 2 Temperature-curvature relation of [RAINBOW/ $0^{\circ}$ ],  $L_y/L_x=1, L_x/H=100, H_r/H=0.35$ .



## **Summary Report of Structural Health Monitoring Project for Smart Composite Structure Systems**

Nobuo TAKEDA

### **Abstract**

The present R&D status of our structural health-monitoring group (SHMG) is summarized. Activities of the SHMG are conducted as a university-industry collaboration program at the University of Tokyo along with 10 research organizations. The research themes include: (1) development of high-performance sensor system technology with newly-developed sensors, (2) development of a damage detection and self-diagnosis system for structural integrity based on micro-mechanical damage identification, and (3) development of application technology for model structures. The sensor technology includes: (1) development of small diameter optical fiber sensor, (2) damage suppression in composite laminate systems with embedded shape-memory alloy films, and (3) development of maximum strain memory sensors with electrically conductive composite systems. The sensor output is correlated with the underlying damage evolution in structures such as aircrafts, satellites, high-speed trains and large-scale civil infrastructures.

### **Introduction**

Light-weight composite material systems have been progressively used as structural members in various applications. However, more use has been proposed as primary structural members under severe operating conditions. In such applications, durability evaluation and health monitoring systems are two key technologies to be investigated.

---

Nobuo Takeda, Department of Advanced Energy, Graduate School of Frontier Sciences, and Department of Aeronautics and Astronautics, School of Engineering, The University of Tokyo, 7-3-1 Hongo, Bunkyo-ku, Tokyo 113-8656, Japan, E-mail: [takeda@compmat.rcast.u-tokyo.ac.jp](mailto:takeda@compmat.rcast.u-tokyo.ac.jp)

The author has been proposing a so-called "experimental micro-mechanics of composites" to bridge the gap between material fabrication and macroscopic mechanical properties. Based on in-situ observation using optical, scanning electron, and/or scanning acoustic microscopes with loading devices, microscopic deformation and damage has been quantified. Moreover, theoretical models have been established for damage evolution. These efforts can provide the methodology for the durability evaluation or the damage tolerance design of composites [1-9].

In real structural applications, however, since the strains applied to the composite structures are random and uncertain, the real-time strain monitoring is necessary to predict the present damage status in composites based on the above durability evaluation method. Moreover, if the damage can be detected by using sensors, more reliable estimation of the damage status or the residual life can be made.

In Japan, a new "R&D for Smart Material/Structure System (SMSS)" project started in October 1998 as one of the Academic Institutions Centered Program supported by NEDO (New Energy and Industrial Technology Development Organization), Japan. This SMSS project includes four sub-themes: (1) structural health monitoring, (2) smart manufacturing, (3) active/adaptive structures, and (4) actuator materials development. The author acts as a group leader in the structural health monitoring group, which consists of 10 research organizations. Our structural health monitoring group (SHMG) is currently developing a health monitoring system, which conducts a real-time damage detection and self-diagnosis as well as damage control in light-weight composite structural systems.

The research themes include:

- (1) development of high-performance sensor system technology with newly-developed sensors,
- (2) development of a damage detection and self-diagnosis system for structural integrity based on micro-mechanical damage identification, and
- (3) development of application technology for model structures.

The sensor output is correlated with the underlying damage evolution in structures such as aircrafts, satellites, high-speed trains and large-scale civil infrastructures. The latest results in SHMG research efforts are reported for each research theme.

#### **Detection of Transverse Cracks in CFRP Laminates with FBG Sensors – Univ. Tokyo**

Fiber Bragg Gating (FBG) optical fiber sensors have been developed to measure strain, temperature and so on, through the shift of the wavelength peak in the reflected

light. A uniform strain within the gage section (typically 10 mm) is normally assumed. When an FBG sensor is embedded in 0-degree ply to detect transverse cracks in a 90-degree ply, a non-uniform strain distribution due to the initiation and evolution of transverse cracks causes the wavelength distribution in the reflected light (Fig. 1) [10]. Figure 2 shows the stress and crack density as a function of strain measured by a strain gage and a FBG sensor. A careful examination of the wavelength distribution can be used to detect the evolution of transverse cracks in composite laminates (Fig. 3). With increasing transverse crack density, the shape of the reflection spectrum was distorted; the intensity of the highest peak became small, some peaks appeared around it, and the spectrum became broad. As the crack density was close to saturation, the spectrum became narrow again and the highest peak recovered its height. These experimental observations can be well explained by the theoretical prediction [10].

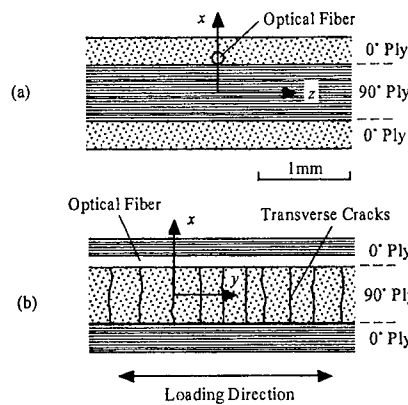


Fig. 1 Cross-sections of CFRP cross-ply laminate with an embedded FBG sensor (a) normal, and (b) parallel to loading

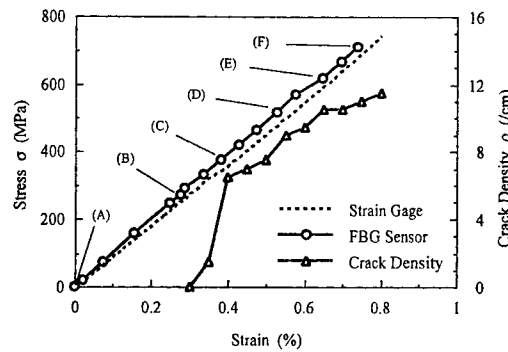


Fig. 2 Stress and crack density versus strain measured by strain gage and FBG sensor

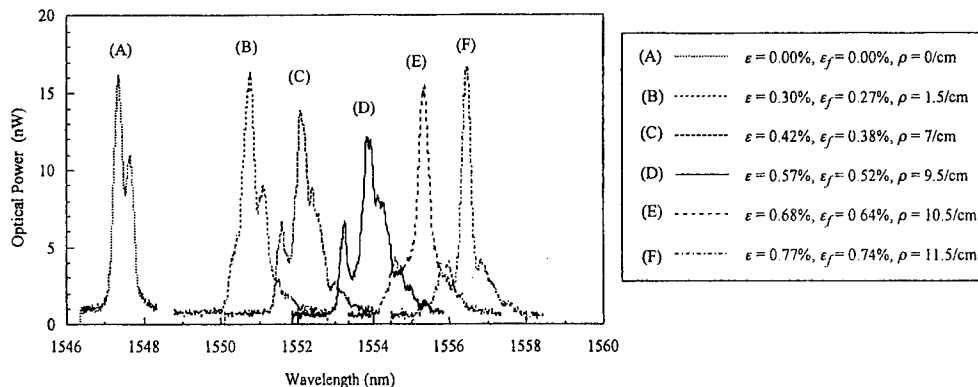


Fig. 3 Reflection spectra at various tensile strains corresponding to (A)-(F) in Fig. 2

### Development of Small-Diameter Optical Fiber Sensors – Hitachi Cable

The first notable accomplishment in our university-industry collaboration is the development of small-diameter optical fibers and the application to the FBG sensors. The developed optical fiber is with 40  $\mu\text{m}$  in cladding diameter and 52  $\mu\text{m}$  in polyimide coating diameter, which is easily embedded within one CFRP ply of 125  $\mu\text{m}$  in thickness. Such optical fibers have mechanical properties similar to those of conventional optical fibers with 125  $\mu\text{m}$  in cladding diameter and do not cause any reduction in strength of composites when embedded parallel to reinforcing fibers in laminas [11]. The developed FBG sensors also have optical sensitivities similar to those of conventional 125  $\mu\text{m}$ -cladding diameter FBG sensors. The polyimide coating is highly compatible with epoxy or other high-temperature polymer matrix of CFRP composites under high-temperature exposure during fabrication and also in high-temperature use.

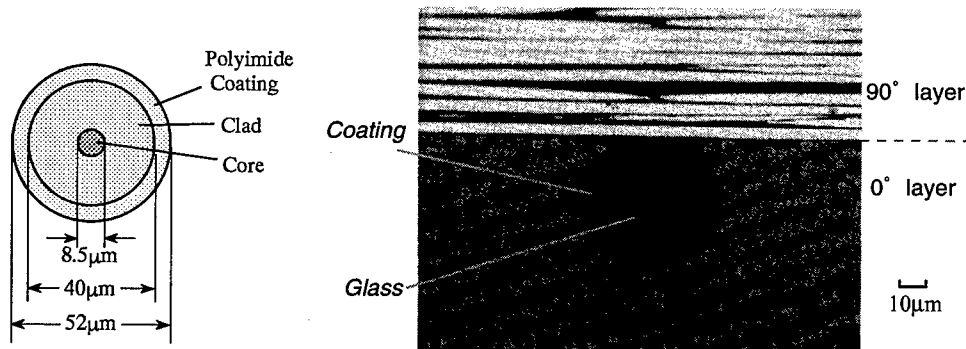


Fig. 4 Small-Diameter OFS      Fig. 5 Small-diameter optical fiber embedded within lamina

### Identification of Impact Damage Parameters in Composites Using Embedded Optical Fiber Sensors – Kawasaki Heavy Industries

Real-time detection of impact load on composite laminates was successfully made with embedded small-diameter optical fibers [12]. Figure 5 shows a small-diameter optical fiber embedded parallel to reinforcing carbon fibers in  $[0_2/90_2]_s$  cross-ply laminates. Instrumented Charpy impact tests were made, and the optical loss during impact was recorded as a function of time simultaneously with the impact load and the surface strains measured by strain gages (Fig. 6). The bending loss can be observed only during impact loading. The magnitude of optical loss is found to be proportional to the magnitude of the impact load.

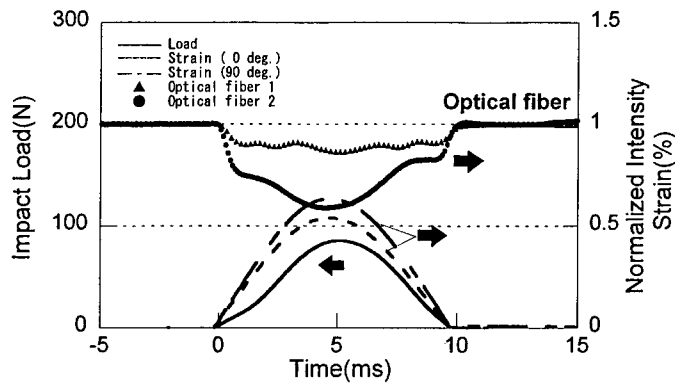


Fig. 6 Impact responses of normalized optical intensity, impact load and specimen surface strains in  $[0_2/90_2]_s$  cross-ply laminates

### Strain and Damage Monitoring of CFRP Space Satellite Structures Using Optical Fiber Sensors – Mitsubishi Electric

Honeycomb sandwich panels with thin CFRP face sheets are normally used as space satellite structures, and are subjected to severe thermal and mechanical environmental conditions. Low-cost fabrication is highly required for future satellites and a structural health monitoring system is essential during fabrication as well as in practical use [13]. Figure 7 shows a specimen for simple compression test of a honeycomb sandwich panel where a small-diameter optical fiber is embedded within CFRP face sheets. The change in optical intensity can be an excellent indicator of compression failure in such structures as shown in Fig. 8.

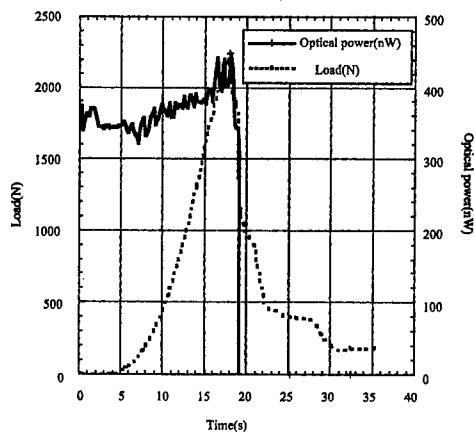
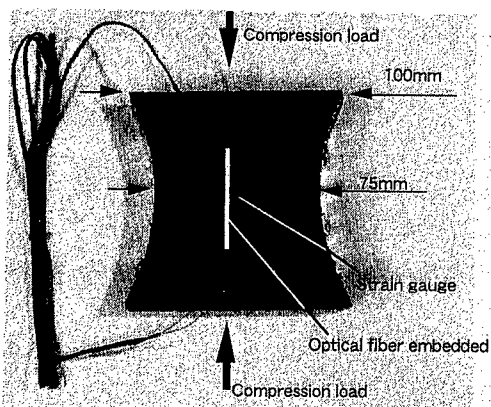


Fig. 7 Compression test of sandwich panel Fig. 8 Optical power loss by compression failure

## Damage Suppression and Control in CFRP Laminates with Embedded SMA Films – Fuji Heavy Industries

Shape memory alloy (SMA) films are embedded and used to suppress and control microscopic damages in CFRP laminates such as transverse cracks and delamination [14]. Improvement of interlaminar shear strength (ILSS) between SMA films and CFRP laminas has been investigated using sputtering, sol-gel, ion-plating and anodic-oxidation. A high ILSS was obtained similar to that of CFRP laminates alone. SMA films were stretched into the plastic deformation region. Then, they were embedded in CFRP laminates with the deformation kept by the fixture jig during the fabrication in order to introduce the shrinking stress in 90-degree plies. Such shrinking stresses were found to suppress the evolution of transverse cracks in cross-ply laminates.

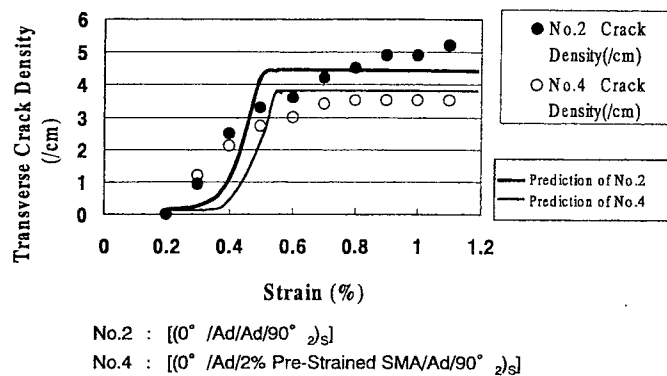


Fig. 9 Transverse crack density as a function of strain at room temperature for without (No. 2) and with (No. 4) embedded 2% pre-strained SMA films

## Quantitative Evaluation of Electric Properties of CFGFRP Hybrid Composites as a Maximum Strain Memory Sensors – Toray

Failure of low-elongation carbon fibers in CFGFRP hybrid composites under tensile loading causes the increase in electrical resistance and can be used to detect the maximum strain applied to composites after unloading. A systematic study was conducted to evaluate the relation between fiber failures and electrical resistance quantitatively [15].

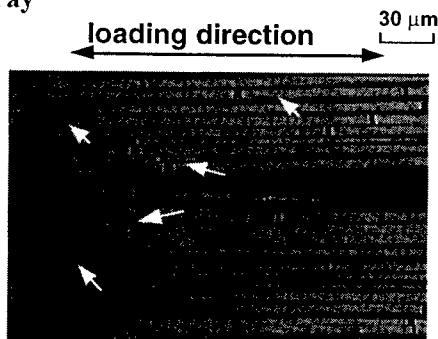


Fig. 10 Fiber failure in CFGFRP

Figure 10 shows the fiber failures observed in CFGFRP hybrid composites in tension. Based on such quantitative observations, a Monte Carlo simulation was conducted to predict the change in electrical resistance due to tensile strain and fiber failures. As shown in Fig. 11, a good agreement was obtained between the experimental results and the prediction.

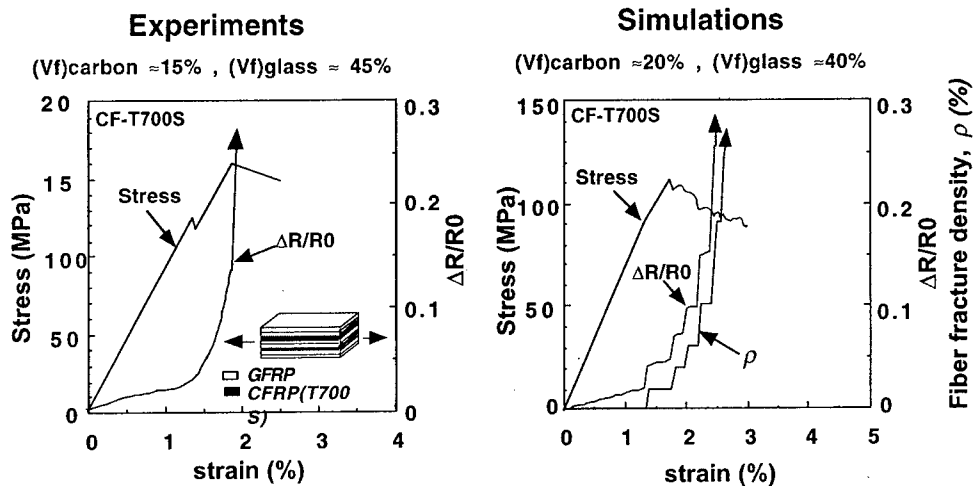


Fig. 11 Comparison between experimental results and prediction

### Self-Diagnosis Function of Electrically-Conductive FRP Containing Carbon Particles - JFCC

Carbon particles or flakes were dispersed into the epoxy matrix to introduce the high electrical conductivity in glass fiber unidirectional or textile composites [16].

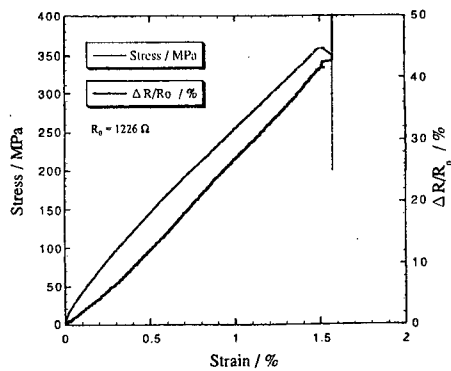


Fig. 11 Electrical resistance and stress vs. strain

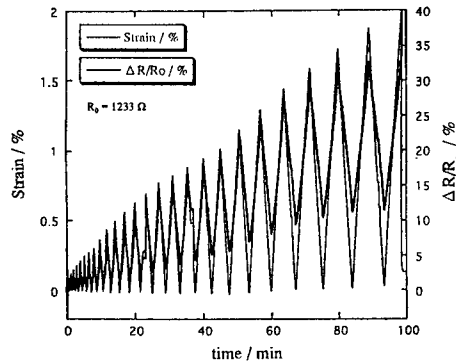


Fig. 12 Maximum and residual resistance

Compared with CFGFRP hybrid composites, higher sensitivity could be obtained. Moreover, a linear resistance change due to tensile strain was achieved in a wider strain range, as shown in Fig. 12. The residual resistance after unloading increased with increasing applied maximum strain. This composite has an appropriate self-diagnosis function as a low-cost sensor to be embedded in concrete infrastructures.

### **Impact Damage Monitoring of Composite Structures Using Integrated Acoustic Emission (AE) Sensor Network – Aerospatiale Matra**

An integrated AE network system is being developed for practical industrial use in aircraft structures [17]. A Learning by Experience approach was developed to assess the AE behavior of a composite structure. The principle is to generate artificial AE events due to impact loading at several arbitrary points on the test specimen (Fig. 13). Recording the acquired waveform parameters enables the system to learn the structure. Then, the system can receive real AE events upon impact in real-time in order to estimate the impact amplitude and to make an accurate localization of the source of impact (Fig. 14).

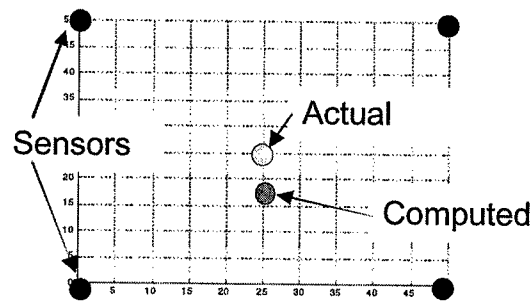


Fig. 13 Specimen and AE event generator    Fig. 14 Interpolation and localization of impact

Due to lack of space, only titles are cited for three other research themes :

- (1) **Integrated Global and Local Strain Measurement Using Distributed BOTDR (Brillouin Optical Time Domain Reflectmetry) and FBG Sensors – Mitsubishi Heavy Industries** : Improvement of spatial resolution, temperature compensation and dynamic strain measurement are conducted. Integrated BOTDR and FBG strain measurement systems are being made for aerospace structures [18].



**(2) Damage Detection of Transparent Composites Using Light Transmission and Reflection Measurement for High-Speed (Magrev) Train – Hitachi :**

Damages such as transverse cracks, delamination and fiber failures in semi-transparent alumina fiber reinforced epoxy composites are detected using light transmission and reflection technique under severe electro-magnetic and low-temperature conditions for load-supporting structures in Magrev trains [19].

**(3) Development of FBG Sensor Elements and Real-Time Monitoring Systems for Large-Scale Infrastructures – Shimizu :** A multiplex FBG sensor element network system is established for structural health monitoring of infrastructures. In particular, a real-time monitoring system is installed to record strains and deformations in hysterisis dampers for urban earthquake mitigation [20].

## Conclusions

The latest results were summarized in the structural health monitoring project for smart composite structure systems in Japan. Some original accomplishments were made based on the correlation studies on the sensor output and the underlying damage evolution in composites.

This research was conducted as a part of the “R&D for Smart Material/Structure System” Project within the Academic Institutions Centered Program supported by NEDO (New Energy and Industrial Technology Development Organization), Japan.

## References

1. N.Takeda and S.Ogihara, 1994. “In-situ Observation and Probabilistic Prediction of Microscopic Failure Process in CFRP Cross-ply Laminates”, *Comp. Sci. Tech.*, 52(2): 183-196.
2. N.Takeda and S.Ogihara, 199. “Initiation and Growth of Delamination from the Tips of Transverse Cracks in CFRP Cross-ply Laminate”, *Comp. Sci. Tech.*, 52(3): 309-318.
3. S.Ogihara and N.Takeda, 1995. “Interaction between Transverse Cracks and Delamination during Damage Progress in CFRP Cross-Ply Laminates”, *Comp. Sci. Tech.*, 54(4): 395-404.
4. N.Takeda, S.Ogihara and A.Kobayashi, 1995. “Microscopic Fatigue Damage Progress in CFRP Cross-Ply Laminate Composites”, *Composites*, 26(12): 859-868.
5. N.Takeda, T.Kosaka and Y.Okabe, 1996. “High-Resolution Ultrasonic Detection of Sub-surface Transverse Cracks in CFRP Laminates -Simulation and Experiments”, *Sci. Engr. Comp. Mater.*, 5(3/4): 169-184.
6. N.Takeda, H.Niizuma, S.Ogihara and A.Kobayashi, 1997. “Application of Micro-Line/

- Grid Methods to Temperature-Dependent Microscopic Deformation and Damage in CFRP Laminates", *Exp. Mech.*, 37(2): 182-187.
7. N.Takeda, S.Ogihara, S.Suzuki, and A.Kobayashi, 1998. "Evaluation of Microscopic Deformation in CFRP Laminates with Delamination by Micro-Grid Methods", *J. Comp. Mater.*, 32(1): 83-100.
  8. N.Takeda, S.Ogihara, N.Nakata, and A.Kobayashi, 1998. "Characterization of Microscopic Failure Process and Deformation in Glass/Nylon Composites by Micro-Grid Method", *Comp. Inter.*, 5(4): 305-321.
  9. N.Takeda and S.Ogihara, 1998. "Micromechanical Characterization of Local Deformation in Interlaminar-Toughened CFRP Laminates", *Composites: Part A*, 29A: 1545-1522.
  10. Y.Okabe, S.Yashiro, T.Kosaka and N.Takeda, 2000. "Detection of Transverse Cracks in Composites by Using Embedded FBG Sensors", *Proc. SPIE*, Vol. 3986, in press.
  11. K.Satori, Y.Ikeda, Y.Kurosawa, A.Hongo and N.Takeda, 2000. "Development of Small-Diameter Optical Fiber Sensors for Damage Detection in Composite Laminates", *Proc. SPIE*, Vol. 3986, in press.
  12. H.Tsutsui, T.Sanda, Y.Okabe and N.Takeda, 2000. "Real-Time Detection of Impact Load on Composite Laminates with Embedded Small-Diameter Optical Fiber", *Proc. SPIE*, Vol. 3986, in press.
  13. S.Kabashima, T.Ozaki and N.Takeda, 2000. "Damage Detection of Satellite Structures by Optical Fiber with Small Diameter", *Proc. SPIE*, Vol. 3986, in press.
  14. T.Ogisu, M.Nomura, N.Andou, J.Takaki, D.-Y.Song and N.Takeda, 2000. "Development of Damage Suppression System Using Embedded SMA Foil Sensor and Actuator", *Proc. SPIE*, Vol. 3986, in press.
  15. D.-Y.Song, N.Takeda, A.Kitano and K.Yoshioka, 2000. "Quantitative Evaluation of CFRP and CFGFRP Hybrid Composites as a Maximum Strain Memory Sensor", *Proc. SPIE*, Vol. 3986, in press.
  16. Y.Okuhara, S.-G.Shin, H.Matsubara, H.Yanagida and N.Takeda, 2000. "Self-Diagnosis Function of FRP Containing Electrically Conductive Phase", *Proc. SPIE*, Vol. 3986, in press.
  17. J.Saniger and L.Reithler, 1999. "Impact Assessment and Monitoring in Composite Structures with Acoustic Emission Sensors: A Learning by Experience Approach", *Proc. 1st Symp. Smart Mater.*, 119-122.
  18. T.Yamaura, Y.Inoue, H.Kino and K.Nagai, 1999. "Development of Structural Health Monitoring System Using Brillouin Optical Time Domain Reflectometer", *Proc. 2nd Int. Workshop on Structural Health Monitoring*, 533-542.
  19. H.Aoyama, K.Tanaka, H.Watanabe and N.Takeda, 1999. "Health Monitoring Technology for Alumina-Fiber-Reinforced Plastics", *Proc. 6th Japan Int. SAMPE Symp.*, 967-970.
  20. A.Mita, 1999. "Emerging Needs in Japan for Health Monitoring Technologies in Civil and Building Structures", *Proc. 2nd Int. Workshop on Structural Health Monitoring*, 56-67.

*Proceedings of the 9th US-Japan Conference on Composite Materials*

## **Design of Intelligent Composite Structures**

F.-K. Chang

---

F.K.Chang Department of Aeronautics and Astronautics, Stanford University, Stanford, CA94305-4035

## **Health Monitoring of Composite Structures Using Optical Fiber Sensors**

C. S. Hong, C. Y. Ryu, and J. W. Park

### **Abstract**

There has been a great interest in developing techniques for structural health monitoring of composite structures as well as infrastructural systems. This paper presents a technique for strain monitoring using fiber Bragg grating sensor, and damage detection using extrinsic Fabry-Perot sensor for composite materials and structures. An improved FBG sensor system using a wavelength-swept fiber laser (WSFL) has been applied for strain monitoring and EFPI sensor system utilizes signal processing scheme using wavelet for damage detection of composite structures. The real time monitoring of quasi-static and dynamic strains were demonstrated by the constructed FBG sensor system for investigation of the system performance. EFPI fiber optic sensor was also applied to the delaminated composite beams to monitor the buckling occurrence and delamination growth. The signals of the fiber optic sensor from buckling or delamination growth were quantitatively evaluated by short time Fourier transform.

### **Introduction**

Optical fiber sensors have shown a potential to serve real time health monitoring of the structures. They can be easily embedded or attached to composite structures and are not affected by the electro-magnetic field. Also, they have the flexibility of the sensor size ( $\mu\text{m}$ ~ $\text{km}$ ) and very highly sensitive. These advantages of OFS make it to be the potential solution for sensor systems of smart structures[1].

There are several types of OFS based on the intensity of light, interferometer and FBG methods [2-3]. Two types of OFS with the most promise at this time are interferometer sensors and FBG sensors. FBG sensor is easy to be multiplexed and has many advantages of linear response, free from spectral intensity, and absolute measurement, etc.

---

C. S. Hong, C. Y. Ryu and J. W. Park, Department of Aerospace Engineering, Korea Advanced Institute of Science and Technology, 373-1 Kusong-dong, Yusong-gu, Taejeon, Korea

FBG sensors based on the wavelength division multiplexing(WDM) technology attract considerable research interest and appear to be ideally suitable for structural health monitoring of infrastructures which require a large number of sensors. As the spectral signature renders the measurement free from intensity fluctuations, it guarantees reproducible measurements despite optical losses due to bending and/or connectors. Proper monitoring of measurands in FBG sensor systems requires accurate measurement of the Bragg center wavelength, and the ability to track rapid shifts of the wavelength especially in the structures under dynamic loading.

There are several reports using FBG sensors for dynamic strain response of the bridge [4-5]. However, these schemes have shown some drawbacks associated with low signal powers by using a narrow spectral slice from a broad source spectrum. Moreover, these results showed poor spectral resolution determined by the resolution of the tunable filter or the spectrometer itself. Recently, the interrogation technique based on the WSFL was developed and demonstrated [6]. This technique offers several attractive features such as high signal powers, and narrow instantaneous spectral line width which allow for a large number of individual sensors within the array. As an example problem, laminated composites with a delamination were under compression to monitor the buckling phenomena. The second part of this paper with EFPI sensor will presents (1) the detection of buckling and the delamination growth using a fiber optic sensor, and (2) the offer of signal processing technique to quantitatively evaluate the fiber optic signal when the buckling and delamination initiate. For that purpose, a compressive test was performed. The signal of fiber optic sensor during buckling onset or delamination growth was analyzed by short time Fourier transform and wavelet transform.

## A Fiber Bragg Grating Sensor System

### Theory of Strain Measurement

A fiber Bragg grating is a periodic, refractive index perturbation that is formed in the core of an optical fiber by exposure to an intense UV interference pattern. Gratings can be formed in telecommunications compatible fibers to operate at any wavelength by the holographic technique or a phase mask to form the fringes. We used FBG sensors fabricated by this phase mask technique.

The Bragg wavelength that is retroreflected at each grating sensor can be written as following Bragg condition.

$$\lambda_B = 2n_e \Lambda \quad (1)$$

Where  $\lambda_B$  is the Bragg wavelength,  $n_e$  is the effective index of the fiber core, and  $\Lambda$  is the grating pitch. The basic principle of operation used in a FBG based sensor system is to monitor the shift in wavelength of the returned "Bragg" signal

with the changes in measurand such as strain and temperature. The wavelength shift is caused by the physical elongation of the grating pitch of the FBG sensor. The Bragg wavelength shift caused by temperature or strain can be expressed as following simple relation,

$$\Delta\lambda_B = \lambda_B [(\alpha + \xi)\Delta T + (1 - p_e)\Delta\varepsilon] \quad (2)$$

$$p_e = \left(\frac{n^2}{2}\right) [p_{12} - \nu(p_{11} + p_{12})] \quad (3)$$

where  $\alpha$  is the thermal expansion coefficient,  $\xi$  is the thermo-optic coefficient,  $p_e (=0.225)$  is the photoelastic constant and  $p_{11}$ ,  $p_{12}$  are strain-optic tensors. If FBG sensors are in the same environmental temperature, we can ignore the temperature dependent part in Eqn. 2. Considering this condition, the strain can be measured by detecting the Bragg wavelength shift. Finally the relation between strain and Bragg wavelength shift is conclusively as follows.

$$\varepsilon = \frac{1}{(1 - p_e)} \frac{\Delta\lambda_B}{\lambda_B} \quad (4)$$

The accurate detection of Bragg wavelength shift is important to strain measurement. For the purpose, the WSFL is constructed and employed to the present FBG sensor system that is described in detail in reference [6].

Fig. 1(a) shows a schematic of the configuration of the WSFL and (b) the grating array with a reference FBG and a Fabry-Perot(F-P) etalon.

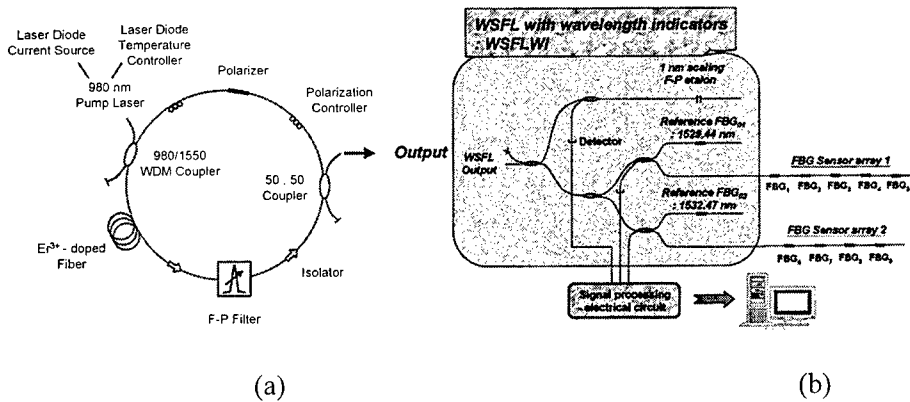


Figure 1 Configuration of (a) the wavelength-swept fiber laser and (b) the grating sensor array.

The signal processing program of strain measurement using FBG sensors is summarized in the reference [7]. We considered the program to be able to select adequate sampling frequency as to types of strains (static or dynamic).

#### Dynamic Test of the FBG Sensor System

To demonstrate dynamic strain measurement, we applied rectangularly and sinusoidally varying strain to FBG sensors. Two FBGs (each Bragg wavelength is 1547.84 nm and 1552.23 nm) were bonded with FM73 adhesive film made by CYNAMID Co. on the surface of two piezo ceramics. Material properties of piezo ceramic made by Fuji Co. (model : Fuji C-82) are  $E_1 = E_2 = 59 \text{ GPa}$ ,  $\nu_{12} = 0.34$ ,  $\rho = 7400 \text{ Kg/m}^3$ ,  $d_{31} = d_{32} = -260 \times 10^{-12} \text{ m/V}$  and its thickness is 0.4 mm. Piezo ceramics are modulated with square and sinusoidal waveform each other by a function generator. Fig. 6(a) is the signal detected from piezo ceramic and (b) is the plotting of strain measured by FBG sensor system. These results show good agreement.

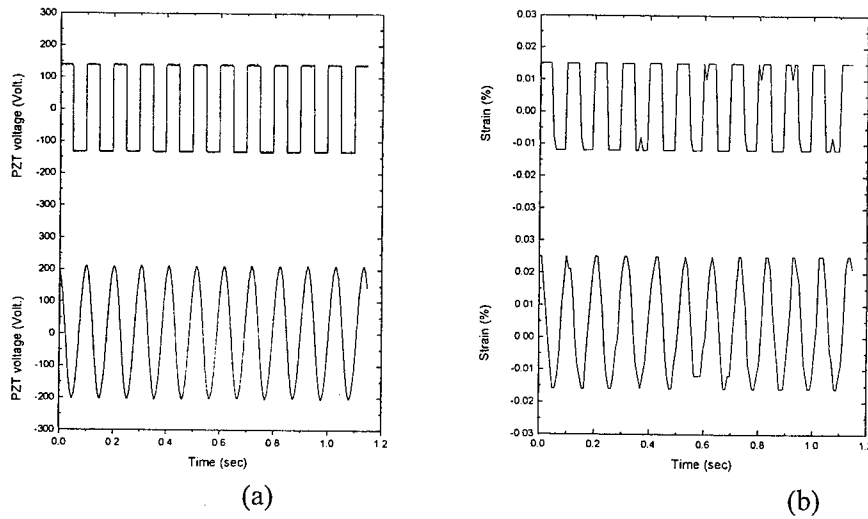


Figure 2 (a) Voltage signals to the piezo ceramic. (b) Strains measured by FBG sensor.

### Strain Measurements of Laminated Composite

The experiments of strain measurement of laminated composite panel under compressive axial loading were carried out using a FBG sensor system. The behavior of the composite panel is simultaneously monitored by measuring strains using multiplexed FBG sensor array. The composite panel was fabricated using graphite/epoxy prepreg, and its material properties are  $E_1 = 130 \text{ GPa}$ ,  $E_2 = E_3 = 10 \text{ GPa}$ ,  $G_{12} = G_{13} = 4.85 \text{ GPa}$ ,  $G_{23} = 3.62 \text{ GPa}$ ,  $\nu_{12} = \nu_{13} = 0.31$ ,  $\nu_{23} = 0.52$ ,  $X_T = 1933 \text{ MPa}$ ,  $X_C = 1051 \text{ MPa}$ ,  $Y_T = 51 \text{ MPa}$ ,  $Y_C = 141 \text{ MPa}$  and  $S = 61 \text{ MPa}$ . The geometry, dimensions and the boundary conditions of the composite panel are shown in Fig. 8. Three FBG sensors were bonded on the surface of the composite panel. The Bragg wavelengths are FBG1 = 1532.65 nm, FBG2 = 1546.01 nm and FBG3 = 1548.77 nm. In order to compare strains measured by FBG sensors with those by electric strain gauges(ESG), ESG1 and ESG2 were symmetrically bonded to FBG1 and FBG2. ESG3 was bonded to FBG3 on the back of the panel.

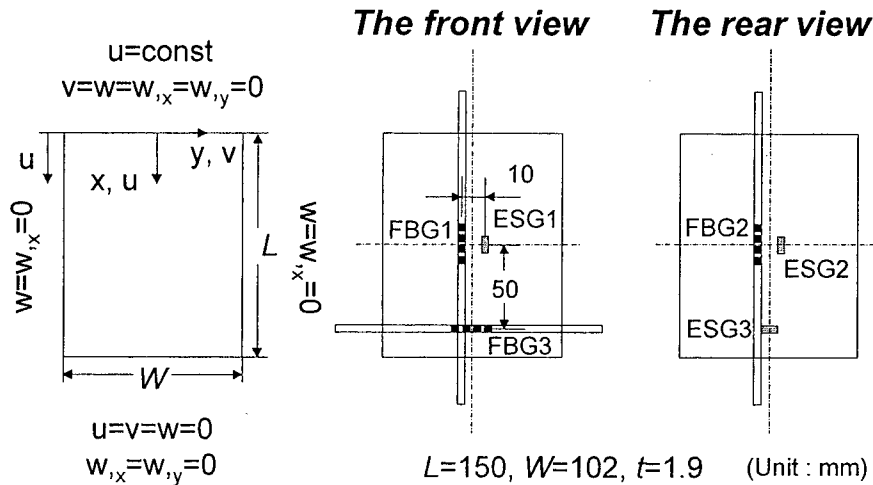


Figure 3 Configuration of the specimen.

The strains measured by FBG sensors are compared with those by ESGs. As shown in Fig. 10, the strains measured by FBG1,2 sensors and ESG1,2 show good agreement up to the final failure of the composite panel. FBG3 sensor and ESG3 were transversely bonded to compressive loading direction and on the other side of the composite panel, therefore they were under the different strain states. Differences between strain from FBG1 and strain from FBG2 before buckling are caused by misalignment in the test or imperfection of the specimen. Buckling stress determined by mean value of strains from FBG1 and FBG2 was 35 MPa. Fig. 11 shows strains of FBGs to the time, which are monitored real-timely during an experiment.



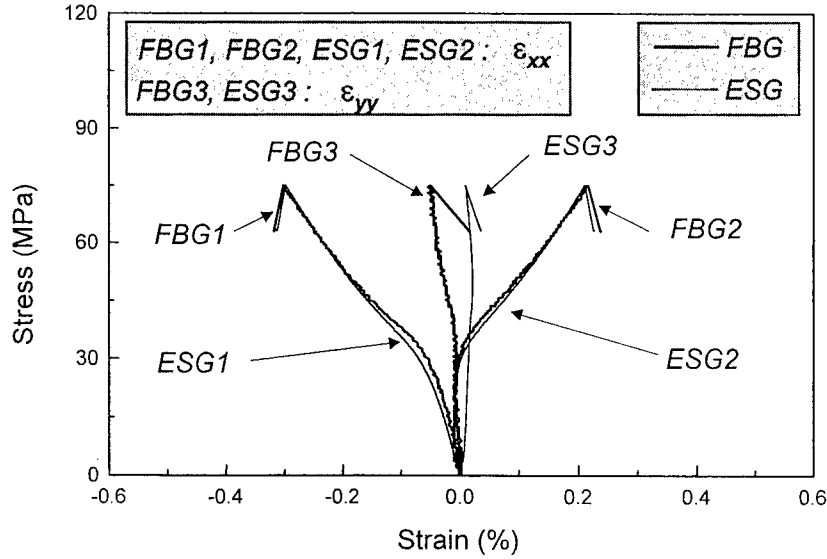


Figure 4 Comparison of strains measured by FBG and ESG.

#### Detection of Buckling and Delamination Growth

In this study, we discuss the detection of onset of buckling and the delamination growth using a fiber optic sensor. And a signal processing technique is introduced to quantitatively evaluate the fiber optic signal when the buckling and delamination initiate. For that purpose, a compressive test was performed. short time Fourier transform(STFT) is introduced in order to more accurately evaluate the signal of EFPI when buckling occurs or delamination grows. STFT is mainly to correct the deficiency of Fourier transform when dealing with non-stationary signals. The STFT of a signal  $f(t)$  is defined as follows:

$$STFT(\tau, \omega) = \int_{-\infty}^{+\infty} f(t)g(t-\tau)e^{-i\omega t} dt \quad (7)$$

The result can be interpreted as the Fourier transform of the signal  $f(t)$  windowed by a function  $g(t)$  around time  $\tau$ . STFT gives more accurate information about the time and frequency domain at the same time.

The delaminated specimens were made of graphite/epoxy prepreg (HFG Co., CU-125 NS). Teflon film was used to form the delamination and inserted into the mid-plane of the specimen. The specimen. 'a' is the length of delamination. 'L<sub>s</sub>' is the length of the test section in the specimen. In the case of the surface-attached, the

stacking sequence of the specimen was  $[0_8//0_8]_T$  where  $//$  means the position of delamination. Figure 10 (a) is the signals of the specimen with surface-attached EFPI and  $\bar{a} = 0.5$  up to failure. In this specimen, buckling occurred at  $u \cong 0.15 \text{ mm}$ . The first event of delamination growth occurred at  $u \cong 1.05 \text{ mm}$  and delamination gradually grew to  $u \cong 1.6 \text{ mm}$ . The second event occurred at  $u \cong 4.2 \text{ mm}$ . Figure 10 (b) is the STFT of the EFPI signal. This two transforms gives us the information about buckling occurrence and delamination growth.

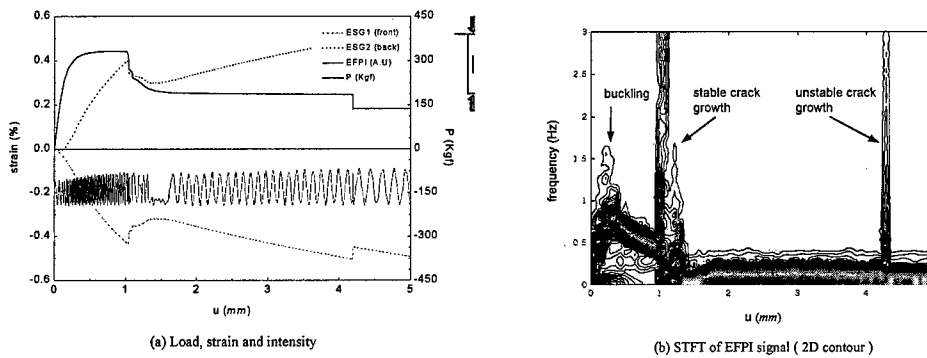


Figure 10. Signals of sensors, STFT of EFPI signal up to failure  
( $\bar{a}=0.5$ , surface attachment,  $[0_8//0_8]_T$ , continued)

## Conclusions

We constructed an improved FBG sensor system by using a WSFL. Dynamic strains were measured by the constructed FBG sensor system, which turns out to show the effective system. Three FBG sensors in an optical fiber were used to measure strains of the laminated composite panel under compressive axial loading with multiplexing technique. Experiments showed that the constructed FBG sensor system and the real-time signal processing program could successfully measure the strains of multi-points in composite laminates. Experiments showed that the constructed FBG sensor system and the real-time signal-processing program could successfully measure the strains of multi-points. The fiber optic sensor, EFPI, successfully detected the buckling occurrence and delamination growth of the delaminated composites. In addition, STFT can quantitatively evaluate the onset of buckling and delamination. These can be applied as a useful tool in the signal process of fiber optic sensor.

### Acknowledgements

The authors would like to thank the Ministry of Science and Technology and Critical Technology 21 program (Machinery Design Technology Enhancement) for their support and interest in this work.

### References

1. Udd, E., "Fiber Optic Smart Structures", *Proceedings of the IEEE*, Vol. 84, No. 1, 1996, pp. 60-67.
2. Kwon, I. B., Kim, C. G. and Hong, C. S., "Simultaneous Sensing of the Strain and Failure Instants of Composite Beams Using Fiber Optic Michelson Sensor", *Composites Science and Technology*, Vol. 57, 1997, pp. 1639-1651.
3. Park, J. W. and C. S. Hong, "Signal Characteristics in the Delaminated Composite Specimen with Fiber Optic Sensor," *Proceedings of the 5<sup>th</sup> Japan International SAMPE Symposium*, Tokyo, Japan, 1997, pp. 893-898.
4. Kodindouma, M. B. and Idriss, R. L., "An integrated sensing system for highway bridge monitoring," *Proceedings of SPIE*, Vol. 2719, 1996, pp.132-140.
5. Davis, M. A., Kersey, A. D., Berkoff, T. A., Jones, R. T. and Idriss, R. L., "Dynamic strain monitoring of an in-use interstate bridge using fiber Bragg grating sensors," *Proceedings of SPIE*, Vol. 3043, 1997, pp.87-95.
6. Yun, S. H., Richardson, D. J. and Kim, B. Y., "Interrogation of fiber grating sensor arrays with a wavelength-swept fiber laser", *Optics Letters*, Vol. 23, No. 11, 1998, pp. 843-845.
7. Hong, C. S., C. Y. Ryu, B. Y. Koo, C. G. Kim, and S. H. Yun, "Strain Monitoring of Smart Bridge Using Fiber Bragg Grating Sensor System with Wavelength-Swept Fiber Laser," *Proceedings of SPIE*, Vol. 3988, March 2000, paper no. 3988-40, Newport Beach, Ca.

# **Low Cost Composite Structures, I**

---

## **Design and Manufacturing Considerations In The Raytheon Premier I Business Jet**

**Ric Abbott**

### **Abstract**

During the design phase of the Premier I, Design Build Teams identified the optimum balance of cost and performance for each airframe component. Material cost, labor content, and assembly cost were weighed against the potential effects on aircraft range, payload, and landing distance.

The resulting wide range of design and manufacturing concepts include some new to commercial aviation and others which have been used historically. These include: hand laid composites, machine laid composites, resin transfer molded composites, machined aluminum, cast aluminum, machined titanium, and other combinations of traditional and new methods.

This paper describes the design and manufacturing considerations for major parts of the airframe, including:

- Fiber placed composite fuselage shells
- Wing assembly from machined aluminum parts
- Hybrid metal/composite empennage
- Cast aluminum emergency exit door
- Resin transfer molded flaps

### **Introduction**

The Premier I is a new business jet designed to bring higher performance to the entry level jet market. Major program objectives were to reduce cost to less than most business jets and to keep the weight below the FAA Part 23 single pilot maximum of 12,500 lb take off weight. Significant aircraft performance objectives were:

Cruise speed	530 mph
Maximum altitude	41,000 feet
Range with five passengers and pilot	1500 miles
Runway length	3100 feet

Trade studies were conducted for all major components during the preliminary design phase to reduce labor content while meeting structural performance targets of strength, stiffness, and durability. A large amount of the airframe is of composite (carbon fiber/epoxy), See Figure 1.

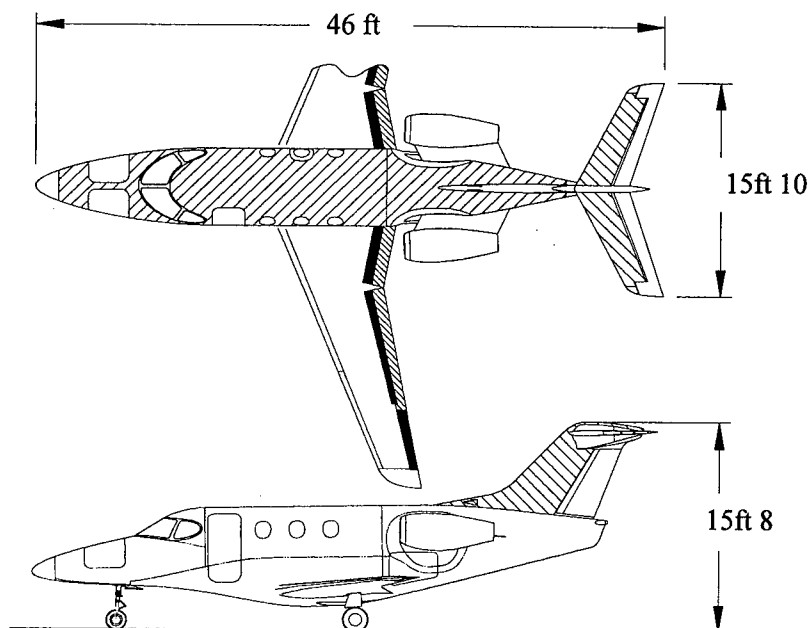


Figure 1, Premier I Composite Structure

Weight was traded for lower cost based on value of a pound of useful load, see table I. Reduced part count was found to be the key to reduced labor content.

Table I. Cost to Transport a Pound of Useful Load

USER	VEHICLE	PRICE \$	USEFUL LOAD LB	COST \$ per LB
ARMY	5 TON TRUCK	76,000	15,000	5
LAWYERS	BMW 540	54,000	1500	36
NAVY	SEAL BOAT	18 MILL	40,000	450
AIRLINE	B 767-300	95 MILL	160,000	594
AIR FORCE	C-17	202 MILL	310,000	650
CORPORATE	BIZ JET	6.2 MILL	7940	780
MARINES	V-22	104 MILL	32,000	3250

## Composite Structures Design and Manufacturing

The fuselage is built in two main sections, the forward pressure cabin and nose, and the unpressurized aft section. Both are fiber placed with prepreg tape either side of nomex honeycomb. See figures 2 and 3.



Figure 2 One Piece Forward Fuselage

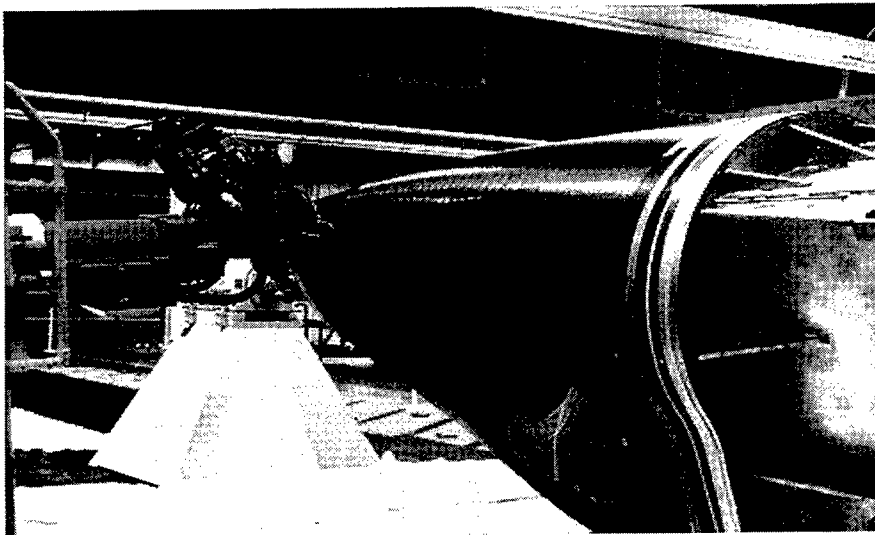


Figure 3 Aft Fuselage Fiber Placement

After fiber placement, the shells are transferred to female molds for autoclave cure. This method provides a load bearing shell without internal frames or ribs, in other words a true monocoque structure. By definition a single piece cure gives the lowest possible part count. The automated lay up contributes to a low labor content. A bonus benefit to the one piece cure concept is that these fuselage shells are extremely dimensionally repeatable. This reduces the cost of subsequent assembly operations. Interior structural installations are bench sub-assembled, mostly from machined aluminum parts (with pilot holes), and fit inside the shells with accuracy not seen in traditional riveted metal fuselages. The forward and aft sections are not joined until the installation of interior structures is complete. See figure 4.



Figure 4 Fuselage Assembly

The two sections are then connected with a structural splice using a combination of rivets and adhesive, but without external fasteners. External fasteners of monel or titanium present a paint and appearance problem and can be a source of increased damage in the event of a lightning strike. The aft pressure bulkhead is installed with an attachment angle (of carbon fiber) which sits directly onto the inside of the fuselage splice. The single piece pressure cabin has one further benefit in production; much less time is spent on pressure sealing as there are so few joints, rivets and therefore leak paths.

The aft pressure bulkhead is hand layed from prepreg tape and fabric and autoclave cured in conventional cure tools. The design is based on utilizing the fiber in a load carrying membrane without added frames or ribs. This approach produces a part with moderate labor content but the lowest possible weight. See figure 5,



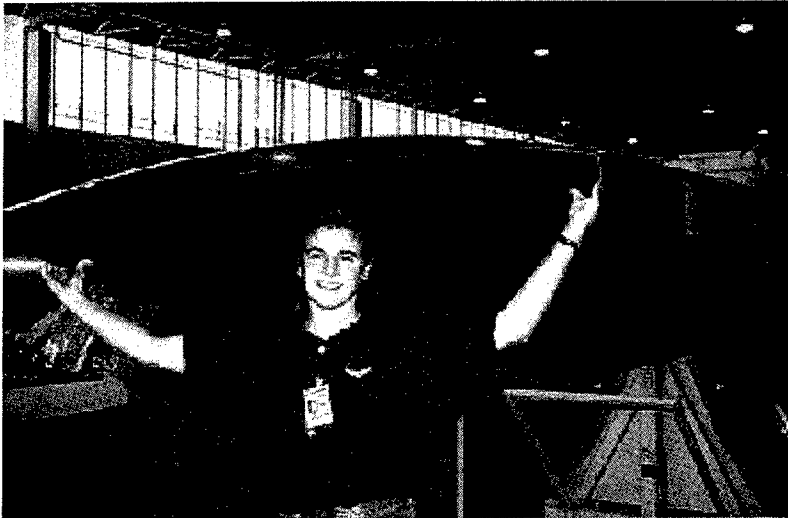


Figure 5, Aft Pressure Bulkhead

The wing flaps are built up from dry fiber fabric and braided carbon fiber sleeves. Mandrels over which the braids are positioned are placed into a mold, and surrounded with fabric which will form the skins. The mold is closed, a vacuum is applied, the resin is injected and held under high pressure while the cure is affected. This produces a single cure cycle flap body ready for the attachment of metal end ribs. These flaps are much lighter and have significantly less labor content than the metal flaps on a previous jet of similar size and performance. See figure 6.



Figure 6 Resin Transfer Molded Wing Flap

The empennage is a hybrid of metal and composite. The horizontal stabilizer is composite with the exception of the centerline rib, whereas the vertical stabilizer has metal spars and ribs with just the skin of composite.

### **Metallic Structures**

Wings for the Premier I are of riveted aluminium construction and are assembled from spars, ribs, and skins machined from 7475 alloy. This approach was chosen based on the known technology for manufacturing and design as opposed to that for a composite wing. The track record of manufacturing thin-skin, stringer-stiffened structure in composites did not give rise to confidence in the economics of such a concept. Economical primary structures have been built at Raytheon Aircraft but in most cases these were based on honeycomb load bearing skins. And in the case of a high performance wing with low thickness to chord ratio, honeycomb skins are unacceptable because of the penalty on fuel volume. The choice of 7475 aluminum alloy was based on a good blend of properties for machining, strength, fracture toughness, and corrosion resistance. The multi-spar load bearing skin design provides low part count, low labor content in assembly, simple wingtip-to-wingtip load paths, and a very simple wing to fuselage assembly. See figure 7 and 8.

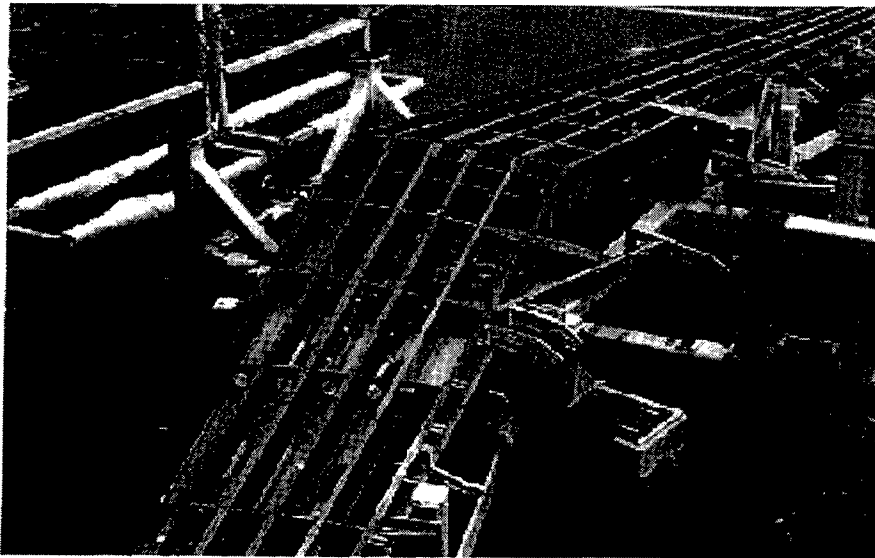


Figure 7 Low Part Count Wing Assembly

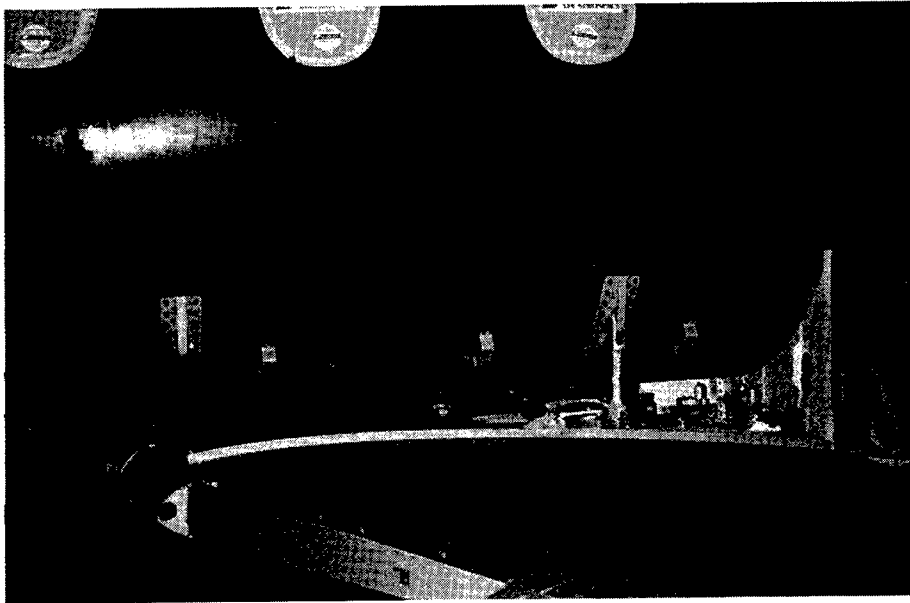


Figure 8 Simple Wing to Fuselage Assembly

The forward pressure bulkhead, and most of the fuselage interior structure are also machined from 7475 aluminum. These were based on economy and electrical properties. In a previous generation all-composite aircraft, considerable expense was incurred in the installation of composite interior parts to which were then added metallic straps and jumper cables in order to maintain a safe conductive path for lightning strike energy. As the avionics black boxes are carried in the nose section, many electrical and avionic entries are required through the forward pressure bulkhead into the cockpit area. The metallic forward bulkhead facilitates simple structural openings with appropriate reinforced areas as well as a convenient electrical ground path. The electrical ground path is carried through the cabin via the under-seat longerons and then continues through the aft fuselage to the engine pylons and stabilizers.

The elevator and rudder are of conventional riveted and bonded sheet aluminum. Also of traditional construction are the landing gears, utilizing forged and/or machined aluminum and some Titanium.

Many castings are used, mostly in the flight control system, including some of titanium. However the framework in the emergency exit door is comprised of the largest critical casting ever used at Raytheon Aircraft and represents a rigorous test case for modern casting technology. An outer skin of 2024 aluminum sheet is bonded and riveted to the cast D357 frame as a damage tolerance precaution. Although weight saving is limited by minimum casting wall thickness, this emergency exit is lighter and less labor intensive than a similar door in conventional riveted aluminum. See figure 9.



Figure 9 Cast Aluminum Emergency Exit Frame

### Conclusions

Team based studies to reduce part count and trade weight for cost will reduce production costs.

The Premier I program achieved 50% reduction in part count, 25% reduction in weight, and 25% reduction in selling price compared to a previous generation business jet.

Raytheon Aircraft Company  
PO Box 85  
Wichita KS 67201-0085

## **Development Program and a Status of Advanced Composite Design and Manufacturing Technology for Future Supersonic Transport**

H. Tamura

---

H. Tamura Japan Aircraft Development Corporation

## **Low Cost Manufacturing Approach for Composite Outer Wing of SST**

H.Tamura, K.Kosugi, S.Maekawa, Y.Hirose, T.Sana and T.Hatakeyama

### **Abstract**

Studies on low cost manufacturing processes for composite outer wing of SST (Super Sonic Transport) are undertaken from 1998. This paper presents the study plan and results of the first two years. An integral skin/stringer panel made of Gr/Bmi(Graphite/Bismaleimide) is set for structural concept. For automated fabrication of structural details, a FPM (Fiber-Placement Machine) is constructed and suitable lay-up conditions are established. To minimize distortions of large sized composite panel, distortion sources are listed up. Curing tests of simplified elements are conducted for evaluations of distortion sources. For the first step of assembly automation, an auto drilling device is constructed and evaluated.

### **Introduction**

The key technology for the realization of SST is to design and manufacture light weight structure with low cost. Materials to be used for SST should be heat resistant because the structures will be heated aerodynamically. Some heat resistant composites such as Gr/Bmi(Graphite/Bismaleimide) and Gr/Pi(Graphite/Polyimide) are the candidate materials for the SST structures. However, heat resistant composites are not easy material for manufacturing, so expensive tooling and skilled labor are required for current manufacturing technology.

A study to develop low cost manufacturing processes for the outer wing structure made of Gr/Bmi has been started 1998. The study is conducted by Kawasaki Heavy Industries Ltd.(KHI) with supervision of Japan Aircraft Development Corporation(JADC). This paper features current results on 1)composite lay-up automation, 2) low distortion fabrication of composite parts, and 3)drilling/assembly automation.

---

H.Tamura, Japan Aircraft Development Corporation, Toranomom Daiichi Bldg., 2-3, Toranomom 1-Chome, Minato-Ku Tokyo, 105-0001, Japan

K.Kosugi, S.Maekawa, Y.Hirose, T.Sana and T.Hatakeyama: Aerospace Division, Kawasaki Heavy Industries, Ltd., 1,Kawasaki-Cho,Kakamigahara City,Gifu-Pref. 504-8710, Japan

This program is a part of Advanced Composite Design & Manufacturing Technology (ACDMT) program funded by Ministry of International Trade and Industry of Japan(MITI) via R&D Institute of Metals and Composites for Future Industries(RIMCOF).

### Structural Concept of the Outer Wing

Figure 1 shows the structural concept of the outer wing. The structure consists of integrally stiffened panels, a front spar, a rear spar, 4 mid-spars and ribs. Ribs are located at every 600mm pitch. The cruise speed of the SST is assumed to be Mach 2.2 and Gr/Bmi can be used for the structural component materials of the outer wing. The upper and lower panels consist of skins and I-section stringers made of Gr/Bmi.

Preliminary sizing efforts of the integral skin-stringer panel was done using FEM based internal loads. The skin thickness and stringer shapes were determined to prevent panel from buckling and keep the applied strain within allowable. The stringers are located about every 200mm pitch and co-cured on the skins. Current analysis results indicate that the skin thickness will be 8 to 10 mm at the root of the outer wing.

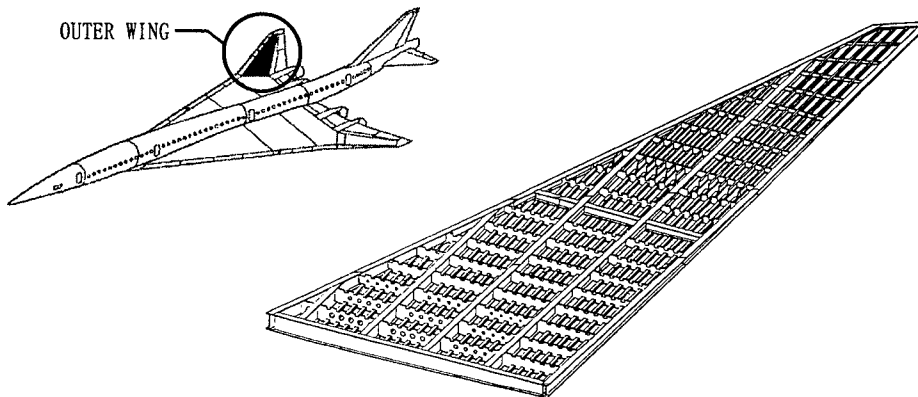


Figure 1 Structural Concept of the Outer Wing

### Composite Lay-up Automation - Fiber-Placement

As manual manufacturing processes, such as hand lay-up, result in a high cost, fabricating processes should be replaced to automation. Though ATL (Automated Tape-Laying) machines offer lowering the cost of pre-preg lay-up, application of ATL's are limited to flat or gentle single-curvature parts with large area, such as simple skins. For cost reduction of complex parts fabrication, development of the fiber-placement technology may be the best solution.

Figure 2 shows application area of FPM (Fiber-Placement Machine) and ATL on skin-stringer panel. To apply the FPM to local pad-up, such as circumference of access holes, reinforcement design methodology suitable for the machine are required. And, for applying the FPM to longitudinal parts like stringers, production methodology suitable for the machine are needed.

A FPM, including the fiber-placement head and the moving platform, has been constructed (Figure 3). The fiber-placement head put five tapes of 5mm width, and pressurize these tapes so as to lay-up is completed. To evaluate the FPM performances, conventional CFRP tapes were sliced to spools for the machine, and some trial parts including a flat panel with padded-up area and a triangular prism were fabricated. Spools of Gr/Bmi pre-preg for FPM were tried to manufacture and suitable lay-up conditions for the machine has been established. Next step, a sub-sized skin/stringer panel will be fabricated for further technology development. Also, trade-off study of the fabrication cost, including material cost and tooling cost, will be performed.

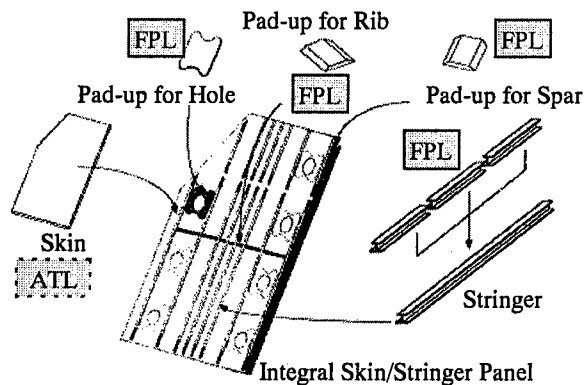


Figure 2 Application of FPM and ATL

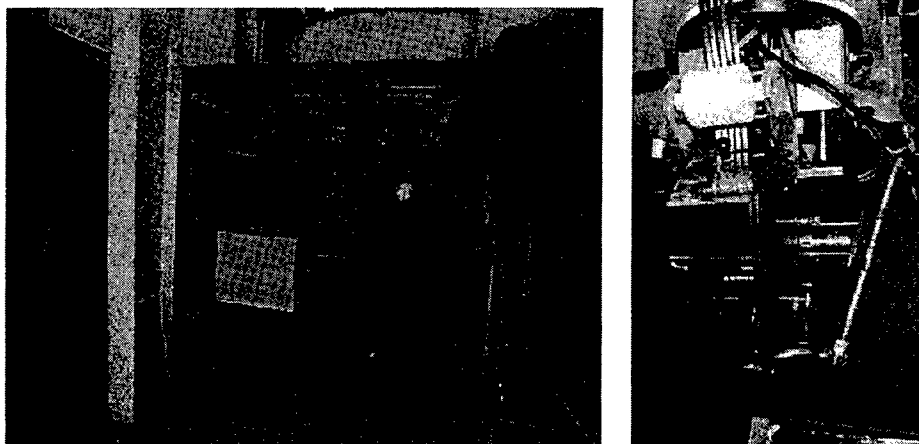


Figure 3 Constructed FPM



## Low Distortion Fabrication of Composite Parts

Lay-up mold tools for composite parts tends to be designed without consideration on parts distortion. But large parts of composites may be distorted after curing. If distortion of stiff parts cannot be corrected by finger-push at assembly, the mold tool should be re-worked to cancel the distortion. This is time consuming and expensive to remedy the deficiency through trial and error. The aims of the study are to enable distortion estimation and correcting mold surfaces, to reduce trial fabrications. This development is undertook in two approaches.

### Evaluation of Distortion Mechanism

Distortion mechanism should be researched to estimate distortion value. The thermal variation in the tool, difference of the CTE(Coefficients of Thermal Expansion) between the tool and the laminate, friction between the tool and the laminate can be the cause of distortions. And shrinkage of resin during cure can be one of the causes of distortions, for instance, the enclosed angle of channel or angle components are "spring-in".

Temperature variation in tool between the windward and the leeward point in the autoclave brings prepreg curing time lag. Temperature distribution of a large(8m length) tool at curing was measured. Maximum temperature gap was 40°C. The influence of this temperature variation was investigated by curing tests of simple specimens with simulated temperature distribution. The distortion after curing was measured and compared to that of specimen without temperature variation. The result was that temperature variation didn't take much effect to distortion.

Distortions caused by CTE difference between the molding tool and the laminate were investigated. Figure 4 shows an example of the test results. Long, simple specimens of various lay-ups were cured with 3 tips of base-plate materials, without caul plates. It is indicated that distortions are correlative with the CTE difference between near tool surface of the stacked pre-preg and the tool. Another test with caul plates indicates that CTE difference between the base plate and the caul plate results in larger distortion.

Spring-in angles of various lay-ups are shown in Table I. Except the all 0 degree lay-up, spring-in angles were about 1 degree for this Gr/Bmi material system.

### Low Deflection Tool Design

Molding tool itself deflects by thermal expansion and its own weight. Analysis of deflection and development of designing the high stiffness/low heat capacity tool are undertaken. With consideration about ease and cost of tool fabrication, most suitable material for large sized tool bed may be aluminum alloy. On the other side, caul plates may be made of CFRP for ease of tool fabrication and bagging operations. As indicated in the test results on distortions caused by CTE

difference, same material is hoped for caul plate and molding tool. So, one answer is that "slip plates" made of CFRP may inserted between aluminum tool bed and pre-pregs. These tooling concepts will be verified by analysis and tests in the next step of the study.

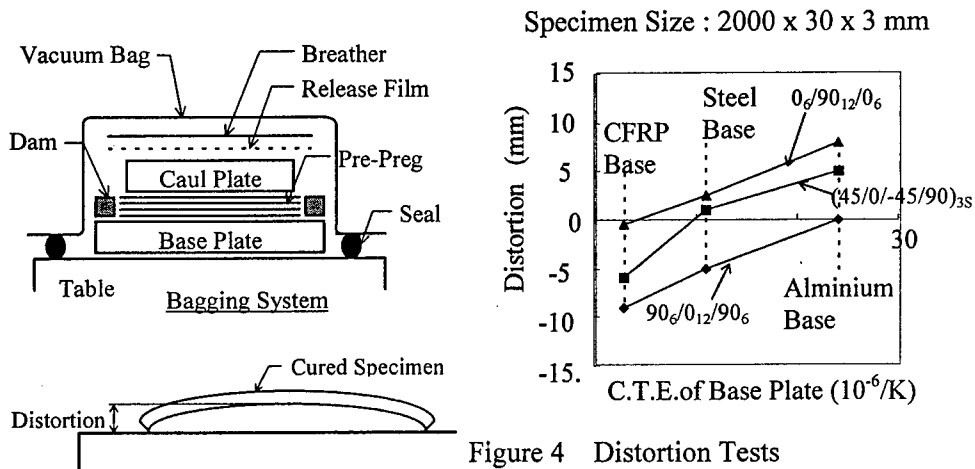


Figure 4 Distortion Tests  
- Mold Material and Lay-up

Table I Spring-in Test Results

Lay-up	Thickness	Tool Angle	Spring-in	
(0) <sub>16</sub>	2 mm	90 deg	- 1 deg 19'	
(0/90) <sub>4S</sub>			1 deg 05'	
(45/0/-45/90) <sub>2S</sub>			1 deg 09'	
(45/0/-45/90) <sub>4S</sub>	4 mm		1 deg 04'	
(45/0/-45/90) <sub>2S</sub>	2 mm	91 deg	1 deg 08'	

### Auto Drilling/Fastening

Conventional fastening process of a thick composite part with a metal part is complicated because they are drilled separately and reamed together. Also a conventional fastening machine is too huge to limit applicable structural shapes for accessibility restriction. For assembly automation, a machine to automate drilling thick composite and metal parts at the same time by one drill, and a small fastening machine to improve accessibility are needed. Furthermore these drilling and fastening machine will be integrated to establish systematic assembly process(Figure 5).

As the first step for developing the auto drilling/fastening system, a prototype drilling end-effector is developed(Figure 6). This end-effector is set on a industrial robot arm, and drill through holes for composite and metal joints. Drilling tests for both Gr/Bmi laminates and titanium alloy material are conducted, and automatic

through drilling conditions are established. It is confirmed that automatic drilling technology is effective for thick and hard-to-cut materials.

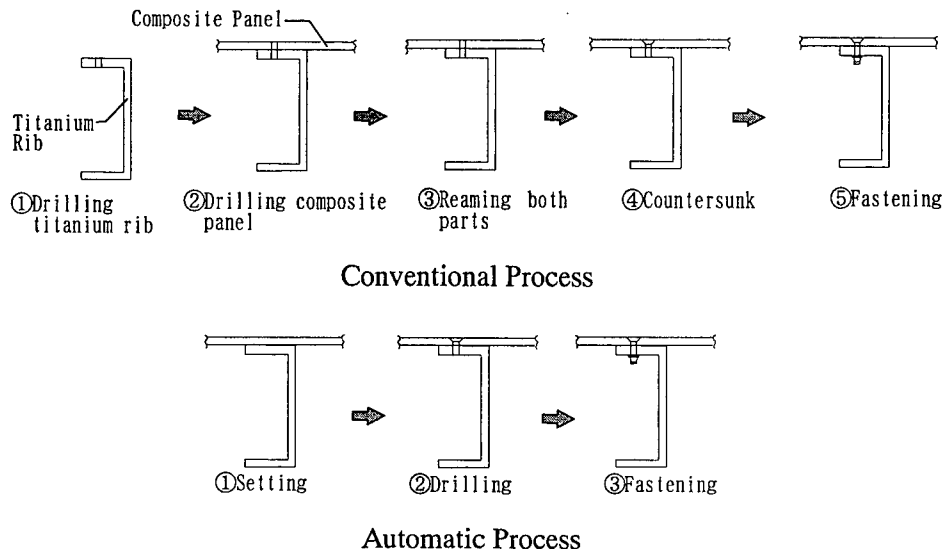


Figure 5 Auto Drilling/Fastening Concept

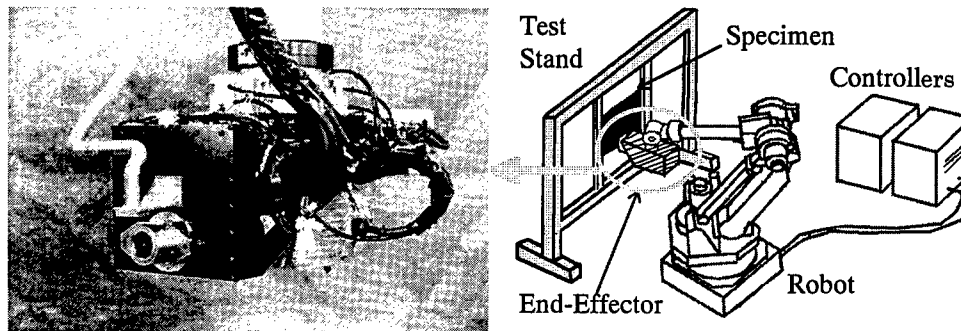


Figure 6 Auto Drilling End-Effector on the Robot Arm

### Demonstration and Evaluation Plan

The development of automated manufacturing processes and tooling concept for minimum distortion are to be demonstrated by the large (8m length) article. This article is a part of upper skin/stringer panel for the outer wing. Tooling concept for minimum distortion and automated manufacturing machine are evaluated by integral skin-stringer panel article.

- Checking local and general distortion.
- NDI and destructive inspections at typical structural details.
- Strength test of small panel cut from integral panel.
- Quality evaluation of structure assembled by auto drilling/fastening machine.

## Conclusions

This project has just started in 1998 and will solve technical issues on the way. The achievements of first two years (designated "Done"), and plans for next step of the research program (designated "Next") is summarized bellow. To reduce the expensive labor cost, fiber placement and the auto drilling/fastening technology will be established. To improve geometric qualities of composite parts, and to reduce the trial-and-error manner of composite tooling/fabrication, low distortion fabrication technology will be required. These manufacturing technologies will be evaluated through the application to trial manufacturing and testing of the large sized panel for the outer wing of SST.

### \*Fiber-Placement

Done A FPM(Fiber-Placement Machine) is constructed. Suitable lay-up conditions for Gr/Bmi pre-preg are established.

Next Trial fabrication tests of structural details will be conducted.

### \*Low Distortion Fabrication

Done Distortion sources are listed up and evaluated by curing tests of simplified elements.

Next Analytical method will be developed and evaluated by trial fabrication tests.

### \*Auto Drilling / Fastening

Done An auto drilling device is constructed and evaluated.

Next An auto fastening device will be constructed and evaluated. Then the system will be evaluated through trial assembly tests.

### \*Structural Article Fabrication and Evaluation

Done Preliminary design of the large sized panel is conducted. Evaluation test concept is developed.

Next The large sized panel will be fabricated for trial. Details taken from the panel will be evaluated by structural tests.

## Acknowledgments

The authors would like to thank RIMCOF, especially Dr. A.Sakamoto and Mr.M.Noda for professional and dedicated support.

## **Study on processability, composite properties and fiberplacement processing for high temp. composites**

Yasuhiro Yamaguchi, Hiroshi Mizuno,  
Hideki Horizono, Yoshihiro Sugiyama  
Yoshitaka Ishimuro, Kazuhiko Ishikiriya  
Hirobumi Tamura

### **Abstract**

In this study, curing mechanism and processability of candidate polyimide composite material for Supersonic Civil Transport(SCT) primary structure were evaluated. After considering manufacture process, mechanical and thermal properties were evaluated. This composite show excellent tough mechanical properties. Finally, automated fiber processing method were evaluated for the first stage development.

KEY WORDS: High temperature composites, Phenylethynyl terminated polyimide, fiberplacement, SCT

### **1. Introduction**

#### **1.1 Requirements for SCT structure**

Flight cruising speed of SCT is planed Mach 2.0~2.4, and to establish light weight SCT structure, high temperature composites are expected for primary structure. Then its surface temperature is estimated at 110~180°C, this max. temperature is over Aluminum available temperature.(Fig. 1)

And, its life cycle is considered 30,000 cycle, 60,000hr. These require composite structure long term durability at high temperature. Before we can apply high temperature composite for primary structure, there are some hurdles to cross. One is development of durable high temperature composite material. The other is development of low cost manufacturing process.

### **2. Evaluation of curing mechanism and processability**

#### **2.1 Curing mechanism evaluation**

Yasuhiro Yamaguchi, Hiroshi Mizuno, Hideki Horizono, Yoshihiro Sugiyama, Mitsubishi Heavy Industries, Ltd., 10, OYE-CHO, MINATO-KU, NAGOYA, 455-8515, JAPAN  
Yoshitaka Ishimuro, Kazuhiko Ishikiriya, Toray Research center, Co., 3-3-7, SONOYAMA, OTSU, SHIGA, 520-8567, JAPAN  
Hirobumi Tamura, Japan Aircraft Development Corporation, 1-2-3, TORANOMON, MINATO-KU, TOKYO, 105-0001, JAPAN

Phenylethynyl terminated polyimide composite (MR50K/PETI-5) are one of the candidate materials for SCT primary structure. PETI-5 are tough thermoset polyimide which have flexible chemical structure and of which cross linking density are low level, developed by NASA Langley research center. Then, PETI-5 shows excellent toughness, but  $T_g$  is not so high compared with other polyimide<sup>1)</sup>.

At first, curing mechanism of this material were evaluated to establish the autoclave process. Chemical reaction of PETI-5 is shown in Fig.2.

As shown in the Fig.2, solvent (N-methyl-2-pyrrolidone (NMP)) and product  $H_2O$  by imidization are generated during autoclave process. And, cross linking reaction follows after imidization. For establishment of autoclave process, it was key point to clear these imidization and cross linking reaction behavior, and gas generation behavior. At first, to clear the behavior, Fourier transform infrared spectroscopy (FT-IR) and Thermo Gravimetry- Gas Chromatography /Mass Spectrometry (TG-GC/MS) analysis were carried out. The results are shown in Fig.3, 4. From the analysis, following results were obtained.

- Almost 80% polyamic acid in this PETI-5 resin of the MR50K/PETI-5 prepreg has already reacted to imide oligomer. Thus, the amounts of the evolved gas (gaseous NMP, product  $H_2O$ ) during autoclave curing were estimated slight compared with insitu polymerized monomer reactant type polyimide like PMR-15.
- Almost product  $H_2O$  have already evolved until the temperature reach to  $250^\circ C$ .

To evaluate cross linking reaction in detail, Temperature Modulated Differential Scanning Calorimetry (TM-DSC) analysis which has features of capability to distinguish reversible and nonreversible reaction, was carried out for the prepreg. By this evaluation, endothermic which are correspond to crystal melt and exothermic which are correspond to cross linking reaction were able to find out. The results are shown in Fig.5, indicating that PETI-5 behaves as thermoplastic before cross linking, whereas it behaves as thermosetting resin after the melting because the cross linking take place. There are three stages regarding the cross linking reaction as follows.

- ① Non reaction stage
  - ② Low rate reaction stage: On this stage, imide oligomer start to melt, and the cross linking reaction take place.
  - ③ High rate reaction stage: On this stage, almost oligomer have already melted, and hence the cross linking reaction are accelerated with increasing temperature.
- From these findings, the autoclave profile was determined as shown in Fig.6.

## 2.2 Processability

Fabrication test of thick (128 ply) isotropic composite were conducted by the one shot curing. For thick composite fabrication like this, it was reported that for PMR-15, 2 or 3 shot curing were applied to prevent delamination during fabrication process<sup>2)</sup>.

On the other hand, very thick (128 ply) phenylethynyl terminated polyimide composite (MR50K/PETI-5) were able to fabricated by the one shot curing as shown in Fig.7. So, this material were considered to have excellent processability

caused by low level gas products.

### 3. Mechanical and Thermal properties

#### 3.1 Mechanical properties

Next, the mechanical properties of Unidirectional composites and Isotropic composites were evaluated. These results were shown in the Fig. 8,9 with another matrix resin composites (Nadic terminated polyimide(T800H/PMR-15) , Heat resistant epoxy).  $G_{Ic}$  and  $G_{IIc}$  were evaluated by Double Cantilever Beam test and Mixed Mode Flexure test respectively.

According to these results , the difference in tensile and compression strength were insignificant. These properties were considered to be clearly influenced by carbon fiber.

On the other hand, Fracture energy and Compression strength after impact of MR50K/PETI-5 showed significantly excellent properties. Particularly,  $G_{Ic}$  was higher value compared with another polyimide and epoxy composites. To confirm this high toughness, toughness of another ply pattern ( 0/90 ply pattern) laminate which was selected to prevent fiber bridging and nesting during crack propagation on the toughness test, was also evaluated. 0/90 composite also showed nearly equal high toughness.

These tough properties were considered to be caused by tough resin properties and interfacial properties between carbon fiber and matrix resin. As described before, PETI-5 have been introduced flexible chemical structure in its main structure. And its average molecular weight are controlled 5,000, so, cross linking density are low level. Then, PETI-5 resin have excellent toughness. This might be one reason for high toughness of MR50K/PETI-5 composite.

#### 3.2 Thermal properties

Thermal properties were important to apply this composite for fuselage structure. Thermal conductivity for 0 ° direction and perpendicular to in plane direction were evaluated. Results are shown in Fig.10 with the PMR-15's data.

As shown in figure, these composites showed similar value. However, MR50K/PETI-5's thermal conductivity were a few lower level compared with T800H/PMR-15. The reason of this phenomena are considered to be influenced by resin properties. It is difficult to measure resin's thermal properties, so, the reason of the thermal conductivity little difference was not so clear.

MR50K/PETI-5 composites showed similar order thermal conductivity as T800H/PMR-15. And the data of T800H/PMR-15 have been already applied to designing main structure for another vehicle. Thus, there are no problem from point of thermal properties that MR50K/PETI-5 composites are applied for structure.

### 4. Fiber placement processing

As described, development of low cost manufacturing process is key technology to establish SCT composite structure.

From this point of view, automated fiber processing method were evaluated for the first stage development. Automated Fiber Placement (AFP) machine were installed at our facility as shown in Fig.11. On this machine, narrow 8 tows are laid individually, thus, this machine can lay for complex shape parts.

To consider the lay up condition, viscosity behavior were evaluated as shown in Fig.12. MR50K/PETI-5 prepreg showed lowest viscosity at 120~130°C, and highest viscosity at 220~240°C. From this results, lay up condition, and gas torch temperature were determined.

Properties of cured composite laid by AFP are shown in Fig.13 and table.1.

Microstructure observed by optical microscope was similar to that by hand laid method.

And, inter laminar shear strength (ILSS) was a few higher compared with hand laid composite. This high ILSS may be caused by high compaction pressure and straightness during lay up process by AFP.

## 5. Summary

Processability and properties of MR50K/PETI-5 polyimide composites were evaluated, and the following have been clarified:

### (1) Curing mechanism

Imidization process and cross linking behavior were evaluated. From these results, autoclave profile was determined.

### (2) Processability

Thick (128 ply) MR50K/PETI-5 were able to fabricated by the one shot curing.

### (3) Mechanical properties

MR50K/PETI-5 composite showed excellent tough properties..

### (4) Automated fiber processing method were evaluated for the first stage

development. ILSS of the composite by AFP was similar to hand lay up method. From these results, It was cleared MR50K/PETI-5 have excellent processability, and tough mechanical properties.

### Acknowledgment:

This work was performed mostly under contract of the R&D Institute of Metals and Composites for Future Industries(RIMCOF).

## 6. References

1. P.M.Hergenrother, R.G.Bryant, B.J.Jensen, J.G. Smith, et.al., 1994. "Chemistry and properties of phenylethynyl terminated imide oligomers and their cured polymers", *39<sup>th</sup> International SAMPE symposium*, 961-968 •
2. Miki Morino, Hiroshi Mizuno, Tomohiro Ito, "Fabrication for thick polyimide composites", *Reinforced plastics*, 40(11)



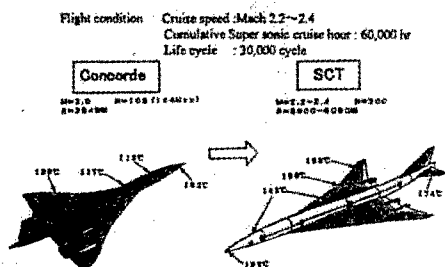


Figure 1 Requirements of composites for SCT structure

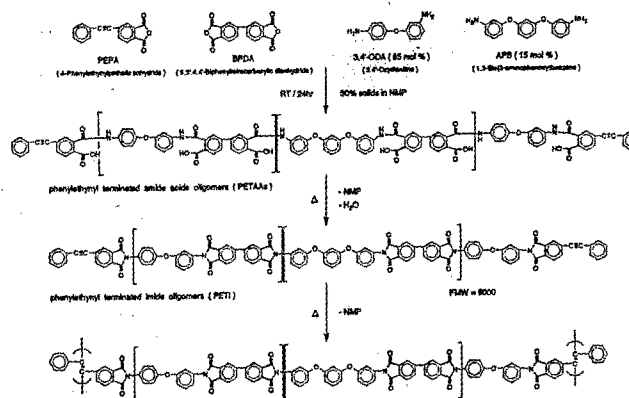


Figure 2 Chemical reaction of PETI-5

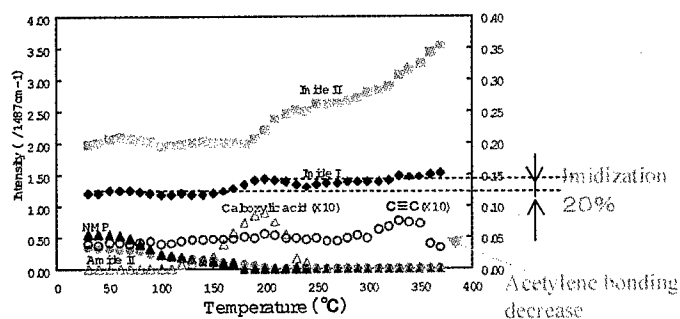


Figure 3 Chemical structure change

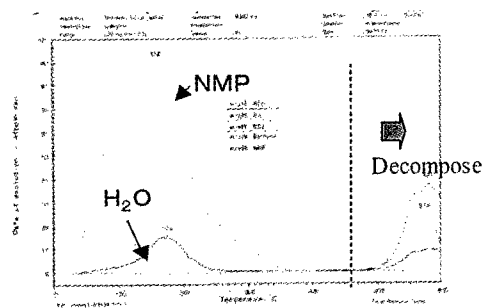
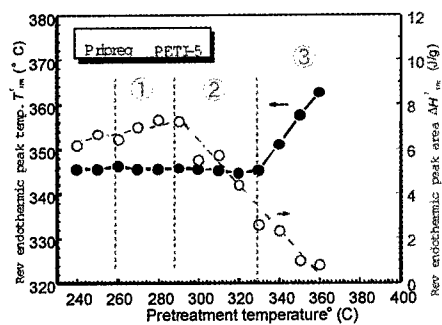
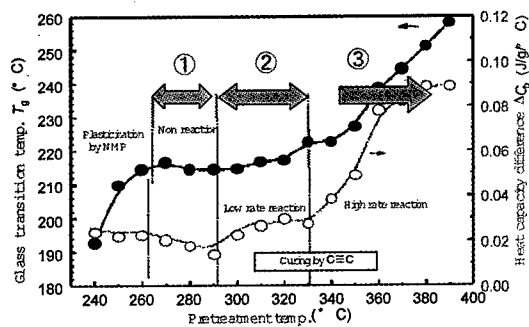


Figure 4 TG-GC/MS



Reversible endothermic peak behavior



Glass transition behavior

Figure 5 Temperature modulated DSC

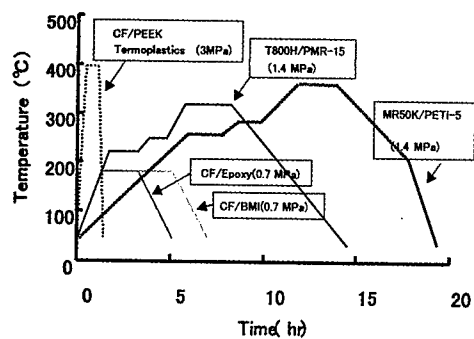


Figure 6 Autoclave profile

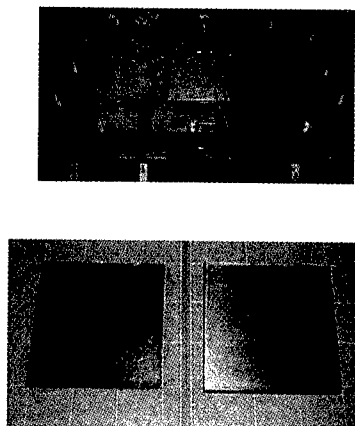


Figure 7 Bagging &amp; Manufactured composites

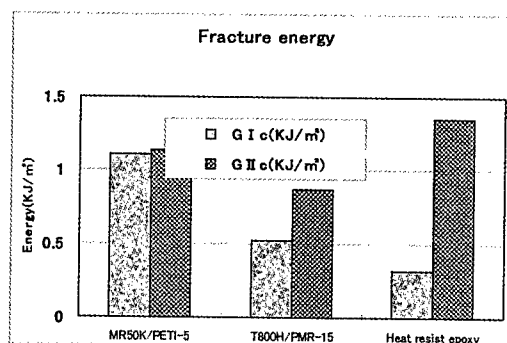
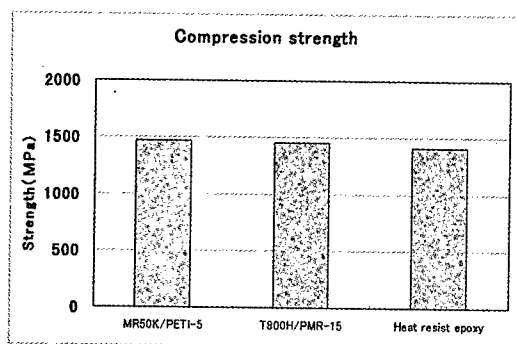
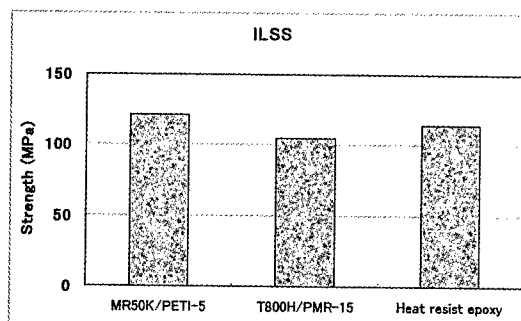
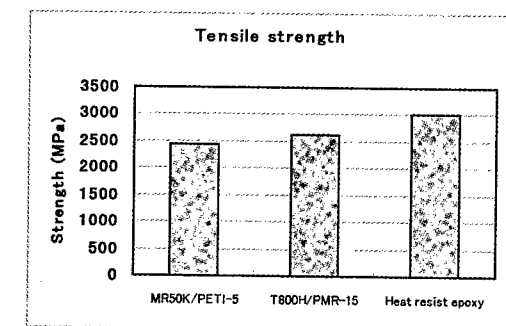


Figure 8 Mechanical properties of UD laminate

CF:Medium Modulus  
 $(\sigma_t: 5490 \text{ Mpa})$   
 $(E_t: 295 \text{ Gpa})$   
 RT/DRY  
 $n=3$

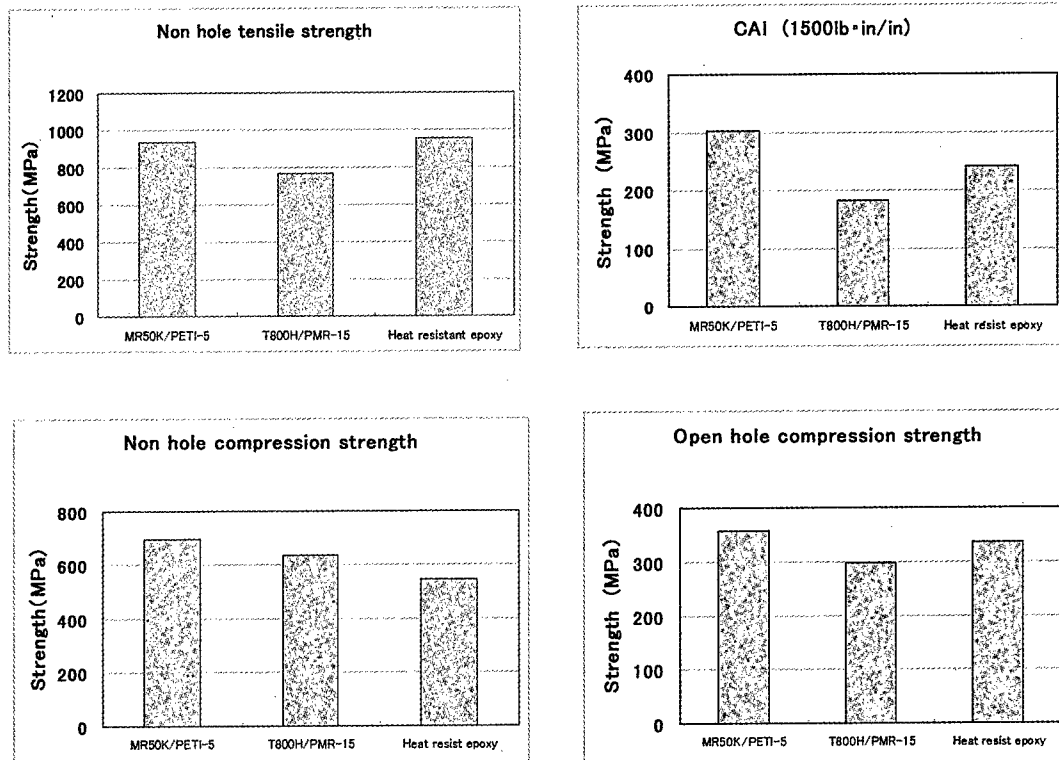


Figure 9 Mechanical properties of quasi isotropic laminate

CF:Medium Modulus  
 $(\sigma_t:5490\text{Mpa})$   
 $(E_t:295\text{Gpa})$   
 RT/DRY  
 $n=3$

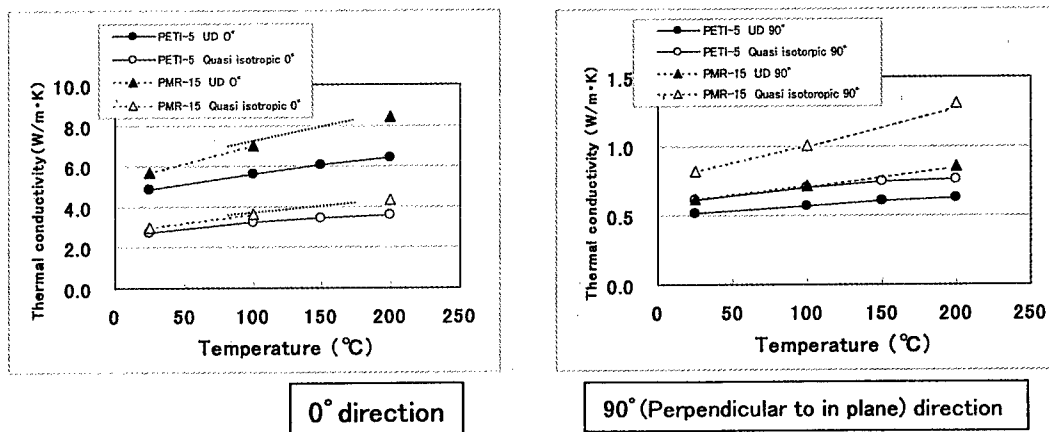


Figure 10 Influence of matrix resin on the Thermal conductivity

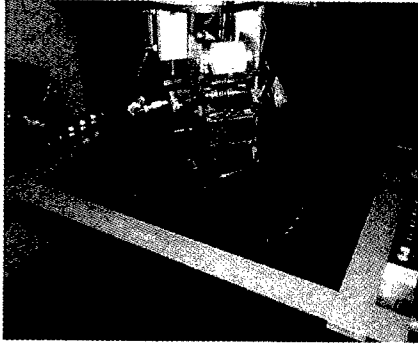


Figure 11 MR50K/PETI-5 Lay up by AFP

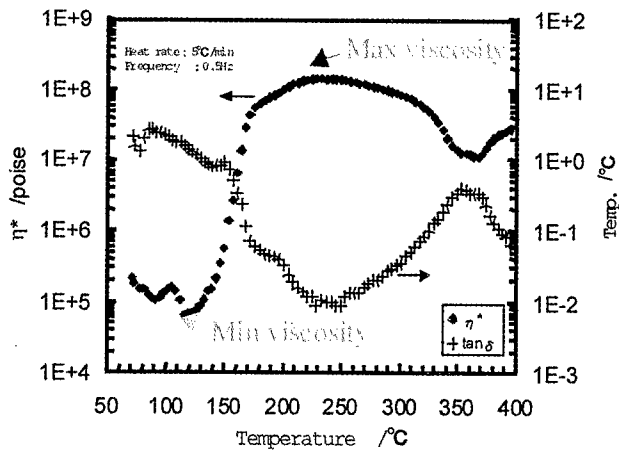


Figure 12 Viscosity change



Figure 13 Cross section optical microscopy

Table I Properties of MR50K/PETI-5 by AFP

T/P	Lay up pattern	Ply number	dimension (mm)	thickness (mm)	Vf (%)	Interlaminar shear strength (MPa)	
						AFP	Hand lay up
MR50K/PETI-5	[45/0/-45/90] <sub>2s</sub>	16	300 × 300	2.352	54.4	97.8	90.0

# **Low Cost Composite Structures, II**

---

## **Property Characterization in On-Line Consolidation of Thermoplastic Composites**

**Cathy Kuo**

Illinois Mathematics & Science Academy  
Aurora, Illinois, U.S.A.

**Selcuk I. Guceri and Chrisoph Pistor**

Mechanical Engineering  
University of Illinois at Chicago  
Chicago, IL

### **ABSTRACT**

Laser-assisted on-line consolidation of thermoplastic composites was previously developed for fabrication of composite components in a filament-winding configuration. In this technology, a laser beam is aimed at the consolidation point of the incoming tape and the substrate to heat and melt the thermoplastic matrix which is subsequently solidified under the pressure of consolidation roller. Investigations showed that highly localized melting/solidification process diminished the formation of residual stresses and produced high quality composite parts.

More recent studies extend this technology to winding of non-circular components which required continuous control of the laser power. This is achieved by developing a control system that adjusts the laser power based on the local consolidation speed and the nip-point temperature. A rastering capability is also introduced to be able to wind wide tapes by rastering the laser energy beam along the seam line.

This presentation reports on the recent developments in this novel technology and presents data on mechanical characterization of products which is achieved through a fixture to determine the internal yield pressure for circular rings. Microscopic characterization is also carried out to determine processing related material damage and quality of interlayer bonding.

## **A Study on the Induction Heating of Carbon Fiber Reinforced Thermoplastic Composites**

H.J.Kim, S.Yarlagadda and J.W.Gillespie, Jr.  
N.Shevchencko and B.K.Fink

### **Abstract**

Recent work in the literature has identified a new heating mechanism during induction processing of carbon thermoplastic prepreg stacks: contact resistance between fibers of adjacent plies. An experimental methodology has been developed to estimate the contact resistance through heating tests based on the properties of composite and geometry. Measured values indicate comparable resistance values at the contact region, compared to resistance in the fiber direction, for AS-4/PEI prepreg stacks under vacuum pressure. The measured values can serve as inputs for induction heating models and process models of carbon thermoplastic prepreg stacks.

### **Introduction**

Heat generation in carbon fiber reinforced thermoplastic composites, during induction processing, occurs due to induced eddy currents flowing along conductive loops in the composite, as shown in Figure 1. In each conductive loop, heating occurs wherever there is a voltage drop due to electrical resistance or impedance. The resultant heating is "volumetric" in nature, as it is an internal heat generation mechanism dependent on intrinsic properties of the composite.

The primary advantage of the induction heating of conductive fiber reinforced composites is the possibility of high volumetric heating rates, leading to higher throughput, compared to conventional manufacturing. Traditional manufacturing processes rely on conduction, convection or radiation heat transfer through the thickness of composite, requiring time for the composite to equilibrate at the desired process temperature. However, in the case of induction heating, volumetric heating occurs leading to higher heating rates and process velocities. In addition, induction heating is a multi-ply process, leading to further reductions in cycle times [1].

Research on induction heating of carbon fiber reinforced composites has looked at heating models for consolidated laminates, for the development of process models. Initial efforts on the induction heating of composites were carried out to investigate the possibility of induction based process for fusion bonding at the

---

H. J. Kim, S. Yarlagadda and J. W. Gillespie, Jr.  
Center for Composite Materials, University of Delaware, Newark, DE 19716, United States  
N. Shevchencko and B. K. Fink  
US Army Research Laboratory, Aberdeen Proving Ground, MD 21005, United States

interface of thermoplastic composites with nickel coated graphite prepreg or amorphous film between the composites [2-5].

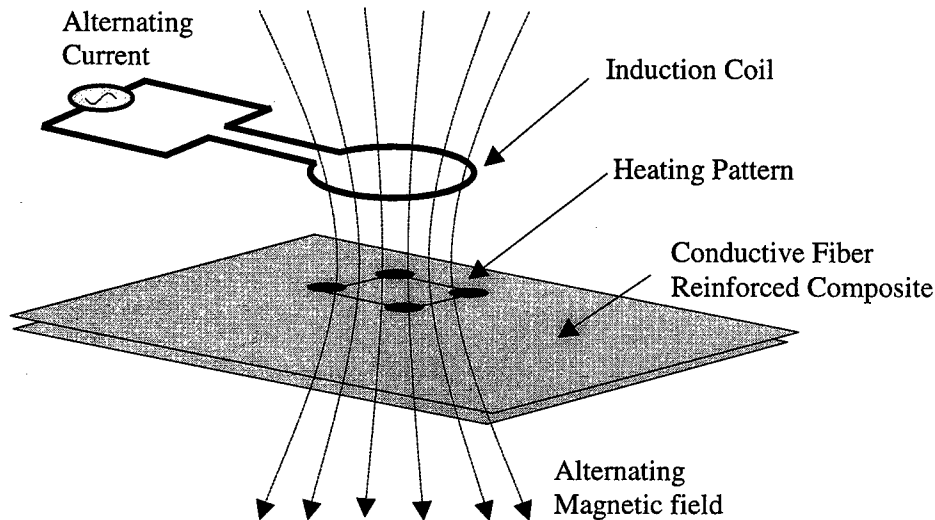


Figure 1 Schematic of the Induction Heating Process

Miller et al. [6, 7] proposed theoretical models for induction heating of carbon thermoplastic laminates based on the assumption that Joule heating along the carbon fiber was the primary heating mechanism, and good electrical contact between fibers of adjacent plies (through-thickness) was necessary for effective induction heating. They applied induction heating to production systems such as die-less forming.

On the contrary, Fink et al. [8, 9] proposed that the dominant heating mechanism is dielectric polymer heating at the regions (junctions) where fibers of adjacent plies overlap. The contention was that the fibers of adjacent plies are not in complete contact, but separated by a small polymer gap. They formulated models for in-plane heat generation and through-thickness heat generation and correlated them with experiments.

Recent work [10] on the induction heating of carbon/thermoplastic prepreg stacks has raised the possibility of a third heating mechanism: fiber contact resistance at junctions of adjacent plies. Experiments on induction heating of two-ply prepreg stacks have verified this concept. Preliminary results were presented for qualitative comparison with heating tests. The present work examines the third mechanism in more detail.

The focus of this work is on quantifying contact resistance values during induction heating of carbon thermoplastic prepreg stacks. The goal is to establish the relationship between heating and the process parameters, both qualitatively and quantitatively.



## Heating Mechanisms and Electrical Models

In a carbon fiber reinforced composite, there are two heating regions: fibers, and junctions (where fibers from adjacent plies overlap) as shown in Figure 2. Fibers can generate heat due to their intrinsic resistance and junctions can generate heat due to dielectric hysteresis if the fibers are separated by a small polymer gap, or contact resistance heating if the fibers are in direct contact.

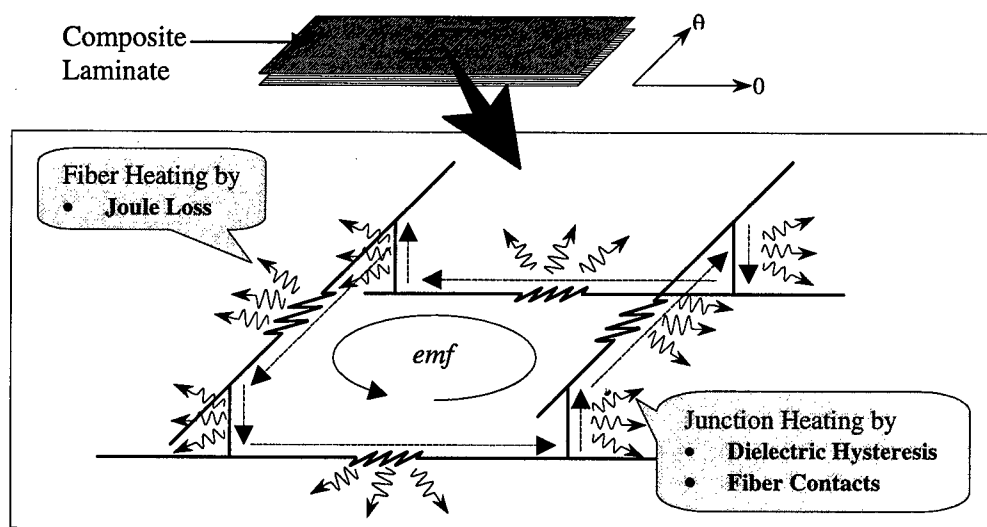


Figure 2 Schematic of the Fiber Heating and Junction Heating at Each Conductive Loop of the Cross-plyed or Angle-plyed Laminate [10]

### Discussion

In a consolidated laminate or a prepreg stack under pressure, all three mechanisms may occur to varying degrees depending on the prepreg quality and processing conditions. One can have regions where fibers of adjacent plies are in complete contact (junction resistance heating) or separated by a small polymer gap (dielectric hysteresis heating) along with Joule heating in the carbon fibers. Pressure and temperature dictate the degree of contact between adjacent plies and determine the through-thickness electrical behavior of the composite.

Of the three possible mechanisms, it is necessary to determine which mechanism is dominant under what conditions. A consolidated laminate can have a different dominant heating mechanism compared to an unconsolidated prepreg stack. Currents in the composite are induced only if there are conductive loops and the formation of loops is dependent on not only the ply properties (electrical conductivity), but also the through-thickness conductivity. Hence, different processing conditions can lead to different heating scenarios. A numerical model is being developed that incorporates all three heating mechanisms and will be used for

parametric studies and correlated with experiments. This work focuses on quantifying contact resistance values for use in the numerical model.

### Evaluation of Contact Resistance

The contact resistance value is a function of prepreg surface characteristics, process pressure and temperature. Figure 3 shows a schematic of a test setup to measure contact resistance as a function of process parameters and prepreg material.

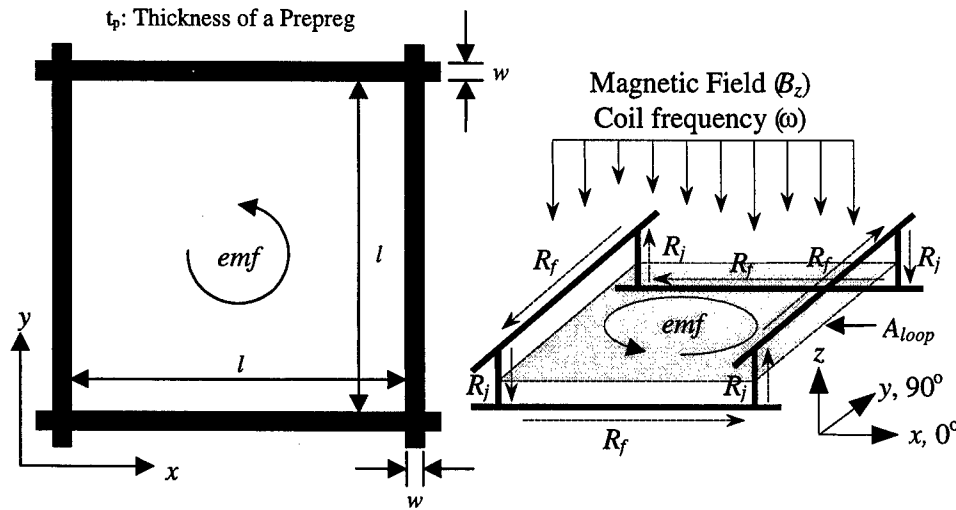


Figure 3 Schematic for the Heating Test with Prepreg Strips

The emf induced along the prepreg loop (Figure 3) is calculated from the magnetic field as shown in Eqns. (1, 2). It is assumed that loop and the coil are parallel in space, and therefore only the z-component of the magnetic field induces emf in the loop.

$$\vec{B} = \frac{\mu_0 I_c}{4\pi} \int \frac{\vec{r} \times d\vec{s}}{r^2} \quad (1)$$

$$emf = \omega A_{loop} B_z \quad (2)$$

The current in the loop ( $I$ ) is calculated based on Kirchhoff's Voltage Law as in Eqn. (3). Note that, since there are 4 strips and 4 junctions in the conductive loop, 8 resistor elements in total were used to implement the voltage conservation law.

$$emf = 4(R_f + R_j)I \quad \text{or} \quad I = \frac{emf}{4R_f(R_f + R_j)} \quad (3)$$

From Eqn. (3), the ratio of the heat generated in each strip ( $p_f$ ) and junction ( $p_j$ ) can be calculated by,

$$\frac{p_j}{p_f} = \frac{I^2 R_j}{I^2 R_f} = \frac{R_j}{R_f} \quad (4)$$

As seen in Figure 3, if the length of the composite strip is given, the resistance can be expressed as,

$$R_f = \rho_f \frac{l}{A_s} = \rho_f \frac{l}{v_f w_s t_s} \quad (5)$$

The contact resistance at the junction ( $R_j$ ) is denoted as  $\Lambda$  and is to be determined. Combining Eqn. (4) and (5), the heat generation ratio is,

$$\frac{p_j}{p_f} = \frac{R_j}{R_f} = \frac{\Lambda}{\rho_f} \left( \frac{v_f w_s t_s}{l} \right) \quad (6)$$

The volume occupied by each element (junction and prepreg strip) is,

$$V_f = w_s t_s l, \quad V_j = 2w_s^2 t_s, \quad \& \quad \frac{V_j}{V_f} = \frac{l}{2w_s} \quad (7)$$

Combining Eqn. (6) and (7), the ratio of heating intensity at the junction and composite strip can be expressed as,

$$\frac{p_j'''}{p_f'''} = \frac{p_j/V_j}{p_f/V_f} = \frac{\Lambda v_f t_s}{2\rho_f} \quad (8)$$

For small time scales, the measured rate of temperature change is a good approximation of the heating intensity of each element is shown in Eqn. (8). It is assumed that the volumetric heat capacity ( $\rho C_p$ ) is constant in each element.

$$\frac{\Delta T}{\Delta t} \approx \frac{p'''}{\rho C_p} \quad (9)$$

Based on measured rates of temperature change in each element, contact resistance at the junction can be estimated from:

$$\Lambda = \left( \frac{2\rho_f}{v_f t_s} \right) \frac{(\Delta T/\Delta t)_j}{(\Delta T/\Delta t)_f} \quad (10)$$

## Results and Discussion

Test material for strip heating test was AS-4/PEI carbon thermoplastic prepreg from Cytac Fiberite, with an effective fiber volume fraction of 60%. Table I list the relevant process parameters and material properties used in the study.

Table I Process Parameters and Material Properties for Strip Heating Tests

Input Parameter	Value
Coil Frequency ( $f$ )	2.38 MHz
Inner/Outer Diameter of Coil	6.35 cm (2.5"), 2.54 cm (1.0")
Coil-part Distance	3.81 cm (1.5")
Number of Turns	3
Fiber Diameter of AS-4 ( $d_f$ )	8 $\mu\text{m}$
Fiber Resistivity of AS-4 ( $\rho_f$ )	0.00153 $\Omega\text{-cm}$
Thickness of AS-4/PEI Prepreg	127 $\mu\text{m}$ (5 mil)
Width of Composite Strip ( $w_s$ )	3.175 mm (0.125")
Length of Composite Strip ( $l$ )	101.6 mm (4.0")

A 2.5 kW Lepel induction unit was used to generate the alternating magnetic field. Strips of AS-4/PEI prepreg were vacuum-bagged on a non-conductive base plate and positioned near a pancake coil and heated at constant power levels. The strip configuration is shown in Figure 3 and formed a [0/90°] loop. During the experiment, temperature at four junctions and four center positions of the composite strip were measured with an AGEMA Thermovision 900 Infrared camera. Figure 4 shows a typical heating pattern of the composite strip and J1-J4 and S1-S4 denote the positions where temperature measured during the experiments.

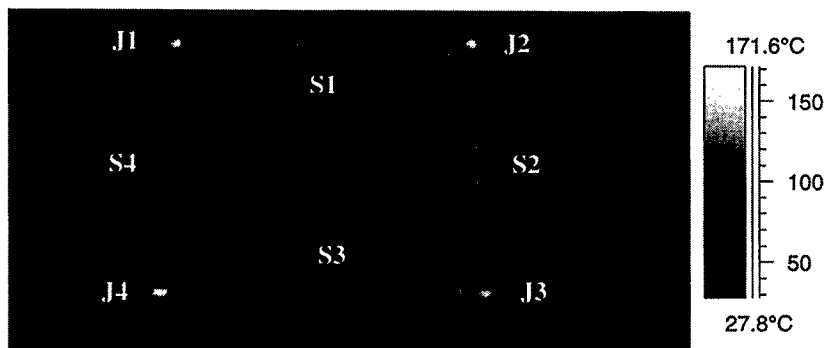


Figure 4 Typical Heating Pattern of Composite Strip and the Measuring Positions for Temperature

Heating experiments were carried out at 3 different induction power levels and fixed loop size (4" x 4") of the composite strips. The temperature measured was

averaged and Figure 5 shows the plot of the temperature change with time. In all the tests, the maximum heating temperature was maintained below  $T_g$  of PEI.

Figure 5 reiterates the dominance of junction heating for unconsolidated prepreg stacks. The time scales are short to minimize heat losses due to conduction, convection or radiation for calculation of heat generated in each element. The ratio of heating rates between the junction and the strip is approximately an order of magnitude and the deviation is reasonably small. Table II shows the ratios between junction heating and strips heating for different power levels.

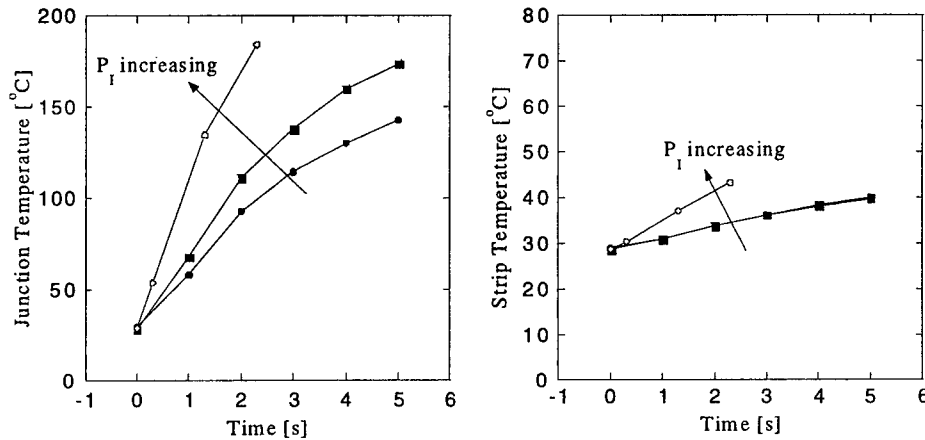


Figure 5 Temperature Change at the Junction and Center of the Strip with Time

Table II Ratio of Temperature Change Rate between the Junction and Strip

Time (s)	$P_1$	$P_{12}$	$P_{13}$
1	$\frac{(\Delta T/\Delta t)_j}{(\Delta T/\Delta t)_f} = 14.0$	$\frac{(\Delta T/\Delta t)_j}{(\Delta T/\Delta t)_f} = 18.2$	$\frac{(\Delta T/\Delta t)_j}{(\Delta T/\Delta t)_f} = 14.2$
2	$\frac{(\Delta T/\Delta t)_j}{(\Delta T/\Delta t)_f} = 11.0$	$\frac{(\Delta T/\Delta t)_j}{(\Delta T/\Delta t)_f} = 14.9$	$\frac{(\Delta T/\Delta t)_j}{(\Delta T/\Delta t)_f} = 12.1$

Based on the ratios in Table II, the junction contact resistance  $\Lambda$ , can be calculated as

$$R_j = \Lambda = \left( \frac{2\rho_f}{v_f t_s} \right) \left[ \frac{(\Delta T/\Delta t)_j}{(\Delta T/\Delta t)_f} \right]_{\text{averaged}} = \left( \frac{2 \times 1.53 \times 10^{-5}}{0.6 \times 127 \times 10^{-6}} \right) \times 15.5 = 6.22 (\Omega) \quad (11)$$

The above value is for vacuum pressure and AS-4/PEI, with temperatures maintained below  $190^\circ\text{C}$  ( $T_g$  of PEI). For temperatures over  $190^\circ\text{C}$ , there is

development of intimate contact and decrease in contact resistance is expected. Work is in progress to estimate  $\Lambda$  for other conditions and prepregs (surface roughness variation). The estimated contact resistance serves as input for the heating model of the system.

## Conclusions

An experimental methodology has been outlined for the measurement of contact resistance between adjacent plies in a carbon thermoplastic prepreg stack. Contact resistance heating has been shown to be the dominant heating mechanism in induction heating of unconsolidated prepreg stacks. Measured values serve as input to induction heating models for simulation of heating mechanisms during induction processing of carbon thermoplastics. Work is in progress to study the influence of process parameters such as, temperature (above polymer  $T_g$ ), pressure and surface quality of prepreg.

## References

1. S.Zinn and S.L.Semiatin, 1988. *Elements of Induction Heating: Design, Control and Applications*. Palo Alto, CA, Electric Power Research Institute, pp. 9-25.
2. T.Nagumo, H.Nakamura, Y.Yoshida, and K.Hiraoka, April 1987. "Evaluation of PEEK Matrix Composite." *32nd International SAMPE Symposium*, 396-407.
3. A.Benatar and T.G.Gutowski, October 1986. "Methods for Fusion Bonding Thermoplastic Composites." *SAMPE Quarterly*, 18(1): 34-41.
4. A.Benatar and T.G.Gutowski, January/February 1987. "A Review of Methods for Fusion Bonding Thermoplastic Composites." *SAMPE Journal*, 33-39.
5. F.N.Cogswell, P.J.Meakin, A.J.Smiley, M.T.Harvey, and C.Booth, May 1989. "Thermoplastic Interlayer Bonding for Aromatic Polymer Composites." *34th International SAMPE Symposium*, 2315-2325.
6. A.K.Miller, C.Chang, A.Payne, M.Gun, E.Menzei, and A.Peled, July/August 1990. "The Nature of Induction Heating in Graphite-fiber, Polymer-matrix Composite Materials." *SAMPE Journal*, 26(4): 37-54.
7. W.Lin, O.Buneman, and A.K.Miller, November/December 1991. "Induction Heating Model for Graphite Fiber/Thermoplastic Matrix Composites." *SAMPE Journal*, 27(6): 45-51.
8. B.K.Fink, R.L.McCullough, and J.W.Gillespie Jr., Mid-March 1992. "A Local Theory of Heating in Cross-ply Carbon Fiber Thermoplastic Composites by Magnetic Induction." *Polymer Engineering and Science*, 32(5): 357-369.
9. B.K.Fink, J.W.Gillespie Jr., and R.L.McCullough, April 1996. "Experimental Verification of Models for Induction Heating of Continuous-Carbon-Fiber Composites." *Polymer Composites*, 17(2): 198-209.
10. S.Yarlagadda, H.J.Kim, J.W.Gillespie,Jr., N.Shevchencko and B.K.Fink, May 2000. "Heating Mechanisms in Induction Processing of Carbon Fiber Reinforced Thermoplastic Prepreg." *45th International SAMPE Symposium and Exhibition*.

## **Needs for Predictable Damage Growth Design of Aircraft Composite Structures**

H.Kikukawa and H.Tamura

### **Abstract**

The discrepancy of DTD method is made clear by comparison between composite structures and aluminum structures. The importance of damage detectable and predictable growth design concept is emphasized to maintain the flight safety of composite structures for aging aircraft or new designed aircraft in extremely long life service. From review of the current study about fracture mechanics of composite materials, a need for new establishment of damage growth rules and growth rates is drawn for some kinds of damage. We formed a working group to study the methodology for this need. An interim information on the activities is provided.

### **Foresight of Composite structures**

The development of new materials and processes has been in the forefront of advancing aerospace technology for many years. The emphasis of these developments was on ever greater capabilities (higher strength-to-weight, elevated temperature operation, more sensitive nondestructive inspection techniques, etc). The realities of operation of aerospace systems in the 1990's and thereafter require environmentally friendly, affordable materials and structures [1] which are capable of extremely long life service and/or are compatible with repair and new design method to estimate life.

### **Aging Aircraft**

Aircraft are often in service longer than their original design life. This trend is expected to continue. Figure 1 shows the age distribution of commercial transport aircraft in service at the end of 1998. The total number of them is about 25,000. Looking on the design life as 20 years, 30% of them (i.e. about 7,500 aircraft) is over the design life. Airworthiness of aging aircraft must be maintained as long as the aircraft remain in service. Almost all the aging aircraft at present has aluminum alloy

---

H.Kikukawa and H.Tamura, Japan Aircraft Development Corporation, Toranomon Daiichi BLDG., 2-3, Toranomon, 1-chome, Minato-ku, Tokyo, 105-0001 Japan

structure, however aircraft having composite structure will also be over the design life in near future.

### **Discrepancy of DTD Methods**

The comparison of DTD (Damage Tolerance Design) methods between composite structures and aluminum structures is shown in Figure 2. For aluminum structures, we applied DTD based on damage detectable and growth concept for a long time, therefore we can apply effective dispositions for damage occurrence due to aging. For composite structures, however, we have applied the design based on damage undetectable and no-growth concept up to this time, accordingly we cannot always apply the appropriate safety dispositions to damage growth.

### **Needs of PDGD for Composite Structures**

Failure mechanics and progression to failure are typically illustrated in Figure 4.4.6.1 (loaded in tension) and Figure 4.4.6.2 (loaded in compression) of a handbook [2]. We need the criteria and methodology for Predictable Damage Growth Design (PDGD) to maintain the flight safety of composite aircraft structures. The main purpose of PDGD is on estimation of Time Before Catastrophic Failure (TBCF). For this purpose, the fracture mechanics have to newly establish growth rules and damage growth rate in addition to failure models, failure criteria and residual strength as shown in Figure 3.

Damages in composite structure are divided into the following four kinds by their sources.

- (a) Pre-existing Damage      (b) Damage Initiation
- (c) Impact damage            (d) Discrete Source Damage

Of these damages, PDGD is needed for (a), (b) and (c) because of the origin (small defects) of damage growth in service. As discrete source damage (d) raises only an issue of residual strength under large size defects, the estimation of TBCF is almost not necessary.

For pre-existing damage, we can apply the method shown in Figure 4 similar to DTD of aluminum structure. The details of this method were described in a journal paper [3].

For damage initiation, we need to develop PDGD method for growth from matrix cracks. We would like to know how long the strength and rigidity can be maintained under increasing matrix cracks. Figure 5 shows sample data of that behavior in which CF/thermoplastic polyimide composite laminate IM7/PIXA maintains the strength and rigidity under increasing matrix cracks at damage initiation phase in thermal cycle and to high temperature exposure. In strain cycle, the strength and rigidity are maintained over 2 or 3 lives as the matrix cracks cease to increase. In the cases of numerous thermal cycle and high temperature long time exposure, can we get the same result? It is desirable that the PDGD method is



analytical, because experimental method takes too much time for us to get the test results.

As recent composite materials have very high fracture toughness, the damage sizes occurred by impact are smaller and are difficult to detect. Figure 6 shows the visibility of impact damage vs. impact energy. Current materials such as T300/3601 and T500/3620 give easily visible sizes of damage 2.5 inch diameter at 1,500 in.-lb/in. impact energy, however new tough materials such as IM600/PIX-M give only 1 inch diameter damage sizes. We cannot visually detect this size of damages. For impact damage, we also need to develop PDGD method for growth from small nonvisible impact damages, although we can use another experimental method such as Post Impact Fatigue (PIF) shown in a brochure [4].

### **Working Group Activities to Study PDGD Methodology**

This working group named MDTACS is active in R&D Institute of Metals and Composites for Future Industries (RIMCOF). A broad range of study on damage tolerance and durability of composite materials and structures is in progress. The main activities at present are as follows and the topics in the discussion are shown in Figure 7.

- (1) Introduction of the current damage tolerance evaluation method for aircraft composite structures (Y.Toi [5]).
- (2) Needs for predictable damage growth design (H.Kikukawa [6]), treated in detail in this paper.
- (3) Analysis method to predict matrix crack occurrence and increase (I.Kimpara and K.Kageyama [7]), Figure 7(a).
- (4) 3-D failure criteria newly put in FEM program to analyze damaged composite structures (M.Zako [7] [14]), Figure 7(b).
- (5) Interpretative discussion about CAI (T.Ishikawa [8] [15]), Figure 7 (c).
- (6) Long-term durability performance for advanced polymer matrix composites (K.Hirano [9] [10]), Figure 7(d).
- (7) Long-term prediction of fatigue life (Y.Miyano [11]), Figure 7(e).

In addition to above damage tolerance and durability study, the health monitoring technology [12] [13] is also discussed to improve the detectability of small damage such as matrix cracks.

### **Concluding Remarks**

The current design for composite structures is limited to the scope L1 based on damage undetectable and no-growth concept in Figure 8. The establishment of PDGD methods will have capability to design the life extended to scopes L2 and L3, as we can estimate TBCF based on damage growth rate and failure criteria.

Structural design and technology improvement provide rational method for operators to achieve the extended utilization of aging aircraft by now and further to secure the flight safety of new designed aircraft in extremely long life service by

developing PDGD criteria and methodologies of composite structures.

## References

1. R.Abbott, 1998. "Damage Tolerance Evaluation of Composite Honeycomb Structures." *Proceedings of 43<sup>rd</sup> International SAMPE Symposium*, 376-386.
2. MIL-HDBK-17E, 1997. "Polymer Matrix Composites"
3. H.Kikukawa and T.Ugai, 1997. "Growth Behavior of Interlaminar Delamination at Edge of Circular Hole of CFRP." *Journal of JSASS*, 45, 522:24-30.
4. D.Moon, 1999. "Fabrication of Sticked Composite Wing Box." *Composite Durability Workshop at Stanford University*.
5. An annual report(SST) of RIMCOF, 1999, Appendix, 340-353.
6. H.Kikukawa, 1999. "Needs for Damage Growth Design Criteria of Aircraft Composite Structures." *Composite Durability Workshop at Stanford University*.
7. An annual report(SST) of RIMCOF, 2000, to be issued.
8. T.Ishikawa, M.Matsushima, Y.Hayashi, 1998. "Comparison and Discussion about CAI Properties Obtained by SACMA and NASA Methods." *8<sup>th</sup> Japan-US Conference on Composite Materials*, 476-485.
9. K.Hirano, 2000. "The Effects of Stress Ratio and Temperature on the Open-Hole Fatigue Behavior of Advanced Polymer Matrix Composites. " to be presented at *2<sup>nd</sup> International Conference on Fatigue of Composites*, June 4-7, 2000.
10. K.Hirano, 2000. "Japanese High Speed Research Program and the Related Long-term durability Performance for Advanced Polymer Matrix Composites." to be presented at *3<sup>rd</sup> APCATS'2000*, Oct. 4-8, 2000, Kunming, China.
11. Y.Miyano and M.Nakada, 1999 "Long Term Prediction of Fatigue Life of Unidirectional CFRP" *Proceeding of 4<sup>th</sup> International Conference on Progress in Durability Analysis of Composite Systems*
12. Y.Okabe, S.Yashiro, T.Kosaka and N.Takeda, 2000. "Detection of transverse cracks in composites by using embedded FBG sensors." *Proceedings of SPIE*, Vol.3986, in press.
13. H.Tsutsui, T.Sanda, Y.Okabe and N.Takeda, 2000. "Real-Time Detection of Impact Load on Composite Laminates with Embedded Small-Diameter Optical Fiber." *Proceedings of SPIE*, Vol.3986, in press.
14. M.Zako, T.Tsujikami and T.Tsumura, 1994. "Development of Finite Element Method considered An Anisotropic Damaged State for Composite Materials." *Proceedings of the 37<sup>th</sup> Japan Congress on Materials Research*, 174-179.
15. T.Ishikawa, M.Matsushima, Y.Hayashi, 1999. "Unified Description of CAI Strengths Obtained by Two Standard Methods (SACMA&NASA)." *Proceedings of 41<sup>st</sup> JSASS/JSME Structures Conference*, 57-60.

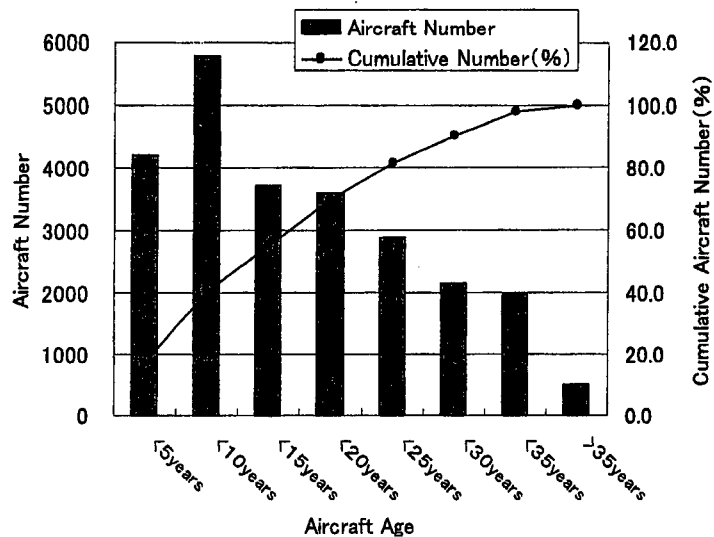


Figure 1 Civil aircraft in Service at 1998 end

Comparison Item	Aluminum Structure		Composite Structure	
	Current Design	Current Design	New Design in near term	New Design in far future
Design Criteria and Principles	Detectable & Growth	Undetectable & No-growth	Undetectable & Growth	Detectable & Growth ( Smart Structure)
Damage Detectability				
in MFG	NDI	NDI	NDI	NDI
in Ground Service	Visible, etc	Tapping, etc	Tapping, etc	Sensing by embedded
in Flight	None	None	None	Sensors
Damage Growth				
-Analysis Method	Applicable	Not applicable	Applicable	Applicable
-Suppression	None	None	None	Suppressing by Actuators, ex. SMA
Sustaining of Residual Strength				
for detectable parts	Crack Arrest, Multi-Load Path & Repair	Repair	Repair or Replacement	Sensing of smaller Damage & Repair
for undetectable parts	Slow Crack Growth by DT alloy	Refurbishment	Slow Damage Growth	Growth Suppression by Actuators
Sustaining of Safety for Aging Aircraft	DTD applicable	DTD not applicable	Damage Growth Design applicable	DTD applicable

Figure 2 Comparison of Damage Tolerance Design Methods

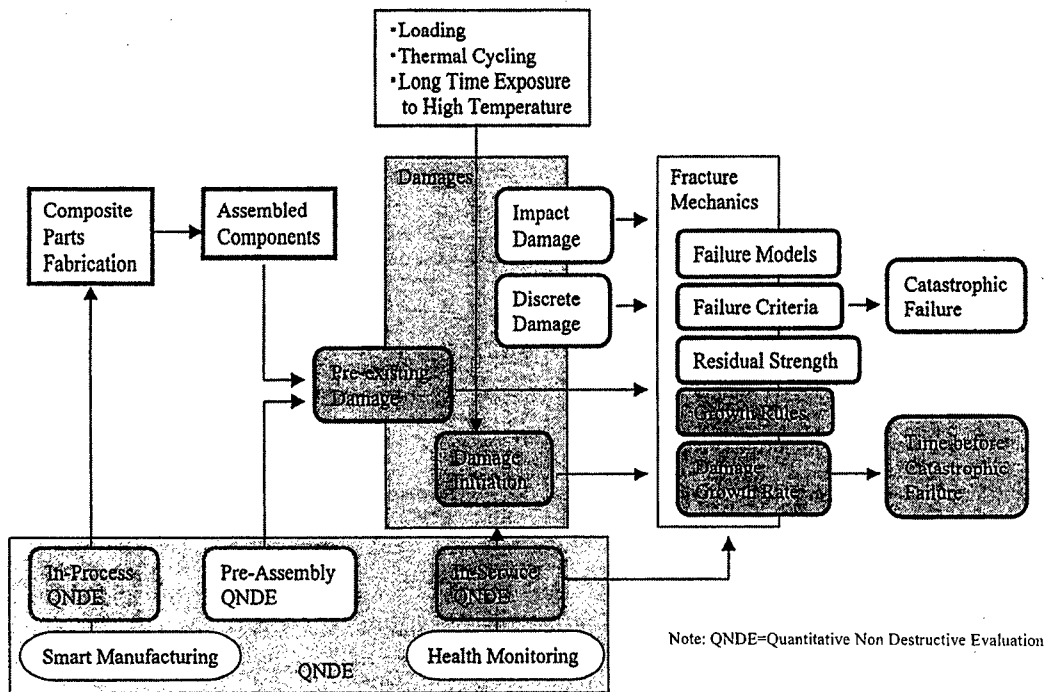


Figure 3 Damage Growth Design to estimate Time Before Catastrophic Failure

#### Design Criteria

- Damage Size and Location
- Delamination Growth Analysis
  - ex.  $db/dN = C[\Delta\tau\sqrt{b}]^n$
  - $\Delta\tau = f(b)(\tau_{max} - \tau_{min}) - \tau_{th}$
- Residual Strength Analysis
  - Single Damage
    - ex.  $\sigma_c = k(\pi^2 E/12)(mh/b)^2$
  - Multiple-Layer Damage

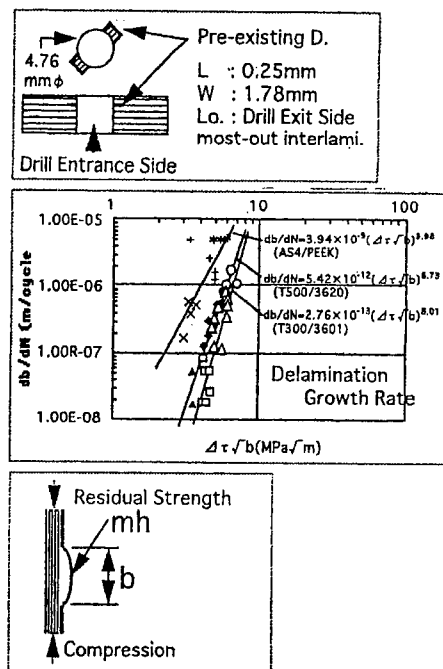


Figure 4 Design Criteria for Delamination Growth from Pre-existing damage

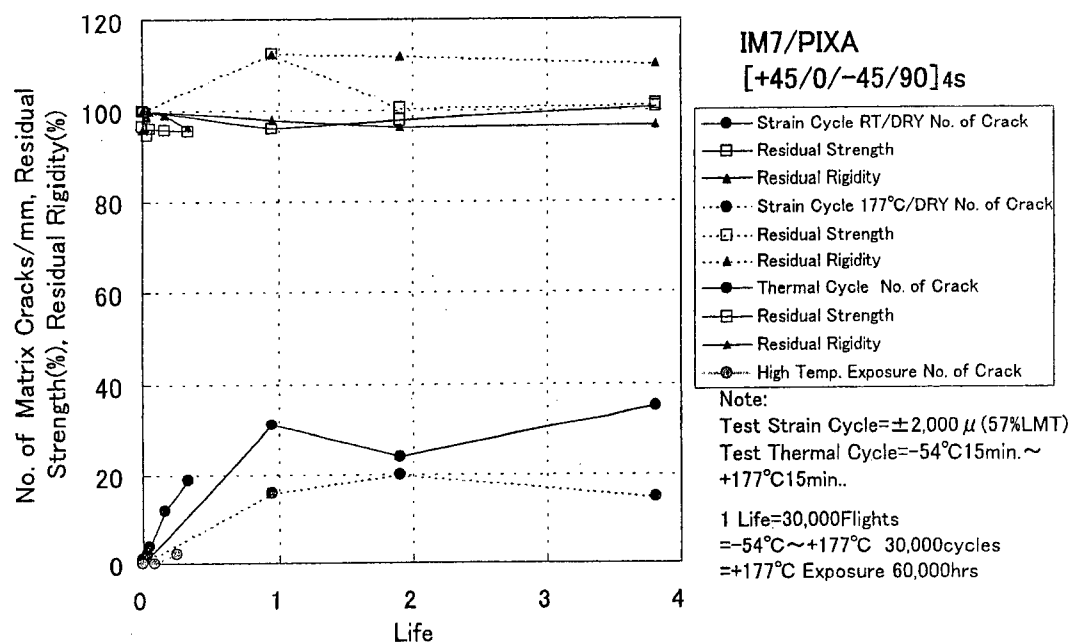


Figure 5 Damage Initiation: Increasing of Matrix Crack, Residual Strength and Rigidity

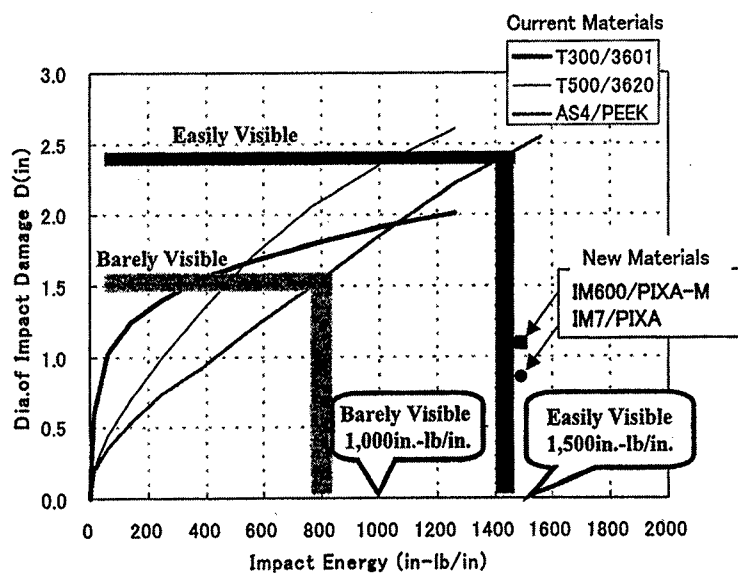


Figure 6 Visibility of Impact Damage vs Impact Energy

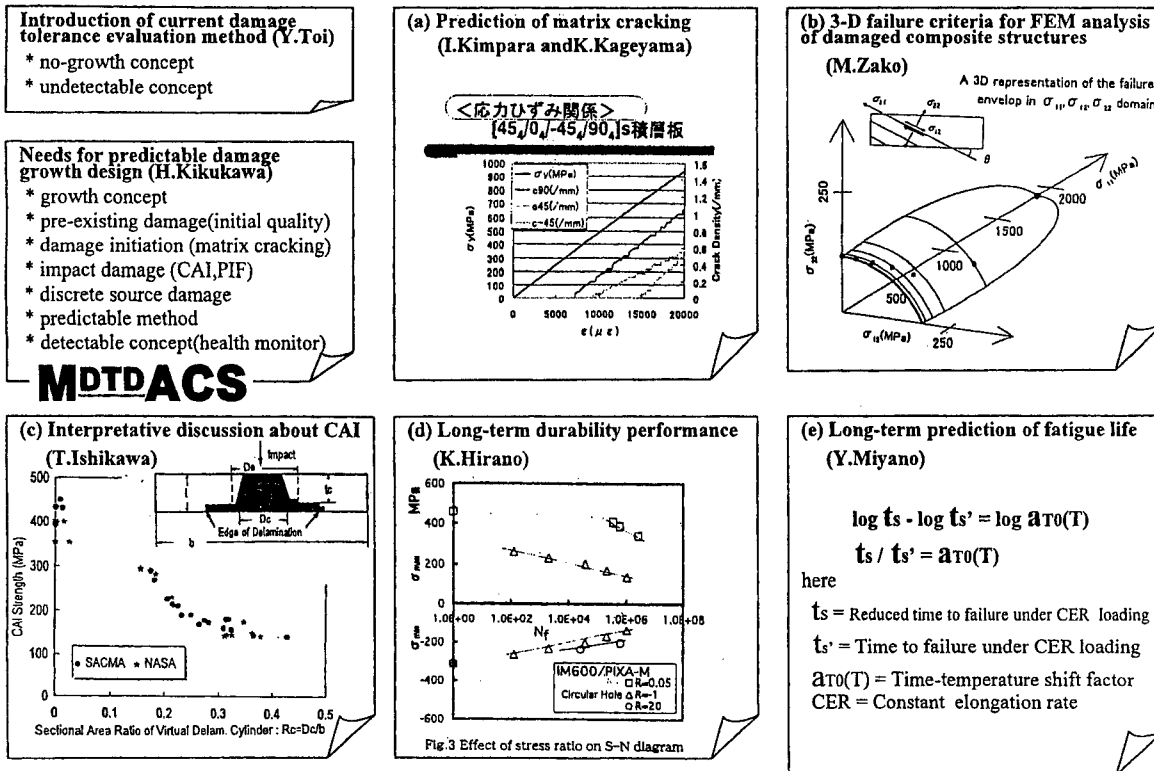
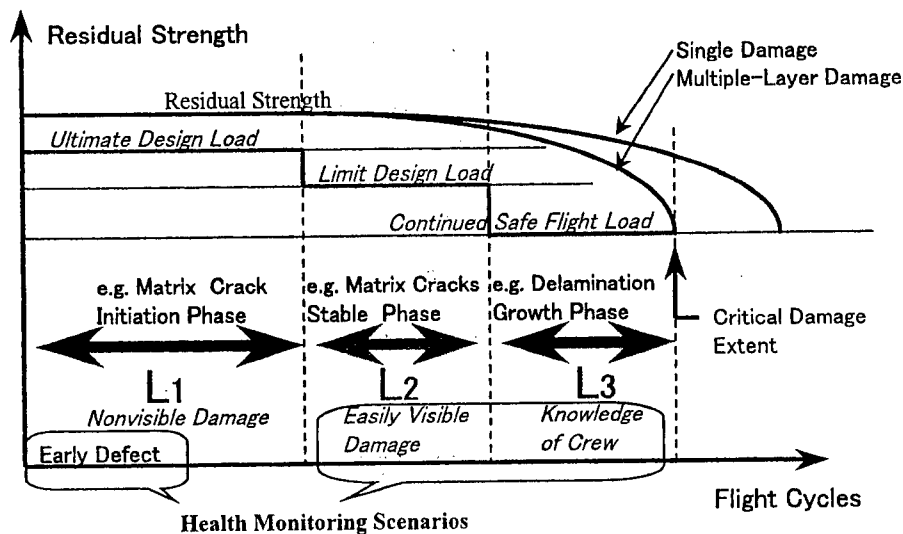


Figure 7 Working Group Activities



Note: Design requirements in italics

Figure 8 Coming Events to Failure and Life Length(L1,L2,L3) to be predicted

## **Cost Reduction in Compression-after-Impact (CAI) Tests : Proposal of Half SACMA Specimen Size**

Takashi Ishikawa, Masamichi Matsushima, Eiichi Hara, and Goichi Ben

### **Abstract**

Test methods for Compression-after-Impact (CAI) tests with low cost potential are investigated for current requirement in aircraft industries. Deep understanding of the mechanics of CAI during tests is the foundation of the test method consideration. The authors' knowledge of the two standard test methods (SACMA and NASA) is utilized. A review of the mechanism in these two methods is given first. The finding is an effective parameter for interpreting the CAI strength trend over a wide range of impact energy and different specimen sizes. Based on such basic knowledge, a new method, actually a size of the specimen of Half SACMA, is proposed here. The review of the already proposed size in JIS R (Reference in Japan Industrial Standard) is also conducted in this report. Trends of CAI strengths are obtained and discussed within a selected conventional brittle carbon/epoxy. Guidelines for minimize the specimen size for low cost is basically obtained.

### **Introduction**

Compression after impact (CAI) tests are considered as crucial evaluation for composite structure design particularly for aircraft wings. Allowable strain limit is mainly defined from CAI results for composite primary structures and it governs weight reduction ratios. As another purpose of CAI, it is considered to be a material screening parameter for evaluating new composite system for structural applications. Although CAI tests does not seem to be the best for this purpose, thousands of CAI tests have been conducted in advanced composite material supplier companies. Therefore, necessity of CAI tests is enhanced in both aircraft and composite industries. On the other hand, high cost of CAI test is also well recognized against recent strong requirement for low cost composite programs. Thus, it is very important to establish appropriate CAI test methods with low cost potential. Of course, deep understanding of mechanics in CAI tests is indispensable background for establishing the new test methods, actually the new reduced sizes.

Among several proposed CAI test methods, NASA method<sup>1)</sup> and SACMA method<sup>2)</sup> are most broadly accepted ones. Although NASA method was proposed earlier, it is not well conducted and understood because it requires a costly large thick plate of 48 plies. Only one advantage of this size is that it simulates well the real behavior of

---

Takashi Ishikawa and Masamichi Matsushima, National Aerospace Laboratory, 6-13-1 Ohsawa, Mitaka, Tokyo 181-0015, Japan  
Eiichi Hara and Goichi Ben, College of Industrial Technology, The Nihon University, 1-2-1, Izumi, Narashino-shi, Chiba 274, Japan  
Yoichi Hayashi, Tokyo Business Service, 6-14-1, Nishi-Sinjuku, Sinjuku-ku, Tokyo 160-0023, Japan

delaminated panel of aircraft wing structures. SACMA method was proposed as a substitute of an eventually distributed company proprietary method, Boeing Method, and it is widely conducted in the worldwide scale. Hence, it is worthwhile first to compare and examine the behavior and results of NASA and SACMA tests. The review of the authors' previous work is given here first to clarify the relationships between CAI results by these two methods. Key finding is to establish the best parameter to interpret trends of CAI behavior over wide range of impact energy and methods (specimen size). Based on such understanding, the present paper proposes a new smaller size of specimen of HALF SACMA with low cost potential. Results by more smaller size specimens suggested in composite CAI in JIS<sup>3)</sup> (Japan Industrial Standard), denoted as JIS R, are also obtained and discussed. An improvement point for JIS R is identified. A guideline of usage and limitation of these smaller CAI specimens are recognized. Some further investigation is required for identifying mechanical behavior of CAI for modern toughened composites.

### Review and Proposal of Test Methods and Specimen Size

Brief reviews of the two CAI test methods of interest and the proposed and discussed sizes are given here: NASA method consists of a thicker plate of 48 plies,  $\{(45/0/-45/90)_6\}_{sym}$ , 6-7mm in thickness and  $127 \times 254$ mm in size. Note that the exact NASA method is defined as that an impact should be applied first to a wider plate (178 mm) closer to the actual bay width of stiffened panel structures and that it should be cut into the above size next and tested.

However, only one deviation is introduced here so as that an impact is applied after cutting into the specified size to reduce testing costs as much as possible. Even so, fabrication costs were enormous for these NASA specimens as shown below. SACMA method consists of a thinner plate of 32 plies,  $\{(45/0/-45/90)_4\}_{sym}$ , 4 - 4.5 mm in thickness and  $102 \times 152$ mm in size. HALF SACMA proposed here complies of the same laminate and a half size in terms area, that is,  $76 \times 102$ mm in size. Note that if we cut the regular SACMA specimen into half, the original zero direction is changed into 90 direction. JIS R is not defined but suggested as a reference in JIS CAI method<sup>3)</sup>. The specified JIS R consists of a  $\{(45/0/-45/90)_2\}_{sym}$ , 2-2.5 mm laminate in thickness. However, because of the problems in impact itself (rebound prevention) and buckling, a modification of double thickness is introduced here so that the mother laminate is the same as SACMA. The specimen size is defined as  $50 \times 80$ mm. Loading fixture concepts are so defined as similar in these methods that two loading and side edges are clamped and simply supported, respectively.

In order to facilitate the later discussion, costs of the standard and proposed CAI specimens are shown in Fig.1 with the baseline tension specimen ( $25 \times 250$ mm) data.

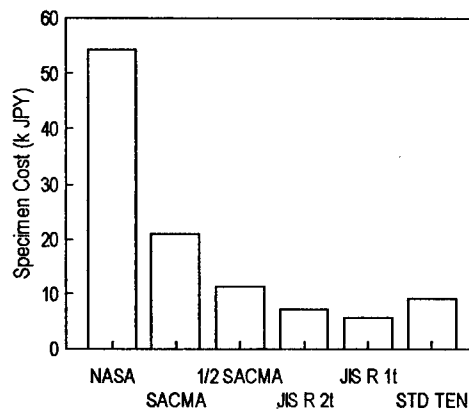


Fig.1 Example of Costs for Several CAI and Baseline Specimens



All specimens were fabricated with the same material to make a meaningful comparison, KA/410 carbon/epoxy of the first generation brittle CF/epoxy by Mitsubishi Rayon Co. similar to US T300/5208 system. The reason why this system was chosen is that it is sensitive to impact delamination and so to CAI test methods. More than 100 plates are fabricated for four test methods. An impact was given by an instrumented drop weight machine with the above deviation in NASA method. A picture frame type plate holder was used in NASA method and the plate holder using rubber bushes was used in SACMA method. Because the latter was considered as controversial, similar picture frame type holders to NASA method were used for HALF SACMA and JIS R methods. In some SACMA specimens, a picture frame type fixture was designed and tried.

Summary of testing specifications for comparison of these four methods is listed in Table 1. Although it is commonly defined that loading edges must be clamped in these methods, the authors would like to point out that the illustrated test fixtures in Refs. 1 and 2 are not adequate to generate clamping forces at the loading edges. One proposal here is to add two screws in each loading edge at locations outer than specimen width.

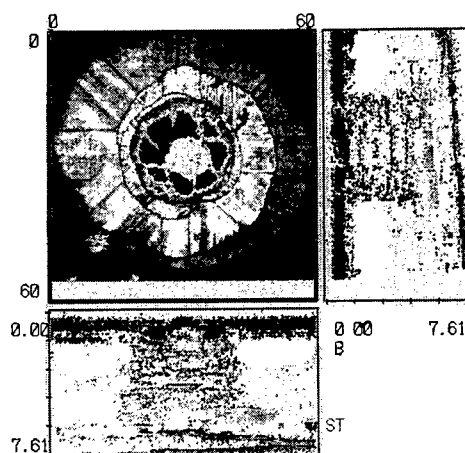
**Table 1 Summary of Four CAI Methods (Specimen Size) Used in This Paper**

	NASA	SACMA	HALF SACMA	JIS R
Specimen Size(mm)	127×254×6-7	102×152×4-5	76×102×4-5	50×80×4-5
Stacking Sequence	{{(45/0/-45/90) <sub>6</sub> }} <sub>sys</sub>	{{(45/0/-45/90) <sub>4</sub> }} <sub>sys</sub>	As Left	As Left
Impact Procedure	Impact and Cut	Direct	Direct	Direct
Supporting Device	Picture Frame	Clamping with Rubber Bush	Picture Frame 60×80	Picture Frame Org.:Circle 35φ
Boundary Condition		(Picture Frame)		Mod.:40×70
(Common)	Clamped at Loading Edges and Simply Supported at Side Edges			

### Baseline Knowledge about Accumulated Delamination Shape by Impact

Specimens after impact were examined by ultrasonic C-scanners for determining delamination geometry. Krautkramer SDS 3300 was mainly used in this investigation. This system can provide plan views of accumulated delamination (C-scope) and their side views (B-scope) by processing ultrasonic echo data and probe locations. By integrating these views, it is possible to identify 3-dimensional delamination geometry created by specified impacts. Figure 2 depicts one typical case of hat shaped delamination where impact energy level was low (NASA:1.48J/mm).

Although 3-D shape in Fig.2 is not



**Fig.2 Example of Hat Shaped Accumulated Delamination (NASA; Low Impact Energy)**

clear by a black and white print unfortunately, it consists of an upper cylindrical portion and a lower truncated cone and looks like a "hat". In NASA methods, it almost always appears in low and high impact energy cases. Almost pure cylindrical shape of delamination only appears in low energy cases in SACMA method for this sort of brittle CF/epoxy. In Ref. 4, it was shown that delamination shape became more cylindrical for tougher composites like CF/PEEK than a current brittle system. This point will affect the whole CAI behavior and be discussed later.

In order to give a basis for later discussions, a schematic of the delamination geometry will be summarized here and a concept of effective diameters of delamination will be introduced. Figure 3 indicates the schematic of the B-scope of delamination perpendicular to the compression direction and definitions of the two effective diameters denoted  $D_c$  and  $D_e$ . Sectional area of delamination in the B-scope,  $A_s$ , can be obtained by a summation of several trapezoid areas and it could be related better to total delamination area than projection area. Based on the knowledge that the brim portion of the hat shape does not govern the delamination buckling behavior, we consider the sectional area of the hypothetical cylinder ( $A_c$ ) of the same diameter of delamination ( $D_c$ ) as the crown part without the brim. The sectional area of this top crown is denoted as  $A_t$ . If we introduce the ratios of  $A_c$  and  $A_e$  to the sectional area of the plate,  $A_s$ , denoted by  $R_c$  and  $R_e$ , the following simple geometrical relations can be derived between  $D_c$ ,  $D_e$ , width and thickness of the plate,  $b$  and  $t$ :

$$A_c = tD_c, R_c = A_c/A_s = tD_c/(tb) = D_c/b \quad 1)$$

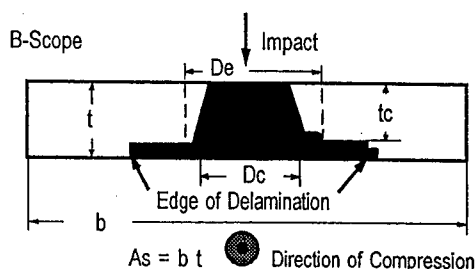
$$A_t = t_c D_c, A_c = t D_c \quad 2)$$

$$A_e = tD_e, R_e = A_e/A_s = tD_e/(tb) = D_e/b \quad 3)$$

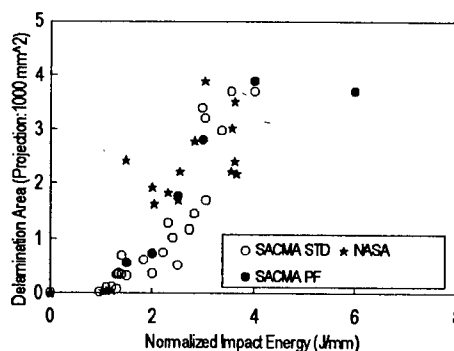
After establishing these simple relations, the CAI strength behavior will be examined.

Before going into the detail, an overview behavior in relationships between impact energy normalized by a plate thickness and projected delamination area is shown in Fig. 4. Here, the projection area is defined as the envelope of the largest delamination radii. Note that this projected area is not the total area

of delamination. An important finding in this figure is an implication that a threshold value of the normalized impact energy appears just above 1 J/mm for delamination occurrence in both methods. Theoretical prediction of a basic mechanics of this sort of threshold was given by Suemasu et al.<sup>5)</sup> and the present data can be considered as collateral evidence of their theory. The other clear finding is a leveling-off in delamination



**Fig.3 Schematic of B-Scope and Delamination Section**



**Fig.4 Relationships between Normalized Impact Energy by Thickness and Projected Area of Delamination**

area particularly in SACMA method. This phenomenon can be easily interpreted as that delamination edge almost reaches vicinity of an impact frame and that more propagation becomes impossible. Such a restriction will be referred as delamination saturation later and it can be regarded as a sort of size effect in CAI tests and implies that we should be sensitive to the limitation of smaller CAI specimens and applied impact energy level.

### Review of CAI Strength Behavior: Examination of NASA and SACMA Results

Prior to the discussion about new CAI specimen results, trends in CAI strengths governed by normalized impact energy by the plate thickness obtained are indicated in Fig.5 for both well-known methods, and examined in detail. This sort of plot is considered as typical "CAI behavior" considered in the early strength design of aircraft primary structures. It can be seen that two methods provide similar CAI strength properties over 2 J/mm and that some discrepancy is found between 1 and 2 J/mm. To be exact, SACMA results show more serious drop in CAI strengths than NASA results beyond the impact energy level of delamination threshold. Global tendency described in Fig.5 is somehow similar to that in Ref.6, although the horizontal axis scale of its key figure, Fig.1 of Ref. 6, must be wrong. If we assume its axis is the same as here considering that the tested material is similar, the present and Ref. 6 results are compatible to each other.

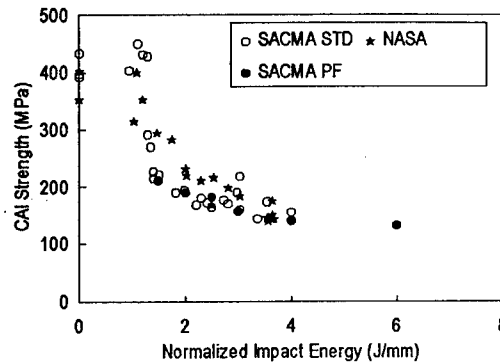


Fig.5 Relationships between Normalized Impact Energy and CAI Strengths

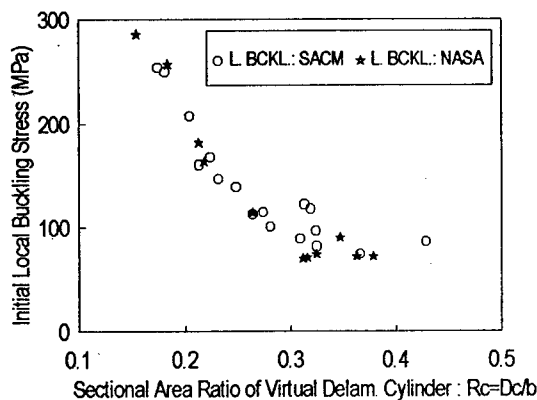
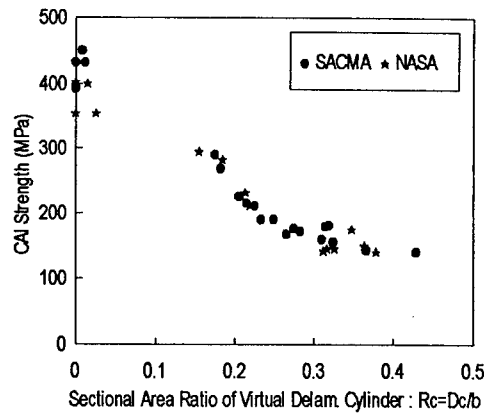


Fig.6 Relationships between Initial Buckling Stress and Ratio of  $D_c$  to Plate width  $b$

From here on, the results of SACMA and NASA methods will be examined rigorously by using the above-defined geometrical parameters. The first finding is that the relationships between initial buckling stress of delaminated plies in CAI specimens and ratio of  $R_c (= D_c/b)$  coincide quite favorably for both methods as shown in Fig.6, although some scatter can be found around  $R_c = 0.3$ . In Ref. 7, an idea that initial buckling is solely controlled by the equivalent diameter,  $D_e$  in this paper, was proposed based on the speculation of uniform strain distribution of the substrate plate. However, it was revealed that such uniform strain distribution is not true in the actual CAI tests in the authors' Ref.8. Thus, it seems more appropriate to employ the ratio of a diameter to the plate width in order

to compare initial buckling stress in different specimen sizes. The reason why  $D_e$  was chosen rather than  $D_c$  is the experimental finding that the brim region in the accumulated delamination does not affect local initial buckling in this area. The recent numerical calculation (Ref.9) by FEA supports this experimental finding. Therefore, the ratio of  $R_c$  is chosen in Fig.6. Although a presentation is skipped, a similar graph to Fig.6 using  $R_c$  was prepared. The result is not as good as Fig.6 due to the above-mentioned experimental finding.

Because a trial plot for buckling of Fig.6 led to a favorable result, a similar plotting was attempted for describing relationships between CAI strengths and  $R_c$ , with recognition that CAI strengths and local initial buckling stresses show a good correlation. Figure 7 depicts the result and a very good accordance in the CAI strengths from both methods can be seen by employing the ratio of  $R_c$ . Thus, as long as these two methods, SACMA and NASA, a common way to interpret the CAI strengths could be found. Small comment about discrepancy between the two data groups at no impact or low energy impact is stated here. NASA specimens at low impact failed in a sort of material failure of shear instability type happened at a tip of side edge supports. This mode is similar to the one happening in a compression of thick composite rods conducted under insufficient fixture rigidity or insufficient prevention of out-of-plane deflection. Because the shear failure mode in SACMA specimens is not so clear as NASA, it might lead to the discrepancy.

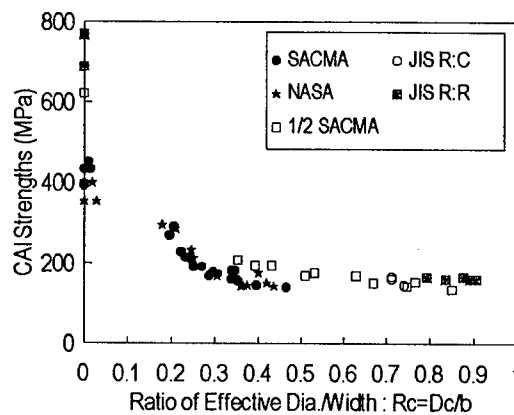


**Fig.7 Relationships between CAI Strengths and Ratio of  $R_c$**

#### Examination of CAI Strengths Obtained by HALF SACMA and JIS R and Discussion about Those Specimens

Once unified way of interpretation of CAI strengths was found, this procedure is also applied to the proposed CAI specimen results, HALF SACMA, and the other point of interest, JIS R results. Figure 8 depicts the trial plot of all CAI strength data including duplicated data in Fig.7 for the purpose of comparison. The results of HALF SACMA gradually tend to the lowest CAI strengths by SACMA and NASA. Although the reason of difference in strength trends is not clear yet,

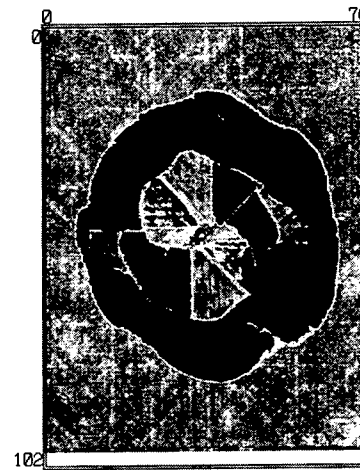
a possible cause might be a ratio of the plate thickness to width. To clarify this, further investigation is required. Another finding here is that JIS R specimens provide slightly



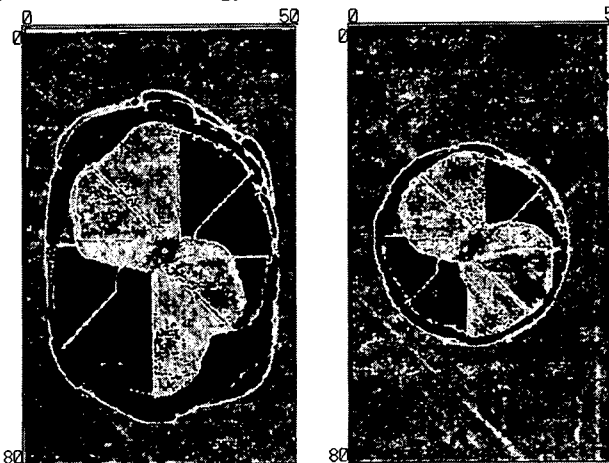
**Fig.8 Relationships between CAI Strengths and Ratio of  $R_c$  for the Employed 4 Methods**

higher strengths than others. Again, modification to double thickness and the thickness to width ratio may play some roles in these CAI strengths. More clear dependency on the size can be found in no-impact strengths for smaller specimens. This phenomenon is caused by a proximity effect of global buckling stress to the failure stress. The detail will be given in the oral presentation.

From here on, some discussions about the delamination saturation phenomena in the newly proposed smaller specimens will be given. Delamination saturation is defined as that impact delamination edges reach the clamping frame and that no more increase in delamination area is possible proportionally to the impact energy. For HALF SACMA specimen, a typical delamination shape is given in Fig. 9 for a middle energy level of 3.0J/mm where there is still a little margin of delamination to the frame edge. In case of JIS R specimen (modified rectangular window) with the same energy, delamination already reaches the frame and its shape becomes away from a circle as shown in Fig. 10(a). In the original JIS R specimen with a circular window in the frame, the delamination saturation



**Fig.9 Delamination Shape for HALF SACMA with 3.0J/mm**



**Fig.10 (a) JIS R:Rect. 3.0J/mm**

**(b) JIS R:Circular 2.0J/mm**

**Delamination Shape for Two JIS R Specimens**

occurs at lower energy level below 2J/mm. Figure 10(b) depicts the saturated circular delamination by 2J/mm with a diameter of 37mm which exceeds a window diameter of 35mm. Thus, it is impossible to obtain a relationship between the impact energy and CAI strength reduction if we adopt JIS R with a circular window type. There will be a slight possibility for JIS R specimen with a rectangular window up to 2.5J/mm for this material. However, severe limitations for tests are expected and the worse thing is non-conventional (slightly higher) CAI strengths might be obtained by JIS R as shown in Fig. 8. If we look at the results by HALF SACMA, the lowest CAI strength reaches the level of SACMA or NASA. Moreover, the relationship between impact energy and the CAI strength reduction can be obtained even if some modification from SACMA or NASA is required. Because the present material is quite brittle one, overall behavior (limitation from the size) tends to the better direction in the case of tougher composites. This is one strong reason why the brittle CF/epoxy is used here although

future research in this aspect will be required for modern tough CF/polymer composites.

In conclusion, the best compromise CAI specimen between performance and cost so far explored is HALF SACMA if we remind the cost data in Fig.1 Its cost remains in the range of standard tension of 16 plies and it can provides the reasonable CAI strengths if we are aware of the whole behavior experimentally.

## Conclusions

Experiments on CAI using the two standard methods, the presently proposed one and newly proposed in JIS were conducted for conventional brittle CF/epoxy and the following findings were obtained.

1. CAI strengths by two standard method data coincide well each other if a ratio of effective diameter to the specimen width is employed as the baseline variable. For obtaining this ratio, a ultrasonic C-Scan machine with B-Scope capability is required.
2. NASA method leads to slightly higher CAI strengths at low impact or no impact.
3. Conventional expression of the results as the relationships between normalized impact energy and CAI strengths can be used for practical purpose.
4. HALF SACMA specimens can provide a relationship between impact energy and CAI strength reduction although it may be a little different from SACMA or NASA.
5. The original JIS R specimens with a circular window provide the poorest data because the delamination saturation occurs at low impact energy. Slight improvement may be possible if we adopt a modification of a rectangular window.
6. HALF SACMA specimen can be considered as the best compromise between cost and data quality if we remind its cost is in the range of the standard tension coupon.
7. Points of improvement for both standard methods are identified: Impact support in SACMA method should be a picture frame type. Screws outside of loading edges of the specimens generating clamping force are required for them.

## Acknowledgements

The authors would like to express their sincere gratitude to the students who supported these CAI tests, Mr. K. Matsui, Mr. S. Nakashima, and Mr. E. K.G. Lim.

## References

1. NASA, 1983 and 1985.: Reference Publication (RP) 1092 and RP 1142.
2. SACMA, 1988.: SRM 2-88, .
3. Association for Japans Industrial Standard, 1996.: JIS K-7089-1996 (in Japanese).
4. Ishikawa, T, et al. 1995. : Composite Science and Technology, 55, pp.349-363.
5. Suemasu, H. et al. 1998 : Journal of Composite Materials, 32(2), pp.123-140.
6. Spiegel, B. 1991. : Proc. of 23<sup>rd</sup> Internatl. SAMPE Tech. Conf., pp. 219-232.
7. Dost, E.F. et al.1988. :Proc. of 3rd Tech. Conf., Am. Soc. of Comp., pp.354-363.
8. Ishikawa, T, et al. 1998. : Proc. of 8<sup>th</sup> Japan US Conf. Comp. Mat., pp.476-485.
9. Wakabayashi, H. et al. 1999.: Proc.of 1999 Annu. Meeting for Com. Mat., Japan Society for Comp. Mat., pp. 21-22. (in Japanese).

# **Smart and Intelligent Composites**

---

## **Delamination Monitoring of Graphite/epoxy Composites by Electric Resistance Change**

A.Todoroki, Y.Tanaka, Y.Shimamura and H.Kobayashi

### **Abstract**

Delamination cracks are usually invisible or difficult to find by visual inspections. The difficulty of detection of the delaminations brings increased significance of development of smart structures for detection of delaminations of laminated composites. In the present study, an electric resistance change method is adapted for identifications of delamination crack location and size of graphite/epoxy laminates, and usefulness of the method for identification of delamination cracks is experimentally investigated by using cross ply laminates. Three-point-bending tests are conducted to introduce delamination cracks using specimens that have multiple electrodes on the top surface. Firstly, response surfaces to predict electric resistance change are constructed from measured electric resistance change. Secondly, designs of experiments are conducted for inverse problem to predict delamination crack position and size from electric potential changes. Finally, response surface to predict delamination crack position and size are constructed. Using the response surface method with designs of experiments, delamination crack position and size are predicted within practical precision.

### **Introduction**

Laminated composite plates have a weak point at delamination resistance. The low delamination resistance causes delamination cracks by slight impacts such as tool drops. Since the delamination cracks are usually invisible or difficult to find by visual inspections, the delamination causes low reliability for primary structures of laminated composites. In order to improve the low reliability, easy-handling detection systems of delamination cracks in-service are required. Health monitoring system to detect the delamination cracks is one of the desired approaches for practical laminated composite structures.

In the present study, an electric potential method is attempted to identify internal delamination cracks. An electric potential method is usually applied to conventional metallic structures to detect cracks or defects. The electric potential

---

A.Todoroki, Y.Shimamura and H.Kobayashi, Department of Mechano-aerospace Engineering, Tokyo Institute of Technology, 2-12-1, Ohokayama, Meguro-ku, Tokyo 152-8552, Japan

Y.Tanaka, Graduate student of Tokyo Institute of Technology



method does not require expensive instruments. Since the method adopts reinforcement carbon fiber as sensor for delamination detection, the method does not cause strength reduction, and applicable to existing structures. Moreover, the electric potential method does not cause increase of weight. Therefore, the electric potential method has been adopted by several researches [1,2].

Authors have already investigated the applicability of the electric potential method for measurements of delamination crack length for the edge cracks of mode I and mode II tests [3]. The electric potential method for the edge cracks was also applied to the laminated composite specimens that had multi-direction fiber angles in authors' paper [4], and the applicability was experimentally shown in the paper. For practical composite structures, however, delamination cracks are usually inside cracks. The inside cracks were also detected by the electric potential method in the previous paper [5]. In order to investigate the effect of electrode position, several FEM analyses were conducted in the previous studies [6-8]. In those papers, it was shown that identification of the location and size of the delamination cracks in a beam type specimen is impossible for the method using electric resistance change among 3 electrodes (2 segments) that are mounted on the specimen top surface due to the large orthotropic electric resistance. The studies also showed that measurements using more than four electrodes are necessary for exact identification of the delamination crack position and size.

In the present study, identification of delamination crack size and position is experimentally attempted by using response surface methodology. The response surface methodology is adopted as a convenient tool for inverse problems to obtain delamination location and size from electric resistance changes. The response surface methodology uses design of experiments and regression curve fittings. Usually equal spacing sampling is adopted for direct problems, but the equal spacing sampling is not always appropriate for inverse problems. The design of experiments helps to find appropriate sampling for the inverse problems. Specimens are fabricated from cross ply laminates, and seven-electrodes are mounted on the specimen top surfaces. Three-point-bending tests are conducted to introduce practical delamination cracks into the specimens, and electric resistance changes between the electrodes are measured. Using the measured electric resistance change, response surfaces are constructed, and delamination crack identification using the response surfaces is experimentally shown to be effective.

### **Principle of electric potential method of laminated composites**

Graphite fiber has a high electric conductivity, and the plastic matrix of graphite/plastics is insulation resistance. For ideal graphite/plastics composites, electric resistance in fiber orientation is almost zero. The electric resistance of transverse orientation is ideally infinity.

Practical graphite fiber in a unidirectional ply is serpentine. The curved graphite fiber constructs a large graphite-fiber-network in a ply by fiber contacts with each other. The fiber-contact-network causes finite electric resistance even in the transverse orientation. In the same way, the fiber network produces the finite electric resistance in the thickness orientation in a ply. The electric resistance in transverse direction is much lower than the electric resistance of the fiber orientation. Authors

have revealed that the electric conductivity ratio of the transverse direction to the fiber direction is approximately  $10^{-1}$ , and the electric conductivity ratio of the thickness direction to the fiber direction is approximately from  $10^{-3}$  to  $10^{-4}$ . That data tells that there is very strong anisotropy between the electric conductance of fiber direction and the conductance of thickness direction.

If a delamination crack starts growing in the resin rich interlamina, the crack breaks the fiber-contact-network between plies. The breakage of the contact network causes increase of the electric resistance of the graphite/plastics composites. Therefore, delamination crack can be detected by the electric resistance change of graphite/plastics composite laminates.

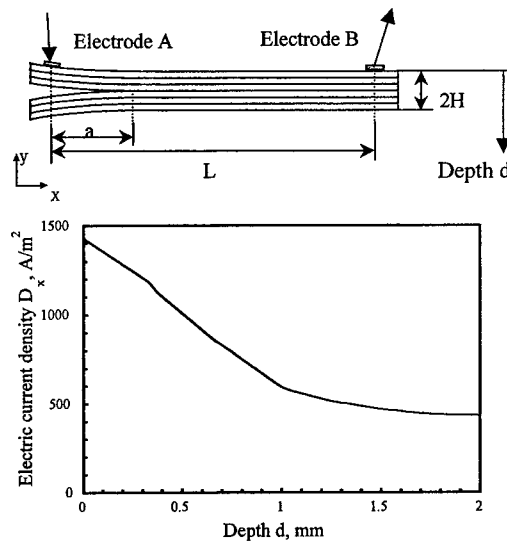


Figure 1 Electric current density distribution of  $[0_8]_T$  laminate

The strong anisotropy of the electric resistance causes a problem for identifications of the delamination cracks. Figure 1 shows the electric current of FEM analysis of the case of electric conductivity ratio of  $10^{-4}$  of the  $[0_8]_T$  laminate. Electric current flows in fiber direction much more than the thickness direction as shown in Figure 1. This causes that the electric resistance changes even at far points from the point where delamination crack is introduced. This electric resistance change at the location far from the delamination crack makes identification of delamination position difficult, and it requires more than 4 electrodes for the identification of exact delamination position. This is revealed in the previous study using FEM analysis[8].

### Response Surface Methodology

The response surface methodology is a widely adopted tool for quality engineering fields [9]. The response surface methodology comprises regression surface fitting to obtain approximate responses, design of experiments to obtain minimum variances of the responses and optimizations using the approximated

responses.

In the present study, the response surface methodology is adopted as a solver of inverse problems. For the present study, predictions of delamination positions and sizes from measured electric resistance changes are one of the inverse problems. The response surface methodology gives three advantages for the problems. One of the advantages is that the inverse problems can be approximately solved without consideration of fracture mechanisms. For most of the composite materials, it is very difficult to understand the exact fracture mechanisms especially about electric resistance. The second advantage is that the approximated response surfaces can be evaluated using statistical tools. The last advantage is that the minimum variances of the response surfaces can be obtained using design of experiments with the small number of experiments.

For most of the response surfaces, the functions for the approximations are polynomials because of simplicity. For the cases of quadratic polynomials, the response surface is described as follow.

$$y = \beta_0 + \sum_{j=1}^k \beta_j x_j + \sum_{j=1}^k \beta_{jj} x_j^2 + \sum_{i=1}^{k-1} \sum_{j=i+1}^k \beta_{ij} x_i x_j \quad (1)$$

The unbiased estimators of the coefficients  $\beta$  is obtained using the well-known least square method. In order to judge the goodness of the approximation of the response surface, the adjusted coefficient of multiple determination  $R^2_{adj}$  is used.

$$R^2_{adj} = 1 - \frac{SS_E / (n - k - 1)}{S_{yy} / (n - 1)} \quad (2)$$

where  $n$  is total number of experiments,  $k$  is total number of variables,  $S_{yy}$  is the total sum of squares and  $SS_E$  is the square sum of errors. Each coefficient of the response surface can be tested using t-statistic.

Design of experiments (DOE) is applied to reduce the variant of each coefficient in the approximated responses. In the present study, the D-optimal design is adopted [9].

Computation of changes of electric resistance of a specimen is one of direct problems, and the calculations of delamination position and size from the electric resistance changes are inverse problems. In the present study, the delamination position and size is estimated inversely from the measured change of resistance data.

The changes of resistance data of multiple segments between electrodes of the specimens are measured using many specimens that have various delamination size and position. In the present study, the delamination location and size is quantized into levels to obtain large noise margin. The delamination position is quantized into 6 levels (spacing 45mm). The delamination size is quantized into 3 levels. The level-1 is the size from 0 mm to 4mm. The level-2 is the size from 4 to 7mm. The level-3 is the size from 7 to 12 mm.

For the direct problem to obtain responses of the strain due to delamination introduction, full factorial DOE is adopted because the total number of combinations is only 18 and the measured data may include large experimental error.

The optimal DOE for the direct problems is not always optimal DOE for the inverse problems. In the present study, using the response surfaces of the direct problem, many approximated change of resistance data are generated. From the approximated change of resistance data, DOE for the inverse problems are conducted.

Using the data selected by the DOE for the inverse problems, the response surfaces for the inverse problems are constructed. In the case of selections of the data point for the inverse problems, the experimental data points that were conducted for the direct problems are always selected. The total number of data points for DOE for the inverse problems must be larger than the number of experiments. Usually to obtain accurate response of the direct problems is easier than to obtain the response of the inverse problems, and the inverse response surface requires more data points to obtain accurate response surfaces for the inverse problem. This is because the direct response surface data is adopted for the construction of the inverse response surfaces.

The response surface methodology (RSM) is similar to the Artificial Neural Network (ANN) of the famous back propagation training. The RSM has advantages of easy calculations and the availability of the strong statistical tools and DOE in compensation for the decrease of fitness compared with the ANN. The decrease of the fitness can be recovered by adopting area segmentations.

### Specimens and experimental procedures

#### Specimens

Material used in the present paper is graphite/epoxy. The type of unidirectional prepreg sheet is A125-Rc33% produced by Shin-Nihon Steel Chemistry Co.. The stacking sequence is  $[0_2/90_2]_s$ . The cure condition is  $180^\circ\text{C} \times 1\text{MPa} \times 2\text{hr}$ . In order to measure the change of electric resistance, electrodes of 0.02mm thickness copper foil are mounted on the prepreg laminates and integrally cured.

Seven electrodes are mounted on a specimen top surface in the present study. Using the laminates, beam type test specimens of 290mm long, 15mm wide and about 1mm thick were produced. The beam specimen configuration is shown in Figure 2. The reason of mounting all electrodes on the same top surface is to simulate to identify invisible inner delamination cracks by mounting electrodes just on the inner surface of shell type structure such as the aircraft.

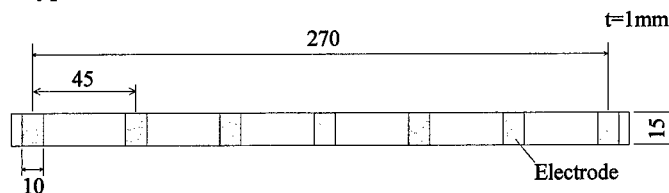


Figure 2 Specimen configurations

#### Electric circuit

Since electric resistance change due to delamination crack growth is very small, the resistance change is measured using the bridge circuit as shown in Figure 3. The electric resistance change can be measured as strain using the static strain amplifiers. The electric resistance change is expressed using measured "strain" data

as follow.

$$\frac{\Delta R}{R k_s} = \varepsilon \quad (3)$$

where,  $\Delta R$  is the electric resistance change due to generation of a delamination crack,  $R$  is the initial electric resistance,  $k_s$  is a gage factor, and  $\varepsilon$  is the measured strain. Note that the word "strain" does not means deformation of the specimen but means electric resistance change ratio in the present study. The gage factor is 2.

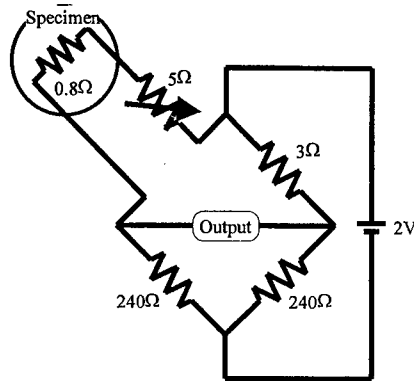


Figure 3 Bridge circuit

### Experimental procedures

In order to create delamination cracks in the beam specimens, three-point-bending tests were conducted. The middle point is loaded from the other surface on which the electrodes are mounted. This is to simulate the electrodes locate inside of the structures and the load comes from the outside. The loading from the other side induced a larger delamination crack is in the  $0^\circ$ - $90^\circ$  interface near the electrodes. For all tests, MTS closed-loop material testing machine was used. Tests were conducted under displacement control condition at cross head speed of 1.3mm/min.

After the creation of a delamination crack, each electric resistance change of six segments were measured as static strain change. Delamination location and size were detected using the ultrasonic C-scan. The delamination position is the center point of the delamination crack from the specimen center.

### Experimental results and discussion

#### Identification of delamination location

The inverse response surfaces were constructed from only experimental data of 54 cases without using design of experiments for comparison. In the inverse response surface for the estimation of the delamination location, the delamination location is a response, and the strain data are variables. Quadratic polynomials are adopted in the response surface.  $R_{ad}^2$  of the response surface is 0.642.

Using the method based on the design of experiments described before, new response surfaces were constructed.  $R^2_{ad}$  of the response surface is 0.698. The value is improved compared with the response surface based only on the experimental data (0.642). The estimated results using the improved response surface are shown in Figure 4. In this figure, the abscissa is exact levels of delamination location, and the ordinate is estimated level. For example, when the estimated level is exactly fine, the data locates on the diagonal line in the figure. The lattice pattern on the figure represents each width of level of the delamination location. The symbols of solid circle are estimated positions of 90 cases that are used for construction of the response surface. The symbols of open circle are estimated positions of 6 cases that are not used for the construction of the response surface though the 6 cases are not pure experimental data but calculated from the direct response surfaces.

The number of the exactly estimated level of the delamination position is 52 in 90 cases that were used for construction of the response surface, and the exact performance is 57.8 %. When the adjacent levels of the delaminating locations are admitted as fair estimations, the number of fair estimations is 84, and the fair estimation performance is up to 93.3%. In the cases of the estimations of the cases that were not used for the construction of the response surface, the exact performance is 50%, and the fair performance is 83.3%. The performances of the response surface using design of experiments are clearly improved compared with the performances of the response surface using experimental data only.

#### Identification of delamination size

The inverse response surface was constructed from only experimental data of 54 cases without using design of experiments for comparison as the same way discussed before. The delamination size is a response, and the strain data are variables in the inverse response surface for the estimation of the delamination size. Quadratic polynomials are adopted in the response surface.  $R^2_{ad}$  of the response surface is 0.439.

Using the method based on the design of experiments described before, a new response surface to estimate the delamination size was constructed. As the same way of the response surface of delamination location, the response surface of the estimation of the delamination size is optimized using t-statistics.  $R^2_{ad}$  of the response surface is 0.700. The estimated results are shown in Figure 6. The abscissa, the ordinate and the symbols are similar to Figure 5.

The number of the exactly estimated level of the delamination size is 76 in 90 cases that were used for construction of the response surface, and the exact performance is 84.4 %. In the cases of the estimations of the cases that were not used for the construction of the response surface, the exact performance is 66.7%.

Compared with the estimation performance by the response surface from the experimental data only, the response surface using the design of experiments gives fairly good performance. Although the exact estimation performance of the small level 1 crack has relatively smaller than the performances of larger cracks, the fair performance of the level 1 crack is up to 100%.

Based on these experimental results, it can be concluded that delamination identification is practically possible using electric resistance change with response surfaces without consideration of mechanisms.

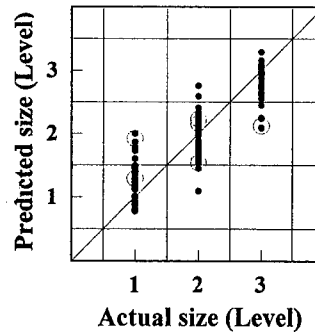
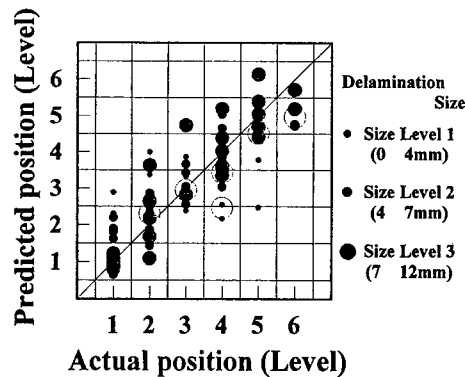


Figure 5 Predicted results of location levels      Figure 6 Predicted results of size

## Conclusions

- (1) The electric potential method with response surfaces is applicable for smart structure of delamination identifications of graphite/epoxy composites.
- (2) Using response surfaces and design of experiments, the inverse problems of identification of delamination cracks is easily obtained by low computational cost.

## REFERENCES

- 1.P.E.Irving and C.Thiagarajan, Fatigue damage characterization in carbon fibre composite materials using an electric potential technique, *Smart Materials and Structures*, 7, (1998) 456-466.
- 2.J.C.Abry, S.Bochard, A. Chateauminois, M.Salvia and G.Giraud, In situ monitoring of flexural fatigue damage in CFRP laminates by electric resistance measurements, *Proceedings of 4th ESSM and 2nd MIMR conference*, Harrogate,(1998) 389-396.
- 3.Akira Todoroki, Katsuya Matsuura and Hideo Kobayashi, Application of Electric Potential Method to Smart Composite Structures for Detecting Delamination, *JSME International J., Series A*, 38-4, (1995)524.
4. Akira Todoroki, Hideo Kobayashi and Katsuya Matsuura, Application of Electrical Potential Method as Delamination Sensor for Smart Structures of Graphite/epoxy, *US-Japan Workshop on Smart Materials and Structures*, Edited by K.Inoue, S.I.Y.Shen and M.Taya, University of Washington TMS, 1997,47-54
5. Akira Todoroki, Delamination Detection by Electric Resistance Change for Graphite/PEEK Composites, *Proceedings of the 5th Japan International SAMPE Symposium*, (1997),899-904
- 6.Akira Todoroki and Hiroshi Suzuki, Evaluation of Orthotropic Electrical Resistance for Delamination Smart Detection of Graphite/Epoxy Composites by Electrical Potential Method, *Proceedings of 1st Asian-Australian Conference on Composite Materials (ACCM-1)*, 1998, 630-1 ~ 630-4
- 7.Akira Todoroki and Hiroshi Suzuki, Health Monitoring of internal delamination cracks for graphite/epoxy by electric potential method, *Proceedings of the 4th European and 2nd MIMR Conference*, (1998),
8. Akira Todoroki and Hiroshi Suzuki, Identification of delamination crack of graphite/epoxy laminates by electric potential method for health monitoring, *Proceedings of the 2nd Japan-France Seminar on Intelligent Materials and Structures*, Universite Louis Pasteur, 1998,
- 9.R.H.Myers and D.C.Montgomery, "Response Surface Methodology: Process and Product Optimization Using Designed Experiments", John Wiley & Sons. Inc.(1995)

## **Internal Strain Measurement of FW FRP Pipe with Optical Fiber Sensors**

T.Kosaka, K.Osaka, M.Sando and T.Fukuda

### **Abstract**

A smart manufacturing is one of the most important technologies in the field of smart composites. Fiber optic sensors are suitable for smart composites as sensors and used to measure internal strain or temperature. Then, sensor technologies using optical fiber sensors have been studied for measurement of internal strain, temperature and detection of damages in composite laminates. High functional FW molded composites have abilities of the high reliability and the low total cost including maintenance cost. It is very important to study the smart manufacturing technique of FW molded composites for development of the practical products.

In this paper, internal strain measurements of FW molded pipes with EFPI (Extrinsic Fabry-Perot Interferometer) optical fiber sensors were conducted in the curing process. A vinyl ester (RIPOXY) and an epoxy resin are used as the matrix resin. From the experimental results of GF/Ripoxy pipe in the room temperature (RT) cure, it is found that the end of cure can be detected. At the curing stage of GF/Epoxy pipe, curing shrink was detected. Internal strain outputs of GF/Ripoxy pipe in the after-curing process shows large residual strain at the cooling stage due to the resin rich region around the embedded optical fiber sensor. Internal strain in GF/Epoxy pipe represented thermal shrink very well. It is found that the internal strain of FW pipe can be measured with optical fiber sensor. Then, It is concluded that optical fiber sensors are useful for smart manufacturing of FW molded composites, but more detail investigations are necessary for quantitative cure monitoring.

### **Introduction**

Smart manufacturing technologies include techniques of control and monitoring of manufacturing process such as a cure-monitoring, and a manufacturing technique of smart composites such as embedding technique of sensors and actuators. Smart manufacturing technologies are important for smart composites, and many studies of them have been conducted. However, there are few studies on their application to FW molded composites. FW composites with sensor functions have added values of high reliability and low maintenance cost. Therefore, it is important to establish manufacturing



process of high functional FW composites.

Optical fiber sensors have many advantages of small size, lightweight, high flexibility and so on, and are most suitable for embedding in FW composites. A spectroscopy-based optical fiber sensor measures changes of chemical constitution in the resin system, a refractive index sensor does changes of refractive index of the resin, and an optical fiber strain sensor does internal strain which indicate curing and thermal shrink of the resin [1,2]. Optical fiber strain sensors also can be used for health monitoring in operation. Then, an EFPI optical fiber sensor was used as a strain sensor in this study.

In this paper, internal strain measurements of FW GF/Ripoxy and GF/Epoxy pipes with embedded optical fiber sensors in the curing process were conducted. Dielectric parameters and temperatures of the pipes were also measured to observe the curing state and the time history of temperature. Some experiments were conducted to understand the relation between the internal strain and the curing state.

## Experimental System

### EFPI Optical Fiber Sensors

Figure 1 shows a schematic diagram of a sensing part of EFPI optical fiber sensor used in this study (FISO Technologies, non-compensated type strain gage). The sensing part has an air gap and is covered with a silica tube. The diameter of sensing part is  $310\mu\text{m}$ , the gage length is about  $1.0\text{mm}$  and the cavity length is about  $16\mu\text{m}$ . A transfer function of the EFPI sensor is written as:

$$T = \frac{F \sin^2(2\pi d/\lambda)}{1 + F \sin^2(2\pi d/\lambda)} \quad (1)$$

where,  $d$  is a cavity length,  $\lambda$  is a wave length of a light and  $F$  is a finesse parameter. When a broadband light is used as a light source, the cavity length can be derived from equation (1) by measuring the transfer function of EFPI [3]. This measurement system has the ability of absolute and stable measurement of the cavity length. FTI-Bus500 (FISO Technologies, Co. Ltd.) was also used as the strain measurement system which obtained the strain from the interference broadband light through a correlator, and it is capable of providing precise, absolute, and perfectly linear measurements. The strain is calculated from the cavity length change  $\Delta d$  as follows:

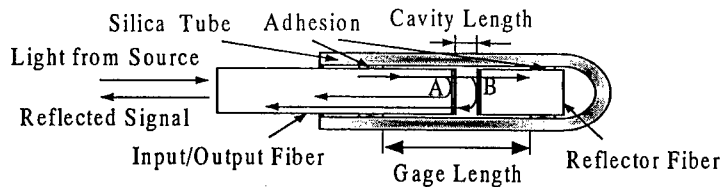


Fig.1 Schematic diagram of sensing part in EFPI optical fiber sensor

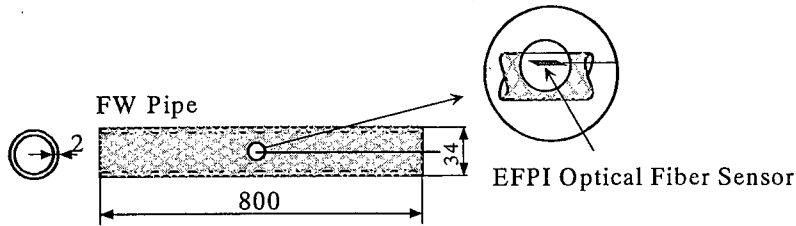


Fig.2 Embedding configuration of optical fiber sensor and the dimensions of FW pipe (unit:mm)

$$\varepsilon = \frac{\Delta d - d_0 \alpha_0 \Delta T}{L_G} \quad (2)$$

where,  $d_0$  is a initial cavity length,  $\alpha_0$  is a coefficient of thermal expansion of silica,  $\Delta T$  is a temperature change and  $L_G$  is a gage length shown in Fig.1. In this experiment, the effect of temperature change can be negligible because  $d_0 \ll L_G$ .

#### FW FRP Pipe

In this paper, E-glass fibers (Nippon Sheet Glass, Co. Ltd.) and two kinds of resin, which are a vinyl ester, RIPOXY R-802 (Showa High Polymer, Co. Ltd.) and an epoxy, EPIKOTE 807 (Yuka Shell Epoxy, Co. Ltd.), were used to fabricate FW GFRP pipes. GF/RIPOXY pipe was cured at RT (26°C) for 20 hours in the RT curing process and at 110°C for 100 minutes in the after-curing process, and GF/EPOXY pipe was cured for 2 hours at 100° and for 4 hours at 175°.

A FW molding machine was improved to easily embed optical fiber sensors. The embedding configuration of the optical fiber sensor and the dimensions of FW pipe are shown in Fig.2. The winding method was a helical winding and the winding angle is 45°. The optical fiber sensor was initialized before the embedding. The winding was

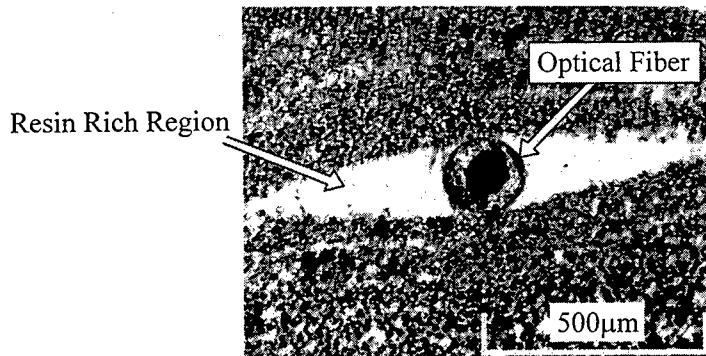


Fig.3 Cross sectional photograph of embedded optical fiber sensor in FW GF/Ripoxy pipe

stopped at the half thickness, and then the sensor was embedded toward the length of FW pipe. After the winding process, the optical fiber sensor was connected again to the strain measurement system. Figure 3 shows a photograph of cross section of embedded optical fiber sensor in GF/Ripoxy pipe. The resin rich region around the embedded optical fiber was seen because the embedding direction was not parallel to the reinforcing direction.

### Experimental Methods

Three kinds of experiments conducted in this paper are shown as follows:

- A. Internal strain and dielectric parameters measurements of FW pipe
- B. Internal strain and dielectric parameters measurements of resin
- C. DSC (Differential Scanning Calorimeter) analysis of resin

The experiment A was conducted to measure the internal strain of FW pipe by the embedded EFPI optical fiber sensor. The measuring system of internal strain and dielectric parameters of FW pipe is shown in Fig.4. The internal strain outputs were recorded by a personal computer through a serial line per 15 seconds. Eumetric 100A (Micromet Instruments, Inc.) dielectric sensor system was used for the dielectric parameters measurements. The measuring cycle of the dielectric parameters was 2 minutes and the setting frequencies were 0.1Hz, 1 Hz, 10 Hz and 100 Hz. The thermocouple was used for the temperature measurement in 2 minutes cycle. For the cure monitoring, the most important dielectric parameter is an ion viscosity, which indicates movability of the electric charges and dipoles in high polymer chains [4]. An ion viscosity is obtained from a permittivity and a loss factor, where the former is a real part of a complex dielectric constant and the latter is an imaginary part. The dielectric sensor and the thermocouple were attached on the surface of FW pipe.

The experiment B is for investigation of effects of the reinforcing fiber strands on the strain outputs. The EFPI optical fiber sensor, the dielectric sensor, and the thermocouple were put in the resin which filled an aluminum cup. The curing condition and the measurement system were same as the experiment A. The thermal history of resin in the curing process is studied by the experiment C.

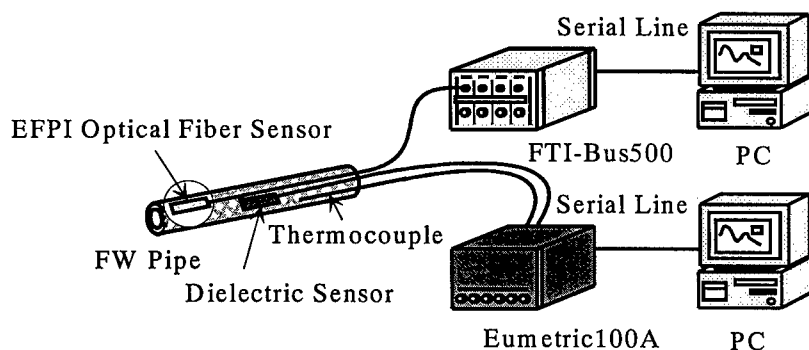


Fig.4 Measuring system of internal strains and dielectric parameters of FW pipe

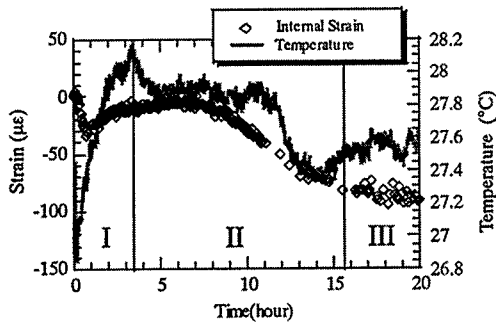


Fig.5 Relation among internal strain, temperature and time in FW GF/Ripoxy pipe in RT-cure.

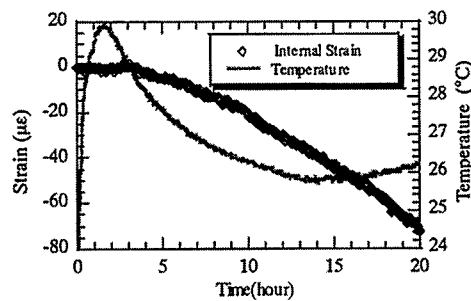


Fig.6 Relation among internal strain, temperature and time in Ripoxy resin in RT-cure.

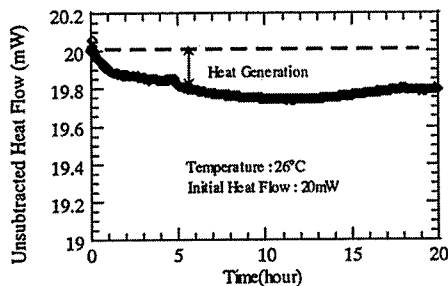


Fig.7 DSC Analysis of Ripoxy in RT-cure.

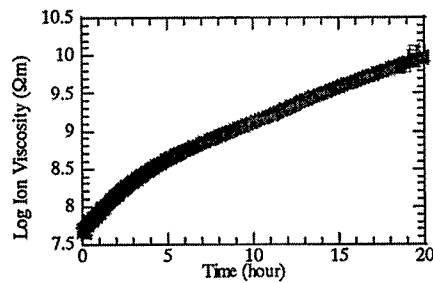


Fig.8 Relation between log ion viscosity and time in GF/Ripoxy pipe in RT-cure.

## Experimental Results and Discussions

### FW GF/Ripoxy Pipe - RT-cure

The experimental results of the internal strain and temperature measurements of GF/Ripoxy pipe and Ripoxy resin in the RT-curing process are shown in Fig.5 and Fig.6, respectively. From the experimental results, the behavior of internal strain outputs of the optical fiber sensor in the FW pipe can be divided into three stages as follows (shown in Fig.5):

Stage I : temperature increases, strain increases.

Stage II : temperature decreases, strain decreases.

Stage III : temperature is constant, strain decreases.

At the stage I, the strain and the temperature increased by almost  $30\mu\epsilon$  and then became constant. From the experimental results of DSC shown in Fig.7, it is found that the increase of temperature at the stage I was caused by the heat reaction of resin. Figure 5 shows that the strain was constant at the stage I because the optical fiber sensor was not constrained by the liquid state resin. Thus, the increase of strain in the

FW pipe is probably caused by thermal expansion of the reinforcing fiber strands which constrain the optical fiber.

At the stage II, the results of the FW pipe and resin show that the strain began to decrease. It indicates that the optical fiber was constrained by the resin as well as by the fiber strands. The decrease of strain indicates both thermal and curing shrinks because the temperature was falling down due to the decrease of heat generation. The starting time of the decrease of temperature curve is different from that of strain curve because their embedded positions are different.

At the stage III, the temperature converged to a constant value but the strain outputs continue to decrease. Figure 8 shows that cure reaction did not finished completely in 20 hours, because the ion viscosity continue to increase and the convergence represents the end of cure. Therefore, the strain outputs represent curing shrink. It is concluded that the curing shrink can be measured by using the embedded optical fiber sensor in the curing process of FW GF/Ripoxy pipe. However, the thermostatic setting should be necessary to detect the end of cure due to the high sensitivity of the sensors to thermal strain of the resin.

#### FW GF/Ripoxy Pipe - After-cure

Figures 9 and 10 show the experimental results of internal strain and temperature measurement of GF/Ripoxy pipe and Ripoxy resin in the after-curing process, respec-

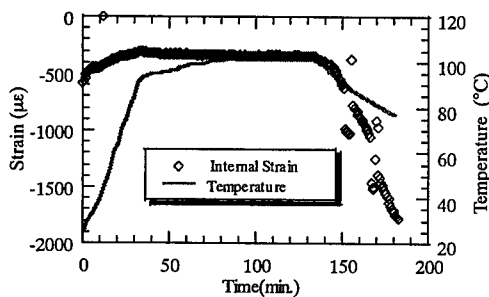


Fig.9 Relation among internal strain, temperature and time in FW GF/Ripoxy pipe in after-cure.

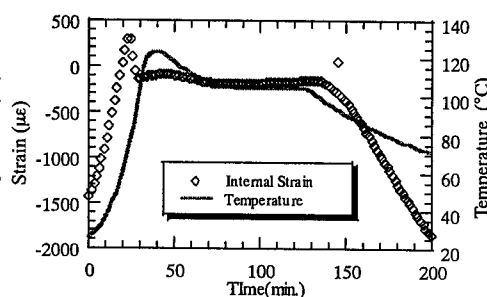


Fig.10 Relation among internal strain, temperature and time in Ripoxy resin in after-cure.

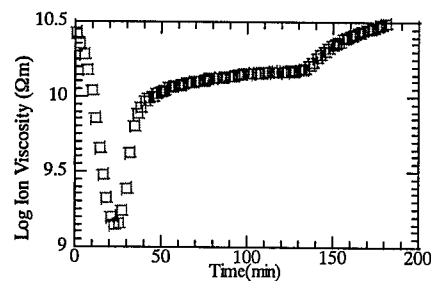


Fig.11 Relation between log ion viscosity and time in GF/Ripoxy pipe in after-cure.

tively. The internal strain went up with rise in temperature at the heating stage (0-35 min.) with the thermal expansion coefficient less than at the cooling stage (135-180min.). Figure 11 shows that the resin was melt at the heating stage. Thus, it is concluded that the optical fiber in the FW pipe was constrained mainly by the glass fiber strands.

At the cooling stage, the thermal expansion coefficients obtained from the experiment A and the experiment B are almost same. It means that there was the resin rich region around the optical fiber sensor in FW pipe. Then, in this experiment, the large thermal residual strain of the optical fiber sensor in FW pipe was detected. These facts suggest that the embedding configuration affect the strain outputs of the optical fiber sensor.

### FW GF/Epoxy Pipe

Figures 12 and 13 show the experimental results of internal strain and temperature measurement of GF/Epoxy pipe and Epoxy resin, respectively. The time history of log ion viscosity of GF/Epoxy pipe is shown in Fig.14. At the heating stage, no strain change was detected before the start of cure at 35 min. The difference of strain behavior of FW pipe between GF/Ripoxy and GF/Epoxy at the heating stage may result in the resin rich region around the optical fiber. Figures 12 and 13 show the curing shrink was detected at the curing stage where the temperature was constant. The measured curing shrink of FW pipe was much smaller than that of resin due to constraint of reinforcing fiber strands. The internal strain of FW pipe follows temperature at the cooling stage,

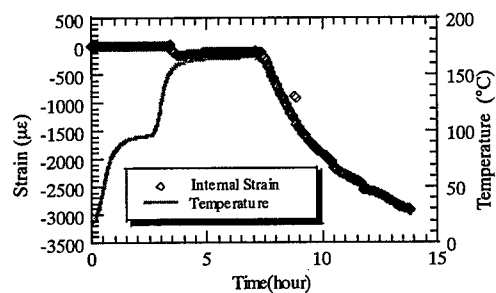


Fig.12 Relation among internal strain, temperature and time in FW GF/Epoxy pipe.

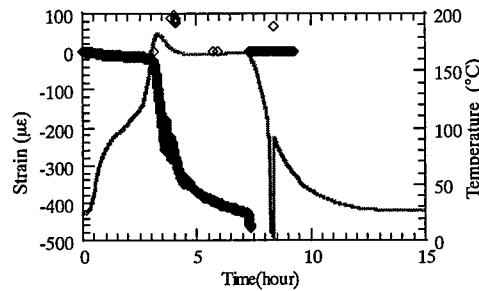


Fig.13 Relation among internal strain, temperature and time in Epoxy resin .

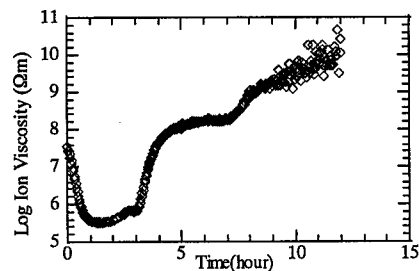


Fig.14 Relation between log ion viscosity and time in GF/Epoxy pipe.

then it represents a thermal shrink very well. The strain output of epoxy resin at the cooling stage could not be obtained because the sensor was broken. The thermal expansion coefficient of optical fiber sensor in the FW pipe at the cooling stage was  $19.5 \times 10^{-6}/^{\circ}\text{C}$ , which is equivalent to the value at the 40% volume fraction. It suggests that the pipe has low volume fraction, or the resin rich region affects the strain outputs.

## Conclusions

The behaviors of the EFPI optical fiber sensor embedded in the FW GF/Ripoxy and GF/Epoxy pipe were investigated. It is found that the curing shrink can be measured by using the EFPI optical fiber sensor in the curing process of the FW pipe. From the experimental results in after-curing process of GF/Ripoxy, it is concluded that the embedding configuration strongly affects on the sensor outputs. Thus, it is necessary to select the sensor range with considering the thermal residual stress. Internal strain in GF/Epoxy pipe represented thermal shrink very well. More detail investigations are necessary for reliable measurements of internal strains.

## References

1. G. R. Powell, P. A. Crosby, D. N. Waters, C. M. France, R. C. Spooncer, and G. F. Fernando, "In-situ cure monitoring using optical fibre sensors-a comparative study", *Smart Material Structure*, 7, 1998, 557-568
2. C. Doyle, A. Martin, T. Liu, M. Wu, S. Hayes, P. A. Crosby, G. R. Powell, D. Brooks and G. F. Fernando, "In-situ process and condition monitoring of advanced fibre-reinforced composite materials using optical fibre sensors", *Smart Material Structure*, 7, 1998, pp.145-158
3. C. Belleville and G. Duplain, "White-light interferometric multimode fiber-optic strain sensor", *Optic Letters*, Vol.18, No.1, 1993, pp.78-80
4. J. Mijovic, J. M. Kenny, A. Maffezzoli, A. Trivisano, F. Bellucci and L. Nicolais, "The principles of dielectric measurements for in situ monitoring of composite processing", *Composites Science and Technology*, 49, 1993, pp. 277-290

## **Strain Monitoring of IACC Yachts Using Fiber Optic Distributed Sensors**

Hideaki Murayama, Kazuro Kageyama, Isao Kimpara,  
Akiyoshi Shimada and Hiroshi Naruse

### **Abstract**

We have developed a monitoring system of ship structures by using some fiber optic sensors. In this paper a health monitoring system using a fiber optic distributed strain sensor, namely a Brillouin optical time domain reflectometer (BOTDR), for International America's Cup Class (IACC) yachts is described. The BOTDR is capable of measuring the strain on an arbitrary fiber section. Most components of the IACC yachts consist of an aluminum honeycomb core sandwiched between carbon fiber reinforced plastic (CFRP) laminates. We equipped two IACC yachts with fiber optic strain sensors designed to measure the distributed strain and to detect any deterioration or damage to the yacht's structures using BOTDR. In this paper, a structural health monitoring technique for IACC yachts is proposed. And some important information about structural conditions of the IACC yachts could be obtained from our system through the periodical strain measurement in the field.

### **Introduction**

The concept of structural health monitoring, in which a structure is instrumented with a network of sensors to monitor the structural integrity, has lately become a subject of special interest. We have been especially interested to apply the health monitoring technologies using fiber optic sensors to a ship structure. In our past study, we applied some fiber optic sensors, such as fiber Bragg grating sensors (FBG), to structural monitoring of a ship [1][2].

The America's Cup is one of the world's famous yacht races. The yacht is called International America's Cup Class (IACC) yacht and it is about 24 m long with a mast about 35 m high. An IACC yacht has extremely lightweight structures and most components of the yacht are sandwich structures which consist of two carbon fiber reinforced plastic (CFRP) faces (called skin) kept separated by an aluminum

---

H. Murayama, K. Kageyama and I. Kimpara, Dept. of Environmental and Ocean Engineering,  
Univ. of Tokyo, 7-3-1, Hongo, Bunkyo-ku, Tokyo 113-8656, Japan

A. Shimada and H. Naruse, NTT Access Network Service Systems Laboratories, 1-7-1,  
Hanabatake, Tukuba-city, Ibaraki 305-0805, Japan



honeycomb core. In yachts assembled using CFRP sandwich composite materials, delamination, skin/core debonding and debonding between adhered members are major failure modes. Because of such structural failures, some yachts were critically damaged in the past America's Cup races. This means that winning requires technology that can monitor a yacht's structural integrity.

To implement reliably comprehensive monitoring and condition-assessment in IACC yachts, highly distributed and robust sensing system is required. Fiber optic sensors are recognized as one of the candidates for sensing component of health monitoring, because of their long-term reliability and ability to achieve quasi-distributed or distributed measurement.

The Brillouin optical time domain reflectometer (BOTDR) is a fiber optic distributed sensor based on Brillouin scattering, and it can measure strain and temperature in arbitrary regions of a sensing fiber. The optical effect only depends on the fiber material, so that the bare fiber itself acts as sensing element without any special fiber processing or preparation. This sensor system needs 3-6 minutes for acquisition time, which makes it suitable for monitoring static phenomena.

A strain measurement system using a BOTDR developed by Nippon Telegraph and Telephone Corporation (NTT) was applied to Asura and Idate. They are the two IACC yachts of Nippon Challenge syndicate that is Japanese entry in the America's Cup 2000. We equipped the yachts with fiber optic sensors to monitor a deformation and to detect deterioration or damage of the yachts. Sensing fibers were fixed along the hull and around the bulkhead. The former was used to measure the deformation of the yacht's structure and to detect any changes or deterioration in its longitudinal stiffness. The latter was used to detect debonding between the hull and the bulkhead supporting the mast. We successfully measured strain distributions of the yachts under dead load and the results were used to assess its structural condition.

### **Health Monitoring for IACC Yacht Structures**

In terms of structural design for an IACC yacht, it is important for the designers to provide the yacht with a sufficient longitudinal stiffness as if subjected to large longitudinal bending loads. The longitudinal stiffness also has a significant effect on speed, because the efficiency of sail power is proportional to the stiffness supporting the tension of the forestay. The forestay is a wire that extends from the head of the mast to the bow of a ship. And debonding between structural members has sometimes caused critical damages of yachts in past America's Cup. Many teams have especially suffered from debonding between the hull and the bulkhead.

So we determined to monitor the longitudinal stiffness of the yacht and the deformation of the adhered boundary between the hull and the bulkhead supporting the mast. When a yacht has any failures, such as debonding between the hull and the deck, the stiffness of the yacht's structure will be decreased. And we can expect that the failure cause a change to a strain distribution of the yacht. Our concepts of health monitoring with fiber optic sensors for IACC yachts are shown Fig. 1.

Our goal was to provide Nippon Challenge with structural information before

rather than during races because there is no chance for the crew to consider and solve the structural problems while sailing. After races or practices, the yachts were usually brought on land. So we had to assess the structural integrity using strain data for the yacht that was only subjected to static forces on land.

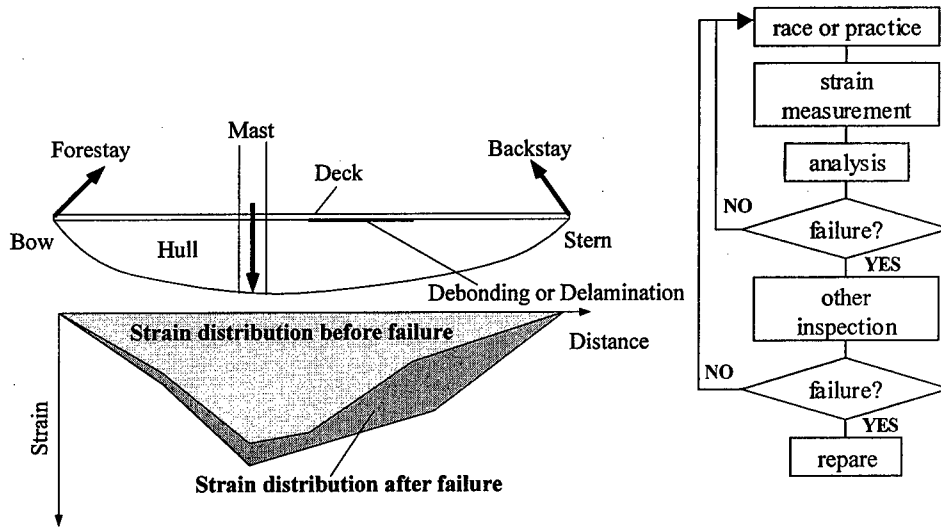


Figure 1 Concepts of health monitoring for IACC yacht structure

### Sensing System

When a pulsed signal is launched into an optical fiber, it is continuously backscattered as it propagates. Time resolution of the emerging backscattered light then reveals the spatial distribution of any external field that is capable of modulating, in a deterministic way, some characterizing property of the light, this latter being demodulated by the detector [3]. This means the capability of distributed sensing using fiber optic sensors. The Brillouin scattering is generated by nonlinear interaction between incident photons and acoustic phonons. And the Brillouin frequency  $\nu_B$  of an optical fiber depends on the glass temperature and strain. It was thus proposed that one could measure the strain and temperature of a fiber by analyzing the Brillouin scattered light [4]. The coefficients of  $\nu_B$  change,  $\partial \nu_B / \partial \epsilon$  and  $\partial \nu_B / \partial T$  are given by

$$\partial \nu_B / \partial \epsilon = 496 \text{ MHz} / 10^4 \mu \epsilon \quad (1)$$

$$\partial \nu_B / \partial T = 1.2 \text{ MHz} / K \quad (2)$$

respectively. The propagation delays of light traveling in the fiber are related to the distance  $x$  along the fiber. So the width  $W$  of the transmitted pulse signal gives the

special resolution  $\delta x$  as

$$\delta x = V_c W / 2 \quad (3)$$

where  $V_c$  is the velocity of light in the fiber [5]. We obtained 1 m spatial resolution from 10 ns pulses. The sensor accuracy of a BOTDR developed by NTT was assumed  $\pm 60 \mu\text{e}$  for deformation [6].

### System Integration

The sensing fibers were installed in the yachts under construction. They consisted two parts; one was fixed to the hull in the longitudinal direction and the other was adhered in the circumferential direction near the joint between the hull and the bulkhead supporting the mast. In this paper, the sensing fibers will be called the longitudinal sensing fiber and the circular sensing fiber respectively.

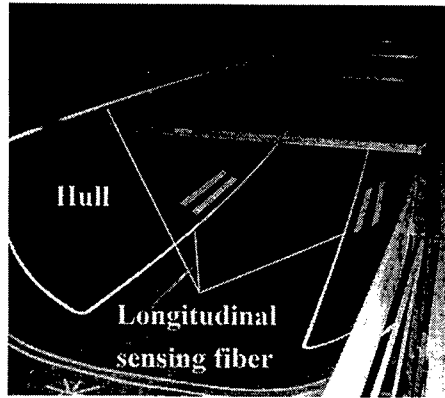


Figure 2 The sensing fiber covered with CFRP sheets

The optical fibers with 0.25 mm diameter were used as the sensing fibers. They were adhered on the inner surface of the hull and covered with CFRP sheets to protect them from various potential sources of damage including machine tools and shoes. The longitudinal sensing fiber covered with CFRP sheets in Idateen is shown in Fig. 2. We used a CAD application in order to calculate the actual positions and the length of the sensing fibers. Figure 3 shows the locations of the sensing fibers in Idateen. The longitudinal sensing fiber was set from a to i, and the circular sensing fiber set from j to m. The lengths between the gauge marks are also shown in Fig. 3.

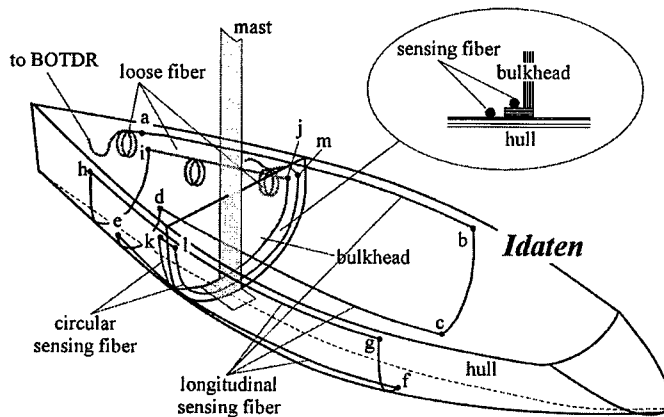


Figure 3 The sensing fibers in the Japanese IACC yacht

Longitudinal sensing fiber	Length (m)
a-b	10.3
b-c	1.6
c-d	8.3
d-e	1.7
e-f	8.3
f-g	1.6
g-h	10.5
h-i	4.3
total	46.6
Circular sensing fiber	Length (m)
j-k	6.2
k-l	0.2
l-m	6.2
total	12.6

## Distributed Strain Measurements of IACC yachts

### Measurement System

Distributed strain measurements using the BOTDR were implemented during maintenance periods when the yachts were on the slipways after races or practices. Figure 4 shows the measurement system. It consisted of fiber optic sensors, a BOTDR, and two computers; one for local control and the other for remote control. It was possible to control this system from our laboratory via a network.

During measurements, both the temperature distribution of the yacht and the structural condition were required to be kept constant. This is because BOTDR strain measurement results are affected by temperature change and it takes 3-6 minutes for the BOTDR to complete a measurement. Therefore, the strain measurements were carried out under static loading conditions after sunset.

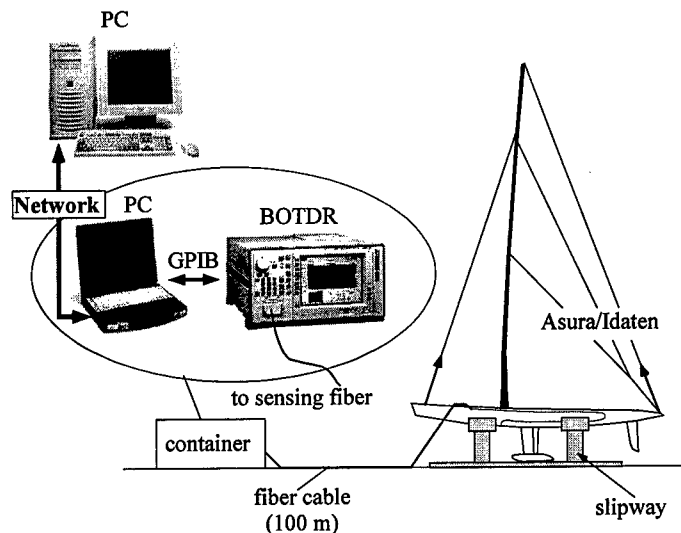


Figure 4 The measurement system in the Nippon Challenge base camp

### Results and Discussion

As shown in Fig. 3, the longitudinal sensing fiber was fixed to the hull with adhesive and it traveled back and forth twice in the longitudinal direction. During a longitudinal bending, it was capable of measuring the strain distribution of both the tensile and compressive side of the yacht.

Figure 5 shows the difference in the strain distributions under the different loading conditions. The forestay tension was set at 4 tons in one condition and it was set at 0 tons in the other condition. We are able to see the state of the hull that was

bent by the forestay.

The circular sensing fiber traveled back and forth along the boundary between the hull and the bulkhead supporting the mast. So it could measure a deformation in the boundary.

Figure 6 shows the difference in the strain distributions under the different loading conditions. The sidestay tension was set at 30 tons in one condition. The sidestay is often called a shroud. And in the other condition the mast was removed from the yacht so that we set the sidestay tension at 0 tons. We are able to see the structural state of the boundary between the hull and the bulkhead loaded by the sidestay tension.

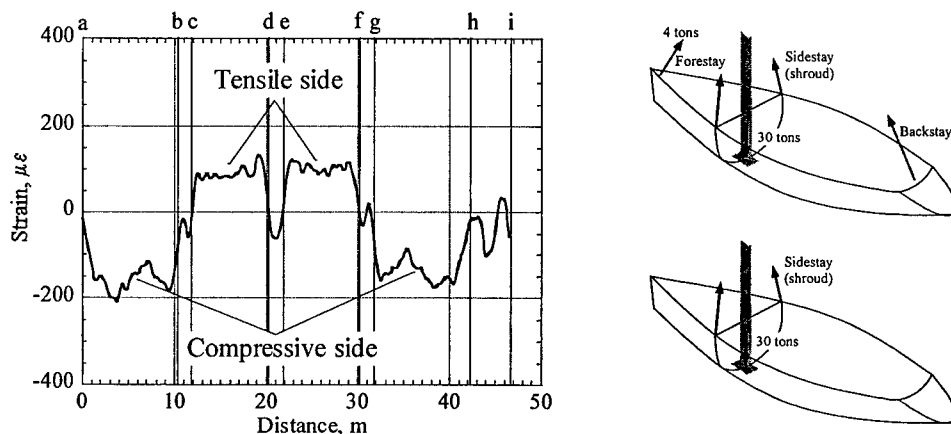


Figure 5 Strain distribution of the longitudinal sensing fiber and the loading condition

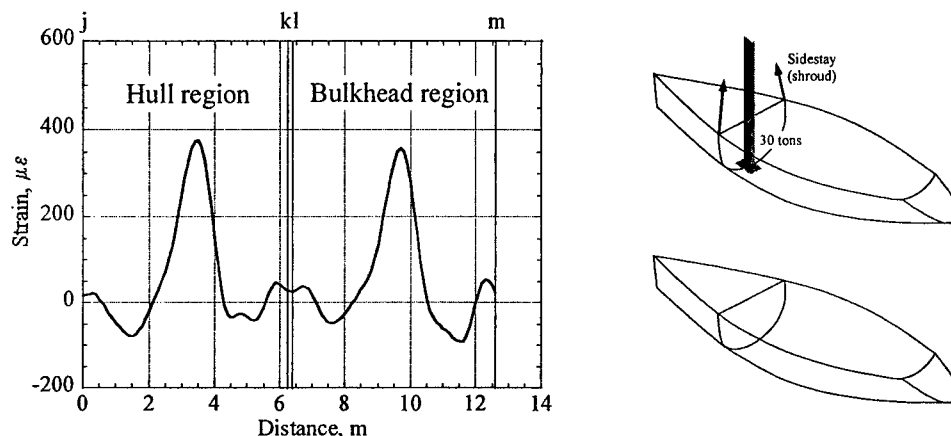


Figure 6 Strain distribution of the circular sensing fiber and the loading condition

These results mean that longitudinal strain distributions measured periodically under the 4 tons forestay tension can provide some information about any deterioration in the longitudinal stiffness of the yachts. Similarly, circular strain distributions measured periodically under the 30 tons sidestay tension can provide some information about damage or debonding of the adhered boundary between the hull and the bulkhead. Therefore, we conducted the structural health monitoring of the IACC yachts (Asura and Idaten) by assessing the difference between the latest strain distribution and the earlier data measured under the loading conditions.

## Conclusions

We successfully measured strain distributions of the IACC yachts by using the fiber optic distributed sensor. And the strain distributions of the sensing fibers acquired from the BOTDR were used to assess the structural integrity of the yachts. Fortunately, the system had not detected any failures because the Japanese yachts did not suffer critical damage during races. But based on our results, Nippon Challenge had been able to plan structural strategies.

## Acknowledgements

We thank Dr. Miyata of Tokyo University who is also the technical director of Nippon Challenge syndicate and Mr. K. Uzawa of GH Craft Ltd. for their kind support and helpful advice. Thanks are due to Mr. M. Katori, Mr. Y. Murata, G. Hayashi and all other staff of Nippon Challenge for the measurement operations that were carried out in the base camp.

## Reference

1. K. Kageyama, I. Kimpara, T. Suzuki, I. Ohsawa, H. Murayama and K. Ito, 1998. "Smart marine structures: an approach to the monitoring of ship structures with fiber-optic sensors", *Smart Materials and Structures*, 7:472-478
2. H. Murayama, I. Kimpara, K. Kageyama, T. Suzuki, I. Ohsawa and M. Kanai, 1997. "Application of Optical Fiber Sensors to Marine Structure", *Proc. of the Japan International SAMPE Symposium*, 1305-1310
3. A. J. Rogers, 1992. "Non-linear Distributed Optical-fiber Sensing", *SPIE Proc.*, 1797 :50-62.
4. A. W. Brown, M. D. DeMerchant, X. Bao and T. W. Bremner, 1999. "Analysis of the precision of a Brillouin scattering based distributed strain sensor", *SPIE Proc.*,

3670:359-365

5. A. Shimada, H. Naruse, K. Uzawa, H. Murayama and K. Kageyama, 2000. "Development of Integrated Damage Detection System for International America's Cup Class Yacht Structures Using a Fiber Optic Distributed Sensor", *SPIE Proc.*, 3986:in press
6. H. Ohno, Y. Uchiyama and T. Kurashima, 1999. "Reduction of the effect of temperature in a fiber optic distributed sensor used for strain measurements in civil structures". *SPIE Proc.*, 3670:486-496

## **Effects of Pressure on Measurement of Strains in EFPI Optical Fiber Sensors Embedded in FRP Laminates**

Katsuhiko Osaka, Tatsuro Kosaka, Yasuhiro Kawasaki and Takehito Fukuda

### **Abstract**

In the authors' previous study, the internal strain measurement of GFRP laminates by using EFPI optical fiber sensors showed unreliable outputs in a cooling process of an autoclave molding. Its cause seems to be the discrepancy of the optical fiber axis in the optical fiber sensor caused by the molding pressure. In the present paper, compression and shear tests of epoxy specimens where the optical fiber sensor was embedded were conducted to investigate effects of the pressure on the internal strain output. In the experiment, the strain output was monitored under the compressive and the shear load. The stress distributions were calculated by the FEM method to know the pressure applied to the sensor. The relation between the strain output and the calculated pressure on the sensor was obtained. From the results, it was found that the load equivalent to the autoclave molding pressure almost does not affect the strain output.

### **Introduction**

Recently, smart composites, which include sensors processors and actuators have been studied. The optical fiber sensors are suitable for the smart composites because of the advantage of small size, light weight, high strength and flexibility. An EFPI (Extrinsic Fabry-Perot Interferometer) optical fiber sensor is one of the most promising technologies to measure internal strains of materials.

In the previous study, the real-time measurement of internal strains in GFRP laminates with EFPI optical fiber sensors during an autoclave molding was conducted[1]. The experimental result of the internal strain measurement by the EFPI optical fiber sensor embedded in the GFRP cross-ply laminate along a direction perpendicular to the reinforcing fibers is shown in Figure 1. Though compressive strains should be measured in the cooling stage, the tensile strains are monitored as shown in the figure. These tensile strains may be caused by the discrepancy of the optical fiber axis in the sensing part of the optical fiber sensor under the molding pressure. Therefore, it is necessary to investigate the effects of the pressure applied to the sensor on its output for the reliable measurement.

In the present paper, compression and shear tests of epoxy specimens, where the EFPI optical fiber sensor was embedded, were conducted to examine the effects of the

---

K. Osaka, T. Kosaka and T. Fukuda, Department of Intelligent Materials Engineering, Osaka City University, 3-3-138 Sugimoto, Sumiyoshi-ku, Osaka, 558-8585, Japan  
Y. Kawasaki, Graduate School of Osaka City University



pressure on the strain output. The stress distributions of the specimens under the compression and the shear test were calculated by the FEM method to evaluate the pressure applied to the sensor.

## Experimental Method

### EFPI Optical Fiber Sensor

The constitution of the sensing part of the EFPI optical fiber sensor used in this study is shown in Figure 2. The sensing part is covered with a silica glass tube. The gage length is about 1.1mm and the diameter is about  $310\text{ }\mu\text{m}$ . A phase difference between a light from (A) and that from (B) changes with the length variation of the air gap.

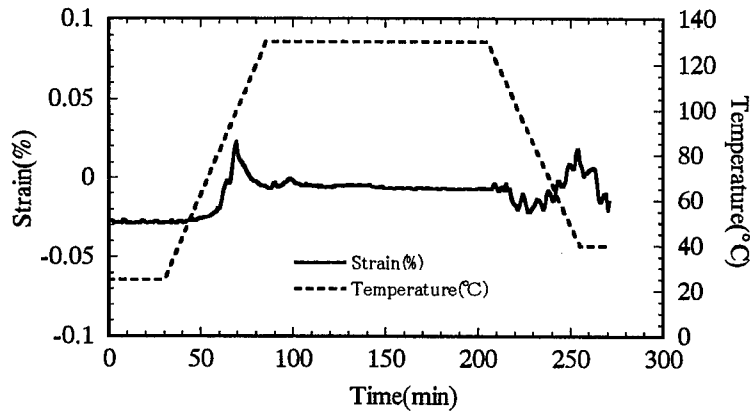


Figure 1 Result of internal strain measurement using the EFPI optical fiber sensor in the GFRP cross-ply laminate.

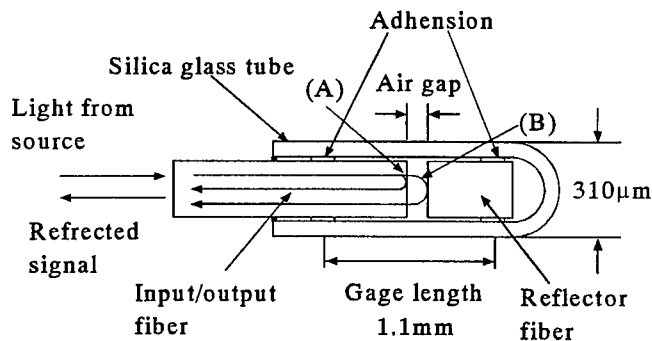


Figure 2 Sensing part of the EFPI optical fiber sensor.

## Specimens

Because the sensing part of the optical fiber sensor is very small (about  $310\text{ }\mu\text{m}$  diameter and about  $5\text{ mm}$  length) and fragile, it is difficult to load the surface of the optical fiber directly. Therefore, thin epoxy specimens where the optical fiber sensor was embedded were made and were used for the compression and the shear test. A bisphenol A type epoxy and a modified cycloaliphatic polyamine were used for the specimens. They were cured at  $60\text{ }^{\circ}\text{C}$  for 3 hours. The shape and dimensions of the compression and the shear test specimen are shown in Figure 3.

## Shear and Compression Tests

The loading jigs for the shear test are shown in Figure 4. The position of the air gap

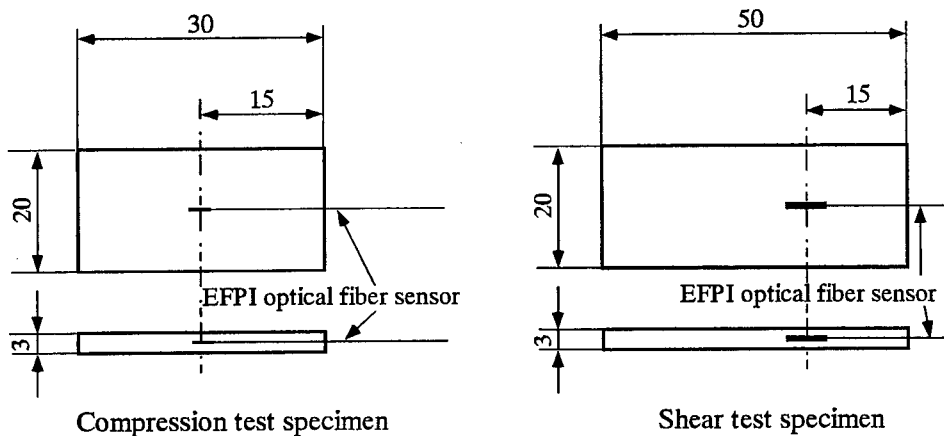


Figure 3 Shape and dimensions of the compression and the shear test specimen.

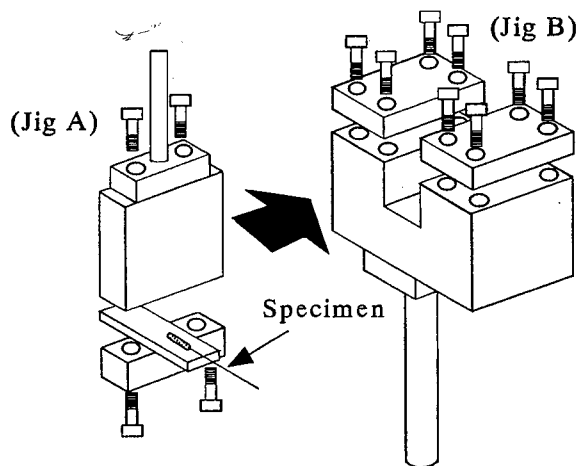


Figure 4 Shear test jigs.

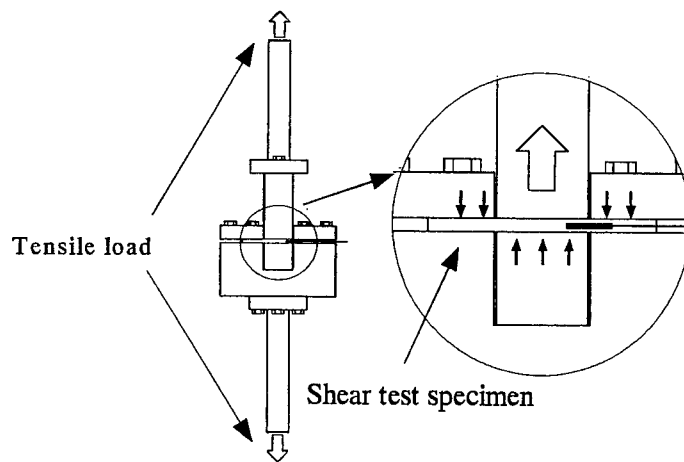


Figure 5 Loading setup for the shear test specimen.

of the optical fiber sensor is adjusted to the edge of the jig A, and the specimen is fixed. The jig A is placed in the jig B, and is fastened by flat plates. In the loading test, as shown in Figure 5, when the tensile load is applied to the jigs, a shear deformation is applied to the sensing part of the optical fiber sensor through the specimen. In the compression test, the specimen was set between two disc jigs in the test machine and the load was provided.

A INSTRON type tensile test machine (SHIMADZU Corp: Autograph AG-5000C) was used in these tests. The test speed was 0.01 mm/min. The output of the optical fiber sensor was monitored by FTI-Buss500 strain measurement system (FISO Technologies Inc.). The displacement was measured by a video-style noncontact extensometer, and the load was measured by a load cell.

## Experimental Results

Typical results from the shear test are shown in Figures 6 and 7. In Figure 6, the internal strain is plotted against the load. In Figure 7, the displacement is plotted against the load. The specimen is loaded up to about 3000 N. Figure 6 shows that the strain increases with the shear load. The strain is too small to be detected under the load of 300 N. As shown in Figure 7, the displacement curve has a linear relation with the applied load up to about 2500 N. But, the relation between the strain output and the load is nonlinear. In Figure 8, the internal strain obtained from the compression test is plotted versus the mean compressive stress applied to the specimen. The strain curve is almost expressed by two straight lines having different inclinations with the exception of an initial nonlinear part.

## Effects of the Pressure

Our interest is in the effect of the pressure on the strain output of the EFPI sensor.

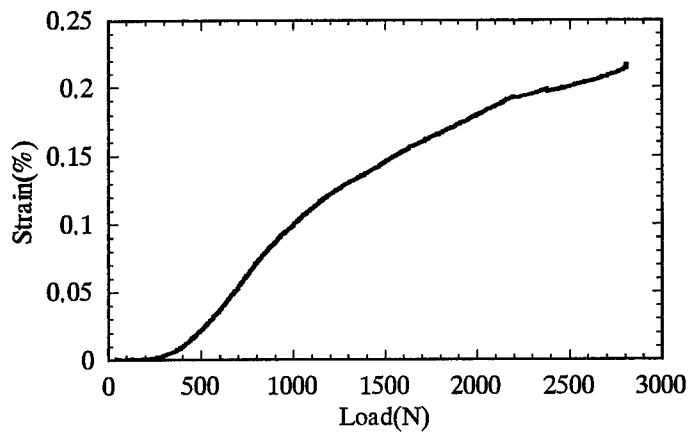


Figure 6 Strain output versus load applied to the specimen for the shear test.

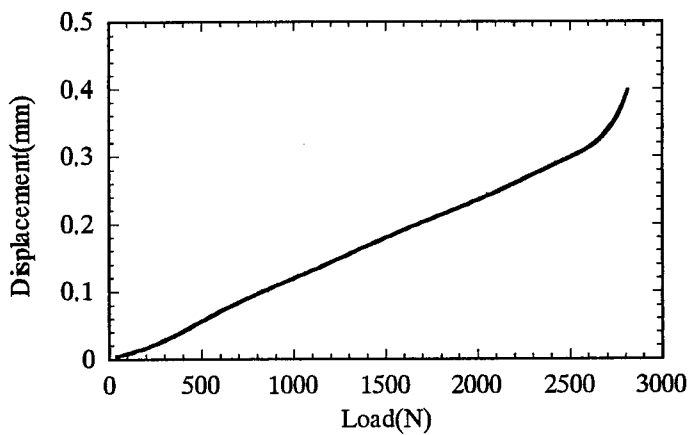


Figure 7 Load versus displacement curve for the shear test.

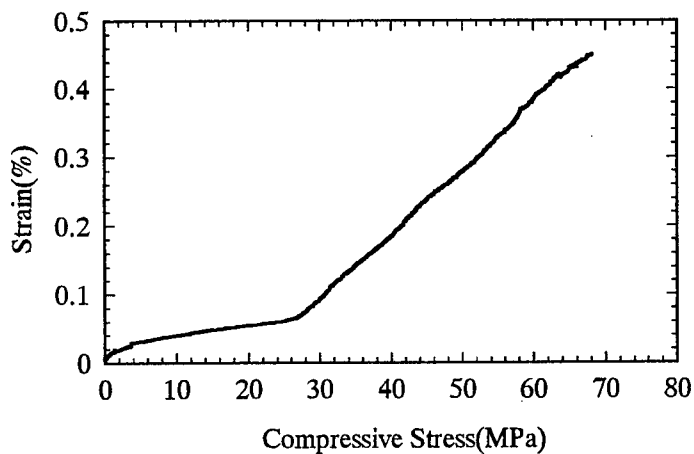


Figure 8 Strain output versus mean compressive stress applied to the specimen for the compression test.

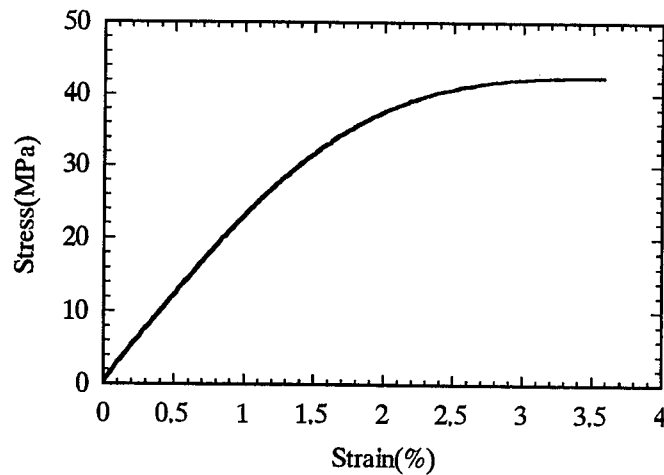


Figure 9 Strain versus stress curve of the epoxy used for the specimen.

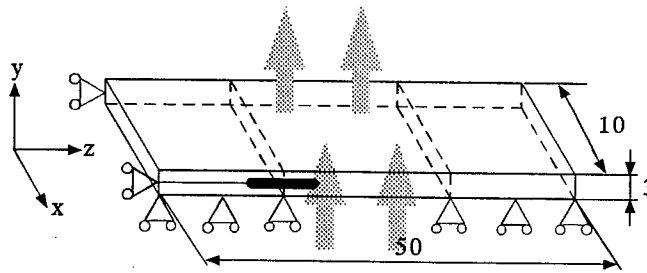


Figure 10 FEM model for the shear test.

In order to obtain the pressure applied to the sensor, the stress distributions of the specimens under the applied compressive and shear deformations were calculated by the FEM method. To obtain material properties of the specimen, its tensile tests were conducted. Figure 9 shows the representative stress-strain curve obtained from the tests. The curve has a non-linearity over 0.8 % strain. With use of this stress-strain curve, the elastoplastic analyses of the specimens were performed. The FEM model for the shear test is shown in Figure 10. The  $\epsilon_z$  strain component along the center axis of the optical fiber is so small, as compared with the strain output, that its contribution to the strain output is negligible. It means that only the share deformation affects the strain output. The average of  $\sigma_y$  stress components of elements adjacent to the surface of the sensing part (in Figure 11) is considered as a representative value to evaluate the effect of the molding pressure. Accordingly, the strain output for the shear test is plotted against the  $\sigma_y$  stress in Figure 12. The shape of the output curve is the same as that in Figure 6. From this result, it is found that the stress equivalent to the autoclave molding pressure (0.5 MPa) hardly affects the strain output. The result for the compression test is shown in Figure 13. In the figure, the strain in the sensing part of the EFPI sensor calculated by FEM is also shown, together with the strain output from the sensor. The strain output shows a little higher value than the calculation under 22 MPa. And smaller strains are

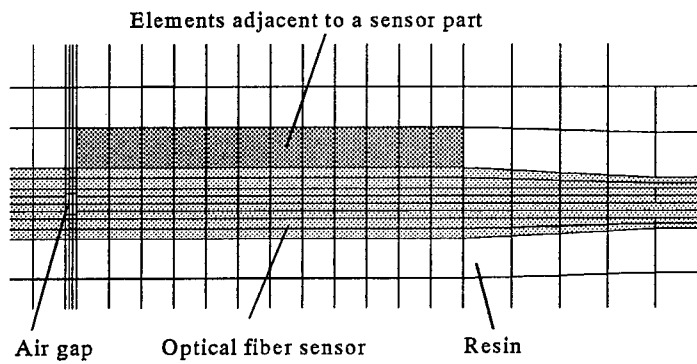


Figure 11 Sensing part of the optical fiber sensor in the FEM model.

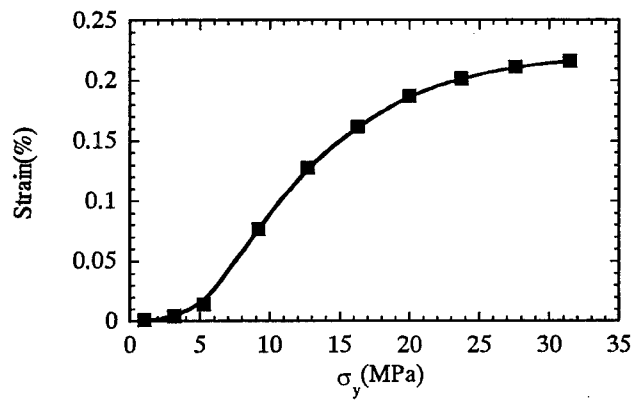


Figure 12 Relation between the calculated  $\sigma_y$  and the experimental strain output for the shear test.

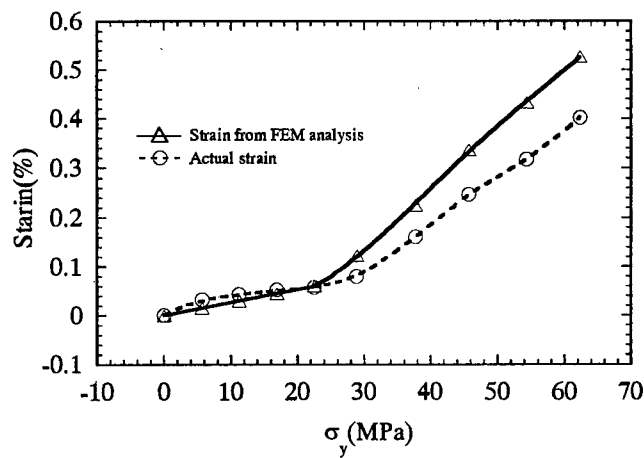


Figure 13 Relation between the calculated  $\sigma_y$  and the experimental strain output for the compression test.

detected up to 60 MPa. The cause of these differences between the detected and calculated strains seems to be effects of situations of the embedded sensor and restrictions of the deformation in the sensing part of the sensor by the pressure. But an exact cause should be examined in detail. In the compression test, it is also found that the stress equivalent to the autoclave molding pressure (0.5 MPa) hardly affects the strain output.

From both the shear and the compression test, it was found that the stress equivalent to the autoclave molding pressure (0.5 MPa) hardly affects the strain output. Therefore, in the cooling stage of the autoclave molding, the strain output of the optical fiber sensor embedded in the FRP laminate may be affected by the stress concentration due to a heat shrinkage and a nonuniform distribution of the reinforcing fibers. To discuss quantitatively, it is necessary to investigate an optical behavior of interference light of the EFPI optical fiber sensor when the shear deformation is applied.

## Conclusions

The compression and the shear test of the thin epoxy specimens where the EFPI optical fiber sensor was embedded were conducted to evaluate the effects of the pressure on the strain output. From the experimental results, it was found that the strain output is affected by the shear deformation. In order to obtain the pressure applied to the sensor, the stress distributions of the specimens were calculated by the FEM method. The strain output versus the stress applied to the sensor, which was calculated from the stress analysis, was obtained. From this relation, it was found that the compressive and the shear deformation caused by the autoclave molding pressure hardly affect the strain output. Therefore, in the cooling stage of the autoclave molding, the strain output may be affected by the stress concentration due to a heat shrinkage and a nonuniform distribution of the reinforcing fibers.

## Acknowledgments

This work was performed under the management of Research and Development Institute of Metals and Composites for Future Industries (RIMCOF) and New Energy and Industrial Technology Development Organization (NEDO). And it is a part of Smart Materials and Structures, R&D Projects on Cooperation with Academic Institutions coordinated by Agency of Industrial Science and Technology (AIST) which belongs to the Ministry of International Trade and Industry (MITI).

## Reference

1. K. Osaka and T. Fukuda, "Strain monitoring in curing of composites using EFPI sensor", Proc. of the 44th International SAMPE Symposium and Exhibition, pp.1993-2004(1999)

## **Application of Embedded FBG Sensors for Detection of Damages in CFRP Composites**

Y.Okabe, S.Yashiro, T.Kosaka, and N.Takeda

### **Abstract**

Fiber Bragg Grating (FBG) sensors were applied for the detection of transverse cracks in CFRP laminates. An uncoated FBG sensor was embedded in  $0^\circ$  ply on the border of  $90^\circ$  ply in a CFRP cross-ply laminate. The reflection spectra from the FBG sensor were measured at various tensile stresses. As a result, the reflection spectra was found to change its form with increase of the transverse crack density in the  $90^\circ$  ply. For confirming that the change was caused by transverse cracks, the spectra were calculated theoretically. The calculated result reproduced the change in the measured spectrum form very well. These results show that the occurrence of transverse cracks can be detected from the change in the form of the reflection spectrum, and the spectrum width at the half-maximum is a good indicator for the quantitative evaluation of the transverse crack density on real-time.

### **Introduction**

The failure process of CFRP laminate involve unique microscopic damages, such as transverse cracks and delaminations [1]. Especially, transverse cracks in off-axis plies occur at much lower stress than the ultimate tensile strength of the laminates. Hence, it is important to detect the occurrence of the transverse cracks on real-time for effective and reliable use of the CFRP laminates practically.

A candidate for the sensing device of the transverse cracks is a FBG sensor. The FBG sensor is a kind of optical-fiber sensors. Optical-fiber sensors are ideal sensors for smart materials and structures, because they are small, light weight, immune to electrical interference, and environmentally more stable. In addition, FBG sensors have more advantages such as potentially low-cost, inherent self referencing capability, unique multiplexing capacity along a single fiber, and independence of connector or fiber losses [2]. Hence the FBG sensors have been embedded in various structures for health monitoring [3]. They are usually used for the measurement of strain or temperature that are almost uniform in the gage length of the sensors. However, the FBG sensors are also very sensitive to non-uniform strain distribution along the entire length of the gratings [4]. The strain distribution influences the form of the reflection spectrum from the FBG

---

Y.Okabe, S.Yashiro, and N.Takeda, Komaba Open Laboratories, The University of Tokyo, 4-6-1 Komaba, Meguro-ku, Tokyo 153-8904, Japan  
T.Kosaka, Faculty of Engineering, Osaka City University, 3-3-138 Sugimoto, Sumiyoshi-ku, Osaka 558-8585, Japan



sensor. Thus, the sensors have a potential for detecting the damage that causes non-uniform strain distribution in composite materials.

In this research, uncoated FBG sensors were embedded on the border of off-axis ply in CFRP laminates for the detection of the transverse cracks, which appeared in the off-axis ply. Then the reflection spectra were measured at various tensile stresses, and the change in the spectrum form was investigated. For confirming that the change was caused by transverse cracks, the spectra were calculated theoretically. As a result, it was found that the occurrence of transverse cracks could be detected from the change in the form of the reflection spectrum, and the spectrum width at the half-maximum was a good indicator for the quantitative evaluation of the transverse crack density on real-time.

## Experimental Procedure

### Materials

The FBGs used in this research are formed in common single-mode optical fibers by NTT-AT Corporation. The optical fibers are coated with UV-cured resin, whose outside diameter is  $250\mu\text{m}$ . Core and cladding are 10 and  $125\mu\text{m}$  in diameter respectively. The length of the gratings is 10mm, and the grating period is about 530nm.

These FBG sensors were embedded in CFRP composites T800H/3631 (Toray Industries, Inc.). The resin coating was removed before the FBG sensors were embedded. The laminate configuration is cross-ply  $[0_2/90_4/0_2]$ . As shown in Fig. 1, by embedding in contact with  $90^\circ$  ply without UV epoxy coating, the FBG sensor is sensitive to the transverse cracks that run through the thickness and width of the  $90^\circ$  ply. Moreover, since the optical fiber is embedded in  $0^\circ$  ply to be parallel to the carbon fibers, the optical fiber is hardly broken by the occurrence of transverse cracks in the  $90^\circ$  ply.

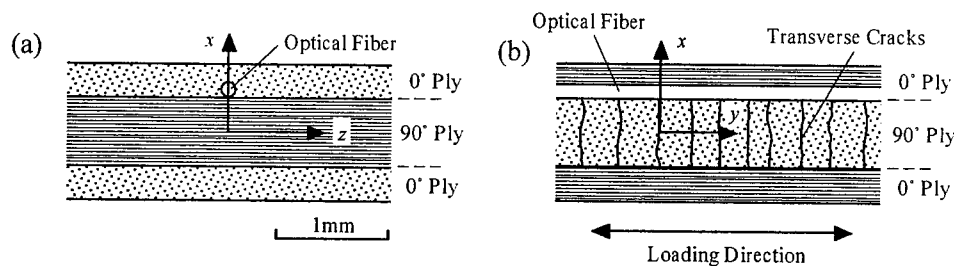


Figure 1 Cross sections of a CFRP laminate in which an uncoated FBG sensor was embedded; (a) perpendicular to the loading direction and (b) parallel to the loading direction.

### Measurements

The schematic of the experimental system is shown in Fig. 2. Quasi-static tensile load is applied on the specimen at room temperature. The reflection spectrum was

obtained using an optical spectrum analyzer (Ando Electric Co., Ltd., AQ-6315A) at various values of the tensile strain, which was measured with a strain gage attached on a surface of the specimen. Simultaneously, the tensile load was measured with a load cell, and a polished edge surface of the specimen was replicated in cellulose acetate film with methyl acetate as a solvent. From the replica film, the number of transverse cracks can be counted after the test.

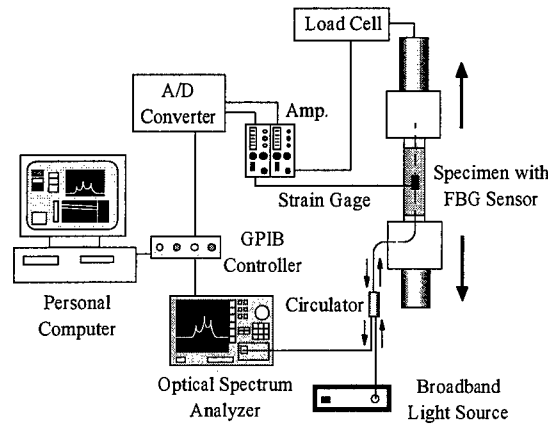


Figure 2 Schematic of the experimental system.

## Experimental Results

Figure 3 shows the stress  $\sigma$  and the crack density  $\rho$  measured for the specimen including the embedded optical fiber as a function of the strain  $\epsilon$  measured by the strain gage. The crack density was defined as the number of transverse cracks per unit length along the loading direction in  $90^\circ$  ply. In this graph, open circles are also plotted using the strain  $\epsilon_f$  that was obtained from the wavelength shift  $\Delta\lambda$  on the highest peak in the reflection spectrum [5].

The reflection spectra at vari-

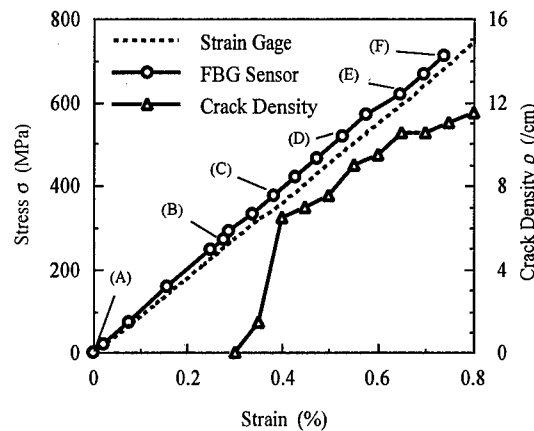


Figure 3 Crack density and stress as a function of the strain  $\epsilon$  measured by the strain gage or the strain  $\epsilon_f$  determined from the reflection spectrum from the FBG sensor.

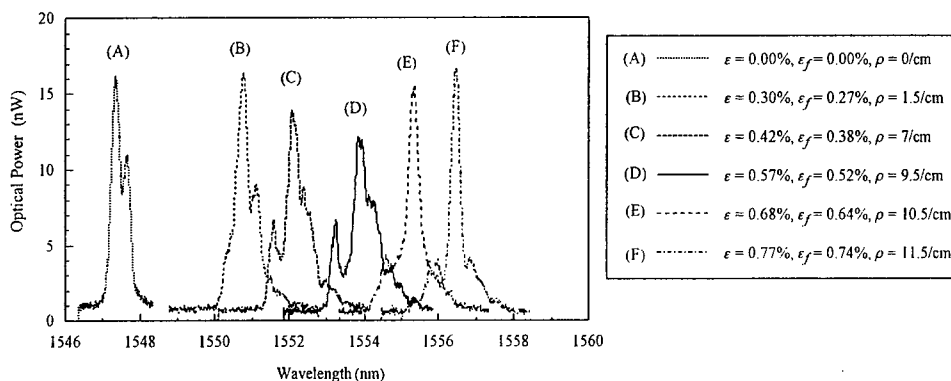


Figure 4 Reflection spectra measured at various tensile strains. These correspond to the data (A) ~ (F) in Fig. 3.

ous tensile strains are shown in Fig. 4. They correspond to the data (A) ~ (F) in Fig. 3. With increase in the crack density  $\rho$ , the form of the reflection spectrum was distorted; the intensity of the highest peak became small, some peaks appeared around it, and the spectrum became broad. As the crack density is close to saturation, the spectrum became narrow again and the highest peak recovered its height. This change in the spectrum form is expected to be due to the strain distribution caused by the transverse cracks in  $90^\circ$  ply. This will be confirmed later.

### Analysis

For confirming that the change in the spectrum form was caused by transverse cracks, the spectrum was calculated theoretically. In the calculation, the axial strain distribution in the FBG sensor was assumed to be the same with the longitudinal strain distribution along the loading direction in the  $0^\circ$  ply.

At first, the non-uniform strain distribution caused by transverse cracks was calculated. The positions where transverse cracks occurred were determined from the replica films. As an example, Fig. 5 shows the positions of transverse cracks at the strain of the data (C) in Fig. 3. Then McCartney's theory [6] was applied for each region between two neighboring cracks. The theory is derived on the assumption that the cross-ply laminate contains an array of parallel transverse cracks which are all equally spaced. In reality, intervals between neighboring transverse cracks  $2L$  are not uniform. However, the effect of the difference is supposed to be small for the calculation of approximate strain distribution in this case, and the theory is applied for each region. In this analysis, generalized plane strain conditions are assumed, and calculated strains in  $0^\circ$  ply are the values averaged through the thickness of the  $0^\circ$  ply. The longitudinal strain  $\epsilon_y$  in  $0^\circ$  ply was calculated along the entire length of the FBG sensor as a function of the longitudinal position  $y$  as shown in Fig. 6. The mechanical properties of T800H/3631 used for the calculation are summarized in Table I.

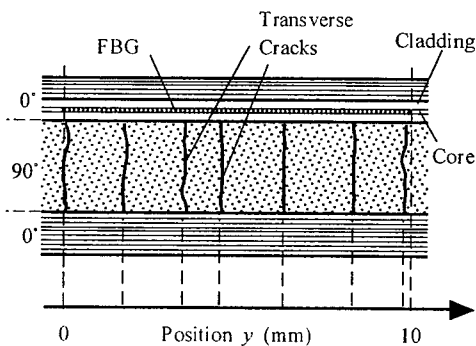


Figure 5 Positions of transverse cracks obtained from the replica film for the data (C) in Fig. 3.

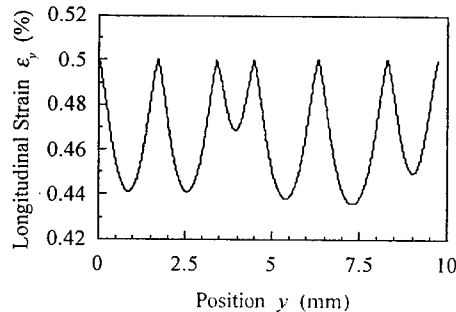


Figure 6 Longitudinal strain  $\epsilon_y$  in  $0^\circ$  ply along with the entire length of the FBG sensor. The tensile strain  $\sigma$  is 376.6MPa, and the positions of transverse cracks are shown in Fig. 5.

Next, the distributions of grating period  $\Lambda$  and average refractive index  $n$  along the FBG sensor were calculated from the axial strain distribution  $\varepsilon_y$ . Then, the reflection spectrum were simulated from the distributions of  $\Lambda$  and  $n$ . This calculation was conducted using the software "IFO\_Gratings" developed by Optiwave Corp. This program can calculate the spectrum by solving the couple mode equations using transfer matrix method. The calculated results are shown in Fig. 7. These spectra correspond to those in Fig. 4.

Compared with the measured reflection spectra, the calculated ones have larger wavelength shifts. This is mainly because the elastic properties of CFRP used for the analysis were slightly different from the actual values. Thus, the calculated axial strain was larger than the actual strain, and the wavelength shift became larger. However, the calculated results reproduce the change in the spectrum form, such as the change in the highest peak, spectrum width, and the positions of other peaks, very well. These agreements show that the change in the spectrum form was caused by the occurrence of the transverse cracks. When the transverse crack density is small, the strain distribution is non-uniform by the transverse cracks, and the reflection spectrum is disturbed. As the crack density is close to saturation, each interval of two neighboring cracks decreases and the variation of the axial strain becomes small. Hence, the spectrum form becomes narrow and has one large peak. These results show that the occurrence of transverse cracks can be detected from the change in the form of the reflection spectrum.

Table I Mechanical Properties of T800H/3631 unidirectional laminates [7-8]. The direction of fibers is expressed by the index 1.

Elastic Moduli (GPa)	$E_1$	148
	$E_2$	9.57
	$G_{12}$	4.50
Poisson's Ratios	$\nu_{12}$	0.356
	$\nu_{23}$	0.49
Thermal Expansion Coefficients ( $\times 10^{-6}/^{\circ}\text{C}$ )	$\alpha_{11}$	-0.6
	$\alpha_{22}$	36.0
Manufacturing Temperature( $^{\circ}\text{C}$ )	$T_0$	185

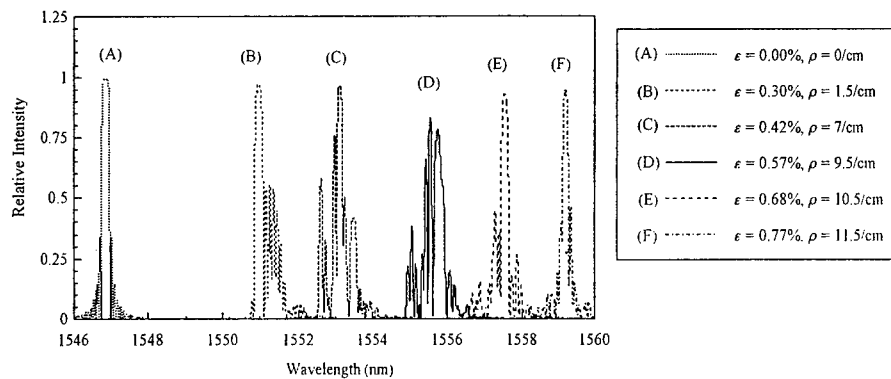


Figure 7 Calculated reflection spectra which correspond to the measured spectra in Fig. 4.

### Dependence of Spectrum Width on Crack Density

With increase in the crack density, the width of the reflection spectrum changed. Thus, the spectrum width defined as Full Width at Half Maximum (FWHM) was plotted as a function of the transverse crack density in Fig. 8. In the experimental result, the FWHM increased drastically at about 7/cm in the crack density. On the other hand, the calculation result show the increase of FWHM at earlier stage of the crack accumulation. This difference at the early stage is due to the spectrum form after the specimen was fabricated. Though the calculated spectrum at 0.00% in  $\varepsilon$  was narrow and had only one large peak, the measured spectrum already had two peaks and its width was large. This is because the transverse thermal residual stresses were applied to the FBG sensor during the curing process [9]. The effect of residual stresses will be discussed in the next section. However, considering the calculation result, the spectrum width has a potential to be a good indicator to evaluate the transverse crack density quantitatively on real-time.

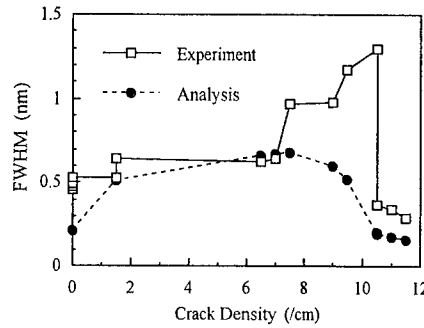


Figure 8 Relationship between the spectrum width and the crack density.

### Effect of Transverse Residual Stresses on the Spectrum Form

In this section, the effect of residual stresses on the spectrum form was confirmed theoretically using FEM analysis. The thermal load was applied by cooling from the manufacturing temperature of 185°C to the room temperature of 19.5°C. The mechanical properties of the optical fiber are shown in Table II. From the FEM analysis, the difference between the principal stresses  $\sigma_2$  and  $\sigma_3$  on the transverse plane of the optical fiber was determined;  $|\sigma_2 - \sigma_3| = 74.58 \text{ MPa}$ .

The difference of the wavelength between the two peaks caused by the transverse stresses is given by the following equation [9].

$$\delta\lambda = \frac{\lambda_0 n_0^2 (1 + \nu_f)}{2E_f} [(p_{11} - p_{12})(\sigma_2 - \sigma_3)] \quad (1)$$

The  $\lambda_0$  and  $n_0$  are the center wavelength and average refractive index at stress-free condi-

Table II Properties of the FBG sensor. The strain-optic coefficients were quoted from Reference [10].

Elastic Moduli (GPa)	$E_f$	73.1
	$G_f$	31.5
Poisson's Ratio	$\nu_f$	0.16
Thermal Expansion Coefficient ( $\times 10^{-6}/^\circ\text{C}$ )	$\alpha_f$	5.0
Initial Wavelength ( $\mu\text{m}$ )	$\lambda_0$	1.5473
Initial Average Refractive Index	$n_0$	1.4490
Strain-Optic Coefficients	$p_{11}$	0.113
	$p_{12}$	0.252

tion, and  $p_{11}$  and  $p_{12}$  are strain-optic coefficients. These values are also shown in Table II.

The  $\delta\lambda$  obtained from the data (A) in Fig. 4 was 0.30nm, and that calculated using the eq. (1) was 0.27nm. These two values are almost the same. Consequently, the split of the spectrum into two peaks after the manufacturing of the specimen was confirmed to be caused by the transverse residual stresses.

## Conclusions

In this research, the FBG sensors were embedded in CFRP cross-ply laminates to be applied for the detection of transverse cracks. Since an uncoated FBG sensor was positioned in  $0^\circ$  ply on the border of  $90^\circ$  ply, the form of the reflection spectrum from the FBG sensor was distorted sensitively, as the transverse crack density in  $90^\circ$  ply increased by tensile loading.

Then, the reflection spectrum corresponding to the measured one was calculated theoretically. The calculated spectrum reproduced the change in the spectrum form very well. From these agreements, it was confirmed that the change in the spectrum form was caused by the non-uniform strain distribution, which was induced by the transverse cracks. Hence, the occurrence of transverse cracks can be detected from the change in the form of the reflection spectrum.

Furthermore, the spectrum width was found to be a good indicator for the quantitative evaluation of the transverse crack density on real-time. However, for the detection of the transverse cracks at early stage of the damage progress, one problem exists. It is that the spectrum splits into two peaks and is broad already before tensile load is applied, because of the transverse thermal residual stresses. If the FBG sensor can be embedded without the non-axisymmetric thermal residual stress, the transverse crack density can be evaluated more reliably by the spectrum width. The authors are now developing small-diameter FBG sensors. Such sensors are expected to be more effective to reduce the residual stresses.

## Acknowledgements

This research was conducted as a part of the "R&D for Smart Materials Structure System" project within the Academic Institutions Centered Program supported by NEDO (New Energy and Industrial Technology Development Organization), Japan.

## References

1. N. Takeda and S. Ogiwara, 1994. "In situ observation and probabilistic prediction of microscopic failure processes in CFRP cross-ply laminates," *Compos. Sci. Technol.*, 52: 183-195.
2. A. D. Kersey, M. A. Davis, H. J. Patric, M. LeBlanc, and K. P. Koo, 1997. "Fiber grating sensors," *J. Lightwave Technol.*, 15(8): 1442-1463.

3. Y. J. Rao, 1999. "Recent progress in applications of in-fibre Bragg grating sensors," *Optics and Lasers in Engineering*, 31: 297-324.
4. K. Peters, M. Studer, J. Botsis, A. Iocco, H. G. Limberger, and R. P. Salathé, 1999. "Measurement of stress concentrations using embedded optical fiber Bragg grating sensors," *Proceedings of SPIE*, Vol. 3670, pp. 195-206.
5. R. J. Van Steenkiste and G. S. Springer, 1997. *Strain and temperature measurement with fiber optic sensors*. Lancaster, PA: Technomic Pub. Co., pp. 162-171.
6. L. N. McCartney, 1992. "Theory of stress transfer in a  $0^\circ$ - $90^\circ$ - $0^\circ$  cross-ply laminate containing a parallel array of transverse cracks," *J. Mech. Phys. Solids*, 40(1) 27-68.
7. N. Takeda, S. Kobayashi, S. Ogihara, and A. Kobayashi, 1998. "Experimental characterization of microscopic damage progress in quasi-isotropic CFRP laminates: effect of interlaminar-toughened layers," *Adv. Composite Mater.*, 7(2) 183-199.
8. N. Takeda, H. Niizuma, S. Ogihara, and A. Kobayashi, 1995. "Experimental evaluation of thermal residual stress in CFRP cross-ply laminates," *Materials System*, 14 73-78 (in Japanese).
9. J. M. Menéndez and J. A. Güemes, 1999. "Strain measurements inside thick CFRP laminates at the vicinity of bolted joints," *Proceedings of SPIE*, Vol. 3670, pp. 184-194.
10. A. Bertholds and R. Dändliker, 1988. "Determination of the individual strain-optic coefficients in single-mode optical fibers," *J. Lightwave Technol.*, 6(1): 17-20.

**MMC**

---



## **Fracture Behavior and Its Influence on Superconducting Property of Nb<sub>3</sub>Al Composite Wire**

S. Ochiai, T. Sawada, M. Ohno, M. Hojo and K. Watanabe

### **Abstract**

Static and fatigue behavior at room temperature and its influence on the superconducting current and upper critical magnetic field at 4.2K of a Nb<sub>3</sub>Al multifilamentary composite were studied. In spite of the large scatter and strong length-dependence of strength of filaments, the strength of composite had very little scatter and only slight dependence on length. These features were described well by the Monte Carlo simulation. When the composite was fatigued, the damages progressed in the order of Stage I(formation of cracks in the clad copper), II(stable propagation of the cracks formed in the clad copper into the inner core portion, causing fracture of the Nb<sub>3</sub>Al filaments) and III(unstable propagation of the main crack, causing overall fracture of the composite). The critical current of both statically pre-stressed and fatigued composites was retained until the occurrence of fracture of Nb<sub>3</sub>Al filament. Due to the maximum stress-dependence of fatigue damage growth, the critical current of the portion apart from the main crack became low for the intermediate maximum stress but not for low and high maximum stresses.

### **I. Introduction**

As mechanical and electromagnetic stresses are exerted during fabrication and/or service of superconducting composites, it is needed to clarify the mechanical behavior and its relation to the superconducting property.

The aim of the present paper is to study the static and fatigue behaviors at room temperature and the influences of the introduced damages on the critical current ( $I_c$ ) and upper critical magnetic field  $H_{c2}$  at 4.2K of Nb<sub>3</sub>Al superconducting composite. From the technical standpoint, the present work intends to approximate the 4.2K static and fatigue behavior associated with periodic changes in magnet energization through room temperature testing, since the Nb<sub>3</sub>Al filaments and copper deform elastically and plastically, respectively, at both 4.2K and room temperature and therefore the accumulation process of damages is similar at both temperatures.

### **2. Experimental procedure**

---

S. Ochiai, T. Sawada, M. Ohno and M. Hojo, Mesoscopic Materials Research Center, Graduate School of Engineering, Kyoto University, Sakyo-ku, Kyoto 606-8501, Japan  
K. Watanabe, Institute for Materials Research, Tohoku University, Sendai 980-8577, Japan

The multifilamentary Nb<sub>3</sub>Al superconducting composite wire was fabricated by means of the Jelly-roll method [1] at Sumitomo Electric Industries. The composite wire with an overall diameter of 0.812mm was composed of 241 filaments with an average diameter of 34  $\mu$ m and copper as a stabilizer. The volume fraction of filaments was 0.42.

Static tensile tests were carried out for the composite wires and the extracted filaments at a strain rate of  $3.3 \times 10^{-4}$ /s. The experimental results were simulated by the Monte Carlo method combined with the shear lag analysis[2-4]. The fatigue test for the composite wire was carried out at room temperature at the stress ratio  $R(= \sigma_{c,min} / \sigma_{c,max}$  where  $\sigma_{c,min}$  and  $\sigma_{c,max}$  are the minimum and maximum stresses applied to the specimens during fatigue test, respectively)=0.1. Two series of composite specimens were used for measurement of critical current and residual strength. In the series (1), first the specimens with a length of 110 mm were fatigued to fracture as shown in Fig.1(a). After the fatigue fracture, the longer one between the two broken halves was used for the measurements of the residual strength at room temperature and critical current  $I_c$  at 4.2K. In this series, the measured  $I_c$ -values reflect the damage apart from the main fatigue crack. In the series (2), as shown in Fig.1(b), the specimens with a gage length of 25mm were fatigued for pre-fixed stress cycles under the same condition as in the series (1), and then  $I_c$ -values were measured. In this series, the measured values reflect the main fatigue crack.

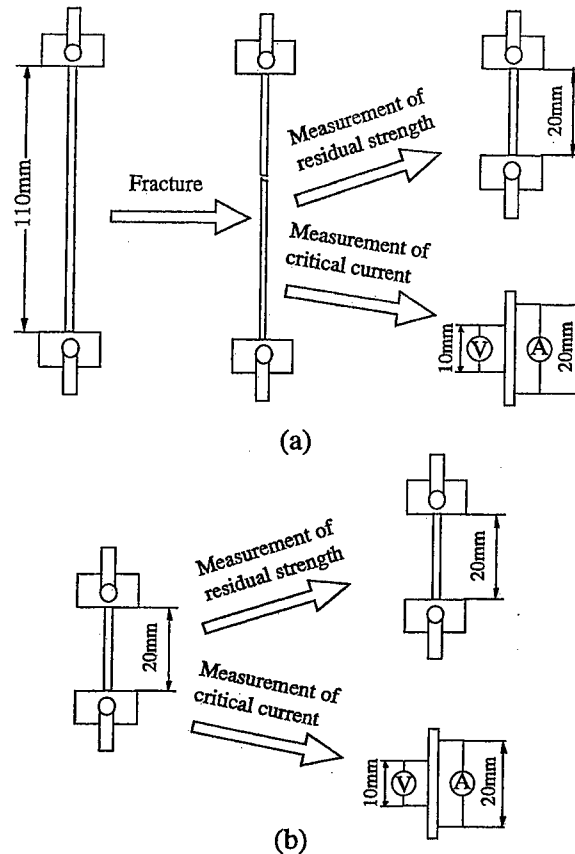


Fig.1 Two procedures for the measurements of residual strength  $\sigma_{c,r}$  at room temperature and critical current  $I_c$  at 4.2K. The specimen with a gauge length 110 mm is broken by fatigue, and the longer segment between the two broken halves is used for the measurements. In this procedure, the extent of the damages other than the main crack in the fatigue-fractured specimens can be detected. (b) The specimen with a gauge length 25mm is fatigued for a given number of stress cycle. The fatigued specimen is tensile-tested directly at room temperature to measure  $\sigma_{c,r}$ . Also the fatigued specimen is cooled to 4.2K to measure  $I_c$ . In this procedure, the extent of all damages, especially the main crack can be detected.

The fracture surface was observed with a scanning electron microscope (SEM). Critical current was measured at the magnetic field  $H$  from 12 to 15 T by a  $1 \mu\text{V}/\text{cm}$  criterion using a WM-5 magnet of the High Field Laboratory for Superconducting Materials, Tohoku University.

### 3. Results and Discussion

#### 3.1 Relation of strength distribution of $\text{Nb}_3\text{Al}$ filaments to that of composite

The experimental results showed that the scatter of strength of the composite is very small compared with that of the filaments as shown in the Weibull plot in Fig.2, and also the length dependence of composite strength is very small compared with that of the filaments as shown in Fig.3. These features could be reproduced by the Monte Carlo-shear lag simulation method [2-4]. Figure 4 shows the distribution of composite strength obtained by the simulation for

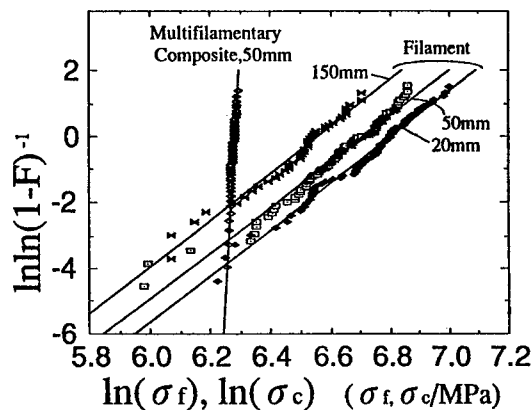


Fig.2 Weibull-plots for the measured strengths of the extracted  $\text{Nb}_3\text{Al}$  filaments( $\sigma_f$ ) and the multifilamentary composite( $\sigma_c$ ).

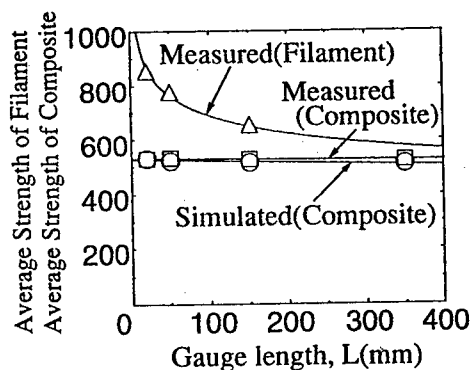


Fig.3 Measured average strengths of the  $\text{Nb}_3\text{Al}$  filament  $\sigma_f(\text{ave})$  and composite  $\sigma_c(\text{ave})$ , plotted against gage length  $L$ , together with the result of simulation.

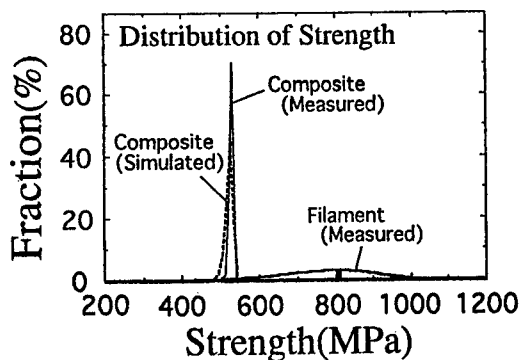


Fig.4 Comparison of the strength distribution of the  $\text{Nb}_3\text{Al}$  filament with that of the multifilamentary composite. The gage length for both filament and composite was 50 mm.

$L=50$  mm, together with the measured distributions of the filaments and composite for comparison. The length dependence of the simulated average strength of the composite is superimposed in Fig.3. The simulated strength distribution and length dependence of the composite strength are fairly in good agreement with the experimental ones.

### 3.2 Influences of damages induced by static loading on the critical current $I_c$ and upper critical magnetic field $H_{c2}$ at 4.2K

When the composite is pre-stressed at room temperature, two possible phenomena controlling the  $I_c$ - and  $H_{c2}$ -values at 4.2K occur: one is the change in strain of  $Nb_3Al$  filaments due to the intrinsic strain-dependence of  $I_c$  and  $H_{c2}$  and another is the breakage of the filaments. In order to check which gives major effect for the present composite, the residual strain of  $Nb_3Al$  at 4.2K was calculated by the method presented in Refs. [5-7]. When the filament volume fraction  $V_f$  is high such as 0.4 as in the present composite, the stress of copper in the composite at 4.2K always reaches its tensile yield stress for any stress state at room temperature, since the thermally induced strain in copper due to cooling from room temperature to 4.2K is higher than twice the yield strain of copper. As the residual stress of the  $Nb_3Al$  at 4.2K is in equilibrium with that of copper, it is nearly independent of applied stress on composite. Thus, in the present specimens, the  $I_c$  and  $H_{c2}$  are not changed by the strain-effect.

Figure 5 shows values of (a)  $I_c$  and (b)  $H_{c2}$  estimated from the Kramer plot [8] plotted against  $\sigma_c$ . Both  $I_c$ - and  $H_{c2}$ -values remain nearly constant for  $\sigma_c < 550$  MPa, as expected. The slight reduction in  $I_c$  for  $\sigma_c > 550$  MPa can be attributed to the fracture of the weaker  $Nb_3Al$  filaments since the scatter of strength of the  $Nb_3Al$  filaments is large.

### 3.3 Fatigue behavior

From the fatigue test of the extracted  $Nb_3Al$  filaments, it was confirmed that the  $Nb_3Al$  filaments themselves are not broken by fatigue in the present condition.

Figure 6 shows the relation of the maximum stress ( $\sigma_{c,max}$ ) to the number of stress cycles to failure,  $N_f$ , of the composite (S-N curve). As the progress of the

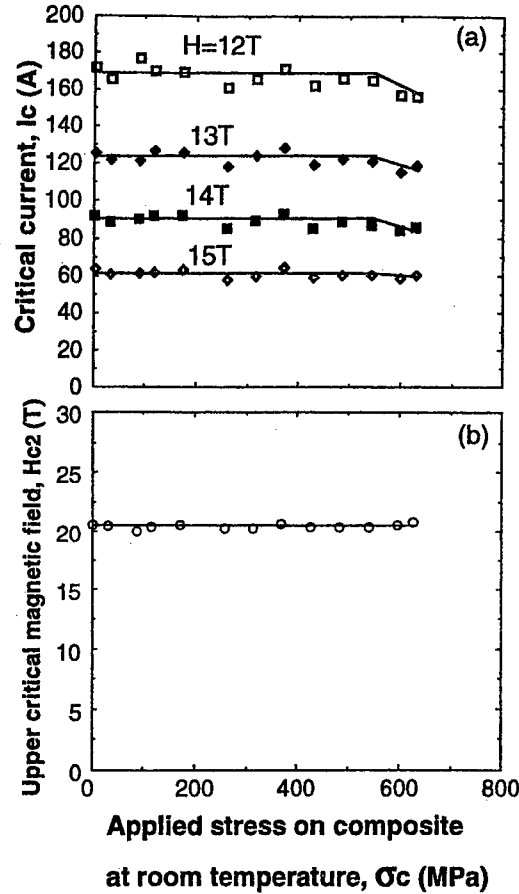


Fig.5 Variations of (a) the critical current  $I_c$  at the applied magnetic field  $H=12$  to  $15T$  and (b) upper critical magnetic field  $H_{c2}$  after the first cycle as a function of the maximum stress applied on composite at room temperature  $\sigma_{c,max}$ .

damage is dependent on the maximum stress as stated already, three maximum stresses (510, 380 and 210 MPa) were chosen as the representatives of (1)high, (2)intermediate and (3)low stress levels, respectively, for the test of the series (2).

From the observation of the fracture surface of the specimens fatigued for various cycles, the progress of the fatigue damage with increasing number of cycles could be divided into three stages; Stage I in which cracking of the clad copper arises, Stage II in which fracture of both copper and  $\text{Nb}_3\text{Al}$  filaments in the inner portion inside the clad copper arises, and Stage III at which the overall fracture of the composite occurs. The morphological feature and the aforementioned result (the  $\text{Nb}_3\text{Al}$  filament itself is not fractured by fatigue), suggest that the fatigue crack nucleates and proceeds preferentially in the copper and the fatigue crack generated by fracture of copper causes fracture of the filaments.

In the series (1), the residual strength in the regions of low and high  $\sigma_{c,\max}$  was not so much different from that for the static strength, while that in the region of intermediate  $\sigma_{c,\max}$  was low (Fig.7). This means that the fatigue damage was small in the portion apart from the fracture surface at high and low  $\sigma_{c,\max}$ , but it was large at intermediate  $\sigma_{c,\max}$ . In the series (2), the strength was reduced slightly in Stage I due to the cracking of the clad copper and significantly in Stage II due to the breakage of the filaments. From the results of observation of fracture surface and measurement of residual strength, the progress of

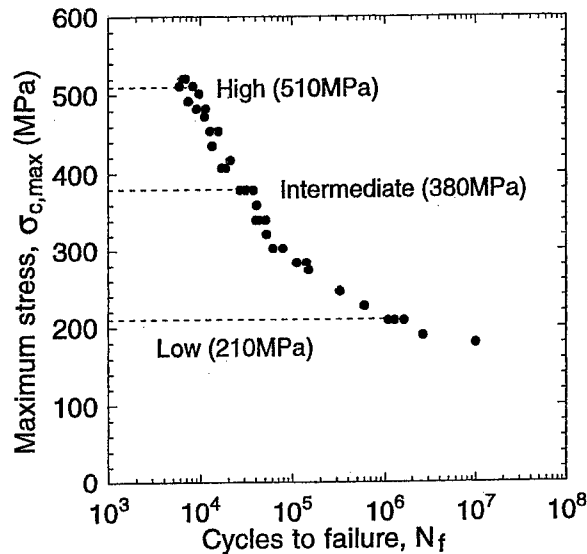


Fig.6 Measured S-N curve of the composite wire and the notation of the high, intermediate and low maximum stresses at which the fatigue tests were carried out in this work as a function of number of cycles.

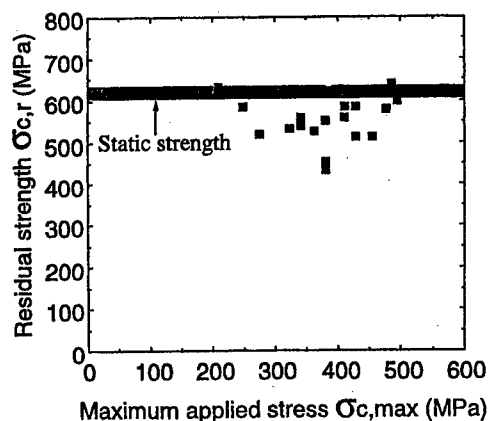


Fig.7 Measured residual strength of composite in series(1), plotted against maximum applied stress  $\sigma_{c,\max}$ . The hatched area shows the scatter band of the static strength.

(b)  $H_{c2}$  of the series (1) samples plotted against  $\sigma_{c,max}$ . The  $H_{c2}$ -value was constant, not affected by fatigue. This means that, as similarly as the static pre-stressing, the cyclic stressing at room temperature gives only a very slight change in the strain of  $Nb_3Al$  at 4.2K so that no detectable change occurs in  $H_{c2}$ .

On the other hand, the  $I_c$ -value in Fig.8(a) was changed by fatigue; the  $I_c$ -value was low in the intermediate range of  $\sigma_{c,max}$  while such a reduction in  $I_c$  was not found for the same stress range in the case of static stressing. In the low and high  $\sigma_{c,max}$  regions, the  $I_c$ -values were the same for the static and cyclic stressing. The reason for this can be attributed to the occurrence of fracture of the superconducting current-transportable  $Nb_3Al$  filaments at intermediate  $\sigma_{c,max}$  and to the non-occurrence at low and high  $\sigma_{c,max}$ .

Figure 9 shows the measured values of  $I_c$  plotted against  $N$  for high, intermediate and low maximum stresses for the series (2) samples. Following features can be read.  
(i) The  $I_c$ -value is reduced in Stage II but not in Stage I. This suggests that the fracture of the current-transportable filaments is the main reason for the reduction in  $I_c$  but not the fatigue damages in the clad copper.

(ii) At any  $\sigma_{c,max}$ , the  $I_c$  is reduced only when  $N$  exceeds about 90% of the failure cycle, suggesting that once the damages including fracture of current-transportable filaments arises (namely once Stage II starts), they grow quickly.

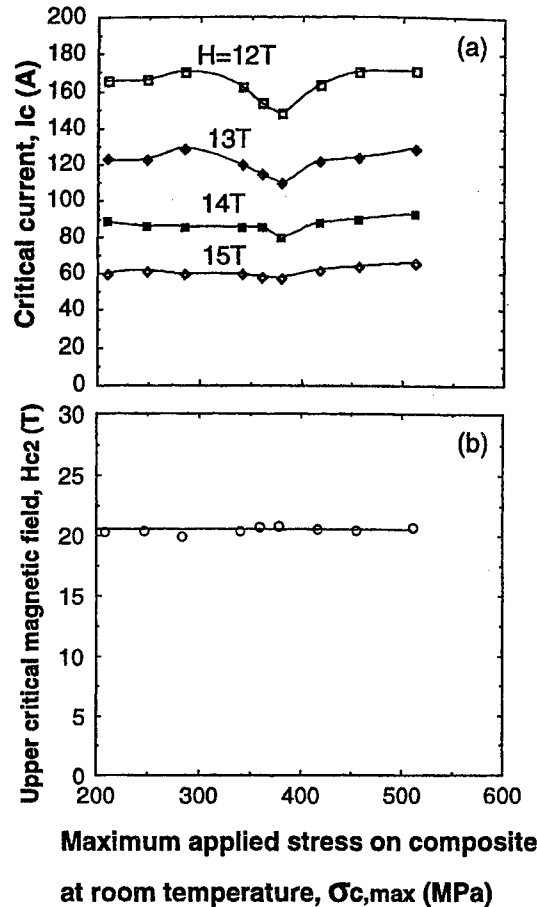


Fig.8 Variations of (a) the critical current  $I_c$  at the applied magnetic field  $H=12$  to  $15T$  and (b) upper critical magnetic field  $H_{c2}$  of the composite fractured by the fatigue as a function of the maximum applied stress on composite  $\sigma_{c,max}$ . The specimens for the measurement were taken out of the longer segment of the broken specimens (Fig.1(a))

#### 4. Conclusions

(A) Static behavior and its influence on critical current:

(i) The scatter of tensile strength of the multifilamentary composite is very small in spite of the large scatter of strength of the  $\text{Nb}_3\text{Al}$  filaments.

(ii) The strength of the composite has a very slight dependence on length, although the strength of the  $\text{Nb}_3\text{Al}$  filaments decreases markedly with increasing length.

(iii) The features mentioned above were explained and simulated well by the Monte Carlo simulation method combined with the shear lag analysis.

(iv) The critical current decreases at high applied stress due to the breakage of  $\text{Nb}_3\text{Al}$  filaments.

(B) Fatigue behavior and its influence on critical current:

(i)  $\text{Nb}_3\text{Al}$  filament itself is not fractured by fatigue when it is not embedded in copper, but is fractured when embedded due to the propagation of the fatigue crack nucleated in the copper.

(ii) The growth pattern of the fatigue cracks is dependent on the maximum applied stress; when the maximum stress is high, the fracture behavior of the composite tends to be similar to that for static loading; when the maximum stress is intermediate, many cracks can grow at different cross-sections; and when the maximum stress is low, one crack among many grows preferentially.

(iii) Due to the features mentioned above, the critical current of the portion apart from the broken-ends of the fatigue-fractured specimens becomes low for the

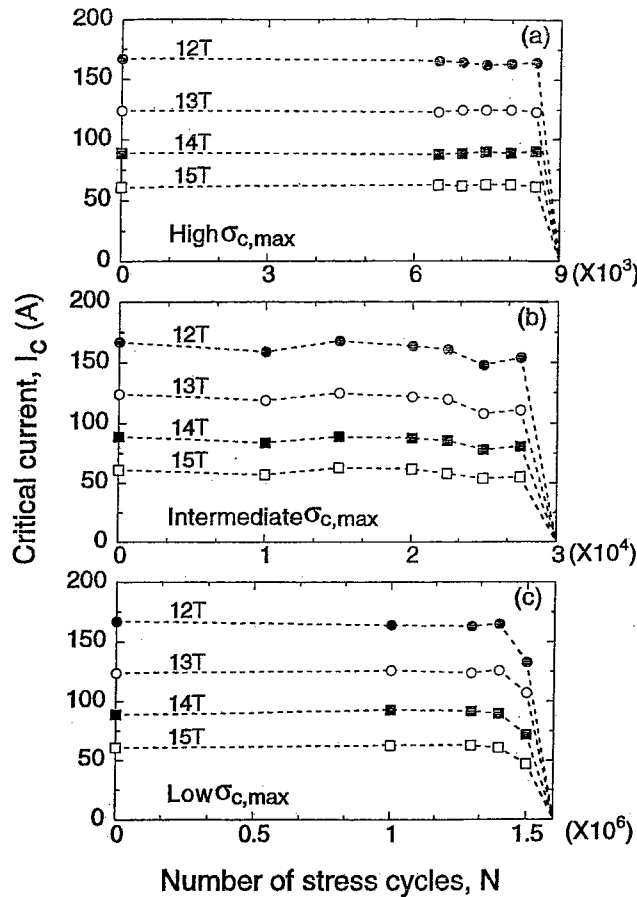


Fig.9 Variations of the critical current  $I_c$  with  $N$  of the specimens fatigued at (a) high ( $\sigma_{c,max} = 510\text{MPa}$ ), (b) intermediate ( $380\text{MPa}$ ) and low ( $210\text{MPa}$ ) maximum stresses.

intermediate maximum stress but not for low and high maximum stresses.

(iv) With increasing number of stress cycles, the damages progressed in the order of the following three stages; Stage I: formation of cracks in the clad copper, Stage II: stable propagation of the cracks in the clad copper into the inner core portion, causing fracture of the  $\text{Nb}_3\text{Al}$  filaments, and Stage III: unstable propagation of the main crack, causing overall fracture of the composite.

(v) The critical current remained nearly constant in Stage I but was reduced in Stage II. The reduction in Stage II arose from the fracture of the current-transportable filaments. The Stage II occurred in the late stage of fatigue life.

(vi) The accumulation process of damage varied with the stress level; at the intermediate stress level, many cracks in the clad copper grew into the core region but at the low stress level, one of the many cracks in the clad copper grew into the inner core region. Accordingly, the critical current of the portion apart from the main crack was low for intermediate stress but not for low stress.

### Acknowledgement

The authors wish to express their gratitude to Sumitomo Electric Industries for the supply of samples and to The Mitsubishi Foundation, Tokyo, for the grant-in-aid.

### References

1. T. Ando, K. Takahashi, M. Sigimoto, M. Nishi, H. Tsuji, Y. Yamada and M. Nagata, 1993. "Development of  $\text{Nb}_3\text{Al}$  Cable-in-conductor Fusion Superconductors", *IEEE Trans. Appl. Supercond.* 3(1):492-495.
2. S. Ochiai, T. Sawada, S. Nishino, M. Hojo and K. Takahashi and Y. Yamada, 1996. *Cryogenics*, 36(3):249-253.
3. S. Ochiai, 1994. *Mechanical Properties of Metallic Composites*, Marcel Dekker Inc. New York, pp.473-510.
4. S. Ochiai, T. Sawada and M. Hojo, 1997. "Application of Monte Carlo Simulation to Tensile Behavior of FRM", *Sci. Eng. Comp. Mater.*, 6(2):63-76.
5. S. Ochiai and K. Osamura, 1992. "Influence of Cyclic Loading at Room Temperature on Critical Current of  $\text{Nb}_3\text{Sn}$  Superconductor Composite Wire", *Cryogenics*, 32(6):584-590.
6. S. Ochiai, K. Osamura and K. Watanabe, 1992. "Estimation of Strength Distribution of  $\text{Nb}_3\text{Sn}$  in Multifilamentary Composite Wire from Change in Superconducting current due to Pre-loading, *J. Appl. Phys.* 74(3):440-445.
7. S. Ochiai, S. Nishino, M. Hojo and K. Watanabe, 1995. "Relation of the Strength Distribution of  $\text{Nb}_3\text{Sn}$  to the Critical Current of a Pre-stressed Multifilamentary Superconducting Composite Wire", *Supercond. Sci. Tech.* 1.8(7):863-869.
8. E. J. Kamer, 1973. "Scaling Laws for Flux Pinning in Hard Superconductors", *J. Appl. Phys.* 44(3):1360-1370.



## **Fabrication and Mechanical-properties of Titanium Metal Matrix Composite rings**

Nobuhiko Yunoki, Tatsuhito Honda, Katsuyoshi Moriya, Shigeto Nishide,  
Michihiro Uyama

### **Abstract**

Metal Matrix Composite (MMC) rings were developed for the application for gas-turbine compressor. The developed MMC rings were thin simple-shaped rings and bladed rings (Bling). The MMC rings were consist of monolithic titanium clad and hoop-reinforced MMC core. The MMC core was reinforced with SiC continuous fiber. For the fabrication of MMC core ring, titanium matrix coated SiC fiber was used. The fiber wire was wound to make preform, and the preforms were stacked and hot-pressed. The titanium clad and the MMC core were integrated into one-piece ring with HIP. The results show this process can minimize the disorder and fiber breakage during consolidation. Uniform wire diameter, precise winding, and hot pressing are effective for successful processing.

The burst spin strength of ring and Bling achieved 98% of coupon tensile strength[1]. After the cyclic spin test under the condition that was equal to LCF-life of coupon specimen, any defect was not detected in the MMC rings.

### **Introduction**

Research Institute of Advanced Material Gas-Generator (AMG) aims to establish basic technologies for next generation gas turbine, which should have the

---

Nobuhiko Yunoki, Tatsuhito Honda, Katsuyoshi Moriya, Shigeto Nishide and Michihiro Uyama,  
Research Institute of Advanced Material Gas-Generator (AMG), 1-13-4, Kitaotsuka, Toshima-ku,  
Tokyo, 170-0004, Japan

feature of low fuel consumption with reduced weight, and should be environmentally acceptable. High efficiency and high performance compressor for future gas turbine requires higher rotating speed and lower weight than the conventional gas turbine. Due to their high specific properties and high temperature capability, SiC continuous fiber reinforced Titanium Metal Matrix Composites (MMC) are attractive compressor material. This study describes MMC Bling fabrication and mechanical properties of MMC Bling.

## Experimental Procedure

### Materials

The clad material of the Bling was Ti-6Al-4V. The MMC core material was SiC/Ti-6Al-4V. In this study the Matrix Coated Fiber Process was applied to fabricate the MMC core. This process uses pre-coated fibers called as the Titanium Matrix Composite (TMC) wire, supplied by Atlantic Research Corporation, 0.240mm in diameter. The TMC wires were consist of inner SiC fiber and outer Ti-6Al-4V layer. SiC fibers (SCS-6 supplied by Textron Systems, 0.140mm in diameter) are EB-PVD coated with Ti-6Al-4V. Fig.1 shows the cross section of the TMC wire.

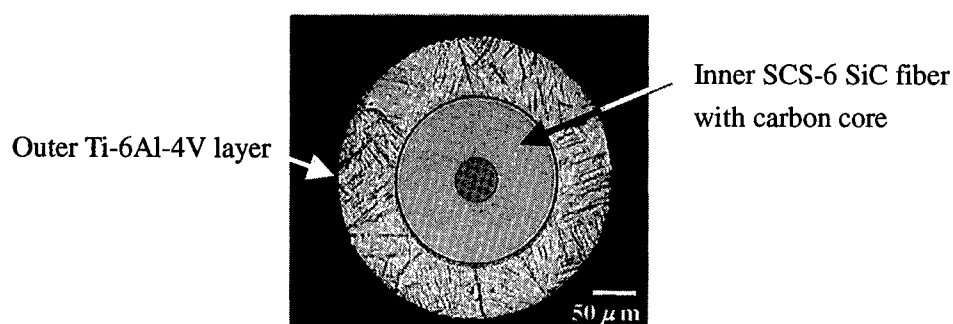


Fig.1 Cross section of TMC wire

The fabrication process of MMC ring is illustrated in Fig.2. The TMC wire was wound to make preform, and the preforms were stacked and hot-pressed. The titanium clad and the MMC core were integrated into one-piece ring with HIP. The hot press condition was 800°C, 20MPa for 3Hrs. The HIP condition is 800°C,

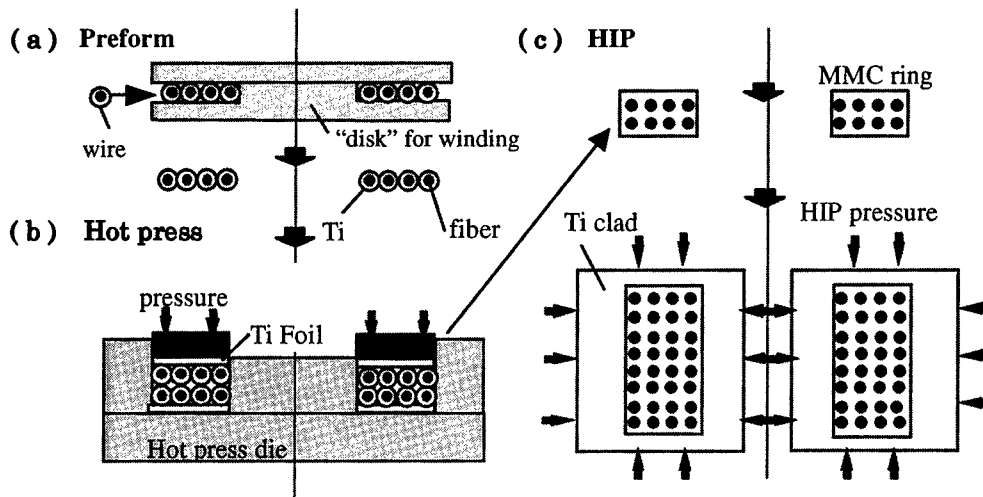


Fig.2 MMC ring fabrication process

140MPa for 3Hrs. The HIP'd ring was machined to the designed shape. Fig.3 shows the cross section of the MMC core, whose volume fraction is 33%. It is obvious that the Matrix Coated Fiber Process using TMC wire is effective for excellent fiber distribution.

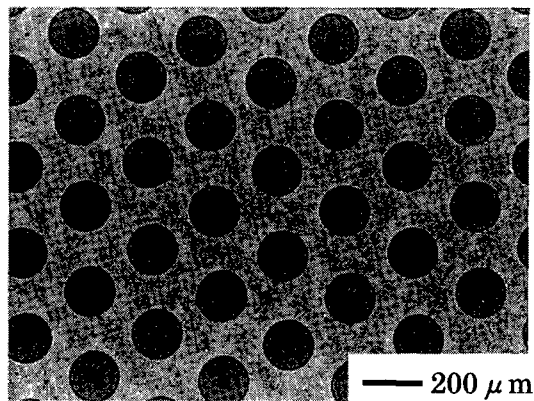


Fig.3 Cross section of the MMC core

#### MMC Rings (thin simple-shaped ring and bladed ring)

Two kinds of MMC ring were fabricated, thick bladed ring (Bling) and thin simple-shaped ring. The MMC ring is shown in Fig.4, which is 180mm in outer

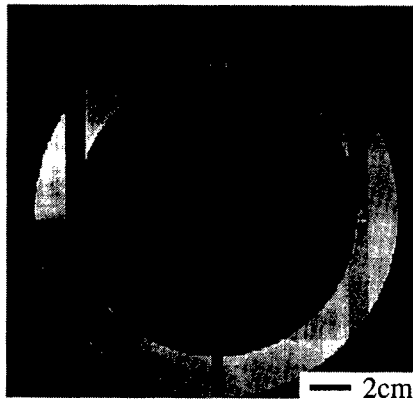


Fig.4 MMC ring

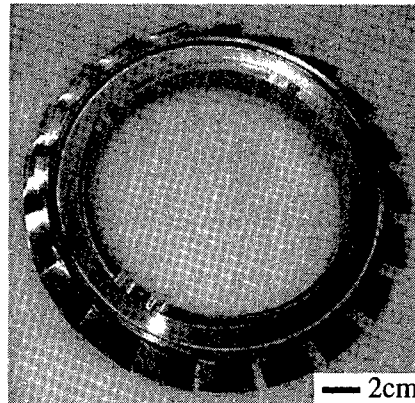


Fig.5 MMC Bling

diameter and 140mm in inner diameter, 3.2mm in thickness, including MMC core of 170-150mm in diameter and 3mm in thickness. The MMC Bling is shown in Fig.5, including MMC core of 170-150mm in diameter and 13mm in thickness. The MMC core ring was reinforced with fibers unidirectional in hoop. The blades were not reinforced. The cross section of the MMC Bling is shown in Fig.6.

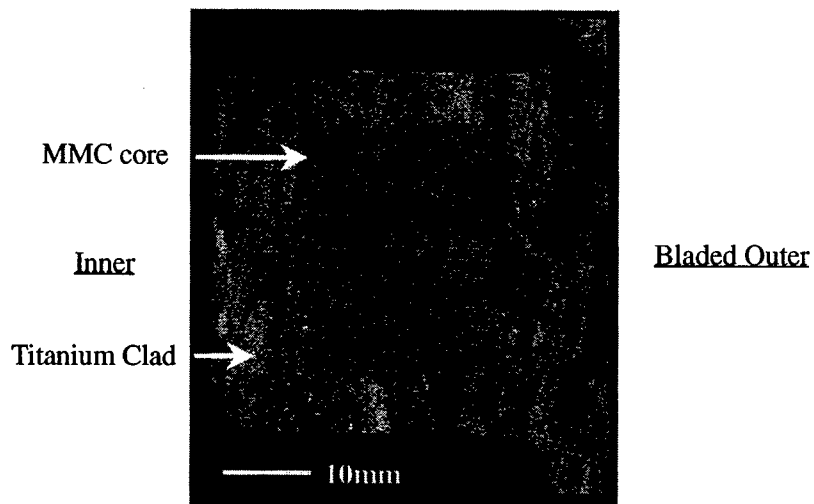


Fig.6 Cross Section of the MMC Bling

#### Burst and Cyclic Spin Test

Spin tests were conducted to certify the burst stress and the LCF-life of MMC

rings, in order to compare with mechanical properties of MMC coupon specimen. The tests were carried out in a vacuum chamber at room temperature. The Spin test equipment is shown in Fig.7.

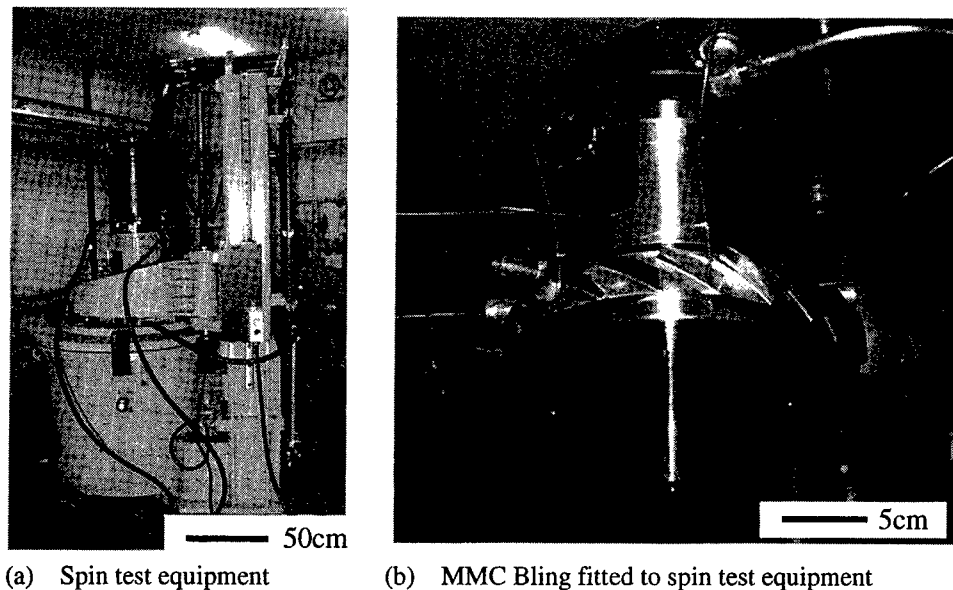


Fig.7 Spin test equipment

## Results and Discussion

### Burst spin test

MMC coupon specimen were fabricated by hot press for evaluation of mechanical properties. The volume fraction of the MMC coupon specimen was 33%. After fabrication, specimen were heat-treated for 3Hrs at  $800^{\circ}\text{C}$  in order to simulate the HIP process for MMC rings. The UTS and the Young's modulus of MMC coupon specimen were 1684MPa and 199GPa respectively. Sofue et al [2] reported that the UTS and the Young's modulus of their HIP'd SCS-6/SP700(Ti-4.5Al-3V-2Mo-2Fe) were 1770MPa and 203GPa respectively, 32% in the volume fraction. The result of Sofue et al were almost equal to our result. It is considered that the Matrix Coated Fiber Process is proper method to fabricate MMC.

The Bling was destroyed into six pieces at 55,830rpm. The blade tip speed

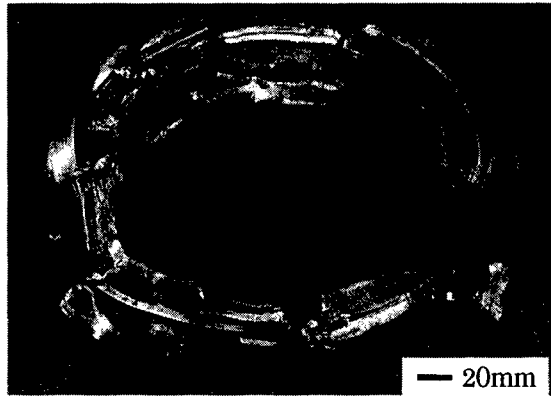


Fig.8 MMC Bling after the Burst Spin Test

reached to 619m/s. According to the FEM estimation, maximum burst stress at 55,830rpm was 1678MPa in the bore of the MMC core. The MMC Bling after the burst spin test is shown in Fig.8. This result indicated the MMC exhibited 98% tensile strength of the same volume fraction (33%) coupon specimen. The primary failure was due to the tensile overload in the hoop direction, and secondary fracture was supposed to be flexural fracture under centrifugal forces. However, colliding with the containment damaged most pieces. The fracture surface of burst Bling is shown in Fig.9. The primary fracture surface indicates ductile flat fracture of matrix from tensile overload. It indicates MMC hoop direction failure. And the MMC core was partially de-laminated from the titanium clad after the burst.

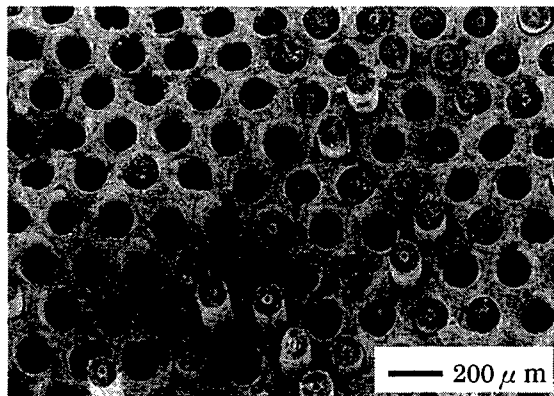


Fig.9 Fracture surface of burst Bling

### Cyclic spin test

The LCF-life of the MMC coupon specimen and the cyclic spin test condition for MMC rings are shown in Fig.10. The test condition of the cyclic spin test for

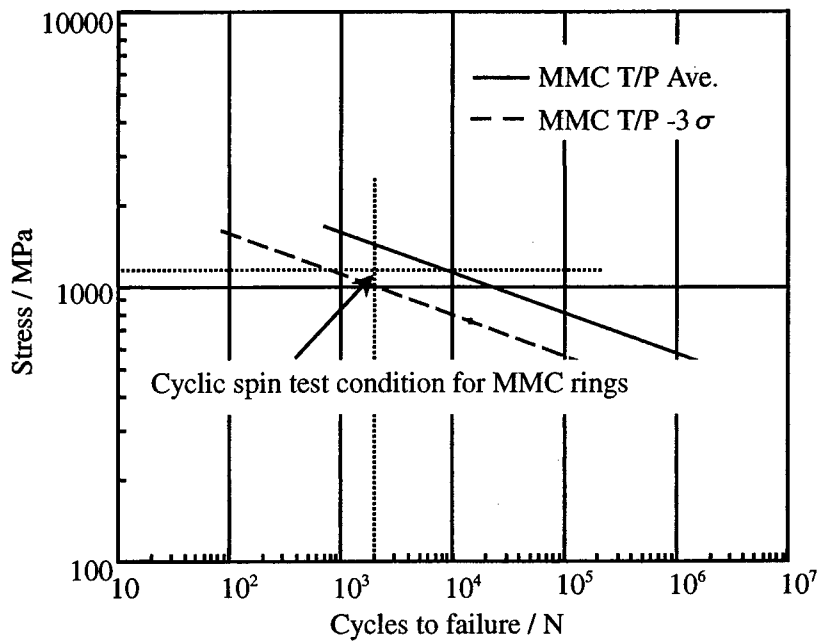


Fig.10 Cyclic spin test condition for MMC rings

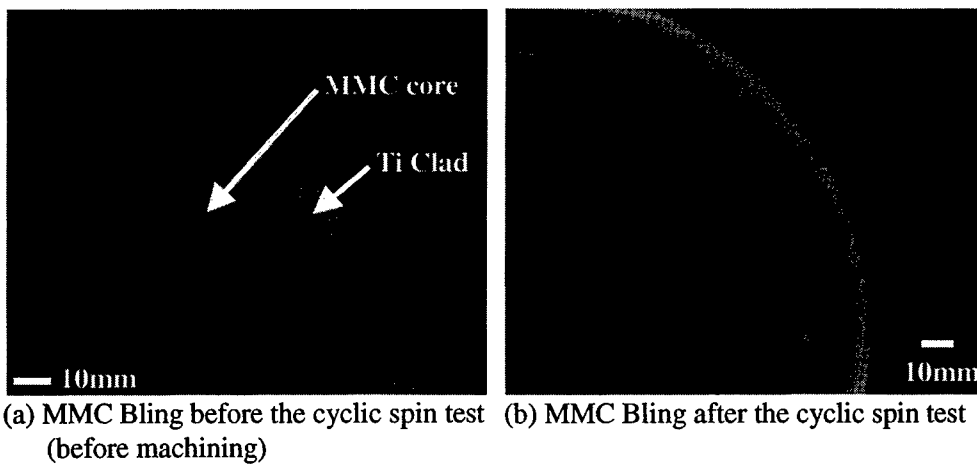


Fig.11 Results of the X-ray inspection

MMC rings was 2000cycles in vacuum at room temperature. Under this condition, hoop stress was about 1100MPa at the bore of the MMC core. This condition is between the average and  $-3\sigma$  of MMC coupon specimen LCF-life. After the cyclic spin test, both the thin simple-shaped MMC ring and MMC Bling were evaluated by X-ray and fluorescent penetrant inspection. The results of the X-ray inspection are shown in Fig.11. De-lamination between titanium clad and MMC core was not detected. Any crack was not detected by the fluorescent penetrant inspection. The MMC rings were completely sound after the cyclic spin test.

### Conclusion

1. MMC (SCS-6 SiC fiber/Ti-6Al-4V matrix) bladed ring was successfully fabricated by Matrix Coated Fiber Process using Titanium Matrix Composite wire.
2. UTS of thin simple-shaped MMC ring and MMC Bling were equal to the UTS of MMC coupon specimen.
3. The LCF-life of MMC rings were equal to the LCF-life of MMC coupon specimen LCF-life. It is considered that the shape of the specimen did not effect on mechanical properties of MMC and Matrix Coated Fiber Process is proper method to fabricate MMCs.
4. After the cyclic spin test, any defect was not detected in MMC rings.
5. The results of this study showed that the developed MMC are potentially applicable for rotating components.

### Reference

1. K. Moriya et al, 1999. "Fabrication of Titanium Metal Matrix Composite Bling", *Proceedings of the 12th International Conference on Composite Materials (ICCM-12)*, 1999.7
2. Y. Sofue et al, 1999. *Proceedings of the Gas Turbine Society of Japan*, 14th:pp117-122



## **Mechanical properties of aluminum borate whisker reinforced AZ91D magnesium alloy composites by semi-solid process**

Makoto Yoshida, S. Takeuchi, J. Pan, G. Sasaki, N. Fuyama, T. Fujii, and Hideharu Fukunaga

### **Abstract**

In order to develop light weight piston for automobile engine, aluminum borate whisker reinforced AZ91D magnesium alloy composites was fabricated with semi-solid material process by the squeeze casting. By controlling the solid fraction, fs, and the rate of the infiltration into the preform, it was successful to reinforce a part of the cast alloy without deformation of the preform. The tensile strength of the alloy/composites interface by semi-solid (50% fs) process was 120 MPa, and it was equal to the strength by conventional 0% fs process. However, the flexural strength of the composite by 50% fs process was about 10% lower than the strength of 0% fs process, 498 MPa. After solid solution and aging treatment, the flexural strength of the composites in both 0% and 50% fs process were decreased. This will be caused by the notch effect of Mg<sub>2</sub>Si compound produced between SiO<sub>2</sub> binder of the preform and magnesium during heat treatment.

### **Introduction**

Recently, magnesium alloys have been used to reduce the weight of machine parts for automobiles. As for the application of the alloys to the piston in the engine, like a certain conventional aluminum alloy piston, suitable reinforcement of the piston-head is necessary to increase high temperature strength nearly at 300°C. The aluminum borate (Al<sub>18</sub>B<sub>4</sub>O<sub>33</sub>, shorted to AlBO) whisker are utilized for the reinforcement of MMC, because of its excellent mechanical properties and lower cost compare to SiC whisker. On the other hand, semi-solid material processing has been developed. The remarkable advantages of this process are the lower amount of shrinkage cavity, macro-segregation and lower process temperature compared with conventional casting[1-3]. In this study, the condition to fabricate partial reinforced AZ91D magnesium alloy by semi-solid squeeze cast process was investigated in succession to our previous work[4-5]. The mechanical properties of the AlBO/AZ91D MMC and the MMC/alloy joints were then examined.

---

Makoto Yoshida, S. Takeuchi, J. Pan, G. Sasaki, H. Fukunaga, Dept. of Mechanical Engineering Hiroshima Univ. Kagamiyama 1-4-1, Higashi-Hiroshima 739-8527, Japan. N. Fuyama, T. Fujii, Western Hiroshima Pref. Industrial Research Institute, Aga-minami 2-10-1, Kure 737-0005 Japan.

## Experimental Procedure

### Processing

To prevent the preform from deformation during the infiltrating process of semi-solid material, fabricating condition was examined in our previous work. The preform with 18% Vf. and 5 MPa compressive strength was then obtained by sintering AlBO whisker (Shikoku Kasei Co. Ltd., Alborex M12) with 5 mass% SiO<sub>2</sub> sol binder vs total amount of the whisker[6]. The preform which has dimensions of L100, H30, T10 was set in a cavity of the dies as shown in Fig. 1. The semi-solid AZ91D alloy was prepared by heating the master billet, which was produced by rapid solidification of the molten alloy [7]. The solid fraction fs. was controlled at 0%(750°C), 20%(590°C), 33%(580°C), or 50%(570°C) by controlling the temperature of the billet. The speed of the plunger with diameter of 60 mm and 309 mm stroke, was set at three levels 50, 100 or 200 mm/s. Approximately 100 MPa pressure was applied to the material at the end of squeeze casting.

### Characterization of the Material

The tensile strength of the MMC/Alloy joints and three point flexural strength of the MMC was measured at room temperature by an autograph (Shimadzu, AG-5000D). After squeeze casting, some specimens were heat-treated in the condition of T6 (two steps solution treatment: 390°C 43.2 Ks, 410°C 57.6 Ks, aging hardening :

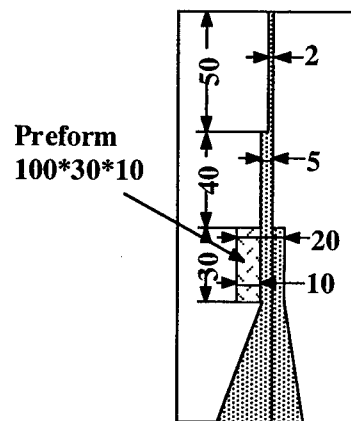


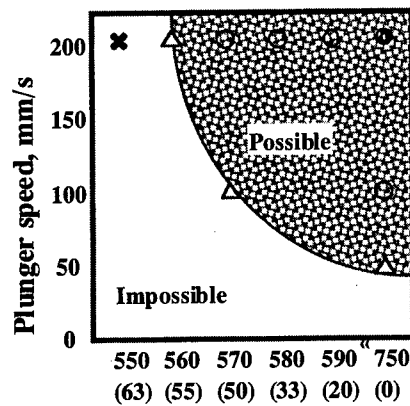
Figure 1 Dimensions of dies and the location of the preform in the cavity.

170°C, 57.6 Ks). In order to examine the damage of the whisker after squeeze casting, distribution of the whisker length was measured by SEM observation of the extracted whisker by etching of dilute HCl solution. The products of chemical reaction between AlBO and alloy were determined with XRD.

## Results and Discussion

### Optimization of the squeeze cast process

The suitable process area between plunger speed and solid fraction is shown in Fig. 2. At the conditions of ring-mark on the map, semi-solid alloy was completely



Temperature, °C (solid fraction, %)

Fig. 2 Suitable process area between plunger speed and solid fraction.

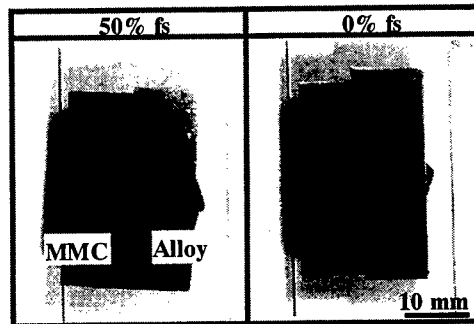


Fig. 3 Cross section of the specimen after squeeze casting.

infiltrated into the preform without the deformation as shown in Fig. 3. As to the conventional squeeze casting process, the preform tends to deform at higher infiltration rate. However, this result reveals opposite tendency. In this process, decrease of the temperature of the billet must be inevitable during the stroke of the plunger, especially in the case of using cold sleeve. Then the lower plunger speed will lead to the larger decrease of the billet-temperature before finishing the infiltration of the semi-solid alloy. This tendency will be more obvious than the semi-solid process of aluminum alloy because of smaller specific heat of magnesium alloy. The hot-sleeve system should be effective to enlarge suitable process area. Hereafter, the maximum solid fraction in the map, 50% fs is chosen to fabricate cast materials beside conventional 0% fs process at 200 mm/s plunger speed.

#### Microstructure

Optical microscope images including MMC/alloy interface are shown in Fig. 4. It is found that in the as-cast 50% fs specimen,  $\alpha$ -Mg solid phase piles up on the preform during the infiltration process of the semi-solid material as reported in the previous work[4]. After T6 treatment of 50% fs specimen, mosaic structure was formed, which was composed of  $\alpha$ -Mg grains (white grains) and black color grains. The black grains contain  $Al_{12}Mg_{17}$  intermetallic compound, which is precipitated from  $\alpha$ -Mg solid solution. On the other, as to the 0% fs specimen, more uniform morphology was obtained than the 50% fs specimen. Therefore in order to disperse precipitates uniformly, longer solid solution treatment is necessary for the material by semi-solid process than that for the conventional 0% fs process. This must be caused by the difference in the scale of the morphology between semi-solid process and conventional 0% fs process.

#### Mechanical Properties

To examine the bonding strength of the MMC/alloy interface, tensile test was

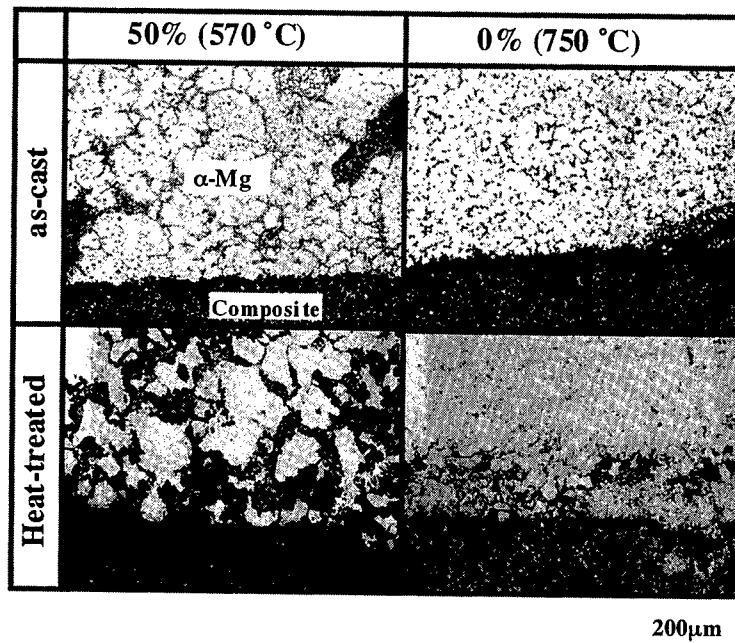


Fig. 4 Microstructure of the specimen including MMC/alloy interface.

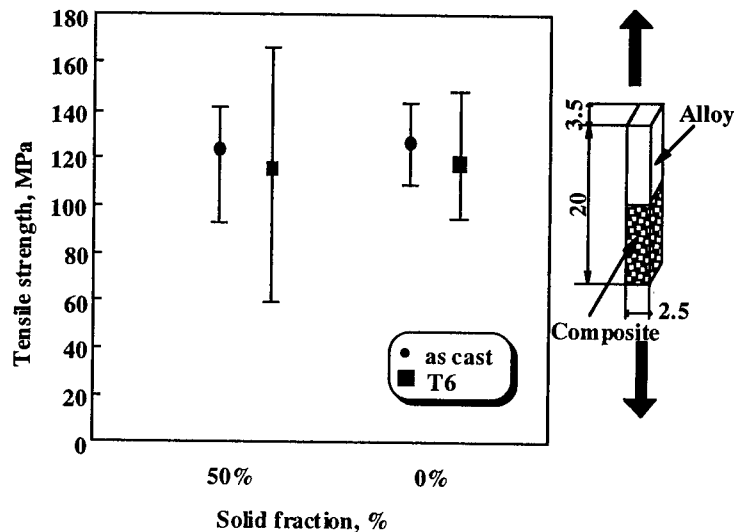


Fig. 5 Tensile strength of the MMC/alloy interface.

carried out. The result is shown in Fig. 5. All specimens were ruptured at the interface. It is found that the average bonding strength of 50% fs specimens are equal to the strength of 0% fs specimens. However the measurements of the T6 treatment of 50% fs specimens vary wider than that of as-cast specimens. This would be due to the scale of the grain size which is enlarged by the T6 treatment as mentioned above. The flexural strength of the composites are shown in Fig. 6(a). In our previous work, the aluminium content in the matrix of 50% fs specimens is higher than that of 0% fs

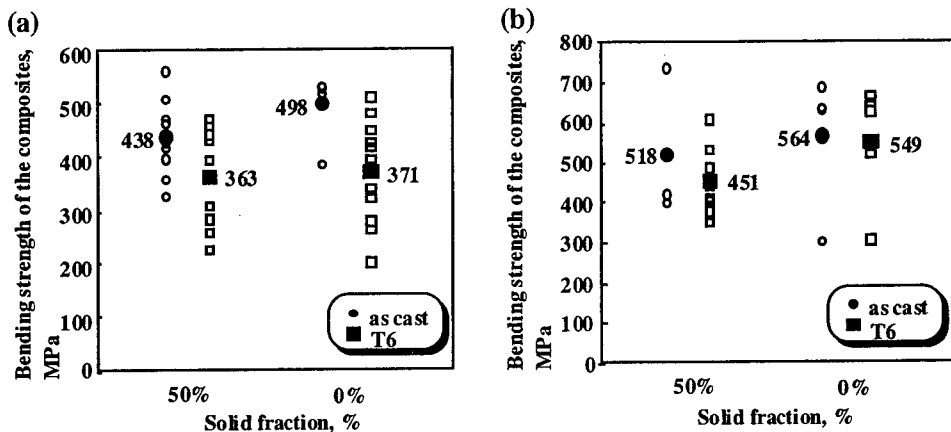


Fig. 6 Flexural strength of the composite, (a) with SiO<sub>2</sub> binder, (b) without inorganic binder to prepare the preform.

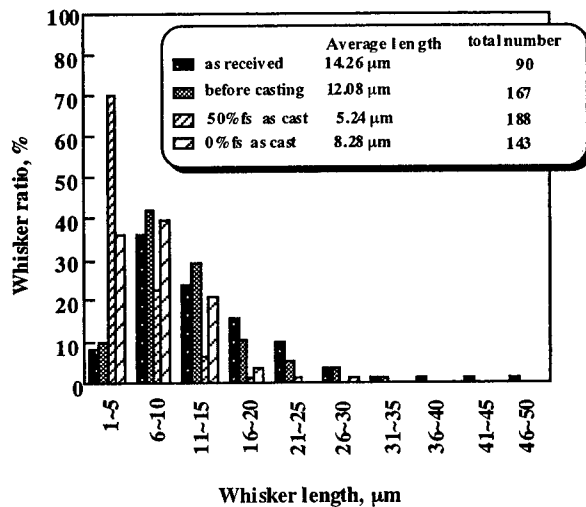


Fig. 7 Distribution of the whisker length.

specimens. This led to the higher Vickers hardness than that of 0% fs specimens. However average flexural strength of the 50% fs specimen is 12% lower than that of 0% fs specimen. The distribution of the whisker length (Fig. 7), reveals that the average length in the 50% fs specimen is 5 μm, which is 37% lower than that in the 0% fs specimen. This will be caused by the higher pressure of the semi-solid process to the preform during the infiltration of liquid phase than the pressure of conventional process. Furthermore, after T6 treatment, regardless of the solid fraction, the flexural strength decreased by 16% (in 50% fs) or 26% (in 0% fs). In order to investigate the cause of this phenomenon, the preforms without inorganic binder such as SiO<sub>2</sub> binder were prepared. As the result of the squeeze cast, the preforms were compressed and deformed by the pressure of the infiltration, however the decrease of the strength after T6 treatment was reduced in both 50% fs (13%) and 0% fs (4%) specimens (Fig.

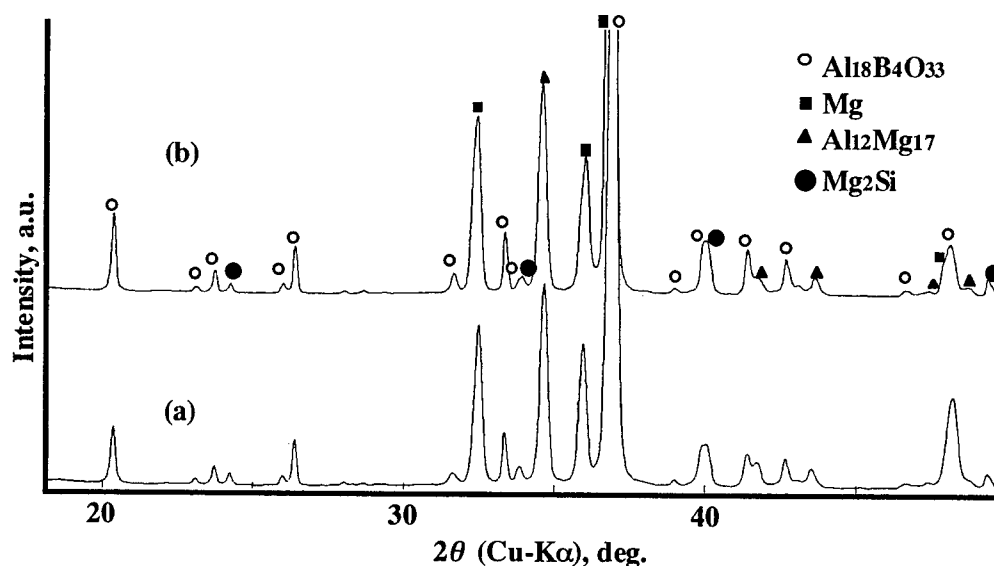
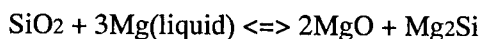


Fig. 8 XRD patterns of AlBO/AZ91D composites, (a) as-cast, (b) T6 treated. (solid fraction = 0% process)

6(b)). The result of the XRD for the composites (0% fs) implies the chemical reaction between  $\text{SiO}_2$  sol on the surface of the whisker and magnesium in molten alloy produces  $\text{Mg}_2\text{Si}$  intermetallic phase. This phase was identified in both as-cast and T6 treated materials. The formula of the reaction should be written as follow. The Gibbs free energy change indicates that this reaction is possible thermodynamically.



Nishino et al [8] pointed out that the formation of the  $\text{Mg}_2\text{Si}$  induce the notch effect to the whisker and this leads to the decrease in the strength of the composites. Thus during the solid solution treatment of aging treatment, the particle of produced  $\text{Mg}_2\text{Si}$  phase grows up like the "Ostwart ripening", then the notch effect will become obvious. Therefore it will be necessary to select alternative inorganic binder which is chemically stable to the magnesium and is effective to strengthen the preform.

## Conclusion

Aluminum borate whisker reinforced magnesium alloy matrix composites was fabricated with semi-solid material process by the squeeze casting.

- (1) Without deformation of the preform, it is possible to fabricate MMC/alloy jointed material by squeeze casting up to 50 % solid fraction.
- (2) The average bonding strength of the MMC/alloy interface of 50% fs specimens is 120 MPa, which is equal to the strength of 0% fs specimens.

- (3) The average flexural strength of the composite, fabricated by squeeze casting of 50 % fs material, was 438 MPa. However as the result of heat-treatment, the strength decreased to 368 MPa. This will be caused by the notch effect of  $Mg_2Si$  phase produced by the chemical reaction between  $SiO_2$  sol and magnesium.

### Acknowledgements

The authors would like to thank the Small and Medium Enterprise Agency in Japan, for financially supporting the present research.

### References

1. D.B. Spencer, R. Mehrabian and M.C. Flemings, 1972. Met. Trans., 3:1925
2. M.C. Flemings, R.G. Riek and K.P. Young, 1976, Mat. Sci. and Engineering, 25:103-117.
3. D.M. Lee, B.G. Kim, J.S. Lee, and C.H. Lee, 1997. "Fabrication, microstructures, and tensile properties of magnesium alloy AZ91/SiCp composites produced by powder metallurgy", Mat. Sci. and Tech., 13:590-595.
4. M. Yoshida, S. Takeuchi, J. Pan, G. Sasaki, N. Fuyama, T. Fujii, and H. Fukunaga, 1999. "Preparation and characterization of aluminum borate whisker reinforced AZ91D magnesium alloy composites by semi-solid process." Adv. Composite Mater., 8(3): 259-268.
5. M. Yoshida and H. Fukunaga et al. Japan Patent H11-25082
6. Sikoku kasei Co. Ltd. 1993. Alborex Technical Instruction.
7. Patent 8-74015, UBE INDUSTRIES, LTD.
8. Nishino et al, J. Japan Institute of Light Metals, 47:208-213.

## **Effect of Whisker Surface Treatment on the Strength of $\text{Al}_{18}\text{B}_4\text{O}_{33}$ /Al Alloy Composites**

J.Pan, A.Okamoto, M.Yoshida, G.Sasaki, H.Fukunaga,  
N.Fuyama and T.Fujii

### **Abstract**

In order to increase the whisker preform strength and decrease the interfacial reactivity between  $\text{Al}_{18}\text{B}_4\text{O}_{33}$  whisker and aluminum alloy, three kinds of whisker surface treatments have been carried out. They were  $\text{SiO}_2$  binder addition, magnesium deposition coating and spinel ( $\text{MgAl}_2\text{O}_4$ ) coating, respectively. By a low vacuum evaporation technique (under vacuum 10Pa at 650°C for 1h), magnesium was deposited on the whiskers uniformly. Magnesium deposition reacted with the whisker at 800°C for 0.5h in air to create a  $\text{MgAl}_2\text{O}_4$  layer (8-10nm in thickness) on the whisker. Three kinds of surface treated and no treated whiskers were used to reinforce AC4CH aluminum alloy by squeeze casting method. Those surface treatments could increase the strength of whisker preform and hence decreased the preform deformation during squeeze casting. However,  $\text{SiO}_2$  binder did not prevent the interfacial reaction. Being similar to no treated whisker composite,  $\text{SiO}_2$  added whisker composite had a deterioration of strength after T6 treatment. Magnesium coating just avoided the interfacial reaction of  $\text{Al}_{18}\text{B}_4\text{O}_{33}$  whisker with the matrix but did not prevent that with the magnesium coating itself. After T6 treatment, the strength decrease due to whisker damage and the strength increase from the matrix age strengthening did not change the total strength of composites.  $\text{MgAl}_2\text{O}_4$  coating existed as an effective barrier to prevent the interfacial reaction. During T6 treating, no any further whisker damage happened and the matrix was strengthened. This enabled composite strength to have a considerable enhancement.

### **Introduction**

Aluminum borate ( $\text{Al}_{18}\text{B}_4\text{O}_{33}$ —AlBO) whisker can be competitive with SiC whisker as a reinforcement of metal matrix composites, because it has an excellent property and a low cost [1,2]. Aluminum matrix composites reinforced by this whisker have been used practically in automobile engines [3,4]. But the interfacial reaction that leads to the degradation of whisker

---

J.Pan, A.Okamoto, M.Yoshida, G.Sasaki and H.Fukunaga, Dept. of Mechanical Engineering, Hiroshima University, Kagamiyama 1-4-1, Higashi-Hiroshima 739-8527, Japan  
N.Fuyama and T.Fujii, Western Hiroshima Prefecture Industrial Research Institute, Aga-minami 2-10-1, Kure 737-0005 Japan



strength must be controlled for a wide application. AlBO whisker reacts with the magnesium included in aluminum alloy from about 520°C, and with aluminum directly at about 730°C [5,6]. Such temperatures belong to the fabrication and heat treatment ones for the composites. As a result of the interfacial reaction, the heterogenous products like spinel ( $\text{MgAl}_2\text{O}_4$ ),  $\gamma$ - $\text{Al}_2\text{O}_3$  are formed at the whisker surface [6-9]. This leads to deterioration in reinforcement efficiency owing to the whisker consumption and whisker length shortening [10-12]. In addition, because magnesium in the matrix alloy is also exhausted by the reaction with whisker, the age strengthening of the matrix after T6 treatment cannot appear [12,13]. Therefore, a suitable barrier to avoid the direct contact between AlBO whisker and aluminum matrix is necessary. Squeeze casting is a simple process to fabricate AlBO/Al alloy composites. Generally, an inorganic binder such as  $\text{SiO}_2$  is added into the whisker in order to decrease the whisker preform deformation. But  $\text{SiO}_2$  binder seems not to prevent the whisker reaction with the matrix alloy. Under these considerations, a new surface treatment method for AlBO whisker has been developed. That is, a uniform magnesium coating is deposited on AlBO whisker by vacuum evaporation of magnesium, and then a homogenous spinel ( $\text{MgAl}_2\text{O}_4$ ) layer is formed by the reaction between this magnesium deposition and the whisker during heat treatment. This surface coating is expected not only to act as binders of the whisker preform, but also as an interfacial reaction barrier. The aim of the present work is to investigate the effect of the different surface treatments on the preform strength and the composite strength after T6 treatment.

### Experiment Methods

AlBO whisker, manufactured by *Shikoku Chemical Industry* (Japan), was used as the reinforcement. Pure magnesium (purity: 99.95%) and an AC4CH aluminum alloy (Al-7.3Si-0.37Mg) were employed as the coating metal of whisker and the matrix alloy of composites, respectively. Magnesium coating on whisker was carried out in a vacuum furnace as shown in Fig.1, where a piece of pure magnesium was vapoured and then deposited on the whiskers. The furnace was heated under vacuum (10Pa). When the temperature arrived at 650°C, the vacuum valve was closed and the furnace chamber was in a sealed state. After heating at this temperature for 1h, electricity supply was switched off, AlBO whisker cooled down together with the furnace naturally.

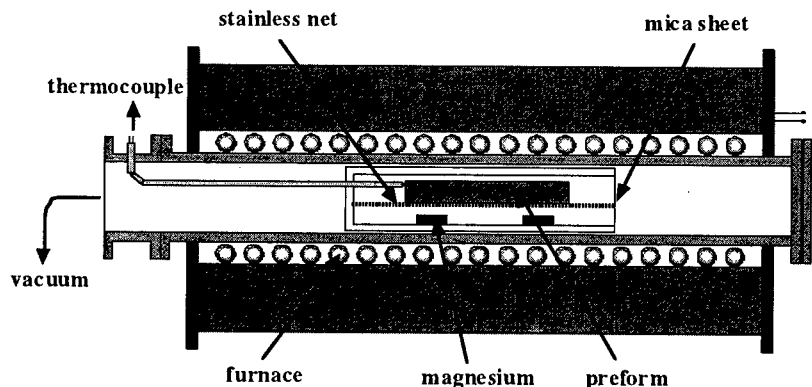


Fig.1 Schematic diagram of AlBO whisker coating apparatus.

Mg-deposited whiskers were taken out from the apparatus and then heated in air for 0.5h to form a spinel layer on the whisker by the reaction of the magnesium deposition with AlBO whisker. No treated whisker, 3 mass% SiO<sub>2</sub> added whisker, Mg-deposited whisker and spinel coated whisker reinforced AC4CH alloy composites were fabricated by squeeze casting, respectively. The preform preheating temperature, aluminum alloy melt pouring temperature, die preheating temperature and squeeze pressure were 700°C, 760°C, 200°C and 100MPa, respectively. The as-cast composites were T6 treated under the following conditions: solution treating at 525°C for 8h, water quenching and aging at 160°C for 6h. SEM (HITACHI/ S-800), EPMA (JEOL/ JXA-9800RL) and XRD (MAC SCIENCE/ MXP<sup>18</sup>VA) were used to identify the composition and structure of the deposition and the coatings on AlBO whiskers. Mg-deposited AlBO whiskers after heat treatment were observed using TEM (TOPCON/ EM-002B). The compressive strength of the whisker preforms and tensile strength of AlBO/AC4CH composites were evaluated with a mechanical tester (SHIMADZU/ Autograph AG-100kNG).

## Results and Discussion

EPMA analysis result of Mg-deposited AlBO whisker shows that the atomic ratio Mg:Al is 13.5:86.5. Since the magnesium coat is a thin layer, aluminum from the whisker has been detected. From this result it can be confirmed at least that magnesium has been coated on the whisker successfully. XRD patterns of the different whiskers are exhibited in Fig.2. For the Mg-deposited whiskers, magnesium existence can hardly be found (Fig.2b). This is attributed to that magnesium maybe just was a cluster, did not become a perfect crystal. When the Mg-deposited whisker was heated at

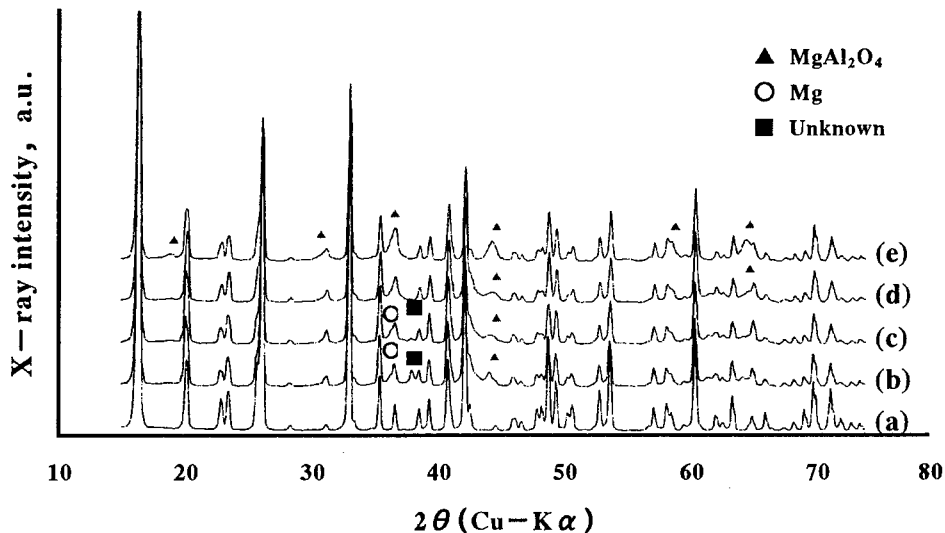


Fig.2 XRD patterns of the as received whiskers, Mg-deposited whiskers, and the Mg-deposited whiskers after heated at different temperatures.

(a) as received, (b) Mg-deposited at 650°C, (c) heated at 600°C, (d) heated at 700°C, (e) heated at 800°C.

600°C, the peaks of magnesium and spinel were not still identifiable (Fig.2c). But in the cases of heat treatment at 700°C and 800°C, obvious  $\text{MgAl}_2\text{O}_4$  peaks can be confirmed (Fig.2d and 2e). For the whisker after heated at 800°C, the atomic ratio Mg:Al was 12.6:87.4, which was almost the same as that before heat treatment. It may be imagined that the reaction between magnesium and AlBO whisker occurs as follow:



The calculation of Gibbs free energy ( $\Delta G = -5.97 \times 10^6 \text{ J/mol}$ ) indicates that this reaction is possible thermodynamically.

AlBO whiskers that coated with magnesium at 650°C for 1h in vacuum and then heat treated at 800°C for 0.5h in air were observed under transmission electron microscope. Fig.3 reveals a surface profile image of the whisker. A continuous reaction layer with a thickness of 8-10nm is covering up

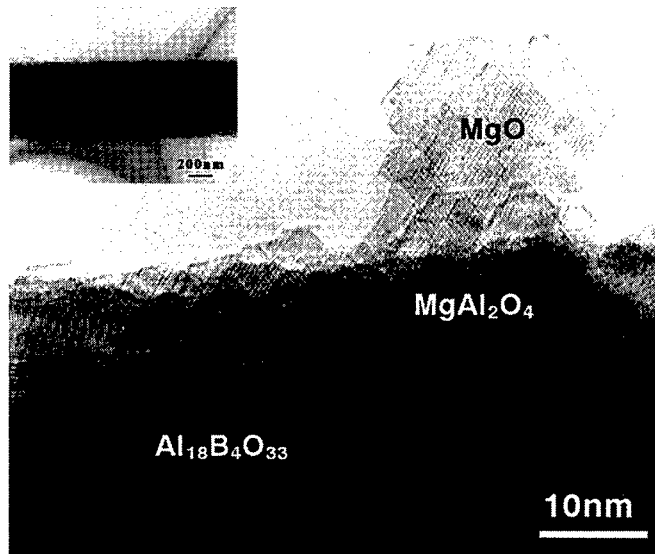


Fig.3 Surface profile HRTEM image showing the interface between AlBO whisker and  $\text{MgAl}_2\text{O}_4$  coat (the top left one is a low magnification image).

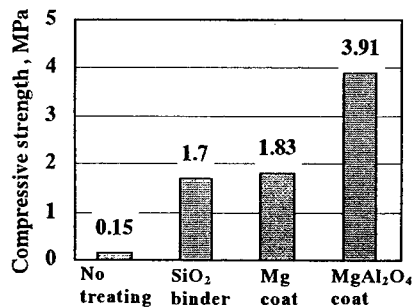


Fig.4 Compressive strength of four kinds of AlBO preforms.

Table 1 Change of whisker volume fraction in preform (composite) before and after squeeze casting.

	Volume fraction (%)		Shrinkage ratio (%)
	Before casting	After casting	
No treating	19.0	24.0	20.8
$\text{SiO}_2$ binder	16.5	16.8	1.8
Mg coat	19.0	19.2	1.0
$\text{MgAl}_2\text{O}_4$ coat	19.0	19.0	0.0

the whole whisker. It adheres to the whisker keeping with a specific crystal orientation. The identification shows that it is a spinel phase  $\text{MgAl}_2\text{O}_4$ . This result is coincident with that of EPMA and XRD. Such a spinel layer bonded with AlBO closely may become a good barrier to prevent the reaction of the whisker with the matrix alloy. In the outside of the spinel layer, MgO particles as shown in the same figure were discovered in some locations. This MgO particle with a size of 20-30nm, is attributed to the oxidation of magnesium coating on AlBO whisker during heat treatment.

The preforms of no treated whisker,  $\text{SiO}_2$  binder added whisker, Mg-deposited whisker and  $\text{MgAl}_2\text{O}_4$  coated whisker were prepared, respectively. Their compressive strengths are shown in Fig.4. For the preform without binder addition, the strength was very low. If 3 mass%  $\text{SiO}_2$  was added into the preform, the strength had approximately ten-fold increase. Magnesium could also be regarded as a binder since the strength of Mg-deposited AlBO preform was as high as that containing binder  $\text{SiO}_2$ . The preform having  $\text{MgAl}_2\text{O}_4$  coat is the strongest. SEM observation shows that the whiskers are connected with  $\text{SiO}_2$  binder, Mg coat or  $\text{MgAl}_2\text{O}_4$  coat (photographs are omitted), which is considered as the reason why those three preforms obtained a fairly high strength. Table 1 gives the change of the whisker volume fraction before and after casting. It can be seen that the stronger the preform was, the less the changes of volume fraction and preform shrinkage were. Therefore, Mg coat and  $\text{MgAl}_2\text{O}_4$  coat created by the present process may become good binders for the whisker preform.

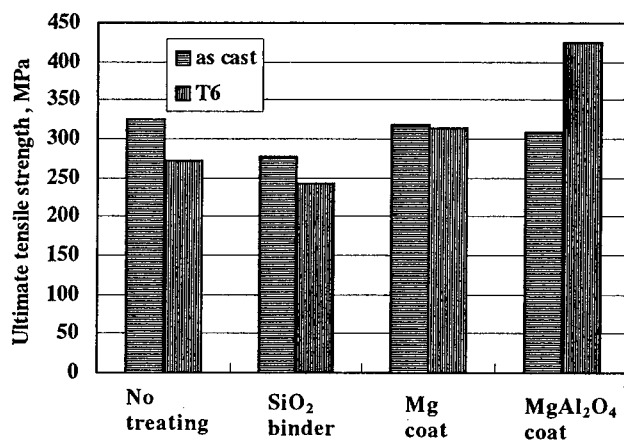


Fig.5 Tensile strength of AC4CH aluminum alloy composites reinforced by the four kinds of AlBO whiskers ( $V_f=20\%$ ).

From a lot of studies it has been indicated that AlBO whisker reacts with magnesium included in the matrix during T6 treatment [5,7,10]. The whisker is damaged, and besides, the magnesium existing as the main element of age strengthening phase ( $\text{Mg}_2\text{Si}$ ) is exhausted. As a result, the composite strength after T6 treatment drops drastically. Fig.5 shows the ultimate tensile strength of the four kinds of whiskers reinforced AC4CH alloy composites in the as-cast and T6 states. No treated AlBO/Al composite had about 16% strength

deterioration after T6 treatment. Similarly,  $\text{SiO}_2$  added AlBO/Al had about 13% strength loss in T6 state. This strength degradation is contributed to the whisker damage and the consumption of magnesium in the matrix. However, in the case of Mg-deposited whisker, it may be imagined that the whisker reacts just with this magnesium coating but not with the magnesium in matrix alloy. Although this reaction damages the whisker, the matrix composition does not occur and hence the age strengthening appears the matrix alloy because. Therefore, the composite strength degradation was stopped after T6 treatment. Furthermore, in the case of  $\text{MgAl}_2\text{O}_4$  coated AlBO/Al composites, because the reaction between the whisker and magnesium coating has been completed before squeeze casting, further whisker damage due to interfacial reaction can be avoided during T6 treatment. Therefore, composite strength in T6 state had a considerable enhancement. Fig.6 exhibits XRD patterns of the whiskers extracted from the four kinds of AlBO/Al composites in the as-cast and T6 states. Fig.7 gives the corresponding SEM photographs of those whiskers. For the whiskers from the no treated and  $\text{SiO}_2$  added AlBO reinforce-

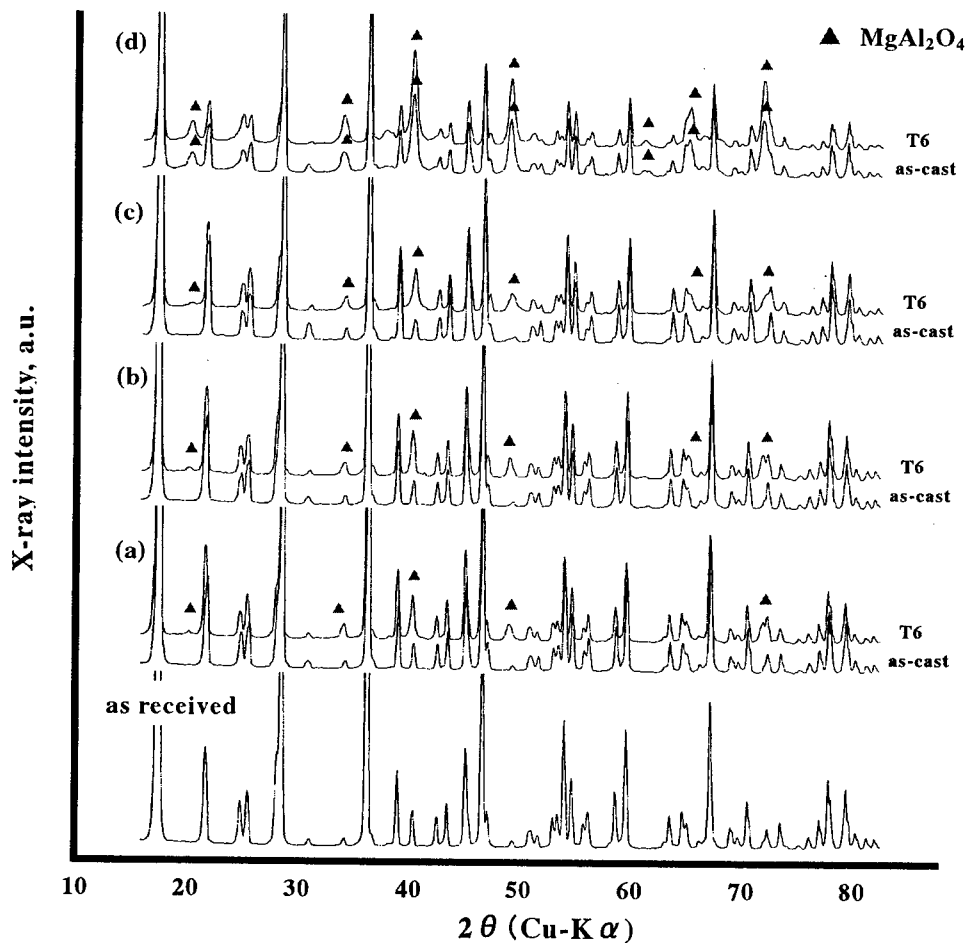


Fig.6 XRD patterns of the as received whiskers and the extracted whiskers from different AlBO/Al composites in the as-cast and T6 states. (a) No treated AlBO, (b)  $\text{SiO}_2$  added AlBO, (c) Mg coated AlBO, (d)  $\text{MgAl}_2\text{O}_4$  coated AlBO.

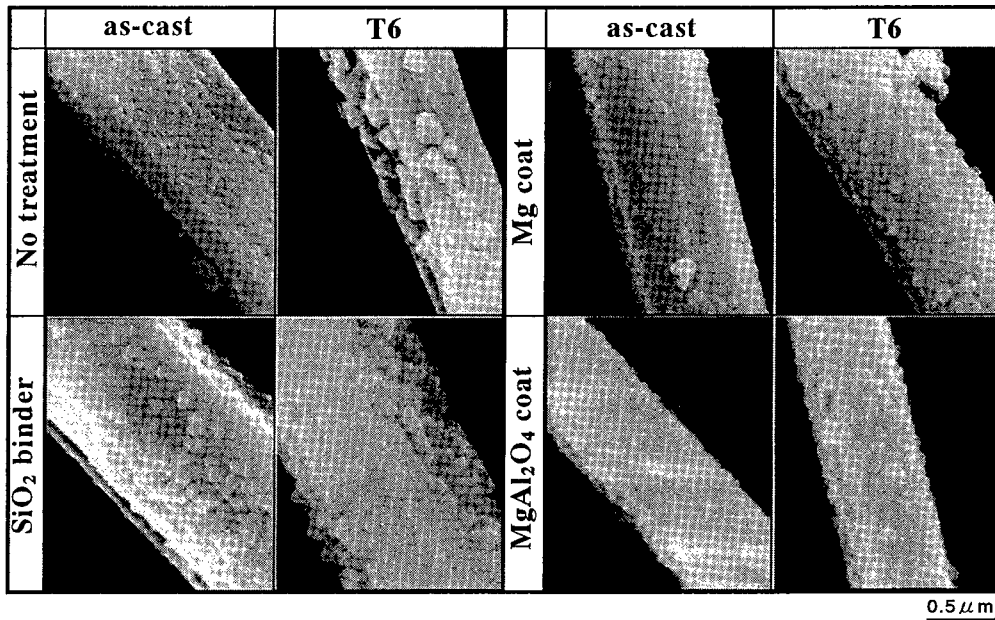


Fig.7 SEM photographs of the extracted whiskers from different treated AlBO whisker reinforced AC4CH alloy composites in the as-cast and T6 state.

ed composites in the as-cast state, although no  $\text{MgAl}_2\text{O}_4$  was found by XRD analysis (Fig.6a and 6b), SEM observation showed that many particlelike substances were covering the whisker. It means that an interfacial reaction occurred when the composites were fabricated. After T6 treatment, obvious  $\text{MgAl}_2\text{O}_4$  peaks appeared in their XRD patterns. The whisker was nibbled by the further chemical reaction between AlBO and the matrix alloy (Fig.7). Whisker surface became very rough and lots of large particlelike products were adhering to the whiskers. AlBO whisker damage by such an interfacial reaction resulted in composite strength degradation drastically. In the case of Mg coated AlBO whisker reinforced composite, XRD patterns of the whiskers from the as-cast and T6 states composites were similar to those of the no treated and  $\text{SiO}_2$  added AlBO composites (Fig.6c). A difference may be seen from SEM observation. The surface appearance of the Mg-deposited whisker from T6 treated composite revealed further damage than that of the as-cast composite, but the degree became much slight comparing to that of no treated and  $\text{SiO}_2$  added AlBO composites (Fig.7). The interfacial reaction was prevented partially and magnesium in the matrix alloy was not exhausted. It may be considered to the reason why the strength of Mg coated AlBO composite did not decrease after T6 treatment. Finally, in the XRD patterns of the extracted whiskers from  $\text{MgAl}_2\text{O}_4$  coated AlBO composite,  $\text{MgAl}_2\text{O}_4$  peaks appeared in the as-cast state (Fig.6d). This is attributed to the chemical reaction between AlBO whisker and Mg coating during the treatment before squeeze casting. After T6 treatment, XRD peaks almost did not change. The surface state of AlBO whisker does not have any visible differences comparing to that from the as-cast composite (Fig.7). In another word, the whisker damage due to interfacial reaction has been stopped. The age strengthening effect by T6 treatment leads to the composite strength increase considerably.

## Conclusions

1. By a vacuum evaporation method, a uniform magnesium coating has been deposited on AlBO whiskers successfully. By the heat treatment of the Mg-deposited whiskers at 800°C for 0.5h in air, a continuous  $\text{MgAl}_2\text{O}_4$  layer of 8-10nm formed on the whiskers.
2.  $\text{SiO}_2$ , magnesium and  $\text{MgAl}_2\text{O}_4$  coating can be regarded as the binders to strengthen the AlBO whisker preform. The deformation of preform using those binders was avoided when composites were fabricated.
3. Adding  $\text{SiO}_2$  in the whisker preform did not change the interfacial reaction behavior and hence the strength of  $\text{SiO}_2$  added AlBO/AC4CH alloy composite still dropped down after T6 treatment.
4. Mg-deposited AlBO whisker could be kept from reacting with the matrix alloy during T6 treating, so the composite strength degradation was avoided.
5.  $\text{MgAl}_2\text{O}_4$  coating on AlBO whiskers played a role of barrier to prevent the interfacial reaction. T6 treatment increased composite strength considerably.

## References

1. K.Suganuma, T.Fujita, N.Suzuki and K.Niihara, 1990, *Journal of Materials Science Letters*, 9: 633-635.
2. Shikoku Chemicals industry Co. Ltd., 1992, *ALBOREX Technical Report*, pp.2-4.
3. Y.Shintari, Y.Okochi and M.Sugiyama, 1997, *Proceedings of the 5th Japan International SAMPE Symposium*, pp.399-404.
4. T.Kitamura, K.Sakane, H.Wada, H.Hata and Y.Shintari, 1997, *Proceedings of International Workshop on Advanced Materials for Functional Manifestation of Frontier and Environmental Consciousness*, pp.11-18.
5. L.J.Yao, G.Sasaki and H.Fukunaga, 1997, *Materials Science and Engineering A*, 225: 59-68.
6. L.J.Yao, G.Sasaki, J.Pan, M.Yoshida and H.Fukunaga, 1998, *Metallurgical and Materials Transactions A*, 29: 1517-1524.
7. K.Suganuma, G.Sasaki, T.Fujita and N.Suzuki, 1991, *Journal of Japan Institute of Light Metals*, 41(5): 297-303.
8. K.Nagatomo and K.Suganuma, 1994, *Journal of Japan Institute of Metals*, 58(1): 78-84.
9. M.Shibata and Y.Takemoto, 2000, *Journal of Japan Institute Metals*, 64(1): 1-6.
10. X.G.Ning, J.Pan, J.H.Li, K.Y.Hu, H.Q.Ye and H.Fukunaga, 1993, *Journal of Materials Science Letters*, 12:1644-1647.
11. G.Sasaki, M.Yoshida, J.Pan and H.Fukunaga, 1999, *Materials Science Research International*, 5(4): 276-279.
12. J. Pan, G. Sasaki, L. J. Yao and M. Yoshida and H. Fukunaga, 1999, *Materials Science and Technology*, 15(9): 1044-1048.
13. X.G.Ning, J.Pan, K.Y.Hu and H.Q.Ye, 1992, *Materials Letters*, 13: 377-381.

## CMC and C/C

---



## **Multiple Micro-cracking and Tensile Behavior of Orthogonal 3-D Woven Si-Ti-C-O Fiber / Si-Ti-C-O Matrix Composite**

T. Ogasawara, H. Ito, T. Ishikawa, and N. Watanabe

### **Abstract**

This paper presents the experimental results of multiple micro-cracking and tensile behavior of the orthogonal 3-D woven Si-Ti-C-O fiber (Tyranno™ Lox-M) / Si-Ti-C-O matrix composite with nano scale carbon interphase. The composite was processed by a polymer impregnation and pyrolysis (PIP) method. It was revealed that the inelastic stress/strain behavior was governed by the matrix cracks in the transverse (90°) fiber bundles above 65MPa, the matrix cracks in longitudinal (0°) fiber bundles above 180 MPa, and the fiber fragmentation above 300MPa. A methodology for estimating unidirectional tensile behavior of the orthogonal 3-D composite was provided by using and modifying the established theories in literatures. Comparison of the predicted and measured strains indicated good correspondence by the procedure.

### **Introduction**

Monolithic ceramics possess excellent performance for high temperature materials. However, because of brittleness, it is difficult to use them for aerospace applications such as jet engine, rocket engine, and thermal protection system of a future space-plane. For the reason, a great amount of effort has been devoted to the development of ceramic matrix composite (CMC) with continuous ceramic fiber. The National Aerospace Laboratory of Japan, Ube Industries Ltd., Shikibo Ltd., and Kawasaki Heavy Industries Ltd. have conducted a joint program to develop and evaluate a continuous fiber reinforced ceramic matrix composite. The composite is referred to as "Nusk-CMC" from the initials of the collaborators.

The composite contained Tyranno™ Lox-M grade fiber (Si-Ti-C-O fiber) with an additional surface modification in order to improve interface properties. Thus, the fiber/matrix interface is controlled by the heat treatment of the fiber, and a SiO<sub>x</sub>-rich layer surrounding an inner carbon-rich layer is formed at the fiber surface.

---

Toshio Ogasawara and Takashi Ishikawa, Structures Division, National Aerospace Laboratory, Mitaka, Tokyo, 181-0015, Japan

Hiroshi Ito\* and Naoyuki Watanabe, Aerospace Systems Department, Tokyo Metropolitan Institute of Technology, Hino, Tokyo, 191-0065, Japan

(\*Present affiliation; Mitsubishi Heavy Industries, Ltd.)

Using these technologies, the composite exhibits excellent tensile strength at room temperature [1].

Nusk-CMC shows nonlinear stress-strain behavior under unidirectional tensile loading, which is due to multiple micro-cracking in the transverse and the longitudinal fiber bundles. Analytical models for estimating stress-strain behavior of unidirectional and cross ply ceramic matrix composites have been reported in literatures. However, no mechanical model regarding to orthogonal 3-D woven CMCs has been reported.

This paper presents the experimental results of multiple micro-cracking and tensile behavior of the orthogonal 3-D woven Si-Ti-C-O fiber / Si-Ti-C-O matrix composite (Nusk-CMC) fabricated by a PIP processing. The constituent properties were estimated by hysteresis loop analysis in unload/reload testing. A methodology for estimating unidirectional tensile behavior of the orthogonal 3-D CMCs was proposed.

### Experimental Procedure

The composite under investigation contained Tyranno™ Lox-M fibers woven into an orthogonal 3-D configuration with fiber volume fractions of 19%, 19%, and 2% in the x, y, and z directions, respectively. The number of layer was 16 for x-axis and 17 for y-axis. Optical micrograph illustrating the composite fiber architecture has been presented in Fig.1. Each fiber bundle contains 1600 fibers. The composite preform plate (240 x 120 x 6 mm) was treated at elevated temperature in a CO atmosphere, resulting in formation of a 10 nm SiO<sub>x</sub>-rich layer surrounding an inner 40 nm carbon-rich layer at the fiber surface [1]. The nano-scale carbon-rich layer acts as desirable interphase between fiber and matrix in the composite. Poly-titano-carbosilane was used as the matrix precursor with repeated impregnation and pyrolysis cycles until satisfactory densification was achieved. The average bulk density of the composite was 2.20 g/cm<sup>3</sup> after machining. Tensile specimens were machined from the composite plates such that the loading direction was parallel to the y-axis.

Tensile testing was conducted on a servo-hydraulic testing system (Model 8501, Instron, USA) at room temperature in air. The specimen had 30 mm in gauge length, 4 mm in thickness and width, and 110 mm in the overall length. The specimen was loaded by using hydraulic wedge grips. A clip gauge-type extensometer (Model

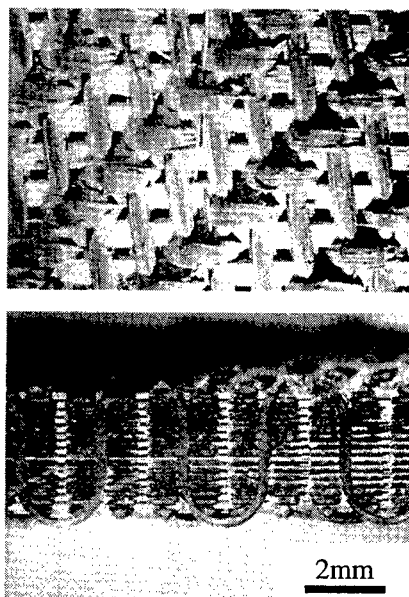


Figure 1 Optical Microphotographs of Si-Ti-C-O Fiber/ Si-Ti-C-O Matrix Composite (Nusk-CMC) Illustrating the Orthogonal 3-D Woven Fiber Configuration

632.11C-20, MTS, USA) was used to measure the longitudinal strain. The gauge length of extensometer was 25 mm. The tensile test was performed under a constant displacement rate of 0.5 mm/min.

Matrix cracking characteristics were established by a replica film method. The side surface of specimen was polished by #4000 diamond whetstone prior to testing. Surface replicas were taken by using acetate replica films with 0.08mm thickness under load at various stages of the loading. Tensile test was conducted with periodic unload/reload cycles to perform hysteresis measurements.

## Experimental Results

### Stress/Strain Behavior and Multiple Micro-Cracking

The stress/strain curves and hysteresis loops measured in unload/reload tensile testing is summarized on Fig.2. The curve of the composite indicates linear elastic behavior up to the proportional limit of 65MPa with an initial elastic modulus,  $E=141$  GPa. The composite exhibits distinct inelastic deformation above 65MPa to the ultimate tensile strength (423.8MPa). Figs.3 show the optical micrographs of the replica films illustrating matrix cracks in the longitudinal ( $0^\circ$ ) and transverse ( $90^\circ$ ) fiber bundles. The photographs (a) to (e) in Figs.3 correspond to the load stage (a) to (e) in Fig.2, respectively. The following damage process for each load stage is understood.

- (a) Stress/strain curve is linear. No microscopic damage is observed (<65 MPa).
- (b) The propagation of matrix cracks in the transverse fiber bundles is observed above 65 MPa. In this paper, the term transverse crack used for matrix crack in transverse ( $90^\circ$ ) fiber bundles.
- (c) The onset and evolution of matrix cracks in the longitudinal fiber bundle are observed above 180 MPa. The matrix cracks that originate in the transverse fiber bundles only partially penetrate the longitudinal fiber bundles. In this paper, the term matrix crack is used for the matrix crack in longitudinal ( $0^\circ$ ) fiber bundles.
- (d) The matrix crack density in longitudinal fiber bundles increases with the applied load up to 300 MPa. A small amount of the transverse crack propagation is also observed.
- (e) The matrix crack densities in

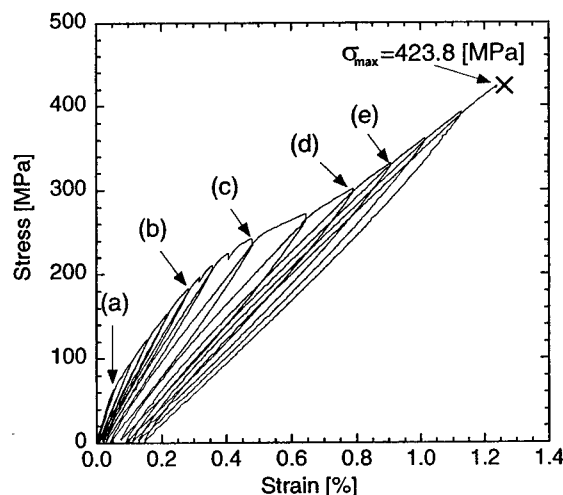


Figure 2 Stress/Strain Curve of NUSK-CMC in Loading-Unloading Test

both the transverse and the longitudinal fiber bundles are saturated above 300MPa.

#### Matrix Crack Densities of Transverse and Longitudinal Fiber Bundles

Crack density measurements made for the composite is plotted in Fig.4. It shows that the matrix cracking stress, 150MPa and that matrix cracks saturate at 300MPa with crack saturated spacing 45.4  $\mu\text{m}$ . Domergue et al. reported that composite failure intervene prior to matrix crack saturation in Nicaron (Si-C-O) fiber / CVI-SiC matrix cross ply composite [2]. However, it is apparent that matrix crack saturation occurs for the composite. The difference may be attributed to differing interfacial characteristics in these CMCs.

The propagation of the transverse crack is more complicated. The onset of transverse crack propagation is 65 MPa, and the crack density increases up to 120 MPa rapidly. Transverse crack density gradually increase above 200 MPa again,

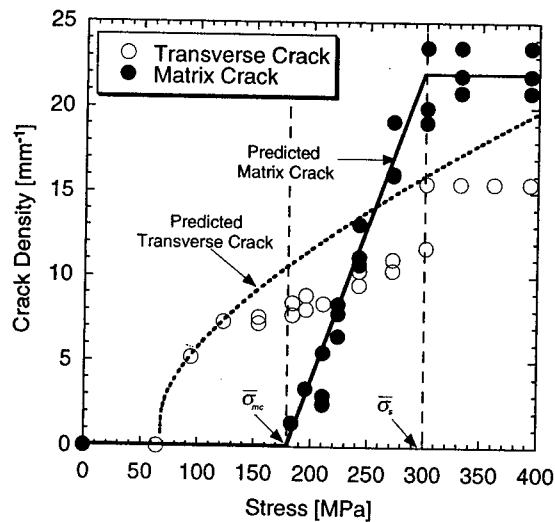
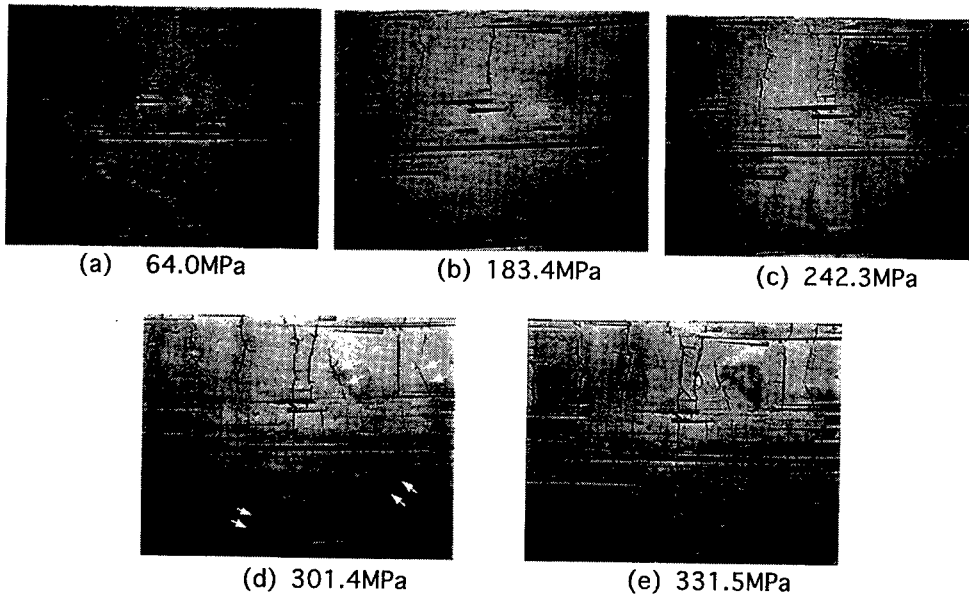


Figure 4 Transverse and Longitudinal (matrix) Crack Densities of Nusk-CMC as a Function of Applied Stress



Figures 3 Optical Microphotographs of Surface Replica Film Showing Matrix Cracks in the Longitudinal (0°) and the Transverse (90°)

and it is completely saturated above 300 MPa. In this stage, oblique transverse cracks indicated by the white arrows in Fig.3(d) are observed. Since the composite has translaminar fiber bundles, no delamination at the interlaminar between 0° and 90° fiber bundles was observed. Thus, these cracks might be propagated by a shear stress at the interlaminar.

## Discussion

### Methodology for Estimating the Stress/Strain Behavior of Orthogonal 3-D CMC

The inelastic stress/strain behavior found upon tension must be governed by the transverse crack, matrix crack, fiber debonding, interfacial sliding, and fiber fragmentation. In this paper, the stress/strain behavior of the orthogonal 3-D woven composite was estimated by using and modifying the established theories in literatures [1-8]. For estimating the in-plane elastic modulus of orthogonal 3-D woven composites, the parallel serial approach (PSA) proposed by Ishikawa et al. was applied [1]. A unit cell of the 3-D composite was simplified and divided into cross ply laminates. The elastic moduli of divided cross ply laminates were calculated by shear-lag model [3].

As the calculation of matrix crack density in longitudinal fiber bundle is significantly difficult, an empirical equation proposed by Evans and Zok was used for estimation of matrix crack density as a function of applied stress [4]. The stiffness changes due to the matrix crack in the longitudinal fiber bundles were calculated by an elastic analysis model of Hutchinson and Jensen [5], or a shear-lag model by Karandikar and Chou [6]. Fiber / matrix interface properties were estimated from hysteresis analysis of loading-unloading data by using Vagaggini, Domergue, and Evans theory [7].

The stress/strain behavior of the orthogonal 3-D CMC was estimated by accounting stiffness change of each laminate. After matrix crack saturation, inelastic stress/strain curve was estimated by Curtin's theory [8] with in-situ fiber strength data reported by Davies et al [9].

### Initial Young's Modulus

The fiber bundle dimensions in the 3-D composite were determined by optical microscopic observations. The initial Young's modulus estimated by the PSA solution is 121 GPa, which is smaller by 9% than the experimental result (141 GPa). The difference between the estimation and the experiment may be attributed to the approximation of *pocket* where is no fiber bundle region in 3-D woven fabric.

### Transverse Crack Density

As described above, transverse crack density was evaluated by a shear-lag model. Since the stiffness changes due to transverse crack density are considerable in low crack density region, the transverse crack propagation parameters were estimated

from the data at the onset of the cracking. By fitting the estimated curve and the experimental data, a critical energy release rate and an effective shear stiffness were determined as  $\mathcal{G}_{ic} = 8.0 \text{ J/m}^2$ , and  $K = 698 \text{ GPa/mm}$ , respectively.

The estimated curve is compared with the experimental data in Fig.4. A deviation of estimated curve from the experimental data becomes gradually considerable with increase of the transverse crack density. Fig.5 shows the effect of transverse crack density on the Young's modulus of the composite, which was calculated by the shear-lag model. The initial stage of transverse crack propagation reduces the Young's modulus rapidly. However, the influence of transverse crack density on stiffness change gradually decreases. And then, the stiffness change is hardly observed above  $10 \text{ mm}^{-1}$ .

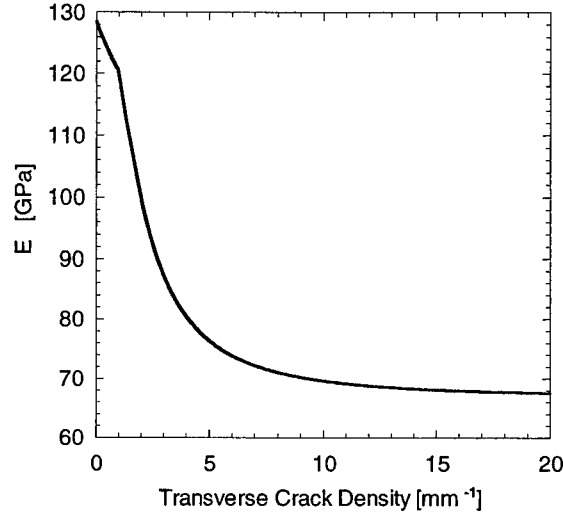


Figure 5 Relationship between Young's Modulus of the Orthogonal 3-D CMC and the Transverse Crack Densities in  $90^\circ$  Plies

Thus, the estimated  $\mathcal{G}_{ic}$  and  $K$  from the experimental data at the onset of the cracking may result in good approximation for calculating the stiffness change due to the transverse cracking.

#### Simulation of Stress/Strain Curve

A simple empirical formula was used to approximate the matrix crack density in the longitudinal fiber bundles. The approximated line is shown in Fig.4 with  $\bar{\sigma}_{mc} = 180 \text{ MPa}$ ,  $\bar{\sigma}_s = 300 \text{ MPa}$ , and  $\bar{l}_s = 45.4 \text{ mm}$ . The strains caused by transverse cracking were predicted using shear-lag model. The stiffness reduction due to matrix cracking of the longitudinal plies was calculated by using Hutchinson and Jensen theory or Karandikar and Chou theory. The total strain of the 3-D composites was calculated by the PSA solution with accounting the stiffness change due to multiple micro-cracking.

The simulated stress/strain curves are shown in Fig.6. Comparison of the predicted and measured strains indicates good correspondence, which indicates the estimation of stress partitioning is fairly well through the whole region of stress/strain diagram. The predicted curve by Hutchinson and Jensen theory is almost same as that by Karandikar and Chou theory.

The average applied stress,  $\bar{\sigma}_{lu}$  in the longitudinal fiber bundles under a composite stress,  $\bar{\sigma}$  is approximated by using a stress partitioning factor  $\lambda$ .

$$\bar{\sigma}_{lu} = \lambda \bar{\sigma}$$

The stress partitioning factor  $\lambda$  is plotted in Fig.7 as a function of applied. It can be understood that the effect of the transverse crack is significantly important for stiffness reduction of the orthogonal 3-D composite. Though the composite shows large failure strain ( $> 1.2\%$ ), it is understood that the contribution of the transverse cracking in  $90^\circ$  fiber bundles is significantly.

After the matrix crack saturation, the numerical results agree with the stress/strain curve as well as the ultimate tensile strength of the composite by Curtin's theory and *in-situ* fiber strength data.

The simulated stress/strain curves show rapid stiffness decrease at 70 MPa in comparison with the experimental results, which is caused by rapid increase of transverse crack density in the calculation. Xia et al reported the similar numerical result [10]. The constant critical energy release rate ( $\mathcal{G}_{IC} = 8.0 \text{ J/m}^2$ ) was assumed for the simulation. The deviation from the experimental results may be caused by

the approximation. In fact, the origins of transverse cracking may be pores, matrix rich regions, and weak interface between fiber and matrix. Therefore, the critical energy release rate of the transverse cracking has considerable scattering. Furthermore, the effect of stress concentration due to non-uniform microstructure can not be ignored for transverse cracking stresses distribution. The similar discussion has been conducted for matrix crack criterion in detail [4].

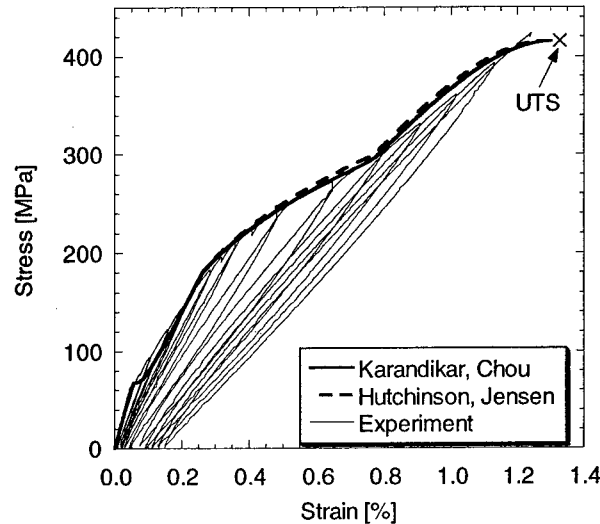


Figure 6 Comparisons between Simulated and Experimental Stress/Strain Behavior of the Orthogonal 3-D Composites

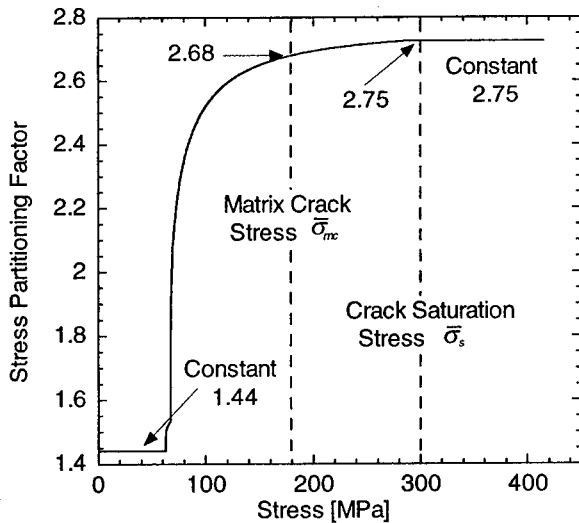


Figure 7 Stress Partitioning Factor  $\lambda$  of the Orthogonal 3-D Composites with Applied Stress  $\bar{\sigma}$

## Conclusion

Multiple micro-cracking and tensile behavior of the orthogonal 3-D woven Si-Ti-C-O fiber / Si-Ti-C-O matrix composite (Nusk-CMC) fabricated by a PIP processing have been investigated in the study. The methodology for estimating unidirectional tensile behavior of the orthogonal 3-D ceramic matrix composite has been provided by using and modifying the established theories in literatures. Comparison of the predicted and measured strains indicates good correspondence by the procedure.

## References

- [1] T. Ishikawa, K. Bansaku, N. Watanabe, Y. Nomura, M. Shibuya, T. Hirokawa, 1998. "Experimental Stress/Strain Behavior of SiC-Matrix Composites of Matrix Elastic Modulus", *Comp. Sci. Technol.*, 58: 51-63.
- [2] J.-M. Domergue, E. Vagaggini, A. G. Evans, 1995. "Relationships between Hysteresis Measurements and the Constituent Properties of Ceramic Matrix Composites: II", *J. Am. Ceram. Soc.*, 78: 2721-31.
- [3] C. H. Park, H. L. McManus, 1996. "Thermally Induced Damage in Composite Laminates: Predictive Methodology and Experimental Investigation", *Comp. Sci. Technol.*, 56: 1209-1219.
- [4] G. Evans, F. W. Zok, 1994. "The physics and mechanics of fibre-reinforced brittle matrix composites", *J. Mater. Sci.*, 29: 3857-3896.
- [5] J. W. Hutchinson, H. M. Jensen, 1990. "Models of Fiber Debonding and Pullout in Brittle Composites with Friction", *Mechanics of Materials*, 9: 139-163.
- [6] P. Karandikar, T.-W. Chou, 1993. "Characterization and Modeling of Microcracking and Elastic Modulo Changes in Nicalon/CAS Composites", *Comp. Sci. Technol.*, 46: 253-263.
- [7] E. Vagaggini, J.-M. Domergue, A. G. Evans, 1995. "Relationships between Hysteresis Measurements and the Constituent Properties of Ceramic Matrix Composites: I, Theory", *J. Am. Ceram. Soc.*, 78: 2709-2720.
- [8] W. A. Curtin, 1991. "Theory of Mechanical Properties of Ceramic-Matrix Composites", *J. Am. Ceram. Soc.*, 74: 2837-2845
- [9] I. J. Davies, T. Ishikawa, M. Shibuya, T. Hirokawa, J. Gotoh, 1999. "Fibre and interfacial properties measured in situ for a 3D woven SiC/SiC-based composite with glass sealant", *Composites:PartA* 30: 587-591.
- [10] Z. C. Xia, R. R. Carr, and J. W. Hutchinson, 1993. "Transverse Cracking in Fiber-Reinforced Brittle Matrix, Cross-Ply Laminates", *Acta metall. Mater*, 41: 2365-2376.



## **Scanning Electron Microscopy Study of Failure in Glass-Sealed SiC/SiC-based Composite (NUSK-CMC) Creep Tested at 1100 and 1200 °C in Air**

I. J. Davies, T. Ogasawara, T. Ishikawa, and N. Suzuki

### **Abstract**

A scanning electron microscopy (SEM) investigation was carried out for glass-sealed 3-D woven SiC/SiC-based composite that had failed following creep testing at 1100 and 1200 °C in air. It was shown that most specimens failed due to oxygen ingress into the composite that initiated at the specimen corner. The main path for oxygen movement with specimens was found to be along z fibre bundles. A simple analysis of the glass evaporation rate showed higher evaporation rates to always exist at the specimen corners and this could help to explain initiation of long-term creep failure at the specimen corners.

### **Introduction**

Although ceramic matrix composites (CMCs) exhibit potential for many applications as high temperature structural materials in the aerospace and space fields, a continuing problem is that of oxidation of the fibre/matrix interface [1], which tends to suppress crack deflection at the fibre/matrix interface and changes the mode of failure from pseudo-ductile to brittle. One method to overcome this problem has been to coat [2] or impregnate [3] the CMC with an oxidation barrier material in order to reduce oxygen diffusion into the material and hence provide longer operational lifetimes at elevated temperatures (*e.g.*, >1000 °C) in an oxidising atmosphere.

One such CMC with an oxidation protection system has been developed in collaboration between the National Aerospace Laboratory (Japan), Ube Industries Ltd., Shikibo Ltd., and Kawasaki Heavy Industries Ltd., and has been named "NUSK-CMC". The composite, based on the SiC/SiC system, has been the subject of previous investigation by the authors [4-9]. Recent work has concentrated on the creep behaviour when tested at 1100 to 1300 °C in air [8,9]. For example, the effect of creep stress on time to failure for glass-sealed specimens tested at 1100 and 1200 °C in air [8,9] has been presented in Figure 1. The main features of the data are the "knee-points" at  $1 \times 10^6$  sec (1100 °C) and  $3-4 \times 10^5$  sec (1200 °C) and coincident

---

I. J. Davies, Advanced Fibro-Science, Kyoto Institute of Technology, Matsugasaki, Sakyo-ku, Kyoto 606-8585, Japan

T. Ogasawara, T. Ishikawa, and N. Suzuki, Airframe Division, National Aerospace Laboratory, Mitaka City, Tokyo 181-0015, Japan

with significant crystallisation of the glass sealant [9]. Increased crystallisation was believed to result in failure due to increased viscosity and/or volume contraction of the glass sealant [9], thus leading to accelerated specimen failure. Other factors such as specimen geometry are also believed to play a role in accelerated creep failure for this composite.

The present investigation is divided into two sections, the first of which summarises results from a SEM investigation of fracture surfaces following creep testing at 1100 and 1200

°C in air. The latter section provides an analysis to account for the effect of specimen geometry on accelerated specimen due to differential glass evaporation.

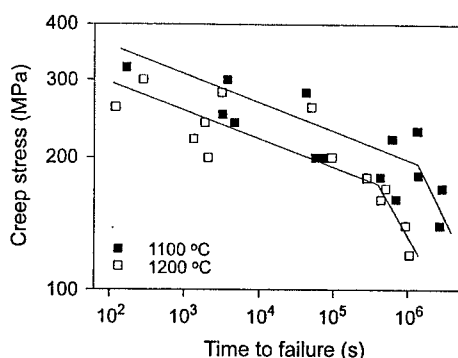


Figure 1: Time to failure as a function of creep stress for specimens tested at 1100 and 1200 °C in air (adapted from [9]).

## Experimental Procedure

The composite system under investigation has been described in detail elsewhere together with details of the creep testing apparatus [8,9]. Essentially, the composite comprised of surface-modified Tyranno<sup>®</sup> Si-Ti-C-O fibres woven into an orthogonal 3-D architecture with fibre volume fractions of approximately 0.19, 0.19, and 0.02 in the x, y, and z directions, respectively. Matrix consolidation was achieved from the repeated impregnation and pyrolysis of a polymer similar to polytitanocarbosilane. Following machining to the required test dimensions, specimens were repeatedly impregnated with a proprietary SiO<sub>2</sub>-Na<sub>2</sub>O-based glass system in order to fill residual open porosity and seal the specimen surface. Following creep testing at 1100 and 1200 °C in air, specimen fracture surfaces from a total of 17 specimens were examined using a SEM (JSM-6300F, JEOL, Japan).

## Results and Discussion

### Summary of the SEM Investigation

Due to constraints of space, in this section, conclusions made from analysis of 17 specimens have been illustrated through a limited number of specimens. A fracture surface exhibiting characteristics typical of most specimens has been presented in Figure 2(a) whilst accompanying fibre bundle positions, approximate oxygen path within the specimen (*black arrows*), and boundary between oxidised and unoxidised regions (*broken line*) have been included in Figure 2(b). Oxygen ingress into the specimen appeared to initiate at both ends of the z fibre bundle at the specimen corner (Figure 3(a)) and then moved relatively quickly along the z fibre bundle before proceeding along the x and y fibre bundles. Indeed, it was noted

generally that the z fibre bundles were the preferred oxygen route within specimens, perhaps as a result of the continuous carbon layer present at the fibre/matrix interface. The symmetrical convex shape of the oxidised region suggests that oxygen ingress occurred at similar times at both ends of the z fibre bundle. Combined with the fact that the present specimen failed after only 120 sec. of creep loading, it was concluded that both ends of the z fibre bundle at the specimen corners had not been sufficiently coated/sealed with the glass protective layer.

Despite the specimen in Figure 2 failing after a relatively short creep loading time, it was in fact the case that nearly all specimens (15 out of 17) showed initial oxygen ingress at their

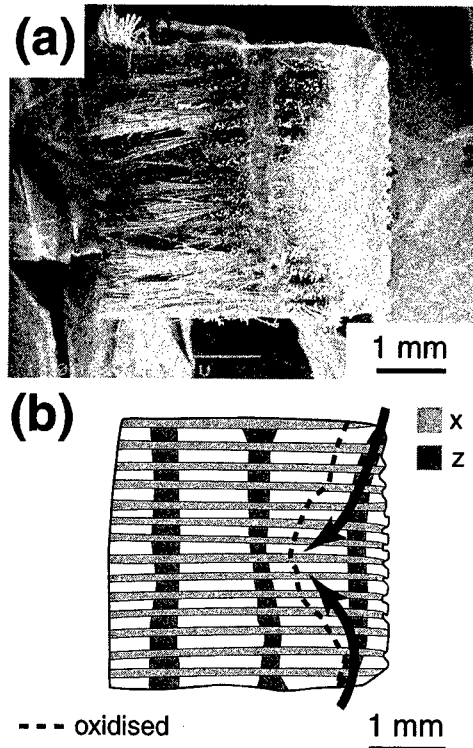


Figure 2: General view of a specimen that failed after 120 sec under a stress of 260 MPa at 1200 °C in air.

corners and this was attributed to several factors: (i) reduced initial glass layer thickness at the corners, (ii) selective evaporation of Na atoms and resulting crystallisation of the glass layer having a greater effect at the corners, and (iii) increased glass evaporation at the corners due to geometrical effects. The first factor was generally applicable to specimens with creep lifetimes on the order of several minutes, including that shown in Figure 2. The second factor was found to apply particularly to specimens with extended creep lifetimes and has been covered in details elsewhere [9]. The contribution from the third factor has been analysed in the second section of this report.

Figure 3(b) illustrates a single y direction fibre bundle in which the left side is seen to exhibit significant fibre

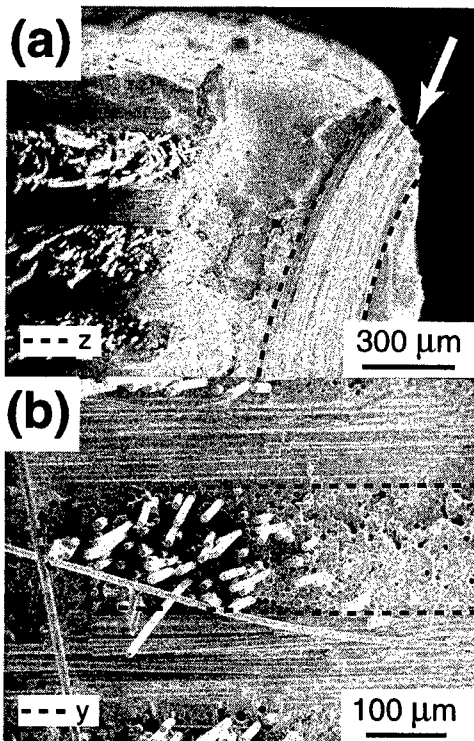


Figure 3: Detailed view of a specimen that failed after 120 sec under a stress of 260 MPa at 1200 °C in air.

pullout (typically 100  $\mu\text{m}$ ) whilst the right side shows negligible pullout. From considering the effect of fibre/matrix interface shear strength,  $\tau$ , on fibre pullout length [4-6], it can be reasonably be assumed that the left side of the fibre bundle comprises of a low  $\tau$  region whilst the right side comprises of high  $\tau$  region. The reason for this difference is that the fibre bundle in question was positioned at the boundary of the oxidised and unoxidised regions. Therefore, the oxidised region (right side) showed negligible fibre pullout as  $\tau$  had increased (due to oxidation of the interface) to such an extent that microcrack deflection at the fibre/matrix interface no longer came into play [10] whereas  $\tau$  for the relatively unoxidised region (left side) was still low enough to allow microcrack deflection

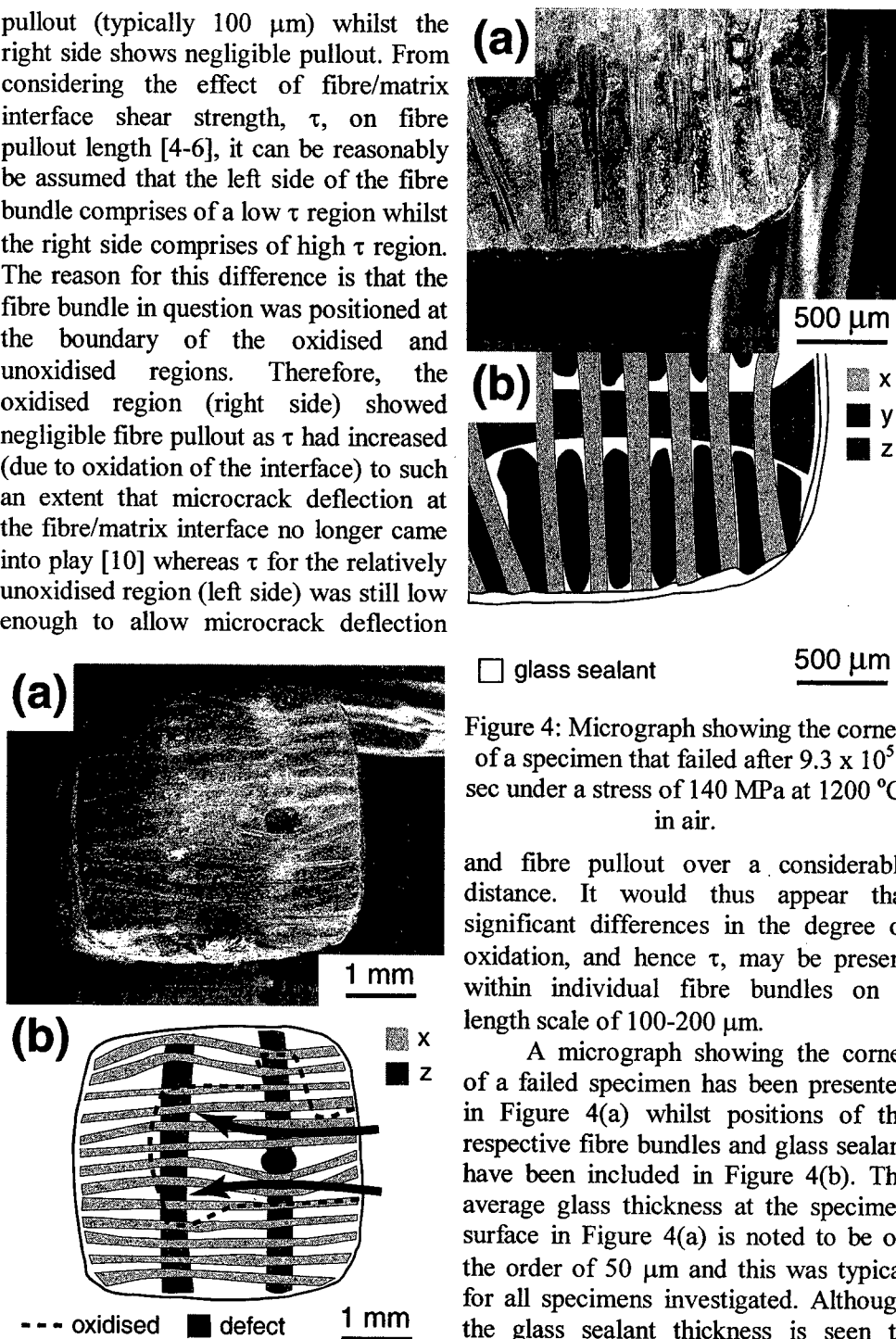


Figure 4: Micrograph showing the corner of a specimen that failed after  $9.3 \times 10^5$  sec under a stress of 140 MPa at 1200  $^{\circ}\text{C}$  in air.

and fibre pullout over a considerable distance. It would thus appear that significant differences in the degree of oxidation, and hence  $\tau$ , may be present within individual fibre bundles on a length scale of 100-200  $\mu\text{m}$ .

A micrograph showing the corner of a failed specimen has been presented in Figure 4(a) whilst positions of the respective fibre bundles and glass sealant have been included in Figure 4(b). The average glass thickness at the specimen surface in Figure 4(a) is noted to be on the order of 50  $\mu\text{m}$  and this was typical for all specimens investigated. Although the glass sealant thickness is seen to decrease to almost zero at the specimen corner, initial oxygen ingress into this specimen was not thought to have

Figure 5: General view of a specimen that failed after  $9.3 \times 10^5$  sec under a stress of 140 MPa at 1200  $^{\circ}\text{C}$  in air.

occurred at this position. Instead, when viewed at a lower magnification (Figure 5), it would seem that oxygen ingression occurred at the middle left side (Figure 5(b)), despite the glass thickness being approximately 50  $\mu\text{m}$  at this position. Instead, consideration of the forces upon loading suggested a stress concentration to be present at the point of oxygen ingression due to the presence of a foreign object/defect observed within the specimen.

Overall, it was concluded that almost every specimen failed due to oxygen ingression at the specimen corner. Failure at short stress lifetimes (order of a few minutes) was attributed to incomplete coating/sealing of z bundles at the specimen surface whereas failure at the longest stress lifetimes was believed to a large part dependent on selective loss of Na and crystallisation of the glass sealant [9]. It will be shown in the next section that evaporation loss for the glass sealant is enhanced at the specimen corners due to a geometrical effect.

#### Analysis of glass evaporation at a curved surface

The aim of this section is to show that a significant contributory factor to oxygen ingression occurring at specimen corner edges may be to that of differences in the glass evaporation rate between the specimen corner edges and sides.

If we consider a sphere of radius,  $R$ , surrounded by a glass layer of thickness,  $t$ , then, from the standpoint of geometrical effects, the initial evaporation rate,  $E$ , from a point in the glass layer at a distance,  $r$ , from the sphere centre may be reasonably assumed to be a function only of  $x$  for any given direction,  $\phi$  and  $\theta$ , as shown in Figure 6. From simple geometry,  $x$  may be given in terms of  $r$ ,  $R$ ,  $t$ , and  $\phi$  by:

$$x = r \cos \phi + \sqrt{(R+t)^2 - r^2 \sin^2 \phi} \quad (1)$$

The initial evaporation rate,  $E(x)$ , at any given point, for fixed  $\phi$  and  $\theta$ , will be a decreasing function of  $x$  and would be expected to decrease disproportionately with increasing  $x$ . The evaporation rate would also be expected to increase with temperature,  $T$ , and decrease with activation energy,  $Q$ . A suitable function for  $E(x)$  is that of:

$$E(x) = Ae^{-\left(\frac{Q \cdot x}{k \cdot T}\right)} \quad (2)$$

where  $A$  is constant and  $k$  is the Boltzmann constant. The total evaporation rate from a given point requires integration over the valid range of  $\phi$  and  $\theta$ , i.e.,

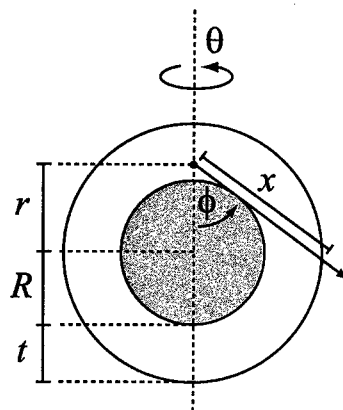


Figure 6: Schematic diagram showing the geometry assumed when calculating evaporation rate for a glass-coated sphere

$$E(r, \phi, \theta) = A \int_0^{2\pi} \int_{\phi_{\min}}^{\pi} e^{-\left[ \frac{Q(r \cos \phi + \sqrt{(R+t)^2 - r^2 \sin^2 \phi})}{kT} \right]} \partial \phi \partial \theta \quad \text{with } \phi_{\min} = \sin^{-1} \left( \frac{R}{r} \right) \quad (3)$$

The next step is to integrate  $E(r, \phi, \theta)$  over the entire glass layer and is achieved through transformation of the integration to the spherical coordinates,  $r$ ,  $\omega$ , and  $\psi$ , *i.e.*,

$$E' = \int_0^{2\pi} \int_0^{\pi} \int_R^{R+t} r^2 \sin \omega \left[ A \int_0^{2\pi} \int_{\phi_{\min}}^{\pi} e^{-\left[ \frac{Q(r \cos \phi + \sqrt{(R+t)^2 - r^2 \sin^2 \phi})}{kT} \right]} \partial \phi \partial \theta \right] \partial r \partial \omega \partial \psi \quad (4)$$

Simplifying this expression and normalising the evaporation rate with respect to the sphere surface area results in the following normalised initial evaporation rate:

$$E = \frac{2\pi A}{R^2} \int_R^{R+t} r^2 \int_{\phi_{\min}}^{\pi} e^{-\left[ \frac{Q(r \cos \phi + \sqrt{(R+t)^2 - r^2 \sin^2 \phi})}{kT} \right]} \partial \phi \partial r \quad (5)$$

This expression may not be further reduced analytically and thus must be solved numerically. In order to simplify calculations, all terms were set to unity apart from those specifically being varied in the following discussion. In addition,  $E$  was further normalised with respect to the case of a flat plate (*i.e.*,  $R \rightarrow \infty$ ).

The effect of sphere radius on  $E$  has been presented in Figure 7, where it is clear that  $E$  increases with decreasing  $R$ , particularly for  $R/t < 10$ , *i.e.*, the evaporation rate is larger in small  $R$  regions such as corners and points. This result appears to confirm the assumption in previous work [9] regarding the possibility of oxygen ingress at the specimen corners being due to an increased evaporation rate at this position. Therefore, it may well be the case that creep lifetime may be enhanced for specimens containing corner edges with larger values of  $R$ . This result would also indicate the necessity for continuous smooth surfaces in glass sealed CMCs. For the present case, the value of  $E$  for  $R \rightarrow 0$ ,  $E(0)$ , was 2.9 times that of the flat plate value,  $E(\infty)$ , although it should be noted that the exact value of this ratio will depend on factors such as  $Q$  and  $T$ .

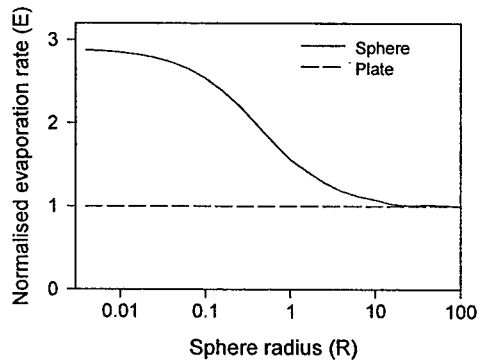


Figure 7: Effect of sphere radius on evaporation rate for a glass-coated sphere.

The effect of changing  $T$  and  $Q$  on  $E$  as a function of  $R$  has been presented in Figures 8(a) and 8(b), respectively. As expected, the effect of increasing either  $T$  and decreasing  $Q$  was to increase  $E$ . The ratio of  $E(0)$  to  $E(\infty)$  was constant to within 5% as  $T$  and  $Q$  changed by a factor of six and thus it would appear that  $T$  and  $Q$  have negligible effect on the ratio of evaporation rates between flat and curved surfaces. On the other hand, however, the actual numerical difference between  $E(0)$  and  $E(\infty)$  increased significantly for increasing  $T$  and/or decreasing  $Q$  so that oxygen ingress at specimen corners would be more likely to occur under these situations.

From considering the geometry of Figure 6 it might be useful to determine which parts of the glass layer make the largest contribution to  $E$ . Shown in Figure 9 is the effect of changing  $R$  on the relative contribution to  $E$  from different parts of the glass layer. The first trend is that, as expected from the earlier data, contributions from each region were always higher for smaller values of  $R$ , i.e.,  $E \uparrow$  as  $R \downarrow$ . The curves for  $R=10$  and  $R=100$  were almost coincident, suggesting that, for the present calculations, an appropriate definition for what constitutes a "corner" might be  $R/t < 10$ . The second

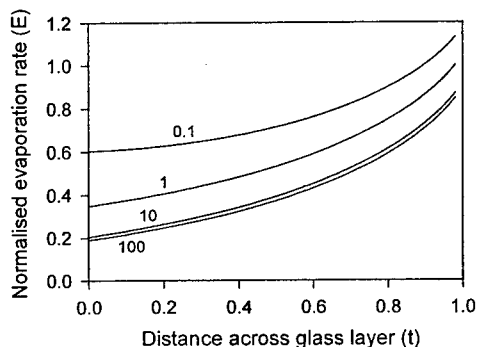


Figure 9: Effect of sphere radius on the positional dependence across the glass layer thickness to the evaporation rate.

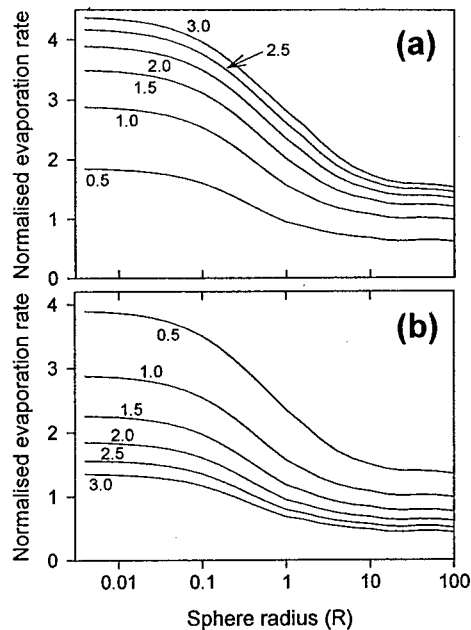


Figure 8: Effect of varying different parameters on evaporation rate for a glass-coated sphere: (a)  $T$ , and (b)  $Q$ .

trend noted is that, for each curve, values were minimum at  $t=0$  (interface between the glass and sphere) and increased to a maximum at  $t=1$  (outside surface of the glass layer). The ratio for contributions at  $t=1$  and  $t=0$  increased with increasing  $R$ , meaning that, for a flat plate, a larger proportion of the evaporation comes from close to the outer glass surface whereas for  $R \rightarrow 0$  there is a larger contribution from the body of the glass layer.

Overall, it is concluded that the surface of glass-sealed materials should be as flat and smooth as possible in order to minimise differential evaporation.

## Conclusions

In this study, results were summarised from a SEM investigation of fracture surfaces from 17 specimens of glass-sealed 3-D woven SiC/SiC-based composite that had failed following creep testing at 1100 and 1200 °C in air. In addition, the problem of glass evaporation from a curved surface was analysed in order to more fully understand the failure mechanism in these specimens. The SEM study concluded that nearly all specimens failed due to initial oxygen ingress at the specimen corner edges and this was attributed to a number of factors. In addition, the main pathway for oxygen movement within specimens was found to be along z fibre bundles. Results of the analysis showed indicated evaporation from the glass surface layer to always be higher at curved surfaces such as corner edges when compared to flat regions.

## References

1. R. Naslain, 1995. "Challenging ceramic matrix composites for applications in severe environments", *Adv. Composite Mater.*, 5(1):35-44.
2. H. Hatta, T. Aoki, Y. Kogo, and T. Yarii, 1999. "High-temperature oxidation behavior of SiC-coated carbon fiber-reinforced carbon matrix composites", *Composites: Part A*, 30:515-520.
3. J. B. Davis, D. B. Marshall, K. S. Oka, R. M. Housley, P. E. D. Morgan, 1999. "Ceramic composites for thermal protection systems", *Composites: Part A*, 30:483-488.
4. I. J. Davies, T. Ishikawa, M. Shibuya, and T. Hirokawa, 1999. "Fibre strength parameters measured in situ for ceramic matrix composites tested at elevated temperature in vacuum and air", *Comp. Sci. Technol.*, 59(6):801-811.
5. I. J. Davies, T. Ishikawa, M. Shibuya, and T. Hirokawa, 1999. "Optical microscopy of 3-D woven SiC/SiC-based composites", *Comp. Sci. and Technol.*, 59(3):429-437.
6. I. J. Davies, T. Ishikawa, M. Shibuya, T. Hirokawa, and J. Gotoh, 1999. "Fibre and interfacial properties measured in situ for a 3-D woven SiC/SiC-based composite with glass sealant", *Composites Part A*, 30(4):587-591.
7. T. Ogasawara, T. Ishikawa, T. Matsuzaki, M. Suzuki, M. Shibuya, J. Gotoh, and T. Hirokawa, 2000. "Durability of 3-D woven Si-Ti-C-O fiber/Si-Ti-C-O matrix composite evaluated by arc jet test", *J. Ceram. Soc. Jap.*, 108(1):80-88.
8. T. Ishikawa, N. Suzuki, I. J. Davies, M. Shibuya, T. Hirokawa, and J. Gotoh, 1999. "Creep behavior and modeling of SiC-based PC ceramic matrix composites with glass sealing in high temperature air", *Key Eng. Mater.*, 164/165:197-200.
9. T. Ogasawara, T. Ishikawa, N. Suzuki, I. J. Davies, M. Suzuki, J. Gotoh, and T. Hirokawa, 2000. "Tensile creep behavior of 3-D woven Si-Ti-C-O fiber / SiC-based matrix composite with glass sealant", *J. Mater. Sci.*, 35:785-793.
10. M. -Y. He and J. W. Hutchinson, 1989. "Crack deflection at an interface between dissimilar elastic materials", *Int. J. Solids Structures*, 25(9):1053-1067.



## **Strength Improvement by Densification of C/C Composites**

H. Hatta, Y. Kogo, H. Hamada, T. Shigei, Y. Sawada, S. Somiya

### **Abstract**

The tensile strength of Carbon/Carbon composites (C/Cs) was examined as a function of the density in the range above  $\rho=1.6 \text{ g/cm}^3$ . Three processing routes of preformed yarn, resin char, and HIP processes were adopted to densify the C/C composites. The density was increased to  $1.95 \text{ g/cm}^3$  through these routes. The interfacial strength between the fiber and matrix was significantly and unexpectedly varied by repeating the HIP process, though the detailed source mechanisms could not be identified. After the tensile strength was re-examined, the ultimate tensile strain was found to be expressed by a monotonic decreasing function of the interfacial strength. This implies that weakening fiber interfaces is a key factor for obtaining C/C composites with the higher tensile strength.

### **Introduction**

Carbon fiber reinforced carbon matrix composites (C/Cs) usually possess a much lower strength than that expected from the rule of mixture. Hence, it is extremely important for the improvement of the C/C strength to understand the mechanisms yielding such strength degradations. So far, several source mechanisms for strength degradation have been studied. They include the effect of the heat treatment temperature [1,2], the fiber/matrix interfacial strength [3,4], and the defects in the C/Cs [5,6].

Continuous fiber reinforced ceramic matrix composites (CFCCs) also possess a much lower elongation than that of the reinforcing fibers [7]. Many mechanical models have been proposed [7] to explain the strength of the CFCCs. An established conclusion in these studies is that the interfacial strength between reinforcing fibers and the matrix has predominant influence on the ultimate tensile fracture strain. C/C composites usually show similar mechanical behavior to that of CFCCs, but the mechanics of the CFCCs has not been well applied to understand the fracture behavior of C/Cs.

In the present study, special attention was placed on the effect of the bulk density the C/Cs on the tensile strength in accordance with the traditional

---

H. Hatta, ISAS; 3-1-1 Yoshinodai, Sagamihara, 229-8510 Japan

Y.Kogo, Science University of Tokyo; 2641 Yamazaki, Noda, Chiba 278-8510 Japan

H.Hamada, Kyoto Institute of Technology; Matsugasaki Sakyo-ku, Kyoto 606 Japan

T.Shigei, Research Lab. Toho Rayon, 234-Kamitokari, Chousen-Chou, Shuntou, Shizuoka 411-8720

Y.Sawada, ONRI, AIST-MITI, 1-8-31 Midorigaoka, Ikeda, Osaka, 563-8577 Japan

S.Somiya, Keio University; 3-14-1 Hiyoshi, Kohoku-Ku, Yokohama-Shi, Kanagawa, 223-8522 Japan

discussions in the C/C community [5,6]. One of the features in this study was to compare the strengths of the C/Cs densified by various processing routes. In addition, the effect of the interfacial strength on the tensile strength of the C/Cs was attempted to be evaluated. Based on this evaluation, a discussion on the possibility of applying the strength theory of the CFCCs to the fracture behavior of the C/Cs was made.

## Experimental Procedure

### Materials

The C/C composites tested in this study were of a cross-ply laminate type fabricated by three processing routes, i.e., the preformed yarn, resin char, and the hot isotropic press (HIP) processes. The Across Co. supplied the C/Cs fabricated by the preformed yarn method (PYs). The density  $\rho$  of the PYs was about  $1.8 \text{ g/cm}^3$ . The PYs were then densified up to  $\rho = 1.96 \text{ g/cm}^3$  by the repeating resin char cycles; pitch infiltration at  $60^\circ\text{C}$  in 10 MPa Argon, carbonization at  $600^\circ\text{C}$  in 10 MPa air, and graphitization at  $2000^\circ\text{C}$  in a vacuum. Hereafter, the densified PYs will be denoted by DPYs.

The C/Cs made by the resin char processing route were derived from a phenolic resin matrix carbon fiber reinforced composite (CFRP). The fiber volume fraction in the CFRP was 60%. After carbonization of the CFRP at  $600^\circ\text{C}$ , the resultant porous C/C plates were densified by up to 6 cycles of pitch infiltration and carbonization. They were then heat-treated at  $2000^\circ\text{C}$  for graphitization. The C/Cs densified by this resin char method were denoted as RC-I and RC-U according to their reinforcing fibers IM-600 and UM-46, respectively.

The C/Cs densified by the HIP treatment were reinforced with IM-600 fibers, and at first, prepared through the same processing route as the resin-charred C/Cs up to the first carbonization process. The HIP treatment was then repeated up to 5 cycles using a pitch precursor. The maximum temperature and the pressure of the HIP treatment were  $2300^\circ\text{C}$  and 200 MPa, respectively. The HIP-treated samples were denoted by HIP-1 to -5, in which the number stands for the repeated cycle(s) in the HIP densification. After 5 cycles, defects in the HIPed C/Cs observed by a SEM were almost completely filled by carbon material.

### Experimental Procedure

The tensile and in-plane shear strengths at each densification step were measured along with their stress-strain curves using the specimens shown in Fig. 1. The in-plane shear strengths were obtained by the Iosipescu method. All the tests were performed using an Instron type testing machine under a cross head speed of  $0.1 \text{ mm/min}$ .

## Experimental Results

### Tensile Behavior

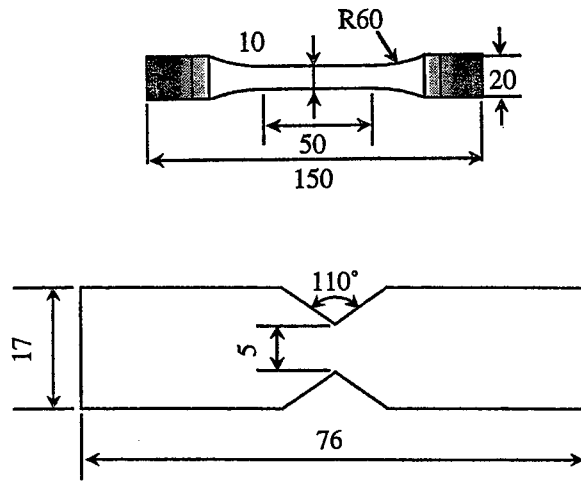


Fig.1 Specimen configurations for tensile (a) and in-plane shear (b) tests.

#### (1) Strength

Figure 2 summarizes the results of all the tensile strength measurements as a function of bulk density  $\rho$ . As shown in this figure, the tensile strength of the C/Cs densified by the resin char method, RC-I and RC-U, exhibited the typical behavior [5,6], i.e., a monotonic increasing function of  $\rho$ . On the other hand, the tensile strength of the HIP-treated specimens (HIPs) decreased with increasing  $\rho$  and that of the DPYs was only slightly improved..

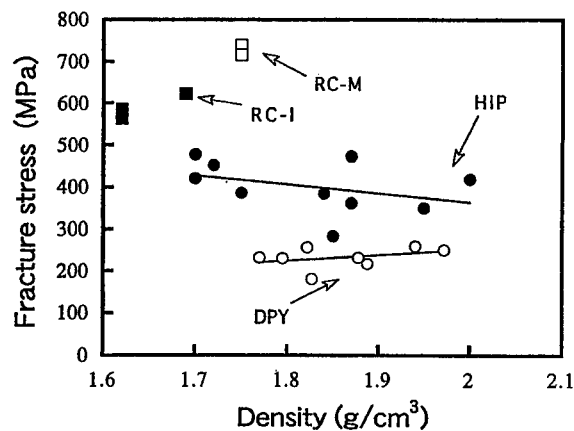


Fig.2 Tensile fracture stresses of all the specimens as a function of bulk density.

## (2) Stress-strain relation

a) DPYs To understand the underlying mechanisms yielding the tensile strength improvement of the DPYs by the densification, Young's moduli, the ultimate fracture strains, and the strengths were measured as shown in Fig. 3. All the stress-strain relations of the DPYs were linear up to the ultimate fracture and the fracture strains were almost constant. However, Young's modulus of the DPYs shown in Fig. 4 was slightly improved by the densification. The solid straight line in Fig. 4 denotes the estimated Young's modulus using the rule of mixture. Young's moduli of defects-included matrices,  $E_m$ , were estimated by the Halpin-Tsai equation. In the calculation of  $E_c$ , it was assumed that all the flaws in the C/Cs were spherical voids and the density of a flawless matrix was 2.1 GPa.

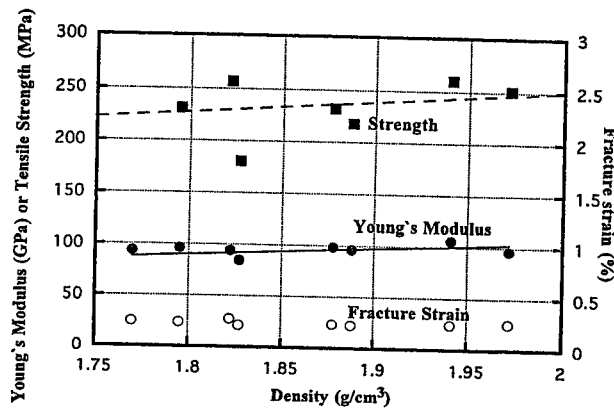


Fig.3 Experimentally determined Young's moduli, tensile strengths, and tensile strain as a function of bulk density. The former two are compared with the predicted values shown by the solid and dashed lines.

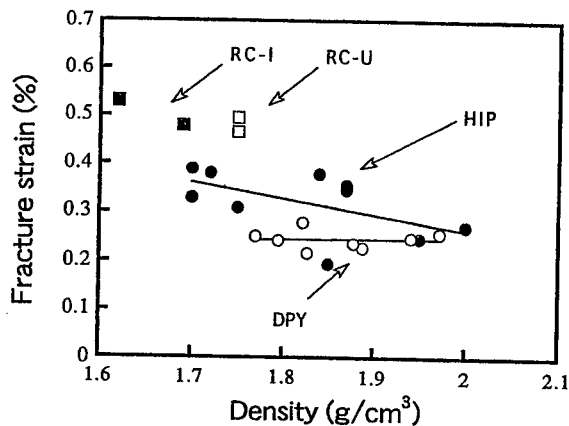


Fig.4 Tensile fracture strain of all the specimens as a function of bulk density.

The agreement of the predicted and observed Young's moduli shown in Fig. 3 indicates that the improvement in Young's modulus is attributed to the filling of the defects in the carbon matrix. This predicted Young's modulus was then multiplied by the averaged fracture strain to obtain the dashed line in Fig. 3. As shown in this figure, the experimentally observed strength agrees well with this calculated line. Hence the slight improvement in the strength of the DPYs by the densification was solely due to the improvement in Young's modulus.

b) HIPs While Young's modulus of the HIPed C/Cs (HIPs) was improved by the repeated densification cycles, the ultimate fracture strain degraded with increasing density as shown in Fig. 5. Thus the strength reduction in high density HIPs was solely due to the degradation of the fracture strain. Figure 5 shows typical stress-strain curves of the HIPs for three different density levels. Similar to all the DPYs tested, the HIP 5 cycles (HIP-5) exhibited a linear stress-strain curve up to an ultimate fracture strain of about 0.25%. On the other hand, the HIP-1 and -3 showed fracture strains higher than 0.25%. It is interesting that nonlinear stress-strain relations also appeared at a strain of about 0.25%.

In order to identify sources of the non-linearity in the stress-strain curves, two straight lines, the upper and lower bounds, were calculated. The upper thin chain and dotted line in Fig. 5 was obtained by using the simple rule of mixture under the assumption that the C/C includes no defects. On the other hand, the lower thin chain and dotted line was drawn by assuming that the entire matrix is fractured, namely, only the fibers parallel to the loading direction sustain an applied load. The deviations from the linear relation for the HIP-1 and -3 were nearly the same as or larger than the difference between the two bounds. These results demonstrate that fiber damage gave rise to the nonlinear behaviors.

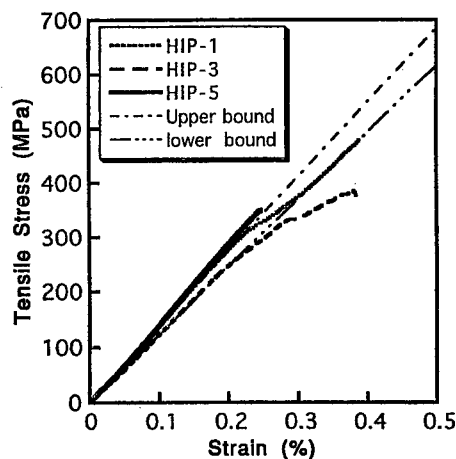


Fig.5 Effect of HIP cycles on the tensile stress-strain curves of the C/C composites.

#### Shear Behavior

One of the well known deficiencies in the mechanical properties of C/Cs is

extremely low shear resistance [8]. This is mainly attributed to weak interfaces between the fibers and matrix. Thus, in-plane shear fracture might be related to the interfacial strength. Typical stress-strain curves under in-plane shear loads are shown in Fig. 6. From these curves and the acoustic emission (AE) count rates, two shear stress levels were chosen as representative points for shear damage. The characteristic shear stress for the onset of AE is denoted by  $\tau_{AE}$ . Micro-interfacial damage might initiate at this shear stress. The other is the maximum shear stress,  $\tau_{max}$ , which is supposed to be the initiation stress of fiber damage. Figure 7 shows  $\tau_{AE}$  and  $\tau_{max}$  for the various C/Cs. As shown in this figure,  $\tau_{AE}$  and  $\tau_{max}$  consistently increase with density. Note that the C/Cs with a low tensile fracture strain (see Fig. 5) possess high values of  $\tau_{AE}$  and  $\tau_{max}$  whereas the C/Cs with a high tensile fracture

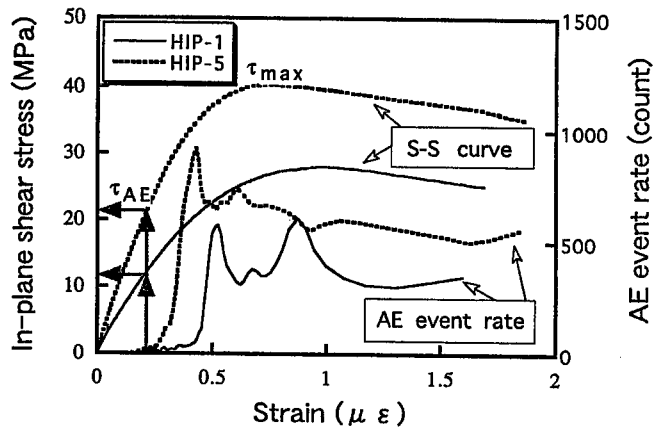


Fig.6 Typical stress-strain curves and AE event rates obtained in in-plane shear tests.

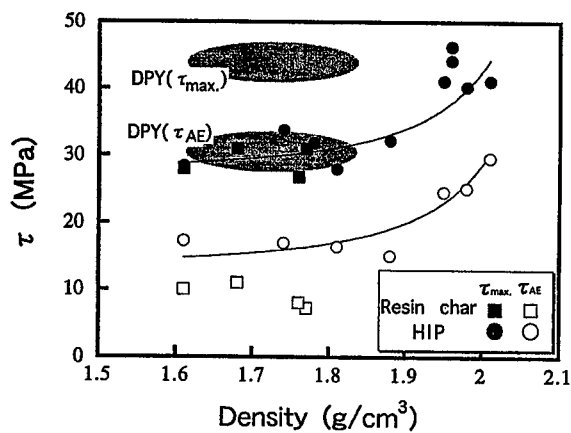


Fig.7 In-plane shear fracture stresses of HIPs and DPYs as a function of bulk density.

strain have low values. Thus the tensile fracture strains were plotted as a function of  $\tau_{AE}$  and the results are shown in Fig. 8. In this figure, all the tested C/Cs treated by the various densification processes lie on a single curve. However, when  $\tau_{max}$  is used instead of  $\tau_{AE}$ , a similar single curve cannot be obtained. Under the assumption that interfacial fracture starts at  $\tau_{AE}$ , this figure indicates that the tensile strength of the C/Cs is predominantly controlled by the interfacial strength between the fibers and matrix as in the case of the CFCCs.

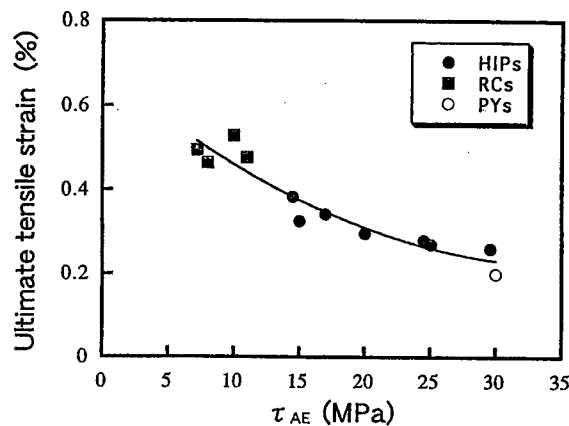


Fig.8 Relation between the initial shear fracture stresses and the ultimate tensile strains.

## Discussion

Fracture patterns of the HIPs are considered to follow the fracture transition model from the local to global load sharing regimes developed in the field of the CFCCs [7]. A typical stress-strain, S-S, curve of the CFCCs is like the dashed line shown in Fig. 9. The S-S curve becomes nonlinear when multiple-cracking of the matrix begins. If the interfacial strength between the fiber and matrix is sufficiently high, the ultimate fracture occurs near the onset point of the nonlinearity due to the local load shearing regime, LLS. On the other hand, in CFCCs with a weak interfacial strength, the matrix cracking is always accompanied by interfacial sliding. This leads to a high ultimate strain due to the global load shearing regime, GLS. During the matrix cracking and accompanying interfacial sliding, Young's modulus should be reduced due to the reduction of the matrix contribution. After the saturation of the matrix cracking, the second linear portion appears in the S-S curve of the CFCCs only when the fiber interfaces are sufficiently weak [9].

Among the C/Cs in the present study, the tensile fractures of HIP-5s, PYs, and DPYs are classified into the LLS. In these C/Cs, the S-S curves for these C/Cs were almost linear, and the ultimate tensile fracture strains were about 0.25%. Ultimate strains of 0.2 to 0.3% were widely reported for low strength C/Cs with linear S-S curves [10]. Thus intensive matrix cracking is expected to occur around this strain.

On the other hand, GLS fracture with a nonlinear S-S curve was observed in

the low density C/Cs of HIP-1, RC-I, and RC-U. The transition point from the LLS to the GLS may be located around HIP-3. From the GLS point of view, the nonlinearity in the S-S curves in C/Cs should be insignificant because the contribution of the matrix is much lower than that in the CFCCs; the elastic modulus of a matrix carbon is over one order lower than that of a carbon fiber. In addition, since the matrix cracking is usually almost saturated even in as-received laminated C/Cs [11], the matrix cracks appearing in the nonlinear region may be much less than CFCCs. Thus we can conclude that even for the HIP-1, fiber fracture is probably the main source of the nonlinearity. This suggests that the interfacial strength is too high for complete realization of GLS even for the low density C/Cs in this study. In other words, there might be still room for improvement of the ultimate elongation of C/Cs if the interfacial strength can be further reduced.

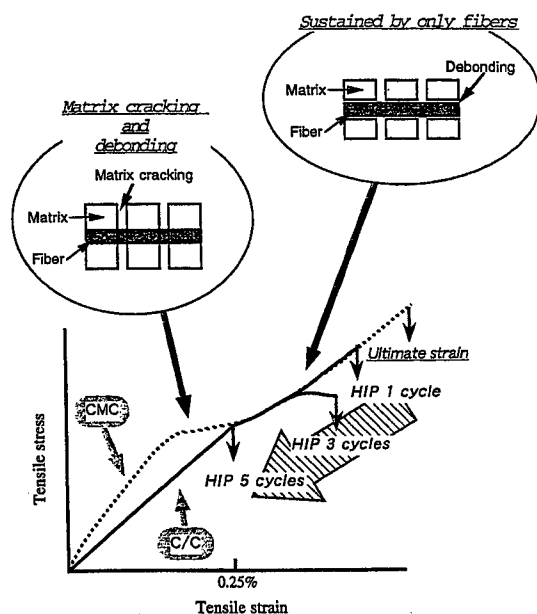


Fig.9 Comparison of typical stress-strain curves of C/Cs with that of CFCCs.

## References

- 1 Chang WC, Ma CCM, Tai NH, Chen CB. *J Mater Sci*1994; 29: 5859-5867.
- 2 Domnanovich A, Peterlik H, Wanner A, Kroimp K. *Comps Sci Tech* 1995; 53: 7-12.
- 3 Manocha LM, Yasuda E, Tanabe Y. *Carbon* 1988; 26 333-337.
- 4 Trouvat B, Bourrat X, Naslain R, 23rd Biennial Conf. on Carbon. (Strasbourg, France): American Carbon Society, 1997; 536-537.
- 5 Weissshaus H, Kenig S, Siegmman A. *Carbon*, 1991; 29: 1203-1220.
- 6 Weissshaus H, Kening S, Kastner E, Siegmman A. *Carbon* 1990; 28: 125-135.
- 8 McNulty JC, Zok FW. *J. Am. Ceram. Soc.* 1997; 80: 1535-1543.
- 11 Heredia FE et al., *J. Am. Ceram. Soc.*, 1994; 77: 2817-2827.
- 12 Evans AG, Zok FW *J Mater Sci* 1994; 29: 3857-3896.
- 13 Sugawara T. *Kogyo zairyou, (Engineering Materials in Japanese)* 1999; 47: 59-64.
- 14 Kogo Y, Hatta H, Kawada H, Machida T. *J. Comps. Mater.* 1998; 32: 1273-1294.



## **Suppression of Through-the-Thickness Cracking in SiC Coating Deposited on C/C Composites**

T. Aoki, H. Hatta, T. Hitomi, H. Fukuda, I. Shiota

### **Abstract**

Two new concepts are proposed to suppress cracking in the oxidation-resistant SiC coating for C/C composites. The first idea is a SiC/C multi-layered coating. The aim of this coating is to prevent through-the-thickness cracking by reducing the thickness of each SiC layer. When the coating fractures occurs, for example, by external load, this coating is thought to be still effective by the mechanism of crack deflection. The other is a sinusoidal SiC coating. This coating suppresses through-the-thickness cracking by reducing thermal stress in the coating using the CTE anisotropy of C/C composites. In the present paper, both the concepts were demonstrated to be promising and possibility was suggested to completely suppress through-the-thickness coating cracks by combining the two concepts.

### **Introduction**

The most serious disadvantage for application of Carbon/Carbon composites, C/Cs, is that they are easily oxidized under high temperature environments. Although several oxidation-resistant coatings, such as CVD-SiC and  $\text{Si}_3\text{N}_4$ , and oxide glass [1-3], were examined, due to a lack of reliability of these coatings, the C/Cs have been applied only to the secondary structures to which critical design parameters were not strength of material [4].

As shown in **Fig.1**, upon cooling after the coating treatment, a huge mismatch in thermal expansion between a ceramic coating and a C/C substrate gave rise to a large number of through-the-thickness coating cracks. These through-the-thickness cracks allow the oxygen diffusion to the C/C substrate, and lead to severe oxidation-degradation in the substrate [5-6]. To improve the oxidation-resistance of C/C composites, therefore, the suppression of the through-the-thickness coating cracks is required.

In the present paper, newly designed SiC/C multi-layered and sinusoidal SiC coatings were examined for the suppression of through-the-thickness cracks in the SiC coating on C/C composites. These coatings were applied by the chemical

---

T. Aoki, Science University of Tokyo, 2641 Yamazaki, Noda-shi, Chiba-ken, Japan 278-8510.

H. Hatta, ISAS; 3-1-1, Yoshinodai, Sagami-hara-shi, Kanagawa-ken, Japan 229-8510.

T. Hitomi, Kogakuin University, 2665-1 Nakano-chou, Hachioji-shi, Tokyo-to, Japan 192-8510.

H. Fukuda, Science University of Tokyo; 2641 Yamazaki, Noda-shi, Chiba-ken, Japan 278-8510.

I. Shiota, Kogakuin University, 2665-1 Nakano-chou, Hachioji-shi, Tokyo-to, Japan 192-8510.

vapor deposition, CVD. Plausibility of these coatings was discussed from both experimental and theoretical points of views.

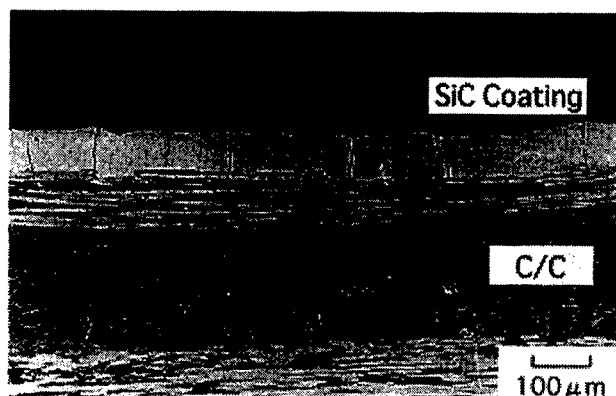


Fig.1 Cross sectional view of a CVD-SiC single-layer coating applied on a C/C composite.

### Coating concepts

#### SiC/C multi-layered coating

The multi-layered coatings examined in this study are composed of extremely thin SiC and pyrolytic carbon layers laminated alternately. The main role of the SiC layer is oxidation protection and that of the pyrolytic carbon layers is to eliminate mechanical interactions among the SiC layers and to isolate each SiC layer.

When the thickness of a coating becomes less than a critical value, the coating cracks disappear. This phenomenon occurs due to the reduction in the energy release rate during the formation of a through-the-thickness crack [7]. As discussed afterward, the critical thickness for the present SiC coating is 200nm. We also experimentally confirmed that a relatively thick pyrolytic carbon layer (about 15μm) on a C/C composite did not induce cracks. Thus if SiC layers with the thickness less than 200 nm and pyrolytic carbon layers are alternately laminated, we can possibly obtain a crack-

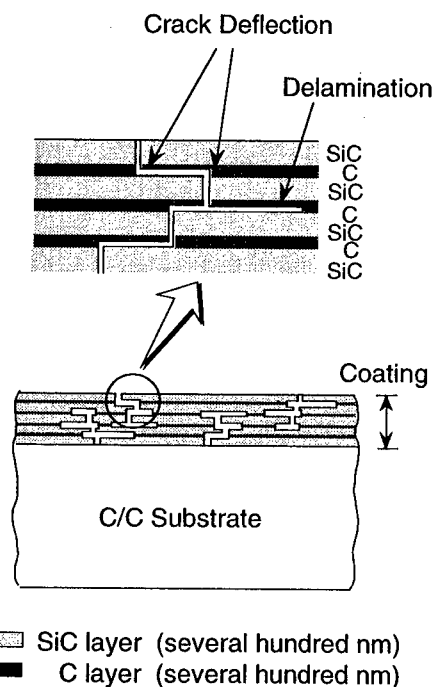


Fig.2 Schematic description of the expected cracking behavior in SiC/C multi-layered coating.

less thick coating.

Even if the multi-layered coating cracks by thermal and/or external loads, the cracks should be strongly deflected in the carbon layers, as shown in Fig. 2. Since the pyrolytic carbon layer is prone to have orientation of their crystalline hexagonal planes parallel to the interfaces, the crack propagation resistance along the layers should be extremely low. As shown in Fig. 2, we can expect for the deflected cracks lowering the probability of through-the-thickness cracks. In addition, even if the through-the-thickness crack eventually appears, the crack pass from the surface to the substrate becomes extremely longer; we can expect a much lower oxidation rate owing to the low gradient of oxygen concentration in the coating [6]. When the SiC coating becomes thinner, the density of coating crack increases and the crack opening of each crack naturally becomes narrower. By the oxidation reaction of SiC,  $\text{SiO}_2$  is formed and by this reaction the volume expands to about twice. This swelling reduces the opening of the coating crack [6]. This effect is more pronounced when the crack opening is smaller.

#### Sinusoidal SiC coating

Shioya *et al.* reported that by making a coating surface sinusoidal, tensile thermal stresses in the coating can be reduced [8]. In addition to this effect, in the present study, we have used the CTE anisotropy of C/C composites to reduce the thermal stress in the SiC coating. While the in-plane CTE of C/Cs is smaller than that of SiC coating, that in the out of plane direction is much larger than that of SiC. Thus, when SiC coatings are applied on the substrates with the reinforcing fibers inclined certain angles with the surface, we can diminish the CTE mismatch in both materials. This implies that by making the surface sinusoidal, i.e. wavy shape, drastic reduction in thermal stresses can be achieved and suppression of coating cracking may be made for UD- and 2D-laminated C/C composites.

#### Experimental procedure

Two kinds of unidirectional reinforced C/C composites were used for the coating substrate. The first C/C was produced by the Preformed-Yarn method and supplied by Across Co., Japan (PY-C/C). The other was fabricated by Sentan Zairyou Co., Japan (SZ-C/C). The reinforcing fiber of the PY-C/Cs was TORAYCA-M40 (Toray Co., Japan) and the volume fraction of the fibers,  $V_f$ , and the final sintering temperature, HTT, were 50% and 2000°C, respectively. The SZ-C/Cs were reinforced by XN-35 (Nippon Graphite Fiber Co., Japan) and HTT was 2500°C.

SiC/C multi-layered and sinusoidal SiC coatings were formed by the chemical vapor deposition using  $\text{SiCl}_4$ ,  $\text{C}_3\text{H}_8$  and  $\text{H}_2$  gases. Both the SiC and pyrolytic carbon layers were deposited at 1200°C under total gas pressure, 10 Torr.

#### Results and discussions

##### Critical thickness for CVD-SiC single-layered coating

The critical thickness of the SiC single-layered coating was examined using the unidirectional PY-C/C with the dimensions of  $15 \times 15 \times 3$  mm. **Figure 3** shows the variation of the observed crack spacing,  $2\lambda$ , the distance between adjacent cracks, as a function of the coating thickness. As shown in this figure,  $2\lambda$  decreases up to  $0.2 \mu\text{m}$  with decrease of coating thickness. The coating cracks, however, almost disappeared at a thickness of  $0.2 \mu\text{m}$  although localized small cracks were still slightly observed only above matrix rich regions of the substrate C/C. These cracks terminated when the cracks reached the region where carbon fibers existed just underneath the coating. The coating thickness, when coating crack almost disappeared, was defined as the critical thickness,  $h_c$ .

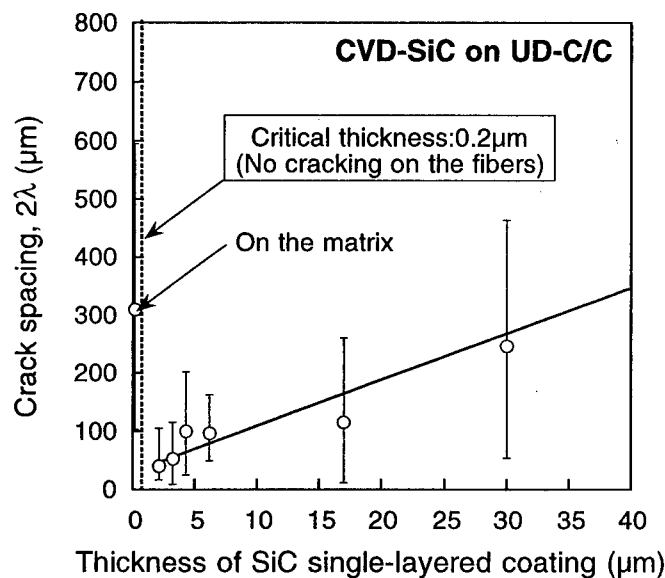


Fig.3 Relationship between the observed crack spacing and thickness of CVD-SiC single-layered coating.

In order to reconfirm the critical thickness from the analytical point of view, the energy release rate,  $G_{ch}$ , during the formation of a through-the-thickness channeling crack was calculated using a finite element analysis. Detailed calculation procedure was shown elsewhere [9]. **Figure 4** shows the calculation results of  $G_{ch}$  under the loading of thermal stress due to the temperature drop from CVD temperature,  $1200^\circ\text{C}$ , to room temperature. Since the coefficient of thermal expansion, CTE, of the present SiC coating has not exactly been known, the calculations were performed using two typical CTEs for the coating. In addition, the critical energy release rate  $G_{IC}$  of the SiC coating was assumed to be  $30 \text{ J/m}^2$  ( $K_{IC} = 3.6 \text{ MPa}\sqrt{\text{m}}$ ). As shown in this figure,  $G_{ch}$  decreases with decreasing the coating thickness and at a thickness less than  $0.2 \mu\text{m}$ ,  $G_{ch}$  becomes lower than  $G_{IC}$ . Thus it is expected that, if the thin crack-less SiC coatings are alternately laminated with the pyrolytic carbon coatings, a thick and crack-less multi-layered coating can be formed.

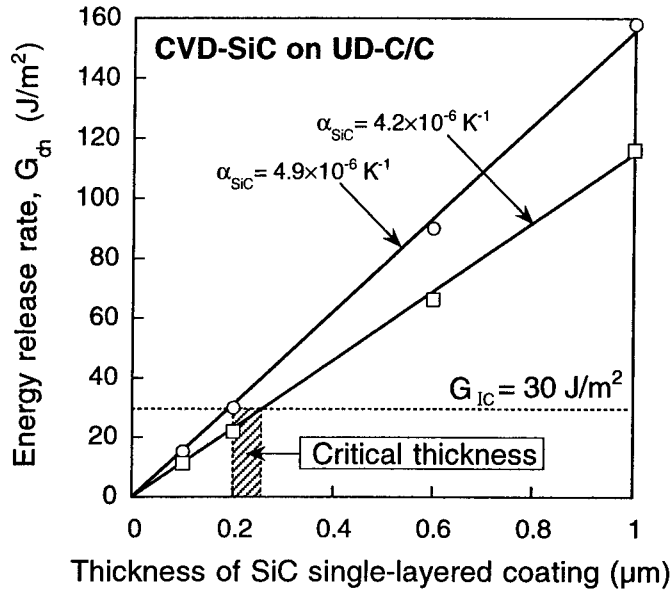


Fig.4 Calculated energy release rates for channeling cracking as a function of thickness of CVD-SiC single-layered coating.

#### Plausibility of SiC/C multi-layered coating

To confirm the validity of the present concept, SiC/C multi-layered coatings were deposited on the off-axis substrates cut from unidirectional SZ-C/Cs. In this experiment, the cutting angle between coating plane and the carbon fiber axis,  $\theta$ , shown in Fig.5 was varied. The substrate dimensions in this case were  $20 \times 10 \times 3$  mm. The off-axis substrates were used so as to increase the in-plane CTE of the substrates. By this procedure, we can set the critical thickness,  $h_c$ , freely and then we can choose  $h_c$  at values we can easily form the multi-layered coatings.

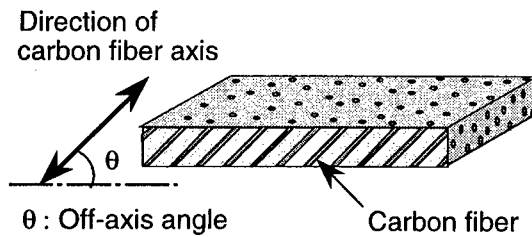


Fig.5 The off-axis C/C substrate prepared for SiC/C multi-layered coating.

Beuth [10] has given  $h_c$  by setting the energy release rate,  $G_{ch}$ , during the formation of a through-the-thickness channeling crack [11] equal to  $G_{IC}$ , as;

$$h_c = \frac{2E_{SiC}G_{IC}}{\sigma_{SiC}^2 \pi g(\alpha, \beta)} \quad (1)$$

where  $E_{SiC}$  is Young's modulus,  $G_{IC}$  the mode-I critical energy release rate of the

coating,  $\sigma_{SiC}$  the tensile stress in the coating given by

$$\sigma_{SiC} = \frac{E_{SiC}}{1 - \nu_{SiC}} (\alpha_{SiC} - \alpha_{in-plane}) \Delta T \quad (2).$$

In Eq. (1),  $g(\alpha, \beta)$  is a function of Dunders parameters,  $\alpha$  and  $\beta$  [10], being modulus ratios of the coating and substrate.

**Figure 6** shows the critical thickness,  $h_c$ , calculated from Eq.(1) for the SiC single-layered coating as a function of  $\theta$ . The shaded band corresponds to the uncertainty of material constants, and  $h_c$  was thus expected to lie within the shaded area.

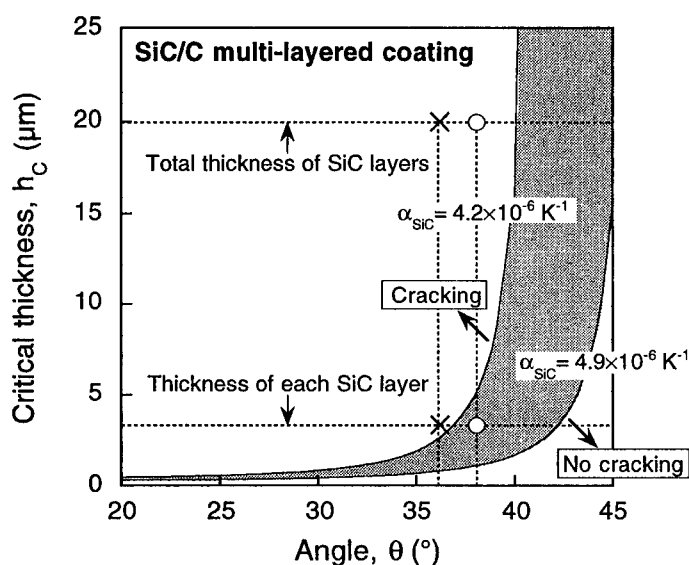


Fig.6 Calculated critical thickness,  $h_c$ , of CVD-SiC single-layered coating as a function of the cutting angle,  $\theta$ .

**Figure 7** shows the cross sectional views of a SiC/C multi-layered coating applied on the off-axis substrate. The total thickness of the coatings was about 24  $\mu\text{m}$ , and thicknesses of the each SiC and pyrolytic carbon layers were about 4  $\mu\text{m}$  and 0.8  $\mu\text{m}$ , respectively. In the coating with the 38° substrate, many through-the-thickness cracks can be seen in the coating. On the other hand, in the 36° coating, no through-the-thickness crack was observed. The difference in the observed morphology can be clearly explained in Fig.6. In the 38° coating, the thickness of each SiC layer, equal to about 4  $\mu\text{m}$ , is lower than the critical thickness ( $h_c \approx 5 \mu\text{m}$ ). Thus isolation of the each SiC layer by inserting the pyrolytic carbon layers between SiC layers lead to crack-less coating. In the 36° coating, however, each SiC layer was thicker than  $h_c$ , causing through-the-thickness cracks.

We also formed single-layered SiC coatings on the same off-axis substrates,  $\theta = 36^\circ$ -38°, and coating thickness, 20  $\mu\text{m}$ . In these coatings, we clearly observed through-the-thickness cracks. This example, therefore, successfully demonstrated that the SiC/C multi-layered coating is effective to suppress the through-the-thickness cracks in the coating on C/C composites as shown in Fig.7.

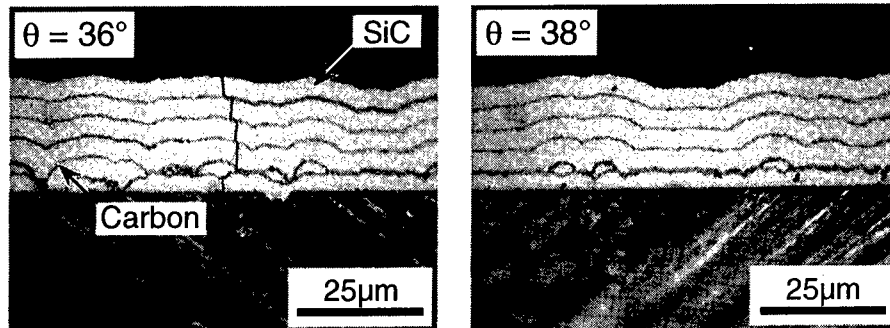


Fig.7 Cross sectional views of a SiC/C multi-layered coating applied on the off-axis substrates.

#### Plausibility of sinusoidal SiC coating

The principle stress in a sinusoidal SiC coating was calculated by use of the finite element analysis. **Figure 8** shows the calculated result for a configuration with coating thickness  $125\mu\text{m}$ , wave height  $3.6\text{mm}$ , and wave length  $4\text{mm}$ , which was assumed to be applied on a unidirectional C/C composite. The Y axis represents the in-plane normal stress in the sinusoidal coating normalized by the stress in the flat coating. As shown in this figure, a large stress was obtained only at the coating surface and near the interface at the bottom and top of the wavy coating. Hence we can expect the cracks induced at these points arrest with in the coating. Note that if we do not assume the anisotropic substrate, i.e., isotropic substrate, then we got higher stress in the coating. This anisotropic effect is a difference from Shioya's analysis. **Figure 9** shows the cross sectional view of a sinusoidal SiC coating applied on QI-C/C substrate. Coating cracks were successfully suppressed by use of the sinusoidal configuration. Thus the remaining problem is the optimization of sinusoidal

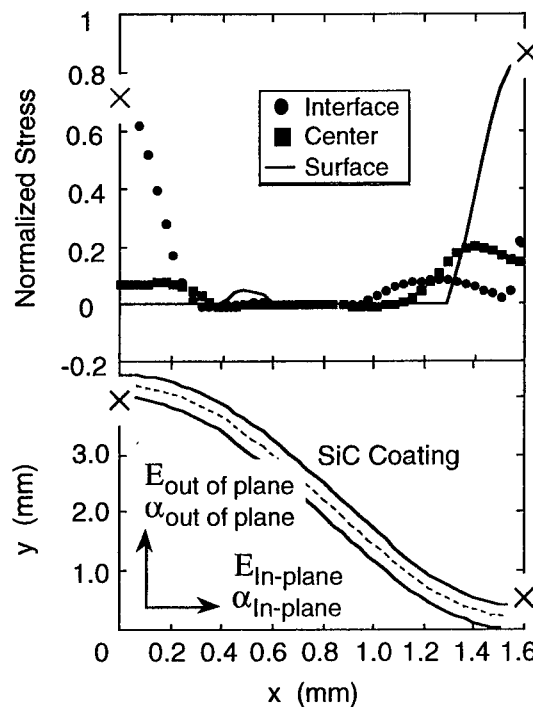


Fig.8 Normalized principle stress in a sinusoidal SiC coating.

configuration to make the wave flatter and how to utilize this concept to the 3D-configuration.

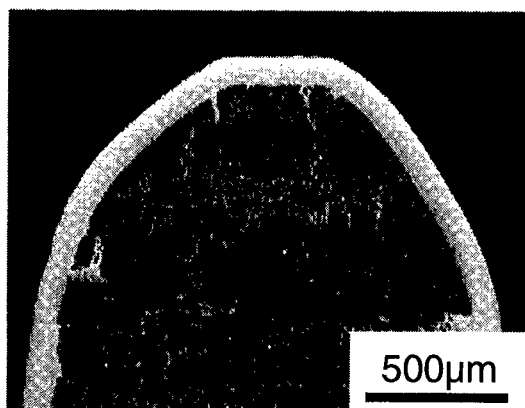


Fig.9 Cross-sectional view of a sinusoidal SiC coating.

## References

1. E. Fitzer, "The Future of Carbon-Carbon Composites," *Carbon*, **25** [2] 163-190 (1987).
2. J.R. Strife and J.E. Sheehan, "Ceramic Coatings for Carbon-Carbon Composites," *Ceramic Bulletin*, **67**, 369-374 (1988).
3. W. Kowbel, J.C. Withers, and P.O. Ransone, "CVD and CVR Silicon-Based Functional Gradient Coatings on C-C Composites," *Carbon*, **33** [4] 415-426 (1995).
4. G. Savege, "Applications of Carbon-Carbon Composites"; pp. 323-359 in *Carbon-Carbon Composites*, Chapman & Hall, London, 1993.
5. H. Hatta, T. Aoki, Y. Kogo, and T. Yarii, "High Temperature Oxidation Behavior of SiC-coated C/C Composites," *Composites, Part A*, **30**, 515-520 (1999).
6. T. Aoki, H. Hatta, Y. Kogo, H. Fukuda, Y. Goto, and T. Yarii, "High Temperature Oxidation Behavior of SiC-coated C/C Composites," *Trans. Japan Soc. Metal*, **62** [4] 404-412 (1998) (in Japanese).
7. M.D. Thouless, "Crack Soacing in Brittle Films on Elastic Substrates," *J. Am. Ceram. Soc.*, **73** [7] 2144-2146 (1990).
8. T. Shioya, K. Uenishi, "A method of thermal stress reduction in oxidation-protective layers by surface geometry modification", Proc. of the 1995 Yokohama Int. Gas Turbine Congress, Yokohama, III, 93-98 (1995).
9. H. Hatta, T. Aoki, T. Hitomi, H. Fukuda, I. Shiota, "Suppression of Through-the-Thickness Cracks in SiC coating on C/C Composites", Submitted for pub. in *Compos. Interface*.
10. L. Beuth, "Cracking of Thin Bonded Films in Residual Tension," *Int. J. Solids Structures*, **29** [13] pp.1657-1675 (1992).
11. M.S. Hu nad A.G. Evans, "The Cracking and Decohesion of Thin Films on Ductile Substrates," *Acta Metall. Mater.*, **37** [3] 917-925 (1989).



## **Development of Glass Fiber Reinforced Carbon Composite**

**S. Somiya and T. Nojiri**

### **Abstract**

Glass fiber reinforced carbon composites (GF/C) has been developed with the Glass-fiber reinforced plastic. Presently it becomes a worldwide important problem to recycle the used FRPs. There are two purposes of this research on the production of GF/C composites based on GFRP. One of them is the development of the material having high heat resistance and high specific strength than some other FRPs. The second purpose is the invention of recycling method of used GFRP. Especially, suitable method of carbonizing treatment had been developed. And the mechanical properties of carbonized composites were evaluated.

The specific strength and specific modulus of GFRP usually shows very high as same as CFRPs and AFRPs. In other hand these material cannot escape from the visco-elasticity caused by resin matrix. When almost FRPs were used in high temperature conditions, the limits on the temperature for practical using is usually lower than 120°C excepting a few high performance high-polymers. It is well known that composing some fiber into resin, the deflection temperature of resin composite is clearly improved. But FRP cannot escape from the deformation caused by the viscosity of resin matrix. The temperature between 150°C and 250°C is very shiver circumstance for FRPs and light metal alloys in practically. After carbonizing of GFRP, the composite was assumed to show non-visco-elastic material and show the stable mechanical properties at the high temperature.

When FRPs were burned completely, all plastics in FRP changed into gases such as CO, CO<sub>2</sub> and NO<sub>x</sub>. These are typical materials for air pollution to the earth. To decrease the amount of these gases caused by burning of plastics, a new method was proposed, which is carbonizing of plastics in used FRP. The carbonizing method for C/C composites is not possible to apply for the production of this GFRP directly. Because the carbonizing temperature for C/C materials is higher than the melting point of glass fiber composed in GFRP. When the carbonizing temperature is lower than C/C composite, it is well known that the bonding strength between carbon particles in matrix carbon becomes very low. To develop the new material on glass fiber reinforced carbon, it is important to strengthen bonding between carbon particles in matrix and carbon and glass fibers. In this research, the purpose is the development of a glass fiber reinforced Carbon composites based on used glass fiber reinforced epoxy resin.

---

S. Somiya and T. Nojiri, Faculty of Science and Technology, Dept. of Mechanical Engineering, Keio University, 3-14-1 Hiyoshi, Kouhoku-ku, Yokohama 223-8522, Japan.

### Material, Carbonizing Method and Evaluation Method

The base material was GFRP-laminate that consisted of 4 laminas. The lamina consisted of a pre-preg sheet (SU263/F6986S03) made by Yokohama-rubber Co., which was constructed with S-glass continuous fiber and Epoxy resin. The fiber volume fraction of lamina was about 66% before carbonizing. The cure temperature in molding was 121°C and the holding time at the temperature was 2 hours. Thickness of laminate was 0.8mm. Used specimen for the weight loss test by carbonizing GFRP was a strip of 10×10×1mm and put it on the ceramic base in the furnace for the metal heat-treatment directly for carbonizing. The specimen for tensile test was prepared on a strip style of 15×180×1mm. Four iron-tabs attached on both ends of them. The hot air can reach to them freely. When the tensile test-specimen was made, the pressure about 0.003 MPa was used, because without the pressure, the material expanded to the thickness direction during carbonizing treatment. When the material expanded, tabs did not attach on them. The press was controlled set by the heat resistance ceramic block.

In this research, the temperatures of heat treatment were from 200°C to 350°C for carbonizing of GFRP. The heat process for carbonizing showed in Fig.1. The first heating cycle was for raising the temperature in the oven, after then specimen was set in the hot furnace quickly. The weight loss due to the heat treatment was measured. After heating for a certain time, the specimen pulled out from the oven and cooled it in room temperature. And the change of mass was measured with an electronic balance over an accuracy of 0.01mg. The tensile strength was measured maintaining the crosshead speed of the test-machine at 0.1 mm/min.

### Evaluation of Quality of Carbonized GFRP and GF/C Composites

The temperatures at 200°C, 250°C, 300°C and 350°C were chosen for carbonizing temperature. Because, when the treatment temperature was over 400°C, in air condition, all plastic began to burn out at the early stage of carbonizing process and changed into gas material except glass fiber completely. And at the temperature conditions of lower than 200°C, it was recognized that the weight loss was very small and the outlook of the surface of GFRP did not change until 1400min. Fig.2 shows the weight loss of carbonized materials according to increase the carbonized time on each temperature. In this figure, the longitudinal axis shows the percentage of weight loss on matrix resin. The mass of embedded fiber was calculated using Mixture's law and the change of carbonized materials was also calculated.

From this figure, at 250°C, the weight loss of carbonized FRP quickly occurred on early stage of the heat treatment until 600min, in other hand over this time the weight loss reached to a certain value that is about 63%. The outlooks of the specimen completely changed from brown to black at the time from 200min to 600min. Over the 600min, the color of material did not show any change, but the roughness of surface increased. At 250°C, the rate of decreasing of mass was rapid than that of it at 200°C. But over the temperature of 350°C, the amount of carbonized material constantly decreased to zero quickly. After burning, glass fiber remained unchanged.

## Mechanical Properties

There are some reports for the strength of carbonized carbon composite but are few reports for glass fiber carbon composites[1,2]. The degradation of mechanical properties was evaluated by the tensile strength of treated GF/Carbon composites. Some specimens, which were prepared at 250°C under some time conditions, were tested by tensile load. The properties of stress and strain curve, tensile strength and modulus were discussed.

Fig.3 shows the stress-strain curve on the heat-treated specimens. The shape of S-S curves of GFRP was a straight line. The shape of GFRP treated by 200°C and 24 hours was the same as the GFRP. The shape of GF/C composite treated by 250°C and 12 hours was changed from the typical pattern on FRP materials. There is a knee phenomenon on it and over the knee point the shape shows the saw pattern as like as the ceramic composite, which was developed during the low fracture strain of matrix than the fracture strain of reinforcements. But according the increase of the time, the strength and the fracture strain decreased as shown in the shape of 250°C and 24 hours. This results show that the fracture mode due to the ductility of resin matrix and the brittle fiber change into the fracture mode caused by the brittleness of matrix and fiber as a ceramic composite.

Fig.4 shows the carbonizing dependence of tensile strength. Even though the weight loss over 600min kept constant, the strength decreased. From these results, the strength depended on the carbonizing. It means that the matrix lost ductility and adhesive strength between fiber and matrix according to carbonizing. But, on the material treated by the condition at 250°C and 24hours, the strength showed a half of tensile strength of GFRP. The value is the same as the strength of some FRTP and is suitable for the structural materials.

The fracture mode of heat-treated materials was changed by the heating time too. The typical fractured phenomenon on GFRP with the tensile test was the breakage of strands and the splits along the strands. After tensile test, test piece was usually consisted of much split strips which were build by a few strands adhered with resin. The strips were oriented to the almost longitudinal direction. It looked like some swords. But, on the GF/C material treated by the condition at 250°C and 24 hours, all specimens looked like a painting brush. Glass fibers were seen without the cover of matrix. It means that carbon matrix around fibers was broken and dispersed by the dynamic vibration due to fiber breakage. Because of the adhesive strength between carbon and fibers was decreased by carbonizing treatment. From this fact, the next problem for the development of useful GF/C composites is the strengthening of carbonized matrix and the adhesive strength.

## Conclusion

The glass fiber reinforced carbon composite was developed from the used glass fiber reinforced epoxy resin. In this study used GFRP was consisted of long glass fibers and epoxy resin and the suitable carbonizing condition was researched. The major findings are as follows:

- 1) For used GFRP, it is found that the better temperature condition was 250°C over 24 hours. At the temperature, carbonizing phenomenon achieved a constant weight loss.
- 2) The tensile strength of carbonized material are decreased according to the heat

treatment time and reached to a half at 250°C and 24 hours. But, it is recognized that the value is higher than the strength of almost all other FRTPs.

3) When suitable temperature and heating time was choused, it is found that used GFRP is able to change into useful industrial products.

### Acknowledgements

The author gratefully acknowledges the financial support on the research fond of Keio University.

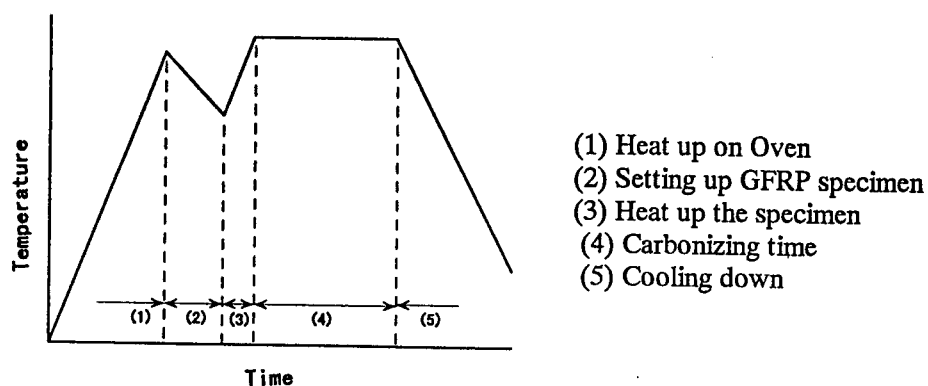


Figure 1. Schematic drawing of heating sequence with time for carbonizing of GFRP

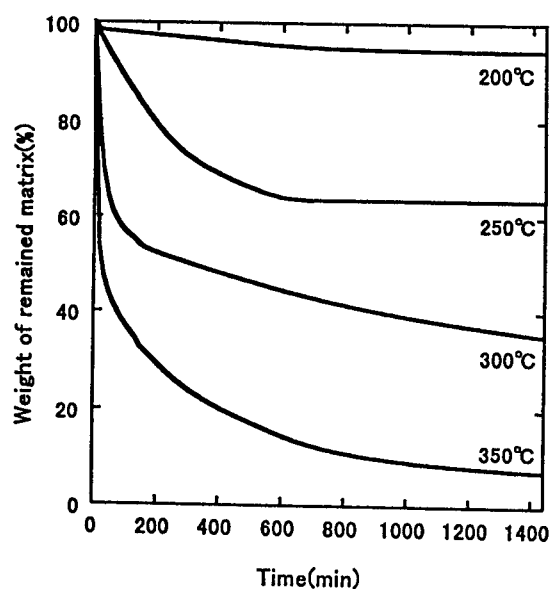


Figure 2. Weight loss of GFRP during carbonizing treatment from 200°C to 350°C

# Fiber and Repair

---

## **A Back Stress Constitutive Model for High Temperature Deformation of SiC Monofilaments**

Charles E. Bakis<sup>1</sup>, Richard E. Tressler<sup>2</sup>, and S. Jared Strait<sup>1</sup>

### **Abstract**

Individual CVD SiC monofilaments (type SCS-6, Textron Systems) were tested in air, under step-wise constant dead-weight loading, at constant temperatures ranging from 1200°C to 1300°C and stresses ranging from 50 MPa to 357 MPa. Experimental results from stepwise creep-recovery tests indicated that these SiC monofilaments exhibit strain recovery under certain stress decrement conditions. A back stress based constitutive equation was implemented to model the creep and recovery data. An evolution equation for predicting back stress during primary creep was evaluated. This evolution equation, coupled with the back stress based constitutive law, was used to predict the creep response of SCS-6 monofilaments under step-wise variable loads. Good correspondence between preliminary predictions and experiments indicates the potential suitability of the back stress constitutive model for the high temperature deformation of SCS-6 monofilaments under complex loadings.

### **Introduction**

Creep is the time dependent deformation of a structural component subjected to a mechanical load for an extended period of time, typically at a high homologous temperature. Ceramic structural components in heat engines and heat exchangers are often subjected to high temperature loading conditions, and thus knowledge of their creep behavior over time is critical for predicting their safety and life. While considerable work has been performed to characterize the creep behavior of metals and metal alloys under various loading conditions, there is far less information available concerning the creep behavior of current generation advanced ceramics. Similarly, while there is a multitude of information concerning creep under constant load conditions, little is available concerning creep under variable loads.

Variable structural loads arise in most practical applications. Components that operate under different conditions, such as engines operating at different speeds, will be subjected to stress conditions that change in an almost step-wise manner. Ceramic matrix composites undergo internal stress redistribution during creep due to

---

<sup>1</sup> Dept. of Engineering Science & Mechanics, 212 Earth-Engineering Sciences Building, The Pennsylvania State University; University Park, PA 16802 USA.

<sup>2</sup> Dept. of Materials Science and Engineering, 101 Steidle Building, The Pennsylvania State University; University Park, PA 16802 USA

the different propensities for creep and different thermal expansion coefficients among the constituents of the composite. The objective of this paper is to experimentally characterize the creep behavior of SCS-6 CVD SiC monofilaments (Textron Systems, Wilmington, MA, USA) subjected to step-wise constant loads and to evaluate the predictive capability of a simple back-stress based model for creep for this type of loading history. A model proven to be accurate with step-wise constant loads is also likely to be appropriate for smoothly varying loads as well.

SCS-6 monofilaments, valued for their excellent creep resistance and strength ( $\sim 4.3$  GPa [1]), are used mostly as reinforcements in titanium matrix composites and to a lesser extent in ceramic matrix composites. Considering both of these applications, creep-inducing temperatures in the vicinity of 1200-1400°C can be encountered either in processing or in service. Deformation models for this temperature range are needed for improved process development and service life prediction of metal and ceramic matrix composites utilizing SCS-6 monofilaments.

## Theory

A commonly used one-dimensional constitutive model for ceramic creep strain,  $\epsilon_c$ , as a function of stress,  $\sigma$ , time,  $t$ , and absolute temperature,  $T$ , is given by eq. (1),

$$\epsilon_c = A\sigma^n t^p \exp(-pQ/RT) \quad (1)$$

where  $A$ ,  $B$ ,  $n$ ,  $p$ , and  $Q$  are constants that depend on the material and external conditions such as environment and  $R$  is the universal gas constant (8.314 J/(mol·K)). Underlying mechanisms controlling each of these terms in the case of steady-state creep ( $p = 1$ ) are explained in the review by Cannon and Langdon [2]. Variants of eq. (1) have been applied to SCS-6 monofilaments, where time exponent  $p = 0.2-0.4$ , stress exponent  $n$  is near 1, and apparent thermal activation energy  $Q = 500-600$  kJ/mol [3,4]. Based on these parameters, it is thought that carbon or silicon grain boundary diffusion controls the creep behavior of SCS-6 fibers.

One of the shortcomings of eq. (1) is its inability to predict strain recovery, or reverse creep, in SCS-6 fibers when the stress is reduced following a period of forward creep. Previous investigators used an anelastic constitutive equation to explain this phenomenon [1], but this approach was noted to not apply to larger magnitudes of creep strain that could occur in service [4]. An alternative approach for modeling strain recovery is to introduce the notion of back stress [5]. The uniaxial back stress concept reflects the idea that creep deformation takes place due to only the effective stress (represented by the difference between the applied stress,  $\sigma$ , and the back stress,  $\sigma_0$ ), rather than the applied stress. The approach has been applied to metallic materials demonstrating either primary or steady-state creep [6]. Previously, terms in the back-stress constitutive model have been evaluated using models of dislocation controlled creep, although the fundamental approach applies to other governing mechanisms as well [6].

Based on this background, the following constitutive model (eq. 2) is now proposed for use with SCS-6 monofilaments,

$$\dot{\epsilon}_c = A(\sigma - \sigma_0)^m \exp(-B/T) \quad (2)$$

where temperature effects are represented by the exponential term ( $B=Q/R$ ), the time rate of change of back stress is given by eq. (3),

$$\dot{\sigma}_0 = h\dot{\epsilon}_c - r(\sigma - \sigma_0)^z \quad (3)$$

and  $A$ ,  $m$ ,  $B$ ,  $h$ ,  $r$ , and  $z$ , are material constants to be determined by experimentation.  $A$  depends on the external conditions of the test,  $m$  represents the degree of stress dependence,  $h$  is a hardening term representing the time rate of change of the back stress with respect to strain,  $r$  is a recovery term representing the time rate of change of the back stress with respect to effective stress, and  $z$  reflects the degree of effective stress dependence in the rate of change of back stress. The value of  $z$  is assumed to be 1.0 for diffusion mechanisms [7]. Determination of  $h$ ,  $r$ , and  $z$  is typically accomplished by the strain transient dip test if experiments are stress-controlled or the stress transient dip test if experiments are strain controlled [5].

It must be noted that major assumptions have been made in adopting eq. (2) for the creep of SCS-6 monofilaments. These are (a) that grain boundary diffusion mechanisms are consistent with the development of back stress within the material and (b) that all thermal effects can be lumped into one parameter,  $B$ . None of these assumptions have been rigorously proven in this effort and thus are considered avenues of future research.

## Experiments

The SCS-6 monofilaments used in this investigation are manufactured by the chemical vapor deposition of silicon carbide onto a pyrolytic graphite core. The carbon core diameter is 33  $\mu\text{m}$  and the nominal diameter of the entire fiber is 142  $\mu\text{m}$ , including a 2- $\mu\text{m}$ -thick surface coating consisting of amorphous carbon covered by carbon-rich silicon [1]. At least four concentric layers of SiC of differing composition or morphology are commonly recognized in the cross-section [8]. Stainless steel sleeves were bonded to the ends of the specimens and ball-jointed pin-vises were used to secure the specimen to the load train.

The creep test method uses dead weights for load and capacitive transducers to measure elongations outside the furnace. Reference [9] contains the details of the apparatus as well as an explanation and verification of the remote strain measurement method. In the case of variable stress conditions, the weights were applied in series such that they could be removed or increased as necessary to generate the desired stress history. Temperature and total displacement of the load train were monitored continually. Only creep strains were extracted from the elongation measurements, though. Variable load experiments were conducted in air, in the as-received condition, at temperatures of 1200 and 1300°C and stresses of 0-



357 MPa. Previous work has shown that creep results from SCS-6 monofilaments tested in air and argon are comparable [3].

Strain transient dip tests were used to determine the evolution equation for back stress in eq. 3 [10]. The method allows the determination of back stress by quickly lowering the applied stress to a level that instantaneously halts forward creep for a specified time following the load dip. When the applied stress has been reduced to the level of the back stress, the effective stress (and creep rate) remains zero until recovery gradually alters the back stress. Since the SCS-6 creep behavior is entirely primary, many separate tests were run at the same stress and temperature but different times to determine how the back stress evolved with time. In this investigation, if the slope of a straight line fitted to the strain transient data in the 30 minutes following a stress drop remained less than  $1.6 \times 10^{-6} \epsilon/\text{hr}$  in absolute value, the effective stress was assumed to be zero.

## Results

Strain transient dip tests were carried out at temperatures of 1300 and 1200°C and constant applied stresses of 357 and 278 MPa to determine the evolution of back stress and assess the ability of eq. (3) to model the back stress under a range of testing conditions. It was found that the back stress could be measured only within  $\pm 10$  MPa due to the small magnitude of strains involved. Hence, upper and lower bounds of back stress at various times were both used to evaluate separate best-fit parameters in eq. (3) by a nonlinear regression analysis [11]. The strain rate used in the direct integration of eq. (3) was determined directly from experimental data. The parameter  $z$  was assumed equal to 1 for the diffusion-controlled creep process being modeled. The best-fit parameters are listed in Table I and the goodness of fit between the evolution equation and experimental data is shown graphically in Fig. 1. The flatness of the back stress curve approaching 50 hr is reflective of a nearly steady-state creep behavior.

Table I. Back stress evolution equation parameters, from tests at 357 MPa/1300°C.

	Upper Bound Value	Lower Bound Value
$h$ (MPa/ $\epsilon$ )	18991	13026
$r$ (1/hr)	$4.0 \times 10^{-5}$	$4.0 \times 10^{-3}$

While both temperature and applied stress contribute to the creep rate present in the first term of the back stress evolution equation, it was unclear whether these parameters would have an independent effect on the evolution of back stress in SCS-6 monofilaments. A preliminary parametric study was therefore conducted to establish whether temperature or applied stress should be independently represented in the  $h$  or  $r$  parameters in eq. (3) and Table I.

To investigate the potential stress dependency, strain transient dip tests were performed at 1300°C with an initial applied stress of 278 MPa. Back stress values were obtained and compared to predicted results based on the evolution parameters given in Table I for the 1300°C/357 MPa conditions. The measured back stress

values fell within the upper and lower bound predictions based on the parameters of Table I, indicating that  $h$  and  $r$  do not significantly depend on initial applied stress in the range investigated (Fig. 2).

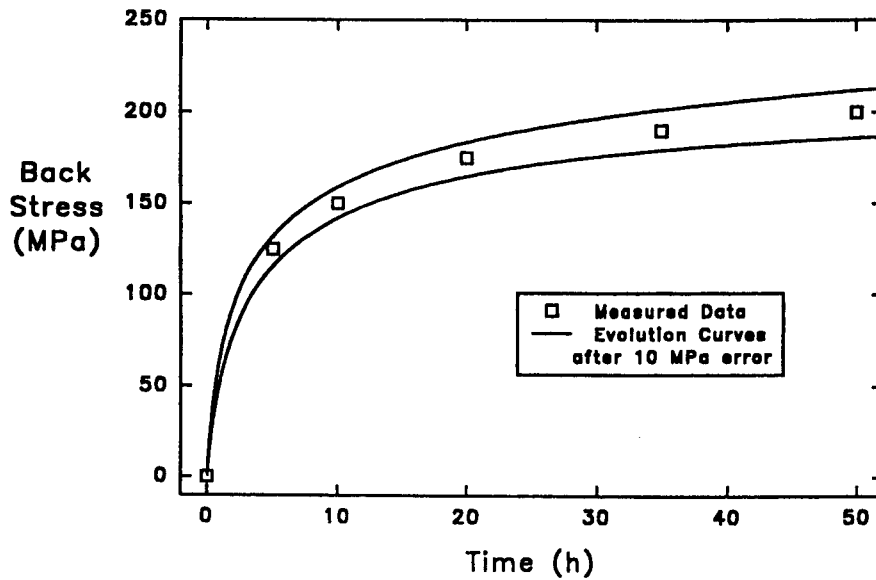


Figure 1. Comparison of experimental back stress data from experiments at 1300°C/357 MPa to predictions using eq. (3) and the best-fit parameters of Table I.

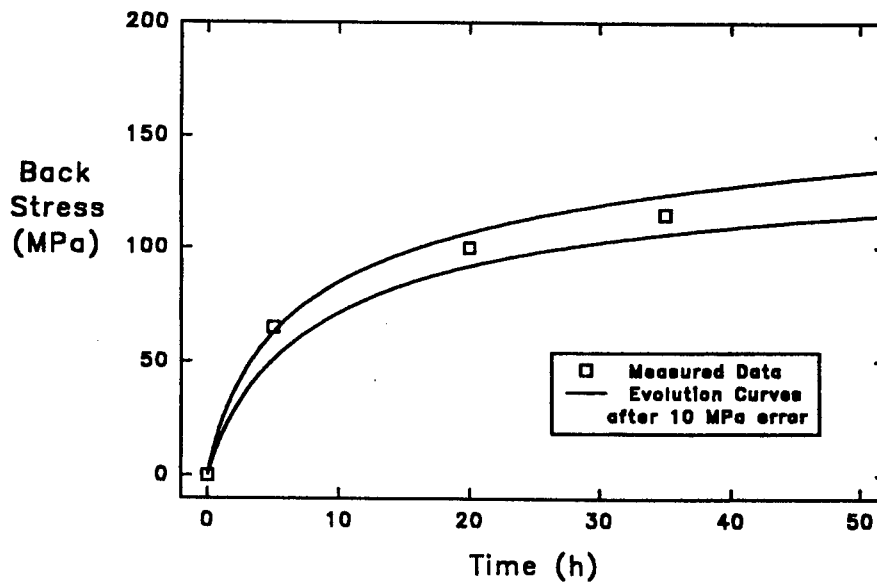


Figure 2. Comparison of experimental back stress data from experiments at 1300°C/278 MPa to predictions using eq. (3) and the best-fit parameters of Table I.

Similarly, to investigate the potential temperature dependency, transient dip tests were conducted at 1200°C with an initial applied stress of 357 MPa, and the results were compared to predictions based on parameters in Table I. Once again, the back stress results fall within the upper and lower bound predictions, indicating that temperature does not appear to have an independent effect on the evolution of back stress (Fig. 3).

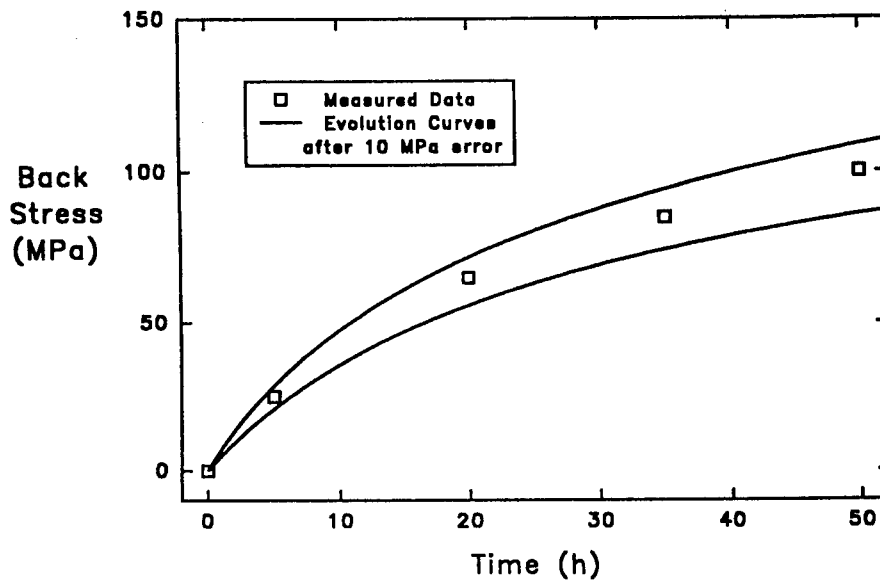


Figure 3. Comparison of experimental back stress data from experiments at 1200°C/357 MPa to predictions using eq. (3) and the best-fit parameters of Table I.

With a complete back stress evolution equation determined, attention was next focused on developing the parameters present in the proposed constitutive law (eq. 2). The value for  $B$  was determined to be 66153°C based on an approximate value of  $Q$  of 550 kJ/mol [3,4]. Forward and backward creep data from two-step load tests were used to establish values for  $A$  and  $m$ . The loadings comprised 12- and 25-hr intervals of the 357/50 MPa load sequence and 12-hr intervals of the 357/100 MPa sequence, at 1300°C. Forward and backward creep data from these tests were curve fitted, as described previously, providing independent parameters for each portion of the load history.

Results of the nonlinear curve fit for the creep and recovery portions of the two-step loading experiments are summarized in Table II. Note that the effective stress exponent,  $m$ , in eq. (2) is significantly higher in magnitude for the recovery portion of a cycle, indicating that the effective stress has a more dominant role in determining strain recovery rate than in driving forward creep.

Using the parameters given in Tables I and II, upper and lower bound predictions of creep strain for a step-wise discontinuous loading were calculated. The mean value of these predictions is plotted, along with experimental data, in Fig. 4, for 50-hr load steps at 278, 190, 357, and 0 MPa, at 1300°C.

Table II. Constitutive law parameters for eq. (2), assuming  $t$  given in hr,  $\sigma$  in MPa, and  $T$  in K.

	Forward Creep Value	Backward Creep Value
$A (1/\sigma^m)$	0.6025	$2.525 \times 10^{-17}$
$m$	6.0	15.0

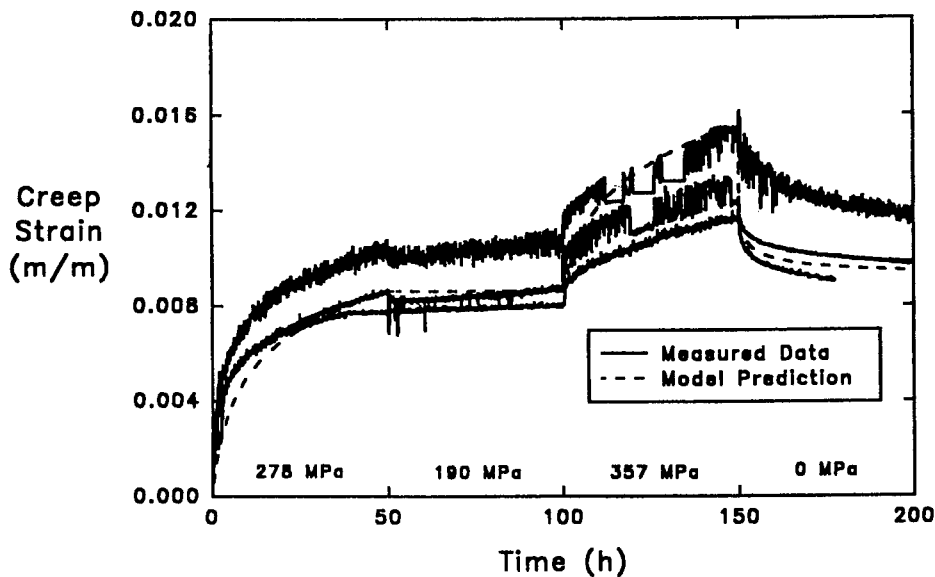


Figure 4. Experimental and mean predicted creep strains during a step-wise discontinuous loading.

## Conclusions

Strain transient dip tests have confirmed that back stress evolves within SCS-6 monofilaments during forward creep and can be measured to within  $\pm 10$  MPa. A back stress-based constitutive law was proposed and evaluated utilizing the results of step-wise creep-recovery tests. This constitutive law effectively predicted the creep response for a complex load history. Experiments demonstrated that the evolution of back stress may be fully characterized using constant hardening and recovery terms, and that additional parameterization of these evolution constants for temperature or applied stress appears to be unnecessary. Additional testing over a broader range of test conditions would be beneficial to reinforce these conclusions.

## Acknowledgments

This work was supported by NASA under grant no. NAGW-1381. Dr. Charles Lewinsohn helped set up and maintain the experimental apparatus. Mr. Gregory

Morscher of NASA Glenn Research Center contributed the monofilament used in this investigation. Dr. Steven Arnold, also of NASA GRC, participated in several valuable technical discussions on constitutive equations.

## References

1. J. A. DiCarlo, 1986. "Creep of Chemically Vapor Deposited SiC Fibers," *J. Materials Science*, 21:217-224.
2. W. R. Cannon and T. G. Langdon, 1983. "Review, Creep of Ceramics," *J. Materials Science.*, 18:1-50.
3. G. N. Morscher, C. A. Lewinsohn, C. E. Bakis, R. E. Tressler, and T. Wagner, 1995. "Comparison of Bend Stress Relaxation and Tensile Creep of CVD SiC Fibers," *J. American Ceramic Soc.*, 78:3244-3252.
4. C. A. Lewinsohn, L. A. Giannuzzi, C. E. Bakis, and R. E. Tressler, 1999. "High-Temperature Creep and Microstructural Evolution of Chemically Vapor-Deposited Silicon Carbide Fibers," *J. American Ceramic Soc.*, 82(2):407-413.
5. J. Cadek, 1987. "The Back Stress Concept in Power Law Creep of Metals: A Review," *Materials Science and Engineering*, 94:79-92.
6. R. Gasca-Neri, C. N. Ahlquist, and W. D. Nix, 1970. "A Phenomenological Theory of Transient Creep," *Acta Metallurgica*, 18:655-661.
7. K. Milicka and F. Dobes, 1990. "Using Constitutive Equations for Describing Creep Curves of Zinc," *Metallic Materials*, 28(6):388-398.
8. X. J. Ning and P. Pirouz, P., 1991. "The Microstructure of SCS-6 SiC Fiber," *J. Materials Research*, 6:2234-2248.
9. C. A. Lewinsohn, C. E. Bakis, H. T. Hahn, and R. E. Tressler, R. E., 1992. "Creep Testing of CVD Silicon Carbide Fibers," *Proc. American Soc. Composites, 7th Tech. Conf.*, Technomic, Lancaster, PA, pp. 779-791.
10. C. N. Ahlquist and W. D. Nix, 1969. "A Technique for Measuring Mean Internal Stress During High Temperature Creep," *Scripta Metallurgica*, 3:679-682.
11. D. W. Marquardt, 1963. "An Algorithm for Least Squares Estimation of Parameters," *J. Soc. Industrial and Applied Mathematics*, 11:431-441.

## **A Representative Diameter for the Evaluation of Brittle Monofilament Strength**

T. Morimoto

### **Abstract**

A new method has introduced for determining an imaginary diameter  $\phi_{\text{imaginary}}$  of the monofilaments with the variation in the diameters along the length. Each monofilament is possible to be treated uniform in the diameter with the  $\phi_{\text{imaginary}}$  for the statistics on the fracture probability under tensile loading. The Weibull model is coupled in the method with the diameter distribution along the gauge.

We define the  $\phi_{\text{imaginary}}$  as a representative diameter  $\phi_R$  when a consistent value is found on the  $\phi_{\text{imaginary}}$  independent of the fiber length. An important contribution of this work is to introduce the existence of the  $\phi_R$  for the theoretical predictions of the fracture probability of a commercial brittle monofilament, Tyranno ZMI Si-Zr-C-O fiber (UBE Industry Co.).

### **Introduction**

The ultimate tensile strength of a brittle monofilament has been characterized with the Weibull model as a function of fiber length.[1][2] However the length has been questioned on the strength characterization, as the "length dependence" has not been clearly shown with the Weibull model.[3][4] One of the important reason has been reported variation in the diameter along the length of monofilaments.[5][6]

---

Tetsuya MORIMOTO, National Space Development Agency of JAPAN (NASDA), Tsukuba Space Center, 2-1-1 Sengen, Tsukuba-shi, Ibaraki-ken, 305-8505 Japan

In the previous work the authors have shown a clear dependence of the fracture strength on the volume of Si-Zr-C-O commercial fiber.[7] Variation in the diameter along the gauge length was focused as a factor affecting the reliability of the statistics. In this work we present a new method suitable for determining an imaginary diameter as the representative for the Weibull model of length dependence.

### A Representative Diameter

We define a representative diameter as a value giving the least error of the fracture probability for a brittle monofilament with a gauge length under a load. The diameter is derived through the following procedure.

First, diameter distributions are measured for the each fiber beforehand the tensile tests. Then second, the sections with a uniform diameter are selected for preparing the samples of a consistent volume. The samples are tensile tested giving the Weibull parameters on the volume effect in the form:

$$P = 1 - \exp \left[ - \frac{V}{V_0} \cdot \left( \frac{\sigma}{\sigma_s} \right)^m \right] \quad (1)$$

where 'P' is the probability of a fiber having a strength less than or equal to  $\sigma$ , ' $V_0$ ' is an imaginary unit of volume,  $V$  is the volume of a fiber under the tensile loading of  $\sigma$  and ' $m$  and  $\sigma_s$ ' are the Weibull shape and scale parameters, respectively.

A probability of fracture is given with the parameters for a fiber when the diameter distribution is known. Therefore third, the applied load and the diameter distribution along the gauge length are used as the parameters for predicting the fracture probability of each fiber tensile tested.

Then fourth, an imaginary diameter  $\phi_{imaginary}$  is given for the Weibull model of the length dependence through equating the fracture probabilities between the one with the diameter  $\phi_{imaginary}$  and the one of diameter distribution, as depicted in equation (2).

$$P = 1 - \exp \left[ - \frac{(\pi \cdot \phi_{imaginary}^2 / 4)^{1-m} \cdot L \cdot \left( \frac{T}{\sigma_s} \right)^m}{V_0} \right]$$

$$\equiv 1 - \exp \left[ \frac{- \int_0^L (\pi \cdot \phi^2(l)/4)^{1-m} dl}{V_0} \left( \frac{T}{\sigma_s} \right)^m \right] \quad (2)$$

Where ' $T$ ' is the tensile load, ' $L$ ' is the fiber length and the fiber cross section is assumed to be circle. Therefore the following relationship is derived between the  $\phi_{\text{Imaginary}}$  and the distributions of  $\phi(l)$  along the fiber length ' $L$ .'

$$\phi_{\text{Imaginary}} \equiv \left( \frac{\int_0^L \phi^{2(1-m)}(l) dl}{L} \right)^{\frac{1}{2(1-m)}} \quad (3)$$

The imaginary diameter  $\phi_{\text{Imaginary}}$  is regarded suitable as the representative diameter  $\phi_R$  for analyzing the tensile fracture probability when a consistent value exists independent of the fiber length ' $L$ .'

### Sample Fibers

Tyranno ZMI Si-Zr-C-O commercial fiber (UBE Industry Co.) was selected to examine the validity of the representative diameter  $\phi_{\text{Imaginary}}$  for the probability on the tensile strength. The fiber has the characteristics according to the quality inspection data sheet: the diameter is 11  $\mu\text{m}$ , the tensile strength is 3.4 GPa, the fracture strain is 1.7%, the density is  $2.48 \times 10^3 \text{ Kg/m}^3$  and the elastic modulus is 200 GPa. Table I is the chemical compositions.

Table I The Compositions of Si-Zr-C-O fiber (wt. %)

Si	C	O	Zr
56.6	34.8	7.6	1.0



The fibers are depicted in Fig. 1 showing circular cross sections. Therefore this fiber is possible to be used for examining the validity with the equation (3) of the imaginary diameter  $\phi_{\text{imaginary}}$  as a representative diameter  $\phi_R$ .

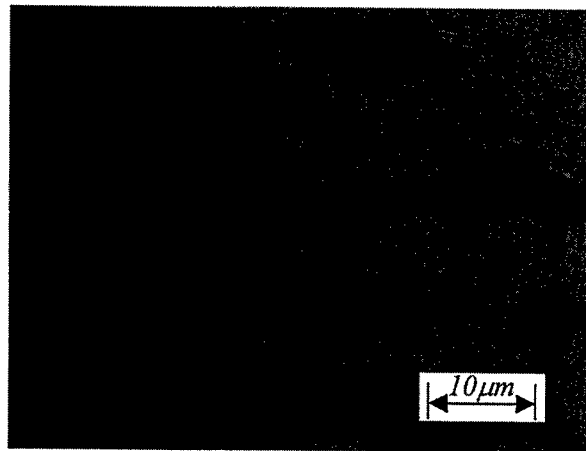


Figure1 Cross Sections of Tyranno ZMI Fibers

## Experimental

The diameters of sample fibers were measured optically with a laser scan micrometer LSM-500 (Mitutoyo MTI Corp.) of the repeatability within  $\pm 0.1 \mu\text{m}$  error. Figure 2 depicts the measurement setup.

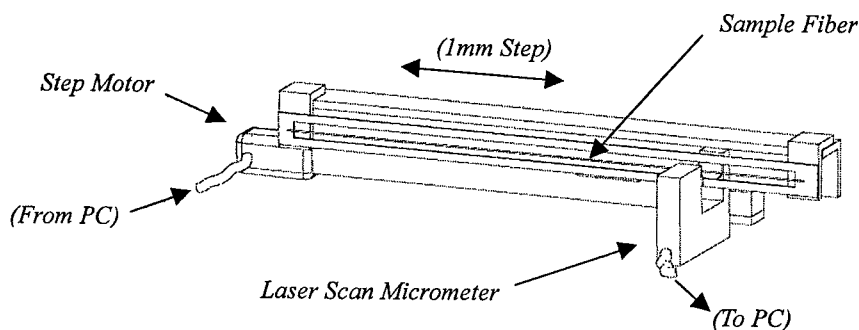


Figure 2 Measurement setup

The fiber to be measured was mounted on a holder as depicted in figure 3. The prepared sample was then attached to the uni-directional stage with 1mm step movement for the measurement.

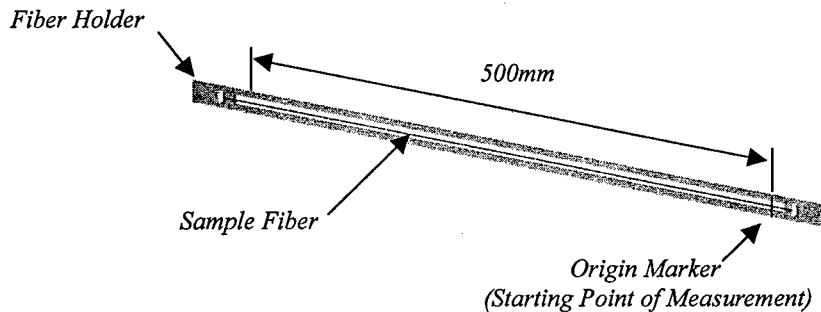


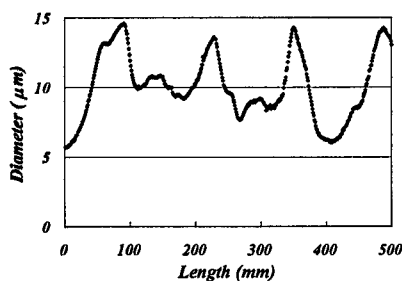
Figure 3 Sample preparation

Tensile samples were prepared for deriving the Weibull parameters  $m$  and  $\sigma_R$  with the consistent volume of  $1.5 \times 10^{-12} \text{m}^3$  out of the sections of uniform diameter.

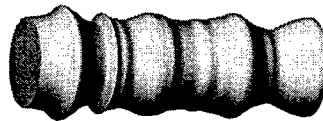
For examining the existence of the representative diameter  $\phi_R$  samples were tensile tested for the gauge length of 10mm, 100mm, 200mm, 300mm and 400mm. Shimadzu EZ-Test 500N tensile machine was used for the tests under a constant cross head speed condition of 10 mm/min.

## Results and Discussions

In figure 4 an example of diameter measurement along 500mm (a) and the schematic shape (b) is given.



(a) A shape of fiber



(b) Schematic shape

Figure 4 Fiber shape

Individual fiber diameters vary significantly along the gauge length as is seen in the figure. This implies that the uniformity assumption is not always applicable for the monofilament diameter on the Weibull analysis. Moreover variation is found in this case more than 10 times in the cross sectional area or tensile stress along the gauge on some fibers making the Weibull analysis difficult. Therefore 30 tensile samples were prepared from the sections of  $\phi_{MAX}/\phi_{MIN} < 1.05$  with the volume of  $1.5 \times 10^{-12} \text{ m}^3$  where  $\phi_{MAX}$  is the maximum and  $\phi_{MIN}$  is the minimum diameter along the gauge. The cumulative distribution of the tests and the data fitting for deriving the Weibull shape and scale parameters  $m$  and  $\sigma_5$  are shown in figure 5 (a) and (b), respectively. The results yielded to the shape parameter  $m=5.3$  and the scale parameter  $\sigma_5=4.9 \text{ GPa}$ .

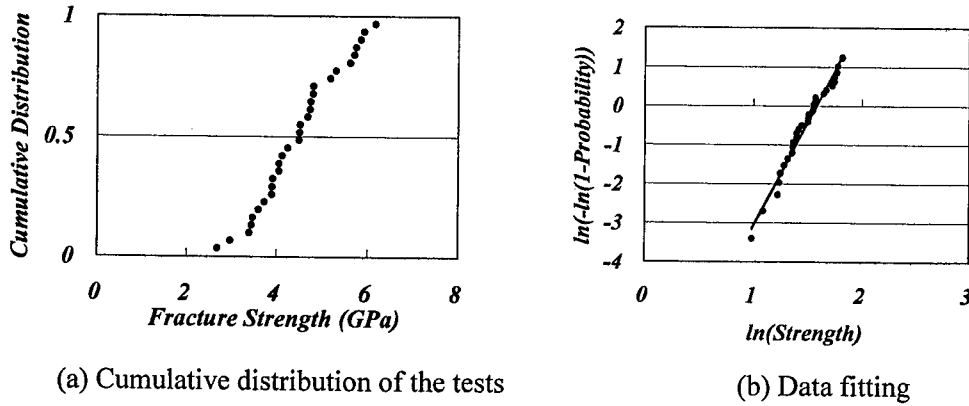


Figure 5 Test results

The fracture probability  $P$  was given for the Tyranno ZMI Si-Zr-C-O fibers with the results over as

$$P = 1 - \exp \left[ - \frac{\int_0^L (\pi \cdot \phi^2(l)/4)^{-4.3} dl}{1.5 \times 10^{-3}} \cdot \left( \frac{T}{4.9 \times 10^{-3}} \right)^{5.3} \right], \quad (4)$$

where  $\phi$  is the cross section diameter in  $\mu\text{m}$ ,  $L$  is the length in  $\text{mm}$  and  $T$  is the tensile load in  $\text{N}$ . The equation (3) is then given as follows.

$$\varphi_{\text{Imaginary}} \equiv \left( \frac{\int_0^L \varphi^{-8.6}(l) dl}{L} \right)^{-\frac{1}{8.6}} \quad (5)$$

Results obtained above were verified for a representative diameter  $\varphi_R$  through the correlation on the imaginary diameter  $\varphi_{\text{Imaginary}}$ . After measuring the diameter in 1mm step 3 data sets were tensile tested for the gauge length of 10mm, 100mm, 200mm, 300mm and 400mm. The fracture loads decreased with the fibers of longer gauge length while the fracture probabilities did not show the tendency as is shown in figure 6 (a) and (b).

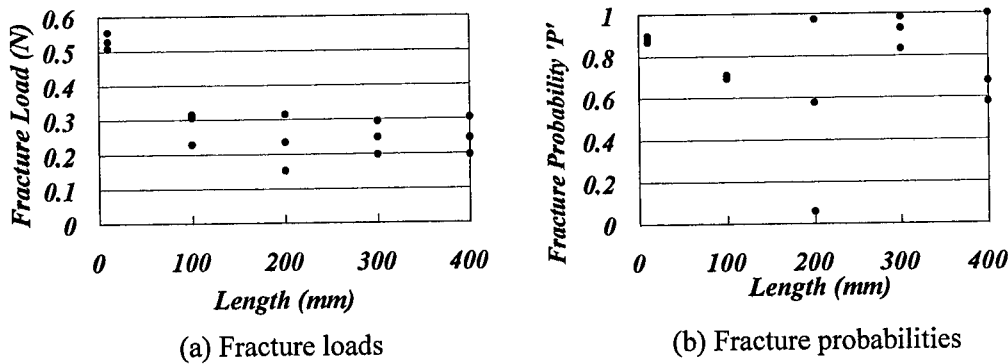


Figure 6 Tensile tests of Si-Zr-C-O fibers

The imaginary diameter  $\varphi_{\text{Imaginary}}$  showed a negligible slope on the gauge length as depicted in figure 7. Therefore the existence is confirmed for a representative diameter  $\varphi_R$  with the value  $9.7\mu\text{m}$ .

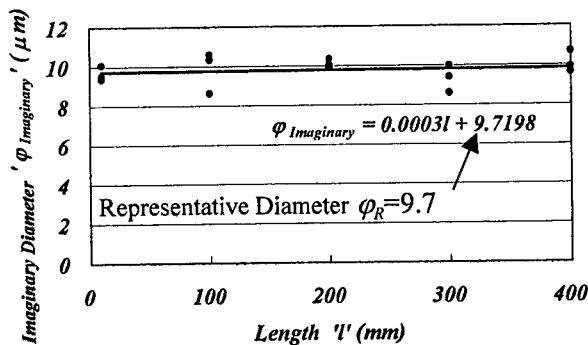


Figure 7 Representative diameter

## Conclusions

The statistics has studied on the strength of brittle monofilaments with variation in the diameter along the gauge length. A new method has introduced for determining an imaginary diameter  $\phi_{\text{imaginary}}$  of the monofilaments. The Weibull model is coupled in the method with the detailed measurements of the diameter along the gauge length. With the method each monofilament is regarded uniform in the diameter with the  $\phi_{\text{imaginary}}$  for the statistics on the fracture probability under tensile loading. We define the  $\phi_{\text{imaginary}}$  as a representative diameter  $\phi_R$  when a consistent value is found on the  $\phi_{\text{imaginary}}$  independent of the gauge length.

Tyranno ZMI Si-Zr-C-O fiber was selected for the demonstration of the method. Large variation was found in the diameter along the gauge of each fiber. However the imaginary diameter  $\phi_{\text{imaginary}}$  was found independent of the gauge length showing a representative diameter  $\phi_R$  exists on the Tyranno ZMI commercial fiber.

## References

1. Coleman, B.D., "On the Strength of Classical Fibers and Fibre Bundles." *Journal of the Mechanics and Physics of Solid*, 1958 7: pp.60-70.
2. Zwaag, S., "The Concept of Filament Strength and the Weibull Moduls." *Journal of Testing and Evaluation*, 1989: pp. 292-298.
3. Wilson, D. M., "Statistical Tensile Strength of Nextel™ 610 and Nextel™ 720 Fibers." *Journal of Materials Science*, 1997 32: pp.2535-2542.
4. Yuntian T. Zhu, et. al., "Analysis of Size Dependence of Ceramic Fiber and Whisker Strength." *Journal of American Ceramic Society*, 1997 80(6): pp.1447-1452.
5. T. Morimoto, et. al., "A New Method for Measuring Diameter Distribution along Ceramic Fiber." *Ceramic Engineering and Science Proceedings*, 1998 19 (3) pp.47-54
6. H. Fukuda, et. al., "Strength Distribution of Monofilaments Used for Advanced Composites." *Proceedings of the 9<sup>th</sup> International Conference on Composite Materials (ICCM/9)*, 1993 6: pp.687-694.
7. T. Morimoto and R. M. Aoki, "The Weibull Moduli of Si-Zr-C-O Fiber with Diameter Variation Along the Gauge Length." *Proceedings of the 12<sup>th</sup> International Conference on Composite Materials (ICCM/12)*, (CD-ROM)

## **Crack Growth Analysis in Cracked Aluminum Panels Repaired with a Bonded Composite Patch**

Y. Shibuya, S. Fujimoto, M. Sato, H. Shirahata,  
H. Fukunaga and H. Sekine

### **Abstract**

Crack growth of cracked aluminum panels repaired with a bonded composite patch is analyzed to evaluate an effect of the repair. An efficient finite element analysis using Mindlin plate element is developed. The technique is extended to a three-layer model, which consists of patch, adhesive and plate layers. The crack growth behavior of an aluminum panel with the composite patch is discussed on the basis of Paris relation.

### **Introduction**

Aging aircraft accumulated fatigue cracks during their operation are in need of repairs to extend the service life. A repair method using composite patches to reinforce the cracked structure has been promising due to the high specific stiffness and strength of the composite.

Repairs with bonded composite patches have been studied as a possible technique. Rose[1] developed an analytical model to characterize bonded reinforcements. Asymmetric repair of structure like as a single-sided patch causes out-of-plane bending. Mindlin plate finite element has been used to evaluate the stress intensity factor[2,3]. Muller and Fredell[4] present simple design guideline for multiple bonded repairs in close proximity. Experimental studies have been made for disbond effect on fatigue crack growth[5] and measurement of stress intensity factor in bonded crack patching[6].

In this study, the crack growth in cracked aluminum panels repaired with a bonded composite patch is considered to predict the residual life of the structure. In case of a single-sided patch, it is needed to include the effect of out-of-plane bending in the analysis. A finite element analysis using Mindlin plate element is developed. The method is extended to three-layer model, which consists of patch, adhesive and

---

Y. Shibuya, Department of mechanical Engineering, Akita University, 1-1, Tegata Gakuen-machi, Akita 010-8502, Japan

S. Fujimoto, Graduate School of Engineering, Tohoku University, Aoba-yama 01, Aoba-ku, Sendai 980-8570, Japan

M. Sato, H. Shirahata, H. Fukunaga and H. Sekine, Department of Aeronautics and Space Engineering, Tohoku University, Aoba-yama 01, Aoba-ku, Sendai 980-8570, Japan

plate layers. The adhesive is modeled as a thin elastic layer. The modified crack closure method is used to calculate the stress intensity factor in the cracked panel.

Numerical results on the stress distribution and stress intensity factor are compared with three-dimensional finite element analysis. The crack growth behavior of the cracked panel with the bonded composite patch is discussed on the basis of Paris relation, where experiment result for monolithic aluminum panel is used.

### Analytical Model

Consider a cracked aluminum panel with a bonded composite patch as shown in Figure 1. The crack is located in the center of the panel, and the composite patch over the crack is adhesively bonded to the panel. A Cartesian coordinate system( $x, y, z$ ) is placed on the panel. Length of the crack is  $2a$ , and diameter of the patch is  $D$ . Length and width of the panel are  $2L$  and  $2W$ , respectively. Thicknesses of the patch, adhesive and panel are  $t_r$ ,  $t_a$  and  $t_p$ , respectively. The panel is subjected to cyclic applied stress with amplitude  $\Delta\sigma_0$  at  $y = \pm L$ .

### Finite Element Analysis

#### Mindlin Plate Element

The structure with a single-side patch causes three-dimensional stresses due to asymmetry of the structure. Mindlin plate element is employed as a suitable model to reduce the cost in computation. The cracked panel and composite patch are modeled by using Mindlin plate element, and the adhesive is modeled as an elastic continuum replacing the normal and shear spring elements.

The adhesive layer is modeled by springs for the transverse shear stiffness in

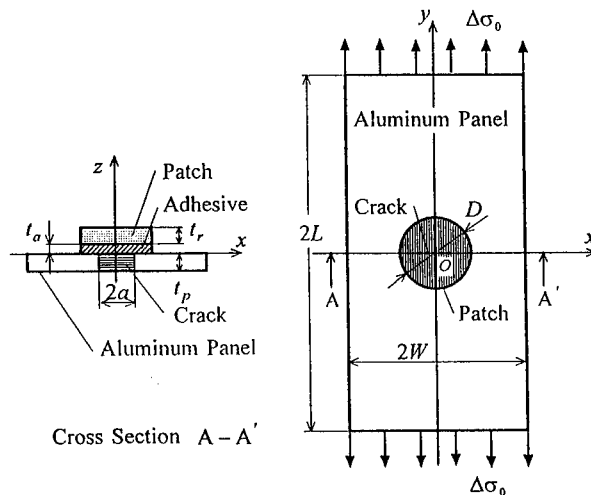


Figure 1 A cracked panel repaired with a bonded composite patch

the  $x-z$  and  $y-z$  planes and the axial stiffness in the  $z$  direction as shown in Figure 2. Stresses of the adhesive are proportional to discontinuity of displacements between the patch and panel at the interface. Displacements of the patch and panel at the interface are expressed from Mindlin plate theory as

(a) Interface between the composite patch and adhesive ( $z = t_a$ ):

$$u^{ra} = u^{0r} - \frac{t_r}{2} \theta_x^{0r}, \quad v^{ra} = v^{0r} - \frac{t_r}{2} \theta_y^{0r}, \quad w^{ra} = w^{0r} \quad (1)$$

(b) Interface between the adhesive and panel ( $z = 0$ ):

$$u^{ap} = u^{0p} + \frac{t_p}{2} \theta_x^{0p}, \quad v^{ap} = v^{0p} + \frac{t_p}{2} \theta_y^{0p}, \quad w^{ap} = w^{0p} \quad (2)$$

where  $u$ ,  $v$  and  $w$  are displacements of  $x$ ,  $y$  and  $z$  directions, respectively. And  $\theta$  is the rotation of the panel. Superscripts  $r$  and  $p$  indicate the patch and panel,  $0r$  and  $0p$  indicate central planes of the patch and panel, and  $ra$  and  $ap$  indicate interfaces at  $z = t_a$  and  $z = 0$ , respectively.

Stress components in the adhesive  $\tau_{zx}$ ,  $\tau_{zy}$  and  $\sigma_{zz}$  are related to discontinuity of displacements between the composite patch and panel as

$$\begin{aligned} \tau_{zx} &= \frac{G_a}{t_a} (u^{ra} - u^{ap}), & \tau_{zy} &= \frac{G_a}{t_a} (v^{ra} - v^{ap}), \\ \sigma_{zz} &= \frac{2(1 - \nu_a)G_a}{(1 - 2\nu_a)t_a} (w^{ra} - w^{ap}) \end{aligned} \quad (3)$$

where  $G_a$  and  $\nu_a$  are the shear modulus and Poisson's ratio of the adhesive, respectively.

The modified crack closure method[7] is used to calculate the strain energy release rate. In the crack closure method, the virtual crack extension  $\Delta a$  is taken to be small in comparison with the crack length. The strain energy release rate is calculated as the work to close the crack with opening displacement. The total strain energy rate  $\bar{G}$  is written as

$$\bar{G} = \bar{G}_v + \bar{G}_\theta \quad (4)$$

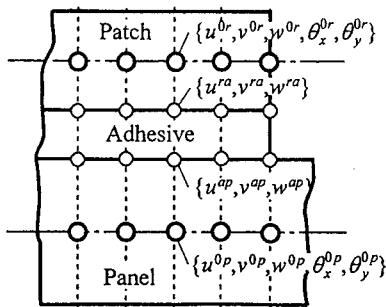


Figure 2 Adhesive layer model

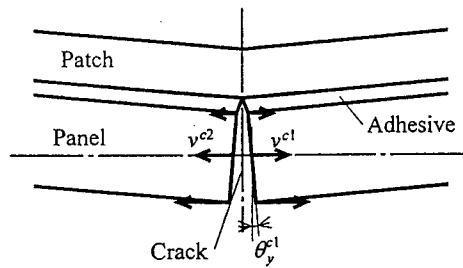


Figure 3 Cross section of crack tip



where

$$\bar{G}_v = \frac{1}{2 \Delta a} [F_y^c (v_{c2} - v_{c1})] , \quad \bar{G}_\theta = \frac{1}{2 \Delta a} [M_y^c (\theta_{c2} - \theta_{c1})]$$

Here,  $F_y^c$  and  $M_y^c$  are the nodal force and moment, respectively. The stress intensity factors at the crack tip for in-plane stress and pure bending moment are obtained from the strain energy release rate as

$$K_v = \sqrt{\frac{E_p \bar{G}_v}{t_p}} , \quad K_\theta = \sqrt{\frac{3 E_p \bar{G}_\theta}{t_p}} \quad (5)$$

where  $E_p$  is the Young's modulus of the panel. As the stress intensity factor is linearly distributed over the thickness of the panel, the stress intensity factors at  $z = 0$  and  $z = -t_p$  are written as

$$K = K_v - K_\theta \quad (z = 0) , \quad K = K_v + K_\theta \quad (z = -t_p) \quad (6)$$

### Three-dimensional Finite Element Analysis

To validate the three-layer model, three-dimensional finite element analysis is made. Typical quarter model is shown in Figure 4. The detail of mesh near the crack tip is shown in Figure 4(b). The stress intensity factor is calculated by performing J-Integral.

### Numerical Results and Discussion

The repaired structure treated in this study is a glass/epoxy composite patch and aluminum panel(2024-T3). The composite patch is a  $[0 / 0 / 0 / \pm 45 / 0 / 0]_s$ .

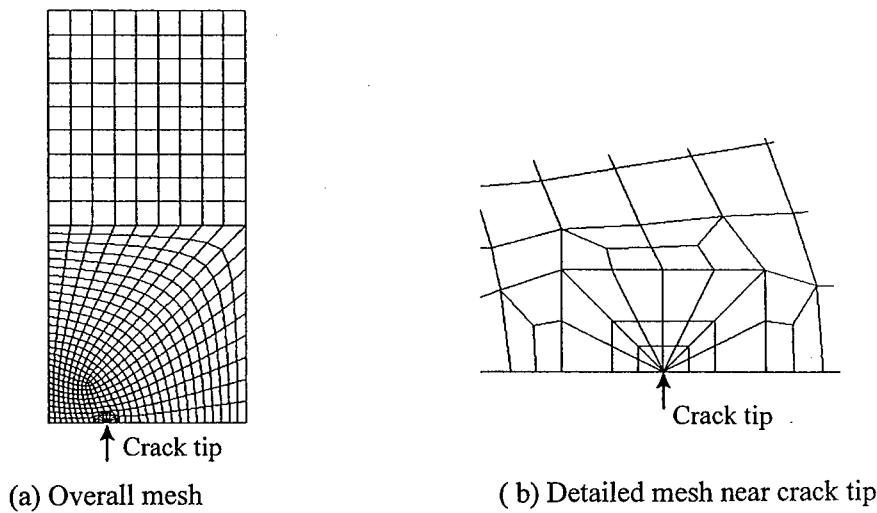


Figure 4 Three-dimensional Finite element mesh

laminate. The adhesive is AF163-2K. Dimensions and material properties of the panel, adhesive and composite are given as follows:

(a) Aluminum panel

$$L = 125\text{mm}, W = 60\text{mm}, t_p = 2\text{mm}, E_p = 72.39\text{GPa}, \nu_p = 0.33$$

(b) Adhesive

$$t_a = 0.1\text{mm}, G_a = 0.439\text{GPa}, \nu_a = 0.34$$

(c) Lamina of composite patch

$$D = 50\text{mm}, t_r / 14 = 0.229\text{mm}, E_L = 44.12\text{GPa}, E_T = 9.65\text{GPa}, G_{LT} = 4.13\text{GPa}, \nu_{LT} = 0.28$$

The panel is subjected to cyclic applied stress with the amplitude  $\Delta\sigma_0 = 58.5\text{MPa}$ .

Amplitude of stress intensity factors  $\Delta K$  calculated by using Mindlin plate element are shown in Figure 5. Stress intensity factor for a unpatched panel is constant over the thickness. As the stress intensity factor for a patched panel is linearly distributed over the thickness due to out-of-plane bending, it is indicated at three planes for free surface ( $z = -t_p$ ), midplane ( $z = -t_p/2$ ) and interface ( $z = 0$ ). The slope of the stress intensity factor changes near  $a = 25\text{mm}$ . The length corresponds to radius of the patch. If the crack extends to the region out of patch, the growth rate can be found to be large from the slope of the curve.

Analyses for Mindlin plate element and three-dimensional element are compared in Figure 6 for the crack length  $a = 17.5\text{mm}$  and  $a = 35\text{mm}$ . Solid lines are for Mindlin plate element, and broken lines are for three-dimensional element. For unpatched case, difference between those analyses is small. The value for three-dimensional element becomes slightly higher for patched case. Profile of the distribution over the thickness is similar in both analyses.

Stress distribution  $\sigma_{yy}$  of the cracked panel repaired with the patch at the surface  $z = 0$  is shown in Figure 7 for  $a = 17.5\text{mm}$  and  $a = 35\text{mm}$ . The stress concentration is found at the crack tip. As the crack exceeds out of patched region as

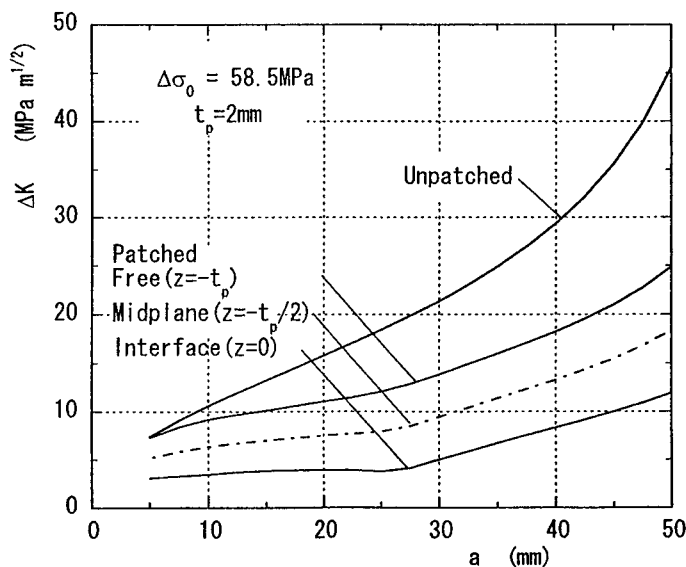


Figure 5 Amplitude of stress intensity factor by Mindlin plate element

$a = 35\text{mm}$ , the distribution become much complicate. Figure 8 shows stress distribution  $\sigma_{yy}$  including deformed form in view from unpatched surface in similar with Figure 7. In case of  $a = 35\text{mm}$ , deformation near the patched region become large due to interaction the crack and the patch. Relatively high stress occurs at the adhesive layer along the crack.

Crack growth behavior of the cracked panel with the bonded composite patch is tried to evaluate on the basis of following Paris relation.

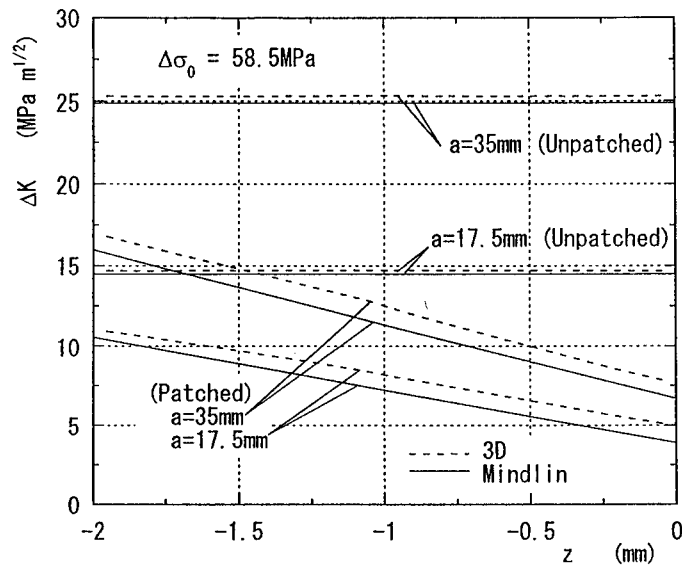


Figure 6 Comparison of analyses between Mindlin plate element and 3D element

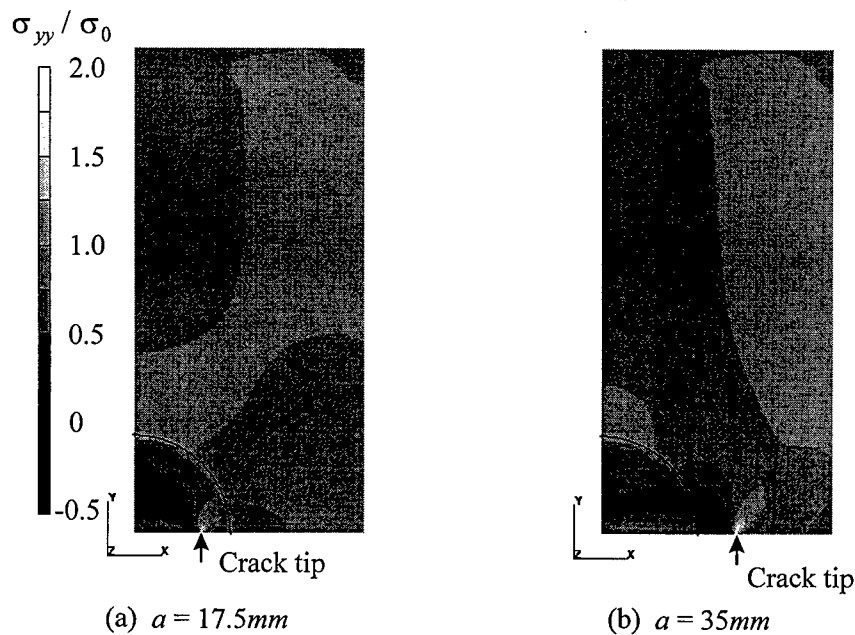


Figure 7 Stress distribution  $\sigma_{yy}$  of aluminum panel at the surface  $z = 0$ .

$$\frac{da}{dN} = C(\Delta K)^n \quad (6)$$

where  $N$  is the number of cyclic load, and  $C$  and  $n$  are material constants obtained from experiments. Figure 9 shows crack growth behavior under cyclic load. The marks in the figure indicate experimental data for crack growth. First, monolithic aluminum panel is tested from initial crack length  $2a_0=11.5$  mm. Material constants  $C$  and  $n$  are fitted from these experimental data. The values

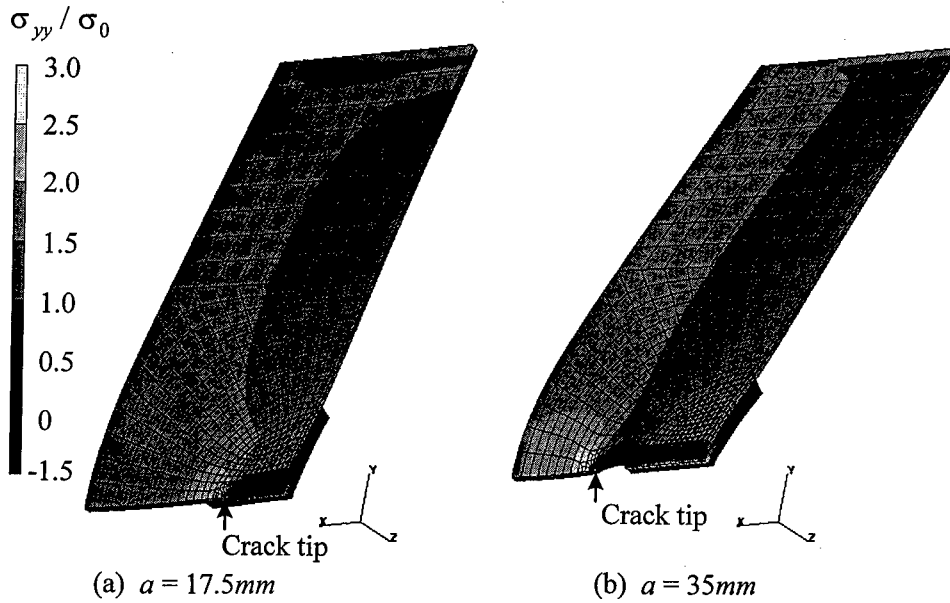


Figure 8 Stress distribution  $\sigma_{yy}$  and deformed form

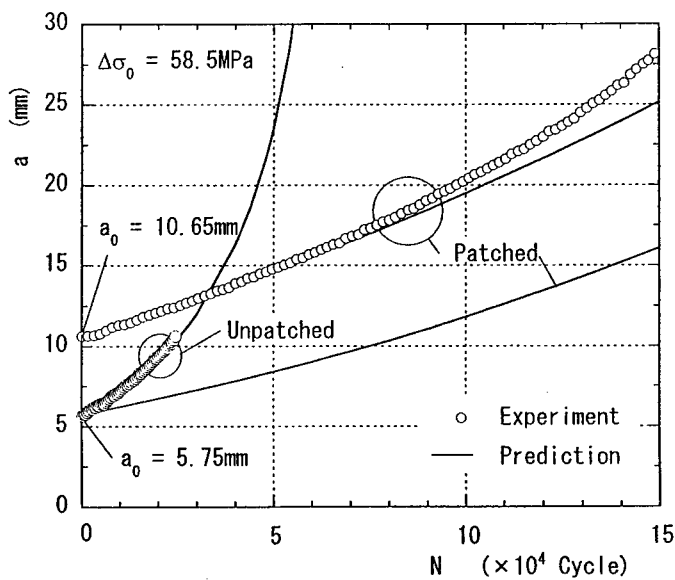


Figure 9 Crack growth behavior under cyclic load

are  $n=2.60$  and  $C = 1.15 \times 10^{-6} (\text{MPa}\sqrt{\text{m}})^{-2.60} \text{mm/cycle}$ . Solid lines in the figure are results by solving Eq.(6) with Runge-Kutta method numerically for unpatched and patched panels. Stress intensity factor at the midplane of the panel, which is calculated by Mindlin plate element, is used in the prediction of crack growth. In case of unpatched panel, the curve is fitted well to experimental data. For the patched panel, the growth of the crack is slow in comparison with unpatched case due to effect of repair. For initial crack length  $2a_0=21.3 \text{ mm}$ , the predicted result agrees well with experimental result except for large number of cyclic load. The stress intensity factor at large crack length may be underestimated because of extending delamination of patch with crack growth.

## Conclusions

Aluminum panels repaired with a bonded composite patch under cyclic load are considered. Using Mindlin plate element, stress intensity factor is evaluated and used to predict the crack growth of the panel. The predicted result agrees well with experimental result except for large number of cyclic load.

## Acknowledgement

This work was partly supported by Grant for Research and Development Applying Advanced Computational Science and Technology, Japan Science and Technology Corporation.

## References

1. L.R.F. Rose, 1982, "A Cracked Plate Repaired by Bonded Reinforcements," *International Journal of Fracture*, 18: 135-144.
2. C.T. Sun, J. Klug, and C. Arendt, 1996, "Analysis of Cracked Aluminum Plates Repaired with Bonded Composite Patches," *ALAA Journal*, 34: 369-374.
3. S. Naboulsi, and S. Mall, 1998, "Nonlinear Analysis of Bonded Composite Patch Repair of Cracked Aluminum Panels," *Composite Structures*, 41: 303-313.
4. R. Muller, and R. Fredell, 1999, "Analysis of Multiple Bonded Patch Interaction Simple Design Guideline for Multiple Bonded Repairs in Close Proximity," *Applied Composite Materials*, 6: 217-237.
5. R. Muller, R. Fredell, C. Guijt, and J. Dally, 1999, "Experimental Verification of Rose's Constant K Solution in Bonded Cracked Patching," *Applied Composite Materials*, 6: 205-216.
6. J.J. Denney, and S. Mall, 1997, "Characterization of Disbond Effects on Fatigue Cracks Growth Behavior in Aluminum Plate with Bonded Composite Patch," *Engineering Fracture Mechanics*, 57: 507-525.
7. E.F. Rybicki and M.F. Kanninen, 1977, "A Finite Element Calculation of Stress Intensity Factors by a Modified Crack Closure Integral," *Engineering Fracture Mechanics*, 9: 931-938.

## **Experimental Study of Repair Efficiency for Single-Side Composite Patches Bonded to Aircraft Structural Panels**

M. Sato, A. T. Yokobori, Jr., Y. Ozawa, T. Kamiyama, T. Miyanaga,  
P. W. R. Beaumont and H. Sekine

### **Abstract**

Fatigue response of cracked aluminum panels repaired with single-sided composite patches under thermal and humidity conditions was investigated from the experimental results. The repair efficiency was evaluated on the basis of Paris relation. The effects of thermal and humidity conditions on the repair efficiency were discussed by comparing with the numerical results.

### **Introduction**

In the repair of aging aircraft structures, crack patching using high strength composite materials is a simple and effective repair method for damaged components such as cracked aluminum panels in fuselage or wing. The composite patches bonded to cracked aluminum panels increase the damage tolerance and extend their fatigue lives by slowing crack growth.

This simple and highly effective repair method has been given attention and it becomes a major concern to evaluate the repair efficiency for the design of composite patch. Baker [1] showed experimentally and analytically that repair efficiency is reduced by significant cyclic disbonding in the bondline of the single-sided bonded patch repair. Denny [2] experimentally examined the effect of disbond locations and size in bonded reinforcement. Sun et al. [3] developed a finite element method for analyzing stress intensity factor of cracked panels repaired with single-

---

M. Sato and H. Sekine, Department of Aeronautics and Space Engineering, Tohoku University, 01 Aramaki-Aza-Aoba, Aoba-ku, Sendai 980-8579, Japan

A. T. Yokobori, Jr., Fracture Research Institute, Tohoku University, 01 Aramaki-Aza-Aoba, Aoba-ku, Sendai 980-8579, Japan

Y. Ozawa, Faculty of Education, Fukushima University, 2 Sugumichi, Asakawa, Matsukawa-Machi, Fukushima 960-1296, Japan

T. Kamiyama, Aerospace Division, Fuji Heavy Industries Ltd., 1-1-11 Yonan, Utsunomiya, Tochigi 320-8564, Japan

T. Miyanaga, Nippon Steel Chemical Co., Ltd., 15-1 Shinminato, Kisarazu, Chiba 292-0836, Japan

P. W. R. Beaumont, Department of Engineering, University of Cambridge, Trumpington Street, Cambridge, CB2 1PZ, U. K.

sided patch and investigated the interfacial disbond growth. Thermal effect on adhesively bonded composite repair was taken into consideration in the finite element analysis [4,5].

It is important to clarify the effects of thermal and humidity conditions on the repair efficiency because the repaired components in aging aircraft are exposed to the severe environmental conditions in the actual flight. This paper describes the results of fatigue tests for the cracked aluminum panel repaired with a single-sided composite patch under thermal and humidity conditions. From the experimental results, the effects of thermal and humidity conditions on the repair efficiency is discussed.

The repair efficiency for the bonded composite patch to the cracked aluminum panel is evaluated by the value of stress intensity factor at the fatigue crack tip. In this study, the stress intensity factor range of the repaired aluminum panel is calculated on the assumption that the relationship between the stress intensity factor range  $\Delta K$  and crack growth rate  $da/dN$  for the repaired aluminum panel obeys the Paris relation of the unrepaired aluminum panel. The Paris relation of unrepaired aluminum panel is shown as follows:

$$\frac{da}{dN} = C(\Delta K)^n \quad (1)$$

where  $C$  and  $n$  are the material constants of unrepaired aluminum panel. Using Paris relation with the data of  $da/dN$ , the  $\Delta K$  is calculated as follows:

$$\Delta K = \left( \frac{1}{C} \frac{da}{dN} \right)^{\frac{1}{n}} \quad (2)$$

The repair efficiency  $RE$  is defined as follows:

$$RE = 1 - \frac{\Delta K_p}{\Delta K_u} \quad (3)$$

where  $\Delta K_p$  and  $\Delta K_u$  denote the stress intensity factor ranges for the patched and the unpatched specimens.

## Test Specimens and Experimental Procedure

### Materials and Test Specimens

The specimens used in this study were designed to simulate the repair of aging aircraft structural panels. The geometry of the specimen is schematically shown in Figure 1. A rectangular aluminum panel (2024-T3 or 7075-T6) has a fatigue crack perpendicular to longitudinal direction (loading direction). The dimensions of the panel are  $250(L) \times 118(W) \times 2(t_{Al})$  mm and the nominal length of fatigue crack  $2a$  is 25 mm. The fatigue crack was pre-cracked from 10 mm machining cut to the desired nominal length. The bonded reinforcement was a circular glass/epoxy composite (Cytec Industries Inc.) with tapered end. The laminate configuration of the composite

patch is  $[0^\circ/0^\circ/0^\circ/\pm 45^\circ/0^\circ/0^\circ]_s$  with the fibers of  $0^\circ$  in the loading direction. The dimension of the patch is 50 mm in diameter with 3.2 mm in thickness. This thickness was designed according to the stiffness ratio,  $E_P t_P / E_{Al} t_{Al}$ , equal to 1.1 which provided a thickness  $t_P$  of 3.2 mm. Here,  $E$  and  $t$  are the Young's modulus and thickness, respectively, and the subscripts  $P$  and  $Al$  denote the composite patch and the aluminum panel. The composite patch completely bonded to one side of the cracked aluminum panel over the fatigue crack by using the adhesive film of AF-163-2K (3M Inc.) in the standard bonding process.

### Experimental Procedure

Fatigue tests are carried out by the use of the servohydraulic fatigue testing machine with thermal or humidity control unit. The thermal or humidity conditions are strictly controlled by those control units during the fatigue tests. In the fatigue tests under thermal conditions, specimens are kept at 353K ( $80^\circ\text{C}$ ), 300K ( $27^\circ\text{C}$ ) and 223K ( $-50^\circ\text{C}$ ) by this thermal control unit. On the other hand, the humidity control unit is used in the fatigue tests under humidity conditions. Before the fatigue tests, specimens are kept in the humidity conditions of 20%RH, 50%RH and 90%RH for 30 days in the chamber settled in the fatigue testing machine and the experiments under humidity conditions are conducted in the same environmental conditions.

The specimens are subjected to fatigue load in the longitudinal direction as shown in Figure 1. A sinusoidal loading with a 79.4 MPa peak stress, a stress ratio of 0.25 and a cycle frequency of 0.5 Hz are employed. Crack length is optically measured from the unpatched side of aluminum panel by using a traveling microscope. When the crack length is over 60 mm, the experiment is terminated.

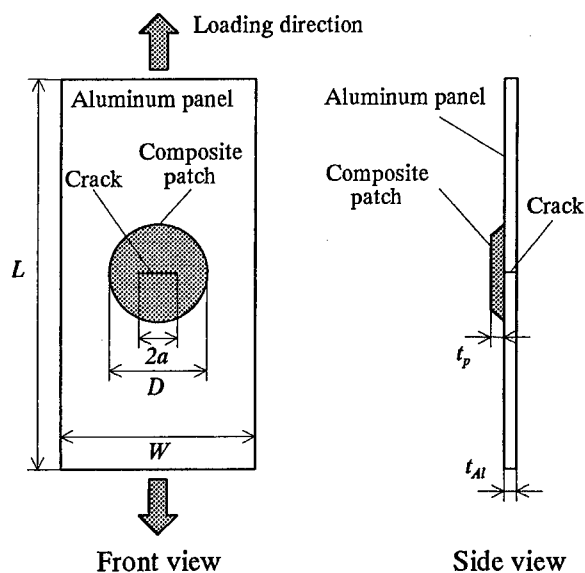


Figure 1 Cracked aluminum panel repaired with a single-sided composite patch



## Results and Discussion

### Fatigue Tests under Thermal Conditions

The results of fatigue tests under the thermal conditions for the cracked 2024-T3 aluminum panel repaired with a single-sided composite patch are shown in Figure 2. The data of the crack length for the repaired panels were measured at an interval of 1050~2140 cycles and the data at an interval of 6170~6604 cycles are shown. For the patched specimens in all thermal conditions, the disbond growth along the fatigue crack was observed after the fatigue test. However, the crack patching effect is revealed in retarding crack growth compared with the unpatched case. Compared the results under the thermal conditions, it is evident that there was a significant effect of thermal condition on the crack growth behavior.

The relationship between the crack growth rate  $da/dN$  and the crack length  $a$  is shown in Figure 3. The data of  $da/dN$  are calculated from the experimental data shown in Figure 2 by using seven point ASTM method [7]. To express the global relationship between  $da/dN$  and  $a$ , the data of  $da/dN$  are fitted with a quadratic curve,  $Aa^2 + Ba + C$ , by the method of least squares. The crack growth rates for the patched specimens are drastically reduced compared with those for the unpatched specimen. Those results also indicate the dependency of crack growth rate on thermal conditions. The crack growth rates at high temperature are larger than those at low temperature.

The repair efficiency under the thermal conditions is shown in Figure 4. The values of  $RE$  under the thermal conditions are obtained by using Paris relation with the data of  $da/dN$  on the quadratic curves shown in Figure 3. As the values of  $C$  and  $n$  in Paris relation,  $(C, n) = (3.64 \times 10^{-8}, 3.73)$ ,  $(7.15 \times 10^{-9}, 4.28)$  and  $(1.69 \times 10^{-10}, 5.54)$  are used respectively, for the specimens under the thermal condition of 353K, 300K and 223K. These values are obtained by using the experimental data in Ref. [6]. From those results, the effect of thermal conditions on the repair efficiency is

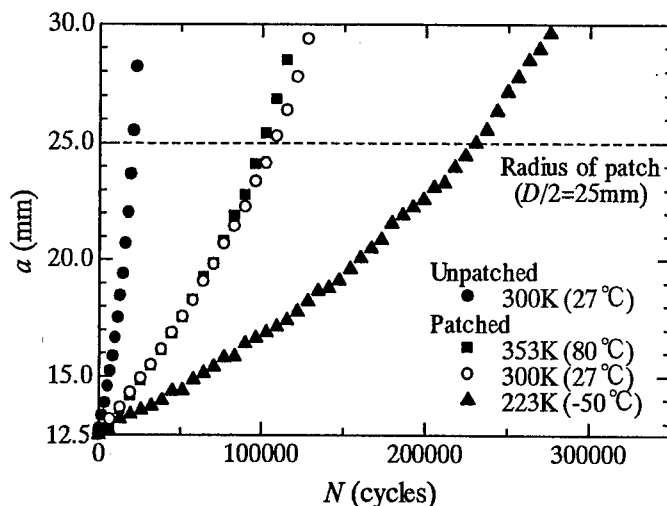


Figure 2 Crack length versus fatigue cycles under thermal conditions (2024-T3)

clarified. The repair efficiency at the high temperature takes the higher value than that at the low temperature. Compared repair efficiency at 223K with that at 353K, the maximum reduction in repair efficiency is about 0.08 in the value of  $RE$ . In Figure 4, the repair efficiency obtained by the finite element analysis using Mindlin plate elements is also shown. Two broken lines show the values of  $RE$  at the mid-plane and free surface of the cracked panel repaired with a completely bonded patch.

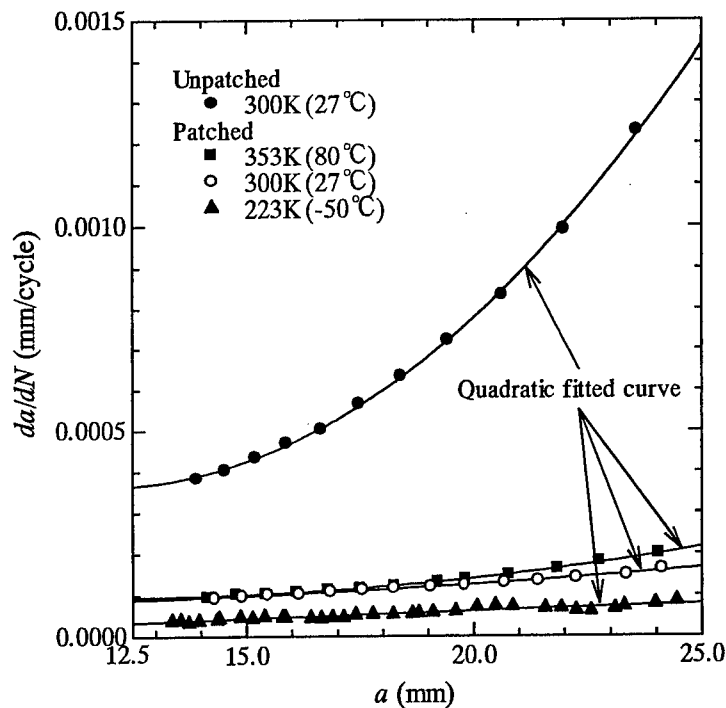


Figure 3 Crack growth rate versus crack length under thermal conditions (2024-T3)

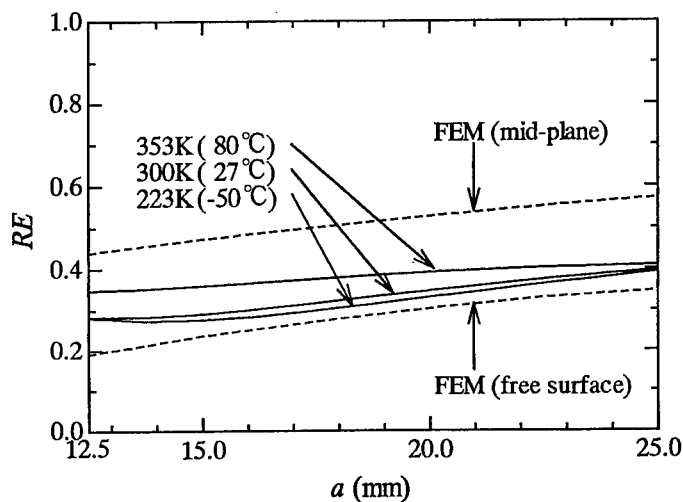


Figure 4 Repair efficiency under thermal conditions (2024-T3)

Compared with the numerical *RE* at the mid-plane, the *RE* under the thermal condition takes the lower value and shows the reduction in repair efficiency. The out-of-plane bending of the panel and the disbond growth with the extension of crack length can be considered to cause this reduction. The reduction due to the disbond growth is not clear because the reduction due to the out-of-plane bending is overestimated in this numerical analysis. However, a drastic change of the repair efficiency can not be found even the crack length extends.

### Fatigue Tests under Humidity Conditions

Figure 5 shows the results of fatigue tests under the humidity conditions for the cracked 7075-T6 aluminum panel repaired with a single-sided composite patch. The data of the crack length for the repaired panels were measured at an interval of 730~1062 cycles and the data at an interval of 2400~2885 cycles are shown. The crack growth is hasten when the specimen is under the high humidity condition. In all humidity conditions, the patched specimen exhibits a sufficient repair effect in retarding crack growth compared with the unpatched case, though the disbond grew during the fatigue test.

Figure 6 shows the crack growth rate versus crack length relationships for the patched specimens under the humidity conditions. The data of  $da/dN$  are calculated by using seven point ASTM method [7]. The data of  $da/dN$  are fitted with a quadratic curve,  $Aa^2+Ba+C$ , by the method of least squares. The effect of crack patching is obviously shown in this figure. Moreover, it is evident that the crack growth rates under the humidity conditions are significantly influenced by moisture absorption into the patch. For example, the crack growth rates for the specimen in 90%RH were greater than those in 25%RH.

Figure 7 shows the repair efficiency under the humidity conditions. The values of repair efficiency *RE* shown by solid lines are calculated by using Paris relation

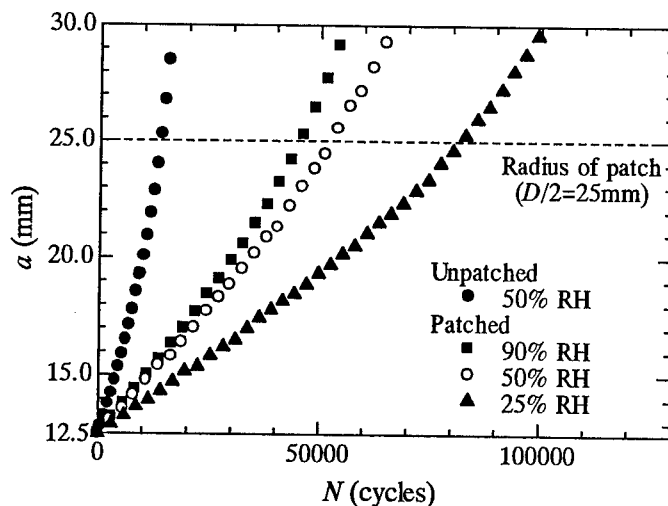


Figure 5 Crack length versus fatigue cycles under humidity conditions (7075-T6)

with the data of  $da/dN$  on the quadratic fitted curves shown in Figure 6. As the values of  $C$  and  $n$  in Paris relation,  $3.99 \times 10^{-8}$  and 3.76 are used respectively, which are obtained from the experimental results of the unrepaired aluminum panel. The effect of humidity conditions on the repair efficiency is clarified from those results. The values of  $RE$  in the low humidity condition are larger than those in the high humidity. Compared the repair efficiency in 90%RH with that in 25%RH, the maximum

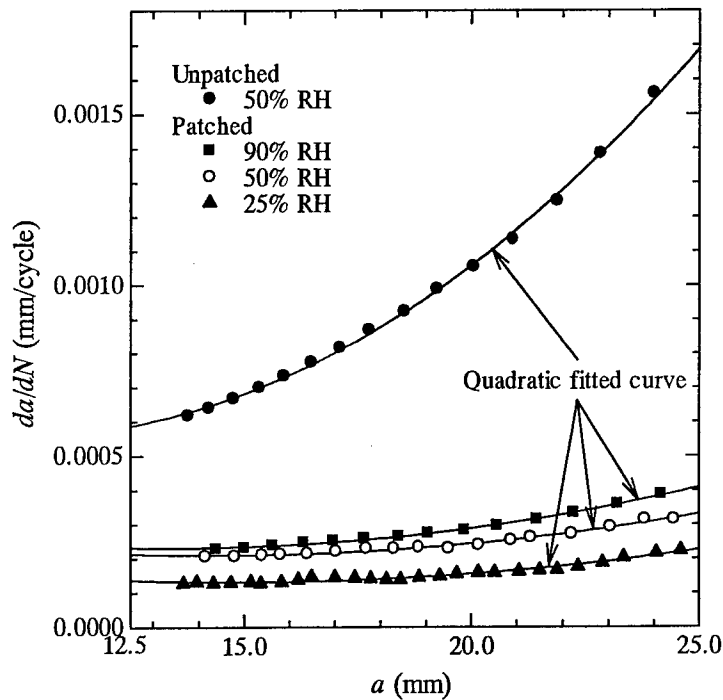


Figure 6 Crack growth rate versus crack length under humidity conditions (7075-T6)

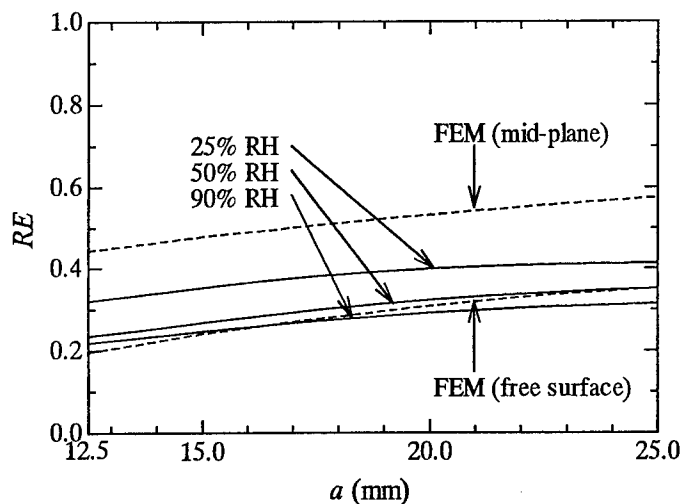


Figure 7 Repair efficiency under humidity conditions (7075-T6)

reduction in repair efficiency is about 0.11 in the value of  $RE$ . In Figure 7, the repair efficiency at the mid-plane and free surface obtained by the finite element analysis are also shown as broken lines. Compared with the numerical  $RE$  at the mid-plane, the repair efficiency under the humidity conditions takes lower value than the numerical one. This mismatch may be caused by the reduction of repair efficiency due to the out-of-plane bending and disbond growth. In this figure, the drastic change of repair efficiency with the extension of crack length can not be found, though the disbond should be grew as the crack length extends.

## Conclusions

The repair efficiency for the single-side composite patches bonded to aircraft structural panels is investigated through the fatigue tests under thermal and humidity conditions. The repair efficiency is evaluated on the basis of Paris relation, and the effects of thermal and humidity conditions on the repair efficiency is clarified. Compared with the numerical results of repair efficiency, the reduction of repair efficiency due to the out-of-plane bending of the aluminum panel and disbond growth during the fatigue tests is also discussed.

## Acknowledgment

This work was partly supported by Grant for Research and Development Applying Advanced Computational Science and Technology, Japan Science and Technology Corporation.

## References

1. A. A. Baker, 1993, "Repair Efficiency in Fatigue-Cracked Aluminum Components Reinforced with Boron/Epoxy Patches." *Fatigue and Fracture of Engineering Materials and Structures*, 16(7):735-765.
2. J. J. Denny, and S. Mall, 1997, "Characterization of Disbond Effects on Fatigue Crack Growth Behavior in Aluminum Plate with Bonded Composite Patch." *Engineering Fracture Mechanics*, 57(5):507-525.
3. C. T. Sun, J. Klug, and C. Arendt, 1996, "Analysis of Cracked Aluminum Plates Repaired with Bonded Composite Patches." *AIAA Journal*, 34(2):369-374.
4. S. Naboulsi, and S. Mall, 1997, "Thermal Effects on Adhesively Bonded Composite Repair of Cracked Aluminum Panels." *Theoretical and Applied Fracture Mechanics*, 26:1-12.
5. G. Renaud, and J. S. Hansen, 1998, "Thermal Model for Cracked Structures Repaired with Composite Patches" *AIAA Journal*, 36(12):2229-2235.
6. T. Yokobori, S. Konosu, and A. T. Yokobori, Jr., 1977, "Micro and Macro Fracture Mechanics Approach to Brittle Fracture and Fatigue Crack Growth." *Fracture*, 1:665-682.
7. American Society for Testing and Materials, 1992, "Standard Test Method for Measurement of Creep Crack Growth Rates in Metals." *ASTM standard*, E1457.

# Fracture Toughness

---

## **Mode II Interlaminar Properties under Static and Fatigue Loadings for CF/Epoxy Laminates with Different Fiber Surface Treatment**

M.Hojo, S.Matsuda, S.Ochiai, N.Tsujioka, Y.Nakanishi, Z.Maekawa and A.Murakami

### **Abstract**

Effect of fiber-surface treatment on delamination fatigue under mode II loading was investigated for unidirectional CF/Epoxy laminates. Two types of laminates were made from surface-treated or surface-non-treated carbon fiber, and a common epoxy matrix. Tests were carried out using end notched flexure (ENF) specimens. Stabilized mode II static tests showed that the fracture toughness of the surface-treated CFRP was 30% higher than that of non-treated CFRP. Fatigue crack growth resistance of the surface-treated CFRP was higher than that of non-treated CFRP at higher crack growth rate. However, the effect of fiber surface treatment was negligible near the threshold region. At higher growth rate, the interfacial fracture occurred prior to the matrix fracture near the crack tip for the non-treated CFRP. Then, the fracture mechanism was controlled by the interfacial fracture. On the other hand, the resin fracture with plastic deformation occurred prior to the interfacial fracture near the crack tip for the surface-treated CFRP. Then, the fracture mechanism was controlled by the resin fracture. Near the threshold region, the ratio of the resin fracture was rather large without respect to the fiber-surface treatment. The main fracture mechanisms near the threshold region was only controlled by the matrix resin. This fact was well correlated to the fact that the threshold value was insensitive to the fiber-surface treatment.

### **Introduction**

The most common damage mechanism in laminated composite structures is delamination. Although this topic has been investigated for more than twenty years, most of these approaches are rather macroscopic, and the role of mesoscopic components of composite laminates such as resin and interface has not been understood in detail.

---

M.Hojo, S.Ochiai and Y. Nakanishi, Mesoscopic Materials Res. Ctr., Graduate School of Engineering, Kyoto University, Kyoto 606-8501, Japan

S.Matsuda and A.Murakami, Dept. Chemical Engineering, Himeji Institute of Technology, Himeji 671-2201, Japan

NTsujioka, Asahi Chemical Co. Ltd., Moriyama 524-0002, Japan

Z.Maekawa, Div. of Advanced Fibro-Science, Kyoto Institute of Technology, Kyoto 606-8585

Several researches have already been carried out to investigate the effect of the surface treatment of fiber on the macroscopic fracture behavior [1,2]. However, these research works are based on laminates produced in laboratories. Thus, it is rather difficult to clarify only the effect of the fiber surface treatment because other mesoscopic factors such as the geometrical arrangement of fiber also changes simultaneously for laminates made in house.

We have launched a series of research works to investigate the effect of surface treatment on the composite properties by producing fibers and prepregs at an industrial manufacturing plant. The influences on the interfacial strength and the static mode I interlaminar properties have already been reported [3,4].

In the present study, the effects of fiber surface treatment on the interlaminar fracture toughness and the delamination fatigue crack growth behavior under mode II loading were investigated for unidirectional CF/epoxy laminates. The mechanism of the effect of the fiber-surface treatment was discussed on the bases of fracture mechanical consideration and microscopic observation.

## Experimental Procedure

### Material and Specimen

The carbon fiber used in this study is PAN based AT400 (Asashi Chemical, strength=3.9GPa, modulus=240GPa). The surface treatment of fiber was carried out by the anodic oxidation method [5] in 8% nitric acid aqueous at the amount of electricity of  $27.6 \text{ C/m}^2$ . The surface oxygen content on the carbon fiber surface was 0.15 by X-ray photoelectron spectroscopy (XPS), and the acid function was  $12 \times 10^{-6} \text{ eq/m}^2$  by neutralization titration. Non-treated fiber was also used for comparison. Two types of laminates were made from surface-treated or surface-non-treated carbon fiber and a common bisphenol A type epoxy matrix (modified epoxy resin with lower cross-linking density and higher toughness). These are designated as surface-treated CFRP and non-treated CFRP. Unidirectional laminates,  $(0)_{26}$  ( $V_f=54\%$ ), of the thickness of 3mm were molded in an autoclave. The manufacturing process of fiber and prepregs was fully

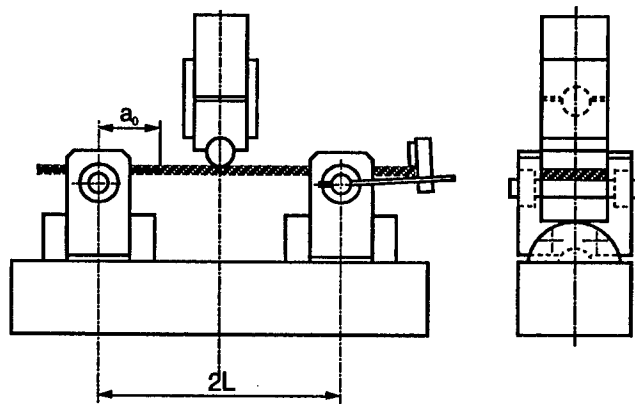


Figure 1 ENF specimen and loading apparatus.



controlled to avoid any influences such as irregularity coming from handmade prepregs etc. This controlled process is essential because interlaminar fracture properties are very sensitive to the distribution of fibers and matrix in mesoscopic scale at the resin rich prepreg interface.

End notched flexure (ENF) specimens (width:  $B = 25$  mm, nominal thickness  $2h = 3$  mm, length: 170 mm) were used for tests under static and fatigue loadings. Figure 1 shows the specimen and the loading apparatus. The distance between both supports,  $2L$ , was 100 mm, the length of the starter slit was 25 mm, and the crack length,  $a$ , is defined as the length between the crack tip and the support. Universal joints were used for the loading point and the supports in order to avoid uneven loading in the width direction of the specimen. Starter slits were introduced into the specimen by inserting 6  $\mu\text{m}$  thick polyimide films (coated with a release agent) during molding at mid-thickness. Specimen edges were polished using abrasive papers and diamond paste to make crack-length measurement easier. For static tests, precracks were introduced under mode II fatigue loading. For fatigue tests, no precrack was introduced.

#### Calculation of Fracture-Mechanical Parameters

Energy release rate,  $G$ , was calculated from the relation between the compliance,  $C$ , and the crack length,  $a$ , using the following equation:

$$G = P^2/(2B) dC/da \quad (1)$$

where  $P$  is the applied load. The relation between  $C$  and  $a$  is expressed by the following equation [6]:

$$E'BC(2h)^3 = \xi_0 + \xi_1 a^3 \quad (2)$$

where  $E'$  is the flexural modulus. Parameters  $\xi_0$  and  $\xi_1$  are computed from experimental calibration by using a least square program for each specimen.

#### Static and Fatigue Tests

Tests were carried out in a computer-controlled 10 kN servohydraulic testing machine (Shimadzu, EHF-ED-1) [6]. Static interlaminar fracture toughness tests were carried out by controlling the crack shear displacement (CSD,  $\delta$ ) to stabilize the crack growth. The CSD rate was 0.03 mm/min based on JIS K7086-1993. The initial values of the fracture toughness,  $G_{IIc}$ , were calculated at the onset of nonlinearity of the initial load-displacement curve (NL), 5% offset point (5%), and the maximum load point ( $P_{max}$ ). The fracture toughness values during crack propagation are expressed as  $G_{IIR}$ .

Delamination fatigue crack growth tests were carried out with our original software[6,7]. In each test, the stress ratio,  $R$ , of the minimum load to the maximum load was kept constant to be 0.5. The load-shedding rate,  $1/G(dG/da)$ , was also controlled to be  $-0.1\text{mm}^{-1}$ . The frequency of stress cycling was 10Hz. The length of the crack was

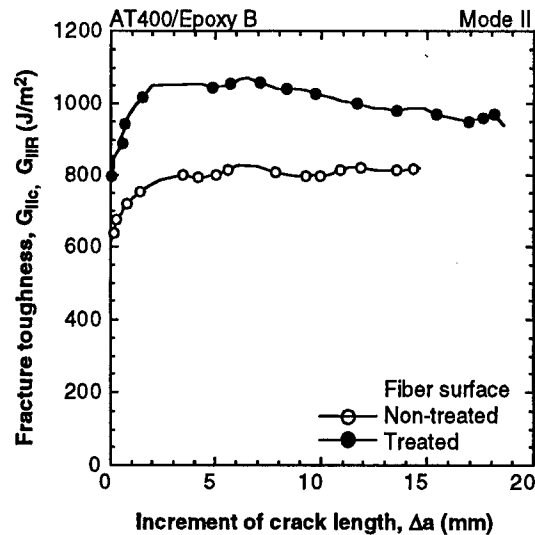


Figure 2 Effect of fiber surface treatment on mode II static crack growth resistance curves.

computed from Equation (2). The tests were carried out in laboratory air.

## Experimental Results and Discussion

### Static Fracture Toughness

The relation between the fracture toughness and the increment of the crack length is shown in Figure 1. The fracture toughness values increased with the increment of the crack length,  $\Delta a$ , and then levelled off where  $\Delta a$  was larger than 3 mm for both laminates [6]. For the case of the non-treated CFRP,  $G_{IIc}$  at NL point was 610 J/m², and that at  $P_{max}$  point (= 5% point) was 750 J/m².  $G_{IIc}$  at NL point was 770 J/m², and that at  $P_{max}$  point (= 5% point) was 1000 J/m² for surface-treated CFRP. The average of the propagation values where  $\Delta a$  was larger than 3 mm,  $G_{IIa}$ , was 810 J/m² and 1010 J/m² for non-treated and surface-treated CFRP, respectively. The fracture toughness of the surface-treated CFRP was 25 to 30% higher than that of non-treated CFRP. This increase was almost the same for the initial values and the propagation values.

### Fatigue Crack Growth Behavior

Figure 3 compares the fatigue crack growth behavior between surface-treated and non-treated CFRP. The crack propagation rate,  $da/dN$ , is expressed as a power function of the maximum energy release rate,  $G_{II,max}$ , in the region where  $da/dN$  is larger than  $10^{-9}$  m/cycle. Below this region,  $da/dN$  deviates to the lower rate from the power functions, and there exists the growth threshold for fatigue cracks. The figures associated with the straight lines indicate the exponents of the power functions. The threshold

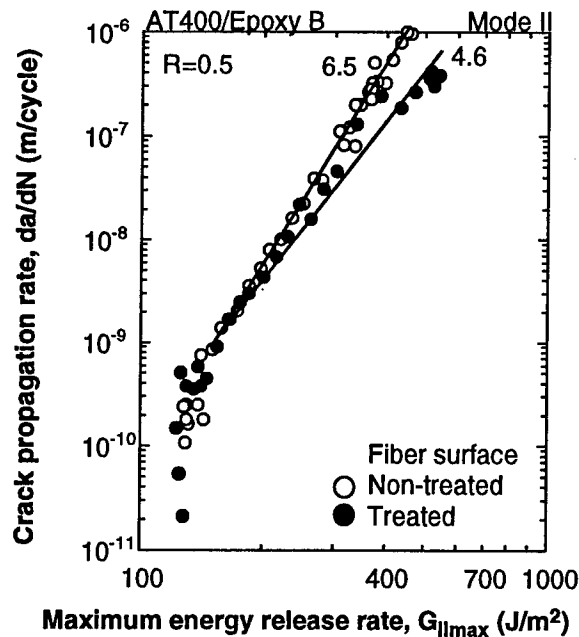


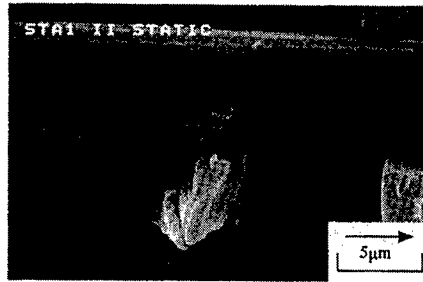
Figure 3 Effect of fiber surface treatment on mode II fatigue crack growth behavior.

value,  $120 \text{ J/m}^2$ , was insensitive to the fiber surface treatment. In the higher rate region,  $da/dN$  for surface-treated CFRP was smaller than that for non-treated CFRP. The exponents of the power functions also showed the same tendency. Thus, the fatigue crack growth resistance of the surface-treated CFRP is higher with higher ductility.

#### Fractographic Observation

Figures 4 and 5 show the scanning electron micrographs of the fracture surfaces under static and fatigue loadings for surface-treated and non-treated CFRP. For the case of static fracture toughness tests, interfacial fracture was dominant for the non-treated CFRP. Debonding of resin at the interface was often observed. On the other hand, the areal ratio of interfacial fracture and resin fracture was almost the same for the surface-treated CFRP. The fracture of resin brings hackles (microcracks perpendicular to the principal stress) and their plastic deformation. This is why the fracture toughness of the surface-treated CFRP was higher.

For fatigue fracture, interfacial fracture was about 60% at the high rate region, and about 40% near the threshold region for the non-treated CFRP. Large hackles of the interval of  $10 \mu\text{m}$  were observed at the high rate region. For the case of the surface-treated CFRP, 70% of the fracture surface was resin fracture at the high rate region, and the areal ratio increased to 90% near the threshold region. Only small hackles of the interval of 1 to  $5 \mu\text{m}$  were observed at the high rate region. Near the threshold, resin part was rather flat, and composed of small hackle like patterns of the interval of less than



(a) Static fracture

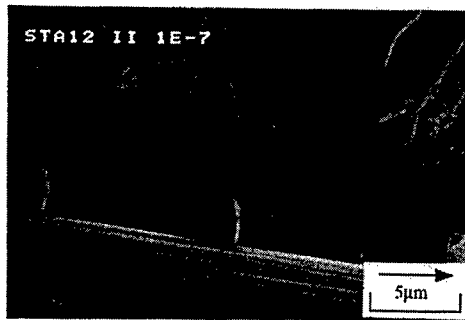
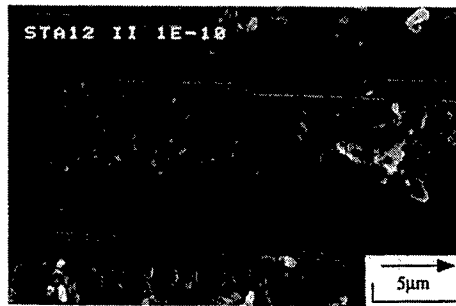
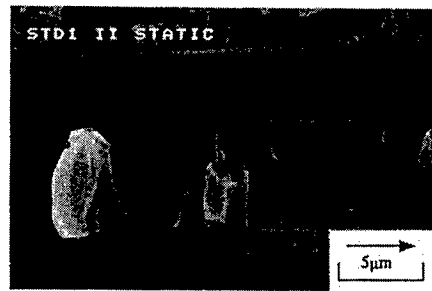
(b) Fatigue,  $da/dN = 1 \times 10^{-7}$  m/cycle.(c) Fatigue,  $da/dN = 1 \times 10^{-10}$  m/cycle.

Figure 4 Scanning electron micrographs of fracture surfaces for non-treated CFRP.



(a) Static fracture

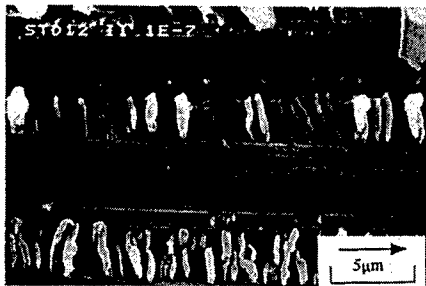
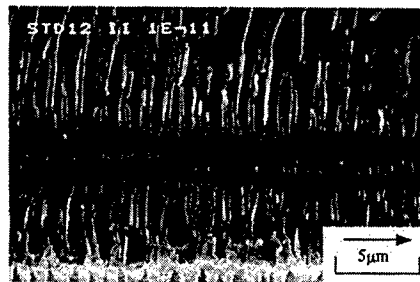
(b) Fatigue,  $da/dN = 1 \times 10^{-7}$  m/cycle.(c) Fatigue,  $da/dN = 1 \times 10^{-10}$  m/cycle.

Figure 5 Scanning electron micrographs of fracture surfaces for surface-treated CFRP.

Table I. Summary of features of fracture surfaces, observed using scanning electron microscopy.

	Non-treated CFRP			Treated CFRP		
	Static fracture	Fatigue fracture		Static fracture	Fatigue fracture	
		$1 \times 10^{-7}$ m/cycle	$1 \times 10^{-10}$ m/cycle		$1 \times 10^{-7}$ m/cycle	$1 \times 10^{-10}$ m/cycle
Main fracture path	Interface	Interface	Resin	Interface/Resin	Resin	Resin
Areal ratio of interfacial fracture	80%	60%	40%	50%	30%	10%
Interval of hackles	10 $\mu$ m	10 $\mu$ m	< 1 $\mu$ m	10 $\mu$ m	1-5 $\mu$ m	< 1 $\mu$ m
Microscopic delamination between fiber and matrix	○	○	○	×	×	×
Plastic deformation	○	×	-	○	○	-

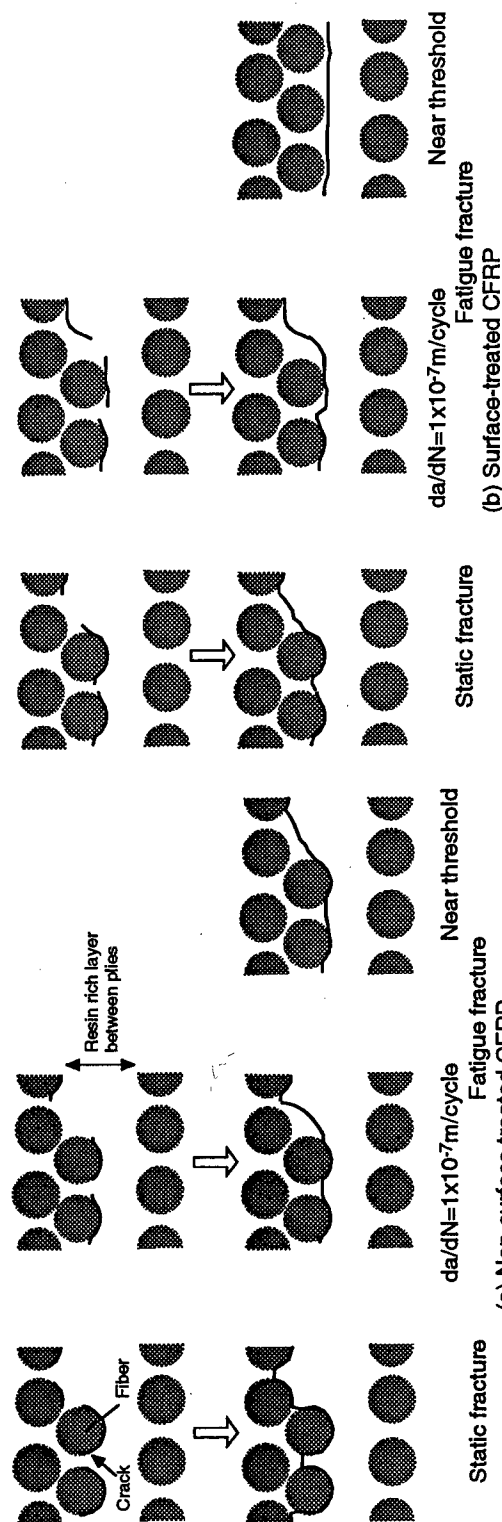


Figure 6 Schematic drawing of fracture process in transverse section of CFRP with and without fiber surface treatment.

1  $\mu\text{m}$  without respect to the surface treatment. The main fracture mechanism near the threshold region was controlled by the matrix resin for both surface-treated and non-treated CFRP, and this was well correlated to the fact that the threshold value was insensitive to the fiber surface treatment. The results of the fractographic observation was summarized in Table I.

Observation of transverse section of the specimen near the crack tip was also carried out in order to clarify whether interfacial fracture or resin fracture first occurred at the crack tip under fatigue loading. While the interfacial fracture occurred prior to the matrix fracture for the non-treated CFRP in the higher growth rate region, the matrix fracture occurred in advance for the surface-treated CFRP. This difference was schematically shown in Figure 6. This difference of the fracture mechanism is responsible for the higher  $da/dN$  and the larger exponent of the power function of the non-treated CFRP.

### Concluding Remarks

Fiber surface treatment had different effect on mode II interlaminar fracture under static and fatigue loadings. Interlaminar fracture toughness of surface-treated CFRP was about 25 to 30% higher than that of non-treated CFRP. On the other hand, the growth threshold of the delamination fatigue crack was insensitive to the fiber surface treatment. This difference of the effect of the surface treatment was explained by the difference of the fracture path in mesoscopic scale based on the microscopic observation.

### References

1. L.M.Manocha, 1982. "Role of Fiber Surface-Matrix Combination in Carbon Fiber Reinforced Epoxy." *J. Materials Science*, 17: 3039-3044.
2. M.S.Madhukar and L.T.Drzal, 1991. "Fiber-Matrix Adhesion and Its Effect on Composite Mechanical Properties." *J. Composite Materials*, 25: 932-957.
3. N.Tsujioka, Z.Maekawa, H.Hamada, and M.Hojo, 1997. "Effect of Surface Oxidation and Sizing Treatment of Carbon Fiber on Interfacial Adhesion." *J. Society of Materials Science, Japan*, 46: 163-169.
4. M.Hojo, S.Ochiai, N.Tsujioka, M.Kotaki, H.Hamada, and Z.Mekawa, 1995. *High Technology Composites in Modern Applications, Proc. COMP'95*: Univ. of Patras, Greece, pp. 30-36.
5. Y.Nakanishi and N.Ikuta, 1996. "Interphase of FRP and Its Chemical Control." *J. Society of Materials Science, Japan*, 45: 1307-1315.
6. M.Hojo, S.Matsuda, T.Higuchi, and S.Ochiai, 1997. "Fracture mechanism for Mode II Propagation of Delamination Fatigue Cracks in CF/PEEK Laminates." *J. Society of Materials Science, Japan*, 46: 366-373.
7. M.Hojo, S.Ochiai, C.-G.Gustafson, and K.Tanaka, 1994. "Effect of Matrix Resin on Delamination Fatigue Crack Growth in CFRP Laminates." *Engineering Fracture Mechanics*, 49: 35-47.

## Highly Accurate Mode-Separated Energy Release Rates for Delamination Cracks

Hae-Soo Oh<sup>1</sup>

### Abstract

Following Irwin's argument, the energy release rates are computed by using nodal forces a head of the crack front and relative displacements behind the crack front. Furthermore, the quarter-point singularity elements were used for most finite element computations. Recently, Babuska and Oh introduced a new approach, called the method of auxiliary mapping (MAM), that can effectively handle singularities in the framework of the  $p$ -Version of the FEM. In this paper, this new approach is modified so that it can yield highly accurate mode-separated energy release rate for the cracks in composite materials. The results obtained by this method are more accurate than those obtained by the conventional methods. It is known that the mode separated energy release rates for interfacial cracks of bimetals do not converge. However, we claim that in practical point of view, the mode-separated energy rates of interlaminar cracks of a laminate, whose layers are of the same material and may have different fiber orientations, converge.

## 1 Mode-Separated Energy Release Rate

Consider a crack with area  $a$  in a deformable ideally brittle (the plastic deformation is negligible) continuum subjected to arbitrary loading. If the applied load is time independent and the crack grows slowly, and if  $\gamma$  represents the energy required to form a unit of new material surface, we have ([3])

$$G = -\frac{\partial \Pi}{\partial a} = \frac{\partial \Gamma}{\partial a} = 2\gamma, \quad (1.1)$$

which represents the fracture criterion for the crack growth. Here  $\Pi = U - W$  is the potential energy of the system. If the work of the body force is ignored, Equation (1.1) takes the form

$$G = -\frac{\partial U}{\partial a}, \quad (1.2)$$

that is called the **Strain Energy Release Rate**.

Consider the two dimensional case where the crack extends along its own direction in a self-similar manner. Then the central difference approximation (CDA) for the energy release rate is the following.

$$G \approx \frac{U(a + \Delta) - U(a - \Delta)}{2\Delta}. \quad (1.3)$$

---

<sup>1</sup>Department of Mathematics, University of North Carolina at Charlotte, Charlotte, NC 28223. e-mail: hso@math.uncc.edu

On the other hand, by observing that the work necessary to extend the crack from  $a$  to  $a + \Delta$  is the same as that necessary to close the crack tip from  $a + \Delta$  to  $a$ , Irwin ([8],[9]) obtained the energy release rate as

$$\begin{aligned} G = & \lim_{\Delta \rightarrow 0} \frac{1}{2\Delta} \int_0^\Delta \sigma_y(r, 0) [u_y(\Delta - r, \pi) - u_y(\Delta - r, -\pi)] dr \\ & + \lim_{\Delta \rightarrow 0} \frac{1}{2\Delta} \int_0^\Delta \tau_{xy}(r, 0) [u_x(\Delta - r, \pi) - u_x(\Delta - r, -\pi)] dr, \end{aligned} \quad (1.4)$$

which is known as the virtual crack closure technique (VCCT). Here  $u_x$  and  $u_y$  represent the  $x$ - and the  $y$ - component of the displacement vector, respectively. Two integrals in this formula are called the opening mode (Mode I) and the sliding mode (Mode II), respectively. They are denoted by  $G_I$  and  $G_{II}$ , respectively.

In ([14]), the Central Difference Approximation (1.3) was discarded because (a) the computation involves differences of large numbers divided by a small number and hence the resulting value is not accurate, and (b) this procedure involves two finite element runs. However, in this paper, (1.3) is employed to estimate the total energy release rate. Moreover, it is shown that CDA Approach (1.3) is even better than the VCCT Approach in computations of total energy release rates.

It is easy to show that the mode-separated energy release rates are  $\Delta$ -independent. However, if a crack is along the interface of two dissimilar materials, displacement functions and stress tensor are oscillating singular near the crack tip. Because of the oscillating factor, the mode-separated energy release rates  $G_I$  and  $G_{II}$  are  $\Delta$ -dependent. Actually, it has been known in the computational mechanics community ([2],[4],[10],[13]) that  $G_I$  and  $G_{II}$  of bimaterial interface cracks do not converge.

We believe that the mode-separated energy release rates for interfacial cracks of isotropic bimaterials do not converge. However, in this paper, by applying the method of auxiliary mapping (MAM) developed by Bábúška and Oh ([5]), it is claimed that, in practical point of view,  $G_I$  and  $G_{II}$  for interfacial cracks of laminates, whose layers are of the same materials, virtually converge.

Conventional methods to compute the energy release rate are to use nodal forces ahead of the crack tip and relative displacements behind the crack tip with quarter point singular elements in the framework of the  $h$ -version of FEM. On the other hand, our method is to use the Power and the Exponential Auxiliary Mappings, defined below, to deal with singularities of type  $r^\lambda \sin(\varepsilon \log r)$ .

## 2 A New Approach to compute Energy Release Rates

For brevity, we consider  $G_I$  in two dimensional case. Let us consider the line integral

$$\frac{1}{2\Delta} \int_0^\Delta \sigma_y(x, 0) \delta u_y(x - \Delta, 0) dx, \quad (2.1)$$



where  $\delta u_y(x - \Delta, 0) = [u_y(\Delta - r, \pi) - u_y(\Delta - r, -\pi)]$  is the relative displacement. Suppose the stress tensor  $\sigma_y$  and the  $y$ -displacement  $u_y$  are oscillating singular functions. Then, in order to get accurate energy release rate, we have to overcome the following problems:

- Low accuracy of FE solutions in the presence of the singularities and the poor approximability due to the oscillating factor  $\varepsilon$ .
- Low accuracy in Numerical Integration of singular functions in case of using singular basis functions, constructed through quarter point singularity elements method or MAM, for the Finite Element solution.

We are going to deal with these problems by introducing two mappings which map the  $\xi$ - $\eta$  plane to the  $x$ - $y$  plane in the following. We define the **power auxiliary mapping** by

$$\varphi_{pow}^\beta(\xi, \eta) = (\hat{r}^\beta \cos(\beta\hat{\theta}), \hat{r}^\beta \sin(\beta\hat{\theta})), \quad (2.2)$$

and the **exponential auxiliary mapping** by

$$\varphi_{exp}^{(\beta_1, \beta_2)}(\xi, \eta) = (e^{\beta_1 \xi} \cos(\beta_2 \eta), e^{\beta_1 \xi} \sin(\beta_2 \eta)) \quad (2.3)$$

respectively. Here  $(\hat{r}, \hat{\theta})$  is the polar coordinates of  $(\xi, \eta)$ .

Let  $\Omega_S = [-h, h] \times [-h, h]$  be the square neighborhood of the crack tip, where  $h$  is the layer thickness. For example, discretize  $\Omega_S$  into eight triangular elements and 16 quadrilateral elements as shown in Fig. 1. Then  $(\varphi_{pow}^2)^{-1}(\Omega_S) = \hat{\Omega}_S$  consists of eight curved triangular elements and 16 curved quadrilateral elements as shown in Fig. 1 (Note that the mapped triangular elements have one curved side and the mapped quadrilateral elements have two curved sides).

Let  $E$  be an element in  $\Omega_S$  and  $\hat{E} = (\varphi_{pow}^2)^{-1}(E)$  be the corresponding element in  $\hat{\Omega}_S$ . Let  $\hat{\Psi}_{\hat{E}}$  be the elemental mapping of blending type from the standard element  $\Omega_{st}^{(*)}$  to  $\hat{E}$ . Then the induced singular elemental mapping  $\Psi_E^S : \Omega_{st}^{(*)} \rightarrow E$ , defined by

$$\Psi_E^S = \varphi_{pow}^2 \circ \hat{\Psi}_{\hat{E}},$$

generates the singular shape functions on  $E$  which resemble the crack singularity. For the elements which are not in  $\Omega_S$ , we assign the standard linear elemental mapping. Then the curved sides in  $\hat{\Omega}_S$  can be parameterized so that the singular elemental and the standard elemental mappings can induce an "exactly and minimally conforming" (continuous singular basis functions) finite element space  $S^p(\Omega, \mathcal{T}, \mathcal{M})$ . Here  $\mathcal{T}$  denotes a specific mesh on the physical domain  $\Omega$ ,  $p$  is the polynomial degree uniformly assigned to the elements in  $\mathcal{T}$ , and  $\mathcal{M}$  is the vector of elemental mappings assigned to each element in  $\mathcal{T}$ .

Suppose a fiber-reinforced material is a laminate whose layers are of the same material and may have different fiber orientation. Then it can be proved by using similar arguments to those in ([7],[12]) that the oscillating factors of inter-laminar cracks of such laminates are expected to be very small. In other words, the mode-separated energy release rates  $G_I$  and  $G_{II}$  for such fiber-reinforced materials are

virtually constant when

$$10^{-9} \leq \frac{\Delta}{h} \leq 10^{-1}.$$

Moreover, if  $\frac{\Delta}{h} \leq 10^{-9}$ , then  $\Delta$  is smaller than the diameter of the fiber and hence the  $\Delta$ -neighborhood of the crack tip does not contain any fiber. In other words, the  $\Delta$ -neighborhood of a crack consists of a homogeneous material (resin only) and hence we may claim that  $\varepsilon = 0$  whenever  $\frac{\Delta}{h} \leq 10^{-9}$ . Therefore we have the following.

**Theorem 2.1** *The mode-separated energy release rates for the inter-laminar crack of a laminate whose layers are of the same material and may have different fiber orientations virtually converge.*

### 3 Computational Results

**A: Cracks in homogeneous materials.** Since the displacement functions near crack tip of homogeneous isotropic materials are non-oscillating singular functions, the mode-separated energy release rates converge. In this section, the new method presented in section 2 yields better results than the conventional method that use quarter point (or cubic) singularity elements in the framework of the  $h$ -version.

We assume that  $\nu = 0.3$ ,  $E = 10^6$  and the computations are for plain strain.

**Example 1. Center-cracked tension specimen (CCT):** We consider a Center-Cracked Plate  $[-b, b] \times [-h, h]$  with crack length  $2a$  under uniform tension  $S$  as shown in Fig. 2(a). Suppose we choose  $S = 100$ ,  $b = 1.0$ ,  $a = 0.8$ ,  $h = 2$ . Then by appendix 2.1 of [3], we obtain  $G_I = 0.0754556$ .

Fig. 3 shows that the relative error of the best  $G_I(p = 9)$  is 0.02%. Nevertheless, the best  $G_I$  in ([9]), obtained by using cubic singularity elements, has 0.3% in the relative error. By comparing  $G_I$  and  $G_{(I)}$  from Table 1, one can see the superiority of the new method over the conventional  $p$ -method (that is, 0.02% verses 11% in relative error when  $p = 9$ ). Relative errors in percent of total strain energy,  $G_I$ ,  $G_{(I)}$ , and  $G_{total}$  are depicted in Fig. 3.

**Example 2. Single Edge-Notched specimen (SEN):** The second example is Single edge-notched plate  $[-a, b - a] \times [-h, h]$  under uniform tension  $S$  as Fig. 2(b).

In this example, we use the crack length  $a = 0.55$  and  $b = 1.0$ ,  $h = 2.0$ , and the remote uniform traction load is  $S = 100$ . Then by appendix 2.1 of [3], we have  $K_I = 440.6271928$  and  $G_I = (1 - \nu^2)K_I^2/E = 0.176678$ .

Fig. 2(d) is a finite element mesh for the new method which consists of eight triangular elements and 28 quadrilateral elements. For the mapping zone (the neighborhood of the crack tip) for the new method, we select the eight triangular elements and the eight quadrilateral elements that are next to the triangular elements. And the SENS was analyzed in the same ways as the previous example. The results are displayed in Fig 4.

Fig. 4 shows that the relative error of  $G_I$  is 0.6% when  $p = 9$ . However, the best  $G_I$  in [9], obtained by using cubic singularity elements, has 3.3% in the relative error.

By comparing  $G_I$  and  $G_{(I)}$  from Fig. 4, once again, one can see the superiority of the new method over the conventional  $p$ -method (i.e., 0.6% versus 11.8% in relative error when  $p = 9$ ). Relative errors in percent of total energy,  $G_I$ ,  $G_{(I)}$ , and  $G_{total}$  are depicted in Fig. 4.

**B. Interfacial Cracks between orthotropic layers** Now, we consider the inter-laminar cracks of laminates of fiber-reinforced layers. If layers are of the same material and may have different fiber directions, the oscillating factor  $\varepsilon$  (the order of discontinuity between layers) expected to be very small.

For various tests of inter-laminar cracks of laminates that consist of fiber-reinforced layers with various fiber angles,  $G_I$  and  $G_{II}$  are virtually constant when  $10^{-9} < \Delta/h < 10^{-1}$ . Moreover, if  $\Delta/h < 10^{-9}$ , then the crack tip is well inside the homogeneous materials (resin). In other words, in fiber-reinforced composite materials, if  $\Delta$  is very small, then physics of the  $\Delta$ -neighborhood of the material is changed from orthotropic (fiber and resin) to isotropic (resin only). Hence the oscillating factor  $\varepsilon$  is 0 for such case.

In order to compare our results with the results reported in [2], the engineering properties of ply with unidirectional fiber used in examples of this subsection are the same as those in [2].

### Example 3.

The first laminate specimen [0/90/0] consists of plane strain drop-ply configuration of  $0^\circ$  and  $90^\circ$  graphite-epoxy plies as shown in Fig. 5, which is Test case # 1 of [2]. In this example, the thickness  $h$  of the layer next to the inter-laminar crack is 0.125, the crack length is 0.4, and  $\Delta$  denotes the side length of the inner most eight triangular element. The singular zone for our method is the 40 elements inside the square neighborhood  $[-0.125, 0.125] \times [-0.125, 0.125]$  of the crack tip.

The new method is applied to estimate  $G_I$  and  $G_{II}$  when  $\Delta/h$  is  $10^{-1}, \dots, 10^{-7}$ . Table 1 is the results when the degree of basis functions are 4, 8, and 9. The results in Table 1 show that the energy release rate is virtually  $\Delta$ -independent whenever the finite element solution for stress functions are highly accurate (that is, the polynomial degree of basis functions are  $\geq 8$ ). On the other hand, if  $p$ -degree is  $\leq 4$ ,  $G_I$  is increasing and  $G_{II}$  is decreasing as  $\Delta \rightarrow 0$ . This is a similar pattern as those reported in [4].

The computation costs are comparable. In this  $p$ -version finite element analysis, 90 quadrilateral elements and eight triangular elements are used. On the other hand, in [2], 763 eight-noded quadrilateral interpolation elements are used for the finite element analysis of this test problem. The singular and non-singular near-tip meshes consist of 18 rings of elements meshed over a length equal to  $h/2$ . However, the near-tip meshes of the new method consist of five rings of elements over  $[-h, h] \times [-h, h]$  near the crack tip,  $h = 0.125$ .

Actually, the new method does not require such a very fine mesh. If we put only two rings with side length, for example,  $r_1 = h/10, r_2 = h/2$ , then the

$\frac{\Delta}{h}$	$G_I$			$G_{II}$		
	p = 4	p=8	p=9	p=4	p = 8	p = 9
1.0E-1	2.676E-2	2.723E-2	2.725E-2	0.361E-2	0.396E-2	0.396E-2
1.0E-2	2.678E-2	2.725E-2	2.727E-2	0.359E-2	0.395E-2	0.394E-2
1.0E-3	2.676E-2	2.725E-2	2.727E-2	0.359E-2	0.395E-2	0.394E-2
1.0E-4	2.672E-2	2.725E-2	2.727E-2	0.359E-2	0.395E-2	0.394E-2
1.0E-5	2.646E-2	2.725E-2	2.727E-2	0.377E-2	0.395E-2	0.394E-2
1.0E-6	3.874E-2	2.726E-2	2.727E-2	0.172E-2	0.396E-2	0.394E-2
1.0E-7	3.272E-2	2.726E-2	2.727E-2	0.232E-2	0.396E-2	0.394E-2

Table 1:  $G_I$  and  $G_{II}$  for the inter-laminar crack of Drop-ply configuration for the Test #1 of [2] (Fig. 7(a)).

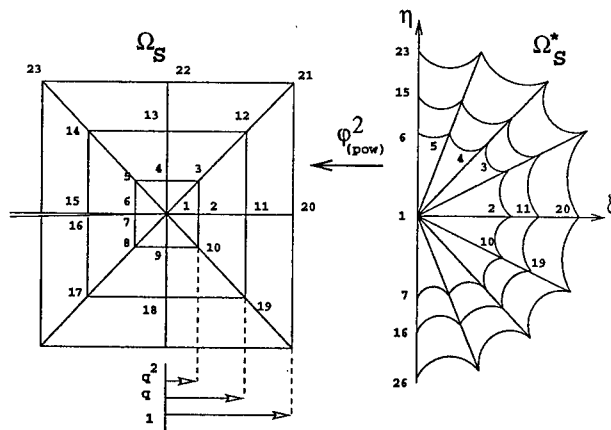


Figure 1: Scheme of Neighborhood  $\Omega_S$  of crack tip and the Mapped Neighborhood  $\hat{\Omega}_S$ .

number of elements is reduced from 98 to 74 and the mapping zone for the new method consists of eight quadrilateral elements and eight triangular elements. The accuracy of the finite element solution obtained by 74 elements mesh is virtually the same as that obtained by the 98 elements mesh. The reason to put five rings in the mesh is to apply the definition of energy release rate when  $\Delta$  is extremely small.

## References

- [1] I.Babuška and H.-S.Oh,1990. " *The p-Version of the Finite Element Method for Domains with Corners and for Infinite Domains*". Number. Meth. PDEs., 6:371-392.

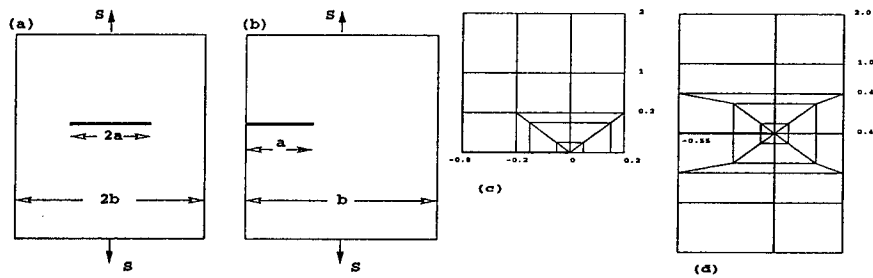


Figure 2: Schemes of (a) Center Cracked Tension (CCT) specimen, (b) Single Edge Notched (SEN) specimen, (c) Finite Element Mesh of one quarter of CCT specimen, (d) Finite Element Mesh of SEN specimen.

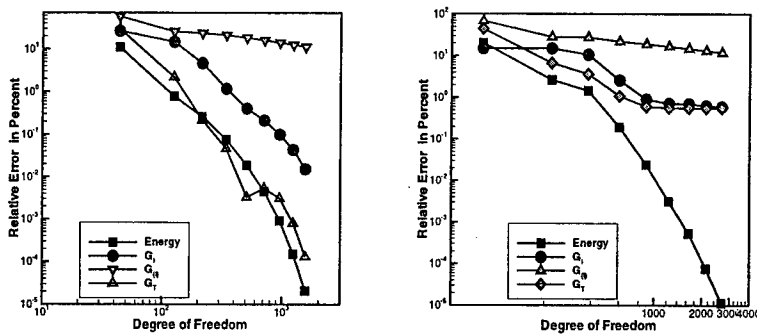


Figure 3: Relative Error (%) of  $G_I, G_{II}$  (Mode I energy release rate without applying the new method),  $G_{total}$  of CCT specimen.

Figure 4: Relative Error (%) of  $G_I, G_{II}$  (Mode I energy release rate without applying the new method),  $G_{total}$  of SEN specimen.

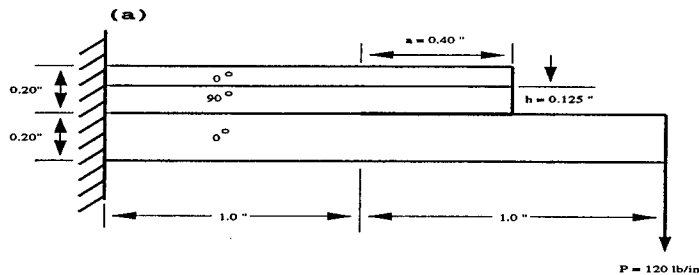


Figure 5: Scheme of Drop-ply configuration for the Test Problem 3.

*lamination Models.*" Int. J of Fracture, 77: 305-321.

- [3] E.E.Gdoutos, 1993. *Fracture Mechanics: An Introduction*, Kluwer Academic Publishers.
- [4] M.G.Manoharan, M. G. and C.T.Sun, 1990. " *Starin Energy Release Rates of an Interfacial Crack between Two Anisotropic Solids under Uniform Axial Strain.*" Composites Science and Technology, 39:99-116
- [5] H.-S.Oh, and I.Babuška, 1995. " *The Method of Auxiliary Mapping For the Finite Element Solutions of Plane Elasticity Problems Containing Singularities.*" J. of Computational Physics, 121:193-212.
- [6] H.-S.Oh, H.Kim, and S.-J.Lee, 2000. " *The Mapping Techniques and the h-p Version of the Finite Element Method for Elliptic Boundary Value Problems Containing Oscillating Singularities.*" submitted to Comput. Meth Appl. Mech and Eng.
- [7] J.Qu and J.L.Bassani, 1989. " *Cracks on Bimaterial and Bicrystal Interfaces.*" J. Mech. Phys. Solids, 37(4):417-433.
- [8] E.F.Rybicki and M.F.Kanninen, 1977. " *A Finite Element Calculation of Stress Intensity Factors by a Modified Crack Closure Integral.*" Eng. Fracture Mechanics, 9:931-938.
- [9] I.S.Raju, 1987. " *Calculation of Strain Energy Release Rates with Higher Order and Singular Finite Elements.*" Engineering Fracture Mechanics, 28(3):254-274.
- [10] C.T.Sun and M.G.Manoharan, 1989. " *Starin Energy Release Rates of an Interfacial Crack between Two Orthotropic Solids.*" J. of Composite Materials, 23:460-477.
- [11] Z.Suo, 1990. " *Singularities, interfaces and cracks in dissimilar anisotropic media.*" Proc. of the Royal Society of London, A427:361-364.
- [12] T.C.T.Ting, 1986. " *Explicit Solution and Invariance of the Singularities at an Interface Crack in Anisotropic Composites.*" Int. J. Solids Structures, 22(9):965-983.
- [13] M.Toya, 1992. " *On mode I and mode II energy release rates of an interface crack.*" Int. J. of fracture, 56:345-352.
- [14] J.T.Wang and I.S.Raju, 1996. " *Strain Energy Release Rate Formula for Skin-Stiffener Debond Modeled with Plate Elements.*" Eng. Fracture Mechanics, 54(2):211-228.

## **Propagation Behavior of Mixed-Mode Delamination Fatigue Cracks in Graphite/Epoxy and Graphite/Thermoplastic Laminates**

H. Tanaka and K. Tanaka

### **Abstract**

The propagation behavior of delamination fatigue cracks under mixed-mode I+II loading was studied with two kinds of unidirectional laminates, graphite/epoxy (T800H/#3631) and graphite/PEEK (AS4/PEEK). Mixed-mode fatigue tests were conducted by the mixed-mode bending (MMB) method under several mode ratios. The crack propagation rate,  $da/dN$ , was correlated to the maximum strain energy release rate. A fracture mechanics equation was proposed for predicting the crack propagation rate under various mixed-mode ratios and stress ratios. The predicted crack propagation behavior was in good agreement with experimental results.

### **Introduction**

Interlaminar fracture, or delamination, represents one of the most prevalent life-limiting failure modes in composite structures. It is important to characterize the crack propagation behavior under any combination of mode I and mode II loadings because delamination cracks are generally subjected to mixed-mode loading.

In the present paper, the propagation behavior of delamination cracks under mixed-mode I+II cyclic loading was investigated with graphite/epoxy laminates and graphite/PEEK laminates by the mixed-mode bending (MMB) method. The effects of the mixed-mode ratio and the stress ratio on the relationship between the crack propagation rate and the strain energy release rate were discussed. A mixed-mode fatigue criterion for predicting the crack propagation rate under various mixed-mode ratios and stress ratios was proposed.

### **Experimental Procedure**

#### **Materials and Specimens**

Two unidirectional laminates, T800H/#3631 graphite/epoxy and AS4/PEEK

---

H. Tanaka, Research Center for Advanced Waste and Emission Management, Nagoya University,  
K. Tanaka, Department of Mechanical Engineering, Nagoya University,  
Furo-cho, Chikusa-ku, Nagoya 464-8603, Japan

graphite/thermoplastics, were used in the present study. A starter crack was formed by inserting a Kapton film of 12 $\mu\text{m}$  in thickness at the mid-plane of the laminates. Split laminate beam specimens were cut from these laminates, and have a width of 20mm and a height of 6.1~6.2mm. The values of the mode I interlaminar fracture toughness,  $G_{IC}$ , measured by using the double cantilever beam (DCB) specimens are 0.144kJ/m<sup>2</sup> for T800H/#3631 laminates and 2.0kJ/m<sup>2</sup> for AS4/PEEK laminates, and represent the values at the onset of a crack from a starter film. The mode I fracture toughness increased with crack extension because of the development of fiber bridging. The values of the mode II fracture toughness,  $G_{IIC}$ , determined by the end-notched flexure (ENF) and the end-loaded split (ELS) tests are 0.76kJ/m<sup>2</sup> for T800H/#3631 laminates and 2.2kJ/m<sup>2</sup> for AS4/PEEK laminates.

### Mixed-Mode Bending Test

The MMB method proposed by Reeder and Crews [1] was used for mixed-mode tests under various ratios of mode I to mode II loading. The mode I and mode II stress intensity factors,  $K_I$  and  $K_{II}$ , were first determined from the linear analysis by the boundary element method. The effect of the geometrical nonlinearity on the stress intensity factors was taken into account on the basis of the modified beam theory proposed by Reeder and Crews [1]. The details of the results were reported elsewhere [2].

The mode I and mode II components of the strain energy release rate,  $G_I$  and  $G_{II}$ , were calculated from the stress intensity factors as follows

$$G_I = H_I K_I^2, \quad G_{II} = H_{II} K_{II}^2 \quad (1)$$

where  $H_I$  and  $H_{II}$  are functions of elastic constants. The total strain energy release rate is given by

$$G = G_I + G_{II} \quad (2)$$

### Fatigue Testing

Fatigue tests were conducted in air at room temperature. The frequency of stress cycling was 10Hz. The propagation behavior of pure mode I and II fatigue cracks was examined by the DCB and ENF tests, respectively. Mixed-mode fatigue tests were conducted by the MMB method. For T800H/#3631 laminates, the mixed-mode ratios,  $G_I/G_{II}$ , were 0.030, 0.19, 0.57 and 1.37. For each  $G_I/G_{II}$  ratio, tests were carried out under stress ratios,  $R$ , of 0.2 and 0.5. For AS4/PEEK laminates, the stress ratio was  $R=0.2$  and the  $G_I/G_{II}$  ratios were 0.15, 1.2 and 11. For mode II and mixed-mode tests, the crack propagation rate was obtained under  $G_{\max}$ -decreasing and  $G_{\max}$ -increasing conditions. The crack length was measured with a travelling microscope at a magnification of 200. On the other hand, for mode I tests, the propagation rate was determined under  $G_{\max}$ -constant conditions. The crack length was measured by the compliance method.



## Experimental Results and Discussion

### Crack Propagation Behavior

The crack propagation rate,  $da/dN$ , of T800H/#3631 laminates is correlated to the maximum value of the total energy release rate,  $G_{\max}$ , in Fig. 1. For each mixed-mode ratio,  $da/dN$  is given by a power function of  $G_{\max}$  in the region of  $da/dN > 10^{-9}$  m/cycle. Below this region, there exists the threshold for fatigue crack propagation. For both stress ratios,  $da/dN$  is highest for mode I loading and lowest for mode II loading. All the data of mixed-mode loading fall between the results of mode I and mode II loadings, and  $da/dN$  is higher for higher  $G_I/G_{II}$  ratios. The  $G_I/G_{II}$ -ratio effect on the  $da/dN$ - $G_{\max}$  relationship for  $R=0.5$  is larger than that for  $R=0.2$ .

Figure 2(a) shows the stress-ratio effect on the  $da/dN$ - $G_{II\max}$  relationship for T800H/#3631. For each  $G_I/G_{II}$  ratio,  $da/dN$  is higher for lower  $R$ -values. For higher  $da/dN$  and higher  $G_I/G_{II}$  ratios, the difference in  $da/dN$  due to changing the  $R$ -value is reduced, indicating that  $da/dN$  is mainly controlled by the maximum load.

The same data of  $da/dN$  are plotted against the range of the mode II energy release rate,  $\Delta G_{II}$ , in Fig. 2(b), where the energy release rate range is defined by

$$\Delta G_{II} = H_{II} \Delta K_{II}^2 = H_{II} (K_{II\max} - K_{II\min})^2 \quad (3)$$

The propagation rate is higher for higher  $R$ -values. For lower propagation rates and lower  $G_I/G_{II}$  ratios, the contribution of the load amplitude to propagation is larger.

Figure 3 shows the  $da/dN$ - $G_{\max}$  relationship for AS4/PEEK laminates. The influence of the  $G_I/G_{II}$  ratio on the  $da/dN$ - $G_{\max}$  relationship is minimal for AS4/PEEK laminates in contrast to T800H/#3631 laminates.

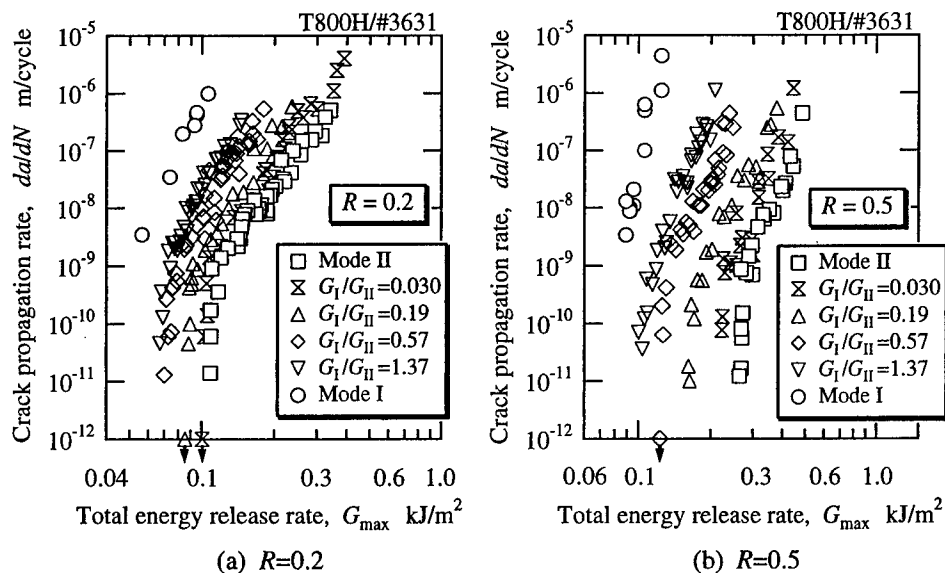


Figure 1 Relationship between crack propagation rate and total energy release rate for T800H/#3631 laminate

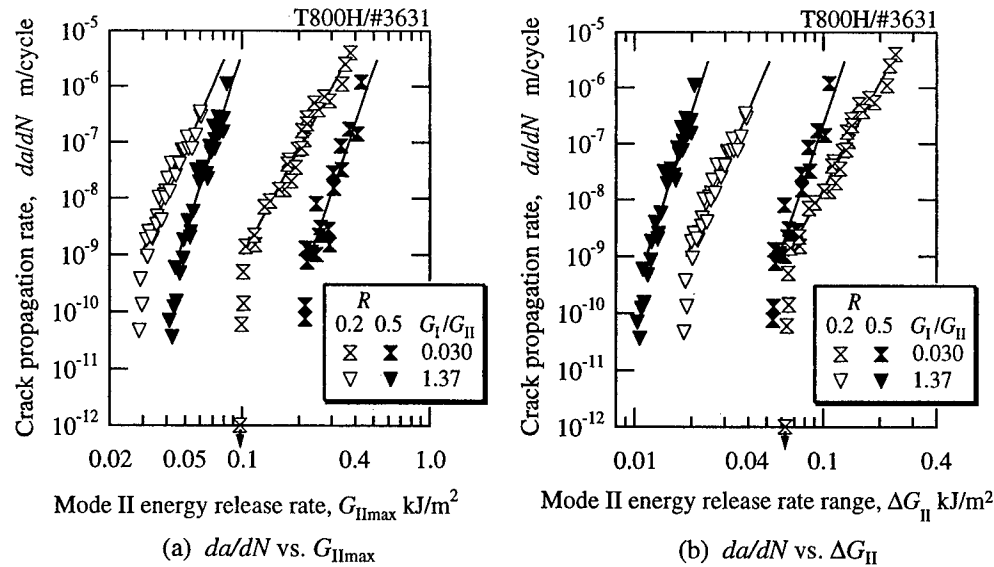


Figure 2 Effect of stress ratio on relationship between crack propagation rate and energy release rate for T800H/#3631 laminate

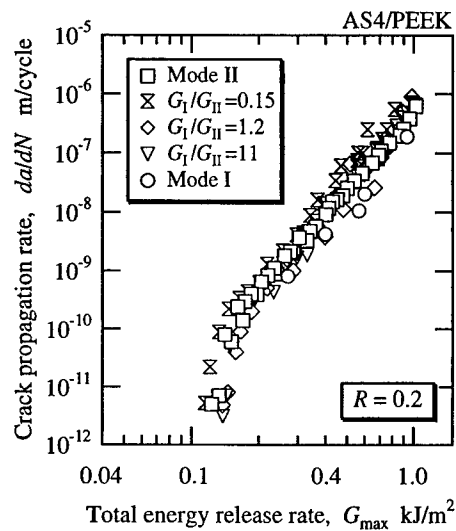


Figure 3 Relation between  $da/dN$  and  $G_{\max}$  for AS4/PEEK laminate

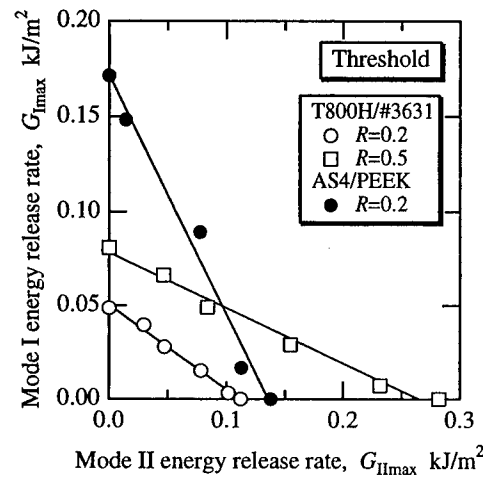


Figure 4 Mixed-mode fatigue threshold condition

Figure 4 shows the maximum values of mode I and mode II energy release rates,  $G_{I\max}$  and  $G_{II\max}$ , at the fatigue threshold. For each  $R$ -value, the threshold condition is well approximated by the following equation:

$$G_{I\max}/G_{I\max th} + G_{II\max}/G_{II\max th} = 1 \quad (4)$$

where  $G_{I\max th}$  and  $G_{II\max th}$  are the threshold energy release rates for pure mode I and

pure mode II loadings, respectively, and are functions of the  $R$ -value. For T800H/#3631 laminates, the  $G_{II\max th}$  value is larger than the  $G_{I\max th}$  value.

### Mixed-Mode Fatigue Criterion

On the basis of the experimental results, a simple fracture mechanics equation for the fatigue crack propagation rate under various stress ratios and mixed-mode ratios is proposed. Figure 5(a) depicts the relationship between  $da/dN$  and  $G_{\max}$ . As shown in the figure, the following power law relationship is postulated

$$da/dN = V_H (G_{\max}/G_C)^m = V_L (G_{\max}/G_{\max th})^m \quad (5)$$

From this equation, we have

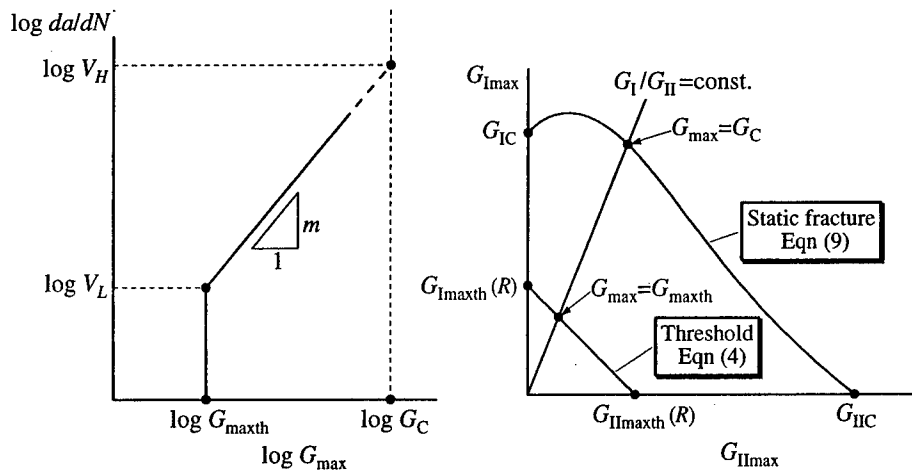
$$m = [\log(V_H/V_L)] / [\log(G_C/G_{\max th})] \quad (6)$$

where  $V_H$  and  $V_L$  represent the propagation rates at  $G_{\max}=G_C$  and  $G_{\max}=G_{\max th}$ , respectively, and are assumed to be material constants. The threshold total energy release rate,  $G_{\max th}$ , is determined from eqn (4) and the  $G_I/G_{II}$  ratio as follows

$$G_{\max th} = \left(1 + \frac{G_I}{G_{II}}\right) / \left(\frac{G_I/G_{II}}{G_{I\max th}} + \frac{1}{G_{II\max th}}\right) \quad (7)$$

For T800H/#3631 laminates, the effect of the stress ratio on the values of  $G_{I\max th}$  and  $G_{II\max th}$  is presented in Fig. 6. These values are well approximated by the following equation proposed by Hojo *et al.* [3]:

$$G_{I\max th} = G_{I\max th(R=0)} / (1-R)^{2(1-\gamma_{Ith})}, \quad G_{II\max th} = G_{II\max th(R=0)} / (1-R)^{2(1-\gamma_{IIth})} \quad (8)$$



(a)  $da/dN$  vs.  $G_{\max}$  (b) Threshold and static fracture conditions

Figure 5 Prediction of crack propagation behavior

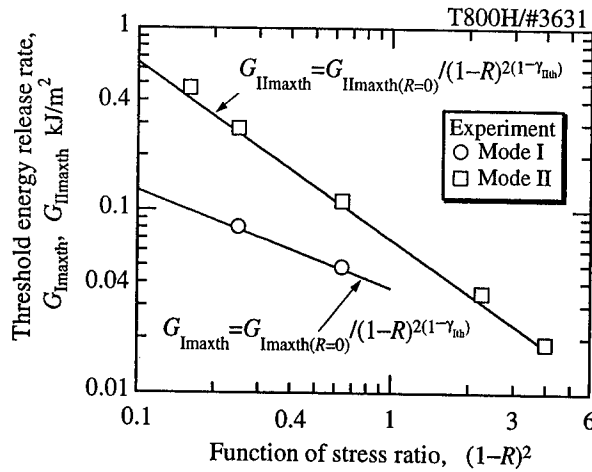


Figure 6 Effect of stress ratio on threshold energy release rate of mode I and mode II cracks for T800H/#3631 laminate

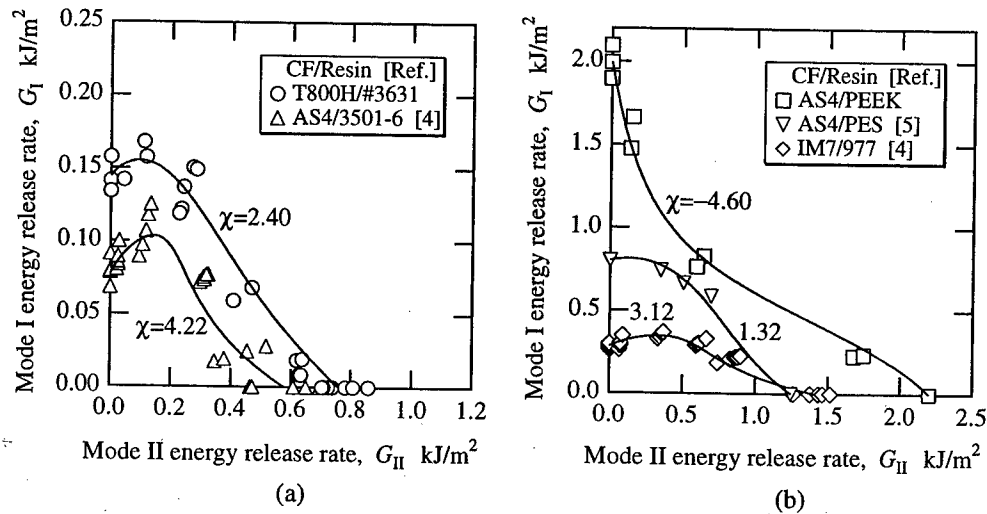


Figure 7 Mixed-mode fracture condition under static loading

The fracture toughness,  $G_C$ , is obtained from the  $G_I/G_{II}$  ratio and the mixed-mode criterion for static fracture as shown in Fig. 5(b). In the present study, we propose the following mixed-mode criterion:

$$\frac{G_I}{G_{IC}} + \frac{G_{II}}{G_{IIC}} - \chi \frac{G_I}{G} \frac{G_I}{G_{IC}} \frac{G_{II}}{G_{IIC}} = 1 \quad (9)$$

where  $\chi$  is a material constant. Figure 7 shows the results of mixed-mode static tests for the present laminates as well as for different laminates in the literature [4,5]. For both brittle and tough laminates, the experimental results are well described by eqn (9) as shown in the figure with the solid lines.

Table I Material constants used for predictions

(a) T800/#3631

$G_{IC}$ (kJ/m <sup>2</sup> )	$G_{IIC}$ (kJ/m <sup>2</sup> )	$\chi$	$V_H$ (m/cycle)	$V_L$ (m/cycle)	$\gamma_{Ith}$	$\gamma_{IIth}$	$G_{I\max th(R=0)}$ (kJ/m <sup>2</sup> )	$G_{II\max th(R=0)}$ (kJ/m <sup>2</sup> )
0.144	0.76	2.40	$3.2 \times 10^{-5}$	$1.0 \times 10^{-9}$	0.46	0.02	0.037	0.068

(b) AS4/PEEK

$G_{IC}$ (kJ/m <sup>2</sup> )	$G_{IIC}$ (kJ/m <sup>2</sup> )	$\chi$	$V_H$ (m/cycle)	$V_L$ (m/cycle)	$G_{I\max th(R=0.2)}$ (kJ/m <sup>2</sup> )	$G_{II\max th(R=0.2)}$ (kJ/m <sup>2</sup> )
2.0	2.2	-4.6	$7.9 \times 10^{-6}$	$1.0 \times 10^{-10}$	0.17	0.14

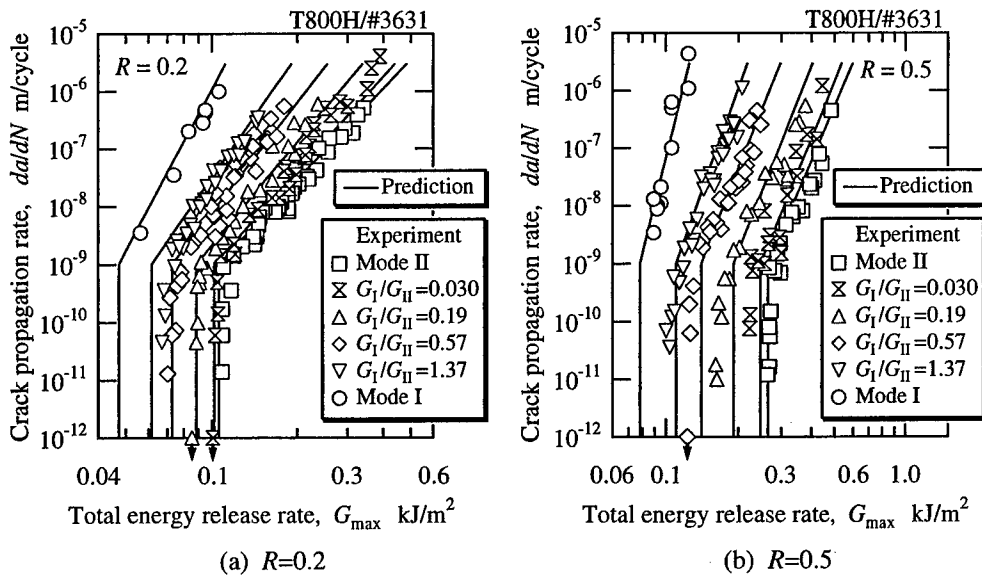


Figure 8 Predictions of crack propagation rate for T800H/#3631 laminate

Table I summarizes the constants used for the prediction. For AS4/PEEK, substituting the values of  $G_{I\max th(R=0.2)}$  and  $G_{II\max th(R=0.2)}$  in the table into eqn (7), the  $G_{\max th}$  value at  $R=0.2$  is obtained. On the other hand, for T800H/#3631, the  $G_{I\max th}$  and  $G_{II\max th}$  values determined from eqn (8) are used for calculating the  $G_{\max th}$  value.

In Figs. 8 and 9, the predicted crack propagation rates are compared with the experimental results. For both brittle T800H/#3631 and tough AS4/PEEK composites, the agreement between the experimental results and the predictions from the proposed method is very good over the full range of  $G_I/G_{II}$  ratios.

## Conclusions

(1) When compared at the same value of the maximum total energy release rate,  $G_{\max}$ , the crack propagation rate,  $da/dN$ , is higher for higher  $G_I/G_{II}$  ratios for

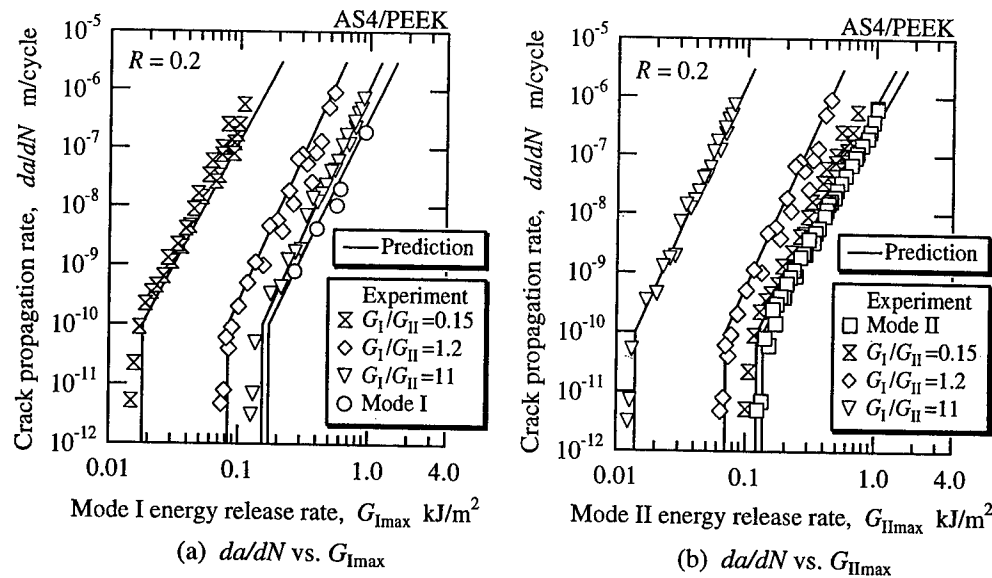


Figure 9 Predictions of crack propagation rate for AS4/PEEK laminate

T800H/#3631 laminates. On the other hand, the influence of the  $G_I/G_{II}$  ratio on the  $da/dN$ - $G_{\max}$  relationship is minimal for AS4/PEEK laminates.

(2) For each  $R$ -value, the condition of the fatigue threshold is approximated by the following equation:  $G_{I\max}/G_{I\max th} + G_{II\max}/G_{II\max th} = 1$ , where  $G_{I\max th}$  and  $G_{II\max th}$  are the threshold energy release rates for pure mode I and II loadings, respectively.

(3) A fracture mechanics equation for predicting the crack propagation rate under various stress ratios and mixed-mode ratios is proposed. For both laminates, the agreement between the experimental results and the predictions is very good over the full range of  $G_I/G_{II}$  ratios.

## References

1. J.R.Reeder and J.H.Crews, Jr., 1991. "Nonlinear Analysis and Redesign of the Mixed-Mode Bending Delamination Test." *NASA Tech. Memo.*, 102777.
2. H.Tanaka and K.Tanaka, 1995. "Mixed-Mode Growth of Interlaminar Cracks in Carbon/Epoxy Laminates under Cyclic Loading." *Proc. 10th Int. Conf. Comp. Mater.*, Vol. I: 181-188.
3. M.Hojo, K.Tanaka, C.-G.Gustafson and R.Hayashi, 1987. "Effect of Stress Ratio on Near-threshold Propagation of Delamination Fatigue Cracks in Unidirectional CFRP." *Comp. Sci. Tech.*, 29: 273-292.
4. J.R.Reeder, 1993. "A Bilinear Failure Criterion for Mixed-Mode Delamination." *ASTM STP 1206*: 303-322.
5. S.Hashemi, A.Kinloch and J.G.Williams, 1990. "Mechanics and Mechanisms of Delamination in a Poly (ether sulphone)-Fibre Composite." *Comp. Sci. Tech.*, 37: 429-462.

## Evaluating The Fracture Toughness of Glass Fiber /Epoxy Interface Using Slice Compression Test - Propagation Behavior of Interfacial Debonding -

K. N. TSAY, K. TOGE, H. KAWADA

### Abstract

The slice compression test (SCT) is used to evaluate interfacial properties by loading/unloading a specimen of the composite between two plates, one has low modulus and the other has high modulus. The specimen used is an epoxy resin, containing a single  $\text{SiO}_2$  glass fiber, with a  $200\ \mu\text{m}$  diameter. The interfacial debonding is monitored by using a microscope and a video camera. Then, the energy release rate is calculated by the finite element analysis.

From the *in-situ* observation, it is found that the interface fracture initiates when the radial stress around the fiber changes from compression to tension due to the Poisson's effect (applied stress  $\geq 40\text{MPa}$ ). The length of the crack is proportional to the stress as the load increases. It is also found analytically that the energy release rates remain constant once the interface fractures, independent of the initial crack length. It is suggested that the critical energy release rate can be appropriate for the interface fracture criterion.

### Introduction

The mechanical performance of polymer matrix composite (PMC) is closely related to its interfacial properties. To evaluate these interfacial properties, fiber pull-out [1], push-out [2], and push-in [3] tests have been developed. However, these tests can only evaluate a single fiber specimen, and a special indenter and complicated testing machines are required. The SCT [4-7] can be carried out using a universal testing machine. It involves compressing a polished slice of the composite material which has been cut normally to reinforce the fiber between the hard and soft plates. The hard plate has a high modulus and high strength while the soft plate has a low modulus and a low yield stress. Up to a certain load, the fiber-matrix interface initially debonds, the crack grows and finally fibers protrude, making permanent

---

K.N.Tsay, Department of Mechanical Engineering, National Taiwan University, Taipei, Taiwan  
R.O.C

K.Toge, Graduate School of Mechanical Engineering, Waseda University, 3-4-13-4-1 Okubo,  
Shinjuku, Tokyo 169-8555, Japan

H.Kawada, Department of Mechanical Engineering, Waseda University, 3-4-1 Okubo, Shinjuku,  
Tokyo 169-8555, Japan

imprints on the soft plate. Upon the release of loading the fibers at the bottom surface partially relax back into the matrix and retain residual protrusion. Y. Kagawa and K. Honda [8], C.H. Hsueh [4,5], N. Shafry [6,7] and D.G. Brandon have done the theoretical and experimental studies concerning SCT for ceramic-matrix composite.

The SCT was originally developed for evaluating the interfacial properties of ceramic-matrix based composites. It has seldom been applied to the PMC. Furthermore, no failure criterion for the interface debonding by the use of the SCT is available. One of the authors [9] first applied the slice compression test to PMC. They tried to develop a stress-based failure criterion for the slice compression test. But the singularity of the stress field near the crack tip is difficult to evaluate the interfacial properties.

In this paper, the SCT is also applied to polymer matrix composite. The progressive debonding process is observed using circular polariscope. By observing the development of photoelastic fringes in the matrix, the debond length can be accurately measured and correlated to the loading stress. A numerical analysis is carried out to identify the stress field before, upon and after the initial debonding occurs. In the current work, finite element analysis is also performed to calculate the energy release rate for interface fracture criterion.

## Experimental Procedure

### Materials and Specimen Preparation

Epicote 828 was used as the matrix, containing a single glass fiber ( $\text{SiO}_2$ ) with a  $200\ \mu\text{m}$  diameter (Fig.1). The curing temperature is  $373\text{K}$  with a heating rate of  $1\text{K}\cdot\text{min}^{-1}$ . The material properties of the constituents are listed in Table1. The specimens were then cut normal to fiber direction, thickness  $6\pm 0.5\text{mm}$ , and both surfaces were polished up to  $1\ \mu\text{m}$  with a diamond paste. However, most of the interfaces between the fiber and the matrix were debonded near the surface after being polished.

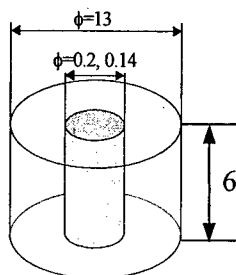


Table 1. Material properties of constituents

	$\text{SiO}_2$	$\text{SiC}$	Epoxy
E (GPa)	78	406	3.0
$\nu$	0.14	0.15	0.37
$\alpha_z(10^{-6}/\text{K})$	0.5	5	65
$\alpha_r(10^{-6}/\text{K})$	0.5	2.63	65

Fig.1. Illustration of specimen Geometry

### Measurements



The SCT was carried out at room temperature using a standard compression testing machine. The specimen was located parallel to the loading direction and sandwiched between the soft plate, annealed Al1050 (thickness: 3mm,  $E=60\text{MPa}$ , initial yield stress  $\approx 10\text{MPa}$ ), and the hard plate, SUS303 ( $E=193\text{GPa}$ , initial yield stress  $\approx 689\text{MPa}$ ). A relatively slow rate of compression,  $0.05\text{mm/min}$ , was employed. The microscopic images were transferred to the recorder and displayed on a LCD monitor (Fig.2). The specimens were transparent because of the epoxy matrix. The tip of the interfacial debonding could be traced under the appropriate reflection of the light and the corresponding debonded length could be determined on the LCD monitor directly.

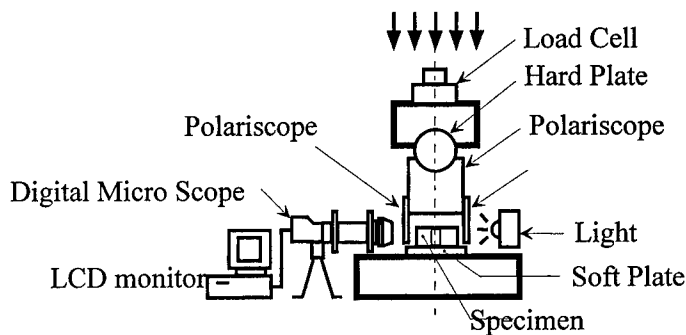


Fig.2 Schematic drawing of SCT

### Experimental Results

It has been observed that a crack initiated near the soft plate and propagated along the  $\text{SiO}_2$  fiber/Epoxy matrix interface. The crack growth was monitored using a digital microscope and a recorder when the applied load was increased continuously as presented in Fig.3. Relative debonding lengths are plotted in Fig.4 as a function of the compressive applied stress. The relative debonding lengths distribute into two main lines due to the different initial debonding lengths. There is no apparent crack propagation when the loads under  $40\text{MPa}$ . The crack propagation initiates when the load is over  $40\text{MPa}$ . So we can infer that the interfacial stress distribution changed when the load was up to  $40\text{MPa}$ .

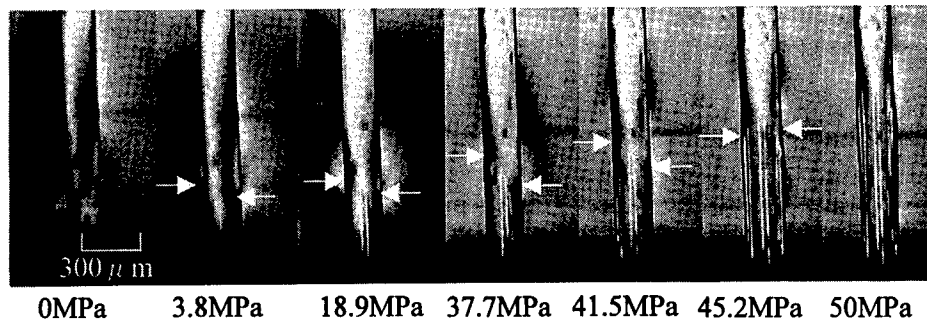


Fig.3. Interfacial debonding propagation

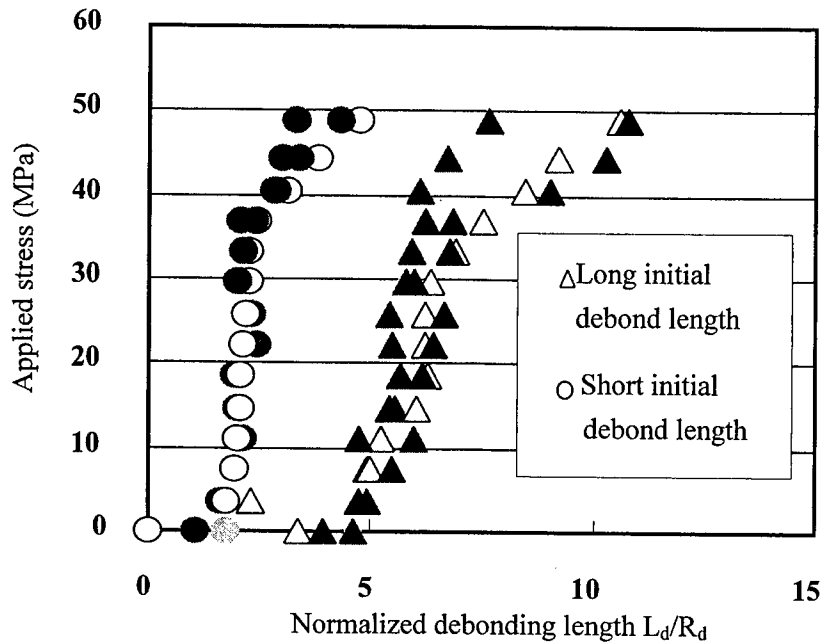


Fig.4. Relation between applied stress and debonding length

### Analysis and Discussion

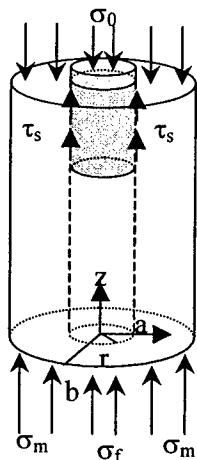


Fig.5. Composite cylinder model for SCT analysis

To analyze the interfacial stress distribution when the specimen is stressed, a composite-cylinder model is adopted (Fig.5) to simplify the problem. In this case, the radial stress is the main effect that affects the debonding process. There are two sources of radial stress at the interface of the composite: (1) residual clamping stress  $\sigma_c$  which is due to the mismatch of the thermal expansion of the coefficient during cooling from the curing temperature when the thermal expansion coefficient of the matrix is higher than the fiber and (2) the stress  $\sigma_p$  is due to the Poisson's expansion of the specimen in the radial direction when the specimen is subjected to axial compression stress.

The radial stress  $\sigma_p$  can be related to loading stress  $\sigma$  as follows: [4]

$$\sigma_p = \frac{\left( \frac{\nu_f E_m}{E_f} + \frac{a^2 \nu_m}{b^2 - a^2} \right) \sigma_f - \frac{b^2 \nu_m \sigma}{b^2 - a^2}}{D} \quad (1)$$

where  $E$  and  $\nu$  are Young's modulus and Poisson's ratio, and the subscripts,  $f$  and  $m$ , show the fiber and the matrix, respectively.

$D$  is given as

$$D = \frac{b^2 + a^2}{b^2 - a^2} + \nu_m + \frac{(1 - \nu_f) E_m}{E_f} \quad (2)$$

The clamping stress  $\sigma_c$  is derived by [10]

$$\sigma_c = A \left[ \left( \frac{1 + \nu_f}{E_f} + \frac{f}{1 - f} \frac{1 + \nu_m}{E_m} \right) \alpha_m - \left( \frac{1}{E_f} + \frac{f}{(1 - f) E_m} \right) \alpha_f - \left( \frac{\nu_f}{E_f} + \frac{f \nu_m}{(1 - f) E_m} \right) \alpha_z \right] \Delta T \quad (3)$$

where  $\alpha$  is a thermal expansion of the coefficient, the subscripts  $z$  denote the axial direction of the specimen,  $f$  is the fiber volume fraction, and  $\Delta T$  is a change in the temperature.

$A$  is given as follows:

$$A = \left\{ \frac{(1 + \nu_f)(1 - 2\nu_f)}{E_f^2} + \frac{f(2 - \nu_f - \nu_m - 4\nu_f \nu_m) + 1 + \nu_m}{(1 - f) E_f E_m} + \frac{f(1 + \nu_m)(1 + f - 2f\nu_m)}{(1 - f)^2 E_m^2} \right\}^{-1} \quad (4)$$

The interface debonding and sliding process of the PMC interface using SCT is schematically shown in Fig.6. Before loading, only the residual clamping stress closes the interface. The effect from the stress induced by the Poisson's effect increased with the applied stress. Finally, the contact between the fiber and the matrix vanishes at the specimen's surface when the load reaches to the critical value. When  $\sigma_p = \sigma_c$ , the interface starts opening and the applied stress at this time is calculated by eqn.(1) = eqn.(3) which is 44.3MPa. So, the experimental result can be explained by the crack propagation which initiates when the applied stress is about 40MPa.

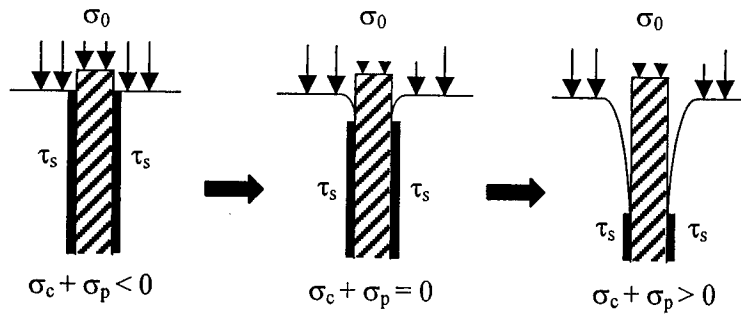


Fig.6. Debonding process of PMC with SCT.

## Finite Element Analysis

### Finite Element Model

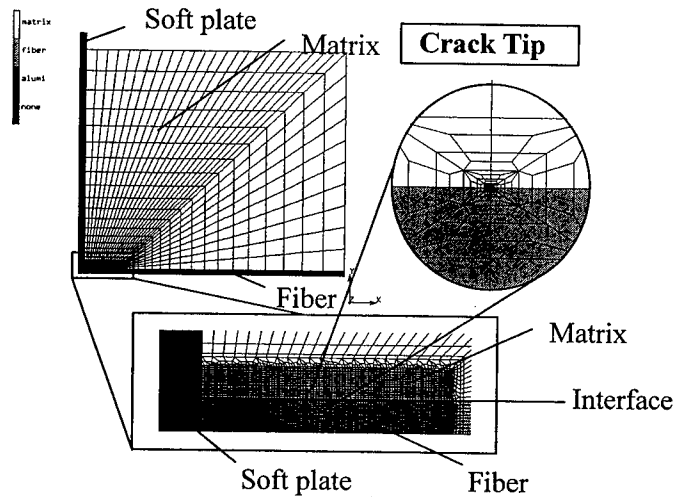


Fig.7. Finite Element Model

The FE analysis was carried out using an axisymmetric mesh (Fig.7) with eight-noded elements and linear-elastic material properties. The stress-intensity factor was calculated by the extrapolation method. The energy release rate was obtained from the FE results by the relationship between the energy release rate and the stress-intensity factors for bimaterial cracks [11]:

$$G = \frac{1}{4 \cosh^2(\varepsilon\pi)} \left\{ \frac{1-\nu_f}{G_f} + \frac{1-\nu_m}{G_m} \right\} (K_1^2 + K_2^2) \quad (5)$$

where  $G_f$  and  $G_m$  are the fiber and matrix shear modulus, and  $\varepsilon$  is a bimaterial constant. Equation (5) is strictly valid in plane-strain conditions, which are a good approximation for the interface region in an axisymmetric model, provided that at least the fiber is rigid compared to the matrix; this was expressed [12] in the results of the FE analysis.

### Finite Element Results for Energy Release Rate

The relationship between the debonding length and the energy release rate are presented in the FE results (Fig.8). An interesting region can be found in the range of medium crack lengths in both the initial crack length conditions, where the energy release rate itself shows only a slight change in this range and runs through a slight region, denoted also as a 'plateau range' in this paper. To evaluate the debonding process of the PMC composite, a critical energy release rate can be defined as a criterion.

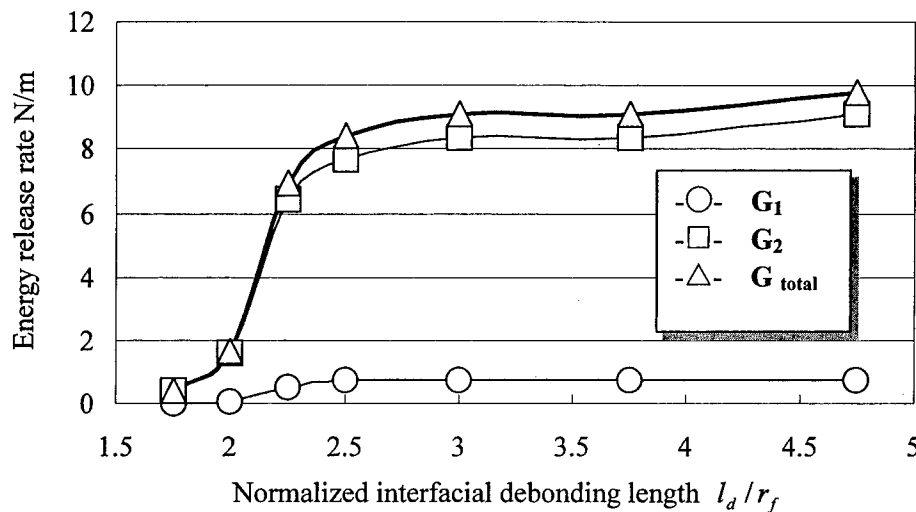


Fig.8. Dependence of energy release rate on debonding length

### Conclusions

(1) The slice compression test is used to evaluate the interfacial debonding process of the  $\text{SiO}_2/\text{epoxy}$  composite. The obtained applied stress that opens the interface is compared to the results proposed by our group [9], the relation of the fiber protrusion and the loading stress, on the same system. There is has a good agreement between two view points.

- (2) The interfacial debonding proceeds after the interface opening, when the compressive loading stress overcomes a particular value because of the Poisson's effect.
- (3) The critical energy release rate can be defined to be able to evaluate the interfacial debonding propagation in both the lengths of the initial debonding.

## References

1. Favre, J. P., Advances in pull-out testing and data analysis, *Composites Science and Technology*, 1991, **42**, 151-187
2. A. F. Kalton, C. M. Wrad-Close and T.W. Clyne, Development of the tensioned push-out test for study of fibre/matrix interfaces, *Composites*, **25**, 1994, 637-644
3. D. B. Marshall, *Acta metall. mater.* **40**, 3, 427-441(1992)
4. C. H. Hsueh, Analyses of slice compression tests for aligned ceramic matrix composites, *Acta metall. mater.* **41**, 12, 3585-3593(1993)
5. C. H. Hsueh, Slice compression tests versus fiber push-in tests, *J.Compos. Mater.*, **28**, 7, 638-655(1994)
6. N.Shafry, D. G. Brandon and M. Terasaki, *Euro Ceramics*, **3**, 3453(1989)
7. C. H. Hsueh, D. G. Brandon, N. Shafry, Experimental and theoretical aspects of slice compression tests, *Materials Science and Engineering A205*, 91-100(1996)
8. Y. Kagawa and K. Honda, *Ceram. Eng. Sci. Proc.* **12**, 7-8, 1127-1138(1991)
9. N. Taniguchi, K. Toge, H. Kawada, Evaluation of the mechanical properties of PMC interface using slice compression test, *Composite Interface 2000 proceeding*
10. C.H. Hsueh and P.F. Becher. *J. Am. Cerem. Soc.*, **71**, C438(1988)
11. J.R. Rice, Elastic fracture mechanics concepts for interfacial cracks. *J.Appl. Mech.*, **55**, 98-103(1988)
12. C. Atkinson, J. Avila, E. Betz, R.E. Smelser, The rod pull out problem, theory and experiment. *J. Mech. Phys. Solids*, **30**, 97-120(1982)
13. R.S. Dhaliwal, H.S. Saxena, Wenhua He, J.G. Rokne, Stress intensity factor for the cylindrical interface crack between nonhomogeneous coaxial finite elastic cylinders, *Engineering Fracture Mechanics*, **6**, **43**(1992)

## **Interlaminar Fracture Toughness of Composite Laminates with Whisker Reinforced Interlamination**

<sup>1</sup>W. X. Wang, Y. Takao, T. Matsubara and H.-S. Kim

### **Abstract**

In the present study, an attempt is made to improve the interlaminar fracture toughness of composite laminates by distributing whiskers along the interface of composite laminates. A commercially available T800H/3631 CFRP prepreg and  $\beta$ -SiC whisker are employed. A simple spray method is developed to distribute whiskers on the prepreg. Unidirectional laminates of 24 plies with whisker reinforced interlamination are made. The conventional DCB (double cantilever beam) and ELS (end loaded split) tests are conducted to investigate the Mode I and Mode II interlaminar fracture toughness, respectively. Microscopic analysis of the edge, cross-section and fracture surface of specimens is performed by optical microscopic and SEM (scanning electron microscope) to investigate the distribution of whiskers and effects of whiskers on the fracture toughness.

### **1. Introduction**

Fiber reinforced composite materials are well known for their high ratios of stiffness to weight and strength to weight. These advanced characteristics enable composite laminates to be used positively in aerospace and aeronautical structures, as well as in other wide applications. However, the low interlaminar strength of composite laminates is one of major shortcomings, which delayed the widespread use of composite laminates in primary aircraft structures. Interlaminar fracture or delamination becomes a fatal damage frequently observed in composite laminates in service. For this reason, many efforts have been made to improve the interlaminar strength.

The study on stitching method [1,2] seems to be one of the most frequently reported researches. Stitching through the thickness of a laminate is valid in the improvement of interlaminar fracture toughness. However, it may reduce the strength

---

<sup>1</sup>W. X. Wang, Y. Takao, T. Matsubara and H.-S. Kim, Research Institute for Applied Mechanics, Kyushu University, 6-1, Kasuga-Koen, Kasuga, Fukuoka, 816-8580, Japan

of other directions. Another well known research is the development of 3-D braided composites (for example, [3]). Doubtless, the 3-D braided composite has relatively high strength in all directions because of no obvious layers existing. The major shortcomings of 3-D composites are high cost and the complexity of manufacturing process. Furthermore, a particulate interlayer toughening technology[4] has been developed in recent years to improve the interlaminar toughness and is employed practically in the aeronautical structures. High impact resistance is achieved by the use of this technology. Whiskers and short fibers were also employed to improve the interlaminar toughness by adding whiskers (or short fibers) with ferromagnetic coating into the matrix during the manufacturing process of prepreg [5], where a magnetic moment method was developed to control the orientation of whiskers. Much improvement was obtained for the Mode I interlaminar fracture toughness and little effects were found for the Mode II one. But, high cost and complexity in the manufacturing process are still obstacles for practical application. It is noted that many other researches, which are not described here because of limitation of pages, have been also conducted. However, up to now, all of these methods are not seemed to be widely used in practical applications. Moreover, the effects of high or low temperatures are hardly considered in the most of above mentioned researches.

In the present study, an attempt is made to improve the interlaminar fracture toughness of composite laminates by distributing whiskers along the interface of composite laminates, where a simple spray method is developed to distribute whiskers on the prepreg. Unidirectional laminates of 24 plies with whiskers distributed along the mid-plane are made. The conventional DCB and ELS tests are conducted to investigate the Mode I and Mode II interlaminar fracture toughness, respectively. Microscopic analysis of the cross-section and fracture surface of specimens is performed by the use of SEM to investigate the distribution of whiskers and effects of whiskers on the fracture toughness.

## 2. Materials and Specimens

A commercial TORAYCA T800H/3631 prepreg and TOKAIWHISK TWS-2  $\beta$ -SiC whisker are used as the basic material and reinforcement, respectively. The diameter and length of whiskers are around 0.3-0.6  $\mu\text{m}$  and 5-15  $\mu\text{m}$ , respectively. A spray method is developed to distribute whiskers randomly on the prepreg surface. Figure 1 shows the images of original prepreg and distributed whiskers. It can be seen that the whiskers are randomly distributed on the prepreg surface. In practical application, whiskers may be distributed selectively to the prepreg surfaces during the layout process of a laminate. The curing processes of the laminate are the same to the conventional ones without adding whiskers.

In order to investigate the effects of whiskers on the interlaminar fracture toughness, unidirectional  $[0]_{24}$  laminates are made to conduct interlaminar fracture



testing. Whiskers are distributed along the mid-plane of the laminate. A Kapton film of  $25\text{ }\mu\text{m}$  thickness is inserted between the plies at the mid-plane to make a initial crack of 50 mm length. The thickness of the laminate is nearly 3.3 mm. Before fracture testing, microscopic analysis of the side-view and cross-section of the laminate is performed by using the SEM to obtain the distribution of whiskers in the laminate after curing.

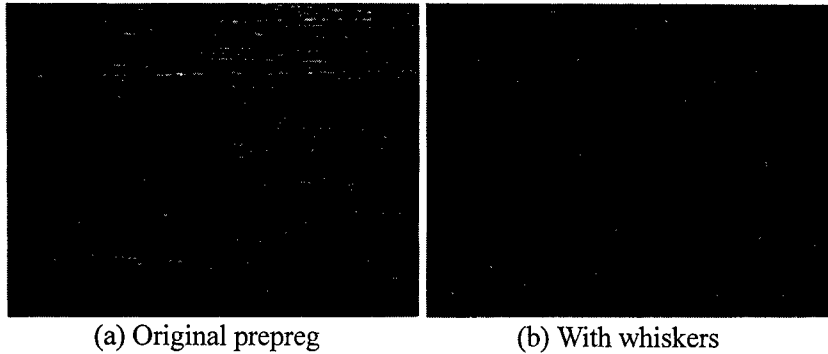


Fig. 1 Optical images of the prepreg surface with and without whiskers

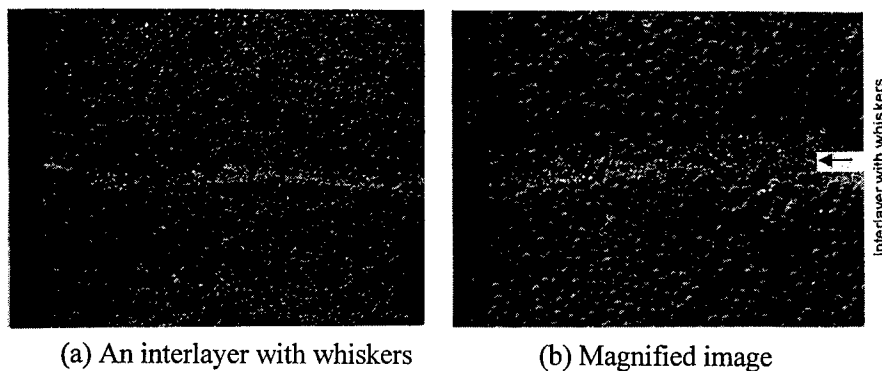


Fig. 2 Cross-section images of the laminate with an whisker reinforced interlayer

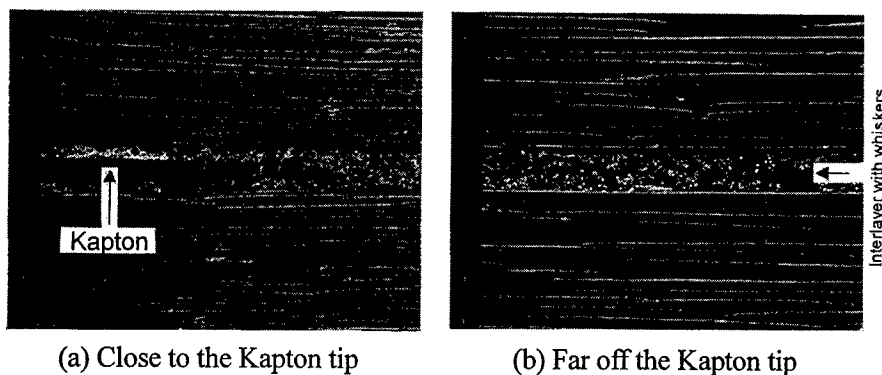


Fig. 3 Side view images of the laminate with an whisker reinforced interlayer

Figures 2 and 3 shows the SEM images of the edge and cross-section of the laminate. It is seen that a whisker reinforced interlayer of nearly 20  $\mu\text{m}$  is formed along the mid-plane. White spots and short lines within the interlayer represent whiskers. Good coherence between whiskers and matrix is observed from the higher magnification SEM analysis. It is expected that the whisker reinforced interlayer may play a useful role in the improvement of the interlaminar fracture toughness.

Specimens are straight-sided, approximately 25 mm wide and 150mm long for DCB testing, 25mm wide and 170 mm long for ELS testing. The edges of the specimen are painted in white and scaled to enable easy observation of the crack growth length. Two hinges are bonded to the specimen to transfer the loading and the crack length is measured as the distance between the center of the hinge pivot pin and the crack tip in the case of DCB testing. An optical system with a microscope, a CCD camera and a video recorder is used to observe the crack growth in the both of DCB and ELS testing cases.

### 3. DCB and ELS tests and results

Tests are conducted by using a material testing machine of MTS system. Eight specimens are tested in the DCB testing and four specimens are tested in the ELS testing. The specimen is loaded under a cross-head rate of 1 mm/min. After the crack is extended by about 5 to 10 mm the specimen is unloaded by applying the same cross-head rate. The cycle of loading and unloading is repeated until the crack is extended by about 100 mm in the DCB testing and two steps of 20mm crack extension are taken in the ELS testing to suppress the large deflection and to obtain a crack extension of 40 mm. The fracture toughnesses of Mode I  $G_{IC}$  and Mode II  $G_{IIC}$  are reduced from the conventional compliance methods[6,7], respectively, as follows:

$$G_{IC} = \frac{3}{2(2H)} \left(\frac{P}{B}\right)^2 \frac{(BC)^{2/3}}{\alpha_1}, \quad \frac{a}{2H} = \alpha_1 (BC)^{1/3} + \alpha_0 \quad (1)$$

$$G_{IIC} = \frac{9P^2 a^2 C}{2B(L^3 + 3a^3)} \quad (2)$$

where  $P$  is applied load,  $a$  is crack length,  $C$  is compliance,  $B$  is specimen width,  $2H$  is specimen thickness,  $L$  is specimen length and  $\alpha_1$  is calculated from Eq. (1) based on the experimental data of crack length  $a$  and compliance  $C$ .

Typical load to displacement curves for DCB and ELS tests are depicted in Fig. 4. There is no obvious difference from conventional load to displacement curves without whiskers, except for the locally protruded part on the curve of DCB testing. This protruded part reflects the resistance of whiskers to crack growth. The critical energy release rates of Mode I  $G_{IC}$  and Mode II  $G_{IIC}$  are shown in Fig. 5. In order to compare the present results with the ones without whiskers, the previous experimental results [8] are depicted together the present results. The solid lines express the averaged values of

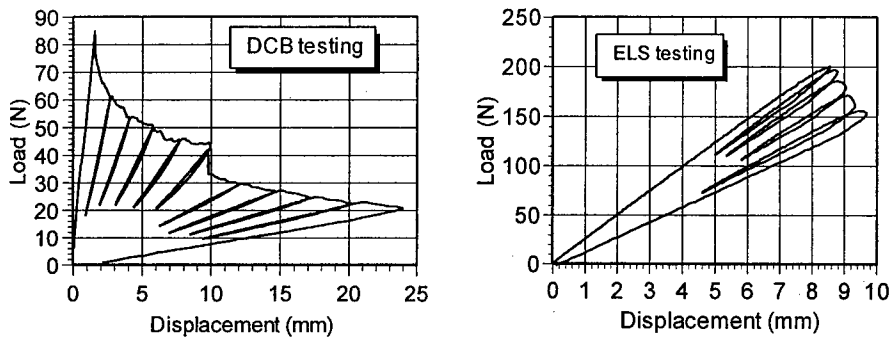


Fig. 4 Typical Load-Displacement curves for DCB and ELS tests.

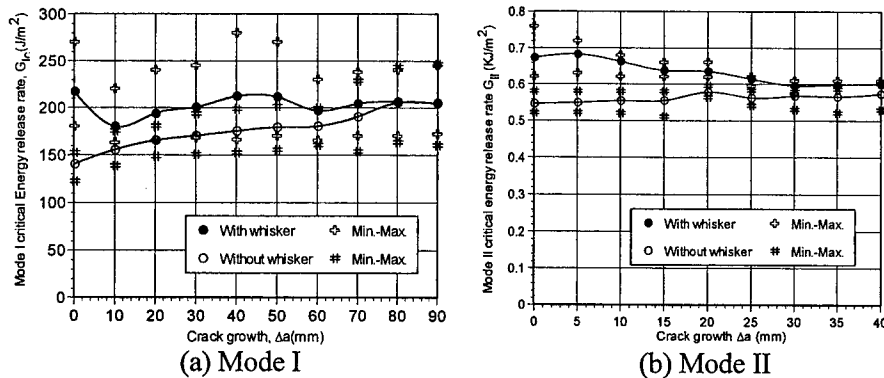


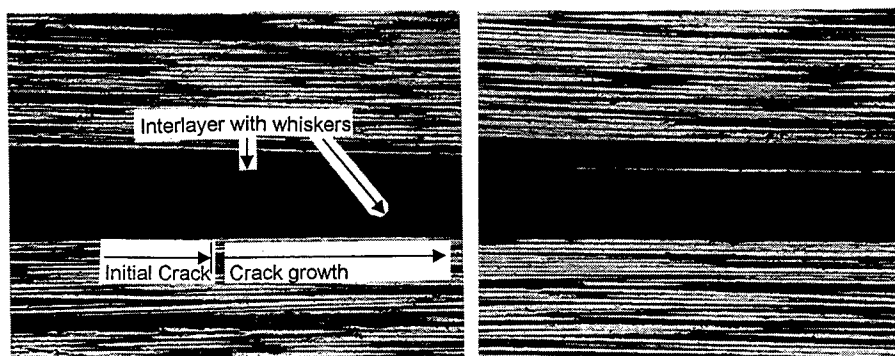
Fig. 5 The critical energy release rates of Mode I and Mode II interlaminar fracture

the experimental results. The cross marks indicate the maximum and minimum values of the present results with whiskers and the sharp marks indicate those of the previous results without whiskers. The  $G_{IC}$  and  $G_{IIC}$  with whiskers are found to be higher than those without whiskers in a wide region of crack growth. Especially, high initial  $G_{IC}$  and  $G_{IIC}$  are observed. As the crack grows by a long distance, two kinds of results with and without whiskers almost have the same values. To understand these phenomena, a microscopic analysis of the tested specimens is performed by the use of optical microscopic and SEM.

#### 4. Microscopic analysis of tested specimens

Figure 6 shows the side view images of a specimen after DCB testing and Fig. 7 shows the ones of a specimen after ELS testing. In both testing cases, the crack usually initiates from one corner of the Kapton film and grows firstly in the whisker reinforced interlayer. This behavior leads a high initial fracture toughness. Then, the crack grows curvedly in the interlayer or along the interface between the interlayer and the fiber

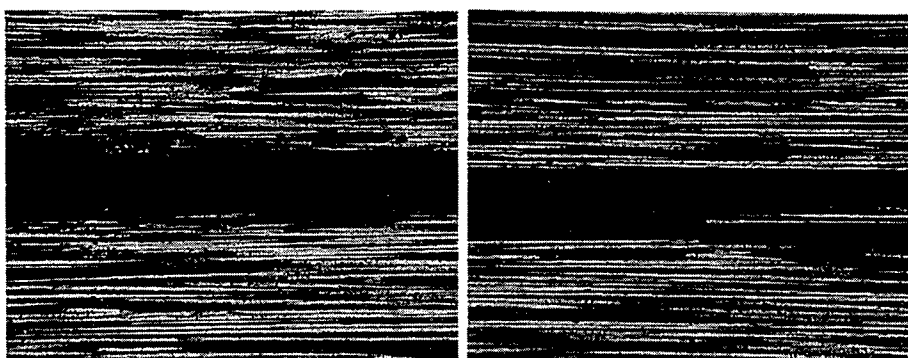
reinforced matrix layer. Finally, as the crack reaches a relatively long distance the crack growth is always out of the whisker reinforced interlayer. This is why the critical energy release rates in both cases with and without whiskers almost have the same values when the crack grows by a relatively long distance. A typical crack growth path is depicted in Fig.8 based on the observation of the cracked specimens. The through-width images of crack growth can be found in the following microscopic analysis of fracture surfaces.



(a) Close to the initial crack tip

(b) Far off the initial crack tip

Fig. 6 Images of side view of crack growth path in the DCB testing case



(a) Close to the initial crack tip

(b) Far off the initial crack tip

Fig. 7 Images of side view of crack growth path in the ELS testing case

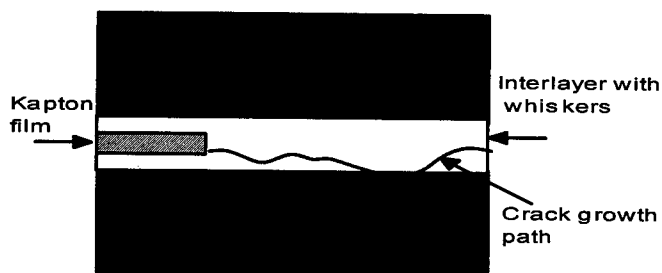
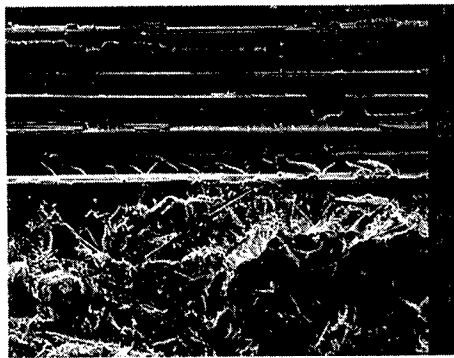


Fig. 8 Illustration for crack growth

Figure 9 and 10 give the SEM images of the fracture surfaces at different regions of crack growth in both testing cases. In Figs. 9 (a) and 10 (a), two partial surfaces with and without whiskers can be seen. It is pointed out that the fracture surface in the direction of width usually consists of these two partial surfaces in the whole region of crack growth. In the initial region of crack growth, the region with whiskers occupies most of the surface. In contrast, in the region of a long crack growth, the region without whiskers is much larger than that with whiskers. From the images of the partial regions with whiskers, it is seen that many whiskers appear on the surface and that the damage situations at these regions are quite complicated. The pullout and breaking of whiskers during the crack growing process can be considered to be the major reason which leads a high fracture toughness. Figures 9 (b) and 10 (b) show the images of fracture surfaces without whiskers at the region of a long crack growth, which are similar to the images of conventional Mode I and Mode II fracture surfaces of unidirectional carbon/epoxy laminates without whisker reinforced interlayer.

From the micro-analysis of Figs. 6 to 9, it is understood that these microscopic images are coincident with the results of  $G_{IC}$  and  $G_{IIC}$  given in Fig.5 and they reveal that the whisker bridging play an important role in enhancing the interlaminar fracture toughness compared with that without whiskers.

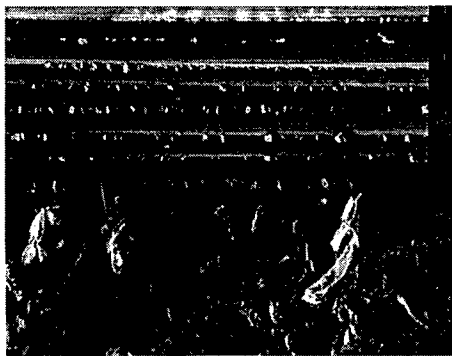


(a) Initial region of crack growth

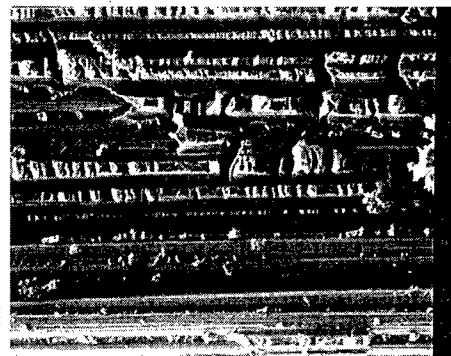


(b) Far off the initial region

Fig. 9 SEM images of fracture surfaces in the DCB testing case



(a) Initial region of crack growth



(b) Far off the initial region

Fig. 10 SEM images of fracture surfaces in the ELS testing case

## 5 Conclusions

In the present study, an attempt is made to improve the interlaminar fracture toughness of composite laminates by distributing whiskers along the interface of composite laminates. Unidirectional laminates of 24 plies with  $\beta$ -SiC whiskers distributed along the mid-plane are manufactured for Mode I (DCB) and Mode II (ELS) tests. A spray method is developed to distribute whiskers on the prepreg. The manufacture process is simple and applicable in practical structures. Microscopic analysis of the edge and cross section of the laminate is performed. The SEM and images of the side-view and cross section reveal that a whisker reinforced interlayer is formed along the mid-plane.

The DCB and ELS tests are conducted to investigate the effects of the whisker on the Mode I and Mode II fracture toughness. The initial  $G_{IC}$  and  $G_{IIC}$  exhibit an improvement of nearly 50 % and 25 % compared with those without whiskers, respectively. Microscopic analysis of the crack growth path and fracture surface of cracked specimens by the optical microscope and SEM exhibits that the whisker bridging plays an important role in enhancing fracture toughness of the interlaminar. Hence, it is understood that the present method with whiskers distributed on prepreps is valid to improve the interlaminar fracture toughness of laminated composites.

## References

1. Mignery, L. A., Tan, T. M., and Sun, C. T., "The use of stitching to suppress delamination in laminated Composites", *ASTM STP* 876, pp. 371-385 (1985).
2. Dransfield, K. A., Jian, L. K., and Mai, Y. -W., "On the effects of stitching in CFRPs-I. Mode I delamination toughness", *Compos. Sci. Technol.*, 58, pp. 815-827 (1998).
3. Ito, M., and Chou T. W., *Proceedings of ICCM-10*, Vol. 3, pp. 213-220 (1995).
4. Odagiri, N., Kishi, H., and Yamashita, M., "Development of TORAYCA prepreg P2302 carbon fiber reinforced plastic for aircraft primary structural materials", *Adv. Composite Mater.*, 5, pp.249-252 (1996).
5. Yamashita, S., Hatta, H., Takei, T., and Sugano, "Interlaminar reinforcement of laminated composites by addition of oriented whiskers in the matrix", *J. Comp. Mater.*, Vol. 26, pp. 1254-1268 (1992).
6. Japanese Industrial Standard group, "Testing Method for Interlaminar Fracture Toughness of Carbon Fiber Reinforced Plastics," (in Japanese), *JIS K 7086-1993*, pp. 651-665.
7. K. Kageyama, "Fracture mechanics of composite materials", (in Japanes), *J. the Japan Society for Composite Materials*, Vol. 18, No. 4, pp. 158-165, (1992).
8. H.-S. Kim, "Damage behavior and fracture toughness of composite laminates under various temperature envirnments", Dissertation, Kyushu University, (2000).

## **Delamination Growth Simulation of Composite Plates by Using Finite Element Method**

Y.Shimamura, A.Todoroki, H.Kobayashi and H.Nakamura

### **Abstract**

Recently, applications of integrated composite structures have been attempted to many structures of vehicles. In order to improve the cost performance and reliability, it is necessary to judge the structural integrity of the composite structures with damage. For the judgment, we have developed a simulation method using finite element method with two-dimensional plane stress elements. The simulation method includes both intralaminar and interlaminar fracture mechanisms. Analytical damage growth and stiffness degradation of a CF/epoxy laminate with an open hole were compared with experimental results. As a result, it is shown that the proposed simulation method can roughly predict the delamination growth and stiffness degradation of composite laminates.

### **Introduction**

Recently, applications of integrated large composite structures have been attempted to many structures of vehicles. In order to improve the cost performance and reliability of the integrated composite structures, it is necessary to judge the structural integrity of the composite structures with defects that were found by nondestructive inspection. For the judgment, we need a fracture simulation technique of composite structures. Many researches on the fracture simulation method using FEM have been reported by now. The main objective in the studies, however, is to predict fracture strength of structures, and damage growth has not been investigated in detail. Most of the researches carried out simulations considering only intralaminar fracture mechanisms, and did not consider delamination. Several papers have reported delamination simulation [1]-[4], but all these reports require three-dimensional elements or quasi three-dimensional elements for FEM analysis. The analyses are very expensive and time-consuming.

In order to analyze the damage growth of composite laminates inexpensively, we have developed a fracture simulation technique using FEM with plane stress elements

---

Y.Shimamura, A.Todoroki, H.Kobayashi and H.Nakamura, Department of Mechano-Aerospace Engineering, Tokyo Institute of Technology, O-okayama 2-12-1, Meguro-ku, Tokyo 152-8552, Japan

that includes both intralaminar and interlaminar fracture mechanisms. For the intralaminar fractures, i.e. matrix cracking and fiber breaking, reduction of moduli of laminae is applied to the fractured laminae, and stress-strain matrices of elements are calculated based on the classical lamination theory. For the interlaminar fracture, i.e. delamination, reduction of effective engineering moduli of elements based on the classical lamination theory and rule of mixtures is applied to the delaminated elements. This approach does not require thickness-direction analysis. Analytical damage growth and stiffness degradation of a CF/epoxy laminate with an open hole were compared with experimental results. As a result, it is shown that proposed simulation method can roughly predict delamination growth and stiffness degradation of composite laminates.

## Simulation Method

### Judgement of Intralaminar Fractures

Tsai-Hill criterion was adopted as a fracture criterion of intralaminar fractures.

$$\left(\frac{\sigma_L}{F_L}\right)^2 - \frac{\sigma_L \sigma_T}{F_L^2} + \left(\frac{\sigma_T}{F_T}\right)^2 + \left(\frac{\sigma_{LT}}{F_{LT}}\right)^2 = 1 \quad (1)$$

where  $\sigma_L$ ,  $\sigma_T$ ,  $\sigma_{LT}$  are longitudinal stress, transverse stress and shear stress, respectively, and  $F_L$ ,  $F_T$  and  $F_{LT}$  are longitudinal tension strength, transverse tension strength and shear strength, respectively. If compressive stress components are involved, the corresponding compressive strength should be used.

Fiber breaking of the lamina is judged if  $\sigma_L \geq F_{Lt}$  or  $\sigma_L \leq F_{Lc}$ , and matrix cracking of the lamina is judged if  $F_{Lc} \leq \sigma_L \leq F_{Lt}$ , where  $F_{Lc}$  is longitudinal compress strength. Reduction of moduli of the lamina that was judged as intralaminar fractures is as follows.

$$\begin{aligned} \text{Matrix cracking : } E_T^* &= \frac{1}{100} E_T, G_{LT}^* = \frac{1}{100} G_{LT} \\ \text{Fiber breaking : } E_L^* &= \frac{1}{100} E_L, E_T^* = \frac{1}{100} E_T, G_{LT}^* = \frac{1}{100} G_{LT}, \nu_{LT}^* = \frac{1}{100} \nu_{LT}, \end{aligned} \quad (2)$$

where  $E_L$ ,  $E_T$ ,  $G_{LT}$ ,  $\nu_{LT}$  are longitudinal modulus, transverse modulus, shear modulus and major Poisson's ratio, respectively, and superscript \* means degraded modulus.

### Judgement of Interlaminar Fractures

In the present approach, delamination is regarded as reduction of effective engineering moduli of plane stress elements of FEM. By dividing the difference



between the total strain energy before and after delamination by the element area, we can obtain the total strain energy release rate  $G$  of the elements due to delamination. If strain components  $\{\varepsilon_1 \ \varepsilon_2 \ \varepsilon_6\}$  are unchanged before and after delamination, the total strain energy release rate  $G$  is expressed as

$$G = \left( \frac{1}{2} \varepsilon^T D_{lam} \varepsilon - \frac{1}{2} \varepsilon^T D_{delam} \varepsilon \right) \cdot St / S \quad (3)$$

where  $D_{lam}$  and  $D_{delam}$  are stress-strain matrices of the laminate without and with delamination, respectively, and  $S$ ,  $t$  are the element area, element thickness, respectively [5]. It is assumed that longitudinal moduli of X direction and Y direction and shear modulus are calculated independently by using Whitcomb & Raju's method [6].

A criterion of delamination onset is described as

$$G > G_c \quad (4)$$

where  $G_c$  is the critical energy release rate.

### Simulation Procedure

The simulation procedure is described as follows.

- (1) The D matrix is calculated based on the classical lamination theory.
- (2) Strain components of each element are determined by FEM analysis with 2-dimensional plane stress elements.
- (3) Stress components of each lamina are calculated by using the classical lamination theory.
- (4) A fractured lamina or a delaminated element is estimated one by one according to Yamada's method [7].
- (5) Reduction of moduli is applied to the fractured lamina or the delaminated element.
- (6) The above process is repeated until a given displacement is achieved.

In the simulation, triangle plane stress elements are adopted. In each element, an additional fracture is not judged after delamination for simplicity of calculation.

### Comparison of Experimental and Analytical Results

#### Damage Growth

Using CFRP laminates of stacking sequence  $[30_2/-30_2/0_2/90_2]_S$  with an open hole, static tension tests were conducted under displacement control. An

extensometer was mounted on the specimens to measure displacements over 50mm-gauge length. In order to observe delamination and matrix cracking, applied load was held at several steps and then unloaded. Ultrasonic inspection method (Hitachi AT5000) was used for the observation.

Damage growth obtained in the experiment is shown in Fig. 1. In the first step, matrix cracking in 90° lamina emanated from the hole edges where the stress concentration occurred. Further increase of the displacement brought delamination between 0° lamina and 90° lamina from the free edges of the specimen. The delamination propagated into loading direction as increase of the displacement.

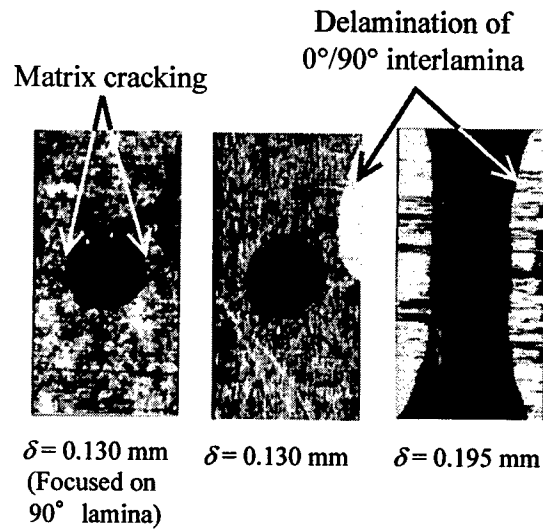


Figure 1 Experimental Damage Growth in  $[30_2/-30_2/0_2/90_2]_s$  Laminate

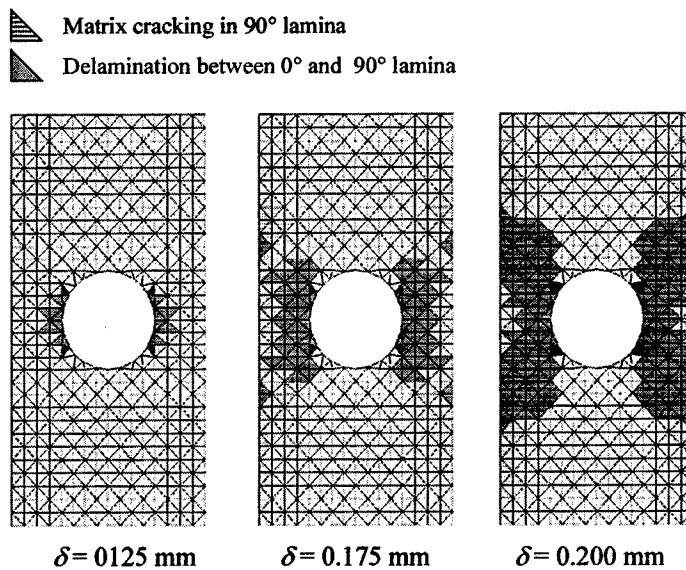
Damage growth simulation of the laminate with an open hole was conducted by using the proposed simulation method. In the analysis, a mesh division of 524 nodes and 928 elements was adopted, and a displacement was given at the upper edge of the mesh division. Material properties used in the analysis are listed in Table I. In Table I, subscripts  $L$  and  $T$  denote longitudinal and transverse, respectively.

The results obtained from the simulation are shown in Fig. 2. Dark elements represent delamination between 0° and 90° lamina, and striped elements represent matrix cracking in 90° lamina. Delamination and matrix cracking in other lamina were not observed in the simulation.

In the early stage of damage growth, matrix cracking in 90° lamina and delamination between 0° lamina and 90° lamina were occurred from the hole edges. Further increase of the displacement brought delamination from the free edges of the specimen, and it propagated in the similar way as the experimental results. The profile of the analytical damage growth roughly agrees with the experimental one.

Table I Material Properties of CFRP

Longitudinal modulus, $E_L$	161.7 GPa
Transverse modulus, $E_T$	9.43 GPa
Shear modulus, $G_{LT}$	5.06 GPa
Major Poisson's ratio, $\nu_{LT}$	0.32
Longitudinal tension strength, $F_{Lt}$	2000 MPa
Transverse tension strength, $F_{Tt}$	30 MPa
Shear strength, $F_{LT}$	550 MPa
Longitudinal compress strength, $F_{Lc}$	160 MPa
Transverse compress strength, $F_{Tc}$	60 MPa
Critical energy release rate, $G_C$	294 J/m <sup>2</sup>

Figure 2 Analytical Damage Growth in  $[30_2/-30_2/0_2/90_2]_S$  Laminate

### Stiffness Degradation

Load versus displacement curves are shown in Fig. 3. Solid line represents an experimental result and broken lines represent analytical results. In order to investigate the influence of the value of the critical energy release rate, simulations in case of  $G_C \pm 10\%$  were also conducted. Since delamination propagated beyond the mounted points of the extensometer when the displacement reached at  $\delta = 0.24 \text{ mm}$  and excessive stiffness degradation was observed in the experimental result, we show the load-displacement relation until  $\delta = 0.24 \text{ mm}$ . The analytical results show good agreements with the experimental result regardless of the value of  $G_C$ .

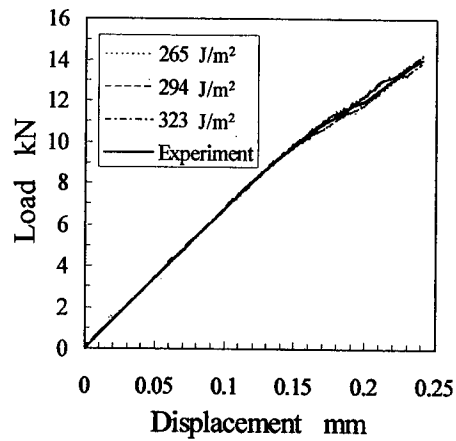


Figure 3 Load versus Displacement Curves

#### Delamination Area

Increase of delamination area is shown in Fig. 4. Vertical axis means delamination area normalized by the meshed area. Open circles are experimental results and other symbols are analytical results. Rapidly increase of delamination area after  $\delta = 0.13$  mm was reproduced by the analysis. Delamination area increased in proportion to  $G_C$ . As a result, it is shown that the simulation method can roughly predict damage propagation and stiffness degradation of composite laminates.

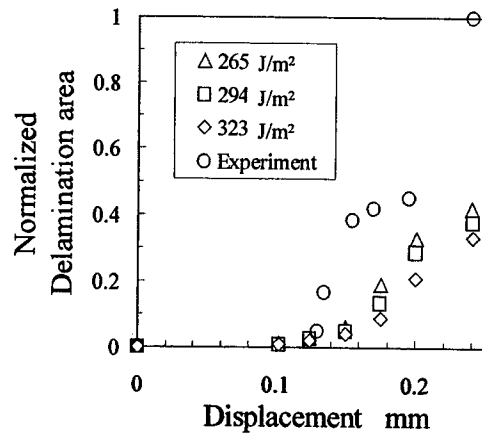


Figure 4 Increase of Delamination Area

## Conclusions

A FEM simulation method of damage growth for composite laminates was proposed, and analytical results were compared with experimental results. As a result, it is shown that the simulation method can roughly predict delamination growth and stiffness degradation of composite laminates.

## References

1. M.Zako, and T.Tsujikami, 1994. "Development of Simulation Program for Delamination of Laminated Composite." *J.Soc.Mat.Sci.,Japan*, 43(489):684-689. (in Japanese)
2. D.J.Chen, W.S.Chan, and B.P.Wang, 1996. "An Efficient Method to Simulate One- and Two-dimensional Delamination Growth in Composite Laminates." *Journal of Reinforced Plastics and Composites*, 15:944-957.
3. R.Rinderknecht, and B.Kröplin, 1997. "A Computational Method for the Analysis of Delamination Growth in Composite Plates." *Computers & Structures*, 64(1-4):359-374.
4. S.Kamiya, H.Sekine, and Y.Yagishita, 1998. "Computational Simulation of Interlaminar Crack Extension in Angle-Ply Laminates Due to Transverse Loading." *Journal of Composite Materials*, 32(8): 744-765.
5. Y.Shimamura, A.Todoroki, H.Kobayashi, H.Nakamura, and T.Inada, 1998. "Inexpensive Simulation of Delamination Growth in Composite Plates by Using FEM with Two-dimensional Elements." *Proceedings of Computer Methods in Composite Materials VI*, Southampton, UK: Computational Mechanics Publications, pp. 237-244.
6. J.D.Whitcomb, and I.S.Raju, 1985. "Analysis of Interlaminar Stresses in Thick Composite Laminates with and without Edge Delamination." *Delamination and Debonding of Materials, ASTM STP 876*, Philadelphia, PA: American Society for Testing and Materials, pp. 69-94.
7. T.Miyoshi, M.Shiratori, M.Zako, and S.Sakata, 1976. *Yuugenyoushou*. Tokyo, JAPAN: Jikkyousyuppan, pp. 39-41. (in Japanese)

# **New Concept Composites, I**

---

## **Effects of Rolling on the Microstructure and the Mechanical Properties of Injection-Molded Sheets of PP/LCP Blend**

M. Kawagoe, J. Qiu, W. Mizuno and M. Morita

### **Abstract**

The effects of rolling process on the mechanical properties, especially on the fatigue behavior, were investigated on the injection-molded sheet of polypropylene (PP) blended with liquid crystalline polyester (LCP) by 20wt% in relation to the microstructural changes by rolling. The sheet specimens were rolled out along the flow direction under injection to several rolling ratios, defined as sheet thickness reduction divided by initial sheet thickness, at a rolling speed of 3m/min in air at 25°C. By the rolling treatment the PP and LCP phases were still separated in skin, intermediate and core layers formed during injection molding, but they were much flattened and closer each other. The LCP phase appeared to be strongly oriented in the rolling direction. The crystallinity in the PP phase analyzed by the micro-FT infrared spectroscopy (FTIR) was, as a whole, lowered by the rolling process, preserving a general trend of higher crystallinity in the core region. As the rolling ratio increased, the molecular orientation was lowered and raised in the intermediate and the core layers, respectively, and as a result its distribution became more uniform. The rolling process reduced the storage modulus  $E'$  and inversely raised the loss tangent  $\tan\delta$  in wide temperature range. The ductility was generally so enhanced by the rolling treat-

---

M. Kawagoe and M. Morita, Department of Mechanical Systems Engineering, Toyama Prefectural University, Kosugi, Toyama 939-0398, Japan

J. Qiu, Department of Machine Intelligence and Systems Engineering, Akita Prefectural University, Honjo, Akita 015-0055, Japan

W. Mizuno, Central Research Institute, Toyama Industrial Technology Center, Takaoka, Toyama 933-0981, Japan

ment, although the tensile strength was hardly affected. The fatigue test revealed that the lifetimes of specimens rolled to 20 and 40% are commonly shorter than that of unrolled specimen showing brittle fracture. By contrast the specimen rolled to 60% was observed to form no crack and to show uniform large deformation, and in addition was not fractured even after the loading cycles of  $10^6$ . For all the rolled specimens  $\tan\delta$  once increased and then decreased indicating a peak at about  $10^3$  cycles. This behavior may be caused by realignment of molecular chains promoted under cyclic tensile loading.

## Introduction

Polypropylene (PP) blended with liquid crystalline polyester (LCP) is often regarded as an *in situ* composite, because LCP with high rigidity due to a rod-like molecular structure can well be dispersed and aligned in the flow direction under the injection molding in the form of fine fiber [1-3]. The PP/LCP blend is expected to develop in future for replying various industrial demands by their high mechanical performance and recycle ability [4]. On the other hand, thermoplastic polymers are well rolled even at room temperature to improve various mechanical and processing properties like deep drawing characteristics [5,6]. In this study, the combined effects of blending and rolling on the mechanical properties, particularly on the fatigue behavior, are examined on an injection-molded sheet of PP mixed with LCP by 20wt% with reference to the microstructural changes caused by the rolling process.

## Experimental

### Materials

The commercially available pellets of PP (M1700, Asahi Chemical Co. Ltd) and LCP (Rodrun LC3000, Unitika Co. Ltd) were used as raw materials. They were mixed to a weight ratio of PP/LCP=80/20 without any compatibilizer, and then extruded by a single screw extruder (Raboplastomil, Toyo Seiki Co. Ltd). The blended pellets were injection-molded to the dumbbell-shaped specimens with gauge length of 90mm, width 10mm and thickness 2mm under a mold temperature at 230°C and an injection speed of 22cm<sup>3</sup>/s. The gauge region was cut from the



dumbbell-shaped specimen, and offered to the rolling process.

### Rolling Procedure

The two-step rolling mill of 50mm in diameter (Oono Roll Co. Ltd) was used. The sheet specimens were rolled out along the flow direction under injection to several rolling ratios  $\xi$ , defined as the sheet thickness reduction divided by the initial sheet thickness, at a rolling speed of 3m/min in air at 25°C. An increment in the distance between two rollers was adjusted in 100 $\mu$ m for one cycle of rolling process.

### Evaluations of dynamic viscoelasticity and fatigue properties

The dynamic viscoelastic factors, the storage modulus  $E'$  and the loss tangent  $\tan\delta$ , were measured by means of a dynamic viscoelastic meter (Fatigueron VFA-1KNA, Orientec Co. Ltd). The tests were carried out under a fixed displacement of 25 $\mu$ m at frequencies of 1, 5, 10 and 35Hz and temperature ranging from -150 to 170°C. Since different rolling ratios produce different thicknesses of specimen, a heating rate was set to a low value of 1°C/min for uniformly heating the specimens.

The fatigue tests were conducted by using the same equipment as the above for the viscoelastic analyses. The variations in  $E'$  and  $\tan\delta$  under cyclic loading were simultaneously and continuously measured until fracture. The testing conditions were controlled to give sinusoidal tensile stress with a ratio of 0.02 at a frequency of 5Hz. The testing temperatures were set from -50 to 50°C, covering the glass transition temperature ( $T_g$ ) of PP (about -10°C). The tests were mainly conducted at -10 and 20°C, after waiting for about 20min to hold the testing temperature.

### Observation of inner morphology and fracture surface

The inner morphology in the blend was observed under transmitted light by means of an optical microscope (Axioplan, Carl Zeiss, Inc). A thin slice 20 $\mu$ m thick was cut from the as-molded and the rolled specimens in the flow direction by using a microtome (HM325, Microm Inc). The fracture surfaces obtained by the fatigue tests were observed by a scanning electron microscopy (SEM) with a field emission gun

(S4000, Hitachi Co. Ltd), after being sputter-coated with a thin layer of gold.

### Evaluations of crystallinity and molecular orientation in PP phase

For understanding the changes in molecular orientation and crystallinity in the PP phase by the rolling process, the microspectroscopic analyses were performed by means of a Fourier transform infrared spectrometer (FTIR) with a microscope (FTIR 8900 $\mu$ , Japan Spectroscopic Co. Ltd). The thin films of 20 $\mu$ m thickness were again sliced from the as-molded and the rolled specimens in the injection or rolling direction by the microtome. The measurements were done for a small area of 120 $\times$ 40 $\mu$ m<sup>2</sup> from the surface to the core regions under transmission mode. The crystallinity in PP phase was relatively evaluated by a ratio of absorbances at the wavenumbers of 998 and 947cm<sup>-1</sup>, which correspond to the crystalline and the non-crystalline phases, respectively. For the evaluation of molecular orientation the absorbances of PP at 998, 899, 841 and 809cm<sup>-1</sup> were measured under polarized light in the directions parallel ( $A_{\parallel}$ ) and perpendicular ( $A_{\perp}$ ) to the flow (rolling) direction. A dichroic ratio  $R (=A_{\parallel}/A_{\perp})$  for each wavenumber was obtained for evaluating the molecular orientation function  $f$ .

## Results and Discussion

### Microstructure

The optical micrographs of inner morphology of blended specimens rolled to several rolling ratios represent that even by the rolling process the PP and LCP phases still are clearly separated in the skin, intermediate and core layers formed during the injection molding, but they are much flattened and closer each other with increasing the rolling ratio. The LCP phase was observed to be clearly oriented in the rolling direction.

Figure 1 shows the distributions of IR absorbance ratio corresponding relatively to the crystallinity in PP phase in the specimens rolled to different rolling ratios. The relative crystallinity is, as a whole, lowered with increasing the rolling ratio, preserving a general trend of higher crystallinity in the core region resulted from slow cooling during the process of injection molding. The distributions of molecular

orientation in PP phase expressed by a orientation function  $f$  are shown in Figure 2 with reference to the rolling ratio. In the unrolled specimens ( $\xi = 0\%$ ) the molecular orientation is highest in the intermediate layer, and lowest in the core layer. Since the intermediate layer is relatively quickly cooled and subjected to large shear stress during the injection molding, the densification of microstructure and the large residual stress may be brought about in this layer, leading to higher value of  $f$ . When the rolling ratio is increased, the crystals and/or crystallites in the core (the spherulites were not identified) may be broken and allowed to orient the molecules under rolling, but the molecular orientation in the intermediate region may be relieved in the rolling (flow) direction, probably due to molecular flow in another direction perpendicular to the rolling direction and to relaxation of residual stress under the rolling process. As a result the difference in the molecular orientation between the intermediate and the core layers becomes smaller. The rolling treatment thus may homogenize the microstructure all over the cross section of specimen formed by the injection molding process. Such microstructural changes may affect the mechanical properties, as mentioned below.

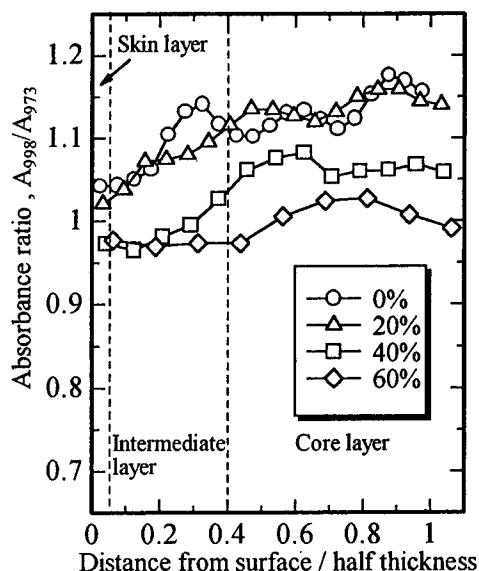


Fig. 1 Effects of rolling on the distribution of relative degree of crystallinity

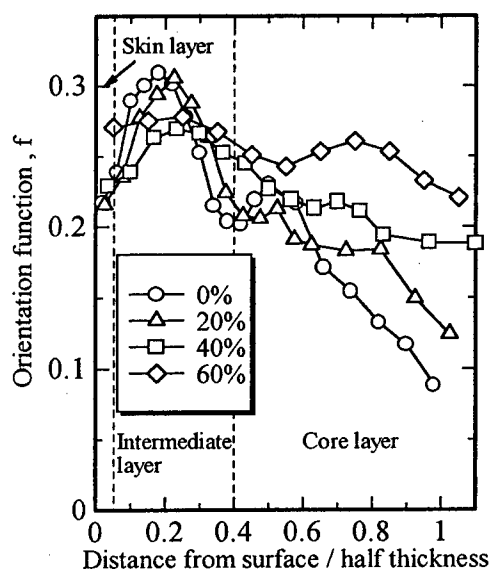


Fig. 2 Effects of rolling on the distribution of molecular orientation

### Dynamic viscoelastic and tensile properties

The effects of rolling treatment on the viscoelastic behavior are shown in Figure 3, in which the applied frequency is 1Hz. In general the storage modulus  $E'$  and the loss tangent  $\tan\delta$  are lowered and raised, respectively, as the rolling ratio is increased up to 40%, but it is not so clear for the ratio of 60%. Within the temperature range from  $-20$  to  $20^\circ\text{C}$  covering the  $T_g$  (about  $-10^\circ\text{C}$ ) of PP, an increase in the rolling ratio results in an increase in  $\tan\delta$ . For the rolling ratio of 60%, however, the  $\tan\delta$  curve becomes so broader as that its peak at  $T_g$  can not be clearly observed.

The tension tests revealed that in general the ductility (strain to fracture) is so enhanced by the rolling treatment, although the tensile strength is hardly affected. For example, the rolling ratio of 40% caused large fracture strain of 100% at  $10^\circ\text{C}$  and 30% even at  $-10^\circ\text{C}$ . Incidentally the fracture strain and the tensile strength of unrolled specimen were measured at  $10^\circ\text{C}$  to 5% or less and 53MPa, respectively.

### Fatigue behavior

The variations in the storage modulus  $E'$  and the loss tangent  $\tan\delta$  during the fatigue process for various rolling ratios are shown in Figure 4, in which the testing temperature is  $20^\circ\text{C}$  and the stress amplitude is 15MPa. The experimental data for the neat PP specimen are also represented. The unrolled specimen ( $\xi = 0\%$ ) showed brittle fracture after the loading cycle of  $4.7 \times 10^5$ .  $E'$  and  $\tan\delta$  remain almost constant for long time, and are drastically lowered and raised, respectively, just before fracture. The specimens rolled to 20 and 40% are broken for shorter period than the unrolled specimen, showing interesting features of a momentary reduction in  $E'$  and an inverse trend in  $\tan\delta$  curves at about  $10^3$  cycles. The dramatic decrease in  $E'$  and increase in  $\tan\delta$  observed just before fracture in these specimens suggest the thermal failure to take place by heat generation due to the hysteresis loss under cyclic tension. By the contrast the specimen rolled to 60% was observed to form no crack and to show uniform large deformation, and in addition was not fractured even after the loading cycles of  $10^6$ . Thus higher rolling ratio of 60% may provide higher resistance to fatigue fracture. The  $\tan\delta$  value in this specimen also indicates a peak at about  $10^3$  cycles. Such a trend of  $\tan\delta$  may indicate an advancing process of realignment of molecular chains in the loading direction under cyclic tension.

The fatigue behavior at  $-10^{\circ}\text{C}$  (near  $T_g$  of PP) was fundamentally similar to that at  $20^{\circ}\text{C}$ . In this case the specimen rolled to 40% showed a similar trend to that rolled to 60% rather than 20%.

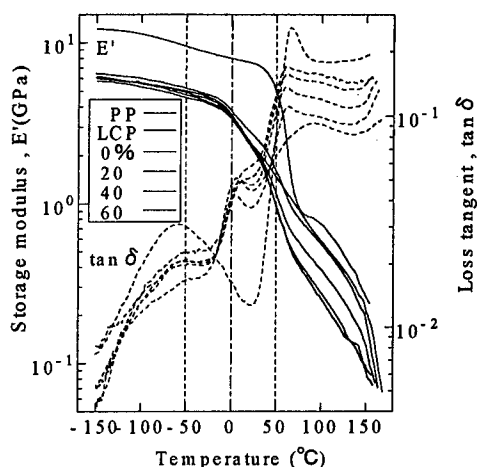


Fig. 3 Effect of rolling on the dynamic viscoelasticity

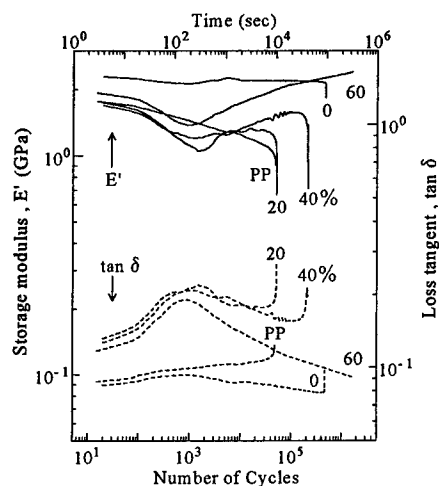


Fig. 4 Effects of rolling on variations in  $E'$  and  $\tan\delta$  during fatigue process ( $\sigma_{\max} = 15 \text{ MPa}$ ,  $20^{\circ}\text{C}$ )

## Conclusions

The effects of rolling on the microstructure and the mechanical properties were examined for the injection-molded sheet of PP/LCP containing LCP by 20wt%. By the rolling process the crystallinity is generally lowered, and the distribution of molecular orientation in the flow direction becomes more uniform all over the cross section of specimen. The tensile and fatigue properties of PP are generally improved by blending LCP and enforcing the rolling treatment, especially at lower temperature and for the rolling ratio above 40%. The rolling process thus may homogenize the microstructure of injection-molded sheet to lead to the improvement of mechanical properties.

### Acknowledgements

M. Nomiya is gratefully acknowledged for her assistance in operating the FTIR. M. Kataoka and M. Matsui are also thanked for their help in conducting the experiments.

### References

1. G.Kiss, 1987. *Polymer Engineering and Science*, 27, 410
2. H.J.O'Donnell and D.G.Baird, 1995. *Polymer*, 36, 3113
3. M.Kawagoe, M.Nomiya, J.Qiu, M.Morita, and W.Mizuno, 1997. *Polymer*, 38, 113
4. K.Sasaki and T.Tomita, 1993. *Kobunshi Ronbunshu*, 50, 855
5. T.Machida, K.Oki, F.Hamayoshi, and Y.Arakawa, 1984. *Plasticity and Machining*, 25-278, 206
6. T.Nakayama and Y.Fujito, 1993. *The Proceedings of the 44<sup>th</sup> Japanese Joint Conference for the Technology of Plasticity*, 111

## **Mechanical Properties of PE Fiber Reinforced Thermoplastics Composites**

Tatsuro Fukui, Hiroyuki Hamada

### **Abstract**

In this study, unidirectional UHMWPE fiber reinforced PE film by film stacking method was prepared. The most important fabrication point of this composite was molding temperature. The molding temperature should be determined between the melting temperature of fiber and matrix. This molding temperature may expect the strong interphase properties of PE/PE composite. In this study, the effects of thermal properties for molding temperature in film stacking method were investigated by using DSC simulation run.

### **1. Introduction**

The demand of thermoplastics composite materials has been increasing from a viewpoint of the ecological issue. The interface construction is very important on the design of composite materials. For example, in the case of glass fiber reinforced thermoplastics composites, interface is generally treated by silane coupling agent or matrix modification with additional or binder agent. In the case of composite materials with polyethylene fiber and epoxy resin, the adhesion between fiber and matrix was not so good. Therefore composites that consist of same materials but different shape such as fiber shape and matrix phase can create high interfacial strength.

Generally, melting temperature of fibrous shape material is higher than that of bulk material due to molecular orientation in thermoplastic materials. Therefore processing temperature between two melting temperature enable fabrication of

---

Tatsuro Fukui, Masaharu Iwamoto, Hiroyuki Hamada : Division of Advanced Fibro-Science, Kyoto Institute of Technology, Matsugasaki, Sakyo-ku, Kyoto 606-8585, Japan, Tel. +81-75-724-7844, Fax. +81-75-724-7800

composites with high interfacial strength and maintaining reinforcing effects of fibers. When its fibrous shape is remained in the composites, reinforcing effects are expected. This concept can be applied any kinds of thermoplastic materials. The advantage of this material is not needed to pay any attention the adhesion between fiber and matrix because the interface disappears. This is essential for construction of this composite. Therefore we call this composite "Interface-less Composites".

DSC measurements were performed in order to understand interfacial properties in PE/PE composite. Particularly, temperature profile in DSC measurements was set same as actual processing conditions, so that the results obtained in this paper should be used for determination of an optimum processing condition.

## 2. Experiments Method

### *Materials*

Ultra-high-molecular-weight polyethylene (UHMWPE) fibers (Dyneema SK60, 400d, 390 filaments, TOYOBO Co., Ltd.) were used in this study as a reinforcement. Matrix resin used was a linear-low-density polyethylene film supplied by Sumitomo Chemical Industry Co., Ltd.

### *Differential Scanning Calorimeter (DSC) measurements method*

Perkin-Elmer's Pyris 1 DSC was used to measure melting point of fiber and matrix and to simulate molding process. In the only fiber and matrix film, 1.2mg were weighed precisely and placed into the DSC. The temperature of DSC was programmed first ; heating sample up to 200°C by 10°C/min <1<sup>st</sup> heating>, under pure nitrogen atmosphere (25 ml/min), cooled to 25°C by 10°C/min. Then the sample was scanned by 10°C/min of heating rate from 25-200°C <2<sup>nd</sup> heating>.

Figure 1 shows temperature and time profile for DSC cure. In the simulation run, 1.4 mg of fiber PE and 2.4 mg of film PE were weighed precisely and placed into the DSC. The temperature of DSC was programmed first to simulate molding process; heating sample up to 135-155°C by 10°C/min <1<sup>st</sup> heating>, under pure nitrogen atmosphere (25 ml/min), holding the respective molding for 30 minutes and cooled to 25°C by 10°C/min. Then the sample was scanned by 10°C/min of heating rate from 25-180°C <2<sup>nd</sup> heating>. Only the difference between the actual sample and the simulated sample was with and without of molding pressure.



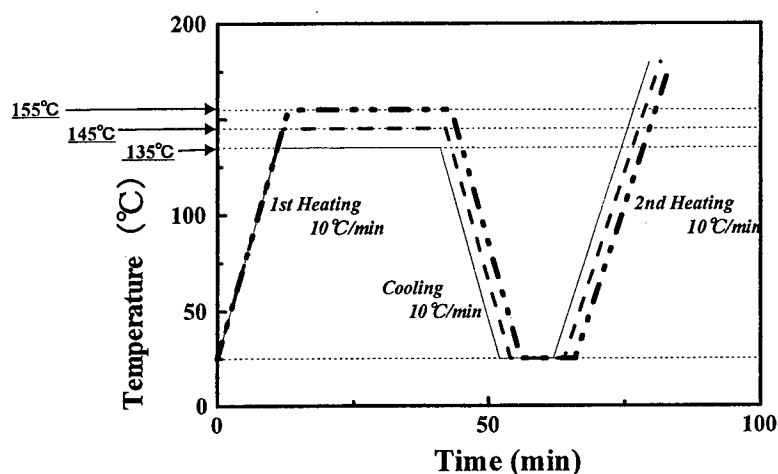


Figure 1 Temperature and time profile for DSC cure.

### 3. Results & Discussion

The melting condition of PE fiber was discussed. Melting condition of the fiber was examined in heated oven. The fiber was exposed for approximately 20 min in the oven. Figure 2 shows SEM photographs of UHMWPE fiber surface after heating history under free tension condition. At the 135°C fiber did not melt, at the 145°C it was melted a little, and at the 155°C most of fiber was melted.

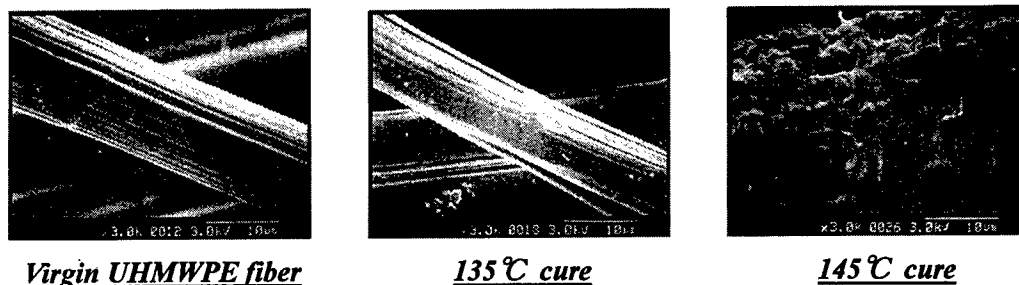
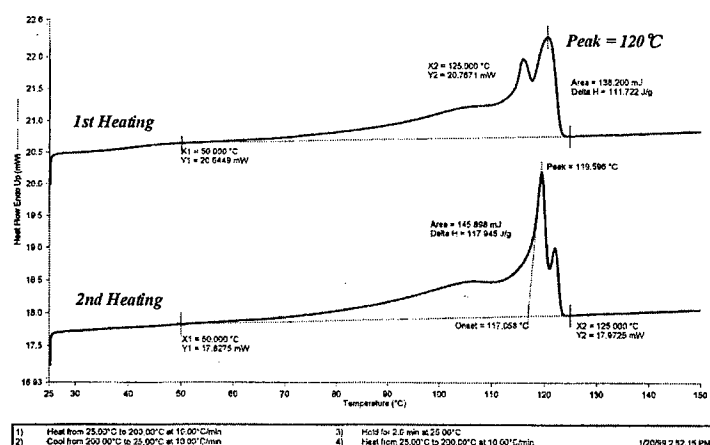
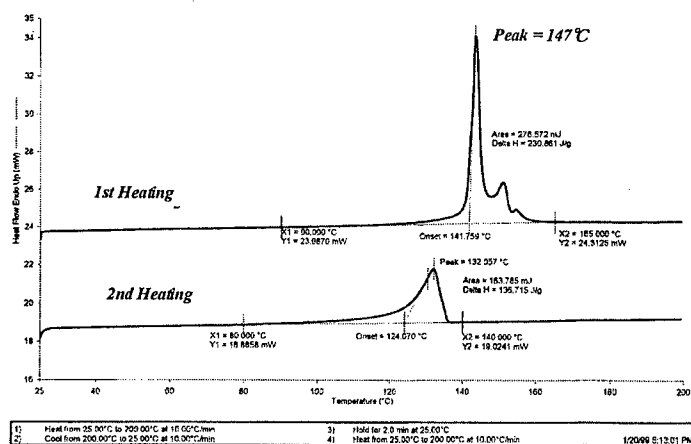


Figure 2 Surface of UHMWPE fiber after heating history under free tension condition.

Figure 3 shows DSC curves of (a) polyethylene film and (b) UHMWPE fiber. Melting temperature of PE film was 120°C and that of PE fiber was 147°C, as confirmed by DSC measurements.



(a) Polyethylene film



(b) UHMWPE fiber

Figure 3 DSC curves of (a) polyethylene film and (b) UHMWPE fiber.

Figure 4 shows DSC curves of simulation run. A peak at 120°C is fusion peak of the straight chain linear-low-density polyethylene film. Other peak at 140-160°C shown on DSC curve of thermally treated (molded) at 135, 145, and 150°C respectively was fusion peak of UHMWPE fiber. These were confirmed by separate testing of fiber and film material only. Also other peak observed at 132°C on DSC curve of 145, 150 and 155°C treated samples are re-fusion peak of UHMWPE fiber.

It is estimated that the UHMWPE do not fuse at around 130°C, for a very high peak is observed at 143°C and no peak is found at 132°C.

For other DSC curves of 145, 150, and 155°C treated samples are indicating the fusion took place and reduced size of peak around 140-160°C show the degree of fusion at around 132°C. First shoulder peak around 140-160°C in 135°C treated sample is shifting toward peak around 132°C in 145°C treated sample. Second and third shoulder peak around 140-160°C in 135°C treated sample remain in 145°C treated sample. If the actual molding temperature was higher than 145°C, peak around 140-160°C may become smaller and other peak may appear at around 132°C. The orientation of material is maintained and the fiber do not fuse completely. From these results, 145°C treated samples showed better performance for inter-faceless composites.

To exhibit better properties of PE/PE composite material, it is essential that making the reinforcement PE partially solved to matrix and improves adhesion. The condition of molding temperature may be expected near the melting point for good adhesion in actual molding.

Thus selecting the amount of partially fused reinforcement UHMWPE fiber is the key point of interface designing of the composite PE/PE material.

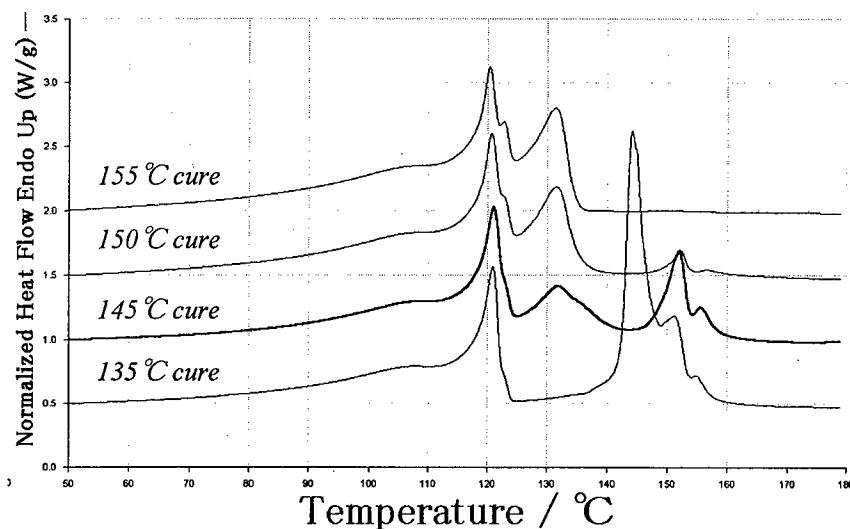


Figure 4 DSC curves of simulation run.

#### 4. Conclusion

In this study, the effects of thermal properties by molding temperature in film stacking method were investigated by DSC. In order to determine the molding temperature for "Interface-less Composite", DSC measurement was conducted both reinforcement PE fiber and matrix film. According to these results, it was cleared that 145°C treated samples showed better performance for this composites.

This concept can be used in any kinds of thermoplastic materials and in addition this composite greatly contribute recycled problem because of same materials. Further investigation would be requiring for the amount of partial fusion and crystalline structure of the material etc.

#### 5. Reference

- [1] Teishev Albert, Incardona Silvia, Migliaresi Claudio, Marom Gad, Polyethylene fibers-polyethylene matrix composites: preparation and physical properties, *Journal of Applied Polymer Science*, 50-3, 1993, pp.503-512.
- [2] Economy J., Andreopoulos A.G., Morphological Modification of UHMPE Fibers, *Polymer Advanced Technology*, 5-7, 1994, pp.349-357.
- [3] Wang Qi, Ait-Kadi Abdellatif, Kaliaguine Serge, Catalytic grafting. A new technique for polymer/fiber composites. II. Plasma treated UHMPE fibers/polyethylene composites, *Journal of Applied Polymer Science*, 45-6, 1992, pp.1023-1033.
- [4] Lacroix F., Werwer M., Schulte K., Solution impregnation of polyethylene fibre/polyethylene matrix composites, *Composites Part A*, 29A-4, 1998, pp.371-376.
- [5] Gutowski W.S., Pankevicius E.R., Wu D.Y., Controlled Interfaces of Ultra-High Modulus Polyethylene and Aramid Fibres for Advanced Composites, *Materials Science Forum*, 189-190, 1995, pp211-220.

## **Effects of Thermal Cycling on Degradation of High-Temperature Polymer Composite Materials for the Next-Generation SST Structures**

T. Shimokawa<sup>1</sup>, H. Katoh<sup>1</sup>, Y. Hamaguchi<sup>1</sup>, S. Sanbongi<sup>2</sup>, H. Mizuno<sup>3</sup>,  
H. Nakamura<sup>4</sup>, R. Asagumo<sup>5</sup>, and H. Tamura<sup>6</sup>

### **Abstract**

The objective of this study was to investigate the effect of thermal cycles encountered by an SST in service on the degradation of high-temperature polymer matrix composite materials. One cycle of thermal cycling was designated as the sequence from room temperature (RT) to -54°C, up to +177°C, and back to RT. Thermal cycling tests were conducted up to 10,000 cycles on three kinds of carbon fiber/high-temperature polymer composite material: IM7/PIXA, IM7/K3B, and G40-800/5260. At scheduled thermal cycles, microcracks initiated on the sectional surface of the laminates were observed and counted by using an optical microscope. Static mechanical tests indicated the open-hole compressive strength before and after thermal cycles. In addition, a simple FEM analysis using basic data of the T800H/PMR-15 carbon/polyimide composite was conducted to estimate the thermal stress generated in the laminate.

### **Introduction**

The structures of the next-generation supersonic transport (SST) require the long-term durability of structural materials under a variety of conditions involving temperature, loads, and fluids, not only in constant states but also with cyclic fluctuations. Structural weight moreover must be drastically reduced to achieve

---

<sup>1</sup> Structures Division, National Aerospace Laboratory, 6-13-1 Ohsawa, Mitaka, Tokyo 181-0015, Japan

<sup>2</sup> National Space Development Agency of Japan, 2-4-1 Hamamatsu-cho, Minato, Tokyo 105-8060, Japan

<sup>3</sup> Engineering Research Department, Nagoya Aerospace Systems, Mitsubishi Heavy Industries, Ltd., 10 Oye, Minato, Nagoya 455-0024, Japan

<sup>4</sup> Research & Laboratory Department, Utsunomiya Plant, Aerospace Division, Fuji Heavy Industries, Ltd., 1-1-11 Yonan, Utsunomiya 320-8564, Japan

<sup>5</sup> Aerospace Engineering Department, Aerospace Division, Kawasaki Heavy Industries, Ltd., 1 Kawasaki, Kakamigahara 504-0971, Japan

<sup>6</sup> Japan Aircraft Development Corporation, 1-2-3 Toranomon, Minato, Tokyo 105-0001, Japan

commercial success requiring extensive use of high-temperature polymer-matrix composite materials.

The National Aerospace Laboratory (NAL) is carrying out joint research programs with three major aircraft manufacturing companies in Japan and the Japan Aircraft Development Corporation (JADC) to evaluate the long-term durability of high-temperature polymer-matrix composite materials nominated for use in SST. This research was conducted as part of joint effort, to evaluate the effects of thermal cycling on the strength degradation of high-temperature polymer-matrix composite materials.

Microcracking has been demonstrated to be a serious problem for high-temperature polymer matrix composite materials and a particular concern under hygrothermal (i.e., cyclic moisture and temperature) conditions for thermoset and thermoplastic polyimides [1]. Hergenrother [2] also indicated the importance of an absence of microcracking after thermal cycling under stress for SST structural high-temperature composites. Microcracking is thought to facilitate oxidation and to accelerate the degradation of mechanical strength of polymer matrix composites. Mazzio and Mehan [3] reported the strength degradation of graphite-epoxy composites by thermal cycling; however, they dealt with unidirectional fiber laminates only and provided no data for microcracking. Fahmy and Cunningham [4] demonstrated the effects of thermal cycles on the tensile strengths, moduli, and thermal expansion coefficients of graphite-epoxy laminates and the degradation of these properties attributed to matrix cracks. There are no reports however dealing the quantitative relationship between microcracking by thermal cycling and compressive strength for high-temperature polymer-matrix composites.

This study involved thermal cycling tests up to 10,000 cycles for three kinds of high-temperature polymer-matrix composite for use in the structures of the Next-Generation SST. The number of microcracks initiated was counted and the open-hole compressive strength investigated by static mechanical tests at room temperature before and after thermal cycling. In addition, an analysis based on a simple finite element model was conducted to estimate the thermal stress generated in a laminate using the basic lamina data of the T800H/PMR-15 carbon/polyimide composite.

### **Materials, Specimens, and Testing Procedure**

The materials tested were three varieties of carbon/high-temperature polymer composite made from two kinds of carbon/polyimide prepreg systems: IM7/PI-XA and IM7/K3B, and a carbon/bismaleimide prepreg system - G40-800/5260. Nominal lamina-thickness of each of the IM7/PI-XA, IM7/K3B, and G40-800/5260 prepreg systems was 0.134 mm. The laminates had a quasi-isotropic stacking-sequence of 32 plies (45/0/-45/90)<sub>4S</sub>. Figure 1 illustrates the specimen configurations for microcrack observation and open-hole compression tests. The cross-sections observed for microcracks were the orthotomic surfaces to 0, 45, and 90 degrees of fiber direction as indicated in Fig. 1 and polished before thermal cycling. The size of the compressive specimens is short only in length in comparison with that recommended in SACMA SRM 3-88. The clamped area is 40 mm from each end of the specimen.

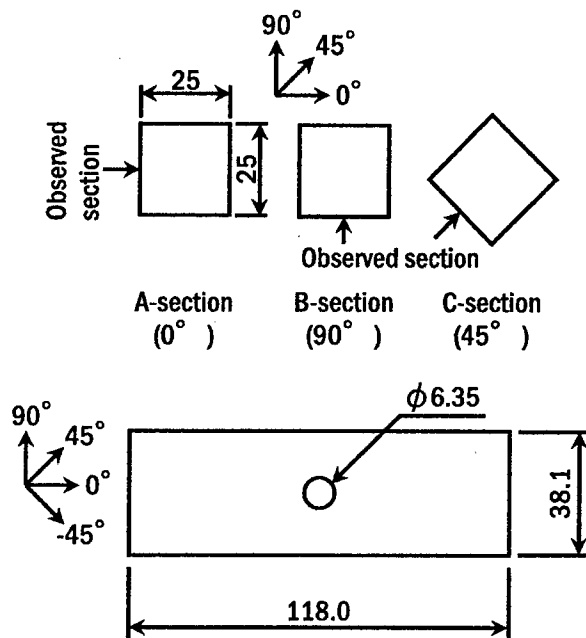


Figure 1 Specimen configurations for microcrack observation and open-hole compression tests.

Fast thermal cycling tests were conducted for specimens in a hot-cold chamber in order to maintain accurate retention time at the specified maximum and minimum temperatures and to keep the testing period as short as possible. Figure 2 shows the test system, i.e., a TSA-70H thermal-shock testing system manufactured by the TABAI ESPEC Company. This system has a hot air chamber and that of cold air with cold storage plates above and below the testing chamber respectively. The temperature inside the testing chamber is controlled by circulating air via opening and closing of the doors on both sides of the chamber. The test thermal cycle consisted of a minimum temperature of  $-54^{\circ}\text{C}$  and a maximum temperature of  $+177^{\circ}\text{C}$  with retention time of 15 minutes. The averaged heat-up and pull-down rates were approximately  $44^{\circ}\text{C}/\text{min.}$  and  $94^{\circ}\text{C}/\text{min.}$  respectively. Figure 3 shows an example of the testing thermal cycle measured by a thermocouple embedded in a specimen of the same size for microcrack observation. One thermal cycle required approximately 38 minutes.

At scheduled thermal cycles, transverse microcracks were observed using an optical microscope only in the layers in which the fiber direction was 90 degree to the observed surface, due to the visibility of this type of microcracks. The number of initiated microcracks was then counted.

The compression test specimens were taken out from the test-chamber at the scheduled cycles, static compression tests conducted after dehumidifying of the specimens in a vacuum drying-oven.

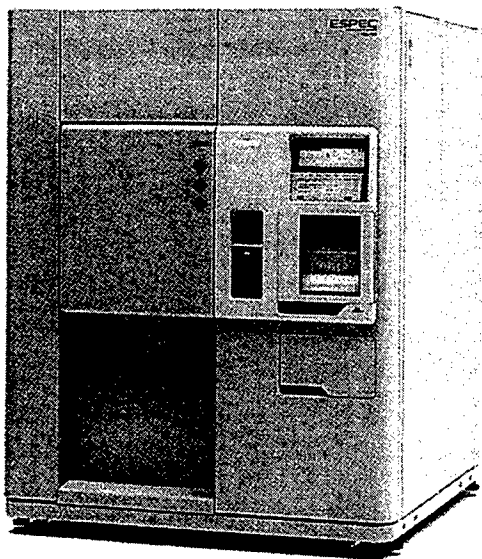


Figure 2 Thermal cycling test system.

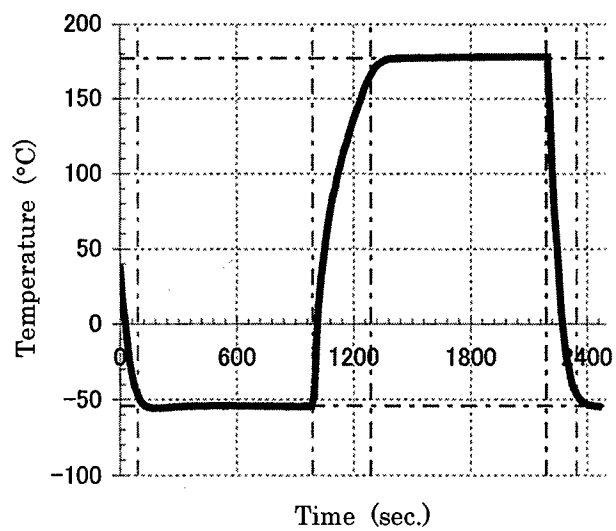


Figure 3 Test thermal cycle measured in a specimen of the same size as that used for microcrack observation.



## Test Results

### Number of Microcracks Initiated

Figure 4 shows a typical example of the type of microcrack observed. Each one of the three kinds of specimen shown in Fig. 1 was used in the observation of microcracks for one test case. The region observed in each section is the central area of 10mm long  $\times$  laminate thickness. The total number of microcracks was defined as the sum of the numbers found in the orthotomic surfaces to 0 and 90 degree fibers and two times the number in the orthotomic surface to 45 degree fibers. No delamination-microcracking was observed in this study.

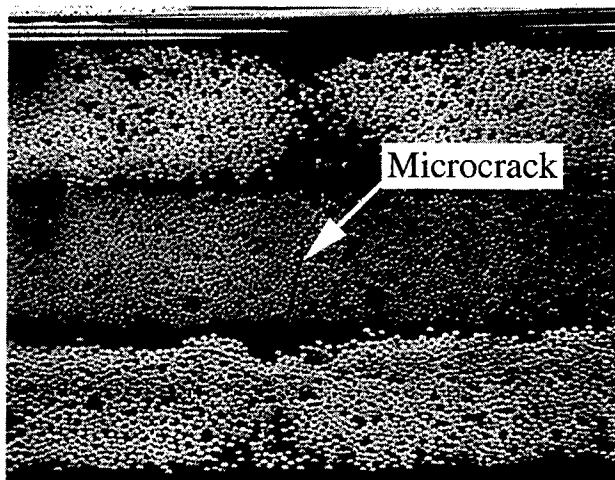


Figure 4 A typical transverse microcrack.

Figure 5 presents the relationship between number of microcracks observed and thermal cycles for three kinds of carbon fiber/high-temperature polymer-matrix composite. Thermal cycling tests on both polyimide-matrix composites, IM7/PI-XA and IM7/K3B, were carried out up to 10,000 cycles, and on a bismaleimide matrix composite, G40-800/5260, up to 1,000 cycles. In the case of IM7/PI-XA, microcracks were found even in the first 10 cycles. The extent of microcracking was considerable and increased up to 10,000 cycles. In the case of IM7/K3B, microcracking was not confirmed until 1,600 cycles and found at 5,000 cycles. A remarkable increase in the number of microcracks was observed from 5,000 cycles to 10,000 cycles. In G40-800/5260, the initiation of microcracks was confirmed at 1,000 cycles, and the number of microcracks at 1,000 cycles comparable with that of IM7/PI-XA.

In the case of G40-800/5260, extra thermal cycling tests using a different maximum temperature of +149°C were conducted up to 1,000 cycles. Microcrack initiation was not found at 1,000 cycles.

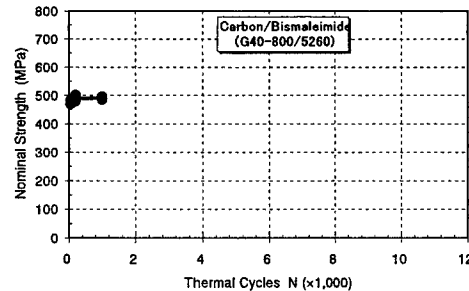
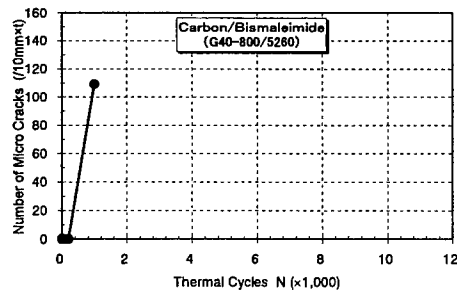
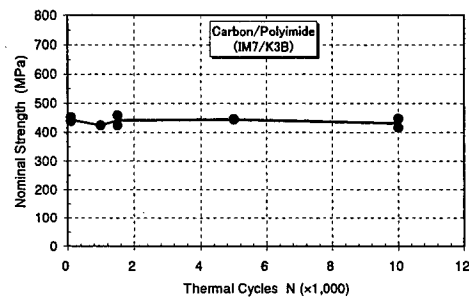
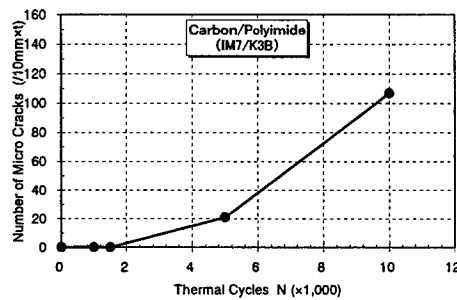
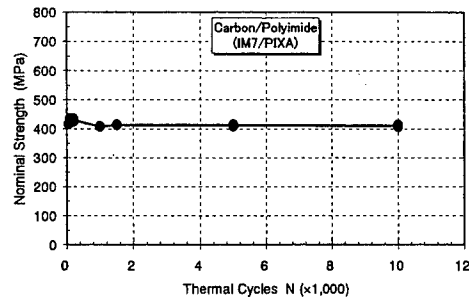
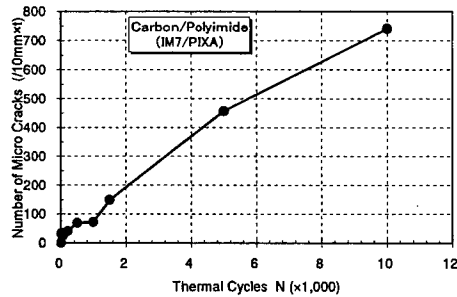


Figure 5 Number of microcracks initiated in the sectional area of 10mm x thickness as a function of thermal cycles.

Figure 6 Open-hole compressive strength at room temperature before and after thermal cycles.

### Open-Hole Compressive Strength

Static compression tests were carried out at room temperature. Figure 6 illustrates the relationship between open-hole compressive strength and thermal cycles for three kinds of carbon fiber/high-temperature polymer composite. As a rule two specimens were used for each test.

No degradation of open-hole compressive strength was observed up to 10,000

cycles for either IM7/K3B or IM7/PI-XA, though the number of microcracks increased up to 10,000 cycles as shown in Fig. 5, nor did open-hole compressive strength decrease up to 1,000 cycles for G40-800/5260. Considerable microcracking was found however at 1,000 cycles.

This study confirmed that transverse microcracks do not affect open-hole compressive strength, an important property when considering materials for use in composite SST structures. Compressive strength degradation may however occur if a microcrack grew inter layers, i.e. as a delamination crack, with a further increase in thermal cycles.

#### Thermal Stress Calculation Using a Simple Finite Element Model

A simple finite element model as shown in Fig. 7 was used to evaluate internal thermal stresses in the laminates. Since basic lamina data for the composite materials used in this study do not exist, the internal thermal stresses were calculated using the basic lamina data of a T800H/PMR-15 carbon/polyimide laminate obtained in joint research by NAL and NASDA (the National Space Development Agency of Japan). The objective of this calculation was to estimate the numerical values of the thermal stresses.

First it was assumed that a tensile elastic modulus of  $0^\circ$  lamina is constant regardless of temperature, and the temperature difference is  $180^\circ\text{C}$ . The thermal transverse tensile-stress generated in the layer of the central element in this model was calculated to be  $42.7\text{MPa}$ . If the temperature difference is  $300^\circ\text{C}$ , this stress will be  $71.1\text{MPa}$ . The tensile strength of the fiber transverse direction of T800H/PMR-15 was approximately  $63.7\text{MPa}$  at room temperature.

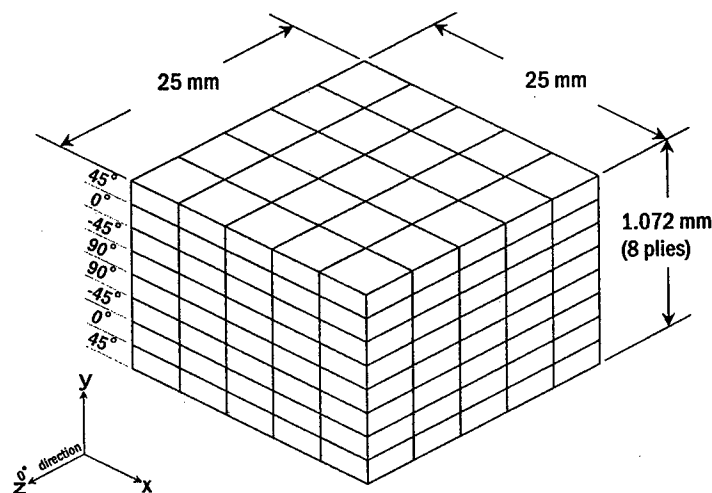


Figure 7 Simple finite element model of the laminate.

A microcrack may occur in one thermal cycle at a temperature difference of at least 269°C, because 63.7MPa corresponds to the thermal stress at a 269°C difference in temperature, when a linear variation of thermal stress is assumed between temperature differences of 180°C and 300°C.

This study employed a 231°C difference between the maximum and minimum temperatures. A microcrack may not initiate in one thermal cycle for T800H/PMR-15. However, if thermal fatigue were taken into account, the situation would be very severe. Therefore, thermal fatigue would be very severe for microcracking in the high-temperature polymer composite materials tested in this study.

## Conclusions

Major results obtained by the thermal cycling tests and an FEM analysis are as follows:

- (1) The number of microcracks initiated per 10mm×thickness as a function of thermal cycles was found. This number varied according to the material.
- (2) The open-hole compressive strength before and after thermal cycles did not change during the course of this study, therefore, thermal cycles and the initiation of transverse microcracks did not affect the open-hole compressive strength.
- (3) The calculated tensile-stress level generated by one thermal-cycle of 231°C temperature difference was under the limit for crack initiation; however, if thermal fatigue were taken into account, this thermal-stress cycle would be very severe.

## References

- [1] National Research Council, "U.S. Supersonic Commercial Aircraft - Assessing NASA's High Speed Research Program," National Academy Press, Washington DC, 1997, p. 72.
- [2] P.M. Hergenrother, "Composites, Adhesives and Sealants for High Speed Commercial Airplanes," Chemical Innovations, Feb. 2000 (to be published).
- [3] V.F. Mazzio and R.L. Mehan, "Effects of Thermal Cycling on the Properties of Graphite-Epoxy Composites," ASTM STP 617, 1977, pp. 466-480.
- [4] A.A., Fahmy and T.G., Cunningham, "Investigation of Thermal Fatigue in Fiber Composite Materials," NASA-CR-2641, July 1976.

## Novel Carbon Fiber Reinforced Composites with Newly Developed Silicon Containing Polymer MSP

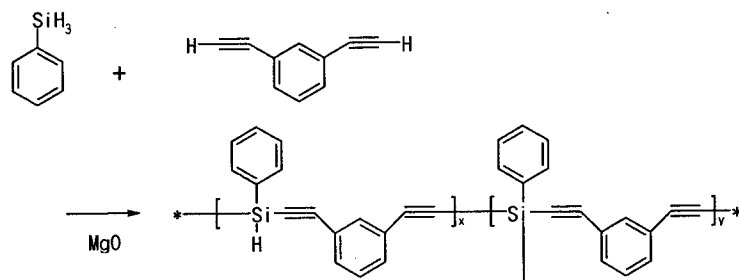
T. Ogasawara, T. Ishikawa, M. Itoh, T. Abe, R. Yokota and M. Ando

### Abstract

The objective of the study was to investigate the processing, material characteristics and mechanical properties of novel carbon fiber reinforced composite with newly developed silicon containing polymer. The polymer, poly [(phenylsilylene) ethynylene -1, 3- phenyleneethynylene], abbreviated MSP, has low thermosetting temperature (423 - 480 K), no volatility with cure, light weight (density 1.14 g/cm<sup>3</sup>), and excellent heat-resistance. In this study, carbon fiber reinforced composites with MSP were made by prepreg consolidation of plain 2-D woven prepreg sheets, and resin transfer molding (RTM) with a stitched plain 2-D woven fabric. Compressive testing were conducted for evaluating the mechanical properties of the composites. However the strengths of the composites were not fairly well at elevated temperature. It was attributed to embrittlement and shrinkage of the polymer during heat treatment above 473 K.

### Introduction

The polymer, poly [(phenylsilylene) ethynylene -1, 3- phenyleneethynylene] (abbreviated MSP), was developed by Mitsui Chemicals Ltd in 1994 [1]. The polymer is made by dehydrogenative coupling polymerization reactions between phenylsilane and m-diethynylbenzene (Scheme 1) [1-2].



<Scheme 1>

Toshio Ogasawara and Takashi Ishikawa, Structures Division, National Aerospace Laboratory, 6-13-1, Ohsawa, Mitaka, Tokyo, 181-0015, Japan  
Masayoshi Itoh and Takaharu Abe, Mitsui Chemicals, Inc., Sodegaura, Chiba, 299-0265, Japan  
Rikio Yokota, Institute of Space and Astronautical Science, Sagamihara, Kanagawa, 229-8510, Japan  
Masato Ando, Toho Rayon Co., Ltd., Nagaizumi, Shizuoka, 411-8720, Japan

The polymer has reactive  $\text{-Si-H}$  and  $\text{-C}\equiv\text{C-}$  bond, therefore, it is cross-linked above 423 K by hydrosilylation reaction between  $\text{-Si-H}$  and  $\text{-C}\equiv\text{C-}$ . The Diels-Alder reaction between  $\text{-C}\equiv\text{C-}$  and  $\text{-C}\equiv\text{C-}$  proceeds above 473 K and a very highly thermally stable structure is formed. Thermogravimetric analysis data of the cured polymer in argon atmosphere is shown in Fig.1. It can be seen that the pyrolysis temperature is higher than 800 K, and the char yield is more than 94% at 1273 K.

Engineering applications of MSP have been studied for several years, such as fiber reinforced composites [3], glassy carbon [3,4], electrical insulators and ablative materials [5]. MSP has some advantages as matrix material of high temperature polymer based composites in comparison with polyimides. Thus, it has low thermosetting temperature (423-480 K), no volatility with cure, and high decomposition temperature ( $> 800$  K). However, little investigations about the MSP matrix composites have been reported.

In this study, carbon fiber reinforced composites with MSP polymer were fabricated by prepreg consolidation, and resin transfer molding (RTM) method. To establish a processing of the MSP / CFRP composites, MSP polymer were characterized by using thermal analyses such as TGA, DSC, TMA, and FT-IR. Mechanical properties of the composites were evaluated by compressive testing at elevated temperature as well as room temperature.

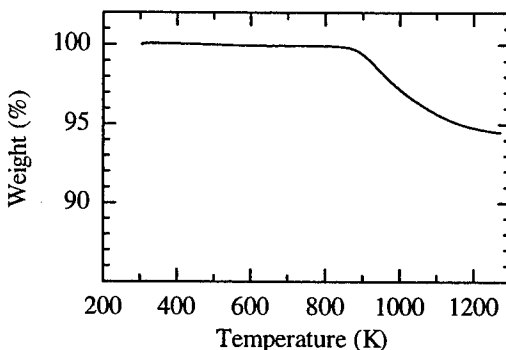


Figure 1 Thermogravimetric Analysis (TGA) Data of MSP polymer (Type-S) in Argon Atmosphere

## Experimental Procedure

### Polymer Properties

The polymers used in this study were a pale yellow amorphous solid (Type S) for prepreg preparation, and a viscous yellow liquid (Type L) for an RTM fabrication. Weight-average molecular weight ( $M_w$ ) of the polymer was 7417 for S-type polymer and 2124 for L-type polymer, respectively. The viscosity of L-type polymer was 10 Pa·s at 323 K, and 1 Pa·s at 363 K, it was low enough to apply the polymer to an RTM processing.

### Kinetic Analysis of Cure

Kinetic analyses of cure process in epoxy resin have been reported in a lot of literatures based on a differential scanning calorimeter (DSC) technique [6]. The work is concerned with a estimation procedure for the determination of the kinetic parameters. It is assumed that the rate of heat generation during cure is proportional

to the rate of the cure reaction. Then, the degree of cure  $C$  of the polymer may be defined as

$$C = H(t)/Q$$

$H(t)$  is the heat evolved from the beginning of the reaction to final time, and  $Q$  is the total or ultimate heat generation during cure. The reaction of thermosetting polymer systems can be realistically assumed by the following kinetic expression.

$$dC/dt = k(T)f(C)$$

Where,  $C$  = degree of cure,  $T$  = temperature,  $t$  = time,  $k(T)$  = reaction rate constant expressed as a function of temperature, and  $f(C)$  = equation as a function of  $C$  dependent on type of reaction. Simple equations for  $k(T)$  and  $f(C)$  can be expressed as follows.

$$k(T) = A \exp\{- (E/RT)\}$$

$$f(C) = (1 - C)^n$$

Where,  $A$  is a constant,  $E$  is an activation energy,  $R$  is gas constant ( $=8.31$  J/mole/K), and  $n$  is a reaction order. Using these equations, the degree of cure was modeled throughout the range of applicable temperature (25-773 K).

#### Processing and Characterization of Composites

Materials and processing parameters of the composites (MSP-CFRP) fabricated by prepreg consolidation method are listed in Table 1. MSP polymer / carbon fabric prepreg was formulated by a solution impregnation process using toluene as solvents. An IM-600-3k plain weave fabric (Toho Rayon, Japan) was used for reinforcement. Prepreg sheets were stacked by hand lay-up, and the laminates were consolidated by using a hot-press at 423 K for 3 h. By the prepreg consolidation technique, high quality composite laminates without voids were obtained.

The processing parameters of MSP matrix composites fabricated by RTM method are listed in Table 2. An IM-600-3k plain weave fabric stitched with glass fibers (Unitica Co. Ltd., Japan) was used for a preform. The polymer was heated at 368 K and impregnated into a fiber preform with 0.98 MPa. After a polymer impregnation, it was heated at 453 K for 4 h. High quality composites were also obtained by RTM processing. The composite laminates were post-cured at 473K, 573K, or 673K for 2 hours under nitrogen gas atmosphere.

Chemical structures of the polymer were characterized by using a Fourier transform infrared spectrometer (FT/IR-610, JASCO, Japan). Thermal expansion and shrinkage behaviors were evaluated by a thermal mechanical analyzer (TMA-6300, Seiko Instruments, Japan).

#### Mechanical Testing

Compressive tests were conducted on a mechanical type testing machine (Model 8228, Instron, USA). The test configuration was similar to ASTM-D695-85. Nominal sample size was 25.4 mm in width, 105.5 mm in length, and 4 mm in thickness without tabs. Compressive tests were conducted under a constant displacement rate of 1.0 mm/min. Specimens were held for 10 minutes after

reaching the test temperature with heating rate of 3 °C/min. Elastic modulus was measured by using strain gauges affixed on both sides of specimen surface at room temperature.

Table 1 Materials and Processing Parameters of MSP/CFRP Fabricated by Prepreg Consolidation

Carbon fiber	IM-600-6K (Toho Rayon)
Carbon fabric	Fabric; plain weave (0°/90°) W6E01 Areal Weight; 200 g/m <sup>2</sup> Count warp and fill; 492 yarn/m
Polymer	MSP type-S (STM-3S, Mitsui Chemicals) Solid type, Mn=3050, Mw=7417
Polymer content	38 wt%
Fiber fraction	48-50 vol% (x:y =1:1)
Ply	20 ply (For compressive test, thickness 4.5 mm)
Cure temperature	Pre-cure; 423 K, 3 h Post-cure; (a) 473 K, 2 h, (b) 673 K, 2 h
Fabricator	Toho Rayon Co., Ltd.

Table 2 Materials and Processing Parameters of MSP/CFRP Fabricated by Resin Transfer Molding (RTM)

Carbon fiber	IM-600-6K (Toho Rayon)
Carbon fabric	Fabric; plain weave (0°/90°) W6E01 Areal Weight; 200 g/m <sup>2</sup> Count warp and fill; 492 yarn/m
Stitched glass fiber	B150 1/4 10.4z x-2 (Unitica Ltd.)
Polymer	MSP type-L (STM-5L-A, Mitsui Chemicals) liquid type, Mn=804, Mw=2124
Fiber fraction	54-56 vol% (x:y:z=1:1:0.02)
Ply	20 ply (For compressive test, thickness 4.5 mm)
Cure temperature	Pre-cure; 453 K, 4 h Post-cure; (a) 473 K, 2 h, (b) 673 K, 2 h
Fabricator	Japan Aircraft MFG Co., Ltd.



## Results and Discussion

### Kinetics of Cure and Thermosetting Reaction

Typical DSC data of MSP polymer (type-S) are plotted in Fig.2. The estimated parameters for kinetics of cure are listed in Table 3, which were estimated by Friedman method [7]. The heat generation of type-L polymer was approximately twice as much as that of type-S.

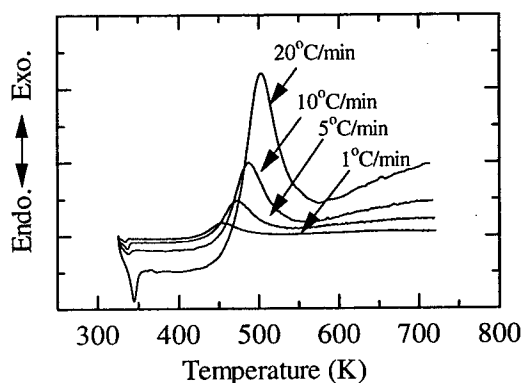


Figure 2 DSC data of MSP resin (Type-S): Heating rate was 1, 5, 10, and 20 °C/min, respectively.

Fig.3 shows the FT-IR spectra of non-cured and cured MSP (type-S) polymer at 423, 473, 573 K for 2 h., respectively. The decrease in an IR absorption peak around  $3300\text{ cm}^{-1}$  ( $\text{-C}\equiv\text{C-H}$ ) is obviously observed. Thus, the heat generation measured by DSC may correspond to hydrosilylation reaction between  $\text{-Si-H}$  and  $\text{-C}\equiv\text{C-H}$  of terminal in MSP polymer. Any other obvious difference between non-cured and cured polymer at 473 K could not be observed in the FT-IR spectra. Heat generation due to the Diels-Alder reaction between  $\text{-C}\equiv\text{C-}$  and  $\text{-C}\equiv\text{C-}$  above 473 K could not be measured by DSC. However, an absorption peak around  $2200\text{ cm}^{-1}$  decreases with heat treatment temperature, which suggests the decreases in  $\text{-Si-H}$  bond by hydrosilylation reaction, and  $\text{-C}\equiv\text{C-}$  bond by the Diels-Alder reaction.

Table 3 Cure Kinetic Parameters of MSP polymer (type-S and type-L)

	MSP type-S (STM-3S)	MSP type-L (STM-5L-A)
$A$ (1/s)	$2.2 \times 10^7$	$3.7 \times 10^9$
$E$ (kJ/mole)	90	112
$n$	1.2	1.2
$Q$ (J/g)	179	365

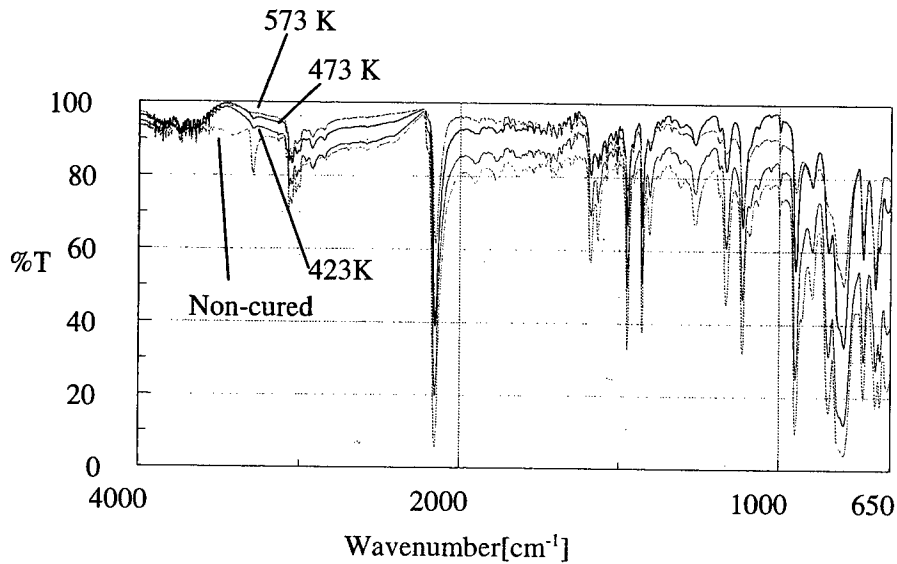


Figure 3 FT-IR Spectra of Non-cured and Cured MSP Polymer (Type-S)

#### Mechanical Properties

Fig.4 shows compressive strength data of the composites at room temperature, as a function of heat treatment temperature. The compressive strengths of the composite cured at 473 K were not fairly well in comparison with typical graphite / epoxy composites [7]. Furthermore, the strength degradation of the composites was considerable after heat treatment above 573 K, and the compressive strengths were quite poor. It should be noticed that the strength degradation due to heat treatment is irreversible.

The stitched composite was a little bit stronger than the non-stitched composites at high temperature. Young's modulus at room temperature was 61.8 GPa for the composite laminate processed by prepreg consolidation, and 71.7 GPa for the stitched composite laminate processed by RTM, which corresponds to the fiber volume fraction as shown in Table 1 and 2.

Compressive strength data at elevated temperature are plotted in Fig.5. The compressive strengths of the composites cured at 473 K considerably decreased with temperature. Although the strengths of the composite cured at 673 K were almost constant up to 573 K, the strengths were quite poor. It can be observed that

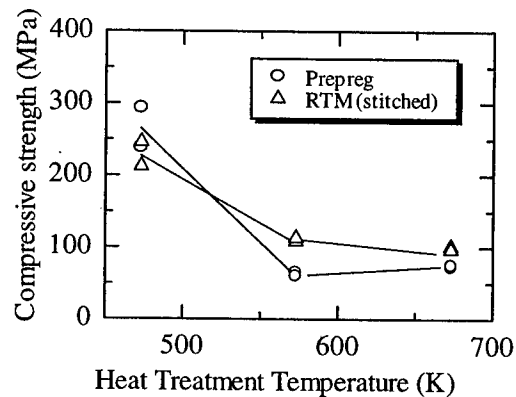


Figure 4 Compressive Strengths of the MSP-CFRP at Room Temperature as a Function of Heat Treatment Temperature

the compressive strength was a little bit improved by stitched fibers.

Fig.6 shows an SEM micrograph of the composite after heat treatment at 673K. A lot of matrix cracks were observed in transverse fiber bundles and resin rich regions. The compressive strength of the composites was degraded by these cracks. Thermo-mechanical analysis (TMA) data of MSP type-S polymer cured at 423 K is shown in Fig.7. After heat treatment at 473 K for 2 h., large volume shrinkage was observed above 550 K. The shrinkage was caused by post-curing reaction due to the Diels-Alder reaction, and subsequent increase in the cross-link density. As a result, residual stress in matrix increased after cooling, and a lot of matrix cracks were propagated in transverse fiber bundles. Furthermore, the polymer became brittle with cross-link density, the embrittlement also influenced the strength degradation of the composites.

To improve the mechanical properties of MSP polymer, polymer blend design with thermoplastic polymer such as polyimides seems to be the most effective method. Furthermore, basic polymer structure design for reducing the cross-linking density is also important for improving the toughness. Although stitched fibers in composite are certainly effective, it is impossible to improve the strength of MSP-CFRP sufficiently.

## Conclusion

In this study, carbon fiber reinforced composites with silicon containing polymer MSP were made by prepreg consolidation of plain 2-D woven prepreg sheets, and resin transfer molding (RTM) with a stitched plain 2-D woven fabric. The processing of MSP matrix composites have been established by prepreg consolidation and RTM method with polymer cure kinetics analysis. Compressive tests were conducted for evaluating the mechanical properties of the composites.

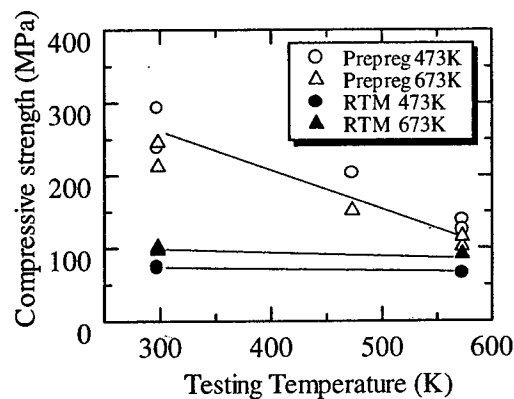


Figure 5 Compressive Strengths of CF/MSP Composites Cured at 473 or 673 K



Figure 6 SEM Photograph of the MSP-CFRP Heat-Treated at 673 K

However the strength of the composites were not fairly well at elevated temperature. It was attributed to embrittlement and shrinkage of the polymer during heat treatment above 473 K. Although MSP polymer has a lot of attractive properties as matrix of high temperature polymer based composite, the improvement of mechanical properties after heat treatment is indispensable for realistic engineering applications.

#### Acknowledgment

The authors thank Mr. S. Iwasawa and Mr. Y. Iwahori of Japan Aircraft MFG. Co. Ltd. for their assistance in development of resin transfer molding process.

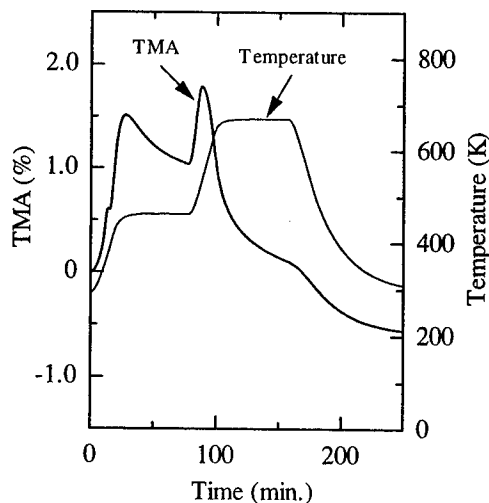


Figure 7 TMA Data of MSP Type-S Polymer Cured at 423K in Argon atmosphere

#### References

- [1] M. Itoh, M. Mitsuzuka, K. Iwata, K. Inoue, 1994. "A Novel Synthesis and Extremely High Thermal Stability of Poly[(phenylsilylene)ethynylene-1,3-phenyleneethynylene]", *Macromolecules*, 27: 7917-7919.
- [2] M. Itoh, K. Inoue, K. Iwata, M. Mitsuzuka, T. Kakigano, 1997. "New Highly Heat-Resistant Polymers Containing Silicon: Poly (silylene ethynylene phenylene ethynylene)s ", *Macromolecules*, 30: 694-701.
- [3] M. Itoh, K. Inoue, K. Iwata, J. Ishikawa, Y. Takenaka, 1997. "A Heat-Resistant Silicon-Based Polymer", *Adv. Mater.*, 9[15]: 1187-1190.
- [4] M. Narisawa, H. Takao, J. Hoshino, K. Okamura, M. Itoh, 1997. "Formation of Amorphous Carbon containing Silicon from a New Organosilicon Precursor", 1996, *J. Ceram. Soc. Jpn*, 104: 812-815
- [5] T. Ogasawara, T. Ishikawa, T. Yamada, R. Yokota, M. Itoh, S. Nogi, 2000. "Thermal Response and Ablation Characteristics of Novel Carbon Ablator with Silicon Containing Polymer for Re-entry Capsule", *Proc. 22<sup>nd</sup> ISTS (International Symposium on Space Technology and Science)*, 2000-c-35p.
- [6] D. Frank-Susich, D. Laanamen, D. Ruffner, 1992. "Computer-Aided Cure Optimization", *Proc. 37<sup>th</sup> Int. SAMPE Symposium*, March 9-12: 1075-1088.
- [7] H. L. Friedman, 1965. "Kinetics of Thermal Degradation of Charforming Plastics from Thermogravimetry. Applications to a Phenolic Plastic", *J. Polym. Sci. (Chem)*, 6: 183-195.
- [8] For example, *The composite materials handbook-MIL 17: Materials Properties*, Vol.2. Lancaster, PA: Technomic Publishing Company, Inc., pp. 4.1-4.220.

## **New Concept Composites, II**

---

## Flexural and compressive properties of polymer matrix composites containing a mixture of carbon and silicon carbide fibres: Part 2 - Compression

Ian J. Davies<sup>1</sup>, H. Hamada<sup>1</sup>, and M. Shibuya<sup>2</sup>

<sup>1</sup> Advanced Fibro-Science, Kyoto Institute of Technology,

Matsugasaki, Sakyo-ku, Kyoto 606-8585, Japan

(Tel: 075 724 7850, Fax: 075 724 7800, e-mail: [davies@ipc.kit.ac.jp](mailto:davies@ipc.kit.ac.jp))

<sup>2</sup> Corporate Research and Development, Ube Industries Ltd., Ube City, Yamaguchi, Japan

### ABSTRACT

Whilst carbon fibre reinforced plastic (CFRP) composites are known to possess excellent tensile mechanical properties, the relatively poor longitudinal compressive properties of carbon fibres [1] often shows itself in decreased compressive performance of the resulting CFRP composite. Therefore, in applications involving compressive or flexural loads, it may well be the case that overall mechanical properties of CFRP composites, particularly strength, will be limited by the compressive properties of the carbon fibres.

One method to circumvent this problem is through selective reinforcement of CFRP composite with ceramic fibres that have superior compressive properties, such as those based on the SiC system. Although a limited amount of research has been conducted into the mechanical properties of fibre reinforced plastic (FRP) composite containing a mixture of carbon and silicon carbide fibres [2,3], the carbon fibres used as a comparison (HTA-6000) had relatively poor tensile strength (3.6 GPa) and thus would also be expected to exhibit poor compressive strength. A more accurate approach might be to compare a FRP composite containing SiC fibres together with high strength carbon fibres.

In light of this, the authors have conducted an investigation into the flexural and compressive properties of 8 layer unidirectional FRP composites containing a mixture of SiC fibre (Tyranno Si-Ti-C-O fibre, Type S1, Ube Industries Ltd., Ube City, Japan) and high compressive strength carbon fibre (Type T700S, Toray, Tokyo, Japan) in an epoxy matrix. The first part of this investigation dealt with the flexural properties [4] of FRP composites with different amounts and configurations of C and SiC fibres as shown in *Table 1*. Specimens were machined to cross-sections of 6.5 x 2 mm and tested in the 3 point bend configuration with a span of either 32 mm (span-to-depth of 16) or 64 mm (span-to-depth of 32). A span-to-depth ratio of 32 was found necessary to prevent shear failure in the specimens containing 78 vol% of SiC fibres. Compared to specimens containing only carbon fibre, those with 12 to 50% of SiC fibre had increased flexural strength (11~20%) (*Fig. 1(a)*), specific flexural strength (5~6%) (*Fig. 1(b)*), estimated fracture energy ( $\geq 100\%$ ) (*Fig. 2(a)*), and specific fracture energy ( $\sim 100\%$ ) (*Fig. 2(b)*). It would thus appear that CFRP composites subject to flexural loads may benefit from partial substitution of carbon fibres by SiC fibres.

In the present work, the behaviour of 8 layer unidirectional FRP composite subject to compression testing will be investigated with the stacking sequence of specimens chosen to be the following: C/C/C/C/C/C/C/C, SiC/C/C/C/C/C/C/SiC, C/C/C/SiC/SiC/C/C/C, SiC/SiC/C/C/C/C/SiC/SiC, SiC/SiC/SiC/C/C/SiC/SiC/SiC, and SiC/SiC/SiC/SiC/SiC/SiC/SiC/SiC.

## REFERENCES

- [1] N. Oya, D. J. Johnson, and H. Hamada, to be published in proceedings of the Twelfth International Conference on Composite Materials, Paris, France, July 1999
- [2] O. Hiroyuki and H. Tsujihata, *Goseijyushi Kogyo* (Industrial Synthetic Resins), 4 (1991) 151
- [3] O. Hiroyuki and H. Tsujihata, *Goseijyushi Kogyo* (Industrial Synthetic Resins), 3 (1992) 106
- [4] I. J. Davies, H. Hamada, and M. Shibuya, in Proceedings of the 6th Japan International SAMPE Symposium and Exhibition (JISSE-6), Tokyo, Japan, October 1999, in press

Table 1: Specimens previously tested in flexure by the present authors [4].

Layer arrangement	Number of layers	Specimen name	Density (gcm <sup>-3</sup> )	Estimated composition (vol%)		
				SiC fibre	C fibre	Matrix
C/C/C/C/C/C/C/C	8	8c	1.60	0.0	70.0	30.0
SiC/C/C/C/C/C/C/C	8	1s	1.70	9.8	61.3	29.0
SiC/SiC/C/C/C/C/C/C	8	2s	1.75	19.5	52.5	28.0
SiC/SiC/SiC/C/C/C/C/C	8	3s	1.79	29.3	43.8	27.0
SiC/SiC/SiC/SiC/C/C/C/C	8	4s	1.87	39.0	35.0	26.0
SiC/SiC/SiC/SiC/SiC/SiC/SiC/SiC	8	8s	2.09	78.0	0.0	22.0

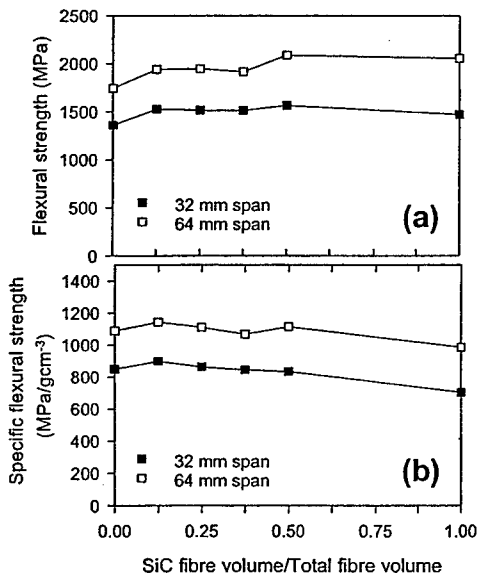


Figure 1: Flexural properties as a function of SiC fibre volume fraction:  
 (a) flexural strength, and  
 (b) specific flexural strength [4].

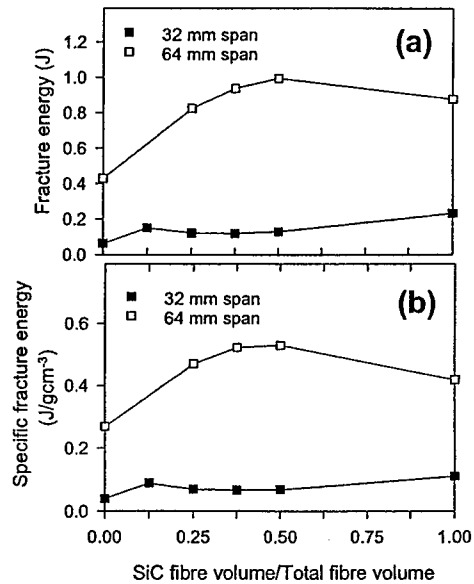


Figure 2: Flexural properties as a function of SiC fibre volume fraction:  
 (a) estimated fracture energy, and  
 (b) specific fracture energy [4].

## **Development of carbon fiber composites using biodegradable plastics and their mechanical properties**

Jianye Jiang, Kazuya Okubo and Toru Fujii

### **Abstract**

Carbon fiber composites using biodegradable plastics (CFRBP) have been developed. Plain weave carbon fabrics and biodegradable thermoplastics were used as reinforcement and matrix, respectively. CFRP (carbon fiber reinforced plastics) was also fabricated using conventional epoxy matrix and the same carbon fabrics for comparison. CFRBP was fabricated by hot pressing. Its tensile strength, bending strength and inter-laminar fracture toughness were measured at room temperature. The experimental results showed that the tensile and bending strengths of CFRBP were slightly lower than those of CFRP using epoxy matrix, but the interlaminar fracture toughness of CFRBP was about 300% as high as that of CFRP. Therefore, CFRBPs have a potential in strength as engineering materials for structural elements supporting severe loads.

### **Introduction**

PMC (polymer matrix composites) such as carbon or glass fiber reinforced plastics (CFRP/GFRP) are now widely used not only in the aerospace industry but also in the sport goods and automobile industries as primary structural members since they have high specific strength and modulus [1]. Thermosetting resin matrices are used for those composite materials although FRTP (fiber reinforced thermoplastics) is also very popular. Therefore, it is very difficult for both CFRP and GFRP to be recycled after their use is terminated. Wasted FRPs are mostly buried although some of them are burned. They won't be naturally decomposed under the ground. What is one of the most difficult problems for FRP using thermoset plastics is that compositions of FRP cannot be separated with less energy once they are fabricated. Material recycling has not been practical today even for FRTP (using thermoplastics) from viewpoints of cost and quality, and some recycling systems including energy recycling are still under development. If compositions of FRP such as fibers and fillers are separated without consuming a lot of energy, we may expect to solve some problems accompanying with FRP waste.

Now, biodegradable plastics are being developed and focused as future materials reducing burdens against environment accompanied with waste. However, they cannot be used to replace some engineering plastics due to their poor mechanical proper-

---

Jianye Jiang, Venture Laboratory, Graduate School, Kyoto Institute of Technology, Matsugasaki, Sakyo-ku, Kyoto 606-8585, Japan

Kazuya Okubo, Toru Fujii, Department of Mechanical Engineering and Systems, Doshisha University, Kyo-tanabe, Kyoto 610-0321, Japan



ties as well as the cost [2]. Reinforcing biodegradable plastics with high strength fibers such as glass fibers is one of ideas to improve their strengths. If we use biodegradable plastics as matrix for one of strength oriented PMC, fibers and fillers would be taken out from composites at relatively low energy consumption by putting them into composites. Even if fiber composites using biodegradable plastics would be thrown away in the nature, their matrix will be biodegraded. And we may expect inorganic fibers and fillers will give less burdens against environment.

Recently, we have developed carbon fabric composites using biodegradable plastics (CFRBP: Carbon Fiber Reinforced Biodegradable Plastics). Their tensile strength, bending strength and interlaminar fracture toughness were examined in this paper. Whether the newly developed CFRBP is applicable to primary structural members is examined by comparing the mechanical properties above mentioned to those of CFRP using the same carbon fabrics and conventional epoxy matrix.

#### How to Fabricate CFRBP by Hot Pressing.

Two types of PAN-based plain weave carbon fabrics (CO6343-T300 and CO6343B-T300: TORAY) were used as reinforcement. Fiber bundles of the former CO6343-T300 are twisted while those of the later CO6343B-T300 are straight. The matrix used for CFRBP was one of biodegradable thermoplastics, made from corn (LACEA H-100PL: MITSUI CHEMICALS). LACEA is poly-lacticacid biodegradable thermoplastics (PL). Laminates from which specimens will cut are fabricated as follows.

First, biodegradable plastic films whose thickness is about 0.25 mm are alternatively stacked with plain weave carbon fabrics (Fig.1). Then, stacked films and fabrics are hot-pressed for 10 minutes at 190 °C under vacuum. Laminates are pressed at 7.84 MPa (80 kgf/cm<sup>2</sup>). Dimensions of the laminates are about 300 mm long, 200 mm wide and 3 mm in thickness. Some spherules occur in PL (H-100PL) during cooling process at a low cooling rate [3]. Such spherules increase the rigidity and the strength although the material may loose the toughness [4]. Therefore, in order to examine the effect of cooling rate on the mechanical properties, two cooling rates; roughly 50 °C/min. (designated as "H") and 1 °C/min. (designated as "L") are applied when the laminates are removed from the hot pressing mold. The carbon fiber volume content of CFRBP is about 40%.

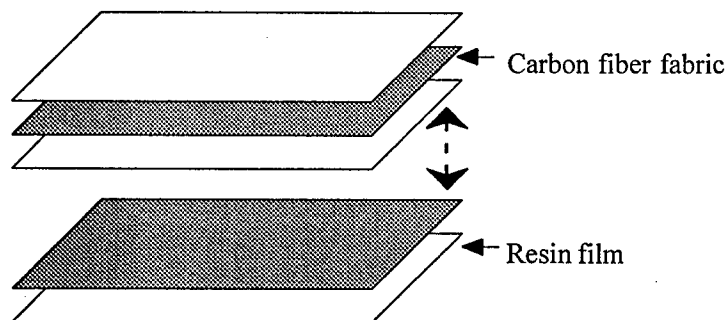


Fig.1 Schematic illustration of stacking sequence of CFRBP

## Test Specimens and Experimental Procedure

For comparison, CFRP laminates were also fabricated by the hand-lay-up method using epoxy resin (Epikote 828: Yuka-Shell) and the same carbon fabrics as used for CFRBP. The hardener was acid anhydride. They were cured at 90 °C for 1 hour and 120 °C for 3 hours under the pressure of 4.9 MPa (50 kgf/cm<sup>2</sup>).

Laminates used in this study are classified as shown in Table 1. "B" in the table shows that the specimens contain straight fiber bundles. Twisted fiber bundles are used for specimens without "B". Letters "L" and "E" after "/" designate the matrix material (either PL or epoxy). The last letters "-H" and "-L" identify the cooling rate. For example, the "CFB/L-L" means the specimen was fabricated using straight fiber bundles as reinforcement and PL as matrix cooled at the low cooling rate.

Tensile and (three point) bending strengths of both CFRBP and CFRP were measured under static loading according to JIS K7054 and JIS K7055. A universal-testing machine was used. Dimensions of the parallel sided specimens are 200 mm long and 25 mm wide having the original thickness of laminates for the tensile tests. They are 80 mm long and 15 mm wide for bending tests. The cross-head speed is 1 mm/min. for tensile tests. The span is 50 mm, and the cross-head speed is 2 mm/min. for bending tests.

Double Cantilever Beams (DCB) specimens cut out from laminates were used in order to measure the interlaminar fracture toughness. The testing speed is 1mm/min.. A pair of aluminum blocks with circular holes are glued to both beams as loading tabs. The fractured surface of specimens failed under tensile loading of CFRBP and CFRP is observed using a scanning electron microscope (SEM).

## Results and Discussion

### (1) Tensile S-S relations of PL and CFRBP under static loading

Typical tensile stress-strain curves of PL (bulk) cooled from its melting point to room temperature rapidly (L-H) and slowly (L-L) are shown in Fig.2. The tensile stress-strain curve of the L-L specimen is linear up to the fracture while that of the L-H

Table 1 Types of CFRBP and CFRP

Laminates	Carbon Fiber	Matrix	Cooling rate (°C/cm <sup>2</sup> )
CF/L-L	CO6343-T300	LACEA	1
CF/L-H	CO6343-T300	LACEA	50
CFB/L-L	CO6343B-T300	LACEA	1
CFB/L-H	CO6343B-T300	LACEA	50
CF/E	CO6343-T300	epoxy	1
CFB/E	CO6343B-T300	epoxy	1

specimen is non-linear at stress higher than 50% of its fracture stress. L-L specimens became sensitive to tiny flaws due to crystallization, and failed in a brittle fashion at a low stress. The tensile strength of L-H specimens is about four times higher than that of L-L specimens. However, the initial modulus of L-L specimens is about 35% higher than that of L-H specimens.

Typical tensile stress-strain curves of CFRBPs (CF/L-H and CF/L-L) are shown in Fig.3. The tensile stress-strain curve of CF/L-H is almost linear up to failure. On the other hand, the CF/L-L specimen shows a non-linear relationship beyond the stress of 75% of its fracture stress. The tensile strength of CF/L-L was lower (about 92%) than that of CF/L-H. CF/L-H fails in a brittle fashion although the matrix may be ductile as can be seen in Fig.2. The matrix of CF/L-L must be brittle due to slow cooling and internal damage such as matrix cracking may occur at a relatively early stage. Transverse cracks may occur at 350~400 MPa for CF/L-L and the S-S curve bends at that point. Successive damage following the transverse cracking weakens the stress transfer between fibers, and the local stress concentration is enhanced. Then, it is deduced that the final failure occurs at lower stress than the stress for CF/L-H while the observed tensile modulus is higher than that of CF/L-H since the modulus of the matrix for CF/L-L is higher than that for CF/L-H.

As above mentioned, PL is crystallized. Its modulus becomes high while it sacrifices the toughness due to spherules (see Fig.4) at a low cooling rate. Figure 5 shows

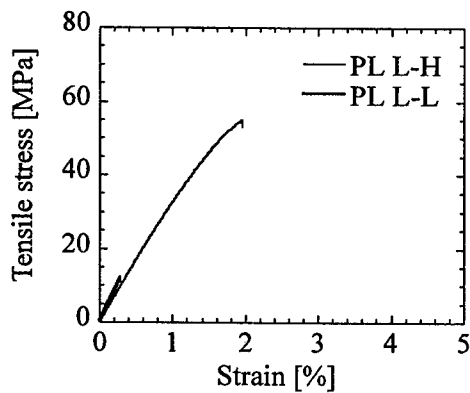


Fig.2 Tensile stress-strain curves of PL/L-H and PL/L-L

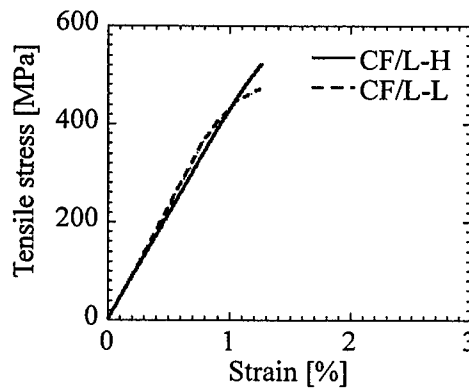


Fig.3 Tensile stress-strain curves of CF/L-H and CF/L-L

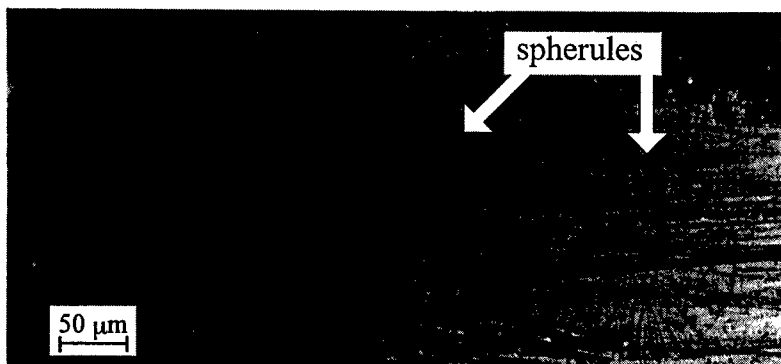


Fig.4 Spherules at low cooling rate

the failed specimen of CF/L-H and CF/L-L. Many delaminations between fiber and matrix in the CF/L-L can be identified. It is considered that the low cooling rate reduces the strength of CFRBP because delamination easily occurs in the material even if the matrix would have high tensile strength <sup>†</sup>.

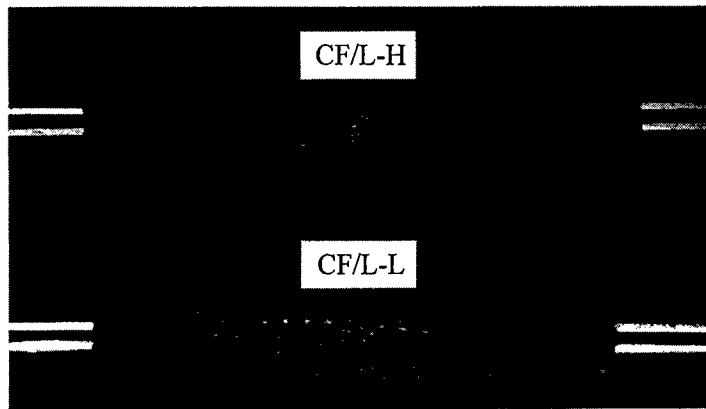


Fig.5 The failed specimens of the CF/L-H and CF/L-L

(2) Tensile strength, bending strength and fracture toughness of CFRP and CFRBP, and their comparisons

The tensile and bending strengths of CFRP and CFRBP are given in Fig.6. It is found from this figure that the strengths of CFRP (CF/E, CFB/E) are higher than those of CFRBP (CF/L-L, CF/L-H and CFB/L-L, CFB/L-H). The tensile and bending strengths of CFRBP using straight fiber bundles are higher than those of CFRBP using twisted fiber bundles. The test results also show that a high cooling rate increases

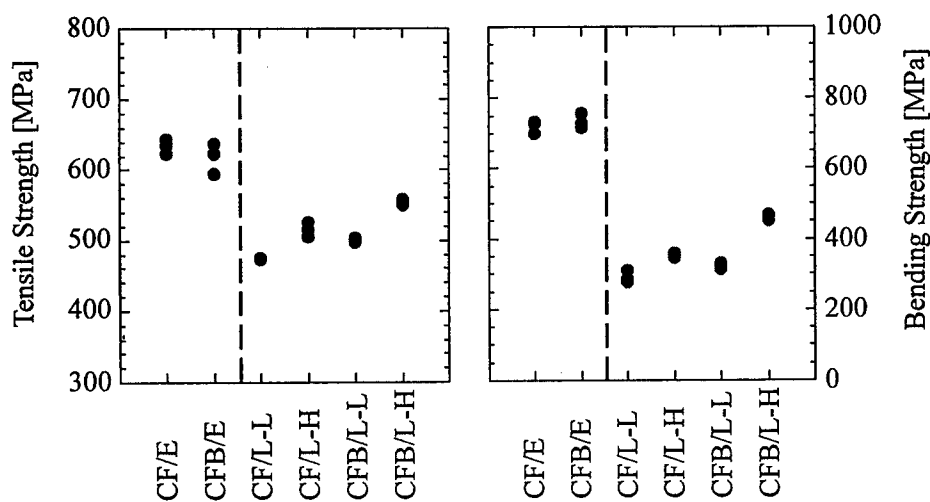


Fig.6 Tensile strength and Bending strengths of composites

<sup>†</sup> Figure 2 is not well confirmed that the tensile strength of PL containing spherules is higher than that of PL whose microstructure is amorphous

bending strength of CFRBP as well as for tensile strength.

Figure 7 shows the comparison of interlaminar fracture toughness among CF/E, CF/L-H and CFB/L-H. It is found that the interlaminar fracture toughnesses of CF/L-H and CFB/L-H laminates are about 280% and 300% higher than that of CF/E (CFRP using twisted fiber bundles). Both CFRBPs (CF/L-H and CFB/L-H) used in this study have high fracture toughness compared to the present CFRP.

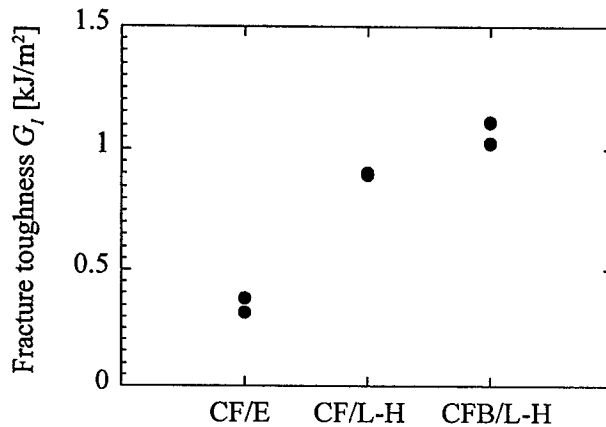


Fig.7 Variation of interlaminar fracture toughness

Figure 8 shows SEM photographs of the fractured surfaces of CF/E and CFB/E specimens failed under tensile loading. It is recognized that some resin remains on the fiber surfaces. It may be concluded that the interfacial strength between carbon fibers and epoxy matrix has high. The SEM photographs suggest that both CFRPs failed in a brittle fashion since some typical hackle patterns were apparently observed on the fractured surfaces of resin.

Tensile fractured surfaces of the CF/L-H and CFB/L-H specimens are shown in Fig.9. An occurrence of ductile failure was microscopically deduced for PL matrix cooled rapidly as well as other undecomposable thermoplastics presently used in the market. The fiber surfaces were smooth, which means that interfacial debonding oc-



CF/E



CFB/E

Fig.8 SEM photographs of fractured surfaces of tensile CF/E and CFB/E specimens

curs between fibers and matrix. The interfacial strength may be lower for CFRBP than that for the combination between carbon fibers and epoxy. Such lower interfacial strength may be one of reasons for lower tensile and bending strengths of CFRBP than those of CFRP although the interlaminar fracture toughness is higher than that of CFRP due to the weaker bonding strength and ductile fracture of the biodegradable plastics (PL).

### (3) Effect of fiber twisting on tensile and bending strengths of CFRBP

Figure 10 (a) also shows another SEM photograph of the fractured surface of CF/L-H (using twisted fiber bundles). Some voids can be found in fiber bundles. Figure 10 (b) shows a cross sectional view of a virgin CF/L-H specimen. An existence of voids in fiber bundles is also identical on the cross section of CF/L-H. On the other hand, CFB/L-H specimens using straight fiber bundles, less voids are observed on their cross section. It is supposed that the strength of CFRBP was reduced due to such voids in the

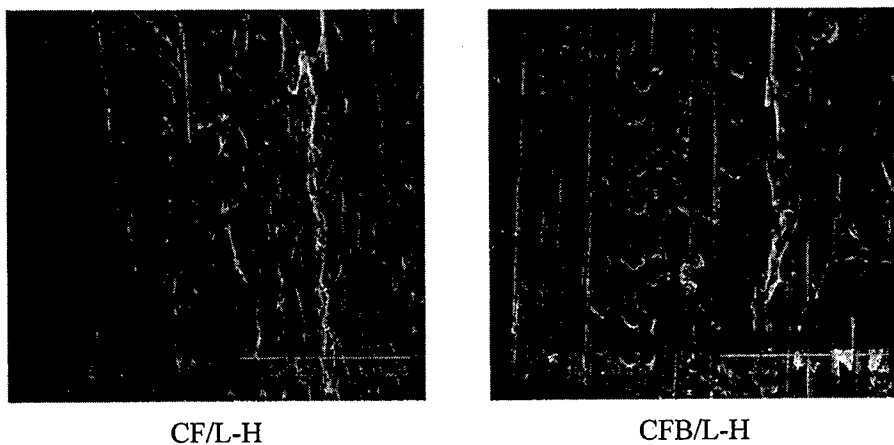


Fig.9 SEM photographs of fractured surfaces of tensile CF/L-H and CFB/L-H specimens

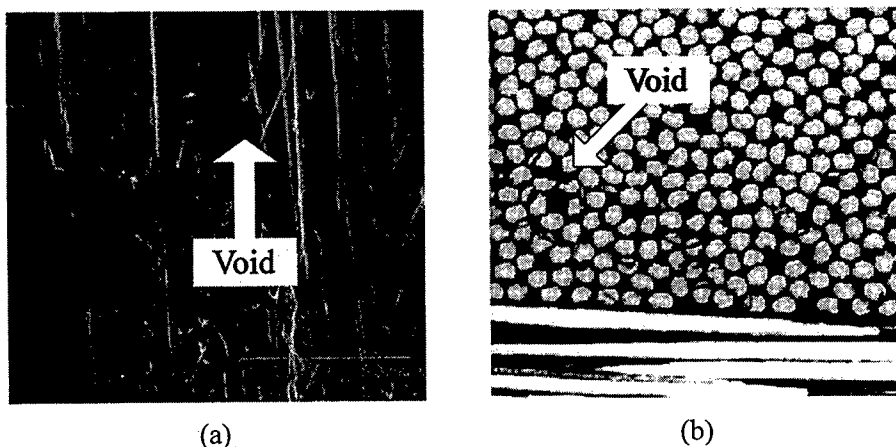


Fig.10 Micro photographs of CF/L-H specimen  
(a) SEM photograph of fracture surface (b) cross sectional view

twisted fiber bundles. Due to high viscosity of PL, the matrix cannot penetrate into fiber bundles of fabrics if they are twisted. Straight fibers are preferable for CFRBP fabricated by hot pressing.

## Conclusion

In this paper, we first examined the tensile strength of biodegradable thermoplastics used as the matrix of CFRBP. Second, CFRBP (Carbon Fiber Reinforced Biodegradable Plastics) and CFRP are fabricated. Their tensile strength, bending strength and interlaminar fracture toughness were examined and compared with each other. The test results showed that the tensile and bending strengths of CFRBP were slightly lower than those of CFRP using epoxy matrix, but the interlaminar fracture toughness of CFRBP was about 300% as high as that of CFRP. Therefore, CFRBPs have a potential in strength as engineering materials for structural elements supporting severe loads.

## Acknowledgments

This work was financially supported by a grant to RCAST at Doshisha University from the Ministry of Education, Japan. Biodegradable thermoplastics used in this study was supplied by the courtesy of MITSUI CHEMICALS, INC, Japan. The authors would like to express our special thanks to Mr. M. Matsuo (MITSUI CHEMICALS, INC.) for helping us.

## References

1. M. Miki, T. Fukuda, S. Motogi and M. Hojo, 1997. *Fukugozairyo (Composite Materials)*, Kyoritsu, pp. 53-61.
2. K. Fukuda, 1999. "Biodegradable thermoplastics." *Plastics Age*, 45, (2):84-85.
3. S. Ikado, 1999. "LACEA." *Plastics Age*, 45, (2):122-124.
4. Tim A. Osswald and H. Georg L. Menges, 1997. *Materials Science of Polymers for Engineers*, Shiguma, pp. 32-34.

## **Energy Absorption Properties of Pultruded Rectangular Pipes**

H.Saito, R.Inai, K.Kameo and H.Hamada

### **Abstract**

Recently FRP rectangular pipes have been used for car energy absorber because of that shape is suited to construction components of car body. It is considered that energy absorption properties and fracture mechanisms of rectangular pipes are different from those of circular pipes, which are well investigated up to this time. In this study, energy absorption properties of pultruded rectangular pipes were investigated and discussed energy absorption properties with comparing with that of circular pipes.

### **1. Introduction**

FRP shows the excellent strength and lighter weight than metal, so that FRP is used in variable areas such as constructions, aircraft, sport gear and so on. Additionally, the tendency of safety improvement in automobile area has been increased, so that much attention have been paid to energy absorption properties of FRP. In automobile area, the rectangular components are mainly used because the shape is suited to construction components. Therefore the rectangular pipe with energy absorption properties is useful as component of both weight saver and energy absorber.

---

H.Saito and R.Inai, Division of Advanced Fibro Science, Graduate School,  
Kyoto Institute of Technology, Matsugasaki, Sakyo-ku, Kyoto 606-8585, Japan  
K.Kameo, Division of Polymer Science, Graduate School, Kyoto Institute of Technology,  
Matsugasaki, Sakyo-ku, Kyoto 606-8585, Japan  
M.Iwamoto and H.Hamada, Division of Advanced Fibro Science, Kyoto Institute of Technology,  
Matsugasaki, Sakyo-ku, Kyoto 606-8585, Japan



In this study, the energy absorption properties of pultruded rectangular pipes were investigated. The pultrusion process can fabricate constant products continuously and save production cost, so that the pultruded products is suitable for component of automobile[1,2]. In testing, static and impact crushing tests were performed to consider testing speed influence. And to investigate the shape effect on energy absorption properties, rectangular and circular pipes were compared.

## 2. Equipments and Experimental Method

Pipe was fabricated by unsaturated polyester resin as matrix, unidirectional glass roving and glass mat as reinforcement and polyester non-woven fabric as skin lamina. The circular pipe was constructed as same as rectangular pipe. In the static test, the pipe was cut off in 75mm length for specimen and 30 degree-taper was made at the one end of specimen as shown in Figure 1.

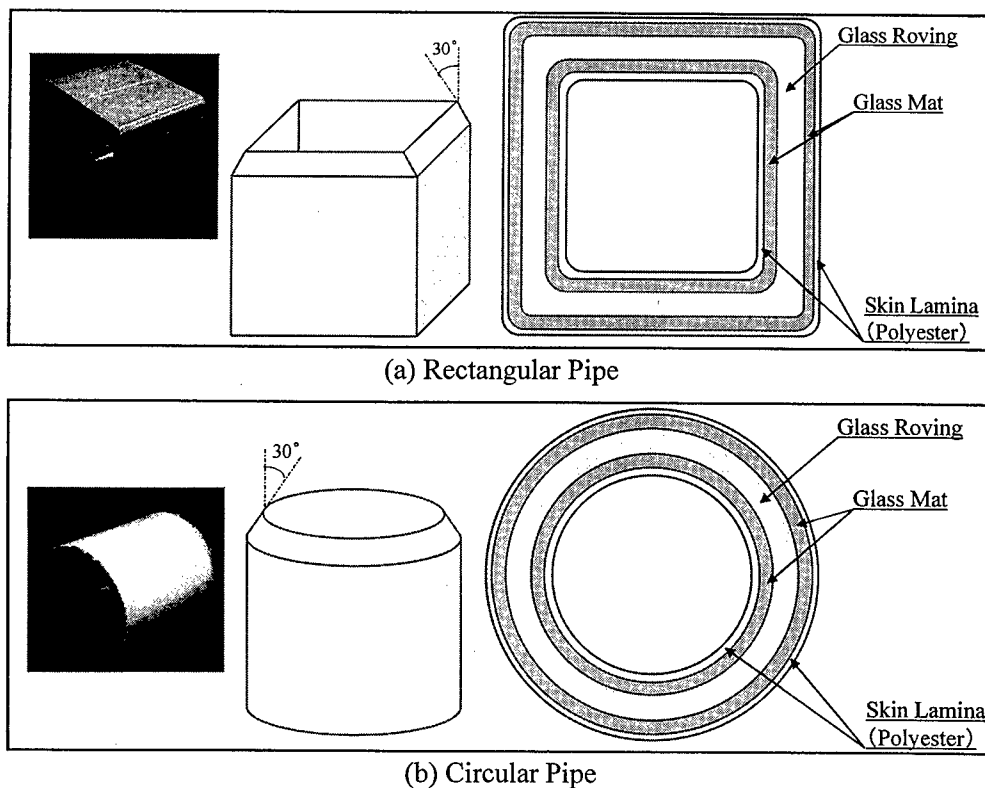


Figure 1 Construction of Pultruded Pipes

In the impact test, the pipe was cut off in 150mm. The taper has the role of fracture initiation and is necessary to occur progressive crushing[3,4]. Progressive crushing is one of fracture aspects and performs good energy absorption property with proceeding under constant load. Compression load was applied to longitudinal direction at constant speed of 5mm/min. in the static test, and 20, 30 and 40km/h in the impact test.

### 3. Results and Discussion

Photograph and load-displacement curve of *static* testing are shown in Figure 2. Fracture parts of rectangular pipe were extended in direction of each pipe face. In the first stage of progressive crushing, fracture of skin lamina and glass mat concentrated in corner of pipe, and skin lamina and glass mat delaminated together from glass roving. This fracture aspect was occurred in external face as same as internal face. The glass roving was divided into outer direction and inner direction. In the load-displacement curve shows the characteristic of progressive crushing.

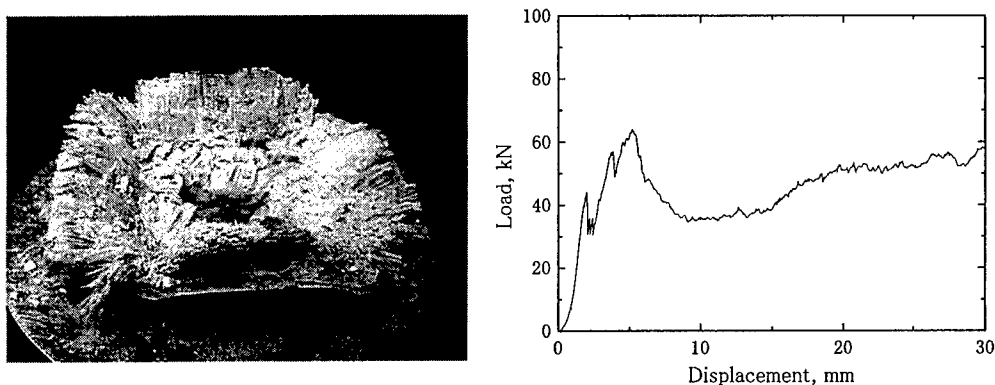


Figure 2 Photograph and load-displacement curve of *static* testing  
(Rectangular pipe)

Here, in general, when comparing energy absorption properties quantitatively, specific energy absorption value ( $E_s$  value) is used[5].  $E_s$  value is calculated by mean crushing load ( $\bar{P}$ ), area of cross section ( $A$ ) and density of material ( $\rho$ ) as follows:

$$E_s = \bar{P} / A\rho \quad (1)$$

From this equation,  $E_s$  value of rectangular pipe was calculated as 27.6kJ/kg.

Figure 3 shows cross-sectional photograph of rectangular pipe. (a) is photograph that is observed at normal face, and (b) is photograph that is observed at corner face. In these photographs, wedge was generated by mainly fiber fracture. Wedge generation causes expansion of fracture region named fronds. A longitudinal crack generates at the center of the material. In the photograph of (a), the fronds spread out in outer side of the pipe. On the other hand, fronds in inner side showed bending and buckling. Cracking was progressed at the center of cross section. In the photograph of (b), the fronds almost spread out only inner side of the pipe, because corner of pipe showed cracking at outer side edge and buckling at inner side edge in initiation stage. Finally, cracking was shown at the center of cross section as shown in figure 3 (b).

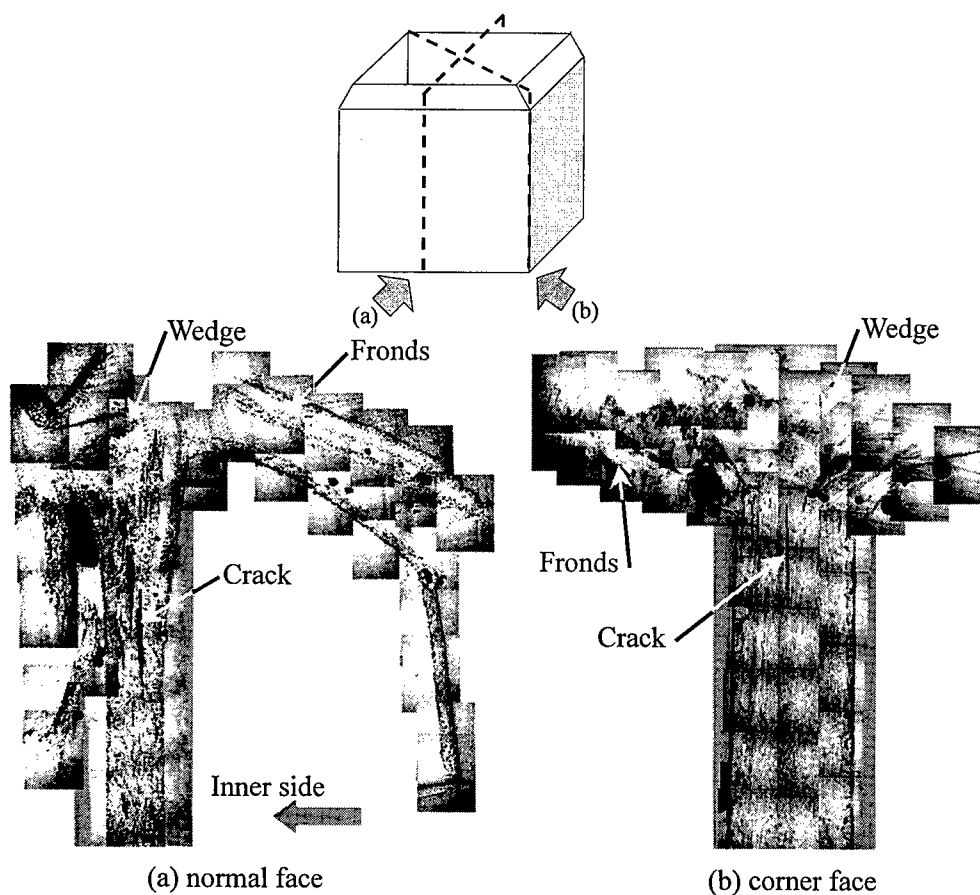


Figure 3 Cross-sectional photograph of rectangular pipe in static test

In the static crushing test of the circular pipe, the fracture parts were extended in direction of radial pattern as shown in Figure 4. As same as rectangular pipe, the skin lamina and the glass mat delaminated together from the glass roving, and the glass roving was divided into outer direction and inner direction. From load-displacement curve, specific energy absorption value was calculated as 47.8kJ/kg.

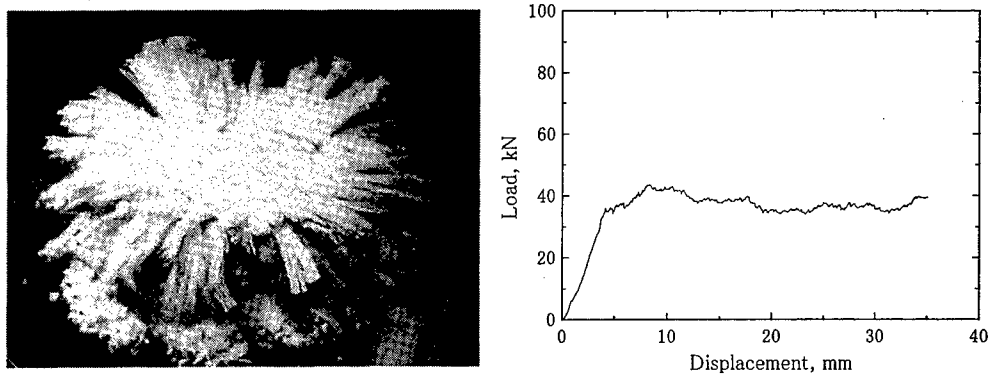


Figure 4 Photograph and load-displacement curve of *static* testing  
(Circular pipe)

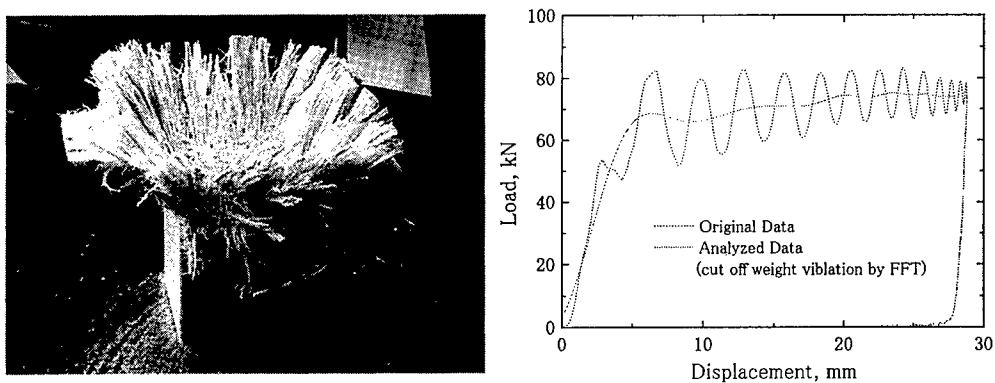


Figure 5 Photograph and load-displacement curve of *impact* testing  
(Rectangular pipe)

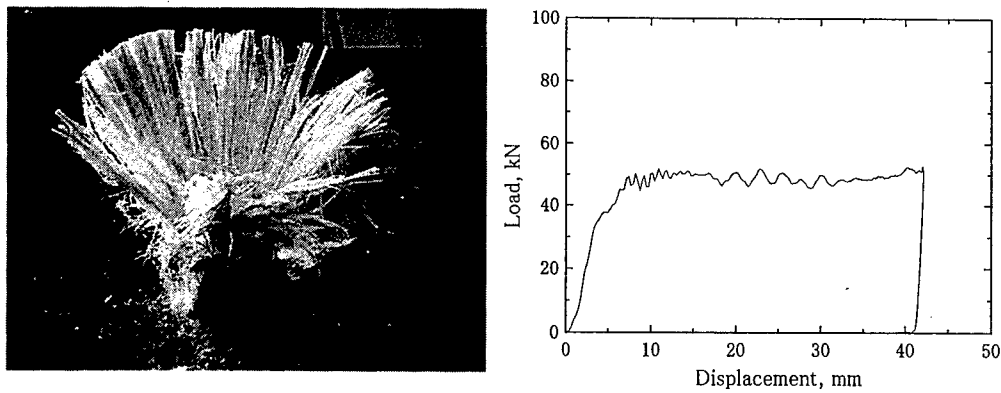


Figure 6 Photograph and load-displacement curve of *impact* testing  
(Circular pipe)

Photograph and load-displacement curve of *impact* testing are shown in Figure 5 and Figure 6. The fracture aspect and characteristics of both rectangular and circular pipes were as same as static test. On the other hand, load-displacement curves show higher constant load values in both rectangular and circular pipe, and specific energy absorption values from these curves also showed higher values than static tests as shown in Table 1. Moreover, although the rectangular pipe showed almost same  $E_s$  values in different test speed, the circular pipe showed higher  $E_s$  values in lower test speed[6]. In further investigations, the effects of test speed or the different energy absorption properties should be clarified.

Table 1 Specific energy absorption values of pipes in different testing condition

	Static	Impact		
	5.0mm/min.	20km/h	30km/h	40km/h
Circular pipe	47.8	62.2	59.6	51.6
Rectangular pipe	27.6	42.3	42.3	42.7

#### 4. Conclusion

The pultruded rectangular and circular pipes show typical progressive crushing in compression test. Although in both rectangular and circular pipes, fracture aspects were almost same in static and impact test, specific energy absorption values were different. Rectangular pipes have different two fracture aspects between flat faces and corners of pipes. Fracture aspects in corners of pipes may have key of energy absorption performance of rectangular pipe, so that it is necessary to investigate fracture behaviors in corners of rectangular pipes.

#### Reference

1. A.Fujita, T.Nakatani, T.Uozumi, K.Kameo, A.Nakai and H.Hamada, "Crush Energy Absorption of Braided Composite Rods", Proceedings of the fifth Japan SAMPE Symposium, 1997, pp.1231-1234
2. Y.Hisa, T.Uozumi, A.Fujita, H.Hamada, A.Nakai and A.Yokoyama, "Braiding Pultrusion Process (BPP)", 27<sup>th</sup> International SAMPE Technical Conference, 1995, pp.371-379
3. H.G.S.J.Thuis and V.H.Metz, "The Influence of Trigger Configurations and Laminate Lay-up on the Failure Mode of Composite Crush Cylinders", Composite Structure, Vol.25, 1993, pp.37-43
4. I.Sigalas, M.Kumosa and D.Hull, "Trigger Mechanisms in Energy-Absorbing Glass Cloth/Epoxy Tubes", Composite Science and Technology, Vol.40, 1991, pp.265-287
5. D.Hull, "A Unified Approach to Progressive Crushing of Fiber-Reinforced Composite Tubes", Composite Science and Technology, Vol.40, 1991, pp.377-421
6. P.H.Thornton, "The Crush Behavior of Pultruded Tubes at High Strain Rates", Journal of Composite Materials, Vol.24, 1990, pp.594-615

# Composite Mechanics, I

---

## Use of Glass Fibers in Tailoring Laminated Composites with Directionally Negative and Near-Zero Coefficients of Thermal Expansion

K. Wakashima, T. Suganuma and T. Ito

### Abstract

An analysis, together with experiments, has been made toward an intention indicated by the title of the paper. A simple closed-form expression is derived for the in-plane coefficients of thermal (thermoelastic) expansion (CTEs) in laminates of the type  $[(\pm\theta)_n]_s$  from a consideration of the so-called "normal-shear coupling" in anisotropic elasticity. By incorporating micromechanical expressions to estimate the lamina elastic properties and CTEs, it is found that negative CTEs can occur if a polymer of very low modulus and very large CTE is used as the matrix material, and polypropylene is a candidate. This prediction is confirmed experimentally. Some stiffness-enhanced designs using  $0^\circ$  plies are also suggested.

### 1. Introduction

Laminated composites of fiber-reinforced plastics (FRPs) can exhibit "anomalous" thermoelastic behavior, which is characterized by *negative* coefficients of thermal expansion (CTE) in one particular in-plane direction of the laminates. Experimentally, this behavior was reported first by Fahmy and Ragai [1] in carbon/epoxy composites and later by Strife and Prewo [2] in Kevlar/epoxy composites, both with simple  $\pm\theta$  angle-ply lay-ups of unidirectionally fiber-reinforced plies. To our knowledge, no composite systems other than these have been identified as materials having such directionally negative CTEs. Does this imply that the anomaly in laminate CTEs never occurs in all FRPs that utilize glass fibers? If the answer is not affirmative, conventional "low-cost" glass fibers may find new "engineered" applications. With this possibility in mind, the work presented here was undertaken.

In the following, we first deal with a simple, but most fundamental, bidirectionally fiber-reinforced laminate of the type  $[(\pm\theta)_n]_s$  to show that a closed-form expression

---

K. Wakashima†, T. Suganuma and T. Ito, Precision and Intelligence Laboratory, Tokyo Institute of Technology, 4259 Nagatsuta, Midori-ku, Yokohama 226-8503, Japan

†E-mail: wakashim@pi.titech.ac.jp

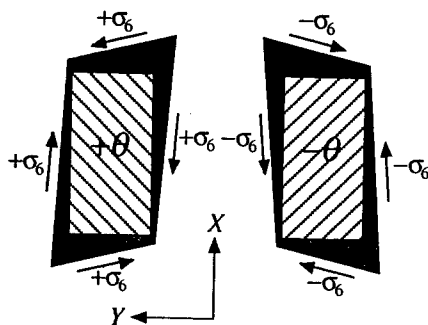


for the laminate CTE in its in-plane principal direction can be derived from a consideration of *normal-shear coupling* in the so-called *generally orthotropic* off-axis laminae. Using this macromechanical expression along with a set of micromechanical expressions for predicting the lamina effective properties and CTEs, we then make a calculation to seek a candidate for the matrix material (along with its volume fraction) to be combined with glass fibers. Experimental results that follow will verify our prediction. Finally, with attention focused on laminated composite beams with *near-zero* CTEs, an ongoing effort to enhance the beam stiffness in bending by incorporation of  $0^\circ$  plies is briefly described.

## 2. Simple $\pm\theta$ Angle-Ply Laminates

### 2.1. Closed-Form Expression for the Laminate CTE

As is well known, thermoelastic properties of fiber composite laminates in general can be predicted by classical laminated plate theory (CLPT). However, this route of analysis requires rather complicated, but just algebraic, computations and does not necessarily illuminate the principles involved in our problem. Giving special attention to a simple  $\pm\theta$  angle-ply laminate, we may take an alternative way of analysis. By making reference to Fig. 1 which illustrates a significant effect of normal-shear coupling characteristic of generally orthotropic (just like monoclinic) off-axis uni-



$$\bar{S}_{66}(\theta)\sigma_6 = -(\alpha_L - \alpha_T)\sin 2\theta$$

$\bar{S}_{16}(\theta)\sigma_6$  : Extra elastic strain by normal-shear coupling

**Fig. 1**—Schematic picture illustrating the importance of normal-shear coupling for in-plane thermal expansion behavior of a symmetric, balanced,  $\pm\theta$  angle-ply laminate. A rectangular piece of off-axis UD lamina does not remain rectangular after free expansion because of its anisotropic CTEs, i.e.  $\alpha_L < \alpha_T$ . When the  $+\theta$  and  $-\theta$  laminae are bonded together to form the laminate, equal-in-magnitude, but opposite-in-sense, in-plane shear stresses  $+\sigma_6$  and  $-\sigma_6$  are to be induced in the respective laminae. The elastic strains associated with these stresses must cancel out the mismatch in the in-plane shear component of strains due to anisotropic thermal expansion of the laminae; hence

$$\bar{S}_{66}\sigma_6 = -(\alpha_L - \alpha_T)\sin 2\theta.$$

Since the off-axis laminae each behave just like a monoclinic material, the shear stresses above cause elastic length changes in the  $X$  direction, i.e. extra normal strains,  $\bar{S}_{16}(\theta)\sigma_6$  and  $-\bar{S}_{16}(-\theta)\sigma_6$ , are equally induced in the respective laminae, and these can be negative in a certain range of  $\theta$ .

directional (UD) laminae in the  $\pm\theta$  laminate, it is easy to derive a closed-form expression for the laminate CTE under consideration:

$$\alpha_X(\theta) = \alpha_L \cos^2 \theta + \alpha_T \sin^2 \theta + \frac{\bar{S}_{16}(\theta)}{\bar{S}_{66}(\theta)} (\alpha_T - \alpha_L) \sin 2\theta \quad (1)$$

Here,  $\alpha_L$  and  $\alpha_T$  are the longitudinal and transverse CTEs of UD lamina;  $\bar{S}_{66}(\theta)$  and  $\bar{S}_{16}(\theta)$  are the in-plane shear and normal-shear coupling compliances of  $+\theta$  off-axis UD lamina in the  $X$ - $Y$  coordinates fixed to the laminate, and these are given in terms of four effective elastic constants of UD lamina (i.e., the longitudinal Young's modulus  $E_L$ , the transverse Young's modulus  $E_T$ , the longitudinal shear modulus  $G_L$ , and the longitudinal Poisson's ratio  $\nu_L$ ) as

$$\bar{S}_{66}(\theta) = \left( \frac{1+2\nu_L}{E_L} + \frac{1}{E_T} \right) \sin^2 2\theta + \frac{1}{G_L} \cos^2 2\theta \quad (2)$$

$$\bar{S}_{16}(\theta) = \left\{ \frac{1}{E_L} \cos^2 \theta - \frac{1}{E_T} \sin^2 \theta + \left( \frac{\nu_L}{E_L} - \frac{1}{2G_L} \right) \cos 2\theta \right\} \sin 2\theta \quad (3)$$

The expression above is quite informative in its form; the first two terms represent the free expansion of off-axis UD lamina and the last term an interactive synergistic effect due to the lamination. When  $E_L \gg E_T$ , one gets an approximate equation:

$$\frac{\alpha_X(\theta) - \alpha_L}{\alpha_T - \alpha_L} \approx \sin^2 \theta - \frac{\sin^2 \theta + \frac{1}{2} \left( \frac{E_T}{G_L} \right) \cos 2\theta}{\sin^2 2\theta + \left( \frac{E_T}{G_L} \right) \cos^2 2\theta} \sin^2 2\theta \quad (4)$$

Consider a special case of  $E_T / G_L = 1$ ; then,

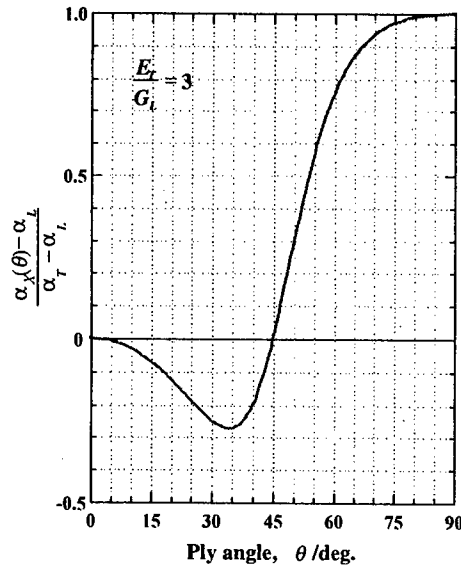
$$(\alpha_X(\theta) - \alpha_L) / (\alpha_T - \alpha_L) = -\sin^2 \theta \cos 2\theta \quad (5)$$

which gives a minimum value of  $-1/8$  at  $\theta = 30^\circ$ , i.e.  $\alpha_X = (9\alpha_L - \alpha_T)/8$  at this ply-angle. In fiber-reinforced plastics,  $\alpha_T \gg \alpha_L$  because  $\alpha_L$  is as small as the axial CTE of the fiber whereas  $\alpha_T$  is dominated by the matrix CTE. Hence, it is evident that the condition  $\alpha_L < 0$ , which is usually met in carbon/epoxy and Kevlar/epoxy systems, is not essential for the laminate CTE  $\alpha_X(\theta)$  to be negative. Actually,  $E_T / G_L \approx 3$  in most cases of practical interest (see foot note †) and then, the ratio

$(\alpha_X(\theta) - \alpha_L)/(\alpha_T - \alpha_L)$  becomes more negative in a range of  $\theta$  smaller than about  $45^\circ$  and takes a minimum value of  $-0.27$  at  $\theta \approx 33.5^\circ$ , as shown in Fig. 2. Thus, the approximation above suggests that  $\alpha_X(\theta)$  can take negative values if  $\alpha_T/\alpha_L \geq (1.27/0.27) \approx 4.7$ .

## 2.2. Requirements for the Matrix Properties

The analysis shown above has been made entirely on a "macromechanical" basis. For further examination to elucidate the possibility of glass fiber systems that we are particularly interested in, we need "micromechanical" information about the lamina elastic properties and CTEs ( $E_L$ ,  $E_T$ ,  $G_L$ ,  $\nu_L$ ,  $\alpha_L$  and  $\alpha_T$ ). To this end, we have used a set of expressions given in Table 1. The following values will be appropriate for the present examination:  $E_f = 75$  GPa,  $\nu_f = 0.2$  and  $\alpha_f = 5 \times 10^{-6} \text{ K}^{-1}$  for the glass fiber, and  $V_f = 0.5$  and  $\theta = 30^\circ$  for the laminate. Assuming  $\nu_m = 0.3$  as a typical value of Poisson's ratio for most polymeric matrices, we have calculated the laminate CTE  $\alpha_X(\theta)$  as a function of both Young's modulus  $E_m$  and CTE  $\alpha_m$  of the matrix. Results of this calculation is summarized as a 2-D contour map representation in Fig. 3. Here, diagrams (a) and (b) show the longitudinal and transverse CTEs of UD lamina, respectively. As is evident from diagram (c), negative CTEs will occur if matrices of *very low modulus* and *very large CTE* are used, a candidate of which is polypropylene (PP). Note that the anomaly in laminate CTEs is never expected with such polymers of conventional GFRPs as epoxy and polyester.



**Fig. 2**—The laminate CTE,  $\alpha_X(\theta)$ , plotted against the ply angle  $\theta$ , calculated from Eq. (4) with  $E_T/G_L = 3$ . Note that the condition  $E_L \gg E_T$  is assumed in Eq. (4).

† Using approximate expressions for  $E_T$  and  $G_L$  given in Table. 1, one may derive  $E_T/G_L \approx 4(\mathcal{P} + V_f)(1 + QV_f)/(1 + V_f)[(\mathcal{P} + V_f) + (1 + QV_f)]$  with  $\mathcal{P} \equiv (11 - 16\nu_m)/3(1 - 2\nu_m)$  and  $Q \equiv (11 - 16\nu_m)/(17 - 28\nu_m)$ , where  $V_f$  is the fiber volume fraction and  $\nu_m$  the matrix Poisson's ratio. Putting  $V_f = 0.5$  and  $\nu_m = 1/3$  gives  $E_T/G_L \approx 3$ .

Table 1 Equations used to calculate the effective elastic properties and CTEs of unidirectional lamina.

Longitudinal Young's modulus

$$E_L = (1 - V_f)E_m + V_f E_f + \frac{4V_f(1 - V_f)(v_f - v_m)^2}{(1 - V_f)/k_f + V_f/k_m + 1/G_m} \cong (1 - V_f)E_m + V_f E_f \quad (a)$$

Longitudinal Poisson's ratio

$$v_L = (1 - V_f)v_m + V_f v_f + \frac{V_f(1 - V_f)(v_f - v_m)(1/k_m - 1/k_f)}{(1 - V_f)/k_f + V_f/k_m + 1/G_m} \cong (1 - V_f)v_m + V_f v_f \quad (b)$$

Plane-strain bulk modulus

$$k_r = k_m + \frac{V_f}{1/(k_f - k_m) + (1 - V_f)/(k_m + G_m)} \cong \frac{k_m + V_f G_m}{1 - V_f} \quad (c)$$

Longitudinal shear modulus

$$G_L = G_m + \frac{V_f}{1/(G_f - G_m) + \frac{1}{2}(1 - V_f)/G_m} \cong \frac{1 + V_f}{1 - V_f} G_m \quad (d)$$

Transverse shear modulus

$$G_r = G_m + \frac{V_f}{1/(G_f - G_m) + (1 - V_f)(k_m + 2G_m)/2G_m(k_m + G_m)} \cong \frac{(1 + V_f)k_m + 2G_m}{(1 - V_f)(k_m + 2G_m)} G_m \quad (e)$$

Transverse Young's modulus

$$E_r = \frac{4}{1/G_r + 1/k_r + 4v_L^2/E_L} \cong \frac{4}{1/G_r + 1/k_r} \quad (f)$$

Longitudinal CTE

$$\alpha_L = \alpha_m + \frac{\alpha_f - \alpha_m}{1/K_f - 1/K_m} \left( \frac{3(1 - 2v_L)}{E_L} - \frac{1}{K_m} \right) \quad (g)$$

Transverse CTE

$$\alpha_r = \alpha_m + \frac{\alpha_f - \alpha_m}{1/K_f - 1/K_m} \left( \frac{3}{2k_r} - \frac{3(1 - 2v_L)v_L}{E_L} - \frac{1}{K_m} \right) \quad (h)$$

where  $V_f$  = the volume fraction of fiber (of circular cross-section);  $K$  = the bulk modulus;  $k$  = the plane-strain or transverse bulk modulus for transversely isotropic materials undergoing lateral dilatation without longitudinal extension ( $k = K + G/3$  for isotropic materials); subscripts f and m refer to fiber and matrix, respectively. It is assumed that both constituents of the composite are isotropic.

Table 2 Elastic properties of 45 vol.% glass fiber/polypropylene unidirectional lamina, calculated from constituent elastic constants†.

Longitudinal Young's modulus, $E_L$ / GPa	34.5
Transverse Young's modulus, $E_r$ / GPa	3.1
Longitudinal shear modulus, $G_{LT}$ / GPa	1.3
Longitudinal Poisson's ratio, $v_{LT}$	0.25

† Young's modulus ( $E$ ) and Poisson's ratio ( $v$ ) of glass fiber (GF) and polypropylene (PP)

are:  $E_{GF} = 75 \text{ GPa}$ ,  $v_{GF} = 0.2$ ,  $E_{PP} = 1.3 \text{ GPa}$  and  $v_{PP} = 0.3$ .

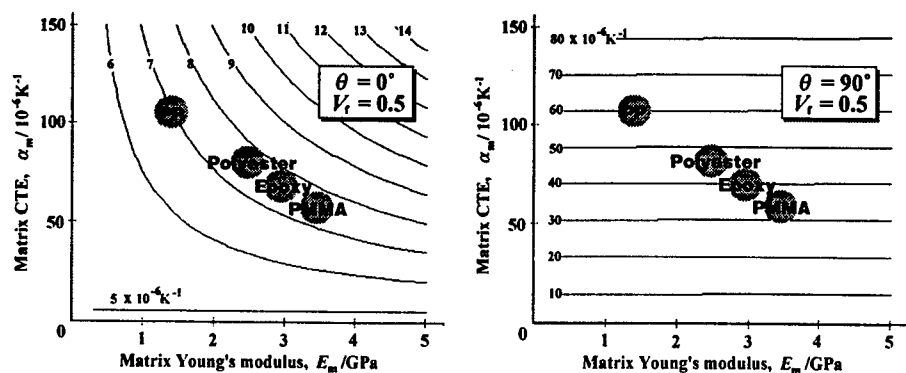


Fig. 3—Contour maps showing the laminate CTEs as a function of the matrix Young's modulus,  $E_m$ , and the matrix CTE,  $\alpha_m$ , for  $\theta = 0^\circ$  and  $90^\circ$  (top; right and left) and for  $\theta = 30^\circ$  (right).

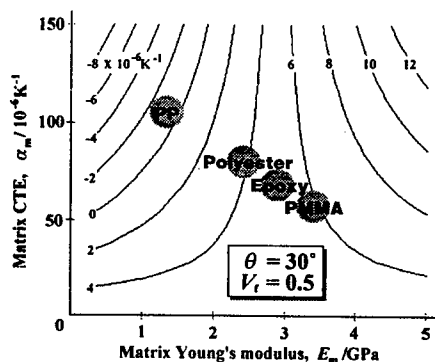


Fig. 4 (Left)—Typical thermal expansion curves on heating for  $\pm\theta$  angle-ply laminates of 45 vol.% glass fiber/polypropylene composite, measured in the  $X$  direction at a heating rate of  $0.5^\circ\text{C}/\text{min}$ .

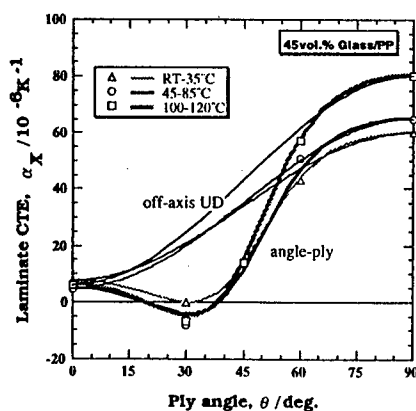
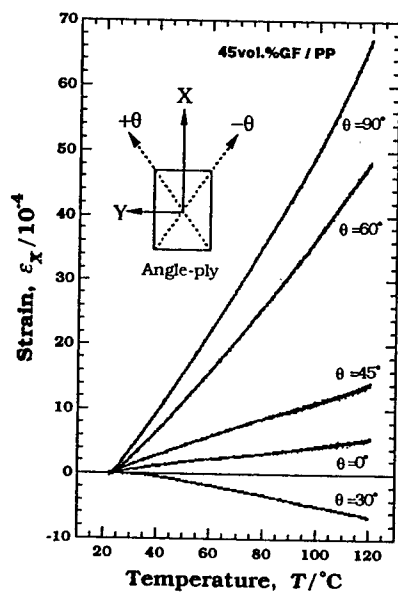


Fig. 5 (Right)—Comparison between measured and calculated in-plane CTEs of  $\pm\theta$  angle-ply laminates. The calculation, based on Eq. (1), uses the measured CTE values at  $\theta = 0$  and  $90^\circ$  as input data for  $\alpha_L$  and  $\alpha_T$ . Calculated angular dependence of CTE for the off-axis UD lamina is also shown by dotted lines to illustrate the effect of the lamination.

### 2.3. Experimental Verification

To verify our prediction for the glass/PP composite system experimentally, 8-ply laminates of three different lay-ups,  $[0^\circ_8]$ ,  $[(\pm 30^\circ)_2]_s$  and  $[(\pm 45^\circ)_2]_s$ , were fabricated using 45 vol.% UD-glass/PP prepreg tapes of thickness 0.2 mm, and in-plane thermal expansions in two principal directions of these laminated orthotropic materials were measured in the range from room temperature (RT) to 120 °C by means of scanning laser extensometry. Results are shown in Fig. 4, which displays typical strain-temperature curves on heating. It is evident that the negative CTE response occurs in the laminate with  $\theta = 30^\circ$ . Close inspection of the thermal expansion data reveals that the slope of each curve changes at temperatures around 40 and 90 °C. Thus the average CTE values were determined separately in three different ranges: (I) RT to 35 °C, (II) 45 to 85 °C and (III) 100 to 120 °C. In Fig. 5, results are plotted and compared with predictions by Eqs (1) to (3). Here, the observed CTE values at  $\theta = 0^\circ$  and  $90^\circ$  are used as the input data for  $\alpha_L$  and  $\alpha_T$  in Eq. (1), together with the calculated lamina elastic constants listed in Table 2. A good agreement can be seen for all other data points with the predicted curves.

## 3. Laminates with Near-Zero CTEs

### 3.1. A Primitive Example

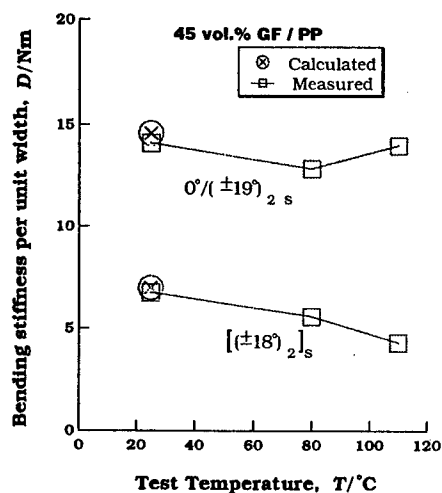
As is evident from the diagram shown in Fig. 5, the simple lamination with  $\pm\theta$  plies of the 45 vol.% glass/PP composite gives near-zero CTEs at certain values of  $\theta$  while the determination of these  $\theta$  values depends on the temperature ranges indicated. If attention is focused on range II (45-85 °C) for example, the  $\theta$  value of either 18° or 39° is suggested. Of these, the former angle is of interest for two reasons. First, a greater axial stiffness is expected in that laminate. Second, fiber misorientations that may be encountered in making experimental "small-size" laminates will have a comparatively small effect. Thus, a  $[(\pm 18^\circ)_2]_s$  laminate was prepared, and its thermal expansion measured. The result confirmed our prediction; its average CTE in the range 45-85 °C was about  $0.6 \times 10^{-6} / \text{K}$ , which can be well compared with the value  $0.17 \times 10^{-6} / \text{K}$  predicted.

### 3.2. Stiffness-Enhanced Designs

The directionally near-zero CTE behavior will be of practical interest, especially if the laminate is formed into slender configurations with various cross-sectional shapes. In making such axially very low-expansive solid or hollow beams as elements for structural application, their stiffnesses in axial bending (and also in stretching

**Table 3**—Calculated and measured CTEs of the  $[0^\circ/(\pm 19^\circ)_2]_s$  laminate.

CTE $\alpha/10^{-6}\text{K}^{-1}$	Temperature Range		
	25–35°C	45–85°C	100–120°C
Calculated	3.5	0.15	0.41
Measured	3.0	-0.14	-2.9



**Fig. 6**—Axial bending stiffnesses of two different laminated beams,  $[(\pm 18^\circ)_2]_s$  and  $[0^\circ/(\pm 19^\circ)_2]_s$ , measured at 25, 80 and 110 °C by four-point flexural testing using specimens of length 180 mm, width 15 mm and of different thicknesses 1.6 and 1.9 mm for the respective laminates, with outer span 120 mm and inner span 40 mm. Constant load was applied in a stepwise manner and the resulting surface strain was measured with a foil strain gage. The strain response in the duration of 2 h was nearly constant at 25 and 80 °C but slightly changed at 110 °C. Linearity between moment and curvature was good especially at 25 and 80 °C.

possibly) will be an important consideration. Thus, the incorporation of axially reinforcing  $0^\circ$  plies as outer skin layers is of further interest. While this is now under examination, some preliminary data show quite encouraging results. For instance, a 10-ply laminate of the type  $[0^\circ/(\pm\theta)_2]_s$ , the simplest case for stiffness enhancement, is expected to have an average CTE of  $0.15 \times 10^{-6}/\text{K}$  in the range 45–85 °C when  $\theta = 19^\circ$ . Also, preliminary estimates by CLPT show that the axial bending stiffness of this particular laminate is about twice greater than that of the  $[(\pm 13^\circ)_2]_s$  laminate (although this naturally involves a thickness effect). Experimental results generally confirmed the above predictions, as summarized in Table 3 and Fig. 6.

Of further interest are such laminates of sandwich construction as  $[0^\circ/(\pm\theta)_2/(PP)_n]_s$ , which will be discussed elsewhere.

## References

1. A. A. Fahmy and A. N. Ragai, 1970. "Thermal Expansion of Graphite-Epoxy Composites." *J. Appl. Phys.* **41** (13), 5112–5115.
2. J. R. Strife and K. M. Prewo, 1979. "The Thermal Expansion Behavior of Unidirectional and Bidirectional Kevlar/Epoxy Composites." *J. Composite Materials* **13** (October), 264–277.

## **Full-Field Singular Stresses in a Composite Laminate Weakened by a Cylindrical Cavity: Theory and Experiment**

Endel V. Iarve and David H. Mollenhauer

### **Abstract**

Analytical and experimental investigation of strain fields arising in composite laminates in the vicinity of an open hole and ply interfaces was performed. The singular stress fields, arising at the ply interface and hole edge intersections, were analytically examined by using a novel technique based on superposition of an asymptotic and spline approximation solution. The Moiré interferometry technique, providing high spatial resolution and allowing rapid strain variations across a laminate thickness to be recorded, was utilized to experimentally measure the strain distributions throughout the thickness of a  $[+30_2/-30_2/90_4]_{3s}$  laminate. The singular solution and the experimentally measured strain showed good agreement for most strain components with some discrepancy for the interlaminar normal strain component.

### **Introduction**

Bolted joining remains a primary joining method of load carrying composite structural elements in modern aircraft. Significant efforts to develop methods for composite bolted joint strength prediction put forth in the past by government agencies [1], as well as proprietary programs [2], led to the development of several computer codes, which were adopted by various airframe and helicopter manufacturing companies as standard tools for composite bolted joint strength prediction. A common mechanical foundation for all of these tools is classical lamination theory combined with either stress or fracture mechanics failure criterion containing empirical geometric, material, and loading related constants needed to describe the experimentally obtained failure envelope. Definition of these empirical parameters requires extensive experimental effort.

The objective of the present research is the development of analytical tools based on three-dimensional stress and failure analysis at the ply level. The present paper is focused on analytical and experimental characterization of the stress fields in laminated composites near singularities arising at the ply interface and hole intersections. The singular stress fields were analytically examined by using a novel technique based on superposition of an asymptotic and spline approximation

---

Endel V. Iarve, University of Dayton Research Institute, 300 College Park Ave., Dayton, OH 45469, U.S.A.

David H. Mollenhauer, United States Air Force Research Laboratory, AFRL/MLBC, Bldg. 654, Wright Patterson AFB, Ohio 45433-7750, U.S.A.



solution, described in Iarve and Pagano [7]. The Moiré interferometry technique, providing high spatial resolution and allowing rapid strain variations across a laminate thickness to be recorded, was utilized for experimental characterization.

A method of superposition of a hybrid and displacement approximation was developed to provide accurate stress fields in a multilayered composite laminate including the singular neighborhood of the ply interface and the hole edge. Asymptotic analysis was used to derive the hybrid stress functions. Morley [3] pioneered the idea of superposition of the analytical and finite element solutions in problems with local field singularities. Yamamoto and Tokuda [4] applied this method to crack stress intensity factor determination, using a multiple term asymptotic expansion for the analytical solution. They used a boundary collocation method to obtain the coefficients of the terms contained in the analytical solutions. Yamamoto and Sumi [5] considered an axisymmetric problem of a twisted round isotropic bar with an annular crack. The asymptotic solution, which was used as the basis for the analytical solution near the crack tip, was equivalent to a local plane strain solution, which does not satisfy the axisymmetric equilibrium equations throughout the domain. The asymptotic solution for the round isotropic bar problem, which was reduced to a single unknown function – the circumferential displacement component, was augmented by a higher-order term, added to the asymptotic solution to satisfy the equilibrium equations. However, in a general orthotropic case these complementary terms are not obvious and have not been reported in the literature.

For the curvilinear edge singularities in orthotropic plies, considered in the present paper, the analytical solution in a finite domain near the singularity is unknown. The present paper extends the superposition approach to problems where no analytical solutions in the finite domain are known. The model developed is based on Reissner's variational principle and is intended to reflect the singularities which arise at each interface at the boundary of the hole. Hybrid approximation functions to be developed have the following characteristics:

- (1) They include the asymptotic solution, thus representing the directional nonuniqueness of the solution. It is only in this manner that one can embed the proper singular field. The fact that the asymptotic solution results from the three-dimensional problem by truncating the spatial derivatives in the circumferential direction [6] will be used to construct hybrid stress functions.
- (2) Two independent (B-spline) displacement functions are considered. One is related to the regular and the other to the singular portion of the stress field. It is undesirable to use the asymptotic displacement functions in the displacement approximation because the calculation of their derivatives in the circumferential direction, required in the variational formulation, is only possible numerically. The displacements related to the singular stresses will be also approximated with splines. Thus the approximations of stresses and displacements are made independently.

### Problem Definition

Consider a rectangular orthotropic laminate containing a circular hole having a diameter  $D$ . The laminate consists of  $N$  plies of total thickness  $H$  in the  $z$ -direction and has a length  $L$  in the  $x$ -direction and width  $A$  in the  $y$ -direction. An open hole of diameter  $D$  with the center at  $x=x_c$  and  $y=y_c$  is considered. Uniaxial stretching in the

x-direction is applied via displacement  $u_x=u_0>0$  at  $x=L$  and  $u_x=0$  at  $x=0$ . A cylindrical coordinate system  $r,\theta,z$  is introduced at the center of the hole, so that  $\theta=0$  is parallel to the x-axis.

### Asymptotic Analysis

A local coordinate system  $\eta,\psi,z$  is introduced at the interface between plies  $s$  and  $s+1$ . The origin is at the point  $r=D/2$ ,  $z=z^{(s)}$ ,  $\theta$  so that  $\eta$  is the distance from a singular point, and  $\psi$  is an angle defining the direction in which the origin of the coordinates is approached:  $-\pi/2 \leq \psi \leq 0$  belongs to the  $s$ -ply and  $0 \leq \psi \leq \pi/2$  - belongs to the  $s+1$ -ply. Free-edge boundary conditions are imposed at  $\psi=\pm\pi/2$ , and displacement and traction continuity is imposed at  $\psi=0$ . In the limit of  $\eta \rightarrow 0$  the following asymptotes for the stress distribution were obtained, with the accuracy of an arbitrary multiplicative factor:

$$a_{ij}^m = \eta^{\lambda_m - 1} f_{ij}(\lambda_m, \psi, \theta) \quad (1)$$

The values of  $\lambda$  are determined to provide a nontrivial solution under the imposed boundary conditions.

### Spline Approximation of Displacements

Cubic B-splines are used for the displacement approximation which, according to [6], can be written as:

$$u_i = \mathbf{C}_i \mathbf{X} \mathbf{U}_i^* + \delta_{ix} \mathbf{X} \mathbf{E}_0^* \cdot u_0, \quad (2)$$

where  $\mathbf{X}$  is a vector of three-dimensional spline approximation basis functions. Superscript star denotes the transpose operation. Boundary matrices  $\mathbf{C}_i$  and constant vector  $\mathbf{E}_0$  are defined so that approximation (2) provides a kinematically admissible displacement field. Curvilinear coordinates  $\rho$  and  $\phi$  were introduced to map the laminate with a cutout into a region  $0 \leq \rho \leq 1$  and  $0 \leq \phi \leq 2\pi$ . Vector  $\mathbf{X}$  is a tensor product of one-dimensional basis spline functions of  $\rho, \phi$  and  $z$  coordinates, respectively.

### Hybrid Approximation

It was shown by Iarve and Pagano [7] that it is beneficial to consider as independent displacement functions the total displacement (2) and the displacement  $u_{ij}^s$  related to the singular stresses. The singular displacement is approximated similar to (2), and the boundary condition matrices are defined to satisfy the condition of zero radial displacement at the hole edge. The hybrid stress approximation is proposed as follows

$$\sigma_{ij} = \sum_m K_m(\theta)(a_{ij}^m - s_{ij}^m) + \sigma_{ij}^u, \quad (3)$$

where  $\sigma_{ij}^u$  is calculated by using Hooke's law from displacements (2) and  $a_{ij}^m$  is given by eqn. (1). Functions  $s_{ij}^m$  are spline approximations of functions  $a_{ij}^m$ . They are defined by auxiliary solutions [7]. Unknown coefficients  $K_m$  are computed by

requiring the stresses (3) to satisfy interlaminar  $\sigma_{rz}$  continuity at the collocation points.

### Moiré Interferometry Experiments

The free-edge strains in laminated composites were studied for curved surfaces. The research focused on the development and use of Moiré interferometry techniques applied to the open hole problem in laminated composites. Moiré interferometry [8] was chosen because the excellent spatial resolution and full-field nature of this optical displacement measuring technique would allow rapid strain variations across a laminate thickness to be recorded. Three specimens were examined in this study. An aluminum specimen was used to develop and validate the experimental procedures. Two composite specimens, fabricated from IM7/5250-4 prepreg with ply lay-ups of  $[0_4/90_4]_{3s}$  and  $[30_2/-30_2/90_4]_{3s}$ , were then examined with the refined techniques. The procedure required that a replica of the grating on the cylindrical surface of the hole be made while the specimen was loaded. This cylindrical-shaped deformed grating replica was then examined directly in a Moiré interferometer. A schematic of this procedure is shown in Figure 1. This multi-step procedure was developed mainly to eliminate an uncertainty

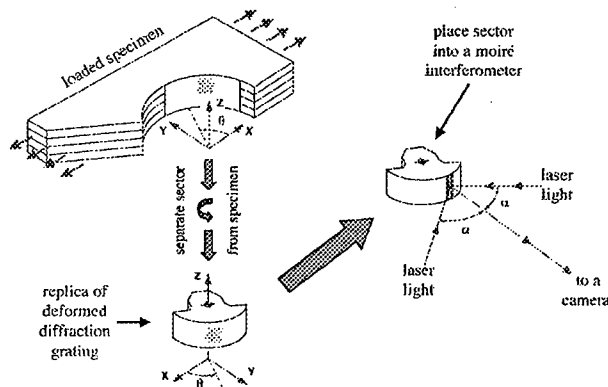


Fig 1: Schematic of the procedure for recording fringe patterns from the deformed curved specimen grating by examining a curved replica in a Moiré interferometer.

associated with the  $\theta$ -direction displacement variation. The resulting fringe patterns were narrow strips, approximately  $3^\circ$  wide, which were recorded at various angular locations around the hole. A mosaic of  $U_\theta$  fringe patterns from  $48^\circ$ - $69^\circ$  on the cylindrical surface of the  $[30_2/-30_2/90_4]_{3s}$  specimen is shown in Figure 2. Clearly, sub-ply variations of displacement can be obtained from these fringe patterns. Distributions of strain at various angular locations around the periphery of the holes were calculated from the recorded displacement fringe patterns. Representative results from the  $[30_2/-30_2/90_4]_{3s}$  specimen are subsequently presented. A comprehensive report of the research can be found in [9], which is available for download from the World Wide Web, however a less refined analytical solution was used for comparison in that work.

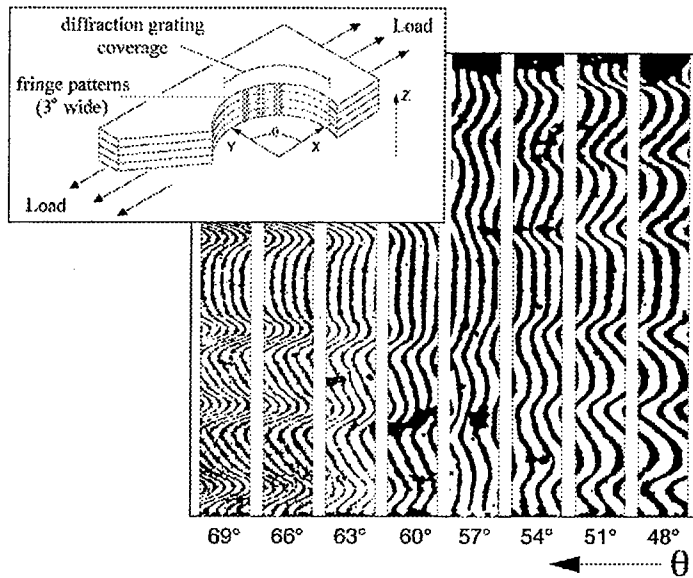


Fig 2:  $U_\theta$  fringe pattern mosaic from the  $[30_2/-30_2/90_4]_{3s}$  specimen.

## Results and Discussion

The convergence and accuracy of the numerical procedure are addressed in [6,7]. Comparisons of the analytically and experimentally obtained interlaminar distributions of three strain components at the edge of an open hole in an IM7/5250-4 laminate are shown in Figures 3-5. The stacking sequence  $[30_2/-30_2/90_4]_{3s}$  was utilized to enhance the interlaminar stress and strain values. The elastic properties of the unidirectional ply were  $E_1 = 151$  GPa,  $E_2 = E_3 = 9.45$  GPa,  $G_{12} = G_{13} = 5.9$  GPa,  $G_{23} = 3.26$  GPa,  $\nu_{12} = \nu_{13} = 0.32$ , and  $\nu_{23} = 0.45$ . The in-plane dimensions of the plate were  $L = 0.147$  M,  $A = 0.0736$  M,  $x_c = L/2$ ,  $y_c = A/2$ ,  $D = 0.0254$  and the ply thickness  $h = 0.00134$  M. Uniaxial loading was applied in the x-direction with the far-field stress equal to 50 MPa.

The mesh was chosen so that  $n_s = 1$  or one sublayer per ply in the z-direction;  $\rho$ -coordinate was subdivided into a total of  $m = 16$  intervals, with  $m_1 = 12$  intervals in the cylindrical transformation region, which was a hole radii wide ( $\kappa \rho_h = 1$ ). The consecutive interval length ratio was  $q = 1.2$ , where  $q = (\rho_{i+1} - \rho_i) / (\rho_i - \rho_{i-1})$ . The  $\theta$  coordinate in all cases was uniformly divided into 36 intervals.

Comparisons of the analytically and experimentally obtained distributions of three strain components at the edge of an open hole in laminate are presented in Figures 3-5. The analytical results on the figures are referred to as SVELT results, where SVELT is the software package implementing the theory described above. Distributions of  $\epsilon_\theta$  at  $66^\circ$ , the  $\gamma_{\theta z}$  component at  $75^\circ$ , and the  $\epsilon_z$  at  $90^\circ$  are compared with predictions made with the present model. Within these figures, the vertical dotted lines represent the idealized ply boundaries. The filled triangles represent the approximate ply boundaries of the actual specimen. The numbers across the top of

these charts represent the fiber orientation of the particular ply. The results from the experiment and the numerical model are extremely close for

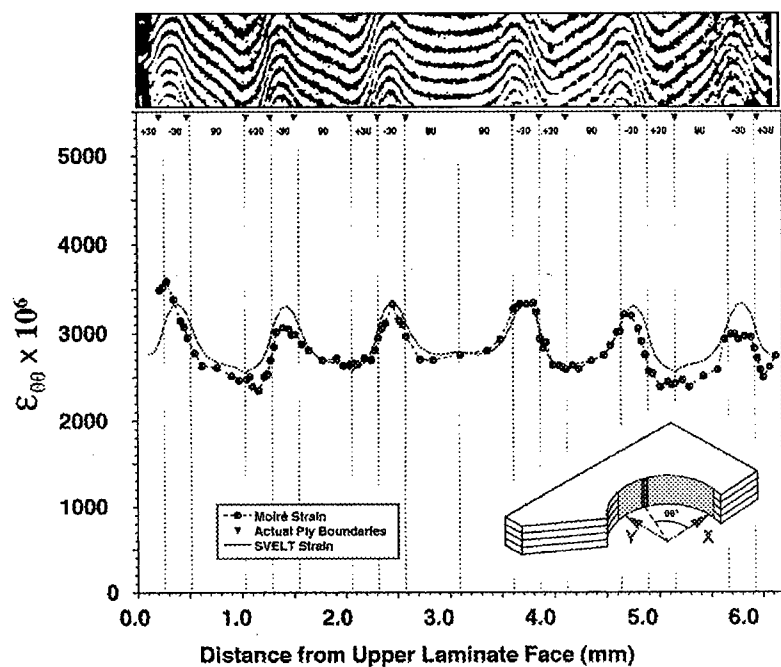


Fig 3: Comparison of the distribution of  $\epsilon_{\theta}$  through the laminate thickness at  $66^\circ$  for the  $[30_2/-30_2/90_4]_{3s}$  laminate.

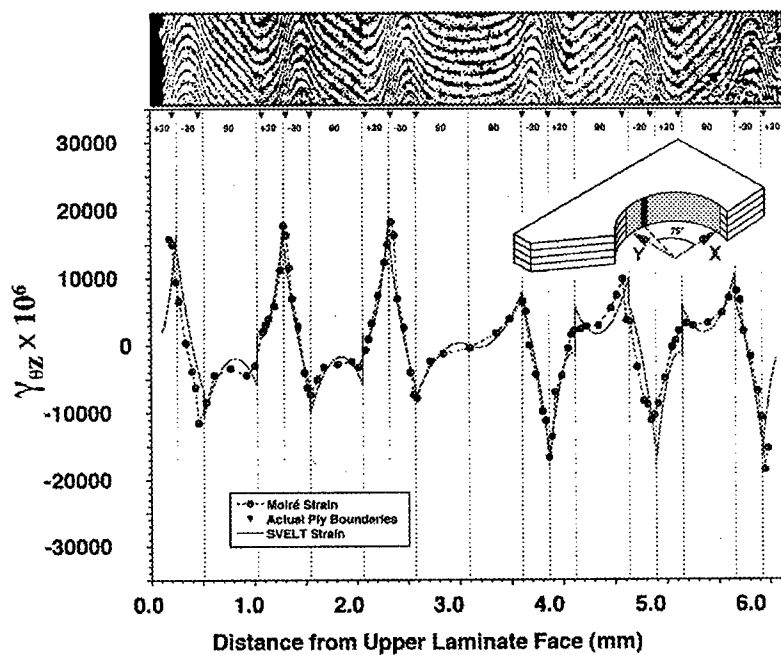


Fig 4: Comparison of the distribution of  $\gamma_{\theta z}$  through the laminate thickness at  $75^\circ$  for the  $[30_2/-30_2/90_4]_{3s}$  laminate.

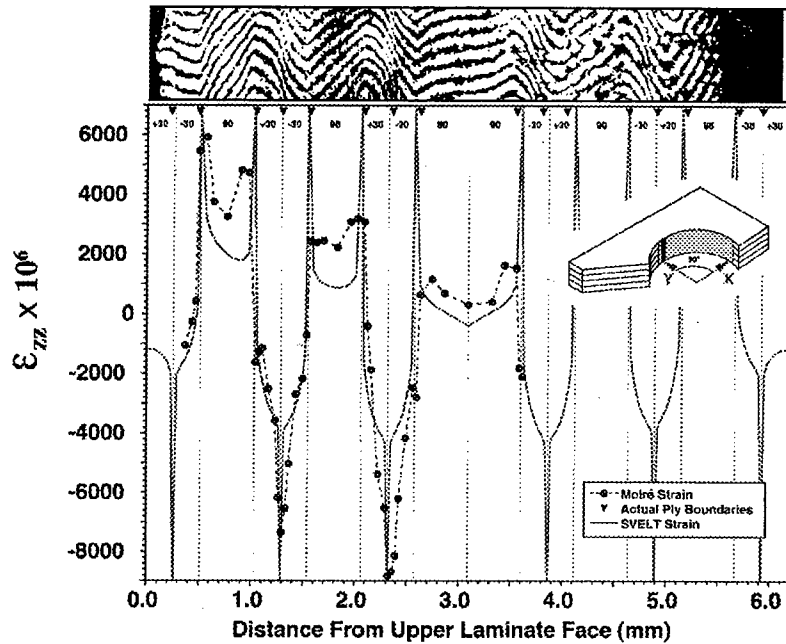


Fig 5: Comparison of the distribution of  $\varepsilon_z$  through the laminate thickness at  $90^\circ$  for the  $[30_2/-30_2/90_4]_{3s}$  laminate.

$\varepsilon_\theta$  and  $\gamma_{\theta z}$ . It is worthwhile to point out the difference of the two strain component distribution patterns, i.e.,  $\varepsilon_\theta$  has a smooth thickness distribution, whereas the  $\gamma_{\theta z}$  component has sharp peaks at the ply interfaces. It is in agreement with the theoretical prediction that the hoop strain component is bounded and  $\gamma_{\theta z}$  exhibits singular behavior. Similar verification is found at all angular locations examined. The present model accurately predicts the strain trends and strain magnitudes measured by Moiré. The comparison between the model predictions and Moiré for  $\varepsilon_z$  is not as close. The strain trends measured by the Moiré experiments are closely matched by the spline model prediction, however, the strains are consistently lower in magnitude than the Moiré measurements. This discrepancy is under investigation. The suspected cause is the discrepancy between the transverse normal stiffness of the specimen and the value used in the model, although a micromechanical origin is also being considered.

## Conclusions

Singular full-field stress distribution in composite laminates with open holes was obtained by using a novel technique based on superposition of hybrid and displacement approximation. Moiré interferometric measurements of the through-the-thickness distribution of strain components inside the hole of a  $[30_2/-30_2/90_4]_{3s}$

laminate was performed. Very close agreement of the theoretical and experimental results was observed for the hoop and interlaminar transverse shear strain components. Some quantitative difference for the interlaminar normal strain component is under investigation.

## References

1. Snyder, D. S., J. G. Burns, & V. B. Venkayya. (1990). Composite Bolted Joints Analysis Programs. *J. of Composite Technology & Research*, Spring, Vol. 12 (1) (41-51).
2. Eisenmann, J. R. (1976, April). Bolted Joint Static Strength Model for Composites Materials. *Third Conference on Fibrous Composite Materials in Flight Vehicle Design, Part II* (NASA TM X-3377).
3. Morley, L. S. D. (1970). A Finite Element Application of the Modified Rayleigh-Ritz Method. *Int. J. for Numerical Methods in Engineering* 2 (85-98).
4. Yamamoto, Y., & N. Tokuda. (1973). Determination of Stress Intensity Factors in Cracked Plates by the Finite Element Method. *Int. J. Numerical Methods in Engineering* 6 (427-439).
5. Yamamoto, Y., & Yoichi Sumi. (1978). Stress Intensity Factors for Three-Dimensional Cracks. *Int. J. of Fracture* 14(1) (17-38).
6. Iarve, E. V. (1996). Spline Variational Three Dimensional Stress Analysis of Laminated Composite Plates with Open Holes. *Int. J. of Solids and Structures*, Vol. 33, No. 14 (2095-2117).
7. Iarve, E. V., & N. J. Pagano. (2000, In Press). Singular Full-Field Stresses in Composite Laminates with Open Holes. *Int. J. of Solids and Structures*.
8. Post, D., B. Han, & P. Ifju. (1994). High Sensitivity Moiré. *Experimental Analysis for Mechanics and Materials*. New York: Springer-Verlag Inc.
9. Mollenhauer, D. H. (1997). Interlaminar Deformation at a Hole in Laminated Composites: A Detailed Experimental Investigation Using Moiré Interferometry. *Doctor of Philosophy Dissertation* available for download at the Virginia Polytechnic Institute and State University library's Web page <http://scholar.lib.vt.edu/theses/theses.html>.

## **Interaction of Shear Wave with Fiber Orientations in Composite Laminate: Model and Experiment**

D.K.Hsu and D.Fei

### **Abstract**

Linearly polarized transverse (shear) waves propagating in the thickness direction of a composite laminate interact strongly with the fiber directions in the discrete plies of the laminate. Shear waves transmitted through or reflected from a laminate therefore contain information about its stacking sequence and layup orientation. In the case of transmission, one can also exploit the analogy with the polarizer-analyzer configuration in optics. It has been shown that the interaction between shear waves and fiber directions can lead to high sensitivity for the detection of certain errors in the layup of stacking sequence of a laminate. This paper describes a complete analytical model for the propagation of shear waves in a laminate using local and global transfer matrices. Transmitted and reflected signal amplitude as a function of angle and time (or frequency) can be predicted for a given input. Experimental results are also shown for a transmission setup that uses electromagnetic acoustic transducers (EMATs) for the generation and reception of normal incidence shear waves in cured and uncured composite laminates.

### **Introduction**

Due to the highly anisotropic elastic properties of the plies in a fiber-reinforced composite laminate, transverse (shear) waves propagated through the laminate, or reflected from its back surface, carry rich information about the fiber orientation and ply stacking sequence in the laminate. Such signals can therefore be used in the nondestructive detection of ply layup or stacking sequence errors in composite laminates. Some attempts have been reported for exploiting the strong interaction between shear wave polarization and fiber orientation for nondestructive evaluation (NDE) purposes [1-4]. For example, Hsu et al [2,4] have used the "crossed polarizer" configuration in which the transmitting and receiving transducers on the two faces of the laminate were perpendicular to each other and both were rotated in unison over a full circle. The transmitted signal was found to have good sensitivity for certain ply orientation and stacking sequence anomalies. However, it is not until recently that a complete analytical model was developed by Fei and Hsu [5-7] for the propagation of shear waves in composite laminates and verified by a series of experiments. The analytical model led to a result that is very compact and tractable. The four transfer functions  $F_{ij}$  ( $i,j=1,2$ ) that contain the most information

---

D.K.Hsu and D.Fei, Center for Nondestructive Evaluation, Iowa State University, Ames, IA 50011, USA



can be determined experimentally for a given laminate by four measurements, with the transmitter angle and receiver angle at (0,0), (0,90), (90,0), and (90,90). The model takes into account all the reflected waves at the interfaces in the laminate by including the four partial waves in each layer that are polarized parallel to and perpendicular to the fiber, and propagating in the forward and reversed directions. The model for the transmission geometry has been experimentally verified using both cured and uncured laminates; it has now been extended to the case of reflection (pulse-echo).

An experimental problem with making reproducible shear wave measurements has been the need for a shear wave couplant. Keeping the coupling condition constant has been especially problematic for measurements that require frequent change of the angular orientation of the shear wave transducers. To alleviate this problem, researchers at Iowa State University used EMAT probes for the generation and detection of normal incidence shear waves in a non-contact manner. The composite sample was sandwiched between two aluminum blocks and the EMAT probes were placed on the outside faces of the two blocks. The EMATs can be rotated freely with computer-controlled stepping motors in an angular scan. For uncured laminates, the pressure applied on the blocks was sufficient for shear waves to transmit through. For solid cured laminates, shear couplant was still used between its surfaces and the aluminum; however, the coupling condition was not disturbed by rotation and hence remained constant. The analytical model was used to predict the transmitted signals for a number of laminate layup with various likely ply orientation errors and stacking sequence anomalies. The comparison of model and experimental results for selected cases is presented in this paper.

## Modeling

An idealized layered model, shown in Fig. 1(b), has been established to model the EMAT-generated shear wave transmission measurement shown in Fig. 1(a). The EMAT transmitter and receiver are modeled as linearly polarized plane shear wave generator and receiver, respectively. The aluminum blocks are modeled as two isotropic half spaces and the composite is modeled as a material structure that contains many plies, each of which is modeled as a homogeneous transversely-isotropic material with the plane of isotropy normal to the fiber direction. All the boundaries, including the ply-ply interfaces within the laminates and the aluminum-laminate interfaces, are assumed to be perfect so that the continuity conditions of displacement (or velocity) and stress can be applied.

To model the transmission output, we express the shear wave field in each ply as a summation of four partial wave fields: two fast shear waves propagating up and down, and two slow shear waves propagating up and down. Then we use the velocity and stress continuity conditions at each interface, including ply interfaces in the sample and sample-aluminum interfaces, to set up and solve the equations for the unknown transmission fields. Velocity continuity conditions, instead of displacement continuity conditions, are used so that the final equation can be expressed in terms of acoustic impedance, which is more compact and physically meaningful. The transfer matrix technique [8] is used to simplify the above solution process. But instead of

using transfer matrix directly, we use inverse transfer matrix to simplify the final expression. A brief description of the derivation process is given below. A more complete description can be found in [7].

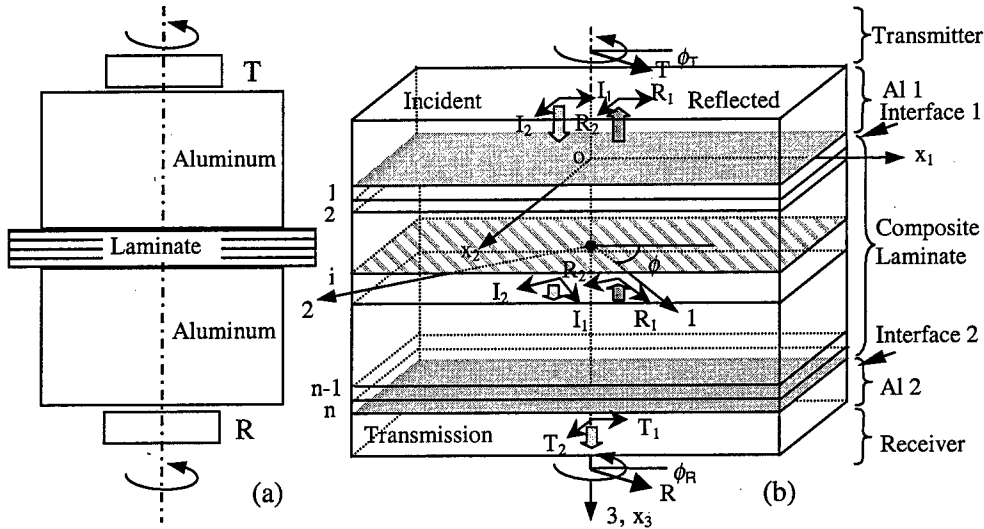


Figure 1 Model idealization. (a) measurement configuration; (b) model.

### Shear Wave Generation and Detection

As shown in Fig. 1(b), using the linear polarization assumption, the two displacement components of the incident shear wave can be expressed as

$$\begin{bmatrix} I_1 \\ I_2 \end{bmatrix}_{Al_1}^+ = V_i \beta_T(\omega) \begin{bmatrix} \cos \phi_T \\ \sin \phi_T \end{bmatrix} \quad (1)$$

where  $I_1$  and  $I_2$  are the displacement components of the incident shear wave,  $V_i$  is the source voltage,  $\omega$  is angular frequency,  $\beta_T(\omega)$  is the efficiency factor for the transmitter, and  $\phi_T$  is the polarization direction of the transmitter. For detection in the transmission mode, we have

$$V_o = \beta_R(\omega) \begin{bmatrix} T_1 & T_2 \end{bmatrix} \begin{bmatrix} \cos \phi_R \\ \sin \phi_R \end{bmatrix} \quad (2)$$

where  $T_1$  and  $T_2$  are the displacement components of the transmitted shear wave,  $V_o$  is the output voltage,  $\beta_R(\omega)$  is the efficiency factor for the receiver side, and  $\phi_R$  is the polarization direction of the receiver.

### Transfer Functions

By applying the velocity and stress continuity conditions at each interface in

the sample, we can relate the velocity-stress vectors at the top and bottom interfaces of the whole sample by a global inverse transfer matrix  $B$ , as follows,

$$P_{sample}^- = BP_{sample}^+ \quad (3)$$

where velocity-stress vector  $P(=[v_1 \ v_2 \ \sigma_{13} \ \sigma_{23}]^T)$  contains the velocity and stress components associated with the shear wave field, and  $B(=B_1B_2...B_{n-1}B_n)$  is a product of the local inverse transfer matrices  $B_i$  ( $i=1,2,...,n$ ) whose detailed expressions are given in [7].

In aluminum medium 1, the velocity-stress vector at interface 1 can be expressed as

$$P_{Al_1}^+ = (-i\omega) \begin{bmatrix} 1 & 0 & 1 & 0 \\ 0 & 1 & 0 & 1 \\ -Z & 0 & Z & 0 \\ 0 & -Z & 0 & Z \end{bmatrix}_{Al_1} \begin{bmatrix} I_1 \\ I_2 \\ R_1 \\ R_2 \end{bmatrix}_{Al_1} \quad (4)$$

where  $Z$  is the acoustic impedance of the shear wave in aluminum,  $R_1$  and  $R_2$  are the displacement components of the reflected shear wave, respectively. In medium 2, there are only two transmitted partial waves and the velocity-stress vector at the top interface is given by,

$$P_{Al_2}^- = (-i\omega) \begin{bmatrix} 1 & 0 \\ 0 & 1 \\ -Z & 0 \\ 0 & -Z \end{bmatrix}_{Al_2} \begin{bmatrix} T_1 \\ T_2 \end{bmatrix}_{Al_2} \quad (5)$$

Combining Eqs (3), (4) and (5) and applying velocity-stress continuity conditions at the two aluminum-sample interfaces, we can set up the equations for the unknown reflected and transmitted components in aluminum media. Solving the equations, we get the transmitted components  $T_1$  and  $T_2$  in the form of

$$\begin{bmatrix} T_1 \\ T_2 \end{bmatrix} = \begin{bmatrix} F_{11} & F_{12} \\ F_{21} & F_{22} \end{bmatrix} \begin{bmatrix} I_1 \\ I_2 \end{bmatrix} \quad (6)$$

where  $F_{ij}$  ( $i,j=1,2$ ) are the transfer functions that relate the arbitrary incident inputs with the transmission outputs. The detailed expressions for  $F_{ij}$ 's can be found in [7].

### Output Voltage

The expression for the output voltage can be obtained by combining Eqs (1), (2) and (6), which leads to

$$V_o = V_i \beta_T(\omega) \beta_R(\omega) \begin{bmatrix} \cos \phi_R & \sin \phi_R \end{bmatrix} \begin{bmatrix} F_{11} & F_{12} \\ F_{21} & F_{22} \end{bmatrix} \begin{bmatrix} \cos \phi_T \\ \sin \phi_T \end{bmatrix} \quad (7)$$

From Eq. (7), we can see that the layup information is contained in the transfer functions, and therefore there is no simple relationship between the transmission output and the layup. We can, however, detect the layup error by changing the frequency and the orientation of the transducers and monitoring the output accordingly. In essence, the transfer functions contain the maximum information that can be obtained from the transmission or reflection measurement. These transfer functions can be determined in principle by just four measurements: with (1)  $\phi_T = \phi_R = 0^\circ$ ; (2)  $\phi_T = \phi_R = 90^\circ$ ; (3)  $\phi_T = 0^\circ$ ,  $\phi_R = 90^\circ$ ; and (4)  $\phi_T = 90^\circ$ ,  $\phi_R = 0^\circ$ , respectively.

### Angular Scan Patterns

It has been found that the angle-frequency patterns (transmission spectra at different angles), for either "aligned" (where the EMATs are parallel to each other during an angular scan) or "crossed" (where the EMATs are normal to each other during an angular scan) configurations, are very sensitive to layup errors [6,7]. Figure 2 shows the modeled crossed angle-frequency patterns for a cross-ply graphite/epoxy laminate with and without stacking sequence errors. It can be seen that the changes of pattern due to layup errors are very obvious. Extensive model calculations for other types of laminates with other types of layup errors also show that the angle-frequency patterns or the equivalent angle-time patterns (transmission waveforms at different angles) are very sensitive to layup errors.

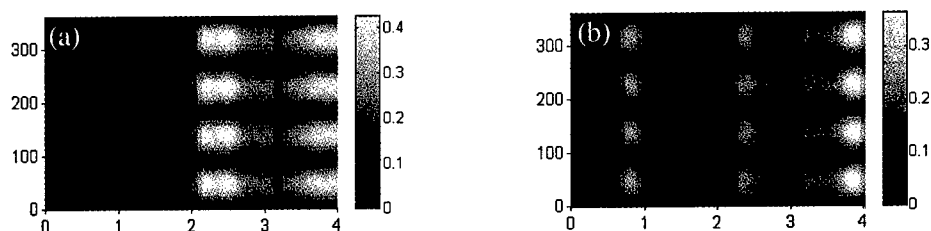


Figure 2 Modeled crossed angle-frequency patterns for graphite/epoxy laminates with and without errors. Layup:  $[(0/90)]_{2S}$ . (a) without error; (b) crossed, plies 2 and 3 are exchanged. For all patterns, the horizontal axis is frequency in MHz and the vertical axis is angle of the transmitter in degrees.

### Reflection Method

Compared to the transmission method, the reflection method has a big advantage of single-side access. To model the reflection output, the same procedure as the above can be used. Referring to Fig. 1, since there is no separate receiving transducer and the associated aluminum block necessary in a transmission measurement, interface 2 is traction free. Using Eqs (3) and (4) and the velocity-stress continuity condition at interface 1, we can again set up the equations and solve the unknown reflected fields  $R_1$  and  $R_2$ . Similar to Eq.(6), we have

$$\begin{bmatrix} R_1 \\ R_2 \end{bmatrix} = \begin{bmatrix} H_{11} & H_{12} \\ H_{21} & H_{22} \end{bmatrix} \begin{bmatrix} I_1 \\ I_2 \end{bmatrix} \quad (8)$$

where  $H$  contains the first two rows and columns of a matrix  $X$ , which is given by

$$X = \begin{bmatrix} 1 & 0 & -B_{11} & -B_{12} \\ 0 & 1 & -B_{21} & -B_{22} \\ Z & 0 & -B_{31} & -B_{32} \\ 0 & Z & -B_{41} & -B_{42} \end{bmatrix}^{-1} \begin{bmatrix} -1 & 0 \\ 0 & -1 \\ Z & 0 \\ 0 & Z \end{bmatrix} \quad (9)$$

The above expression can be further simplified using symbolic evaluation. Using Eq. (8) and the linear polarization assumption of the shear wave generation and detection, we can also get the expression for the reflected output, which is just Eq.(7) with  $\phi_T$  and  $F$  respectively replaced by  $\phi_R$  and  $H$ .

## Experiment

### Experimental System

An azimuthal EMAT scan system [5,6] has been developed for experimental verification of the model. In the scan system, the composite sample is sandwiched between two aluminum blocks. For cured composite laminates, a shear couplant was used at the composite-metal interfaces. In the case of uncured laminates, no couplant is needed and the shear wave can be detected effectively via the pressure applied on the sample. Two stepper motors, controlled by a computer through a motor driver, are used to rotate the EMATs (with a central frequency of about 1.3MHz and a bandwidth of about 1MHz) simultaneously. The EMAT transmitter is driven by a burst pulser (RITEC BP-9400). The transmitted signals, after being amplified and filtered, are acquired by the computer for further analysis. The azimuthal scan can be either "aligned" or "crossed". Under computer control, a typical azimuthal scan can be done in about 3 minutes.

### Results and Discussions

The first case studied is a 24-ply unidirectional graphite/epoxy laminate. Figure 3 (a) and (b) show the experimental and model-predicted crossed angle-time patterns, respectively. The angle-time pattern shows a 2D plot of the transmission waveforms obtained at different angular positions of EMATs during the scan. The time-domain model prediction is generated by calculating the spectrum of the reference signal obtained with the two aluminum blocks coupled directly together by couplant, multiplying the result by the transmission coefficient and transforming back into the time domain. It could be seen that the experimental results and the model prediction agree with each other very well. The aligned results are equally good.

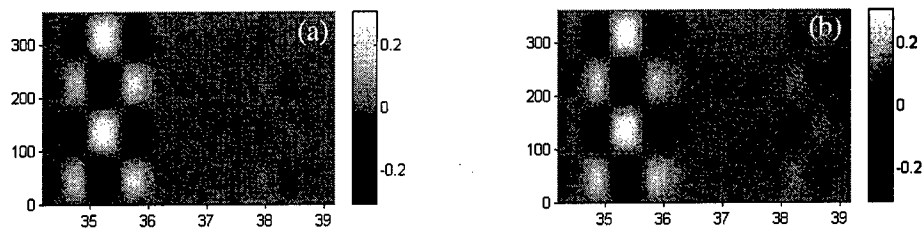


Figure 3 Angle-time patterns for a 24-ply unidirectional graphite/epoxy laminate: (a)experimental; (b)model. For all patterns, the horizontal axis is time in  $\mu\text{s}$  and the vertical axis is angle of the transmitter in degrees.

The second example is a case of an 8-ply uncured quasi-isotropic graphite/epoxy laminate. Figure 4 (a) and (b) show the experimental pattern for the crossed configuration and its model prediction for the sample free of layup errors, respectively. We can see that the model predicted the main features of the experimental pattern. In the experimental pattern, the signal decays faster than the model prediction because of the high attenuation of the uncured laminate, which is not included in the model. Figure 4 (c) and (d) show the crossed experimental pattern and its model prediction for the sample with the 4<sup>th</sup> ply misplaced at  $+45^\circ$ . By comparison, we can see that the changes of the pattern due to the fiber misorientation are very obvious, and that the model predicated such changes of the pattern fairly well. Experiments performed on other laminate layups in the model validations were similarly successful.

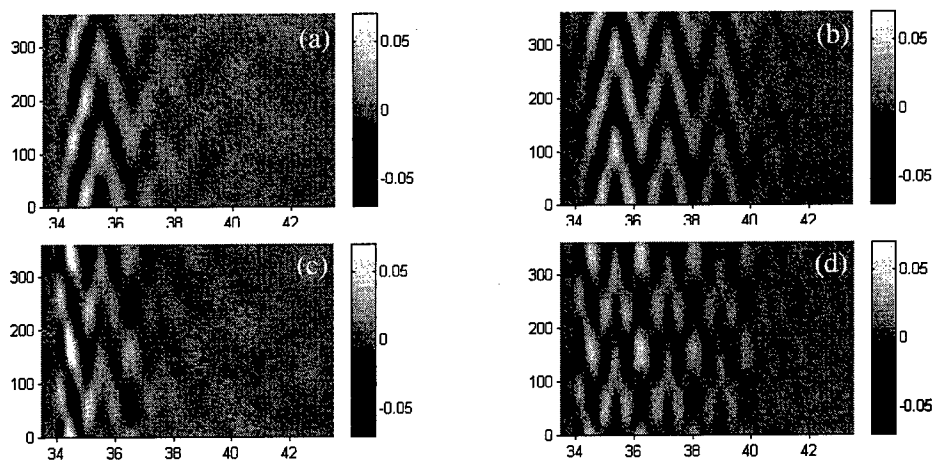


Figure 4 Crossed angle-time patterns for uncured graphite/epoxy laminates with and without layup errors. Layup:  $[(0/45/90/-45)]_s$ . (a)without error, experimental; (b)without error, model; (c)with ply 4 at  $45^\circ$ , experimental; (d)with ply 4 at  $45^\circ$ , model. For all patterns, the horizontal axis is time in  $\mu\text{s}$  and the vertical axis is angle in degrees for the transmitter.

## Conclusions

By developing an analytical model and conducting experimental verification, we have established normally incident shear waves as a quantitative NDE method for the evaluation of composite laminates. The use of EMATs has made it possible to have a computerized angular scan and data acquisition system for transmitted shear waves. The amplitude patterns of the transmitted signal, displayed as a function of time and angle (or frequency and angle), contain distinct features that reflect certain properties of the laminate. The experimental validation of the analytical model in cured and uncured composite laminates has been largely successful. Together with the computerized EMAT angular scan system, the analytical model continues to serve as a useful tool for the nondestructive detection of manufacturing anomalies in composite laminates.

## Acknowledgement

This work was supported by the NSF Industry/University Cooperative Research Center for Nondestructive Evaluation at Iowa State University. One of the authors (D. Fei) acknowledges the support of a fellowship from the Institute for Physical Research and Technology at Iowa State University.

## References

1. I. N. Komsky, I. M. Daniel and Y. C. Yee, Rev. of Prog. in Quantitative NDE, Vol. 11, D. O. Thompson and D. E. Chimenti editors, Plenum Press, 1992, pp. 1615-1622.
2. D. K. Hsu and F. J. Margetan, Adv. Comp. Lett., 2(2), 51-54 (1993).
3. B. A. Fischer and D. K. Hsu, Rev. of Prog. in Quantitative NDE, Vol. 15, D. O. Thompson and D. E. Chimenti editors, Plenum Press, 1996, pp. 1191-1198.
4. D. K. Hsu, B. A. Fischer and M. Koskamp, Rev. of Prog. in Quantitative NDE, Vol. 16, D. O. Thompson and D. E. Chimenti editors, Plenum Press, 1997, pp.1975-1982.
5. D. Fei and D. K. Hsu, Rev. of Prog. in Quantitative NDE, Vol. 18, D. O. Thompson and D. E. Chimenti editors, Kluwer Academic/Plenum Publishers, NY, 1999, pp. 1385-1392.
6. D. Fei and D. K. Hsu, submitted to Rev. of Prog. in Quantitative NDE, Vol. 19, D. O. Thompson and D. E. Chimenti editors, American Institute of Physics, Melville, NY, 2000.
7. D. K. Hsu and D. Fei, SAMPE 2000, Long Beach, CA, May 2000.
8. A. H. Nayfeh, Wave Propagation in Layered Anisotropic Media with Applications to Composites, Elsevier Science, 1995.

## **Finite Element Analysis of Creep in Unidirectional Composites Based on Homogenization Theory**

K. Kondo and R. Takiguchi

### **Abstract**

The creep behavior of continuous fiber reinforced unidirectional composites due to the viscoelasticity of the resin matrix is analyzed based on the homogenization theory utilizing the finite element method. It is assumed that the constituent fiber is transversely isotropic elastic material and the matrix is isotropic linearly elastic and nonlinearly viscoelastic one. The theoretical predictions for the creep behavior of the composites are compared with the experimental results.

### **Introduction**

The fiber reinforced plastics exhibit the creep behavior due to the viscoelasticity of the resin matrix even at the room temperature. Since a variety of composites are being considered for use in aerospace structures at high temperature, it is critical to predict the creep behavior of composites. The creep of unidirectionally reinforced composites were theoretically analyzed by the finite element method utilizing the repeating unit in composites with the regular fiber packing [1] or the homogenization theory [2].

In the present paper, the creep of the unidirectional composite with regular fiber arrangement is analyzed by the finite element method based on the homogenization theory. It is assumed that the constituent fiber is transversely isotropic linearly elastic material while the matrix is isotropic linearly elastic and nonlinearly viscoelastic one.

### **Governing Equations**

We deal with the mechanics of a periodic nonhomogeneous material. The equilibrium equations are given by

$$\frac{\partial \Delta \sigma_{ij}}{\partial x_j} = 0 \quad (1)$$

---

K. Kondo, Department of Aeronautics and Astronautics, University of Tokyo, 7-3-1 Hongo, Bunkyo-ku, Tokyo 113-8656, Japan

R. Takiguchi, Robot Systems Department, Nagoya Works, Mitsubishi Electric Corporation, Nagoya, Japan



and the strain displacement relationship is written as

$$\Delta \varepsilon_{ij} = \frac{1}{2} \left( \frac{\partial \Delta u_i}{\partial x_j} + \frac{\partial \Delta u_j}{\partial x_i} \right) \quad (2)$$

The constitutive equations take the form

$$\Delta \sigma_{ij} = C_{ijkl} [\Delta \varepsilon_{kl} - \dot{\varepsilon}_{kl}^c(\sigma_{t+\theta \Delta t}) \Delta t] \quad (3)$$

where  $\dot{\varepsilon}_{kl}^c(\sigma_{t+\theta \Delta t})$  is the creep strain rate at  $t = t + \theta \Delta t$  ( $0 \leq \theta \leq 1$ ).

The stress boundary conditions are given by

$$\Delta \sigma_{ij} n_j = \Delta \bar{T}_i \quad \text{on } \Omega_T \quad (4)$$

while the displacement boundary conditions are expressed as

$$\Delta u_i = \Delta \bar{u}_i \quad \text{on } \Omega_u \quad (5)$$

## Homogenization Method

### Global and Local Coordinates

We define the local coordinate  $\mathbf{y}$  in a single repetitive cell of periodicity as

$$\mathbf{y} = \frac{\mathbf{x}}{\varepsilon} \quad (\varepsilon \ll 1) \quad (6)$$

where the global coordinates  $\mathbf{x}$  refer to the whole of the body. By using the rule of differentiation

$$\frac{d}{dx_j} = \frac{\partial}{\partial x_j} + \frac{\partial y_k}{\partial x_j} \frac{\partial}{\partial y_k} = \frac{\partial}{\partial x_j} + \frac{1}{\varepsilon} \frac{\partial}{\partial y_j} \quad (7)$$

the equilibrium equations as Eqs.(1) are reduced to

$$\frac{\partial \Delta \sigma_{ij}}{\partial x_j} + \frac{1}{\varepsilon} \frac{\partial \Delta \sigma_{ij}}{\partial y_j} = 0 \quad (8)$$

and the strain-displacement relationship as Eqs.(2) are transformed to

$$\Delta \varepsilon_{ij} = \varepsilon_{x(y)}(\Delta \mathbf{u}) + \frac{1}{\varepsilon} \varepsilon_{y(y)}(\Delta \mathbf{u}) \quad (9)$$

where

$$\varepsilon_{x(y)}(\Delta \mathbf{u}) = \frac{1}{2} \left( \frac{\partial \Delta u_j}{\partial x_i} + \frac{\partial \Delta u_i}{\partial x_j} \right) \quad (10)$$

### Asymptotic Expansion

We assume that the periodicity of material characteristics imposes an analogous periodical perturbation on quantities describing the mechanical behavior of the body. Hence we use asymptotic expansion to describe the displacements and stresses as

$$u_i(\mathbf{x}, \mathbf{y}) = u_i^0(\mathbf{x}) + \varepsilon u_i^1(\mathbf{x}, \mathbf{y}) + \varepsilon^2 u_i^2(\mathbf{x}, \mathbf{y}) + \dots \quad (11)$$

$$\sigma_{ij}(\mathbf{x}, \mathbf{y}) = \sigma_{ij}^1(\mathbf{x}, \mathbf{y}) + \varepsilon \sigma_{ij}^2(\mathbf{x}, \mathbf{y}) + \dots \quad (12)$$

where  $u_i^k$ ,  $\sigma_{ij}^k$  for  $k \geq 1$  take the same value on the opposite sides of the cell of periodicity (i.e. Y-periodic). Substituting Eq.(12) into Eq.(8), the equilibrium equation splits into terms of orders  $\varepsilon^{-1}$  and  $\varepsilon^0$  as

$$\frac{\partial \Delta \sigma_{ij}^1}{\partial y_j} = 0 \quad (13)$$

$$\frac{\partial \Delta \sigma_{ij}^1}{\partial x_j} + \frac{\partial \Delta \sigma_{ij}^2}{\partial y_j} = 0 \quad (14)$$

Introduction of Eq.(11) into Eq.(9) yields

$$\Delta \varepsilon_{ij} = \varepsilon_{x(ij)}(\Delta \mathbf{u}^0) + \varepsilon_{y(ij)}(\Delta \mathbf{u}^1) + \varepsilon \left[ \varepsilon_{x(ij)}(\Delta \mathbf{u}^1) + \varepsilon_{y(ij)}(\Delta \mathbf{u}^2) \right] + \dots \quad (15)$$

The creep strain rate  $\dot{\varepsilon}_{kl}(\sigma_{t+\theta \Delta t})$  in Eq.(3) can be approximated by

$$\dot{\varepsilon}_{kl}^c(\sigma_{t+\theta \Delta t}) = \dot{\varepsilon}_{kl}^c(\sigma_t) + \theta \frac{\partial \dot{\varepsilon}_{kl}^c(\sigma_t)}{\partial \sigma_{rs}} \Delta \sigma_{rs} \quad (0 \leq \theta \leq 1) \quad (16)$$

Substituting Eq.(12) into Eq.(16), we get

$$\dot{\varepsilon}_{kl}^c(\sigma_{t+\theta \Delta t}) = \dot{\varepsilon}_{kl}^c(\sigma_t^1) + \dot{G}_{klrs}(\sigma_t^1) \left\{ \theta \Delta \sigma_{rs}^1 + \varepsilon (\sigma_{rs}^2 + \theta \Delta \sigma_{rs}^2) + \dots \right\} \quad (17)$$

where

$$\dot{G}_{klrs}(\sigma) = \frac{\partial \dot{\varepsilon}_{kl}^c(\sigma)}{\partial \sigma_{rs}} \quad (18)$$

By introducing Eqs.(12), (15), (17) into Eq.(3), the constitutive equation splits into terms of order  $\varepsilon^0$  and  $\varepsilon^1$  as

$$\begin{aligned} \Delta \sigma_{ij}^1 &= \left[ (C_{ijkl})^{-1} + \theta \dot{G}_{kl ij}(\sigma_t^1) \Delta t \right]^{-1} \left[ \varepsilon_{x(kl)}(\Delta \mathbf{u}^0) + \varepsilon_{y(kl)}(\Delta \mathbf{u}^1) - \dot{\varepsilon}_{kl}^c(\sigma_t^1) \Delta t \right] \\ &= \tilde{C}_{ijkl} \left[ \varepsilon_{x(kl)}(\Delta \mathbf{u}^0) + \varepsilon_{y(kl)}(\Delta \mathbf{u}^1) - \dot{\varepsilon}_{kl}^c(\sigma_t^1) \Delta t \right] \end{aligned} \quad (19)$$

$$\Delta \sigma_{ij}^2 = \tilde{C}_{ijkl} \left[ \varepsilon_{x(kl)}(\Delta \mathbf{u}^1) + \varepsilon_{y(kl)}(\Delta \mathbf{u}^2) - \dot{G}_{klrs}(\sigma_t^1) \sigma_{rs}^2 \Delta t \right] \quad (20)$$

### Microscopic and Macroscopic Equations

We decompose the displacement increment in the perturbation into the elastic and creep parts as

$$\Delta u_i^1 = \Delta u_i^{1e} + \Delta u_i^{1c} = \chi_i^{k\ell} \varepsilon_{x(k\ell)}(\Delta \mathbf{u}_0) + \Delta u_i^{1c} \quad (21)$$

where  $\chi_i^{k\ell}$  and  $\Delta u_i^{1c}$  are Y-periodic. Substituting Eq.(21) into Eq.(19), we get the macroscopic evolution equation as

$$\begin{aligned} \Delta \sigma_{ij}^1 &= \tilde{C}_{ijpq} \left[ \delta_{pk} \delta_{q\ell} + \varepsilon_{y(pq)}(\chi^{k\ell}) \right] \varepsilon_{x(k\ell)}(\Delta \mathbf{u}^0) + \tilde{C}_{ijkl} \left[ \varepsilon_{y(k\ell)}(\Delta \mathbf{u}^{1c}) - \dot{\varepsilon}_{k\ell}^c(\sigma_t^1) \Delta t \right] \\ &= \tilde{a}_{ijkl} \varepsilon_{x(k\ell)}(\Delta \mathbf{u}^0) + \Delta r_{ij} \end{aligned} \quad (22)$$

Here, we introduce volume average operator

$$\langle \cdot \rangle = \frac{1}{|\mathbf{y}|} \int_{\mathbf{y}} (\cdot) d\mathbf{y} \quad (23)$$

where  $|\mathbf{y}|$  denotes volume of the unit cell  $\mathbf{y}$ . From Eq.(22), we get the macroscopic constitutive equations

$$\Delta \Sigma_{ij} = \langle \tilde{a}_{ijkl} \rangle \Delta E_{k\ell} + \langle \Delta r_{ij} \rangle \quad (24)$$

where

$$\Delta \Sigma_{ij} = \langle \Delta \sigma_{ij} \rangle, \quad \Delta E_{ij} = \varepsilon_{x(k\ell)}(\Delta \mathbf{u}^0) \quad (25)$$

Introducing Eq.(22) into Eq.(13) and considering that  $\varepsilon_{x(k\ell)}(\Delta \mathbf{u}^0)$  are arbitrary, we get

$$\frac{\partial \tilde{a}_{ijkl}}{\partial y_j} = 0 \quad (26)$$

$$\frac{\partial \Delta r_{ij}}{\partial y_j} = 0 \quad (27)$$

which give the governing equations for  $\chi^{pq}$  and  $\Delta \mathbf{u}^{1c}$ , respectively, as

$$\frac{\partial}{\partial y_j} \left\{ \tilde{C}_{ijkl} \left[ \delta_{kp} \delta_{lq} + \varepsilon_{y(k\ell)}(\chi^{pq}) \right] \right\} = 0 \quad (28)$$

$$\frac{\partial}{\partial y_j} \left\{ \tilde{C}_{ijkl} \left[ \varepsilon_{y(k\ell)}(\Delta \mathbf{u}^{1c}) - \dot{\varepsilon}_{k\ell}^c(\sigma_t^1) \Delta t \right] \right\} = 0 \quad (29)$$

From Eq.(14), we obtain the macroscopic equations as

$$\frac{\partial \Delta \Sigma_{ij}}{\partial x_j} = 0 \quad (30)$$

### Creep Law

The flow rule of creep deformation of the isotropic matrix is

$$\dot{\epsilon}_{ij}^c = \frac{3}{2} \frac{\dot{\epsilon}_e^c}{\sigma_e} \sigma'_{ij} \quad (31)$$

where  $\sigma_e$  and  $\dot{\epsilon}_{ij}^c$  are the effective stress and the effective creep strain increment, respectively, in the form

$$\sigma_e = \left( \frac{3}{2} \sigma'_{ij} \sigma'_{ij} \right)^{\frac{1}{2}}, \quad \dot{\epsilon}_e^c = \left( \frac{2}{3} \dot{\epsilon}_{ij}^c \dot{\epsilon}_{ij}^c \right)^{\frac{1}{2}} \quad (32)$$

It is assumed that the creep of matrix is governed by the Norton-Bailey law as

$$\epsilon_e^c = k \sigma_e^n t^m \quad (33)$$

from which we have the creep law of the time hardening type in the form

$$\dot{\epsilon}_e^c = km \sigma_e^n t^{m-1} \quad (34)$$

Eliminating  $t$  from Eqs.(33) and (34), we obtain the creep law of the strain hardening type as

$$\dot{\epsilon}_e^c = k^{\frac{1}{m}} m \sigma_e^{\frac{n}{m}} \epsilon_e^{\frac{m-1}{m}} \quad (35)$$

### Finite Element Formulation

We solve Eqs.(28) and (29) utilizing the finite element method. Considering that  $\chi_i^{pq}$  is Y-periodic, the Galerkin equation for Eq.(28) can be reduced to

$$\begin{aligned} 0 &= \int_Y \frac{\partial}{\partial y_j} \left\{ \tilde{C}_{ijkl} \left[ \delta_{kp} \delta_{lq} + \epsilon_{y(kl)}(\chi^{pq}) \right] \right\} \delta \chi_i^{pq} dY \\ &= - \int_Y \tilde{C}_{ijpk} \frac{\partial \delta \chi_i^{pq}}{\partial y_j} dY - \int_Y \tilde{C}_{ijkl} \epsilon_{y(kl)}(\chi^{pq}) \frac{\partial \delta \chi_i^{pq}}{\partial y_j} dY \end{aligned} \quad (36)$$

which is the weak form utilized to obtain  $\chi_i^{pq}$  in the finite element method. The Galerkin equation for Eq.(29) can be also transformed to

$$\begin{aligned}
0 &= \int_Y \frac{\partial}{\partial y_j} \left\{ \tilde{C}_{ijk\ell} \varepsilon_{y(k\ell)} (\Delta \mathbf{u}^{1c}) - \dot{\varepsilon}_{k\ell}^c (\boldsymbol{\sigma}_t^{1c}) \Delta t \right\} \delta \Delta u_i^{1c} dY \\
&= - \int_Y \tilde{C}_{ijk\ell} \varepsilon_{y(k\ell)} (\Delta \mathbf{u}^{1c}) \frac{\partial \delta \Delta u_i^{1c}}{\partial y_j} dY - \int_Y \tilde{C}_{ijk\ell} \dot{\varepsilon}_{k\ell}^c (\boldsymbol{\sigma}_t^{1c}) \Delta t \frac{\partial \delta \Delta u_i^{1c}}{\partial y_j} dY \quad (37)
\end{aligned}$$

which it the weak form to obtain  $\Delta u_i^{1c}$ .

### Numerical Procedure

For the case where macroscopic stresses  $\Sigma_{ij}$  (or macroscopic strains  $E_{ij}$ ) are given, we set  $\boldsymbol{\sigma}_t^{1c} = \mathbf{0}$  for  $t = 0$ . Then the incremental computation from the current time  $t = t$  to the subsequent time  $t = t + \Delta t$  is conducted as follows ;

- (1) For given  $\boldsymbol{\sigma}_t^{1c}$ , we calculate  $\tilde{C}_{ijk\ell}$  from Eq.(19), and  $\dot{\varepsilon}_{k\ell}^c (\boldsymbol{\sigma}_t^{1c})$  from Eq.(31). And we obtain  $\chi_i^{pq}$  and  $\Delta u_i^{1c}$  by the finite element method based on Eqs.(36) and (37) with the Y-periodic boundary conditions.
- (2) We calculate  $\tilde{a}_{ijk\ell}$  and  $\Delta \gamma_{ij}$  from Eq.(22), and obtain  $\langle \tilde{a}_{ijk\ell} \rangle$  and  $\langle \Delta \gamma_{ij} \rangle$ .
- (3) We calculate  $\Delta E_{ij} = \dot{\varepsilon}_{k\ell}^c (\Delta \mathbf{u}_0)$  (or  $\Delta \Sigma_{ij}$ ) from Eq.(24).
- (4) We calculate  $\Delta \sigma_{ij}^{1c}$  from Eq.(22), and obtain  $\boldsymbol{\sigma}_t^{1c}$  at  $t = t + \Delta t$ .

### Numerical Results

We analyze a unidirectional graphite-epoxy composite with hexagonal packing as shown in Fig.1. The epoxy resin is considered to be isotropic linearly elastic and nonlinearly viscoelastic material with the mechanical properties

$$\begin{aligned}
E_m &= 476 \text{ Kgf/mm}^2 & \nu_m &= 0.39 & n &= 1 & m &= 0.269 \\
k &= 1.76 \times 10^{-4} \text{ (kgf/mm}^2\text{)}^{-n} \text{ (hour)}^{-m}
\end{aligned}$$

The graphite fiber is assumed to be transversely isotropic linearly elastic material with the mechanical properties

$$\begin{aligned}
E_{Lf} &= 21000 \text{ Kgf/mm}^2 & E_{Tf} &= 1310 \text{ Kgf/mm}^2 \\
\nu_{LTf} &= 0.29 & \nu_{LTf} &= 0.49 & G_{LTf} &= 2190 \text{ Kgf/mm}^2
\end{aligned}$$

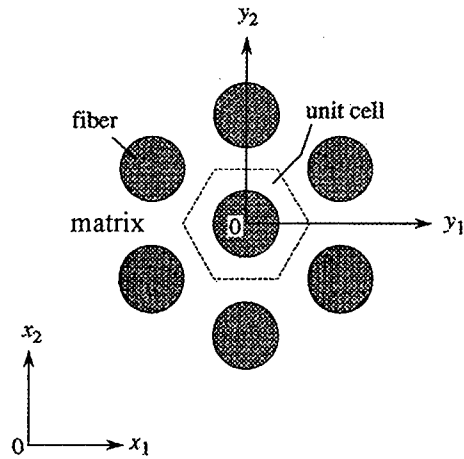


Figure 1 Regular Hexagonal Array Composite and Unit Cell

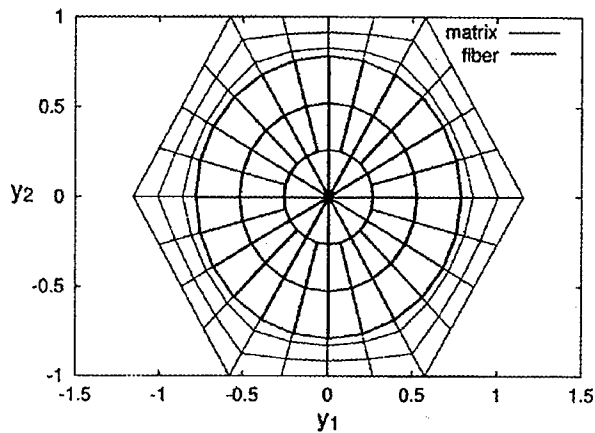


Figure 2 Finite Element Discretization of Unit Cell of Hexagonal Array Composite

A unit cell of periodicity as indicated in Fig.1 is discretized by the eight-node isoparametric quadrilateral finite element as shown in Fig.2.

The macroscopic strain  $E_{11}$  of the graphite-epoxy unidirectional composite subjected unidirectional constant macroscopic stress  $\Sigma_{11} = \bar{\sigma}_1$  is shown as a function of  $t$  in Fig.3 together with the experimental results [1]. And the macroscopic strain  $E_{22}$  vs. the applied stress  $\Sigma_{22}$  is shown in Fig.4

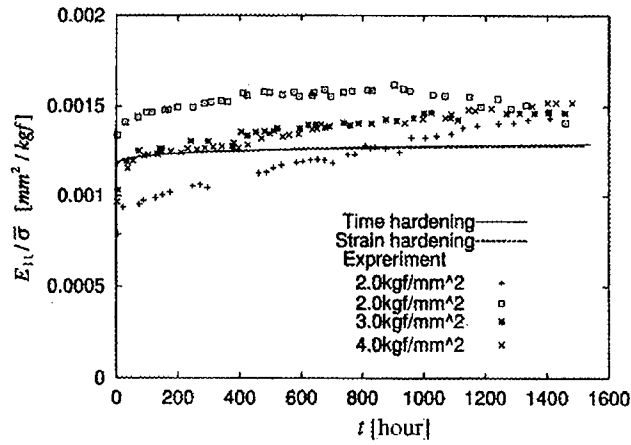


Figure 3 Strain  $E_{11}$  vs. Time  $t$  for Unidirectional Graphite-Epoxy Composite under Applied Stress  $\Sigma_{11} = \bar{\sigma}$

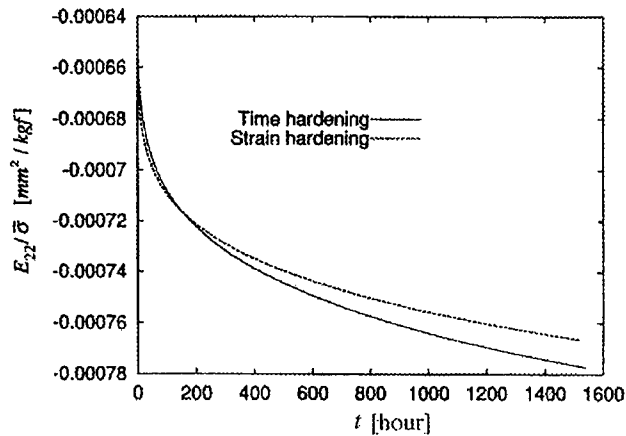


Figure 4 Strain  $E_{22}$  vs. Time  $t$  for Unidirectional Graphite-Epoxy Composite under Applied Stress  $\Sigma_{11} = \bar{\sigma}$

## References

1. K.Kondo and M.Masuyama, 1994. "Greep Behavior of Unidirectional Coposites." *Computational Mechanics*, 14:16-27.
2. X. Wu and N. Ohno, 1998. "A Homogenization Theory for Time-Dependent Deformation of Composites with Periodic Internal Structures." *JSME International Journal, Series A*. 41(3):309-317

## **Correlation between Acoustic Emission Waveform Parameters and the Damage and Failure Mechanisms in CFRP Materials**

O. Siron, H. Tsuda and T. Hamada

### **Abstract**

The mechanical behavior of unidirectional (UD) and 2D-laminate Carbon Fiber-Reinforced Plastic composites was investigated under 4-point bending and tensile loads at room temperature. The mechanical behavior of UD composites was first studied. The mechanical behavior of a quasi-isotropic laminate ( $[+45/90/-45/0]_{2s}$ ) was subsequently investigated under the same loading conditions and correlated to that of the UD plies. The damage and the failure mechanisms were identified by microscope observations on both UD and laminate composites. Two families of damage mode were identified, involving interfiber cracks and inter-layer delamination cracks homogeneously distributed within the composite. The fracture process is assigned to the propagation of the macrocrack in the failure envelope through a large intra and inter-layer delamination process interrupted by fibers/bundles fracture. Acoustic emission measurement was performed during the tests. An approach using a combination of acoustic waveform parameters as indicators of the physical damage is discussed.

### **Introduction**

Carbon Fiber-Reinforced Plastic (CFRP) composites display several advantageous properties for structural application in the aeronautics and space industry. In order to define an accurate design and life prediction of CFRP structures, it is important to identify and to predict the nature of the physical damage occurring within the structure under critical loads. The damage and failure process in CFRP composites is known to involve a sequential accumulation of matrix microcracks, delaminations and fiber/bundle failures. These features have been identified on unidirectional (UD) [1] and 2D-laminate CFRP composites [2-4] under several loading conditions at room temperature.

---

O.Siron and H.Tsuda, Department of Composite Materials, National Institute of Materials and Chemical Research, 1-1 Higashi, Tsukuba 305-8565, Japan

T.Hamada, Department of Materials Science and Technology, Science University of Tokyo  
2641 Yamazaki, Noda 278-8510, Japan



An example of such CFRP composite (T800H/3631) has been investigated in this study. In the first part of this work, the mechanical behavior and the ultimate failure of the composites were investigated under quasi-static loading conditions at room temperature. The originality of this work is to study the mechanical behavior of CFRP composites through multi-scale approach. The mechanical behavior of UD composites under tensile and flexural loads was first studied. The mechanical behavior of a quasi-isotropic laminate composite was subsequently investigated under the same loading conditions and correlated to that of the elementary plies. For both CFRP composites tested, the damage and the rupture processes were identified by optical microscopy.

Non-destructive evaluation (NDE) is useful to follow the integrity of structures during processing and industrial applications. Acoustic emission (AE) analysis was performed during the mechanical tests. In the second part of this study, AE waveform parameters were investigated as damage indicators and related to the physical damage of the composite. Numerous attempts have been done to correlate AE waveform parameters to the physical damage process. Major studies are reviewed in the references [5-9]. In the present work, AE was recorded with a single sensor under several loading conditions generating localized (bending test) and diffuse (tensile test) damage area. From a multi-scale experimental analysis of the composites, a double amplitude/duration analysis of the AE signals was performed. A correlation between the AE waveform parameters and the damage and fracture kinetics identified by optical microscopy was then proposed.

## Materials and Experiments

The materials used are unidirectional (UD) and quasi-isotropic ( $[+45/90/-45/0]_{2s}$ ) CFRP composites (manufactured by Toray Co. Ltd). All these materials were fabricated according to the same process. The prepreg used was T800H / 3631 (Epoxy matrix). The volume fraction of fibers (table I) was 60%. Prepregs were cured at 180 °C during two hours. An analysis by optical microscopy was performed on the as-received UD and 2D composites. No damage (including no porosity) was identified within the specimens. The apparent density of the specimens is  $1.58 \pm 0.02$  g/cm<sup>3</sup>. The length and width of the specimens tested were respectively 200 mm and 20 mm, except for the on-axis UD-composite of which the width has been reduced to 10 mm.

The tensile tests were performed with a universal testing machine at a crosshead speed of 0.5 mm/min. The 4-point loading was chosen because shear components were generated during testing. Furthermore, 4-point bending tests generate gradual loading conditions concentrated between the loading noses, favoring the damage kinetics analysis. Tests were performed according to the ASTM standards [10]. All the specimens were loaded with a device whose lower and upper span were 150 mm and 50 mm respectively. The tests were performed with a universal testing machine with a 1mm/min crosshead speed. The composite strain and the beam deflection were measured respectively with strain gauges and a

displacement sensor. Flexural moduli were calculated from the load/deflection measurements, in accordance with reference 10.

Prior to testing, simulated AE sources (pencil lead broken on the edge of specimens) have been analyzed. Optimized timing parameters used for the AE waveform parameters recording have been defined. The sampling rate was set to 2 MHz. A 300KHz resonance frequency AE sensor was attached to the specimen through a silicone grease coupling. The sensor output was connected to a 40 dB preamplifier and a 150-750 KHz bandwidth plug-in filter. The threshold of the AE system was set to 30 dB. The calibration of the recording system allowed the selection of the appropriate parameters and elimination of the signal noise from the grip device.

Table I Mechanical properties of the CFRP composite materials

(Notations: E: Young's modulus,  $\nu$ : Poisson ratio,  $\sigma$ : stress,  $\epsilon$ : strain, l: longitudinal, t: transverse, b: bending, r: failure, max: maximum)

	Tensile Test		4-pt bending Test	
C-fiber T800H (data provided by Toray Co.)	Density: 1.81 g/cm <sup>3</sup> E <sub>l</sub> = 294 GPa	$\sigma_r = 5.49$ GPa $\epsilon_r = 1.9$ %		
UD [0] <sub>12p</sub>	On-axis: E <sub>l</sub> = 175±3 GPa $\nu_{lt} =$ 0.33±0.01 $\sigma_r =$ 2600±50 MPa $\epsilon_r =$ 1.49±0.01 %	90° off-axis: E <sub>t</sub> = 7.90±0.02 GPa $\sigma_r =$ 80 ±5 MPa $\epsilon_r =$ 1.05±0.1 %	On-axis: E <sub>b</sub> = 155.8±2.1 GPa $\sigma_{max} =$ 1807±44 MPa ( $\epsilon =$ 1.31±0.03 %)	90° off-axis: E <sub>b</sub> = 8.1±0.2 GPa $\sigma_{max} =$ 118±2 MPa ( $\epsilon =$ 1.36±0.02 %)
[+45/90/-45/0] <sub>2s</sub>	E <sub>l</sub> = 61±1 GPa $\nu_{lt} = 0.32$	$\sigma_r =$ 865±32 MPa $\epsilon_r =$ 1.4±0.1 %	E <sub>b</sub> = 47.60±0.15 GPa	$\sigma_{max} =$ 702±12 MPa ( $\epsilon =$ 1.7±0.1 %)

## Results and Discussion

### Mechanical Behavior and Microscope Observations of Damage [8]

The stress-strain relationship of the UD and the laminate composites are linear and interrupted by a brittle fracture process under tensile and bending loading conditions (table I). Optical microscopy inspections of the tested specimens were used to assess the damage and the failure processes of the composites. A few intra-ply cracks and limited inter-ply delamination cracks were identified homogeneously distributed in the laminate composite. The 45° off-axis plies clearly fulfill their function delaying the propagation of the matrix cracks to the on-axis plies. For both of the composites tested, most of the damage is located in the failure envelope, including large intra and inter-layer delamination cracks as well as fiber/bundle failures (figure 1). The damage and fracture processes are mainly due to local shear components.

### Damage and Rupture Processes in Correlation with AE Waveform Parameters [8]

The multi-scale approach adopted in this work allowed to clearly identify the damage and the failure modes involved during the loading of the CFRP composites. Based on the variations in amplitude and duration of the AE events, several domains were defined and correlated to the physical damage. This multi-scale approach provides evidences of a correlation between the initiation and the propagation of matrix microcracking and the low duration and low/medium amplitude events. The initiation and the propagation of the intra and inter-ply delamination cracks were associated to medium duration and medium/high amplitude AE events. Medium duration and highest amplitude events were assigned to fiber/bundle failure. Finally, high duration (and mainly highest amplitude) events were associated to the sudden propagation of the macrocrack including large delamination cracks. Table II summarizes the classification of the AE signal parameters.

## Conclusions

The mechanical behavior of UD and quasi-isotropic CFRP composites was investigated under tensile and 4-point loads. This material exhibits remarkably high elastic and failure properties. Optical microscopy inspections of the tested specimens were used to assess the damage and the failure processes of the composites. A few intra-ply cracks and limited inter-ply delamination cracks were identified, homogeneously distributed in the laminate composite. The 45° off-axis plies clearly fulfill their function delaying the propagation of the matrix cracks to the on-axis plies. For both of the composites tested, most of the damage is located in the failure envelope, including large intra and inter-layer delamination cracks as well as

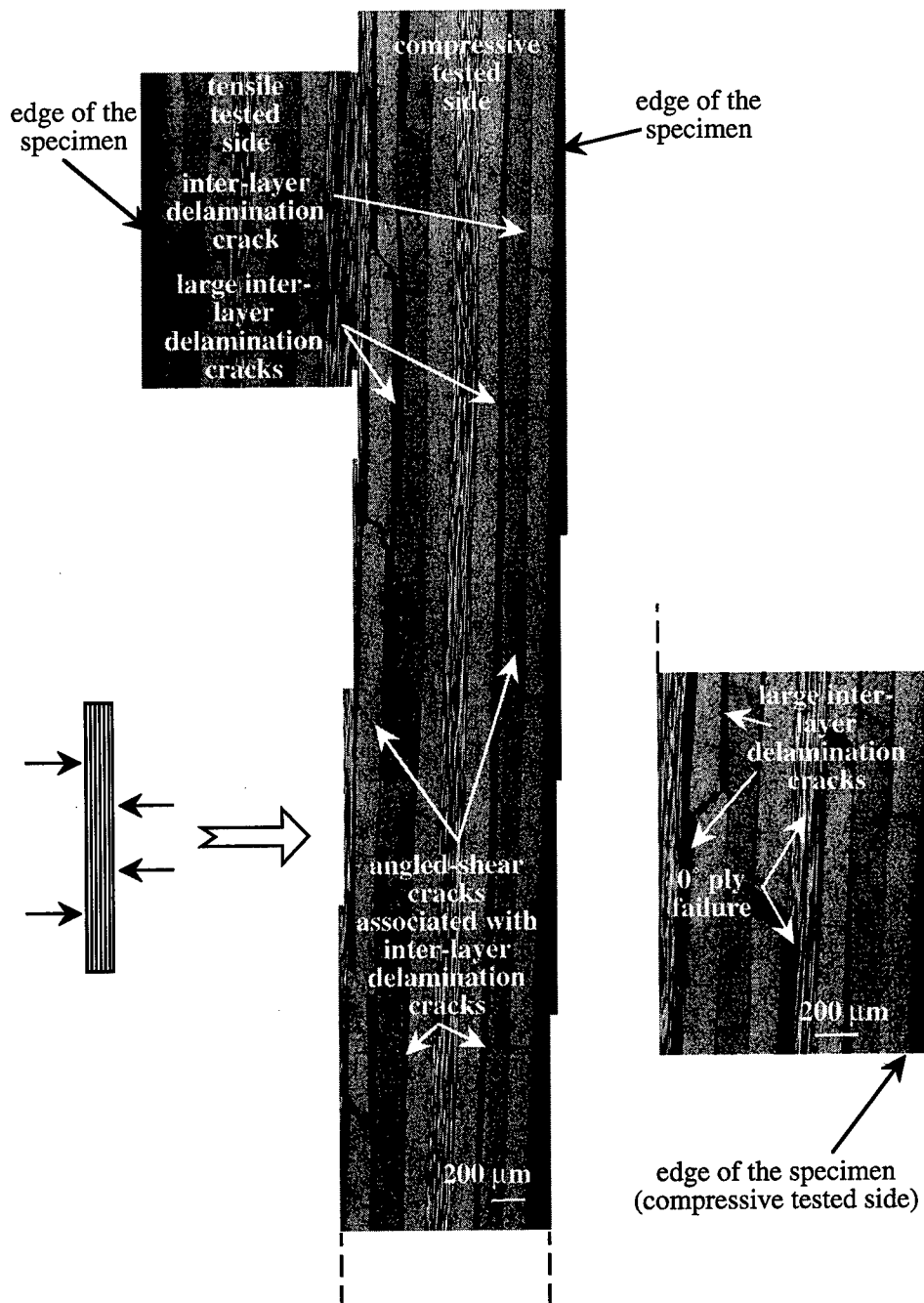


Figure 1 : Optical micrographs showing the fracture process occurred within the  $[+45/90/-45/0]_{2s}$  laminate CFRP composite under 4-point bend test

fiber/bundle failures. The damage and fracture processes are mainly due to local shear components.

AE signals were recorded during the mechanical tests. Based on the microscopy analysis of damage, an approach using AE waveform parameters as damage indicators was proposed. Similar results were obtained on both the CFRP composites tested under tensile and bending loading conditions. This multi-scale approach provides evidences of a correlation between the initiation and the propagation of matrix microcracking and the low duration and low/medium amplitude events. The initiation and the propagation of the intra and inter-ply delamination cracks were associated to medium duration and medium/high amplitude AE events. Medium duration and highest amplitude events were assigned to fiber/bundle failure. Finally, high duration (and mainly highest amplitude) events were associated to the sudden propagation of the macrocrack including large delamination cracks. The next step will involve experiments with several AE sensors ( $\geq 2$ ). The AE waves attenuation could be studied in correlation with the location of the AE sources. These new results will be compared to the classification proposed.

Table II Correlation between the physical damage, the fracture mechanism and the AE waveform parameters.

Amplitude Duration	Low (30 - 35/40dB)	Medium (35/40 - 80dB)	High (80 -100 dB)	
Low ( $< 1000 \mu\text{sec}$ )	<u>Domain I:</u> onset of intra- ply matrix microcrack	<u>Domain II:</u> propagation of matrix microcrack	(80-90/95 dB)	(90/95-100dB)
Medium ( $1000 << 10,000 \mu\text{sec}$ )		<u>Domain III:</u> onset of delamination (initiation of transverse ply failure associated with inter-ply delamination crack)	<u>Domain IV</u> (a): propagation of intra and inter- ply delamination crack	<u>Domain IV</u> (b): fiber / bundle failure
High ( $> 10,000 \mu\text{sec}$ )				<u>Domain V:</u> brutal propagation of macrocrack associated with large delamination crack

## Acknowledgements

This work has been supported by the Japanese Science and Technology Agency.

## References

1. N. SATO, T. KURAUCHI and O. KAMIGAITO, 1986. "Fracture Mechanism of Unidirectional CFRP Composite." *J. Mater. Sci.*, 21: 1005 - 1010.
2. J.E. MASTERS and K.L. REIFSNIDER, 1982. "An Investigation of Cumulative Damage Development in Quasi-Isotropic Graphite/Epoxy Laminates, Damage in Composite Materials." *ASTM STP 775*: 40 - 62.
3. P.W. PETERS and T.W. CHOU, 1987. "On Cross-Ply Cracking in Glass and Carbon Fiber-Reinforced Epoxy Laminates." *Composites*, 18: 40 - 46.
4. S. OGIHARA, N. TAKEDA and A. Kobayashi, 1997. "Experimental Characterization of Microscopic Failure Process Under Quasi-Static Tension in Interleaved and Toughness-Improved CFRP Cross-Ply Laminates." *Comp. Sci. & Tech.*, 57: 267 - 275.
5. F. MERAGHNI, 1994. PhD Thesis, U.T. Compiègne: 99 (in French).
6. O. SIRON, G. CHOLLON, H. TSUDA, H. YAMAUCHI, K. MAEDA and K. KOSAKA, "Microstructural and Mechanical Properties of Filler-Added Coal Tar Pitch-Based C/C Composites: The damage and Fracture Process in Correlation With AE Waveform Parameters." to be published in *Carbon*.
7. O. SIRON, H. TSUDA, 1999. "Damage and Rupture Process of Filler-Added Coal-Tar Pitch-Based C/C Composite Materials Under Quasi-Static Loadings at Room Temperature." *Proceedings of the 6th Japan International SAMPE*, Tokyo, October 26-29: 1135 - 1138.
8. O. SIRON, H. TSUDA, "The Damage and Fracture Processes in CFRP in Correlation with AE Waveform Parameters." submitted to *J. of Mater. Sci.*
9. W.H. PROSSER, K.E. JACKSON, S. KELLAS, B.T. SMITH J. McKEON and A. FRIEDMAN, 1995. "Advanced Waveform-Based Acoustic Emission Detection of Matrix Cracking in Composites." *Materials Evaluation*, 53: 1052 - 1058.
10. ASTM D790-95a, 1996. "Standard Test Methods for Flexural Properties of Unreinforced and Reinforced Plastics and Electrical Insulating Materials." 155 - 163.



# Composite Mechanics, II

---





## Characterization of mechanical behavior of CFRP laminates containing matrix cracks using damage mechanics analysis

S. Kobayashi, S. Ogihara and N. Takeda

### Abstract

A damage mechanics analysis is applied to predict the relation between laminate stress and strain in composite laminates containing transverse matrix cracks. First, the transverse crack density as a function of laminate stress is predicted based on both energy and average stress criteria. Next, the laminate strain increment caused by transverse cracking is also derived as a function of applied laminate stress and transverse crack density, and then the relation between laminate stress and strain can be predicted considering matrix cracking. The analytical prediction of the relation between laminate stress and strain is compared with the experimental results. The analytical prediction slightly underestimates the laminate stress because the strain increment associated with transverse crack opening displacement is overestimated in this analysis. An advantage of the present predictive method is that it can be applied to laminates with arbitrary stacking sequences.

### Introduction

In the failure process of fiber reinforced composite laminates, it is well known that many types of damages occur, that is, fiber-matrix interfacial debonding, transverse

---

S. Kobayashi, Graduate Student, Takeda Lab., Komaba Open Laboratory, The University of Tokyo, 4-6-1 Komaba, Meguro-ku, Tokyo 153-8904, Japan

S. Ogihara, Department of Mechanical Engineering, Science University of Tokyo, 2641 Yamasaki, Noda, Chiba 278-8510, Japan

N. Takeda, Graduate School of Frontier Sciences, The University of Tokyo, 7-3-1 Hongo, Bunkyo-ku, Tokyo 113-8656, Japan

cracks, delamination and fiber breaks. Among them, transverse cracks are the first significant mode of damage observed in the weakest laminae. Transverse cracks cause the increments of strain which result in nonlinear behavior in the relation between laminate stress and strain.

Many studies have been conducted on transverse cracking in laminated composites. Shear-lag analysis [1-4], variational stress analysis [5-7] and approximate elastic analysis [8, 9] were conducted for cross-ply laminates. Moreover, there are few studies to predict the nonlinear relation between laminate stress and strain caused by transverse cracking [10] which is necessary for damage tolerance design.

Recently, Gudmundson and Zang proposed a damage mechanics analysis for the prediction of thermoelastic properties of composite laminates containing matrix cracks [11]. In damage mechanics analysis, generally speaking, parameters relating internal damage state and material properties must be obtained by using a numerical calculation or an experiment. Gudmundson and Zang assumed that the average crack opening displacements for a row of transverse cracks in a ply is approximated by the average crack opening displacements for the same row of cracks in an infinite homogeneous transversely isotropic medium which has the same properties as the ply in consideration, and derived the relation between thermoelastic properties and transverse crack density successfully. This analysis can be applied to general laminates.

In this study, transverse cracking behavior in 90° ply in a composite laminate is predicted based on both energy and average stress criteria [9]. In the damage mechanics analysis, the increment of strain associated with transverse cracking can be derived. The global laminate strain is represented as the sum of the undamaged laminate strain and the above laminate strain increment. An advantage of this method is that it can be applied to general laminates with arbitrary stacking sequences.

## Analysis

Gudmundson and Zang [11] proposed a model for the prediction of thermoelastic properties of composite laminates containing transverse cracks whose surfaces are parallel to the fiber direction and perpendicular to the laminate plane. In the present study, in-plane loading is solely considered. The laminate which consists of  $N$  plies with transverse cracks is considered. The normalized transverse crack density for ply  $k$ ,  $\rho^k$  is defined as

$$\rho^k = \frac{a^k}{d^k} \quad (1)$$

where  $a^k$  is thickness of ply  $k$ ,  $d^k$  is the average distance of transverse cracks.

Using the classical lamination theory, the tractions on prospective crack surface,  $\tau^k$ , which is related to the average crack opening displacement, is represented as

$$\tau^k = A^k \epsilon + (C^k - A^k \alpha_0) \Delta T \quad (2)$$

where

$$\begin{aligned} A^k &= N^k (S^k)^{-1} \\ C^k &= A^k (\alpha_0 - \alpha^k) \end{aligned} \quad (3)$$

and  $\epsilon$  is the applied laminate strains,  $\alpha_0$  is the in-plane thermal expansion coefficient of the undamaged laminate and  $\alpha^k$  is the in-plane thermal expansion coefficient of ply  $k$ . The matrix  $N^k$  in eq. (3) is represented by the unit normal vector  $n_j^k$  on the crack surface in ply  $k$ , as shown in Ref 11.  $S^k$  is the in-plane compliance of ply  $k$ .  $\Delta T$  is temperature change from the stress free temperature,  $T_{sf}$ . In eq.(2), the residual stresses and strains due to other reasons than the mismatch in thermal expansion coefficients are neglected, while they appear in Ref 11.

The average transverse crack opening displacements in ply  $k$ ,  $\Delta u^k$ , linearly depend on all crack surface tractions as

$$\Delta u^k = a^k \sum_{i=1}^N \beta^{ki} \tau^i \quad (4)$$

where  $\beta^{ki}$  ( $k, i = 1, 2, \dots, N$ ) are  $3 \times 3$  matrices which depend on laminate lay-ups, ply properties and transverse crack densities, and shown in Ref 11. According to eqs. (2)-(4), the average increment strain,  $\Delta \epsilon^k$ , due to crack opening displacement in ply  $k$  can be written as

$$\begin{aligned} \Delta \epsilon^k &= (\rho^k / a^k) (N^k)^T \Delta u^k \\ &= \rho^k (N^k)^T \sum_{i=1}^N \beta^{ki} [A^i \epsilon + (C^i - A^i \alpha_0) \Delta T] \end{aligned} \quad (5)$$

In a cracked ply  $k$ , there is a distinction between the effective strains,  $\epsilon^{k(e)}$ , and average strains,  $\epsilon^{k(a)}$ . The effective strains are the strains measured on a global scale, while the average strains are the strains which are experienced by the material. The relation between them can be written as

$$\epsilon^{k(e)} = \epsilon^{k(a)} + \Delta \epsilon^k \quad (6)$$

Under in-plane loading conditions, the laminate effective in-plane strains,  $\epsilon^*$  and

effective strains of ply  $k$  are equal, that is,

$$\boldsymbol{\varepsilon}^* = \boldsymbol{\varepsilon}^{k(e)} \quad (7)$$

By the aid of the classical lamination theory, the relations between stresses and strains for a laminate containing transverse cracks is expressed as

$$\begin{aligned} \boldsymbol{\varepsilon}^* &= \mathbf{S}\boldsymbol{\sigma} + \boldsymbol{\alpha}\Delta T \\ \boldsymbol{\varepsilon}^{k(a)} &= \mathbf{S}^k \boldsymbol{\sigma}^{k(a)} + \boldsymbol{\alpha}^k \Delta T \end{aligned} \quad (8)$$

where  $\boldsymbol{\sigma}$  is laminate in-plane stresses,  $\mathbf{S}$  and  $\boldsymbol{\alpha}$  are in-plane compliance matrix and in-plane thermal expansion coefficients of a laminate with transverse cracks and can be expressed as

$$\mathbf{S} = \left( (\mathbf{S}_0)^{-1} - \sum_{k=1}^N v^k \rho^k (\mathbf{A}^k)^T \sum_{i=1}^N \boldsymbol{\beta}^{ki} \mathbf{A}^i \right)^{-1} \quad (9)$$

$$\boldsymbol{\alpha} = \boldsymbol{\alpha}_0 + \mathbf{S} \sum_{k=1}^N v^k \rho^k (\mathbf{A}^k)^T \sum_{i=1}^N \boldsymbol{\beta}^{ki} \mathbf{C}^i \quad (10)$$

where  $\mathbf{S}_0$  is the in-plane compliance matrix of the undamaged laminate and  $v^k$  is the volume fraction of ply  $k$ .

Next, the laminate strain increment caused by transverse cracking is considered to predict the mechanical behavior of composite laminates with transverse cracking. It is assumed that transverse cracks of amount  $\rho^k$  initiate at a constant laminate stress in the laminate without transverse cracks, as shown Figure 1. The strain increment of laminate strain can be calculated with eq. (5), that is, total laminate strain is expressed as eq. (7). Total laminate strain after transverse cracking also can be calculated considering unloading process as

$$\begin{aligned} \boldsymbol{\varepsilon}^* &= \frac{\sigma(\rho^k)}{E_{LAM}(0)} + \Delta \boldsymbol{\varepsilon}(\rho^k, \boldsymbol{\sigma}) \\ &= \frac{\sigma(\rho^k)}{E_{LAM}(\rho^k)} + \Delta \boldsymbol{\varepsilon}(\rho^k, \mathbf{0}) \end{aligned} \quad (11)$$

In Ref 12, the authors derived the relation between normalized transverse crack density and laminate stress based on both energy and average stress criteria using damage mechanics analysis. Equation 11 indicates that laminate strain can be calculated using laminate stress and transverse crack density.

## Discussion

In order to verify the efficiency of the present analysis, the prediction of the transverse crack behavior by the present analysis are compared to the experimental results obtained by the authors. The material system used in the experiments is bismaleimide-based CFRP, G40-800/5260. Laminate configurations tested are  $[0/90]_s$ ,  $[\pm 45/90]_s$ ,  $[\pm 45/0/90]_s$  and  $[0/90/\pm 45]_s$ . The specimen size was 150 mm long and 25 mm wide. GFRP tabs were glued on the specimens which resulted in specimen gage length of 90 mm. Quasi-static tensile tests were conducted at room temperature (25°C). The crosshead speed was 0.5 mm/min. During the test, the testing machine was periodically stopped, and the specimen was observed by a soft X-ray radiography. The number of transverse cracks in 90° ply was counted to obtain the transverse crack density which was defined as the number of transverse cracks per unit length.

Figure 2 shows the predictions and the experimental results of the relation between laminate stress and strain. Prediction for  $[\pm 45/90]_s$  laminate overestimates the laminate stress. The discrepancy is due to occurrence of delamination and nonlinear relation between shear stress and strain.

Prediction for  $[0/90]_s$  laminate provides larger nonlinearity than other laminates. In the present damage mechanics analysis, average transverse crack opening displacement is approximated by the average crack opening displacements for the same row of cracks in an infinite homogeneous transversely isotropic medium which has same properties as the ply in consideration. However, the existence of high modulus medium around the tip of the cracks causes constraint effect which makes crack opening displacement smaller. This means the present analysis evaluates the average crack opening displacements larger which results in the larger strain increments associated with transverse cracking, that is, nonlinearly of the relation between laminate stress and strain is overestimated in the present analysis. Some modification is necessary for improved prediction. The advantage of the present analysis is to predict the mechanical behavior for arbitrary laminate configurations once critical values are determined.

## Conclusion

A damage mechanics analysis was used to predict transverse cracking in 90° ply in general composite laminates and the relation between laminate stress and strain.

Predictions for transverse cracking behavior based on both the energy and stress criteria were made and compared with the experimental results. A reasonably good agreement was obtained for transverse cracking behavior. Predictions for the relation between laminate stress and strain somewhat overestimated the nonlinearly. An advantage of the present analysis is that it can predict the transverse crack behavior in laminates with arbitrary configurations.

## References

- [1] J. E. Bailey, P. T. Curtis and A. Parvizi, 1979. "On the transverse cracking and longitudinal splitting behavior of glass and carbon fiber reinforced epoxy cross-ply laminates and the effect of Poisson and thermally generated strain." *Proceedings of Royal Society of London*, A. 366; 599-623.
- [2] S. G. Lim and C. S. Hong, 1990. "Prediction of transverse cracking and stiffness reduction in cross-ply laminate composites." *Journal of Composite Materials*, 23; 695-713.
- [3] J. W. Lee and I. M. Daniel, 1990. "Progressive transverse cracking of crossply composite laminates." *Journal Composite Materials*, 24; 1225-1243.
- [4] N. Takeda and S. Ogiwara, 1994. "In-situ observation and probabilistic prediction of microscopic failure processes in CFRP cross-ply laminates." *Composite Science and Technology*, 52; 183-195.
- [5] Z. Hashin, 1985. "Analysis of cracked laminates: a variational approach." *Mechanics of Materials*, 4; 121-136.
- [6] J. A. Nairn, 1989. "The strain energy release rate of composite microcracking." *Journal of Composite Materials*, 23; 1106-1129.
- [7] J. Varna and L. Berglund, 1991. "Multiple transverse cracking and stiffness reduction in cross ply laminates." *Journal of Composite Technology & Research*, 13; 97-106.
- [8] L. N. McCartney, 1992. "Theory of stress transfer in a  $0^\circ$ - $90^\circ$ - $0^\circ$  cross-ply laminate containing a parallel array of transverse cracks." *Journal of Mechanical Physics and Solids*, 40; 27-68.
- [9] S. Ogiwara, N. Takeda and A. Kobayashi, 1998. "Transverse cracking in CFRP cross-ply laminates with interlaminar resin layers." *Advanced Composite Materials*, 7; 347-363.
- [10] H. T. Hahn and S. W. Tsai, 1974. "On the behavior of composite laminates after

initial failures." *Journal of Composite Materials*, 8; 288-305.

[11] P. Gudmundson and W. Zang, 1993. "An analytic model for thermoelastic properties of composite laminates containing transverse matrix cracks." *International Journal of Solids and Structure*, 30; 3211-3231.

[12] S. Ogihara, N. Takeda, S. Kobayashi and A. Kobayashi, 2000. "Damage mechanics analysis of transverse cracking behavior in composite laminates." *International Journal of Damage Mechanics*, printing.

Table 1 Material properties of G40-800/5260 unidirectional composite used in the analysis.

Longitudinal Young's modulus (GPa)	152
Transverse Young's modulus (GPa)	10.0
In-plane shear modulus (GPa)	6.94
Longitudinal Poisson's ratio	0.33
Transverse Poisson's ratio	0.49
Longitudinal thermal expansion coefficient ( $10^{-6}/^{\circ}\text{C}$ )	-0.6
Transverse thermal expansion coefficient ( $10^{-6}/^{\circ}\text{C}$ )	36.0
Stress Free Temperature ( $^{\circ}\text{C}$ )	195

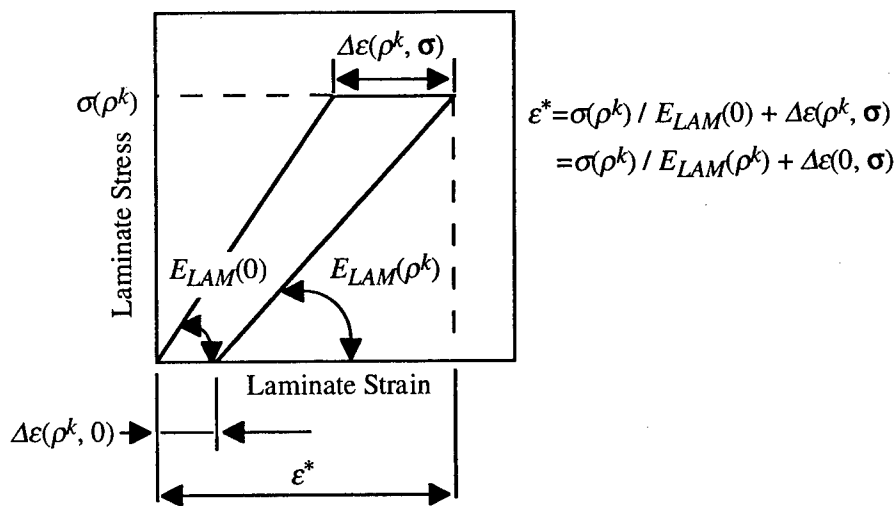


Figure 1 Schematic of stress-strain curve before and after transverse cracking.



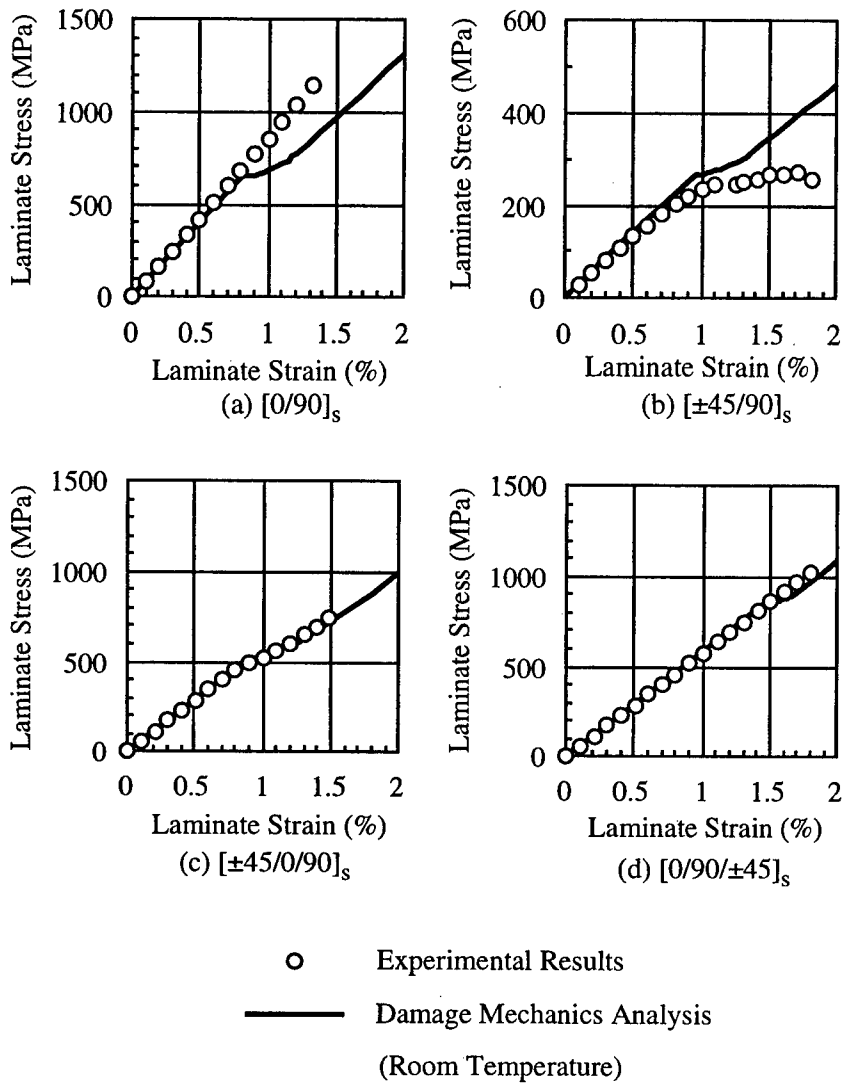


Figure 2 Relation between laminate stress and strain (Experimental results and analytical prediction).

# Bearing Failure Mechanisms of Carbon/Bismaleimide Composite in Mechanically Fastened Joints

Yi Xiao

## Abstract

In this report, the experimental work will be presented in two parts: one fastened joint and two fastened joints. For the problems of one fastened joint, to characterize the bearing strength and failure process of a double lap bolted joint were focused. During the static tensile tests, load-displacement response and acoustic emissions (AE) were monitored and measured to understand the fracture process of joint specimens. Some of them were unloaded at several loading levels, and damage behavior were observed by soft X-ray and Scanning Electron Microscope (SEM) to assess damage progress, failure mechanism and the relationship with the bearing strength. Next, to determine the ratio of loading proportion were focused on the problem of two fastened joints.

## Introduction

Carbon Fiber/Bismaleimide (CF/BMI) composite materials based on the heat-resistant bismaleimide resins have been developed as structural materials of the next generation supersonic transport (SST), and the mechanical characteristic have been investigated under various loading conditions. However, the joining problem by mechanically fasteners is inevitable to the assembly of structural components. Since the failure of the joints can lead to the catastrophic failure of the structures, an accurate methodology to evaluate the bearing strength and to understand the damage process is the most fundamental and essential item in the design of the joints.

The process of bearing failure in a bolted composite joint is very complicated. One of the complicated cause resulted by out-of-plane compression deformation in the vicinity of the hole <sup>(1-4)</sup>. Because of this, a unique form that the fiber microbuckling, matrix cracks and delamination etc. is easy to produced in laminate structures. As for the understanding of the occurrence and progress behavior of such micro damage is necessary to the discovery of the damage allowable on structural design.

As such foundation examination that optimizes the design of the joints for three-dimensional (3-D) textile composites in this report, two-dimensional (2-D)

---

Y. Xiao, Japan Aero Space Technology (JAST) Fellow, [in National Aerospace Laboratory (NAL)], 6-13-1, Osawa, Mitaka-shi, Tokyo, 181-0015, Japan

CF/BMI composites were prepared without through-the-thickness fibers, called z-fibers, which were produced by the same manufacturing process as the 3-D composites except the z-fiber inserting. The experimental work will be presented in two parts: one fastened joint and two fastened joints. For the problems of one fastened joint, to characterize the bearing strength and failure process of a double lap bolted joint were focused. During the static tensile tests, load-displacement response and AE were monitored and measured to understand the fracture process of joint specimens. Some of them were unloaded at several loading levels, the damage behavior was observed by soft X-ray and SEM to understand damage progress, failure mechanism and the relationship with the bearing strength. Next, to determine the ratio of loading proportion were focused on the problem of two fastened joints.

## Experiments

### Materials and Specimens

The material studied in the present work was CF/BMI composite laminate<sup>(5)</sup>. A middle elastic system carbon fiber MR50K (Mitsubishi Rayon Co. Ltd. production) and the Bismaleimide system (CYTEC-5250-4RTM) heat-resistant resins were used. Coupon specimens were fabricated by a resin transfer molding (RTM) process and the average fiber volume fraction was 55%, as a quasi-isotropic  $[45/0/-45/90]_{2S}$  laminate was applied.

The geometrical configuration and testing setup of the specimen in bolted joints are shown in Figure 1. Two types of the fastener arrangements were considered, one fastener (bolt) in series and two fasteners in series. The double lap joining forms were adopted that bolt fastener attached the CFRP specimen and Titanium alloy fixture (with lateral constraints). However, it was returned in the configuration method that made usual CFRP specimen to be the middle lap, and Titanium alloy fixture was used as a middle lap.

### Experiment Method

To establish a simpler experimentally techniques on the bearing strength evaluation of the composite bolted joints, the simply and high functional measurement system has been developed by using non-contact Electro-Optical Extensometer, which does not require the special fixture, and it has been proposed as a practical test method<sup>(6)</sup>. In this study, the tests were carried out to evaluate bearing strength of marking composite materials, by using non-contacting electro-optics extensometer (ZIMMER Co. product MODEL-100B). The measurement system composition is illustrated in Figure 2. ZIMMER electro-optics extensometer converts linear motion of a black-and-white edge (target) into a voltage proportional to displacement, and that is to say, the optical image is converted into electron image by the special photo cathode. In conventional contact form measuring method, metal fittings (yoke) have been installed in which linked both sides edge of the specimen with the pinhead<sup>(7)</sup>. But in present method, only the black-and-white target is established for it.

Tensile load was given using INSTRON-8501 testing machine; the cross-head speed was 1.0 mm/min. During the static tests, load-displacement response and acoustic emissions were monitored and measured to understand the fracture process of joint specimens. Some of them were unloaded at several loading levels, and the damage behavior was observed by soft X-ray and SEM to assess damage progress, failure mechanism and the relationship with the bearing strength.

## Results and Discussion

### One Fastened Joint

#### Bearing Strength

For the specimen of one fastened joint, the typical load-displacement curve ( $P-\delta$  curve) is shown in Figure 4. The bearing strengths were obtained from based on the bearing load at which the pin relative displacement was deformed 4% of the pin diameter, and the ultimate failure load from the peak point of the load. The average bearing strength required from three specimens is shown in Table 1. From Figure 4, it can be found that after the testing start, the load almost linearly was increased, but before it reaches 4% of displacement (about 12KN) the nonlinear behavior has appeared on the load-displacement curve. It indicates that micro damage is beginning to happen inside. The similar tendencies were also shown in other specimen cases.

#### Mechanisms of Bearing Failure

To characterize the inside damage of the joint specimens, the result of monitoring by AE measurement is shown in Figure 5. It was understood that was reflected more clearly the damage behavior in the occurrence associated with load increase, from the AE count rate that shows the activity of the AE signal. When the applied load up to near 12KN, the sharp change of the AE signal was observed. An obviously nonlinear behavior was begun to turn up on the load-displacement curve at the same time. Afterward, the load response gradually was lowered. During the load exceed the 4%P point, there are some large lowering points shown on the load-displacement curve. Furthermore these progresses in stage-by-stage condition occurred, and AE signal is measured clearly. It was considered that corresponding to fiber-matrix splitting and delamination, and the out-of-plane shear cracks were occurred.

Figure 6 shows photographs of the surface view and the X-radiographs of the bearing damage for each specimen under the various load conditions. It was corresponded with the AE measurement results that above expressed, it is conceivable that to evaluate the damage state and scale of the damage production. In the early load stage before reaching 4%P loads, it can be seen that the microscopically damage has occurred, and this is agreeing well with the AE measurement results. When increasing the loads, the damage ranges were become widely around the hole, this tendency continued until reaching to final fracture.

During the tests, some specimens were unloaded at several loading levels to

examine the bearing failure mechanisms, and the tested specimens were cut in parallel along the centerline of circle hole. The micrographs were made of their cross-sections under SEM. Figure 7 shows the section SEM photographs of the bearing damage along loading direction at 70%, 85% and 100% of the maximum load.

At 70% of the maximum load, the peculiar kink band damage in the compressive failure can be seen clearly in the  $0^\circ$  layer, and a local delamination was also occurred under the washer area. Next, the load was increased to 85% of the maximum load, the out-of-plane shear cracks occurred more than before, and fiber-matrix splitting cracks can be also found in the  $0^\circ$  layer. Such the damage patterns were continued until reaching to final fracture, which can be understood at the case for 100% of the maximum load. In other words, it is conceivable that the load reduction is reduced for stage-by-stage on the  $P-\delta$  curve, due to the shear cracks were occurred intermittently.

Based on the section SEM photographs, it can be concluded that the kink band, delamination, fiber-matrix shearing and fiber-matrix splitting failure comprised the major failure modes of the shear cracks. For the growth of the shear cracks can be found that the influence of washer area and bolt clamping conditions is large.

#### Two Fastened Joints

One of problems in the multi-fastened joints design is that the ratio of loading proportion is not equal generally for acting to each fastener. Because of this, to determine the ratio of loading proportion becomes needed to the optimal design of the multi-fastened joints. However, heretofore most of the previous studies have been focused on using finite element analysis to determine it<sup>(8-9)</sup>, have not been shown using with the experimental method to evaluate one.

#### Load Proportioning

In this experiment, only considered a two fastened joint in series, to measure the hole elongation that a extensometer was set up in the side edge of specimen along the transverse of bolt hole as shown in Figure 8. Based on this, the ratio of loading proportion for each bolt can be requested.

Figure 9 shows the typical load-displacement curve of two fastened joint specimen. It can be found that the hole elongation was different with each hole under the loading respond, and an obviously nonlinear behavior shown on the  $P-\delta$  curve. Measured the relative displacements between bolt/hole, which it was replaced to the ratio of loading proportion, is shown in Figure 10.

For the change of loading proportion can be divided in the next three ranges for all the loading responses. (I) initiated deformation range ( $0 \sim 12.5\text{KN}$ ); (II) elastic and elasto-plasticity deformation range ( $12.5 \sim 27\text{KN}$ ); (III) ultimate deformation range ( $27\text{KN} \sim$ ). For range (I), the cause that ratio  $P_i/P$  ( $i = 1, 2$ ) changes sharply, can be estimates as the influence of the fractional forces between washer and CFRP specimen due to the bolt clamping forces. In range (II), because the inclination of the  $P-\delta$  curve (see Figure 9) is almost constant, so that the change of ratio  $P_i/P$  was also regular almost,  $P_1/P = 0.63 \sim 0.58$ , average is 0.6;  $P_2/P = 0.38 \sim 0.43$ , average

is 0.4. In range (III), because the inclination of the  $P-\delta$  curve was decreasing continuously when the load was increased to 27KN, the ratio  $P_i/P$  were gradually appearing with the tendencies that becomes equality,  $P_1/P=0.55$ ,  $P_2/P=0.45$  were obtained in the case of the maximum load.

Figure 11 shows photographs of the surface view and the X-radiographs of the bearing damage for each specimen under tensile loading for 85% and 100% of the maximum load. It was understood that the compressive damage conditions around each hole differs by the difference of the loading proportion in two kinds of the load cases. Whichever, the hole of inside that the loading proportions is large; the damage pattern was seen more largely than the hole of the outside. The final fracture of the joint is in a bearing failure mode.

### Conclusions

To evaluate the bearing strength and damage behavior of the bolted CF/BMI composite joints, the relation between the load-displacement curve, AE characteristic and failure mechanisms was investigated. As for the activity of the AE signal corresponding to the loading record, it can be found that there are big correlations for the damage pattern and progress behavior. Furthermore, corresponding it with the results that observed by X-ray and SEM photograph, the bearing failure mechanisms was able to explain. Based on these, the following remarks can be made:

1. The kink band of  $0^\circ$  layer and delamination appeared to be the dominant mode in the onset damage. The out-of-plane shear cracks and fiber-matrix splitting cracks were the major form of final failure.
2. It was confirmed that the loading proportion is a nonlinear behavior in the multi-fastened joints.
3. To evaluate lateral clamping effect on restrain the out-of-plane deformation, the construction of a 3-D damage model and development of the analysis tools should be become a focus on further investigations.

### Acknowledgments

We thank Y. Hamaguchi of our laboratory for a part of the experimental work in two fastened joints was carried out.

### References

- 1) H. S. Wang, C. L. Hung and F. K. Chang. 1996. "Bearing failure of bolted composite joints Part I: Experiments," *Journal of Composite Materials*, 30(12): 1284-1313.
- 2) P. P., Camanho, S. Bowron and F. L. Matthews. "Failure mechanisms in bolted CFRP," *Journal of Reinforced Plastics and Composites*, Vol. 17, 1998, pp.205-233.
- 3) I. Eriksson, 1990. "On the bearing strength of bolted graphite/epoxy laminates," *Journal of Composite Materials*, 24:1264-1269.

- 4) P. S. Wu and C. T. Sun, April 1997. "Bearing failure in pin contact of composite laminates," Proceedings of the 38<sup>th</sup> AIAA/ASME/ASCE/AHS/ASC Structures, Structural Dynamics and Materials Conference, pp.1974-1983.
- 5) I. Susuki and T. Takatoya, October 1998. Proceedings of The 36<sup>th</sup> Aircraft Symposium, pp.61-64.
- 6) Y. Xiao, Y. Hayashi and T. Ishikawa, April 1999. Proceedings of Annual Meeting of Japan Society for Composite Materials, pp.77-78.
- 7) JIS K 7080, 1991. "Testing methods for bearing strength of carbon fiber reinforced plastics", Japanese Industrial Standard.
- 8) S. M. Wang and Y. X. Han, 1988. "Finite element analysis for load distribution of multi-fastener joints," *Journal of Composite Materials*, 22:124-135.
- 9) C. Poon and Y. Xiong, September 1996. "Bolted Joint Technology in Composite Structures -- Analytical Tools Development", in "Bolted/Bonded Joints in Polymeric Composites", AGARD Conference Proceedings CP-590.

Table 1 Results of the bearing strength required from three specimens.

(Material: MR50K/5250-4RTM Carbon/Bismaleimide)

Specimen	4%D Displacement		Ultimate Failure		Failure Mode
	(KN)	(MPa)	(KN)	(MPa)	
J1-D1	14.21	753.8	15.83	839.8	Bearing
J1-D2	13.95	740.0	15.95	846.7	Bearing
J1-D3	14.73	781.9	16.59	879.9	Bearing

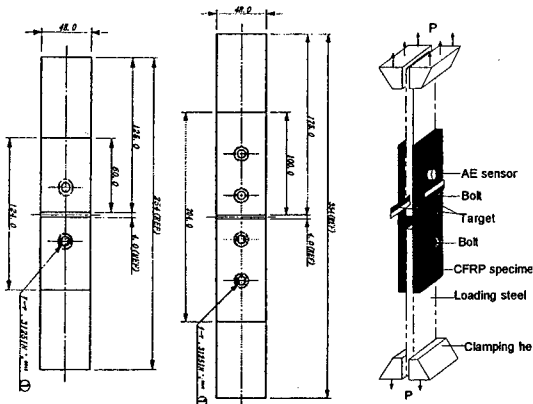


Figure 1 Geometrical configuration and testing setup of the specimen in bolted joints.

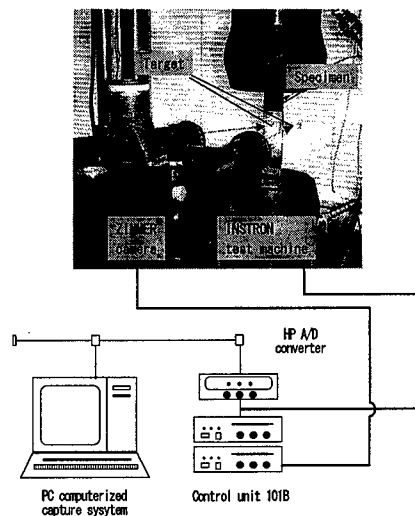


Figure 2 Measurement system using non-contacting Electro-Optics Extensometer.

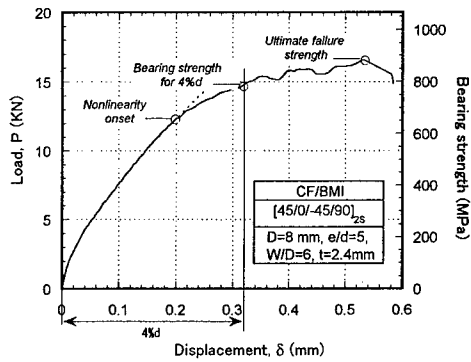


Figure 3 Typical load-displacement curve of bolt-bearing specimens.

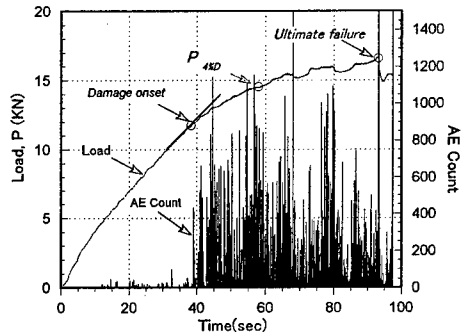


Figure 4 Result of monitoring by AE measurement for damage in bolted joint.

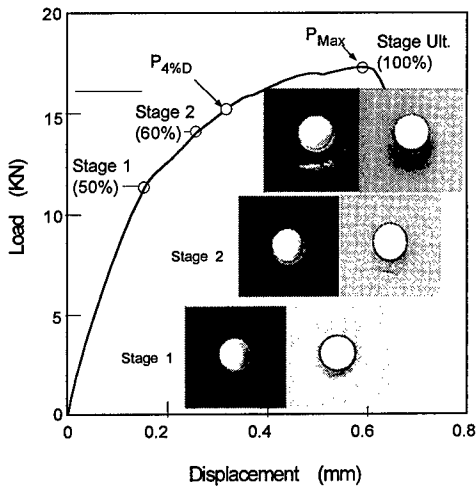


Figure 5 Photographs of the surface view and X-radiographs of the bearing damage under the various load conditions.

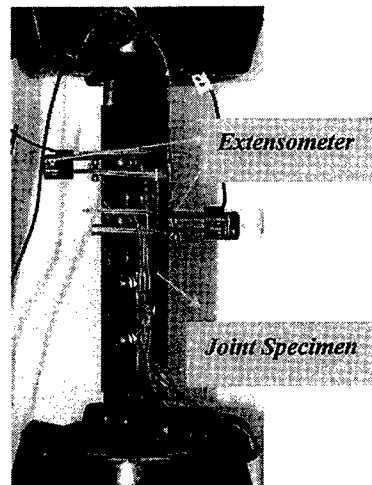


Figure 7 Testing set up for two fastened joint specimen.

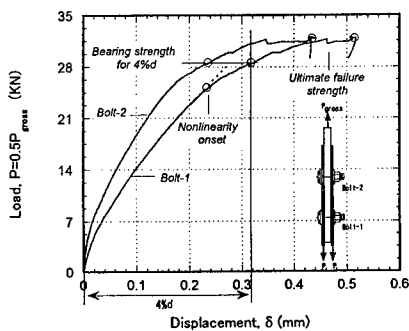


Figure 8 Typical load-displacement curve of two fastened joint specimen.

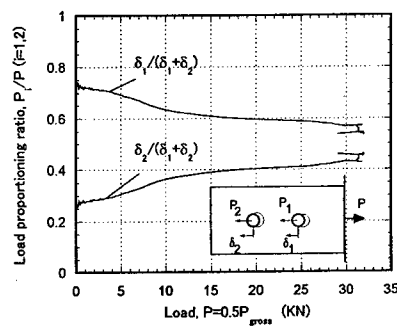


Figure 9 Ratio of loading proportion for two fastened joint specimen.



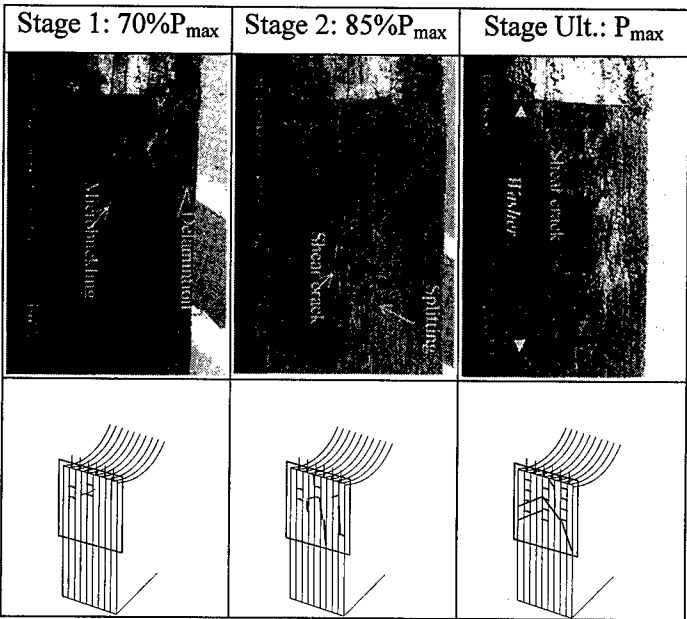


Figure 6 SEM photographs of the bearing damage along loading direction at 70%, 85% and 100% of the maximum load.

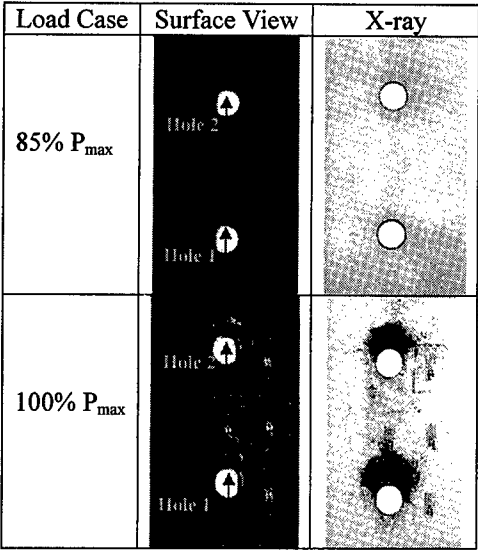


Figure 10 Photographs of the surface view and the X-radiographs of the bearing damage at 85% and 100% of the maximum load.

## **Mechanical Property Analysis of Matrix Hybrid Laminates**

T.Onita, T.Nishiwaki and Z.Maekawa

### **Abstract**

As an example of the material designing method that must satisfy complex required properties, we propose matrix hybrid laminates. In this study, matrix hybrid laminates composed of a common resin with high stiffness and a flexible resin with high damping are fabricated. The influence of the stacking sequence on the static and dynamic properties is investigated by the bending and the vibration tests. It is confirmed that matrix hybrid laminates can have wide ranges of stiffness and damping property by changing the flexible resin ratio and the stacking sequence.

### **Introduction**

The practical structures must have complex mechanical properties in response to the application. As an example, the musical instrument materials must have not only high specific moduli, but also low damping [1]. In the structural components applied to various industrial fields, the high damping as well as the high stiffness and strength must be generally considered. However, it is difficult that a kind of material produce the above complex properties required in these structural components. The compound designing method of plural materials with different properties can satisfy the various requirements, because this method has many designing parameters.

Matrix hybrid laminates are fabricated by the combination of two or more kinds of matrices. The wide ranges of stiffness and damping property may be produced by changing the designing parameters, the flexible resin ratio and/or the stacking sequence. Whereas stiffness of matrix hybrid laminates can be easily calculated by the classical lamination theory [2], the quantitative prediction of the damping property has been difficult. Because the influences of the internal damping of materials, the external damping of air resistance and boundary conditions

---

T.Onita and Z.Maekawa, Graduate Program of Advanced Fibro-Science in Graduate School, Kyoto Institute of Technology, Matsugasaki, Sakyo-ku, Kyoto 660-8585, Japan

T.Nishiwaki, Research and Development Department, ASICS Corporation, Takatsukadai, Nishi-ku, Kobe 651-2271, Japan

must be considered [3]-[8].

In this report, glass cloth reinforced matrix hybrid laminates with various flexible resin ratios and stacking sequences are fabricated. The static and dynamic bending properties of matrix hybrid laminates are investigated by static bending test and vibration test, respectively. Antisymmetric matrix hybrid laminates are also fabricated and investigated by the above tests. For the above all experimental results, the influences of designing properties on both the bending properties are discussed in detail.

## Experimental

### Specimens

As the reinforcement, plane-woven glass cloth (WE18W, Nitto Boseki Co., Ltd.) was used. As the matrices, common resin, vinyl ester (R806, Showa Highpolymer Co., Ltd.) and flexible resin, unsaturated polyester (FK2000, Showa Highpolymer Co., Ltd.) were used. The tensile and damping properties of both the resins used are listed in Table I. The common resin has the higher tensile modulus and strength rather than the flexible one. On the other hand, the flexible resin has the higher logarithmic decrement rather than the common one. Using the above resins, matrix hybrid laminates were fabricated by hand lay-up. All specimens were set up to form a 16-layer, and the nominal thickness of the specimen fabricated was 3mm. The stacking sequences were four types of  $[H_{16}]$ ,  $[F_{16}]$ ,  $[H_4F_4]_s$  and  $[F_4H_4]_s$ , as shown in Fig.1. Here, "[H]" and "[F]" indicate the glass cloth embedded in common and flexible resins, respectively.

Table I Tensile and damping properties for matrix resins used

Material	Tensile modulus (GPa)	Tensile strength (MPa)	Logarithmic decrement
Common resin	4.01	73.0	0.242
Flexible resin	0.37	0.72	1.002

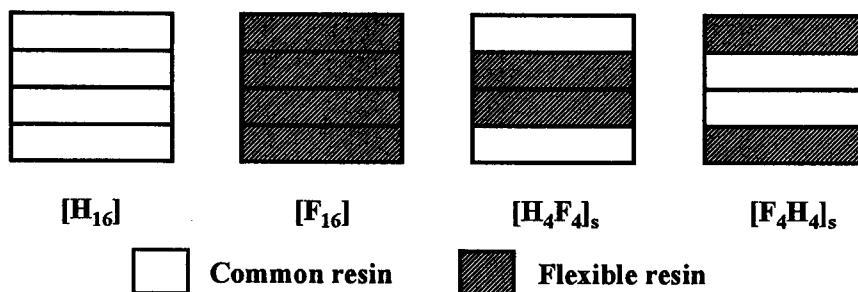


Figure 1 Stacking sequence

### Bending test

A three point bending test was used for the bending modulus and strength measurement. The bending test was performed by the INSTRON testing machine (Model 4206, Instron Japan Co., Ltd.) with computer controlled. The specimen length and width were 60mm and 15mm respectively, and the longitudinal direction was set to be a warp direction. A crosshead speed was 1.0mm/min, and a span length was 48mm.

### Vibration test

Using the FFT analyzer (AD 3542, A&D Co., Ltd.), the vibration test was performed. The specimen length and width were 250mm and 150mm respectively, and the longitudinal direction was set to be a warp direction. The center of the specimen was impacted by an impulse hammer in free boundary condition suspended by a light thread, and the out-plane accelerations at various positions were measured by a light accelerometer. The input and output response data were First Fourier Transformed, and a transfer function was obtained by dividing the output response data by the input data. Here, we focused on the 1st bending eigenvibration mode with the main curvature in the longitudinal direction as shown in Fig.2. The eigenfrequency was obtained from the peak position corresponded to the 1st bending mode in the transfer function. The logarithmic decrement was calculated by a time-domain damping curve obtained from the corner output. The time-domain damping curve was obtained from the Reverse First Fourier Transformation of the short range near the above peak.

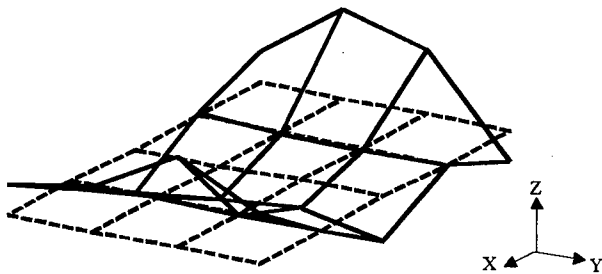


Figure 2 Eigenvibration mode corresponded to the 1st bending frequency

### Results

Typical stress-deflection curves of the matrix hybrid laminates obtained from the three point bending test are shown in Fig.3. The fracture aspect of  $[H_{16}]$  is brittle, conversely, the fracture one of  $[F_{16}]$  is ductile. It is confirmed that the matrix

hybrid laminates,  $[H_4F_4]_s$  and  $[F_4H_4]_s$  possess both the brittle and ductile properties. All the stress-deflection curves are nonlinear. The bending moduli and strength of the matrix hybrid laminates are listed in Table II. Both the bending modulus and strength increase in the order  $[F_{16}] < [F_4H_4]_s < [H_4F_4]_s < [H_{16}]$ . This order is derived from the stacking position of the common resin with the higher modulus. Approaching the position of the common resin layer to the outmost layer causes the higher stiffness, because the outmost layer has the largest curvature under the bending load. It is found that, the bending modulus and strength are on the decrease and fracture deflection is on the increase in comparison  $[H_{16}]$  with  $[H_4F_4]_s$ . On the other hand, the bending modulus and strength are on the increase and fracture deflection is on the decrease in comparison  $[F_{16}]$  with  $[F_4H_4]_s$ .

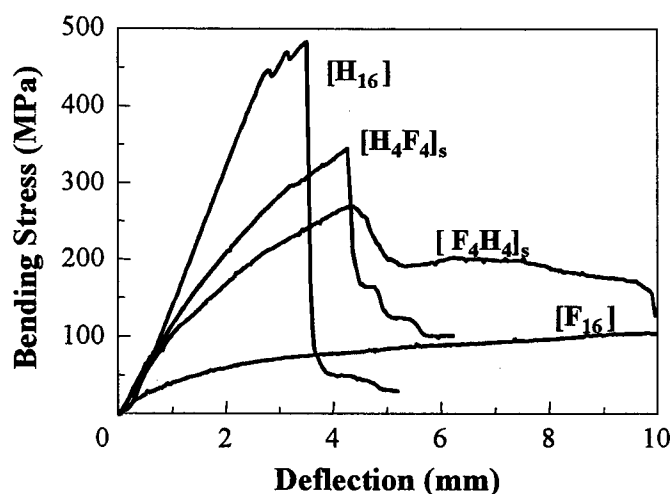


Figure 3 Bending stress-deflection curves of matrix hybrid laminates subjected to the three point bending load

Table II Bending moduli and strength obtained from the bending test

Type	Bending modulus (GPa)	Bending strength (MPa)
$[H_{16}]$	22.0	460
$[F_{16}]$	6.96	113
$[H_4F_4]_s$	16.9	333
$[F_4H_4]_s$	13.4	264

The 1st bending frequencies and the logarithmic decrements of the matrix hybrid laminates obtained from vibration test are listed in Table III. The order in the 1st bending frequency is similarly  $[F_{16}] < [F_4H_4]_s < [H_4F_4]_s < [H_{16}]$ . On the other hand, the logarithmic decrement increases in the order  $[H_{16}] < [H_4F_4]_s < [F_4H_4]_s < [F_{16}]$ . Compared the logarithmic decrement of  $[H]$  with  $[F]$ , it was found that  $[H]$  had the lower damping property. This order is also derived from that the mechanical properties of the outmost layer have a great influence on the damping property of the whole laminate under the bending mode. It is found from the above results that matrix hybrid laminates can have wide ranges of stiffness and damping property, the stacking sequence is an important factor.

Table III 1st bending frequencies and logarithmic decrements obtained from the vibration test

Type	1st bending frequency (Hz)	Logarithmic decrement
$[H_{16}]$	181.1	0.077
$[F_{16}]$	163.4	0.199
$[H_4F_4]_s$	169.9	0.095
$[F_4H_4]_s$	164.9	0.143

## Discussions

As already mentioned the stacking sequence makes a great influence on both the static and dynamic properties. In order to evaluate the static and dynamic properties of matrix hybrid laminates with other stacking sequences, antisymmetric matrix hybrid laminates were fabricated and these properties were investigated by the bending and vibration tests. Figure 4 shows the stacking sequence of antisymmetric matrix hybrid laminates.

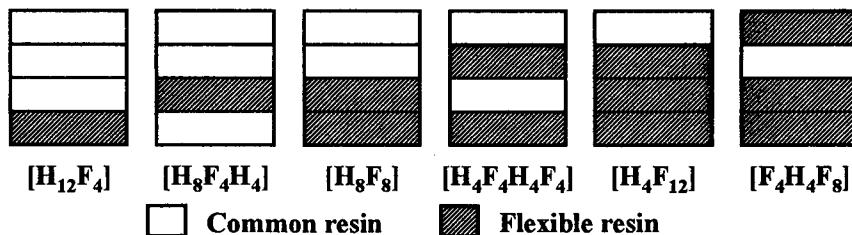








Figure 4 Stacking sequences of antisymmetric matrix hybrid laminates







The bending moduli and strength of antisymmetric matrix hybrid laminates are listed in Table IV. Here, the bending strength is the value on the outmost layer of tensile side calculated by using the laminated beam theory. Because the position of a neutral axis of antisymmetric matrix hybrid laminates varies. In the case that matrix hybrid laminates with the constant flexible resin ratio are compared, the bending modulus and strength of  $[H_8F_4H_4]$ ,  $[H_4F_4H_4F_4]$  and  $[H_4F_{12}]$  is respectively higher than them of  $[H_{12}F_4]$ ,  $[H_8F_8]$  and  $[F_4H_4F_8]$ . This result can be explained by the stacking sequence between the common resin layer and a neutral surface and the total common resin ratio.

Table IV Bending moduli and strength of antisymmetric matrix hybrid laminates

Type	$[H_{12}F_4]$	$[H_8F_4H_4]$	$[H_8F_8]$	$[H_4F_4H_4F_4]$	$[H_4F_{12}]$	$[F_4H_4F_8]$
						
Bending modulus (GPa)	15.4	21.5	9.75	13.5	6.81	6.48
Bending strength (MPa)	391	449	288	390	160	143

The 1st bending frequencies and the logarithmic decrements of antisymmetric matrix hybrid laminates are listed in Table V. In the same comparison as the above,  $[H_8F_4H_4]$  and  $[H_4F_{12}]$  have the higher 1st bending frequency rather than  $[H_{12}F_4]$ , and  $[F_4H_4F_8]$ , respectively. This reason can be also explained by the position of  $[H]$  because all the matrix hybrid laminates fabricated in this section have the constant weight. On the other hand,  $[H_{12}F_4]$  and  $[F_4H_4F_8]$  have the higher logarithmic decrement rather than  $[H_8F_4H_4]$  and  $[H_4F_{12}]$ , respectively. This result is mainly caused by the stacking position of the flexible resin with the high damping. Compared  $[H_8F_8]$  with  $[H_4F_4H_4F_4]$ , we could not observe a difference.

Table V 1st bending frequencies and logarithmic decrements of antisymmetric matrix hybrid laminates

Type	$[H_{12}F_4]$	$[H_8F_4H_4]$	$[H_8F_8]$	$[H_4F_4H_4F_4]$	$[H_4F_{12}]$	$[F_4H_4F_8]$
						
1st bending frequency (Hz)	160.8	172.2	154.6	154.9	155.1	149.6
Logarithmic decrement	0.121	0.087	0.142	0.143	0.170	0.180

Based on the above all results, we created the mechanical property map as shown in Fig. 5. As already mentioned at the outset, the properties cased in both the axes are very important parameter for the designing. In the case of comparison between  $[H_4F_4H_4F_4]$ ,  $[F_4H_4]_s$  and  $[H_8F_8]$  which have the constant flexible resin ratio, the bending strength of  $[H_4F_4H_4F_4]$  is higher than other types, however these three types have the constant value of logarithmic decrement. In the case of comparison between  $[H_4F_4H_4F_4]$  and  $[H_4F_4]_s$ , both the bending strength and the logarithmic decrement of  $[H_4F_4H_4F_4]$  is larger than them of  $[H_4F_4]_s$ . These results indicate that the static bending properties and logarithmic decrement can be independently controlled by changing the stacking sequence and common/flexible resin ratio. In other words, it is confirmed that matrix hybridization is a very effective designing method.

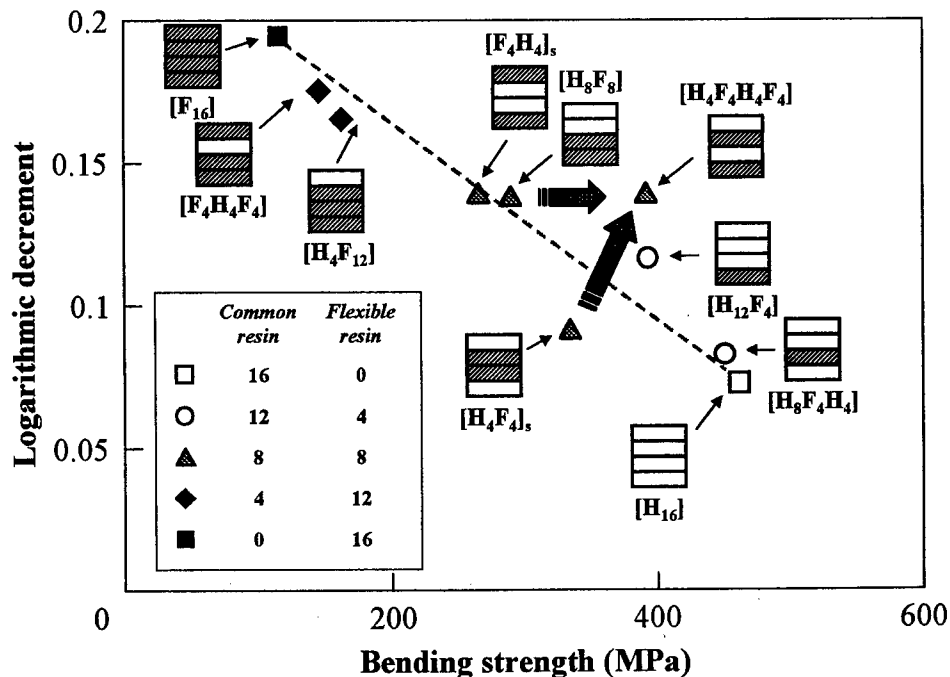


Figure 5 Logarithmic decrements plotted against bending strength for matrix hybrid laminates

## Conclusions

Matrix hybrid laminates with various stacking sequences were fabricated and their static and dynamic properties were investigated by the bending and vibration tests. In matrix hybrid laminates with the constant flexible resin ratio, the bending strength and the logarithmic decrement can be improved by changing the position of the flexible resin layer. It is confirmed that matrix hybrid laminates can



possess wide ranges of stiffness and damping property by changing the flexible resin ratio and the stacking sequence. For the more precise designing, it is effective to develop a numerical model which can consider the influence of the stacking sequence upon the whole mechanical properties.

## References

1. A.Kataoka and T.Ono, 1976. "The Dynamic Mechanical Properties of Sitoka Spruce Used for Sounding Boards." *Mokuzai Gakkaishi*, 22(8):436-443
2. R.M.Jones, 1975. *Mechanics of Composite materials.*, Hemisphere Publishing Corporation, pp.147-210
3. R.Chandra, S.P.Singh and K.Gupta, 1999 "Damping Studies in Fiber-reinforced Composites -a review." *Composite Structures*, 46:41-51
4. M.Coni, B.Benchekchou and R.G.White, 1996. "The Structural Damping of Composite Beams with Tapered Boundaries." *Composite Structures*, 35:207-212
5. T.Iwatsubo, 1993. "Standardization of Methods for Testing Vibration-Damping Property in Laminated Damping Steel Sheets." *JSME C*, 59(566):2921-2925
6. R.M.Crane and J.W.Gillespie Jr, 1991. "Characterization of the Vibration Damping Loss Factor of Glass and Graphite Fiber Composites." *Composite Science and Technology*, 40:355-375
7. A.A.El-hamid Hamada, 1995. "Vibration and Damping Analysis of Beams with Composite Coats." *Composite Structures*, 32:33-38
8. R.Rikards, 1993. "Finite Element Analysis of Vibration and Damping of Laminated Composites." *Composite Structures*, 24:193-204

# **Damage Tolerance**

---

## **DAMAGE AND FAILURE IN FRP COMPOSITE LAMINATES UNDER LOW-VELOCITY IMPACT**

**K. Minnaar, J. Zhai, S. W. Park and M. Zhou<sup>†</sup>**

### **Abstract**

The damage and failure behavior of FRP composite laminates under low-velocity, transverse impact is studied experimentally and numerically. Experiments use a split Hopkinson pressure bar to apply impact on the specimens and monitor their transient responses. The technique allows key mechanical quantities, including contact force history, specimen deformation, and energy dissipation, to be accurately determined from an analysis of the measured longitudinal strain histories of the pressure bars. Total energy dissipation is taken as a macroscopic measure of cumulative damage in the specimen. It is found that the energy dissipation is not proportional to the impact energy but becomes saturated as the impact energy level increases. Impacted specimens are subjected to quasistatic extension to determine their post-impact tensile strengths. The residual strength generally decreases with increasing impact intensity but tends to level off as the impact energy exceeds a certain level. An experimental technique involving a Hopkinson bar and a laser interferometer is used for real-time monitoring of damage progression in a laminate under a low-velocity impact. Numerical simulations of the impact response and damage progression are conducted using a cohesive finite element method. The method employs a cohesive zone model to simulate matrix cracking and interlaminar delamination and a transversely-isotropic elastic model for the bulk behavior of each ply. The effect of interlaminar bond strength on the pattern of damage evolution is investigated. It is found that damage in specimens with a weak interlaminar bond initiates in the form of delamination along interlaminar interfaces, while in the case of a strong interlaminar bond damage initiates in 90° plies in the form of matrix cracking.

### **Introduction**

Fiber-reinforced polymeric (FRP) composite laminates are susceptible to damage in the forms of interlaminar delamination and in-ply matrix cracking. Low velocity impact on such laminates often cause damage that leads to significant reduction in the strength and stiffness of the material. Most of the damage is internal and cannot be easily detected by the naked eye.

In the current investigation, a split Hopkinson pressure bar combined with a three-point bend fixture is used to apply low-velocity impact loading to composite laminates and to monitor their response. This technique allows the contact force, load-point displacement, mechanical work, and energy dissipation to be accurately determined within a fully dynamic framework. The experiments focus on the evolution of energy dissipation associated with impact-induced damage. The total energy dissipated is taken as a macroscopic measure of cumulative damage in the specimen without the tracking of individual damage mechanisms. The impacted specimens are subjected to quasi-static tension to determine their residual

---

K. Minnaar, J. Zhai, S. W. Park and M. Zhou<sup>†</sup>, School of Mechanical Engineering, Georgia Institute of Technology, Atlanta, GA 30332-0405, USA.

<sup>†</sup> Corresponding author, Tel: 404-894-3294, Fax: 404-894-0186, min.zhou@me.gatech.edu

strengths. A correlation between the post-impact strength and impact energy is then analyzed. Further, in an effort to develop a technique for time-resolved assessment of damage progression in composite laminates subjected to transverse impact, a separate experimental setup involving a laser interferometer is used. In this experiment, the velocity of the rear surface (opposite to the impact side) of a laminate is monitored in real time and correlated with the progression of damage inside the specimen.

Numerical simulations are carried out to gain understanding on damage development in the impacted specimens. The simulations use a micromechanical framework for explicit account of crack initiation and propagation. This framework of analysis is based on the cohesive finite element method (CFEM) described by Zhai and Zhou [1-3]. This approach does not require any crack initiation and propagation criteria in the numerical implementation since separation is possible along all finite element boundaries and the cohesive law allows fracture to evolve as a natural outcome of the combined effects of bulk constituent response, interfacial behavior, and applied loading.

## Experimental Investigation

### Materials Analyzed

Two different material systems are used: IM7/K3B for impact response analysis and T300/5208 for real-time monitoring of damage progression. IM7/K3B consists of graphite fibers embedded in a polyimide matrix. The specimens used have a 32-ply quasi-isotropic  $[(45/0/-45/90)_{4s}]$  layup. T300/5208 comprises graphite fibers embedded in a bismaleimide matrix. The specimens have a 16-ply quasi-isotropic  $[(45/0/-45/90)_{2s}]$  layup.

### Experimental Configuration

A split Hopkinson pressure bar (SHPB) is used to apply impact loading on the specimen and to record its response throughout the impact event. Figure 1 shows a schematic illustration of the experimental configuration used. The specimen is sandwiched between the incident and transmitter bars through a miniature three-point bend loading fixture. A compressive stress pulse propagates along the incident bar. Part of this incident pulse is transmitted to the transmitter bar through the specimen/fixture assembly, and part of it is reflected back into the incident bar. The wave propagation in the incident and transmitter bars is monitored through a strain gage mounted on each bar. The SHPB experimental setup employed in the current study allows multiple loading pulses to be applied on the specimen without full intervening unloading, offering an opportunity for analyzing repeated interactions between an impactor and a specimen. Similar tests are conducted on other specimens at different impact levels ranging in impact energy from 0 up to 100 J. Test coupons were cut out of an IM7/K3B plate into dimensions of 152.4 mm x 19.05 mm x 4.47 mm. Details of the analysis can be found in Park and Zhou [4].

Figure 2(a) shows the variation of energy dissipated in specimen with impact energy. The latter is the total energy available during an impact event. The data shows that energy dissipation does not increase in proportion to the impact energy, suggesting that as the damage increases the energy absorption capability tends to become saturated. Following the impact experiments, specimens were subjected to quasistatic extension to determine their residual strengths. Tensile loading is chosen to avoid possible difficulties associated with premature buckling of the impacted specimens under compressive loading. Figure 2(b) shows the post-impact tensile strength of IM7/K3B as a function of energy dissipated during the impact experiments. It can be seen that post-impact residual strength decreases with increasing impact energy. Again, the relationship is not linear but tends to level off as impact energy increases.

### Time-resolved Analysis of Damage Progression

Time-resolved assessment of damage progression in composite laminates under impact loading is an issue of practical significance. A new experimental technique is used to characterize the onset and progression of damage in a composite laminate subjected to low-velocity impact loading. This experiment uses a Hopkinson pressure bar for the loading and a Polytec OFV-511 laser vibrometer for measuring the velocity (or displacement) profile of the rear surface of the impacted specimen, see Fig. 1. The specimen is simply supported and the maximum transverse deflection occurs at the center. The laser interferometer, capable of measuring surface velocities of up to  $10 \text{ ms}^{-1}$ , allows the normal velocity to be recorded throughout the experiment. The strain gage mounted on the incident bar allows the histories of impact force, contact point velocity and displacement, and impact energy delivered to the specimen to be determined. The specimen is subjected to multiple impact loading under the same loading conditions and a rear surface velocity profile is recorded during each impact process. Damage in the specimen accumulates gradually with the successive impact loading. The velocity profiles are then analyzed to derive a possible correlation between the velocity signature and the damage. Experiments are conducted on T300/5208 coupons with dimensions of  $152.4 \text{ mm} \times 12.77 \text{ mm} \times 2.20 \text{ mm}$ . Experiments on IM7/K3B were attempted initially. However, due to its large thickness, no significant damage was found in this material.

Figures 3(a)-(c) show measured velocity profiles of a specimen at three different levels of damage. The time window shown ( $125 \mu\text{s}$ ) matches approximately the duration of the loading pulse applied on the specimen. Figure 3(a) shows the response of a virgin specimen with no damage, while Figs. 3(b) and (c) are from the same specimen with moderate and severe damage, respectively. The figures indicate a gradual change of the velocity profile with increasing amounts of damage. The measurement from the virgin laminate in Fig. 3(a), is characterized by a gradual rise of the velocity profile. The profiles from the damaged laminate in Figs. 3(b) and (c) exhibit distinct features including a short rise time and a characteristic plateau in the early stage of the deformation. The duration of this plateau appears to increase with increasing damage in the specimen. Another feature to be noted is the change in the overall amplitude of the velocity profile. It appears that the mean amplitude of a profile decreases as the damage increases. These observations suggest that certain features of a measured rear surface velocity profile, such as the early-stage plateau and the mean amplitude may provide useful clues to the nature and state of the damage induced in the specimen.

### Numerical simulation

#### Governing Equations

A Lagrangian, finite deformation formulation is used to account for the finite deformation involved in the crack tip regions. The formulation follows from Zhai and Zhou [1], [2] and includes a bulk constitutive law and a cohesive law to explicitly account for crack formation. The volumetric constitutive law is assumed hyperelastic so that

$$\mathbf{S} = \frac{\partial W}{\partial \mathbf{E}}, \quad (1)$$

where  $\mathbf{S} = \mathbf{s} \cdot \mathbf{F}^{-T}$  is the second Piola-Kirchhoff stress and  $\mathbf{E}$  is the Lagrangian strain. The strain energy density  $W$  is taken to be

$$W = \frac{1}{2} \mathbf{E} : \mathbf{L} : \mathbf{E}, \quad (2)$$

where  $\mathbf{L}$  is the fourth-order stiffness tensor and  $\mathbf{E}$  is the Lagrangian strain tensor. Homogenized, effective properties are used for each ply. The resulting transversely isotropic stiffness tensor with five independent components for the bulk constitutive behavior of the ply is

$$\mathbf{L} = \begin{pmatrix} Q_{11} & Q_{12} & Q_{13} & 0 & 0 & 0 \\ Q_{12} & Q_{11} & Q_{13} & 0 & 0 & 0 \\ Q_{13} & Q_{13} & Q_{33} & 0 & 0 & 0 \\ 0 & 0 & 0 & Q_{44} & 0 & 0 \\ 0 & 0 & 0 & 0 & Q_{44} & 0 \\ 0 & 0 & 0 & 0 & 0 & (Q_{11} - Q_{12})/2 \end{pmatrix} \quad (3)$$

where  $Q_{ij}$  are functions of five material constants including the in-plane and out-of-plane Young's moduli, Poisson's ratios, and a shear modulus [5]. In (3), the 1-2 plane is taken to be the plane of isotropy and subscripts 1 and 2 on the stiffnesses are interchangeable.

The constitutive law for cohesive surfaces relates the tractions and the displacement jumps across the crack surfaces. The separation process is also assumed hyperelastic under monotonic loading conditions so that any dissipation associated with separation is neglected (Xu and Needleman, 1994). Assuming the surface potential  $\phi$  exists, the traction on the cohesive surfaces can be derived as

$$\mathbf{T} = -\frac{\partial \phi}{\partial \Delta}. \quad (4)$$

In two dimensions, the specific form of  $\phi$  used here is

$$\phi(\Delta) = \phi_0 - \phi_0 \left( 1 + \frac{\Delta_n}{\delta_n} \right) \exp \left( -\frac{\Delta_n}{\delta_n} \right) \exp \left( -\frac{\Delta_t^2}{\delta_t^2} \right), \quad (5)$$

where  $\Delta_n = \mathbf{n} \cdot \Delta$  and  $\Delta_t = \mathbf{t} \cdot \Delta$  are the normal and tangential displacement jumps with  $\mathbf{n}$  and  $\mathbf{t}$  denoting unit vectors along the surface normal and tangent in the reference configuration, respectively.  $\delta_n$  and  $\delta_t$  are characteristic lengths. Potential  $\phi$  is defined such that  $\phi(\Delta)|_{|\Delta|=0} = 0$  and  $\phi_0 = \phi(\Delta)|_{|\Delta| \rightarrow \infty}$  represents the work of separation. The cohesive parameters include the cohesive strength and the work of separation per unit area. From dimensional considerations, a characteristic length should enter the formulation. Details of the finite element method and the finite element discretization including the cohesive surfaces are available in [1] and [2].

### Problem Analyzed

A composite beam in a three-point bending configuration is analyzed. Two simple supports symmetrically span away from the center of the bottom surface. The span between the supports is 10 mm. The material used is a cross-ply, graphite/epoxy laminate with a ply thickness of 0.5 mm. The layup considered is  $[0^\circ/90^\circ/0^\circ]$ . The bulk constitutive properties of each lamina are those of a transversely isotropic, linearly elastic material. The material properties used by Chang et al. [7] are used here. A constant impact velocity of  $2 \text{ ms}^{-1}$  is applied at the center of the upper surface of the beam. Since no accurate data on the interlaminar bond strength is available for the laminate, two different bond strength levels are considered, representing a weak interlaminar bond and a strong interlaminar bond.

### Results and Discussion

The numerical simulation focuses on the evolution of deformation and failure in a composite beam. In particular, the effect of interlaminar bond strength on the evolution of damage is emphasized. Figure 4 show how the stress field and damage pattern evolve in a

three-ply laminate during an impact process, for the case of a weak interlaminar bond. The major principal stress at two different loading times is contoured in the deformed configurations. Figure 4 shows that delaminations occur first and then matrix cracks develop in the middle  $90^\circ$  ply. The delaminations are mostly in mode-II because of the high shear stresses developed along the interfaces. The combined effect of interlaminar delaminations and matrix cracks leads to a global failure of the beam. In order to analyze the nature of damage growth more quantitatively, the time histories of cumulative crack lengths in the  $90^\circ$  ply matrix, delamination along the top  $0^\circ/90^\circ$  interface, and delamination along the bottom  $0^\circ/90^\circ$  interface, are calculated and compared. The results are presented in Fig. 5(a) and (b), for the weak and the strong interlaminar bonds, respectively. For the weak bond, damage is initiated by delamination along the top  $0^\circ/90^\circ$  interface, followed by matrix cracking in the  $90^\circ$  ply and then delamination along the bottom  $0^\circ/90^\circ$  interface. Damage progresses in a top-to-bottom manner. However, in the case of the strong interlaminar bond, damage first initiates in the  $90^\circ$  ply in the form of matrix cracking, followed by delaminations at the top and bottom interlaminar interfaces. The cumulative length of matrix cracks increases rapidly with time, indicating widespread matrix cracking in the middle layer before a global failure occurs.

## Conclusions

Experimental and numerical studies on the deformation and failure behavior of fiber-reinforced structural composites subjected to low-velocity impact are conducted. The studies use a split Hopkinson pressure bar and a cohesive finite element method. The experiments allow the full histories of applied load, contact point velocity/displacement, and energy input, and energy dissipation in impacted specimens to be determined. Total energy dissipation, taken as a macroscopic measure of cumulative damage in an impacted specimen, increases with increasing impact energy. Beyond a certain level of impact energy, the energy absorption capability of the specimen tends to saturate. The post-impact tensile strength of the material analyzed decreases with increasing impact energy. An experimental technique is developed for time-resolved monitoring of damage progression in composite laminates. The technique uses a split Hopkinson bar and a laser interferometer.

Numerical simulations based on a cohesive finite element are conducted. The framework of analysis allows delamination and matrix cracking to be explicitly resolved. The analysis focused on the effect of interlaminar bond strength on the development of damage in impacted laminates. For laminates with a weak interlaminar bond, it is found that damage initiates in the form of delamination along the top interlaminar interface. For laminates with a strong interlaminar bond, damage initiates in a  $90^\circ$  ply in the form of matrix cracking.

**Acknowledgements:** Support of this work by the Office of Naval Research (Scientific Officer: Yapa D. S. Rajapakse) is gratefully acknowledged.

## References

1. Zhai, J. and Zhou, M. (1998). "Micromechanical modeling of dynamic fracture in ceramic composites." *ASTM STP* 1359 (in press).
2. Zhai, J. and Zhou, M. (1999). "Finite element analysis of micromechanical failure modes in heterogeneous brittle solids." *Int. J. Fracture* (in press).
3. Zhou, M. and Zhai, J. (1999). "Modeling of micromechanical fracture using a cohesive finite element method." *Proc., SHOCK99- APS 11th Topical Conference on Shock Compression of Condensed Matter*, Salt Lake City, UT, June 27- July 2.
4. Park, S. W. and Zhou, M. (1999). "Separation of elastic waves in split Hopkinson bars using one-point strain measurements." *Experimental Mechanics* (in press).

5. Jones, R. M. (1975). *Mechanics of Composite Materials*. Hemisphere Publishing Co., New York.
6. Xu, X. -P. and Needleman, A. (1994). "Numerical simulations of fast crack growth in brittle solids." *J. Mech. Phys. Solids*, **42**, 1397-1434.
7. Chang, F. -K., Choi, H. Y. and Jeng, S. -T. (1990). "Study on impact damage in laminated composites." *Mech. Mater.*, **10**, 83-95.

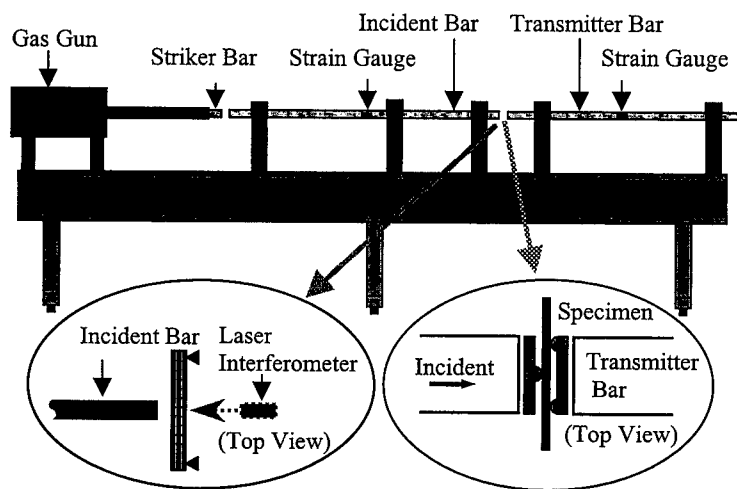


Figure 1 A schematic illustration of the impact experiments on a SHPB system



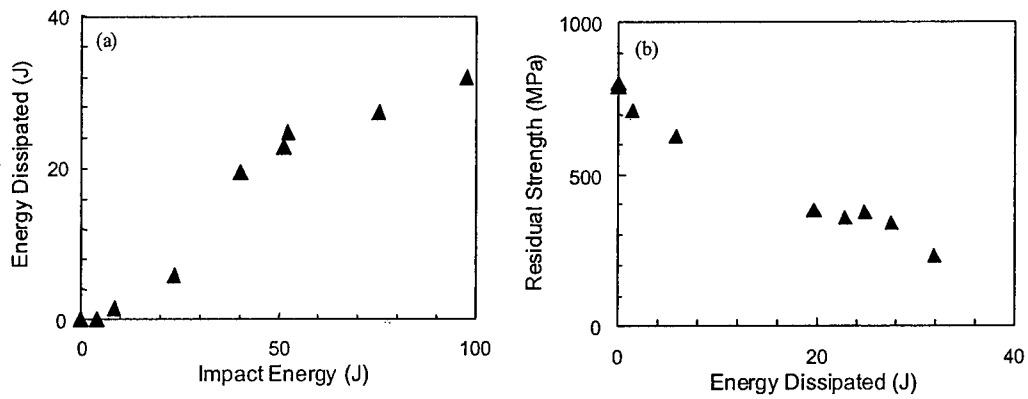


Figure 2 (a) Energy dissipation as a function of impact energy, (b) residual strength as a function of energy dissipated.

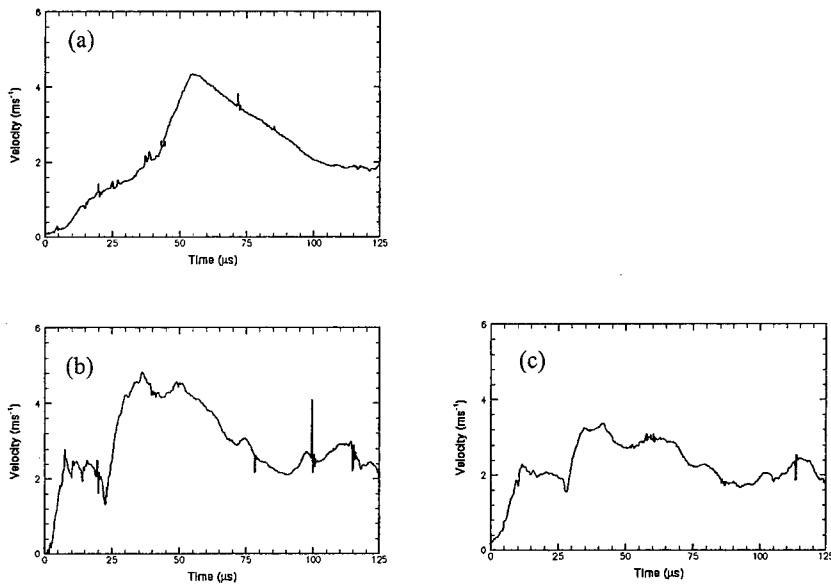


Figure 3 Measured rear-surface velocity profiles from: (a) a virgin specimen; (b) the same specimen with moderate damage; (c) with severe damage

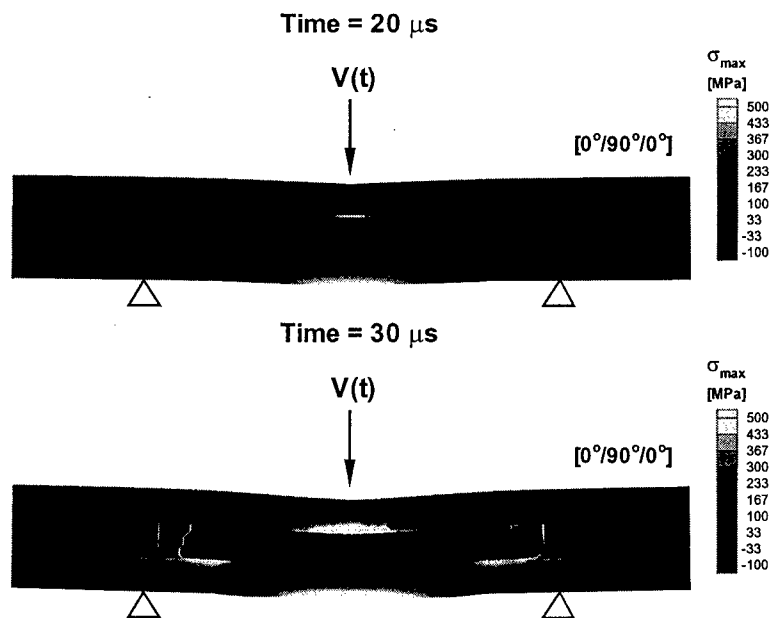


Figure 4 Evolution of the major principal stress and damage for a weak interlaminar bond

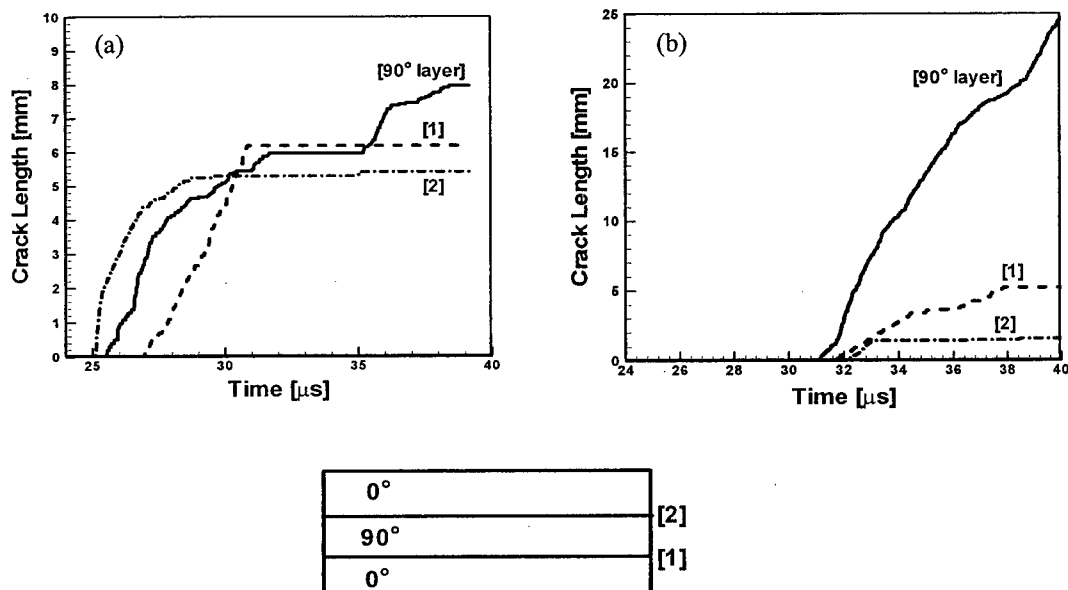


Figure 5 Histories of the crack lengths in a three-ply laminate:  
(a) for weak interlaminar bond; (b) for strong interlaminar bond

## **Damage Accumulation in Composite Laminates during Quasi-Static Transverse Loading**

Y.Aoki\*, H.Suemasu\*\* and O.Majima\*\*

### **ABSTRACT**

A mechanism of damage accumulation in composite laminates subjected to a quasi-static concentrated load is numerically studied by using finite element method to disclose the impact damage problem. The energy release rate distributions are calculated along the delamination edges in square composite laminates with various stacking sequences. Not only circular delaminations but also more realistic impact damage model are investigated to explain the reason why the typical impact damage must be created. The effects of transverse cracks and stacking sequence on the energy release rate are discussed.

**Key Words:** finite element method, delamination, transverse crack, stacking sequence, energy release rate, CAI

### **Introduction**

In recent years, CFRP composite materials are used extensively in many engineering applications, such as aircraft and space structures mainly because of the need for reducing weight. The material is used in the form of laminates for these aerospace applications. But it is known that structures made of composite laminates are susceptible to impact damage such as delamination, transverse cracking etc[1-2]. It is difficult to detect these impact damages from outside of structures. Furthermore, these damages can cause severe reduction of compressive strength[3]. Design loads of the structures are often limited by the degraded compressive performance due to these damages. Therefore, the mechanism of damage accumulation due to impact must be well understood in order to utilize composite laminated structures to their full advantage.

In this paper, special emphasis is placed on the interlaminar delaminations below the impact point, which usually occur in the form of multiple delaminations. A mechanism of damage accumulation in composite laminates subjected to a quasi-static concentrated load is numerically studied by using finite element method to disclose the impact damage problem. The energy release rate distributions are calculated along the delamination edges in square composite laminates with various

---

\* Graduate Student, Department of Mechanical Engineering, Sophia University

\*\* Department of Mechanical Engineering, Sophia University, 7-1 Kioicho Chiyoda-ku Tokyo 102-8554 Japan

stacking sequences. Not only circular delaminations but also more realistic impact damage model are investigated to explain the reason why the typical impact damage must be created. The effects of transverse cracks and stacking sequence on the energy release rate are discussed.

In order to observe the mechanism of the damage initiation and accumulation in the quasi-isotropic composite laminates during static indentation, a transverse concentrated load was applied at the center of glass fiber reinforced composite laminates  $[(0_2/45_2/90_2/-45_2)_2]_s$ . Details of the experiment will not be shown in the present paper. Only the damage state obtained is shown in Figure 1. The damage state was quite similar to those of the impact damage reported by many researchers [for example 3]. It is reasonable to investigate damage accumulation problem of the laminates during the static indentation before studying impact damage problem.

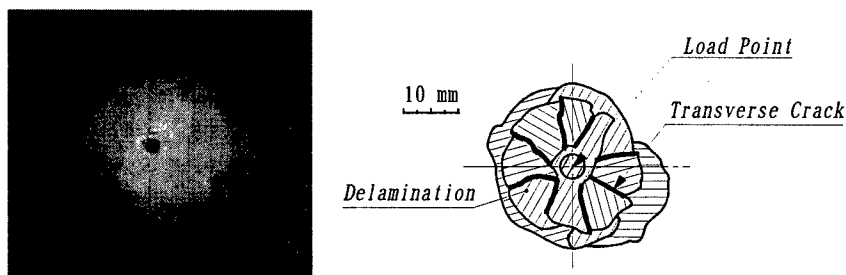


Figure 1 Typical damage shape due to a concentrated static load

## Finite Element Analysis

A composite laminate with eight layers analyzed in the present paper is schematically shown in Figure 2. Firstly we studied the energy release rate distribution along the edges of the circular multiple delaminations in the isotropic plate and cross-ply  $[0/90]_{2s}$  and quasi-isotropic laminates  $[-45/90/45/0]_s$  to study the effect of the fiber orientations on the delamination propagation (Figure 3 (a)). Then, we studied a damage model made of fan shaped delaminations and transverse cracks in a quasi-isotropic laminate as shown in Figure 3 (b). The delaminations are connected each other via transverse cracks and form a circular projected shape.

$E_x=56.5$  GPa,  $E_y=E_z=9.15$  GPa,  $G_{xz}=G_{yz}=4.18$  GPa,  $\nu_{xy}=0.316$ ,  $\nu_{xz}=\nu_{yz}=0.262$  are chosen for the elastic properties of the lamina, except the isotropic plate ( $E=56.5$  GPa,  $\nu=0.316$ ). The dimensions of the square plates are  $150 \text{ mm} \times 150 \text{ mm} \times 4 \text{ mm}$ . All four edges are fixed both in inplane and out-of-plane directions.

A commercially available finite element program (ABAQUS 5.7) is used. A finite element mesh is shown in Figure 4. Three dimensional twenty node isoparametric brick elements are used to model the laminates except the center portions of the delaminated layers where 15 node wedge elements are used. The number of elements and nodes is 5520 and 17496, respectively. Static distributed load is applied on the wedge elements at the center of the plate. In order to prevent the delaminated portions from overlapping each other, spring element having stiffness only in compression direction is introduced between every double node above and below the delamination. The energy release rate is

calculated by using virtual crack closure technique[4]. Very stiff and very flexible spring elements are set to easily obtain the necessary nodal forces and relative displacements between the corresponding nodes, respectively. Geometrical nonlinearity is considered.

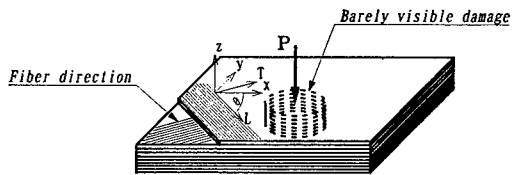


Figure 2 Composite laminate subjected to concentrated load

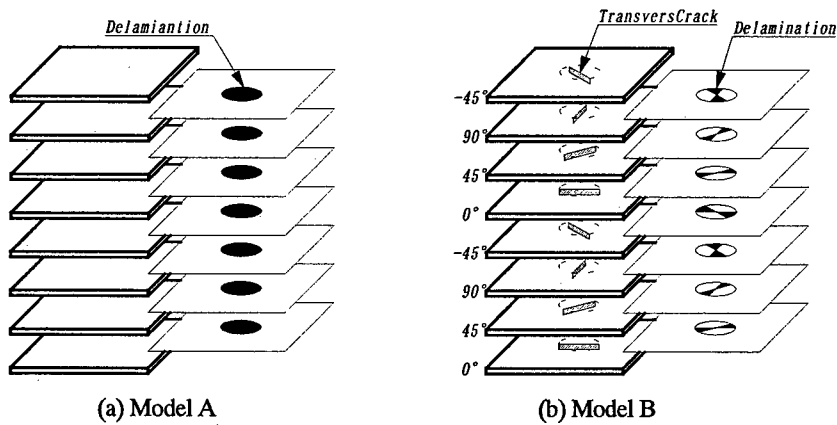


Figure 3 Models of damage analyzed

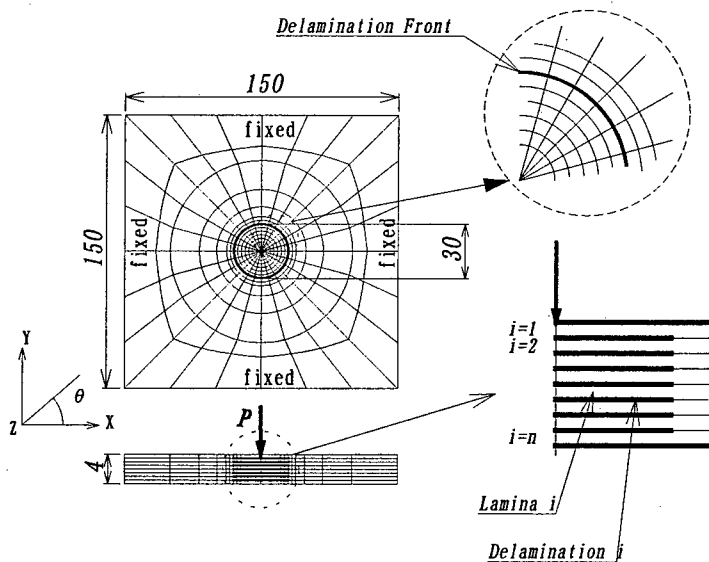


Figure 4 Typical Finite Element Mesh

## Results and Discussion

The relationships between applied load and center deflection are shown in Figure 5. The hardening effect due to large deflection, being unclear for the intact plates until their deflections reach at half the thickness, is extremely significant for the multiply delaminated plate from the low load level. The geometrical nonlinearity must be considered to discuss the instability of the damage in the laminates.

### 1. The case of Model A

We will show the results of the isotropic plate first. The total energy release rate distributions at  $P=10$  kN are plotted in Figure 6 (a). At this load level the center of the plate deflects by 5.38 mm and the effect of geometrical nonlinearity is significant (Figure 5). The distribution is almost circular and effect of the square shape plate is insignificant. The energy release rate, being maximum at the middle surface and symmetric about it in the linear case, increases more rapidly at the delamination front near the bottom surface and becomes asymmetric about middle surface. The tendency is well seen in Figure 6 (b) where the total energy release rate at the edge of  $0^\circ$  direction is plotted. The mode II component is dominant and the other terms are negligibly small.

The energy release rate distributions at the delamination fronts 1,2,4,6 and 7 for cross-ply laminate and quasi-isotropic laminate are plotted in Figures 7 and 8. The energy release rate of the delamination 6 and 7 is much larger than that of the delamination 1 and 2. The energy release rate is maximum at the fiber direction of the layer outside the delaminations and symmetric about the middle surface at linear case. But the effect of geometrical nonlinearity being larger with the increase of the load, the direction of the maximum energy release rate changes from the fiber direction of the layer above the delamination to that below the delaminations for the delamination above the middle surface. The distribution of the energy release rate for the delaminations below the middle surface are deformed in the fiber direction of the layer below the delamination, i.e. outside the delaminations. The maximum values of the energy release rate of the delamination 6 and 7 are even larger than that of center delamination 4 at middle surface for both laminates, though the energy release rates tend to be large at the middle surface. The tendency becomes more eminent with the increase of the load. The energy release rate distributions at the other delaminations have the same tendency as the delaminations 1,2,6 and 7. From the results, we can say that the delaminations tend to propagate in the fiber direction of the layer below the delamination at each interface. It coincides with the experimentally obtained delamination shape (often referred as peanut shape) at each interface.

The components of the energy release rate for the cross-ply and quasi-isotropic laminates are plotted in Figures 9 (a) and (b), respectively. The both results are basically similar to that of the isotropic plate. The mode III component is negligibly small for both cases at any load level. Mode II component is still dominant at the delamination fronts above middle surface. But a mode I component existing at the delaminations near the bottom surface is not very small compared to the mode II component and must be considered to discuss the instability of the delaminations.

### 2. The case of Model B

The total energy release rates at the delamination fronts at  $P=362$  N and  $P=10$  kN for model B are plotted in Figure 10. The plots of Figure (a) shows the energy release rates at the delaminations

above the middle surface and (b) shows those below the middle surface. At the low load of  $P=362$  N, the energy release rate is maximum at the delamination 4 which locate at middle surface. The gap of the energy release rate is not large between the neighboring delaminations, which are connected via a transverse crack. At large load of  $P=10$  kN, the energy release rate below the middle surface tends to be larger than that above the middle surface similar to the case of the circular delaminations. At this load, the geometrical nonlinearity is not so significant for this model as for Model A, because the delaminated area of model B is about 1/4 of that of the model A. As the number of the plies is eight and only one round of spiral is considered, the projected shape of the energy release rate distribution is elliptic, i.e. the predicted projected damage thought to be a little elliptic. But the shape is not strongly elongated. The difference of the energy release rate is not significant as shown in both Figures, because all the delamination edges are almost aligned to the fiber direction of the layer outside the delamination. If the more number of the plies are considered, the projected shape is thought to be more round. The more important is that even the present model with the transverse cracks and delaminations does not explain the experimentally observed damage shape, in which the largest delamination always locates near the bottom surface. Some dynamic effect may contribute to the formation of typical impact damage.

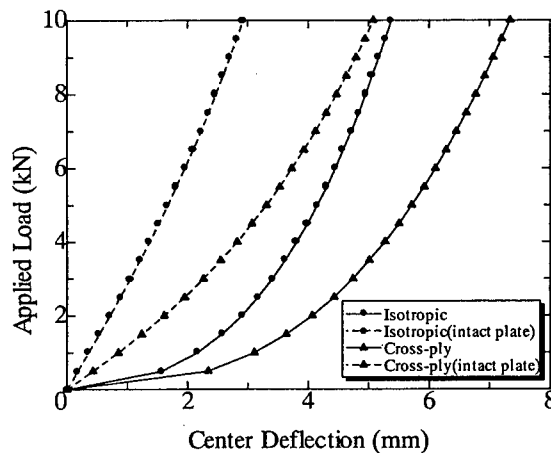


Figure 5 Relationship between applied load and center deflection

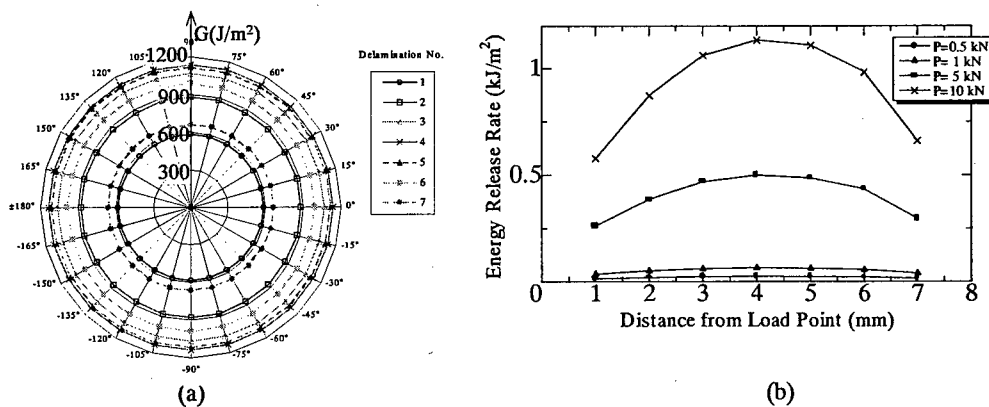


Figure 6 Energy release rate distribution at  $P=10$  kN for isotropic plate

## Delamination No.

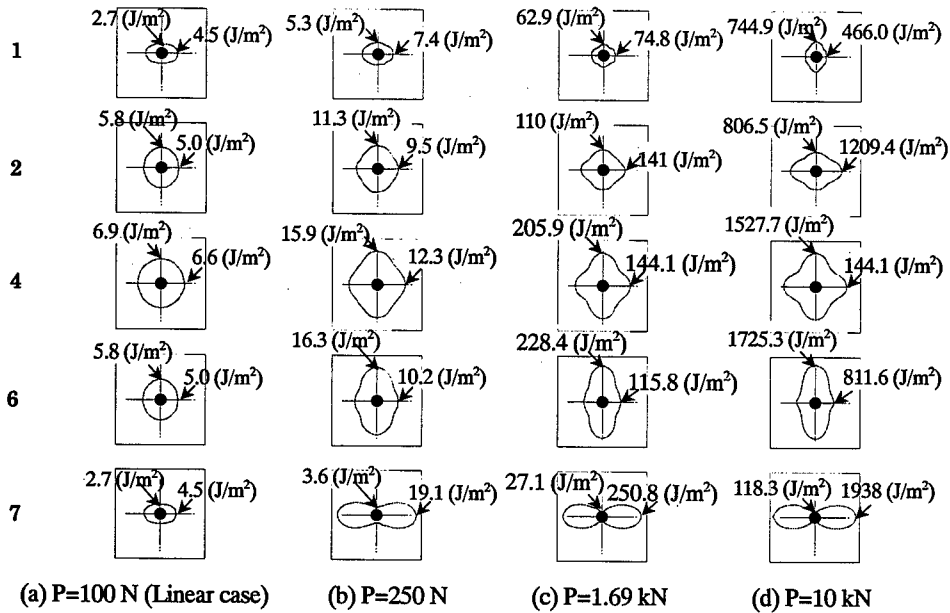


Figure 7 Changes of energy release rate distribution with the increase of the load for cross-ply laminate

## Delamination No.

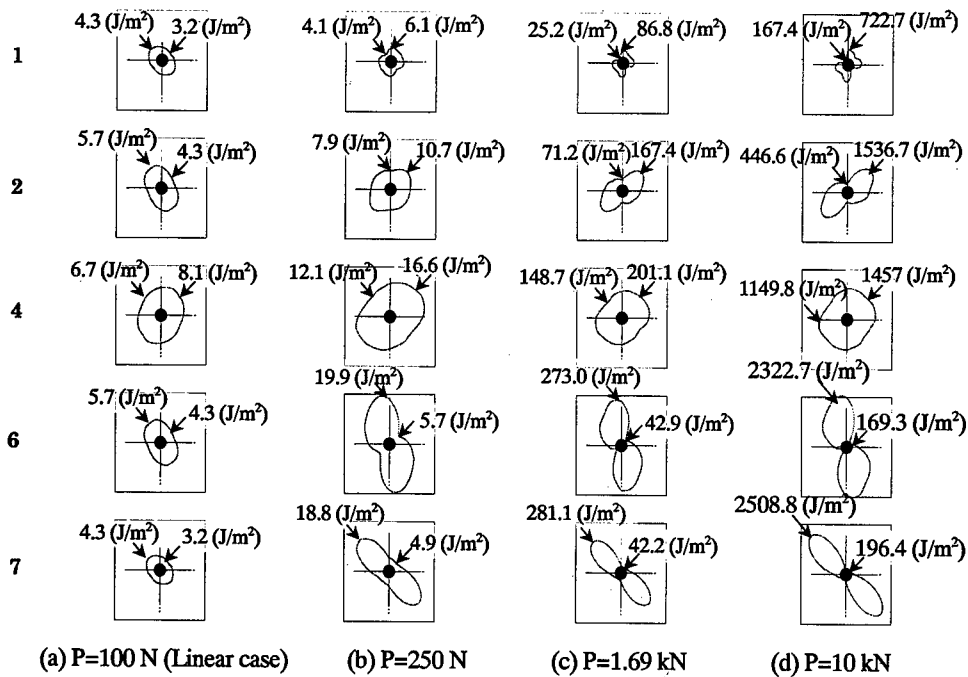


Figure 8 Changes of energy release rate distribution with the increase of the load for quasi-isotropic laminate



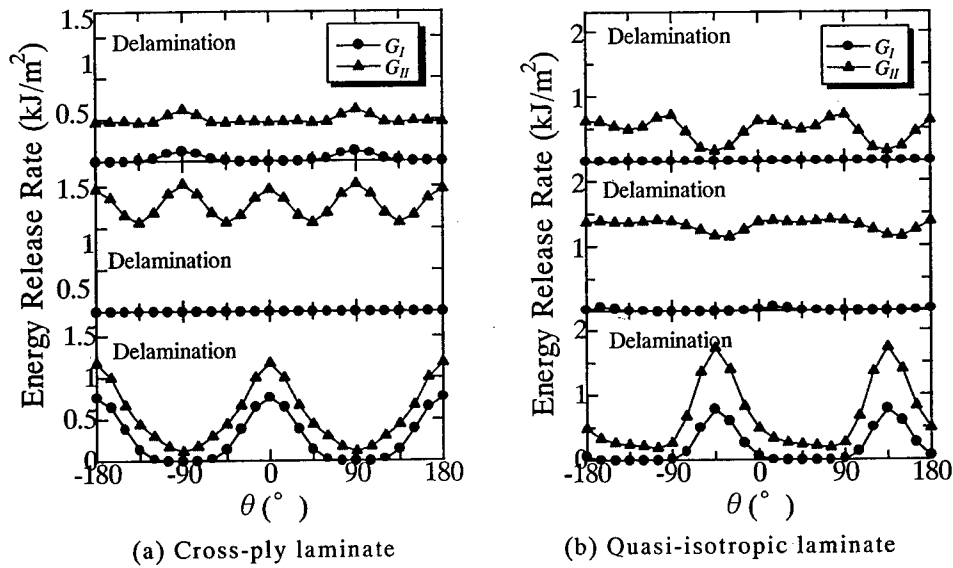


Figure 9 The distribution of mode I and mode II components for cross-ply laminate and quasi-isotropic laminate

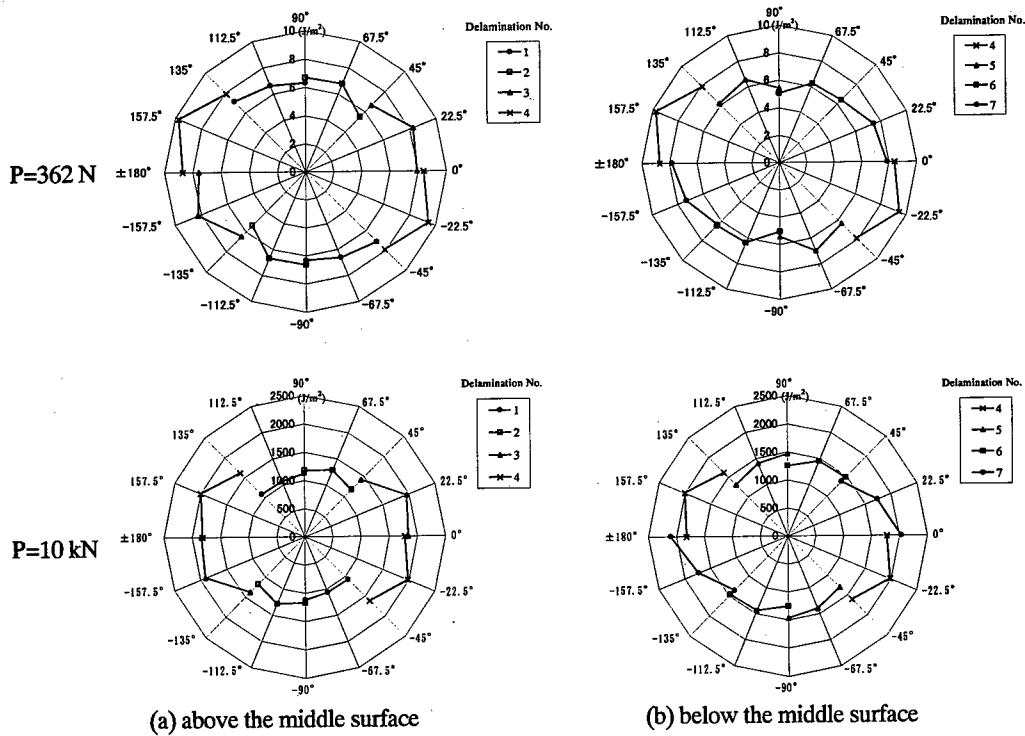


Figure 10 Change of energy release rate distribution for Model B

## Conclusion

Two types of damage models are numerically analyzed by using finite element method and energy release rate distributions are obtained. From the analysis, we may have the following conclusion.

- The effect of geometrical nonlinearity must be considered to discuss the instability of delaminations in the laminate.
- The energy release rate distribution is almost circular for the square isotropic laminates.
- Though the energy release rate tend to be large at the middle surface at low load level, the position of the maximum value moves to the back surface with the increase of the load
- The energy release rate, being large in the fiber direction of the lamina just outside the delamination at low load level, rapidly increases in the fiber direction of the lamina just below the delamination with the increase of the load.
- The energy release rate distribution for the model B is a little elliptic but the expected delamination shape may not be significantly elongated.

The large delamination near the back surface often observed in the impact damage cannot be clearly shown from the numerical result of the present models. More factors must exist during the damage accumulation process.

## Acknowledgement

The authors acknowledge the effort of Mr. Shimizu to conduct the experiment. A part of the present research is supported by Grant-in-aid for scientific research 09650116.

## Reference

1. Shang-Lin Gao, Jang-Kyo Kim and Xing-Juan Xian, "Characterization of Impact Damage in CFRPS Using a Scanning Acoustic Microscope", Proceedings of ICCM-11, Gold Coast, Australia, 14th-18th July 1997.
3. S.A.Hichen and R.M.J.Kemp, "The Effect of Stacking Sequence on Impact Damage in a Carbon Fiber/Epoxy Composite, Composites, 26, 1995
3. T.Ishikawa, et al, Some Experimental Findings in CAI Tests of CF/PEEK and Conventional CF/EPOXY Flat Plates, Composite Science and Technology, 55, 1995
4. Shivakumar.K.N, Tan.P.W and NewmanJ.C, "A Virtual Crack-Closure Technique for Calculating Stress Intensity Factors for Cracked Three Dimensional Bodies", International Journal of Fracture, 36, 1988, pp R43-R50
5. Y.Aoki, H.Suemasu, "A Numerical Study on Mechanism of Damage Accumulation in Composite Laminates Under a Quasi-Static Concentrated Load", Proceedings of 3rd Joint Canada-Japan Workshop on Composites, Kyoto, Japan, 6th-8th March 2000.

## **Damage Progression of Composite Laminates Under Low-Velocity Impact**

Nobuhide Uda, Kazuo Kunoo, Kousei Ono, Tadashi Nagayasu  
Toru Izumiya, and Kazunori Machida

### **Abstract**

We conducted low-velocity impact tests and quasi-static contact tests of carbon fiber/PEEK cross-ply laminates. Major damage modes were matrix cracks and delaminations. Experimental observations gave that both the impact and quasi-static contact damages result from complex failure processes, but show a lot of similarities. We analyzed the damage initiation and growth behavior in the quasi-static contact test in order to fundamentally understand the impact damage progression of laminated composites. We developed a finite element model combined with a failure criterion and fracture mechanics considering delamination arrest.

### **Introduction**

The application of composite materials to aircraft primary structures is increasing due to their light-weight and high-strength nature. However, the excellent mechanical properties of the composite materials can be significantly reduced by a low-velocity impact, such as dropped tools during maintenance and runway stones during taxing. Test data [1] show that compression strength after impact (CAI) of composite structures is seriously reduced, even if impact damage is not detectable by visual inspection. A number of investigations have been conducted to estimate the sensitivity of CAI to low-velocity impact damage. The available literature has been classified into the following two aspects. The first is the experimental and theoretical investigations [1,2 etc.] of the effect of impact-induced damage on the post-impact compressive strength. The second aspect concerns the relationship between the impact energy and the size of the damage area [3-9 etc.]. The works belonging to the second aspect have considerably revealed details of the impact damage in composite laminates, by using a finite element method (FEM) with a failure criterion [3,4], a FEM combined with a failure criterion and fracture mechanics [5-7], and a FEM with a failure criterion and fracture mechanics considering crack arrest [8,9]. However, quantitative comparison between the experimental and analytical results on the impact damage has been insufficiently made because of the extremely complex damage process. The objective of our work is to precisely predict damage initiation and development in composite laminates subjected to a low-velocity impact.

---

Department of Aeronautics and Astronautics, Kyushu University  
6-10-1 Hakozaki, Higashi-ku, Fukuoka, 812-8581, Japan

## Experiments

We conducted low-velocity impact tests and quasi-static contact tests of laminates with a stacking sequence of  $[0_4/90_4]_{2S}$ . We made the specimens of the AS4/PEEK prepreg APC-2. Specimens were 150-mm long and 100-mm wide. The thickness was about 4.2 mm. The specimens were clamped on all four edges by a metal frame and had 125 mm x 75 mm spans. Strain gages were mounted at each location on both the front and opposite sides of the load point as illustrated in Fig. 1.

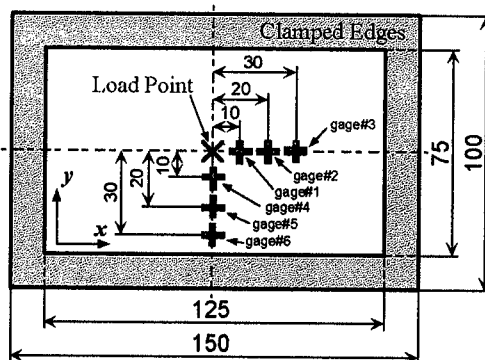


Figure 1 Specimen geometry and strain gage locations.

## Low-Velocity Impact Tests

The impact tests were conducted using a dropped-weight test machine. The dropped weight assembly consists of a 16-mm diameter hemispherical steel impactor, a load cell, and an aluminum member slid on a guidance assembly. The total weight of the impactor assembly was 4.67 kg. The velocity of the impactor was measured using a laser displacement sensor.

Contact force and deflection histories of a plate subjected to an impact of energy level 20.6 J are represented in Fig. 2. Contact started at the time  $t \approx 2$  ms and lasted until  $t \approx 7.6$  ms. The force-time curve had a relatively high frequency oscillation as shown in Fig. 2. The oscillation started somewhere during the loading stage and seemed to terminate at around the time of the maximum deflection of the plate,  $t \approx 4.7$  ms.

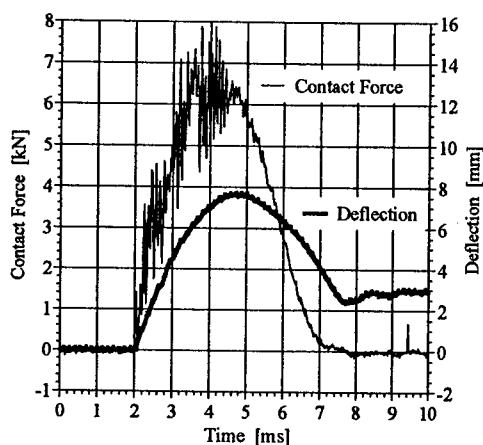


Figure 2 Contact force and deflection histories of the specimen subjected to an impact of energy level 20.6 J.

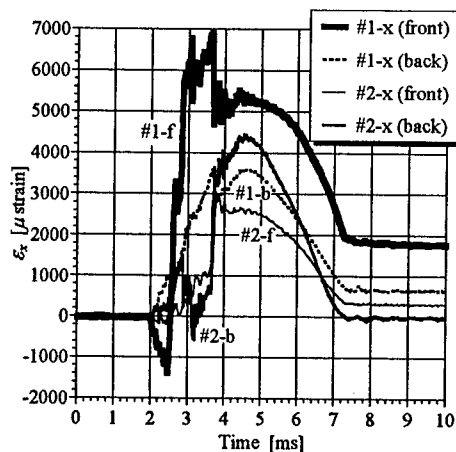


Figure 3 x-direction strain histories of the specimen subjected to an impact of energy level 20.6 J.

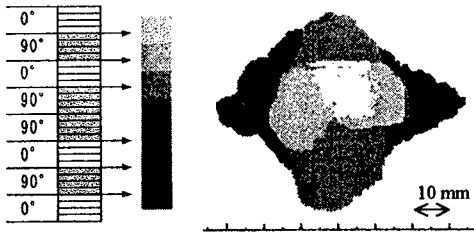


Figure 4 C-scan map of the specimen subjected to an impact of energy level 20.6 J.

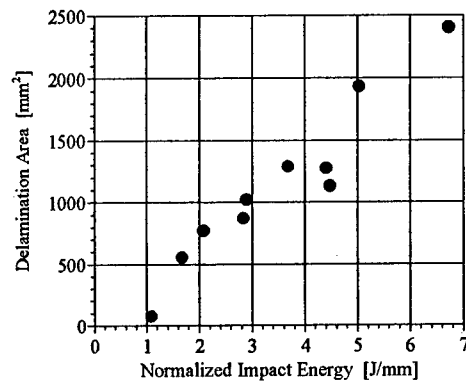


Figure 5 Relationships between normalized impact energy and projected delamination area.

Figure 3 depicts  $x$ -direction strain histories of this plate during impact. At the beginning of the impact test, the strain histories of each pair of the strain gages on both the front and opposite sides of the impact point were symmetric about the zero strain axis, indicating a pure bending behavior. The strain value of the #1 gage at the front side, however, altered abruptly from compression to tension at 0.5 ms after the contact. We can estimate force level at the time using Fig. 2. The sudden strain change at the #1 front side occurred at  $F \approx 4.4$  kN. A change of the strain history at the #2 back side was observed at 0.3 ms after the sudden change at the #1 front side. The strain values of all the gages were smoothly decreased after the time of the maximum deflection of the plate,  $t \approx 4.7$  ms. It is therefore considered that the impact damage was initiated beneath the impact point and damage near the back surface was occurred later, and no damage was caused during the unloading stage after  $t \approx 4.7$  ms.

After impact tests an ultrasonic C-scan inspection was conducted to assess damage caused. Figure 4 shows a C-scan map of the impact energy case shown in Figs. 2 and 3. The C-scan map represents the delamination depth using a gray scale shown in Fig. 4. Figure 4 depicts that the delaminations grew in a shape of peanuts at all the interfaces. The peanut shape delaminations were oriented in the fiber direction of the layer below the interface. The impacted specimen had a 0.94-mm deep indentation as a permanent deformation at the impact point, a local buckling of fibers at the surface near the impact point, and several transverse cracks at the back surface.

We evaluated delamination damage using the projected delamination area measured by processing the C-scan image. Figure 5 shows the delamination area as a function of the impact energy normalized by the specimen thickness. It is observed from Fig. 5 that there exists an impact energy threshold beyond which delamination occurs, but below which no delamination can be found.

#### Quasi-Static Contact Tests

The quasi-static contact tests were done using an Instron 8501 test machine.

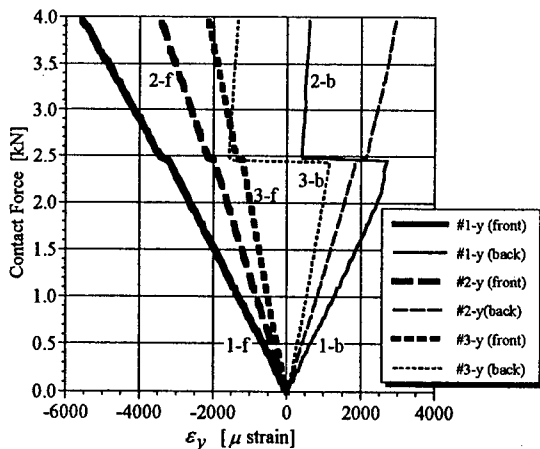


Figure 6 Contact force and  $y$ -direction strain relationships of the specimen statically loaded to  $F = 3.96$  kN.

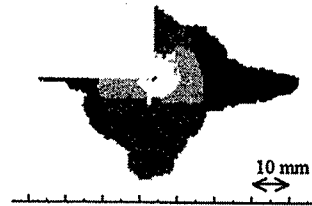


Figure 7 C-scan map of the specimen statically loaded to  $F = 8.10$  kN.

The stroke speed of the indenter was 0.01 mm/sec. The impactor head of the dropped weight assembly was used as the indenter for the contact test. To experimentally obtain the contact force and delamination extension relationship, a specimen was loaded to a preselected contact load, and unloaded. The specimen was inspected at each load stage by the ultrasonic C-scan to evaluate delamination caused.

A specimen was loaded to  $F = 3.96$  kN,  $F = 5.97$  kN,  $F = 7.96$  kN and  $F = 8.10$  kN. Figures 6 and 7 are contact force and strain relationships, and a C-scan map, at the load stage captioned, respectively.

Figure 6 depicts contact force and  $y$ -direction strain relationships of the specimen loaded to  $F = 3.96$  kN. A jump of strain is observed at  $F \approx 2.5$  kN in the relationship obtained from the strain gages at the back surface. This event indicates that a transverse crack occurred in the fiber direction in the 0-degree layer of the plate bottom. The C-scan map of the specimen indicated that little delamination occurred in the specimen.

The C-scan map in Fig. 7 is of the specimen loaded to  $F = 8.10$  kN. The upper left quarter of the C-scan map is disappeared because fine C-scan pulse echo was not gotten well at the region for a hindrance which strain-gage leads caused. Figure 7 shows the delaminations at each interface grew larger.

#### Comparison Between the Impact Tests and the Quasi-Static Contact Tests

Figure 8 shows contact force and  $x$ -direction strain relationships obtained from both the impact and quasi-static contact tests. The strain gages were mounted at the same location #1 in both the tests as shown in Fig. 1. Figure 8 indicates that the strain history roughly coincides with each other except for the oscillation in the impact test. The strain histories at the front side of the specimen were changed at  $F \approx 4.5$  kN in both the tests. The C-scan maps inform us that delaminations occurred as far as at the interface lower of the middle 90-degree layer in the specimen at  $F \approx 4.5$  kN.

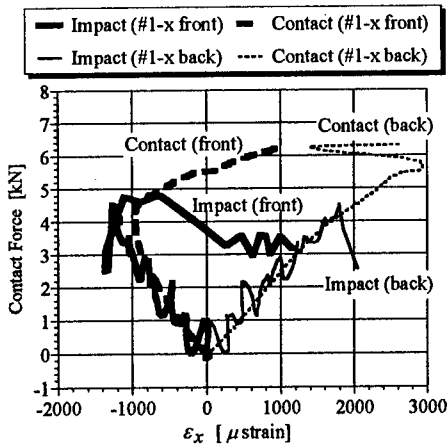


Figure 8 Contact force and x-direction strain relationships obtained from the impact test and the quasi-static contact test.

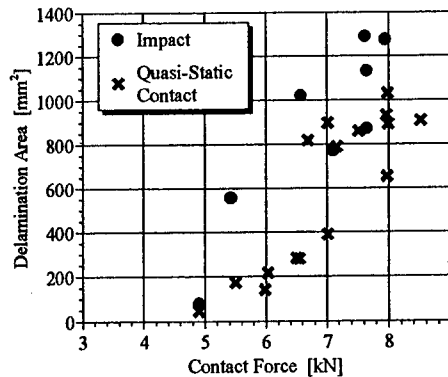


Figure 9 Contact force and delamination area relationships obtained from the impact tests and the quasi-static contact tests.

Figure 9 shows contact force and delamination area relationships obtained from both the impact and quasi-static contact tests. The threshold force for the onset of delaminations in the impact test is almost the same as that in the quasi-static test. In the case of the quasi-static test, the contact force beyond the threshold level caused the delaminations at the interfaces beneath the loading point. Increasing the contact force further led to growth of the delaminations at all the interfaces as depicted in Fig. 7. In the case of the impact test, however, when the contact force was just above the threshold level, the delaminations were instantaneously extended at all the interfaces as shown in Fig. 4. The reason for this is that the fracture toughness of APC-2 decreases with increasing loading rate [10].

### Analytical Study

Experimental observations gave that both the impact and quasi-static contact damages result from complex failure processes, but show a lot of similarities. Therefore, we analyzed the damage initiation and growth behavior in the quasi-static contact test in order to fundamentally understand the impact damage progression of laminated composites. We postulated that three-dimensional effect is minimized because the stacking sequence of the specimen is cross-ply. Hence damage behavior of cross-ply laminates caused by a line-nose indenter was analyzed using a two-dimensional finite element model. Because of symmetry in the loading and the geometry, only one-half of the specimen was modeled with 3000 isoparametric quadrilateral plane strain elements.

### Contact Force

The quasi-static loading is applied by a line-nose indenter as shown in Fig. 10.

The contact force  $F$  during loading was determined using the Hertzian contact law by the equations

$$F = \kappa \alpha^{1.5}, \quad (1)$$

$$\text{where } \kappa = \frac{4}{3} \sqrt{R} \frac{1}{\left[ (1-\nu_s^2)/E_s + 1/E_T \right]}. \quad (2)$$

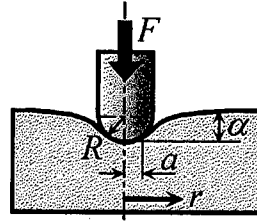


Figure 10 Description of the contact region.

$\alpha$  is the indentation depth, and  $\kappa$  is the modified constant of the Hertz contact theory [11].  $R$ ,  $E_s$ , and  $\nu_s$  are the radius, the Young's modulus, and the Poisson's ratio of the indenter, respectively.  $E_T$  is the Young's modulus normal to the fiber direction in the uppermost composite layer.

The contact force  $F$  is distributed over a small area around a central point. According to the Hertzian model, the pressure distribution about this central point can be approximated by

$$p(r) = \frac{2F}{\pi a^2} \sqrt{a^2 - r^2}, \quad (3)$$

$$a = \sqrt[3]{\frac{F R^{1.5}}{\kappa}}, \quad (4)$$

where  $r$  is the distance from the central point, and  $a$  is the width of the contact region [12].

### Failure Analysis

Based on the experimental findings, we assumed basic damage mechanism as follows: (1) Intraply matrix cracks, i.e., shear cracks and transverse cracks, are the initial damage mode. (2) Delaminations occur only at interfaces which are adjacent to the ply group in which the intraply matrix cracks occur.

In order to predict the onset of the matrix cracks, we adopted the maximum stress theory. We assumed that the matrix crack would propagate throughout the thickness of the ply group which contained the cracked ply.

Delamination occurs when the strain energy available to form the delamination exceeds the energy required to cause delamination.

$$\hat{S} \geq \Gamma dA, \quad (5)$$

where  $\hat{S}$  is the strain energy available to create a delamination of an area  $dA$ , and  $\Gamma$  is the energy required to delaminate a surface of unit area. During a slow stable fracture,  $\hat{S}$  equals to  $\Gamma dA$ . Fast fracture occurs when  $\hat{S}$  becomes higher than  $\Gamma dA$ .



Table I Material properties of APC-2 composites.

$E_L = 135 \text{ GPa}$ , $E_T = 10.5 \text{ GPa}$ , $G_{LT} = 5.7 \text{ GPa}$ , $G_{TR} = 5.7 \text{ GPa}$ , $\nu_{LT} = 0.33$ , $\nu_{TR} = 0.33$ $F_L = 1920 \text{ MPa}$ , $F_T = 90 \text{ MPa}$ , $F_{LT} = 167 \text{ MPa}$ , $F_{TR} = 167 \text{ MPa}$ , $G_{IIC} = 1.5 \text{ kJ/m}^2$
--

The unstable fracture continues until  $\hat{S}$  decreases or  $\Gamma dA$  increases so that the available strain energy is insufficient to create a new delamination surface. The delamination size is therefore controlled by an arrest criterion as follows.

$$\hat{S} \leq \Gamma_{\text{arr}} dA, \quad (6)$$

where  $\Gamma_{\text{arr}}$  is the delamination arrest toughness.

We adopted the delamination formation model proposed by Finn and Springer [6], which assumes that the strain energy available to create a delamination at an interface is supplied from the adjacent ply group in which the intraply matrix cracks occur.

In the finite element analysis, the intraply matrix crack was introduced by separating the nodes on the crack into two independent nodes. The delamination was modeled by replacing the nodes on the delamination with nodes which have independent degree-of-freedom only in sliding direction, but are connected in through-the-thickness direction to prevent overlapping. We neglected an effect of friction.

### Analytical Results and Discussion

We analyzed damage growth behavior of  $[0_4/90_4]_{2S}$  and  $[90_4/0_4]_{2S}$  subjected to the quasi-static line loading. The material properties of APC-2 composites used in the calculations are listed in Table I. We assumed  $\Gamma = \Gamma_{\text{arr}} = G_{IIC}$ .

Figures 11 and 12 show intraply matrix cracks and delaminations in the  $[0_4/90_4]_{2S}$  under a line loading 144 N/mm and in the  $[90_4/0_4]_{2S}$  under 93 N/mm, respectively. The fiber direction of the 0-degree layer is horizontal in the Figures. In

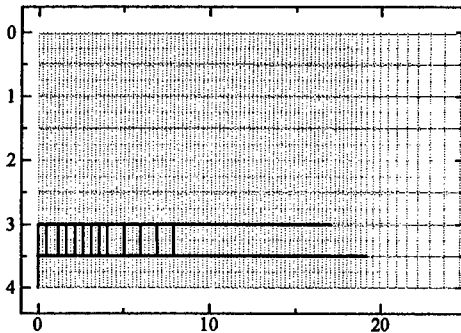


Figure 11 Intraply matrix cracks and delaminations in the  $[0_4/90_4]_{2S}$  under a line load 144 N/mm.

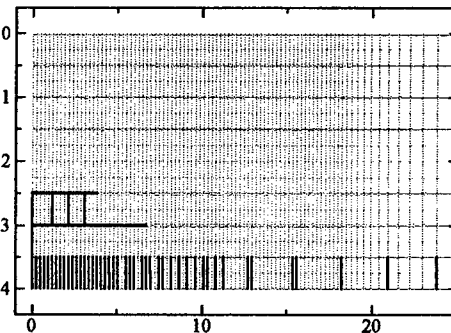


Figure 12 Intraply matrix cracks and delaminations in the  $[90_4/0_4]_{2S}$  under a line load 93 N/mm.

the case of the  $[0_4/90_4]_{2S}$ , a lot of matrix cracks occurred in the second ply group from the plate bottom, which is a 90-degree layer. Delaminations grew at both the upper and lower interfaces of the cracked 90-degree layer. The delamination at the lower interface was larger than that at the upper interface. This depicts that delamination is propagated in the fiber direction of the layer below the interface.

## Conclusions

1. The responses of laminates in the low-velocity impact and quasi-static contact tests are very similar.
2. The threshold force for the onset of delaminations in the impact test is almost the same as that in the quasi-static test. In the case of the impact test, however, when the contact force is just above the threshold level, the delaminations are instantaneously extended at all the interfaces. The reason for this is that the fracture toughness of APC-2 decreases with increasing loading rate.
3. The experiments show that delaminations occur at interfaces which are adjacent to the ply group in which intraply matrix crack occur, and a delamination at an interface is propagated in the fiber direction of the layer below the interface. The analytical results coincide with these experimental findings.

## References

1. T.Ishikawa, T.Sugimoto, M.Matsushima and Y.Hayashi, *Composite Science and Technology*, Vol.55, No.4, 1995, pp.349-363.
2. H.Suemasu, T.Kumagai and K.Gozu, *AIAA Journal*, Vol.36, No.7, 1998, pp.1279-1285.
3. H.Y.Choi and F.K.Chang, *Journal of Composite Materials*, Vol.26, No.14, 1992, pp.2134-2169.
4. J.P.Hou, N.Petricin, C.Ruiz and S.R.Hallett, *Composites Science and Technology*, Vol.60, 2000, pp.273-281.
5. S.Liu, Z.Kutlu and F.K.Chang, *Composite Materials: Fatigue and Fracture*, ASTM STP 1156, American Society for Testing and Materials, 1993, pp.86-101.
6. S.R.Finn and G.S.Springer, *Composite Structures*, Vol.23, 1993, pp.177-190.
7. G.A.O.Davies, D.Hitchings and J.Wang, *Composites Science and Technology*, Vol.60, 2000, pp.1-7.
8. H.Razi and A.S.Kobayashi, *AIAA Journal*, Vol.31, No.8, 1993, pp.1498-1502.
9. H.Wang and T.V.Khanh, *Journal of Composite Materials*, Vol.29, No.2, 1995, pp.156-178.
10. H.Maikuma, J.W.Gillespie, Jr. and D.J.Wilkins, *Journal of Composite Materials*, Vol.24, No.2, 1990, pp.124-149.
11. S.H.Yang and C.T.Sun, *Composite Materials: Testing and Design*, ASTM STP 787, American Society for Testing and Materials, 1982, pp.425-449.
12. S.P.Timoshenko and J.N.Goodier, *Theory of Elasticity*, McGraw-Hill, 1982.

## **Impact Perforation of Orthotropic and Quasi-isotropic CFRP Laminates by a Steel Ball Projectile**

H.Kasano

### **Abstract**

This paper considers the perforation characteristics of orthotropic and quasi-isotropic carbon fiber composite laminates struck by a steel ball projectile, both analytically and experimentally. Two analytical models are introduced, which are developed on the basis of the conservation laws of momentum and/or energy. High velocity impact tests by a steel ball projectile are also conducted on the CFRP target plates. By combining these models with the test results simple semi-empirical expressions for estimating /predicting the perforation characteristics of these CFRP laminates are presented. The ballistic limit velocities estimated from the semi-empirical expression agree well with those obtained by applying the statistical approach to the test data. Comparison of the residual velocities also shows a fairly good agreement between those predicted from the expression and obtained from the impact tests.

### **Introduction**

Impact perforation of plates by projectiles covers a variety of protective structures in civil applications as well as in military ones. In the design of the protective structures, perforation characteristics is of critical importance and a most commonly used measure of the preventability of perforation is a ballistic limit velocity, which is the greatest projectile velocity the structure can resist the perforation. Therefore many investigations on the estimate of ballistic limit velocities have been made [1] and [2]. On the other hand, a residual velocity of a projectile after perforating a target plate is equally important, and so work on the prediction of residual velocity have also been done as much. Most of these have been concerned exclusively with concrete and metallic plates. In recent years, however, the attention is also being attracted to the fiber composite laminates such as glass, carbon, and aramid fiber reinforced plastic composites, since they are expected to be used in structural applications threatened by high velocity impact [3] - [5]. Recent works on impact perforation of fiber composite laminates struck by foreign objects traveling at high speed have been reviewed by the present author [6].

The purpose of this work is to examine the perforation characteristics of carbon fiber composite laminates struck by a steel ball projectile, both analytically and

---

H.Kasano, Department of Mechanical Systems Engineering, Takushoku University,  
815-1, Tate-machi, Hachioji City, Tokyo 193-0985, Japan

experimentally. Two analytical models are introduced. The first model is based solely on the energy conservation law, while the second on both the momentum and the energy ones. High velocity impact tests by a steel ball projectile are also conducted on the orthotropic and the quasi-isotropic CFRP composite laminates. By combining these models with the test results, simple semi-empirical expressions for estimating/predicting the perforation characteristics are presented.

## Perforation Mechanics

### General Expressions for Residual Velocity and Ballistic Limit Velocity

Consider a steel ball projectile impinging on a target plate and passing through it as shown in Fig. 1. A residual velocity  $V_R$  of the projectile after perforating the target plate is a function of many factors associated with a projectile, a target plate, and impact condition. Hence, in general, it may take the form of

$$V_R = F(a_1, a_2; V_i, \Psi) \quad (1)$$

in which,  $a_1$ : material properties of a projectile and a target plate,  $a_2$ : initial geometry of a projectile and a target plate,  $V_i$ : impact velocity of a projectile and  $\Psi$ : obliquity =  $(\phi, \theta)$ . A ballistic limit velocity  $V_b$  is another perforation characteristics and it is the velocity beyond which a specified projectile perforates a specified target plate and below which it will not. Hence, it is defined mathematically as follows:

$$V_b = \max \{V_i; V_R=0\} = \inf \{V_i; V_R>0\} \quad (2)$$

Thus, by putting  $V_R = 0$  and  $V_i = V_b$  in Eq.(1), we have

$$0 = F(a_1, a_2; V_b, \Psi)$$

and, from this equation, the ballistic limit velocity must have the following form:

$$V_b = G(a_1, a_2; \Psi) \quad (3)$$

The ballistic limit velocity given by Eq.(3) being regarded as one of the parameters affecting the residual velocity, the expression (1) may also be rewritten in the form

$$V_R = \bar{F}(a_1, a_2, V_b; V_i, \Psi) \quad (4)$$

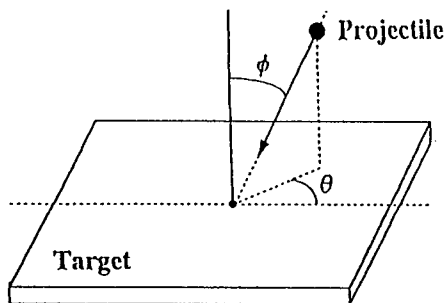


Figure 1 A Steel Ball Impinging on and Passing through a Target Plate

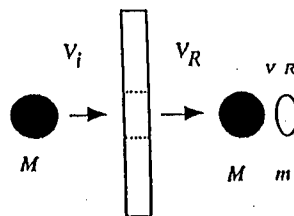


Figure 2 Perforation Process Accompanied by a Plate-fragment

### Governing Equations

For simplicity, we consider only a normal impact ( $\phi=0$ ) of a steel ball projectile on a target plate. The projectile is assumed here to pass through the plate accompanied by a plate-fragment as illustrated in Fig.2., in which  $V_i$ : impact velocity of a projectile,  $V_R$ : residual velocity of the projectile,  $v_R$ : flying velocity of the plate-fragment,  $M$ : mass of the projectile,  $m$ : mass of the fragment removed from the plate due to perforation. This perforation process is described by three fundamental conservation laws in the impact dynamics: conservation of mass, momentum, and energy. Since mass is assumed to be conserved in this system, the following two conservation laws provide the governing equations for the analysis:

$$MV_i = MV_R + m v_R + I \quad (5)$$

$$\frac{1}{2} MV_i^2 = \frac{1}{2} MV_R^2 + \frac{1}{2} m v_R^2 + E_p \quad (6)$$

in which  $I$ : impulse transmitted to the plate and  $E_p = E_p(V_i)$  total energy lost during the perforation process.

### Analytical Modelling

Two analytical models are introduced to estimate the ballistic limit velocity and predict the residual velocity for CFRP target plates. Model A employs the conservation law of energy alone, in which the perforation energy  $E_p$  is assumed to be independent of the impact velocity exceeding the ballistic limit velocity and it remains constant. Meanwhile, in Model B [7], the conservation laws of momentum and energy are used, where the perforation energy is separated into two parts, i.e., inelastic deformation energy  $E_{pf}$  associated with a free impact of a projectile and a target plate, and the shear deformation energy  $E_{ps}$  required for the removal of the fragment from the plate. The latter is also assumed to remain constant for the impact velocity greater than the ballistic limit velocity. These two models formally lead to the same expressions for estimating/predicting the ballistic limit velocity and the residual velocity as follows:

$$V_b = \sqrt{V_i^2 - V_R^2 / \alpha^2} \quad (7)$$

$$V_R = \alpha \sqrt{V_i^2 - V_b^2} \quad (8)$$

in which, the mass coefficient  $\alpha$  is given by

$$\alpha = \left( \frac{M}{M+m} \right)^{1/2} \quad \alpha = \frac{M}{M+m} \quad (9)$$

for Model A and B, respectively.

For a pair of  $V_i$  and  $V_R$  along with  $\alpha$  obtained from an impact test, the corresponding  $V_b$  is calculated from Eq.(7). A mean value of these  $V_b$ 's thus obtained for some different pairs of  $V_i$  and  $V_R$  can be regarded as an estimated ballistic limit velocity. The ballistic limit velocity being determined, the residual velocity is predicted from Eq.(8) as a function of the impact velocity.

## Target Materials and Impact Tests

### Target Materials

CFRP composite laminates are chosen as the target materials. The panels are first fabricated by laying up uni-directional carbon fiber prepreg sheets, where three kinds of stacking sequence are employed, and then they are cut into square plates of 90 mm by 90 mm. The orthotropic plates have the stacking sequence of  $[0/90/0]_n$ s, in which  $n=2$  and 3 are adopted in the impact tests. The quasi-isotropic plates, on the other hand, are of  $[0/+45/-45/90]_n$ s and  $[-60/0/60]_n$ s, where  $n=1, 2$ , and 3 are used. These plates are denoted by  $A_n$ ,  $B_n$ , and  $C_n$ , respectively. The plate-thickness ranges between 0.9 mm and 3.6 mm.

### Impact Testing Machine

Figure 3 shows a gas-gun type impact testing machine. A steel ball projectile of 5 mm in diameter and 0.51g by weight is propelled by releasing high pressurized nitrogen gas in a chamber and it impinges on a target plate. The testing machine is capable of firing the projectile at a maximum velocity of around 330 m/s. The impact velocity  $V_i$ , which is the velocity of the projectile just before impact is determined from the time of the projectile traveling between two specified points measured by a laser velocity detector located at the end of the barrel. The residual velocity  $V_R$  after perforating the target plate is also determined in a like manner by an infrared rays sensors located behind the plate.

### Test Procedure

The target plates are mounted in the fixture and struck normally by a steel ball projectile. The right and left edges are both clamped by the frames in the testing, while the upper and lower edges are free. The impact velocities vary between about 180m/s~280m/s for  $A_n$  plates, 120m/s~320m/s for  $B_n$  and  $C_n$  ones. For each test, an impact velocity  $V_i$ , the corresponding residual velocity  $V_R$ , and mass of the plate-fragment  $m$  are measured.

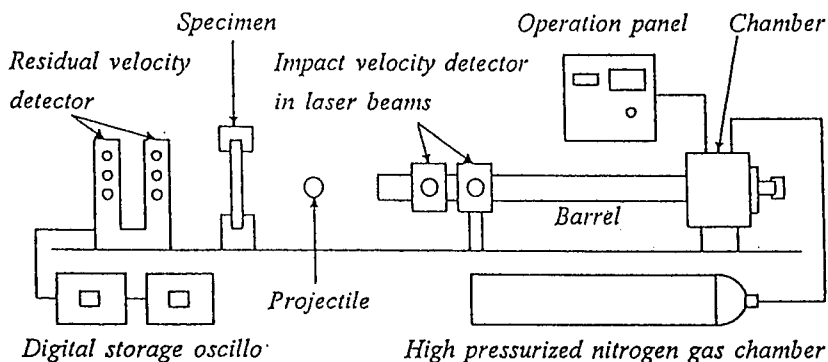
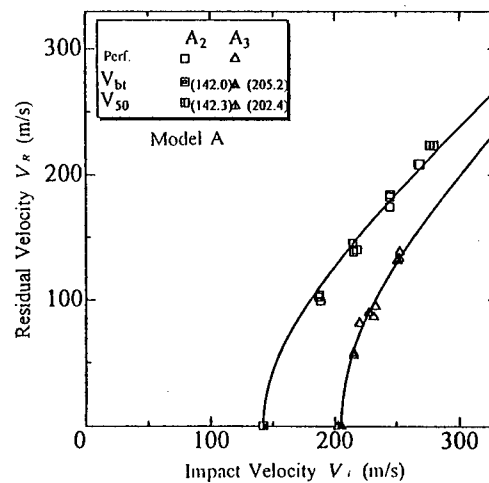


Figure 3 Schematic of Impact Testing Machine

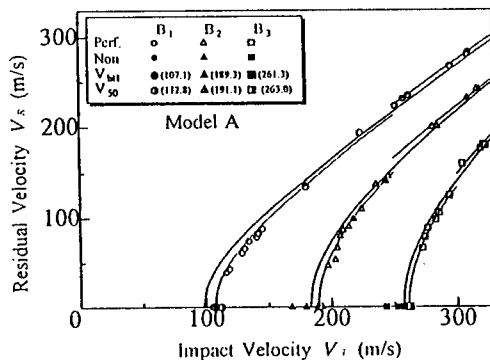
## Results and Discussions

Figure 4 shows the residual velocity as a function of impact velocity for the  $A_n$ ,  $B_n$ , and  $C_n$  target plates, in which the open symbols represent the experimental results. The residual velocity increases parabolically near at the ballistic limit velocity and then linearly increases with an increasing impact velocity. The ballistic limit velocities shown in the figures are obtained by substituting a pair of residual and impact velocities together with a mass coefficient into Eq.(7) and then by averaging the values thus obtained for some pairs of  $V_i$ ,  $V_R$ , and  $\alpha$ . In this way, a ballistic limit velocity is estimated for each target plate. The ballistic limit velocity being substituted into Eq.(8), the residual velocity is predicted for a given impact velocity. Solid lines represent the predictions from the semi-empirical expression for a residual velocity of a projectile when an impact velocity is given. Comparison of the predictions with the experimental results shows a fairly good agreement.

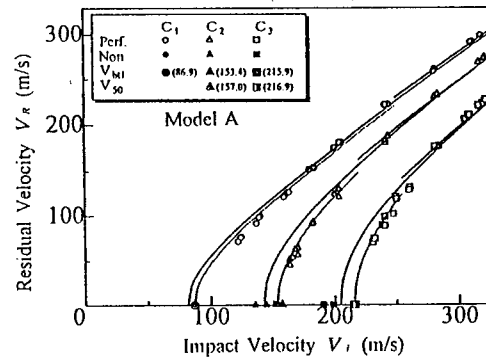
Figure 5 shows the total perforation energy  $E_p(V_i)$  lost during the perforation and the loss of the kinetic energy  $E_{p0}(V_i)$  of the projectile as a function of impact velocity. Both energies remain almost constant for the impact velocity exceeding and close to the ballistic limit velocity. As the impact velocity increases, however, the total perforation energy tends to slightly decrease, while the loss of the kinetic energy increases. This is more remarkable for quasi-isotropic  $B_n$  and  $C_n$  plates than orthotropic  $A_n$ . For further increased impact velocity, both energies come to an almost constant value again. This fact requires the modification of the analytical



(a)  $A_n$  Plate



(b)  $B_n$  Plate



(b)  $C_n$  Plate

Figure 4 Residual Velocity as a Function of Impact Velocity

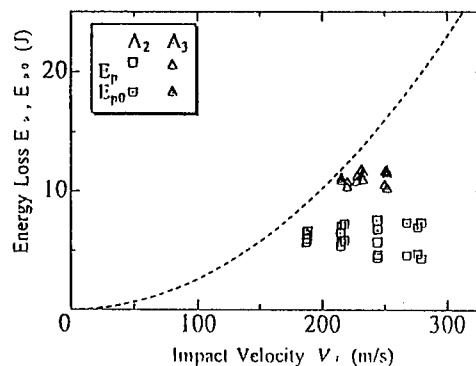
modeling, in which a constant total perforation energy is assumed for the impact velocity over the ballistic limit velocity. Therefore, the assumption is applied separately to the two impact velocity ranges close to and far away from the ballistic limit velocity. The ballistic limit velocities  $V_{bl1}$  shown in Figs. 4 (b) and (c) are those estimated from the modified analytical models for the impact velocity range close to the ballistic limit velocity. The ballistic limit velocity thus obtained is found to be in good agreement with  $V_{50}$ , i.e., that of a 50% probability of perforation, which is estimated by applying the statistical approach to the test data.

Figure 6 shows the variation of four kinds of ballistic limit velocities  $V_{bl}$ ,  $V_{bl1}$ ,  $V_{bl2}$ , and  $V_{50}$  with an increasing plate-thickness  $t$  for  $B_n$  and  $C_n$  plates, where  $V_{bl}$  is estimated from the analytical model and  $V_{bl2}$  from the modified one for impact velocity range far away from the ballistic limit velocity. All these ballistic limit velocities increase almost linearly with an increasing plate-thickness and  $V_{50}$  provides the greatest ballistic limit velocity followed by  $V_{bl1}$ ,  $V_{bl}$ , and  $V_{bl2}$  the smallest.

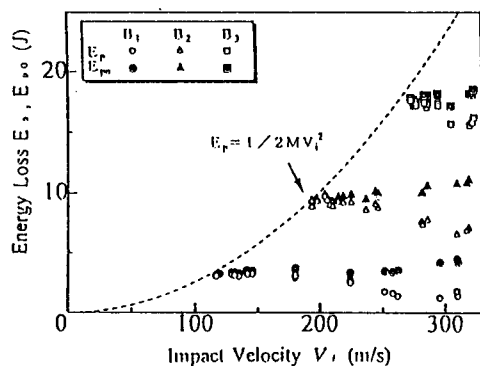
Figure 7 shows the comparison of ballistic limit velocities  $V_{bl}$  between two quasi-isotropic CFRP laminates with different stacking sequence ( $B_n$  and  $C_n$ ). Since both are almost the same, the difference of the stacking sequence in quasi-isotropic laminates is found to little affect the ballistic limit velocity. In addition, the ballistic limit velocities of the orthotropic laminates  $A_2$  and  $A_3$  are confirmed to be almost the same as those of  $B_n$  and  $C_n$  for the identical plate-thickness. The ballistic limit velocities of aluminium A5052 plates ( $A_{ln}$ ) and quasi-isotropic GFRP laminates ( $Gf_n$ ) are also shown in Fig. 7 for comparison [8].

## Conclusions

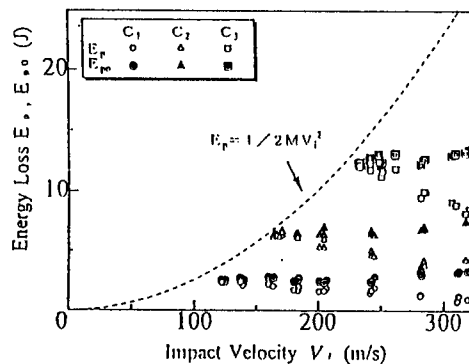
Perforation characteristics of the orthotropic and the quasi-isotropic carbon fiber composite target plates by a steel ball projectile have been investigated both experimentally and analytically. Two analytical models are introduced, i.e., one is model A based solely on the



(a)  $A_n$  Plate



(b)  $B_n$  Plate



(c)  $C_n$  Plate

Figure 5 Energy Loss as a Function of Impact Velocity



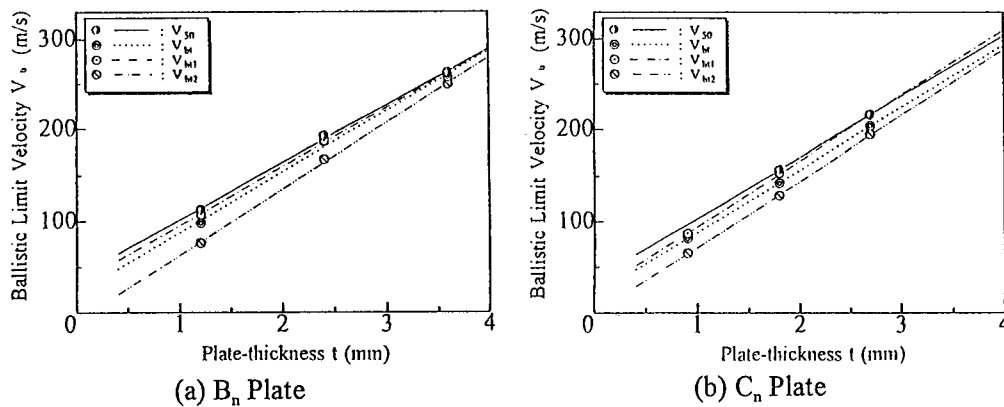


Figure 6 Four kinds of Ballistic Limit Velocities as a Function of Plate-thickness

conservation law of energy and the other model B based on the conservation laws of momentum and energy. By combining these models with the impact test results, simple semi-empirical expressions for estimating a ballistic limit velocity and predicting a residual velocity are obtained.

**Acknowledgements-** The author wishes to thank Messrs. Y.Okayasu and H.Arai for their assistance in conducting the experimental work and data reduction.

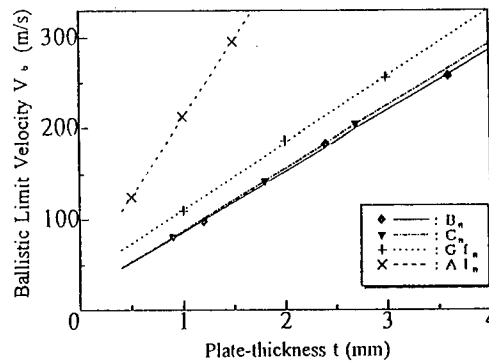


Figure 7 Comparison of Ballistic Limit Velocities for  $B_n$  and  $C_n$  Plates

## References

1. M.E.Backman and W.Goldsmith, 1978. "The Mechanics of Penetration of Projectiles into Targets." *Int. Journal of Engineering Science*, 16:1-99.
2. G.G.Corbett, S.R.Reid, and W.Johnson, 1996. "Impact Loading of Plates and Shells by Free-Flying Projectiles." *Int. Journal of Impact Engineering*, 18(2): 141-230
3. S.Abrate, 1991. "Impact of Laminated Composite Materials." *Applied Mechanics Review*. 44(4): 155-190.
4. S.Abrate, 1991. "Impact on Laminated Composites." *Applied Mechanics Review*. 47(11): 517-544.
5. S.Abrate, 1998. *Impact on Composite Structures*, Cambridge University Press.

6. H.Kasano, 1999. "Recent Advances in High-Velocity Impact Perforation of Fiber Composite Laminates." *JSME International Journal*, Series A, 42(2): 147-157.
7. R.F.Recht and T.W.Ipson, 1963. "Ballistic Perforation Dynamics." *Journal of Applied Mechanics*, 30: 384-390.
8. Unpublished

## **Damage Tolerant Behaviors of a Biomimetic CFRP Laminate**

Toshio Tanimoto

### **Abstract**

The present work examines the damage tolerant behaviors of synthetic composites by using composite architectures observed in biological materials. The static, impact, and compression after impact (CAI) behaviors of biomimetic CFRP laminates with stacking sequences similar to those found in animal hard tissues are compared to those of a standard quasi-isotropic and a cross-ply laminates.

The dependence of the extent of damage in the samples with a hole under tensile loading on the laminate lay-up was analyzed by a finite element analysis. The damage tolerance is then related to the actual damage extension from the hole perpendicularly to the applied load. It is shown that the damage tolerance of biomimetic laminate is more advantageous than the two other laminates. The implications of the findings for the design of damage-tolerant laminates are further discussed.

It is also shown from the results of compression after impact test that the sensitivity of biomimetic laminate to the presence of delamination damage is significantly lower than that of quasi-isotropic and cross-ply laminates.

### **Introduction**

Many biological materials have interesting specific properties. They could provide concepts to improve man-made fiber-reinforced composites [1]. Their microstructure, which is determined to a large extent by the nature of the constituent materials and biosynthesis, is believed to confer them superior specific properties and resistance to damage [2]. In order to do this, we need to clearly understand the strong as well as weak points of laminates with a biomimetic reinforced structure. Our previous work discussed the damage tolerance of a biomimetic laminate in terms of the extent of an equivalent damage zone, which depends on the architecture of the laminate [3].

This work examines the mechanical properties of a type of biomimetic composite laminate with fiber reinforcement architecture similar to that observed in biological materials such as fish scales or insect cuticles [1,4]. The static, impact, and compression after impact (CAI) behaviors of a biomimetic CFRP laminate are

---

Toshio Tanimoto, Shonan Institute of Technology, 1-1-25 Tsujido-Nishikaigan, Fujisawa 251-8511, Japan

compared to those of a standard quasi-isotropic and a cross-ply laminate. The sensitivity of a biomimetic laminate to the presence of a damage area, here modeled as an open hole, and compares the residual tensile strength and fracture patterns to those of conventional quasi-isotropic and a cross-ply laminates.

This paper also discusses the compression after impact (CAI) properties of the biomimetic laminate with delaminations of varying damage and compared to that of quasi-isotropic and cross-ply laminates.

### Specimen Preparation and Experimental Method

The fiber or fibril orientation in many biological laminates varies through the thickness of the material in steps that deviate from  $90^\circ$  by a fairly constant angle [2]. As such composite laminates often have a protective or structural function, it was assumed that their damage tolerance must be advantageous. Based on findings in the literature [1-5], a regular angle difference of  $78^\circ$  between successive plies was adopted for the biomimetic laminates in present study (Figure 1). This angle step gives laminates with a double helical layup and, in multiples of 16 plies, a quasi-isotropic elastic behavior.

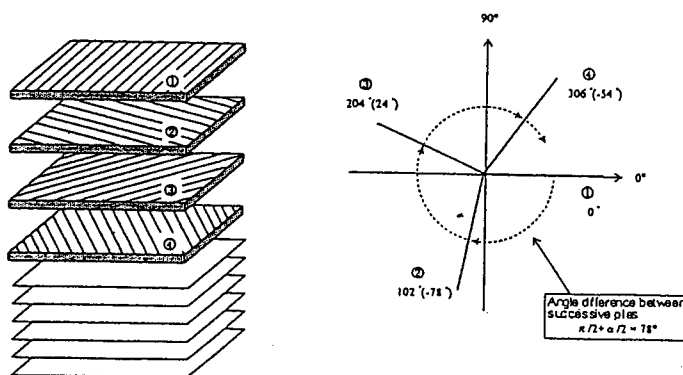


Figure 1 Lay-up Definition of the Biomimetic CFRP Laminate.

The samples were made from unidirectional (UD) AT400/EP carbon fiber-reinforced epoxy preregs (Asahi Kasei Corporation, Japan). The cured material had a longitudinal modulus of 117GPa and transverse modulus of about 11GPa. Laminated plates consisting of 16 plies of prepreg were cured in an autoclave at a pressure of 6bar and  $130^\circ\text{C}$  for two hours. The heating rate was  $2.5^\circ\text{C}/\text{min}$  and the samples were slow cooled under pressure by turning off the heat in the autoclave, in order to minimize internal stresses. The resulting laminates had a thickness of  $1.98\text{mm} \pm 0.06\text{mm}$ . The cured plates were cut into 20mm wide samples with a water-cooled rotary diamond saw. The test pieces were conditioned at room temperature and 65% humidity for two days or more prior to testing. The lay-ups of the samples for this study are given in Table I.

Table I Definition of Sample Types.

Designation	ID	Laminate Lay-up	$\theta^*$
Cross-ply	CP	L $[0/90]_{4S}$	90° (half plies)
		T $[90/0]_{4S}$	
Quasi-isotropic	QI	L $[0/+45/90/-45]_{2S}$	45° (half plies)
		T $[90/-45/0/45]_{2S}$	
Biomimetic	BM	L $[0/-78/24/-54/48/-30/72/-6/-84/18/-60/42/-36/66/-12/90]_T$	78° (24° for each helix)
		T $[90/12/-66/36/-42/60/-18/84/6/-72/30/-48/54/-24/78/0]_T$	

$\theta^*$  : Angle difference between plies

Tensile tests were performed on the samples without hole and with a central, 2.5mm, 4mm or 5mm diameter hole corresponding to a hole diameter to sample width ratio of 1/8, 1/5 and 1/4. The CFRP samples were clamped between two 5mm thick acrylic plates during drilling, in order to keep damage around the hole during machining to a minimum. The samples without and with a hole had a gauge length of 120mm and 80mm, respectively. Tapered GFRP tabs were bonded to the sample ends to reduce the likelihood of damage or slippage in the grips. The samples were tested in tension up to failure at crosshead speed of 1mm/min. The extension of plain samples was measured by strain gauges bonded to each side of the samples. The stress was calculated for the sample net cross-section. Failure loads were accepted only for samples which failed in the free gauge length.

The dimensions of the test specimens used for four-point bending were 15mm in width, 120mm in length and 2mm in thickness. The supporting span length was 80mm, while the loading span length was 40mm. The samples were tested at the constant speed of 2.5mm/min in four-point bending of a beam.

The static bending and tensile samples were cut out from two different direction of each laminate, longitudinal (L) and transverse (T) directions.

The impact tests were conducted at a speed of 4.4m/sec on a closed-loop electro-hydraulic impact testing machine. The impact load was applied with a 12.7mm diameter rod on the central portion of the 75mm x 75mm CFRP plates, in which the outside of 60mm diameter was clamped between steel plates by using four springs to give a constant force (Figure 2).

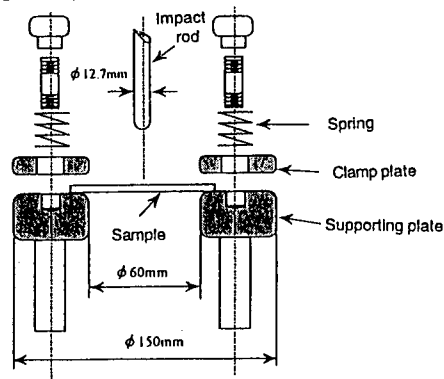


Figure 2 Penetration Impact Test Equipment.

## Experimental Results and Discussion

The biomimetic and the standard quasi-isotropic laminates had nearly the same fracture strength and elastic modulus in tension, while the cross-ply laminate was much stronger and stiffer [6]. The symmetric quasi-isotropic and cross-ply laminates had no extension/flexural coupling. All samples failed on the free length, away from the grips. The failed zones had different appearances. The cross-ply samples broke along a straight line, perpendicular to the sample's axis, and damage was localized in the vicinity of the fracture. On the other hand, the damaged area in the quasi-isotropic and biomimetic laminates extended over a length corresponding to more than twice the width of the tensile sample, and extensive splitting took place. The biomimetic laminate samples also failed in compression in the longer half of the broken sample, upon recoil at tensile failure. This may be due to a lower apparent compressive strength of the unsymmetric biomimetic laminate.

Table II Four-point Bending Properties of the Laminates Compared.

ID	Bending strength $\sigma_b$ [GPa]	Flexural rigidity EI [N·m <sup>2</sup> ]
CPL	1.21	1.77
CPT	0.88	1.44
QIL	0.91	1.35
QIT	0.68	0.74
BML	0.76	1.13
BMT	0.82	1.02

Table II compares the four-point bending properties among cross-ply (CP), conventional quasi-isotropic (QI) and biomimetic (BM) laminates. The bending strength and rigidity of the quasi-isotropic laminate are influenced remarkably by the directions of laminate, longitudinal (L) and transverse (T) directions. On the other hand, those of biomimetic laminate did not differ significantly, even if the sample was cut in the different direction from the laminate. This is more clearly observed in the load-deflection curves for three different laminates [6]. This indicates that the biomimetic laminate has an improved isotropic characteristic when compared with conventional quasi-isotropic laminate.

The static tensile strength of the biomimetic laminate with holes of varying diameter is compared to that of quasi-isotropic and cross-ply laminates. The first two have similar elastic moduli and strengths without a hole. The change of the strength ratio with an increase of hole diameter is compared in Figure 3 between quasi-isotropic and biomimetic laminates.

The strength ratio of quasi-isotropic sample is monotonically decreasing as the hole diameter increases within the present work, while the strength ratio of biomimetic sample becomes almost constant for the hole diameters beyond 2.5mm, independently of loading direction. The change of strength ratio with hole diameter in the longitudinal direction of quasi-isotropic sample is quite different from that in the transverse direction. The sensitivity of biomimetic laminate to the presence of a hole is significantly lower than that of quasi-isotropic laminate. The biomimetic laminate

has a higher resistance to the notch for the larger hole diameters than the quasi-isotropic and cross-ply laminates. The damage tolerance of the laminate depends apparently on the architecture of the laminate.

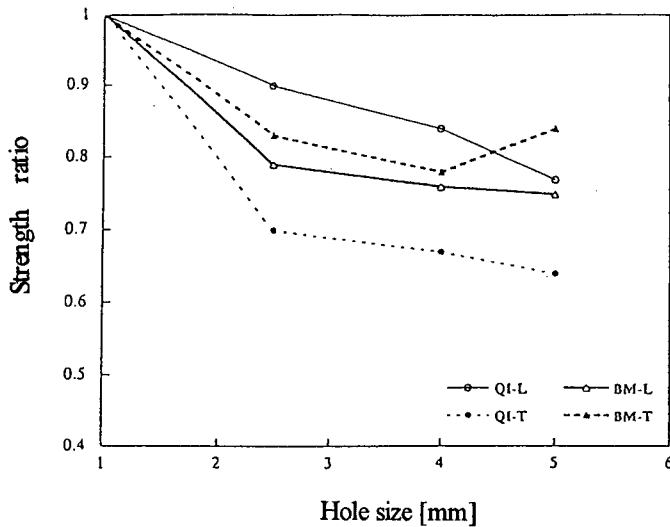


Figure 3 The Change of the Strength Ratio with Hole Diameter.

As a result of penetration impact test, the peak load and energy until peak load,  $U_{peak}$  as well for quasi-isotropic sample are slightly higher than those for biomimetic sample, while the cross-ply laminate has the lowest values (Table 3). The total energy until failure,  $U_{total}$  for biomimetic sample is almost the same as that for quasi-isotropic sample. Here, if a ductility index is defined as the ratio of energy after peak load,  $(U_{total} - U_{peak})$  to energy until peak load,  $U_{peak}$ , the ductility index value for biomimetic sample is the highest of all laminates investigated. It is very interesting to note that the load-deflection behavior of biomimetic laminate is more ductile than those of the two other laminates, while undergoing impact loading.

Table III Absorbed Energy during Impact and Calculated Ductility Index.

ID	Impact rate [m/s]	Maximum Load [kN]	$U_{total}$ [J]	$U_{peak}$ [J]	Ductility Index
CP	4.4	1.78	124	39	2.16
QI	4.4	1.95	152	58	1.63
BM	4.4	1.83	155	49	2.19

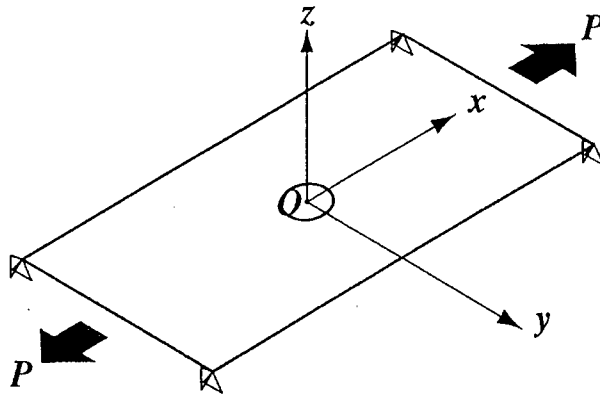


Figure 4 Finite Element Analysis.

The dependence of the extent of damage in the samples with a hole under tensile loading on the laminate lay-up was analyzed by a finite element analysis using a commercial FE code (see Figure 4). The damage tolerance is related to the actual damage extension from the hole perpendicularly to the applied load. The critical damage zone  $D^*$  was calculated as the ratio of damage zone size to the specimen width size,  $D/W$  at the ultimate load of the sample with a hole, as shown in Figure 5. This critical damage zone value is taken as an indicator of the damage tolerance of the laminate. A larger critical damage zone at failure means a higher damage tolerance. As can be compared in Table IV, the calculated critical damage zone  $D^*$  at failure load level for the samples with the  $\phi 4\text{mm}$  hole was about 47% larger in the biomimetic laminate than in the standard quasi-isotropic laminate. The value of  $D^*$  for the cross-ply laminate was the lowest, at less than 60% of the value for the biomimetic laminate. The higher value of  $D^*$  indicates a more extensive lateral propagation of the damage before failure of the sample. Whereas the cross-ply laminate fails catastrophically, the biomimetic laminate had a more extensive spatial distribution of the damage before final failure. The broader distribution of angles between plies and the loading direction is expected to lead a wider range of interlaminar shear stresses near edges and hole, and thus to a more progressive evolution of damage.

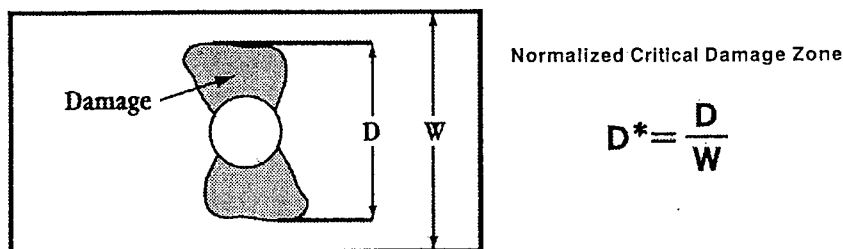
Figure 5 Critical Damage Zone  $D^*$ .



Table IV The Calculated Critical Damage Zone Value.

ID	D*
Cross-ply (CP)	0.500
Quasi-isotropic (QI)	0.571
Biomimetic (BM)	0.843

The compression after impact (CAI) properties of the biomimetic laminate with delaminations of varying damage is compared to that of quasi-isotropic and cross-ply T800H/3631 laminates. The change of the residual compressive strength with an increase of damage area is compared in Figure 6. The residual compressive strength for quasi-isotropic laminate and cross-ply laminate are monotonically decreasing as the damage area increases within the present work, and the rate of decreasing the residual strength for the biomimetic sample is apparently lower than that for the quasi-isotropic sample. In addition, the compressive strength of biomimetic laminate becomes almost constant for the damage area beyond 500mm<sup>2</sup>. The sensitivity of biomimetic laminate to the presence of delamination damage is significantly lower than that of quasi-isotropic laminate. The biomimetic laminate has a higher resistance to the impact damage than the quasi-isotropic and cross-ply laminates, particularly for the larger damage area. The damage tolerance of the laminate depends apparently on the architecture of the laminate.

As the biomimetic laminates have a more complex layup, an optimized design involves a tradeoff between performance and manufacturability.

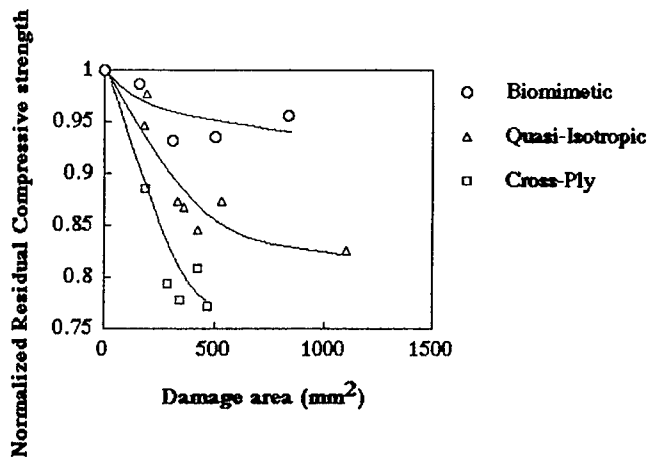


Figure 6 The Change of Residual Compressive Strength with Damage Area.

### Concluding Remarks

This paper presents results on the residual compressive strength properties of a biomimetic laminate after it has been impact damaged. It examines the sensitivity of a biomimetic laminate to the presence of a damage area, here modeled as a delaminated area. The sensitivity of biomimetic laminate to the presence of delamination damage is significantly lower than those of conventional quasi-isotropic and a cross-ply laminates. It is quite an important conclusion that the biomimetic laminate has a higher resistance to the impact damage, particularly for the larger damage area than the quasi-isotropic and cross-ply laminates. The damage tolerance of the laminate depends apparently on the architecture of the laminate.

Judging from the results of both the notched strength in tension and impact energy after reaching peak load, it is reasonable to consider that the damage tolerance of biomimetic laminate is better than that of the standard quasi-isotropic laminate.

The above-mentioned results obtained in the present work seem important issues for the actual design of damage-tolerant laminates in application to structures. As the biomimetic laminates have a more complex layup, an optimized design involves a tradeoff between performance and manufacturability.

### REFERENCES

1. Neville, A.C. 1993. *The Biology of Fibrous Composites: Development beyond the Cell Membrane*, Cambridge University Press.
2. Li, S., Zhang, R., Fu, S., Chen, X., Zhou, B., Zeng, Q. 1994. "A Biomimetic Model of Fiber-reinforced Composite Materials", *Journal of Materials Science and Technology*, Vol. 10, No.1, pp. 34-38.
3. Kim, P. and Tanimoto, T. 1997. "Damage Tolerance of Biomimetic Laminates", *Proceedings of the 11th International Conference on Composite Materials*, Vol. , pp. 10-15
4. Gunderson, S. L., Whitney, J. M. 1992. "A Controlled Unsymmetric Ply Orientation for Improved Isotropic Properties", *Advances in Experimental Mechanics*, ASME Vol. AMD-146, pp. 99-109.
5. Giraud, M. M., Castanet, J. 1978. Meunier, F. J., Bouligand, Y., "The fibrous Structure of Coelacanth Scales: A Twisted 'Plywood'", *Tissue and Cell*, Vol. 10, No. 4, pp. 671-686.
6. Tanimoto, T., Taguchi, M., Kim, P., 1998. "Mechanical Properties of Biomimetic CFRP Laminates", *Proceedings of the 8th US-Japan Conference on Composite Materials*, pp. 780-789.

# **Composites for Infrastructure, I**

---

## **The Application of Composites for the Rehabilitation of Concrete Bridge Infrastructure**

A. S. Crasto, R. Y. Kim, J. P. Mistretta

### **Abstract**

This paper describes recent efforts at the Materials Directorate of the U.S. Air Force Research Laboratory (AFRL) to demonstrate the feasibility of rehabilitating concrete beams in bridge decks with fiber-reinforced composites. Early work in this program built on the success in Europe in repairing bridge beams by bonding thin composite plates to their lower surfaces. Materials and processes were appropriately selected, validated with flexural tests on scaled-down and full-sized concrete beams and implemented in a vehicular bridge in the field. The durability of this rehabilitation scheme was evaluated from actual exposure in service. From the results emerged a novel concept, the use of composite rods (instead of plates), embedded in longitudinal grooves in the lower face of the beam to improve flexural strength and stiffness. In addition to improved affordability, convenience and performance, this approach provides the unique ability to rehabilitate *deteriorated* concrete beams, in service, without the necessity of strengthening or otherwise preparing the concrete. The results demonstrate the viability of this repair scheme.

### **Introduction**

With the institution of the interstate highway system in the U.S. in 1956, a large number of bridges were added to the national inventory. Many of these bridges are 40-50 years old (past their average life span) and in a state of disrepair. By one estimate [1], reconstruction of these bridges will average \$80 per square foot of deck area for a total of about \$200 billion in today's dollars. However, annual expenditures in this area are insufficient to overcome annual deterioration. This points to the need to repair or rehabilitate these aging bridges, thereby extending their useful lives and allowing staggered replacement in line with state or federal budgets. Rehabilitation itself is not inexpensive, and new and innovative materials, processes and designs are required to further lower costs.

Repair of concrete bridges has progressed from external post-tensioning and additional supports to flexural stiffening or strengthening of concrete beams with bonded steel plates. The advantages of the latter are lower cost, ease of application and maintenance, elimination of special anchorages, and the ability to strengthen the

---

A. S. Crasto and R. Y. Kim, University of Dayton Research Institute, 300 College Park, Dayton, OH 45469-0168, USA; J. P. Mistretta, AFRL/MLBC, Wright-Patterson AFB, OH 45433.

structure while it remains in use. The bonded plate serves as a second layer of reinforcement that can increase flexural strength by as much as 40% [2] and provide crack control for the concrete member. Corrosion at the steel/adhesive interface over time, however, results in deterioration in bond strength and reinforcing efficiency which led to a switch to carbon fiber-reinforced plastics (CFRP) as the reinforcing material of choice. CFRP offers distinct advantages over steel in this capacity with higher specific stiffness and strength, excellent durability in a saline environment, resistance to corrosion by acids and salts over a wide range of temperatures, and the ability to be tailored to provide the desired mechanical properties. Although much costlier than steel, composites have lighter weight and better corrosion resistance that can result in significant reductions in fabrication and long-term costs. Research in this area originated in the mid-eighties in Switzerland [3] and has continued to expand [4-6], with many commercial repair systems currently on the market.

Successful incorporation of nontraditional materials and processes (M&P) in the repair of concrete structures requires an interdisciplinary teaming effort between the M&P experts and the civil engineering industry. A second requirement is implementation of the technology in the field to evaluate its performance under actual service conditions. Accordingly, the AFRL Materials Directorate established a partnership with an architectural firm, Lockwood, Jones & Beals, Inc., the Butler County Engineer's Office in Ohio and the University of Dayton Research Institute to develop repair methodologies using fiber-reinforced composites and implement them in the field. This paper describes the results of those studies, including laboratory evaluations, scale-up to tests on full-sized beams, and field implementation.

### **Rehabilitation with Externally Bonded Composite Plates**

Unidirectional composite plates were fabricated from graphite/epoxy prepreg (AS4C/1919 from Hercules, Inc.) for this work, and the surfaces mechanically abraded to improve adhesion. For lab studies, the plates were bonded to 2.6-m x 46-cm x 15-cm deep construction-grade, steel-reinforced concrete beams with an ambient-cure, two-part epoxy adhesive (EA9460 from Dexter Hysol, Inc.). The relevant composite, concrete, adhesive and reinforcing steel properties are given in Table I. Since joints are both practical and necessary in field rehabilitation with composite plates, various joint configurations were evaluated before settling on a doubler joint. Each doubler joint had a minimum plate overlap of 15.2 cm and was constructed with the same adhesive used to bond the composite to concrete. The two-part adhesive was mixed in accordance with the manufacturer's instructions, applied to the beam's tensile surface, and overlaid with the composite plates. The entire plate area was then enclosed in a vacuum bag, sealed against the sides of the concrete beam and evacuated, to generate a pressure of approximately 82 kPa for a minimum of 24 hours. Bonding in this manner resulted in excellent adhesion, with the vacuum bag promoting intimate contact between adhesive and adherends during adhesive cure. Consequently, in all subsequent flexural testing, the composite plate did not peel away from the concrete beam up to final failure.

The composite-reinforced 2.6-m beams were tested in four-point flexure in accordance with ASTM C78-84, with leather pads between the loading pins and

beam to evenly distribute the applied load. Typical results, shown in Figure 1, demonstrate a substantial increase in beam stiffness and moment capacity with bonded composite plates. Failure in the control beam initiated via tensile cracks in the concrete and continued with yielding of the steel rebar. Failure in the plate-reinforced beam also initiated via tensile cracking of the concrete, albeit at higher loads. Subsequent failure depended on the cross-sectional area of composite plate and the location of the composite joint. This failure ranged from longitudinal splitting and partial fracture of the outer plate in the doubler joint followed instantaneously by its debonding from the inner plate in the joint, to compressive failure of the concrete followed by tensile fracture of the composite plate in the central region of the beam. These results provided guidance for the design and application of composite plates (with joints) in full-sized concrete bridge beams.

This rehabilitation technology was scaled up to tests on three 8.5-m beams. The beam dimensions and composite joint locations are shown in Figure 2. Beam 1 was the control beam. Beam 2 was flipped over for ease of bonding of the composite plates to its tensile surface, while composite plates were bonded overhead to the tensile surface of Beam 3 to simulate their application in the field. For convenience of bonding (in the field) the width of the plate was reduced for Beam 3; the plate cross-sectional area was maintained the same as in Beam 2, however, by adding another ply to the composite. Failure of Beam 1 under flexural loading occurred via yielding of the steel rebar at a bending moment of approximately 400 kN-m. Beyond this point the beam continued to deflect with no significant increase in bending moment, with the concrete eventually failing in compression at a maximum bending moment of 435 kN-m. Failure in Beam 2, reinforced with  $[0]_4$  composite plates, initiated via longitudinal splitting of the plate in the region of maximum bending moment. Ultimate failure was precipitated by fracture of the concrete in compression. This was followed instantaneously by failure via composite/composite debonding in the joint accompanied by failure in the concrete adjacent to the composite. This failure scenario confirms the existence of a strong bond between the concrete and composite. On the other hand, interfacial failure at a lap instead of composite tensile fracture (following concrete compressive failure) suggests the need to improve the composite/composite bond. Ultimate failure occurred at a maximum bending moment of 565 kN-m, representing a 30 percent increase in moment capacity over the control beam. The failure sequence in Beam 3 paralleled that observed in Beam 2 with two notable exceptions: ultimate failure was precipitated by debonding of the composite/composite lap (the reduced plate width results in a reduced lap area), and occurred at a lower maximum bending moment of 530 kN-m.

From a comparison of the flexural test data for these three beams (Figure 3), it is apparent that the ratio of composite to reinforced concrete utilized in this study did not enhance beam stiffness. It may be concluded from the results that due to the difficulty in working overhead with Beam 3, the application of adhesive and the adhesive bond obtained were not as efficient as with Beam 2, resulting in the observed failure in the composite lap joint instead of concrete compressive failure. Up until ultimate failure, however, no plate peeling was observed either at the ends of the plate or in the composite joints. These results validate the improvements seen in tests on the scaled-down concrete beams and provide the materials, process and design for an approach to the rehabilitation of concrete beams.

### Field Implementation of Plate Bonding

The technology developed in these lab studies was applied in the field to demonstrate the feasibility of strengthening concrete beams in a vehicular bridge deck. The bridge, on Fear Not Mills Road in Butler County, Ohio was built in 1994. It has a single span of 8.05 m and a width of 9.14 m, face to face of the rail, with a conventionally reinforced precast concrete box-beam superstructure and an asphalt wearing surface. The 10 box beams that comprise the deck are identical to those used in the scaled-up lab studies. Composite plates, identical to those employed in Beam 3, were bonded to each of the two exterior box beams of the bridge deck using doubler joints. The only difference from Beam 3 was an increase in the composite/composite lap length in the joint from 15.2 cm to 22.9 cm. The exterior box beams were selected since they receive the most severe exposure to the natural environment as well as to gasoline, oil, deicing chemicals, etc. The lower faces of the beams were sandblasted to remove the outer weak cement layer, followed by a high-pressure water wash. All aggregate projecting below the plane of the lower face was mechanically ground down. Composite plates were bonded as described earlier, with pressure during adhesive cure once again applied with a vacuum bag.

These rehabilitated beams were retained in service (with corresponding exposure to the elements, temperature fluctuations, deicing chemicals and static and dynamic loads) for one year. Over this period of time bond integrity was monitored using an acoustic tap-hammer technique to detect regions where the composite plate debonded from the adhesive layer. Measurements were made one, three and 10 months after the rehabilitation. The percentage of debonded area increased slightly with time from one to 10 months. After a year in service, one of these exterior was removed and tested in flexure under conditions identical to those used for Beam 3. A comparison of the test results is shown in Figure 4. As is evident from the plot, a year's exposure to the outdoor application environment (and the resulting increase in composite/adhesive debonded area) resulted in a minimal reduction in the maximum bending moment of the beam. The sequence of failure events was also similar to that of Beam 3. Post-failure examination of the composite/composite lap region revealed areas between composite and adhesive that were initially unbonded, in addition to those that debonded later, in service. This points to a need to optimize the plate bonding conditions to minimize such unbonded areas on adhesive cure. In five to six years from the rehabilitation date, the other plate-reinforced exterior beam will be similarly removed and tested.

### Rehabilitation with Embedded Composite Rods

Although composite reinforcement of aging infrastructure has demonstrated benefits, various materials, material forms and processes may be employed to this end. Initial attempts focused on bonding precured composite plates to the concrete, followed by the lay-up and *in-situ* cure of composite prepreg on the concrete member. There are a number of disadvantages to rehabilitating concrete bridge beams with composite *plate* reinforcement:

- Precured plates have to be fabricated in sizes that are practical and convenient to transport to the field, necessitating the development of strong, efficient plate joining techniques for beams with long spans.
- Plate reinforcement typically covers the entire lower surface of the rehabilitated concrete beam, restricting the drainage of absorbed water that may accumulate at the bondline, accelerating its degradation.
- Optimum bonding requires proper surface preparation and application of pressure during adhesive cure, to promote intimate contact between adhesive and adherends and minimize voids.
- Free-edge, thermal and residual stresses, in conjunction with the service environment, can promote plate debonding and consequent loss of reinforcing capability over time.

Some of these disadvantages can be overcome by using composite rods (of the same cross-sectional area as the plate) embedded in parallel, longitudinal grooves cut into the tensile face of the beam. Continuous lengths of pultruded rods can be transported to the field in rolls and cut to the necessary length, thereby avoiding composite joints. Since the rods cover a small fraction of the beam's lower surface, drainage of absorbed water is not hindered. The surface-to-volume ratio of a rod is substantially lower than for a plate; this, coupled with the fact that the rods are completely embedded in the adhesive makes them less susceptible to interfacial degradation in service. Pultruded rods are also less expensive to fabricate than precured composite plates and easier to employ in the field, requiring no pressure application during adhesive cure. This approach to use pultruded CFRP rods to strengthen structural members is the subject of a patent application by Lockwood, Jones and Beals, Inc. One disadvantage of this rehabilitation technique is the difficulty in cutting grooves on the lower surface of a concrete beam in the field.

Experiments were conducted with unidirectional, pultruded composite rods from DFI Pultruded Composites, Inc. The composite consists of a matrix of seven parts vinyl ester (Hetron 922HV) and one part polyester (Aropol 703) from Ashland Chemical Co., reinforced with T-300 PAN-based carbon fiber. Longitudinal rectangular grooves were machined on the lower faces of beams using a portable masonry cutter and lined with beads of the same epoxy adhesive used for plate bonding. Composite rods, the length of the beam, were sanded, wiped clean with acetone, and embedded in the epoxy within the grooves. The adhesive was then allowed to cure overnight under ambient conditions. In initial studies, four composite rods (with a total cross-sectional area of  $1.97 \text{ cm}^2$ ) were used in 2.6-m beams to replace the plate ( $1.45 \text{ cm}^2$  cross-sectional area) employed in earlier studies. The larger cross-sectional area of the rods was compensated by their closer proximity (in the grooves) to the beam's neutral axis. The test data for the two reinforcement types were similar. The failure modes, however, were different. Ultimate failure in both beams initiated with compression fracture of the concrete. In the plate-reinforced beam, secondary, catastrophic failure occurred almost instantaneously through composite fracture or composite/composite lap failure. In the rod-reinforced beam, however, secondary failure was noncatastrophic, with limited debonding and partial fracture of the embedded rods, allowing the beam to sustain the applied load with gradual deformation up to the limits of the test fixture. Total extension of the rods during loading did not exceed 1%, and post-failure



examination revealed no slippage of the rods at the ends of the beam. In this method of rehabilitation, machining the longitudinal grooves for the composite rods entails cutting through the steel stirrups that support the steel rebars during beam fabrication. However, this does not appear to adversely affect the mechanical performance of the beam in flexure.

The success with rod reinforcement of 2.6-m beams led to a scale-up of this reinforcing scheme to as-fabricated 8.5-m beams. Eleven composite rods (with a total cross-sectional area of  $5.43 \text{ cm}^2$ ) were embedded in parallel grooves equally spaced on the lower surface of the beam. This beam was tested in flexure, and the data are compared in Figure 5 with those from flexural tests on similar beams with plate reinforcement and without any composite reinforcement. The beam with rod reinforcement stacks up well against the beam with plate reinforcement, even though the comparison favors the latter because of its higher composite cross-sectional area ( $6.13 \text{ cm}^2$ ). For an equivalent or slightly larger rod area (to compensate for the closer proximity of the rods to the beam's neutral axis), the beam would have a significantly higher maximum bending moment (at ultimate failure) compared to a beam with plate reinforcement. This difference in maximum bending moments may be explained by the differences in failure modes. In the beam with plate reinforcement, premature composite/composite lap failure triggers ultimate failure of the beam; in the beam with rod reinforcement, the concrete fails first in compression, at a higher applied bending moment, followed by noncatastrophic secondary failure events (partial rod debonding and fracture).

In laboratory tests, rehabilitation with composites is generally evaluated on as-fabricated concrete beams or those subjected to controlled damage. Little work has been reported on the rehabilitation with composites of beams *aged in service* in which, in addition to mechanical damage, the constituent properties have been severely degraded. Any reinforcing scheme is only as good as its weakest link. The drawback with using external plate bonding to rehabilitate concrete beams deteriorated in service is that the plate is bonded to weakened concrete which becomes the locus of failure under flexural loading, at significantly lower bending moments than in virgin beams. Therefore, while laboratory tests demonstrate the efficacy of this rehabilitation scheme, the question remains as to whether weakened concrete severely undermines the reinforcing capacity of the bonded composite plate. In rehabilitation with embedded composite rods, on the other hand, this problem does not arise; grooves may be machined down to a depth at which the concrete has its original strength, and the composite rods embedded with adhesive in this sound concrete. This was the approach taken to evaluate this reinforcing concept with three 10.4-m beams recovered from a bridge deck, replaced after 80+ years in service.

All three beams cut from the concrete bridge deck were of slightly different dimensions, in different states of disrepair, and had different amounts of steel reinforcement. Consequently, it was not possible to use the results from the flexural testing of any one beam as a baseline for comparison. Grooves were therefore first machined in two of the beams. They were then preloaded in flexure to obtain a baseline, reinforced with composite rods, and then tested again in flexure to failure. Figure 6 shows a schematic of the cross section of one of the beams (Beam 3). Composite reinforcement for this beam consisted of two rods 15.9 mm in diameter, and two rods 19 mm in diameter, located as shown in the figure. The flexural test

data for this beam (the most deteriorated of the three beams) are displayed in Figure 7. This beam was loaded up to the first sign of steel yielding, as evidenced from the start of a knee in the corresponding load trace, then unloaded, and reinforced with the composite rods. As evidenced from the trace for the second loading, the rod-reinforcement results in a significant increase in flexural stiffness and an approximately 40 percent increase in maximum bending moment at which the steel yields. Ultimate failure is precipitated by compressive fracture of the concrete. This event is not catastrophic, however, and the beam continues to deflect while sustaining significant load. Post-failure examination revealed no slippage of the composite rods within the epoxy adhesive; secondary failure occurred in the concrete below the machined grooves and through partial fracture of the composite rods before the test was terminated. An interesting feature in the secondary failure process was the tensile fracture of an exposed steel rebar.

### Summary

Concrete bridge beams can be significantly strengthened by external reinforcement with fiber-reinforced composites. Composite rods, embedded in grooves in the beams' tensile faces offer several advantages over externally bonded composite plates, chief among which is the ability to use the former to rehabilitate deteriorated concrete.

### Acknowledgments

The authors gratefully wish to acknowledge contributions from the following, to this work: Mark Henderson of LJB Engineers and Architects, Inc.; Bill Ragland, Ron Cornwell, Chuck Fowler and Jim Lute of the University of Dayton Research Institute; Dave Hart and Larry Kretz of AFRL/FIBT; and Dean Foster of the Butler County Engineer's Office. This work was sponsored by the U.S. Air Force under Contract No. F33615-95-D-5029.

### References

1. N. H. Bettigole, "Rebuilding Our Bridges - Why and How," ASTM Standardization News (July 1994), pp. 24-27.
2. R. N. Swamy and R. Jones, "Plate Bonding Technology - The Painless Technique of Structural Rehabilitation," Proc. ACI Int. Conf., SP-128, Vol. II, American Concrete Institute, Detroit (1991).
3. H. P. Kaiser, "Strengthening of Reinforced Concrete with Epoxy-Bonded Carbon-Fiber Plastics," Doctoral Thesis, Diss. ETH No. 8918, ETH Zurich, Switzerland (1989).
4. U. Meier, et al., "Strengthening of Structures with CFRP Laminates: Research and Applications in Switzerland," in Advanced Composite Materials in Bridges

and Structures, K. W. Neale and P. Labossiere, eds., Canadian Society for Civil Engineering, Montreal, Canada (1991), p. 243.

5. H. Saadatmanesh and M. R. Ehsani, "Fiber Composite Plates can Strengthen Beams," Concrete International (Mar. 1990), pp. 65-71.
6. A. Sharif, et al., "Strengthening of Initially Loaded Reinforced Concrete Beams Using FRP Plates," ACI Structural Journal (Mar.-Apr. 1994), pp. 160-168.

TABLE I Material Properties for Concrete Test Beam Constituents.

Property	Composite Plate	Composite Rod	Steel Rebar	Concrete	Adhesive
Fiber volume, %	59	56	-	-	-
Yield stress, MPa	-	-	414	-	-
Tensile modulus, GPa	138	122	200	-	2.8
Tensile strength, MPa	1930	-	-	-	30
Ultimate strain, %	1.4	-	-	-	3.5
Flex. strength, MPa	-	1326	-	-	-
Compr. strength, MPa	-	-	-	5.1	-

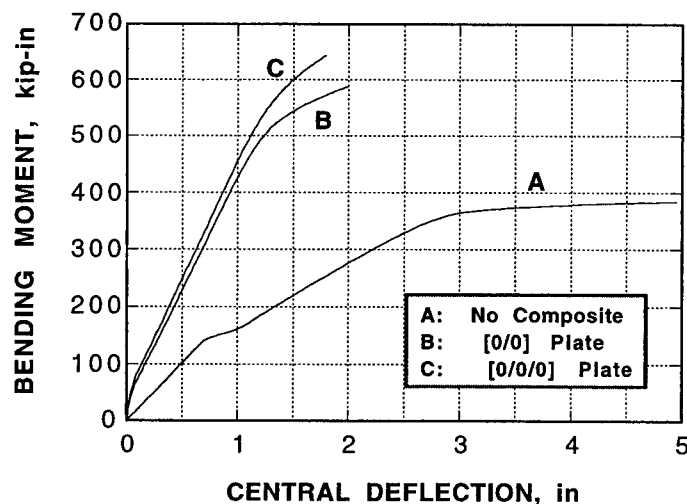


FIGURE 1. Bending moments vs. measured deflections of 2.6-m reinforced concrete beams with and without externally bonded composite plates.

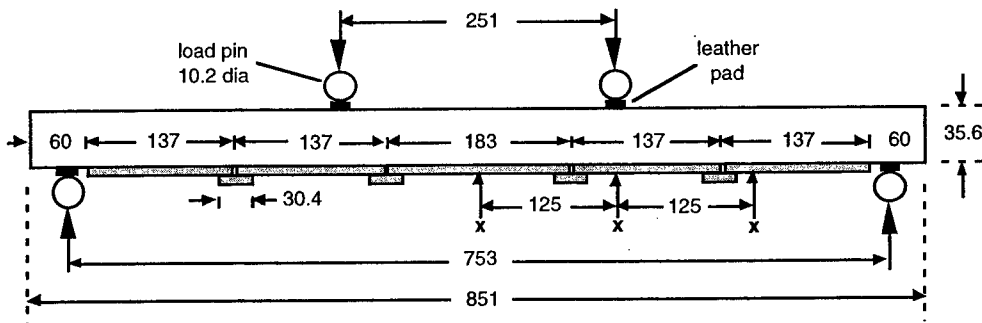


FIGURE 2. Experimental set-up for flexural testing of 8.5-m concrete beam with bonded composite plates (all dimensions in cm).

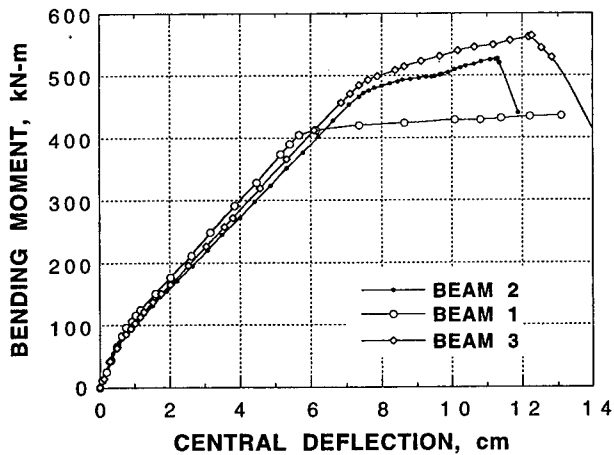


FIGURE 3. Bending moments of three 8.5-m reinforced concrete test beams vs. measured deflections. Beam 1: no composite reinforcement; Beam 2:  $[0]_4$  plate reinforcement; Beam 3:  $[0]_5$  plate reinforcement.

FIGURE 4. Comparison of maximum bending moments of 8.5-m concrete beams without external reinforcement, and with external composite plate reinforcement (unaged and aged for one year), vs. measured central deflections.

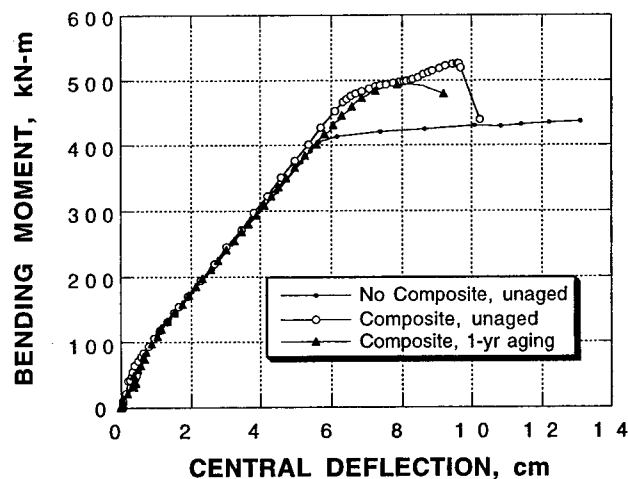


FIGURE 5. Comparison of maximum bending moments of 8.5-m concrete beams without external reinforcement, reinforced with composite plates, and reinforced with composite rods, vs. central deflections.

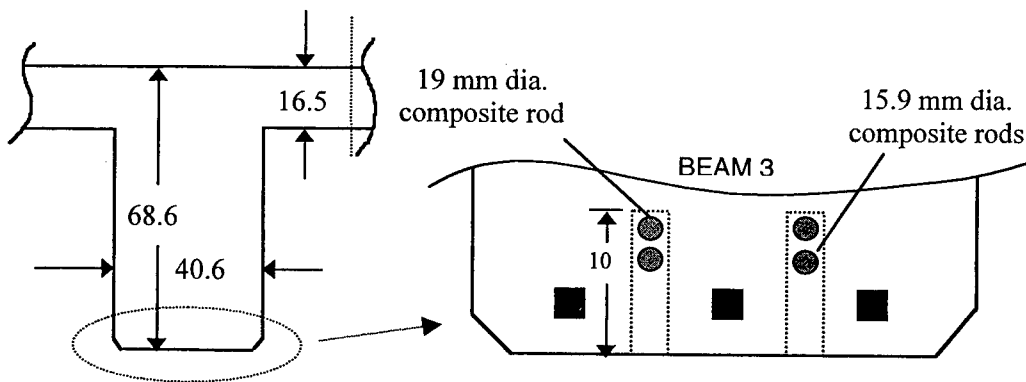
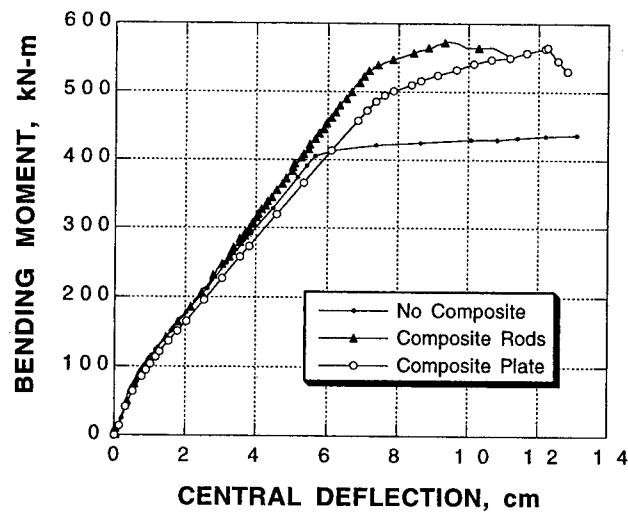
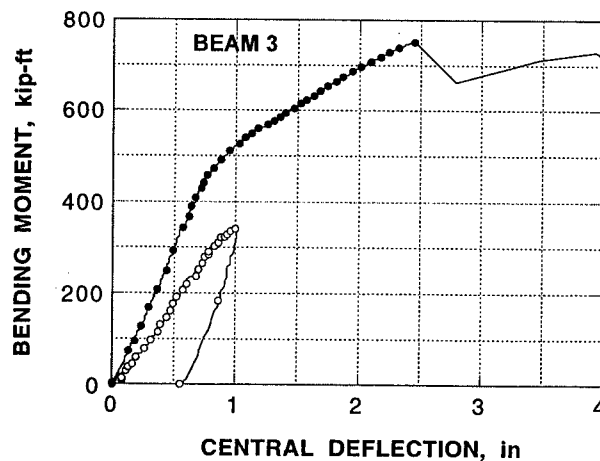


FIGURE 6. Schematic of Beam 3 from deteriorated bridge deck, tested in flexure. (Dimensions in cm)

FIGURE 7. Comparison of maximum bending moments of deteriorated 10.4-m concrete beams as functions of central deflections, shown before and after reinforcement with composite rods.



## **Composite Spoolable Tubulars**

**O. Ochoa**

### **Abstract**

The computational assessment of a composite spoolable tubular, under the typical working loads of a riser, and the bending loads due to storage is presented. Finite element models with axisymmetric geometry, material properties, and boundary conditions are utilized for the axial, pressure loads, and an axisymmetric model with nonaxisymmetric loads (Fourier series boundary conditions) is used for the bending analysis. The tube wall is composed of inner and outer polyethylene liners, hoop-wound glass/epoxy reinforcements within rubber cradles and an outer layer of unidirectional glass/epoxy layer. The analytical results are utilized to identify minimum spool radius with minor matrix cracking.

### **Analysis**

#### **Geometry and Loads**

The complex cross-sectional geometry is shown in Figure 1. The internal diameter of the tubular is 8 in. and the wall thickness is 1.8 in. The outermost unidirectional glass/epoxy layer provides axial support whereas the hoop wound layers support the pressure loads in the circumferential direction, and the rubber cradle segments optimize the tube flexural stiffness for storage on spools. The polyethylene (HDPE) serves as a protective layer from the harsh offshore environment.

The anticipated working field loads are 1,800 psi external pressure, 3,000 psi internal pressure, and an axial load of 500 kips. Furthermore, the tube undergoes bending while in storage on spools. The material properties and the strength allowables of the four constituents in the cylindrical coordinate system are presented in Tables I - II.

#### **Fully Axisymmetric Finite Element Analysis – Pressure and Axial Loads**

MARC commercial finite element software [1] is used to analyze the models, while MENTAT is utilized for pre- and post-processing. The MARC element number 28 with two degrees of freedom, the global axial displacement,  $w$ , and global radial

---

O. Ochoa, Department of Mechanical Engineering, Texas A&M University,  
MS 3123, College Station, Texas, 77843-3123, United States

displacement,  $u$ , at each node is utilized. A repeating unit of the cross-section is analyzed to infer the behavior throughout the tube since the pressure and axial loads induce stress states that are periodic along the length of the tube. Further simplification occurs due to symmetry and the final mesh is applied to a region which is 0.75" in axial length, with a 4" internal diameter and 5.8" external diameter as shown in Figure 2. The nodes at  $z = 0$ , along edge  $AD$ , are constrained in the axial direction.

#### Axisymmetric Finite Element Analysis with Nonaxisymmetric Loads (Bending)

Since in the case of a cylinder under bending, the geometry and material properties are axisymmetric, while the loads and resulting displacements are not, a Fourier series representation is incorporated. The MARC Fourier series element, number 62, is an eight-noded quadrilateral for axisymmetric geometry, but, unlike element 28, offers the option of boundary condition input described by a Fourier series. This element, which is utilized to model bending behavior in this study, has an extra degree of freedom at each node,  $v$ , describing the global circumferential displacement.

Axial displacements are again constrained along edge  $AD$  ( $w = 0$ ), as well as a single node constrained in the circumferential direction ( $v = 0$ ) at mid-length of  $AD$  to prevent rigid body motion. MARC element 62 does not allow the input of bending moments, therefore an axial traction,  $T$ , is applied so as to cause elongation in the tube above the neutral axis, and contraction below it, representing the equivalent moment in the tube. Multi-point displacement constraints are also applied to keep the loaded end planar. The traction load is specified with a one-term Fourier series,  $T = T_n \cos(\theta)$  and applied along edge  $BC$  of the model. The axial traction is distributed into a series of nodal forces, which for a constant tubular cross-sectional area, are related to the traction as

$$T = \sum_{j=1}^N F_j A \cos(\theta) \quad (1)$$

where  $F_j$  is the nodal force amplitudes,  $A$  is the cross-sectional area of the tube, and  $N$  is the number of nodes in the radial direction of the model. The distributed line load,  $q_j$ , that acts on a nodal circle of radius  $r_j$  is determined by

$$q_j = \frac{F_j}{2\pi r_j} \cos(\theta) \quad (2)$$

The distribution of a line load with cosine variation acting on a cylindrical ring imposes a moment couple about the plane that passes through  $\theta = \pi/2$  and  $\theta = 3\pi/2$  and is evaluated as

$$M = \sum_{j=1}^N F_j r_j \quad (3)$$

The nodal force amplitudes and radii of the nodes along the loaded edge of the model are obtained during post-processing, and are substituted into equation (3) to determine the bending moment acting on the tube.

## Results

The deformed shape obtained from the "fine" mesh model of the tube under the pressure and axial loading is shown in Figure 3. As denoted, the model elongated axially, and contracted through the thickness of the wall. The largest radial displacement occurred in the lower right hand corner of the model where the internal pressure is acting on the most compliant material, rubber. Some bending is observed in the hoop-wound glass regions, particularly in the vertical sections.

The ratio of the allowable stress to the local stress is evaluated for each region and are listed as the factor of safety in Table III. Note that in the hoop-wound region, a factor of safety of only 0.26 for tensile axial stress and 0.51 for tensile radial stress indicate transverse matrix cracking. This mode maybe eliminated if the tube is manufactured such that these sections are not bonded to each other, allowing interfacial slipping. The local bending in the hoop-wound glass introduces matrix cracking in the radial direction, indicating that its slenderness ratio may not be ideal.

## Bending

The radius of curvature in the tube is calculated and the curvature of the tube at the point of contact with the spool is considered to be the minimum bend radius and is equivalent to the radius of the spool. The initial case is a moment loading of  $8.97\text{e}5$  ft-lb which creates a curvature of 108 in. at the external radius of the tube, and therefore requires a spool radius,  $R_s$ , of 96 in.

Results are obtained for the planes  $\theta = 0$  and  $\theta = \pi$ , where the maximum axial extension and contraction occur respectively. The highest axial stress occurs in the unidirectional layer where the maximum magnitude is approximately 498 ksi, tensile in the  $\theta = 0$  plane and compressive in the  $\theta = \pi$  plane. A corresponding strength of materials calculation ( $\sigma_z = -E_z y / \rho$ ) provides a value of 469 ksi which is within approximately 6% of the finite element result. This value however is much larger than the 150 ksi strength allowable in tension and the 90 ksi allowable in compression leading to failure.

As a second case, the bending moment is scaled down. This reduction is proportional to the diameter of the spool used for storage. Thus, a moment of  $1.56\text{e}5$  ft-lb, which yields a spool radius of 578 in (48 ft), is selected for further analysis. The axial stress in the  $\theta = 0$  plane for this case,  $R_s = 578$  in. lead to maximum axial stress of 86.6 ksi. The global extension and rotation that occurs in bending is captured as well as local bending in the hoop-wound glass sections and the polyethylene liner. The rotation of the hoop-wound segment (HG) is compared in Figure 4, revealing that the local bending



under pressure and axial load is more severe than during combined pressure and axial load then during storage.

The stress distribution in the hoop-wound glass experiences stress concentrations due to local bending. The highest axial stresses in this region are approximately 26 ksi at the concentrated areas, but are less than 15 ksi elsewhere in the hoop-wound glass. Also the in-plane shear stress is highest in the hoop-wound glass sections. Axial stress in the unidirectional layer, 86.6 ksi maximum, is safely below the allowable strength of 150 ksi, giving a factor of safety of 1.73. The remaining factors of safety in plane  $\theta = 0$  are listed in Table 4.

## Conclusions

Finite element analysis with fully axisymmetric elements is used to assess the response of the composite tube subjected to pressure and axial loads. Bending response is studied with the addition of Fourier loading to the axisymmetric models. The two-dimensional fully axisymmetric analysis of the flexible composite tube subjected to combined pressure and axial loads revealed that the current design can withstand these loads with some matrix cracking in the hoop-wound glass layers. However, Fourier series analysis for bending loads due to storage on an 8 ft. spool radius revealed failure of the outer most unidirectional glass region of the tube. After further investigation, a spool radius of approximately 48 feet is suggested to eliminate this damage mode.

The finite element analysis techniques used allow simple input of properties and boundary conditions, and are very efficient in computational time. The Fourier models, in particular, are significant because bending behavior in tubes with complex material and geometric configurations can be effectively determined without complications introduced by three-dimensional analysis. As a result, these models are well suited for parametric studies with additional material systems and geometric changes. Incorporation of contact analysis, which would allow interfacial slip is necessary to adequately assess the load distribution within the tube wall.

## References

1. *MARC User's Manual, Vol. A and B. and MENTAT User's Guide*. Palo Alto, CA: MARC Analysis Research Corporation, 1994.
2. Chouchaoui, C. S., and Ochoa, O. O., "Similitude Study for Laminated Cylindrical Tube under Tension, Torsion, Bending, Internal and External Pressure; Part I: Governing Equations", *Composite Structures*, **44/4**, 1199, pp.221-229 and Part II: Scale Models", *Composite Structures*, **44/4**, 1999, pp.231-236
3. Judice, David, Composite Spoolable Tubulars, MS. Thesis, Texas A&M University, 1999

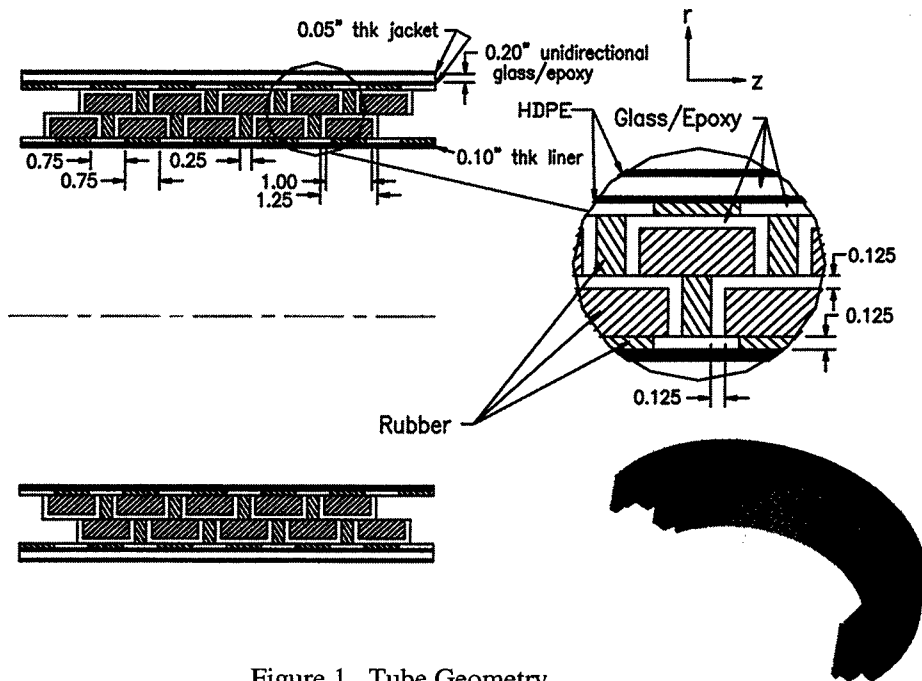


Figure 1. Tube Geometry

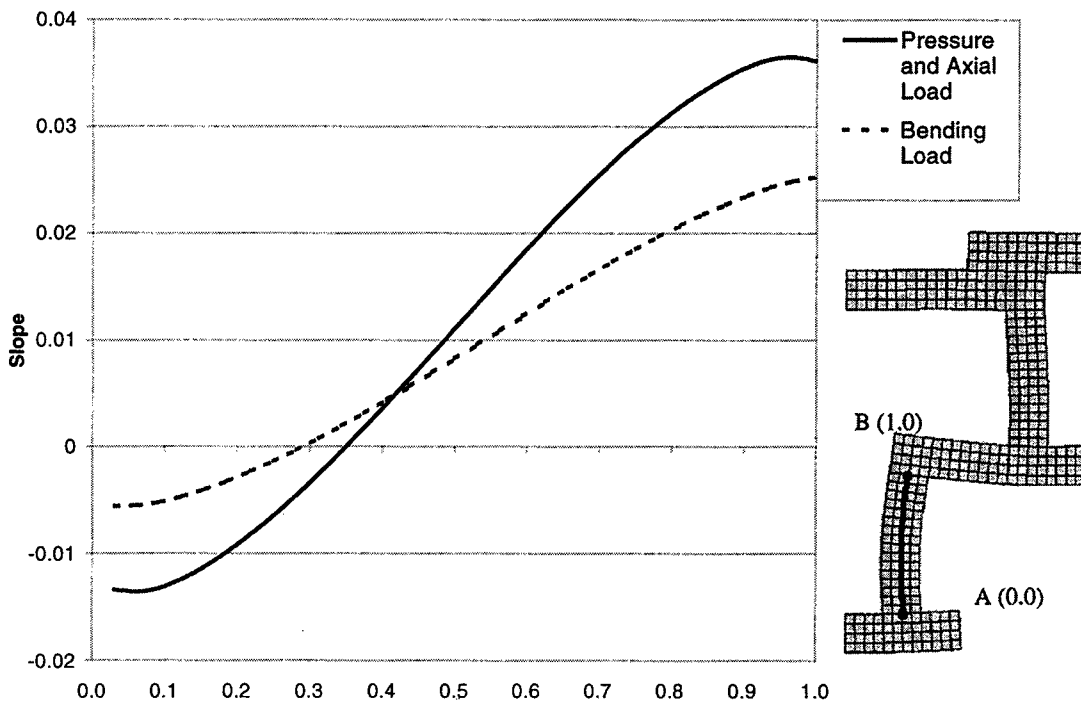


Figure 3. Slope along hoop-wound segment AB

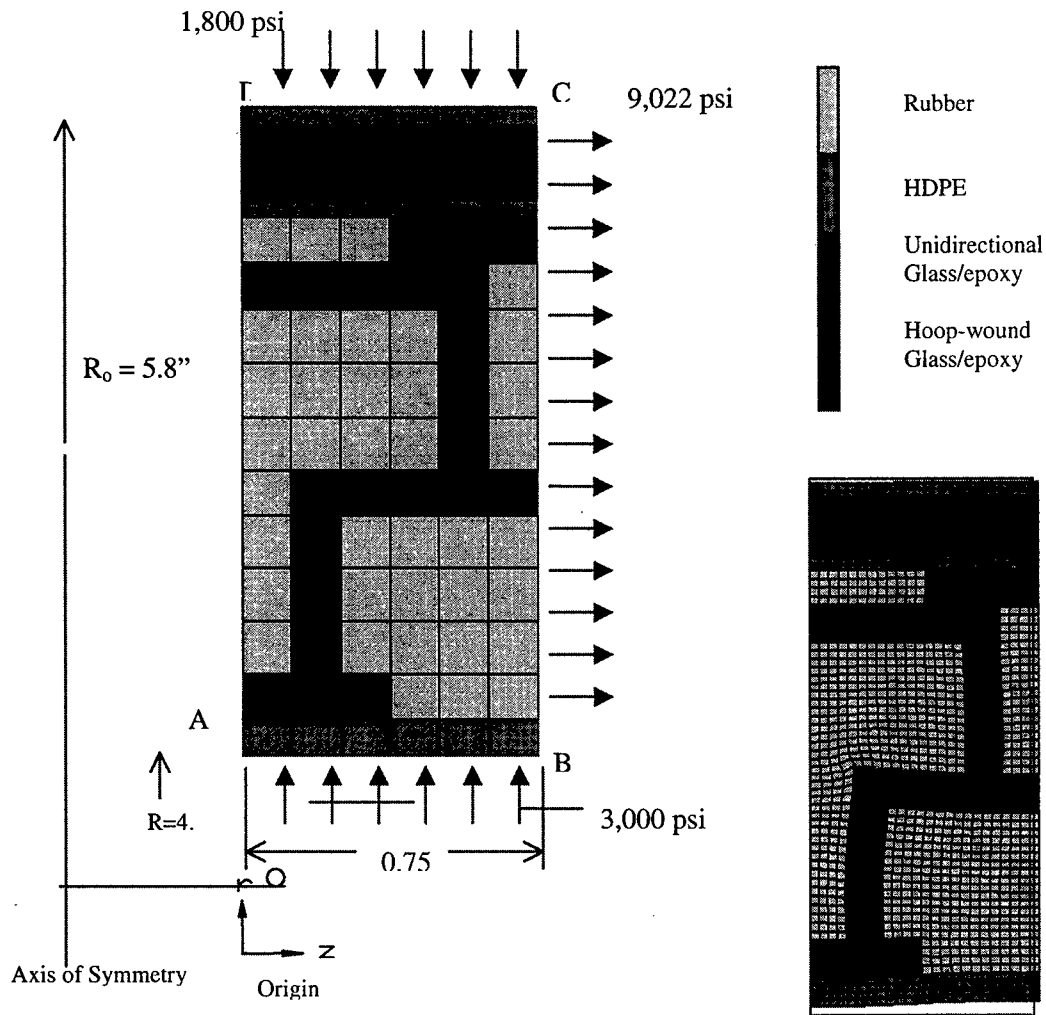


Figure 2. Fully Axisymmetric Finite Element Mesh and Loading

Table I Material Properties

<b>Isotropic:</b>	<b>E (psi)</b>	<b>v</b>							
Rubber	645	0.499 9							
Polyethylene	1.8 e5	0.4							
<b>Orthotropic:</b>	<b>E<sub>z</sub> (Msi)</b>	<b>E<sub>r</sub> (Msi)</b>	<b>E<sub>θ</sub> (Msi)</b>	<b>v<sub>zr</sub></b>	<b>v<sub>θz</sub></b>	<b>v<sub>rz</sub></b>	<b>G<sub>zr</sub> (Msi)</b>	<b>G<sub>zθ</sub> (Msi)</b>	<b>G<sub>rθ</sub> (Msi)</b>
Unidirectional glass/epoxy	8.336	1.657	1.657	0.273	0.0542	-0.309	0.633	0.633	0.633
Hoop-wound glass/epoxy	1.657	1.657	8.336	-0.309	0.273	0.0542	0.633	0.633	0.633

Table II Strength Allowables (ksi)

	<b>Rubber</b>	<b>HDPE</b>
Tensile	--	5.0
Compressive	--	7.9
Ultimate	3.5	--
	<b>Unidirectional Glass/Epoxy</b>	<b>Hoop Wound Glass/Epoxy</b>
Axial Tensile	150	7.0
Axial Compressive	90	20
Radial Tensile	7.0	7.0
Radial Compressive	20	20
Hoop Tensile	7.0	150
Hoop Compressive	20	90
In-plane Shear	9.0	9.0

Table III Factors of Safety for pressure and axial loads

	<b>Axial</b>	<b>Radial</b>	<b>Hoop</b>	<b>In-plane Shear</b>
Unidirectional Glass/Epoxy	1.98 (T)	4.16 (C)	1.60 (T)	7.11 (T) 6.75 (C)
Hoop Wound Glass/Epoxy	0.26 (T) 1.29 (C)	0.51 (T) 1.01 (C)	5.98 (T) 11.3 (C)	1.36 (T) 1.83 (C)
Rubber	1.10 (C)	1.10 (C)	1.10 (C)	94.6 (T) 109 (C)
HDPE	1.57 (T)	1.26 (C)	2.67 (T)	3.07 (C)

	2.87 (C)		2.15 (C)	
--	----------	--	----------	--

Table IV Factors of Safety for bending loads.

	<b>Axial</b>	<b>Radial</b>	<b>Hoop</b>	<b>In-plane Shear</b>
Unidirectional Glass/Epoxy	1.73 (T)	4.48 (T) 7.41 (C)	2.11 (T)	7.99 (T) 6.93 (C)
Hoop Wound Glass/Epoxy	0.27 (T) 2.21 (C)	0.77 (T) 1.75 (C)	18.6 (T) 8.16 (C)	1.64 (T) 2.61 (C)
Rubber	1.88 (T)	1.98 (T)	2.07 (T)	82.4 (T) 122 (C)
HDPE	1.45 (T) 7.40 (C)	2.74 (T) 2.36 (C)	3.13 (T) 4.81 (C)	5.72 (C)

\* (T) - Factor of Safety due to Tensile Stress

(C) - Factor of Safety due to Compressive Stress

## **Ductility of Reinforced Concrete Beams Externally Retrofitted with Carbon Fiber Polymer Composites**

Sarah E. Mouring<sup>1</sup>, Oscar Barton, Jr.<sup>2</sup>, and D. Kevin Simmons<sup>3</sup>

### **Abstract**

This study investigates the effect of externally bonded carbon fiber reinforced polymer (CFRP) laminates on the ductility of reinforced concrete beams used in the repair of damaged bridge structures. Reinforced concrete structures deteriorate over time due to environmental aging, fatigue, excessive loading, chemical attack, and other factors. Strengthening and rehabilitating these concrete structures by externally bonding carbon laminates is one of many economical engineering solutions. Eight rectangular beams with varying internal steel reinforcement were retrofitted with CFRP strips on the tension faces and tested under four-point bending. The beams were instrumented to monitor strains, deflection, and curvature over the entire spectrum of loading, and determine the structural response of the beams. An existing analytical model using the discrete yield and ultimate values of the load-deflection and moment-curvature curves was modified to an energy-based model, and used to predict the ductility of the beams. Numerical results indicated an increase in strength, a decrease in ductility, and validated the analytical model. Ultimately, this study will aid in the development of design guidelines governing the use of CFRP.

### **Introduction**

The application of fiber reinforced polymer (FRP) as external reinforcement to concrete infrastructure repair has received more attention from the Civil Engineering research community than any other engineering concern. A majority FRP research related to civil infrastructure is conducted in Europe and Japan where design codes governing FRP repair already exist. However, this trend is changing slowly with an increasing number of American researchers joining their European and Japanese counterparts in the investigation. Due to this increasing acceptance of FRP as external reinforcement, the American Concrete Institute (ACI) recently has formed Committee 440H tasked to develop a set of guidelines for design with FRP.

In the past two decades, several types of structures, including columns, slabs, and beams, have been retrofitted and tested with FRP. Researchers have reported

<sup>1</sup>Associate Professor, Dept. of Naval Architecture and Ocean Engineering, U.S. Naval Academy, Annapolis, MD, 21402, USA

<sup>2</sup>Associate Professor, Dept. of Mechanical Engineering, U.S. Naval Academy, Annapolis, MD, 21402, USA

<sup>3</sup>Graduate Student, Dept. of Civil and Environmental Engineering, Stanford University, Stanford, CA, 94305, USA

improvements in strength and stiffness of retrofitted members with some studies indicating that the shear and flexural strength of reinforced concrete beams can be increased by 20% to 100% with retrofitted CFRP sheets [1]. Many of the studies on strengthening effects have been both analytical and experimental investigations.

## **Background**

Extensive work has been conducted on the short-term response of concrete beams strengthened in flexure with FRP plates [2,3]. From these and other results, a pivotal belief was formed that given the superior properties of CFRP over other composites, CFRP offers the highest potential for strengthening concrete structures in most cases [3,4]. Studies also have confirmed that the use of epoxy for externally bonding the FRP reinforcement is more advantageous than typical mechanical bonding methods since nuts, bolts, and steel plates are vulnerable to environmental corrosion [5]. Other studies identified mid-span deflection and strain over the entire load spectrum as critical parameters for evaluating the response of a strengthened member [6]. Strain profiles can be used to calculate the stresses at various locations and are necessary to validate the assumptions of reinforced concrete beam flexure theory [7]. The four-point bending test has been shown to be the most appropriate for testing these types of hybrid beams[6,8].

A critical evaluation of the research data shows that there are still many aspects of material and structural behavior arising from the use of FRP that are not yet clearly understood. One such issue is the ductility of retrofitted reinforced concrete beams. Several recent studies, including one by the authors, have examined this topic [9,10,11]. This paper outlines the analytical and experimental study performed by the authors.

## **Experimental Methodology**

A series of eight reinforced concrete beams were designed to represent typical in-service reinforced concrete beams. Standard construction techniques were closely followed and the quality of the constructed beams closely mirrored normal construction standards. All beams had identical nominal dimensions. Each beam was 9½ ft (2.896m) in length, 6 in (1500mm) in width, and had an 18 in (4500mm) nominal depth. The internal longitudinal flexural reinforcement was varied for the beams from #4 to #9 re-bar, but the vertical shear reinforcement had a constant stirrup arrangement designed to minimize the possible occurrence of a transverse shear-induced failure (see Table I). Varying the internal reinforcement while maintaining constant CFRP properties provided a mechanism of accessing the effect of the bonded sheet on the performance of the hybrid beam.

Table I Beam Specimen Designation and Details

Beam	Longitudinal Reinforcement				CFRP Type	No. of Strips
	Number of Re-bars	Size of Re-bars	Area of Steel (in <sup>2</sup> )	Reinforcement Ratio (%)		
4A	2	#4	0.40	0.404	S512	1
4B	2	#4	0.40	0.404	S812	1
5	2	#5	0.62	0.626	S512	1
6	2	#6	0.88	0.889	S512	1
7	2	#7	1.20	1.212	S512	1
8	2	#8	1.58	1.596	S512	1
9A	2	#9	2.00	2.020	S512	0
9B	2	#9	2.00	2.020	S512	1

Each beam was tested under four-point bending. Unique to this test configuration was that the beam was mounted so that its tension face was located on the top rather than the bottom. This allowed ease of access to this surface for the in-situ repair. The constant moment region was three feet under this configuration. This region was more than adequate for strain and displacement instrumentation.

Each beam was instrumented with three vertical linear variable displacement transducers (LVDT's) in contact with the tension face. One at mid-span and two directly under the outer load points. These LVDT's provided the essential data for computing the curvature of the beam. In addition, the concrete beam, CFRP sheet, and steel re-bars were instrumented with strain gages. Recording the strain measurements in these materials allowed one to check the strain compatibility and validate Hooke's Law. Finally, eight LVDT's were mounted horizontally on the sides of each beam, at the mid-span, and provided measurements to compute through-the-thickness strain distribution.

Testing consisted of several steps. First the beam was loaded to initial cracking. After reaching this load, the CFRP sheet was bonded to the tension face of the beam. The bonding of the sheet was performed under load. Loading then was resumed until visible failure of each beam was reached. The parameters of interest included mid-span deflection, strains in concrete and CFRP laminate sheets, and ultimate moment capacity. A digital data-acquisition system was used to monitor loading, mid-span deflection, and deformations in the concrete and in the reinforcement.

Figures 1 and 2 represent load-deflection and moment-curvature results for beam 4A. For this beam, the maximum bending moment at failure was computed as 75.41 kip-ft. Similar results were determined for the remaining beams.



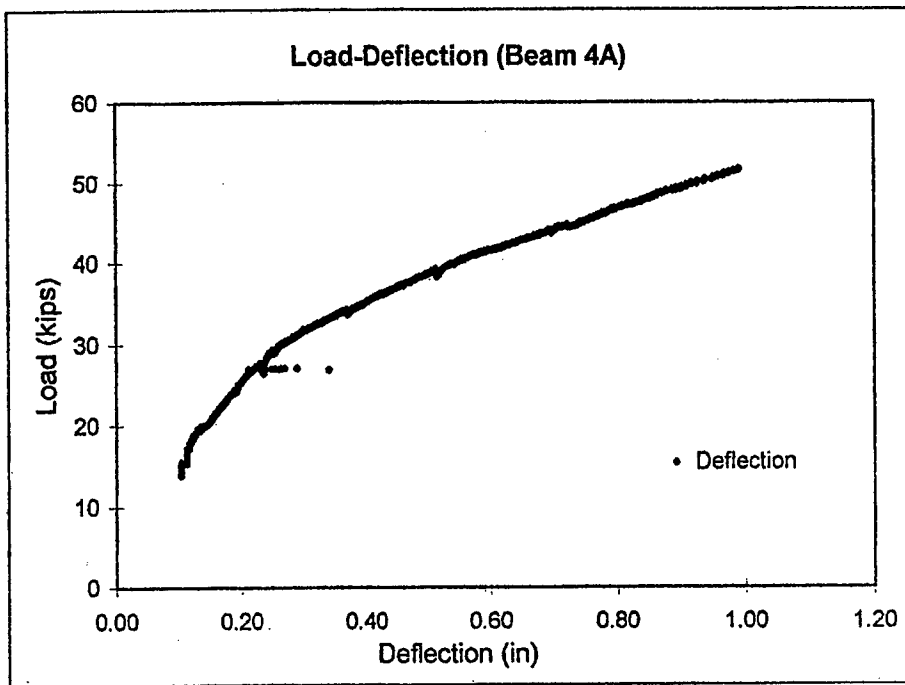


Figure 1 Typical Load-Deflection Curve

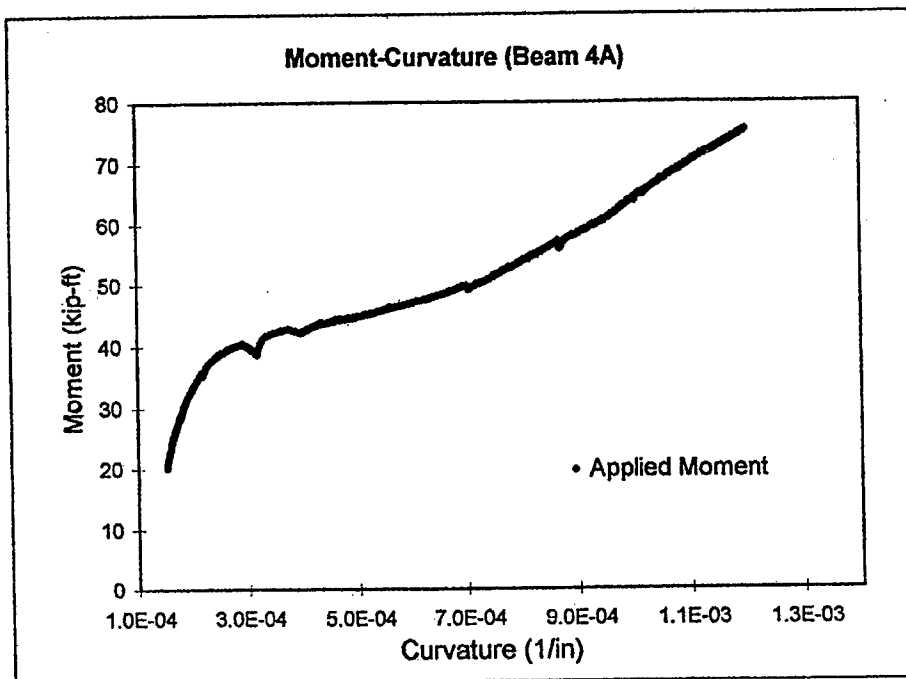


Figure 2 Typical Moment-Curvature Curve

### Analytical Methodology

In order to predict the mode of failure the reinforcement ratio,  $\rho$ , needs to be calculated. As prescribed by ACI 318-95 10.2.7.3, the reinforcement ratio is given by :

$$\rho = \frac{A_s}{bd} \quad (1)$$

where  $A_s$  is the area of steel,  $b$  is the beam nominal width, and  $d$  is the beam effective depth. However, this definition for  $\rho$  is inadequate for reinforced concrete beams with externally bonded CFRP sheets. For these beams, one must account for the area of the CFRP. Therefore, introduce  $A_c$ . Now the reinforcement ratio becomes  $\rho^*$ , and is termed the adjusted reinforcement ratio. It accounts for the difference between the ultimate strength of CFRP and the yield strength of steel by adjusting the area of steel used in the calculation of the reinforcement ratio. The adjusted area of steel,  $A_s^*$ , should be calculated as follows:

$$A_s^* = A_s + n\alpha A_c \quad (2)$$

The compositeness reduction factor,  $\alpha$ , indicates the degree of composite action predicted for the externally applied CFRP laminate, and was chosen to be 0.7 in this study. The composite-to-steel weighting factor,  $n$ , is given by:

$$n = \frac{f_{ult \text{ composite}}}{f_{y \text{ steel}}} \quad (3)$$

where  $f_{y \text{ steel}}$  is the steel yield strength and  $f_{ult \text{ composite}}$  is the composite ultimate strength. Replacing the area of steel with the adjusted area of steel gives  $\rho^*$  as:

$$\rho^* = \frac{A_s^*}{bd} \quad (4)$$

In order to predict the ductility of the beams, an existing analytical model by Spadea, Bencardino, and Swamy [12] using the discrete yield and ultimate values of the load-deflection ( $P-\Delta$ ) and moment-curvature ( $M-\phi$ ) curves was modified to an energy-based model. The modified model evaluates the ductility in terms of the energy at these two points. The energy is the area under the curves at these points. The modified deflection ductility index,  $\mu_\Delta$ , calculated from the load-deflection curve and modified curvature ductility index,  $\mu_\phi$ , calculated from the moment-curvature curve are given as:

$$\mu_{\Delta} = \frac{\int_0^{\text{ultimate}} P(\Delta) d\Delta}{\int_0^{\text{yield}} P(\Delta) d\Delta} \quad (5)$$

$$\mu_{\phi} = \frac{\int_0^{\text{ultimate}} M(\phi) d\phi}{\int_0^{\text{yield}} M(\phi) d\phi} \quad (6)$$

## Discussion and Results

The results of the reinforcement ratio calculations and the predicted modes of failure for the specimens are shown in Table II. The modes of failure were predicted by comparing the adjusted reinforcement ratio,  $\rho^*$ , to the maximum design reinforcement ratio,  $\rho_{max}$ , as specified by ACI Code. (Note:  $\rho_{max}$  is 75% of balanced reinforcement ratio,  $\rho_{balanced}$ .) Since  $\rho^*$  did not exceed  $\rho_{max}$  for any of the beams, a typical tension failure by yielding of steel was predicted for the beams. These predicted modes compared well to the observed failure modes given in Table II. The only difference was found in the results of Beam 9B. Beam 9B displayed a semi-brittle collapse that can be termed as a tension/balanced failure. This data, more than any other, shows the possible dangers associated with CFRP retrofit. As a result of adding CFRP, Beam 9B experienced a change in failure mode from tension to balanced. This is an undesirable sudden concrete compressive failure.

Table II Experimental and Analytical Results

Beam	$\rho^*$	$\rho_{max}$	Predicted Failure	Observed Failure	$\mu_{\Delta}$	$\mu_{\phi}$
4A	0.0078	0.0283	Tension	Tension	5.67	10.2
4B	0.0102	0.0283	Tension	Tension	5.63	7.63
5	0.0101	0.0283	Tension	Tension	3.50	8.94
6	0.0127	0.0283	Tension	Tension	3.77	8.24
7	0.0159	0.0283	Tension	Tension	--	7.81
8	0.0198	0.0283	Tension	Tension	2.55	2.82
9A	0.0202	0.0283	Tension	Tension	1.93	2.05
9B	0.0240	0.0283	Tension	Tension/Balanced	1.60	1.59

Computed ductility indices for deflection and curvature cases also are given in Table II. As expected, the control beam, 9A, which displayed a typical tension failure, had a ductility index greater than 1. Beam 9B experienced an almost balanced failure and correspondingly had a lower ductility index. Beams 4A and 4B, which had the

lowest laminated reinforcement ratios, displayed the most ductile behavior. These beams showed increases in flexural capacity while retaining significant ductile qualities.

As reinforcement ratio increases, the ductility indices decrease. This is because the beam is becoming stiffer as more steel or carbon is added and after the steel has yielded, this stiffness limits the amount of deflection and curvature possible. The reinforcement ratio is approaching the balanced condition when no deflection after yield occurs.

Another observation shows that as the laminate percentage of total reinforcement increases, the ductility indices decrease. The CFRP laminate accounted for 23.3% and 37.3% of the total tensile reinforcement in Beams 4A and 4B, respectively, while for Beams 9A and 9B, the CFRP contribution was 0% and 4.7%, respectively. In both cases, the increases in CFRP contribution corresponded to a decrease in ductility.

Deflection and curvature ductility indices appear to follow similar trends. The curvature ductility index is greater than the deflection ductility index for all beams except Beam 9B, where the values are essentially the same. The differences in these two ductility indices range from as low as 10.85% for Beam 9A to a high of 60.85% for Beam 5. This shows the unpredictable behavior of retrofitted beams and reinforces the need for an increased understanding of the behavior of such beams.

## Conclusions

Several conclusions were drawn from this research: 1) bonding of CFRP composites to damaged reinforced concrete beams is a viable technology for repair, 2) strengthening technology is easy to perform and results in significant improvements in ultimate load capacity, 3) existing ACI guidelines do not accurately model the experimental behavior of CFRP retrofitted concrete beams; however, minor modifications to account for the strength and constituent behavior of CFRP enable reasonably accurate predictions to be made, 4) energy-based definition of ductility better assesses the ductile behavior of reinforced concrete beams than traditional discrete-based definitions, and 5) the use of CFRP as external reinforcement reduces the ductility of an under-reinforced concrete beam, but it is possible to design beams with FRP that still exhibit ductile failure by ensuring that the reinforcement ratio of the retrofitted beam does not exceed the balanced reinforcement ratio.

## Acknowledgments

The experimental research outlined herein was supported, in part, by the Structures Division of the Building and Fire Research Laboratory of National Institute of Standards and Technology (NIST).

## References

1. Norris, T., Saadatmanesh, H., and Ehsani, M. (1997). "Shear and Flexural Strengthening of R/C Beams with Carbon Fiber Sheets". *J. Struct. Engrg.* 123(6), 903-911.
2. Saadatmanesh, H., and Ehsani, M.R. (1991). "Analytical Study of Concrete Girders Retrofitted with Epoxy-Bonded Composite Laminates". *J. Struct. Engrg.*, ASCE 117(11), 3434-3455.
3. Ritchie, P., Thomas, D., Lu, L., and Connelly, M., (1991). "External Reinforcement of Concrete Beams using Fiber Reinforced Plastics". *ACI Struct. J.*, 88(4), 490-500.
4. An, W., Saadatmanesh, H., and Ehsani, M. (1991). "ARC Beams Strengthened with FRP Plates. II: Analysis and Parametric Study". *J. Struct. Engrg.*, 117(11), 3434-3455.
5. Deskovic, N., and Triantafillou, T.C., (1995). "Innovative Design on FRP Combined with Concrete: Short-term behavior." *J. Struct. Engrg.*, ASCE, 127(7), 1069-1078.
6. Buyukozturk, O., and Hearing, B., (1998). "Failure Behavior of Precracked Concrete Beams Retrofitted with FRP". *J. Comp. Constr.*, 2(3), 138-144.
7. Spadea, G., Bencardino, F., and Swamy, R. N. (1998). "A Structural Behavior of Composite RC Beams with Externally Bonded CFRP". *J. Compos. Constr.*, 2(3), 132-137.
8. GangaRao, H. V. S., and Faza, S. (1991). "A Bending and Bond Behavior and Design of Concrete Beams Reinforced with Fiber Reinforced Plastic Rebars". *Final Report to Federal Highway Administration*, West Virginia Univ.
9. Uy, B., and Bradford, M.A. (1995). "Ductility of Profiled Composite Beams. Part II: Analytical Study." *J. Struct. Engrg.*, ASCE, 121(5), 883-889.
10. GangaRao, H.V.S., and Vijay, P. V. (1998). "Bending Behavior of Concrete Beams Wrapped with Carbon Fabric." *J. Struct. Engrg.* 124(1), 3-10.
11. Simmons, D., Mouring, S., and Barton, O. (1999) "The Effect of Externally Retrofitted Carbon Fiber Reinforced Polymer Composites on the Ductility of Reinforced Concrete Beams", *USNA Trident Report No. 268*, U.S. Naval Academy.
12. Spadea, G., Bencardino, F., and Swamy, R. N. (1998). "A Structural Behavior of Composite RC Beams with Externally Bonded CFRP". *J. Compos. Constr.*, 2(3), 132-137.

# **MMA Resin Application for the Continuous Fiber Retrofitting Method**

M. Saito, A. Kobayashi

## **Abstract**

Epoxy resin is normally used in the continuous fiber retrofitting (CFR) method. However, epoxy cannot be applied when the ambient temperature is below 5 °C. Also if the surface is wetted with rain, dew, or mist shortly after the application, a problem with surface whitening may occur.

A new CFR method using MMA resin is introduced in this paper. MMA resin has a higher curing rate than epoxy and can be cured in as quickly as 1 hour even when the ambient temperature is -10°C. The resin has proven to be very useful for difficult situations such as cold weather applications, very fast curing needs, or when rain is expected and unavoidable.

In this paper, the comparisons between MMA and epoxy resins are discussed based on mechanical and physical properties, reinforcing ability, and the methods of application in the CFR method. Also, a number of application examples are described where MMA was chosen as the resin because of the anticipated difficulties which would have developed had epoxy been used.

## **Introduction**

Continuous fiber retrofitting method has been practiced for several years and the number of actual construction projects is already more than 2000. In almost all the

---

M. Saito, A. Kobayashi, TOW SHEET department, Nippon Steel Composite Co., Ltd.,  
3-8, Nohonbashikobuna-cho, Chuo-ku, Tokyo 103-0024 Japan

construction cases, room temperature curing epoxy resin system was used for the application. However, epoxy resin has application limitations. It cannot be applied when the ambient temperature is below 5°C. Also, the full cure of the epoxy may take several days.

MMA resin is another room temperature curing resin system that has advantages such as low temperature curing and rapid curing. Also, contact dermatitis is not a usual problem. In this paper, the comparisons between MMA and epoxy resins are discussed based on mechanical and physical properties, reinforcing ability, and the methods of application in the CFR method. A number of application examples are described where MMA was chosen as the resin because of the anticipated difficulties which would have developed had epoxy been used.

## Experiments

In the comparison between MMA and epoxy resins, basic mechanical property tests (tensile and adhesion tests), accelerated weathering tests, beam bending tests, and seismic retrofitting tests were conducted. In all experimental results, MMA resin demonstrated the same good reinforcing ability as epoxy resin.

FORCA Tow Sheet FTS-C1-30 or FTS-C5-30 was the uni-directional carbon fiber sheet used in all experiments. The MMA resin system is composed of MMA primer (FP-M) and MMA impregnating resin (FR-M1P).

### Tensile and Adhesion Tests

Tensile test specimens and adhesion tests specimens were fabricated using FORCA Tow Sheet FTS-C1-30 with the MMA resin system. Test specimens were cured at 20°C and 0°C. As a comparison, test specimens with epoxy resin were also fabricated and cured at a temperature of 20°C. [1]

Tensile tests and adhesion tests were conducted based on JIS K 7073 and JIS K 5400 testing methods respectively. Tests results are shown in Table I .

Tensile strength and adhesion strength of MMA specimens were equal to that of epoxy specimens, within experimental error, even when the specimens were cured at 0°C.

Table I Test Results of Tensile Strength and Adhesion Strength

No	Resin System	Curing Temp. Deg C	Tensile Test		Adhesion Test	
			Strength MPa	Modulus GPa	Strength MPa	Failure Mode
1	MMA	0	4,020	237	3.2	Concrete Failure
2	MMA	20	4,270	240	2.9	Concrete Failure
3	Epoxy	20	4,140	235	2.5	Concrete Failure

### Accelerated Weathering Tests

Accelerated weathering tests were conducted according to JIS A 1415 (WS type). Test specimens were tensile test specimens while adhesion test specimens used mortar panels with Tow Sheet bonded. The tests were conducted for 2,000 hours exposure time. The test results are shown in Figures 1 and 2.

At 2000 hours exposure, no degradation was observed for tensile strength, Young's modulus, or adhesion strength. [1]

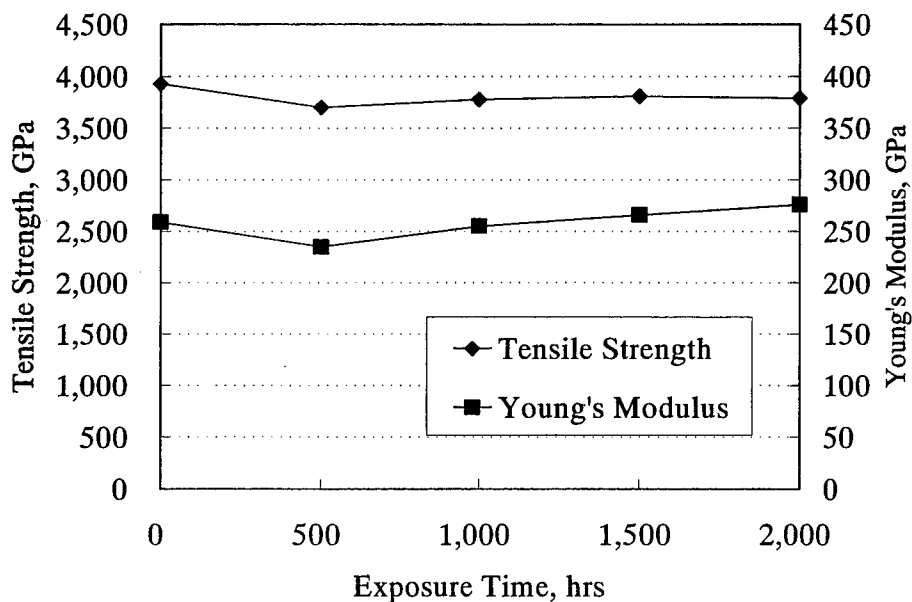


Figure1 Accelerated Weathering Test (Tensile Test)



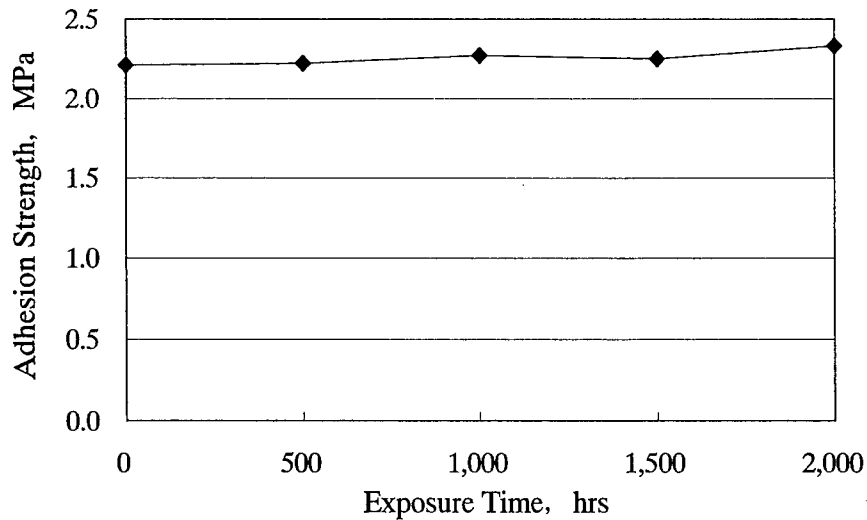


Figure2 Accelerated Weathering Test (Adhesion)

### Beam Bending Tests

The comparison between MMA and epoxy was also conducted on beam bending specimens. Reinforced concrete (RC) beams, 3 m long, 30 cm wide, and 40 cm high were retrofitted with FTS-C5-30 (high modulus type) carbon fiber sheets using MMA or epoxy resin. The sheets were applied on the tensile surface of the RC beam for a 2.3 m length, and either 1ply or 3 plies of sheets were applied with each resin system. Specifications of the concrete beam are described in Figure 3.

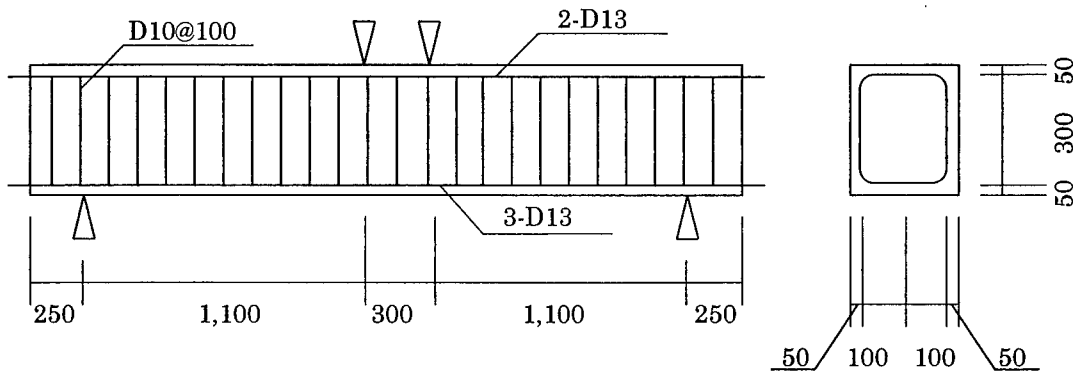


Figure3 Specifications of Concrete Beam

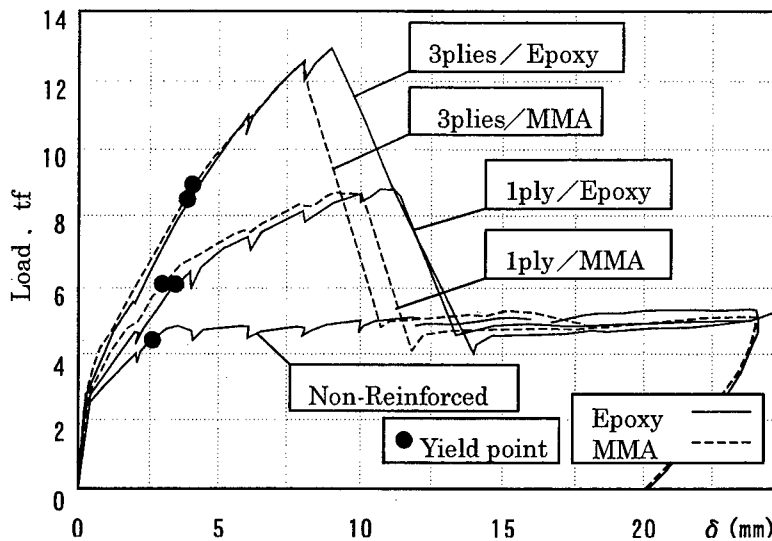


Figure 4 Beam Bending Test Results

Figure 4 shows the load - displacement curves of the beam bending tests. Essentially equivalent results were obtained between MMA and epoxy resin applications for each case of 1ply or 3 plies of carbon fiber sheet.

#### Seismic Retrofitting Tests

Seismic retrofitting tests were also conducted in order to compare the MMA resin system to the epoxy resin system. 1/4 scale RC highway column models were used for the tests. Two plies of carbon fiber sheet (FTS-C1-30) were wrapped around the lower area of each column as shown in Figure 5. Specifications of the test specimens are described in Table II and Figure 5.

Table II RC Column Details

	Resin	Cross Section	Re-bar Ratio, %		Number of plies
			Main Re-bar	Hoop Re-bar	
Non-Reinforced	-	Circle	0.79	0.57	-
CF Reinforced	Epoxy	Circle	0.79	0.57	2 (Hoop direction)
CF Reinforced	MMA	Circle	0.79	0.57	2 (Hoop direction)

After curing, test specimens were subjected to alternating horizontal loads, as would occur in a seismic event. Figure 6 shows the load – displacement results of the seismic tests. The maximum displacement shows the ductility of the specimens. The ductility of the retrofitted specimens was enhanced by 70 to 80%. Again, the MMA test specimen showed equivalent performance to the epoxy specimen.

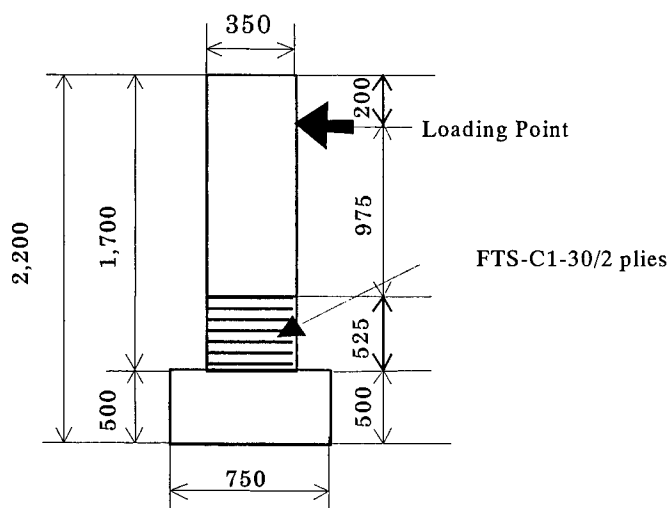


Figure 5. Schematic Diagram of Test Specimens

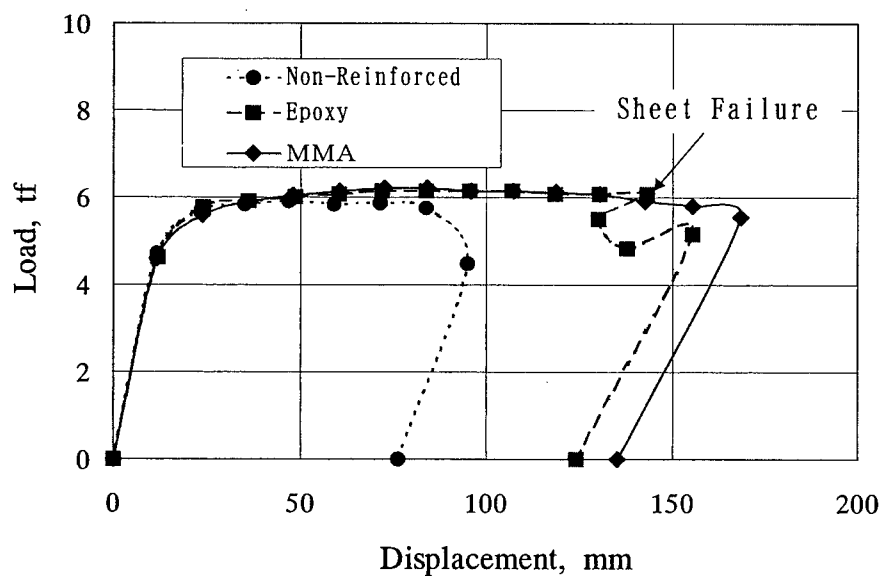


Figure 6. Seismic Loading Test Results

## Construction Examples

### Sakawa River Bridge (Column Wrapping)

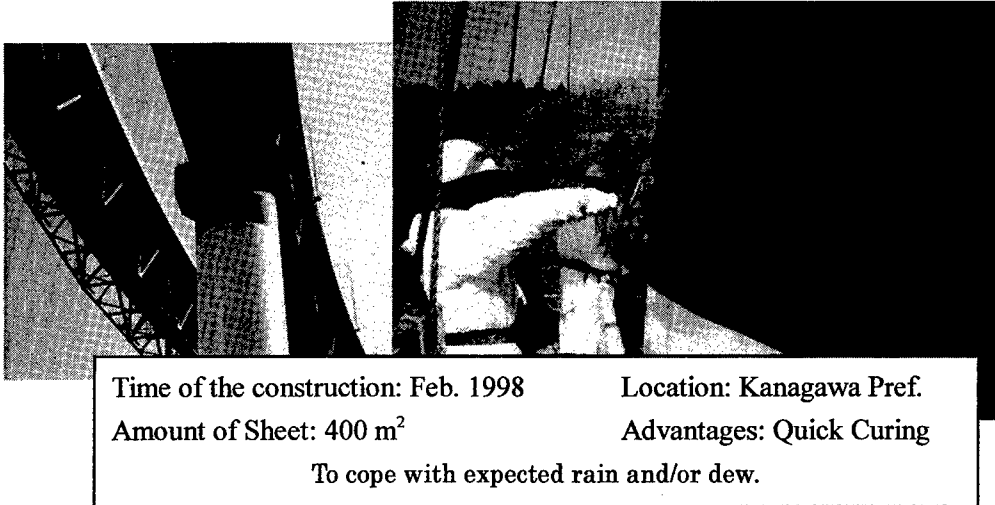


Figure 7. Sakawa River Bridge

### K Tunnel (Tunnel Lining Reinforcement)

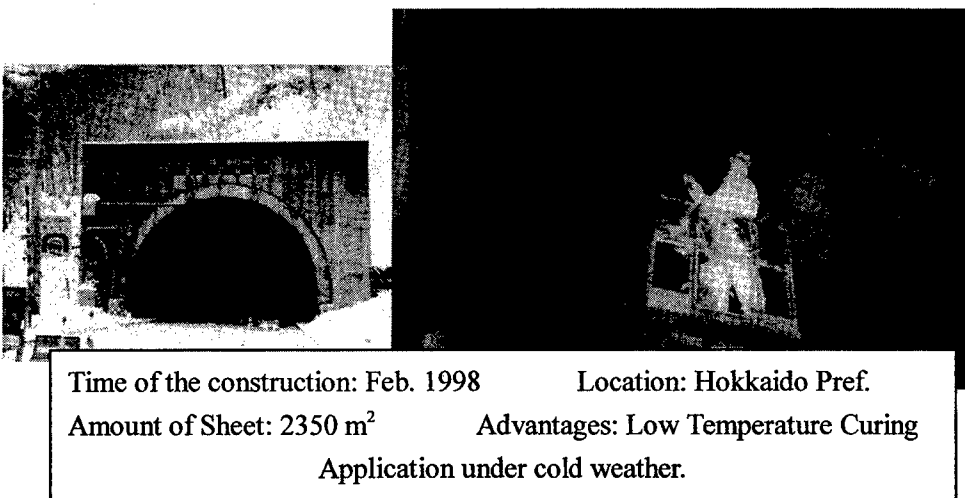


Figure 8. K Tunnel

### H Bridge (Upper Surface Slab Application)

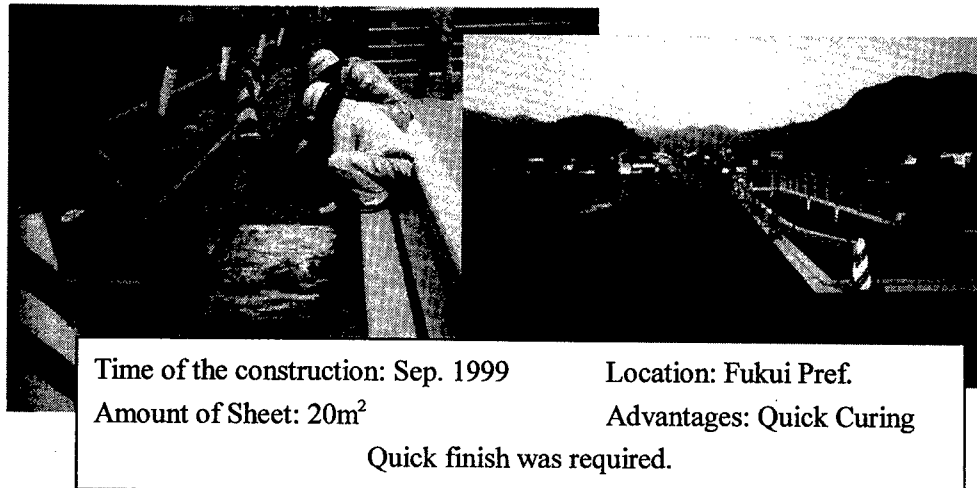


Figure 9. H Bridge

### Conclusion

1. MMA resin system in continuous fiber retrofitting method has the same good reinforcing ability as epoxy resin.
2. MMA resin system was successfully applied to the real retrofitting constructions.

### References

1. M. Saito, M. Nakasu, N. Yajima, T. Shindo, E. Lee, "MMA Resin Application for Carbon Fiber Sheet Reinforcement." Proceedings of Annual Meeting of Japan Society of Civil Engineering, V-463, 1998 : 926-927
2. Y. Matsuzaki, T. Myojoh, H. Honma, M. Kobayashi, K. Fujiwara, K. Nakano, 1998 "Experimental Study on Bending Strength of Reinforced Concrete Beam Reinforced with Carbon Fiber Sheets – About Effect of Resin - " Proceedings of Annual Meeting of Japan Architecture Society, 23096, Sept. 1998 : 191-192
3. M. Imbrogno, M. Saito, H. Kliger, "The Development of Low Temperature Cure Resin Systems for External Sheet Reinforcement of Concrete Structures", 44<sup>th</sup> International SAMPE Symposium, May 1999

# **Composites for Infrastructure, II**

---

## **Behavior of Concrete Columns Confined with Hybrid Composite Materials**

H. Toutanji and M. Saafi

### **Abstract**

Retrofitting of existing concrete columns by wrapping them by fiber reinforced polymer (FRP) sheets, straps, or pultruded FRP shells have been gaining great interest in the research community and industry. New hybrid concrete columns are developed in this study for new constructions. The basic structure of the proposed hybrid column consists of an exterior PVC-FRP shell with a concrete core. The exterior shell is commercially available cylindrical PVC pipe externally reinforced with impregnated continuous fiber in the form of hoops at different spacing. This paper presents the results of experimental and analytical studies of the performance of axially loaded concrete columns confined with PVC-FRP tubes. Test variables include type of confinement, volume of fiber and FRP hoop spacing. The results indicate that the new hybrid columns exhibited high strength and ductility. A new design procedure for concrete confined with PVC-FRP is proposed. Comparisons between experimental and theoretical results showed good agreement.

### **Introduction**

Past research was targeted at developing new reinforcing methods using less FRP in concrete structures to reduce cost. Shitindi<sup>1</sup> proposed FRP spirals to confine concrete instead of FRP tubes. Aramid, glass and carbon spirals were used. The spacing between the FRP spirals ranged between 30 to 80 mm. It was found that the stress-strain behavior of concrete confined with FRP spirals was similar to that confined with steel spirals with ascending and descending branches. Moreover, the ultimate compressive strength of columns was slightly affected by the volume and the type of fiber used. This is due to the fact that the concrete that covers the FRP spiral cracks, resulting in little increase in strength.

The proposed hybrid columns, cast in place, consist of PVC tubes reinforced with fiber reinforced polymer (FRP) hoops. The basic structure includes an exterior PVC-FRP shell with a concrete core. The exterior shell is commercially available

---

H. Toutanji and M. Saafi, Department of Civil and Environmental Engineering, University of Alabama in Huntsville, Huntsville, AL 35899, USA

cylindrical PVC pipe externally reinforced with impregnated continuous fiber in the form of hoops at different spacing as shown in Fig. 1. In the proposed system, the discrete confining pressures provided by the FRP hoops were distributed uniformly over the entire length of the column through the PVC tube. Moreover, the PVC tube has sufficient stiffness to prevent the spalling and cracking of the concrete core before the FRP hoops are activated. In addition, the PVC shell acts as formwork and protects the concrete and the internal reinforcements from environmental effects such as chloride and corrosion, while the FRP provides confinement to the concrete. The volume of fiber, of this reinforcing scheme, is very small compared with other existing confinement methods such as FRP tubes and FRP jackets. The spacing of the FRP hoops is dependent on the strength and ductility requirement of the system. The proposed system does not need reinforcing cages or longitudinal reinforcement unless extra reinforcements are required.

The objective of this paper is to present this new hybrid columns which can be used in highway bridge structure supports or columns in marine and other construction applications. The experimental performance and theoretical analyses of axially loaded concrete-filled PVC-FRP tubes are presented in this paper.

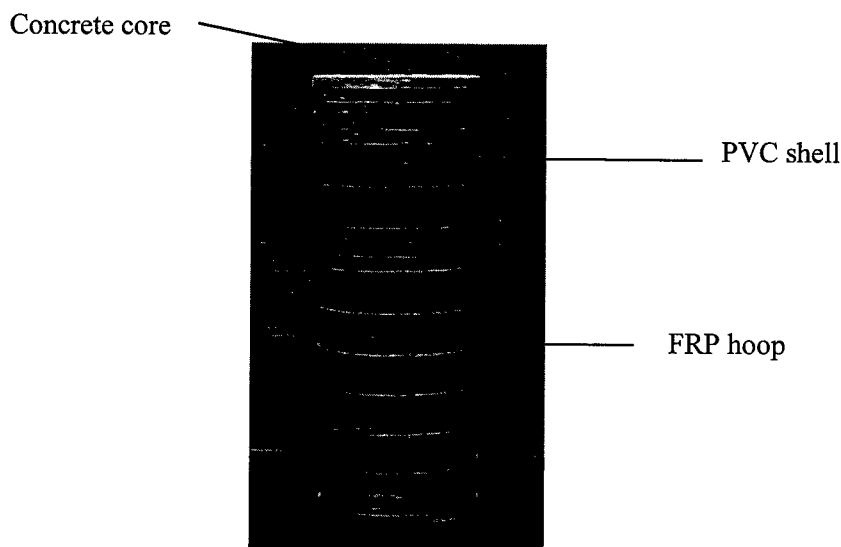


Figure 1 Proposed Hybrid Column System

### Experimental Program

Thirty-eight short concrete columns were tested under a uniaxial compression load. Thirty-six concrete columns confined with PVC-FRP tubes and 2 control concrete columns (concrete encased in PVC tubes) were used. All specimens measured 102 mm in diameter, 305 mm in length, and 6 mm in thickness. The PVC-FRP tubes used in this study were made of glass, aramid and carbon fiber reinforced polymers. The mechanical properties of the fibers, obtained from the manufacturer, are summarized in Table I. The FRP hoops consisted of 75% fiber and 25%



polyester resin and have a cross section of approximately 12 mm,<sup>2</sup> including the resin. The selected spacings of FRP hoops were 30 mm, 38 mm, 40 mm, 50 mm, 60 mm, and 78 mm. The average compressive strength of the concrete was 45 MPa.

Table I Mechanical Properties of FRP Hoops

Specimen	Thickness <sup>†</sup> (mm)	Hoop strength <sup>†</sup> (MPa)	Modulus of elasticity <sup>†</sup> (GPa)
GFRP	0.71	1500	74
AFRP	0.68	2100	120
CFRP	0.99	3000	400
PVC	6	42	3

<sup>†</sup>excluding resin

The FRP strands were continuously wrapped around the PVC tube through grooves that were notched in the tubes. The process was repeated until the proper number of tows had been wound through the grooves. The winding procedure was repeated 6 times for glass and carbon fibers, producing 6 tows, and 3 times for aramid fibers producing 3 tows. After winding, the PVC-FRP tubes were left at room temperature until resin hardened. The concrete-filled PVC-FRP tubes and concrete-filled PVC tubes (control specimens) were tested in compression. Four strain gauges were used, two to measure axial strain and two to measure lateral strain.

## Test Results

The results of strength and deformation at failure are given in Table II. Results show that the strength of PVC-FRP confined concrete increases with the increase of fiber volume. Lateral confinement by the PVC-FRP tubes causes the development of a triaxial stress field within the confined concrete, constraining it during dilation and thereby increasing the load carrying capacity. Figures 2, 3 and 4 show the axial stress plotted as a function of both axial strain and lateral strain for PVC-GFRP, PVC-AFRP and PVC-CFRP specimens, respectively. The figures show that the stress-strain curves of all concrete-filled PVC-FRP tubes are generally bilinear in nature with a small transition zone. The behavior of PVC-FRP tubes confined concrete columns under axial loading can be divided into three regions. In the first region, the behavior of confined concrete is similar to that of plain concrete, this is due the fact that the confining effect of PVC-FRP tube is still not activated by the lateral expansion of the concrete core. In the vicinity of the peak stress of unconfined concrete, the confined concrete reaches a state of unstable volumetric growth caused by excessive cracking. At this point, the confining PVC-FRP tube is activated and starts to gradually restrain the rapid growth of the lateral strains. This region of response is characterized by a transitional curve in the vicinity of the unconfined strength. Finally, a third region is recognized in which the confining PVC-FRP tube is fully activated, and the stiffness is generally stabilized around a constant rate.

Table II Summary of Test Results

Specimen	$s^{\dagger}$ (mm)	$\rho_{com}^{*}$ (%)	$f_{cu}^{*}$ (MPa)	$(f_{cu}-f_{co})/f_{co}$	$\epsilon_{cu}^{\otimes}$ (%)	$(\epsilon_{cu}-\epsilon_{co})/\epsilon_{co}$	$\epsilon_1^{\otimes}$ (%)
Plain	-	-	33	0	0.2	0	0.2
As30	30	0.5	71.35	1.160	1.26	5.30	1.45
As38	38	0.42	64.2	0.945	1.48	6.40	1.42
As40	40	0.4	61.13	0.852	1.57	6.85	1.44
As50	50	0.32	54.8	0.661	1.16	4.80	1.3
As60	60	0.27	48.88	0.480	0.75	2.75	1.2
As78	78	0.002	44.3	0.342	0.63	2.15	0.89
Gs30	30	0.56	62.6	0.896	1.8	8.00	1.52
Gs38	38	0.44	58.9	0.785	1.35	5.75	1.65
Gs40	40	0.42	55.6	0.685	1.29	5.45	1.54
Gs50	50	0.34	52.1	0.579	0.97	3.85	1.06
Gs60	60	0.28	48.2	0.461	0.58	1.90	1.11
Gs78	78	0.22	43.5	0.318	0.31	0.55	0.24
Cs30	30	0.78	93	1.818	1.1	4.50	1.27
Cs38	38	0.62	91	1.758	1.6	7.00	1.23
Cs40	40	0.58	89	1.697	1.77	7.85	1.27
Cs50	50	0.47	78.4	1.376	1.8	8.00	1.25
Cs60	60	0.39	68	1.061	1.43	6.15	1.35
Cs78	78	0.3	62.6	0.897	1.18	4.90	1.06

$^{\dagger}$  FRP hoop spacing,  $^{*}$  FRP volumetric ratio,  $^{*}$  Ultimate strength,  $^{\otimes}$  Ultimate axial strain  $^{*}$  Ultimate lateral strain

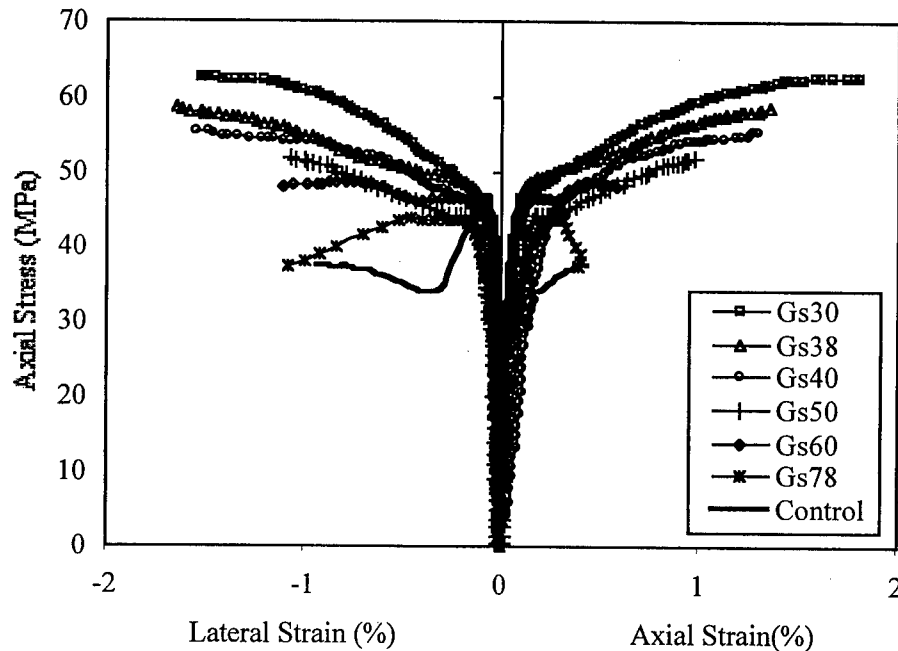


Figure 2 Stress-strain curves of PVC-GFRP Confined Concrete

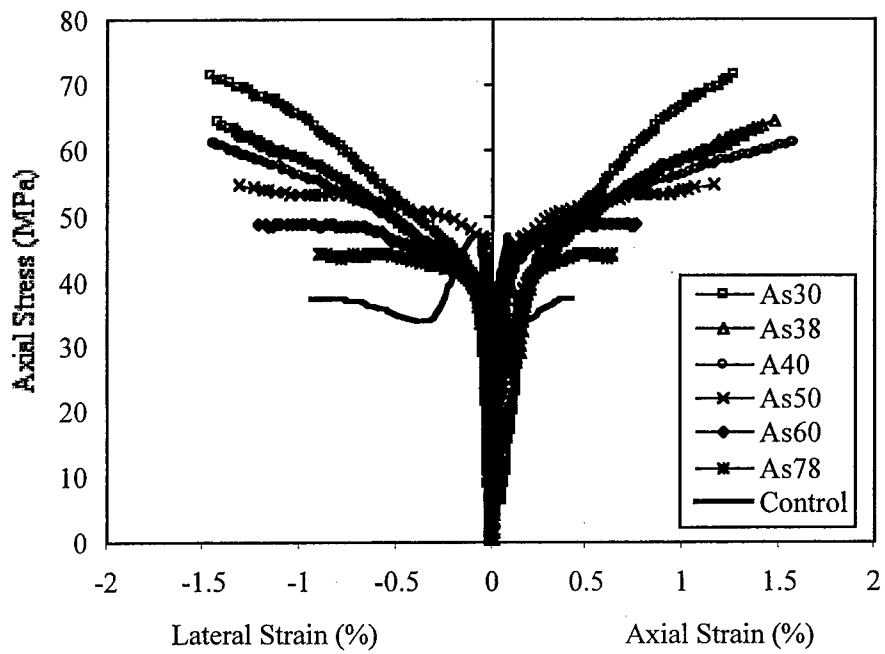


Figure 3 Stress-Strain of PVC-AFRP Confined Concrete

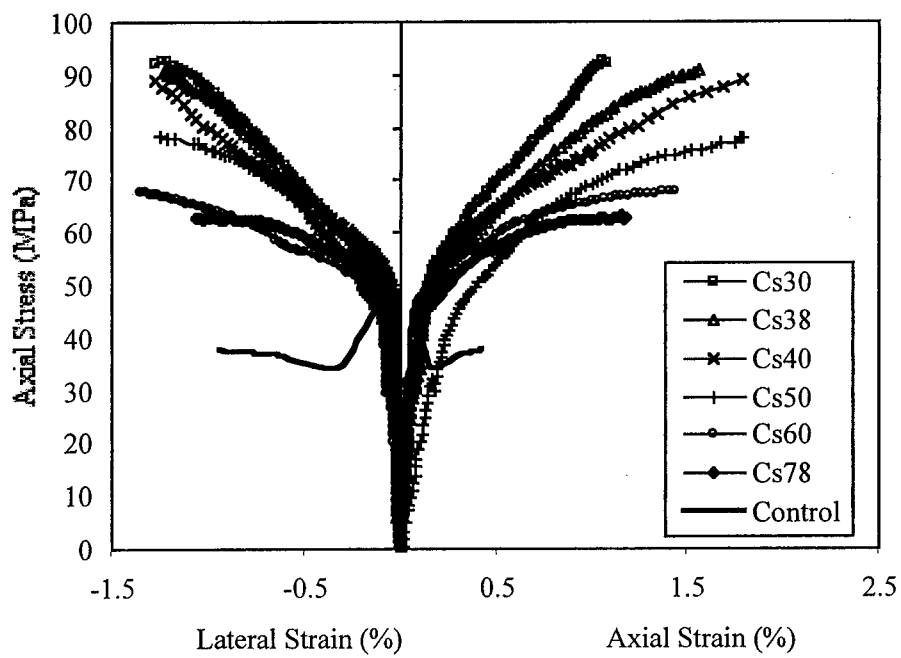


Figure 4 Stress-strain of PVC-CFRP confined concrete

The results also show that in each case, the composite hoops failed when the radial strain reached the ultimate strain of composite. This was the case regardless of the magnitude of axial strain and the spacing of FRP hoops. Figure 5 shows a typical failure for PVC-GFRP, PVC-AFRP and PVC-CFRP tubes confined specimens. Snapping of PVC and FRP hoops could be heard near the end of the loading. Specimens with spacings of 60 and 78 mm, the failure occurred by shear failure of the concrete core and the PVC shell followed by the failure of the FRP hoops. This occurred due to the low volume of fiber confinement as well as the large hoop spacings.

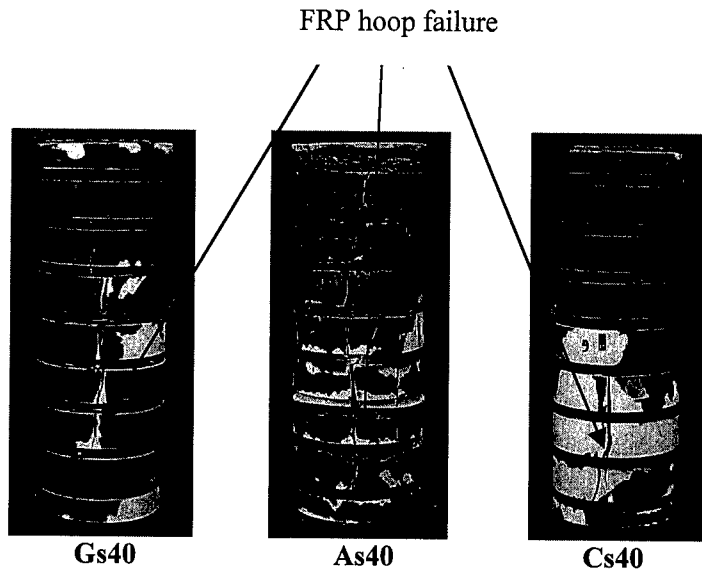


Figure 5 Typical Failure Mode of PVC-FRP Confined Concrete Specimens

### Design Equations for PVC-FRP Confined Concrete

In this section, a design procedure is proposed for PVC-FRP confined concrete, in which the amount of lateral FRP required is a function of the column ductility performance and the level of axial loading. The proposed approach was developed using experimental results. The required lateral FRP confinement in PVC-FRP columns may be calculated using the following equation

$$\rho_{com} = \frac{0.036f'_c}{f_{com}} \left[ 0.6 + 0.4 \left( \frac{P}{A_c f'_c} \right)^3 \right] D_\mu^{0.65} \quad (1)$$

where  $P$  is the applied axial load and,  $A_c$  is area of the concrete core,  $D_\mu$  is the ductility index,  $f_{com}$  is the ultimate strength of confining fiber, and  $f'_c$  is the compressive strength of concrete. The ductility index  $D_\mu$  was obtained from the experimental results by dividing the area under the stress-strain curves of PVC-FRP confined concrete by the area under the stress-strain curve of concrete filled PVC tube. For concrete confined with PVC-FRP, the ductility requirement depends on the category used in the design. Based on our experimental results, three categories were adopted. Category I for low ductility ( $D_\mu < 1$ ), category II for moderate ductility ( $1 < D_\mu < 10$ ), and category III for high ductility ( $D_\mu > 10$ ). Once the required percentage of FRP confining material is determined, the FRP hoop spacing may be selected using the following expression

$$s = \frac{4A_{com}}{\rho_{com}d_c} \quad (2)$$

One can assume a cross-section for the FRP hoop and solve for the pitch required. It was found that when the volume of confining fiber increases beyond a certain limit, the ductility of PVC-FRP decreases. Based on this finding, a conservative limitation on fiber volume ratio  $\rho_{com}$  was adopted for all three confining materials used in this investigation.

$$\rho_{com \min} = 0.2\% \quad (3)$$

$$\rho_{com \max} = 0.8\% \quad (4)$$

When the fiber volume ratio  $\rho_{com}$ , obtained from Eq. (1), is greater than  $\rho_{com \max}$ , this indicates that longitudinal reinforcement such as steel or FRP bars is needed; therefore, the fiber volume ratio  $\rho_{com}$  can be estimated as

$$\rho_{com} = \frac{0.036f'_c}{f_{com}} \left[ 0.6 + 0.4 \left( \frac{P - f_y A_{st}}{A_c f'_c} \right)^3 \right] D_\mu^{0.65} \quad (5)$$

where  $A_{st}$  is the cross sectional area of the longitudinal reinforcement and  $f_y$  is the compressive strength of the longitudinal reinforcement.

The proposed design approach was used to estimate the ultimate compressive load of concrete columns confined with PVC-FRP tubes. At failure, the specimens exhibited moderate ductility; thus, the ductility index in Eq. (1) was assumed to be 5. The ultimate load of the specimens was calculated using Eq. (1) based on the mechanical properties of the FRP hoops and the concrete core. Table III shows a comparison between the experimental and predicted ultimate loads. As can be seen from Table III, good agreement with the test data was obtained.

Table III Comparison between Experimental and Theoretical Ultimate Load Values

Specimen	Volume of fiber (%)	Experimental $P_{uexp}$ (kN)	Predicted $P_{upred}$ (kN)	$P_{uexp}/P_{upred}$
As30	0.5	578.15	588.28	0.98
As38	0.42	520.21	541.28	0.96
As40	0.4	495.33	526.5	0.95
As50	0.32	444.04	486.81	0.91
As60	0.27	396.17	424.11	0.94
As78	0.2	358.96	340.33	1.05
Gs30	0.56	507.25	529.00	0.96
Gs38	0.44	477.27	465.27	1.02
Gs40	0.42	450.52	452.15	0.99
Gs50	0.34	422.17	397.10	1.06
Gs60	0.28	390.56	340.33	1.14
Cs30	0.78	753.58	815.18	0.93
Cs38	0.62	737.37	746.61	0.99
Cs40	0.58	721.17	727.24	0.99
Cs50	0.47	635.27	667.85	0.95
Cs60	0.39	551.00	616.65	0.90
Cs78	0.3	507.25	547.56	0.93

### Conclusions

Tests were performed to study the behavior of axially loaded concrete columns confined with PVC-FRP tubes. The influence of FRP volumetric ratio, the type of FRP composite material, and the spacing between the FRP strips on column strength and axial and lateral deformations were evaluated. The hybrid tubes can provide an effective lateral confinement to the concrete core by increasing the strength and ductility of concrete. The confinement effectiveness diminishes, however, as the hoop spacing,  $s$ , increases. The stress-strain response of PVC-FRP tubes confined concrete is bilinear in both the axial and lateral directions. The first slope of the response depends on the concrete core, whereas the stiffness and the spacing control the second slope. The bent between the two slopes takes place at a stress level slightly higher than unconfined strength of the concrete core. The proposed design equation for concrete confined with PVC-FRP tubes depends on the ductility performance of the columns and the axial load. The proposed design equation produces good comparison with the experimental results.

### Acknowledgements

The authors would like to acknowledge the financial support of the National Science Foundation CAREER Grant No. CMS-9796326 and the generous contributions of materials from Tonen Co. and Master Builders Inc.

### References

1. Shitindi, R., V., 1999. "Behavior of Concrete Cylinders Confined with FRP Spirals," *Ph.D thesis*, Kyoto University, Japan.
2. M. Saafi, H. Toutanji, and Li Zonjin, 1999. "Behavior of Concrete Columns Confined with Fiber Reinforced Polymer (FRP) Tubes," *ACI Material Journal*, 96(4):500-509.

## **Stress-Strain Behavior of Concrete Columns Confined With Advanced Fiber Composite Sheets**

H. Toutanji and Y. Deng

### **Abstract**

Fiber reinforced polymer composite (FRPC) wrap has been established as an effective method for strengthening and rehabilitation of concrete structures. The performance of concrete columns externally wrapped with carbon, glass, and Aramid FRPC sheets is presented in this paper. The confined and unconfined (control) specimens were loaded in uniaxial compression. Axial load and axial and lateral strains were obtained in order to evaluate stress-strain behavior, ultimate strength, stiffness, and ductility of the wrapped specimens. Results show that external confinement of concrete by FRP composite sheets can significantly enhance the strength, ductility and energy absorption capacity of the concrete specimens. An analytical model to predict the entire stress-strain relationship of concrete specimens wrapped with FRP composite sheets was developed. The proposed model consists of two distinct parts. In the first part, the behavior is similar to that of plain concrete, since lateral expansion of the confined concrete is insignificant. The second region, which is mainly dependent on the stiffness of the FRP composite, is recognized in which the FRP wrap is fully activated. Comparison between the experimental results and those of analytical indicates that the model provides satisfactory predictions of the stress-strain response.

### **Introduction**

Problems with the deteriorated national infrastructure and the urgent need for the development of novel and more reliable construction systems, have led to the development of advanced composite materials. Advanced composites promise to provide substantially improved mechanical, durability-and constructability-related properties, essential for successful long-term solutions to the problems of the deteriorated national infrastructure. FRP composites are lightweight, high tensile strength and modulus, corrosion resistance, and durability. In addition, their low density is important because it adds less weight to the existing structures, and

---

H. Toutanji and Y. Deng, Department of Civil and Environmental Engineering, University of Alabama in Huntsville, Huntsville, AL 35899, USA

because the use of heavy equipment for repair with FRP composites is not necessary during rehabilitation.

It has been shown that wrapping FRP fabrics around the perimeter of both circular and rectangular concrete columns effect improves ductility and strength.<sup>1,2</sup> It has also been shown that confinement with FRP improves the behavior of columns submitted to seismic loading.<sup>3,4</sup> FRP fabric wraps consisting of carbon, aramid, or glass fibers bonded by an epoxy resin, have been successfully applied for seismic rehabilitation of bridge piers in the U.S. and Japan.<sup>5,6</sup> Other FRP confinement techniques have been shown to improve the behavior of normal and high-strength concrete.<sup>7</sup> Saadatmanesh et al<sup>8</sup> used the stress-strain model proposed by Mander et al,<sup>9</sup> that analyzes the behavior of concrete columns externally wrapped with fiber composite straps.

The performance of concrete columns confined with FRP composite sheets including experimental and analytical work is presented in this paper. This paper should provide a framework for better understanding of the behavior of fiber-wrapped or FRP-confined concrete columns.

### Experimental Procedure

A total of twenty-four 76 x 305 mm cylindrical specimens were tested, which included 16 FRP-wrapped concrete specimens and 8 plain concrete specimens. The average 28-day compressive strength of the concrete was about 30 MPa. The concrete cylinders were confined by wrapping them in a continuous manner with two laps of unidirectional FRP sheets. Four types of FRP sheets were used: two carbon (C1 and C5), one glass (GE), and one aramid (AR), which were bonded to the concrete with one type of epoxy system. All specimens were confined at a configuration of 0° orientation. In all cases, the outside layer was extended by an overlap of 76 mm to ensure the development of full composite strength. All specimens were left at room temperature for at least 7 days before testing. This was done to ensure that enough time had passed for the epoxy system to cure. A summary of the properties of the FRP composite sheets and the resin epoxy system is presented in Table I.

Table I. Mechanical Properties of FRP Sheets and Epoxy System

FRP sheets and epoxy	Tensile strength (MPa)	Elasticity modulus $E_f$ (GPa)	Ultimate strain (%)	Thickness (mm)
AR	2,059	118	1.75	0.286
GE	1,518	72.6	2.1	0.118
C1	3,485	230.5	1.5	0.110
C5	2,940	372.8	0.8	0.165
Epoxy	55.9	2.35	2.4	-



All specimens were loaded in uniaxial compression until failure, using a hydraulic testing machine. Both ends of the cylinders were capped with sulfur to ensure parallel surfaces and to distribute the load uniformly. The applied load was measured using a load cell. Axial and lateral strains were measured using electronic strain gauges. The axial and lateral strain gauges were installed at the center point of the cylinders. A computerized data logger system was used to obtain the results of the load and strains during the test.

## Results

### Effect of Confinement

Table II presents the experimental results of the wrapped and unwrapped specimens. The compressive strength and the axial and lateral strain values are based on the average of four tested specimens. Results show that the compressive strength of the concrete specimens was improved by about 200% due to confinement with carbon fiber, by about 100% due to glass fiber, and by about 230% due to aramid fiber. The compressive strength of the specimens confined with carbon and aramid fibers are higher than that confined with glass fiber, because the lateral strength developed due to carbon and aramid fibers are much higher than that developed due to the glass fiber.

Table II. Experimental Results for Confined and Unconfined Specimens

FRP sheets	Compressive strength (MPa)	Maximum axial strain (%)	Maximum lateral strain (%)	Lateral elastic modulus, $E_l$ (MPa)	Maximum lateral stress (MPa)
Plain	30.93	0.19	0.18	-	-
AR	140.89	1.83	1.55	1774	32.46
GE	60.82	1.53	1.63	449.7	7.33
C1	95.02	2.45	1.25	1,331.2	16.64
C5	94.01	1.55	0.55	3,228.8	17.76

Figure 1 shows the stress-strain curves of the confined and unconfined concrete cylinders. The curves on the right side represent axial stress-axial strain curves and on the left side show axial stress-lateral strain curves. The stress-strain response of the FRP-wrapped concrete specimens can be divided into two regions. In the first region, the curve ascends rapidly slightly above the ultimate unconfined concrete strength, which is similar to the behavior of plain concrete. In this region, the stress and strain produced over the concrete, due to confinement, are very small. In the second region, the concrete is cracked and the FRP wrap is fully activated, improving the compressive strength, energy absorption capacity and ductility of the specimens. The response in this region seems mainly dependent on the stiffness of the composite sheets.

The stress-strain curves (Fig. 1) show that, at the same stress level, the axial strain for the confined cylinders with carbon fiber was always higher than the lateral strain, whereas with glass and aramid fibers, the axial and the lateral strains were approximately the same. This is due to the fact that the stiffness of confinement of glass and aramid fibers are lower than that of carbon fiber.

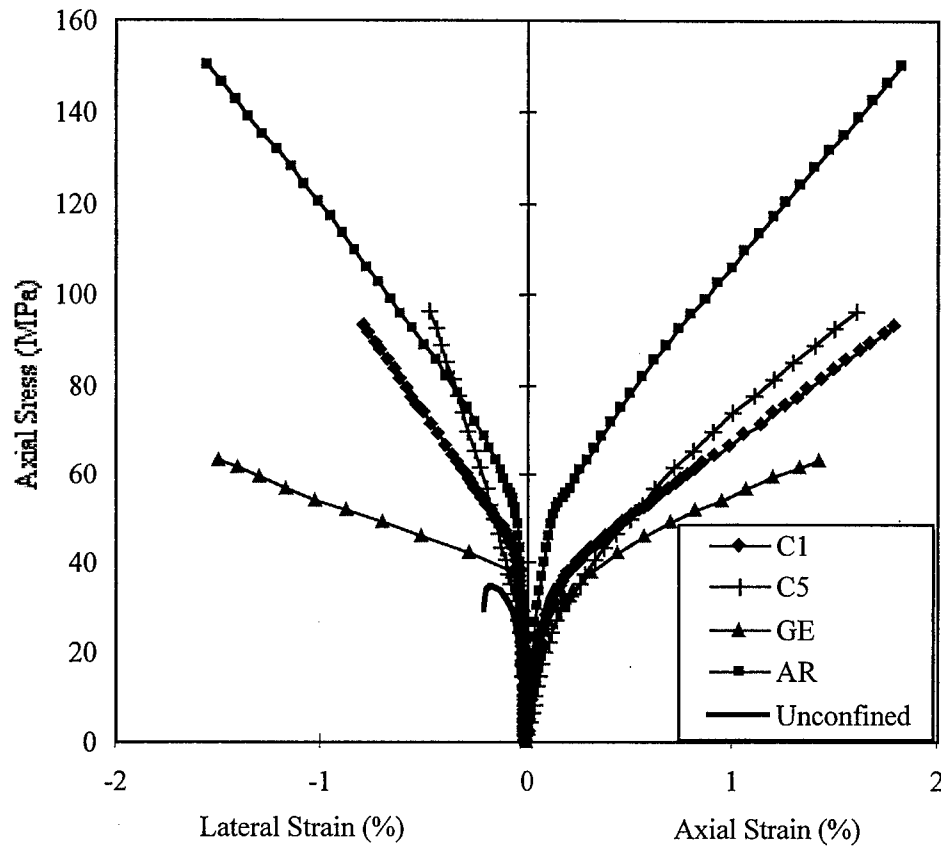


Figure 1 Stress-Strain Curves of Confined and Unconfined Concrete

#### Confinement Modeling (Stress-Strain Relationship)

The proposed model in this study consists of two distinct regions. In the first region, the behavior is similar to that of plain concrete, since lateral expansion of the confined concrete is insignificant. The second region is recognized in which the FRP wrap is fully activated, the stiffness is generally stabilized around a constant rate. The response in this region is mainly dependent on the stiffness of the FRP composite. Boundary conditions are necessary to develop the equations for the first region. For simplicity, the stress-strain relationship equations are first developed for the second region.

### Second Region of the Stress-Strain Response

The axial stress ( $f_a$ ) in every point of the second region is calculated using the following relationship<sup>10,11</sup>

$$f_a = f'_c + k_1 f_l \quad (1)$$

where,  $f'_c$  is the strength of the unconfined concrete,  $f_l$  is the lateral stress applied to the concrete by the FRP composite, and  $k_1$  is the confinement effectiveness coefficient. The values of the coefficient  $k_1$  can be obtained as a function of the ratio between the lateral stress and the concrete strength ( $f_l/f'_c$ ), as shown in Eq. (2)

$$k_1 = 3.5 \left( \frac{f_l}{f'_c} \right)^{-0.15} \quad (2)$$

Substituting  $k_1$  into Equation (1), an expression to calculate the axial stress of FRP-confined concrete specimens in the second region is obtained.

$$f_a = f'_c \left[ 1 + 3.5 \left( \frac{f_l}{f'_c} \right)^{0.85} \right] \quad (3)$$

The axial strain ( $\epsilon_a$ ), of confined concrete is given in equation (4)<sup>11</sup>

$$\epsilon_a = \epsilon_o \left[ 1 + k_2 \left( \frac{f_a}{f'_c} - 1 \right) \right] \quad (4)$$

$k_2$  increases with increasing lateral strain ( $\epsilon_l$ ) and is calculated as<sup>11</sup>

$$k_2 = 310.57 \epsilon_l + 1.90 \quad (5)$$

Substituting  $k_2$  into Equation (4), an expression to calculate the axial strain in every point of the second region of confined concrete with FRP composites is obtained.

$$\epsilon_a = \epsilon_o \left[ 1 + (310.57 \epsilon_l + 1.90) \left( \frac{f_a}{f'_c} - 1 \right) \right] \quad (6)$$

The meeting point between the first and the second regions is adopted when the lateral strain is equal to 0.002. The intersection point at strain of 0.002 seems to produce a good prediction of the experimental data of confined concrete with FRP composites.

### First Region of the Stress-Strain Response

It is assumed that the intersection point between the first and the second regions occurs when the lateral strain is equal to 0.002. By substituting this value in Equations (1), (3) and (6), the following expressions are obtained:<sup>11</sup>

$$\epsilon_{ul} = 0.002 \quad (7)$$

$$\epsilon_{ua} = \epsilon_o \left[ 1 + 0.0448 \left( \frac{E_l}{f'_c} \right)^{0.85} \right] \quad (8)$$

$$f_{ua} = f'_c \left[ 1 + 0.0178 \left( \frac{E_l}{f'_c} \right)^{0.85} \right] \quad (9)$$

$$E_{ul} = 7.557 E_l \left( \frac{f'_c}{E_l} \right)^{0.15} \quad (10)$$

$$E_{ua} = 0.3075 \frac{f'_c}{\epsilon_o} \quad (11)$$

### Comparison between Experimental and Analytical Results

The experimental results obtained in this study are compared with those of analytical obtained by the proposed model, as seen in Fig. 2. To generate the stress-strain analytical curves for concrete confined with FRP composites, it is necessary to know the ultimate unconfined compressive strength and its corresponding strain, the radius of the concrete cylinder, and the elastic modulus and thickness of the fiber sheet. Table III provides data necessary to use the developed model on the results obtained in this study. The ultimate strain of the unconfined concrete is assumed to equal to 0.002. A comparison between the experimental and the analytical curves indicates that the proposed model provides good predictions of stress-strain response of cylinders wrapped with FRP composites.

Table III Data for Applying the Analytical Model

Size of the cylinders		Concrete strength, $f'_c$ (MPa)	Type of fiber	Elasticity modulus of fiber, $E_f$ (GPa)	Thickness of the fiber, $t$ (mm)†	Lateral elastic Modulus, $E_l$ (MPa)*
Radius (mm)	Length (mm)					
38	305	44	Aramid	118	0.572	1,774
38	305	31	Glass	72.6	0.24	450
38	305	31	Carbon	230.5	0.22	1,331
38	305	31	Carbon	372.8	0.33	3,229

† Two layer of FRP wraps

\* Lateral elastic modulus of confined specimens ( $E_l$ ) is calculated as  $E_f * t / R$

The proposed model was developed for cylinders wrapped with FRP composites, in which the fiber is bonded to the concrete with an epoxy system to ensure perfect union between the fiber and the concrete. However, in concrete-filled FRP tubes there is a little bond between the concrete and the FRP tub. Thus, the proposed model overestimates the stress-strain curves of concrete-filled FRP tubes.<sup>12</sup>

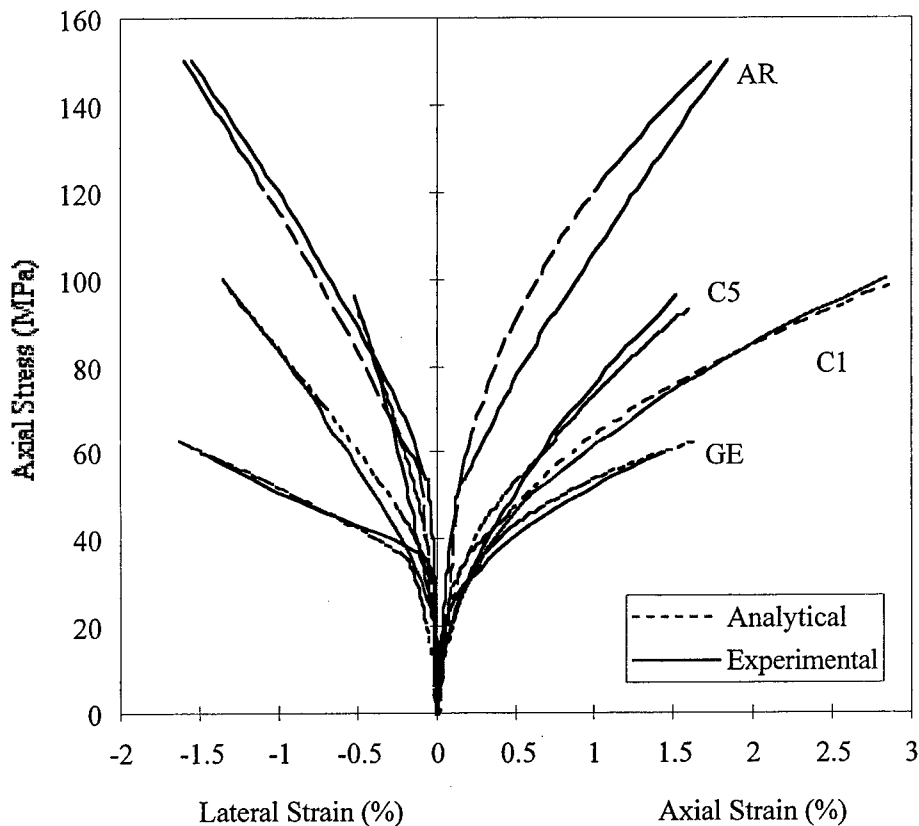


Figure 2 Comparison between Experimental and Analytical Results

## Conclusions

Concrete cylinders confined with four different types of FRP composite sheets were tested in compression, and their stress-strain curves (compressive stress vs. axial and lateral strains) were determined. The confinement with FRP composite sheets constrains the lateral strain, producing a triaxial stress field in the concrete, which results in improving the compressive strength, maximum strain and ductility.

A model to predict the behavior of the axial stress-axial and-lateral strain curves of confined concrete with FRP composite sheets was developed. The model is limited to circular short columns with axial load; the columns are confined with fiber composite sheets at  $0^\circ$  fiber orientation. The proposed model consists of two distinct regions. In the first region, the behavior is similar to that of plain concrete, since

lateral expansion of the confined concrete is insignificant. The second region, which is mainly dependent on the stiffness of the FRP composite, is recognized in which the FRP wrap is fully activated. In this region, the stiffness is generally stabilized around a constant rate. The developed model produces reliable results in predicting both the axial stress-axial strain and axial stress-lateral strain of FRP-wrapped concrete columns.

### Acknowledgements

The authors would like to acknowledge the financial support of the National Science Foundation CAREER Grant No. CMS-9796326. The contribution of materials from Tonen Inc. and Master Builders Inc. is also gratefully acknowledged.

### References

1. H. Katsumata, and K. Kimura, 1990. "Applications of Retrofit Method with Carbon Fiber for Existing Reinforced Concrete Structures," The 22nd Joint UJNR Panel Meeting, US-Japan Workshop, Galthersburg, MD, pp. 1-28.
2. F. Picher, P. Rochette, and P. Labossiere, 1996. "Confinement of Concrete Cylinders with CFRP," Fiber Composites in Infrastructure, *Proceedings of the First International Conference on Composites in Infrastructure*, pp. 829-841.
3. M.J.N. Priestley, F. Seible, and E. Fyfe, 1992. "Column Seismic Retrofit Using Fiber Glass/Epoxy Jackets," *Proceedings of the First International Conference on Advanced Composite Material in Bridges and Structures*, Sherbrooke, Canada, pp. 287-298.
4. H. Katsumata, Y. Kobatale, and T. Takeda, 1987. "A Study on the Strengthening with Carbon Fiber for Earthquake-Resistance Capacity of Existing Reinforced Concrete Columns," *Proceedings of the Seminar on Repair and Retrofit of Structures*, US-Japan Panel on Wired and Seismic Effects, UJNR, pp. 1816-1823.
5. A.A. Mufti, M.A. Erki, and L.C. Jaeger, 1992. "Advanced Composite Materials in Bridges and Structures in Japan," *Canadian Society of Civil Eng.*, Montreal, Canada.
6. M. Kasei, 1993. "Carbon Fiber Reinforced Earthquake-Resistant Retrofitting," Mitsubishi Kasei Corporation, Japan.
7. T. Harmon, K. Slattery, and S. Ramakrishnan, 1995. "The Effect of Confinement Stiffness on Confined Concrete," Non-Metallic Reinforcement for Concrete Structures, *Proceeding of the Second International RILEM Symposium (FRPRCS-2)*, pp. 584-592.
8. H. Saadatmanesh, M.R. Ehsani, and M.W. Li, 1994. "Strength and Ductility of Concrete Columns Externally Reinforced with Fiber Composite Straps," *ACI Structural Journal*, 91(4):434-447.
9. J.B. Mander, J.N. Priestley, and R. Park, 1988. "Theoretical Stress-Strain Model for Confined Concrete," *ASCE Structural Journal*, 114(8):1804-1826.
10. F.E. Richart, A. Brandtzaeg, and R.L. Brown, 1990. "The Failure of Plain and Spirally Reinforced Concrete in Compression," *Bulletin*, University of Illinois Engineering Experimental Station, Champaign, IL.
11. H. Toutanji, 1999. "Stress-Strain Characteristics of Concrete Columns Externally Confined with Advanced Fiber Composite Sheets," *ACI Materials Journal*, 96(3):397-404.
12. D. Cusson, and P. Paultre, 1995. "Stress-Strain Model for Confined High-Strength Concrete," *ASCE Structural Journal*, 121(3):468-477.

## **Durability of steel members reinforced with FRP sheets in marine environments**

Koji Yamaguchi, Isao Kimpara, Kazuro Kageyama and Masahiro Takanashi

### **Abstract**

As bridges and marine structures are being declared unsafe in increasing numbers, economical ways must be found to return such an infrastructure to its previous safe conditions. The use of repairing techniques with externally bonded FRP sheets and structural adhesives is increasing for concrete structure and aircraft because of high rigidity, lightweight and easy fabrication. In this study, environmental durability of steel members reinforced by external FRP sheets were investigated in marine environment. Eight kinds of FRP sheets were prepared: four resins, epoxy, vinylester, isophthalic and orthophthalic polyester resin, and two kinds of fiber, carbon and glass. An approach based on fracture mechanics was applied to evaluate bonding strength between steel members and FRP sheet. "Membrane Peeling" test was proposed and used to evaluate bonding strength between steel and FRP sheet. In the case of carbon fiber, the bonding strength of steel member reinforced by epoxy resin was found to be twice as that of steel member reinforced by the others resin before these test specimens were immersed in seawater. On the other hand, steel member reinforced by epoxy resin got most decreased debonding strength after immersion in seawater for one month.

### **Introduction**

As bridges and marine structures are being declared unsafe in increasing numbers, economical ways must be found to return such an infrastructure to its previous safe conditions. Repair and retrofitting are much more economical than rebuilding. In addition, infrastructure is difficult to be rebuilding since these functions can not be stopped in daily use. The use of repairing techniques with externally bonded FRP sheets and structural adhesives is increasing for concrete structure and aircraft because of high rigidity, lightweight and easy fabrication. Many studies have demonstrated the viability of adhesively bonded patch repairs as a mean to improve the durability and the damage tolerance of cracked metallic structures efficiently and economically.

---

K. Yamaguchi, I. Kimpara and K. Kageyama, Department of Environmental & Ocean Engineering, The University of Tokyo 7-3-1 Hongo, Bunkyo-ku, and Tokyo 113-8656 Japan  
M. Takanashi, Ishikawajima-Harima Heavy Industries Co., Ltd. 1-15 3-choume, koto-ku, Tokyo 135 Japan

There are many needs for steel structure in marine environment to develop new repairing techniques capable of rapidly and cost-effectively rehabilitating structures. The new repair procedure has several advantages over the traditional methods in that it minimizes corrosion, stress concentration, fretting and balance problems on control surface. In this new repair method, the bonding strength between FRP sheets and structure has a lot of influence on the strength of structural members reinforced by FRP sheets, [1,2,3].

In this study, we investigated the durability of steel members reinforced by bonding external FRP sheets in marine environments. An approach based on fracture mechanics was applied to evaluate bonding strength between steel and FRP sheets. "Membrane Peeling" test method was used to evaluate bonding strength between FRP sheets and structures, [4]. Steel members were reinforced by eight kinds of FRP sheets; four kinds of resin, epoxy, vinylester, isophthalic and orthophthalic polyester resin, and two kinds of fiber, carbon and glass were prepared. Tarepoxy resin was covered with steel members reinforced by FRP sheet to avoid corrosion by seawater. These test specimens were immersed in seawater in a month to evaluate the deterioration of reinforced structures. The bonding strength between FRP sheet and steel members were evaluated based on energy release rate.

### Test Method and Data Reduction

A new peeling test was proposed to characterize the peeling strength. A simple data reduction method was proposed for the debonding energy release rate from the viewpoint of fracture mechanics and theory of thin membrane. This simple data reduction method for critical energy release rate expressed as a function of extensional rigidity and deflection-to-debonding-length-ratio.

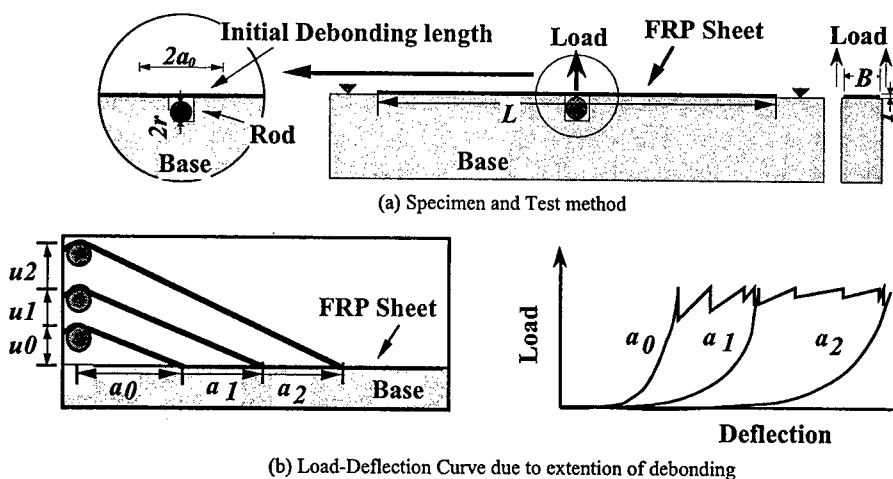


Figure 1 Proposed test method for evaluating debonding energy release rate



## Test method

Consider a test specimen and a testing method as shown in Fig. 1(a), in which a peeling load is applied with a loading rod of radius  $r$  on a FRP sheet of young's modulus  $E$ , width  $B$ , thickness  $t$  and initial debonding length  $2a_0$ , bonded on base material, as shown in Fig. 1(a). The resulting non-linear load-deflection curves due to the extension of debonding are schematically shown in Fig. 1(b). Though this loading method is apparently similar to the one proposed by Lin Ye et al. [5], it is quite different in the assumption that FRP sheet is regarded as an elastic membrane in the present testing method. This assumption made it possible to make a useful simple data reduction as described later. Hence this method is referred to "Membrane Peeling (MP) Test" hereafter.

## Data Reduction

Because a load-deflection curve in this test method is not linear, the conventional "Compliance Method" is not appropriate to be applied to evaluate the energy release rate. "Membrane Peeling (MP) Method" is proposed for evaluating the energy release rate.

A modification of the compliance method is proposed for evaluating the energy release rate. It is assumed that the FRP sheet is a linear elastic membrane, and that the out-of-plane load is applied to the sheet with a loading rod with equal right and left debonding length,  $a$ .

Considering the equilibrium of forces between sheet and rod, the relation between deflection,  $u$ , of the sheet and load,  $P$ , is expressed by

$$P = 2 \cdot EtB \cdot x \left( 1 - \frac{1}{\sqrt{1+x^2}} \right) \quad (1)$$

where  $x = u/a$

Integration of Eqn 1 with respect to  $u$  under the condition that debonding length,  $a$ , is constant and the initial condition of  $U=0$  at  $x=0$  gives the strain energy stored. And differentiation of the strain energy with respect to  $a$ , under the condition that sheet deflection,  $u$ , is constant, gives:

$$G = Et \left( \frac{x^2}{2} + \frac{1}{\sqrt{1+x^2}} - 1 \right) \quad (2)$$

From the Eqn 2, it is noteworthy that the energy release rate is given as a function of  $x=u/a$ , and independent of debonding length,  $a$ . This formula gives the basis for a simple data reduction method for critical energy release rate to be calculated from extensional rigidity and deflection-to-debonding-length-ratio.

When bonding strength is evaluate based on energy release rate in this data reduction, measurement of debonding length is not required and neither is repeated loading and unloading, so that a continuous R-curve of critical energy release rate due to crack extension can be obtained.

In addition, energy release rate was corrected if the debonding length is not equal on right and left. Let the average debonding length between right and left debonding length as  $a$  and the difference between average debonding length and each debonding length as  $s$ . Corrected energy release rate is a function of  $x=u/a$ , and  $\alpha=s/a$ .

$$G = \frac{1}{4} Et \cdot f(x, \alpha) \quad (3)$$

## Material and Experimental Procedure

### Material

Eight kinds of composite specimens were used: two kinds of fiber and four kinds of resin were prepared. The fibers were in tow-sheet form, which is basically a layer of dry unidirectional fiber attached to a glass scrim. Their basic properties are reported in Table I.

Four kinds of resin were used in this study. The first one is epoxy resin, FR-E3P supplied by Nippon Steel Composite Co, Ltd., which is widely used as a matrix in infrastructure application. The second one is vinyl ester resin, Neo-Paul 8250H supplied by JAPAN U-PICA Co, Ltd. The third one is isophthalic polyester resin, U-pica 4521PT-4 supplied by JAPAN U-PICA Co, Ltd. Last one is orthophthalic polyester resin, U-pica 4183PT-4 supplied by JAPAN U-PICA Co, Ltd.

Base material is SM520B steel. This is similar to KA32, which is widely used in ship constructions in Japan.

### Test piece

The size of steel was 30mm in width, 600mm in Length and 40mm in height. In this study, surface treatment of steel was used by a sand blasting. The size of a particle of a sand blasting is #32. And the treated surface was given with the coating of primer, which is vinyl ester resin, Neo-Paul 8355H supplied by JAPAN U-PICA Co, Ltd. after we removed grease on steel surface used by acetone. The FRP sheet was 20mm in width, 0.75mm in thickness, and 500mm in length. These strips were made by hand-

Table I Fiber property

	FTS-C1-30	FTS-GE-30
Fiber	Carbon	E-glass
Weight (g/m <sup>2</sup> )	300	300
Extension rigidity (N/mm)	38,020	8,530
Extension strength (%)	1.5%	2.1%

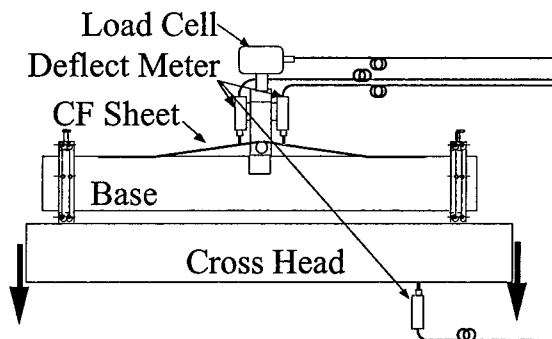


Figure 2 Experiment set-up for "MP Test"

lay-up method on the base material surface. The initial debonding length was  $a_0=45\text{mm}$  used by release film. After 1 day curing, the epoxy resin was covered with steel members reinforced by FRP sheet to avoid corrosion by seawater. These test specimens were immersed in a synthetic seawater ( $40^\circ\text{C}$ ) based on ASTM D1141-52 for one month to evaluate the deterioration of reinforced structures.

#### Experimental Procedure

The cross-head speed was set to  $0.5\text{mm/min}$  with continuous recording of a load-deflection curve. The angles between FRP sheet and upper surface of base material at both ends were measured with deflect meters, which are set at a certain distance away from the rod, as shown in Fig. 2.

#### Result

In the case of glass fibers, among all resins a crack propagated through an intralaminar and effective sectional area of GFRP decreased. For this reason, GFRP sheets were broken and the test was finished. Also, when carbon was used as fiber, a crack

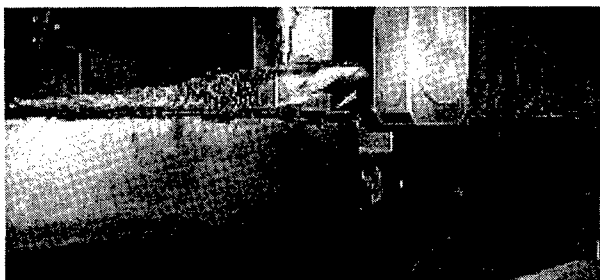


Figure 3 Fiber bridge of CF-orthophthalic

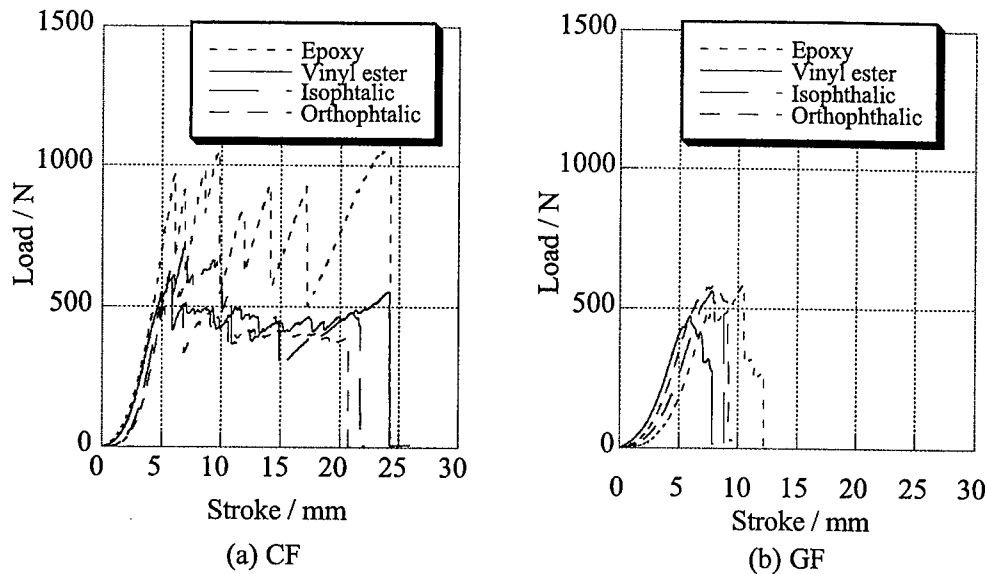


Figure 4 The relation between load and stroke before immersion in sea water

propagates through an intra laminar. However, CFRP was not broken and a crack propagates to the end of edge of CFRP sheet. Crack growth of CF-vinyl ester, -isophthalic and -orthophthalic occurred together with fiber bridge, as shown in Fig.3.

The typical load-stroke curves before immersion in synthetic seawater are shown in Fig.4. In case of CF-epoxy, many stick-slip phenomena were clearly observed. In case of the other resins, this phenomenon was scarcely observed. One reason for this is that fiber bridge prevents unstable crack growth.

Maximum load was observed as shown Table II. In the case of carbon fibers, it is shown that before immersion in the seawater epoxy resin was the highest among the other resins before and after immersion in seawater for one month. But after immersion in seawater for one month the deterioration of maximum load of epoxy resin was the worst among the other resins. Also in the case of glass fibers, after immersion in seawater for one month a deterioration of maximum load of epoxy is the worst among

Table II Comparison by maximum load.(N)

Fiber	Carbon		Glass	
Immersion Time	0-month	1-month	0-month	1-month
Epoxy	1230	830	670	600
Vinyl ester	580	730	730	680
Isophthalic	730	730	550	600
Orthophthalic	620	680	600	590

Table III Comparison by energy release rate (kJ/m<sup>2</sup>)

Fiber	Carbon	
	0-month	1-month
Epoxy	3.14	1.94
Vinyl ester	1.52	1.42
Isophthalic	1.73	1.62
Orthophthalic	1.57	1.61

the other resins. However, maximum load of vinyl ester resin is the highest among the other resins before and after immersion in seawater for one month.

When an average debonding length is from 45mm to 100mm, average energy release rate was observed as shown in Table III. In the case of carbon fibers, an average energy release rate of epoxy resins is the highest of all that of the other resins before and after immersion in seawater for one month. However, a deterioration of average energy release rate of epoxy resin was the worst among the other resins after immersion in seawater for one month. The deterioration of that of epoxy resin was close to 40%. On the other hand, the deterioration of that of the other resins was below 10%.

R-curves of carbon-epoxy before and after immersion in seawater for one month was observed as shown in Fig. 5. A crack growth of carbon-epoxy before immersion in seawater was often unstable. However, after immersion in seawater for one month, "stick-slip" phenomena were less. Debonding energy release rate at critical crack growth in "stick-slip" phenomena decreased from 3.83 kJ/m<sup>2</sup> before immersion in seawater for one month to 2.04 kJ/m<sup>2</sup> after immersion in seawater for one month. This deterioration was about 50%. However, debonding energy release rate at crack stop point in "stick-

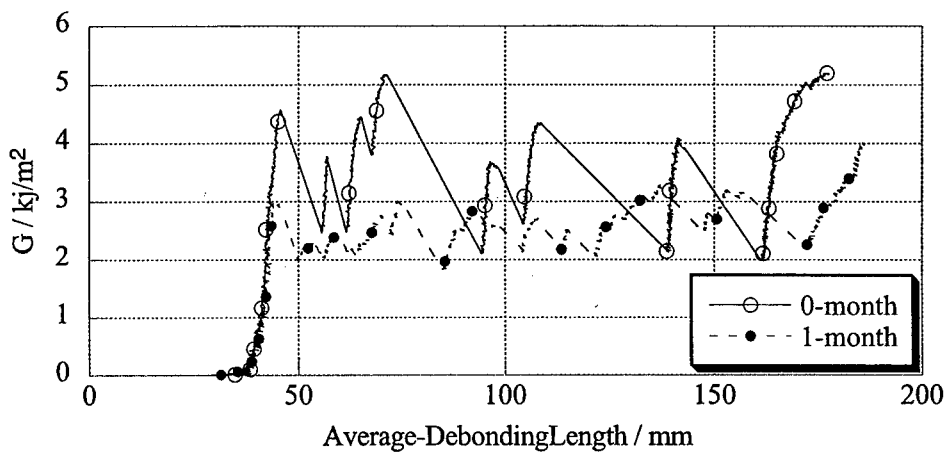


Figure 5 Comparison of CF-Epoxy before and after immersion in sea water about the relation between energy release rate and average debonding length

slip" phenomena decreased from 2.02 kJ/m<sup>2</sup> before immersion in seawater for one month to 1.65 kJ/m<sup>2</sup> after immersion in seawater for one month. This deterioration was about 20%.

## Conclusion

The environmental durability of steel members reinforced by external FRP sheets were successfully evaluated in marine environment based on the proposed "Membrane Peeling" test method. Eight kinds of FRP sheets were prepared: four resins, epoxy, vinylester, isophthalic and orthophthalic polyester resin, and two kinds of fiber, carbon and glass. In the case of glass fibers, a crack propagates through an intra laminar and effective sectional area of GFRP decreased among all resins. For this reason, GFRP sheet was broken. In the case of carbon fibers, the bonding strength of steel member reinforced by epoxy resin was found to be as twice as strong that of steel member reinforced by the others resin before these test specimens were immersed in seawater. On the other hand, steel member reinforced by epoxy resin got most decreased debonding strength after immersion in seawater for one month. The characteristics of deterioration mechanism was discussed based on the measured continuous R-curves.

## Acknowledgement

The authors are also grateful to the Ishikawajima-Harima heavy Industry Co., Ltd., JAPAN U-PICA CO, Ltd. and Nippon Steel Composite Co, Ltd. for providing the specimens and the reinforcing materials.

## Reference

1. Grabovac, I., Pearce P. J., Camiller, I A., Challis, K. and Lingard, J., "Are composites suitable for reinforcement of ship structures?" Proceeding of ICCM12, 1999
2. Nahas, M. N., "Experimental investigation of fatigue of cracked aluminum specimens repaired with fiber composite patches", Journal of Reinforced Plastic and Composite, 1992 vol. II, pp, 932 - 938.
3. Karbhari, V. M. and Shulley, S. B., "Use of composite for rehabilitation of steel structures - determination of bond durability.", Journal of Material in Civil Engineering, 1995, November, pp239 - 245.
4. Kimpara, I., Kageyama, K., Suzuki, T., Ohsawa, I. and Yamaguchi, K., "Characterization of peeling strength of FRP sheets bonded on mortar and concrete", Advanced Composite Material, 1999, vol. 8, No. 2, pp, 177-187
5. Ye, L. , Friedrich, K. , Weimer, C. and Mai, Y-W. , "Surface treatments and adhesion bonding between concrete and a CFRP composite" Advanced Composites Materials, vol.7 (1998), 47-61

## **Mechanical Characterization of Unidirectional CFRP Thin Strip and CFRP Cables under Quasi-Static and Dynamic Tension**

H. Kimura, M. Itabashi and K. Kawata

### **Abstract**

Under uniaxial tension, full stress-strain curves up to fracture and mechanical properties of a variety of CFRP cables having structures of UD, 1, 1×2, 1×3 and 1×7 are evaluated experimentally at three strain rates ranging from quasi-static ( $10^{-5} \text{ s}^{-1}$ ) to dynamic ( $10^2 \text{ s}^{-1}$ ). Obtained tensile properties are tensile strength, chord or tangent modulus, strain at tensile strength and absorbed energy per unit volume. Experimental difficulties on stress and strain detection and specimen fastening are overcome by introducing special instrumental arrangements and expansive-cement fastening technique. For all cables, at quasi-static ( $10^{-5} \text{ s}^{-1}$ ) and intermediate ( $10^{-2} \text{ s}^{-1}$ ) strain rates, the stress-strain relation is linear. On the other hand, at dynamic ( $10^2 \text{ s}^{-1}$ ) strain rate, the stress-strain relation is non-linear and all cables tend to increase elastic modulus and tensile strength. This response obviously leads to increase absorbed energy per unit volume under dynamic tension. However, strain at tensile strength remains almost the same level at these three strain rates. Thus, basing upon the fracture strain criterion, strain rate insensitivity is concluded for all cables.

**Keywords:** UD, CFRP cable, mechanical properties, dynamic tension, fastening, helix angle, infrastructure

### **Introduction**

Extensive research on advanced composite material, such as CFRP, has already been suggested that the material is substitutive to conventional steel for the structure reinforcing applications because of its high tensile modulus and tensile strength comparable with or higher than those of steel. Another performances of the material such as light weight, non-magnetic, non-corrosive, low linear expansion and fatigue resistance have focused engineer's attention on utilizing the material for the tensile

---

H. Kimura, Tokyo Rope Mfg. Co., Ltd., 5707, Shishikura, Kasumigaura, Niihari, Ibaraki 300-0195, Japan

M. Itabashi, Department of Materials Science and Technology, Science University of Tokyo, 2641, Yamazaki, Noda, Chiba 278-8510, Japan

K. Kawata, Professor Emeritus, University of Tokyo, Science University of Tokyo, 2-19-21, Minami-Oizumi, Nerima, Tokyo 178-0064, Japan

element in the applications including civil engineering and bridge construction, not only on steel substitution basis but also with positive concepts extending those material advantages [1]. Furthermore, the recent improvement of manufacturing technology and cost saving efforts for CFRP cables encouraged the research and project in this field. At the present time, CFRP cables are being recognized as an potential reinforcing element for infrastructure applications, for example, concrete beam reinforcing, bridge stay cables, ground anchor tendon, etc [2-3].

The strand structure of the CFRP cables in this study is similar to that of traditional steel cable or synthetic fiber rope in which wires or strings are gathered and twisted into spiral shape. Factors of array of the strand are related to its structure, i.e., the number of pieces of wire, and helix angle of spiral wire. Effects of its structure and helix angle on its tensile behavior at quasi-static strain rate ( $10^{-5} \text{ s}^{-1}$ ) of the CFRP cables has been analyzed [4]. The work found that the structure, i.e., the number of pieces of string in CFRP cables itself, did not apparently affect its tensile properties, while increasing helix angle above about 10 degrees degraded tensile properties except elongation at break. Our next step is to conduct tensile test at higher strain rate level than that, for example,  $10^2 \text{ s}^{-1}$ , at which structures come to be forced as seismic impacts [5]. Strain rate effect on tensile properties of CFRP characterized here can also be compared with those of the other composite materials, AFRP and GFRP, which have been already given by the present authors [6-7].

## Experimental Procedures

### Specimen

All specimen are fabricated from the same specified raw material CF prepreg: epoxy resin impregnated to unidirectionally arrayed carbon fibers (Besfight HTA 12K-P112, Toho Rayon). UD is prepared simply by curing the prepreg as received. Its fiber volume fraction is 57% and cross section is rectangular having a typical dimensions shown in Table I. Figure 1 shows the detail of CFRP cables fabricated. The symbol 1 is a cable of only one string in which the prepreg is twisted in right-hand lay or so called Z lay with 23 mm pitch and is wrapped closely with polyester yarn. The symbol 1×2, 1×3 and 1×7 are cables in which 2, 3 and 7 pieces of the above-mentioned string are twisted into strand structures with left-hand lay or so called S lay, respectively. Thus CFRP cables are prepared by the process consist of laying, wrapping, stranding and final process curing at 130°C. Helix angle as shown in Figure 1, the angle between the spiral string and the axis of the cable, is 9.7 degrees typically in 1×2, 1×3 and 1×7. Smaller and larger angles of 5.0 and 18.7 degrees are also prepared for 1×7 structure. Hence specimens are varied structures of UD, 1, 1×2, 1×3 and 1×7, and helix angles of 5.0, 9.7 and 18.7 degrees for only 1×7 structure as shown in Table I. Outer diameter of CFRP string is 1.3 mm and thickness of wrapped coating is about 0.15 mm. The diameter of CFRP site in a string is about 1.0 mm and its fiber fraction is 64%. Cross-sectional area of the cables is defined as the cross sectional contour of CFRP site normal to the cable axis [4].



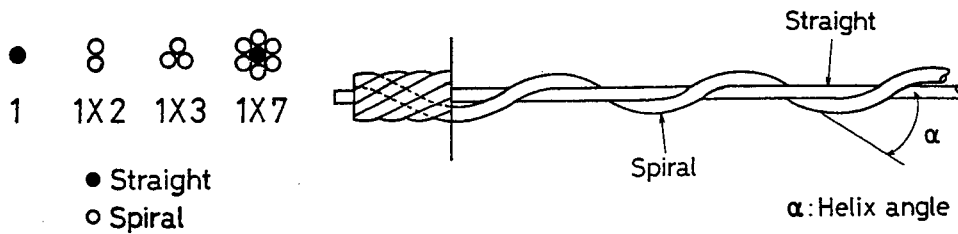


Figure 1 Strings array and helix angle of CFRP cables.

Table I Variation of structure and helix angle of the specimens.

Symbol	Number of pieces of string straight <sup>a</sup>	spiral	Characteristic dimension(s) <sup>b</sup> (mm)	Helix angle (deg.)	Cross-sectional area <sup>c</sup> (mm <sup>2</sup> )
UD	1	—	2.3×0.4	—	0.810
1	1	0	1.3	—	0.724
1×2	0	2	2.6	9.7	1.47
1×3	0	3	2.8	9.7	2.20
1×7 S	1	6	3.9	5.0	5.08
1×7	1	6	3.9	9.7	5.13
1×7 L	1	6	3.9	18.7	5.31

<sup>a</sup> A string is not twisted for UD.

<sup>b</sup> Length of rectangular sides for UD. Diameter of a circumscribed circle for cables.

<sup>c</sup> Total area of CFRP sites in strings normal to the cable axis.

### Specimen fastening

Full stress-strain curves up to fracture for advanced composite materials are relatively difficult to obtain with conventional chucking techniques, for example, screw threads, friction by transverse compression, adhesion and wedges. The present authors introduces a new fastening technique. The end of the specimen are inserted into a loose steel socket hole, the loose gap between the specimen end and socket is filled up with expansive cement. Uniform transverse compressive loading to the specimen over the socket hole length is applied by the expansion of the cement, obstructing pull-out from sockets [8]. In the present case, this technique is the most suitable chucking technique and used for all specimens. However, a conventional fastening system in which specimen ends are embedded with epoxy resin and fixed by the adhesion is still effective at only quasi-static ( $10^{-5} \text{ s}^{-1}$ ) and intermediate ( $10^{-2} \text{ s}^{-1}$ ) tensile test. This system is used partially in this study for 1, 1×2, 1×3 and 1×7 at the two strain rates. As shown in Figure 2, cables were cut into pieces of 310 mm or 230 mm in length, where 80 mm of their both ends were terminated with the filled socket system; thus effective length were 150 mm or 70 mm respectively. Curing condition of the filling material were 20°C for 48 h and 120°C for 4 h for expansive cement and epoxy resin, respectively.

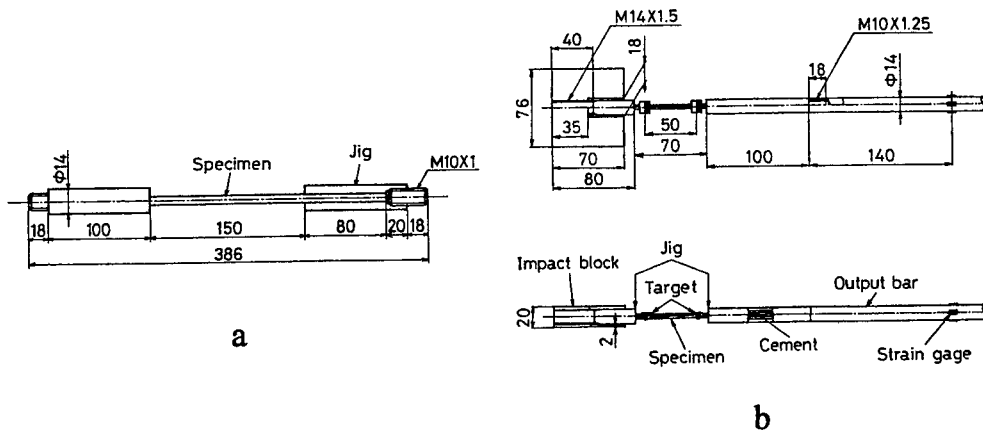


Figure 2 Assembled specimen for (a)  $10^{-5} \text{ s}^{-1}$  and  $10^{-2} \text{ s}^{-1}$  and (b)  $10^2 \text{ s}^{-1}$  tensile test.

### Experimental

For quasi-static ( $10^{-5} \text{ s}^{-1}$ ) and intermediate ( $10^{-2} \text{ s}^{-1}$ ) tension, the special extensometer consists of four eddy-current displacement transducers are devised, allowing initial geometric irregularities of a high-aspect-ratio specimen. The transducer detects the displacement of a target steel plate of 1 mm thickness which is clipped on the specimen with V-shaped attachment. The displacement of the upper and lower target plates are monitored by the transducers at two locations, i.e. the left and right sides and at the same horizontal distances of 30 mm from the specimen. Signals from two sensors for each plate are averaged so that any tilt of the target plate is cancelled around the cable axis at the attachment. The gage length is typically 88 mm. As shown in Figure 3a, the extensometer is instrumented into a 98 kN-universal material testing machine (Shimadzu AG-10TA). Crosshead speed is 0.5 mm/min or 100mm/min for quasi-static ( $10^{-5} \text{ s}^{-1}$ ) and intermediate ( $10^{-2} \text{ s}^{-1}$ ) tensile test, respectively.

On the other hand, under dynamic tension ( $10^2 \text{ s}^{-1}$ ), two-target version of the one bar method gives rational stress-strain relations for even CFRP thin twisted structures. As shown in Figure 3b, the two-target version of the one bar method consists of a high-velocity loading machine and dynamic stress-strain measuring system. In this effective experimental method, in order to cancel the apparent strain induced by the end breakage of the fastening cement, two targets are adhered on the specimen itself to detect accurate elongation. Both displacements of the targets are detected with an electro-optical extensometer (Zimmer model 200X, gage length of an installed lens: 5mm). To secure the accuracy of the dynamic strain detection, the two-target method and a conventional strain gage method are tried simultaneously, as a preliminary experiment. In the former method, two black-and-white paper targets backed by a square aluminum sheet are adhered on the specimen of 50mm-gage length, by small spots of epoxy adhesive. In the latter method, a strain gage (Kyowa KFG-02-120-C1-11, gage length: 0.2mm) is cemented directly on the specimen. However, the surface roughness of it is not perfectly good as a gage station. Prior to

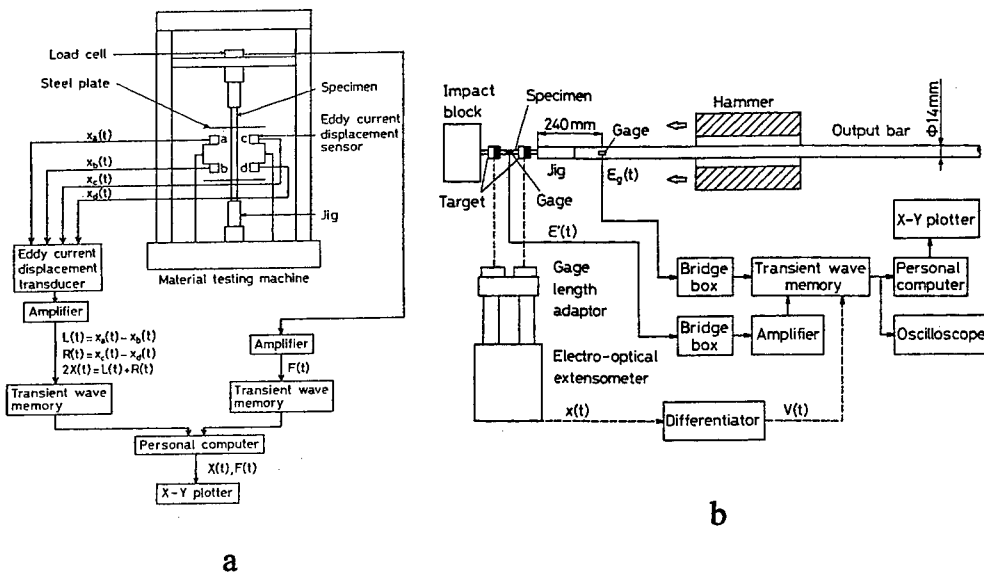


Figure 3 Stress-strain measuring system for CFRP cables at the strain rates of (a)  $10^{-5} \text{ s}^{-1}$ ,  $10^{-2} \text{ s}^{-1}$  and (b)  $10^2 \text{ s}^{-1}$ .

the cementing, epoxy resin is applied on the specimen as thin as possible, as a gage station base. A slingshot loading system is able to give the hammer velocity of 10m/s typically. The dynamic loading to the specimen is applied via a impingement between the hammer and impact block. The signals from both methods are stored by three synchronized digital memories (Kawasaki Electronica TMR-100, resolution: 10 bits, sampling frequency: 1 MHz). After the rupture of the specimen, load and displacement data are reduced to stress and strain values via a personal computer. The agreement of the two strain detection methods is fairly good. After that, only the one bar method is used in this series of experiments.

## Results and discussion

### Stress-strain relations

Typical stress-strain curves of UD are shown in Figure 4a. At quasi-static ( $10^{-5} \text{ s}^{-1}$ ) and intermediate ( $10^{-2} \text{ s}^{-1}$ ) strain rate, both stress-strain curves are linear, and the difference between them is quite small. On the other hand, at dynamic ( $10^2 \text{ s}^{-1}$ ) strain rate, the stress - strain curve is no longer linear. The curve shows increase in elastic modulus initially, which is succeeded by gradual decrease until 1.3% strain. Then at the strain close to the specimen breakage, elastic modulus lowers almost the same of that in quasi-static tension. Thus the stress-strain curve draws a convex in dynamic tension. The behavior for 1×7 at three strain rates, as shown in Figure 4b, is almost similar to that of UD. However, the enhancement of elastic modulus in dynamic tension is less than that of UD; since the increase of elastic modulus at the

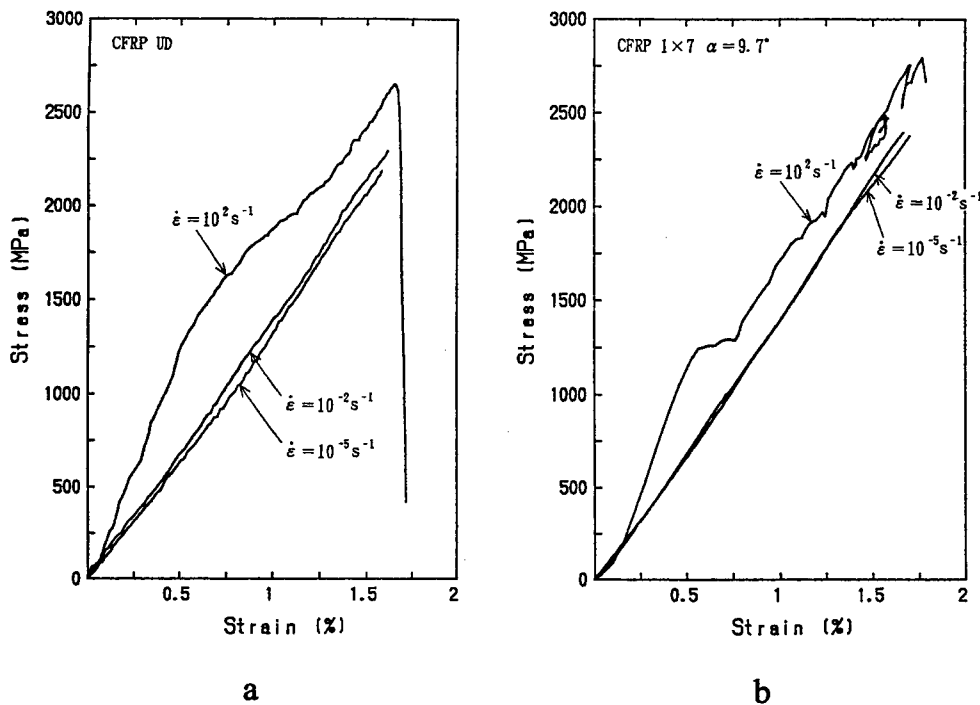


Figure 4 Stress-strain curves of (a) CFRP UD and (b) CFRP 1x7 at three strain rates,  $10^{-5} \text{ s}^{-1}$ ,  $10^{-2} \text{ s}^{-1}$  and  $10^2 \text{ s}^{-1}$ .

initial part is succeeded by a drop from 0.5% to 0.75% strain. Furthermore, at a region close to the specimen breakage, an apparent distortion (a loop) in the stress-strain curve is observed sometimes in dynamic tension. The reason of this distortion is still not clearly found out, but some candidates are considered as such like a local failure in individual strings of 1x7, a collapse of array of strand or a very small scale pull-out from fastened part. All of them possibly cause an instantaneous relaxation of tension, but this is not a fatal problem.

#### Strain rate dependence of tensile properties

From the obtained stress-strain curves, tensile strength, strain at tensile strength, elastic (chord or tangent) modulus and absorbed energy per unit volume are evaluated. At quasi-static ( $10^{-5} \text{ s}^{-1}$ ) and intermediate ( $10^{-2} \text{ s}^{-1}$ ) strain rates, since the stress-strain relation is linear, chord modulus is calculated from the stresses at the strains of 0.2% and 1.0%. On the other hand, at dynamic ( $10^2 \text{ s}^{-1}$ ) strain rate, the stress-strain behavior is not linear as described in the preceding subsection, tangent modulus is adopted as a measure of elastic property. Average tangent modulus here is calculated as a mean value of differential values of the upward part of dynamic curve, using Savitzky-Golay method based upon the least square procedure. Absorbed energy per unit volume is obtained from the area of the stress-strain curve. Tensile properties vs. strain rate for UD and CFRP cables are shown in Figure 5. Mean

values of 4 or 5 data are plotted.

Tensile properties remain almost the same for UD and CFRP cables in quasi-static and intermediate tension. But except on strain at tensile strength, increases of tensile strength, elastic modulus (chord or average tangent modulus) and absorbed energy per unit volume with increasing strain rate from intermediate to dynamic tension, is observed for all CFRPs. The elastic modulus enhanced at dynamic tension increases tensile strength and absorbed energy per unit volume. From the fracture strain criterion, it is found that the whole CFRP cable is strain rate insensitive, since strain at tensile strength is almost constant over the strain rate region tested. This insensitivity is similar to that of AFRP UD [6, 7]

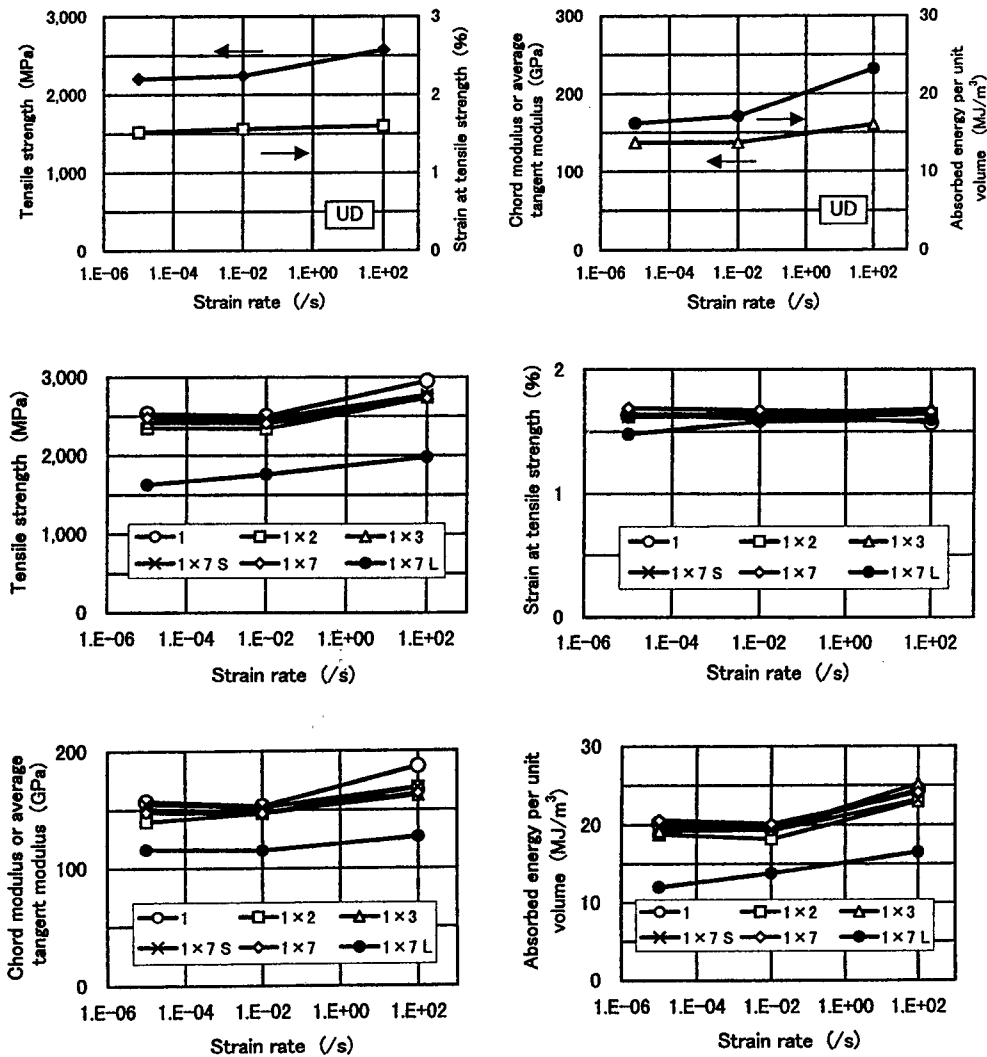


Figure 5 Strain rate effect in tensile characteristics of CFRP UD and CFRP cables.

## Conclusions

Followings are concluded in mechanical characterization of CFRP UD and CFRP cables at the strain rate over seven decades ( $10^{-5}$ - $10^2$  s $^{-1}$ ).

1. The specimen fastening technique using expansive cement works well to fasten CFRP UD and CFRP cables, especially in dynamic tension.
2. Stress-strain relation is linear at quasi-static ( $10^{-5}$  s $^{-1}$ ) and intermediate ( $10^{-2}$  s $^{-1}$ ) rate of strain in tension for CFRP UD and CFRP cables. And no obvious change in their mechanical properties is observed at these range.
3. In dynamic tension ( $10^2$  s $^{-1}$ ), tensile response enhances tensile modulus and the stress-strain relation becomes non-linear. But strain at tensile strength remains almost constant. Accordingly, this increases tensile strength and absorbed energy per unit volume.
4. Basing upon the fracture strain criterion, CFRP UD and CFRP cables have strain rate insensitivity from  $10^{-5}$  s $^{-1}$  to  $10^2$  s $^{-1}$ . This property is similar to that of uni-directional AFRP.

## References

1. S. Swiatecki, Mar., 1998. "Building better bridges with CFRP," Reinforced Plastics, pp. 44-45, 47.
2. N.F. Grace, Oct., 1999. "Continuous CFRP Prestressed Concrete Bridges," Concrete International, pp. 42-47
3. Tokyo Rope, Oct., 1993. "Technical Data on CFCC".
4. H. Kimura, K. Kawata and M. Itabashi, 1996. "Analysis of Tensile Behavior of CFRP Strand Cables with Various Structures," Advanced Composite Materials, Vol. 6, No. 1, pp. 19-32.
5. Ed. by N. Ishikawa, Dec., 1993. *Impact Behavior and Design of Structures*, Subcommittee of Impact Problems, Committee of Structural Engineering, Japan Society of Civil Engineers, pp. 35-36 ( in Japanese).
6. K. Kawata, M. Itabashi and M. Tomi, 1993. "Dynamic Tensile Mechanical Properties of One-Dimensional Continuous-Fiber Reinforced KFRP and GFRP," Proceedings of the 4<sup>th</sup> Zairyo no Shogeki Mondai Symposium, Society of Materials Science, Japan, pp. 1-4 (in Japanese)
7. K. Kawata, M. Itabashi and H. Kimura, Aug., 1996. "Mechanical Characterization on Solids in High Strain Rate Tension," Proceedings of IUTAM Symposium on Constitutive Relation in High/Very High Strain Rate, Noda, Springer-Verlag, Heidelberg, Berlin, New York, Tokyo, pp. 1-16.
8. T. Harada, M. Soeda, T. Enomoto, S. Tokumitsu, M. Khin and T. Idemitsu, Oct., 1997. "Behavior of Anchorage for FRP Tendons Using Highly Expansive Material Under Cyclic Loading," Non-Metallic (FRP) Reinforcement for Concrete Structures, Proceedings of the Third International Symposium, Vol. 2, pp. 719-726.

# **Creep and Fatigue**

---

## **Time-Temperature Dependence of Fatigue Strength of Unidirectional CFRP**

Masayuki NAKADA<sup>1</sup>, Yasushi MIYANO<sup>1</sup>, and Rokuro MUKI<sup>2</sup>

### **Abstract**

The tensile test for resin impregnated carbon fiber strand (CFRP strand) and the bending tests for longitudinal and transverse directions of unidirectional CFRP laminates were carried out for constant strain-rate (CSR) and fatigue loadings under various loading-rates and temperatures. The master curves of these fatigue strengths as well as CSR strengths are constructed from these test results based on the time-temperature superposition principle. It is clarified from these master curves that all these fatigue strengths depend on loading-rate and temperature rather than the number of cycles to failure.

### **Introduction**

The mechanical behavior of polymer resins exhibits time and temperature dependence, called viscoelastic behavior, not only above the glass-transition temperature  $T_g$  but also below  $T_g$ . Thus, it can be presumed that the mechanical behavior of FRP using polymer resins as matrices also depends on time and temperature even below  $T_g$  which is within the normal operating-temperature range. The presumption is confirmed experimentally by Aboudi et al. [1], Sullivan [8], Gates [3], and Miyano et al. [5].

The time-temperature dependence of the flexural strengths for satin-woven CFRP laminates under constant strain-rate (CSR) and fatigue loadings has been studied by Miyano et al. [2,4,6,7]. It was observed that the fracture modes are almost identical under CSR and fatigue loadings over a wide range of time and temperature, and the same time-temperature superposition principle holds for CSR and fatigue strengths. We have shown [7] that the master curve of fatigue strength can be obtained from the CSR strengths under various strain-rates and temperatures and the fatigue strengths at a single frequency under various temperatures.

In this paper, we present the CSR and fatigue tests results of unidirectional CFRP for three kinds of loading under various loading-rates and temperatures: the tensile test for resin impregnated carbon fiber strand (CFRP strand), the bending tests

<sup>1</sup> Materials System Research Laboratory, Kanazawa Institute of Technology, 3-1 Yatsukaho, Matto, Ishikawa 924-0838, Japan

<sup>2</sup> Civil & Environmental Engineering Department, University of California, Los Angeles, Los Angeles, CA90095-1593, U.S.A.



for longitudinal and transverse directions of unidirectional CFRP laminates. The dependence of these fatigue strengths upon number of cycles to failure as well as loading-rate and temperature are discussed based on the time-temperature superposition principle.

## Experimental Procedure

### Preparation of Specimen

Epoxy resin impregnated carbon fiber strand (CFRP strand) was used as the tensile test specimen for the longitudinal direction of unidirectional CFRP, which consists of a high-strength carbon fiber TORAYCA® T400-3K (TORAY) and a general-purpose epoxy resin EPIKOTE® 828 (YUKA SHELL EPOXY). These specimens were produced by filament winding method. The glass-transition temperature  $T_g$  of this epoxy resin is 145°C. The diameter of CFRP strand is approximately 1 mm.

Unidirectional CFRP laminates was used as the bending test specimen for longitudinal and transverse directions, which consists of a high-strength carbon fiber TORAYCA® T300-3K (TORAY) and a general-purpose epoxy resin #2500 (TORAY). These specimens were produced by hot pressing the prepreg sheets made from these fiber and resin. The glass transition temperature  $T_g$  of 2500 is 130°C. The fiber volume fraction of CFRP laminates is approximately 55%.

### Test Procedures

During preliminary tests, pulling-out of strand from the grip ends occurred in both CSR and fatigue tests during loading. This pulling-out was suppressed by two improvements: use of specimen with taper-shaped configuration at both ends bonded by adhesive resin in the grips as shown in the upper portion of this figure, and use of the small temperature chamber as shown in the right side of this figure to keep the grips at room temperature. After these improvements, fracture of all specimens tested for both CSR and fatigue loadings occurred within the central 70mm region of the specimen.

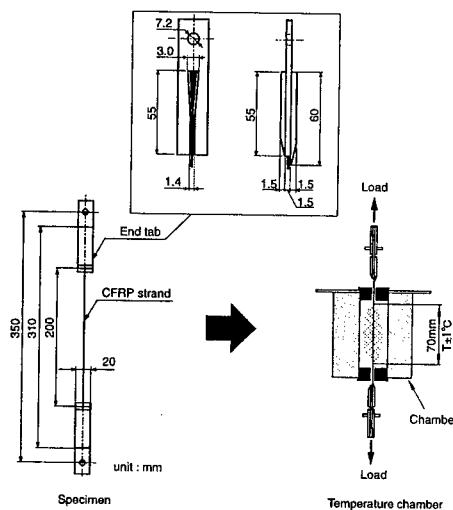


Figure 1 Tensile test specimen and small temperature chamber

The tensile CSR tests were carried out under various constant temperatures by using an Instron type testing machine with a small temperature chamber. Loading rates (crosshead speeds) were 0.01, 1, and 100 mm/min. The tensile fatigue tests were carried out under several constant temperatures at two frequencies  $f=2$  and 0.02Hz by using an electro-hydraulic servo testing machine with a small temperature chamber. Stress ratio  $R$  (minimum stress/maximum stress) was 0.1. The tensile CSR and fatigue strengths  $\sigma$  of CFRP strand are defined by

$$\sigma = P_{\max} \frac{\rho}{t_e} \quad (1)$$

where  $P_{\max}$ ,  $\rho$ ,  $t_e$  are the maximum load of CFRP strand, the density of fiber strand, the tex of fiber strand, respectively, and their dimensions in this order are [N], [g/cm<sup>3</sup>], [g/10<sup>6</sup>m].

Three point bending CSR tests for longitudinal and transverse directions of unidirectional CFRP laminates (to be abbreviated as longitudinal tests and transverse tests below) were carried out by using an Instron type testing machine with a temperature chamber. The nominal dimensions of the test specimens were 80, 10, and 3 mm (length, width, thickness) for the longitudinal tests and were 65, 15, and 3 mm for the transverse tests. The span of the test fixture was 60 mm for the longitudinal tests and was 50 mm for the transverse tests. The tests were carried out under various constant temperatures at three loading-rates  $V=0.02, 2, 200$  mm/min.

Specimens with the same dimensions were used for three point bending fatigue tests. The fatigue tests were carried out under several constant temperatures at  $f=2$  and 0.02Hz by using an electro-hydraulic servo testing machine with a temperature chamber. Stress ratio  $R$  was 0.05. The flexural CSR and fatigue strengths  $\sigma$  of CFRP laminate are defined by

$$\sigma = \frac{3P_{\max}L}{2bh^2} \quad (2)$$

where  $P_{\max}$ ,  $L$ ,  $b$  and  $h$  are the maximum load, the span, width and thickness, respectively, and the dimension of the maximum load is [N] while those of the rests are [mm].

## Results and Discussion

### Master Curve of CSR Strength

The left sides of Fig.2 show the CSR strength  $\sigma_s$  versus time to failure  $t_s$  for three cases: (a) tensile strength for CFRP strand, (b) the flexural strength in the longitudinal direction of unidirectional CFRP laminates, and (c) the flexural strength in the transverse direction of unidirectional CFRP laminates.

The master curve for each  $\sigma_s$  was constructed by shifting  $\sigma_s$  at constant temperatures other than reference temperature  $T_0$  along the log scale of  $t_s$  so that they overlap on  $\sigma_s$  at  $T_0$  or on each other to form a single smooth curve as shown in the right side of Fig.2. Since the smooth master curve for each  $\sigma_s$  can be obtained, the time-temperature superposition principle is applicable for each  $\sigma_s$ .

The time-temperature shift factor  $a_{T_0}(T)$  is defined by

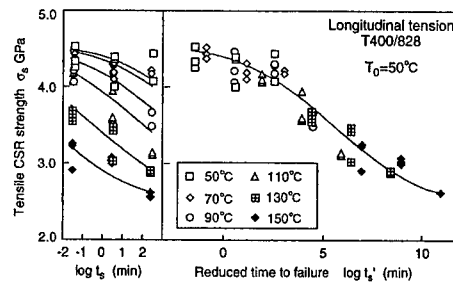
$$a_{T_0}(T) = \frac{t_s}{t'_s} \quad (3)$$

where  $t'_s$  is the reduced time to failure at  $T_0$ .

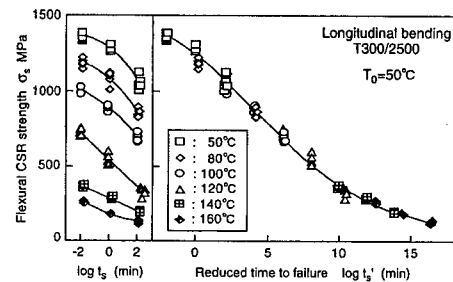
The shift factors  $a_{T_0}(T)$  for  $\sigma_s$  obtained experimentally in Fig.2 are plotted respectively as three kinds of circle in Fig.3. The solid and dotted lines in this figure show  $a_{T_0}(T)$  for the creep compliance of matrix epoxy resin, Epikote 828 and #2500, respectively. The  $a_{T_0}(T)$  for each  $\sigma_s$  agrees well with that for the creep compliance of corresponding matrix resin, which are described by two Arrhenius' equations shown in Eq.(4) with different activation energies  $\Delta H$ . Therefore, the time-temperature dependence of three kinds of CSR strength for unidirectional CFRP is controlled by the viscoelastic behavior of matrix resin.

$$\log a_{T_0}(T) = \frac{\Delta H}{2.303G} \left( \frac{1}{T} - \frac{1}{T_0} \right) \quad (4)$$

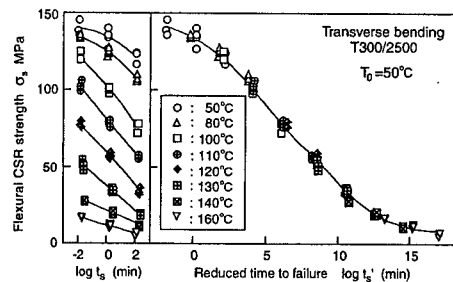
where  $G$  is the gas constant.



(a) Tensile  $\sigma_s$  in longitudinal direction



(b) Flexural  $\sigma_s$  in longitudinal direction



(c) Flexural  $\sigma_s$  in transverse direction

Figure 2 Master curves of  $\sigma_s$  for three kinds of loading

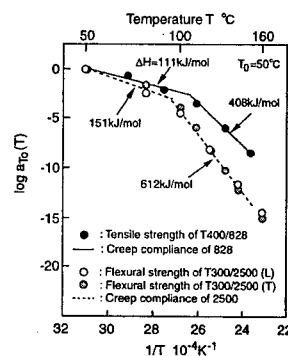


Figure 3 Time-temperature shift factors  $a_{T_0}(T)$  for  $\sigma_s$

### Master Curve of Fatigue Strength

We turn now the fatigue strength  $\sigma_f$  and regard it either as a function of the number of cycles to failure  $N_f$  or of the time to failure  $t_f = N_f/f$  for a combination of frequency  $f$ , temperature  $T$  and denote them by  $\sigma_f(N_f; f, T)$  or  $\sigma_f(t_f; f, T)$ . Further, we regard the CSR strength  $\sigma_s(t_f; T)$  the fatigue strength at  $N_f=1/2$ ,  $R=0$ , and  $t_f=1/(2f)$ ; this is motivated by closeness of the line connecting the origin and  $(\pi, 1)$  and the curve  $[1+\sin(t-\pi/2)]/2$  for  $0 < t < \pi$  [7].

To describe the master curve of  $\sigma_f$ , we need the reduced frequency  $f'$  and the reduced time  $t_f'$  defined by

$$f' = f a_{T_0}(T), \quad t_f' = \frac{t_f}{a_{T_0}(T)} = \frac{N_f}{f'} \quad (5)$$

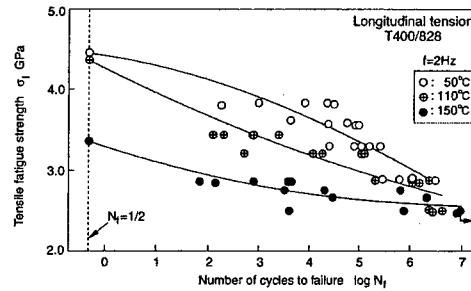
We introduce two alternative expressions for the master curve:  $\sigma_f(t_f'; f, T_0)$  and  $\sigma_f(t_f'; N_f, T_0)$ . In the latter expression, the explicit reference to frequency is suppressed in favor of  $N_f$ . Note that the master curve of  $\sigma_f$  at  $N_f=1/2$  is regarded as the master curve of  $\sigma_s$ . Equation (5) enables one to construct the master curve for an arbitrary frequency from the tests at a single frequency under various temperatures.

The following four figures, Figs.4~7, display  $\sigma_f$ - $N_f$  curves or  $\sigma_f$ - $t_f'$  curves for the three kinds of loading: tension in longitudinal direction, bending in longitudinal direction, and bending in transverse direction.

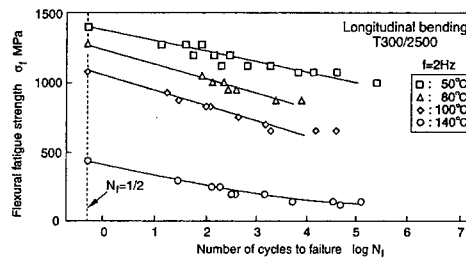
Figure 4 shows  $\sigma_f$ - $N_f$  curves at  $f=2\text{Hz}$  together with  $\sigma_s$  which is regarded as  $\sigma_f$  at  $N_f=1/2$ . In Fig.5,  $\sigma_f$ - $t_f'$  curves at  $T_0=50^\circ\text{C}$  are depicted in solid curves using  $a_{T_0}(T)$  for  $\sigma_s$ ; the master curve for  $\sigma_s$  is indicated in a dashed curve. Figure 6 shows the master curves of  $\sigma_f$  versus  $t_f'$  for fixed  $N_f$ , which are constructed by connecting the points of the same  $N_f$  on the curves of each  $f'$ .

We define the reduced temperature  $T'$  by

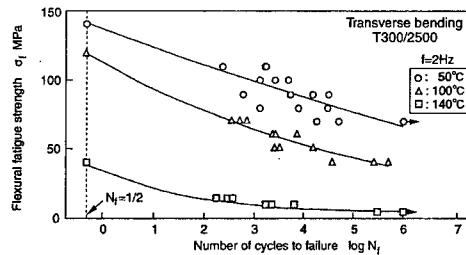
$$\sigma_f(t_{f_0}, T') = \sigma_f(t_{f_0}', T_0) \quad (6)$$



(a) Tensile  $\sigma_f$  in longitudinal direction



(b) Flexural  $\sigma_f$  in longitudinal direction



(c) Flexural  $\sigma_f$  in transverse direction

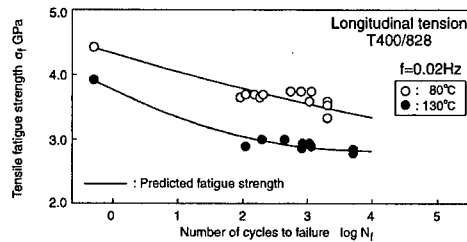
Figure 4  $\sigma_f$ - $N_f$  curves for various temperatures  $T$

$f=0.02\text{Hz}$  predicted in this manner from the data for  $f=2\text{Hz}$  are displayed in Fig.7 together with test data. Since the  $\sigma_f-N_f$  curves predicted on the basis of the shift factor for CSR strength capture fatigue test data satisfactorily, the time-temperature superposition principle for CSR strength also holds for fatigue strength. Therefore, the validity for the construction of master curves of fatigue strength by using the time-temperature shift factor for CSR strength is confirmed.

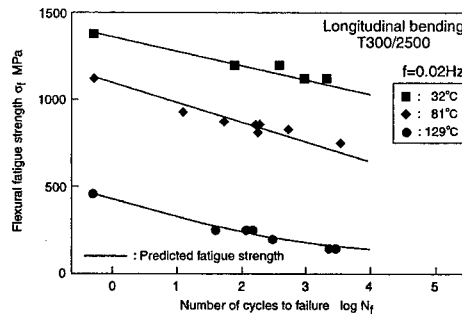
### Characterization of Fatigue Strength for Three kinds of Loading

The fatigue fracture mode for the tensile test in the longitudinal direction of unidirectional CFRP is the tensile fracture in all ranges of time to failure, temperature, and number of cycles to failure  $N_f$ . The fatigue fracture mode for the bending test in longitudinal direction is the compressive fracture on the compression side of specimen triggered by the microbuckling of fiber in all ranges of time to failure, temperature, and  $N_f$ . The fatigue fracture mode for the bending test in transverse direction is the tensile fracture on the tension side of specimen in all ranges of time to failure, temperature, and  $N_f$ .

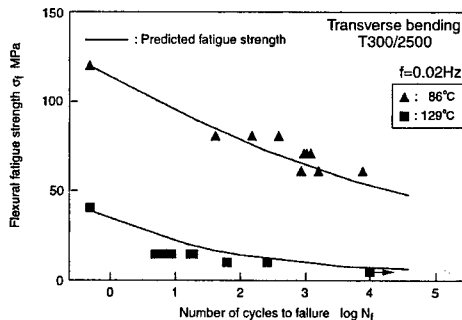
We return to Fig.6 and note that the tensile fatigue strength in longitudinal direction decreases clearly with increasing  $N_f$  in the range of short time to failure and low temperature. On the other hand, the tensile fatigue strength decreases scarcely with increasing  $N_f$  in the range of long time to failure and high temperature in the vicinity of the glass transition temperature of matrix resin. The flexural fatigue strength in longitudinal direction decreases with time to failure and temperature, however this strength depends scarcely on  $N_f$  in all ranges of time to failure and temperature. The flexural fatigue strength in transverse direction decreases with time to failure, temperature, and  $N_f$  in all ranges of time to failure and temperature.



(a) Tensile  $\sigma_f$  in longitudinal direction



(b) Flexural  $\sigma_f$  in longitudinal direction



(c) Flexural  $\sigma_f$  in transverse direction

Figure 7  $\sigma_f-N_f$  curves (predicted from test at  $f=2\text{Hz}$ ) and test data at  $f=0.02\text{Hz}$  for various temperatures  $T$

## Conclusion

The time and temperature dependence of the tensile fatigue strength in longitudinal direction and the flexural fatigue strengths in longitudinal and transverse directions for unidirectional CFRP are characterized based on the time-temperature superposition principle. We have shown that the fatigue strengths of unidirectional CFRP for three kinds of loading depend on loading-rate and temperature rather than the number of cycles to failure.

## References

1. Aboudi, J. and G. Cederbaum, "Analysis of Viscoelastic Laminated Composite Plates", *Composite Structures*, 12 (1989), 243-256.
2. Enyama, J., M. K. McMurray, M. Nakada and Y. Miyano, "Effects of Stress Ratio on Flexural Fatigue Behavior of a Satin Woven CFRP Laminate", *Proceedings of 3rd Japan SAMPE*, Vol. 2: (1993), 2418-2421.
3. Gates, T., "Experimental Characterization of Nonlinear, Rate Dependent Behavior in Advanced Polymer Matrix Composites", *Experimental Mechanics*, 32 (1992), 68-73.
4. McMurray, M. K., J. Enyama, M. Nakada and Y. Miyano, "Loading Rate and Temperature Dependence on Flexural Fatigue Behavior of a Satin Woven CFRP Laminate", *Proceedings of 38th SAMPE*, No. 2 (1993), 1944-1956.
5. Miyano, Y., M. Kanemitsu, T. Kunio and H. Kuhn, "Role of Matrix Resin on Fracture Strengths of Unidirectional CFRP", *Journal of Composite Materials*, 20 (1986), 520-538.
6. Miyano, Y., M. K. McMurray, J. Enyama and M. Nakada, "Loading Rate and Temperature Dependence on Flexural Fatigue Behavior of a Satin Woven CFRP laminate", *Journal of Composite Materials*, 28 (1994), 1250-1260.
7. Miyano, Y., M. Nakada, M. K. McMurray and R. Muki, "Prediction of Flexural Fatigue Strength of CFRP Composites under Arbitrary Frequency, Stress Ratio and Temperature", *Journal of Composite Materials*, 31 (1997), 619-638.
8. Sullivan, J., "Creep and Physical Aging of Composites", *Composite Science and Technology*, 39 (1990), 207-232.

## **Fatigue of High Strength Fiber Caused by Repeated Axial Compression**

Y.Yamashita , S.Kawabata and A.Kido

### **Abstract**

We report a method for measuring the axial compression characteristic of high strength fibers. This is a technique for loading compression force on a fiber by winding it on a plastic rod at an angle of 45 degrees. The fiber was fixed to the rod with an adhesive. The aramid fiber, the carbon fiber, and the E-glass fiber were examined in this research. The relation between the compression fatigue and strength of the fiber became clear by this technique.

### **Introduction**

Previously, we measured the axial compression characteristics of high strength, high modulus fibers. Two techniques were developed. Firstly, we measured the properties of a high packing density micro composite<sup>1)</sup> (1990-1995), and secondly we axially compressed single fibers<sup>2), 3)</sup> (1995-1996). In this paper we report a method of measuring the axial compression characteristics of fibers using torsion. The advantage of this technique is that it is very easily to measure the axial compression fatigue of a fiber. The measurement of the elastic modulus and the yield strength is possible in both the micro composite and the single fiber compression method tests. However, the fatigue measurement was difficult, because of crushing at the composite edge in the composite method, or the falling of the single fiber in the single fiber method. In contrast, using the method described in this paper, it is easy to observe the change in elastic modulus during compression fatigue of a fiber. We report the measured result of high strength fibers.

### **Experiment**

#### *The principle of the measurement*

The deformation  $\gamma$  (shear strain) by torsion in the stress skin (twist angle  $\theta$ ) is given in equation (1).

$$\gamma = \frac{\theta R}{L} \quad (1)$$

---

Y.Yamashita, S.Kawabata and A.Kido, Department of Materials Science, The University of Shiga Prefecture, 2500 Hassaka, Hikone, Shiga, 522-8533, Japan

where  $L$  is the cylinder length,  
and  $R$  is the cylinder radius.  
In particular, the strain in the  $45^\circ$  direction is given  
by equation (2) and (3),

$$\varepsilon_1 = \frac{1}{2}\gamma \quad (\text{Tensile}) \quad (2)$$

$$\varepsilon_2 = -\frac{1}{2}\gamma \quad (\text{Comp.}) \quad (3)$$

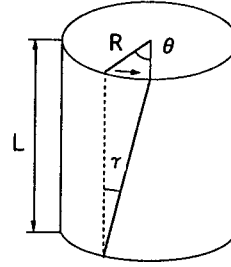


Figure 1

When equation (3) is substituted in equation (1), and  
using diameter  $D$  instead of radius  $R$ , equation (4) is obtained

$$\varepsilon_2 = -\frac{\theta D}{4L} \quad (4)$$

The torsion torque  $T$  of the cylinder is given by

$$T = GI_P \cdot \frac{\theta}{L} \quad (5)$$

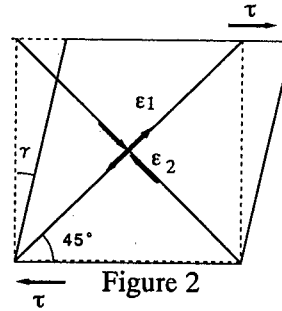


Figure 2

where  $G$  is the shear modulus and  $I_p$  is a shape factor.  $I_p$  is equal to  $(\pi D^4)/32$  for a cylinder, so we have

$$T = G \frac{\pi}{32} D^4 \cdot \frac{\theta}{L} \quad (6)$$

Consider the case in which a fiber is wound around this cylinder at a  $45^\circ$  angle (Figure 3(a)). The compressive strain which is added to the fiber  $\varepsilon_2$ , is given by equation (3). The compression energy  $u_c$  added to the fiber corresponds to the area under the load-elongation curve of the fiber (equation(7) and figure 3(b)).

$$u_c = \frac{1}{2} \cdot \lambda \cdot f \quad (7)$$

Let  $\ell_f$  and  $A$  denote the length and cross-sectional area of the fiber. When equations (8) are substituted into equation (7), we obtain equation (9)

$$f = \sigma \cdot A, \quad \sigma = \varepsilon_c \cdot E_c, \quad \ell_f = \sqrt{2}L, \quad \lambda = \varepsilon_c \cdot \ell_f \quad (8)$$

$$u_c = \frac{1}{2} \cdot \frac{\gamma}{2} \sqrt{2}L \cdot \frac{\gamma}{2} E_c A = \frac{\sqrt{2}}{8} \gamma^2 AL \quad (9)$$



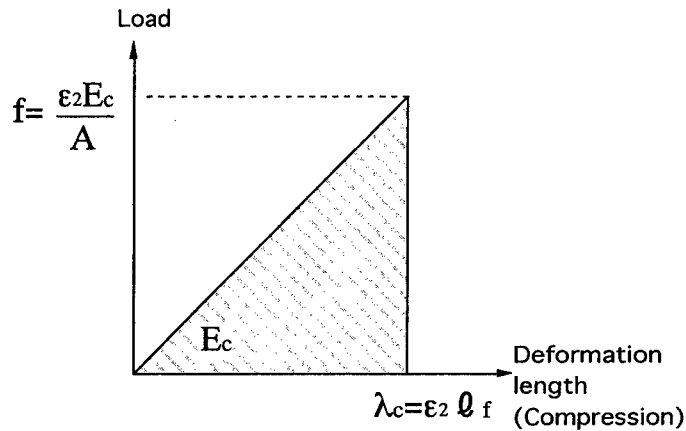
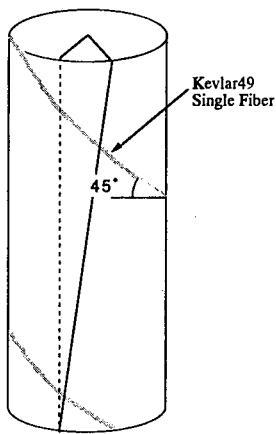


Figure 3(a)

Figure 3(b)

Figure 4 shows the twist energy of the cylindrical composite consisting of the rod and the fibers wrapped around it. The gray area is the twist energy of only the round rod. The area filled with diagonal lines represents the increase due to the presence of the helically wrapped fibers. The fibers are assumed to be wrapped in a single layer. The increase in the energy due to the increase of the torque ( $\Delta T$ ) of the cylindrical composite resulting from the winding of the fiber is denoted by  $u_t$ . The increase in compression energy of the fiber is  $u_c$ . The energy increase from the increase in the torque  $u_t$  can be considered to be equal to  $u_c$  (equation (11)). Hence we can derive equation (12), which gives us the axial compression modulus of the single fiber,  $E_c$ .

$$u_t = \frac{1}{2} \Delta T \cdot \theta$$

$$u_c = u_t$$

$$E_c = \frac{4L}{\sqrt{2}R^2\theta A} \cdot \Delta T$$

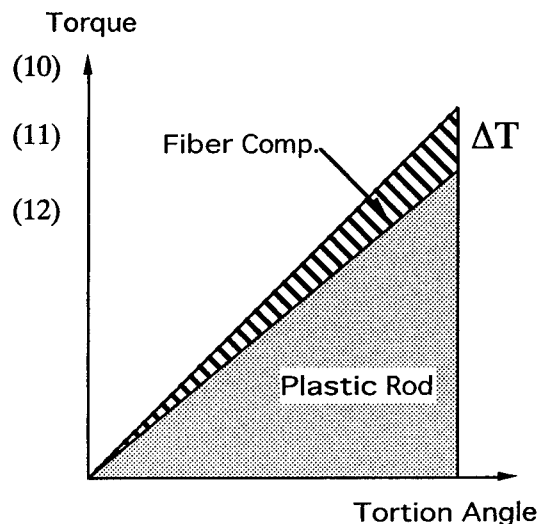


Figure 4

### Sample

The cylindrical rod used as the base unit was made from acrylic or

polycarbonate resin. The rod had a diameter of 3mm. A bundle of fibers (aramid fiber "Kevlar", carbon fiber "T-300" and E-glass fiber ) was spirally wound onto the cylindrical rod at an angle of 45°, and then fixed to the rod by a cyanoacrylate adhesive. The adhesion between the fiber bundle and the rod was good; there was no peeling at this interface. After bonding to the rod, the sample was aged for 24 hours at room temperature. The gauge length of the torsion tester was 30mm. A test sample is shown in figure 5.

### *Measurement*

Figure 6 shows the high load and high performance torsion tester that was used (Kato Tech Ltd.). The maximum twist angle was  $\pm 80^\circ$ . The sample was fixed in a chuck, and then attached to the tester. The relationship between torque and twist angle was recorded on a X-Y recorder or on a personal computer.

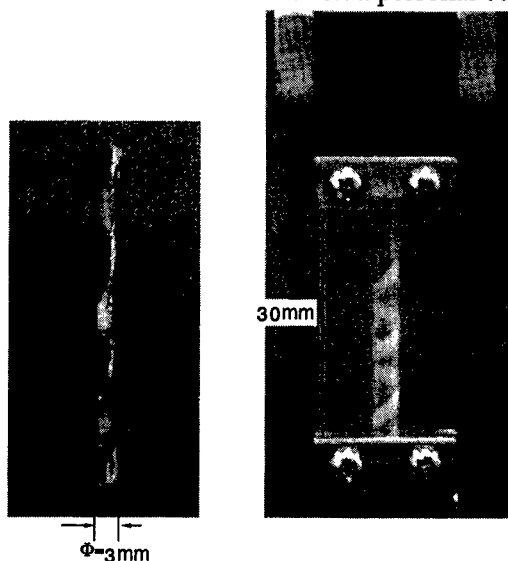


Figure 5 A cylindrical rod sample

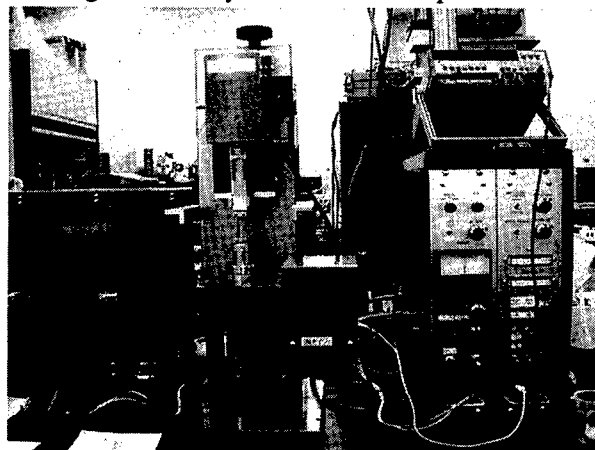


Figure 6 The high performance torsion tester (Kato Tech Ltd.)

## Result and discussion

The suitability of the linear elastic range in torsion of the plastic cylinder was confirmed by a preliminary experiment. The twist measurement of the cylinder was carried out in the linear range. The plastic cylinder did not have a decrease after repeated twisting. Figure 7 (Kevlar29) and 8 (T-300) show the relationship between the twist angle and the torque of both the cylinder and the fiber-cylinder composite. In this case, the round bar was twisted in both the right and left directions. A compressive force is applied to the fiber when the round bar which the fiber is bonded to is twisted to the right. Tensile force is applied when twisted to the left. Compression force and tensile force are alternately applied to the fiber as the round bar is repeatedly twisted to the right and to the left.

The glass fiber was used to verify that the experiment matched the theory. The compression modulus of glass fiber measured by the torsion compression was 81GPa, which almost corresponds to 84.5GPa which is the value of its tensile modulus. Because the relation between compressive strain and compression modulus is obtained from equation (1), (3), and (12), the compressive stress is given by the multiplication of the strain and modulus. The result is shown in figures 9 and 10. It is understood that compression moduli of the aramid and carbon fibers are smaller their tensile moduli. However, the lowering of the elastic modulus by composite collapse as observed in the Kevlar micro composite was not generated. Therefore, the fiber axial

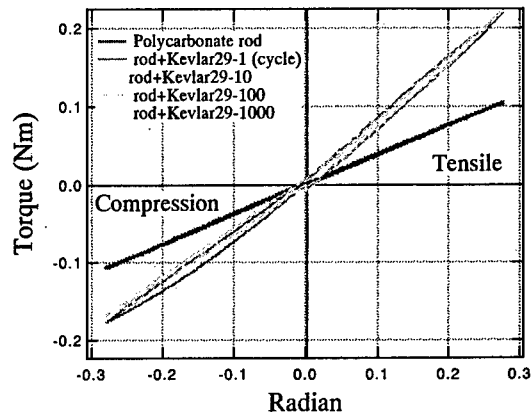


Figure 7 Relationship between torque and

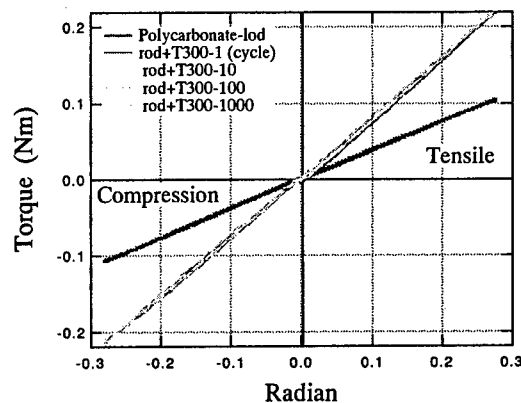


Figure 8 Relationship between torque and twist angle of rod for T-300

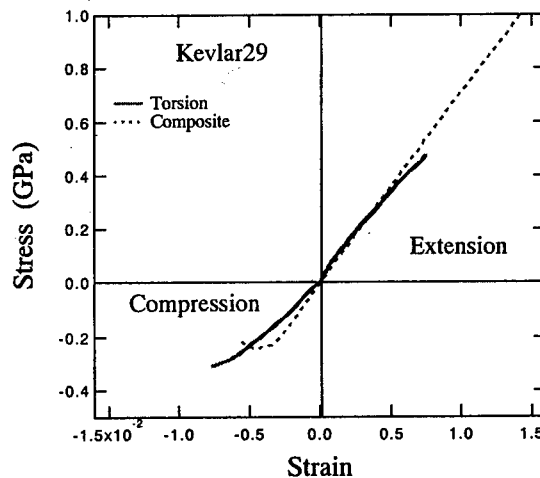


Figure 9 Longitudinal properties of aramid fiber covering the whole compression and extension region

direction compression modulus measurement was easy using this technique.

Figure 11 shows the relationship between the frequency of the compression fatigue and the change in modulus of elasticity of the Kevlar fiber. It was observed that for the cylinder wrapped by Kevlar, the modulus decreased due to compression torsional fatigue. The compression yield strain of the Kevlar fiber is 0.5% according to our composite method. Modulus does not decrease when compressive strain is 0.3%. When the compression fatigue strain exceeded 0.5%, we observed that the modulus began to decrease. It is thought that modulus decreases as the twist cycle increases when the compression fatigue strain exceeds 0.5%. However, a decrease in modulus of the fiber was not observed after tensile torsional fatigue. Figure 12 is a photograph of the Kevlar fibers taken after 1000 compression fatigue cycles. Many kink bands can be seen on the surface of the Kevlar fibers.

Figure 13 shows the change in the modulus when a repetition fiber tensile strain of 0.5%, 0.88%, and 1.0% were used. The tensile modulus of Kevlar single fiber increases a little as a result of tensile fatigue.

It is important to predict the lowering of the elastic modulus by long-time fatigue. Previously, a superposition rule was established between fatigue frequency and strain in the single fiber torsional fatigue test<sup>4)</sup>. That is to say that the fatigue was found to be a function of the product of frequency and strain. However, in this experiment when both the compression force and

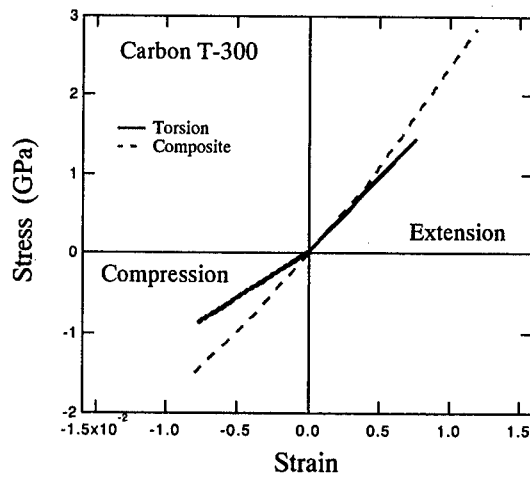


Figure 10 Longitudinal property of carbon fiber

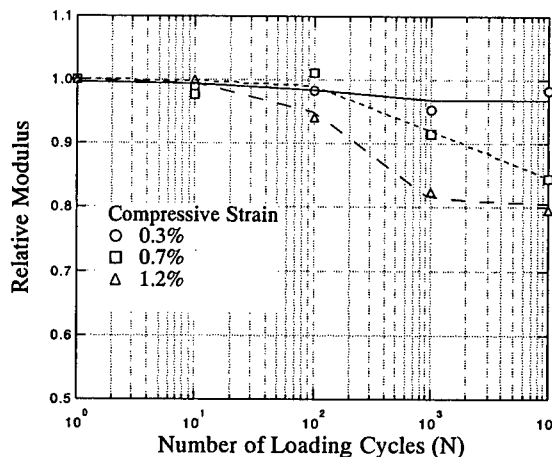


Figure 11 Strain Dependence of the Compressive Modulus

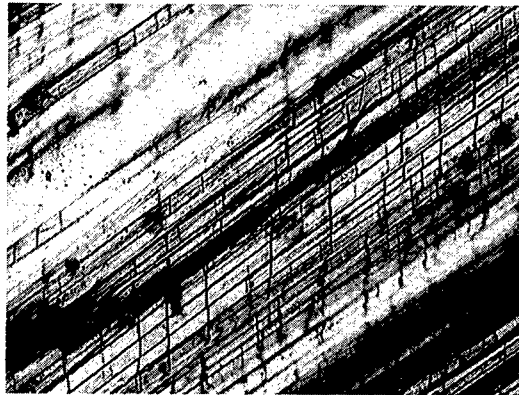


Figure 12 Photograph of after 1000 cycles compression fatigue of Kevlar 49

tensile force fatigues were loaded to the fiber, it was obtained that the decrease in modulus quickened compared with only the compression force (Figure 14). Modulus decreases even the twice fast than the fatigue only of compression. This reason is being examined now. Perhaps, it seems that the amount of the total strain loaded to the fiber is related to the fatigue.

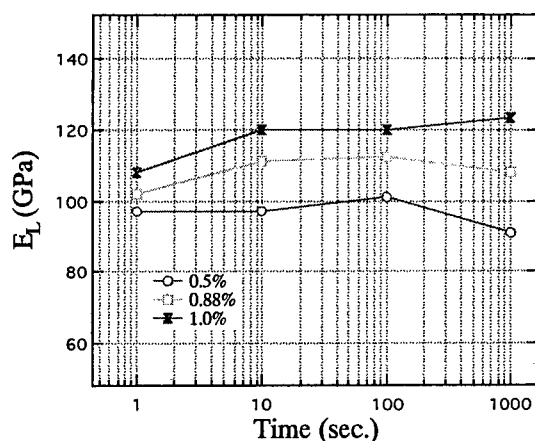


Figure 13 Kevlar49 Tenile Fatigue

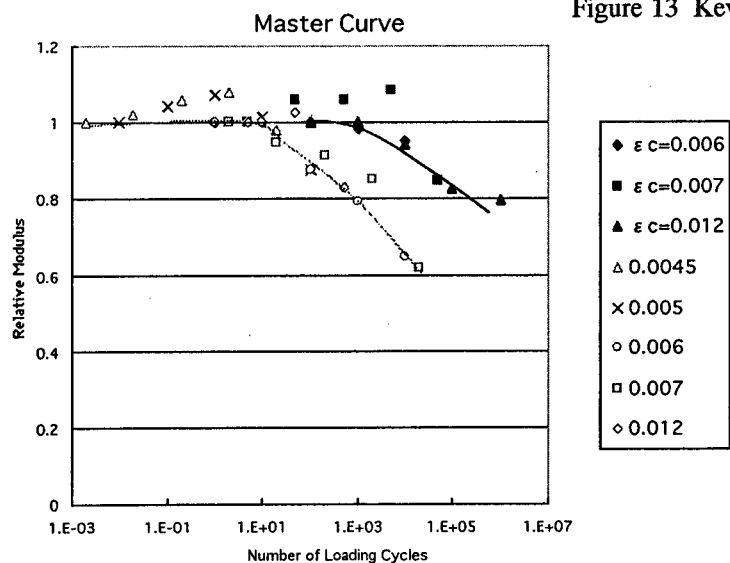


Figure 14 Superposition curves of the compression fatigue  
Solid line/ filled mark shows the compression torsion  
Dotted line/ open mark shows the compression tensile torsion

## Reference

- 1) S. Kawabata, T. Kotani and Y. Yamashita, "Measurement of the Longitudinal Mechanical Properties of High-performance Fibers", J. Text. Inst., **86**, 347-359 (1995)
- 2) Y. Yamashita and S. Kawabata, "Longitudinal Compression Property of Wool Fiber", Pro. 24<sup>th</sup> Text. Research Sympo. At Mt. Fuji, 16-21 (1995)
- 3) Y. Yamashita and S. Kawabata, "Longitudinal Compression Property of Single Fiber", Polymer Preprints Japan, **45**, No.5 858 (1996)
- 4) S. Kawabata, "Prediction of Fatigue Life of Fiber and Durability Design of Fiber Reinforced Rubber", Full text of International Rubber Conference 1995 in Kobe (IRC95 Kobe), The Society of Rubber Industry, Japan, pp147-150 (1995)

## **Study on Creep Behavior of Glass Fiber Reinforced Polycarbonate**

K. K. Biswas, M. Ikueda and S. Somiya

### **Abstract**

In this study creep behavior of glass fiber reinforced Polycarbonate was carried out at elevated temperatures. The result shows that creep behavior of GFRPC composites represented good agreement with Arrhenius reciprocity law of time-temperature. The effect of fiber volume fraction on creep behavior was also been studied. It became possible to estimate the creep behavior of GFRPC composites with any fiber contents using the grand master curve of creep compliance master curves and time and modulus shift factors. So it become possible to design materials for creep by reinforcing quantity of fibers to obtain the required objectives.

**Key Words:** GFRPC, creep compliance, Arrhenius equation, grand-master curve.

### **Introduction**

Plastics, specially fiber reinforced plastics (FRP), are light in weight but yet are sufficiently strong enough to withstand high loads. As a result, in aerospace vehicles, like aircrafts, FRPs are used in substitution of metal alloys. An important aspect of their composite structural performance is the visco-elastic behavior of FRP, which as a polymeric solid, is elastic in that it recovers but is viscous in that it creeps. Due to the fact that FRPs are not simple elastic solids, it is always necessary to take into account not only the stress, but also the time of applied stress. Much research has been done by Struik[1] on time-temperature dependency, especially on the physical aging of amorphous polymers and their composites. Kunio et. al. [2] have also investigated the mechanical properties, specifically with regard to the time-temperature dependency of some visco-elastic bodies. To evaluate the visco-elastic

---

K. K. Biswas, and M. Ikueda, Faculty of Science and Technology, Keio University, 3-14-1 Hiyoshi, Kohoku-ku, Yokohama 223-8522, Japan. e-mail: kanti@msr.st.keio.ac.jp

S. Somiya, Dept. of Mechanical Engineering, Keio University, 3-14-1 Hiyoshi, Kohoku-ku, Yokohama 223-8522, Japan. e-mail: somiya@mech.keio.ac.jp

properties of polymers, temperatures must be specified clearly and taken into consideration. Gates et. al.[3] are also performing research on the time dependency of different kinds of thermoplastics. Visco-elastic materials[4] are characterized by a fundamental concept on the linearly visco-elastic mechanical behavior under uniaxial stress-strain state and its mathematical representation in both the differential equation based on the spring-dashpot model and the integral form due to the superposition principle.

The visco-elastic behavior[5]-[6] of polymer composites is also dependent upon stress and temperature. Because FRPs are used in the primary structural materials of aircraft, spacecraft etc. as well as in their secondary structural materials, high durability and high reliability over long periods regarding their deformation become important issues. They show the changes in visco-elastic behavior at their operational temperatures. The structure of some casings has to withstand high temperature environments. Some pre-stress are introduced in the structures during molding as well as manufacturing. Also in practical uses, the structures have to carry some dead loads. Therefore at higher temperature creep occurs therein. It becomes essential then to study the creep behavior of these structural materials. On the other hand, as these composites are time dependent. Composites of Polycarbonate are widely used in parts of automobiles, vehicles, window glasses, roof rail etc. In the previous studies[7]-[9], creep behavior of stainless fiber-PPE and other composites were been carried out. Thus, it also becomes important to investigate the creep behavior of glass fiber reinforced Polycarbonate.

## Experimentals

### Materials

In this study glass-fiber reinforced Polycarbonate (GFRPC) with various fiber volume fractions were used as test material. The used matrix, Polycarbonate (PC), was a thermoplastic resin. The glass transition temperature of PC was about 150°C. Here, fiber weight fractions of the test specimens were 0% (resin matrix itself), 10%, 20% and 30% and the specimens were denoted hereafter as G0, G10, G20 and G30 respectively. The test specimens were molded by injection molding process to a dimension of 152.1×12.8×6.5mm.

### Experimental Procedure

To eliminate thermal history, the specimens were heated to 160°C ( $T_g + 10^\circ\text{C}$ ) and held for 10 minutes and then quenched to test temperatures in air. Creep tests were carried out by 3-point bending test method using creep test machine in Yamato Fine Oven DH42. Tests were made at several temperatures between 90°C to 140°C, which were below the glass-transition-temperature (150°C) of the composites. Plane wise creep tests were done with a span of 120mm and the applied loads were 1/10th of

their bending strengths. Each test specimen was inserted in the test chamber at room temperature and then raised the temperature to test temperature. Creep deflections at the middle of the specimen were measured with transducer (linear deflection gauge) and data at corresponding times were recorded in an on-line computer. Figure 1 shows the schematic presentation of experimental setup.

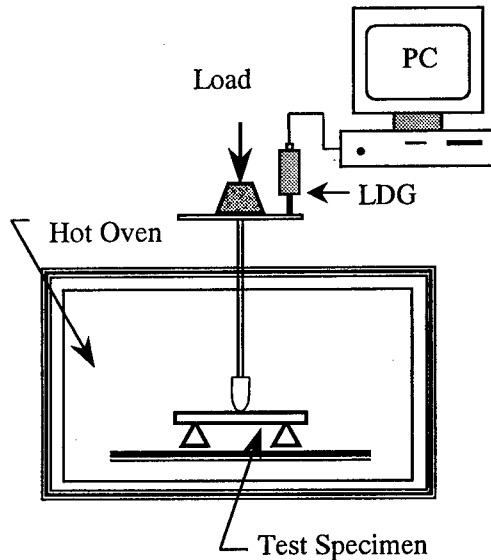


Figure1 Schematic presentation of creep test machine for three-point bending creep test:

## Results and Discussions

### Creep Behavior of GFRPC

Before executing creep test 3 point bending test has been carried out for calculating the flexural strength and flexural modulus. The flexural strength and flexural modulus increase slightly with the increase in fiber volume fraction. Table I shows the mechanical properties of these composites.

Table I Static mechanical properties of GFRPC composites.

Materials	G0	G10	G20	G30
Weight fraction (%)	0	10	20	30
Volume fraction (%)	0.0	5.0	10.6	16.8
Bending modulus (GPa)	2.1	3.5	5.6	7.7
Bending strength (MPa)	85.3	114.7	141.9	163.3



To evaluate the creep behavior of GFRPC, the creep compliance was calculated from the creep data. Figure 2(a) shows the creep compliance curves of G10 composite. At lower temperature from about 90°C to 110°C, the creep compliance were almost invariant with time but an insignificant increasing tendency was observed. At 120°C the rate of increase was considerably higher. In contrast, at higher temperatures, specifically above 130°C, the creep compliance rapidly increased with time. The creep compliance curves exhibited the typical creep behavior i.e. at any constant temperature the creep compliance increased with the increase in time and at a specific time the creep compliance increased with the increase in temperature.

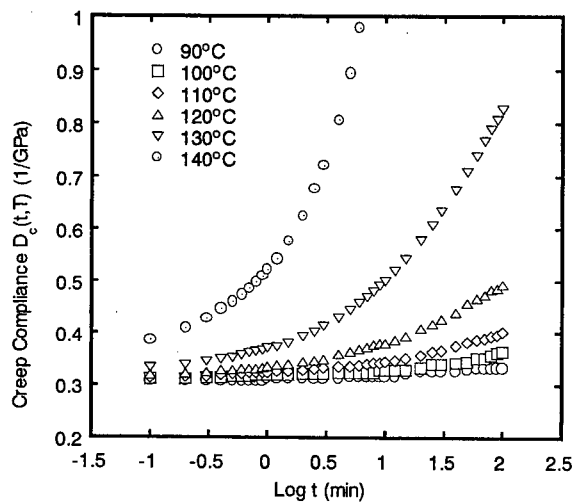


Figure 2(a) Creep compliance curves of glass fiber reinforced polycarbonate (G10).

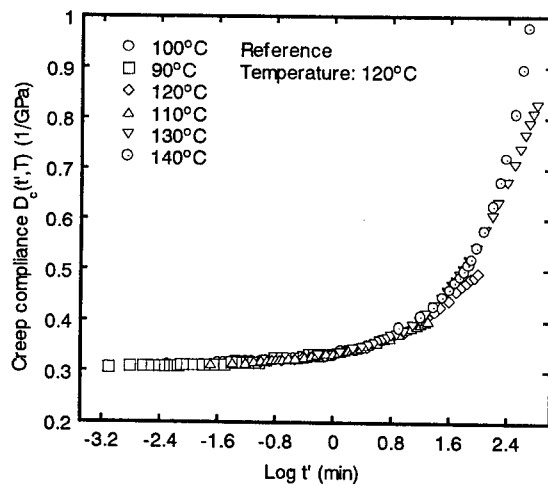


Figure 2(b) Master curve of creep compliance of glass fiber reinforced polycarbonate (G10).

To verify time-temperature dependency of these polymer composites, creep compliance master curves were drawn at 120°C as reference temperature by shifting the creep compliance curves. The Arrhenius time-temperature shift factor could be calculated from the following equation:

$$\text{Log } a_{T_o}(T) = \frac{\Delta H}{2.303R} \left( \frac{1}{T} - \frac{1}{T_o} \right) \quad (1)$$

where,  $a_{T_o}$  = time-temperature shift factor,  $R$  = gas constant (8.31 J mole / K),  $\Delta H$  = energy of activation,  $T_o$  = reference temperature and  $T$  = arbitrary temperature.

The time-temperature superposition was established by drawing the master curve shifting the short-term creep data according to the following steps.

- I. taking a suitable temperature as the reference temperature and fixing the co-ordinates of the data curve of this reference temperature
- II. taking the reference temperature as the base and shifting horizontally the other data curves of all other temperatures along the time axis to make one overlapped smooth curve
- III. obtaining the master curve by replacing the time  $t$  of each shifted curve by the physical time  $t'$  at the reference temperature  $T_o$
- IV. by investigating the relation between temperature and the shift quantity  $a_{T_o}$  of each data curve while drawing the master curve, the time-temperature shift factor of that material is calculated.

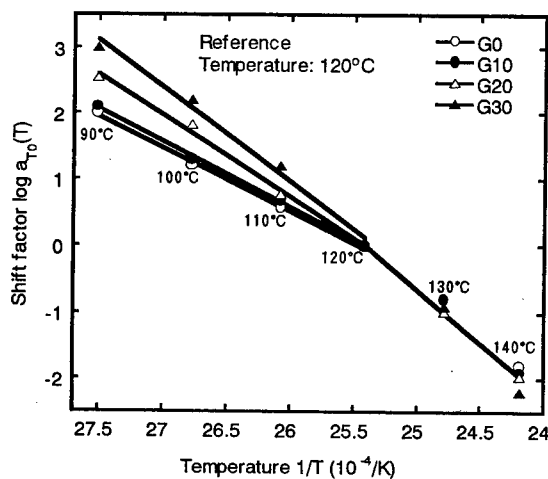


Figure 3 Time-Temperature shift factors of GFRPC and polycarbonate resin.

To draw the creep compliance master curve, time-temperature shift factor during the shifting operation could be defined as follows:

$$\text{Shift Factor, } a_{T_0}(T) = \frac{t}{t'} \quad (2)$$

where,  $t$  = creep time and  $t'$  = physical time.

By applying the above shifting operation, creep compliance master curve and shift factor curve was drawn. To draw the creep compliance master curves, short time side (short-term-creep side) of compliance curves was adjusted to overlap.

Figure 2(b) shows the creep compliance master curves of G10 composite. In this figure, the horizontal axis shows the physical time. The creep compliance curves at lower than the reference temperature ( $120^\circ\text{C}$ ) were shifted towards the shorter time (left) side on the time axis and those at the higher temperatures were shifted towards the longer time (right) side on the time axis. The shift factor curves for each of the composites were plotted on Arrhenius type graph as in Figure 3. Each shift factor curve shows two straight lines indicating that the creep phenomena represents good agreement with Arrhenius reciprocal law of time-temperature.

#### Effect of Fiber Contents on Creep Behavior

It was observed that the creep compliance was lower for composite of higher fiber volume fraction. The result indicates that the GFRPC composites of higher fiber volume fraction can withstand longer time than that of the lower fiber volume fraction. The increase in fiber volume fraction caused to increase in the static elasticity part of the visco-elastic polymer composite. This indicated that increased in fiber contents decreased the creep compliance and thus suppressed visco-elastic deformation.

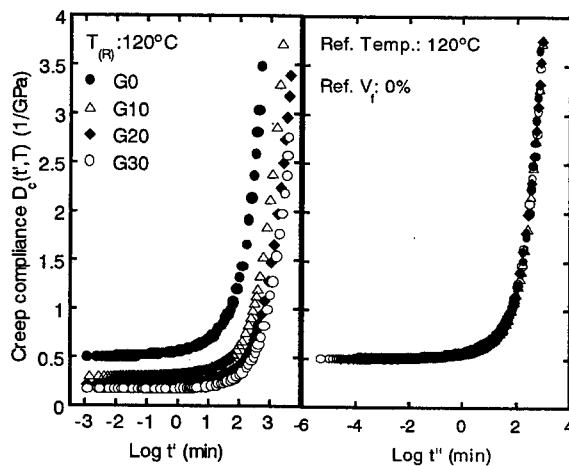


Figure 4 Master curves of creep compliance and grand master curve of GFRPC.

The left side of Figure 4 shows four creep compliance master curves of G0, G10, G20 and G30 composites at 120°C. From this figure it is clear that with the increase in fiber volume fraction, considerable changes of visco-elasticity occurred and the composite could withstand against higher temperature and longer time. Thus the fiber content played a prominent role in creep behavior of GFRPC composites.

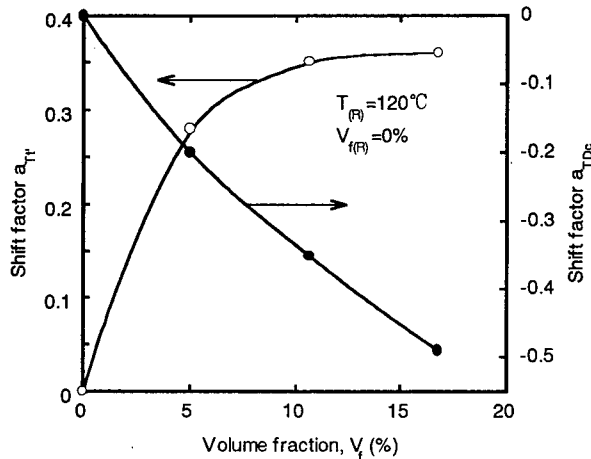


Figure 5 Time and Modulus Shift factors of GFRPC.

The right side of Figure 4 shows the grand master curve of four creep compliance master curves of G0, G10, G20 and G30 composites at 120°C. The grand master curve was drawn by shifting the creep compliance master curves horizontally and vertically to overlap each other. In this case, G0 was used as the reference. In Figure 5, the horizontal and vertical shift factors are denoted as 'time' and 'modulus' shift factor respectively. The grand master curve represents a smooth curve. Thus it became possible to estimate the creep behavior of composites with any fiber contents and at any temperature using the grand master curve of creep compliance master curves and time and modulus shift factors.

## Conclusions

Experiments on the creep behaviors GFRPC composites were performed in this study. Finally, major conclusions, obtained from this study are as follows. At any constant temperature the creep compliance increased with the increase in time. Again at a specific time the creep compliance increased with the increase in temperature. Creep phenomena of GFRPC composites comply with Arrhenius reciprocal law of time-temperature. There were significant effects of fiber volume fraction in creep behavior. With the increase in fiber volume fraction, considerable changes of visco-elasticity occurred and the composite could withstand against higher temperature and

longer time. Thus it became possible to estimate the creep of composites with any fiber contents using the grand master curve of creep compliance master curves and horizontal and vertical shift factors. So it become possible to design materials for creep by reinforcing contents of fibers to obtain the required objectives.

### Acknowledgement

This research has been supported by Grant in Aid for Scientific Research under grant no. 005-10073041.

### References

1. L. C. E. Struik, 1978. *Physical Aging in Amorphous Polymers and Other Materials*. Elsevier Scientific Publishing Co., New York.
2. T. Kunio, 1987. Mechanical Behavior of Visco-elastic Body Dependent on Time and Temperature - Fundamentals of Visco-elasticity. *Material System*, (in Japanese) 6:7-19.
3. T. S. Gates, and M. Feedman, 1995. Time-Dependent Behavior of Graphite/Thermoplastic Composite and the Effects of Stress and Physical Aging. *Journal of Composites Technology and Research*, 17:33-42.
4. M. Takashi, and T. Kunio, 1987. Characterization of Visco-elastic Materials. *Material System*, (in Japanese) 6:21-48.
5. C. M. Howard, and L. Hollaway, 1987. The Characterisation of the Non-linear Viscoelastic Properties of a Randomly Oriented Fiber/Matrix Composite. *Composite*, 18(4):317-323.
6. G. D. Dean, P. E. Tomlins, and B. E. Read, 1995. A Model for Non-linear Creep and Physical Aging in Poly(Vinyl Chloride). *Polymer Engineering and Science*, 35(16):1282-1289.
7. S. Somiya, 1994. Creep Behavior of a Carbon-Fiber Reinforced Thermoplastic Resin. *Journal of Thermoplastic Composite Materials*, 7(2):91-99.
8. K. K. Biswas, S. Somiya, and J. Endo, 1999. Creep Behavior of Metal Fiber-PPE Composites and Effect of Test Surroundings. *Mechanics of Time-Dependent Materials*, 3(1):85-101.
9. K. K. Biswas, and S. Somiya, 1999. Study of the Effect of Aging Progression on Creep Behavior of PPE Composites. *Mechanics of Time-Dependent Materials*, (Accepted).

## **Creep and Recovery of a Quasi-isotropic GFRP Laminate with Damage**

K. Ogi<sup>1</sup> and P. A. Smith<sup>2</sup>

### **Abstract**

An analytical model is proposed for predicting creep and recovery behavior of a quasi-isotropic laminate having transverse cracking. The analysis is based on the shear lag model and viscoelastic theory. The strain is obtained in the Laplace-transformed space and its original function is calculated by expressing relaxation moduli as exponential functions. Creep and recovery tests are conducted for a quasi-isotropic glass/epoxy (GFRP) laminate at a room temperature. The predicted strain response is in reasonably good agreement with experimental results.

### **Introduction**

While much analytical and experimental work has been done on the damage mechanism of composites, time-dependent behavior of damaged composites has received little attention in the literature. Some experimental work [1, 2] has been conducted on time-dependent transverse cracking of cross-ply laminates. Moore and Dillard [1] investigated time-dependent cumulative matrix cracking in graphite/epoxy and Kevlar/epoxy laminates. Raghavan and Meshii [2] conducted constant strain rate and constant stress tests of AS4/3501-6 cross-ply laminates and showed that the matrix crack density and its rate of increase depend on strain rate and stress, respectively. Recently, Ogi and Takao [3, 4] have developed a model to predict the strain response and transverse crack density in a carbon/epoxy cross-ply laminate under monotonic and constant loading. In their model, a shear lag parameter is assumed to be independent of time.

In the present study, time-dependent behavior of a  $[0^\circ/90^\circ/-45^\circ/45^\circ]_s$  quasi-isotropic laminate with transverse cracking is presented. The time-dependent shear lag parameter is considered in the analysis. Numerical simulation is conducted to predict the strain for creep and recovery of the laminate. The predictions are compared with some experimental results of a quasi-isotropic GFRP laminate.

---

<sup>1</sup> K. Ogi, Research Institute for Applied Mechanics, Kyushu University, 6-1, Kasuga-koen, Kasuga, Fukuoka 816-8580, Japan

<sup>2</sup> P. A. Smith, School of Mechanical and Materials Engineering, University of Surrey, Guildford, Surrey, GU2 5XH, UK

## Modeling

### Strain Response

Figure 1 illustrates a  $[0^\circ/90^\circ/-45^\circ/45^\circ]_s$  quasi-isotropic laminate with transverse cracking and its displacement distribution. The displacements in the  $x$  directions are assumed to be expressed as parabolic functions of  $z$  [5]:

$$u_k(x, z, t) = C_1^{(k)} z^2 + C_2^{(k)} z + C_3^{(k)} \quad (k = 1, 2, 3) \quad (1)$$

where the subscript  $k$  of 1, 2, and 3 denotes the  $0^\circ$  layer,  $90^\circ$  layer and  $[\pm 45^\circ]_s$  laminate, respectively, and  $C_i^{(k)}$  ( $i = 1, 2, 3$ ) are functions of  $x$  and time  $t$ . These displacements give a linear distribution of the shear strain  $\gamma_{xz,k}(x, z, t)$ . The shear stresses in the  $x$ - $z$  plane is expressed as a hereditary integral as

$$\tau_{xz,k}(x, z, t) = G_k(t) \gamma_{xz,k}(x, z, 0) + \int_0^t G_k(t - \tau) \frac{\partial \gamma_{xz,k}(x, z, \tau)}{\partial \tau} d\tau \quad (2)$$

where  $G_k(t)$  denotes the through the thickness shear modulus.

The relationship between the axial stress  $\sigma_k$  and strain  $\epsilon_k$  in each layer is given by the viscoelastic constitutive equation:

$$\sigma_k(x, t) = E_k(t) \epsilon_k(x, 0) + \int_0^t E_k(t - \tau) \frac{\partial \epsilon_k(x, \tau)}{\partial \tau} d\tau \quad (3)$$

where  $E_k(t)$  denotes the Young's modulus of each layer. The axial strain in each

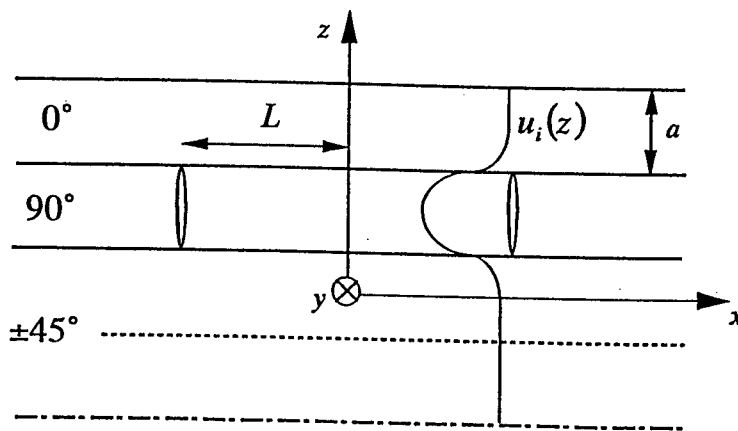


Figure 1 Illustration of a  $[0^\circ/90^\circ/-45^\circ/45^\circ]_s$  quasi-isotropic laminate with transverse cracking in the  $90^\circ$  ply.

layer is decomposed into the mechanical component and thermal component  $\varepsilon_k^T$ .

From the force balance in the laminate and transverse layer we obtain

$$\sigma_1(x, t) + \sigma_2(x, t) + 2\sigma_3(x, t) = 4\sigma_a(t) \quad (4)$$

$$a \frac{\partial \sigma_2(x, t)}{\partial x} + \tau_1(x, t) - \tau_2(x, t) = 0 \quad (5)$$

where  $\sigma_a(t)$  is the applied stress,  $a$  denotes the thickness of each layer, and  $\tau_1$  and  $\tau_2$  denote the shear stresses at the interfaces between the  $0^\circ$  layer and  $90^\circ$  layer and between the  $90^\circ$  layer and  $[\pm 45^\circ]_s$  laminate, respectively.

In order to solve the viscoelastic problem, all the calculations are made in the Laplace transformed space. Solving a differential equation derived from the above equations under the boundary conditions [5], we obtain the strain of the laminate

$$\hat{\varepsilon}_L(s) = \hat{\varepsilon}_0(s) + \varepsilon_1^T / s + (s \hat{\varepsilon}_0(s) + \varepsilon_2^T) \hat{f}(s) \quad (6)$$

with

$$\hat{\varepsilon}_0(s) = \frac{\hat{\sigma}_a(s)}{s \hat{E}_0(s)} \quad (7)$$

$$\hat{f}(s) = \frac{\hat{E}_2(s)}{4\hat{E}_0(s) - \hat{E}_2(s)} \frac{\tanh(\hat{\alpha}(s)L)}{s \hat{\alpha}(s)L} \quad (8)$$

where a circumflex accent denotes Laplace transform,  $\hat{E}_0(s)$  denotes the modulus of an undamaged laminate,  $\hat{\alpha}(s)$  is a shear lag parameter and  $L$  is a half crack spacing. The detail of calculations including the form of  $\hat{\alpha}(s)$  is described somewhere [5].

Inverting eq. (6) to the real space, we obtain the strain response of the laminate as

$$\begin{aligned} \varepsilon_L(t) &= \left[ \varepsilon_0(t) + f(t)\varepsilon_0(0) + \int_0^t f(t-\tau) \frac{d\varepsilon_0(\tau)}{d\tau} d\tau \right] + [\varepsilon_1^T + f(t)\varepsilon_2^T] \\ &= \varepsilon_L^M(t) + \varepsilon_L^T(t). \end{aligned} \quad (9)$$

where  $\varepsilon_L^M(t)$  and  $\varepsilon_L^T(t)$  denote the mechanical and thermal strains, respectively.

### Approximation

We assume that  $\tanh\{\hat{\alpha}(s)L\}$  is approximately unity for small transverse crack density. In addition, it is assumed that the elastic moduli are given as the following functions:



$$E_k(t) = E_k^0 \{e_k + (1 - e_k)e^{-\lambda t}\}, \quad G_k(t) = G_k^0 \{g + (1 - g)e^{-\lambda t}\} \quad (k=1, 2, 3) \quad (10)$$

where  $E_k^0$ ,  $G_k^0$  and  $\lambda$  are positive constants and  $e_k$  and  $g$  are constants between zero and unity. Due to linear elasticity in the fiber direction,  $e_1 = 1$  is assumed. Equation (10) gives the Young's modulus of the laminate

$$E_0(t) = E_0^0 \{e_0 + (1 - e_0)e^{-\lambda t}\} \quad (11.1)$$

with

$$E_0^0 = \frac{E_1^0 + E_2^0 + 2E_3^0}{4}, \quad e_0 = \frac{E_1^0 + E_2^0 e_2 + 2E_3^0 e_3}{E_1^0 + E_2^0 + 2E_3^0}. \quad (11.2)$$

Then the original function of eq. (8) is expressed as [5]

$$f(t) = f(0) \left[ \int_0^t \left\{ \int_0^{t-\tau} \varphi_1(t-\tau-u) \varphi_2'(u) du \right\} \varphi_3'(\tau) d\tau + \int_0^t \varphi_1(t-\tau) \{ \varphi_2'(\tau) + \varphi_3'(\tau) \} d\tau + \varphi_1(t) \right] \quad (12)$$

with

$$\varphi_l(t) = \exp(-\beta_l t) I_0(\alpha_l t) + \lambda e_2 \int_0^t \exp(-\beta_l u) I_0(\alpha_l u) du \quad (l=1, 2, 3) \quad (13)$$

where  $I_0(x)$  is the modified Bessel function of order zero and  $\alpha_l$  and  $\beta_l$  are constants expressed by using viscoelastic constants.

The strain response of an intact laminate  $\varepsilon_0(t)$  to a given applied stress  $\sigma_a(t)$  is calculated by using eqs. (7) and (11.1).

### Creep and Recovery

We consider the following stress history; first, a specimen is pre-loaded for introducing transverse cracking, next, the stress given by the following equation is applied:

$$\sigma_a(t) = \begin{cases} \sigma_0 H(t) & (0 < t \leq t_c) \\ \sigma_0 H(t) - \sigma_0 H(t - t_c) & (t_c < t \leq 2t_c) \end{cases} \quad (14)$$

where  $\sigma_0$  denotes the creep stress,  $H(t)$  denotes a Heviside's step function and  $t_c$  is the duration of creep loading. The thermal strain  $\varepsilon_L^T(t)$  in eq. (9) becomes a

steady-state value  $\epsilon^T_\infty$  at a sufficiently long time after cracking. Then, the strain response to the above stress history is written as

$$\epsilon_L(t) = \begin{cases} \epsilon_L^M(t) + \epsilon^T_\infty & (0 < t \leq t_c) \\ \epsilon_L^M(t) - \epsilon_L^M(t - t_c) + \epsilon^T_\infty & (t_c < t \leq 2t_c) \end{cases} \quad (15)$$

with

$$\epsilon_0(t) = \frac{\sigma_0}{E_0} \left\{ 1 - (1 - e_0) e^{-\lambda e_0 t} \right\} \quad (16)$$

## Experimental

The  $[0^\circ/90^\circ/-45^\circ/45^\circ]_s$  quasi-isotropic laminate was fabricated by a filament winding technique. The final cured thickness was 3.6 mm and the average fiber volume fraction was 0.62. Coupon specimens 230 mm in length and 25 mm in width were cut from the laminate. The aluminum tabs of length 50mm were bonded on the specimens. The loading tests were performed with an electrohydraulic testing machine (MTS 320.14) at a room temperature. The strain was measured with an extensometer (gage length 50 mm) and two strain gages (gage length 30 mm each). First, the specimen was initially loaded so that transverse cracks were generated. Next, the creep test for the cracked specimen was performed at a load of 8.5 kN for 60 min. Then, the specimen was unloaded and kept at 0 kN for 60 min. It should be noted that the transverse crack density dose not increase during the creep and recovery tests. The above procedure was repeated for three initial loads (0.0, 17.5 and 18.9 kN), namely, three transverse crack densities (0.0, 0.275 and 0.567 /mm).

## Results

Figure 2 shows mechanical strains of a quasi-isotropic laminate with and without transverse cracking in the  $90^\circ$  layer. The dotted curves in Fig. 2 (a) show the predicted strains when a constant shear lag parameter is used. It is found that presence of transverse cracks increases the initial strain at the beginning of creep loading and that the strain is slightly underestimated by using the constant shear lag parameter. The initial portions of the creep and recovery curves are not well predicted because the relaxation moduli expressed by exponential functions (eqs. (10) and (11.1)) are not suitable for predicting initial creep behavior. However, the creep and recovery strains approach to steady-state values with time. As a result, the present theory gives good approximation.

## Conclusions

An analytical model is proposed for predicting creep and recovery behavior of a

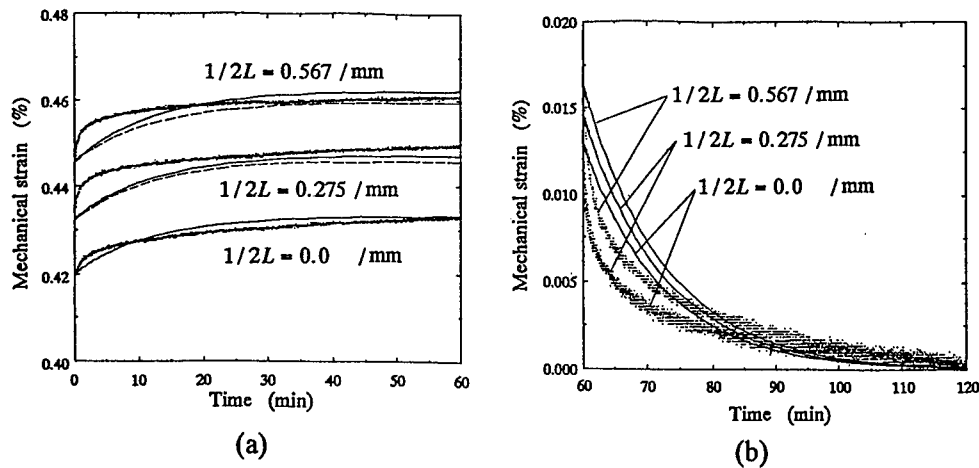


Figure 2 Mechanical strain  $\epsilon_L^M(t)$  of a  $[0^\circ/90^\circ/-45^\circ/45^\circ]_s$  quasi-isotropic GFRP laminate during (a) creep loading (94 MPa) and (b) recovery after unloading.

quasi-isotropic laminate with transverse cracking. The strain response is derived based on the shear lag analysis and viscoelastic theory. Good agreement is obtained between experimental results and predictions except the first stage of creep and recovery. Further experiments will be performed in the near future.

### Acknowledgement

Authors would like to express appreciation of technical support from Mr. Reg Whittingham of University of Surrey. Keiji Ogi is grateful to the Ministry of Education of Japan for providing an opportunity to study at University of Surrey.

### References

- [1] R. H. Moore RH and D. A. Dillard, 1990. "Time-Dependent Matrix Cracking in Cross-Ply Laminates." *Composites Science and Technology*, 39: 1-12.
- [2] J. Raghavan and M. Meshii, 1996. "Time-Dependent Damage in Carbon Fibre-Reinforced Polymer Composites." *Composites Part A*, 27: 1223-1227.
- [3] K. Ogi and Y. Takao, 1999. "Evolution of Transverse Cracking in CF/Epoxy Cross-Ply Laminates under Creep Loading." *Journal of Reinforced Plastics and Composites*, 13 (8): 220-230.
- [4] K. Ogi and Y. Takao, 1999 "Modeling of Time-Dependent Behavior of Deformation and Transverse Cracking in Cross-Ply Laminates," (to be published in *Composites Part A*).
- [5] K. Ogi and P. A. Smith. "Viscoelastic response of Composite Laminates with Transverse Cracking," (in preparation).

## **Bearing Creep Behavior of a Carbon/Bismaleimide Composite Material for the Next-Generation Supersonic Transport**

Hisaya Katoh, Toshiyuki Shimokawa, Hiroshi Tsuda, Akihito Sakai,  
and Ryoji Asagumo

### **Abstract**

The objective of this study was to investigate the bearing creep behavior of a high-temperature composite material. The material tested was a G40-800/5260 carbon/bismaleimide composite material, and testing was carried out at temperatures of 120°C, 150°C, and 180°C. Load levels for creep tests corresponded to 0.3, 0.4, 0.5 and 0.6 of the 4%-yield bearing strength. This study presents the results of these tests as follows: (1) The relationship between bearing tensile strength and elevated temperatures. (2) The relationship between hole deformation and time up to 10,000 hours as a function of the test load level and temperature. (3) The comparison of the observed damage in longitudinal sections at the loaded-hole edges between bearing creep tests and the bearing tensile tests.

### **Introduction**

The structures of the next-generation supersonic transport (SST) require significant lightweight and heat-resistance in comparison with the structures of conventional subsonic transport aircraft. For this reason, high-temperature composites are currently being considered as candidate materials for the structures of SST.

Except in the case of integrated molding, every structure has joints. SST structures are no exception. When composite materials are used in SST structures, large bearing damage may occur as a result of heat exposure under long supersonic

---

Hisaya Katoh and Toshiyuki Shimokawa, Structures Division, National Aerospace Laboratory,  
6-13-1 Ohsawa, Mitaka, Tokyo 181-0015, Japan  
Hiroshi Tsuda, Dept. of Composite Materials, National Institute of Materials and Chemical Research,  
1-1 Higashi, Tsukuba, Ibaraki 305-8565, Japan  
Akihito Sakai and Ryoji Asagumo, Aerospace Division, Aerospace Group, Kawasaki Heavy Industries,  
Ltd. 1 Kawasaki, Kakamigahara, Gifu 504-8710, Japan

flight conditions, due to reinforced fibers being cut off at the hole. Creep at the joints is an important problem in using composite materials for the SST structures. Hatakeyama [1] touched on bolt bearing studies and bearing creep tests in the USA for investigating thermal effects on thick PMC laminates.

Wright et al. [2] reported that the bearing creep of the IM7/K3B carbon/thermoplastic polyimide material did not progress at aged temperatures of 177°C and 204°C for 5,000 and 10,000 hours, though the destruction was occurred when large bearing load was applied. Miyano and Nakada [3] illustrated their creep test results and life prediction of bolted joint of a GFRP pipe under room and elevated temperatures as 25°C, 80°C and 120°C. However, there are no reports examining bearing creep behavior of bismaleimide composite materials at elevated temperatures. This composite material appeared viable for components subjected to relatively mild temperatures on SST, and its manufacturing process is similar to that of epoxy.

This study investigated bearing creep properties of a typical carbon/bismaleimide composite material, G40-800/5260, at elevated temperatures. A pin joint type specimen was chosen, because it is the simplest joint. Bearing tensile tests at elevated temperatures determined the load levels of bearing creep tests. On the way to the creep tests until 10,000 hours at elevated temperatures, the hole deformation of specimens were measured several times. This paper introduces the obtained test results.

## **Specimens and Testing procedure**

### **Specimen Configuration and Test Temperatures**

The prepreg tape of G40-800/5260 carbon/bismaleimide was supplied by the CYTEC Engineered Materials Inc. Laminate panels with a quasi-isotropic stacking sequence, 24 plies (45/0/-45/90)<sub>3S</sub>, and holed coupon specimens were made by the Kawasaki Heavy Industries, Ltd. Figure 1 illustrated specimen configuration and views of the bolt-loading apparatus. The specimen size meets to that described in the bearing strength test standard of MIL-HDBK-17E.

Creep tests were conducted at 120°C, 150°C and 180°C. These temperatures are expected to be encountered by most SST structures when the cruising speed lies between Mach 2.0 and 2.4. 150°C is however the temperature around which the bismaleimide composite material reaches the limits of serviceability. 180°C is considered to be a temperature used in acceleration tests.

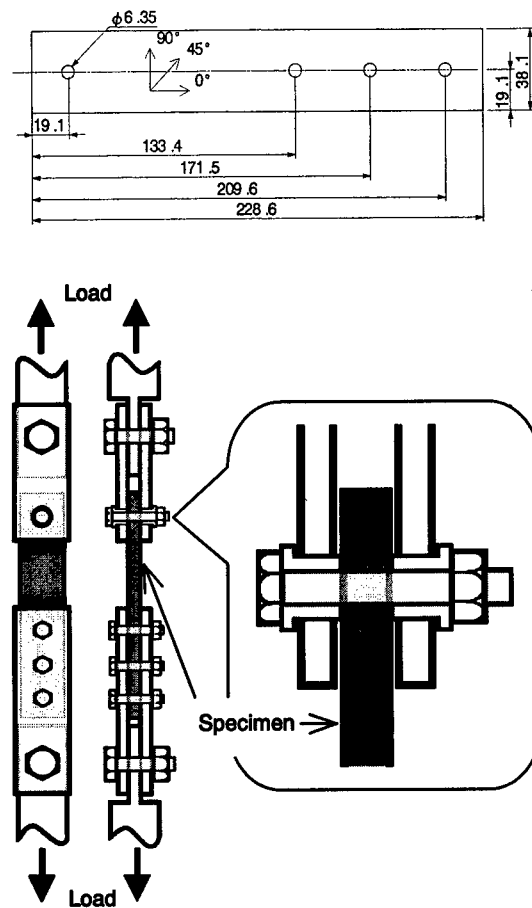


Figure 1 Specimen configuration and bolt-loading apparatus, dimensions in mm.

### Bearing Tensile Test

Before performing bearing creep tests, bearing tensile tests were conducted at room and elevated temperatures. The bearing yield strength defines the strength of the 4% residual deformation according to MIL-HDBK-17E. 4% residual deformation is 0.254 mm in this instance. The torque of the bolt was made finger tight. The finger tight was identified 5 kgf·cm (4.3 in·lb) or less. Test loads for bearing creep were determined on the basis of these results.

## Bearing Creep Test

The load level of creep tests corresponded to 0.3, 0.4, 0.5, and 0.6 of the 4%-yield bearing strength at each temperature, as shown in Table I. One specimen was used for each test condition. The torque of the bolt in bearing creep tests was adjusted to 3.5 kgf-cm (3 in-lb) using a torque wrench. This torque was similar to finger tight. The same torque was necessary in the bearing creep test, to avoid the considerable influence of differences in torque on the test results [2]. Major difference in bearing creep test results was caused by the minor difference of torque, when given tightening torque was small.

Table I Load levels of creep tests.

Temperature (°C)	Maximum load (kN)	4% yield load (kN)	Load (kN)			
			x 0.3	x 0.4	x 0.5	x 0.6
23	28.0	24.8				
120	22.6	21.9		8.7	10.9	13.1
150	21.1	18.3		7.3		11.0
180	19.2	15.6	4.7	6.2	7.8	9.4

Hole deformation was measured using a micrometer at scheduled hours, after detaching specimens from the test fixture. The creep test was then continued using a new set of a nut and a bolt.

## Test Results

### Bearing Tensile Test Results

Figure 2 shows the relationships between load and hole deformation obtained by bearing tensile tests. Bearing yield strength at room and elevated temperatures derived from this figure is listed in Table II. Maximum strength means the bearing stress for the maximum load, and 4% yield strength is the bearing stress generating a

residual deformation of 4% on hole size when unloaded. According to this figure, load-carrying capacity was not reduced, even when the bolted hole was considerably deformed.

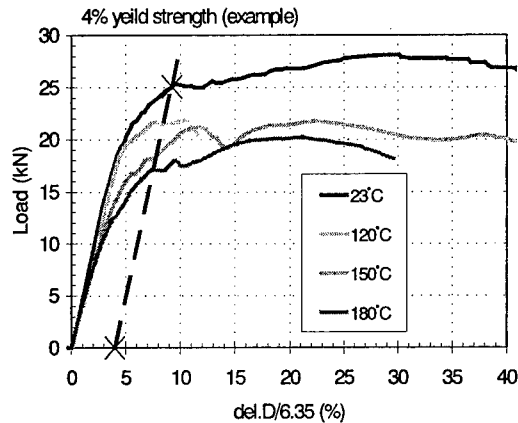


Figure 2 Load versus hole deformation in bearing tensile tests.

Table II Bearing yield strength at room and elevated temperatures.

Temperature (°C)	Maximum strength (MPa)	4% yield strength (MPa)
23	1370	1210
120	1110	1070
150	1030	900
180	940	760

Figure 3 indicates the relationship between bearing tensile strength and temperature. The bearing tensile strength at elevated temperatures was much lower than that at room temperature. Strength at 180°C was approximately 63% of that at room temperature.



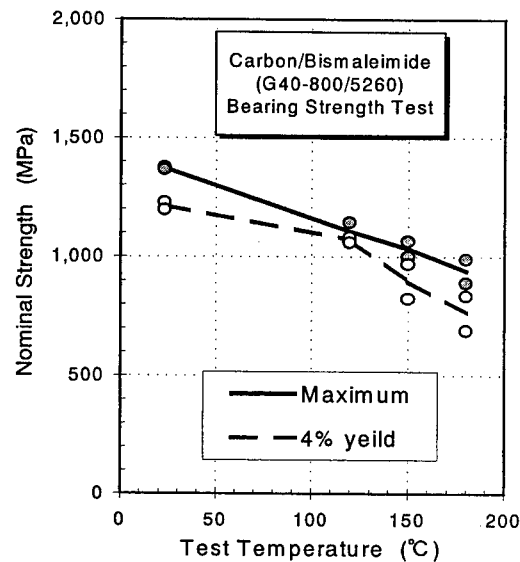


Figure 3 Bearing tensile strength versus temperature.

#### Bearing Creep Test Results

Figure 4 shows the relationship between hole deformation and testing time. The bolt hole deformation was large at the high load level and elevated temperature, though it was small at the low load level. Rapid bearing failure occurred under the conditions of the load level 0.6 at 150°C and 180°C. Gentle bearing failure was found under the conditions of the load level 0.6 at 120°C and the load level 0.5 at 180°C. Almost no bearing failure was produced under the other conditions.

Figure 5 presents the relationship between hole deformation and load level after 120 hours. The deformation may rapidly increase at a load factor of around 0.6, though the curve at 120°C was estimated.

Figure 6 shows photomicrography of the longitudinal cross sections of the loaded hole obtained by a bearing creep test under the condition of the load level 0.6 at 180°C after 240 hours. The left one is a cross section of the side with the bearing load. The damage was observed in the 45° direction for the longitudinal axis. The right one is the opposite side; no damage was observed in this side. This type of damage is similar to the damage formed by the bearing tensile test, but the damaged area is different.

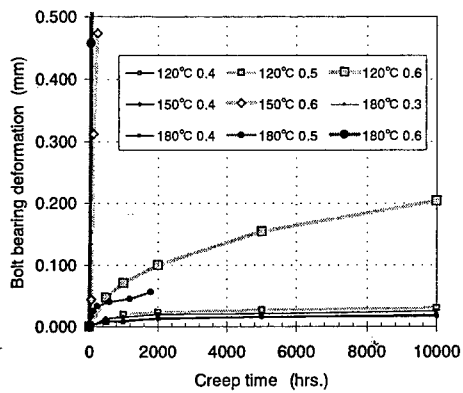


Figure 4 Hole deformation versus testing time.

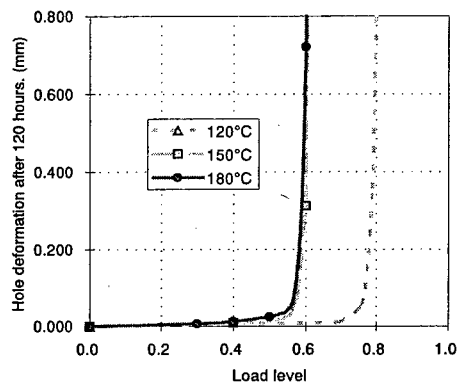


Figure 5 Hole deformation after 120 hours versus load level.

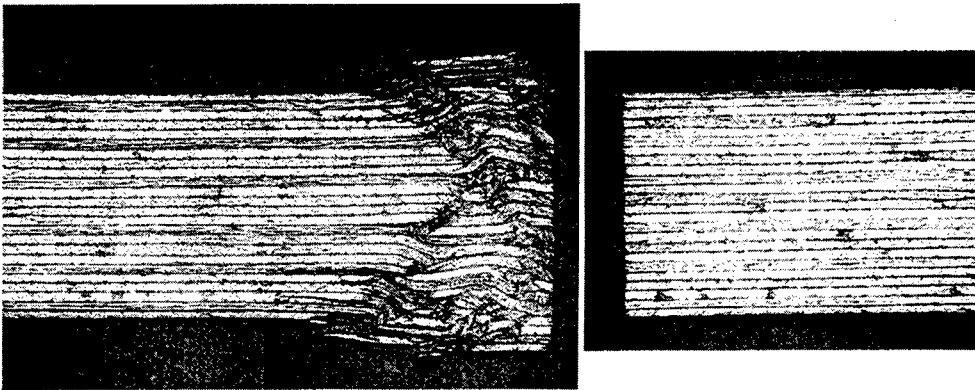


Figure 6 Photomicrography of longitudinal cross sections at the hole edge in a bearing creep test.

## Discussion

No hole deformation was observed after the creep tests at the load level 0.4, the usual design limit stress level. However, considerable hole deformation occurred under the conditions of high load level at 180°C. Gentle bearing failure was produced at the condition of low load and low temperature.

Wright et al. [2] reported that IM7/K3B carbon/polyimide composite indicated the deformations insensitive to time. Meanwhile, this study clarified the

deformation of G40-800/5260 bismaleimide composite sensitive to time in such cases as the condition of the load level 0.6 at 120°C and the load level 0.5 at 150°C.

No deformation was observed in the cases of high fastening torque at a few conditions in which considerable hole deformation occurred under the conditions of high load level. So, the fastening torque contributed considerably to bearing creep deformation.

The applicability of high-temperature composites to supersonic transport structures must be examined by carrying out similar tests for other candidate composites, due to the obvious importance of bearing creep as described above.

## Conclusion

Bearing creep tests clarified the following facts:

- (1) Load-carrying capacity was not reduced, even if the bolt hole deformation was considerably large.
- (2) The bearing tensile strength at elevated temperatures was much lower than that at room temperature. The strength at 180°C was approximately 63% of that at room temperature.
- (3) The bolt hole was deformed at high load levels and elevated temperatures, though deformation was small under the condition of the low load level at 120°C. As the temperature rose, the deformation increased even at the low load level.
- (4) The thickness of the damaged hole increased and oblique shear fractures were observed in a longitudinal section.

## References

1. S. J. Hatakeyama, "The High-speed Civil Transport: A Supersonic Leap in Technology", Proceedings of 11th International Conference on Composite Materials, 1997, I-383-380.
2. R. J. Wright, W. S. Johnson, H. Ahmad, "Bolt Bearing Behavior of Highly Loaded Composite Joints at Elevated Temperatures with and without Cramp-up", Proceedings of 11th International Conference on Composite Materials, 1997, VI-102-110.
3. Y. Miyano and M. Nakada, "Fatigue Life Prediction of Bolted Joint of Composite Materials", Proceeding of Composite Durability Workshop at Stanford Univ., 1999.

# Damage Identification

---

## **Effective Use of Fracture Surface of DCB Specimen for Better Understanding of Interphase**

M.Maeda, Y.Ma, K.Inomata, K.Kitagawa, Y.Fujii, H.Hamada

### **Abstract**

In order to understand the properties of interphase in glass cloth/vinylester composite, precise observation of the fracture surface obtained from DCB test was performed. Two patterns of crack propagation; unstable and stable fracture, were found. The unstable fracture region was used to measure thickness of resin on fracture surface, and the stable fracture region was used to calculate fracture toughness of interphase. FT-IR analysis of fracture surface was also carried out. From both fractographic and chemical viewpoints, size of interphase and fracture toughness of interphase could be estimated.

### **Introduction**

It has been well known that selection of surface treatment of glass fiber is important to design glass fiber reinforced plastics. Silane coupling agent as a surface treatment of glass fiber is normally used to create chemical bond between resin and glass fiber and it makes adhesion between them much stronger. Furthermore, it affects the mechanical properties of whole composite [1]. The resin around glass fiber is modified with silane coupling agent and the region is called interphase. It is considered that mode I interlamina crack propagation behavior should be related to the properties of this interphase. For example, it was reported that Mode I interlamina crack propagation exhibited stable and unstable behavior in terms of interfacial adhesion [2-5]. The unstable crack propagation, which is occurred with fine interface and crack propagated into resin region and in the case of poor interfacial adhesion the crack propagated along the glass cloth. These observations were sufficient to understand "strong" or "poor" adhesion. However, further information such as precise mechanical properties and chemical structure of interphase should be needed to understand the performance of composite material.

In this paper, fracture surface of Mode I fracture toughness test with DCB specimen was observed precisely. Based on these results, the fracture toughness

---

M. Maeda, Y. Ma, K.Inomata, H.Hamada, Advanced Fibro Science, Kyoto Institute of Technology, Matsugasaki, Sakyo, Kyoto 606-8585, Japan

K.Kitagawa, Kyoto Municipal Institute of Industrial Research, Chudoji, Shimogyo, Kyoto 600-8813, Japan

Y.Fujii, Seikow Chemical Engineering & Machinery, Ltd. Shioe, Amagasaki, Hyogo 66-0976, Japan

value of interphase was calculated.

## Material and Experimental

Materials used in this study were plain woven fabrics treated with 1wt% of  $\gamma$ -metacryloxypropyltrimethoxysilane aqueous solution. Methanol solvent was used to remove the phisorbed silane which existed around glass fiber. Two types of woven fabric were prepared, unwashed and washed fabric. The matrix resin used was a bisphenol A type vinylester resin (R806; Showa high polymer Co. Ltd., Japan) containing 43wt% of styrene monomer. The catalyst used was 0.7 phr methylethylketoneperoxide promoted by 0.3 phr cobalt naphthenate solution. The laminates for DCB specimen were fabricated by a hand lay-up method with 20 plies of washed or un-washed woven cloth in 4mm thick. The post-cure was performed at 80°C for 3 hours and at 150°C for 2 hours.

Mode I fracture toughness tests using double cantilever beam (DCB) specimens were carried out. After the testing, the cross-section of the specimen along the longitudinal directions was observed with microscope and the fracture surface was observed using scanning electron microscopy (SEM). The crack length and load-displacement curve and the fracture toughness calculated were linked with the each point on the photographs. The procedure was summarized in figure 1.

The mechanical properties of un-washed and washed specimens are shown in table 1.

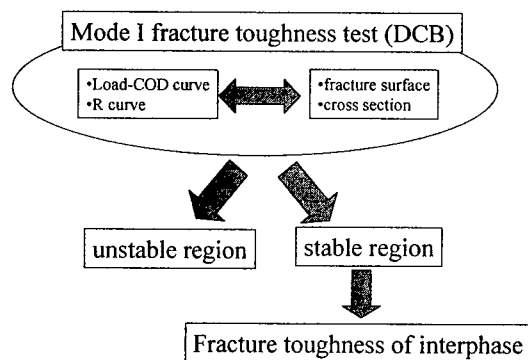


Figure 1 Experimental procedure

Table 1 Tensile and Bending properties

	Tensile modulus (GPa)	Tensile strength (MPa)	Bending modulus (GPa)	Bending strength (MPa)
un-washed	23.7	356	20.1	502
washed	24.8	357	20.4	475

## Result and Discussion

### Fracture toughness and fracture behavior

Figure 2 shows representative load-COD curves and R curves of un-washed and washed specimens respectively, and the fracture toughness value,  $G_{IC}$ , obtained were  $0.34(\text{kJ/m}^2)$  of un-washed specimen and  $0.33(\text{kJ/m}^2)$  of washed specimen. Both specimens mainly exhibited unstable fracture which the load drastically dropped. No obvious difference was found between non-washed and washed specimens.

According to precise observation of cross section and fracture surface, stable fracture, which occurred before unstable fracture, was found. Figure 3 is SEM photographs of fracture surfaces. Unstable region in figure 3 is a fracture surface of the area before load abruptly decreased. From precise observation of whole specimen, almost all area exhibited unstable crack propagation. The glass cloth was observed on fracture surface in stable fracture region, while it was covered with resin in unstable fracture region. Figure 4 is a SEM photograph of fracture surface in washed specimen. Crack did not propagate only along glass fiber, but also into resin even in stable region, because of its woven structure. Therefore the crack propagated both interphase and resin.

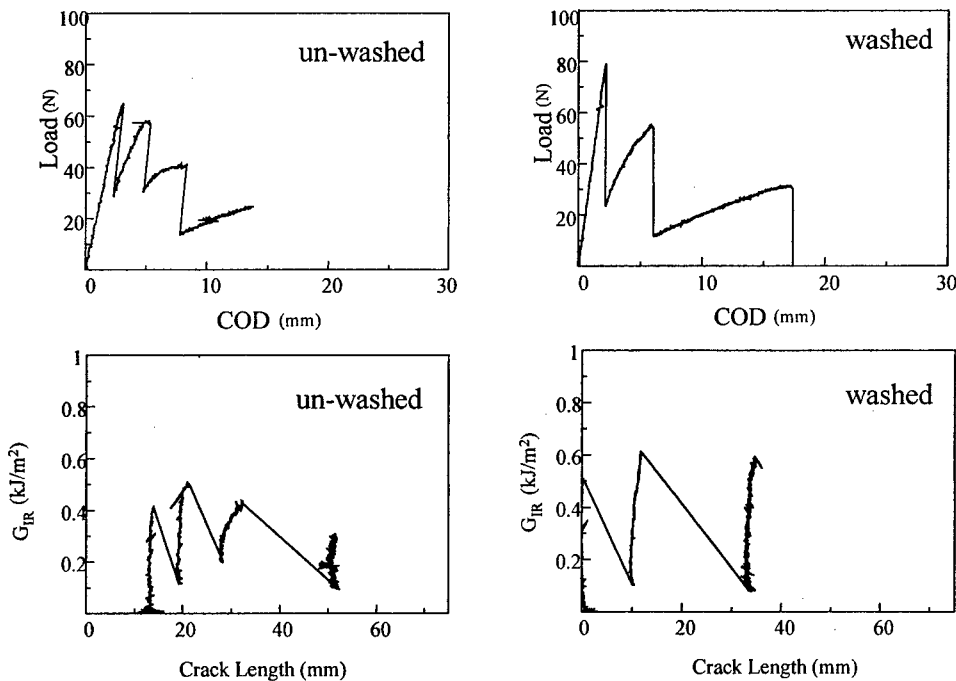


Figure 2 Load-COD curves and R curves

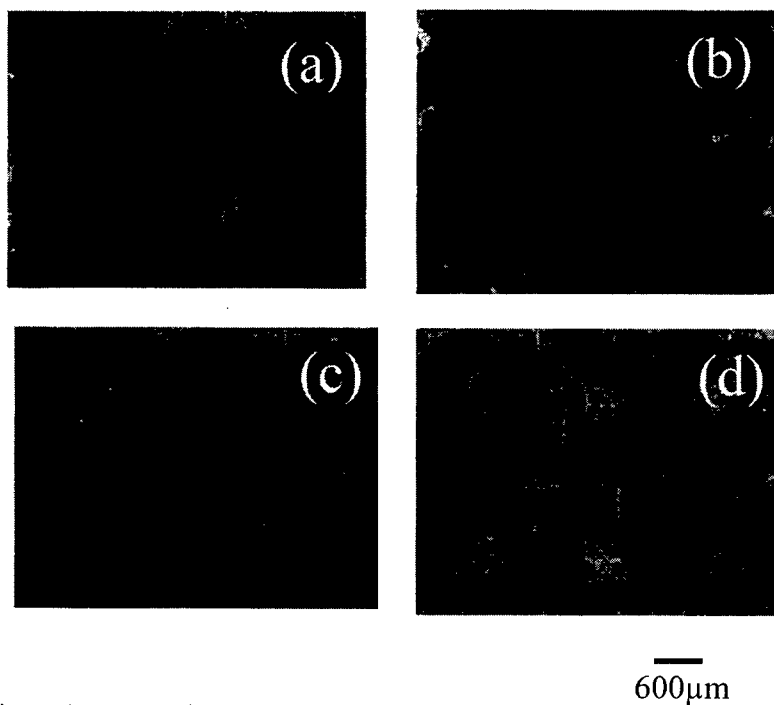


Figure 3 SEM photographs of fracture surface

(a) stable region in un-washed specimen, (b) unstable region in un-washed specimen, (c) stable region in washed specimen, (d) unstable region in washed specimen

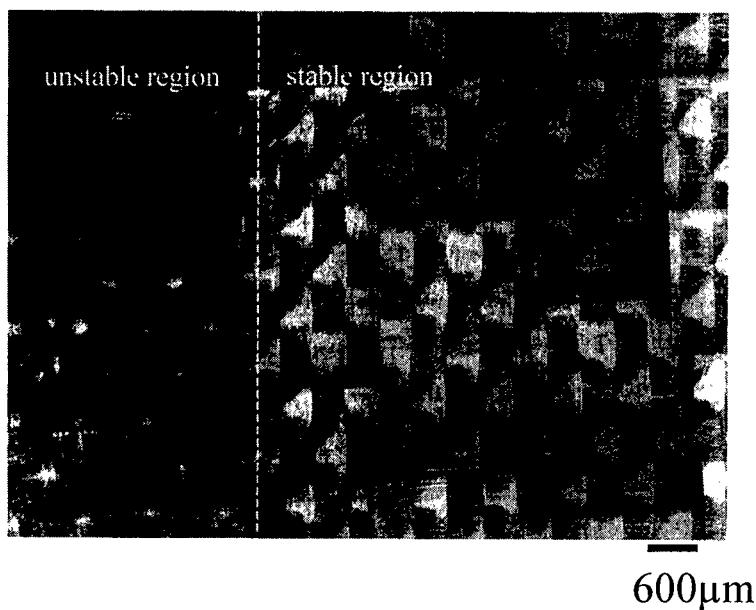


Figure 4 SEM photograph of washed specimen



### Fracture Toughness of Interphase

In stable region which appeared before un-stable crack propagation, crack propagated into both interphase and resin. The crack propagation energy would be the sum of energy in both resin and interphase region. Therefore, experimental value can be expressed by a simple equation as follows;

$$G_{\text{exp}} = \alpha G_{\text{int.}} + (1 - \alpha) G_{\text{resin}} \quad (1).$$

Where,

$\alpha$  ; Fractographic coefficient

$G_{\text{exp}}$ ; Experimental value of fracture toughness (kJ/m<sup>2</sup>)

$G_{\text{int.}}$ ; Fracture toughness of interphase (kJ/m<sup>2</sup>)

$G_{\text{resin}}$ ; Fracture toughness of resin (kJ/m<sup>2</sup>).

Here,  $\alpha$  value was defined as follows;

$$\alpha = \frac{\sum_{i=1}^n l_i}{L} \quad (2).$$

$G_{\text{exp}}$  during stable fracture propagation is a sum of fracture toughness of the interphase ( $G_{\text{int.}}$ ) and the resin ( $G_{\text{resin}}$ ).  $\alpha$  is a ratio of length of interphase crack to that of resin crack. Figure 5 is a schematic drawing to explain the definition of  $\alpha$ .

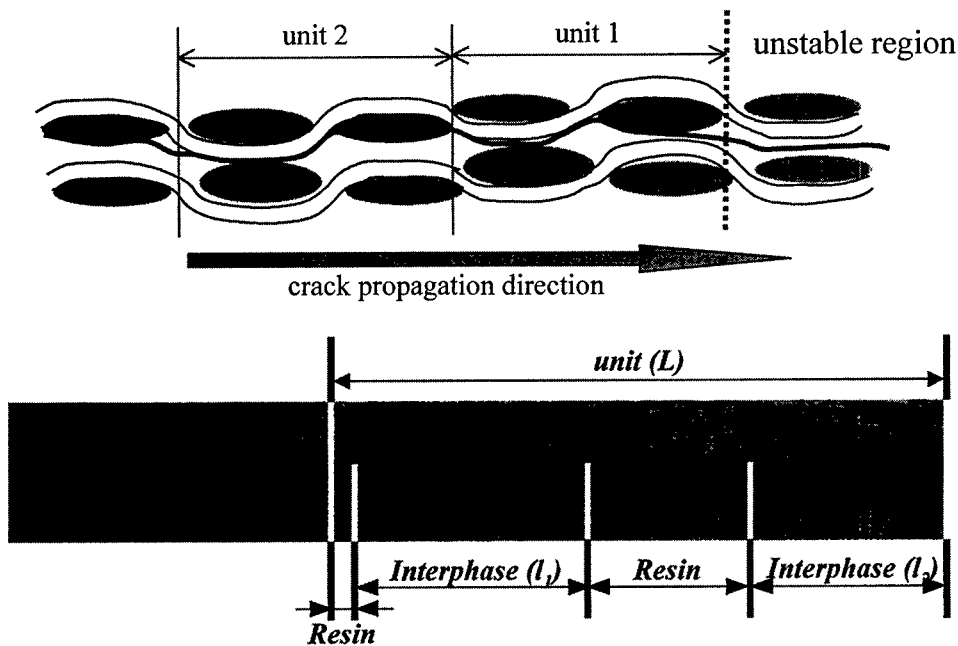


Figure 5 Definition of unit and  $\alpha$ .

value. The  $\alpha$  values obtained from the cross sectional observation in table 2 were used in equation (1). The fracture toughness of resin was  $0.2 \text{ kJ/m}^2$ , that was an experimental value of cured resin. The calculated fracture toughness of interphase also shown in table 2. The  $G_{\text{interphase}}$  of washed specimen was larger than that of un-washed one. It means the effect of physisorbed silane, hence it suggested that removing the physisorbed silane increased the fracture toughness of interphase. A possible explanation of this tendency is that the reacting site of vinyl ester resin and silane coupling agent would increase with removing physisorbed silane with methanol solvent as shown in figure 6. The circles in figure 6 indicate the reacting points created by removing physisorbed silane with methanol solvent. The adhesion between glass fiber and resin in washed specimen should become stronger than that of un-washed specimen, and more energy should be needed for crack propagation in washed specimen.

### Conclusion

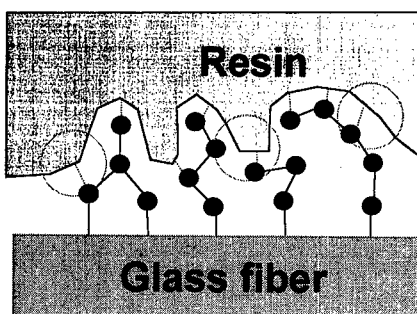
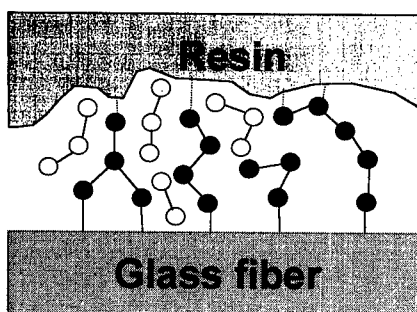
From the precise microscopic observation of cross section, the fracture toughness of interphase was obtained, and the effect of physisorbed silane could be discussed. The possibility to obtain properties of interphase, such as fracture toughness of interphase, from precise observation of fracture surfaces was proposed.

### Reference

1. R.Bequignat, P.Krawczak, W.Cantwell, P.Schramuzzino, M.Desaeger, I.erpoest, H.Hamada, Y.Hrai, M.Kotaki, M.Hojo, J.K.Kim, J.K.Kocsis, T.J.Mackin J.Mayer, T.Morii and T.Tanimoto, Proceedings of international Conference on Composite Materials (ICCM-10), 597-

Table 2  $\alpha$  and fracture toughness

un-washed		washed	
$G_{\text{exp.}}=0.51$		$G_{\text{exp.}}=0.61$	
$G_{\text{int.}}=0.71$		$G_{\text{int.}}=1.06$	
unit	$\alpha$	unit	$\alpha$
1	0.60	1	0.46
2	0.54	2	0.42
3	0.81	3	0.28
4	0.56	4	0.49
		5	0.59
		6	0.61
		7	0.85
		8	0.67



● Chemical-bonded silane

○ Physisorbed silane

Figure 6 Chemical structure model of interphase

603(1995).

2. M.Kotaki, H.Hamada, *Composites part A*, **28A**, 257-266(1997).
3. Y.Suzuki, Z.Maekawa, H.Hamada, T.Sugihara, *Sen-I Gakkashi*, **49**, 117-123 (1993).
4. Y.Suzuki, Z.Maekawa, H.Hamada, M.Kibune, M.Hojo, N.Ikuta, *J. Mater. Sci.*, **27**, 6782-6790 (1992).
5. Y.Suzuki, Z.Maekawa, H.Hamada, A.Yokoyama, T.Sugihara, M.Hojo, *J. Mater. Sci.*, **28**, 1725-1732(1993).
6. N.Ikuta, Y.Suzuki, Z.Maekawa, H.Hamada, *Polymer*, **34** 2445-2446(1993).
7. M.Maeda, K.Kitagawa, Y.Fujii, H.Hamada, Recent Advancement of Interfacial Material Science on Composite Materials, P-31-1-P-31-2(1999).

## **Damage Identification of Laminated Composite Structures Based on Dynamic Residual Forces**

H. Fukunaga, M. Kameyama and Y. Ogi

### **Abstract**

This paper shows a damage identification method based on dynamic residual forces which can be evaluated using an analytical model of undamaged structures and measured vibration data of damaged structures. The method consists of a two-step damage detection procedure. In the first step, a rough damage region is identified from the dynamic residual forces. In the next step, error vectors of the residual forces are minimized to identify the accurate location and extent of structural damage. Effect of measurement points and measurement errors on the identification results is examined through numerical examples on symmetric laminated plates.

### **Introduction**

Structural health monitoring is an important technology to evaluate structural degradation or damage for laminated composites in aircraft wing structures or space structures. Damage inspection methods such as X-ray or ultrasonic testing which have often been used for composite structures can be time consuming and are local assessments. They also require the exposure of structural elements to the inspector and equipment for detecting damage, and thus they may not be appropriate as a real-time nondestructive evaluation. An alternative approach making use of vibration test data or static test data can be useful as the structural health monitoring system. Several approaches have been suggested for the structural health monitoring. Nonlinear optimization techniques have been applied to identify material properties and damage using the static or vibration test data [1]. The use of vibration test data has been attempted to locate structural damage in composite materials [2]. For the evaluation of damage location and magnitude in structures, two main approaches have been suggested where one is based on the flexibility matrix [3][4] and the other is based on the residual force vector [5][6].

The present paper shows a damage identification method of laminated composite structures using dynamic residual forces. The method consists of a two-step damage detection procedure that initially uses dynamic residual force vectors to locate potential

---

H. Fukunaga, M. Kameyama and Y. Ogi, Department of Aeronautics and Space Engineering, Tohoku University, Aramaki Aza Aoba, Aoba-ku, Sendai 980-8579, Japan

damage regions, and next error vectors of the residual forces are minimized to identify the accurate location and extent of structural damage.

### Damage Identification Method

We consider a cantilevered CFRP plate with  $[30/-30/90]_s$  laminate as shown in the finite element model of Figure 1. Table I represents six bending stiffness components of the laminate. The natural vibration equation is given by

$$[K]\{\phi\}_i = \lambda_i[M]\{\phi\}_i \quad (1)$$

where  $K$  and  $M$ , respectively, denote the  $n \times n$  stiffness and mass matrices;  $\lambda_i$  and  $\phi_i$ , respectively, denote the  $i$ -th eigenvalue (square of the circular natural frequency) and the corresponding vibration mode.

We identify the damage location and the damage extent from the eigenvalues  $\lambda_i$  and the corresponding eigenmodes  $\phi_i$ . The measurement of eigenmodes at all degrees of freedom involving the angle of deflection is, in fact, difficult and also not all need to be measured. Partitioning Equation (1) into two terms corresponding to the measured  $\phi_{1i}$  and unmeasured vectors  $\phi_{2i}$  leads to

$$\begin{bmatrix} K_{11} & K_{12} \\ K_{12}^T & K_{22} \end{bmatrix} \begin{Bmatrix} \phi_1 \\ \phi_2 \end{Bmatrix}_i = \lambda_i \begin{bmatrix} M_{11} & M_{12} \\ M_{12}^T & M_{22} \end{bmatrix} \begin{Bmatrix} \phi_1 \\ \phi_2 \end{Bmatrix}_i \quad (2)$$

The damage in laminated composites is modeled as a proper stiffness reduction within an element in the finite element division. The stiffness matrix components are assumed to vary due to damage as follows:

$$[K'_{rs}] = [K_{rs}] + [\Delta K_{rs}] \quad (r, s = 1, 2) \quad (3)$$

From Equations (2) and (3), the equation for natural vibration after damage is given as follows:

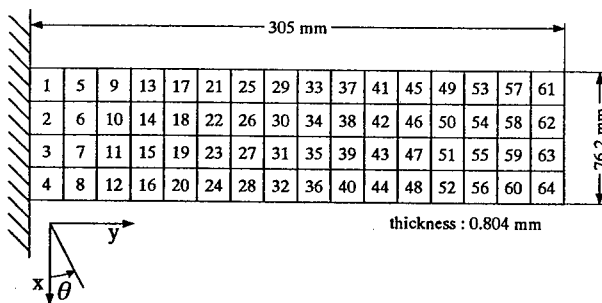


Figure 1 Finite Element Model of CFRP Plate

Table I Bending Stiffness of  $[30/-30/90]_s$  laminate

$D_{11}$	$2.56 \times 10^9$ [N·m]
$D_{12}$	$7.20 \times 10^{-1}$ [N·m]
$D_{16}$	$5.44 \times 10^{-1}$ [N·m]
$D_{22}$	$8.12 \times 10^{-1}$ [N·m]
$D_{26}$	$2.12 \times 10^{-1}$ [N·m]
$D_{66}$	$8.66 \times 10^{-1}$ [N·m]

$$\begin{bmatrix} K_{11} + \Delta K_{11} & K_{12} + \Delta K_{12} \\ K_{12}^T + \Delta K_{12}^T & K_{22} + \Delta K_{22} \end{bmatrix} \begin{Bmatrix} \phi'_1 \\ \phi'_2 \end{Bmatrix}_i = \lambda'_i \begin{bmatrix} M_{11} & M_{12} \\ M_{12}^T & M_{22} \end{bmatrix} \begin{Bmatrix} \phi'_1 \\ \phi'_2 \end{Bmatrix}_i \quad (4)$$

where ' denotes the properties after damage.

From Equation (4), dynamic residual forces are defined as follows:

$$\begin{aligned} \begin{Bmatrix} \Delta R_1 \\ \Delta R_2 \end{Bmatrix}_i &= \begin{bmatrix} \Delta K_{11} & \Delta K_{12} \\ \Delta K_{12}^T & \Delta K_{22} \end{bmatrix} \begin{Bmatrix} \phi'_1 \\ \phi'_2 \end{Bmatrix}_i \\ &= \lambda'_i \begin{bmatrix} M_{11} & M_{12} \\ M_{12}^T & M_{22} \end{bmatrix} \begin{Bmatrix} \phi'_1 \\ \phi'_2 \end{Bmatrix}_i - \begin{bmatrix} K_{11} & K_{12} \\ K_{12}^T & K_{22} \end{bmatrix} \begin{Bmatrix} \phi'_1 \\ \phi'_2 \end{Bmatrix}_i \end{aligned} \quad (5)$$

When eigenmodes at all degrees of freedom can be measured,  $\Delta R_i = \Delta K \phi'_i$  and non-zero residual forces occur only at the damage element. On the other hand, when all components cannot be measured, we cannot determine the values of  $\Delta R_1$  and  $\Delta R_2$  separately. Deleting  $\phi'_2$  in the second row of Equation (5), we can obtain

$$\begin{aligned} \{\Delta Q\}_i &= \{\Delta R_1\}_i - [\lambda'_i M_{12} - K_{12}][\lambda'_i M_{22} - K_{22}]^{-1} \{\Delta R_2\}_i \\ &= ([\lambda'_i M_{11} - K_{11}] - [\lambda'_i M_{12} - K_{12}][\lambda'_i M_{22} - K_{22}]^{-1}[\lambda'_i M_{12}^T - K_{12}^T]) \{\phi'_1\}_i \end{aligned} \quad (6)$$

In Equation (6), the right-hand term can be evaluated since  $K_{ij}$  and  $M_{ij}$  are known and  $\lambda'_i$  and  $\{\phi'_1\}_i$  can be measured. The combined residual force vector  $\Delta Q$  in Equation (6) consists of the residual force vectors  $\Delta R_1$  and  $\Delta R_2$ , and  $\Delta Q$  has the same degree of freedom with the measurement data. It is expected that  $\Delta Q$  is an indicator for the damage location.

We define the normalized damage indicator as follows:

$$\{\varepsilon\}_i = \frac{\{\|\Delta Q\|\}_i}{\sqrt{\{\Delta Q\}_i^T \{\Delta Q\}_i}} \quad (0 \leq \varepsilon_i \leq 1) \quad (7)$$

where  $\{\|\Delta Q\|\}_i$  denotes a vector where the component consists of an absolute value of each component of  $\{\Delta Q\}_i$ , and  $\{\varepsilon\}_i$  represents the normalized damage vector for  $i$ -th mode.

The average damage vector from first to  $m$ -th mode is expressed as follows:

$$\{\varepsilon\}_0 = \sum_{i=1}^m \{\varepsilon\}_i / m \quad (8)$$

The average damage vector has a large absolute value near the damage element. In this paper, we use the damage criterion that the region is damaged when  $|\varepsilon| \geq 0.1$  in all

nodes surrounding the region.

When the damage region is determined by the criterion of Equation (8), we estimate the damage elements within the damage region. In this step, we use the following error vector for  $i$ -th mode:

$$\{E\}_i = ([\lambda'_i M_{11} - K'_{11}] - [\lambda'_i M_{12} - K'_{12}][\lambda'_i M_{22} - K'_{22}]^{-1}[\lambda'_i M_{12}^T - K'_{12}^T])\{\phi'_i\}_i \quad (9)$$

where  $K' = K + \Delta K$  are unknown, and the error vector  $\{E\}_i$  is a function of the  $j$ -th bending stiffness in the  $k$ -th element  $(D'_j)_k$ . When  $(D'_j)_k$  gives the true bending stiffness after damage, the error vector vanishes.

Thus the damage elements can be determined by minimizing the following error vector norm with respect to  $(D'_j)_k$ :

$$\min \sum_{i=1}^m \{E\}_i^T \{E\}_i \quad (10)$$

In the determination of the damage region using the criterion of Equation (8), there are many possible damage elements. Then the minimization problem of Equation (10) has many variables when the bending stiffness components in possible damage elements are used as direct variables. In order to reduce the number of variables and to locate the damage elements roughly, we solve Equation (10) using the following variable linking:

$$(D'_j)_k = (1 - \alpha_k / 100)(\bar{D}_j)_k \quad \begin{pmatrix} j = 11, 12, 16, 22, 26, 66 \\ k = 1, 2, \dots, K \end{pmatrix} \quad (11)$$

where  $K$  and  $\alpha_k$  are, respectively, the number of possible damage elements and the variable in the  $k$ -th element.  $(\bar{D}_j)_k$  is the  $j$ -th bending stiffness in the  $k$ -th element before damage. Thus the number of variables is reduced to  $K$ . In Equation (11), it is assumed that the stiffness components decrease uniformly in the damage elements.

By minimizing the error vector norm of Equation (10) with respect to  $\alpha_k$ , the damage elements are determined. Then it is the next step to obtain the damage magnitude in the damage elements. The damage magnitude can be obtained by the minimization of Equation (10) using the variables  $(D'_j)_k$  in the damage elements. As a nonlinear optimization technique to solve Equation (10), the Davidon-Fletcher-Powell method was adopted with the golden section method in the ADS program [7].

## Numerical Results

As numerical examples, we consider a  $[30/-30/90]_s$  laminated composite plate shown in Figure 1. The plate is divided into  $4 \times 16$  rectangular bending elements where

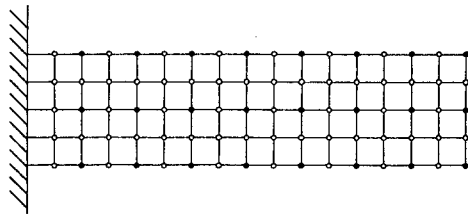
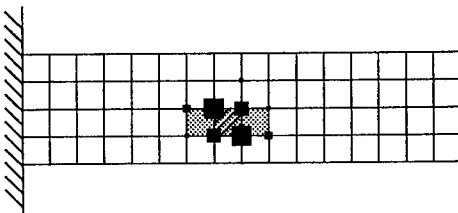
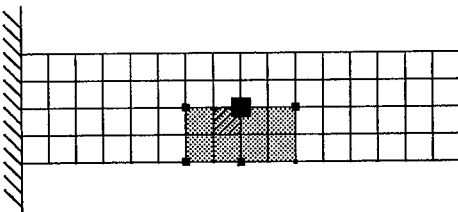


Figure 2 Measurement Points of Deflection Components

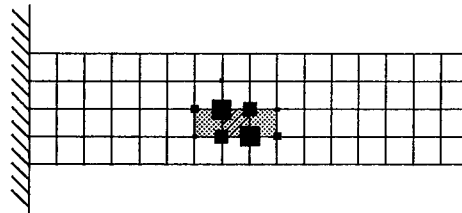


(a) 80-points Measurement

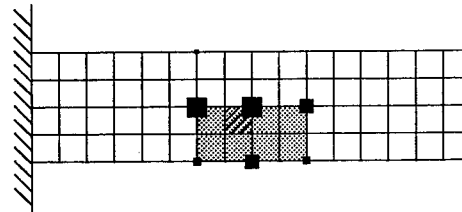


(b) 24-points Measurement

$\square$  :  $0.1 \leq \varepsilon_i < 0.2$  ,  $\blacksquare$  :  $0.2 \leq \varepsilon_i < 0.3$   
 $\blacksquare$  :  $0.3 \leq \varepsilon_i < 0.4$  ,  $\blacksquare$  :  $0.4 \leq \varepsilon_i$



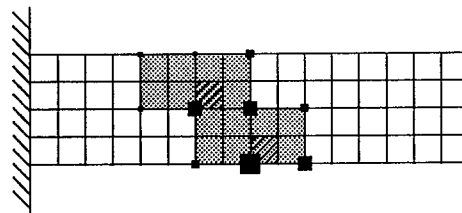
(a) 80-points Measurement



(b) 24-points Measurement

$\square$  :  $0.1 \leq \varepsilon_i < 0.2$  ,  $\blacksquare$  :  $0.2 \leq \varepsilon_i < 0.3$   
 $\blacksquare$  :  $0.3 \leq \varepsilon_i < 0.4$  ,  $\blacksquare$  :  $0.4 \leq \varepsilon_i$

Figure 4 Identification Results for Case 2



$\square$  :  $0.1 \leq \varepsilon_i < 0.2$  ,  $\blacksquare$  :  $0.2 \leq \varepsilon_i < 0.3$   
 $\blacksquare$  :  $0.3 \leq \varepsilon_i < 0.4$  ,  $\blacksquare$  :  $0.4 \leq \varepsilon_i$

Figure 3 Identification Results for Case 1

Figure 5 Identification Results for Case 3

the damage element has one element size. The damage in laminated composites is modeled as a proper stiffness reduction of all bending stiffness components. From the practical viewpoint of vibration tests, the use of less vibration modes and less measurement points is the better. We use only the three lowest vibration modes and the number of measurement points of deflection components in each vibration mode is 80 ( $\odot$  points) and 24 ( $\bullet$  points) as shown in Figure 2.

We consider the following three damage cases:

Case 1 :  $(D_1, D_2, D_3, D_4, D_5, D_6) = (50, 50, 50, 50, 50, 50)\%$  reduction of bending stiffness components in the No.31 element

Case 2 :  $(D_1, D_2, D_3, D_4, D_5, D_6) = (23, 18, 16, 35, 21, 23)\%$  reduction of bending stiffness components in the No.31 element

Case 3 :  $(D_1, D_2, D_3, D_4, D_5, D_6) = (50, 50, 50, 50, 50, 50)\%$  reduction of bending



stiffness components in the No.26 and No.36 elements (24-points measurement)

### Damage Location

It is assumed that the exact vibration data can be measured without any measurement error. In the first step of damage identification, the damage location is identified by using the criterion of Equation (8) based on the combined residual force vector. Figure 3 shows the identification results of damage location for Case 1 where the damage is modeled as the 50% reduction of all bending stiffness components in the No.31 element. The hatched region represents the true damage element, and the shaded region represents the one of  $|\varepsilon| \geq 0.1$  in all nodes surrounding the region.

The magnitude of the average damage vector in Equation (8) is also indicated by the ■ mark. It is seen that the identified damage region includes the true damage element for both cases of 80-points and 24-points measurement although the identified damage region is larger for the less measurement points. Figure 4 shows the identification results of damage location for Case 2 where the damage model corresponds to the 20% reduction of  $Q_{11}$  and the 50% reduction of  $Q_{12}$ ,  $Q_{22}$  and  $Q_{66}$  in unidirectional composites. Figure 5 shows the identification results for Case 3 where the measurement points are 24. It is seen in Figures 4 and 5 that the damage region can also be identified precisely. Thus the present identification method based on the criterion of Equation (8) can adequately locate the damage region into a small region when the measurement error vanishes.

Now we examine the effect of measurement errors on the identification results of damage location. We treat the identification problem of Case 1 where the measurement points are 24. Figure 6 shows the effect of measurement errors where the measurement noise with the normal distribution is added to the deflection components. It is seen that we can locate the damage region accurately for 0.1% measurement error while it is difficult to identify the damage location for 0.5% measurement error.

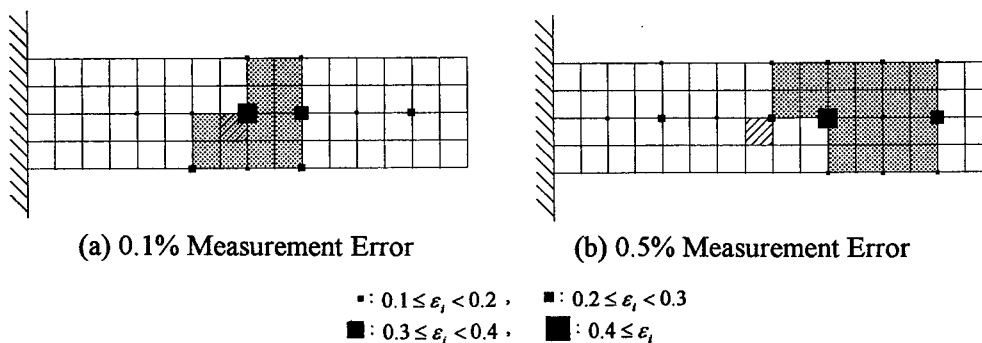


Figure 6 Effect of Measurement Errors on Identification Results for Case 1

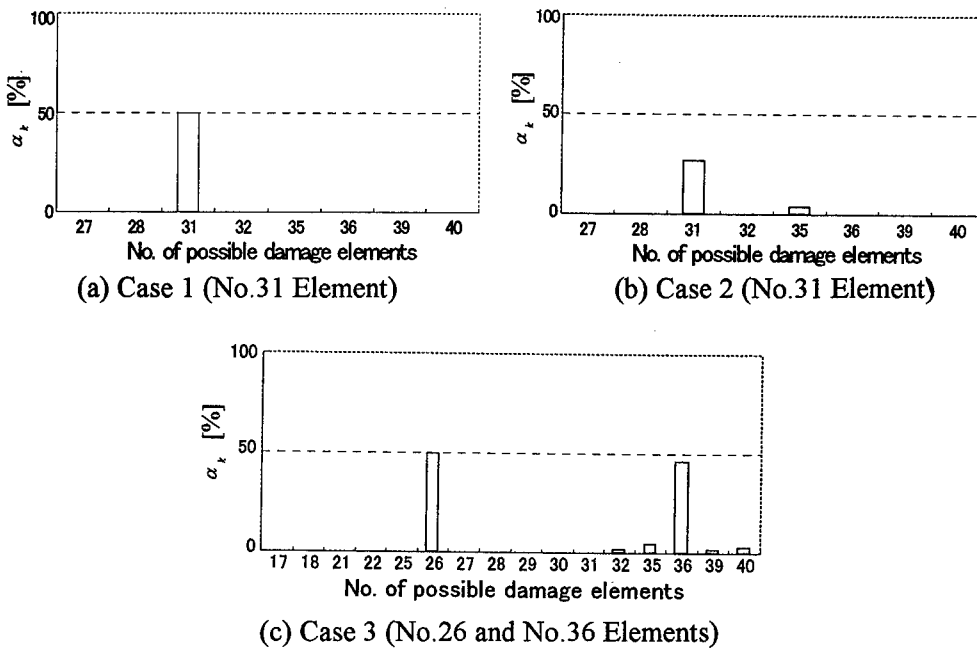


Figure 7 Estimation of Damage Element Using  $\alpha_k$

### Damage Magnitude

When the damage region is determined by the criterion of Equation (8), we estimate the damage elements within the damage region. Here we assume that the exact vibration data can be measured without any error. Assuming that the stiffness components in elements decrease uniformly after damage, the damage element is identified by minimizing Equation (10) with respect to  $\alpha_k$  in the possible damage elements. We consider the case of 24-points measurement. As shown in the shaded region of Figures 3-5, the number of possible damage elements is 8 elements for Cases 1 and 2, and 16 elements for Case 3. Figure 7 shows the estimation results using  $\alpha_k$  for Cases 1-3. As the initial values of a nonlinear optimization technique,  $\alpha_k = 0$  are used. It is seen that the damage element can be identified adequately for Cases 1-3.

When the damage elements are determined as stated above, we obtain the damage magnitude in the damage elements, i.e., the stiffness reduction rate. The damage magnitude is obtained by the minimization of Equation (10) using the variables  $(D'_j)_k$  in the damage elements. Figure 8 shows the identification results for Case 1. The estimated stiffness reduction is shown in the figure with the comparison of exact one when we use the three and six lowest vibration modes. It is seen that only the two bending stiffness components,  $D'_{22}$  and  $D'_{66}$ , are identified for the use of three modes. This is due to the limited sensitivity of other bending stiffness components to the three lowest vibration modes. When we use the six vibration modes, all of the bending stiffness components can be identified precisely.

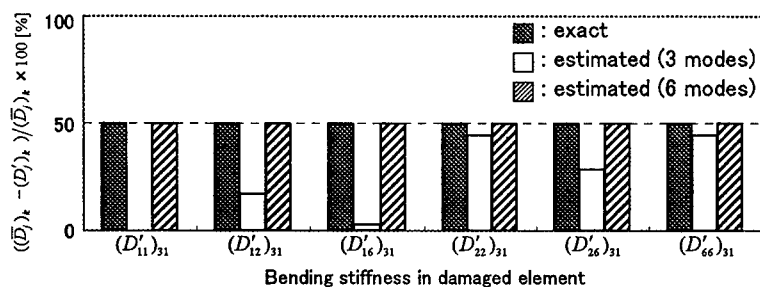


Figure 8 Estimation of Bending Stiffness Using  $(D'_j)_k$  for Case 1

## Conclusions

In the present paper, we suggest a damage identification method of laminated composite structures based on dynamic residual forces. The method consists of a two-step damage detection procedure that initially uses dynamic residual force vectors to locate potential damage regions, and next error vectors of the residual forces are minimized to identify the accurate location and magnitude of structural damage. Effect of measurement points and measurement errors on the identification results is examined through numerical examples on symmetric laminated plates. It is shown that the present method can be useful as a health monitoring of composite structures although the high sensitivity to measurement noise should be improved.

## References

1. P. Hajela and F. J. Soeiro, 1990. "Structural Damage Detection Based on Static and Modal Analysis." *AIAA Journal*, 28(6):1110-1115.
2. P. Cawley and R. D. Adams, 1979. "A Vibration Technique for Non-Destructive Testing of Fibre Composite Structures." *Journal of Composite Materials*, 13(3):161-175.
3. C. S. Lin, 1990. "Location of Modeling Errors Using Modal Test Data." *AIAA Journal*, 28(9):1650-1654.
4. H. Fukunaga, H. Sekine, K. Sasajima and N. Hu, 1999. "Damage Identification of Truss Structures Based on Vibratory Data." *Trans. JSME(C)*, 65(635):2617-2622.
5. J. M. Ricles and J. B. Kosmatka, 1992. "Damage Detection in Elastic Structures Using Vibratory Residual Forces and Weighted Sensitivity." *AIAA Journal*, 30(9):2310-2316.
6. H. Fukunaga, H. Sekine and Y. Tani, 1999. "Stiffness and Damage Identification of Laminated Plates Using Static Deflection." *Journal of Reinforced Plastics and Composites*, 18(13):1173-1185.
7. G. N. Vanderplaats and H. Sugimoto, 1986. "A General-Purpose Optimization Program for Engineering Design." *Computers & Structures*, 24(1):13-21.

## **Damage Detection of CFRP Pipes and Shells by Using Localized Flexibility Method**

Yoshio Aoki, O-IL Byon(Goichi Ben)

### **Abstract:**

This paper presents modal-based structural damage detection. Specifically, we focus on localized flexibility properties that can be deduced from the experimentally determined global flexibility matrix. We present the underlying theory that can be viewed a generalized flexibility formulation in three different generalized coordinates, viz., localized or substructural displacement, elemental deformation-basis and element strain-basis. Then, the present methods are applied to a CFRP pipes and shells having interior damage and the numerical and experimental results show that the elemental strain-basis method is quite useful for detecting the inside damage of the CFRP filament winding pipes.

### **1. Introduction**

CFRP composites have very favorable strength and stiffness-to-weight ratio among engineering materials, which make their aerospace applications highly desirable as weight savings translate directly into higher performance. A major concern in using these composites is their vulnerability to impulsive loading by space debris, pebbles and dusts. This is because crack or damage caused by inter-laminar delaminations or fiber-matrix debonding in the laminated composites, although not visible on the surface, significantly reduces their strength and/or stiffness. A rational method for the detection of damage location and damage modes or mechanisms in composites can therefore facilitate a wider acceptance of composites by the practicing engineers.

To this end, several damage detection methods have been proposed, which include ultrasonic crack detection, wave propagation and scattering, modal testing, among other [1],[2]. We applied the localized flexibility method to damage identification in CFRP laminated beam and showed a good agreement of analytical results with the experimental ones [3]. The objective of the present paper is to offer a model-based damage detection technique by relying on vibrations test data. It should be mentioned that on-site vibration test is becoming economical and mobile as new miniaturized sensors of both contact and non-contact high-fidelity types which are readily available.

---

Y.Aoki, Department Precision Machinery Engineering, College of Sciences and Technology, Nihon University, 7-24-1 Narashinodai, Funabashi, Chiba, 274-8501 Japan

O-IL Byon, Department of Mechanical Engineering, College of Industrial Technology, Nihon University, 1-2-1 Izumi-cho, Narashino, Chiba, 275-8575 Japan

The present paper is organized as follows. First, a brief review of the variational formulation of the partitioned equations of motion for a vibrating structures is described. Second, by solving for the partitioned or substructural displacement, the relation between the partitioned flexibility and the global flexibility is established. The relation of the global frequency response function (FRF) to the partitioned FRF is then established by using the input/output invariance requirement. Third, by decomposing the elemental output displacement vector in terms of the strain amplitudes, a theory for strain output-based damage detection is derived by treating the strain gauge records. The damage location is estimated by the present three localized flexibility changes for CFRP filament winding pipes.

## 2. REVIEW OF LOCALIZED FLEXIBILITY FORMULATION

### 2.1 Global Flexibility Matrix

The discrete energy functional  $\Pi$  for a linear damped structure can be expressed as

$$\Pi(u_g) = u_g^T \left( \frac{1}{2} K_g u_g - f_g^D \right),$$

$$K_g = L^T K L, \quad K = \begin{bmatrix} K^1 & & \\ & K^2 & \\ & & K^{n_s} \end{bmatrix}, \quad f_g^D = f_g - M_g \ddot{u}_g - C_g \dot{u}_g \quad (1)$$

where  $u_g$  is the displacement vector of the assembled structure;  $f_g^D$  is D'Alembert's force vector that consists of the applied force vector  $f_g$ , the resisting inertia force  $M_g \ddot{u}_g$ , and the dissipating force  $C_g \dot{u}_g$ ;  $K_g$  is the assembled stiffness matrix;  $C_g$  is the assembled damping matrix;  $M_g$  is the mass matrix of the assembled structure;  $K$  is the block diagonal collection of unassembled substructural stiffness matrices;  $L$  is the Boolean assembly matrix that relates the global and substructural displacements; the superscript (·) designates time differentiation, and the subscript (g) designates 'an assembled global structure' to distinguish from 'partitioned substructures'. The discrete damped, time-invariant linear equations of motion for vibrating structures can be obtained from the stationary value of the preceding discrete energy functional, viz.,  $\delta\Pi = 0$ :

$$M_g \ddot{u}_g + C_g \dot{u}_g + K_g u_g = f_g \quad (2)$$

The input-output relation, referred to as the *frequency response function* (FRF), is obtained by substituting a harmonic form of the input-output vectors as

$$\begin{bmatrix} u_g \\ f_g \end{bmatrix} = e^{j\omega t} \begin{bmatrix} \bar{u}_g \\ \bar{f}_g \end{bmatrix} \quad (3)$$

and solving for the frequency-domain output  $\bar{u}_g$ :

$$\bar{u}_g = H_g(\omega) \bar{f}_g, \quad H_g(\omega) = (K_g + j\omega C_g - \omega^2 M_g)^{-1} \quad (4)$$

where  $H_g(\omega)$  will be called the 'global' flexibility matrix and becomes to  $K_g^{-1}$  ( $=F_g$ ) in the quasi-static limit ( $\omega \rightarrow 0$ ). This matrix can be obtained in terms of the eigenmodes  $\Phi$  and eigen values  $\Lambda$  as

$$F_g = \Phi \Lambda^{-1} \Phi^T, \quad \Phi^T M_g \Phi = I, \quad \Phi^T K_g \Phi = \Lambda \quad (5)$$

In practice, the size of the experimentally identified global flexibility matrix is given by

$$F_g = \Phi_m \Lambda_m^{-1} \Phi_m^T \quad (6)$$

where the subscript (m) denotes the measured modes and mode shapes which are substantially smaller than the analytical mode size.

## 2.2 Substructural Flexibility Equation

Since our objective is to identify the damage location and reductions of the rigidity and the global flexibility-based damage indicators are known to mask localized damage attributes, we employ a general partitioned flexibility method presented by Park and Felippa [4] to relate the experimentally measured global flexibility matrix in Eq.(6) in term of the corresponding localized flexibility matrices. This is accomplished as follows. First, a structure that is in equilibrium under applied forces is partitioned into substructures or elements. Hence, each of the partitioned substructures would be subject to the corresponding applied forces plus the Lagrange multipliers acting along the substructural partition interfaces. In order to maintain the kinematical compatibility along the partitioned boundaries, the displacement vector of the partitioned substructures  $u$  must satisfy the following relation:

$$u - Lu_g = 0 \quad (7)$$

where  $u$  are the collections of all the substructural displacements. The element-by-element force vector  $f$  that is conjugate with the substructural displacement is given by

$$L^T f = f_g \quad (8)$$

so that the desired FRF must assume the following form:

$$\bar{u} = H(\omega) \bar{f} \quad (9)$$

Observe that Eq.(9) relates the input  $\bar{f}$  that is acting on each substructure defined in Eq.(8) to the output of individual substructural displacements  $\bar{u}$  introduced in Eq.(7). Therefore, by introducing a Lagrange multiplier vector  $\lambda_\ell$  to enforce the kinematic compatibility condition Eq.(7), the system energy functional expressed in terms of the global nodal variables given in Eq.(1) is transformed into the three-variable functional:

$$\Pi(u, \lambda_\ell, u_g) = u^T (\frac{1}{2} Ku - f + M\ddot{u} + C\dot{u}) - \lambda_\ell^T B^T (u - Lu_g) \quad (10)$$

where  $M$  and  $C$  are the substructural mass and damping matrices, and  $B$  is a constraint projection matrix that extracts the partition boundary substructural nodes. The stationary value of the above functional leads to the following equations of motion for partitioned structures:

$$\begin{bmatrix} \ddot{M} + \dot{C} + K & -B & 0 \\ -B^T & 0 & L_b \\ 0 & L_b^T & 0 \end{bmatrix} \begin{Bmatrix} u \\ \lambda_\ell \\ u_g \end{Bmatrix} = \begin{Bmatrix} f \\ 0 \\ 0 \end{Bmatrix}, \quad L_b = B^T L \quad (11)$$

The substructure-by-substructure FRF that is sought after can now be obtained from Eq.(11) as

$$H(\omega) = H_e(\omega) \{ I - BK_B(\omega) [I - L_b H_L(\omega) L_b^T K_B(\omega)] B^T H_e(\omega) \} \quad (12)$$

$$H_e(\omega) = (K + j\omega C - \omega^2 M)^{-1}, \quad K_B(\omega) = (B^T H_e(\omega) B)^{-1}, \quad H_L(\omega) = (L_b^T K_B(\omega) L_b)^{-1}$$

It can be shown that the substructural FRF  $H(\omega)$  can also be obtained in terms of the global FRF  $H_g(\omega)$ , viz.,

$$H(\omega) = L H_g(\omega) L^T = L (K_g + j\omega C_g - \omega^2 M_g)^{-1} L^T \quad (13)$$

Observe that the substructural FRF given by Eq.(12) reveals the substructural compositions consisting of the substructural mass, damping and stiffness matrices. On the other hand, the same FRF obtained by the input/output invariance property given by Eq.(13) masks the substructural compositions, showing only the global quantities. Their combined use leads to an important application in detecting damages as shown below. For the quasistatic limit, i.e.,  $(\omega \rightarrow 0)$ , the two expressions provide the following Ricatti-like equation:

$$LF_g L^T = F\{I - BF_B^{-1}[I - L_b F_L L_b^T F_B^{-1}]B^T F\} \quad (14)$$

$$F = K^{-1}, F_B = (B^T F B), F_L = (L_b^T F_B^{-1} L_b)^{-1}$$

where  $F$  is called the substructural flexibility matrix of block diagonal form.

### 2.3 Deformation-Basis Flexibilities

The substructural flexibility matrix  $F=K^{-1}$  given in Eq.(14) consists of both free-free deformation modes plus the rigid body modes. This poses no difficulty when the experimentally identified global flexibility  $F_g$  in Eq.(6) is a full basis matrix, viz., the eigenvector  $\Phi_m$  is a square matrix. In practice the measured modes are often a fraction of the sensor output numbers, namely, for  $\Phi_m$  ( $s > m$ ) where  $s$  is the number of the sensors and  $m$  is the measured mode numbers. This observation motivated us to transform the free-free substructural flexibility matrix  $F$  into a constrained deformation flexibility which can lead to a sharper indication of damage. Let us decompose the substructural displacements  $u$  further into deformational and rigid parts:

$$u = d + R\alpha \quad (15)$$

where  $d$  is the deformational part,  $R$  describe the substructural rigid-mode shapes, and  $\alpha$  are the rigid-mode amplitudes. In order to eliminate the rigid-body motions from the substructural displacements, we partition Eq.(15) according to:

$$\begin{Bmatrix} u_c \\ u_f \end{Bmatrix} = \begin{Bmatrix} d_c \\ d_f \end{Bmatrix} + \begin{Bmatrix} R_c \\ R_f \end{Bmatrix} \alpha, \quad R = \begin{bmatrix} R^1 & & \\ & R^2 & \\ & & \ddots \\ & & & R^{n_s} \end{bmatrix} \quad (16)$$

where  $R_c$  is a square invertible submatrix corresponding to 'temporarily constrained nodes' and  $R_f$  refers to unconstrained nodes. Hence,  $R_c$  would be a  $(3 \times 3)$  matrix. Similarly, the constrained-node rigid-body amplitudes  $R_c$  for other substructural cases can be chosen. Solving for  $\alpha$  from the first row of Eq.(16), we obtain

$$\alpha = R_c^{-1}(u_c - d_c) \quad (17)$$

We now introduce a deformation measure that represents deformations at nodes  $f$  with respect to nodes  $c$ :

$$v = d_f - R_f R_c^{-1} d_c = Tu = TLu_g, \quad T = [-\bar{R} \quad I], \quad \bar{R} = R_f R_c^{-1} \quad (18)$$

Using this relation, its conjugate force vectors are given by

$$T^T f_v = f \Rightarrow L^T T^T f_v = L^T f = f_g \quad (19)$$

The variational functional Eq.(10) expressed in terms of the substructural displacement  $u$  is transformed into that of the deformation variable  $v$ , which in the quasi-static limit becomes:

$$\bar{\Pi}(v, \lambda_v, u_g) = v^T (\frac{1}{2} K_v v - f_v) - \lambda_v^T B_v^T (v - T L u_g), \quad K = T^T K_v T \quad (20)$$

A simple expression is obtained if the constraint operator  $B_v$  is chosen as a nullspace of  $TL$ , viz.,

$$B_v^T (TL) = 0 \quad (21)$$

So that the stationary condition  $\delta \Pi = 0$  of Eq.(20) yields

$$\begin{bmatrix} K_v & -B_v^T \\ -B_v^T & 0 \end{bmatrix} \begin{Bmatrix} v \\ \lambda_v \end{Bmatrix} = \begin{Bmatrix} f_v \\ 0 \end{Bmatrix} \quad (22)$$

which will be called the deformational quasi-static equations of motion for partitioned structures. A Riccati-like equation which relates the global flexibility to the deformation-basis substructural flexibility can be obtained in a similar manner as for the substructural displacement case Eq.(14):

$$TLF_g L^T T^T = P_v^T F_v P_v, \quad F_v = K_v^{-1}, \quad P_v = I - B_v [B_v^T F_v B_v]^{-1} B_v^T F_v \quad (23)$$

## 2.4 Strain-Basis Flexibilities

We have experienced that the use of the deformational flexibilities  $F_v$  yields an adequate identification of damage locations. In many applications not only identifying damage locations but also damage mechanisms are equally important. For only through understanding damage mechanisms one can develop damage prevention measures. An effective approach to detect damage mechanisms is to utilize strain-basis substructural flexibilities. As an example, a typical substructure consists of membrane, transverse shear and bending strains. By identifying which of the three strains undergo a major strain change, one may deduce the damage mechanisms. The necessary transformation to obtain a strain-basis flexibilities is shown below. Let us assume that the strain output  $s$  can be related to the substructural displacement  $u$  according to

$$s = Du = D L u_g \quad (24)$$

where  $D$  is the discrete strain-displacement relation matrix that can be derived in a variety of ways, e.g., by relying on the finite element shape functions. With this change of basis, one arrives at the following strain-basis functional and the corresponding equations of motion in quasi-static form:

$$\bar{\Pi}(s, \lambda_s) = s^T (\frac{1}{2} K_s s - f_s) - \lambda_s^T B_s^T (s - D L u_g), \quad K = D^T K_s D, \quad B_s^T (DL) = 0 \quad (25)$$

$$L^T D^T f_s = f_g \Rightarrow \begin{bmatrix} K_s & -B_s^T \\ -B_s^T & 0 \end{bmatrix} \begin{Bmatrix} s \\ \lambda_s \end{Bmatrix} = \begin{Bmatrix} f_s \\ 0 \end{Bmatrix}$$

The global flexibility  $F_g$  is then related to the strain-basis substructural flexibility  $F_s$  according to:

$$DLF_g L^T D^T = P_s^T F_s P_s, \quad F_s = K_s^{-1}, \quad P_s = I - B_s [B_s^T F_s B_s]^{-1} B_s^T F_s \quad (26)$$

which can be used not only for localized damage detection but more importantly for identifying damage mechanisms.

## 3. Applications to Damage Detection in Continuum CFRP Composites

To illustrate the applicability of the localized damage detection techniques reviewed in the preceding sections to continuum composites, we first evaluate the methods to analytical problems. Validation of the damage detection methods by the experimental data is then followed.



### 3.1 Analytical Demonstration

In order to demonstrate the validity of present method, CFRP filament winding pipe having 34mm diameter, length of 500mm, 2mm thickness, winding angle of  $45^\circ$  and clamped at the both ends is chosen as an example. The pipe is divided into 12 beam elements in the FEM Analysis and the bending rigidity of 6th element is assumed to be 80% value of other elements owing to the damage. For offering the relative performance of three methods, the global flexibility  $F_g$  is adopted as an inverse of the global stiffness matrix that is obtained from the corresponding FEM analysis. A homotopy iterative procedure [5] is then used to obtain the free-free substructural flexibility  $F$  given in Eq.(14), the deformation-basis flexibility  $F_v$  in Eq.(23) and the strain-basis flexibility  $F_s$  in Eq.(26). For damage detection we have employed the following rigidity ratio  $\delta$ :

$$\delta^{ns} = \frac{\text{diag}(F_{\text{damage}}^{ns} - F_{\text{healthy}}^{ns})}{F_{\text{healthy}}^{ns}} \quad (27)$$

where the superscript (ns) designates the substructural component or degree of freedom.

In Figs.2 - 4, the solid line indicates the change of rigidity ratio by using the 44 eigen values and eigen vectors in the global flexibility matrix  $F_g$  and the broken line with '\*' mark is the change of rigidity ratio by using only the first three eigen values and modes in the  $F_g$ . When the free-free substructural flexibility method is used, the damage is detected at the degree of freedom from 19 to 22 corresponding to 6<sup>th</sup> element as shown in Fig.2. The resulting rigidity ratio as solid line provides the location of damage correctly and the rigidity ratio of the corresponding element shows the assumed value of 0.8. Since the only first three eigenvalues and modes are used for calculating the global flexibility  $F_g$  in Eq.(6), the change of rigidity ratio as broken line with '\*' mark cannot be accurately computed. Nevertheless, the locations of damaged elements are correctly determined. As for the deformation-based flexibility method, the damage should occur at the degree of freedoms from 11 and 12 is shown in Fig.3. Both of results correctly trace except the 11<sup>th</sup> and 12<sup>th</sup> degree of freedom, but their values are overestimated somewhat for the assumed reduced bending rigidity. Finally, Fig.4 shows the damage indication based on the strain-basis flexibilities not only correctly detects the damaged 6<sup>th</sup> element but also computes the almost same rigidity ratio of 0.8. So far as the identification in CFRP filament winding pipe is concerned, the strain-basis damage indication can predict it well within acceptable accuracy ranges.

### 3.2 Application to Experimental Data

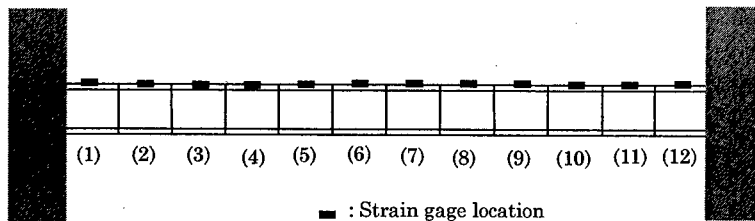


Fig.1 Partition elements and the location of the strain gage

We have carried out the damage detection procedure to experimental strain data obtained on the CFRP filament winding pipe mentioned before. The strain data have been measured at the center of the twelve elements on the CFRP pipe specimens as shown in Fig.1. The 6<sup>th</sup> element of pipe specimen has 50% bending rigidity ratio compared with the other elements. This bending rigidity reduction has been realized by cutting out a half of the cross section area and this area is extended a half of the circumferential length. The CFRP pipe has been then subjected to forced vibration tests under sinusoidal signal from 10Hz to 1200Hz. The frequency response functions (FRFs) have been obtained by using Fast Fourier Transform analyzer and the strains are measured for the first three eigenmodes of healthy and damaged specimens. By using the experimentally determined three global flexibility modes, the rigidity ratios based on the strain-basis flexibility changes are computed and shown in Fig.5. By comparing the experimental case shown in Fig.5 with the analytical case (see Fig.4), it is seen that the damage locations are correctly determined. The bending rigidity of the damaged element is overestimated for the real test case but is well within acceptable accuracy ranges.

#### 4. Conclusions

The change of rigidity ratio that utilizes the three localized flexibilities has been

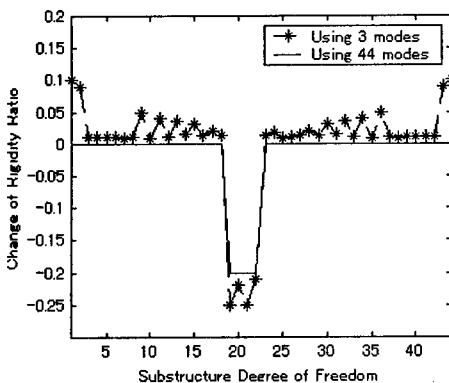


Fig.2 Damage Detection Based on Substructural Flexibility

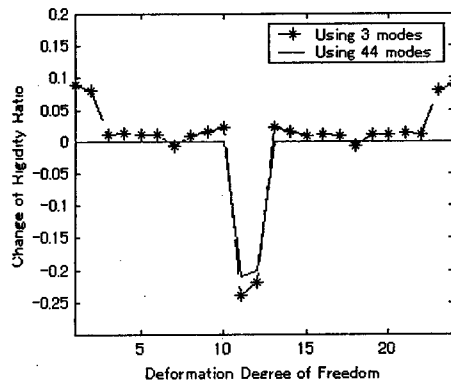


Fig.3 Damage Detection Based on Deformation Flexibility

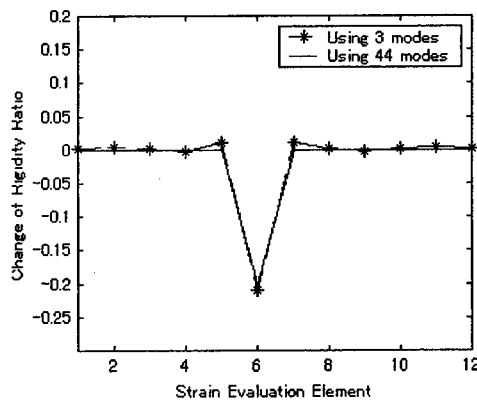


Fig.4 Damage Detection Based on Strain Flexibility

applied to the damage detection of CFRP composite pipes and shells. The free-free localized flexibility and the deformation-basis flexibilities can make use of conventional output data such as acceleration or displacement. The strain-basis localized flexibility can utilize a combination of the conventional modal test output as well as the strain output. Then, the damage detection of CFRP filament winding pipe has been carried out by using strain gage records. The main features of the present study are summarized as follows.

- 1) The relative accuracy fidelities of the three localized flexibilities are evaluated as applied to the damage detection of CFRP composite pipes analytically. All three flexibility methods accurately captured the locations of rigidity changes. Among the three, the strain-basis flexibility method is most accurate.
- 2) By using the global flexibility of CFRP filament winding pipes determined by first three strain eigenmodes, damage detection are carried out by the strain-basis flexibility method. The result demonstrates that damage location is identified with high confidence as well as reasonably accurate change in the bending rigidity.

## References

1. Doebling, S. W. et al, "Damage Identification and Health Monitoring of Structural and Mechanical System form Changes in Their Vibration characteristics: A Literature Survey", Los Alamos National Laboratory, Report No.LA-12767-MS, 1996, Los Alamos, NM.
2. Park, K.C., Reich, G.W. and Alvin, K.F., "Damage Detection Using Localized Flexibilities", Structural Health Monitoring, Current Status and Perspectives, Chang, F.K., Ed., Technomic Pub., 1997, pp125-139
3. Byon, O.I., Aoki, Y., Yamaguchi, T. and Park, K.C., "Damage Detection of CFRP Laminates Composites by Localized Flexibility Method", Proceedings of 12<sup>th</sup> International Conference on Composite Materials, July, 1999, pp375
4. Park, K.C. and Felippa, C.A., "A Variational Framework for Solution Method Developments in Structural Mechanics", Journal of Applied Mechanics, March, 1998, Vol.65/1, pp242-249
5. Richter, S.L. and Collins, E.G., Jr., "A Homotopy Algorithm for Reduced-Order Controller Design Using the Optimal Projection Equations, Proceedings of the Conference on Decision and Control, April, 1989, pp331-338

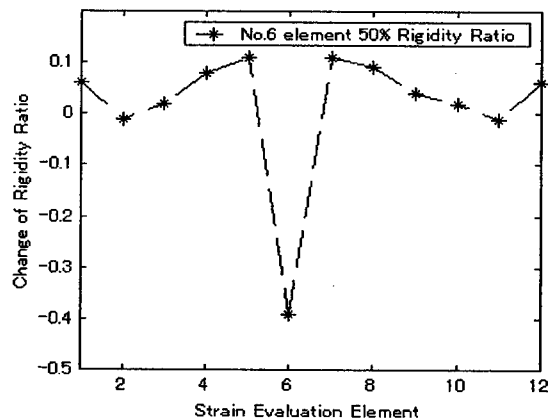


Fig.5 Experimental damage detection based on strain flexibility

## **Damage Detection of CFRP Laminates Using Vibration Analysis Data**

T.Inada, Y.Shimamura, A.Todoroki, H.Kobayashi and H.Nakamura

### **Abstract**

This paper presents a delamination identification method for advanced composite structures using vibration data. Delamination identification of CFRP laminated beams using natural frequency change and response surfaces was conducted. Response surfaces were used for approximation of the natural frequency change in delaminated CFRP beams. In order to identify the delamination sizes and location, an objective function was made from response surfaces and the natural frequencies of the delaminated CFRP beam. By minimizing the objective function, the delamination size and location can be predicted easily and inexpensively. Effectiveness of the present method was verified both analytically and experimentally.

### **Introduction**

Recently, CFRP laminated structures have been applied to many structures of vehicles. Since interlamina strength of the structure is relatively low, internal damage, such as delamination, can be easily induced by impact. In order to assess integrity of the damaged structures, it is necessary to identify the size and location of the damage by using nondestructive testing.

Since modal parameters of damaged structures change from that of undamaged states, damage identification methods based on the modal parameter changes are investigated by many researchers [1-6]. Among the modal parameters, modal strain distribution is effective to localize damage [5,6], but measurement of modal strain distribution is expensive and unrealistic since it needs many sensors on the structure. On the contrary, natural frequencies are global parameters and can be measured easily with a few sensors. However, natural frequency change of structures is complicated, it is very difficult to identify delamination size and location. For this reason, backpropagation neural network (BNN) is often used. BNN is, however, time-consuming for teaching and the regression results cannot be validated by using a statistical testing.

---

T.Inada, Graduate student of Tokyo Institute of Technology, O-okayama 2-12-1, Meguro-ku, Tokyo, 152-8552, Japan

Y.Shimamura, A.Todoroki, H.Kobayashi and H.Nakamura, Department of Mechano-Aerospace Engineering, Tokyo Institute of Technology

This study provides a delamination identification method using natural frequency change and response surfaces. In this method, the natural frequencies are approximated by response surfaces, and the delamination identification is identical with an optimization problem. In order to verify effectiveness of the present method, delamination identification of CFRP cantilever beams was conducted both analytically and experimentally.

### Analytical Model of a CFRP Cantilever Beam

In the present study, the changes of the natural frequencies from an intact state are used for delamination identification. In order to construct delamination identification system, the relationship between the natural frequencies and the delamination size and locations have to be cleared.

An analytical model used to calculate the natural frequency change of delaminated CFRP beams is shown in figure 1 [1,2]. In the model, the cantilever beam is divided into four Euler beams and the natural frequencies are obtained as a result of an eigenvalue problem. The stacking sequence is  $[0/90/90/0]_s$ , and delamination is located at the midplane of the CFRP beam. The length of the beam is 0.25m, and the thickness of the beam is 0.002m. Material properties of CFRP ply used in the analysis are:  $E_1=157\text{GPa}$ ,  $E_2=10.0\text{GPa}$ ,  $\nu_{12}=0.27$ . Although the model did not include bending and extensional coupling terms, it was shown that the natural frequencies calculated from this model are well agreed with the experimental results [1,2]. Normalized value  $a/L$  as delamination size, and normalized value  $l/L$  as delamination location are used. The range of delamination size assumed in analysis is  $0.05 \leq a/L \leq 0.25$ , and the range of delamination location is  $0 < l/L < 1$ .

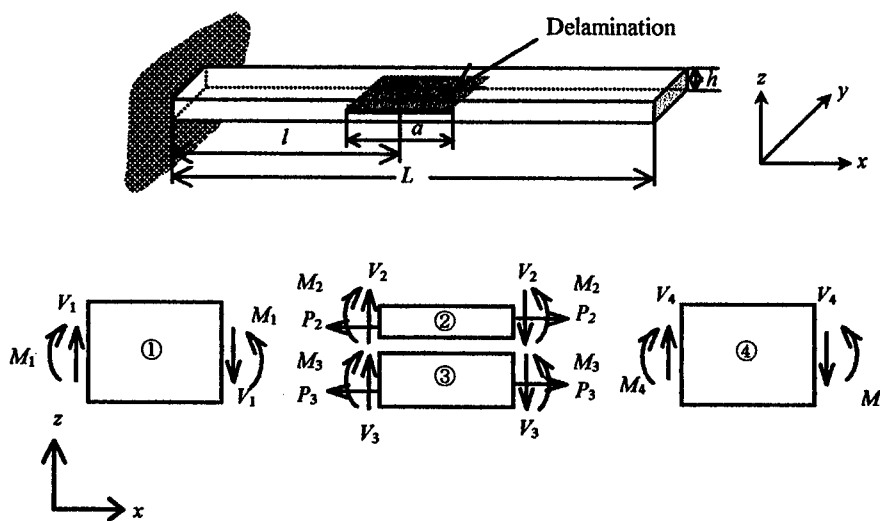


Figure 1 Analytical Model of a CFRP Cantilever Beam with a Delamination

## Damage Identification Method

### Response Surfaces of Natural Frequencies

It is easy to calculate many data sets from analytical models. It is, however, difficult and expensive to calculate many data sets for general complicated structures by FEM analysis. In order to reduce the calculation cost, we adopt response surface methodology (RSM) to complement many data sets from a few data sets that are calculated from analysis. RSM is a method to get an approximate expression of relation between variables and responses, which consists of surface regression by least squares method and design of experiments.

The quadratic polynomial response surface of two variables is expressed as follows.

$$y = \beta_0 + \beta_1 x_1 + \beta_2 x_2 + \beta_3 x_1^2 + \beta_4 x_2^2 + \beta_5 x_1 x_2 \quad (1)$$

In equation (1),  $y$  is the natural frequency,  $x_1$  is the delamination size and  $x_2$  is the delamination location. In order to calculate the coefficients  $\beta$ , the least squares method is used.

Since the natural frequency change of CFRP beams was complicated, high-order response surfaces were used for the approximation. Moreover, the natural frequency change in terms of delamination location was especially complicated, and three response surfaces were used to approximate the natural frequency change of each mode. The feasible region for the delamination size and location was divided into three regions at  $l/L=0.33$  and  $l/L=0.66$ .

### Objective Function for Damage Identification

As mentioned above, we can obtain the approximate expressions of the natural frequency change of the beams with various delamination sizes ( $x_1$ ) and locations ( $x_2$ ) using response surfaces. We define these response surfaces as  $\{\Omega_1(x_1, x_2), \Omega_2(x_1, x_2), \Omega_3(x_1, x_2)\}$  on individual regions, and the natural frequencies of a CFRP cantilever beam with delamination as  $(\omega_1, \omega_2, \omega_3)$ .

By using the response surfaces, the delamination identification is identical with an optimization problem. In order to identify the delamination size and location of the CFRP beam, we make an objective function on individual regions as

$$F = \sum_{i=1}^3 \{\Omega_i(x_1, x_2) - \omega_i\}^2 \quad (2)$$

By minimizing the objective function  $F$ , the delamination size and location are obtained on individual regions. From the three candidates, the global minimum is decided. When the function  $F$  is globally minimized at  $(x_1^*, x_2^*)$ ,  $x_1^*$  means predicted delamination size and  $x_2^*$  means predicted delamination location. The conjugate gradient method was used to minimize the function  $F$ . Since there are many local

minimums in the function, we used random initial values of  $x_1$ ,  $x_2$  and searched the local minimums for these initial values on each region.

### Identification Results

Delamination identification was conducted to verify effectiveness of the present method. The sets of the natural frequencies used for the verifications were also calculated from the analytical model shown in figure 1, and they are not used for making the response surfaces.

In practical use, it is not so important to identify delamination size and location precisely, and it is desirable to obtain identification results simply and quantitatively. For this reason, we classified the identified delamination sizes and locations into levels as shown in Table I.

The reliability as an index of delamination identification results is described as

$$\text{Reliability (\%)} = \frac{\text{The number of data identified in actual level}}{\text{The total number of data}} \times 100 \quad (3)$$

The reliabilities of delamination size and location were calculated and shown in figure 2. In figure 2, the vertical axis means the reliability and the horizontal axis means delamination parameters (i.e. size and location). The reliability of delamination size is 93%, and that of location is 81%. Judging from the results, it is clear that the present method is effective to identify delamination size and locations.

In practical the measured natural frequencies are, however, supposed to contain some errors, and the identification reliability may become worse. In the next section, effectiveness of the present method will be verified in experiments.

### Vibration Tests of CFRP Cantilever Beams

In this section, modal testings of CFRP cantilever beams with various delamination sizes and locations are conducted, and delamination identifications are also conducted from the measured natural frequencies.

Table I Classification of delamination sizes and locations

Size		Location	
Level	Range	Level	Range
1	$0 \leq a/L < 0.1$	1	$0 \leq l/L < 0.2$
2	$0.1 \leq a/L < 0.2$	2	$0.2 \leq l/L < 0.4$
3	$0.2 \leq a/L < 0.3$	3	$0.4 \leq l/L < 0.6$
		4	$0.6 \leq l/L < 0.8$
		5	$0.8 \leq l/L < 1$

### Vibration Tests of CFRP Cantilever Beams

In this section, modal testings of CFRP cantilever beams with various delamination sizes and locations are conducted, and delamination identifications are also conducted from the measured natural frequencies

#### Experimental Setup

Specimens of CFRP beams were obtained from  $[0/90/90/0]_S$  CFRP laminates with delaminations. Delaminations were fabricated by inserting Teflon tapes into the midplane of the laminates. An intact beam and delaminated beams with delamination size of 15mm, 30mm, 45mm and 60mm were obtained from a laminate. Four laminates were fabricated by hot press and 16 kinds of delaminated beams were thus prepared.

The experimental setup is shown in figure 3. An impulse hammer is used to excite the beam and a PVDF sensor is used to measure the response. The measured frequency response is stored in the personal computer, and modal parameters such as natural frequencies are extracted from the frequency response. The cantilever beam was basically 2mm thick, 20mm wide and 250mm long. In order to increase the number of experimental data, the beam length was changed from 240mm to 260mm, and modal testings were conducted. Thus, 29 kinds of data sets of the natural frequencies were prepared.

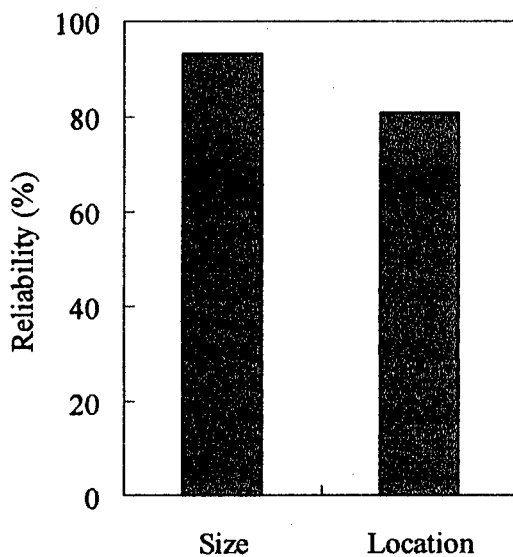


Figure 2 Delamination Identification Results (Analysis)



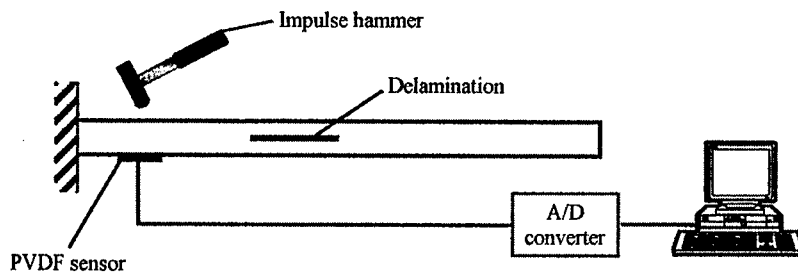


Figure 3 Experimental setup

### Identification Results

Delaminations were identified by substituting the measured natural frequencies into equation (2) and optimizing the equation. The reliability of delamination sizes and locations are shown in figure 4. In figure 4, the vertical axis means the reliability and the horizontal axis means delamination parameters. The reliability of delamination size is 69%, and that of location is 45%. Both of the reliabilities are lower than that of using the analytical data. This is because of incorrectness of measured natural frequencies. Especially, the natural frequencies of first mode contain large errors due to sampling conditions. The natural frequencies of first mode are about 30Hz, and the resolution is not sufficient to measure the natural frequencies of the first mode. By modifying the measuring conditions, we can improve the delamination identification reliability.

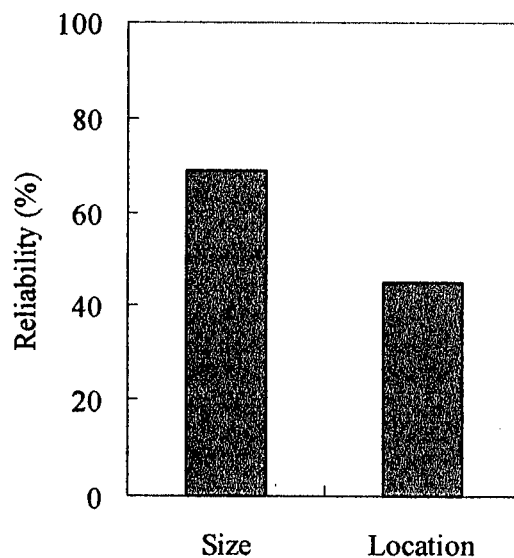


Figure 4 Delamination Identification Results (Experiment)

## Conclusions

This paper describes the delamination identification method for CFRP laminated structures using the natural frequency change and response surfaces. In order to verify the effectiveness of the present method, delamination identification of CFRP cantilever beams was conducted both analytically and experimentally. As a result, it is shown that the present method has high identification reliability when the natural frequencies are measured precisely. The present method is easy and inexpensive because of adopting the response surfaces, and the applications to general structures are also easy since natural frequencies can be measured easily by modal testing.

## References

1. A. C. Okafor, K. Chandrashekhara and Y. P. Jiang, "Delamination prediction in composite beams with built-in piezoelectric devices using modal analysis and neural network", *Smart Mater. Struct.*, 5, 1996, pp.338
2. A. S. Islam and K. C. Crag, "Damage detection in composite structures using piezoelectric materials", *Smart Mater. Struct.*, 3, 1994, pp.318
3. C. H. Keilers, Jr. and F. Chang, "Identifying Delamination in Composite Beams Using Built-In Piezoelectrics: Part II-An Identification Method", *J. Intell. Matls. Sys. & Struct.*, 6, 1995, 664
4. H. Luo and S. Hanagud, "PVDF SENSOR AND ITS APPLICATIONS IN DELAMINATION RESPONSE DETECTION", *AIAA*, 97-1218, 1997, pp.720
5. A. K. Pandey, M Biswas and M. M. Samman, "DAMAGE DETECTION FROM CHANGES IN CURVATURE MODE SHAPES", *J. Sound and Vibration*, 145(2), 1991, pp.321
6. C. P. Ratcliffe, "DAMAGE DETECTION USING A MODIFIED LAPLACIAN OPERATOR ON MODE SHAPE DATA", *J. Sound and Vibration*, 204(3), 1997, PP.505

# **Composite Structure and Tank**

---

## **Development of High Speed Composite Flywheel Rotors for Energy Storage Systems**

K.TAKAHASHI, S.KITADE and H.MORITA

### **Abstract**

A composite flywheel rotor was developed. The rotor was designed, which based on the finite element analysis, and fabricated to achieve the peripheral speed of 1300m/s. The rotor consisted of composite rim and aluminum alloy hub. The inner diameter of the rim was 340mm and outer diameter was 400mm and thickness was 25mm. The rim comprised press fitted multiple concentric rings(multi-ring) to prevent radial tensile failures at high rotational speed. Rings were fabricated by filament winding process using high strength carbon fiber. The configuration of the hub was like a steering wheel with 4 spokes. The cross section area of these spokes was changed to withstand a centrifugal force.

Spin tests of flywheel rotors were performed, using an air turbine driven spin tester in a vacuum chamber. The rotor was spun to maximum peripheral speed at 1310m/s, whose stored energy was 354Wh, and the specific energy density was 195Wh/kg.

### **1. Introduction**

Flywheel energy storage systems offered advantages over electrochemical batteries in situations demanding high power delivery and high specific energy (energy storage per unit weight). In the 1970s and early 1980s, much composite flywheel research [1] was carried out in response to energy storage needs in daily load-leveling, space applications and automotive applications. However the fiber strength was too low to achieve sufficient rotational speed. Recent researches on flywheels [2] have resurged because of developments of new high strength and high modulus fibers. The composite flywheel system with new fibers will be more compact and lighter weight at same storage energy.

Authors have developed an all composite flywheel rotor [3], whose outer diameter has been 400mm (Fig.1). The composite rotor has been reached to maximum peripheral speed of 1203m/s.

In this study, the authors tried to develop a new flywheel rotor which rotated at more than 1300m/s.

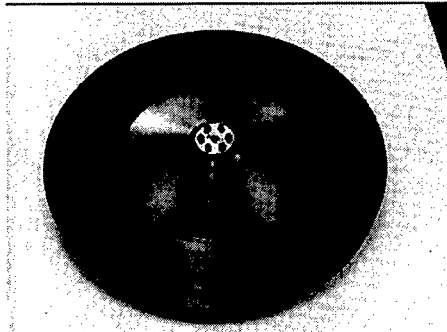


Figure1 Composite flywheel rotor

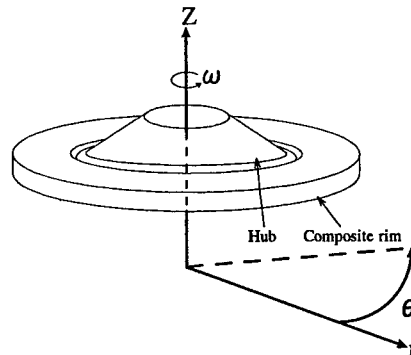


Figure 2 Configuration of the composite flywheel rotor

## 2. Basic concept of the composite flywheel rotor

A flywheel rotor was a rotating body consisting of a rim attached to an axis by a hub (Fig.2). The rotor stored rotating kinetic energy by high speed rotation. The kinetic energy was proportional to weight and square of peripheral speed. The maximum energy density (energy / unit weight) was shown in equation (1).

$$e = K \frac{\sigma_{\theta}}{\rho} \text{ -----(1)}$$

where  $e$  was energy density,  $K$  was a coefficient,  $\sigma_{\theta}$  was hoop stress,  $\rho$  was density.  $\sigma_{\theta}/\rho$  was specific strength. The specific strength of carbon fiber composites was much higher than metals, and a composite flywheel rotor could be reached to high speed rotation and high energy storage.

### (1) Composite rim

The maximum radial stress of a rotating ring depended on radius ratio between inner and outer ( $r_{in}/r_{out}$ ), and the larger  $r_{in}/r_{out}$  was the smaller maximum radial stress. Therefore, only thin filament wound ring could rotate at high speed because of the low transverse strength. To reduce the radial stress, a multi-ring structure was effective (Fig.3). In case a thick single ring was divided in multi rings, the maximum radial stress in each rings at rotation was lower than in the single ring, but the contact radial stress between inner and outer ring became tension (Fig.3 M). In a word, the multi-ring form couldn't be maintained because each rings separated at rotation. To maintain the multi-ring form, contact radial stress between inner and outer ring should be compression in the rotating area. Therefore, the multi-ring design approaches were : (a) the rim consist of press fitted multiple rings (Fig.3 a) and (b) the inner rings are more denser and/or less stiff than outer rings (Fig.3 b). At method (a), initial compressive stress field caused by press-fitting could be reduced radial stress. At method (b), expanding of denser and/or softer inner ring under rotation presented compressive stress in composite rim, and it resulted the reduction of radial stress.

The rim of the all composite rotor [3], which authors have developed, have been

designed using the both two approaches (a) and (b). The outer ring was made of a high modulus fiber (Toray M40J) and the inner rotor was made of standard modulus fiber (Toray T300). All rings were press fitted. This rotor was failed at peripheral speed of 1203m/s.

In this study, the target speed was set at over peripheral speed of 1300m/s. The strength of a thin single ring made of M40J, of which outer diameter was 400mm, was too low for the ring to spin at over 1300m/s. Therefore, Toray T1000G, which had higher strength than M40J, was applied to the outer ring. But the modulus of T1000G is lower than M40J. In case of using a T300 ring inside T1000G ring, the effect (b) could be obtained, but inner radius of the rim had too large deformation at over 1300m/s because T1000G had less modulus than M40J. Therefore, it was difficult to design a hub, which had to expand according to the elongation of composite rim. As results, only effect (a) was used with all T1000G rings. The strength and modulus of T300, M40J and T1000G was shown in Table.1.

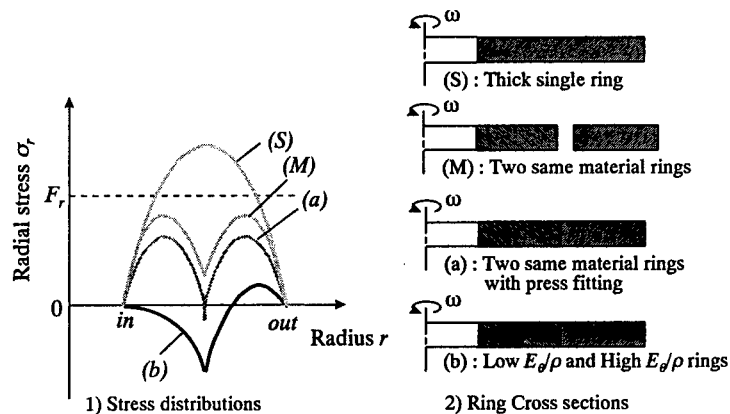


Figure 3 Reduction of the radial stress by multi-ring configuration

Table I Mechanical properties of fibers (T300, M40J, T1000G)

	Strength (MPa)	Elastic modulus (GPa)	Density (g/cm <sup>3</sup> )
T300	4210	230	1.78
M40J	4400	377	1.77
T1000G	6370	294	1.80

## (2) Hub

Under rotational loading, the hub had to expand according to the elongation of composite rim, and the contact stress between hub and rim should be compressive to prevent separation. Therefore, the material of the hub needed to have high strain of failure and relatively low modulus. The material also needed to have stable deformation behavior until high strain (over 1.5%) region to predict precise deformation field in

design work.

The hub of the all composite rotor [3], which authors have developed, have been made of glass fiber composite, because of its high strain of failure and low elasticity to expand with rotational speed. However, the glass fiber composite hub was damaged with delamination and fiber/matrix debonding at low speed. The deformation behavior of glass fiber composite hub was unstable, and it concluded that, the design of glass fiber composite hub for new 1300m/s class rotor was difficult.

In this study, high strength aluminum alloy (7075) was selected for the hub. The aluminum alloy had adequate ultimate strength and modulus like glass fiber composite to rotate at peripheral speed of 1300m/s class, and the deformation behavior was stable. Under the high speed rotation, the strain of the aluminum alloy hub was beyond the elastic region. Therefore, plastic deformation of the hub was considered in design work. The hub was inserted after a soak of liquid nitrogen, to obtain initial contact stress to fit the hub with the rim.

### 3. Flywheel design

#### (1) Configuration of the flywheel rotor

The basic configuration of the flywheel rotor in this study was shown in Fig.4. The rim was 400mm in outer diameter, 340mm in inner diameter and 25mm in axial thickness. The ultimate peripheral speed in the design was 1350m/s.

The rim was a multi-ring structure with 4 rings which were made of the high strength fiber (T1000G). The material of the hub was aluminum alloy (7075). The configuration of the hub was like a steering wheel with 4 spokes. The cross section area of these spokes was changed to withstand a centrifugal force. The detailed configuration was adjusted by analytic.

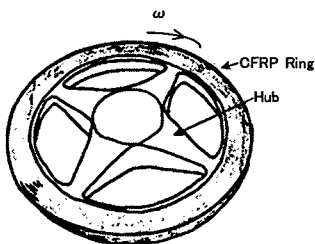


Figure 4 Configuration of the flywheel

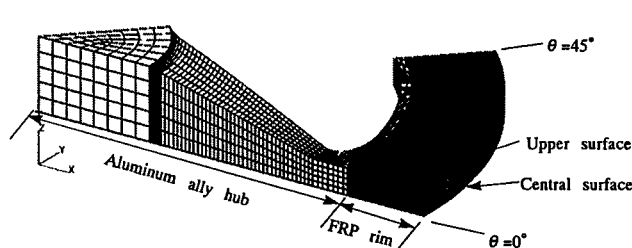


Figure 5 FEM model for composite flywheel

#### (2) Analytical method

The flywheel rotor was designed with a finite element analysis. The model of the analysis was shown in Fig.5. The model was one eighth of circle and a half of thickness

of the rotor, and it was considered the symmetry for the circle and the thickness. The model consisted of 3D elastic-plastic elements, and was considered the effects of contact among each rings and aluminum hub.

The criterion of the flywheel rotor design was as follows;

- (a) Hoop stress limitation in the rim was the ultimate strength of the composite which was made of T1000G. The ultimate stress by a NOL ring test was 3.5 GPa.
- (b) Radial stress limitation in the rim was under 10 MPa.
- (c) Contact radial stress between each rings should be compressive (under 0 MPa).  
Contact radial stress between the rim and the hub should be compressive (under 0 MPa).
- (d) Von-Mises stress limitation in the hub was 570 MPa.

#### (4) The result of the analysis

The radial and hoop stress distribution of the composite rim at 1350m/s were shown in Fig.6 and 7. The radial stress of the composite rim was compressive in all region, and the rim was satisfied with the radial stress criterion (b) and (c). In Fig.7, the bold lines showed failure stresses. Hoop stress was under failure stresses, and it was satisfied with hoop stress criterion (a).

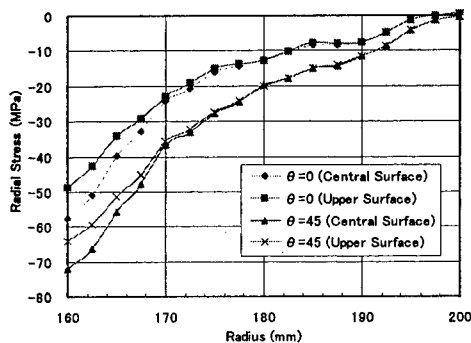


Figure 6 Radial stress distribution of the rim at 1350m/s

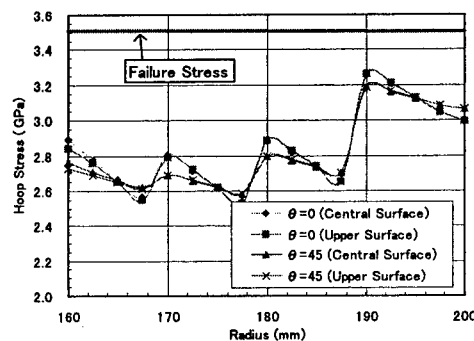


Figure 7 Hoop stress distribution of the rim at 1350m/s

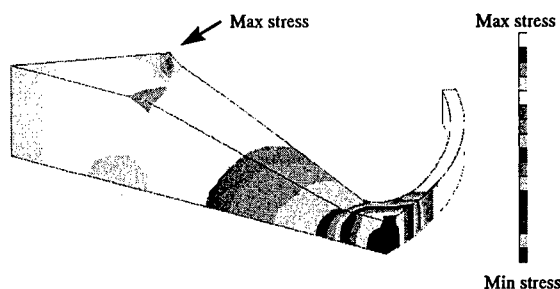


Figure 8 The von-Mises stress distribution in the hub



The stress distribution in the hub was shown in Fig.8. To reduce the stress by centrifugal force, the cross section area of the spoke decreased according to the outside of the spoke. Therefore, von-Mises stress distribution in the spoke was almost uniform. The Maximum stress in the hub occurred in the root of the spoke (indicated in Fig.8). The relation between maximum stress and peripheral speed was shown in Fig.9. The stress rose in proportion to peripheral speed. At about peripheral speed of 1100m/s, plastic deformation of aluminum alloy occurred. Beyond about 1300m/s, the stress rapidly rose, and the stress almost reached to the ultimate limitation at 1350m/s.

From the design work, it was resulted that the most critical stress of the rotor was maximum stress of the aluminum alloy hub.

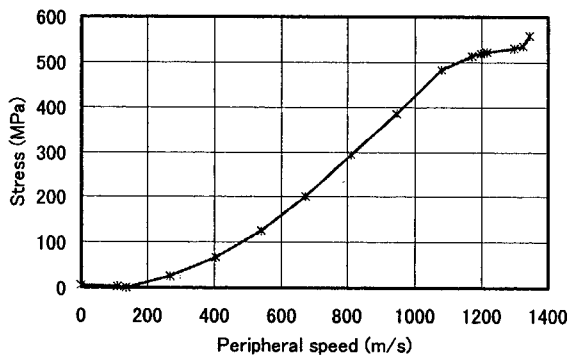


Figure 9 Peripheral speed dependence of the maximum stress in the hub

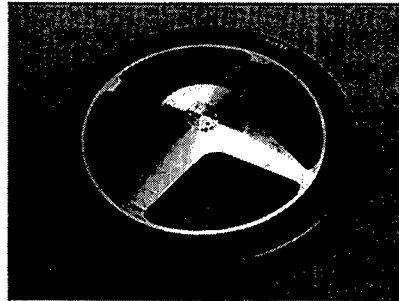


Figure 10 Composite flywheel

#### 4. Fabrication and Spin Test

Composite rings were fabricated by filament winding process using T1000G fiber and epoxy resin. After the winding, the outer diameter of each ring was machined and the multi-ring was assembled by press fitting. After the hub was soaked in liquid nitrogen, the hub was fitted into the rim. The flywheel rotor was shown in Fig.10.

The test of the flywheel rotor was performed using a spin-tester which drove rotors with an air turbine in a vacuum chamber.

##### (1) Machined rotor

The flywheel rotor, of which outer circumference of the rim was machined, was burst at peripheral speed of only 1220m/s. The rotor after the spin test was shown in Fig.11. There wasn't any damage in the hub, and outer part of the composite rim was broken. The result of the test was unexpected from the design, because the composite rim was designed without failure until peripheral speed of over 1300m/s. To observe the failure sequence, another machined rotor was cyclic tested at 1000m/s level.

After the first cycle, whose speed was 1080m/s, the fiber of which length was 50mm and width was 1.0mm was peeled at one spot on the surface of the outer circumference

of the rim. The windage loss by the rotation made the rotor warm.

The second cycle, whose speed was 1020m/s, was performed to check the temperature of the rotor during the rotation using a thermo-seal. The temperature of the rotor rose up to 45 °C, and other fiber peeling was occurred.

At third cycle, the rotation was stopped at 1000m/s because of a noise from the spin tester. After the rotation, the outer part of the rim, whose thickness was 2mm, was peeled (Fig.12). Another damage couldn't be found.

From these results, the initial damage of the rotor was the fiber peeling of outer circumference at low rotating speed of 1000-1100m/s. It was considered that the machining process shortened the carbon fibers at the outer circumference of the rim and decreased its strength.

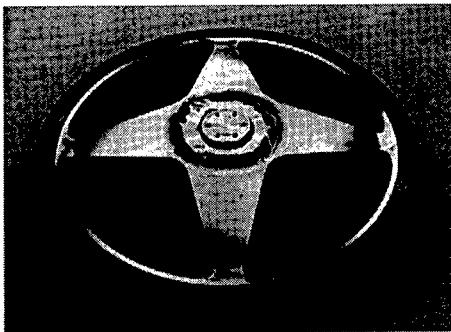


Figure 11 Burst flywheel rotor with machined outer diameter

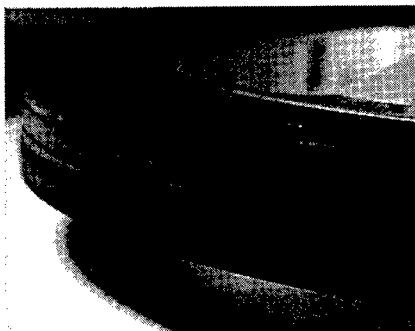


Figure 12 Peeled rim of machined outer diameter

## (2) Re-wound rotor

To prevent initial peeling damage, a new flywheel rotor, whose outer circumference of the rim was re-wounded with a few plies after machining, was fabricated and tested. The rotor burst at peripheral speed of 1310m/s. Fig.13 showed the result of spin test which was the relation between rotational speed and axial vibration. The axial vibration gradually increased from the peripheral speed of 1050m/s (rotational speed 5000rpm) to 1300m/s (6200rpm). When the speed was beyond 1300m/s (6200rpm), the axial vibration rapidly increased, and the rotor burst at the peripheral speed of 1310m/s. This phenomenon could be explained using aluminum alloy hub stress prediction as shown in Fig.9. The flywheel rotor might stably rotate until about 1100m/s. Beyond the speed, axial vibration rose, because plastic deformation of aluminum alloy caused unbalance of rotational axis. Beyond about 1300m/s, the hub burst because plastic deformation rose until ultimate strength of aluminum alloy. It was considered the vibration in the spin test indicated good agreement with the stress behavior in the analysis. The fragments of the broken hub were blocks. The fragments of the broken rim were in pieces.

The composite flywheel rotor stored energy of 354Wh, and the specific energy density of the ring was 195Wh/kg at maximum peripheral speed of 1310m/s.

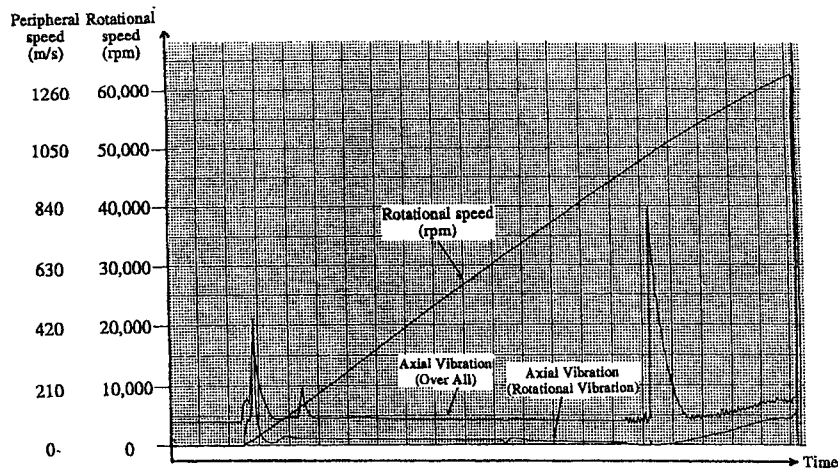


Figure13 Result of the spin test

## 6. Conclusion

Flywheel rotor was designed, fabricated and tested. The rim, which was multi-ring structure, consisted of 4 rings made of the high strength fiber (T1000G). The configuration of the hub made of aluminum alloy (7075) was like a steering wheel with 4 spokes. The cross section area of these spokes was changed to withstand a centrifugal force.

The rotor, whose outer circumference of the rim was machined, burst at 1220m/s. The rotor, whose outer circumference was re-wound, burst at peripheral speed of 1310m/s. The rotor stored energy of 354Wh, and the specific energy density of the ring was 195Wh/kg at 1310m/s. The vibration in the spin test indicated good agreement with the stress in the analysis.

## 7. Acknowledgments

This work was entrusted by New Energy and Industrial Technology Development Organization(NEDO). We appreciate the persons concerned.

## REFERENCES

1. A Hamamoto and T Inutake , 1982."Fabrication and Spin Tests of Composite Flywheel."ICCM-IV , TOKYO : 1759-1766
2. C.W.Gabrys and C.E.Bakis, 1997."Design and Testing of Composite Flywheel Rotors."J. of REINFORCED PLASTICS AND COMPOSITES, 16(6): 488-502
3. K.Takahashi and S.Kitade, 1998."Study of Composite Flywheel Rotors for Energy Storage Systems."ACCM-1, 1: 228-1-228-4

## **Development of H-2A Launch Vehicle Composite Interstage Structure**

M.Kobayashi, S.Sakai and R.Shimizu

### **Abstract**

The Interstage structure of H-2A launch vehicle was developed as CFRP and foam core sandwich structure by co-curing technique. In the design analysis, nonlinear buckling analysis for a sandwich panel cylinder was conducted considering the imperfection effect of actual cylinder shape. The manufacturing process of the co-cured composite cylinder was established in various manufacturing tests. The Interstage structure was qualified by the full-scale strength test. The required cost and weight target was achieved.

### **Introduction**

The National Space Development Agency of Japan (NASDA) has been developing a new low-cost, high-performance launch vehicle named H-2A. The outline of H-2A is shown in Figure 1. The Interstage is a structure that connects the first stage and the second stage of this vehicle. The Interstage of H-2A is a cylindrical structure, 7m length and 4m diameter. The Interstage of the former H-2 launch vehicle was aluminum semi-monocoque structure. For H-2A we developed it as a CFRP and foam core co-cured sandwich structure to reduce cost and weight. Figure 2 shows the outline of H-2A Interstage. This report describes the Interstage development regarding designing, manufacturing and qualification testing.

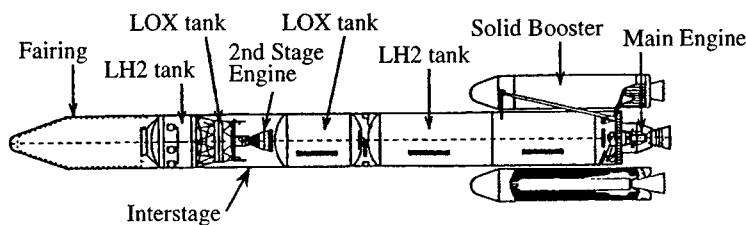


Figure 1 H-2A Launch Vehicle

M.Kobayashi and S.Sakai, Nagoya Aerospace Systems Works, Mitsubishi Heavy Industries, Ltd.  
10, Oye-cho, Minato-ku, Nagoya, 455-8515, Japan

R.Shimizu, Office of Space Transportation Systems, National Space Development Agency of Japan,  
World Trade Center Bldg. 2-4-1, Hamamatsucho, Minato-ku, Tokyo, 105-8060, Japan

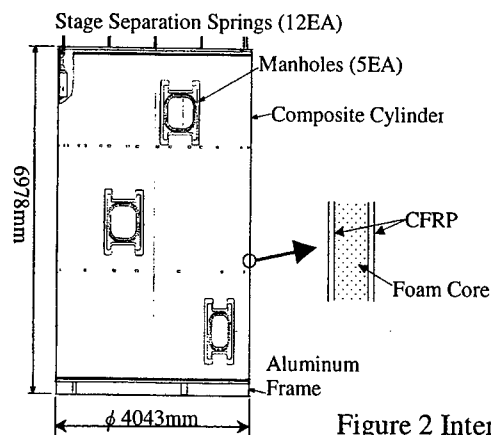


Figure 2 Interstage Structure Outline

## Design

The usual aluminum made semi-monocoque structure consists of many parts, so the processing time and assembling time are required so much. For H-2A Interstage, we designed it as a monocoque cylinder made of CFRP and foam core sandwich in order to reduce the number of parts to 1/10 of H-2. The 4m diameter, 7m length composite cylinder has no partition, and is co-cured from CFRP and foam core. CFRP is 350F cure type inexpensive Gr/Ep fabric prepreg. The foam core is made of polymethacrylimide and each cell of the foam is independent, so this core does not explode under the high temperature and vacuum environment in flight condition, and this is the great advantage over the honeycomb core.

Flight loads on the Interstage are mainly axial compression and bending moment, so compressive stress that is generated by the axial compression and the compression side of the bending moment is critical. The limit load of equivalent axial compression at dynamic pressure maximum is 4.38MN and the ultimate load is 1.25 times the limit load. The fracture modes of this structure are buckling of cylinder, wrinkling of CFRP face and partial destruction of manhole, etc.

## Buckling Analysis

The buckling strength of the sandwich monocoque cylinder was evaluated by non-linear FEM buckling analysis. The model elements of CFRP face are shells and those of foam core are solid elements. Figure 3 shows the buckling modal shape of the first mode. The first modal shape is axial symmetry and the half wavelength of buckling is about 240mm in general. Actual structures are not a perfect cylinder and this initial imperfection affects greatly to the buckling strength. We assumed that the imperfect shape is equal to the first modal shape shown above and conducted the buckling analysis with various imperfection magnitudes. Figure 4 is the analysis result that shows the relation of buckling strength and imperfection. As the result of

manufacturing tests, the actual imperfection value is under 8mm. Consequently it is found that the Interstage structure has the sufficient buckling strength.

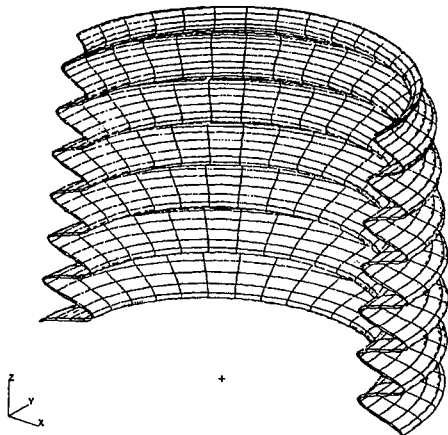


Figure 3 Modal Shape of Axial Buckling

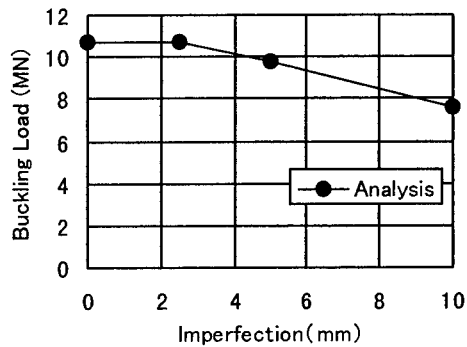


Figure 4 Imperfection Influence on Buckling Strength

## Manufacture

Figure 5 shows the cylindrical lay-up tool for CFRP prepreg and foam core. This tool has rotation equipment on the both ends of the cylinder and operators can lay-up prepreg and core on the all surface of the tool by rotating it.

The composite cylinder is co-cured under heat and pressure in the auto-clave. Under the normal cure pressure condition for this CFRP, we found thickness of the foam core decreases. So we had done some tests and obtained the pressure condition under which the foam core thickness does not change and CFRP properties do not go down.

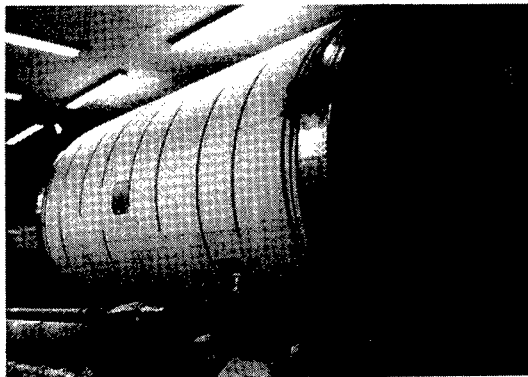


Figure 5 Cylindrical Lay-up Tool

For non-destructive inspection of the sandwich panel cylinder, ultrasonic inspection is applied. A probe, which is like a rubber tire, inputs ultrasound from outside surface of the Interstage and another probe senses it at inside surface. We conducted compressive strength tests with sandwich articles with an artificial defect and obtained defect size influence to strength decrease and decided allowable defect size. Figure 6 shows sandwich panel compressive strength change by the size of square delamination as an example of tests results. We confirmed that the ultrasonic inspection equipment could certainly sense the minimum allowable defect.

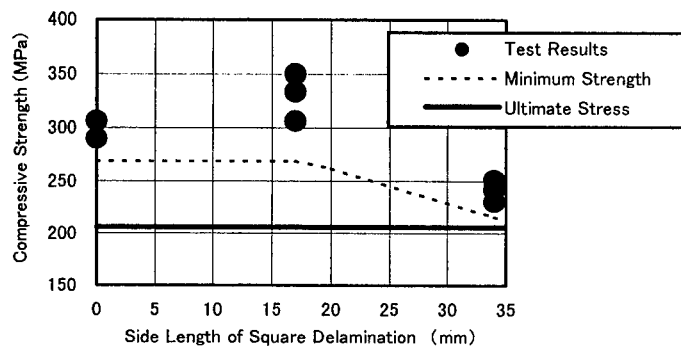


Figure 6 Compressive Strength of Sandwich Panel with a Delamination

In order to evaluate these manufacturing process, a short size (2.1m) cylinder and a full size (7m) article manufacturing tests were done, and finally the whole cylinder co-cure process was established.

Figure 7 shows the completed Interstage assembly.

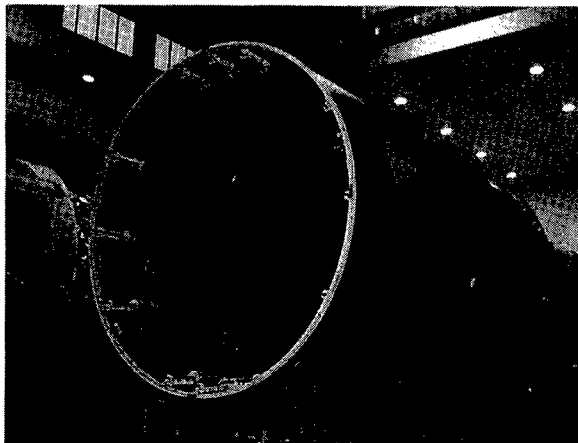


Figure 7 Completed Interstage

## Tests

In the development of the Interstage, many tests were conducted as material data tests for design, partial structure strength tests, manufacturing tests, allowable defect tests, acoustic test, static strength tests (qualification tests) and repair test.

In the static strength tests, flight loads were loaded on a full size test article. Totally 7 cases tests(3 Limit, 3 Ultimate and 1 Over load) were performed, and the test article bore with all loads. The maximum load of equivalent axial compression was 6.72MN.

Lower end of the Interstage connects directly with aluminum alloy liquid oxygen tank, and the tank radius shrinks about 9mm by the cryogenic temperature and tank pressure effect, and so the lower end of the Interstage deforms. In the static strength tests we simulated this situation by using liquid nitrogen and tank simulator and we confirmed the effect of the cryogenic deformation on the composite structure. Figure 8 shows the test setup.

Figure 9 shows the axial strain data of inner and outer CFRP sandwich faces at the critical load phase as a typical test result. Test results shows a good matching with predicted design analysis and adequacy of the analysis is confirmed.

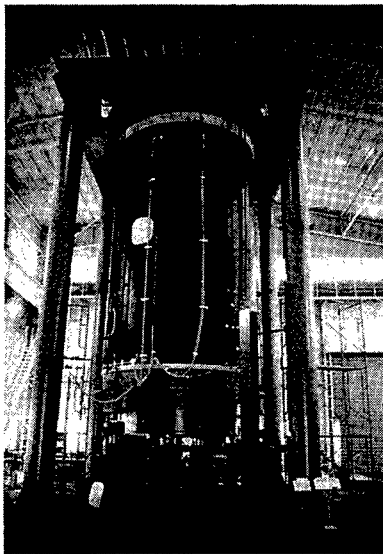


Figure 8 Static Strength Tests Setup

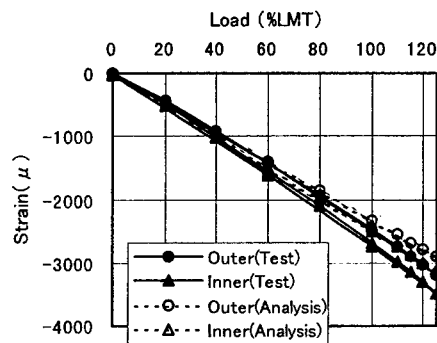


Figure 9 Axial Strain of CFRP Cylinder Lower End

## Conclusion

In the development of the Interstage, it was achieved to establish the manufacturing process of large composite cylinder by co-curing in a short period. Figure 10 shows the comparison of cost item value between this composite Interstage



and an aluminum structure. About 30% cost reduction is achieved. The weight of the Interstage is 820kg except for stage separation spring actuators. This is 20% less than an aluminum structure.

And various useful technical data about sandwich structure of CFRP face and foam core are obtained.

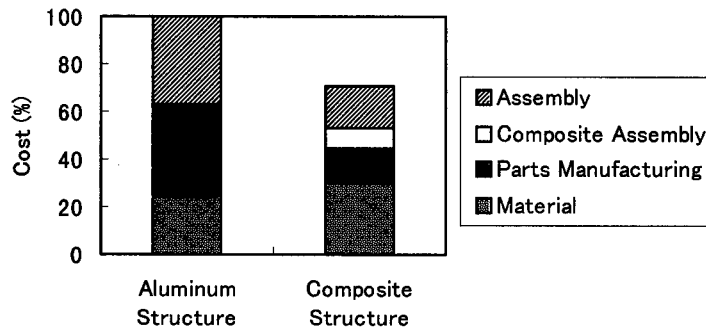


Figure 10 Cost Comparison of Interstage Structure

## **Postbuckled Behavior of Composite Isogrid Stiffened Shell Structure**

Thomas D. Kim\*

### **Abstract**

This paper investigated reliability of a postbuckled composite isogrid stiffened shell structure under the compression load. The outside diameter of isogrid cylinder was 624.8 mm and the length was 368.3 mm and the total weight of the cylinder was measured to be 3.24 kg. A finite element buckling analysis result was compared with the axial compression experimental data. The average critical buckling load of 186.56 kN was obtained by using the Patran finite element analysis (FEA). The isogrid shell was modeled using 3-node triangular elements and the stiffeners were modeled using 4-node quad elements with total of 504 nodes and 900 elements. The postbuckled isogrid cylinder was compression tested to the failure load of 177.35 kN. The postbuckled cylinder continued to resist compression loading even after one or more stiffeners had fractured. The testing evaluation revealed that the stiffener buckling was the critical failure mode and it has been demonstrated to be tolerant to structural damage due to the multiplicity of load paths. The obtained experimental buckling load was low due to the small imperfections in the cylinder but this problem can be overcome by advancement in the manufacturing methods.

### **Introduction**

The development of lightweight and highly efficient structural component is desirable for next generation of aerospace systems [1]. The use of composite materials for space application is particularly attractive because space structures are stiffness driven and requires stringent weight limits. The combination of composite materials and isogrid stiffened design is particularly well suited for critical structures that require buckling resistance and damage tolerances [2]. When the structure is stiffened, it typically means that a ring or oddly shaped pieces of metal are added to the backside of a plate or shell as shown in Figure 1. This stiffening concept increases the buckling resistance and thus the critical loads can be delayed with only a little addition of material. The high performance launch vehicle structures such as interstage and fairings utilize metallic

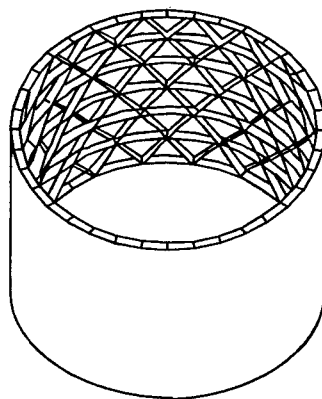


Figure 1 Isogrid Cylinder

\* Asian Office of Aerospace Research & Development  
7-23-17 Roppongi, Minato-ku, Tokyo 106-0032

isogrid designs to transmit and sustain the applied loads. These current stiffened structures are machined from a single solid piece of metal to form the thin skin with stiffeners. This manufacturing process is costly and time consuming requiring more than one year to fabricate a single large cylindrical stiffened structure. The introduction of composite isogrid structure into industry thus has been hampered by lack of understanding isogrid failure behaviors and manufacturing methods. This paper examined the postbuckling characteristics of a composite isogrid under the compressive load. Knowledge of stability behavior is essential for reliable lightweight aerospace structure, which will allow designers to add additional capabilities while reducing life cycle costs.

### Fabrication Method

The isogrid cylinder was fabricated from a carbon fiber reinforced epoxy in form of prepreg tow and unidirectional tape. The Hercules IM7 fiber and the toughened epoxy (977-2) resin system from Fiberite were used. The properties of IM7/977-2 are shown in Figure 2. The manufacturing of isogrid structures has proven to be complex due to buildups at the stiffener node intersections where the fibers cross over [3]. At each intersection, three times the amount of fiber will cross over, making out-of-plane compaction difficult. Excessive buildup, if not designed and fabricated properly, will cause higher loads to be concentrated at the intersections (nodes). These non-uniformly distributed loads at the nodal points can cause a premature failure of the structure. One way to reduce the buildup is by offsetting the fibers at the nodal intersections. This offsetting allows each ply to overlap each other by reducing from three plies to two plies [4].

Cylinder Outside Radius, (mm)	312.42
Cylinder Length, (mm)	368.30
0° Tensile Strength, (GPa)	2.82
0° Tensile Modulus, (GPa)	173
90° Tensile Strength, (MPa)	75.1
90° Tensile Modulus, (GPa)	7.60
0° Compression Modulus, (GPa)	157
Shear Modulus, (GPa)	5.50
0° Flexural Strength, (GPa)	1.64

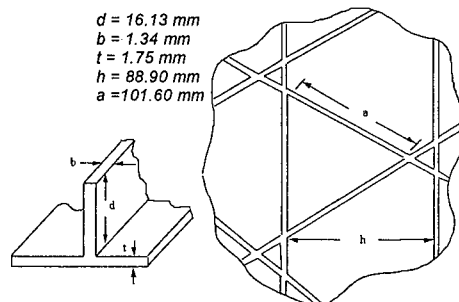


Figure 2 Isogrid Dimensions

Winding prepreg tow into isogrid shaped grooves (slots) formed the stiffeners in the rubber mold as shown in Figure 3. The use of rubber tooling is critical because the rubber is the primarily responsible for lateral compaction of the stiffeners. Between 40 to 50 layups are needed to fill the 1.45 cm deep slots by stacking each tow fiber on top of each other until it was filled to the top. Then the skin was filament wound and it consisted of 12 plies of  $[+90, 0, 90, 0]_s$  orientations. The entire part was bagged and co-cured in an autoclave. This procedure results in

excellent stiffener consolidation and skin finish. After curing, the rubber mold is removed leaving a cylindrical composite isogrid as shown in Figure 3. All curing was done in an autoclave for two hours at 177°C and a pressure of 0.552 MPa.

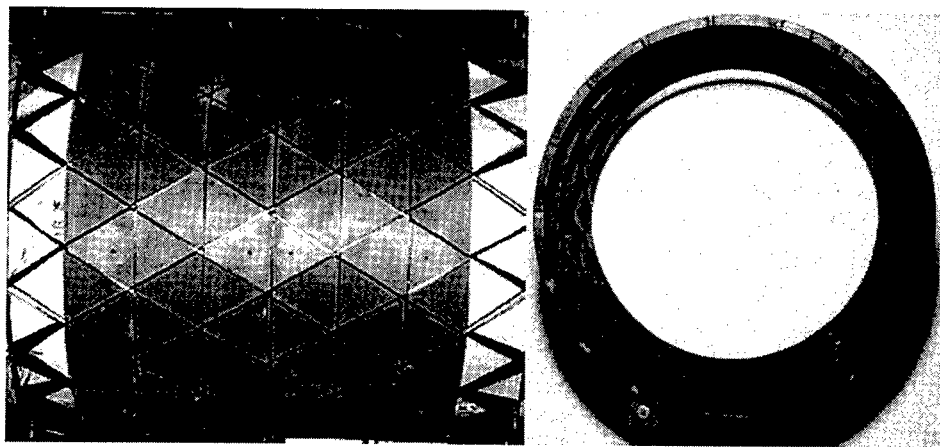


Figure 3 Isogrid Cylinder Fabrication

### Finite Element Analysis

The objective of the finite element analysis was to visualize the behavior of the isogrid cylinder under the compressive load and determine the maximum buckling strength. Five different linear finite element buckling analyses were performed using the parameters listed in Figure 2. The cylinder model was analyzed using Patran pre and post processors. The geometry of isogrid cylinder was generated by measuring various dimensions on the test specimen and averaging the results. The Patran model of the isogrid cylinder consists of 504 nodes and 900 elements. The isogrid skin was modeled using the 3-node triangular elements and the stiffeners were modeled using the 4-node quadrilateral elements. The boundary conditions were modeled as simply supported at both ends to simulate the actual test conditions. The deformed shapes of the isogrid cylinder under the axial compression load are shown in Figures 4. The dark regions represent the stress concentrations around the cylinder where failure might occur. The effect of the stiffener/skin interface was difficult to

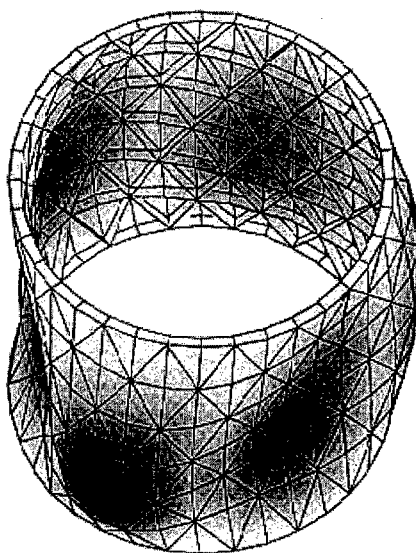


Figure 4 Buckled Shape of Cylinder

determine from this analysis. The FEA results are summarized in Table I. The maximum load ranged from 189.5 kN to 182.4 kN with maximum displacement of 12.73 mm. The results indicate that for isogrid cylinder, the skin thickness parameter had more influence in obtaining higher buckling load. However, the increase in skin thickness will increase weight, which will make the structure less efficient. It was expected to obtain lower buckling load from the experiment due to the fact that the cylinder was slightly damaged from the previous test and also the FEA did not consider minor manufacturing imperfections in the isogrid cylinder.

Table I Finite Element Analysis Results

Patran FEA Model #	Stiffener Thick (mm)	Stiffener Height (mm)	Skin Thick (mm)	Max Load (kN)	Max Disp. (mm)
1	1.36	15.77	1.78	189.50	12.24
2	1.31	16.20	1.74	182.38	12.78
3	1.37	16.07	1.76	189.49	12.14
4	1.33	15.70	1.72	184.60	12.61
5	1.34	16.16	1.76	186.83	12.73

### Axial Compression Test

Shell stiffened structures are susceptible to failure by buckling and extensive research has been reported in the open literature [5,6]. The objective of the compression test on the cylindrical composite isogrid structure was to examine the pre and post buckling characteristics and to determine the maximum load before the failure [7]. The outside diameter of isogrid cylinder was 624.8 mm and the length was 368.3 mm and the total weight of the cylinder was measured to be 3.24 kg. The top and bottom of the cylinder was potted with fiberglass and machined flat in order to evenly transmit the applied loads. The test fixture as shown in Figure 5 was fabricated with a precision ground 3.81 cm thick stainless steel top and base plates in which the cylinder was placed between the plates. The corners of the bottom plate had support pins that secured the cylinder during the compression test. The isogrid cylinder was loaded in compression at a rate of 0.50 mm/min. The displacement controlled MTS load was continuously applied until the cylinder experienced skin buckling and failure of stiffeners near top and bottom edge of the cylinder

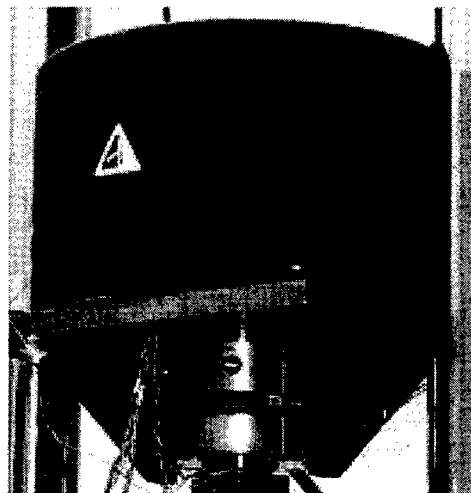


Figure 5 Compression Test Setup

occurred. The test specimen was instrumented with twenty-two strain gauges type CEA-06-125UW-350 supplied by Micro-Measurements as shown in Figure 6. Among the strain gauges, four were uni-directional back-to-back gauges used to measure the axial and bending strains on the stiffener and skin. For the postbuckling test, twenty-two of the previous strain gauges were used. However, some of the strain gauges were damaged from the previous test run and an accurate strain data reading was not expected. Data from all strain gauges and the 80 kip bi-axial MTS test machine was recorded using BAF-8 signal conditioner bridge and Macintosh computer. Labview and Excel software were used to obtain and plot the results.

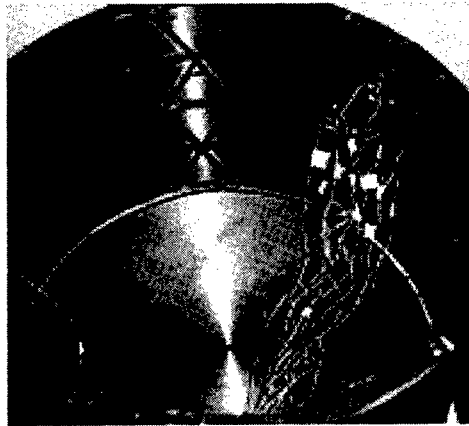


Figure 6 Strain Gauges Location

### Experimental Results

The load versus strain results from the original (test #1) and the post-buckling test were plotted in Figures 8 and 9. In test #1, the compression data showed that at around 40.0 kN, there was a sudden drop of a compressive load. This drop corresponded with the strain gauge values of both stiffeners and skin, which were deviating from each other. This nonlinear curve indicates the incipient buckling occurring on the structure. For example, the skin strain gauges #1, 3, and 9 located on the middle of the triangular pocket area had about 10% strain difference when compared to each other. Similarly, the stiffener strain gauge #5 and #6 also began to deviate from a straight line. As the axial load reached 60.0 kN, the cylinder began to make low pinging noises caused by the polymeric matrix microcracking. The soft pinging noise was followed by a high audible cracking sound at 75 kN and another loud popping sound was heard at 106.75 kN. The test was stopped when the compression load reached 117.9 kN due to significant audible popping noises. The maximum displacement of 7.21 mm was obtained. Visual inspection of the stiffeners revealed two helical stiffeners were indeed separated from the skin located near top and bottom of the cylinder. Only one helical stiffener located near the bottom of the cylinder had a serious fracture damage. A high bending stress most likely caused this damage. However, there were no noticeable damages from the hoop stiffeners. The highest compressive strain value of 4.8% was recorded by the strain gauge #22 and the highest tensile strain value of 1.3% was recorded by strain gauge #7. The testing revealed that both stiffener and skin experience relatively large axial displacement rather than bending displacement.

The test #1 had verified that isogrid stiffeners provided most of the bending stiffness. Therefore, any damage to the stiffeners should result in the reduced buckling resistance of the cylinder. As expected during the postbuckling test, the cylinder exhibited similar buckling behavior as the previous cylinder test up to 82

kN. The helical stiffeners remained in compression and the hoop stiffeners and skin were under tension. At 63 kN, there was a sudden drop in strain followed by a distinctive loud cracking noise at 75 kN and 98 kN respectively. As the load was continuously applied, another sharp drop in strain (load relief) was encountered at 115 kN (On the test #1, the testing was halted at 117 kN). The strain readings fluctuated throughout the test; eventually, the testing was stopped at 177.4 kN. Post visual examination of the cylinder revealed that the upper and lower part of the cylinder (first column) showed extensive damage. As the stiffeners were no longer able to carry the load in this region, the damage intensified. The stiffeners relieved the load by transmitting it to the next set of stiffeners located in the second column before their failure. The maximum displacement of 13.75 mm was obtained as shown in Figure 10.

Strain gauges located near the center of the cylinder had lower strain values when compared to that of strain gauges located near the top and bottom of the cylinder. The hoop stiffener resists the tendency for the helical stiffeners to bow in or out and holds the helical stiffeners stationary. This continues until one of the helical stiffeners can no longer resist high bending moment and fractures. This suggests that the load is being carried by the stiffeners and is transferred to the skin. The skin, being relatively thin does not keep the stiffeners from local buckling. Adding additional skin layer in circumferential direction will increase the axial stiffness, which will restrict the axial displacement in the skin. However, adding additional skin will increase the weight of the structure, which will make the structure less efficient. A better method to increase the axial stiffness without increasing significant weight is by adding an extra hoop stiffener at the buckling node points. This extra hoop stiffener will shorten the column length that will delay the general instability and the concentrated load will be more easily distributed into the structure. The helical stiffeners can increase their column buckling stress by utilizing the shorter end restraints provided by the hoop stiffeners. The inspection of postbuckled cylinder revealed that four helical stiffeners had an actual fracture and another four had separated from the skin near the top and bottom of the cylinder. However, two of the four stiffeners were damaged from a previous test and all of the stiffeners located near the center of the cylinder still did not show any sign of damage as shown in Figure 7. The degradation of buckling resistance was low until a certain progressive damage level was reached. Even if one or more stiffeners were separated from the skin, the damaged stiffener was able to redistribute the load path to carry additional loads.

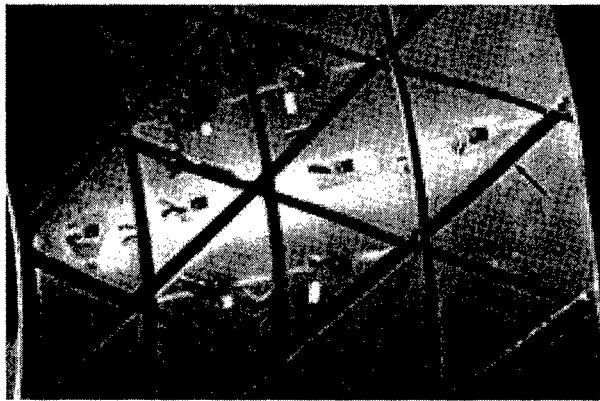


Figure 7 Location of Damaged Stiffener

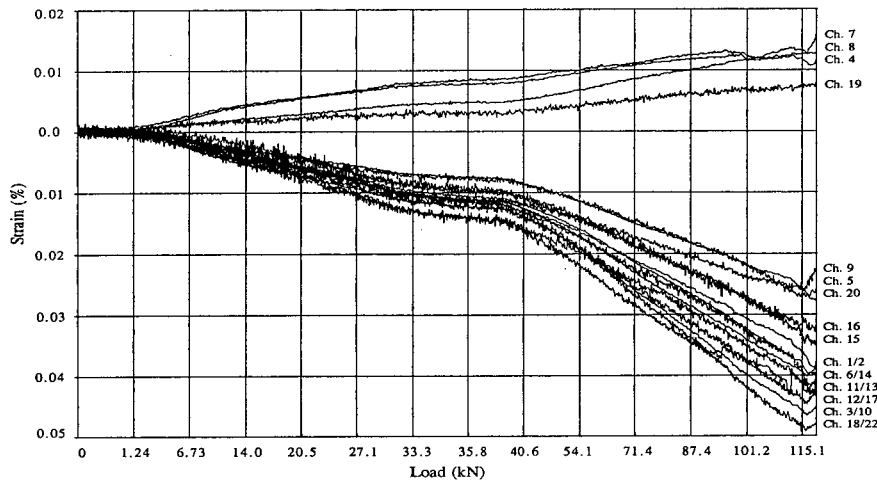


Figure 8 Load vs. Strain Results of Test #1

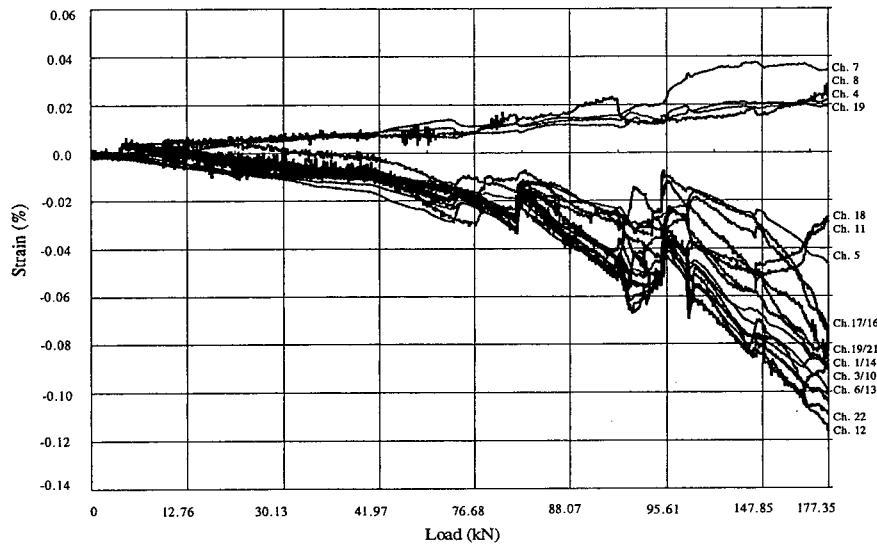


Figure 9 Load vs. Strain from Post-Buckling Test

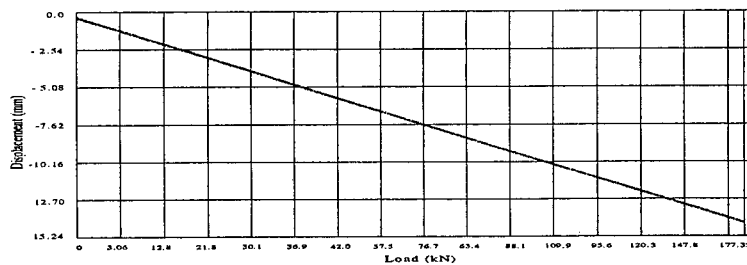


Figure 10 Load vs. Displacement from Post-Buckling Test



## Conclusion

An axial compression test of a postbuckled composite isogrid structure exhibited damage tolerance and buckle resistant characteristics due to multiplicity of loading paths. The postbuckling test of the damaged cylinder exhibited similar buckling behavior as the undamaged cylinder up to 82 kN. The degradation of buckling resistance was gradual until a certain progressive damage level was reached. The compression test verified that the stiffeners are buckling critical and provided most of the bending stiffness. The stiffeners could not resist the excessive bending force and lead to the eventual failure. Even when one or more stiffeners were separated from the skin, the damaged stiffener was able to redistribute the load path to carry additional loads. The skin resisted radial displacements and increased the axial stiffness of the cylinder. Although the skin acted with stiffeners in resisting the initial bending and axial load, cylinder's thin skin eventually could not support the stiffeners from local buckling. The postbuckled cylinder continued to resist compression loading after one or more of the stiffeners had fractured. Continued loading caused the number of fractured stiffeners to increase but the cylinder was able to maintain its basic cylindrical shape. These factors make composite isogrid cylinder attractive for use in lightweight critical structural applications.

## References

1. A. Reddy, R. Valisetty, L. Rehfield, Continuous Filament Wound Concepts for Aircraft Fuselage Structures, *J. Aircraft*, 22, (1985), 249-255.
2. L. Rehfield, A. Reddy, Damage Tolerance of Continuous Filament Composite Isogrid Structure: A Preliminary Assessment, *Composite Materials: Mechanics, Mechanical Properties and Fabrication*, Japan-US Conference, Tokyo, (1981), 471-477
3. T. Kim, C. Rotz, Warping of Flat Composite Isogrid Panels, *1997 IEEE Aerospace Conference*, Aspen, (1997), 271-277.
4. T. Kim, Investigation of Composite Isogrid Stiffened Structures, *Phillips Laboratory Technical Report 95-1112*, (1995), 11-21.
5. P. Seide, A Donnell-Type Theory for Asymmetrical Bending and Buckling of Thin Conical Shells, *J. Applied Mechanics*, 24 (1957), 547-552.
6. L. Li, The Stability of Composite Material Stiffened Conical Shell Under Axial Compression, *Composite Structure*, 38 (1997), 169-175.
7. T. Kim, Fabrication and Testing of Composite Isogrid Stiffened Cylinder, *Composite Structure*, 45 (1999), 1-6.

## **Effect of Transverse Crack on Strength Degradation in Filament Wound Composites**

A. Horide, A. Tanaka, S. Wakayama, Y. Shigenari, K. Miyagawa  
and S. Suzuki

### **Abstract**

The strength tests of FRP rings with defects, i.e. transverse cracks, were carried out by using the ring burst test which developed by the authors. Ring specimens were fabricated by a filament winding (FW) machine. In this study, in order to imitate the defects of matrix crack in hoop layers of CFRP pressure vessel grown in service, the artificial transverse crack was introduced into the CFRP by applying axial load to the CFRP/Aluminum tube. The fracture behavior during the tests of FRP ring specimen with or without transverse crack was characterized by a digital video camera, a high magnification video scope and AE analysis. The burst pressure of specimen without transverse crack were higher than that of the specimens with transverse crack. Comparing both specimens, the cumulative AE energy increased in earlier stage and the total energy is larger in the specimen with transverse crack. Consequently, it was suggested that the artificial transverse crack had significant effects on the fracture behavior and decrease in strength of FW-FRP ring specimen, i.e. hoop ply of pressure vessel, due to the pre-existing microcrack along the fiber direction.

### **Introduction**

FW-FRP pressure vessels have been developed and utilized in the rocket motor case of solid propellant rocket [1] and the fuel gas containers of compressed natural gas (CNG) vehicles [2] because of the high specific strength. However, it was reported that transverse cracks in hoop layers were initiated and propagated at low pressure levels in FW-CFRP pressure vessels, which were designed under small safety factor as the rocket motor case. The burst pressure of FW-CFRP pressure vessel was then decreased due to those flaws. In this study, the term of

---

A. Horide, A. Tanaka, Graduate School, Tokyo Metropolitan University, 1-1 Minami-Ohsawa, Hachioji-shi, Tokyo 192-0397, Japan

S. Wakayama, Department of Mechanical Engineering, Tokyo Metropolitan University, 1-1 Minami-Ohsawa, Hachioji-shi, Tokyo 192-0397, Japan

Y. Shigenari, K. Miyagawa and S. Suzuki, Nissan Motor Co., Ltd. Aerospace Division, 900 Fujiki, Tomioka-shi, Gunma 370-2398, Japan

*transverse crack* indicate the grown defect of matrix crack parallel to fibers due to the transverse stress as mentioned above.

Transverse cracking under tensile loading in composite materials have been studied mostly for cross ply laminates [3], [4]. However, in cross ply laminates, the transverse crack surface and stress direction cross each other at the right angle under the uniaxial stress state. On the contrary, in the case of pressure vessel, transverse crack and hoop stress direction are parallel under the biaxial stress state. Furthermore, the principal reasons of decrease in strength of FW-CFRP pressure vessel have not been found clearly, since the cross sectional observations during the real burst tests of pressure vessel are difficult.

In this study, the artificial transverse cracks were introduced into the FW-CFRP composites. The ring burst test [5], which were developed by the authors, were carried out. Moreover, in order to investigate the fracture behavior during the ring burst test, fracture phenomenon were observed by using a high magnification video system and a digital video camera. Consequently, the effects of transverse crack on strength and fracture behavior of FW-CFRP composites were investigated.

## Experimental Procedure

### Preparation of Ring Specimens with Transverse Cracks

The ring specimens were prepared from carbon fiber prepreg (laminates tensile strength: 2990 MPa, failure strain: 1.7 %). Eight plies of carbon fiber prepreg were wound on an Aluminum tube (outer diameter: 100 mm, thickness: 3 mm) using a filament winding machine. The winding angle between fiber and hoop direction was close to  $0.27^\circ$  as a actual CFRP pressure vessel. The artificial

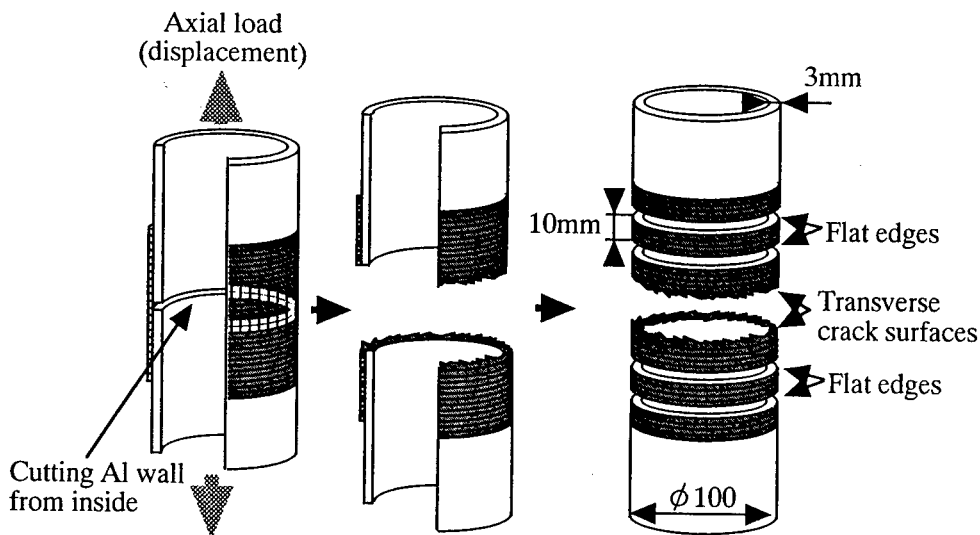


Figure 1 Introducing Method of Transverse Crack in CFRP

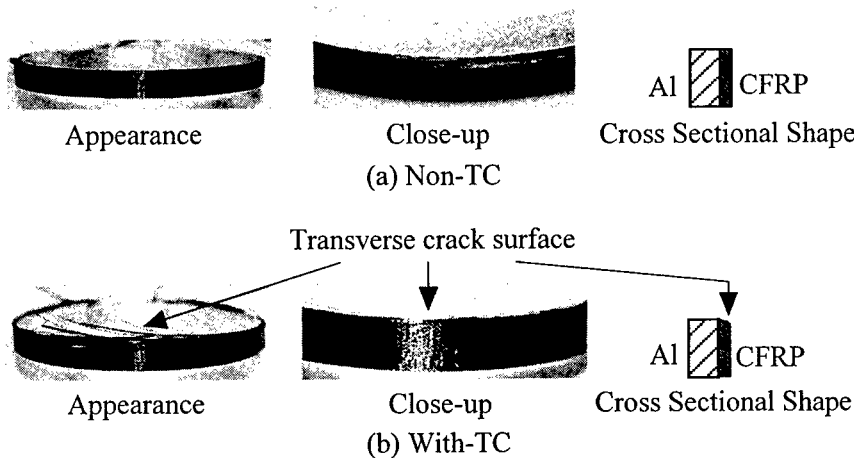


Figure 2 Appearance and Cross Sectional Shape of Specimens

transverse crack was introduced into the CFRP ring specimens as shown in Figure 1. After curing in an autoclave, a part of Aluminum tube was cut from the inside surface, and then artificial transverse cracks (TC) were introduced into the CFRP by applying axial load to the CFRP/Aluminum tube. Finally, the tube was cut into 10 mm width ring specimens with or without transverse crack.

Appearance and cross sectional shape of specimens are shown in Figure 2. Non-TC specimen has both flat edges of ring specimen. With-TC specimen has a transverse crack surface and a flat surface. The flat edges of all specimens were polished by emery paper. Observing a initial flaw on a transverse crack surface by a scanning electron microscope, it was understood that the outer surface of With-TC specimen has relatively many pre-existing microcracks along the fiber direction, but that the edge of Non-TC has few initial micro flow on polished edge.

#### Ring Burst Test and Observation of Fracture Behavior

Ring burst tests [5] were carried out for the evaluation of the strength and the fracture behavior. The system of ring burst test and observation of fracture behavior are shown in Figure 3, schematically. The external appearance of fracture behavior in CFRP ring was observed using a digital video camera. The AE measurement was also carried out in order to detect the microfractures such as the interfacial fractures between fiber and matrix, matrix cracking etc. The total gain was 60 dB (20 dB at the main amplifier and 40 dB at the pre-amplifier), and the threshold level was 45 dB (i.e. 177 $\mu$ V at the input terminal of the pre-amplifier). The AE sensors with a resonant frequency of 500 kHz were attached on the specimen surface, and the distance between the sensors was 60 mm. The AE signals, load and strain data were measured by an AE analyzer. Then the data were sent to a personal computer and analyzed in detail.

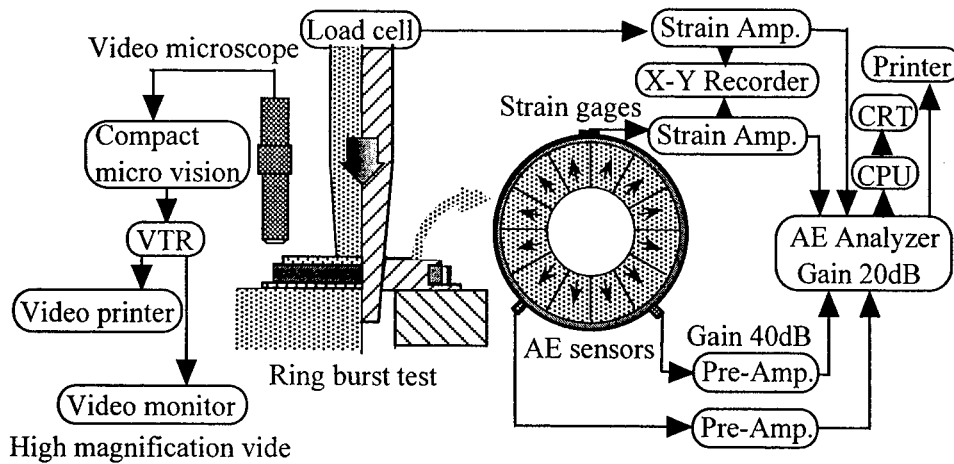


Figure 3 Schematic drawing of Equipments of Ring Burst Test and Observation of Fracture Behavior

## Results and Discussions

### Strength of CFRP with or without Transverse Crack

Experimental strength obtained from ring burst test are tabulated in Table I. In order to compare with the experimental results under combined stress state ( $\sigma_1$ ,  $\sigma_2$  and  $\tau_{12}$  are longitudinal, transverse tensile and shear stress applied to specimen, respectively), the quadratic failure theory in conjunction with laminated plate theory is employed to predict the ultimate failure without defect. The quadratic failure criteria, i.e. Tsai-Hill criteria [6], is used to predict the failure for CFRP laminates,

$$\left(\frac{\sigma_1}{X_1}\right)^2 + \left(\frac{\sigma_2}{X_2}\right)^2 + \left(\frac{\tau_{12}}{X_6}\right)^2 = 1 \quad (1)$$

where  $X_1$ ,  $X_2$  and  $X_6$  are longitudinal, transverse tensile and shear strength, respectively.  $\sigma_1$ ,  $\sigma_2$  and  $\tau_{12}$  are expressed by using hoop stress ( $\sigma_H$ ) and winding angle ( $\phi$ ) as followings,

$$\sigma_1 = \sigma_H \cos^2 \phi \quad (2)$$

$$\sigma_2 = \sigma_H \sin^2 \phi \quad (3)$$

$$\tau_{12} = \sigma_H \sin \phi \cos \phi \quad (4)$$

Then, the predicted hoop strength can be obtained as

Table I Results of Burst Hoop Strain, Pressure and Stress in Ring Burst Test

Winding angle [°]	Edge condition	Burst strain [%]	Burst pressure of CFRP [MPa]	Burst stress of CFRP [MPa]	Tsai-Hill criteria [MPa]
0.27	Non-TC	1.6	54.7	2760	2950
	With-TC	1.4	43.3	2190	-

$$\sigma_H = \left\{ \frac{\cos^4 \phi}{X_1^2} + \left( \frac{1}{X_6^2} - \frac{1}{X_1^2} \right) \sin^2 \phi \cos^2 \phi + \frac{\sin^4 \phi}{X_2^2} \right\}^{-\frac{1}{2}} \quad (5)$$

The material properties obtained from 0, 45 and 90 ° tensile test of unidirectional CFRP laminates were used in failure predictions, i.e.  $X_1$ : 2990 MPa,  $X_2$ : 51 MPa and  $X_6$ : 91 MPa. The predicted failure strength and the experimental results are also shown in Table 1. It was understood from the table that the burst pressure of Non-TC specimen were higher than With-TC specimen. Also the burst pressure are decreased from 80 to 90 % of Non-TC. Consequently, it was suggested that the pre-existing defects on transverse crack surface decreased the strength of hoop wound CFRP.

### Fracture Behavior

Typical hoop strain, pressure and cumulative AE energy - time curves of Non-TC and With-TC specimen are shown in Figure 4 (a) and (b), respectively. Photographs of fractured CFRP specimens for Non-TC and With-TC are also shown in Figure 5 (a) and (b), respectively. In addition, the fracture behavior obtained from a high magnification video system and a digital video camera are summarized as followings.

#### (1) Without Artificial Transverse Crack (Non-TC Specimen)

The macroscopic fracture was not observed until the final burst. It can be seen in Figure 5 (a) that the cumulative AE energy curve was increased at the early stage (50 s-75 s) of deformation of CFRP specimen. It can be considered that the increase in cumulative AE energy corresponds to initiation of contact between the CFRP and Aluminum ring. Furthermore, the cumulative AE energy curve was increased at the final stage of ring burst test (220 s- 290 s, >73 % of burst strain). Therefore, it is suggested that the increase in cumulative AE energy corresponded to the accumulations of microfractures such as matrix crack, interface delamination between the fiber and matrix etc. In Figure 6 (a), a number of fiber breakage were observed in each ply. Therefore, it is understood that the whole width of specimen without transverse crack was failed simultaneously since the hoop stress of almost fibers reached the failure strength and the fiber breakage occurred catastrophically.

#### (2) With Artificial Transverse Crack (With-TC Specimen)

The onset of crack propagation was observed at 185 s by the digital video

camera along the fiber direction from the tip of a torn fiber on transverse crack surface, i.e. initial defect. On the contrary, it is understood from Figure 4 (b) that the cumulative AE energy curve of With-TC was increased in earlier stage (47 % of burst strain) and the total cumulative AE energy was greater than the Non-TC. It was confirmed by the high magnification video camera that the increase in cumulative AE energy corresponds to the onset of crack propagation along the fiber direction. Figure 5 (b) also shows that the fracture path of ring specimen with transverse crack surface propagated spirally from the transverse crack surface. Consequently, it can be concluded that the cracks along the fiber direction propagate from the pre-existing defects before the hoop stress reached the tensile strength.

From the experimental results, it can be suggested that the artificial transverse crack surface had effects on the fracture behavior and the decrease in

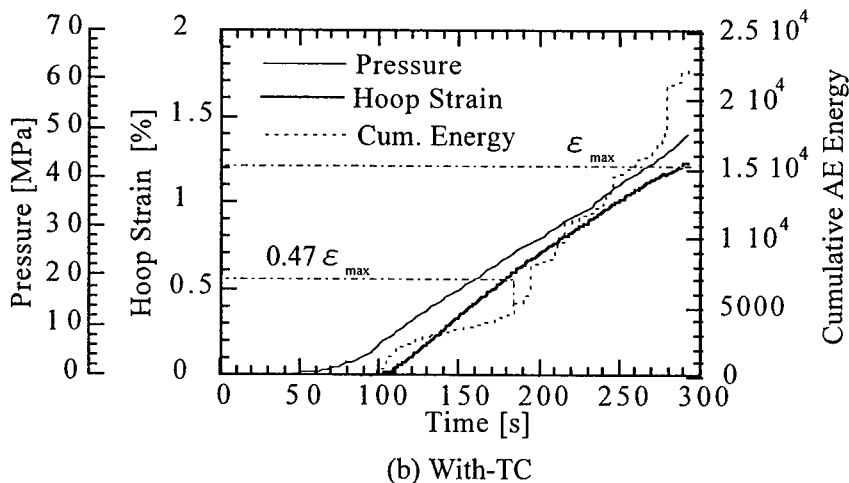
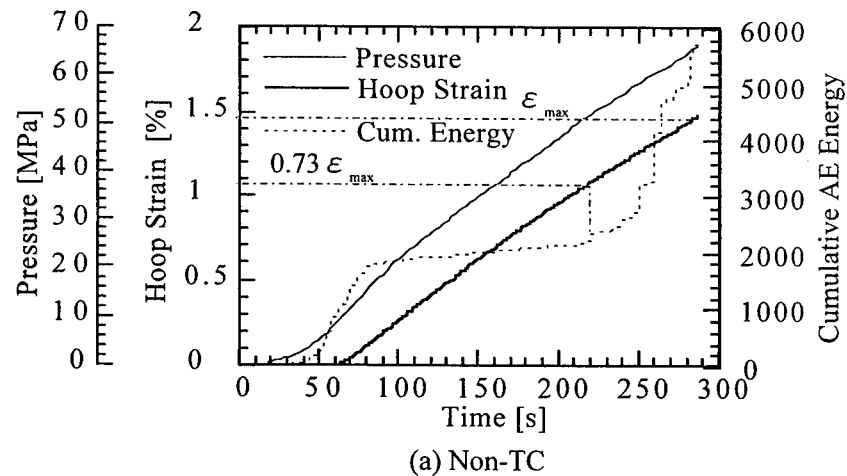


Figure 4 Hoop strain, Pressure and Cumulative AE Energy - Time Curves in FRP with or without Transverse crack

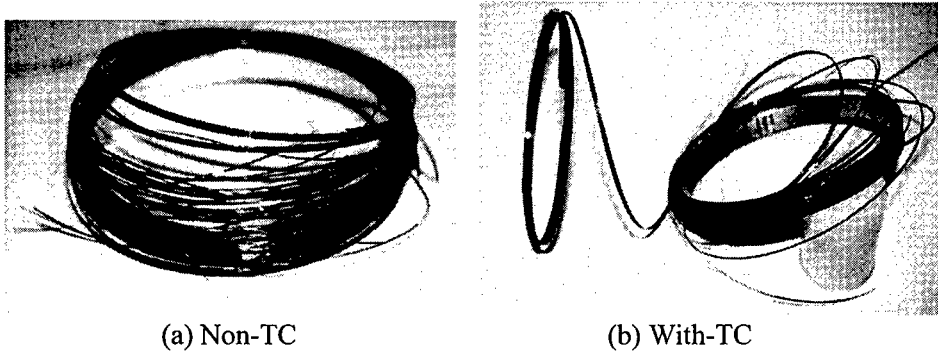


Figure 5 Photographs of Fractured CFRP Specimens

strength of FW-FRP ring specimen, i.e. hoop ply of pressure vessel, due to stress concentration at the pre-existing cracks along the fiber direction.

### Conclusions

In this study, the fracture behavior of FW-FRP composites with artificial transverse cracks was investigated by the combination of the AE measurement and the observation using a high magnification video system and digital video camera. Consequently, the following conclusions were obtained:

- (1) Non-TC specimens without transverse crack failed because the hoop stress of ring specimen reached the failure stress and the fiber breakage occurred.
- (2) The cracks along the fiber direction propagate from the pre-existing crack before the hoop stress of ring specimen reached the tensile strength.
- (3) The pre-existing defects, i.e. cracks along the fiber direction on the edge of ring specimen, had essential effects on fracture behavior and decrease in strength of FW-FRP composites due to the stress concentrations at tip of the defects.

### References

1. T. Narushima, 1997, *J. High Press. Inst. Jpn.* **35**, No. 1, 9-14
2. S. T. Peters and W. Donald Humphrey, 1987, in *Engineering Materials Handbook*, **1**, Composites, ASM International, USA, 503-518
3. S. Motogi, S. Yasuda and T. Fukuda, 1997, *Trans. Jpn. Soc. Mech.* **63**, 2318-2325
4. S. Kobayashi, N. Takeda, M. Oba, S. Ogihara and A. Kobayashi, 1999, *J. Jpn. Soc. Comps. Mater.* **25**, 179-187
5. A. Horide, S. Wakayama and M. Kawahara, 1999, *Trans. Jpn. Soc. Mech. En.* **65**, 635-642
6. S. W. Tsai, *Theory of composites design* 1992, Think composites, A division of ILT corporation, (8-1)-(8-24)



## Edge Effect on the Damage Development of CFRP

T. Yokozeki, Y. Hayashi, T. Ishikawa and T. Aoki

### Abstract

The damage process of transverse cracks in quasi-isotropic CFRP laminates under quasi-static loading are studied. It is necessary to investigate the damage process of transverse cracks in order to apply CFRP composites to cryogenic fuel tanks of Reusable Launch Vehicle (RLV). To investigate edge and specimen configuration effect on transverse cracks, coupon specimens with a range of specimen widths and transverse ply thicknesses are tested under tensile loads. Measurements of edge crack density and detailed observations of transverse crack propagation across the specimen width are made. The results suggest that transverse cracks seem to initiate from free-edges and specimen width has significant effect on transverse crack propagation.

### Introduction

Composite materials are commonly used in many structures. However, the damage process is very complicated. When CFRP coupon specimens are tested under tensile loads, different kinds of damage modes such as transverse cracks, delaminations and fiber fractures develop before the final failure. Transverse cracks are often the first observed damage mode. Although this damage mode is not critical from a final fracture point of view, it induces more severe damage. Moreover, transverse crack is a critical design factor for cryogenic composite fuel tank of Reusable Launch Vehicle (RLV). This is why it is important to investigate the damage process of transverse cracks.

Transverse cracking due to mechanical and thermal loads has been extensively studied, and crack initiation can be predicted very well. However, transverse crack propagation is related not only to the cracking stress state but also the distributive initial flaws, so the analytical models cannot predict the crack propagation very well. Therefore, probabilistic method has been employed. Xu[1] proposed a probabilistic analytical method, the "Characteristic Curve Method" (CCM),

---

T.Yokozeki, Department of Aeronautics and Astronautics, the University of Tokyo, Graduate School of Engineering, 7-3-1, Hongo, Bunkyo-ku, Tokyo 113-8656, Japan

Y.Hayashi, Tokyo Business Service Co.LTD, 6-14-1, Nishi-Shinjuku, Shinjuku-ku, Tokyo 160-0023, Japan

T.Ishikawa, National Aerospace Laboratory, 6-13-1, Ohsawa, Mitaka, Tokyo 181-0015, Japan

T.Aoki, Department of Aeronautics and Astronautics, the University of Tokyo, 7-3-1, Hongo, Bunkyo-ku, Tokyo 113-8656, Japan

to correlate initial flaws and transverse crack densities. The concepts of the "equivalent applied loading" and the "equivalent crack density" are introduced to reveal the physical essence of the damage process. He showed that the characteristic curves for laminates of the same material under the same cure process are approximately same. Specimen configuration has significant effect on transverse crack initiation and propagation. Boniface et al.[2] conducted tensile tests of cross-ply coupon laminates with a range of transverse ply thicknesses. In laminates with thick plies, all cracks span the full thickness and width of the transverse plies whereas for laminates with thin plies, part-width cracks exist over appreciable strain range. Pagano et al.[3] also showed the same trend.

In recent toughened CFRP laminates, transverse cracks are less susceptible to initiate or propagate. In this study, quasi-isotropic coupon specimens of toughened CFRP are tested under quasi-static tensile loads in order to investigate edge and width effect on transverse crack initiation. The widths of coupons are 15mm, 30mm and 50mm. The process of crack growth is studied by observing edge cracks with an optical microscope and grown cracks by X-ray radiography. And a parallel study is carried out using coupons with thin transverse plies to investigate thickness effect on crack initiation and propagation.

## Experiment

The material systems used in this study are IM600/Q133, intermediate modulus carbon fiber and toughened epoxy systems. The specimen configurations are summarized in Table I. Edges of coupon specimens are polished by diamond hand stones. Specimens are checked for defects that may be introduced during cure process by an optical microscope before testing. All tensile tests are carried out using an Instron 8501(hydraulic driven) machine at slow cross head speed(approximately 0.2mm/min) at room temperature. Coupon specimens are instrumented with an extensometer and an acoustic emission sensor, and are initially loaded until the first acoustic event occurs. For damage inspection by X-ray radiography and edge observation using an optical microscope, coupons are removed from the machine after the penetrant is applied to coupon edges. Then these specimens are loaded to the next applied strain level. In this way, the density of part-width or full width transverse cracks can be obtained.

## Results

Figure 1 shows a micrograph and an X-radiograph of cracks in [45/0/-45/90]<sub>s</sub> laminate at applied mechanical strain of 0.62%. By edge observation, many cracks

Table I Specimen configuration

Type	Stacking Sequence	Width[mm]	Thickness [mm]	Gauge Length [mm]
Coupon E	[45/0/-45/90] <sub>s</sub>	15,30,50	1.1	80
Coupon F	[45/0/-45/90/-45/0/45]	15,30,50	1.0	80

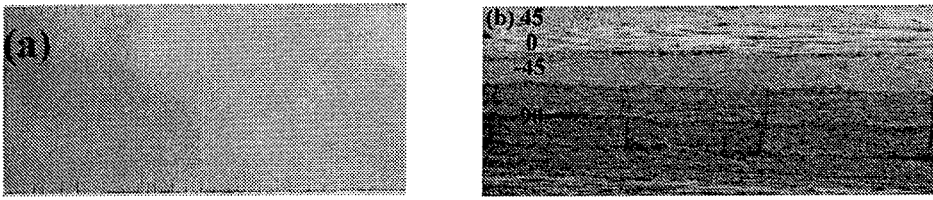


Figure 1 Edge cracks : (a)X-ray radiography (b)Edge observation  
 $\epsilon = 0.62\%$

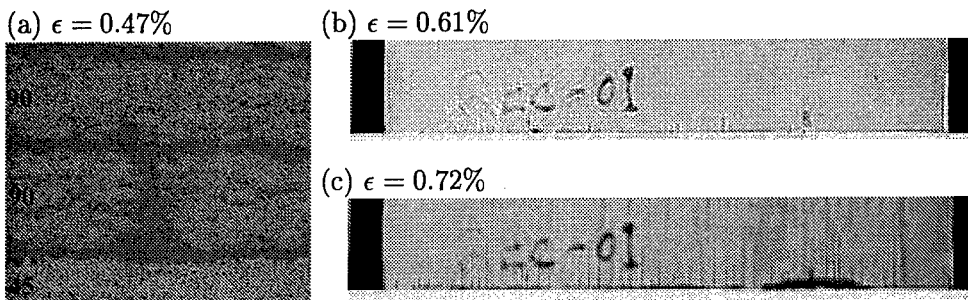


Figure 2 Transverse crack propagation process : (a)edge crack initiation in resin-rich region , (b)edge crack saturation , (c)crack propagation into inner region

can be seen, but few cracks propagate into the inner region. Some specimens are cut and examined for inner damages. There is no crack in the inner region at relative low strain level. These results suggest that transverse cracks seem to initiate from free-edges and propagate into the inner region. At higher strain level, transverse crack propagation and delaminations at free-edges can be observed. Figure 2 shows the damage process of these laminates; (a) edge cracks appear at the resin-rich region in  $90^\circ$  layers; (b) edge cracks are developed and almost saturated only in the edge region; (c) the cracks propagate into the inner region and edge delaminations initiate. In  $[45/0/-45/90/-45/0/45]$  laminates, transverse cracks are less susceptible to initiate or propagate. But damage growth process of both laminates is almost the same. In coupon laminates, there seem to be no specimen width nor transverse ply thickness effect on this damage process within the qualitative meaning.

### Edge cracks

Figure 3 shows the relationship between the applied tensile strain and edge crack density measured by edge observation. The circle, triangle, and square

marks reveal the edge crack densities of the specimen with 15mm, 30mm, and 50mm width respectively. In 90<sub>2</sub> plies, edge cracks seem to initiate at lower strain level than in 90 ply. In conjunction with load increase, the numbers of edge cracks rapidly grow and saturate in both laminates. However, the saturation density of edge cracks in 90 ply is higher than in 90<sub>2</sub> plies. These trends coincide with the conventional results and analyses of transverse full width cracks.

There is a little difference between the laminates with a range of specimen widths about the initiation and growth process of edge cracks. However, this difference is probably caused by edge conditions, not by specimen width. Kitano et al.[4] showed edge condition effect on the transverse cracks. Although edge cracks may be considerably influenced by edge conditions, further investigation is needed.

In recent toughed CFRP laminates, the edge crack density is not the density of transverse full width cracks. And so, the damage inspection of inner region is needed. However, edge crack length along the specimen width is too short to be observed by only X-ray radiography especially at edge crack initiation. This is why both edge observation and X-ray inspection are conducted.

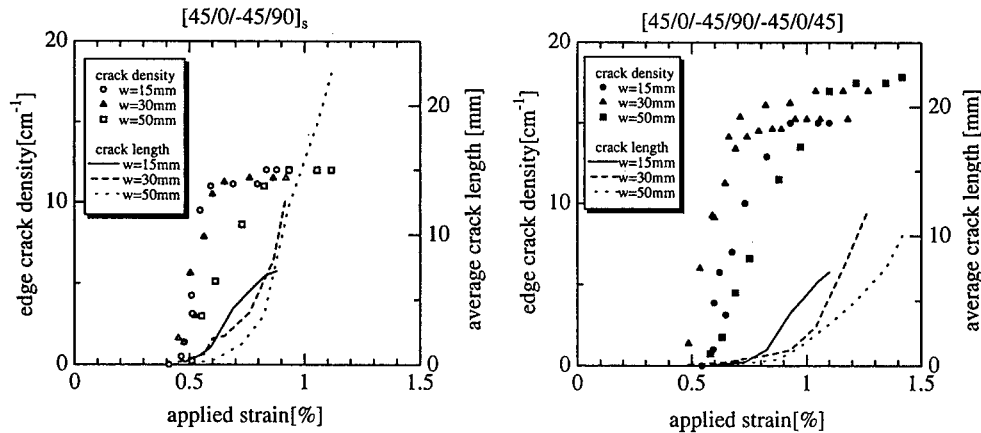


Figure 3 Edge crack density and average crack length as a function of applied mechanical strain

#### Transverse crack propagation

By X-ray radiography, transverse crack length from free-edges along the specimen width can be obtained as shown in Figure 3. The full, chain, and dotted lines show the average crack length of the specimen with 15mm, 30mm, and 50mm width respectively. Although observed values of crack length from free-edges have variation to some degree, the lengths of many cracks are almost the same. Figure 4 shows the transverse crack propagation into the inner regions. The crack density in Figure 4 is the normalized crack density defined as :

$$\rho = \rho_{edge} \frac{2\bar{y}}{w} \quad (1)$$

where  $\rho_{edge}$  is the edge crack density,  $\bar{y}$  is the average crack length from free-edges, and  $w$  is the specimen width. Full width cracks are regarded as two half-width cracks. The cracks barely propagate in the edge crack growth process, and after edge crack saturation, crack propagation into the inner region accelerates. From Figure 4, transverse cracks seem to be less susceptible to propagate through the width in the specimens with wider widths. This trend is remarkable in thin 90° layers. These results suggest that specimen width and transverse ply thickness have significant effect on transverse crack propagation.

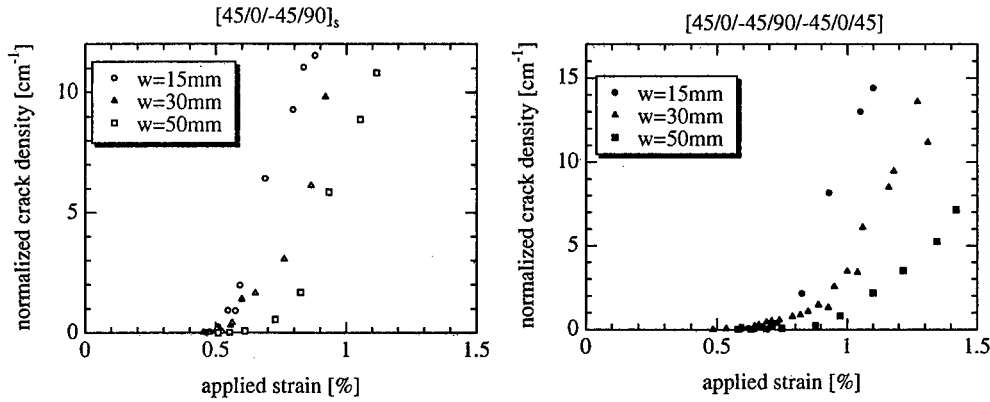


Figure 4 Normalized density of transverse cracks as a function of applied mechanical strain

### Analysis

Edge crack growth process seems to be dependent on edge conditions. In this analysis, transverse cracks are supposed to stem from the distributed initial defects at free-edges. According to Wang's "effective flaw hypothesis" [5], the defects in matrix can be simulated by a distribution of the effective flaws. These flaws are possible to form transverse cracks. Xu[1] derived the relationship between the applied loading and the *in situ* transverse crack density. He defined the "equivalent applied loading" as :

$$\epsilon_{EQ} \approx \frac{\epsilon_{CI}}{\epsilon_{CS}} \sqrt{\frac{\epsilon_{CS}^2 - \epsilon^2}{\epsilon^2 - \epsilon_{CI}^2}} \quad (2)$$

where  $CI$  and  $CS$  represent the crack initiation and the crack saturation state respectively. And the equivalent crack density,  $D_{EQ} = D/D_{CS}$ , is derived as :

$$D_{EQ} = 1 - F_{\epsilon}(\epsilon_{EQ}) \quad (3)$$

where  $F_{\epsilon}(\epsilon_{EQ})$  is the distribution function of the equivalent applied loading. In this study,  $F_{\epsilon}(\epsilon_{EQ})$  can be described by the Weibull distribution function, i.e.,

$$F_{\epsilon}(\epsilon_{EQ}) = 1 - \exp[-(\epsilon_{EQ}/\epsilon_{EQ}^W)^K], \quad D_{EQ} = \exp[-(\epsilon_{EQ}/\epsilon_{EQ}^W)^K] \quad (4)$$

where  $\epsilon_{EQ}^W$  and  $K$  are parameters.

To predict edge crack growth, the crack initiation and the final saturation crack density should be predicted at first. Many models can be applied to the prediction of the crack initiation, and the crack saturation loading should be measured in experiments. The parameters  $\epsilon_{EQ}^W$  and  $K$  are obtained from a fitted curve of experimental data.

The relationship between the equivalent applied loading and the equivalent edge crack density of both laminates with 15mm width is shown in Figure 5. By linear regression, the edge crack growth parameters are obtained. The obtained values of  $\epsilon_{EQ}^W$  and  $K$  are 1.414 and 1.688 respectively. Figure 5 also shows that the distribution function  $F_{\epsilon}(\epsilon_{EQ})$  can be described as the Weibull distribution function very well. By using these parameters, analytical predictions of edge crack density are carried out. Figure 6 shows the experimental data and analytical predictions of edge crack density in 90 plies of both laminates with 15mm width. According to Figure 6, edge crack growth processes of  $[45/0/-45/90]_s$  and  $[45/0/-45/90/-45/0/45]$  laminates seem to be different. However, the fitting parameters obtained from Figure 5 may be regarded as the material properties and not depend on the laminate layups[1]. By using these obtained parameters, edge crack growth can be predicted very well as shown in Figure 6.

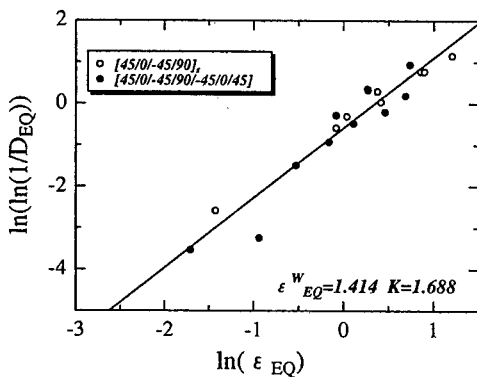


Figure 5 The relationship between the equivalent loading and the equivalent crack density

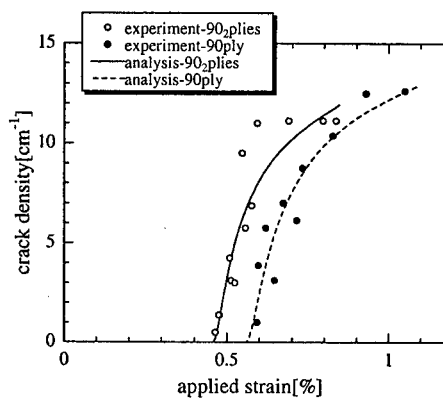


Figure 6 Experimental data and prediction of edge crack growth

## Conclusions

Detailed observations of transverse cracks confirm that transverse cracks initiate from free-edges, and there is a three stage process of edge crack initiation, edge crack saturation, and crack propagation across the width. The existence of free-edges has significant effect on *in situ* transverse cracking. Data of edge crack density show that edge crack growth process is similar to the conventional full width cracking. A probabilistic-analytical method can be applied to the prediction of edge crack growth. By linear regression, edge crack growth parameters are obtained. Edge crack density of  $[45/0/-45/90]_s$  and  $[45/0/-45/90/-45/0/45]$  laminates are predicted very well. There is no relation between the specimen width and edge crack growth.

Measurements of crack length from free-edges suggest that the specimen width influences crack propagation. Transverse cracks are less susceptible to propagate in specimens with wider width. Useful information for cryogenic composite fuel tank of RLV is obtained. Further work to investigate specimen width or transverse ply thickness effect on transverse cracks is needed.

## References

- [1] L. Y. Xu, 1996. "On the Law of the Transverse Matrix Crack Growth in Brittle Polymeric Matrix Composite Laminates under Static Loadings" *Journal of Composite Materials*, 30(3):384-405.
- [2] L. Boniface, P. A. Smith, and M. G. Bader, 1997. "Transverse Ply Cracking in Cross-Ply CFRP Laminates – Initiation or Propagation Controlled?" *Journal of Composite Materials*, 31(11):1080-1112.
- [3] N. J. Pagano, G. A. Schoeppner, R. Kim, and F. L. Abrams, 1998. "Steady-State Cracking and Edge Effects in Thermo-Mechanical Transverse Cracking of Cross-Ply Laminates" *Composites Science and Technology*, 58:1811-1825.
- [4] A. Kitano, K. Yoshikawa, K. Noguchi, and J. Matsui, 1993. "Edge Finishing Effects on Transverse Cracking of Cross-Ply CFRP Laminates" *Proceedings of 9th ICCM*, Madrid:169-176.
- [5] A. S. D. Wang, 1984. "Fracture Mechanics of Sublaminar Cracks in Composite Materials" *Composites Technology Review*, 6(2):45-62.

# Cryogenic Composite Tank

---



## **Applicability of CFRP Materials to the Cryogenic Propellant Tank for Reusable Launch Vehicle (RLV)**

Y. Morino, T. Shimoda, T. Morimoto, T. Ishikawa and T. Aoki

### **Abstract**

It is essential to utilize carbon fiber reinforced plastics (CFRP) for main structural materials of cryogenic propellant tanks in order to realize drastic weight reduction needed for efficient reusable space transportation systems. Recently developed toughened CFRP materials, which are expected to show good cryogenic properties, are considered promising candidates for these kinds of applications. Present study investigates cryogenic properties of candidate materials and structural elements including Y-joint structural models. 300 mm diameter filament wound tank and 600 mm diameter lay up tanks were fabricated and tested. Based on these experimental data, feasibility of CFRP cryogenic tank is discussed and future research tasks are proposed. This research is being conducted under the cooperation contract between NASDA and NAL.

### **Introduction**

Drastic weight reduction of propellant tanks is needed for realization of the practical reusable space transportation vehicles because the large propellant tanks occupy primary part of the airframe. Figure 1 shows some of the RLV concepts, which are investigated in Japan. Utilization of carbon fiber reinforced plastics (CFRP) for cryogenic propellant (liquid hydrogen and liquid oxygen) tanks would be one of the most promising enabling technologies on this purpose. So far there has been very little information or data to verify feasibility of this technology, although some very ambitious demonstrations like DC-XA and X-33 have been carried out in USA. We

---

Y. Morino, T. Shimoda, T. Morimoto, National Space Development Agency of Jpan, 2-1-1 Sengen, Tsukuba, Ibaraki 305-8505, Japan

T. Ishikawa, National Aerospace Laboratory, 6-13-1 Ohsawa, Mitaka, Tokyo 181-0015, Japan

T. Aoki, Department of Aeronautics and Astronautics, University of Tokyo, 7-3-1 Hongo, Bunkyo-ku, Tokyo 113-8656

started this research three years ago aiming to assess the feasibility of the cryogenic composite tanks and to evaluate degree of weight reduction compared with conventional aluminum tanks. Before that time we had very little material data on composite materials at cryogenic temperatures. Consequently, we started from obtaining fundamental material characteristics at various temperatures and conducted some preliminary structural element testing. Recently we initiated small tank testing to detect potential technical problems related to application to the cryogenic pressure vessels. At present we are dealing tanks with no inner lining because of structural simplicity. From the data obtained so far, we discuss applicability of CFRP cryogenic tank and future research directions.

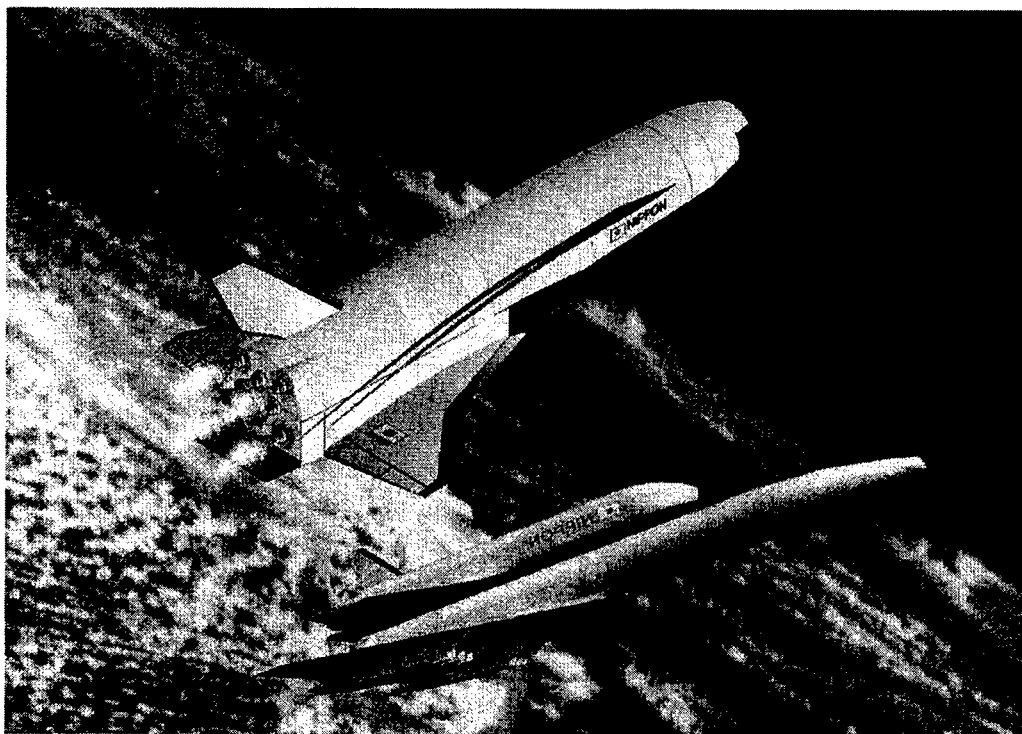


Figure 1 Typical RLV concepts studied in Japan

### Material properties

The expected weight reduction of popular aerospace primary structures by using composite materials would be 20% to 30% if compared with conventional aluminum materials. This ratio would be contributed by improvement of specific strength and specific stiffness together with introduction of one piece forming technology that reduces number of assembly interfaces. This is assuming that CFRP has same specific

strength/stiffness and heat resistance properties as typical aerospace aluminum alloys. Cryogenic environments will impose additional severe requirements about leak tightness and low temperature toughness. Candidate materials include high temperature cured epoxy systems, bismaleimide systems, PEEK systems and others. Several kinds of CFRP materials were tested at from the room temperatures to the liquid helium temperatures<sup>1)</sup>. As a result of these testing, we found that static tensile strength of the quasi-isotropic laminates decreases with respect to temperature decrease in most case and matrix cracks develop at relatively low stress level at the cryogenic temperatures. The latter phenomenon is important in view of propellant sustainability against leaking. Relationship between cracks and leak was observed by experiments with respect to applied loads<sup>2)</sup>. This result seems to suggest that existence of open cracks and connection of these cracks is essential to create serious leaking path. Analytical explanation of these phenomena is being tried in order to identify critical parameters in view of the material selection. From these material data we selected the Toho IM600/#133 for the reference material to be used in the following research because of its overall good properties and available database particularly at cryogenic temperatures. However, systematic selection of the best material for RLV tanks should be made in future based on well-defined requirements and more comprehensive material data that also should be obtained in future.

### **Structural elements**

There are many complex structural elements in the actual rocket tanks, such as stiffened structures, openings for propellant inlet/outlet, attachment of low/high temperature insulation systems, and junctions to the neighboring structures. Composite materials/structures that are used in these portions have complex stress distributions and relatively low production quality, therefore they are susceptible to local defects or insufficient performance. It seems very important to design the tank at sufficiently high reliability even in these complex structural portions. So, it is necessary to take into account these issues in the early R&D phase. In accordance with this considerations, the following basic structural element tests were conducted to identify important technological problems in this area.

#### **Y-joint model testing**

A rocket propellant tank usually consists of a cylindrical section and dome sections. The joining part at the cylinder/dome interface also connects to the neighboring structure and therefore is called "Y-joint" after its cross-sectional shape. Complex loads including internal pressure, external forces and thermal gradients are imposed on this part. In addition, quality of complex layered portion can be worse than simple structural portion. In this respect, Y-joint structural models were fabricated and tested in order to identify potential technical problems concerning design and production for these kinds of structural elements. The assumed tank geometry is a cylinder of 8m diameter with elliptical domes of 2m height (minor radius ratio 0.5). Cross-sectional geometry of fabricated specimen is shown in Figure 2. Here, thickness of the tank around the Y-joint is assumed as 6mm. The width of the specimen is 50 mm (straight). The material is IM600/#133 from Toho-rayon (180°C cured toughened epoxy system). Narrow space between the two branches is filled with 90° layered materials. Three kinds of specimens were made; Type A: quasi-isotropic lay-up with unidirectional prepreg; Type B: same as Type A except for 1 mm over-plying inside surface of the branch portion; Type C: quasi-isotropic lay-up with cloth prepreg, 1mm over-plying. Finite element analysis (FEM) was conducted to calculate stress distribution around the Y-joint of the full-scale tank. Elastic properties of the material are assumed to be orthotropic in in-plane direction and uniform along the thickness direction. Internal pressure of 300 MPa was assumed as a reference load. Calculated deformation around the Y-joint is shown in Figure 3 where the displacements are not scaled. One can see that the lower branch of the Y-joint is pulled down by the dome caused by mismatch of deformation between the dome and cylinder. As a results of this deformation, tearing like loads are imposed on the Y-joint portion. Maximum shear stress in the Y-joint is 65 MPa at the filled area between the Y branches. Referring to this calculation, tearing loads were imposed on the Y-joint model specimens. Tests were conducted at room temperatures and near liquid nitrogen temperatures. In the latter case, specimens were covered with insulation materials and cooled with liquid nitrogen before imposing loads. The measured fracture loads (tearing force) were shown in Figure 4. Specimens without over-ply were fractured at the interface plane between the straight portion and filled portion. Specimens with over-ply were initially fractured at considerably lower loads by the separation of over-ply (shown by black columns) and then fractured in the same mode as the specimen without over-ply. The fracture loads at the straight interface plane were between 300N and 400N. No significant differences were observed for test temperatures and materials. For the purpose of fracture stress comparison with the full-scale model analysis, FEM analysis

of the Y-joint model specimens was conducted corresponding to the test conditions. For the type a specimen, the calculated maximum shear stress at the fracture was 77 MPa and calculated location of the fracture agreed to the experimental observation (interface between the straight branch and filled portion). This value is a little higher than the previously mentioned stress for the supposed propellant tank. However, considering accuracy of the analysis, variation of material quality and necessary margin for design flexibility, etc., it seems that the design arrangements supposed in this study was inappropriate for assumed internal pressure. Accordingly, improvement of Y-joint geometry or application of stronger weaving methods has to be considered in order to establish a feasible tank design.

#### Cryogenic insulation materials

Cryogenic insulation is needed inside or outside of the tank wall in order to prevent excessive boiling off of the cryogenic propellant. The thermal contraction of the insulation material is generally much larger than CFRP substrates and therefore large thermal strain is induced at the adhesive plane of the insulation layer. In addition, large strain induced by the internal pressure is repeatedly imposed to the tank wall as the duty cycle of the RLV. In this respect, low temperature characteristics of insulation materials and CFRP/insulation adhesion are very important for evaluation of insulation systems. As a preliminary evaluation of the insulation materials, several typical plastic foam materials have been tested at low temperatures. Figure 5 shows fracture strains of two typical insulation materials at from room temperature to  $-150^{\circ}\text{C}$ . Airex foam shows better elongation properties than Rohacell foam particularly in low temperatures. From this result, it seems difficult to use the latter as cryogenic RLV rocket tank insulation, although additional cryogenic tests are needed to finalize the conclusion.

#### Small tank testing

##### Filament winding method

Filament winding (FW) method is very efficient method for producing pressure vessels that require low weight and cost. The application of this method to cryogenic propellant tanks is very attractive in spite of possible difficulties in quality control due to tape alignment and cross plying. Usually this method is used together with liners inside. However we first try no lining tank in order to seek drastic weight/cost

performance and structural simplicity. In order to examine the feasibility of FW methods, a small FW tank of 30 cm in diameter was fabricated by use of 1 cm width prepreg tape (IM600/#133) same as the lay-up tank. The cylinder section is 30 cm long and layer construction is  $(90^\circ, \pm 30^\circ, 90^\circ)$ s, resulting the thickness of about 1.1 mm. The domes are spherical shape and helical wound with 4 plies. An aluminum boss flange is attached to the center of the dome. This boss is a part of the mandrel. The bulk of the mandrel is made of plasters in order to put out the FW tank after winding and thermosetting. An adhesive film liner (FM300) was added inside the tank in order to prevent leaking after the fabrication. The cause of the leak was supposed that vapor coming out from the mandrel degraded the quality of the materials and produced the defects such as voids that would become leak passes. The film liner prevented the leaking at the room temperature. Then the tank was filled with liquid nitrogen under no internal pressure as shown in Figure 6. After this cryogenic testing, leaks were detected most of the part of the tank. This means that lining of FM300 was not effective for sealing at the liquid nitrogen temperature. The tank was cut into pieces to inspect cross-sectional microstructures. The microscopic picture of a defective portion is shown in Figure 7. These defective portions were located at the portion where the leaks were observed. We suppose that through these voids or defects internal gas leaked outside when the internal lining layer was destroyed by the internal thermal stresses. Based on these results, improvements of fabrication were made and the fabrication of the second phase tank is being conducted.

#### Lay up methods

As shown in Reference<sup>1) 2)</sup>, we found that micro cracks are formed in typical candidate CFRP materials at considerably low stress level at cryogenic temperatures. However, it is not clear if this phenomena occurs similarly in actual pressure vessels and if this is critical in the sense of leakage or strength. To solve this problem, we are preparing cryogenic pressurization tests of small CFRP tanks made of a typical toughened epoxy system (IM600/#133). Specimen and testing apparatus are shown in Figure 8. The tank is composed of a 60 cm diameter cylinder and spherical dome of same diameter. Total length is about 1.2 m and an aluminum flange is bonded to the top of the CFRP tank. A part of cylinder (0.3 m length) has minimum thickness of about 1.1mm and this part is served for crack evaluation. Three specimens were made. They are different in lay-up configuration of the crack evaluation part. The dome portion is made of cloth prepreg and all the part of the tank is quasi-isotropic in in-plane

directions. The specimen with the upper flange is installed in a vacuum chamber, which has a top disk to close the tank and chamber at the same time. The top disk has various piping systems for loading of cryogenic liquid, pressurization and measurements. The flange of the specimen is kept at the room temperature by electric heaters to avoid unexpected failure of bonding at the cryogenic temperatures. The planned maximum internal pressure is 1.5 MPa at the liquid nitrogen temperature. The maximum hoop stress expected in the crack evaluation portion is about 40 MPa. A helium detector connected to the vacuum chamber will monitor leaking. Damages of the specimen including micro crack formation will be confirmed by destructive inspection after the cryogenic tests.

### Conclusions

In this paper, we described the overview of the RLV cryogenic tank research, most of which have been conducted under cooperation between NASDA and NAL. The research is still in the phase of the preliminary material characterization and a lot of material and structural element testing is needed in future before proceeding to the next intensive research phase such as sub-scale tank testing or flight testing. We believe such kind of step-by-step approach would finally reach the realization of the practical Reusable Launch Vehicles.

### References

1. Y. Morino, T. Ishikawa, T. Aoki, H. Kumazawa, Y. Hayashi, "CFRP Material Characterization Testing for the RLV Cryogenic Propellant Tank", AIAA-99-1927
2. T. Aoki, T. Ishikawa, H. Kumazawa, Y. Morino, "Mechanical Performance of CF/Polymer Composite Laminates under Cryogenic Conditions", AIAA-2000-1605
3. Y. Morino, T. Shimoda, T. Morimoto, T. Ishikawa, T. Aoki, "Feasibility Study of the Cryogenic Composite Tank for Reusable Launch Vehicles", IAF-99-I.3.06

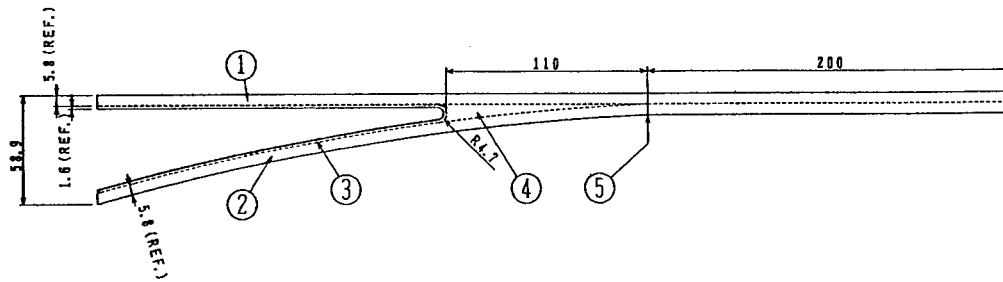


Figure 2 Geometry of the Y-joint



Figure 3 Deformation of the Y-joint

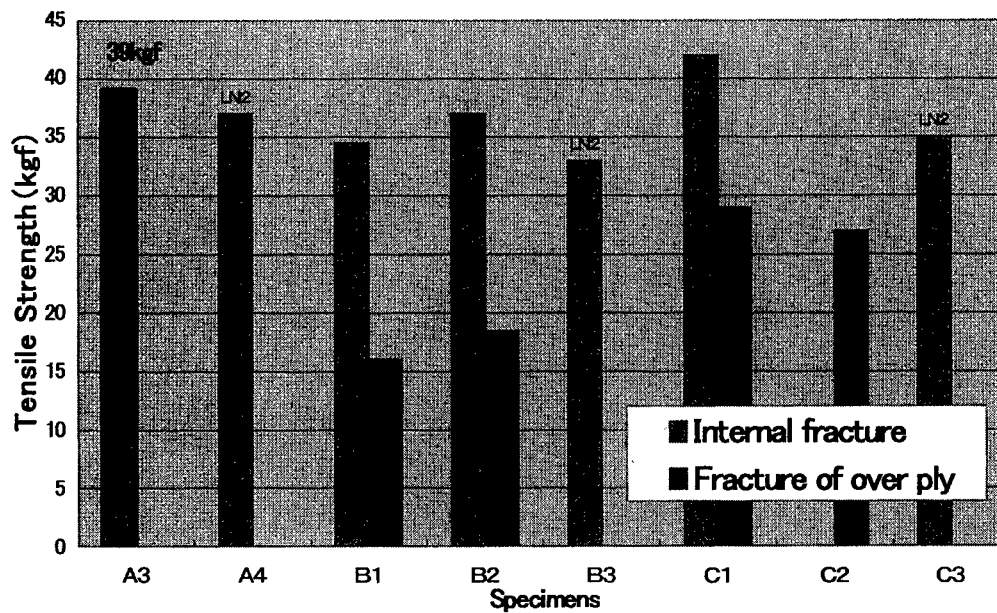


Figure 4 Fracture loads of the Y-joints



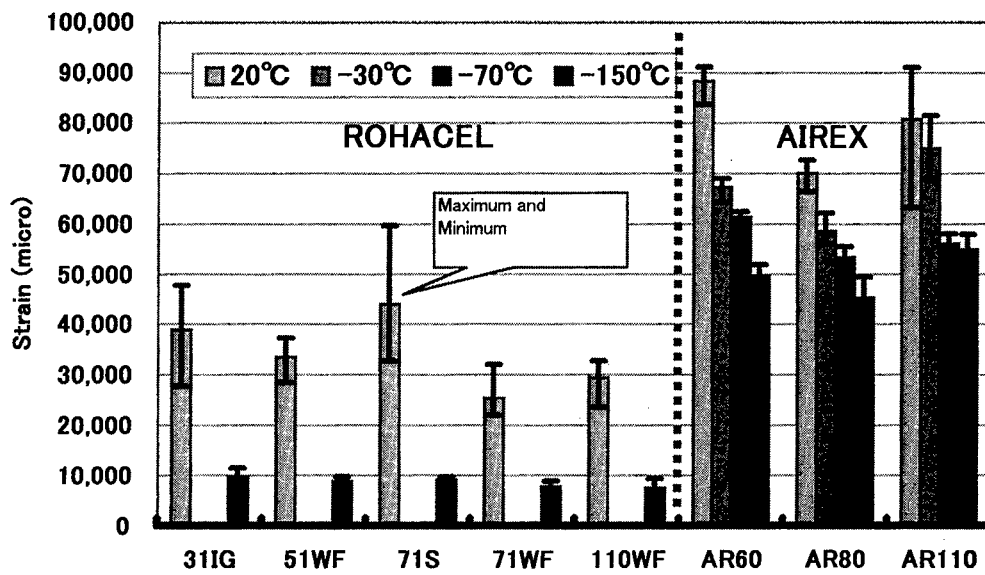


Figure 5 Fracture strains of the various insulation materials



Figure 6 Cryogenic testing of the small FW tank

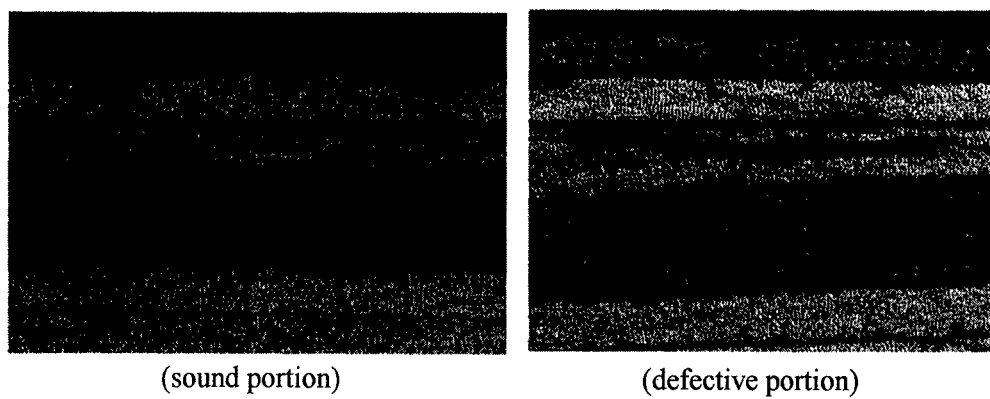


Figure 7 Cross-section of the FW materials

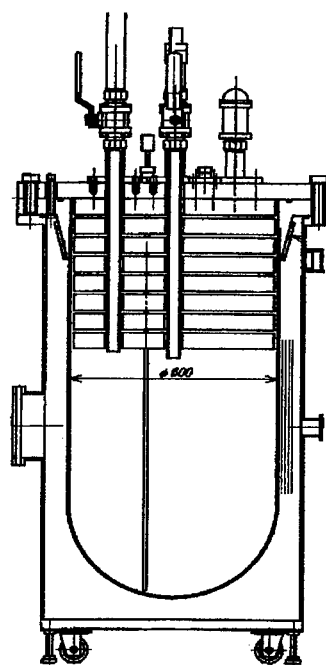


Figure 8 60 cm lay-up tank and cryogenic test configuration

## **Cryogenic Mechanical Properties of CF/Polymer Composites for Tanks of Reusable Rockets**

T. Aoki, T. Ishikawa, H. Kumazawa and Y. Morino

### **Abstract**

Cryogenic properties of different types of CFRPs are experimentally evaluated to survey the basic applicability of different material systems to the cryogenic propellant tanks for future reusable launch vehicles. Temperature dependent material constants, tensile strength and interlaminar fracture toughness are experimentally obtained, together with detailed observations of matrix cracks and delaminations. Up to about 20% reduction in cryogenic static tensile strength is observed for most of the material systems tested. The damage initiation stresses also decreased under cryogenic conditions. The results indicate that the matrix cracks can possibly be one of the major critical issues when current material systems are applied to cryogenic propellant tanks. Numerical predictions of the delaminations and matrix cracks are conducted to theoretically support the experimental consequences.

### **Introduction**

The wide use of composite materials is the major technical challenge for effectively reducing the structural weight of the future reusable launch vehicles. The cryogenic propellant tanks are the dominating structural components of the vehicle structure and thus the application of carbon fiber reinforced plastics (CFRP) to these components is one of the most promising technologies for realizing the aimed weight reduction. In this study, the basic cryogenic mechanical characteristics of CFRP laminates are experimentally and analytically evaluated to discuss their applicability to the propellant tanks.

---

T.Aoki, Department of Aeronautics and Astronautics, University of Tokyo, 7-3-1 Hongo, Bunkyo-ku, Tokyo 113-8656, Japan.

T.Ishikawa and H.Kumazawa, National Aerospace Laboratory, 6-13-1 Ohsawa, Mitaka, Tokyo 181-0015, Japan

Y.Morino, National Space Development Agency of Japan, 2-1-1 Sengen, Tsukuba, Ibaraki 305-8505, Japan

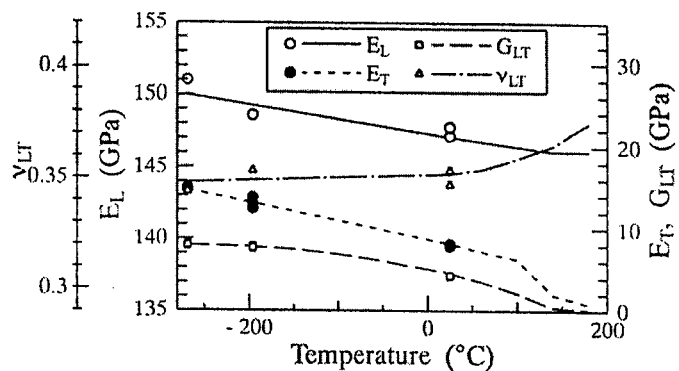
## Materials and Material Properties

The materials are based on different types of epoxy matrices, bismaleimide matrix and PEEK (Table I). Type *Aa*, which is the combination of intermediate modulus fiber and toughened epoxy, is herein set to be the base material and has been investigated in detail.

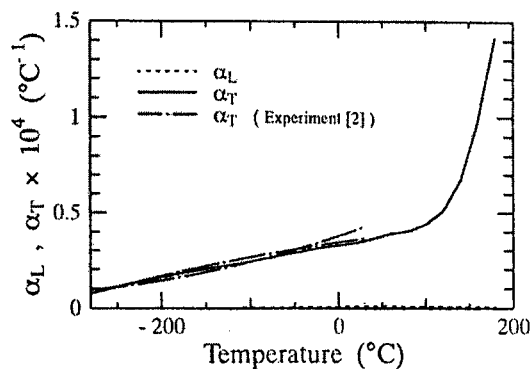
The existing data of cryogenic mechanical properties are often provided for specific discrete temperatures such as  $\text{LN}_2$ (-196°C) or  $\text{LHe}$ (-269°C) conditions [1]. In this respect, it is worthwhile to present the temperature dependent mechanical properties as continuous functions of temperature. The temperature dependent anisotropic elastic constants and thermal expansion coefficients for material *Aa* are obtained based on the experimental measurements and past references (Figure1). They are used later in the analytical predictions of delamination propagation and matrix crack onset. It should be noted that when wide range of thermal loading up from room temperature down to cryogenic condition is of interest, temperature dependent materials properties must be taken into account in the analyses.

Table I CFRP material systems

Material designation	Supplier	Fiber	Matrix resin
<i>Aa</i>	Toho Rayon	IM600	133 (180°C-cure Epoxy)
<i>Ab</i>		HTA	112 (120°C-cure Epoxy)
<i>Ad</i>		HTA	332 (Bismaleimide)
<i>Ae</i>		IM600	PEEK
<i>Ba</i>	Mitsubishi Rayon	MR50K	982 (180°C-cure Epoxy)
<i>Bb</i>		MR50K	154 (120°C-cure Epoxy)
<i>Ca</i>	Mitsubishi Chemical	IM7	977-2



(a) Elastic moduli



(b) Thermal expansion coefficients

Figure 1 Temperature dependent material properties of intermediate modulus CF/180°C-cure toughened epoxy unidirectional composite (Type Aa, IM600/133)

## Analysis

The quasi-isotropic laminate with the single stacking sequence of  $(45/0/-45/90)_{2S}$  is employed here for analytical predictions. The energy release rates are calculated for delamination propagating through inner -45/90 layer interface and matrix crack onset assumed in the central 90<sub>2</sub> layers. The calculation for free-edge delamination is based on the simplified method to calculate the saturated value [2], and that for matrix crack is based on the method proposed by Park and McManus [3]. The analytical results suggest that, for the quasi-isotropic laminates considered herein, the loads at matrix crack onset are drastically lowered under cryogenic condition.

## Experiment

### Experimental Setup

Static tensile tests are conducted using the specimens of nominal thickness and width of 2.2mm and 15mm, respectively. The loading system utilizing 4-rods turret type tension introduction device has been developed and combined with the surrounding double-walled cryogenic chamber. This system is installed in the Instron 4505 Testing Machine (Figure 2). This device facilitates successive loading of up to 4 specimens under single setup of the cryogenic environment so as to spare the cryogenic mediums and setup time. The tests were carried out in the LN<sub>2</sub> and LHe environment to simulate the

cryogenic propellant conditions and at room temperature. The identical setup is also used in the DCB fracture toughness measurements.

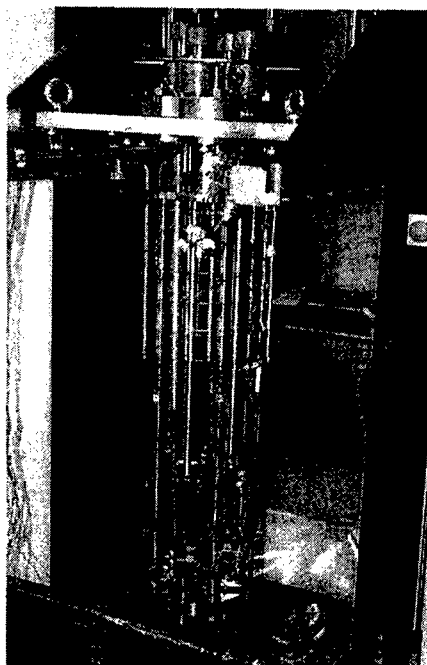


Figure 2 Loading apparatus for cryogenic test

#### Tensile Strength and Associated Damage Observation

The tensile strength of  $(45/0/-45/90)_{2S}$  16 ply, quasi-isotropic laminates of different material systems are obtained. Three specimens are tested for each temperature condition and averaged for later use. The example test results are shown in Figure 3 for type *Ae* material system (IM600/PEEK). The tensile strength for all material systems are summarized in Figure 4. All of the material systems except type *Ad* exhibit strength reduction of up to about 20% at cryogenic conditions compared to those at room temperature.

Matrix crack onset and delamination propagation are investigated based on the acoustic emission (AE) measurements and direct visual observation. The typical stress-strain curves and associated AE counts are shown in Figure 5 in which the indefinite correlation between the AE counts and matrix crack onset is seen under LHe condition. Based on this fact, matrix cracks are visually examined for specific specimens during the cryogenic test by halting the loading and removing the specimen from the experimental

setup. The thermal effect on the onset of matrix cracks, delamination propagation and static strengths of the laminate is summarized in Figure 6. The temperature dependency of the damage initiations for type *Aa* base material system is shown in Figure 7. The matrix cracks tend to take place at drastically lower mechanical load under cryogenic environment, which coincides with the numerical predictions. This poses the possibility of fuel leakage through the chain of these matrix cracks.

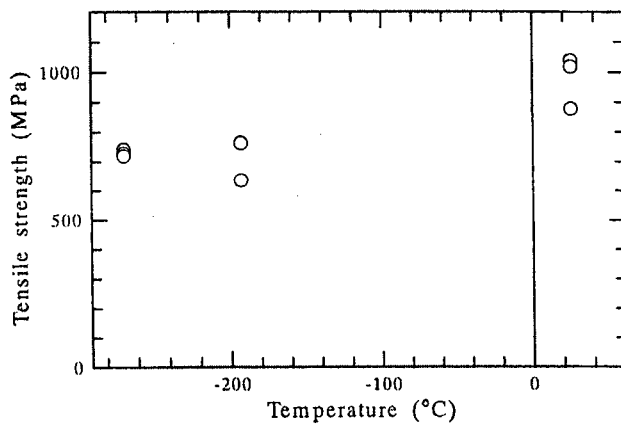


Figure 3 Temperature effect on tensile strength for the quasi-isotropic laminates of type *Ae* material system (IM600/PEEK)

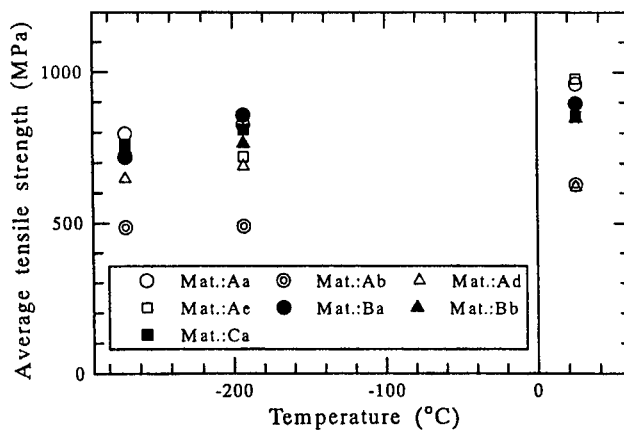
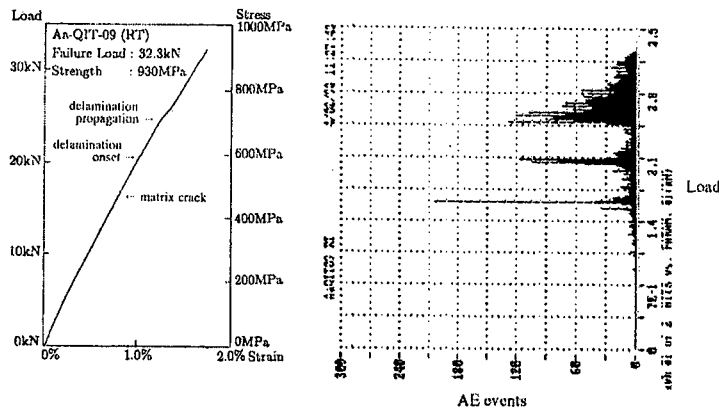
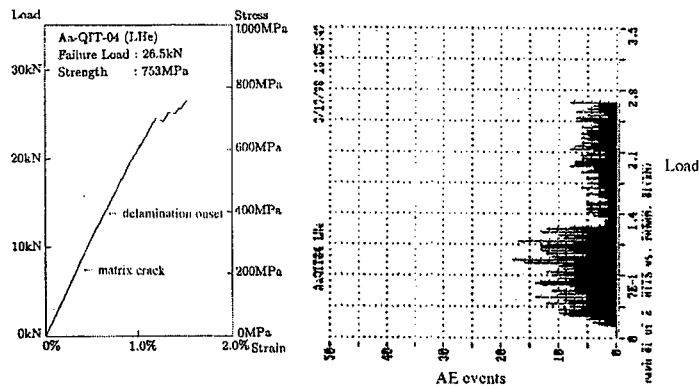


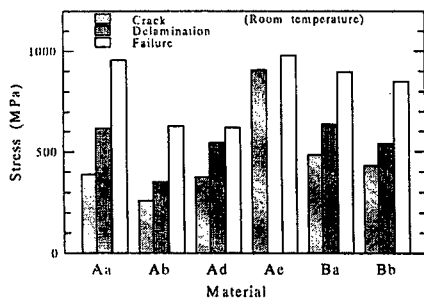
Figure 4 Temperature effect on tensile strength of quasi-isotropic laminates of different material systems



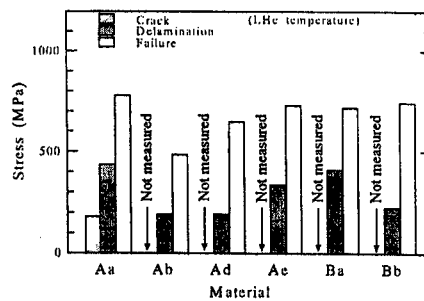
(a) Room temperature



(b) LHe temperature

Figure 5 Tensile stress-strain curves and AE counts for quasi-isotropic laminates of type *Aa* material system (IM600/133)

(a) Room temperature



(b) LHe temperature

Figure 6 Stresses at damage initiations and final failure for different material systems



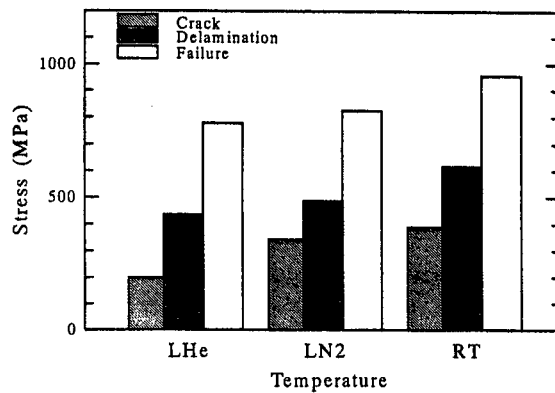


Figure 7 Temperature dependency of stresses at damage initiations for type Aa material system (IM600/133)

#### Interlaminar Fracture Toughness

In order to look into the detailed characteristics of delamination and matrix crack behaviors, it is essential to obtain the interlaminar fracture toughness under cryogenic conditions. The DCB specimens of thickness  $4.5\text{ mm}$  and width  $12.7\text{ mm}$  are used. The interlaminar fracture toughness in terms of energy release rate under room and cryogenic temperatures are plotted in Figure 8. Each plot represents the average propagation value over the full measured crack length range of each DCB specimen.

The fracture toughness is also derived by use of matrix crack initiation measured in the experiment. The temperature dependency, together with the absolute toughness values is in good agreement with the results from DCB specimens. This strengthens the reliability of fracture toughness measured with the DCB specimens showing the increase of the value under cryogenic conditions.

#### Conclusions

The cryogenic performances of different types of CFRPs are experimentally evaluated to survey the basic applicability of the materials to the cryogenic propellant tanks. Temperature dependent material constants, tensile strength, interlaminar fracture toughness are experimentally obtained, together with detailed observations of matrix cracks and delaminations. The results indicate that the matrix cracks can possibly be one of the major critical issues when the current material system is considered for application to the cryogenic propellant tanks. The numerical predictions of the delaminations and matrix cracks are conducted to theoretically support the experimental consequences. The

results suggest that possible application of reliable liner system must also be considered. At the same time the analytical scheme for evaluating the propellant leakage through matrix cracks existing in multiple layers in laminates must be developed to reduce the usage of liner materials for weight savings.

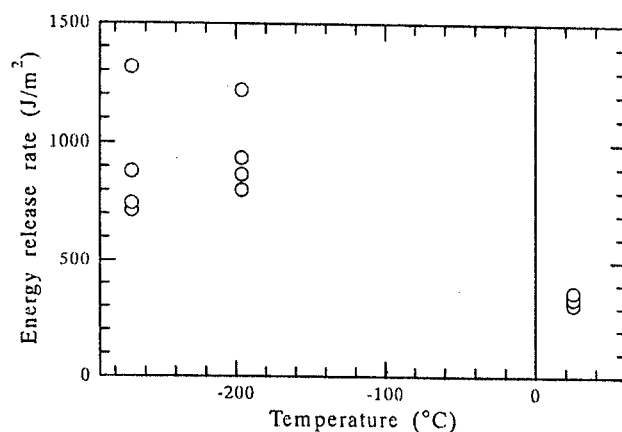


Figure 8 Interlaminar fracture toughness measured with DCB specimens (Type Aa, IM600/133)

## References

1. R.P.Reed and M.Golda, "Cryogenic Properties of Unidirectional Composites", *Cryogenics*, Vol. 34, 1994, pp. 909-928.
2. T.Aoki and K.Kondo, "Delamination Energy Release Rates under Thermal Loading in Fiber-Reinforced Composite Laminates," *Composites Structures*, Vol. 14, 1990, pp. 213-231.
3. C.H.Park and H.McManus, "Thermally Induced Damages in Composite Laminates: Predictive Methodology and Experimental Investigation," *Composites Science and Technology*, Vol. 56, 1996, pp. 1209-1219.

## **Influence of Mechanical and Thermal Loads on Propellant Leak of CFRP Laminates for Tanks of Reusable Rockets**

H.Kumazawa, Y.Hayashi, T.Ishikawa, T.Aoki and Y.Morino

### **Abstract**

In order to apply CFRP composite laminates to cryogenic propellant tanks, it is necessary to research the leakage through CFRP laminates. In this study, experiments and analysis of the leak are investigated for understanding the mechanism of propellant leak. Experiments of leaks through CFRP laminates with matrix cracks are carried out at room temperature, and analysis is developed with a simple assumption between leak and crack opening. In the experiments, CFRP laminate specimens were biaxially loaded and leak rates through the laminates were measured. Then the experiments and the analysis are compared, and it shows the influence of mechanical loads on propellant leak at room temperature. And numerical analysis also predicts that leak rates increase with enlargements of crack openings caused by thermal contractions at cryogenic temperature.

### **Introduction**

For saving of a space transportation cost, it is necessary to develop reusable rockets. One of key issues for the reusable rockets is effectively reducing the structural weight which is mainly occupied by propellant tanks. The application of CFRP to the liquid hydrogen tanks is essential to reduce the weight of the reusable rockets, but cryogenic temperature of the liquid hydrogen affects the properties of CFRP laminates. In toughened CFRP laminates submitted to mechanical loading at cryogenic temperature, matrix cracks easily appear and may lead to the propellant leak. The goal of this study is to investigate the mechanism of the propellant leak due to the chain of the cracks, and influence of mechanical and thermal loads on the propellant leak of CFRP laminates. The results reveal problems for the application of CFRP to the cryogenic propellant tanks.

---

Hisashi Kumazawa and Takahira Aoki, Department of Aeronautics and Astronautics, University of Tokyo, 7-3-1 Hongo, Bunkyo-ku, Tokyo 113-8656, Japan

Yoichi Hayashi, Tokyo Business Service Co. LTD

Takashi Ishikawa, Airframe Division, National Aerospace Laboratory, 6-13-1 Ohsawa, Mitaka, Tokyo 181-0015, Japan

Yoshiki Morino, National Space Development Agency of Japan, 2-1-1 Sengen, Tsukuba, Ibaraki 305-8505, Japan

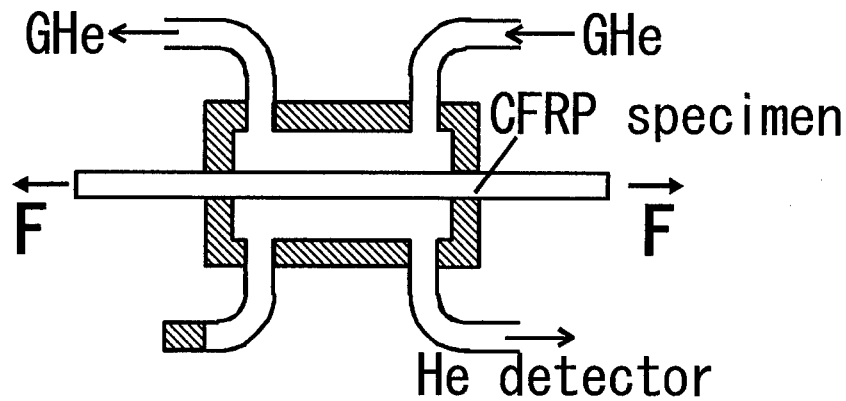


Figure 1 Cross Section of Leak Test

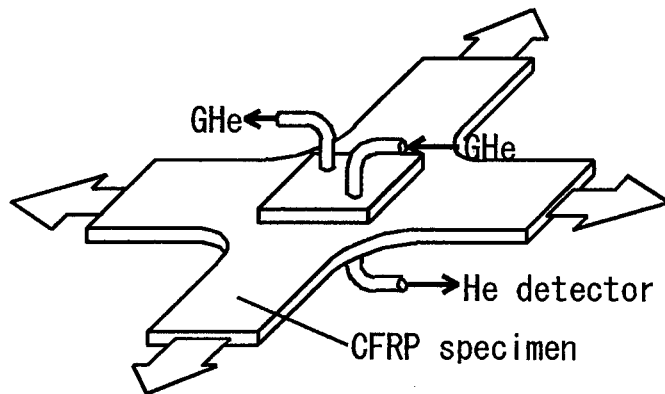


Figure 2 Leak Test Through a Biaxial Loaded Laminate

### Leak Experiment

CFRP laminate specimens for leak experiments are biaxially loaded for modeling on the loading of propellant tanks. Two stainless steel cups are padded to the laminate on both surfaces as shown in Figure 1. Spaces inside the both cups are sealed by O-rings between the laminate and the cup. Helium gas (GHe) flows slowly for keeping atmospheric pressure inside one cup, and a helium leak detector draws a vacuum inside another cup. Pressure difference between both sides of the laminate is atmospheric pressure ( $1.0 \times 10^5 Pa$ ). CFRP specimens padded with these cups are biaxially loaded as shown in Figure 2, and leak rates as functions of loads and load ratio are measured.

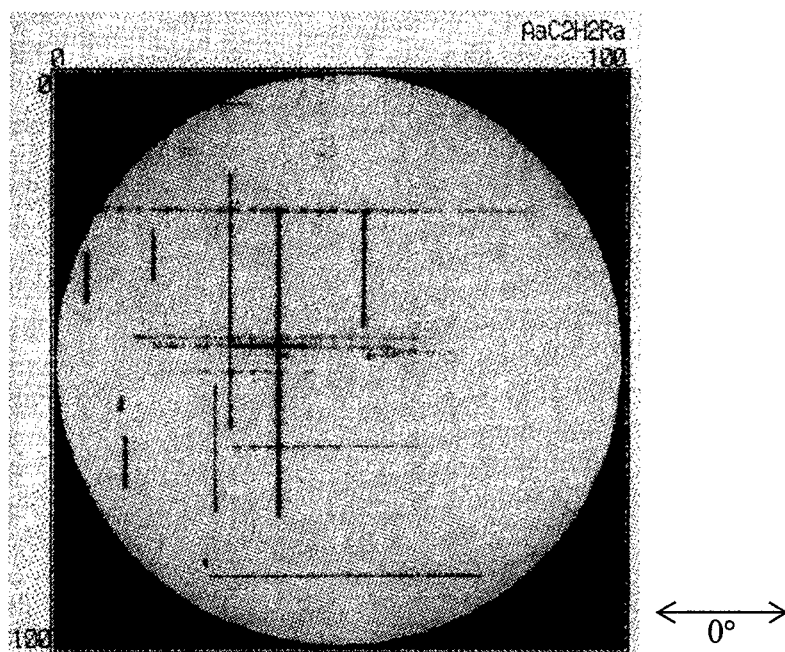


Figure 3 Crack Pattern in Leak Specimen Aa-C2H-02 (Ultrasonic C-scan)

### Specimen

CF/epoxy  $(0/0/90/90)_s$  laminate specimens for biaxial loading were fabricated. The leak test area thickness of the specimens was  $1.2\text{mm}$ . Prior to leak experiments, the loads had been applied to the CFRP laminate specimens to create matrix cracks. If there are not cracks in some layer, leaks don't take place but diffusion is merely detected. The matrix cracks in the leak test area of the specimen (Aa-C2H-02) were inspected by using an ultrasonic testing machine as shown in Figure 3. Figure 3 indicates that matrix cracks exist in both  $0^\circ_2$  and  $90^\circ_4$  layers of the specimen. And then, the chain of these cracks in all layer can induce the leak through the laminate.

Geometry of biaxial specimens is cross shape ( Figure 2 ) and strain field on the leak test area is not calculated simply. Previously strain fields associated with biaxial loads were measured and used for leak analysis of this specimen.

### Leak Analysis

#### Opening Displacements of Cracks

For predictions of leak rates based on crack opening, analysis of  $(0_m/90_n)_s$  cross ply laminate with matrix cracks in both  $0^\circ$  and  $90^\circ$  layers presented by

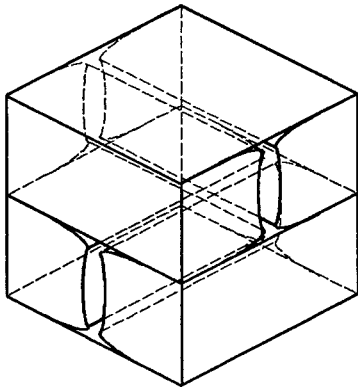


Figure 4 Leak Path at Overlap of Two Matrix Cracks

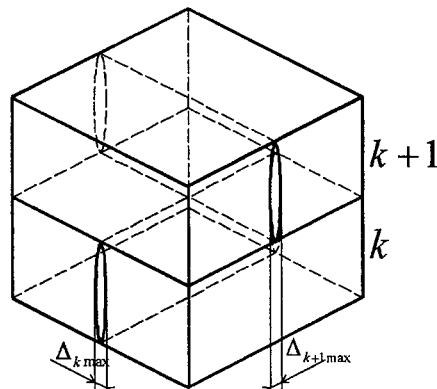


Figure 5 Overlap of Two Matrix Cracks

Henaff-Gardin *et al.* [1] is applied to the calculation of crack opening displacements. In this analysis of the cross ply laminate, displacements in each layer and shape of matrix cracks are assumed to be quadratic functions.

The temperature dependent anisotropic elastic constants and thermal expansion coefficients referred to [2] in which the same CF/epoxy material was employed, are considered in this analysis. Elastic constants for given temperature and thermal strains obtained by integrating thermal expansion coefficients from initial temperature to given temperature are used in the analysis.

#### Conductance for Leak Paths

In vacuum engineering, a relationship between pressure difference, flow rate and conductance is written as

$$Q = C\Delta P \quad (1)$$

where  $Q$  is flow rate,  $C$  is conductance and  $\Delta P$  is pressure difference. Leaks are assumed to occur along the chain of the cracks and thus other permeations, e.g. diffusion, are ignored.

Opening of cracks and microscopic defects at an overlap of two matrix cracks are supposed to make a leak path at the overlap as shown in Figure 4. Helium gas flows through this leak path, and crack opening can affect the sectional area of the leak path at the overlap of cracks. The conductance through the overlap of cracks between  $k$ -th layer and  $(k+1)$ -th layer (Figure 5)  $c_k$  is assumed as

$$c_k = \Omega \bar{\Delta}_k \bar{\Delta}_{k+1} \quad (2)$$

where  $\bar{\Delta}_k$  is a mean opening displacement of cracks in  $k$ -th layer and  $\Omega$  is constant. Although theoretically  $\Omega$  is dependent on thickness of layers and shape of defects at the overlap of matrix cracks,  $\Omega$  is experimentally obtained in this study. Conductances through matrix cracks are supposed to be sufficiently larger than those through the overlap of cracks. Then the conductances through matrix

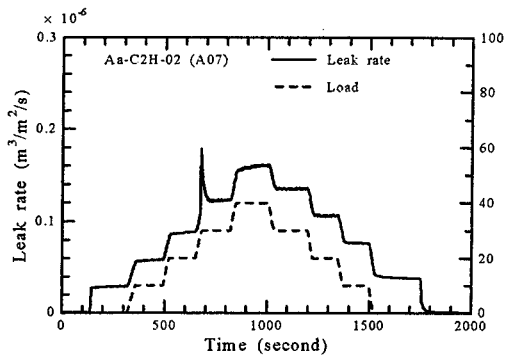


Figure 6 Change of Leak Rate and Uniaxial Load (Aa-C2H-02)

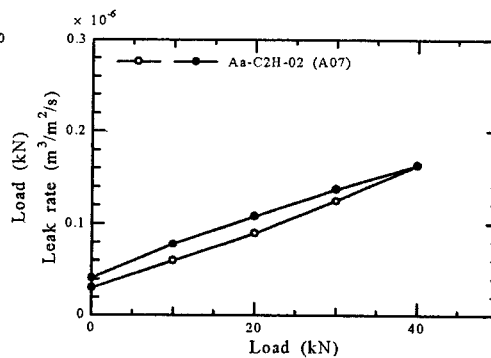


Figure 7 Relationships between Uniaxial Load and Leak Rate (Aa-C2H-02)

cracks are not considered. The conductance through the laminate  $C$  is developed as follows,

$$C = \Omega \left( \sum_k \frac{1}{d_k d_{k+1} \Delta_k \Delta_{k+1}} \right)^{-1} \quad (3)$$

where  $d_k$  is a crack density of  $k$ -th layer. The leak rate is derived from (1) and (3), and finally obtained as a function of the crack densities counted in Figure 3, the crack opening displacements calculated by previously presented method and pressure difference.

## Results and Discussion

### Diffusion

To verify that permeation rates of diffusion is negligible compared with leak, diffusion rates through a similar specimen with no cracks were measured. Results of the diffusion test indicate that detected diffusion rates were very low compared with leak rates, and the effects of diffusion can be ignored.

### Results of Uniaxial Load Test

Through a leak specimen, a leak rate varied with uniaxial load as shown in Figure 6. The leak rate had converted to volume at atmospheric pressure per second in this study. The leak rate immediately rose as the load increased. And decrease of uniaxial load led to decrease of a leak rate. In Figure 6, the curve of the leak rate has a sharp peak at about 700 seconds. The reason of this peak is that slip of O-ring caused by extension of the laminate broke the sealing, and air which flowed into the cup was detected as a helium leak. But the cup connected to a helium leak detector was sealed immediately after the slip of O-ring. Figure 7

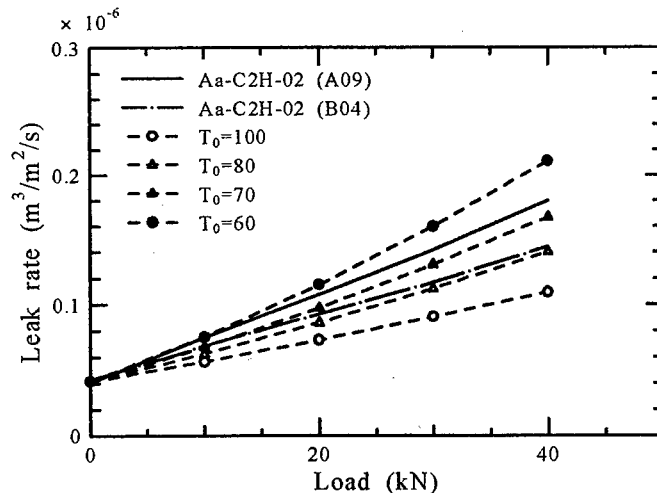


Figure 8 Comparison between Measured Leak Rate and Analytical Leak Rates under Uniaxial Load Aa-C2H-02 (A09) : load to 0° direction in leak experiment, Aa-C2H-02 (B04) : load to 90° direction in leak experiment

shows relationships between uniaxial load and leak rate. In Figure 7, unfilled and filled circles mean leak rates at loading and unloading, respectively. Helium gas flows through the laminate even without mechanical loads because of the crack opening caused by thermal contraction. Figure 7 indicates that the relationship has a hysteresis and the leak rate with no mechanical load rise after a load cycle. The causes of the hysteresis are supposed to be friction and viscoelasticity at neighborhood of the overlap of matrix cracks.

#### Constant $\Omega$

The leak analysis in this study requires an appropriate constant  $\Omega$  in (2). Measured leak rates and numerical predictions are compared in Figure 8. In Figure 8, experimental results are two measured leak rates for the laminate submitted to uniaxial load to 0° and 90° directions, and numerical predictions are leak rates with initial temperature  $T_0$  as 60°C, 70°C, 80°C and 100°C. Change of conductance through matrix cracks in 90° layer causes a difference between two measured leak rates. But calculated leak rates have no difference irrespective of load direction, because the conductance through a matrix crack is not considered in the leak analysis. Constant  $\Omega$  at each numerical result is determined as these predicted leak rates with no mechanical loads adjust to measured one. Figure 8 indicates that the calculated leak rate on condition of initial temperature 70°C ( $\Omega = 61.85 \text{ m}^3/\text{m}^2/\text{s}$ ) is suitable for the measured leak rates through the laminate submitted to uniaxial load. This apparent initial temperature is rather low because supposedly the leak test area of the specimen was compressed due to the contraction of GFRP tabs at room temperature.



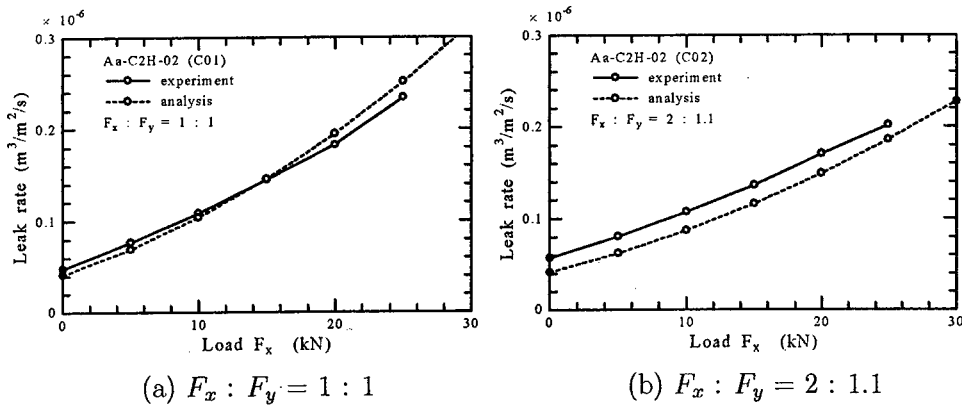


Figure 9 Calculated and Measured Leak Rate as a Function of Load

#### Results of Biaxial Load Test

Figure 9 (a) and (b) show measured leak rates with biaxial load ratio  $F_x : F_y = 1 : 1$  and  $2 : 1.1$  respectively, and calculated one using constant  $\Omega$  determined by the results of uniaxial load test. Leak rates only with increase of load  $F_x, F_y$  are measured. Axis  $x$  and  $y$  indicate  $0^\circ$  and  $90^\circ$  direction, respectively. In Figure 9, the numerical predictions have little differences with the experimental results, which results from the lack of considerations for hysteresis and conductance through the matrix crack in  $90^\circ$  in the leak analysis. Although numerical analysis has a little inaccuracy, each calculated leak rate are approximately in good agreement with the experimental results. Figure 9 reveals that the load ratio and crack opening have influence on the leak rate.

#### Leak Rate at Low Temperature

Leak rate through the same specimen with no mechanical load at low temperature is numerically calculated in Figure 10. Crack densities and constant  $\Omega$  are assumed to remain unchanged at low temperature. Figure 10 shows that decrease of temperature brings increase of leak rate. The increase of the leak rate results from the crack opening displacements enlarged by the thermal contraction.

#### Conclusions

For understanding the mechanism of propellant leak through CFRP laminate, leak analysis based on the opening displacements of matrix cracks has been developed, and leak experiments through the laminate with matrix cracks were carried out at room temperature. The experimental results indicate that

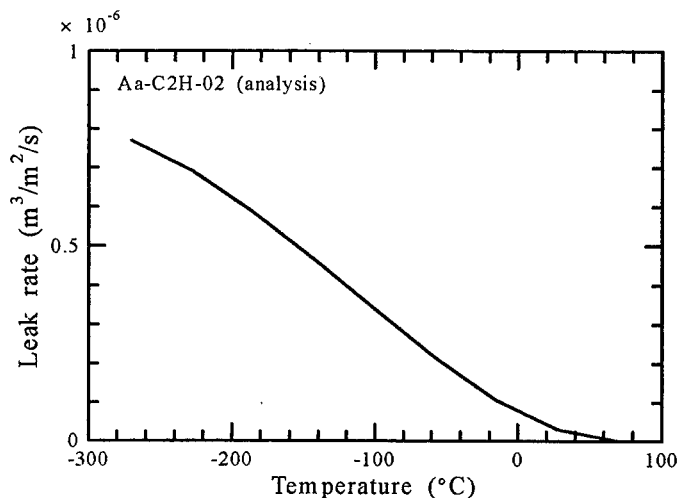


Figure 10 Calculated Leak Rate with no mechanical load at Low Temperature

leaks occur along the chain of the cracks and mechanical loads lead to increase of leak rates through the laminate. Numerical predictions approximately correspond with the measured leak rates at room temperature and indicate that enlargements of crack opening displacements raise leak rate through the laminate. Analytical results show that thermal contraction makes matrix cracks open and leak rate increases at low temperature. The leak analysis in this study based on a simple assumption between conductance and crack opening can be used to evaluate the influence of mechanical loads and thermal strains on propellant leak through CFRP laminates.

The leak rates measured in this experiment were comparable to the allowable permeation rate ( $1.6 \times 10^{-7} \sim 1.6 \times 10^{-6} \text{ m}^3/\text{m}^2/\text{s}$ ) in NASA SSTO (Single Stage To Orbit) project[3]. Therefore it is necessary to develop further investigations for propellant leak through CFRP laminates.

## References

1. C. Henaff-Gardin, M. C. Lafarie-Frenot and D. Gamby, 1996. "Doubly periodic matrix cracking in composite laminates Part 1: General in-plane loading," *Composite Structures*, Vol. 36, pp.113-130.
2. T. Aoki, T. Ishikawa, H. Kumazawa and Y. Morino, July 1999. "Mechanical Behavior of CF/Polymer Composite Laminates under Cryogenic Environment," *Proceedings of 12<sup>th</sup> International Conference on Composite Materials*, Paris, France.
3. M. J. Robinson, "Composite cryogenic propellant tank development," AIAA paper, AIAA-94-1375-CP.

# **Braided and FW Composites**

---

## **Mechanical Properties of Braided Composites with Traditional Braided Structures**

M. Tada, T. Osada, K. Kameo, A. Nakai, N. Takeda and H. Hamada

### **Abstract**

Braids provide excellent preform in reinforcing composite materials. The type of braided structure in use, however, has been depending simply on the availability of the braiding machine setting aside the mechanical functionality of the braid. Historical Japanese and Andean braids are highly complicated and show a variety of braiding structures where we may find mechanically optimized structures that may lead to the replacement of the present braids. This study aims to determine the mechanically optimized braiding structure. We prepared 8 ancient braids with different braided structures, which were determined by volume reconstruction method, and examined tensile and bending modulus and bending strength of the Aramid-Epoxy composite beams. The relation between the braided structures and mechanical properties are then discussed. We have defined new braided structure parameters, braided length reduction rate, reinforcement period and reinforcement frequency, capable of describing the braided structure in a quantitative manner. Good correlations were found between flexural properties and the braided structure parameters.

### **Introduction**

A wide variety of braided structure can be found in the historical braids of Japan and the Andes where exclusive braiding cultures were developed. On the contrary, braided structures available for the present composite materials have been restricted by the availability of the braiding machine and not been optimized in the mechanical functionality. Thus, an investigation into the historical braided structures may lead to an introduction of more rational braided structure in reinforcing composite materials with higher modulus, strength and functionality than those found in the present machine braids. This study thus begins with an investigation of the historical braided structures which will then be translated into the braiding machine processes. Historical braids with 8 different braiding structures were made, and the relation between braided structure and mechanical property was discussed.

---

M. Tada, T. Osada, K. Kameo and H. Hamada, Kyoto Institute of Technology, Matsugasaki, Sakyo-ku, Kyoto 606-8585, Japan

A. Nakai, N. Takeda, University of Tokyo, 4-6-1 Komaba, Meguro-ku, Tokyo 153-0041, Japan

## Experiments

### Specimens

Braids with 8 different braided structures were made by hand with Aramid fiber, Towaron HM7250d from AKUZO Co. The braided structures were each 4 of the round and the square braids selected among the historical braids. Appearance of these braids is shown in Figure 1 and the bundle path diagram of these braids is shown in Figure 2. The name of the historical round braids are Maru-genji, Maru-kara, Maru-Andes and Kongoh, and the name of square braids are Atsumimi-genji, Kaku-kongoh, Kaku-Andes and Kaku-Edo [1], while the alphabetical notation from A to H will be used as the name of the braids in this paper. All the braids were made of the same type of fiber with the same number of bundles (16 bundles) and in the same manufacturing condition to have a difference only in their structures.

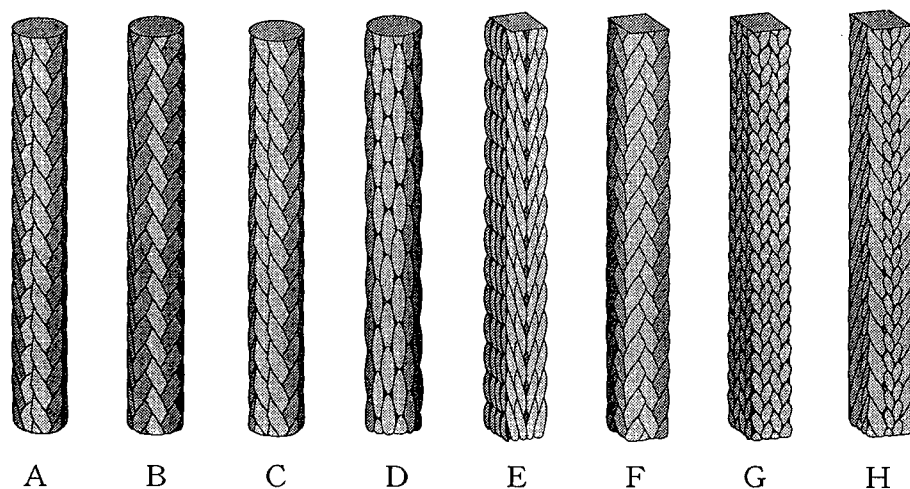


Figure 1 Braids with 8 Different Braided Structures

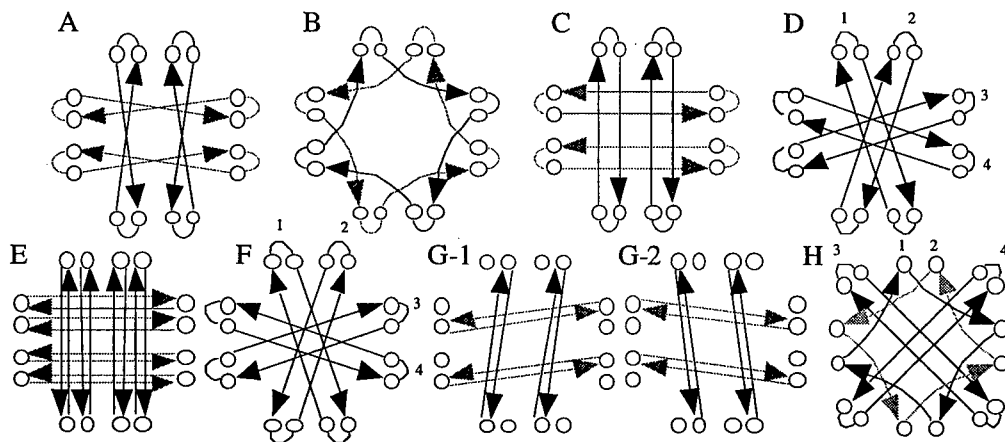


Figure 2 Bundle Path Diagrams of the Specimen Braids

Tensile test of the preform and four-point bending test of composites were performed. Specimens for tensile test were made to have a length of 200 mm in which a 50 mm of grip at both ends were molded with an epoxy resin, EPOMIK R140 from Mitsui Petro Chemical Co., in a round mold with a diameter of 13 mm. All the braids for the four-point bending test were put into a square mold with the epoxy resin at a pressure of 0.5 MPa and cured at a room temperature.

## Test Methods

### (1) 3-D volume reconstruction

To identify the braided structure, every 1mm of the cross section was polished out and photographed by a metallographical microscope. Slices of a cross-section of the braids were captured and the bundle orientations were visualized by the volume reconstruction technique in a computer.

### (2) Tensile test of the preform

The tensile test of the preform was executed with Instoron multi-functional tester 4206 type. The speed of the cross-head was 5 mm per minute. Because the initial length of the specimen may be given after loading and not before loading, the first loading was interrupted at 4 kN and returned to zero, then the second loading was applied up to the same load.

### (3) Four-point bending test of composites

The four-point bending test of composites was executed with Instoron multi-functional tester 4206 type. The speed of the cross-head was 5 mm per minute. The cross-sectional shape of the specimen was determined by that of the mold, 5 to 5.9 mm in width and 7 to 7.2 mm in height, so that the round braids with originally round cross-section took a rectangular cross-section.

## Results

### 3-D Volume Reconstruction

Slices of cross-section of the braids were captured and the bundle orientations were visualized by the volume reconstruction technique leading to an understanding of the clear difference in the braided structures. An example of the volume reconstruction of the square braid G is shown in Figure 3.

### Tensile Test of the Preform

At a load of 4 kN of the second tensile loading, a tangent of the load-displacement curve was obtained for specimens and the tensile modulus was calculated. Specimen A was unable to proceed the test because of the fracture of the grip. The tensile modulus of braids showed distinct difference according to their braided structures: specimen B showed highest and the rest were in an order of E, F, H, C, G and D.

### Four-Point Bending Test

Specimens were molded with resin as a beam and subjected to the four-point bending test. Common to all specimens, displacement was increased as stress increased and, after showing the maximum, stress decreased gradually. Because no apparent fracture was observed for all specimens under the subsequent large deformation, test was terminated. The bending modulus and the bending strength showed distinct difference according to their braided structures: specimen D showed the highest strength and the rest were in an order of G, E, C, F, H, B and A, while specimen G showed the highest bending modulus and the rest were in an order of F, B, D, C, E, H and A.

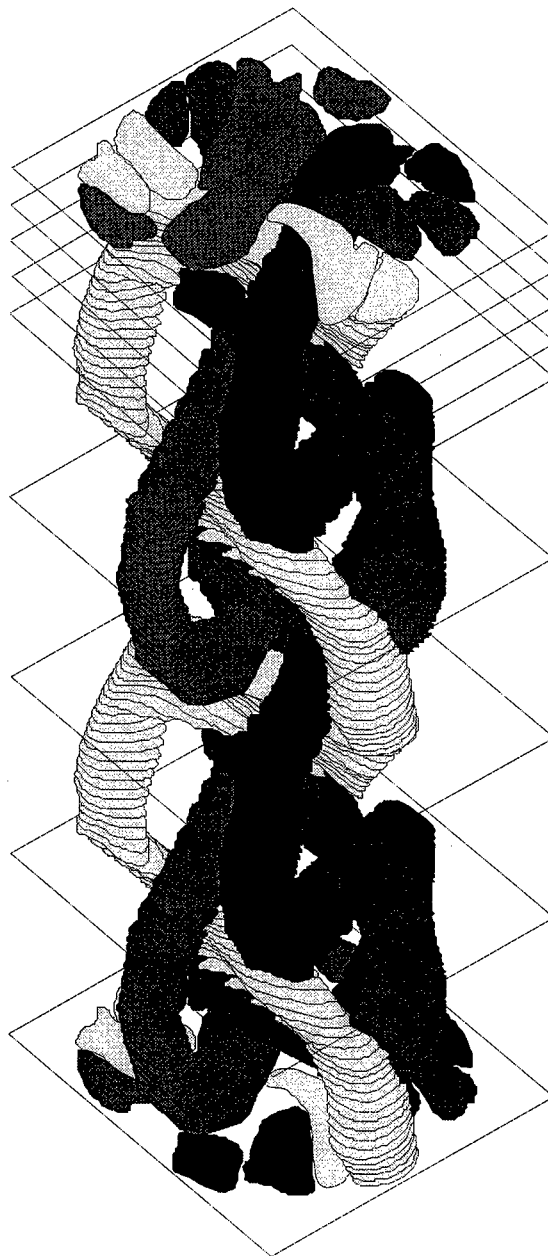


Figure 3 A 3D Reconstruction of Braid G

### Discussion

A 3-D structure of the braids was determined both by the bundle path diagram and the 3-D volume reconstruction techniques [2]. To define the numerical parameters

capable of describing the nature of the braided structure, the bundle arrangements were projected to the elevation and the cross sectional plane. Each 16 bundles in a braid were then treated as periodic functions as shown in Figure 4.

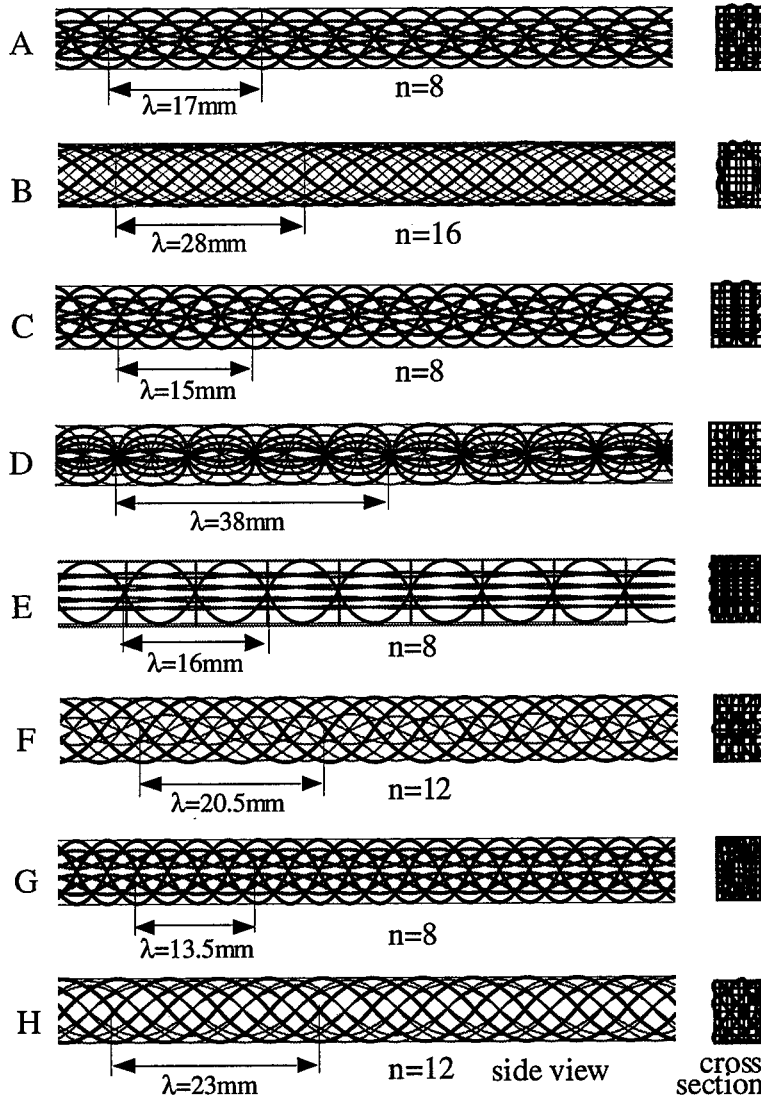


Figure 4 Periodic Structure of Braids

All the specimens were braided with the same volume of bundles. As being braided, the apparent length may be reduced in comparison with the original, straight length. Therefore we defined braided length reduction rate,  $L$ , a ratio of braided length with respect to the original length. The tensile modulus showed good correlation with the braided length reduction rate as shown in Figure 5.

Difference in period of the bundles was determined by the direct measurement of braided bundles before molding. We defined the reinforcement period,  $\lambda$ , similar to the period in a periodic function. Because the number of bundle traveling from the top to the bottom of a beam,  $n$ , may also have significant influence upon rigidity, we



defined the reinforcement frequency,  $\phi$ , as a product of  $n/N$  and the frequency, the inverse number of  $\lambda$ , as follows,

$$\phi = \frac{n}{N\lambda} \quad (1)$$

where  $N$  is the total number of bundle.

The reinforcement frequency  $\phi$  is a parameter describing the frequency of reinforcement in the bending direction.

The braided structure parameters, the bending modulus and the bending strength were determined for all types of braids and are shown in Table I. Because  $N$  was common to all types of braids, we excluded it in the calculation of  $\phi$ .

All the braids were molded in epoxy resin and formed as composite beams to have the same cross-sectional area. Therefore the difference in bending behaviors of the braids may be attributed to the difference in the braided structure.

The bending modulus showed good correlation with the reinforcement frequency as shown in Figure 6. This may be attributed to

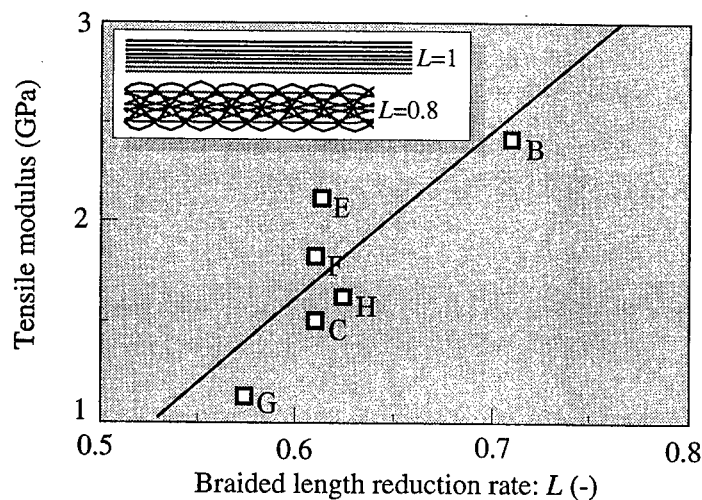


Figure 5 Tensile Modulus and Braided Length

Table I Result of Bending Test

	Bending strength (MPa)	Bending modulus (GPa)	Reinforcement period: $\lambda$ (mm)	Reinforcement frequency: $\phi$ $n/\lambda$
A	117.0	3.460	17.00	0.470
B	119.0	5.630	28.00	0.570
C	145.0	5.040	15.00	0.530
D	170.0	5.200	-	-
E	157.0	4.530	16.00	0.500
F	132.0	5.870	20.50	0.590
G	166.0	6.770	13.50	0.590
H	128.0	4.250	23.00	0.520

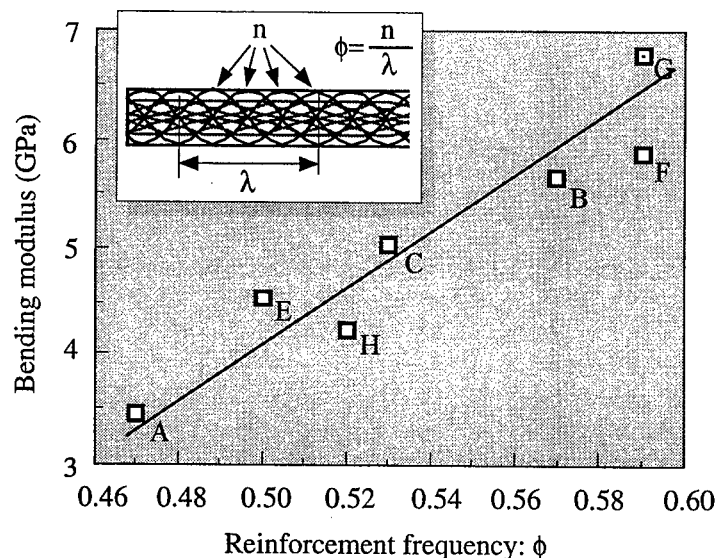


Figure 6 Bending Modulus and Reinforcement Frequency

the fact that the bending rigidity depends not only upon the frequency factors but also the number of bundles that reinforce the beam from the top to the bottom.

## Conclusions

To determine the braided structure optimized in mechanical functionality, we studied the relationship between mechanical properties of 8 different braids and their braided structures. As numerical parameters capable of describing the nature of braided structure, we defined the braided length reduction rate, the reinforcement period and the reinforcement frequency. The tensile modulus showed good correlation with the braided length reduction rate, and the reinforcement period and the reinforcement frequency were successfully accounted for the differences in the bending behaviors of the braids with different braided structures [3].

This study is characterized throughout by the translation of the traditional knowledge into the advanced composite technology with a special emphasis of developing mechanically optimized braiding structures, which may be of academic, industrial and cultural significance.

## References

1. M. Tada, 1998. "Japanese and Andean braids." *Proc. 4th Int. Symp. for Textile Composites*, Kyoto, O-41-1
2. M. Tada, T. Ueda, M. Sakaguti, H. Hamada, 1998. "Deformation behavior of Square Braided Fabrics." *Proc. 4th Int. Symp. for Textile Composites*, Kyoto, P-20-1
3. M. Tada, T. Osada, A. Nakai and H. Hamada, 1999. "Mechanical Properties of Braided Fabrics." *Proc. 6th Japan International SAMPE Symposium*, pp. 509-512

## **Bending Properties of Square Braided Composites with Middle-end-fibers**

Takahisa Ueda, Hiroyuki Hamada, Asami Nakai and Nobuo Takeda

### **Abstract**

The representative braided fabrics are classified into three kinds of braided fabrics, flat braided fabrics, tubular braided fabrics and square braided fabrics, according to the shape and the manufacturing technique. Especially, since the square braided fabric is characterized by that the fiber bundles are continuously braided each other to increase the thickness, it is expectable to prevent the delamination which has been the disadvantage of other laminated type fiber reinforced composites. In this study, the square braided composite material with middle-end-fibers was focused. Three-point bending test was conducted to examine the effects of preforming pressure, tension for middle-end-fiber, number of fiber bundle for middle-end-fiber and the location of the middle-end-fiber. By changing the above parameters, the dimension itself was changed and this means change in fiber volume fraction and structure of braided fabric. Therefore, the bending properties depended on both effects of increase by inserting middle-end-fiber and decreasing by increasing the thickness.

### **Introduction**

Fabric-reinforced textile composites potentially have better out-of-plane stiffness, strength, and toughness properties than tape laminates. Various forms of textile composites, which reinforced with woven, knitted and braided fabric preform, have been considered through much of the modern composite history. Especially braided fabric has a structure which exhibits the ability of long fiber bundle and the composite has excellent mechanical properties since the fiber bundle are continuously oriented through the fabric.

---

Takahisa Ueda, Nippon Pillar Packing Co., Ltd. Nonakaminami, Yodogawa-ku, Osaka, 532-0022, Japan  
Hiroyuki Hamada, Division of Advanced Fibro-Science, Graduate School, Kyoto Institute of Technology, Matugasaki, Sakyo-ku, Kyoto, 606-8585, Japan  
Asami Nakai, JSPS Research Fellow, Takeda Lab., Komaba Open Laboratories, The University of Tokyo, 4-6-1 Komaba, Meguro-ku, Tokyo, 153-8904, Japan  
Nobuo Takeda, Graduate School of Frontier Sciences, The University of Tokyo

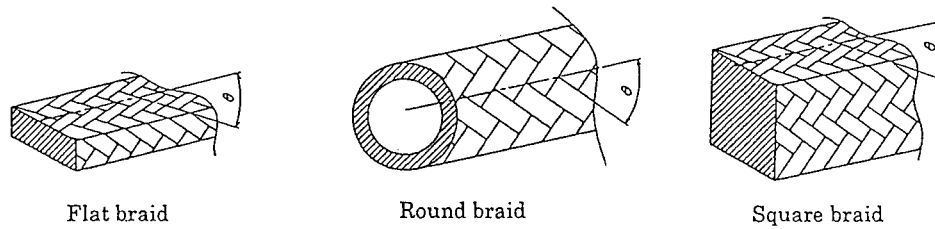


Figure 1 Schematic representation of braided fabric.

The representative braided fabrics are classified into three kinds of braided fabrics as shown in Fig.1, flat braided fabrics, tubular braided fabrics and square braided fabrics, according to the shape and the manufacturing technique. In the flat braided fabrics, fiber bundle path is "1" and the fabric is tape-shaped, and fiber bundle paths are "2" and the fabric is pipe-shaped in the tubular braided fabrics. In the case of square braided fabrics, fiber bundle paths are more than 2 and the fabric is square pillar-shaped. Especially, since the square braided fabric is characterized by that the fiber bundles are continuously braided each other to increase the thickness, it is expectable to prevent the delamination which has been the disadvantage of other laminated type fiber reinforced composites.

All of these braided fabrics can be made with additional (non braiding) fiber bundle system positioned within the intertwining fiber bundles. This additional fiber bundle is called to "middle-end-fiber". The middle-end-fiber can be inserted into braided fabric in the longitudinal direction, and the number and location can be chosen. It is possible to enhance the mechanical properties of braided composites by selecting the number and the location of the middle-end-fiber. This study has currently focused on the square braided composite material with middle-end-fibers. Three-point bending test was conducted to examine the effects of preforming pressure, tension for middle-end-fiber, number of fiber bundle for middle-end-fiber and the location of the middle-end-fiber.

### Square Braided Fabric

The cross section of fabricated square braided fabric is shown in Fig.2(a). The braiding process was made by 4 paths braiding machine with 36 careers. The square braided fabric is braided using the square braiding machine, while moving the spindle which holds the fiber bundle, and it is further taken upward at the same time, to fabricate a braided fabric with the desired braiding angle ( $\theta$ ).

The braiding machine and braiding mechanism used in this study are schematically shown in Fig.2(b). 36 pieces of spindles ③ (only one spindle is shown for each track in this drawing) on 4 tracks ②, pass through and move the intersecting point of each track alternately. On the other hand, this square braided fabric with middle-end-fiber was fabricated by supplying the fiber bundle ④ to the braiding point from the bobbin arranged at the lower side of braiding plate.

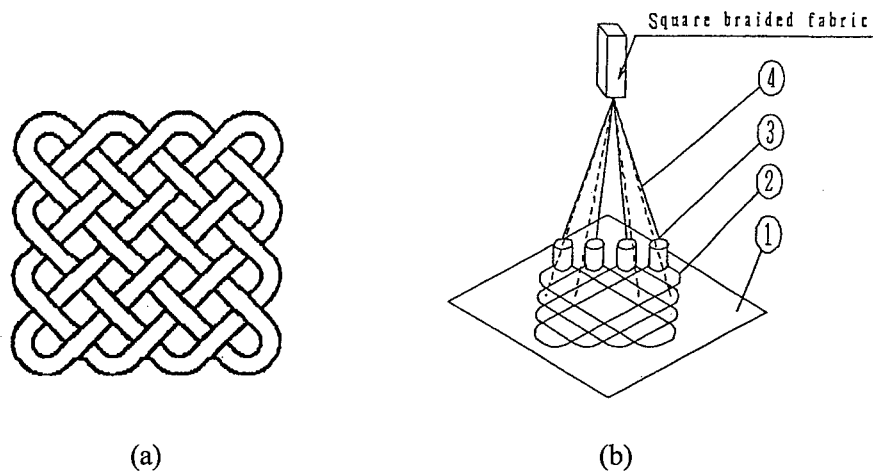


Fig.2 Schematic diagram of braiding path and braiding process

The fiber bundles used was Aramid fiber ( $12\ \mu\text{m}$ , 5000filaments, HM-1055, 8050dTex, AKZO), the resin used was Epoxy resin (EPOMIK R-140, Mitsui Petrochemical Industry Co.) and the curing agent used was Polyamide-amine (Q655, Mitsui Petrochemical Industry Co.). The braided fabric was fitted to the die after impregnating it in resin, to execute the 24-hour room temperature hardening under pressurized condition. It was taken out of die, thereafter, and was hardened in the electric oven at  $100^{\circ}\text{C}$  for 1 hours. The square-shape test piece; width of 10 mm, thickness of approx. 5 – 10 mm and length of 250 mm, was prepared.

Table 1 shows the types of specimens investigated in this study. Two different pre-forming pressure was adopted, 1.47 MPa and 2.94 MPa. Location of middle-end-fiber (Position A, B are indicated in Fig. 3) and number of fiber bundle for 1 middle-end-fiber were changed, 0, 1, 2, 3 fiber bundles. For a specimen, 40N of tension was applied to middle-end-fiber during molding process and effects of tension for middle-end-fiber were investigated.

Table 1 Types of specimen

No.	Fabrication condition			
	Proforming pressure MPa	Middle-end-fiber		Tension for m.e.f(N)
1	1.47	—	0	0
2		A	1	
3			1	
4			2	
5			3	0
6		B	1	
7			2	
8			3	
9	2.94	—	0	0
10		A	1	
11			2	
12			3	
13		B	1	
14			2	
15			3	

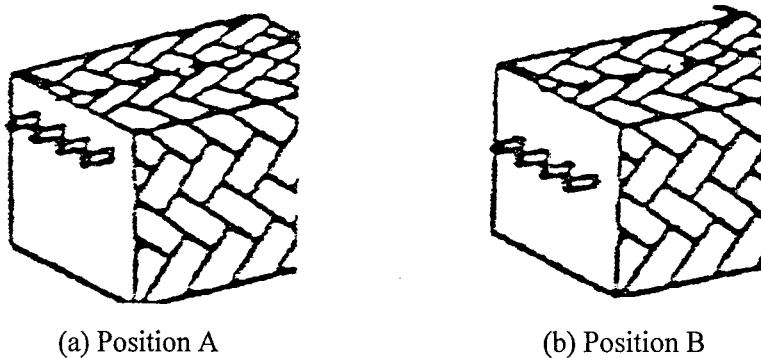
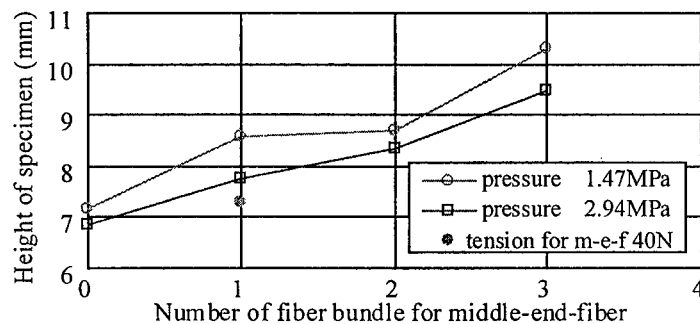


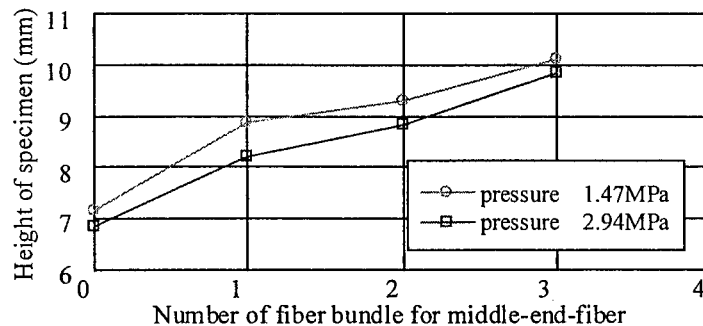
Figure 3 Location of middle-end-fiber

### Experimental Results

Figure 4(a)(b) shows relation between height of specimen and number of fiber bundle for middle-end-fiber. Figure 4(a) shows the results in case that the middle-end-fibers are inserted position A and Fig.4(b) shows in the case of position B. In that molding system, the width of specimen was bounded by molding die, so that change in height means change in fiber volume fraction and structure of braided fabric. For both position A and B, the height of specimen increased with increase in number of fiber bundle for middle-end-fiber and decreased with increase in preforming pressure. In case that the 40N of tension was applied to middle-end-fiber during molding, the height of specimen lower than that without tension.



(a)Position A

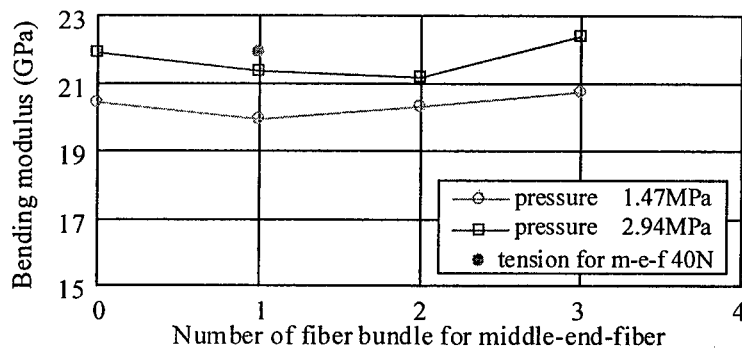


(b)Position B

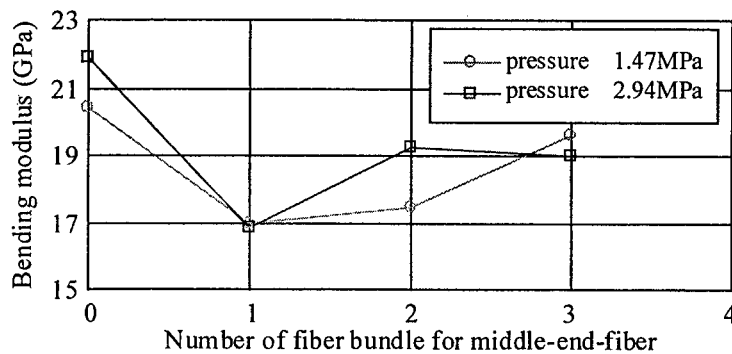
Figure 4 Relation between height of specimen and number of fiber bundle.

Figure 5 (a)(b) shows relation between bending modulus and number of fiber bundle for middle-end-fiber. Figure 5(a) shows the results in case that the middle-end-fibers are inserted position A and Fig.5(b) shows in the case of position B. For position A, there is no improvement of modulus by inserting middle-end-fiber and increasing number of fiber bundle for middle-end-fiber. It is considered that, the modulus is improved by inserting middle-end-fiber and increasing number of fiber bundle but the modulus is decreased by increasing thickness of specimen, consequently the modulus have no improvement apparently. For position B, it is considered that, the modulus is slightly improved by inserting middle-end-fiber, because the inserted position is close to the neutral axis. Therefore, the modulus was decreased by inserting middle-end-fiber with increase in the thickness.

Figure 6 (a)(b) shows relation between bending strength and number of fiber bundle for middle-end-fiber. Figure 6(a) shows the results in case that the middle-end-fibers are inserted position A and Fig.6(b) shows in the case of position B. For position A, the bending strength increased with increase in number of fiber bundle for middle-end-fiber. It is considered that, the final fracture occurred at the compressive side, so that the effects of inserting middle-end-fiber on bending strength are larger than that of change in thickness. For position B, the strength is slightly improved by inserting middle-end-fiber.

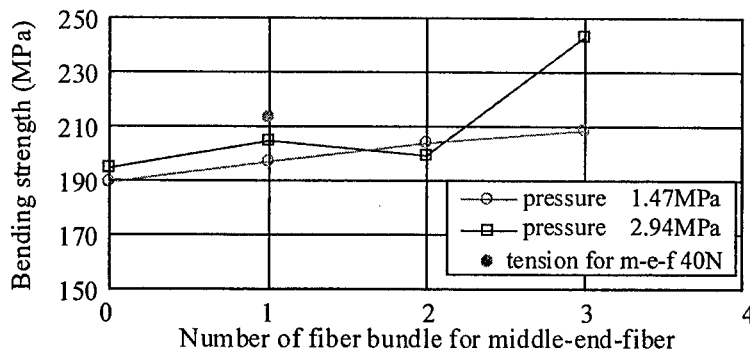


(a)Position A

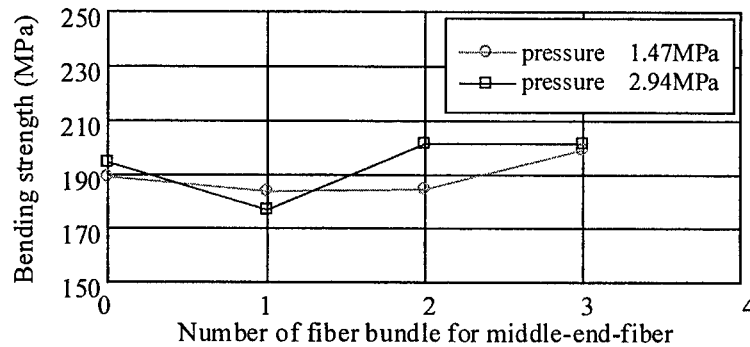


(b)Position B

Figure 5 Relation between bending modulus and number of fiber bundle.



(a) Position A



(b) Position B

Figure 6 Relation between bending strength and number of fiber bundle.

For both bending modulus and bending strength, the property was improved by applying the 40N of tension to middle-end-fiber during molding. From the observation of the braided composites, it was found that the inserted middle-end-fibers were a little undulated by the pressure in the braiding process and molding process. Therefore, the properties were improved by straightening middle-end-fiber with tension.

## Conclusion

In this study, the square braided composite material with middle-end-fibers was focused. Three-point bending test was conducted to examine the effects of preforming pressure, tension for middle-end-fiber, number of fiber bundle for middle-end-fiber and the location of the middle-end-fiber. By changing the above parameters, the dimension itself was changed and this means change in fiber volume fraction and structure of braided fabric. Therefore, considering the bending properties, both effects of increase by inserting middle-end-fiber and decreasing by increasing the thickness should be considered.



## **Micro-fracture Behavior of Flat Braided Composites with a Circular Hole**

Takeru Ohki, Asami Nakai, Hiroyuki Hamada and Nobuo Takeda

### **Abstract**

In this study, attention is paid to braided fabrics as the form of reinforcing fiber in composite materials and the influence of a circular hole on the mechanical properties of a flat braided composite is investigated. Two types of specimens were prepared; a flat braided bar with a braided hole which fiber bundle continuously oriented around the hole and with a machined hole. The effects of a circular hole on fracture behaviors in the braided flat bar was examined by static tensile test. Moreover, in order to evaluate fracture mechanism, micro damage observation and numerical analysis are carried out.

From the results of tensile test, the strength of the flat bar with a braided hole was larger than that of the one with the machined hole. Furthermore, difference of damage propagation in the two types of flat braided composites with a circular hole was confirmed by micro observation and factors that caused initial micro fracture obtained by experiments were identified by numerical approaches.

### **1. Introduction**

The characteristics of long-fiber-reinforced plastic as unidirectional reinforced material are high elasticity and strength in the direction of fiber orientation. However, when the composite materials are used as structural members, connecting them with other members is one of the important problems. Mechanically fastened joints connecting each member by pins or bolts have been well known as one of the simplest joint methods. However, it has been usually said that stress concentration around the hole is caused by the holes. In the case of member made from the homogeneous material, the failure mode and strength are decided due to only joint geometry. Whereas in heterogeneous material such as composite materials, in addition to the joint geometry the fiber orientation state around the hole greatly affects on the failure mode and joint strength. For example, when the hole is produced by machining after fabrication of the composite material, decrease in the strength is attribute to cutting the fiber around the hole. Therefore, particular

---

Takeru Ohki and Hiroyuki Hamada, Kyoto Institute of Technorogy, Matsugasaki, Sakyo-ku, Kyoto 606-8585, Japan

Asami Nakai and Nobuo Takeda, University of Tokyo, 4-6-1 Komaba, Megro-ku, Tokyo 153-0041, Japan

consideration is required in designing the connection parts of composite materials. Here, attention has been paid to braided fabrics as the form of reinforcing fiber in composite materials.

In this study, the influence of a circular hole on the mechanical properties of a flat braided composite is investigated. Two types of specimens were prepared. A flat braided bar with a braided hole which fiber bundle continuously oriented around the hole and with a machined hole. The effects of a circular hole on fracture behaviors in the braided flat bar were examined by static tensile test. Moreover, the micro fracture of each specimen during static tensile test was observed by optical microscope for the detail investigation of the difference caused by fabrication method for creating a circular hole. And, mechanical behavior that caused micro fracture obtained by experiments was identified by numerical approaches employing weaving structural model; continuity of the fiber bundle and precise fiber bundle orientation were considered.

## 2. Fabrication of Specimen and Experimental Equipment

Flat braided fabric was fabricated with glass fiber ( $17\ \mu\text{m}$ , 2000filaments, ER1150 F-165, Nippon Electric Glass Co.) using a 25-carrier braiding machine with the orientation angle of 30 degrees. Figure 1 shows the schematic diagrams of three types of braided flat bar. The specimens were made from flat braided fabric impregnated with epoxy resin (EPOMIK R-140, Mitsui Petrochemical Industry Co.) by hand lay up method. They were cured at room temperature for 24 hours and post curing was carried out at  $100^{\circ}\text{C}$  for 2 hours. The braided hole (symbol "BH") was fabricated by inserting a Teflon pin at the center of the width direction during the braiding process. After curing the specimen, the Teflon pin was removed. In BH specimen, the glass fibers are continuously oriented around the hole as illustrated in Fig.1. On the other hand, the machined hole (symbol "MH") was made by drilling, so that the glass fibers are cut at the rim of the hole in MH specimen.

Figure 2 shows geometric shape and size of specimen. The regular braided flat bar (symbol "F") is same size of specimen as shown in Fig.2. The fiber volume fraction was 45% in these specimens. In the static tensile test, tensile load was applied by an Instron Universal Testing Instrument (Type 4206) with a cross head speed of 1 mm/min. at room temperature.

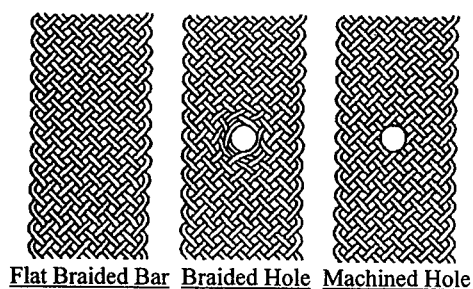


Figure 1 Types of flat braided composite

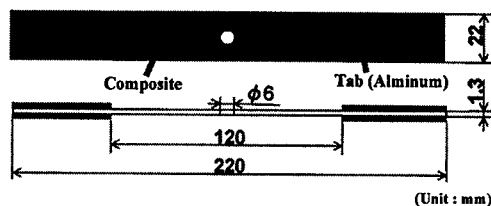


Figure 2 Geometric shape and size

### 3. Results of Static Tensile Test

Figure 3 shows load-displacement curves in the case of the "BH", "MH" and "F" specimens. The displacement was obtained by movement of the cross head of the machine. Although maximum load of MH specimen is 36% lower than that of F specimen, that of BH specimen is no more than 17% lower.

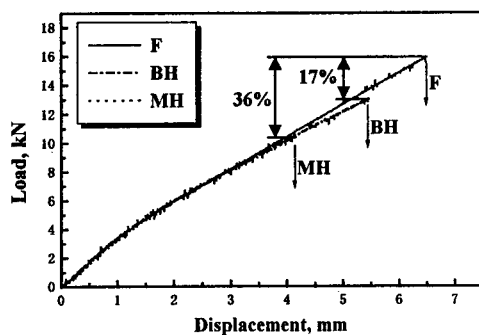


Figure 3 Load-displacement curves of F, BH and MH

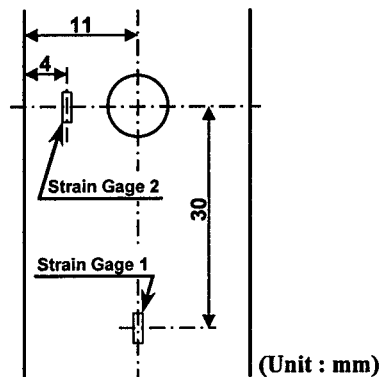


Figure 4 Location of strain gage

For the study of detail deformation behavior, two strain gages were put on the away from a hole (strain gage 1) and the side of a hole (strain gage 2) as shown in Fig.4. Figure 5 shows load-strain curves obtained from strain gage 1 and 2 of the MH and BH specimens.

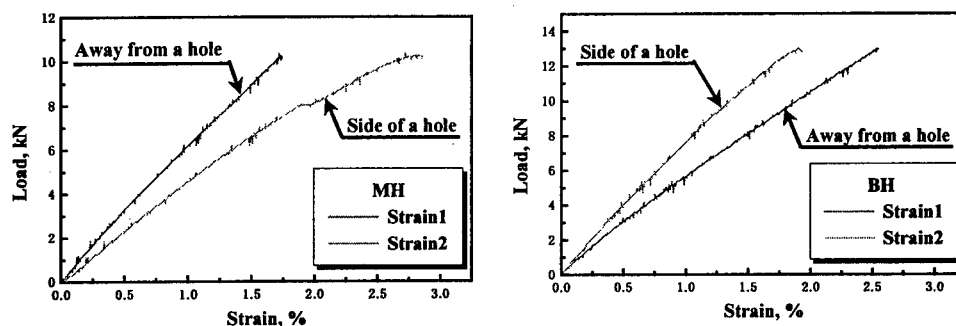


Figure 5 Load-strain curves of BH and MH

In MH specimen, value of strain gage 2 was larger than that of strain gage 1 from initial loading to final fracture. On the other hand, the value of strain gage 2 is continually lower than that of strain gage 1 in the BH specimen.

Figure 6 shows fracture aspects of BH and MH specimens after static tensile test. In the BH specimen, the crack occurred from the edge of specimen and the final fracture did not occur at the hole region. Therefore, in most specimens, a circular hole existed after final fracture as shown in Fig.6. In the MH specimen, the crack occurred at the rim of the circular hole and the specimen was broken at the side of the

hole. The fiber bundle around the circular hole was cut in the MH specimen, whereas in the BH specimen, the continuity of the fiber bundle around the hole is kept because a spacer was used at the fabrication of the hole. In addition to that, the fiber volume fraction of the BH specimen becomes high on both sides of the hole. Accordingly, it is considered that the BH specimen was not broken at the side of the hole, therefore, due to a difference in fracture form, the strength increased.

Moreover, when a tensile load is applied to the flat braided composite, the whitening occurs in the process of deformation. In F specimen, this whitening phenomenon was uniformly observed on the whole specimen and it appeared especially strong at the cross part of fiber bundle. However, in the specimens with circular holes such as BH and MH specimen, the whitening phenomenon is initiated at an angle about 45 degrees from the longitudinal direction around the circular holes. In BH specimen, then the whitening propagates in the longitudinal direction and a great deal of whitening appears at some distance from the circular hole. On the other hand, the whitening phenomenon concentrates around the circular hole in MH specimen. Although the geometric shapes were equal for both of BH and MH specimens, the above-mentioned differences were indicated by stress-strain curves and the specimens showed different fracture aspects.

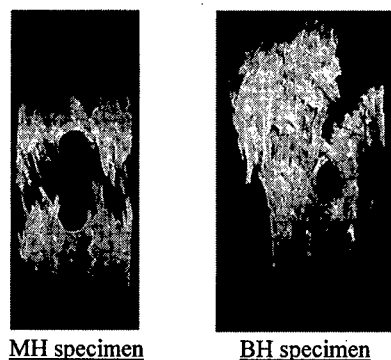


Figure 6 Frature aspects after tensile tests

### 5. Micro observation by Optical Microscope

For explication of difference between BH and MH specimen at micro damage behavior caused by the fabrication method of specimen with a circular hole, the inside of specimen was observed by optical micro scope during static tensile loading.

Figure 7 shows micro damage at side of a hole in each specimen. In MH specimen, matrix crack occurred from the rim of a hole along the direction of fiber orientation in initial fracture. After that, this crack propagated to edge of specimen in the perpendicular direction to longitudinal direction (loading direction) with debonding at the periphery. On the other hand, in BH specimen, matrix cracks occurred at side of a hole along the direction of fiber orientation. However, these matrix crack were at the boundary of fiber bundles with debonding, so that continuously orientated fiber bundle had shifted to the center of a circular hole. Accordingly, as observed in MH specimen, the crack, which occurred at the side of a hole, did not propagate to edge of specimen in the perpendicular direction to

longitudinal direction. Furthermore, in distinction from MH specimen, a lot of fiber fractures were confirmed at the inside of debonding around matrix crack. Consequently, the damage depends on properties of interface between fiber and matrix resin in the type of MH specimen, on the other hand, in the type of BH specimen, it is considered that the damage depends on properties of fiber.

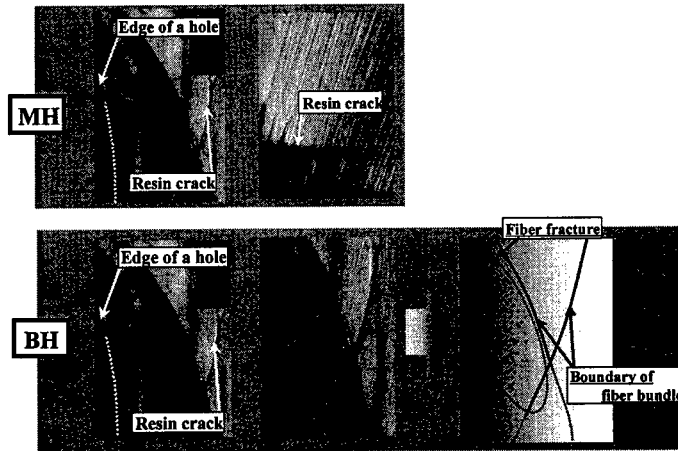


Figure 7 Micro fracture at the side of a hole by optical

## 6. Numerical Analysis

In order to investigate mechanical behavior that caused different micro fracture obtained by experiments, weaving structural model, which was considered continuity of fiber bundle and precise fiber bundle orientation, were employed. Numerical analysis was carried out within the limits of the elastic deformation and the stress components and distribution on each elements were investigated to clarify the factors which caused initial fracture.

The weaving structural model used in this study is shown in Fig.8. Fiber bundle impregnated with resin, cross resin at fiber crossing part and surface resin are represented on the model by connecting 3-D beam elements. Material constants for numerical analysis are shown in Table 1.

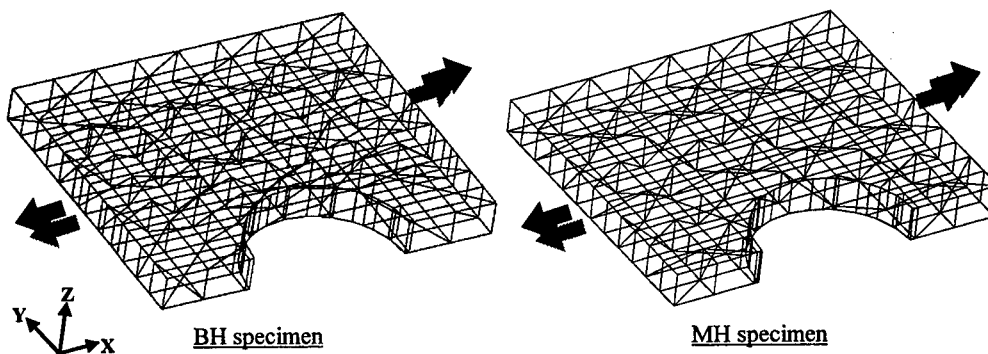


Figure 8 Numerical analysis model

Table 1 Material constants for numerical analysis

	Elastic modulus (GPa)	Poisson's ratio
Fiber bundle element	44.5	0.35
Resin element	2.6	0.35

Figure 9 shows deformation state of finite element division model for BH and MH specimen. The deformation at edge of a hole in the width direction in BH specimen is larger than that in MH specimen. It is considered that finite element model used in this study is suitable for the expression of mechanical behavior with different fiber bundle orientation caused by fabrication method for creating a circular hole, because difference of deformation as shown in this numerical approach had been indicated at the aspects during static tensile tests.

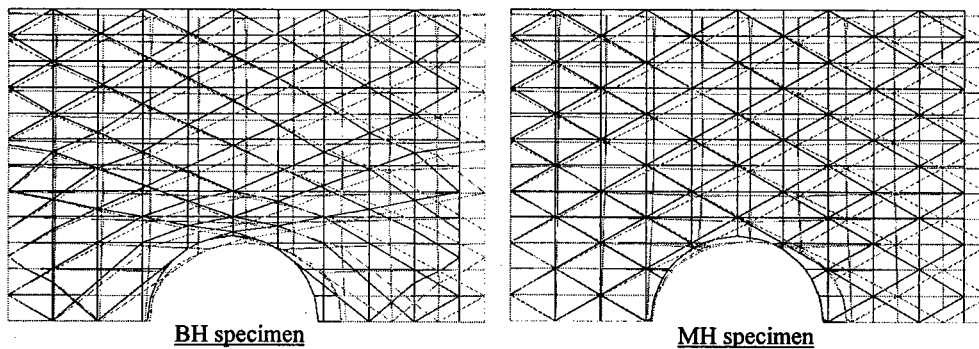


Figure 9 Deformation of finite element division

Next, the stress components and distribution on each elements were investigated. Figure 10 shows normal stress on surface resin elements in longitudinal direction at the side of hole. Here, the fracture of surface resin elements in longitudinal direction corresponds to the matrix crack perpendicular to the loading direction. Normally, it is known that in the homogeneous materials, such as metal, the stress concentration occurs at the tip of notch and decreases with increasing the distance from the tip. In the case of MH, the same tendency was obtained and high stress generated on surface resin at edge of hole, whereas in the case of BH the normal stress was constant regardless of distance from edge of hole.

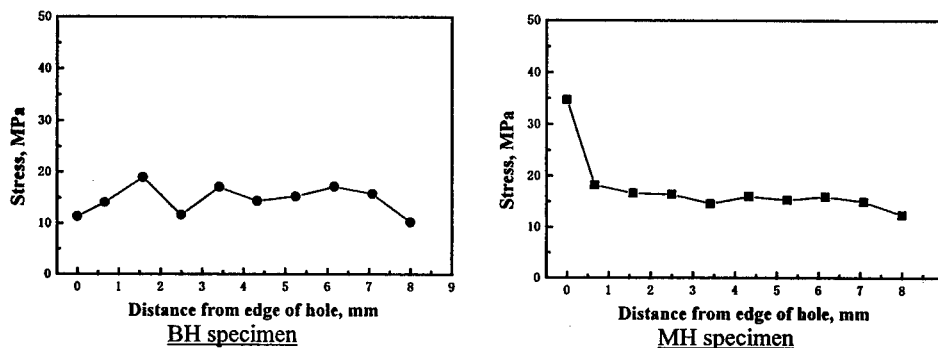


Figure 10 Normal stress of surface resin element at side of a hole

Axial stress on fiber bundle elements that oriented at the side of hole is shown in Fig.11. In the case of MH, the axial stress was constant regardless of distance from edge of hole, while in the case of BH the axial stress was concentrated on the fiber bundle near the edge of hole.

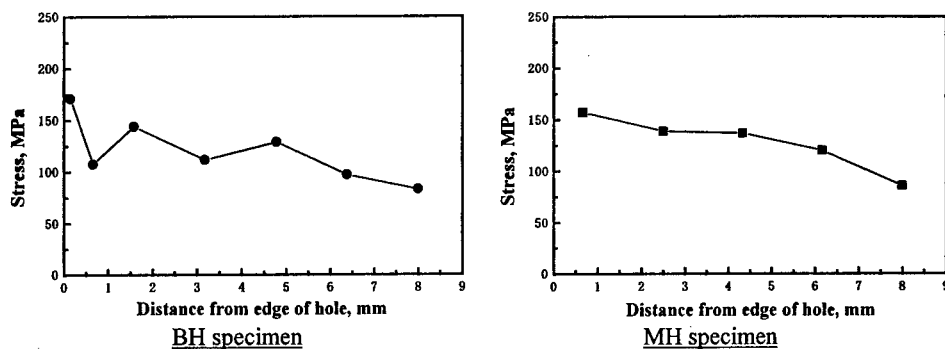


Figure 11 Normal stress of fiber element at the side of a hole

Consequently, mechanical behaviors, which lead to micro fracture observed at the side of a hole by optical microscope as matrix crack and debonding in MH specimen and fiber fracture in BH specimen, is indicated by numerical approach.

## 7. Conclusion

Two types of flat braided composite with circular hole were fabricated. One was a specimen with a braided hole obtained by arranging the braiding fiber bundle around a circular hole using flat braided fabrics (BH specimen), another was a specimen with a machined hole obtained by mechanical processing (MH specimen). In order to study mechanical properties, static tensile test was carried out. Moreover different fracture mechanism caused by fabrication method creating a circular hole was confirmed by micro fracture observation by optical microscope and numerical analysis using weaving structural model.

From the result of static tensile tests, BH specimen showed superior mechanical property MH specimen. And, it was observed that damage at MH specimen depend on the interface between fiber and resin and was confirmed to concentrate around a hole. Whereas, in BH specimen, it was observed that damage depends on continuously oriented fiber in the longitudinal direction. Furthermore, mechanical behavior, which provide different micro damage caused by fabrication method of creating a circular hole, was identified by the consideration of stress distribution at each element; surface resin and oriented fiber bundle elements, on numerical approach using weaving structural model.

Consequently, it is considered that a performance of the reinforcing fiber is properly works at the composite with a circular hole by application of braiding technique.

## **Analysis of Filament-Wound Sandwich Pipe Under Internal Pressure**

M.Xia, K.Kemmochi and H.Takayanagi

### **Abstract**

Using the classical laminated plate theory, a computer model has been developed to investigate stresses and strains of thick-walled sandwich pipes under internal pressure. The analysis is based on treating typical sandwich pipes that are three-dimensional, cylindrical, and orthotropic. The computer model conducts stress and strain analysis of sandwich pipe with different winding angles. The optimum winding angles have been found to be in the range of 60°.

### **Introduction**

In recent years, attention to thick-walled composite pipes has been continuously increased in several industrial areas, including aerospace, vehicles civil engineering and so on. As filament-wound pipes made of fiber-reinforced plastics have many potential advantages over pipes made from conventional materials, a number of investigations to characterize failure mechanisms of filament-wound pipes have been conducted.

Most previous studies on cylindrical fiber-reinforced composite structures have focused on thin-walled cylindrical shells. However, only limited studies have been published dealing with thick-walled cylindrical pipe behaviors. Roy [1] presented a thermal stress analysis of a thick laminated ring assumed to be cylindrically orthotropic. The analysis was based on treating the ring with orthotropic materials in the state of plane stress in the hoop and axial ( $\theta$ - $r$ ) plane. Ben [2] has reported an accurate, finite-cylindrical element method to obtain thermal stresses and the deformation for thick-walled cylindrical pipes. In his work, the effects of thermal residual stresses on the design of thick-walled FRP cylindrical pipes were discussed. Ben did not consider axial loading of cylinders with closed ends in his analyses of cylindrical pipes under internal pressure. Kitao and Akiyama [3] have

---

National Institute of Materials and Chemical Research,  
Agency of Industrial Science and Technology, MITI  
1-1, Higashi, Tsukuba, Ibaraki 305-8565, Japan



analyzed and evaluated the progress of failure in thick-walled FW pipes with different winding-angles under internal pressure.

In this study, we attempt to provide an analytical foundation for the investigation of stress and deformation in a filament-wound sandwich pipe under internal pressure. Considering the complicated material properties of the skin layers reinforced by alternate-ply composites, the analysis is based on treating typical sandwich pipes that are three-dimensional and orthotropic. The stress and strain analyses are carried out for the sandwich pipe with different winding angles.

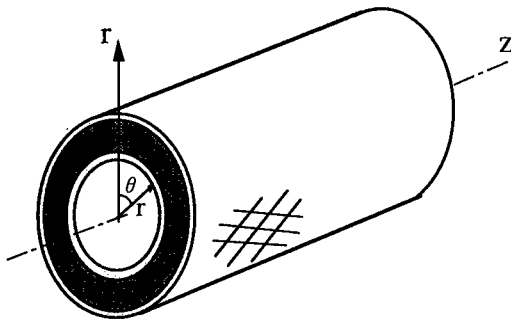


Fig. 1 Filament-wound sandwich pipe in cylindrical coordinates

### Stress Analysis

The sandwich pipe is created using non-reinforced materials for the core layer and alternate-ply materials for the skin layers. The alternate-ply skin layers are those in which the principal material directions of the adjacent layer have an opposite fiber orientation ( $\pm \theta$ ) with respect to the axial direction. Figure 1 shows the cylindrical coordinates for the sandwich pipe.

The equilibrium equation of stress of the  $i$ th layers is

$$\frac{d\sigma_r^{(k)}}{dr} + \frac{\sigma_r^{(k)} - \sigma_\theta^{(k)}}{r} = 0 \quad (1)$$

The radial and hoop strains,  $\epsilon_r^{(k)}$  and  $\epsilon_\theta^{(k)}$ , can be given in the radial displacement  $u_r^{(k)}$ ,

$$\epsilon_r^{(k)} = \frac{du_r^{(k)}}{dr} \quad \text{and} \quad \epsilon_\theta^{(k)} = \frac{u_r^{(k)}}{r} \quad (2)$$

The axial strains  $\epsilon_z^{(k)}$  of all layers are equal to a constant,  $\epsilon_0$ .

The stresses  $\sigma_r^{(k)}$ ,  $\sigma_\theta^{(k)}$ , and  $\sigma_z^{(k)}$  can be expressed in terms of strains

$$\begin{bmatrix} \sigma_r \\ \sigma_\theta \\ \sigma_z \end{bmatrix}^{(k)} = \begin{bmatrix} C_{11} & C_{12} & C_{13} \\ C_{12} & C_{22} & C_{23} \\ C_{13} & C_{23} & C_{33} \end{bmatrix}^{(k)} \begin{bmatrix} \epsilon_r \\ \epsilon_\theta \\ \epsilon_z \end{bmatrix}^{(k)} \quad (3)$$

where  $[C_{ij}]$  ( $i, j = 1, 2, 3$ ) is the off-axis stiffness constants, which can be calculated from the on-axis stiffness constants by using stiffness transformation matrix.

Substituting Eqn. (3) for the stresses in Eqn. (1) and using Eqn. (2), we get the differential equation of the radial displacement, given by

$$\frac{d^2 u_r^{(k)}}{dr^2} + \frac{1}{r} \frac{du_r^{(k)}}{dr} - \frac{C_{22}^{(k)}/C_{11}^{(k)}}{r^2} u_r^{(k)} = \frac{\alpha^{(k)} \epsilon_0}{r} \quad (4)$$

where  $\alpha^{(k)} = (C_{23}^{(k)} - C_{13}^{(k)})/C_{11}^{(k)}$ .

Based on the solution of Eqn. (4), the strain and the stress can be obtained from Eqns. (2) and (3).

The traction condition (pressure  $p_0$ ) at the inner surface and the traction-free condition at the outer surface are written as

$$\begin{aligned} \sigma_r^{(1)}(r_0) &= -p_0 \\ \sigma_r^{(n)}(r_a) &= 0 \end{aligned} \quad (5)$$

here,  $r_0$  and  $r_a$  are the inner and outer radii, respectively.

Continuity of transactions leads to

$$\begin{aligned} u_r^{(k)}(r_k) &= u_r^{(k+1)}(r_k) \\ \sigma_r^{(k)}(r_k) &= \sigma_r^{(k+1)}(r_k) \quad (k = 1, 2, \dots, n) \end{aligned} \quad (6)$$

For a cylinder with closed ends, the axial equilibrium is satisfied by the following relation

$$2\pi \sum_{k=1}^n \int_{r_{k-1}}^{r_k} \sigma_z^{(k)}(r) r dr = \pi r_0^2 p_0 \quad (7)$$

## Numerical Results and Discussion

The analysis of the sandwich pipe was carried out under the internal pressure of 0.1 GPa. The sandwich pipe has an inner radius of 50 mm, a core-layer thickness of 20 mm, and a 2 mm skin-layer thickness. In the present study, the inner and outer skin layers of the sandwich pipe have the same material that is based on a glass and epoxy composite (S2-glass/epoxy). The engineering constants of S2-glass/epoxy and the isotropic material property for the core layer are given in Table 1.

Netting analysis [4] is a simplified approach to the design of cylindrical filament-wound structures under internal pressure loading. Netting analysis assumes that all strength and stiffness properties are derived from the fibers alone

Table 1 Material properties of S2 and resin

Properties	S2-glass/epoxy	Resin (core)
$E_x$ (GPa)	48.3	5.0
$E_y$ (GPa)	19.8	5.0
$G_{zz}$ (GPa)	8.96	1.92
$\nu_{yx}$	0.27	0.3
$\nu_{zy}$	0.60	0.3

and no forces are transmitted by resin. Figure 2 shows the range of the optimum winding angles according to Netting analysis. The optimal winding angles, which are on the crossings of curves and a straight line, can be obtained from Fig. 2. The optimum winding angles for the inner and the outer layers are very similar, and the values have been shown in the range of around 60°.

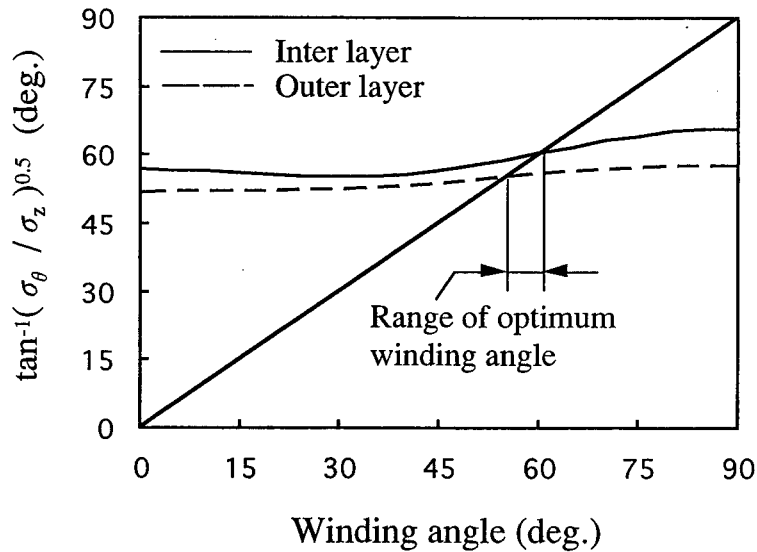


Fig. 2 Map of optimum winding angle

Figure 3 shows the axial, hoop, and radial stress distribution through the wall of the sandwich pipe with a 45°-winding angle. The values of stress distributions are larger at the inner radius than at the outer radius. The skin layers are subjected

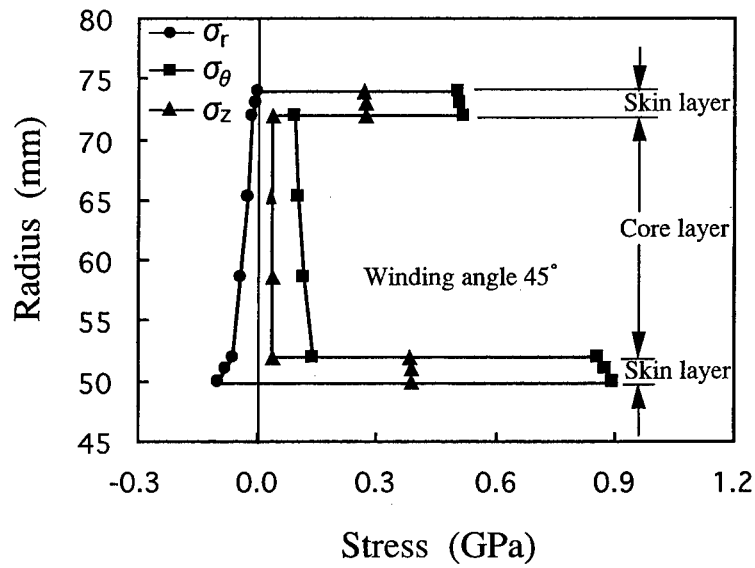


Fig. 3 Stress distributions within a sandwich pipe

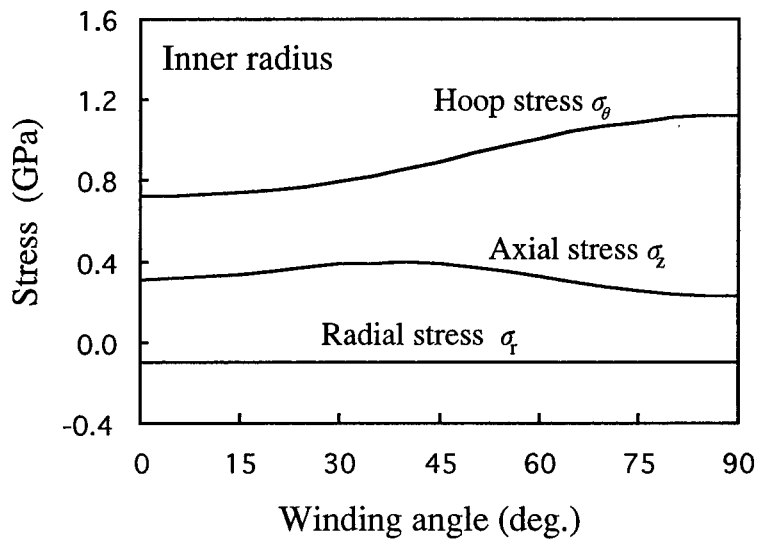


Fig. 4 Effect of the winding angle on hoop, axial and radial stress behaviors

to higher stresses compared to the core layer. Therefore, it is safe to predict that the first failure mode for the sandwich pipe will occur on the inner skin layer.

The hoop, axial and radial stress curves varying with the winding angles at the inner radius are shown in Fig. 4. The hoop and axial stresses for the thick-walled pipe vary with the winding angle. Both the hoop and the axis are subjected to tensile stresses. The hoop stress  $\sigma_\theta$  tends to increase while the axial stress  $\sigma_z$  to decrease when the winding angle is greater than  $35^\circ$ .

## Conclusions

An analytical procedure is developed to assess stresses and strains of the filament-wound sandwich pipe due to internal pressure. This procedure is based on the classical laminated plate theory. The sandwich pipe is considered in 3D analysis and in an orthotropic-material model. The analytical procedure developed here provides a basis for describing the elastic behavior of the filament-wound sandwich pipe.

The optimum winding angles are obtained from netting analysis, which gives a range of around  $60^\circ$ .

## References

- [1] K.,Roy, Ajit, 1991. "Response of thick laminated composite rings to thermal stress." *Comp. Struc.*, 20:125-139.
- [2] G.Ben, 1991. "Structural analyses of thick-walled cross-ply laminated FRP cylindrical shells." (in Japanese) *Trans. Jpn. Soc. Mech. Eng. Part A* 57:134-139.
- [3] K.Kitao, and H.Akiyama, 1994. "Failure of thick-wall filament wound plastic pipes under internal pressure." (in Japanese) *J. Soc. Mater. Sci., Japan*, 43:1134-1140.
- [4] T.T.Chiao, 1996. "Design for commercial filament winding." *SPE Journal*, 22(4):43-47.

# Textile Composites

---

## **In-Plane Strength of 3-D Orthogonal Interlocked Fabric Composite**

N. Watanabe, H. Mibayashi

### **Abstract**

This paper presents the experimental results of compressive behavior of Carbon Fiber/Epoxy 3-D orthogonal interlocked fabric composite. In this experiment, softening property is observed, and all the specimens failed in shearing mode. The average initial modulus is 58.1GPa, and the average strength is 546.7MPa which value is considerably high. In addition, the prediction of in-plane stiffness and ultimate compressive strength are carried out for the model by using 3-dimensional Finite Element Method based on homogenization method. The region where ultimate failure occurs can be predicted from observing the stress distributions. The analysis that includes the softening effect of compressed T300 can simulate the experimental stress-strain curve very well. This fact indicates the possibility that the modulus of load directional fiber tows become high because of the 3-D structural constraint.

### **Introduction**

Fiber reinforced composite materials have many advantages and are frequently used in wide variety of applications. However, most of them are 2-D laminated composites, and their problem is the very low interlaminar fracture toughness. One of the methods for improving the interlaminar toughness is to employ the through-the-thickness fibers in the composites. These 3-D composites offer many advantages, such as the nature of high interlaminar fracture toughness, notch insensitivity, excellent damage tolerance and great potential of manufacturing cost. As for interlaminar toughness of 3-D composites, one of authors has already conducted double cantilever beam (DCB) tests and the results actually show the great interlaminar toughness [1]. The existence of through-the-thickness fibers causes the reduction of fiber volume fraction of the in-plane tows, and it may become defect from the view of in-plane strength. Therefore, investigation of in-plane material properties of 3-D composites and trade-off study between in-plane and interlaminar properties are important. Nevertheless only a few experiments have been already executed in unidirectional tensile load [2, 3], or compressive load [3].

In this study, compressive tests are carried out to in-plane material proper-

---

N. Watanabe and H. Mibayashi, Department of Aerospace Engineering, Tokyo Metropolitan Institute of Technology, 6-6, Asahigaoka, Hino-shi, Tokyo 191-0065, JAPAN

ties. And by making a geometrical model by observing test specimens, FEM analysis based on the homogenization method including the thermal effect is conducted. From this analysis, elastic properties and stress distributions under uni-axial compressive loading are simulated.

## Experimental Procedure

Figure 1 shows schematic of the fiber structure of the 3-D orthogonal interlocked fabric composite tested here. This composite is made of CF/Epoxy, and manufactured in Toyota Automatic Loom Works, LTD. In-plane layers, X and Y tows, are stacked up 20 layers as  $[0^\circ/90^\circ]$ . Out of plane fibers, Z tows are placed with 3mm distance in the in-plane and those are turned back around fibers called "selvage yarn". X and Y tows are made of T300, and contain 12K (12,000 fibers). Z tow is made of 1K T900, selvage yarn is made of 2K T900, and matrix is epoxy 828. The thickness of the composite is nominally 5.96mm. Each fiber volume fraction of X, Y and Z tows are 24.3%, 24.7% and 0.5%, respectively, and total volume fraction is 49.5%. This was made by Resin Transfer Molding (RTM) technique, and the curing temperature in the manufacturing process was  $150^\circ\text{C}$ .

Six specimens were cut out of the composite plate, and the cutting direction was assumed to be X direction in this experiments. The dimension of specimens is  $104.5\text{mm} \times 25.4\text{mm} \times 5.96\text{mm}$ .

Two strain gauges are attached on both sides of each specimen for measuring longitudinal strain, and one strain gauge is put on in the lateral direction for Poisson's Ratio.

Each specimen was fixed in test apparatus to prevent buckling or brooming and the test is mainly according to ASTM-D695. Compressive test is conducted under a constant displacement rate of  $0.5\text{mm/min}$ .

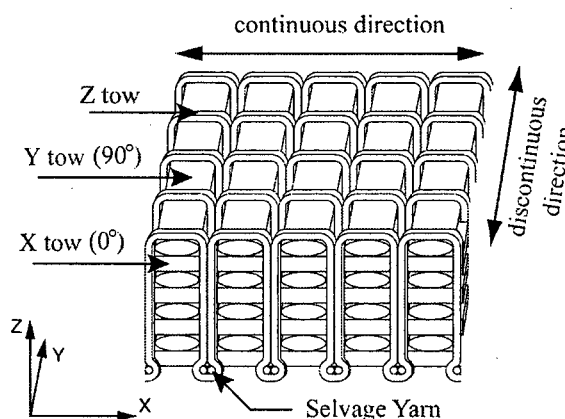


Figure 1 Schematic of the 3-D Composite

## Experimental Results

A typical stress-strain curve is shown in Fig. 2. Although a few slight disorders can be seen on the curve, it is almost linear. But the characteristic of softening is actually appearing so that it is curved a little as an upper convex. This specimen fails at about 1% strain and its strength is approximately 550MPa. Failure configuration is indicated in Fig. 3. Every specimen is fractured in shearing mode as shown in the figure. The crack angle is 42 degree from the compressive axis in this



specimen.

Initial modulus, strength, failure strain and Poisson's ratio obtained from the experiments are tabulated in Table I. The initial modulus is determined as the average value to 0.1% strain because of its disorder in the early stage of the test and the scatter in these value is considerably large. The minimum, maximum and average values of initial modulus are 54.09GPa, 61.97GPa and 58.1GPa, respectively. The maximum difference is 13.6%. As for the strength, the minimum value is 513.2MPa, the maximum is 573.7MPa and the average is 546.7MPa. Its difference is 11.1%. There seems to be no relation between initial modulus and strength properties because high initial modulus specimen does not indicate high strength and *vice versa*. But there is some relation can be seen between strength and failure strain, e.g. low strength specimens as C5 and C6 have low failure strain.

The minimum, the maximum and the average values of Poisson's ratio are 0.043, 0.081 and 0.062, respectively, and the maximum difference is 61.3%. This is quite large. The reason of this large difference is perhaps because of the existence of fibers in lateral to the load direction. Because of that, the lateral strain becomes very small so that tiny things such as the error of the strain gauge or the position of the strain gauge - *i.e.* the difference of strain on fibers or on resin rich region at the surface is obvious - become conspicuous.

Figure 4 indicates the change of tangent modulus in each specimen with the value of strain. From this figure, a tendency can be seen that the modulus decreases as the strain becomes large.

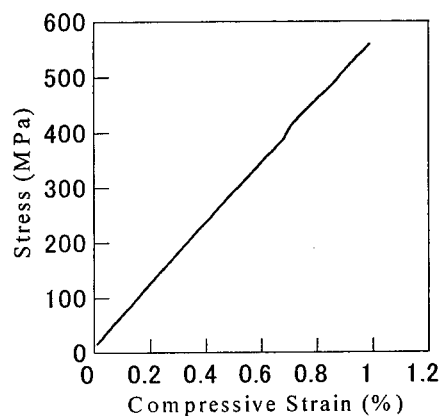


Figure 2 Typical Stress-Strain Curve

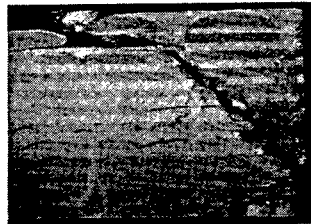


Figure 3 Failure of a Specimen

Table I Results of the Experiments

Specimen No.	Initial Modulus $E_x$ (GPa)	Strength (MPa)	Failure Strain (%)	Poisson's Ratio
C1	58.00	573.7	1.037	0.065
C2	59.17	559.1	0.988	0.043
C3	57.28	549.6	0.992	0.053
C4	54.09	567.6	1.097	0.064
C5	61.97	517.0	0.936	0.081
C6	58.04	513.2	0.961	0.064
Average	58.1	546.7	1.002	0.062

Two major reasons are considered for this phenomenon: One reason is the characteristic of softening of the fiber tow when compressive load is applied [4]. And the other reason is micro fracture that might occur in the composite with loading. But in our observation by using microscope, no such fractures can be found in the region where are far from the failure portion.

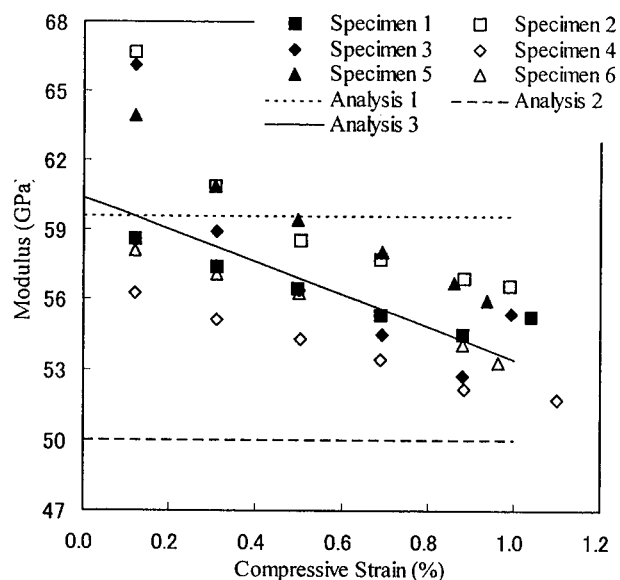


Figure 4 Modulus-Strain Relation of Experimental Results and Analyses

### Analysis

In our analysis, extended homogenization method with considering thermal effect has been adopted. A temperature drop during RTM process is assumed to be 130K. Figure 5 shows pictures of delamination that occurred around curved Z tows mainly due to because of residual thermal stress. Although high stress concentration around Z tow is recognized in the analysis, there are no cracks nor delamination except those regions. And the model is subjected to uni-axial compressive load, where loading direction is parallel to the X axis.

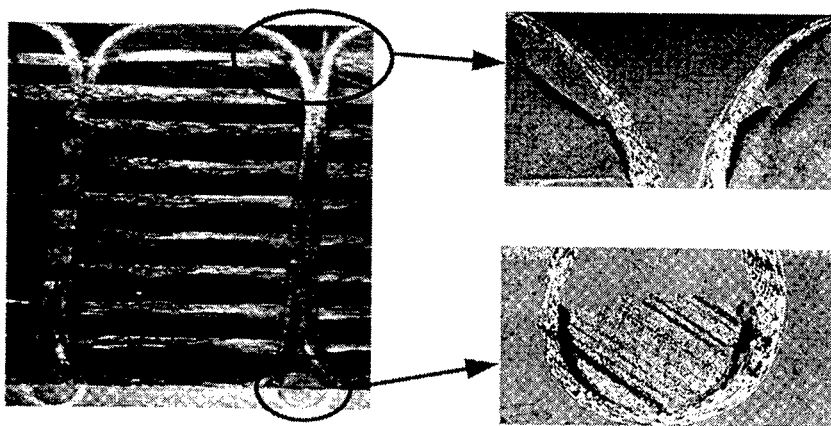


Figure 5 Delamination around a curved Z tow

### Analytical Model

The analytical model used in our analyses has 2,688 elements and 15,065 nodes. Its size is 3mm x 3mm x 0.596mm. The model contains one X tow, one Y tow, one Z tow and pure matrix regions. Material properties of each tow are calculated from the properties of T300, T900 and epoxy 828. The fiber volume fractions of X, Y and Z tows used in the analyses are 54.4%, 54.4% and 50.0%, respectively.

Three types of analyses are conducted by adopting the following assumption about the longitudinal modulus of T300,  $E_f$  in X tow.

Analysis 1 (A1):  $E_f=230\text{GPa}$ . It is the catalogued value.

Analysis 2 (A2):  $E_f=190\text{GPa}$ . It is the initial modulus of T300 in tensile load [5].

Analysis 3 (A3): Using the softening modulus shown in Fig. 6 which is decided to agree with the experimental average modulus-strain line described in Fig. 4.

The modulus of these analyses is shown in Fig. 4. In analyses A1 and A2, the modulus is a constant as shown by dotted line. And the oblique solid line which is used in A3 shows the average of experimental results. This is decided by taking average modulus and descend ratio of the six specimens at 0.5% strain, and then it is extended. The initial modulus of this line is 60.4GPa, and its descend ratio is 6.94GPa/%.

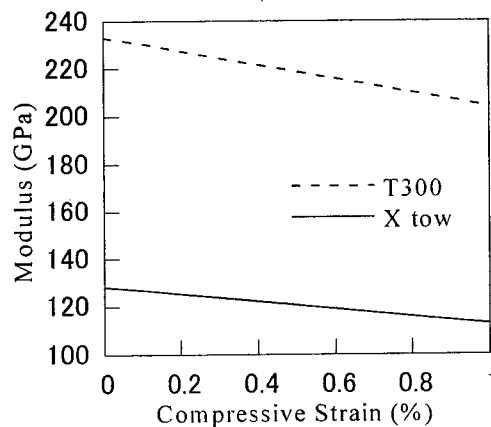


Figure 6 Modulus-Strain Curve of T300 and X tow used in our Analysis

### Analytical Results

Figure 7 shows stress-strain curves of these three analyses and experimental results. As for failure criterion, the maximum strain law is adopted, and the composite is assumed to fail at 1% strain in the analyses. The strength of analyses A1, A2 and A3 are 596.2MPa, 500.5MPa and 530.1MPa, respectively. The line of A1 is close to the experimental results in a low strain region. A2 does not agree with the experimental results from the beginning to the failure, although the modulus of 190GPa of fibers seems to be the most reasonable value without any experimental results. Contrarily A3 has the good agreement with the experimental result. The analytical results are shown in Table II. The initial modulus of A1 and A3 are slightly higher than its experimental value of 58.1GPa. Considering that the experimental value is decided as the average to 0.1% strain the actual initial modulus might become a little higher than this value. Therefore, these analytical values are reasonable. The initial modulus of

A2 is fairly lower by 13.8% than its experimental result. As for the strength, A1 is high by 9.1%, while A2 is low by 8.5%. On the other hand, A3 shows good agreement.  $\sigma_x$  stress distribution at failure load is shown in Fig. 8 as an example. Stress concentration region can be seen in X tow where is between Z tows, and lateral to the load direction. Therefore, it is predicted that the final failure should occur around there. The failure strength is 530.7MPa, and the maximum stress in X tow is 1310MPa.

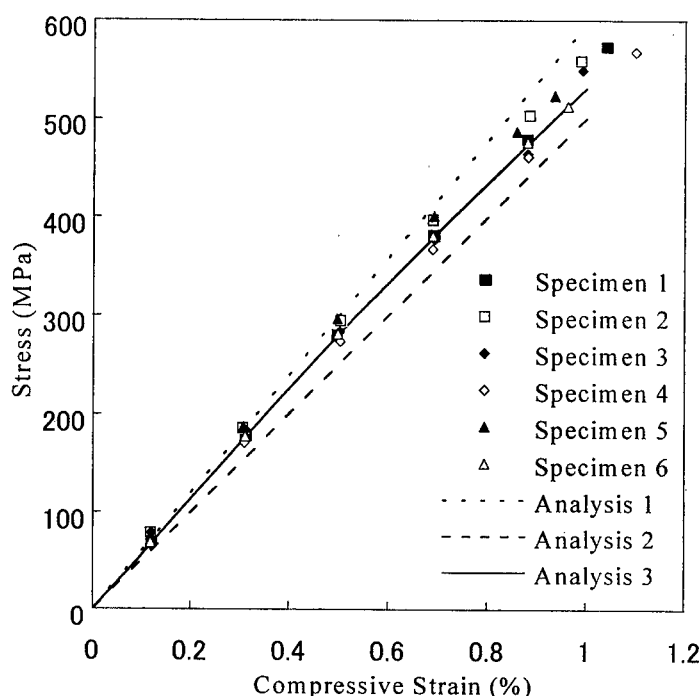


Figure 7 Stress-Strain Curve of the Analytical Results

Table II The Results of Analyses

Analysis No.	Initial Modulus $E_x$ (GPa)	Strength (MPa)	Failure Strain (%)
A1	59.6	596.2	1.0
A2	50.1	500.5	1.0
A3	60.3	530.7	1.0

## Discussion

Figure 6 shows modulus-strain curve of X directional fibers and tows adopted in Analysis A3. The initial modulus of T300 is 233.0GPa, and it is quite high comparing to its initial modulus of experiment in tensile is 190GPa.

By using 190GPa as the modulus of T300 and 3.43GPa as that of Matrix, the modulus of X tow with 54.4% of fiber volume fraction leads to 104.9GPa by the Rules of Mixture (ROM), and it is close to the value solved by FEM based on homogenization method. But initial modulus of X tows used in A3 - that shows good agreement with the experimental result - is 128.3GPa. As for the modulus and strength of unidirectional composite, the values of these in tensile can be calculated comparably easy only from the properties of fibers and matrix, because those values highly depend on mainly the property of the fiber. On the other hand, those values in compression cannot be calculated from only material properties of fibers and matrix easily, and it is determined from the complicated mutual effect between fibers and matrix. And because of the difficulty of the adequate compression test, there

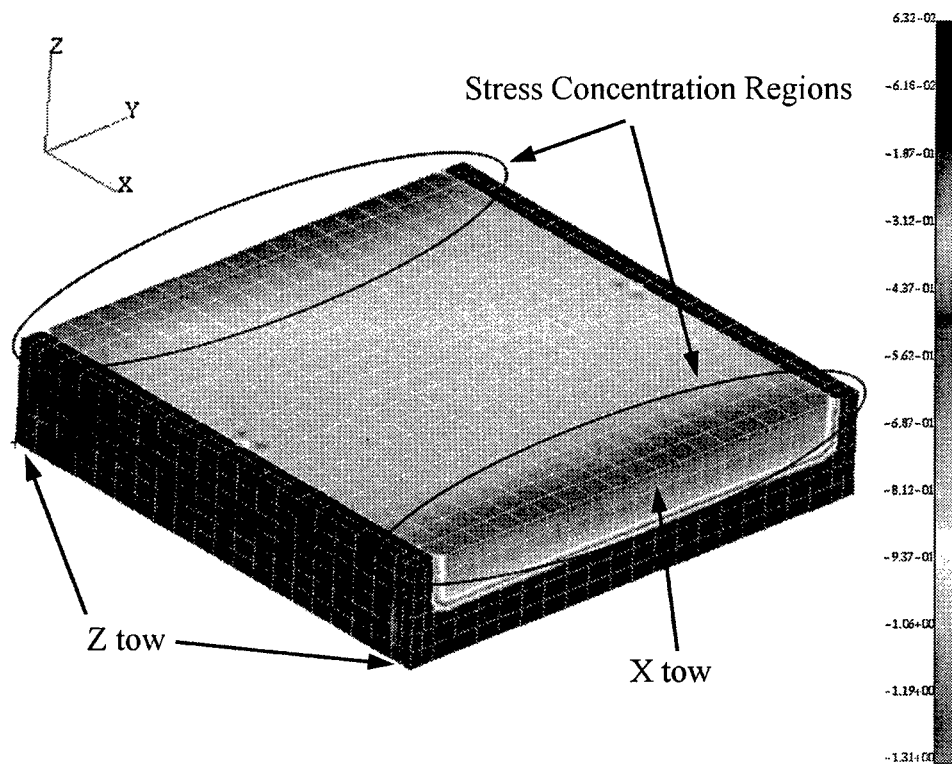


Figure 8  $\sigma_x$  Stress Distribution at Failure

are not enough data to determine these values. But the general tendency is already known, and it is almost the same as the case of tensile or generally lower than that. In this analysis the reasonable initial modulus of X tow is 128.3GPa, and it is 22.3% higher than the value of unidirectional composite with 54.4% of volume fraction at low strain, 104.9GPa. Even considering uncertain compressive modulus, this value is a little high. One possible reason is the structural constraint of 3-D fiber architecture. Because of the existence Y and Z tows, X tows are sandwiched between these tows, and lateral deflections are suppressed. This might become the reason for raising modulus of X tows in compression.

## Conclusion

The compressive test is carried out for the CF/Epoxy 3-D orthogonal interlocked fabric composite. Although the in-plane fiber volume fraction is lower than that of conventional 2-D laminate, it is proved to give high compressive strength of 546.7MPa and its initial modulus is 58.1GPa. All the specimens failed in shearing mode. 3-dimensional FEM analyses based on homogenization method is conducted and the region where ultimate failure occurs can be predicted from the fine stress distribution. The analysis that includes the softening effect of compressed T300 can

simulate the experimental stress-strain curve very well. This fact indicates the possibility that the modulus of load directional fiber tows become high because of the structural constraint, although more detailed experimental observation is required.

### Acknowledge

Authors appreciate Mr. Y. Yashui and R. Kamiya, Toyota Automatic Loom Works, Ltd., for construction of the composites used in the experiment. And authors highly indebted to Dr. T. Ishikawa, Mr. M. Matsushima and Y. Hayashi, Composite Structure Section, Airframe Division, National Aerospace Laboratory, for their great assistant to execute the experiment.

### References

1. Y. Tanzawa, N. Watanabe and T. Ishikawa, "Interlaminar fracture toughness of 3-D orthogonal interlocked fabric composite", *Composite science and Technology*, 59 (1999) 1261-1270
2. N. Watanabe, S. Oshiba and T. Ishikawa, "In-plane mechanical properties of CF/Epoxy 3-D orthogonal interlocked fabric composite", *ICCM-12*, Paris, France (1999)
3. B. N. Cox, M. S. Dadkhah, W. L. Morris and J. G. Flintoff, "Failure mechanisms of 3D woven composites in tension, compression, and bending", *Acta metall. mater.*, Vol. 42, No. 12, pp. 3967-3984 (1994)
4. J. E. Ashton, J. C. Halpin and P. H. Petit, *Primer on Composite Materials, Analysis*, Technomic, Westport, CT (1969)
5. T. Ishikawa, M. Matsushima, Y. Hayashi, "Longitudinal Material Nonlinear Properties of Unidirectional Carbon Composites", *Journal of the Japan Society for Composite Materials*, Vol. 12, No. 1, pp. 8-15 (1986)

## **Micro / Macro Analyses for Mechanical Properties of Textile Composites**

Asami Nakai, Hiroyuki Hamada and Nobuo Takeda

### **Abstract**

We have proposed micro / macro analyses procedure for simulating the mechanical behavior of textile composites in consideration of the structure parameters, interface properties and the resulted micro-fracture process. In this paper, the micro / macro analyses procedure is applied to the plain woven composites with different kinds of coupling agent and the stress-strain behaviors and fracture process are predicted. The present analysis method considering the continuity of fiber bundle, the weaving structures and the interfacial properties, could successfully predict the mechanical behaviors of the whole woven fabric composites.

### **Introduction**

The architecture of a fiber preform in textile composite is complex, so that the parameters controlling the mechanical properties are numerous, e.g. type of fiber bundles, fiber orientation angle, weaving structure, crimp ratio of fiber bundles, fiber volume fraction in the fiber bundle and the composite, and so on. Also, interface properties between fiber and matrix greatly affect the mechanical properties. These factors have the effect on micro fracture behaviors, i.e., debonding between fiber and matrix at interface, debonding at fiber crossing part, transverse crack, filament fracture. These micro fractures contribute to macro fracture behavior of composites.

We have proposed micro / macro analyses procedure for simulating the mechanical behavior of textile composites in consideration of the structure parameters, interface properties and the resulted micro-fracture process. In this paper, the micro / macro analyses procedure is applied to the plain woven composites with different kinds of coupling agent. The stress-strain behaviors and fracture process are predicted.

---

Asami Nakai, JSPS Research Fellow, Takeda Lab., Komaba Open Laboratories, The University of Tokyo, 4-6-1 Komaba, Meguro-ku, Tokyo, 153-8904, Japan  
Hiroyuki Hamada, Division of Advanced Fibro-Science, Graduate School, Kyoto Institute of Technology, Matugasaki, Sakyo-ku, Kyoto, 606-8585, Japan  
Nobuo Takeda, Graduate School of Frontier Sciences, The University of Tokyo

## Materials and Experiments

### Plain Woven Fabric Composites

Materials used in this study were E-glass plain woven fabric (WE18W; Nitto Boseki Co., Ltd.) as reinforcements and unsaturated vinyl ester resin (Repoxyl R806; Showa High Polymer) with 0.7 phr. methyl-ethyl-ketone (MEK) peroxide. Weaving densities of the fabric were 44 fiber bundles / 25 mm in the warp direction and 33 fiber bundles / 25 mm in the weft direction. Each fiber bundle consisted of 400 filaments with 9mm in diameter. Two kinds of coupling agents were used;  $\gamma$ -methacryloxypropyltrimethoxysilane (methacryl silane, designated as MS, A-174; Nippon Unicar Co.) and  $\gamma$ -Glycidoxypropyltrimethoxysilane (epoxy silane, designated as ES, A187, Nippon Unicar Co.). The aqueous solutions of silane coupling agents were acidified with acetic acid at pH 4.0. The concentration of silane coupling agents was 0.4 wt% for both coupling agents. The woven fabric was dipped into the aqueous solutions of the silane agents, which were subsequently squeezed between rollers and were dried for 10 min. at 110°C.

The laminates with ten plies of woven fabric were prepared by hand lay-up such that all warp strands were aligned in one direction, and were cured for 48 h at room temperature, followed by post cure for 3 h at 80°C and for 2 h at 150°C in an oven. Dimensions of the specimen were 2.0 mm in thickness, 130 mm in length, and 10 mm in width. FRP end-tabs were placed on the specimen and the gage length was 70mm.

### Experimental method

The fracture process was clarified by the replica observation at the edge surface. For the replica observation, the surface at one side of edge of the specimen was polished with diamond paste.

Tensile tests were performed using TENSILON UTM-I 500-W (Toyo Measuring Instruments Co., Ltd.) with cross-head speed of 0.5mm/min. During the tensile tests, the testing machine was periodically stopped and the polished edge surface of the specimen was replicated on a replica film (acetyl cellulose film) with methyl acetate as solvent. The replica film was then observed by optical microscopy.

### Experimental results

Elastic modulus of the composites was almost same for MS and ES specimens, whereas ultimate strength and strain of MS specimen (425MPa, 2.67%) were higher than those of ES specimen (408MPa, 2.43%).

Figure 1 shows the onset and growth of micro fractures in the edge surface of the MS specimen obtained by replica observation ((a)strain=0.4%, (b)0.6%, (c)1.2%). The first microscopic damage is transverse cracks in weft fiber bundles (Fig.1 (a)). As the tensile strain increased, the number of transverse cracks increased in the same weft fiber bundles (Fig.1 (b)). At the same time, near the transverse cracks (that is, fiber crossing part), filament fracture in warp fiber bundles was observed (Fig.1 (b)). A filament



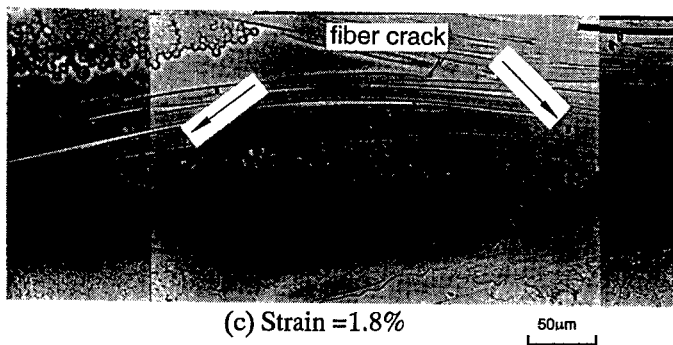
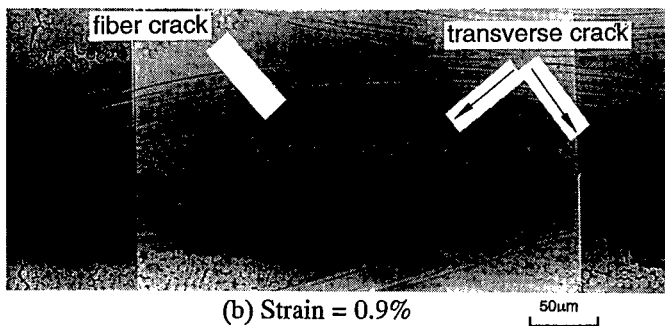
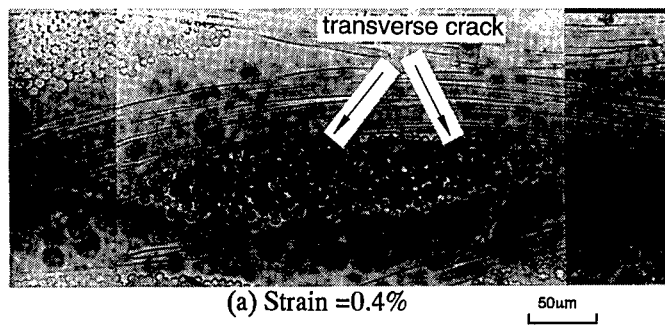


Figure 1 Damage process for tensile test.  
 (a) strain=0.4%, (b) strain=0.9%, (c) strain=1.8%

fracture did not cause the concentration of other filament fractures by stress concentration and the final fracture of the composites. Then, several filament fractures occurred in the same filaments and multiple filament fractures were observed (Fig.1 (c)). Finally, these transverse cracks and filament fractures developed into delamination between fiber bundles and debonding between filament and matrix in the fiber bundles, and then the final fracture occurred due to fracture of fiber bundles. The micro fracture process was same regardless of kinds of coupling agent, whereas the strain at which each micro fracture occurred and the quantities of each fracture were affected by the coupling agent.

Next, each micro fracture obtained by in-situ observation was quantified for (1) transverse cracks in weft fiber bundles, (2) filament fractures in warp fiber bundles, and (3) delaminations at the fiber crossing parts and effects of coupling agents were examined. For transverse cracks, initial fractured strain of MS specimen was higher (0.4%) than that of ES specimen (0.2%) and number of transverse cracks of MS specimen was smaller than that of ES specimen for each strain. We have classified fiber/matrix interface of FRP as shown in Fig.2; (1) Interface around a single fiber filament (class I ), (2) Interface inside of a fiber bundle (class II ), (3) Interface around a fiber bundle (class III ), and (4) Interface between laminas (class IV ). The difference in onset and growth of transverse cracks is caused by interfacial properties inside of a fiber bundle (class II ). Concerning filament fractures, the increasing rate of filament fractures with increasing strain for MS specimen was bigger than that of ES specimen, and final crack interval was smaller than that ES specimen. The behavior of filament fracture results from difference in interfacial properties around a single fiber filament (class I ). As to delaminations at the fiber crossing parts, the delamination was scarcely observed in MS specimens, and the quantity of delamination in ES specimen was much bigger than that of MS specimens. The difference in delamination behavior is caused by interfacial properties around a fiber bundle (class III ).

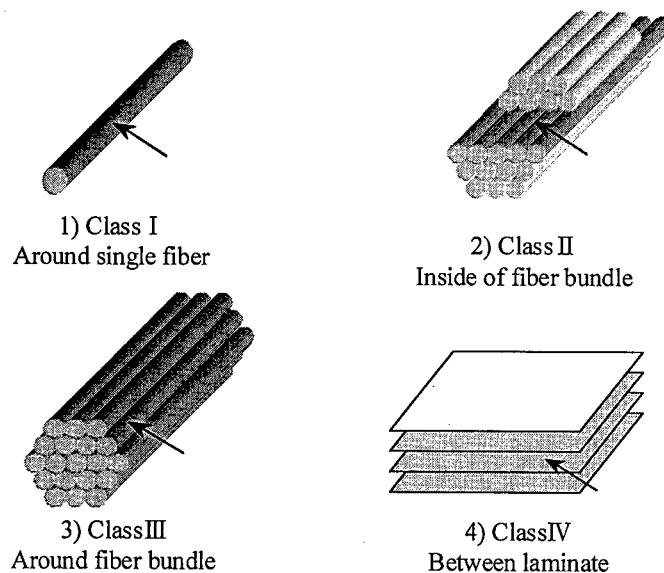


Figure 2 Classification of interface.

## Analysis

### Analytical procedure

We have proposed micro / macro analyses procedure for simulating the mechanical behavior of textile composites in consideration of the structure parameters, interface properties and the resulted micro-fracture process. Figure 3 shows multi-step modeling for mechanical properties of textile composites. Basically, results obtained from micro model are used in the analyses of macro model.

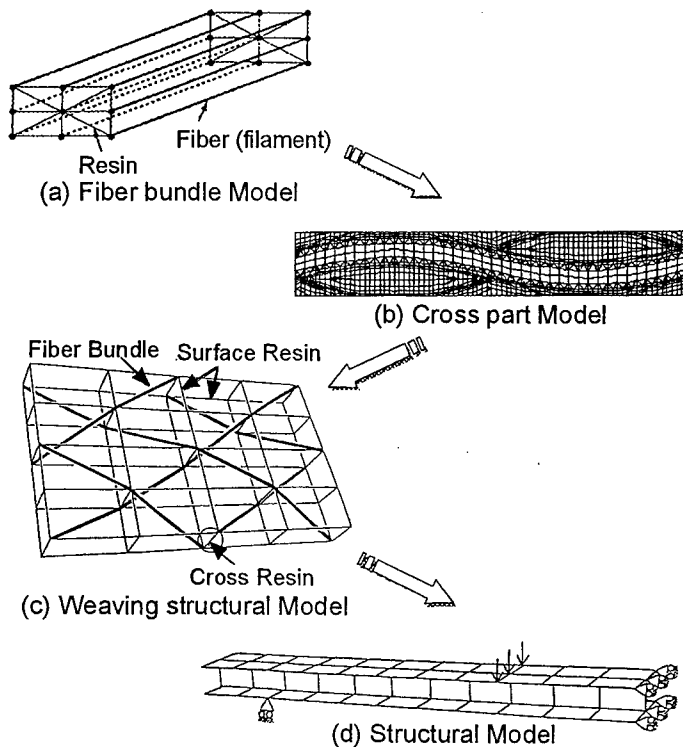


Figure 3 Multi-step modeling for mechanical properties of textile composites.

The present analysis takes into account difference in micro fractures of plain woven fabric composites due to difference in interfacial properties in the following way;

(1) The mechanical behavior of fiber bundles in flat braided composites is explained by the Curtin model (Fiber bundle model). According to the mechanical behavior of fiber bundles obtained by the Fiber bundle model, Young's modulus in fiber bundle elements of the Weaving structural model is reduced successively.

(2) The continuity of fiber bundles and precise weaving structures are represented by a finite element model with 3-D beam elements (Weaving structural model).

(3) Transverse cracks in weft fiber bundles are represented by considering the inter-phase elements inside fiber bundles in the above Weaving structural model.

#### Fiber bundle model

As mentioned above, the reduction of elastic modulus is caused by mainly the filament fractures. Therefore it is necessary to establish the model considering the filament fracture process. Naturally, the fiber strength should be treated as statistical quantities and expressed with the Weibull formulation. Curtin[1] proposed the UTS model for brittle matrix unidirectional composites with multiple matrix cracks.

We have used the model to estimate the reduction in elastic modulus of the fiber bundles. The present model considers that the load is sustained by shear stresses generated at the interface between filaments and matrix, when filaments are broken within the stress recovery length. The matrix yielding shear stress is used as the interfacial shear stress. The load that the matrix carries is neglected in the present analysis, since it is much lower than that by filaments.

The tangent elastic modulus of fiber bundle is represented as a function of strain and given by

$$E(\varepsilon) = \frac{d\sigma}{d\varepsilon} = E_f V_f \left\{ 1 - \frac{1}{2} (m+2) \left( \frac{\varepsilon E_f}{\sigma_c} \right)^{m+1} \right\} \quad (1)$$

In equation (1), the second term in a bracket is expressed to be a damage quantity by multiple filament fractures.

For the material constants, Zhao et al. reported the experimental and theoretical results of filament strengths by means of single fiber composite tests[2]. The results mentioned that the representative strength  $\sigma_0$  of glass filaments with methacryl silane is 1.2 (GPa) and Weibull modulus  $m$  is 4.0 at the gauge length of 10(mm). Thus, the representative strength  $\sigma_0$  is changed from 1.2 (GPa) with the Weibull modulus  $m$  of 4.0. Here, the fiber volume fraction of fiber bundle  $V_f$  used 0.6. The interfacial property around a single fiber filament with different kinds of coupling agents was considered on yielding shear stress  $\tau$ : 12.5 (MPa) for ES specimen and 25(MPa) for MS specimen, respectively.

#### Weaving Structural Model

The finite element division for simulating the mechanical behavior of braided composites is shown Figure 4. This analytical model expresses faithfully the fiber orientation state by connecting beam elements. The thick lines and the fine lines express the fiber bundles and resin in the braided composites, respectively. The resin elements (surface resin elements) were placed at both surfaces of the model, since the resin exists at the surface of the composite. Also, resin existing between crossing fiber bundles was expressed by using beam elements (cross resin elements) in order to consider the transmission of force at crossing point between fiber bundles through resin.

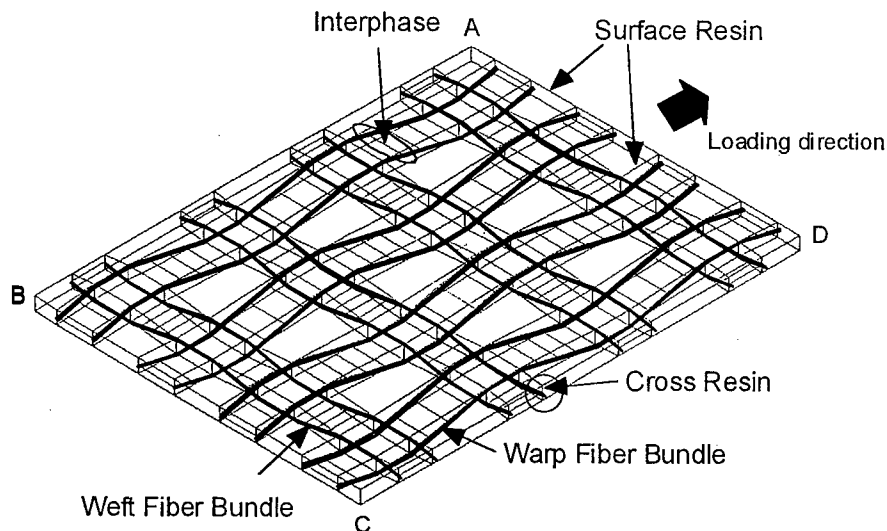


Figure 4 Finite element divisions for plain woven fabric composites.

Transverse cracks occurred at the filament/matrix interface inside of weft fiber bundles, so that in this model, the transverse cracks are regarded as an interfacial fracture. To consider the transverse cracks in weft fiber bundles, the fiber bundle consists of two separated fiber bundles impregnated with resin (fiber bundle elements) and interphase (interphase elements) which connects the two fiber bundle elements.

The material constants are shown in Table 1. The material constants of the fiber element were calculated by the Fiber bundle model and are provided as nonlinear elastic curves. The surface resin element and cross resin element is assumed to possess resin properties and is given as bi-linear elastic curves. However, the material constants of the interphase element are unknown, because this is related to the interfacial properties inside of a fiber bundle. Here, the yielding stress of interphase elements were decided as followings; From the elastic analysis of the weaving structural model, the relation between the applied stress to the model and the calculated stress at the interphase element could be clarified. On the other hand, the tensile stress of the specimen at which an initial transverse crack occurred could be obtained by experiments. Accordingly, in conjunction with the stress at which an initial fracture occurred in experiments and the applied stress to the weaving structural model in analysis, the calculated stress at the interphase element when the initial fracture occurred was obtained. This stress, indeed, is the yielding strength of the interphase element and of course the yielding strength depend on the kinds of coupling agents as shown in Table 1.

Table 1 Material constants of weaving structural model.

	Elastic modulus (GPa)	Yielding stress (MPa)
<b>Fiber bundle element</b>		
Warp	Fiber bundle model	
Weft		
<b>Resin element</b>		
Cross resin	3.5	80
Surface resin	3.5	80
Interphase (MS)	3.5	8.3
Interphase (ES)	3.5	4.2

## Results

Figure 5 shows relation between normal stress and strain of fiber bundle obtained by the Fiber bundle model. As shown in Fig. 5, the elastic modulus of the fiber bundle gradually decreased from 1.5% of strain. The nonlinear behavior depends on the kind of coupling agents and ultimate strength of fiber bundle for ES specimen is lower than that for MS specimen. These results were adapted as data for the reduction in elastic modulus of fiber bundle elements and then the weaving structural model considered the reduction in elastic modulus due to filament fractures.

Figure 6 shows a stress-strain curve of MS specimen predicted by the proposed micro/macro analyses and the corresponded stress-strain curve by experiments. The analytical results provide good agreement with the experimental results. The analytical results of ES specimen also corresponded to the experimental results.

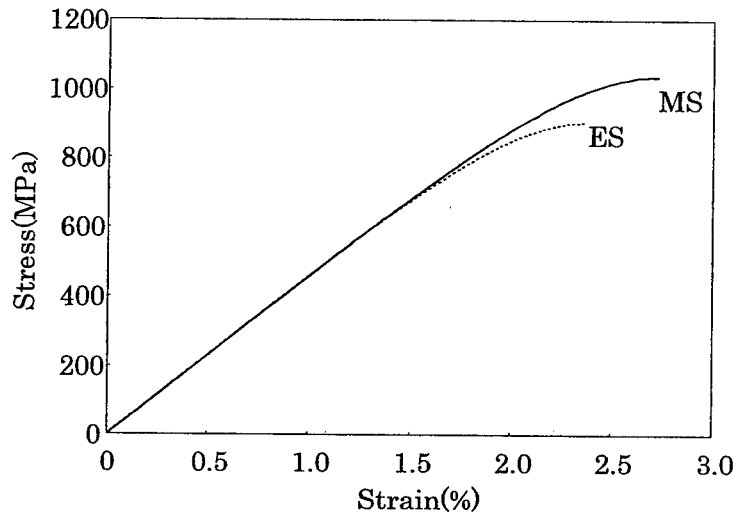


Figure 5 Stress-strain curves of fiber bundle.

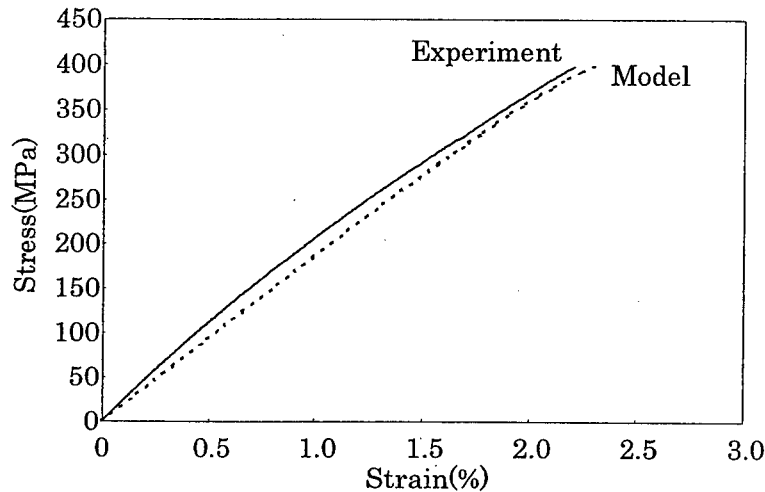


Figure 6 Predicted stress-strain curves for MS specimens.

## Conclusion

For the purpose of investigating the effects of coupling agents on microscopic fracture behavior in textile composites, microscopic in-situ observation was carried out during tensile tests in plain woven fabric composites. Replica method was introduced to examine the fracture process at the edge and the micro-fracture process of plain woven composites was clarified by the results.

A micro / macro analyses considering the interfacial properties and micro fracture mechanism was proposed. The most important feature of the proposed model is 1) to represent the precise weaving structures and interfacial properties by the FE model and 2) to consider the multiple filament fractures by the Curtin model. The present analysis method considering the continuity of fiber bundle, the weaving structures and the interfacial properties, could successfully predict the mechanical behaviors of the whole woven fabric composites.

## **Open Hole Compression Fatigue Test of Stitched CFRP Laminates**

Y.Iwahori, T.Ishikawa and S.Murase

### **Abstract**

Compression-compression (C-C) open hole fatigue test and ultrasonic inspection were conducted to determine the fatigue life of CFRP laminates and the effect of stitching on the delamination damage propagation. The specimens were made from T300 plane woven fabric stitched by Kevlar® 29. The preform was impregnated by resin transfer molding after stitch process. During C-C fatigue test, stress ratio( $R=\min./\max.$ ) was 10. It was concluded that stitched specimens had equivalent or slightly better fatigue resistance than unstitched specimens and arrested damage propagation was observed on some specimens by ultrasonic inspection.

The stitch position effects were evaluated for open hole specimen, fatigue test carried out under tension-tension( $T-T$   $R=0.1$ ) cyclic load condition. In summary, stitching position affects fatigue life. If stitching is too close to the open hole, static strength and fatigue strength were reduced by stitching. It was suggested that the stitching must be avoided in the vicinity to the open hole where stress concentration occurs for static and fatigue loads.

### **Introduction**

Composite materials, especially CF/epoxy 2-D laminates, have capability of light weight design for in-plane high loading structures. On the other hand, interlaminar strength is not strong against through-the-thickness direction load (laminar peeling to out of plane). In some aircraft structural design, weakness of the CFRP properties is critical and CAI (compression after impact), OHC(open hole compression) or resistance of interlaminar peel load such as interface of skin-stringer structure caused by buckled skin panels are typical examples. For these reasons, improvement of the CFRP's interlaminar strength gives a possibility to more light weight structures by damage tolerance or post buckling design. One of the CFRP research activities which through-the-thickness characteristics improvement for aircraft structures, stitching technique with low cost consolidation technique such as RTM(resin transfer molding) and RFI(resin film infusion) are evaluated in US[1] and other countries. In Japan in 1980's, one of the authors(TI) reported that stitched CFRP laminates manufactured by prepreg stitch/autoclave consolidation was evaluated[2]. The results were confirmed in ability of crack arresting and to postpone final fracture in static strength.

Y.Iwahori, Aerospace Engineering Sec. Engineering Dept., Japan Aircraft Mfg. Co. Ltd., 3175 Showa mach, kanazawaku, Yokohama 236-8540, Japan

Takashi Ishikawa, National Aerospace Laboratory, 6-13-1, Ohsawa, Mitaka, Tokyo 181-0015, Japan  
Saburo Murase, Tokyo Institute of Technology, 2-12-1, O-okayama, Meguro-Ku, Tokyo 152, Japan

On the other hand, it was found that static strength of stitched specimen were reduced in tension and compression. The reason for lower strength was that stitch needle gave a damage to CF bundles in prepreg or voids were formed at through-the-thickness thread holes. Recently, however, RTM or RFI technique such as dry-preform consolidation system has been matured and the preform damage by stitching could be reduced by using these methods. The authors' group carried out re-evaluation of stitched CFRP specimens by RTM processes. These results were concluded that 20% CAI strength improvement[3] and equivalent strength in unstitch static strength(compression and tension). They also confirmed interlaminar fracture toughness improvement that had linear relationship between stitch density and interlaminar fracture toughness( $G_{IC}$ )[4]. In fatigue performance, reference[5] reported that the low density stitched specimens had better fatigue resistance than unstitched specimens and also high density stitched specimens under tension-compression(T-C) loading condition.

## Compression Fatigue Test

### C-C Fatigue Test Specimen

Figure 1 shows the geometry of compression-compression(C-C) fatigue test specimen. The specimen consists of 20ply plane woven fabric of T300 3K stitched by Kevlar® 29 1000d yarn. The laminates of test specimen's construction here.  $[\pm 45, [0/90]_2, [\pm 45]_2, [0/90]_2, [\pm 45]_2, 0/90]_s$ . A modified lock-stitch was used and stitch pitch was 3 mm. An open hole of  $\phi 5.7$  mm was formed at the center of specimen. The stitch line placed on 7.5 mm from the center line and 3.5 mm from the edge that parallel to the center line. After stitching on dry preform, it was inserted to mold and

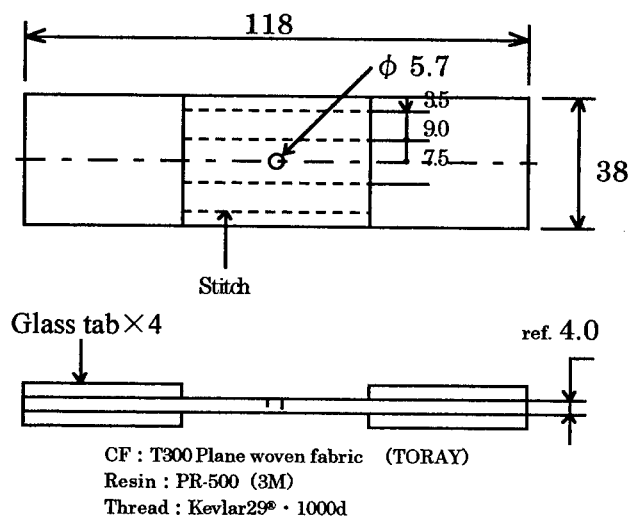


Fig. 1 Compression Fatigue Test Specimen



resin was transferred. The used resin is PR500®, epoxy of 180°C cure type for RTM. The size of specimen is 38\*118\*4.0(w\*L\*t)in mm. GFRP end tabs were bonded to the specimen.

### Static Test Result

The test was conducted by INSTRON 8501 hydraulic driven machine. The static tests were carried out under the displacement-controlled mode and 0.25mm/min cross head speed in both tension and compression tests. Table 1 shows the static test results of tension and compression strengths. It is concluded that stitched and unstitched specimen have almost equivalent strength under the static load conditions.

Table 1 Static Test Results(Average of two specimens)

		load	Max. stress (MPa)	
			Nominal Area	Net Area
Unstitch	Tens.		230.1	269.4
	Comp.		281.8	330.9
Stitch	Tens.		229.3	270.2
	Comp.		282.2	331.9

Nominal Area: Calculated by measured width×thickness.

Net Area: Hole Dia.×t is subtracted from Nominal Area.

### Fatigue Test Result

The fatigue test was conducted under the load-controlled mode and 5Hz sine wave. The fatigue load were set 52%, 54% and 56% based on the static compression strength. Figure 2 shows the picture of C-C fatigue test. As shown in Fig. 2, delamination damage was observed at the both sides of the open hole.

Figure 3 shows the result of the C-C fatigue test, an S-N plot of the maximum stress and the number of cycles up to failure. This figure also shows regression lines of stitched and unstitched strengths data. It is concluded that stitched specimens have equivalent or slightly better fatigue resistance than unstitched specimens under C-C cyclic load condition.

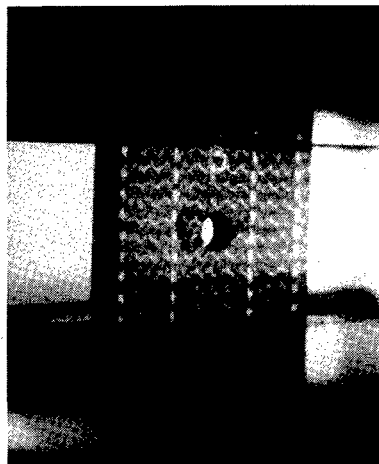


Fig. 2 Picture of Fatigue Test

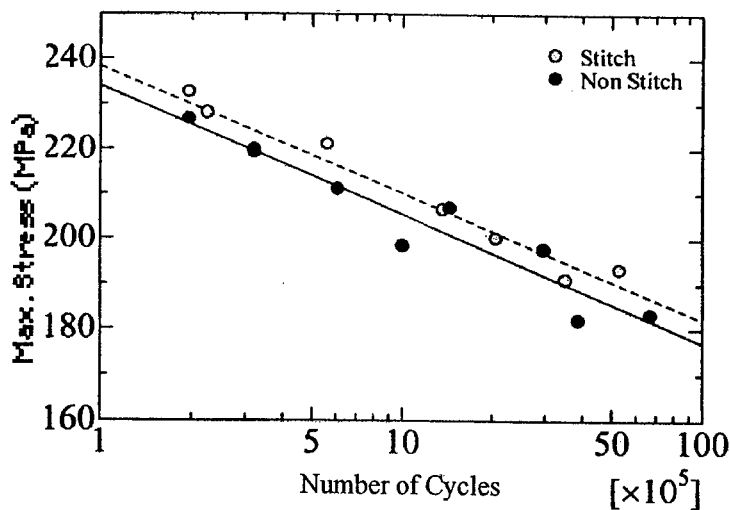


Fig 3 S-N Plotted of C-C Fatigue

#### Ultrasonic Inspection

Figure 4 shows ultrasonic inspection(C-Scan) results after 1280000, 2560000 and 5120000 cycles for a comparison of stitched and unstitched under similar stress levels of -193MPa for stitched and -197MPa for unstitched. Each fatigue life is 5305487 for stitched and 2971216 for unstitched. About the stitched specimen, it seems that the damage did not propagate beyond stitch line from 2560000 to 5120000 cycles. It can be mentioned that damage propagation was arrested by the stitch lines in this case.

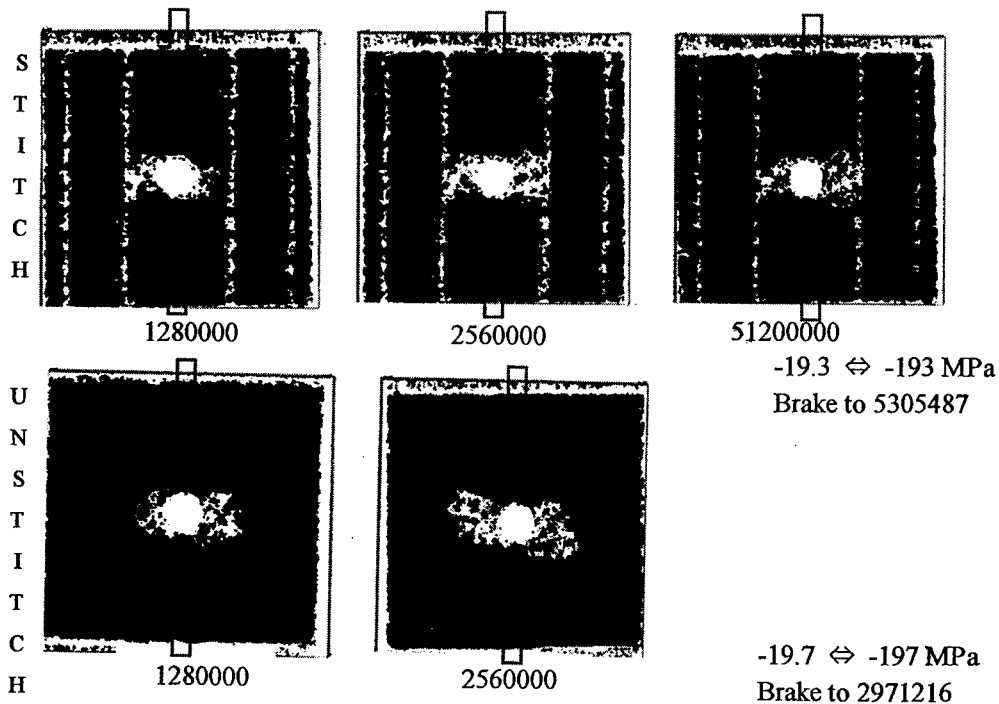


Fig. 4 Ultrasonic Inspection Results for Equivalent Stress Level

## Damage Propagation

Figure 5 shows the data plots of delamination area propagation in the specimens measured from the ultrasonic inspection results. There is a trend that increments in damage area for stitched specimen was larger than those of unstitched specimen. This phenomena is roughly explained as that the damage grows vertically after arrest by stitch lines. It should be noted that simple damage area can not be correlated with fatigue strength.

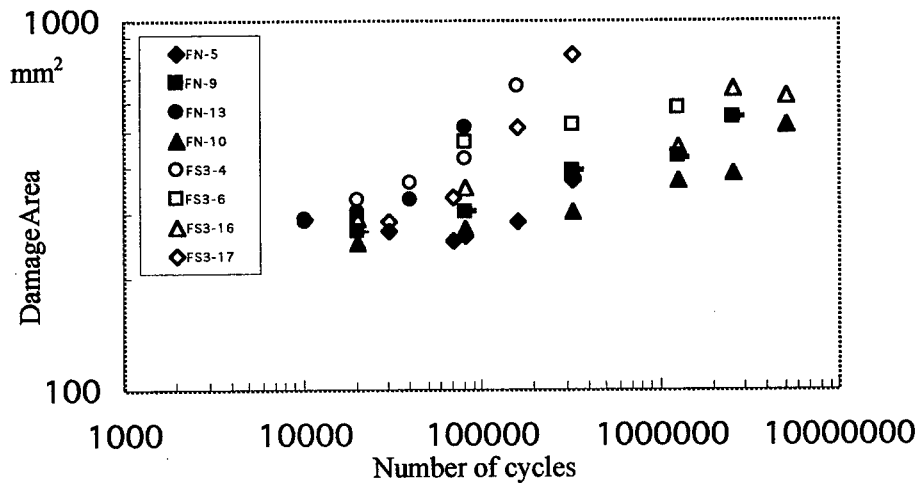


Fig.5 Damage Area Propagation

## Stitch Position Effect in Tension Fatigue

### T-T Fatigue Test Specimen

For the evaluation of a stitch position effect, fatigue tests in tension-tension were conducted. The test specimen geometry is shown in Fig.6. The specimens have  $\phi 5.7$  mm open hole at the center of the specimen similar to the C-C specimen. There were

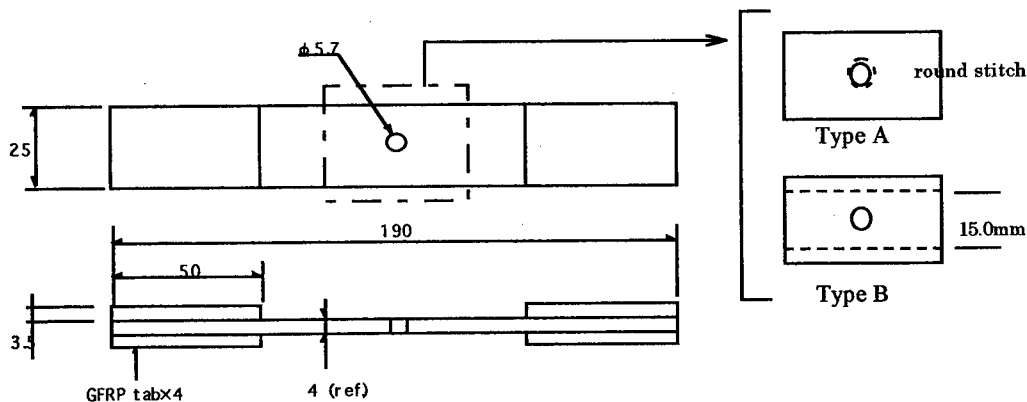


Fig.6 Geometry of T-T Test Specimen

two type of stitch pattern specimens were prepared. Type A specimen has a round stitching close to the open hole (1.0 mm from edge of open hole). Type B has parallel stitches with 7.5mm distance from the center line. Unstitched specimen was prepared for comparison with stitched specimen of type A and B. The used epoxy was different EP828 for type A and PR500 for type B. However, the following conditions are common. The stitch thread is Kevlar®-29 1000d yarn. Stitch pitch is 3 mm. The dry preform of specimen is T300 3K plane woven fabric, number of laminates are 20 ply. The laminate construction is  $[0/90]_{20}$ .

### Static Test Results

The static tension strengths for the T-T test specimens of type A and type B are shown in table 2. For the type A, static strength is inferior to un-stitch strength about 5%. On the other hand, the type B strength is equivalent in static tension. Figure 7 shows a picture of the static test for type A.

Table 2 Static Strength for T-T Specimen

Type	Tension Strength (MPa)	
	A	B
Stitched	304.7	301.4
Un-stitched	320.0	301.6

(Calculated by nominal area and average of two specimens)

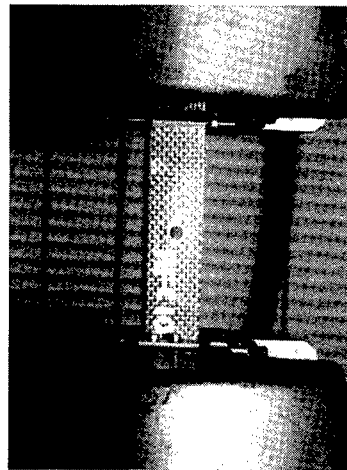


Fig. 7 Picture of Static Test

### Type A Fatigue Test Result

Figure 8 shows the S-N plot of type A fatigue tests of stress ratio : 0.1 ( $R = \min./\max.$ ). Fatigue strength of the type A stitched specimens are inferior to unstitched specimens. It should be noted that the type A stitched strength data show a wider scatter than unstitched specimens.

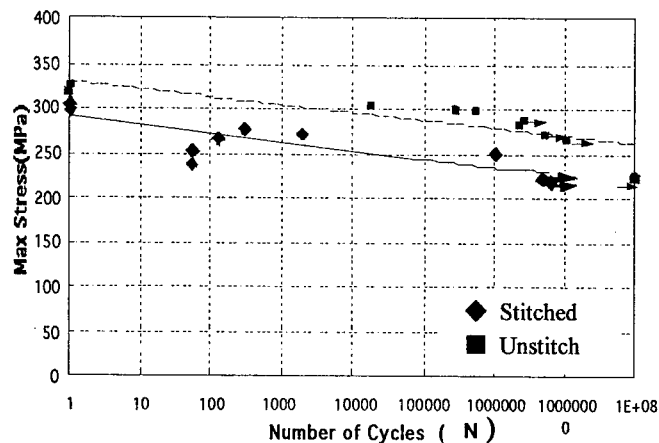


Fig.8 S-N Plot of T-T Test of Type A

### Stitch Effects of Type A

Figure 9 shows ultrasonic inspection results of the type A stitched and unstitched specimen in the T-T fatigue test under similar stress level after 1280000 cycles Fig.

9(a)(b) and 9000000 cycles(Fig 9(c)). Delamination in stitched specimens did not propagate from the open hole to load directions as shown in Fig 9(a) then broke. On the other hand, delamination of unstitched specimen were propagated from open hole to load direction as shown in Fig 9(b), and finally reach to edge of the test specimens as shown in Fig 9(c). After these fatigue tests (from broken specimens), there were observed that broken section of every specimen consisted of stitch thread hole. It was suggested that the stitch thread holes at stress concentration positions could be a trigger of the damage to failure. These thread hole may increase stress concentration from a simple open hole. In other words, the through-the-thickness thread must be avoided in high stress concentration region.

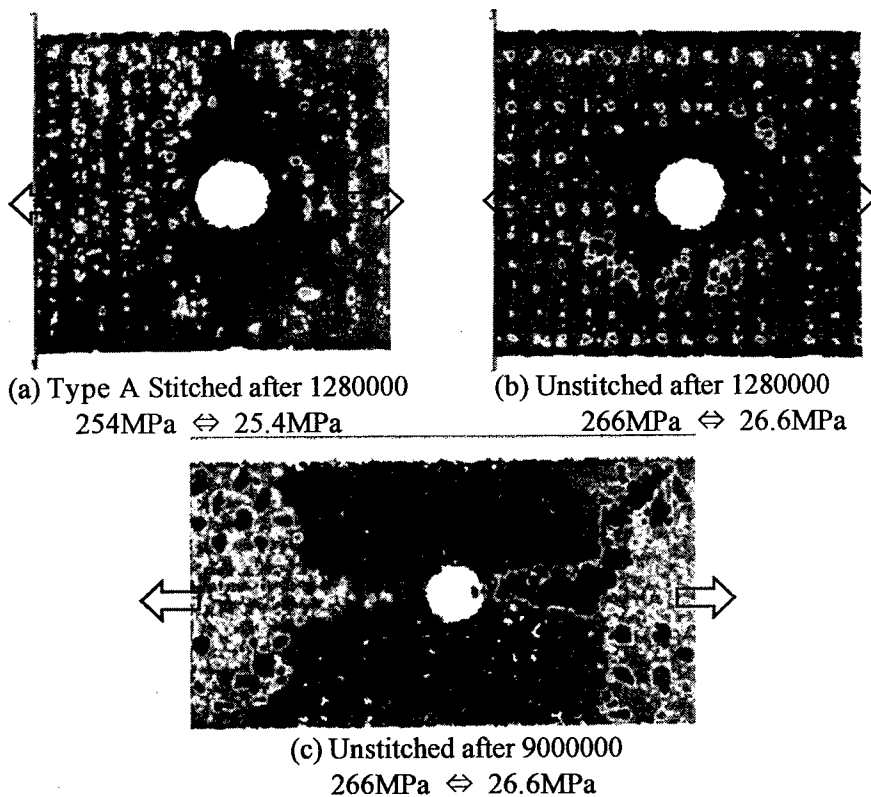


Fig. 9 Ultrasonic Inspection Result of Type A

#### Stitch Effects of Type B

Figure 10 shows ultrasonic inspection results after 2000000 cycles for type B of parallel stitch. No low cycle failure happened in type B stitch. In fatigue tests, the damage area propagated from open hole to the edge similarly to unstitch cases. In type B stitch, after damage area reached to the stitch lines, it was arrested by the stitch lines. Because the parallel stitch lines in type B are allocated away from the stress concentration regions, it has a capability of fatigue damage propagation control. Unfortunately, the fatigue tests are under going and S-N plot is not obtained yet.

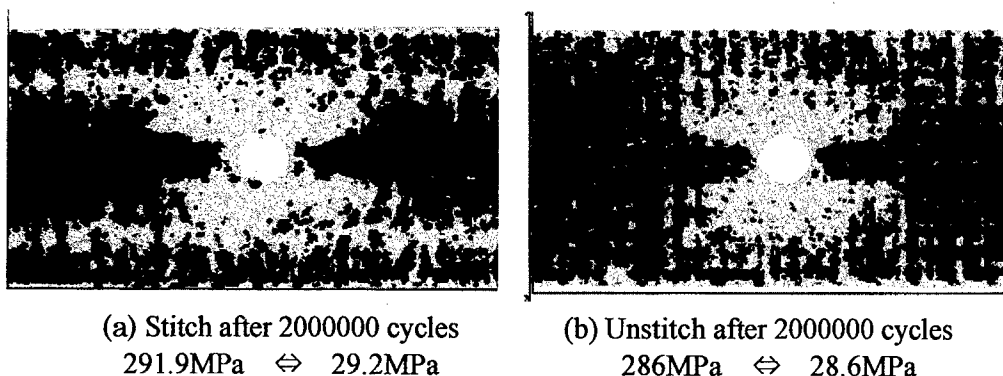


Fig.10 Ultrasonic Inspection of Type B Stitch and Unstitch Specimen

### Conclusions

The C-C fatigue tests and ultrasonic inspections were conducted stitched and unstitched specimens. Also, stitching position for the open hole test specimens was evaluated in T-T tests. The following concluding remarks are obtained.

- 1) Under C-C load, stitch specimen has equivalent or slightly better fatigue resistance than unstitched specimen.
- 2) It was observed in some specimens by ultrasonic inspection that delamination damage propagation was arrested by the stitch line.
- 3) Stitching too close to the open hole leads to reduction in static and fatigue resistance. It is concluded that thread hole became a trigger to the failure. If it exists in the stress concentration zone around a hole, it increases concentration more.
- 4) When stitching technique is applied to structure, stitch thread position must be carefully determined. It is suggested that stitch threads should be avoided in the vicinity of the open hole.

### Reference

- [1] S. W. Beckwith, C. R. Hyland, 1998. "Resin transfer Molding A decade of Technology Advances." *SAMPE Journal*, vol. 34, No.6.
- [2] Y.Tada, T.Ishikawa, 1989. "Experimental Evaluation of the Effects of Stitching on CFRP Laminate Specimens with Various Shapes and Loading" *Key Engineering Materials*, vol.37, pp305-316.
- [3] Y.Tada, M.Matusima et al, 1994. "Stitching Effect upon Strength of Composite Laminates." *Proc., 19th Symposium on Composite Materials*, pp.57-60.
- [4] Y.Iwahori, T.Ishikawa, N.Watanabe, 1999.5. "FEM Analysis of Interlaminar Fracture Toughness on Stitched CFRP Laminates." *Pro., Japan composite materials conference*.
- [5] I.Herszberg, A.Loh, et al, 1997. "Open hole Fatigue of Stitched and Unstitched Carbon/Epoxy Laminates." *ICCM-11, Gold Coast, Australia*, vol. V, pp. V-138-148.

## Delamination Toughness of New 3-D Orthogonal Interlocked Fabric Composite

Naoyuki WATANABE, Naofumi NISHII

### Abstract

The double cantilever beam (DCB) tests were executed for Mode I interlaminar fracture toughness of new type of 3-D orthogonal interlocked fabric composite. Load-deflection curves, the strain energy release rate and fracture mechanism were compared with those of common type. As for the strain energy release rate of two kinds of new type 3-D composite, with low-tension and normal-tension z-fiber, the difference between the two was very small. The toughness of the specimen with continuous z-yarns along the longitudinal direction of the specimen became higher in comparison with discontinuous z-yarns. But toughness of new type of 3-D composites was much higher than the common type. As for the delamination extension analysis, the present FEM model indicated good agreement with the experiments and it was considered to be qualitatively effective.

### 1. Introduction

Fiber reinforced composite materials have many advantages and are frequently used in wide variety of applications, although most of them are two dimensional (2-D) laminated composites. The weakest point in 2-D laminated composites is the very low interlaminar fracture toughness. One of to enhance the interlaminar toughness is to employ the orthogonal interlocked fabric composites.

Several experimental studies about the interlaminar toughness have been done for the orthogonal interlocked fabric composite, as shown in Fig. 1 [1-5]. In Ref. 5 the following several important facts were obtained. The presence of z-fibers caused various kinds of fracture phenomena, and these phenomena increased the interlami-

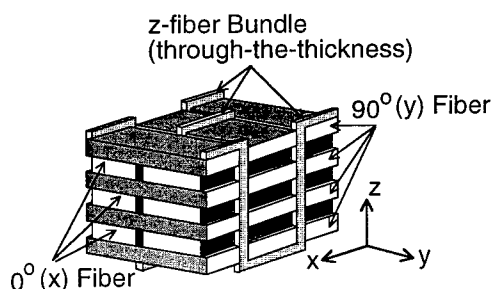


Figure 1 Common type of 3-D orthogonal interlocked fabric composite

Naoyuki WATANABE, Department of Aerospace Engineering, Tokyo Metropolitan Institute of Technology, 6-6, Asahigaoka, Hino-shi, Tokyo 191, JAPAN

Naofumi NISHII, Tokyo Metropolitan Institute of Technology

nar fracture toughness of this material. The strain energy release rate and its scatter became larger as the volume fraction of z-fiber yarn became higher. In addition, the tension of z-fiber during weaving was also changed to evaluate its effect on the fracture behavior. When the tension of z-fiber was loose, the "slack" was longer than that in the normal tension specimen and this long "slack" provided the margin before fiber breakage. Therefore, the bridgings by z-fibers were caused easily and the fracture toughness became high at larger crack opening displacements.

As for the analysis one of authors has carried out the numerical analysis about the 3-D orthogonal interlocked fabric composite, and the effect of through-the-thickness fiber bundle could be evaluated qualitatively as the first approximation. And the numerical simulation was carried out for the delamination extension of actual 3-D composite studied in Ref 5, and the fairly good agreement was obtained [7].

Recently, a new type of 3-D orthogonal interlocked fabric composite has been developed and it is fabricated with a manner similar to the stitching process. Its fiber architecture is indicated in Fig. 2.

In this paper, as for this 3-D composite the double cantilever beam (DCB) tests are executed for Mode I interlaminar fracture toughness and the Mode I strain energy release rate,  $G_{Ic}$  is estimated. From the results, fracture mechanisms of this 3-D composite and the effect of different architecture of z-yarn are evaluated. In addition the validity of delamination analyses using 2-D finite element method which has been developed by one of authors is discussed.

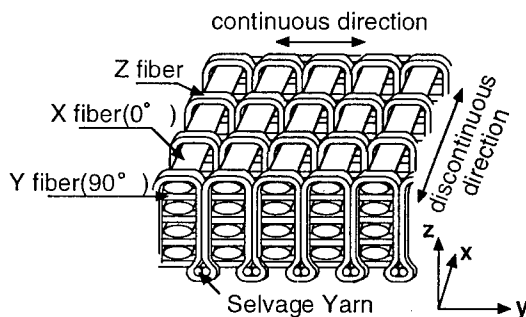


Figure 2 Fiber architecture of new type of 3-D orthogonal interlocked fabric composite

## 2. Experimental Procedure

The orthogonal interlocked fabric composites used in our experiments are made of carbon/epoxy, which are manufactured in Toyoda Automatic Loom Works, Ltd.. This fiber architecture is schematically illustrated in Fig. 2. Each z-fiber bundle was separated by a distance of 3.0 mm. A classification and fiber volume fraction ( $V_f$ ) of the present 3-D composite is given in Table I.

Table I Properties of the new type of 3-D composite

	Fibers		Matrix	Pitch [mm]	$V_f$ [%]			
	In-plane	z			whole	0°	90°	z*
T2	T300	T900	Epoxy#828	3×3	49.3	24.1	24.6	0.5
T'2	T300	T900	Epoxy#828	3×3	49.3	24.1	24.6	0.5

\* includes the portion of selvage yarn



There were two types of the tested materials, which are designated as T2 and T'2. The both are reinforced in the z-direction by carbon fiber T-900. The z-fiber tows of T2 and T'2 are 2K, and its volume fraction is 0.5%. Although this value includes the portion of selvage yarn, the actual  $V_f$  of z-fiber yarn is smaller. Material types without or with prime, T2 and T'2 mean the difference in tension in the z-yarn, within the same fabric architecture, *i.e.*, the primed has smaller tension than non-primed. Thus it is considered that the primed specimen contains longer "slack" than in non-primed specimen.

In addition, the effect of the continuity of z-yarn was evaluated by adopting two cutting directions, x (0°) and y (90°) for non-primed specimens, T2, as shown in Fig. 2. Since the z-fiber bundle is running in y (90°) direction, it is discontinuous in the x (0°) direction specimen and continuous in the y (90°) direction specimen along the delamination extension direction. The letter representing the cutting direction is added in the specimen identification, T2x and T2y.

The modified DCB test is adopted in this study, and  $G_I$  was calculated by the area method based on energy consideration suitable for the 3-D composites. This method and the specimen configuration are explained in Ref. 3 and 4 in detail.

### 3. Experimental Results

#### 3.1 Brief Review of Previous Experimental Results

One of authors has been tested the common type of 3-D orthogonal interlocked fabric composite in Fig. 1 [4, 7]. It has 4-axis in-plane tows and z-fiber yarn and it was manufactured by Nagoya Aerospace System Division, Mitsubishi Heavy Industries, Co. Ltd. Table II indicates comparison of z-fiber volume fraction and the averaged value of  $G_{Ic}$  value between the common and new types of 3-D composites. The z-fiber tows of C1x, C'1x and C1y are 1K, and those of C3x, C'3x, C3y are 3K, where C'1x and C'3x contain longer slack than C1x and C3x. Index notation, x and y, shows cutting direction. From Table II, it is confirmed that the

Table II Comparison of z-fiber volume fraction and  $G_{Ic}$  between the common and new type of 3-D composite

		Volume fraction of z-fibers [%]	Pitch [mm]	Averaged $G_{Ic}$ [N/mm]	Normalized $G_{Ic}$
Common type of 3-D composite	C1x	0.27	3.9×3.9	1.41	5.22
	C'1x	0.23		1.82	7.91
	C1y	0.27		1.75	6.48
	C3x	0.77		4.50	5.84
	C'3x	0.78		9.07	11.6
	C3y	0.77		6.67	8.66
New type of 3-D composite	T2x	0.5* <sup>1</sup>	3.0×3.0	12.9	25.8
	T'2x	0.5* <sup>2</sup>		12.4	24.8
	T2y	0.5* <sup>3</sup>		15.3	30.6

\*1, \*2 \*3: includes the portion of selvage yarn

averaged  $G_{Ic}$  of common type of 3-D composite with longer slack is larger than that with shorter slack. As for the cutting direction, the values of averaged  $G_{Ic}$  for the specimens with continuous z-fibers are larger than that with discontinuous z-fibers.

### 3.2 Typical Load-Deflection Curve for New 3-D Fabric Composite

Figure 3 shows the typical load-deflection curves of T2x and T'2x series. In this figure the load is plotted as the function of the crosshead displacement, namely opening displacement. At the beginning, the load increases almost linearly, then drops abruptly when the crack extends. The crack extends step by step and unstably, and it isn't gradual. That is considered to be due to the existence of the z-direction fiber. The load drops every time the crack extends, and the amount of the load drop is independent of the opening displacement. The peak load decreases gradually as the crack extension. The behavior of T2y such as the maximum load, opening displacement and decent ratio of load is very similar to that of T2x series.

### 3.3 Strain Energy Release Rate

Figure 4 shows the Mode I strain energy release rate,  $G_{Ic}$  for T2x and T'2x as a function of crack length, where  $G_{Ic}$  is obtained from load-deflection curves. The both values of  $G_{Ic}$  increase until the crack length becomes 25 mm and after that they become constant although there

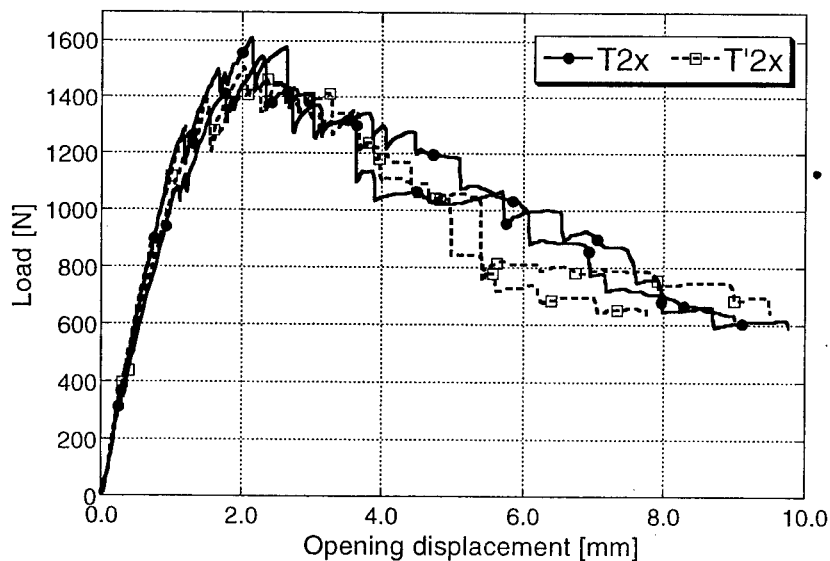


Figure 3 Typical load-deflection curves of T2x and T'2x series

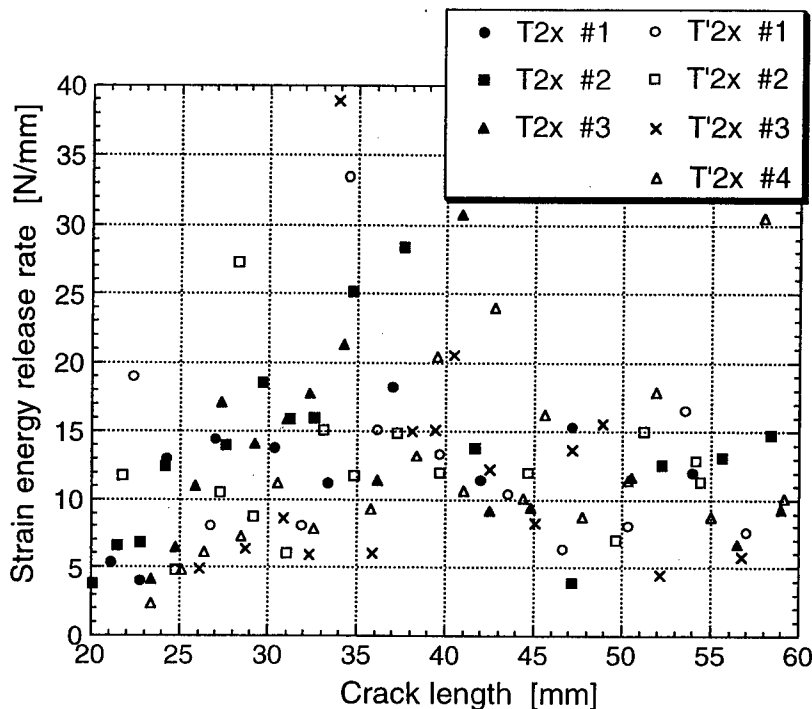


Figure 4 Strain energy release rate for T2x and T'2x as a function of crack length

is some scatter. However, the values of T2x are generally higher than those of T'2x before the crack length reaches 35 mm.

The averaged values of  $G_{Ic}$  for T2x and T'2x are 12.9 N/mm and 12.4 N/mm. The value of T2x is larger than that of T'2x by 3.88 % and the clear difference due to the amount of slack isn't seen in this composite. As mentioned in section 3.1, the averaged  $G_{Ic}$  of the common 3-D composite with longer slack is larger than that with shorter slack. This is because T2x with normal z-fiber tension has enough amount of slack due to specific architecture of z-yarn and adding more amount of slack doesn't give any effect in T'2x. But  $G_{Ic}$  value of T2x and T'2x are 100 times larger than that of usual laminated composites.

On the other hand, the averaged  $G_{Ic}$  of T2y is 15.3 N/mm and is larger than that of T2x by 15.7%. As for the common type of 3-D composite, this tendency is also seen. The averaged  $G_{Ic}$  with continuous z-fiber in the longitudinal direction of specimen for C1y and C3y are larger than those with discontinuous z-fiber of C1x and C3x by 19.4 % and 32.5 %, respectively. But this difference is small for the new type of 3-D composites.

To evaluate  $G_{Ic}$  with considering volume fraction of z-yarn, a following index is introduced.

$$\text{Normalized } G_{Ic} = G_{Ic} / \text{volume fraction of z-yarn}$$

Comparing on this index is tabulated in Table II. The value of normalized  $G_{Ic}$  for T2x, T'2x and T2y are 25.8, 24.8 and 30.6, respectively. The values of T2x and T'2x are more than four times of C1x and C3x and more than two times of C'3x. The value of T2y is nearly five times

of C1y and three and half times of C3y.

From this comparison, it is confirmed that this new type of 3-D composite has prominently high delamination toughness in comparison with the common type of 3-D composite.

### 3.4 Fracture Mechanisms

Figure 5 shows the photograph of the typical fracture mode in T'2x specimen during DCB test. The lines seen on the side were written by pencil in 1 cm intervals for an assistance of crack length measurements. Z-fiber bridging, its pull-out, crack branching and even in-plane fiber bridging were observed in this photograph. These fracture behaviors have been observed in experiments in the common 3-D composite. From

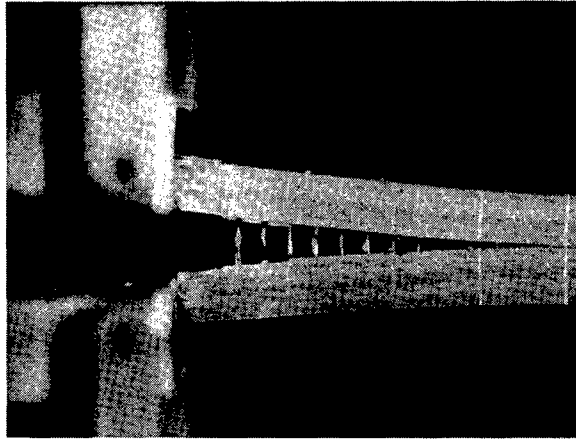


Figure 5 Typical failure mode of T'2x

observation after the test, it is known that almost of z-yarns were broken near the selvage yarn. Its reason is considered to be the stress concentration around the selvage yarn. In some specimens a few secondary cracks parallel to the main crack were observed, also.

### 4. Analytical Model

In this analysis, the behavior of z-fiber during the crack extension has been modeled by Watanabe et al. [6,7], and the detailed explanation is given in Ref. 6

Major points of the fracture phenomena related to the z-fiber bundles are as follows:

- 1) Debonding of through-the-thickness fiber bundle from the in-plane layers
- 2) Absorbing its slack given in manufacturing process
- 3) Tensile fracture and fiber bridging after its fracture

The frictional force which is considered to work between the z-axis fiber bundle and in-plane layers during its pullout is assumed to be neglected.

To simplify the analysis of interlaminar fracture toughness, only one-half of the specimen is modeled, and the crack front is assumed to be straight along the y-direction, then two dimensional finite element analysis is carried out under plane stress condition. In-plane layers of  $0^\circ$  and  $90^\circ$  are homogenized into only one kind of orthotropic layer, and its equivalent elastic constants are assumed to be as follows:

$$E_x = 65.6 \text{ GPa}, \quad E_z = 65.6 \text{ GPa}, \quad G_{xz} = 4.00 \text{ GPa}, \quad \nu_{xz} = 0.32$$

And those of the unidirectional CFRP tab are

$$E_x = 140.0 \text{ GPa}, \quad E_z = 8.5 \text{ GPa}, \quad G_{xz} = 4.37 \text{ GPa}, \quad \nu_{xz} = 0.34$$

Z-axis fiber bundle is modeled as 3-noded rod element with constant sectional area  $A_z$  which has only an axial stiffness and support only an axial force. The fiber tows were 2K and

equivalent longitudinal stiffness and tensile strength of the rod element can be approximated by the rule of mixture approach as

$$\text{T2x: } A_z = 0.132 \text{ mm}, \quad EA_z = 2.78 \times 10^3 \text{ N}, \quad F_{zb} = 57.9 \text{ N}$$

Based on the experimental observation, it is assumed that the values of  $G_{Ic}$  varies linearly from the initial value,  $G_{Ic-inplane}$  while crack extends from initial position to 30 mm from loading point and then maintain the maximum value. The values of  $G_{Ic}$  given in the analysis are as follows:

$$\text{T2x: from } 0.50 \text{ to } 13.0 \text{ N/mm}$$

where the  $G_{Ic-inplane}$  are determined as the values when the crack extends in the in-plane layer between the z-fiber bundles and include no effect of the z-fiber slip.

## 5. Comparison of Experimental Results and Simulation

The delamination analysis was carried out only for T2x composite. Figure 6 shows the load-deflection curves of T2x obtained by experiments and numerical curve. The amount of the slack is determined by the parametric study as 3% of its original length in the present T2x composite. The initial slope and peak load of numerical result are in fairly good agreement with the experiments and then both of result generally agree with each other.

Figure 7 shows the Mode I strain energy release rate,  $G_{Ic}$  for experimental results and numerical one, where  $G_{Ic}$  is obtained from load-deflection curves. The analytical value rises until the crack length reaches 30 mm and after then it is nearly constant, 13.00 N/mm. And the analytical curve is considered to be corresponding to the average curve of the experiments. The averaged  $G_{Ic}$  of analytical is 12.4

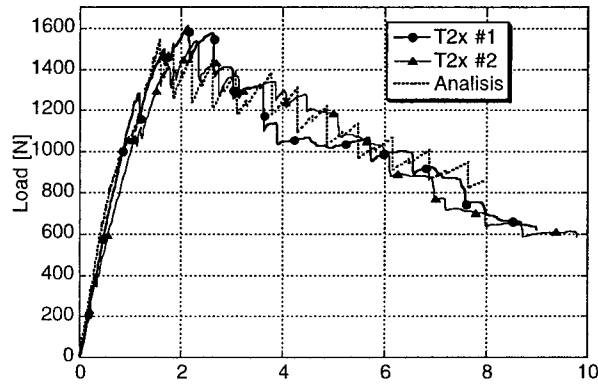


Figure 6 Numerical and experimental load-deflection curves

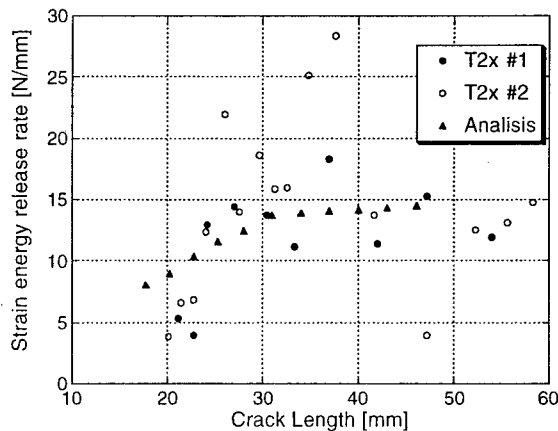


Figure 7 Strain energy release rate for T2x and analysis as a function of crack length

N/mm while the experimental one is 13.0 N/mm, and its error is only 4.6%.

## 6. Conclusions

In the new type of 3-D composite, the difference of the values of averaged  $G_{Ic}$  and the normalized  $G_{Ic}$  due to the amount of slack isn't seen and those values of the specimens with continuous z-fibers are larger than that with discontinuous z-fibers. However, the obtained interlaminar fracture toughness is 100 times larger than that of usual laminated composites and prominently high in comparison with the very tough common type of 3-D composite. In addition, the present FEM model for the delamination extension is considered to be qualitatively effective for T2x.

## Acknowledgments

The authors thank Dr. Takashi Ishikawa, Mr. Y. Hayashi and Mr. M. Matsushima, Composite Structure Section, Airframe Division, National Aerospace Laboratory, for their help in the experiments. The authors also thank Mr. Y. Yashui and R. Kamiya, Toyoda Automatic Loom Works, Ltd., for construction of the materials used in the experiment.

## Reference

1. Guenon, V. A. F., Chou, T. W and Gillespie, J. W., Toughness properties of a three-dimensional carbon-epoxy composite, *Journal of Material Science*, **24** (1989) 4168-75.
2. Ishikawa, H., Ji, M., Anahara, M. and Yasui, Y., The estimation of fracture of orthogonal three-dimensional fiber-reinforced composite by DCB testing, *Proceedings of 71st Annual General Meeting of the Japan Society of Mechanical Engineers*, Tokyo, Japan (1994) 455-7. (in Japanese).
3. Ishikawa, T., Matsushima, M., Bansaku, K., Watanabe, N. and Sunakawa, M., Experimental results of interlaminar fracture toughness and in-plane strength of 3-D woven carbon/epoxy plates, *Proceedings of Seminar of the Japan Society for Composite Materials*, Tokyo, Japan (1996) 51-2. (in Japanese).
4. Tanzawa, Y., Experimental study of interlaminar delamination toughness of 3-D orthogonal interlocked fabric composite, *Proceedings of 38th AIAA SDM Conference*, Orlando, U.S.A. (1997) 2611-20.
5. Tanzawa, Y., Watanabe, N. and Ishikawa, T., Interlaminar fracture toughness of 3-D orthogonal interlocked fabric composite, *Composite Science and Technology* **59** (1999) 1261-1270.
6. Watanabe, N. and Tanzawa, Y., Delamination analysis of 3-D orthogonal interlocked fabric composite, *Proceedings of 37th AIAA SDM Conference*, Salt Lake City, U.S.A. (1996) 877-85.
7. Watanabe, N. and Tanzawa, Y. and Ishikawa, T., FEM simulation of modified DCB test for 3-D orthogonal interlocked fabric composite, *Proceedings of 40th AIAA SDM Conference*, Atlanta, U. S. A. (2000).

## **Static and Dynamic Properties of Tri-axially Woven CFRP**

T.Ozawa and T.Ozaki

### **Abstract**

In this paper, the elastic properties of Tri-axially Woven CFRP from various types of static tensile test and vibration test were investigated. A new technique to estimate Young's Modulus of this material was developed. Practical values for structural design for space components were successfully obtained by combining static and dynamic test.

### **Introduction**

Tri-axially woven CFRP is composed of three sets of yarns – one fill and two warp yarns – interlaced with one another  $60^\circ$  angles. Space structures composed of Tri-axially woven CFRP are expected to be light in weight and to be high in dimensional stability because of its high stiffness and quasi-isotropy in a single ply.

Static properties of this material have been investigated by several researchers [1]-[5]. But it is difficult to predict dynamic performance based on the static evaluation. It is because the cross section of this material is not uniform and has many open holes, which affects dynamic behavior.

In this paper, we carried out tensile and vibration test, and estimated practical Young's modulus of this material.

### **Materials**

Tri-axially woven fabric used in this study was SK920 (Sakase adtech) made of Carbon fiber YT-50 (Nippon Graphite Fiber). Cyanate resin, EX1515 (Bryte Technologies) was applied as a matrix. The prepreg sheets were laminated and the orientation of the laminates was  $(0^\circ / 90^\circ)_n$ , where  $n=1, 2, \dots, 10$ .

### **Tensile Test**

The tensile tests were performed by an INSTRON universal testing machine (MODEL 1185) at room temperature, and the cross-head speed was 0.5mm/min.

---

T.Ozawa and T.Ozaki, ADVANCED TECHNOLOGY R&D CENTER, MITSUMISI ELECTRIC CORPORATION, 1-1-57, Miyashimo, Sagamihara-city, Kanagawa 229-1195, Japan

The specimens were 250mm long, 25mm wide rectangular, and composed of 2,4,6,8,10,12 and 20 plies of lamina. Strain for the evaluation of Young's modulus and Poisson's ratio were measured by using a strain gage. Strain gage used in this study were KFG-5-120-C1-11LM2R (KYOWA Electronic Instruments) and were attached to a single surface of specimen. The set up of the specimen is shown in Figure 1.

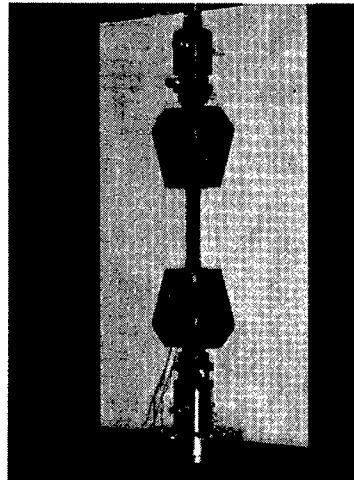


Figure 1 The set up of rectangular specimen for tensile test

The static Young's modulus based on the actually measured and theoretical thickness of the specimens are shown in Table I. The theoretical thickness was calculated from the area weight of the fiber and resin content.

Table I Static Young's Modulus(width:25mm)

	Measured thickness [mm]	Based on measured thickness [GPa]	Theoretical thickness [mm]	Based on theoretical thickness [GPa]	Poisson's ratio
2ply	0.20	33	0.11	60	0.42
4ply	0.34	48	0.22	75	0.39
6ply	0.43	62	0.33	80	0.34
8ply	0.55	67	0.44	83	0.33
10ply	0.70	64	0.55	82	0.33
12ply	0.83	63	0.66	79	0.34
20ply	1.43	67	1.12	81	0.33

Static Young's modulus based on the measured thickness and Poisson's ratio for 6,8,10,12 and 20-ply laminates were almost uniform. But the values for 2 or 4-ply laminates changed with the number of plies.

As for the values based on the theoretical thickness, this change was relatively small, though the same tendency was observed. This is considered to be due to the local transformation in the edge of the specimen, which may occur in 2 or 4-ply specimen.

In order to remove this effect, pipe (40mm inside diameter) specimens were



prepared. The set up of the specimen is shown in Figure 2. The specimens were composed of 2,4,6 and 8-ply laminates.

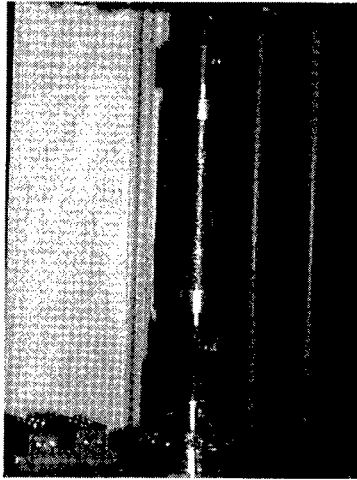


Figure 2 The set up of rectangular specimen for tensile test

The results of the pipe specimen were shown in Table II. Compared with the value in 25mm wide specimen, static Young's modulus was increased in pipe specimen test. Furthermore, the value calculated based on the theoretical thickness in the pipe specimen test was almost uniform.

Therefore, we considered that pipe specimen has little edge effect and was favorable to estimate static properties.

Table II Static Young's Modulus(pipe specimen)

	Based on measured thickness [GPa]	Based on theoretical thickness [GPa]
2ply	42	76
4ply	52	81
6ply	62	81
8ply	68	85

### Vibration Test

We performed free vibration tests with 250mm long, 25mm wide rectangular specimen. In vibration test, 2,4,8,6,8,10,12 and 20 plies of lamina were evaluated. The vibration test apparatus and the set up of the specimen is shown in Figure 3. A support condition was free-end and two support slits equipped at the nodes which were located 56mm from both ends. We measured out-of-plane displacements with a laser displacement sensor (KEYENCE:LB-8100) and the natural frequency were estimated with a FFT analyzer (HP:HP8105).

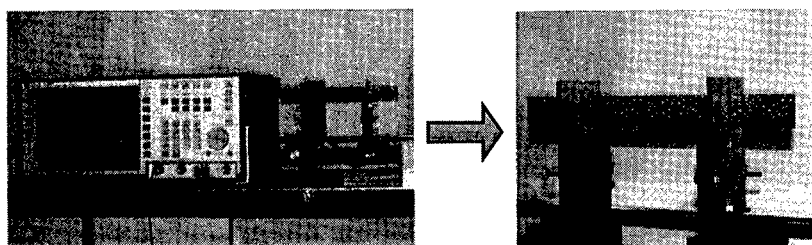


Figure 3 The vibration test apparatus and the set up of the specimen

Dynamic Young's modulus were determined from elementary vibration theory as:

$$f^2 = \frac{1}{(2\pi)^2} \left( \frac{4.73}{l} \right)^2 \left( \frac{EI}{\rho A} \right)^{1/2} \quad (1)$$

where  $f$  is the natural frequency,  $l$  is the length of specimen,  $E$  is the dynamic Young's modulus,  $I$  is the second moment of area,  $\rho$  is the density and  $A$  is the cross sectional area.

Natural frequencies and the evaluated dynamic Young's modulus were shown in Table III. In the vibration test, dynamic Young's modulus based on the measured thickness increased with the number of plies as well as in the tensile test. And the value based on the theoretical thickness except 4-ply laminates were almost uniform. Compared with the results of tensile test, Young's modulus based on the measured thickness was lower and the based on the theoretical thickness was higher. It is mainly due to the difficulty of the definition of the thickness of the specimen, because the dynamic stiffness is affected by the third power of the thickness.

Table III Dynamic Young's Modulus

	Natural frequency [Hz]	Based on measured thickness [GPa]	Based on theoretical thickness [GPa]
2ply	13.3	16	92
4ply	30.1	33	122
6ply	41.5	47	97
8ply	56.5	53	97
10ply	73.3	56	109
12ply	87.4	57	108
20ply	97.8	48	105

### Equivalent Young's Modulus

In the tensile and vibration test, evaluated Young's modulus were different. In order to estimate the practical Young's modulus, we estimated equivalent Young's modulus that reflected static and dynamic properties. In the calculation of the equivalent Young's modulus, both static values of tensile specimen and dynamic values of vibration test specimen were applied. For 2 or 4-ply specimens, the value of

pipe tensile specimen and rectangular vibration test specimens were applied. For 6,8,10,12 and 20-ply specimens, the value of rectangular tensile and vibration specimens were applied.

Reliable values obtained from both tests were stiffness of the specimen. They were obtained by Young's modulus multiplied by second moment of area in the vibration test. If the cross-section is assumed to be rectangular, we can estimate equivalent thickness, equivalent Young's modulus and equivalent density of specimens.

The equivalent values of specimens are shown in Table IV. For all laminates, the equivalent Young's modulus and density are uniform. And the gain of the equivalent thickness is almost uniform with the number of plies.

Table IV Equivalent Thickness, Young's Modulus and Density

	Equivalent Thickness [mm]	Equivalent Young's Modulus [GPa]	Equivalent Density [kg/m <sup>3</sup> ]
2ply	0.12	69	1570
4ply	0.27	66	1437
6ply	0.37	72	1571
8ply	0.49	77	1546
10ply	0.65	69	1471
12ply	0.79	66	1464
20ply	1.22	77	1550

As an example using these equivalent Young's modulus obtained from 2-ply laminates test, we performed cantilever free vibration test for specimens whose length were 200mm and width were 25mm.

The results of experiment and analysis are shown in Table V. For all number of plies, experimental results agreed well with analytical predictions. Therefore, the equivalent values are found to be applicable to all laminates.

Table V Comparison between analytical and experimental natural frequency

	Analysis [Hz]	Experiment [Hz]
2ply	5.8	5.1
4ply	11.5	12.9
6ply	17.3	17.5
8ply	23.1	23.8
10ply	28.8	31.3
12ply	34.6	37.0
20ply	61.1	61.5

## Conclusion

In this paper, we carried out various types of static tensile test and vibration test of Tri-axially woven CFRP. We developed the new technique to estimate practical

Young's modulus. The equivalent value obtained by combining static and dynamic test results of a certain laminates was found to be effective to predict dynamic performance of laminates of any ply.

## References

1. Tsu-Wei Chou, Micro structural Design of Fiber Composites, Cambridge Solid State Science Series, Cambridge (1992).
2. John E. Masters, Raymond L. Foye, Christopher M. Pastore and Yasser A. Gawayed, Mechanical Properties of Triaxially Braided Composite Experimental and Analytical Results, J. of Composites Technology & Research, Vol.15, pp.112-122 (1993).
3. Hiromi Kimura, Hirotaka Shibata, Kenji Kubomura and Hiroshi Ohshibashi, SUPER-HIGH MODULUS TRI-AXIAL FABRICS, 41st International SAMPE Symposium, pp.1139-1148 (1996).
4. Akihito Watanabe, Hiroyuki Tadokoro and Yutaka Arai, TENSILE PROPERTIES OF TWF REINFORCED CF/EP SINGLE PLY COMPOSITES, 43rd International SAMPE Symposium, pp.1874-1882 (1998).
5. E. D. Amato, F. Durante and G. Fedele, Numerical and Experimental Analyses of the Structural Behaviour of Braided Composite Materials, Key Engineering Materials Vol.144, pp.293-300 (1998).

## Poster Session

---

## **Bending Test for CFRP Skin/Foamed Core Sandwich Plates**

H. Fukuda<sup>1</sup>, T. Kawasaki<sup>2</sup>, A. Kataoka<sup>3</sup> and S. Tashiro<sup>3</sup>

### **Abstract**

Bending tests of commercially available sandwich plates with three kinds of CFRP-fabric skins and two types of acrylic foam cores were conducted by means of a three-point bending. The effects of the span and the radius of the loading nose on the bending modulus and strength were examined systematically. Test data on bending rigidity did not coincide with those calculated from a modified beam theory where the effect of the shearing rigidity of the core was incorporated, although the tendency with respect to the span was the same. Based on these results, this paper proposes a desirable data reduction scheme by which methodology, the correlation between theory and experiment could be made clear.

### **Introduction**

Sandwich plates have long history of application to structural elements especially for aerospace use and tremendous research works have been conducted hitherto[1] and recently, a periodical journal for sandwich structures and materials was born[2]. In these researches, sandwiches of aluminum skin (face) and aluminum honeycomb core are of most interest and not a few standards[3] have been established to evaluate the mechanical properties of this kind of sandwiches. Recently CFRP skin/foamed core sandwiches have also been developed which are used in various fields including medical application mainly due to X-ray transmittability with sufficient bending rigidity. In such a case of relatively soft core, the existing test methods are not necessarily sufficient. For example, the deformation may not necessarily coincide with the classical beam theory due to the soft core and the failure pattern may be different from bending failure.

The bending rigidity (EI) can be measured experimentally by conducting a three- or four-point bending test of a sandwich coupon. In the case of the three-point bending,

---

<sup>1</sup> Hiroshi Fukuda, Department of Materials Science and Technology, Science University of Tokyo, Yamazaki, Noda, Chiba 278-8510, Japan.

<sup>2</sup> Takanori Kawasaki, Graduate student, Science University of Tokyo

<sup>3</sup> Atsushi Kataoka and Susumu Tashiro, CAE Laboratory, Toray Industries, 3-3-1 Sonoyama, Otsu, Shiga 520-0842, Japan.

$$EI_{\text{exp}} = \frac{PL^3}{48\delta} \quad (1)$$

holds where  $P$  is the applied load,  $L$  is the span, and  $\delta$  is the midspan deflection. This equation is based on an elementary beam theory.

On the other hand, if we know the elastic constants of the constitutive materials, that is, if we know Young's modulus of the skin, and the shearing modulus of the core, the bending rigidity can be calculated. There are several levels for this.

The simplest one is: if we assume that the applied load (moment) is carried by only the face material and that the role of core is only to keep two skins at a constant distance, the bending rigidity can be calculated, under Euler-Bernoulli's hypothesis, as

$$EI_c = \frac{E_f b t_f t_c^2}{2} \quad (2)$$

where  $E_f$  and  $t_f$  are Young's modulus and thickness of the face material,  $t_c$  is the thickness of the core, and  $b$  is the specimen width. This may be called a composite beam theory although some simplification is done. This also corresponds to the case that the shearing modulus of the core is infinity nevertheless Young's modulus of the core is neglected.

In the case of a soft-core sandwich, shearing deformation of the core takes place. This leads the increase of the deflection, hence the decrease of the bending rigidity. The total deflection,  $\delta_{\text{total}}$ , is the sum of the deflection due to bending,  $\delta_b$ , and the deflection due to the shearing deformation of the core,  $\delta_s$ , that is,

$$\delta_{\text{total}} = \delta_b + \delta_s \quad (3)$$

In the case of a three-point bending, these values can be calculated by

$$\delta_b = \frac{PL^3}{48EI_c} \quad (4)$$

$$\delta_s = \frac{PL}{4t_c b G_c} \quad (5)$$

where  $G_c$  is the shearing modulus of the core. In this case, the bending rigidity,  $EI_m$ , is, referring to eq.(1),

$$EI_m = \frac{PL^3}{48\delta_{\text{total}}} \quad (6)$$

From eqs.(3)-(6),

$$EI_m = \frac{EI_c}{1 + \alpha} \quad (7)$$

is derived where

$$\alpha = \frac{6E_f t_f t_c}{L^2 G_c} \quad (8)$$

Equation (7) may be referred as a modified beam theory where the shearing deformation of core is considered, and the skin is assumed to share the bending moment whereas the role of core is to carry the shearing force. If we neglect the shearing deformation of core,  $\alpha=0$  holds and eq.(7) reduces to a composite beam theory,  $EI_c$ .

In eqs.(7) and (8), it becomes necessary to measure the shearing modulus of the core,  $G_c$ . But as will be described later, it is rather difficult to measure  $G_c$  precisely. In addition, even if precise  $G_c$  value is obtained from core itself, there is no guarantee that the mechanical properties of core are kept unvaried in the sandwich plate. For example, if some amount of resin is impregnated in some portion of core during co-cure process, the core will become harder.

There is a sophisticated way of calculating  $G_c$  by combining the results of a 3-point and a 4-point bending tests of a sandwich coupon[4]. The final result is

$$G_c = \frac{P_3 L_3 t_c \left\{ \frac{8L_3^2}{11L_4^2} - 1 \right\}}{2\delta_3 b(t_f + t_c)^2 \left( \frac{16P_3 L_3^3 \delta_4}{11P_4 L_4^3 \delta_3} - 1 \right)} \quad (9)$$

where the subscripts 3 and 4 denote, respectively, the values for 3- and 4-point bending. However, as far as our experiment is concerned, the scatter of the data by this method was fairly large.

So far we have reviewed several methods to calculate the bending rigidity of a sandwich beam from the mechanical properties of the consistent materials. These theories will later be compared with experimental values.

Going back to the present paper, several kinds of commercially available sandwich plates of CFRP-fabric skin and acrylic foam core were evaluated by means of a three-point bending to make sure their mechanical behaviors. The effects of the span and the radius of curvature of the loading nose on the bending modulus and strength were examined systematically.

During the comparison of the present data with the above existing theories, we found there exist some discrepancies between the two. Then we tried to establish a methodology to correlate the theories and the experiments; this is a primary subject of this paper.



## Experimental Procedure

### Test specimen

In the present study, three kinds of 4-harness satin woven carbon cloths of T300, T700s or M40 with 12000 filaments in a tow are used to make each prepreg sheet for skin. An epoxy resin was used for the matrix and the nominal volume fraction of fiber was 50%. The core material was acrylic foam the inflation ratio of which was mainly 10 times whereas 15times' inflation core was also used for T700s skin sandwich. These raw materials of skin prepreg and core material were co-cured at 80°C by a hot press. Geometries of test specimen are shown in Table 1 where  $h$ ,  $t_f$  and  $t_c$  are the total thickness, the thickness of the skin and the thickness of core, respectively. From these panels, test coupons of width  $b=15\text{mm}$  with various length were prepared. The number of test samples was 4~5 for each case.

**Table 1 Geometries of test specimens**

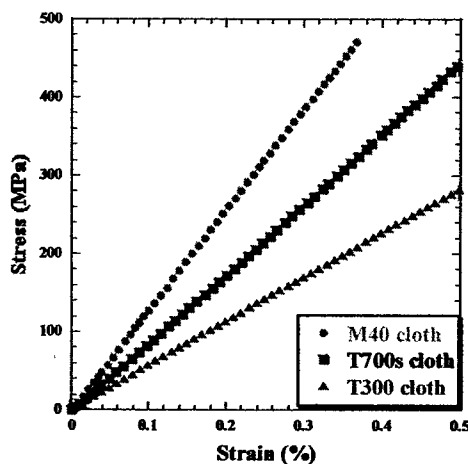
skin	T300	T700s	M40
$h(\text{mm})$	14.4	13.6	13.5
$t_f(\text{mm})$	1.0	0.6	0.6
$t_c(\text{mm})$	12.4	12.4	12.3

**Table 2 Mechanical properties of CFRP skins**

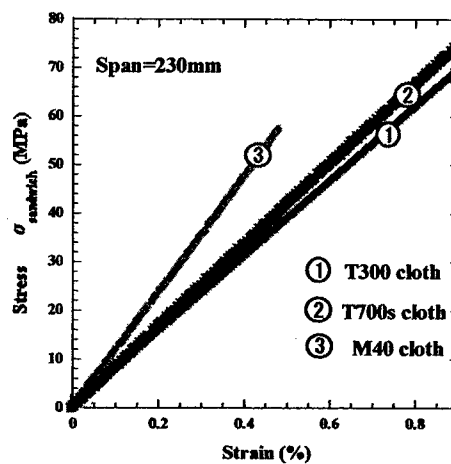
skin	T300	T700s	M40
Young's modulus $E_f$ (GPa)	56.5	89.5	131.0
Tensile strength (MPa)	597	1645	541

### Properties of constitutive materials

Figure 1 demonstrates the stress-strain curves of each skin CFRP material and



**Fig.1 Tensile stress-strain curves of skins (principal axis direction)**



**Fig.2 Tensile strain-stress curves of sandwich coupons**

Table 2 summarizes Young's modulus and the tensile strength. Although tensile tests in the direction of  $45^\circ$  were also done to obtain the shearing modulus of the skin, data are omitted here. Mechanical test data of core materials are also discarded in this paper.

The tensile stress-strain curves of sandwich plates were almost linear as demonstrated in Fig.2 where  $\sigma_{\text{sandwich}}$  indicates the applied load divided by the total cross sectional area of the sandwich coupon.

### Three-point bending

To examine the effect of the span on the bending rigidity and strength, the span was changed from 115mm to 500mm for T300 skin sandwich and for T700s and M40 skin, the span was either 150, 230, or 500mm. The radius of curvature of the loading nose (R) and the supporting nose (r) were fixed to R=6mm and r=3mm, respectively.

The effects of the radius of curvature of the loading nose on the bending modulus and strength were also examined against T300 skin sandwich only. In this case, the span was fixed to either L=230mm or L=500mm and the radius of curvature of the loading nose was varied to R=6, 12, 24, 50, and 100mm.

In all cases, the bending strength was calculated by

$$\sigma_{\max} = \frac{3P_{\max}L}{2bt^2} \quad (10)$$

in accordance with the elementary beam theory.

## Results and Discussion

### Effect of span

In this chapter, only results of three point bending will be described. Figure 3 shows the relation between the span, L, and the equivalent bending rigidity. Lines calculated from modified beam theory are also drawn where  $E_f$  are the experimental values shown in Table 2. For  $G_c$ , a catalog value of 27MPa[5] was used. According to this figure, experimental values are larger than the theoretical values. This point will be discussed later.

Figure 4 is the bending strength

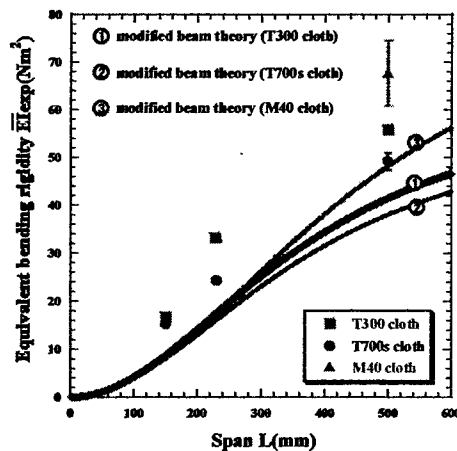


Fig.3 Equivalent bending rigidity vs. span

vs. span for T300 skin sandwich. The bending strength was almost constant when the span  $L$  was larger than 300mm whereas it decreased with decreasing the span in the region of  $L < 300$ mm. This result indirectly shows that for a short-span beam such as  $L < 300$ mm, the failure pattern might be different from the bending failure. This point will be discussed in the next article.

#### Effect of radius of curvature of the loading nose

Bending tests were conducted by also varying the radius of curvature of the loading nose (indenter) where the span was either (a)  $L=230$ mm or (b)  $L=500$ mm. This test was conducted to T300 skin sandwich only. Dots of Fig.5 are the results; square symbols will be discussed later. According to Fig.5, the failure load increased slightly with increasing the radius of the indenter. This suggests that a relatively large loading nose is desirable for the bending test of sandwich beams.

As was shown in Fig.4, a bending failure might not have occurred for short-span coupons. To make clear this point, a kind of indentation test was conducted where the sandwich coupon was pressed on a rigid and flat plate using the same loading nose as those used for the bending test. Figure 6 is the schematic view of the indentation test and the square symbols of Fig. 5 are the results.

One notable point is that, in the case of short span, the failure load by means of 3-point bending was almost the same as that of the indentation test (see Fig.5a). This indicates that for  $L=230$ mm, other failure pattern such as crush of core took place prior to a bending failure. On the other hand, the bending failure is likely to have occurred for  $L=500$ mm because the

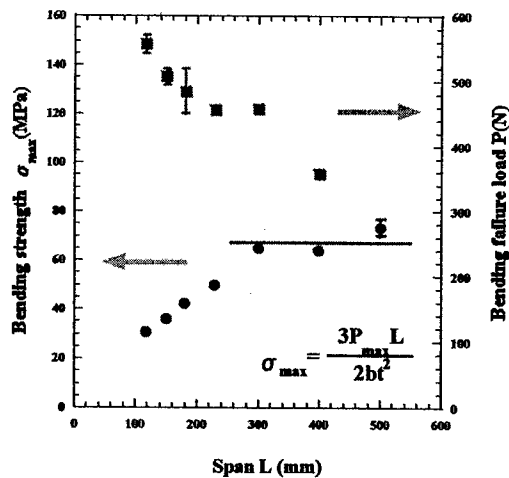


Fig.4 Span vs. bending strength (T300)

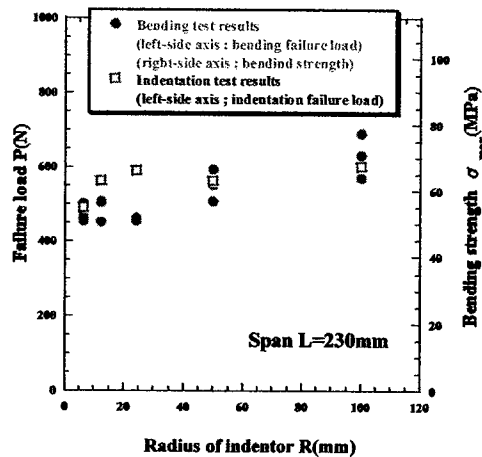


Fig.5(a) Radius of indenter vs. failure load (span  $L=230$ mm)

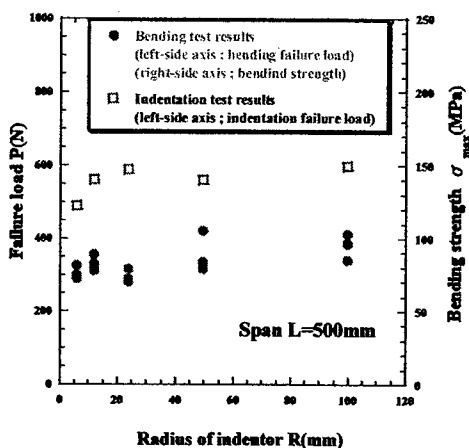


Fig.5(b) Radius of indenter vs. failure load (span  $L=500$ mm)

bending failure load was smaller than that of the indentation test (Fig.5b). Thus, it was again confirmed that a bending test of short span is not desirable.

#### The effect of core

Figure 7 shows the effect of core materials on the equivalent bending rigidity of T700s-skin sandwich. As was expected, the rigidity decreased when the core of 15times' inflation ratio was used, although quantitative discussion is rather difficult at present.

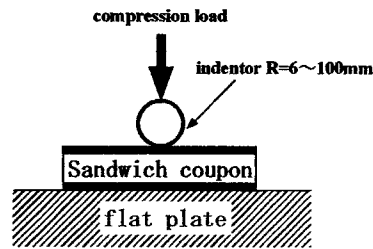


Fig.6 Schematic view of indentation test

#### Methodology of correlating theory and experiment

Going back to Fig.3, the experimental values were larger than those of prediction by means of the modified beam theory. This difference might be due to inaccurate  $G_c$  value used in the theory because it is pretty difficult to measure  $G_c$  in a precise manner.

Our alternative idea is as follows. Choosing an arbitrary span, for example,  $L=230\text{mm}$ , the shearing modulus,  $G_c$ , was inversely calculated from eqs.(2) and (4) so that the calculated bending rigidity meets with the experimental value. In other words, one point collocation was done. Figure 8 shows the case of T700s  $G_c$  value

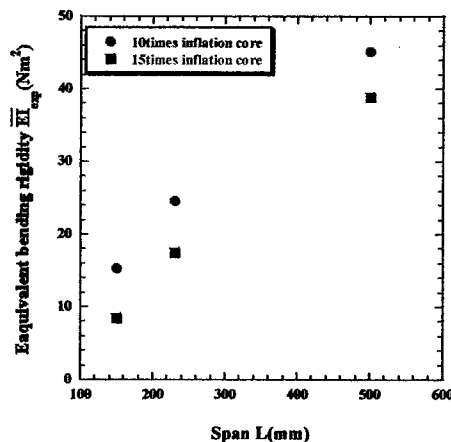


Fig.7 Effect of core materials on the equivalent bending rigidity

was assumed to be 51MPa. The theoretical values agreed very well with the experimental values. That is, if we once conduct a bending test at an arbitrary span length, we can estimate the flexural rigidity at any span length by the aid of the modified beam theory of eqs.(2) and (4); this is a new methodology derived here.

This logic holds to the cases of T300 or M40 face material, too. However,  $G_c$

values necessary to match the theory to experiment were different each other ( $G_c = 83\text{MPa}$  for T300,  $G_c = 65\text{MPa}$  for M40), nevertheless the same core material was used in the experiments. This point was left for future discussion.

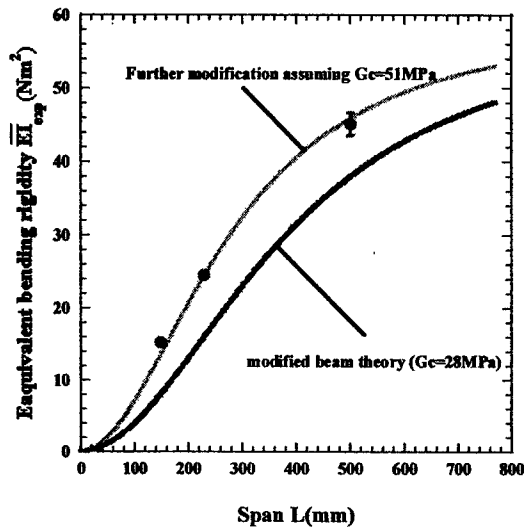


Fig.8 Modification of modified beam theory (T700s cloth)

## Conclusions

In the present paper, we conducted a series of bending tests of CFRP skin/foamed core sandwich beams. Effects of span and radius of curvature of the loading nose on the bending rigidity and bending strength were evaluated systematically and data were accumulated. The effect of core material on the bending rigidity was also demonstrated. Because it was rather difficult to measure the shearing modulus of core itself, some discrepancies of bending rigidity between experiment and theory took place. To correlate experiment and theory, we proposed a methodology of data reduction, which was successfully applied to the present case although some points were left unclear.

## References

1. Vonson, J. R., "The Behavior of Sandwich Structures of Isotropic and Composite Materials," Technomic, Lancaster (1999).
2. "Journal of Sandwich Structures & Materials," Vonson, J. R., editor-in-chief, Technomic, since 1999.
3. ASTM Standards, C 271-297, C-363-369, C-393-394, C-480-481.
4. ASTM C 393-94, "Standard test method for flexural properties of sandwich plates," p.23.
5. Toray Industries, catalog.

## **Effects of Stacking Sequences on Mechanically Fastened Joint Strength of Matrix Hybrid Laminates**

H.Hamada and K.Sugimoto

### **Abstract**

FRP structures consist of many parts which are mainly connected by bolts because of its reliable, repairable and economical effects. The failure modes of mechanically fastened FRP joint can be classified into three types according to the failure aspects around circular hole where the pin or bolt is inserted. These failure modes are called Net-Tension failure, Bearing failure and Shear-Out failure. Generally, mechanically fastened FRP joint failed in Bearing is the most safe among these modes because of its ductile failure propagation. The Bearing failure load can be improved by relieving shear stress concentration around the hole. In this present work, the effects of stacking sequences on bearing load of mechanically fastened joint in matrix hybrid composite laminates with high modulus and flexible resins. It was found by the results of experiment and finite element analysis that the matrix hybrid composite laminates with flexible layer in the vicinity of the surface layer could improve the initial failure load.

### **Introduction**

The concept of the hybrid composites is based on the composites principle where two or more materials are combined together so as to optimize the desirable properties while simultaneously negating the effects of their less desirable properties. The producing cost can be reduced using glass fiber into CFRP that is expensive. Furthermore, the brittle feature of CFRP can be toughened by combining with the glass and aromatic amide fiber which has greater toughness than the carbon fiber.

---

H.Hamada and K.Sugimoto, Division of Advanced Fibro Science, Kyoto Institute of Technology, Matsugasaki, Sakyo-ku, Kyoto 606-8585, JAPAN

In general, hybrid composite consists of the matrix resin and two or more kinds of fibers, which have been developed to improve the damping properties that are considerable problem in the weightless state outer space. Furthermore, the combination of different matrix resins and some interface changed by condition of coupling agents can be applied into hybrid composite. Thus, not only mechanical properties but also acidic and water proof could be improved.

FRP structures consist of many parts which are mainly connected by bolts because of its reliable, repairable and economical effects. The failure modes of mechanically fastened FRP joint can be classified into three types according to the failure aspects around circular hole where the pin or bolt is inserted. These failure modes are called Net-Tension failure, Bearing failure and Shear-Out failure<sup>1-3</sup>. Generally, mechanically fastened FRP joint failed in Bearing has the most safe among these modes. Some combination of these failure modes can occur in actual structures. The strengths and failure modes of mechanically fastened joint depend on the material performance and joint geometry.

Ramakrishna<sup>4</sup> et al. and Cooper<sup>5</sup> et al. investigated mechanical properties of bolted joint of pultruded sandwich composite laminates. In these efforts the skin and core layers were chopped mat and unidirectional strand sheet respectively. Matthews<sup>6</sup> et al. studied on quasi-isotropic laminates combined with the carbon and glass fiber. The hybridization of reinforcement has been investigated widely, but that of matrix has not been studied well.

As mentioned above, Bearing failure mode is desirable in FRP bolted joints because it develops slowly. In the previous effort the authors studied on improvement of bearing strength of carbon quasi-isotropic laminates<sup>7</sup>, in which thermoplastic film was inserted. As a result that higher initial failure load was achieved when the film was inserted into interlamina where the vicinity of surface of laminates. In this present work the optimum stacking sequence of matrix hybrid laminates that effects on bearing strength was investigated.

### **Matrix hybrid stacking sequence**

The plane woven fabric (WE18W, Nitto-Boseki Co. Ltd., Japan) was used as reinforcement. Two kinds of the matrix resin, vinyl ester (RIPOXY R806, Showa High Polymer Co. Ltd., Japan) and unsaturated polyester resins (RIGRAC FK2000, Showa High Polymer Co. Ltd., Japan) were used. The load-displacement

curves for these matrix resins are shown in Figure 1. The vinyl ester indicated high stiffness and ultimate load but brittle failure, on the other hand, the unsaturated polyester had considerably low stiffness and ultimate load and did not broke because of its flexible property. The static properties of these resins are summarized in Table 1. The modulus and strength of the vinyl ester was 10 times as large as that of unsaturated polyester. The hybrid laminates were fabricated by hand-lay-up. Figure 2 shows five kinds of stacking sequences for hybrid laminates. In this figure the word of H and F mean hard and flexible layer respectively. The number of ply was 16 in each laminates. The stacking sequences were symmetry in the thickness direction.

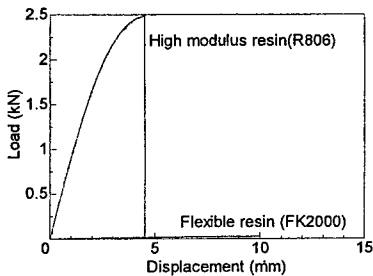


Table 1 Mechanical properties of matrix resin

	Modulus (GPa)	Strength (MPa)	Ultimate strain (%)	Poisson' ratio (-)
Vinyl Ester (R806)	4.01	72.90	4.76	0.456
Unsaturated Polyester (FK2000)	0.38	0.72	-	0.668

Figure 1 Load-displacement curves of matrix resin.

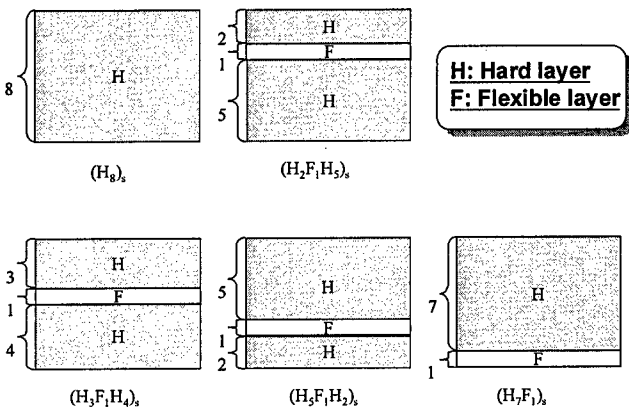


Figure 2 The stacking sequences of matrix hybrid composite laminates.

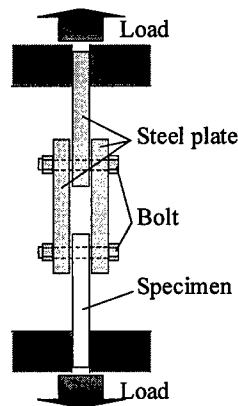


Figure 3 Schematic drawing of joint test.

### Bolted joint test

Figure 3 shows the bolted joint specimen and bolted test set-up. The joint geometry was decided by specimen width ( $w$ ) and, length ( $e$ ) and hole diameter ( $d$ ). In this study, the ratios of width to diameter ( $w/d$ ) and end length to diameter ( $e/d$ )



were 3 respectively, which fails in Bearing failure. The specimen was put between steel plates and jointed by the bolt without any clamping pressure. The Acoustic Emission (AE) was measured simultaneously with bolted joint test under 1mm/min of test speed and 20 degree of temperature.

## Result

The load-displacement curves for matrix hybrid laminates bolted joints are shown in Figure 4. The load linearly increased with increase of the displacement. The initial stiffness of each specimen was almost the same. For  $(H_8)_s$  without flexible layer, the increments of the curve slightly decreased at the lowest load, and bearing strength; failure load, was the highest in the all stacking sequences.

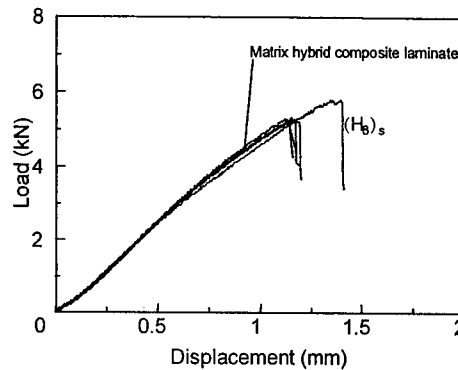


Figure 4 Load-displacement curves for the joint specimen with 12.5% of volume fraction of flexible layer.

Figure 5 shows the load-displacement curves and cumulative AE energy-displacement curves of each stacking sequences. It is recognized that the AE energy is the parameter corresponding to the failure magnitude in the specimen. Accordingly higher AE energy was measured when larger failure such as fiber breakage and delamination occurred. Thus it is considered that the initial failure

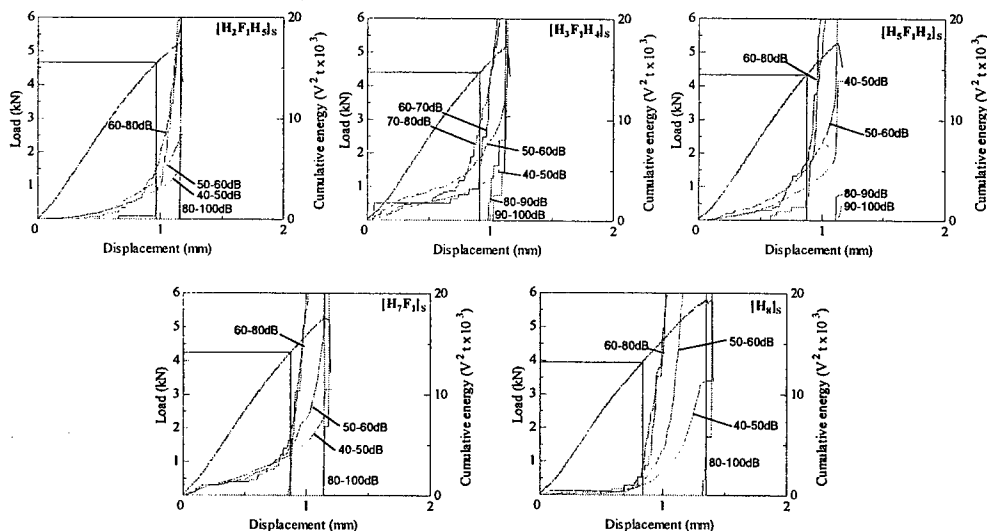


Figure 5 Load-displacement curve and cumulative energy-displacement curve.

occurred when higher AE energy was detected. The initial failure loads of each stacking sequences are shown in Figure 6. In this figure, initial failure load was the lowest in specimen. The flexible layer in the laminates resulted in improve of initial failure load. The initial failure loads were changed by the location of flexible layer. The initial failure load of  $(H_2F_1H_5)_S$  with the flexible layer in the outer layer was the highest, and initial failure load tend to decrease with the flexible layer moving to mid layer. Figure 7 shows the failure propagations of  $(H_2F_1H_5)_S$  and  $(H_8)_S$ . In  $(H_8)_S$ , the upper side of hole failed in the Bearing at 4.5 kN of load, on the other hand that failed at 5.0kN. It is considered that the flexible layer delays the development of failure because the flexible layer reduces stress concentration around the hole.

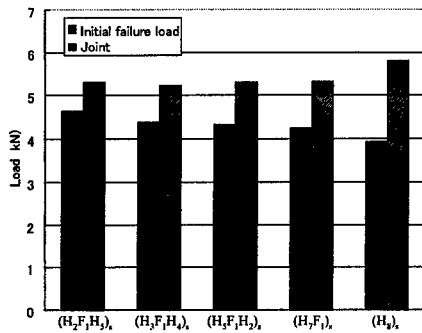


Figure 6 Comparison between initial failure load and joint strength.

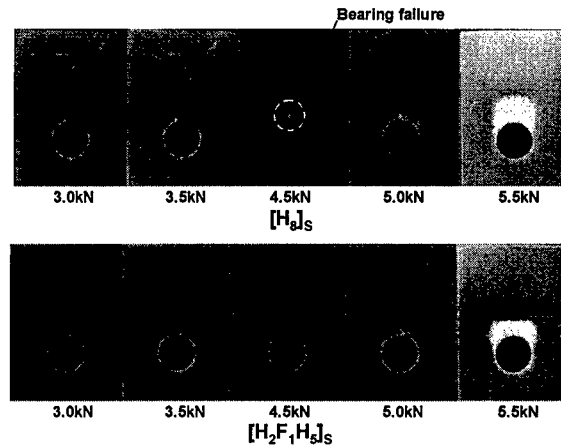


Figure 7 Failure aspects of  $[H_8]_S$  and  $[H_2F_1H_5]_S$ .

### Finite element method stress analysis

In this study, Finite Element Method stress analysis was conducted to confirm the effect of stacking sequence on stress concentration around circular hole in the thickness direction. Analyzed section of joint specimen is shown in Figure 8. Figure 9 shows analytical model of  $(H_8)_S$  and  $(H_2F_1H_5)_S$ . Because of symmetrical stacking sequence, only the half model was used that consists of the 2D plane strain element. Perfect-fit rigid pin and friction less were assumed. The material constant is summarized in Table 1. The fiber volume fraction,  $V_f$  and modulus;  $E_x$  and  $E_y$  were obtained from experiment.  $E_z$  and  $G_{yz}$  were assumed as the modulus in the fiber and transverse direction of uni-directional composite, and they were

calculated by rules of mixture. The material constants of the matrix resin shown in Table 2. As the boundary condition, the nodes at end of the specimen were fixed, and the nodes of pin parts elements with material constant of the steel were loaded along the y-axis.

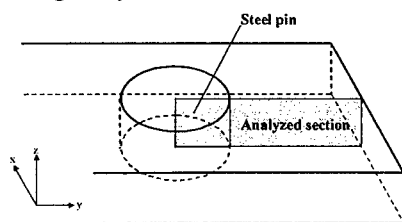


Figure 8 Description of Analyzed section of joint specimen.

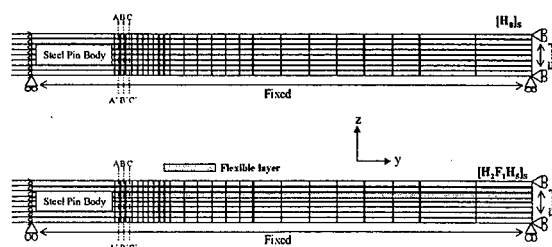


Figure 9 Analytical model for 0° section.

Table 2 Mechanical properties of high modulus and flexible layer

	$E_y$ (GPa)	$E_z$ (GPa)	$E_x$ (GPa)	$\nu_{yz}$	$\nu_{zx}$	$\nu_{xy}$	$G_{yz}$ (GPa)	$V_f$ (%)
High Modulus layer	24.9	10.5	21.8	0.3	0.3	0.3	0.85	44
Flexible layer	15.1	1.22	13.7	0.3	0.3	0.3	0.71	44

Figure 10 shows the relation between shear stress and location in section A-A', B-B' and C-C' as shown in Figure 9. For  $(H_8)_s$  without flexible layer, the shear

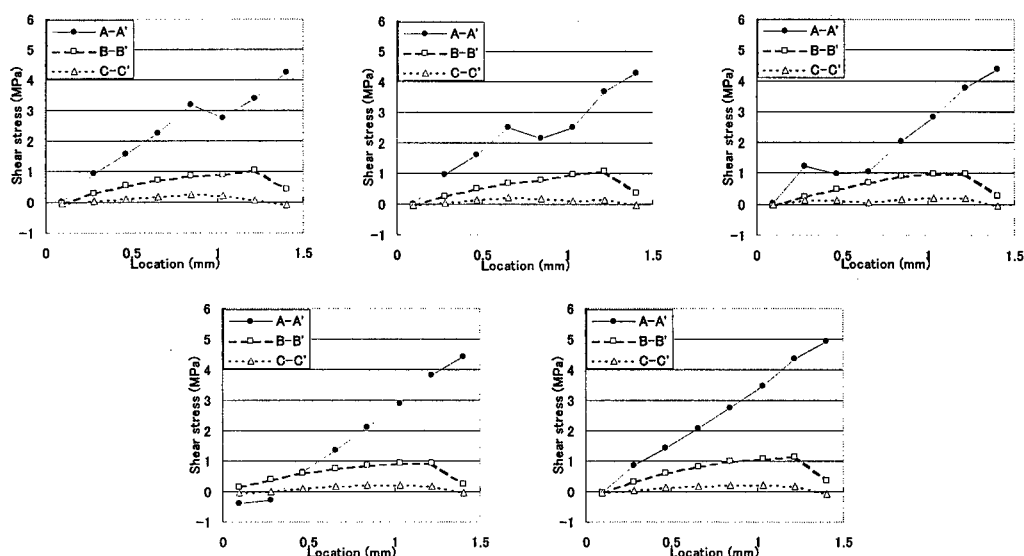


Figure 10 Shear stress distribution around hole.

stress linearly increased from mid layer to outermost layer. On the other hand, the shear stress was reduced at the flexible layer in except for  $(H_8)_s$ . The highest shear stresses of each specimen are shown in Figure 11. The  $(H_8)_s$  specimen indicates the highest shear stress. For the specimen with flexible layer, the shear stress tends to decrease slightly as the flexible layer moving from mid layer to outer most layer. This result, which says that  $(H_2F_1H_5)_s$  can bear higher load, and corresponds to the initial failure load obtained from AE measurement as shown in Figure 6. Therefore it is considered that the matrix hybrid laminates with flexible layer in the vicinity of the outer most layer such as can improve initial failure load because the shear stress concentration is effectively relieved.

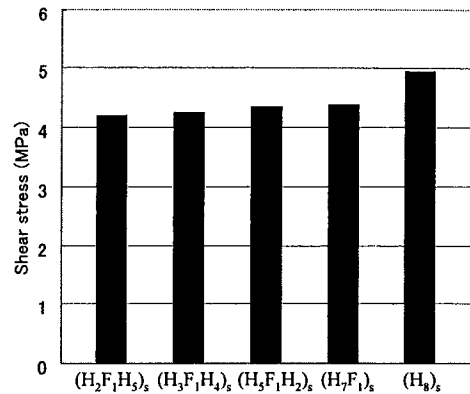


Figure 11 Comparison of maximum shear stress in matrix hybrid laminates.

## Conclusion

In this study, effects of stacking sequences on mechanically fastened joint strength of matrix hybrid laminates were investigated. The matrix hybrid laminates consists of the two kinds of resins, which are vinyl ester with high stiffness, high strength and brittle property and unsaturated polyester resin with low stiffness, low strength and considerably ductile property. The initial stiffness of the joint was almost the same in any stacking sequences. Final failure load of hybrid laminates with flexible layer became lower than that of conventional laminates with only vinyl ester resin, however, the initial failure load was increased by flexible layer in the hybrid laminates because of relieving shear stress concentration. Furthermore the initial failure load of the hybrid laminates that located in the vicinity of outer most layer was the highest among the stacking sequences. The reason of the results is that shear stress in the laminates is higher at the outer most layer. In consequence, the matrix hybrid laminates would make a contribution to improve the design stress and reduce the weight of the structures.

**Reference**

1. Chang F.K. and Scott R.A., Design of composite laminates containing pin loaded holes, *Journal of Composite Materials*, 18, 1984, 279-289.
2. Wilson D.W., Characterization of bolted joint behavior in SMC-R-50, ASTM STP 873, 1985, 73-85.
3. Schutz D. and Gerharz J.J., Strength behavior of carbon fiber reinforced plastic joints, AGARD Report, 727, 1986, 1-1.
4. S.Ramakrishna, H.Hamada and T.Nishiwaki, Bolted joints of pultruded sandwich laminates, *Composite Structures*, 1995, 32, 227-235.
5. C.Cooper and G.J.Turvey, Effects of joint geometry and bolt torque on the structural performance of single bolt tension joints in pultruded GRP Sheet material, *Composite Structures*, 1995, 32, 217-226.
6. Matthews F.L., Roshan A.A and Phillips L.N., The bolt bearing strength of glass/carbon hybrid composites, *Composites*, 13, 1982, 225-227.
7. H.Hamada, Z.Maekawa, K.Haruna, Elevation of Bearing Strength on Mechanically Fastened Carbon/Epoxy Joints by Thermoplastic Film Stacking, *Transactions of the Japan Society of Mechanical Engineers*, 57A, 1991, 101-107.

## **Comparison and Discussion about Compression after Impact (CAI) Properties Obtained by Several Test Method**

Eiichi Hara, Takashi Ishikawa, Masamichi Matsushima and Goichi Ben (O.-Il Byon)

### **Abstract**

Compression after impact (CAI) properties of flat plates made of CF/Epoxy were obtained by three kinds of test methods. The three kinds of methods are referred to as "SACMA", "HALF SACMA", and "JIS R(R: Reference)". From the results, it was clarified that the lower limit values of CAI strengths for the three methods are almost identical to each other. The other finding is that JIS R method is not suitable for examination of impact energy vs. delamination relationships.

### **Introduction**

Levels of compression after impact (CAI) strengths are considered to be crucial design critical values for aircraft composite structures.<sup>1)</sup> Allowable strain limit defined mainly from CAI values governs weight reduction ratios in composite stiffened panels. As another aspect of CAI, it is considered to be a material screening parameter for evaluating new composite system for a structure. Therefore, many CAI tests are conducted in aircraft industries and advanced composite suppliers.

At present, among several proposed CAI test methods, SACMA method<sup>2)</sup> has been employed most widely. In JIS (Japanese Industrial Standard), an almost identical specimen to SACMA was defined as a standard. JIS R method using a very small specimen is described as a reference method in JIS for CAI tests. "HALF SACMA" method was proposed<sup>3)</sup> recently by authors. If we consider low-cost demand in material evaluation, smaller size specimen is highly preferred. Thus, an investigation of size effect on CAI behavior is regarded as a very important subject. This report consists of one part of such an investigation and the emphasis is placed to describe experimental details of the three CAI methods.

---

Eiichi Hara, Graduate School, The Nihon University 1-2-1, Izumi, Narashino-shi, Chiba 275-8575, Japan

Takashi Ishikawa and Masamichi Matsushima, National Aerospace Laboratory, 6-13-1, Ohsawa, Mitaka, Tokyo 181-0015, Japan

Goichi Ben, College of Industrial Technology, The Nihon University 1-2-1, Izumi, Narashino-shi, Chiba 275-8575, Japan

## Specimens

The selected methods in this investigation are the above three. SACMA specimen consists of a plate of 32 plies,  $\{(45/0/-45/90)_4\}$  symmetric, 4-4.3mm in thickness and  $102 \times 152\text{mm}$  in size. JIS R and HALF SACMA specimens consist of the same plate in the thickness and stacking sequence and the size of  $50 \times 80\text{mm}$  and  $76 \times 102\text{mm}$ , respectively. HALF SACMA specimen is a half of SACMA in terms of area. In order to make a meaningful comparison, all specimens were fabricated with the same material, KA/410 carbon/Epoxy (by Mitsubishi Rayon Co. LTD) that belongs to the first generation brittle CF/Epoxy similar to NARMCO 5208 system (US material).

## Test Method

Three test methods (SACMA, JIS R, and HALF SACMA) were conducted in this paper. The difference among the three test methods is basically the sizes of specimens. It should be noted that fixtures for impact and compression tests fitting to each specimen size are required. However, the rest of the test method is regarded as the same in general. The test procedure is divided into the following 3 steps as shown in Figure 1:

- 1 Impact Test
- 2 Non-Destructive Inspection
- 3 Compression Test

The explanation about the above 3 steps is given as follows:

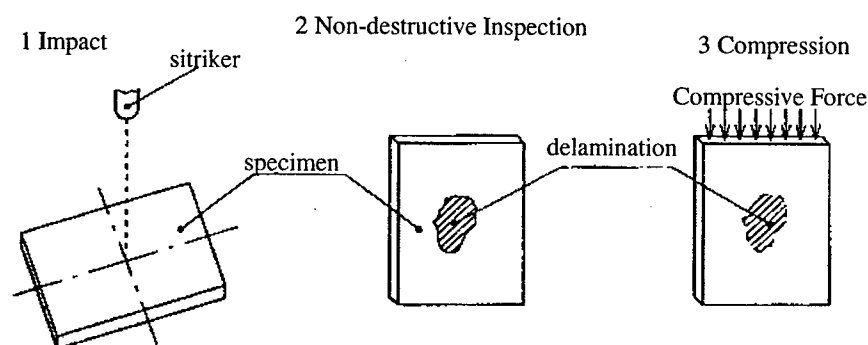


Figure 1 Three Steps of CAI Test

### Impact Test

The purpose of this test is creating delamination in specimen by impacts. The machine used here is a drop-weight type impactor, Dynatup GRC8250. A striker head is a hemisphere of 12.7mm (1/2 inch) in diameter. The striker weight including an extender and an adjustable mass system, is approximately 5.8 [kg]. The view of the impact test is shown in Figure 2. The impact takes place when dropping striker.

All the impact tests were conducted under the specified normalized energy condition by the plate thickness. Note that 6.67 [J/mm] is equivalent to 1500 [lbf\* in/in]. An example of the procedure to calculate the height with the specified impact energy condition is shown in the following:

A simple equation can be written as follows:

$$e = mgh, \quad elt = A \quad (1)$$

where  $e$  : energy for impact [J],  $m$  : mass of striker[kg],  $g$  : the acceleration of gravity ( $=9.8065$ )[m/s<sup>2</sup>],  $h$  : height of the striker [m],  $t$  : thickness of the plate [mm], and  $A$  : specified normalized impact energy[J/mm]. Therefore,  $h$  is determined as,

$$h = e/(mg) = At/(mg) \quad (2)$$

If we consider  $t=4.3$ [mm],  $m=5.80$ [kg],  $A=4$ [J/mm], then we have

$$h = 0.302[\text{m}]=302[\text{mm}]. \quad (3)$$

Here, let us consider the specimen holder at impact tests. The specimen holder at impact in SACMA method is specified as using rubber bushes for holding a

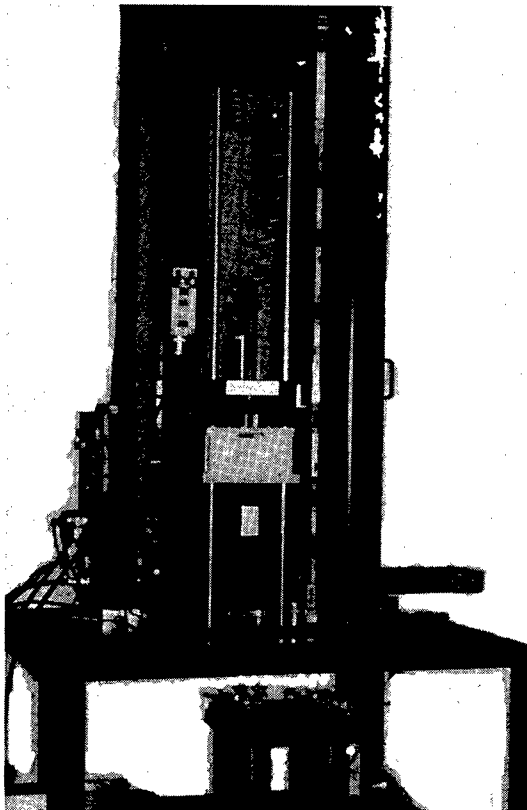


Figure 2 Impact Test Setup (GRC 8250)



specimen as shown in Figure 3. However, these bushes allow a slight rebound of a specimen and then a mechanical boundary condition during impact becomes ambiguous. Therefore, impact tests were also conducted by using a picture frame type holder similar to NASA method where the window shape was rectangle. In HALF SACMA, all the impact tests were conducted using a picture frame type specimen holder as shown in Figure 4. In JIS R, the specimen holder is specified as using a picture frame type with a circle window of 35 mm in diameter. In this report, however, frames with a rectangle window of 40mm by 70mm and with the specified circular window were utilized. Summary of testing specifications for comparison of these three methods is listed in Table I.

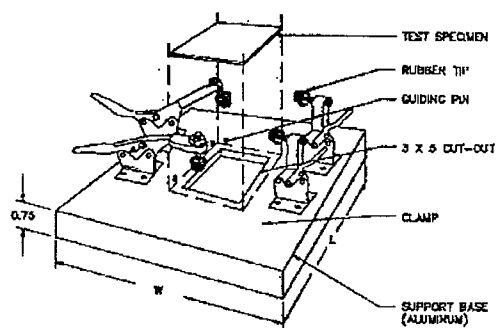


Figure 3 SACMA Impact Test Fixture

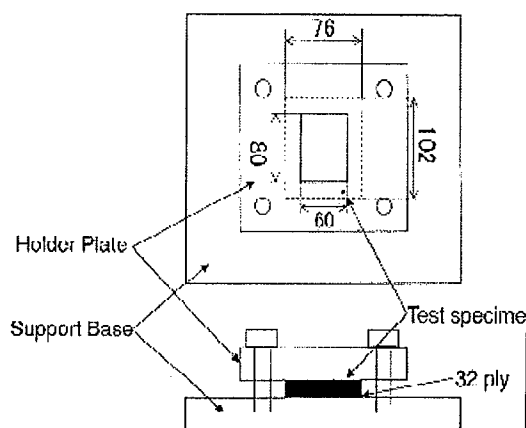


Figure 4 HALF SACMA Impact Test Fixture

Table I Summary of SACMA, HALF SACMA, JIS R Methods

	SACMA	HALF SACMA	JIS R circle	JIS R rectangle
Specimen size(mm)	102*152*4	76*102*4	50*80*4	50*80*4
Supporting Device	Clamping with Rubber Bush and Picture Frame	Picture Frame		
Window Frame Shape	rectangle	rectangle	circle	rectangle
Window Frame size(mm)	76*127	60*80	$\phi$ 35	40*70
Stacking Sequence	{(45/0/-45/90)4}sym.=32ply			
Boundary Condition	Clamped at Loading Edges and Simply Supported at Side Edges			

### Non-Destructive Inspection

The purpose of this step is to investigate delamination in specimen after impact. The machine used here is a ultrasonic C-scanner, SDS5400R system by Krautkramer Japan Co. LTD. Specimens after impact were examined by this system for determining delamination geometry. This system can provide plane views of accumulated delaminations (C-scope) and their side views (B-scope) by processing

ultrasonic echo and probe location data. By integrating these views, it is possible to identify 3-dimensional delamination geometry created by specified impacts. The view of Non-Destructive Inspection is shown in Figure 5. Delamination area is defined here as the projected area of all delamination accumulation, that is, the delamination area here is not the total area of delamination.

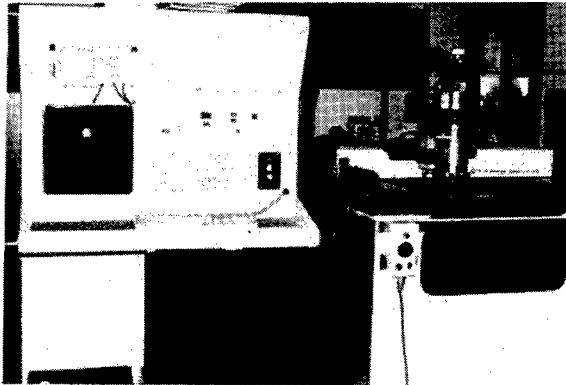


Figure 5 Non-Destructive Inspection by Using a C-scanner

#### Compression test

In this step, the used data acquisition devices were HP Vectra 286/12 (Computer system) and HP 3852A (control unit) with normal strain gages and dial gages for out-of-plane deflections. Number of strain gages were 12 - 6 corresponding to specimen's size. The screw driven Instron 1128 machine was used for all tests. The crosshead speed was determined as 0.2 [mm/min] so as to be appropriate for such tests. The compression test fixture corresponding to each specimen size was used. In all the tests, the boundary conditions were clamped at loading edges and simply supported at side edges.

#### Discussions

The number of test specimen is 23 for SACMA Standard, 6 for SACMA Picture Frame, 12 for Half SACMA, and 13 for JIS R (including quoted tests from authors' previous data<sup>1)</sup>).

#### About Ultrasonic C-scanning

Typical examples of C-scanning data of delaminated plates are shown in Figure 6. Relationships between delamination area and normalized impact energy are shown in Figure 7 where horizontal lines indicate areas of the impact test fixture windows in order of size, JIS R circle ( $962\text{mm}^2$ ), JIS R rectangle ( $2800\text{mm}^2$ ) and HALF SACMA ( $4800\text{mm}^2$ ). It is shown that delamination area is roughly

proportional to the normalized impact energy in HALF SACMA test. It is shown, however, that delaminations spread out to edge of impact test fixture with all normalized impact energy level (2.0J/mm-4.0J/mm) in JIS R circle. Let us denote this phenomenon as delamination saturation. It can be understood that JIS R method with a circle window has a problem that delamination saturation occurs at every normalized impact energy. In JIS R method with a rectangle window, delamination saturation was not occurred up to 4.0J/mm. The tendency in Figure 7 below 4.0J/mm in HALF SACMA is similar to that of SACMA. It is shown that brittle CF/EPOXY like this material shows delamination saturation easily in smaller specimens.

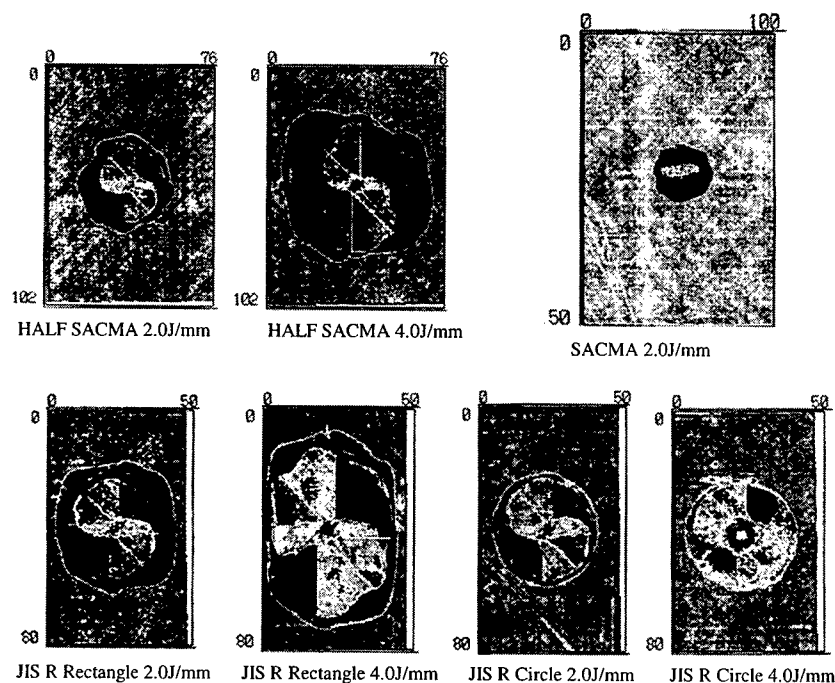


Figure 6 C-scanning Data of Delaminated Plates (unit: mm)

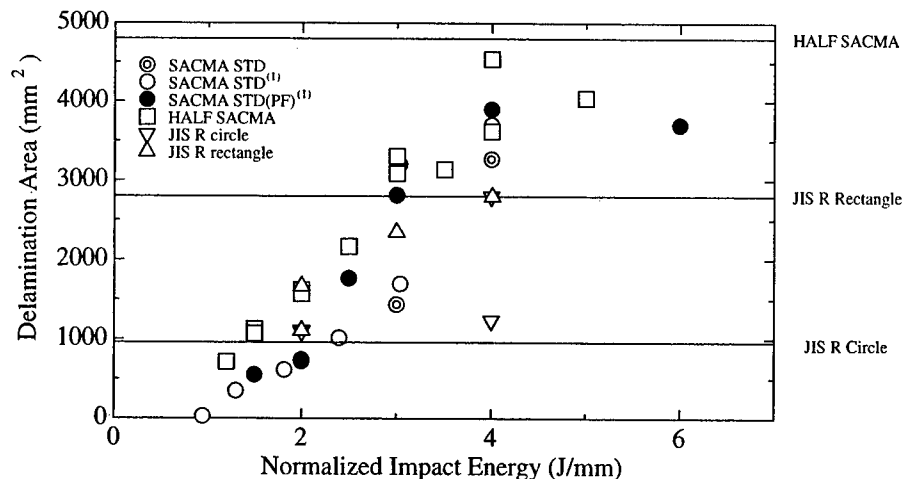


Figure 7 Relationships between Normalized Impact Energy and Delamination Area

### About Compression test

As an example, stress-strain curves for 8 selected channels are shown in Figure 8 for HALF SACMA-05. CAI strength was determined from the maximum stress value. Relationships between CAI strength and normalized impact energy are shown in Figure 9. It is shown that lower limit values of CAI strength in three methods (SACMA, HALF SACMA and JIS R method) are almost identical. It is shown that CAI strength reduction (at 1.3J/mm) is noticeable in HALF SACMA. In no impact cases, however, strength in HALF SACMA is higher than that of SACMA. Moreover, strength in JIS R is even higher than that of HALF SACMA, i.e., the lowest strengths to highest are in order to SACMA, HALF SACMA and JIS R. In other words, a dependency of no-impact compression strengths on the specimen size can be observed. One possible reason for this dependency is a correlation between the lowest buckling stress and the final compressive strength. Of course, JIS R specimen and SACMA show the highest and the lowest buckling stresses, respectively.

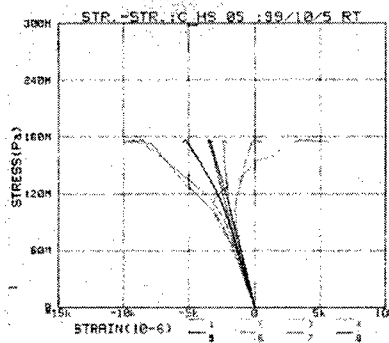


Figure 8 Stress-Strain Behavior in HALF SACMA (Impact: 4.0J/mm)

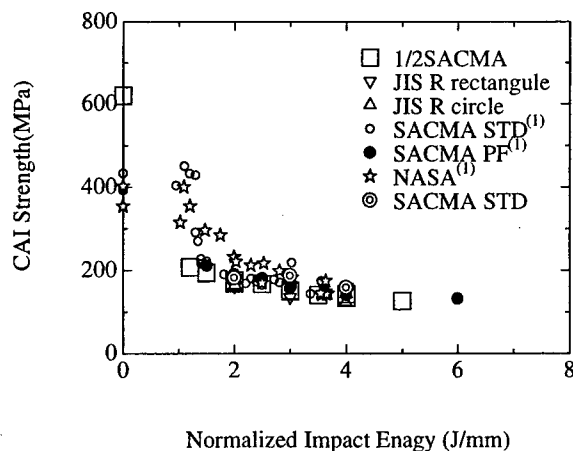


Figure 9 Relationships between Normalized Impact Energy and CAI Strength

## Conclusions

CAI strengths of CF/EPOXY were obtained by using 3 methods, SACMA, HALF SACMA and JIS R. The following findings are unveiled through the experimentation:

1. Projected Delamination area by impact tests in HALF SACMA method is similar to that in SACMA method before the delamination saturation.
2. In JIS R circle method, it is not appropriate to investigate relationships between CAI strength and normalized impact energy because the delamination saturation takes place quite early above 2.0J/mm.
3. Lower limit values of CAI strength remain almost in the same level in all the methods.
4. Some more experiments and discussions will be required to establish HALF SACMA method as the approved standard.

## Acknowledgment

The authors wish to express their gratitude to Mr. Hayashi (Tokyo Business Service Co. LTD), Mr. Nakagawa and Mr. Kouji (students of Sophia University) who cooperated with experimentation.

## References

1. T. Ishikawa, M. Matsushima, and Y. Hayashi, 1998. "Comparison and Discussion about Compression after Impact (CAI) Properties Obtained by SACMA and NASA Methods." Proceedings of 8<sup>th</sup> US/Japan Conference on Composite Materials, pp. 476-485.
2. SACMA, 1988. "Recommended Test Method for CAI Properties." SRM 2-88.
3. T. Ishikawa, M. Matsushima, E. Hara, and G. Ben, 1999. "Comparison of CAI Test Results via SACMA and NASA Methods and Proposal of New Test Method (1/2 SACMA)." Proceedings of the 24<sup>th</sup> Composite Materials symposium, pp. 193-194.
4. E. Hara, T. Ishikawa, M. Matsushima, and G. Ben, 1999. "The experimental Results in Compression-After-Impact (CAI) of small CFRP Plates." Proceedings of the 24<sup>th</sup> Composite Materials symposium, pp. 195-196.

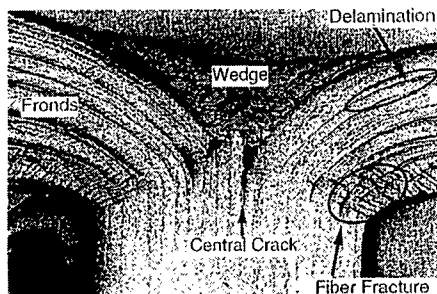
## **Investigation of Fracture Mechanisms of Braided Pultrusion Composites Rods**

Ryuji Inai, Hiroshi Saito, Koji Kameo, Tadashi Uozumi,  
Masaharu Iwamoto, Hiroyuki Hamada

### **Abstract**

FRP rods made by braided pultrusion process (BPP) was used in this study. BPP can fabricate constant quality products continuously, and this fabrication process can restrain fabrication cost comparatively. Moreover, FRP with a trigger made at the end shows a characteristic fracture called progressive crushing. Therefore FRP is attracted to use as energy absorption properties recently. In this study, the energy absorption properties and fracture mechanisms of BPP rods were investigated.

### **1. Introduction**



*Fig.1 Mechanism of Progressive Crushing.*

FRP shows not only the excellent strength with lighter weight than metal, but also high energy absorption properties when a conical chamfer is made at the one end. Therefore FRP has been applied to structural components for various vehicles recently. Particularly, braided composites are expected to use for safety

---

R.Inai, H.Saito, M.Iwamoto and H.Hamada, Division of Advanced Fibro Science, Kyoto Institute of Technology

K.Kameo, Division of Polymer Science Graduate School, Kyoto Institute of Technology, Matsugasaki, Sakyo-Ku, Kyoto, 606-8585, Japan

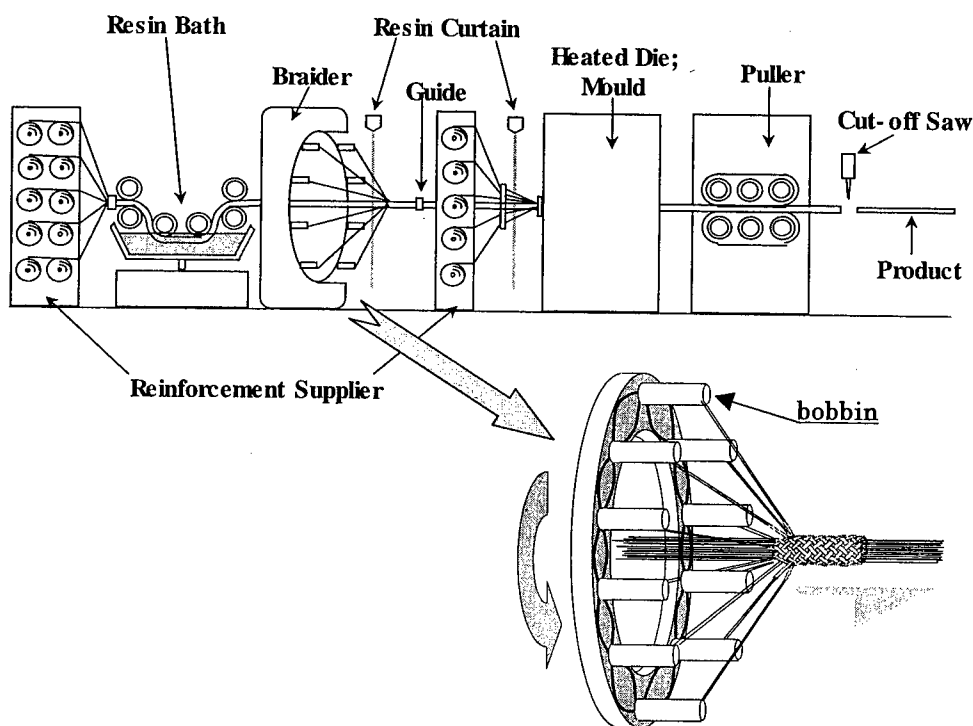
Tadashi Uozumi, Braider Section, Technical Department, Murata Machinery, Ltd

components, because they show the fracture mode called progressive crushing, which proceeds under constant load. Figure 1 shows the representative crushing mechanism of the progressive crushing. The progressive crushing occurred by combination of the various fracture mode; fiber fracture, delamination and cracking and so no, so that the crushing energy absorption value is considered to equal the total sum of the energies of these fractures[1].

In this study, as method to satisfy both cost and strength requirements, braided pultrusion process (BPP)[2][3] was used. The mechanical properties, especially fracture mechanisms of braided rods which consist of both uni-directional fibers and braiding fibers were investigated.

## 2. Braided Pultrusion Process

The construction of braided pultrusion process is shown in Fig.2. From the left, in order, that construct of resin impregnator, braider, heated die, puller and cutter. BPP can fabricate constant quality products in on-line processing continuously. The speed of pultrusion was 200 mm/min.

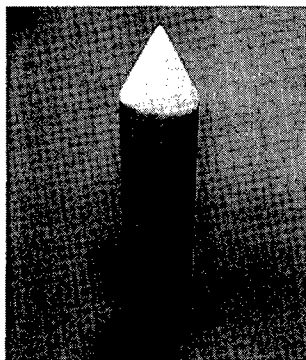


*Fig.2 Schematic Draw of Braided Pultrusion System*

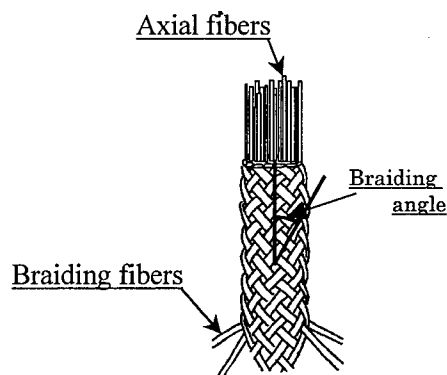
### 3. Material and Specimen

Construction of fabricated rod is shown in Fig.3. The braided rod is constructed by uni-directional axial fibers surrounding braiding fibers. In this study, materials used were epoxy resin as matrix, and glass fibers as reinforcements. The braiding angle was 17 deg. The types of glass fibers were 1150 tex. as braiding fibers and 2310 tex. as uni-directional fibers.

In crushing test, all rods were cut off in 50mm length for use as specimen. For crushing test, a 30degree conical trigger was made at the one end of the specimen rod. Energy absorption properties were evaluated by compression test to longitudinal direction at constant speed, 5mm/min. To investigate fracture mechanism, the cross-section of all rods was observed with the step by step test, and the displacement was 1mm, 3mm, 6mm, 9mm, 12mm, and 15mm.



(a) Photograph of Specimen



(b) Schematic Draw of Specimen

Fig.3 Construction of Braided Perform

### 4. Fracture Mechanism and Energy Absorption Properties

#### 4.1. Energy Absorption Properties

The typical fracture aspect of after testing and the load-displacement curve are shown in Fig.4. The specimen fractured with expanding axial fibers in radial pattern like petals. Load increased with increment of displacement, and indicated approximately constant value after reached maximum value. From these results, the specimen showed typical progressive crushing.

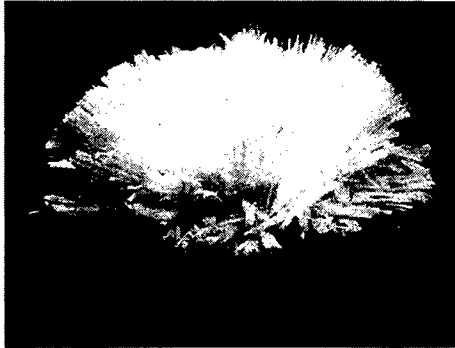
The specific energy absorption value ( $E_s$  value) was calculated to evaluate energy absorption properties.  $E_s$  value is calculated by mean crushing load ( $\bar{p}$ ), area of



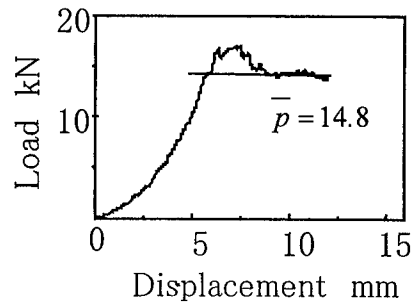
cross section ( $A$ ) and density of material ( $\rho$ ) as follows,

$$Es = \bar{p} / A\rho \quad (1)$$

The unit of  $Es$  is kJ/kg. From equation (1),  $\bar{p}$  was 14.8 kN and  $\rho$  was 2.22 g/cm<sup>3</sup>, so that  $Es$  value was 59.1 kJ/kg.



(a) Photograph



(b) Load-Displacement Curve

Fig.4 Braided Rod of Glass

Table.1[4] lists the  $Es$  value of various material systems. Here, C was the braided rods fabricated by same BPP system.  $Es$  value of G which was obtained in this paper was equivalent to Glass or Kevlar/Epoxy Tubes and was higher than  $Es$  value of Steel Tube. Accordingly, the braided rods which fabricated by BPP has high potential for crushing elements.

Table.1 Comparison of  $Es$  Value

Specimen	$Es$ (kJ/kg)
G	59.1
C	99.9
Glass/Epoxy Tube	53.7
Kevlar/Epoxy Tube	57.9
Steel Tube	33.7
Aluminum Tube	66.9

## 4.2. Fracture Mechanism

The crushing tests were stopped at 1mm, 3mm, 6mm, 8mm, 12mm and 15mm, and the cross-section was observed. Fig.5 shows observed cross-sections in each steps, and Fig.6 shows cross-sectional schematic draws of specimen from the observed photographs.

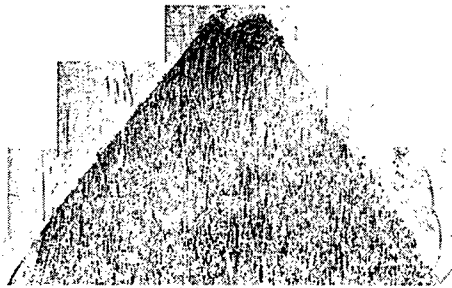
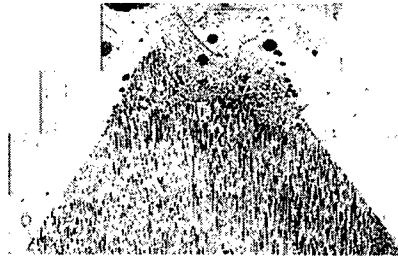
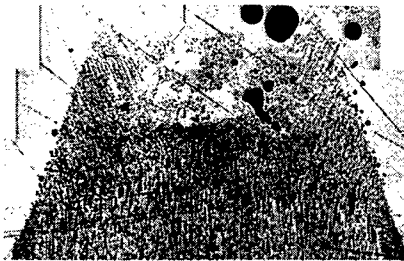
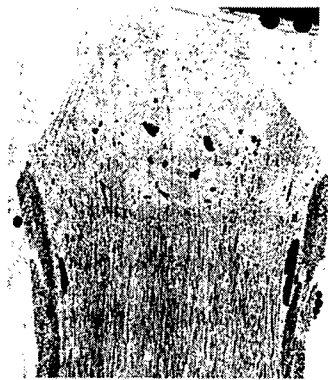
At 1 mm, the wedge was made from shattering axial fibers at the top of specimen. At 3 mm, fronds were recognized as shown in Fig.6(b). The fronds were occurred because the fibers pushed out in circumferential direction by enlargement of wedge. At 6 mm and 8 mm, the fronds spread with enlargement of wedge. At 12 mm, delamination was shown between axial fibers and braiding fibers. At 15 mm, fronds spread largely, but cracks did not occur in zone A as shown in Fig.6(f).

## 5. Conclusion

In this study, to satisfy with cost and strength requirements, braided pultrusion process (BPP) was carried out. BPP can realize constant products quality in on-line processing, so that this fabrication process can save fabrication cost comparatively. The mechanical properties and fracture mechanisms of BPP rods were investigated. First the mechanical properties of BPP rods under compressive load were investigated. Consequently BPP rods had good energy absorption properties by progressive crushing. Especially  $E_s$  value indicated higher value, so that BPP rods has high potential for crushing elements. Next, fracture mechanisms were investigated by the aid of step-by-step observation method. In consequence, BPP rods indicated characteristic fracture mode. This fracture mode would be correlated the fracture toughness of the material.

## 6. Reference

1. H.Hamada, S.Ramakrishna, "Impact Performance of Glass Cloth/epoxy Composite Tubes with Different Surface Treatment", Composite nterface, Vol.4, 1996, pp.1-10
2. A.Fujita, T.Nakatani, T.Uozumi, K.Kameo, A.Nakai, H.Hamada, "Crush Energy Absorption of Braided Composite Rods", Proceedigs of the fifth Japan International SAMPE Symposium, 1997, pp. 1231-1234
3. Y.Hisa, T.Uozumi, A.Fujita, H.Hamada, A.Nakai, A.Yokoyama, "Braiding Pultrusion Process (BPP)", 27th International SAMPE Technical Conference, 1995, pp. 371-379
4. Y.Nakatani, The Research of FRP's Crushing Mechanism and Application, Master's Thesis, (1997), (In Japanese)

*(a) 1mm**(b) 3mm**(c) 6mm**(d) 8mm**(e) 12mm**(f) 15mm**Fig.5 Photograph of Braided Rod*

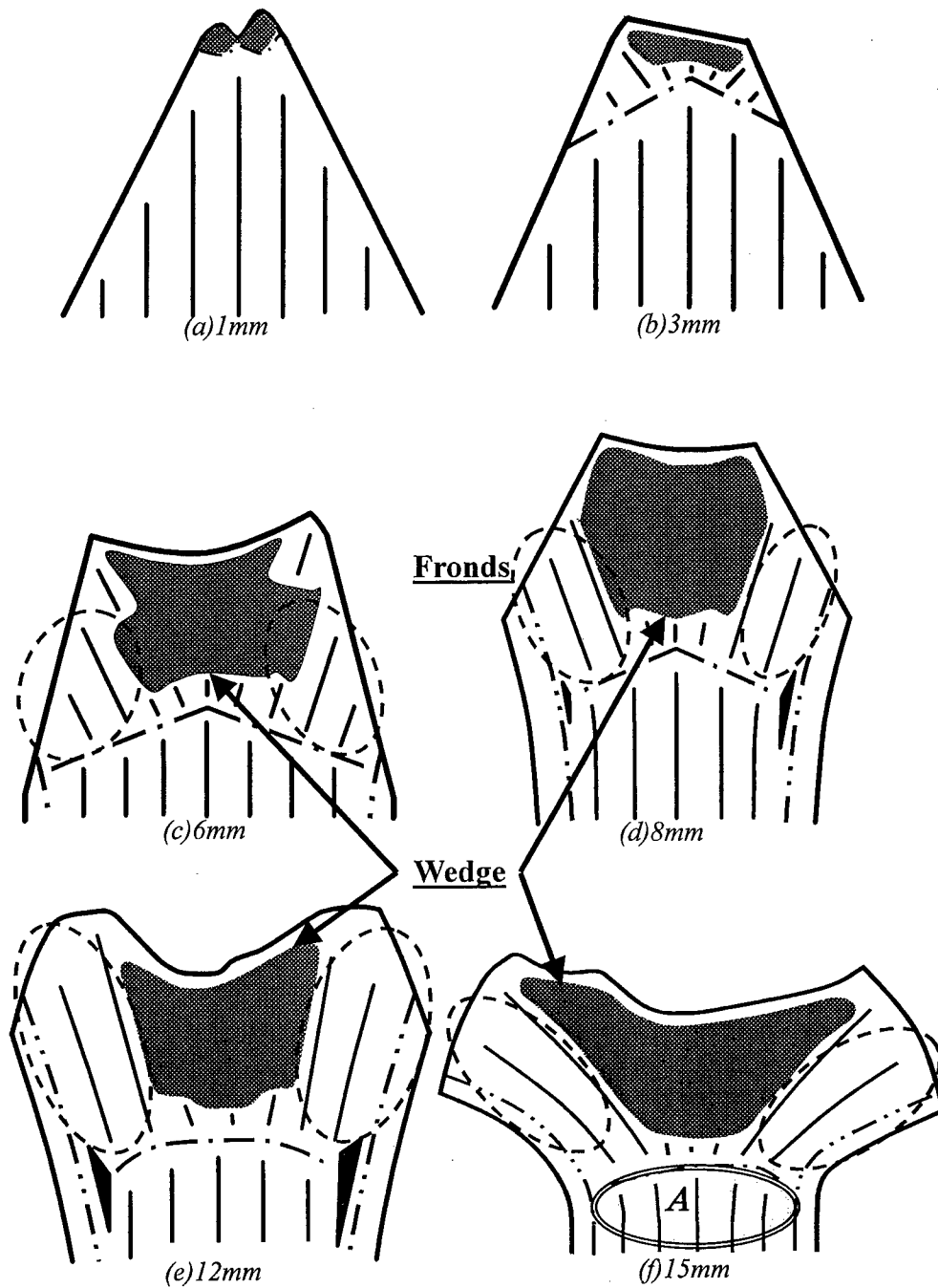


Fig.6 Schematic Draw of Braided Rod

## **Structure and Mechanical Properties of Injection Molded CF/LCP Thin Plates**

Akihiro FUJITA\*, Hiroshi ISHIDA\*\*, Etsuko TANIGAKI\*\*,  
Hiroyuki HAMADA\*\*\* and Fumiaki BABA\*

### **ABSTRACT**

Injection molded Liquid Crystalline Polymer (LCP) has a unique multi layer structure. This study investigates fiber orientation and bending properties of carbon fiber reinforced LCP (CF/LCP). Two types of mold were used under several molding specifications. Bending properties and fracture behaviors of the injection molded CF/LCP thin plates were studied. Moreover, an estimate of bending modulus of the injection molded CF/LCP was obtained by the laminate beam theory. It was observed that all specimens consisted of five macro layers; two skin layers, two intermediate layers, and a core layer. The gate shapes influence the fiber orientation in each layer. The observed differences of fracture aspect due to the gate shape and cutting position are caused by modulus in each layer as the laminated composite. Laminate beam theory is good for fundamental formula of modulus prediction for CF/LCP formed multi layer structure.

### **1. INTRODUCTION**

There is a growing interest in the development of thermotropic liquid crystalline polymers (LCP) especially for high performance materials such as molded articles. LCP consists of rigid, rod-like molecules with the ability to orient themselves in the melt, in which they exhibit both very low melt viscosity and long relaxation time [1]-[5]. By using injection molding for processing, the resulting polymer in the molded articles shows a very high degree of molecular orientation and consequently exhibits superior properties such as high mechanical strength and modulus. The unique multi layer structure and the mechanical properties of injection molded LCP have been widely studied [6]-[11]. Despite many numerous studies in injection molding of LCP reinforced composites [12]-[13], only a few have focused on the interaction between fiber and polymer in fiber reinforced LCP [15].

Akihiro FUJITA and Fumiaki BABA, Advanced Technology R&D Center, Mitsubishi Electric Corporation 8-1-1, Tsukaguchi-honmachi, Amagasaki, Hyogo 661-8661, JAPAN

Hiroshi ISHIDA and Etsuko TANIGAKI, Graduate school, Kyoto Institute of Technology Matsugasaki, Sakyo-ku, Kyoto 606-8585, JAPAN

Hiroyuki HAMADA, Advanced Fibro-science, Kyoto Institute of Technology Matsugasaki, Sakyo-ku, Kyoto 606-8585, JAPAN

In this study, the properties of carbon fiber reinforced LCP (CF/LCP) were investigated. The injection molded CF/LCP thin plates were manufactured using two gate shapes and various injection speeds. Bending properties and fracture behaviors of the injection molded CF/LCP thin plates were investigated and the bending modulus of the injection molded CF/LCP was estimated by the laminate beam theory.

## 2. EXPERIMENTAL PROCEDURES

### 2.1 Materials

Two resins used in this study are non-reinforced liquid crystalline polymer (VECTRA A950, Polyplastics Co.) and carbon fiber reinforced liquid crystalline polymer (VECTRA A230, Polyplastics Co.,  $V_f=30\text{wt}\%$ , fiber length  $=\pm 200\mu\text{m}$ ), and mixed under dry condition. Carbon fiber content are  $0\text{wt}\%$  (A950) and  $20\text{wt}\%$  (A220).

### 2.2 Injection Molding

The two molds used in this study are illustrated in Fig.1. These are the plate cavity molds with side (S) or film (F) gates. The plate dimension is  $70(\text{L}) \times 55(\text{W}) \times 1.0(\text{T}) \text{ mm}$ . A reciprocating screw injection molding machine with a hydraulic accumulator system (V110/75V, Sumitomo Heavy Machinery Co.) is used in this study. Injection molding conditions are summarized in Table 1. The injection speeds range from  $150\text{mm/s}$  ( $68\text{cc/s}$ ) to  $300\text{mm/s}$  ( $136\text{cc/s}$ ), with the  $150\text{mm/s}$  and  $300\text{mm/s}$  speeds regarded as low injection speed (L) and high injection speed (H), respectively. The specimens are identified by the gate shape and injection speed,

Table 1 Injection molding conditions.

Table 2 List of injection molded plates.

Injection Speed	High	Low
Cylinder Temperature ( $^{\circ}\text{C}$ )	320	320
Mold Temperature ( $^{\circ}\text{C}$ )	70	70
Injection Speed (mm/sec.)	300	150
Injection Speed (cc/sec.)	136	68
Injection Time (sec.)	0.14	0.3
Holding Pressure (MPa)	25	50
Holding Time (sec.)	1	3
Cooling Time (sec.)	30	30

CF/LCP (Fiber Volume Fraction:20wt%)		
Sign	Gate	Injection Speed
A220FH	Film	High
A220FL	Film	Low
A220SH	Side	High
A220SL	Side	Low

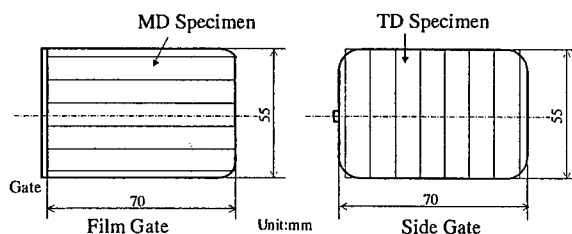


Fig.1 Mold types and specimen cutting position.

and the corresponding notation, S or F, L or H, are added at the end of material name. For example, "A220SH" is A220 fabricated under high injection speed using mold

with side gate.

### 2.3 Experiments

Individual fiber orientation are examined with optical microscope on top of surfaces prepared by specimens are metallographic polishing technique.

Bending test cut out in parallel (MD) and perpendicular (TD) to longitudinal direction of the plate, as illustrated in Fig.1, in order to take into account the effect of cutting location of the specimen. The specimens are cut into strips of 10mm width, and the bending tests are performed for span length of 30 mm at 2mm/min under room condition using universal testing machine (Autograph, SIMADZU Co.).

The fracture characteristics from bending test were examined using metallographic microscope.

## 3. EXPERIMENTAL RESULTS

### 3.1 Observations of Fiber Orientation States

The optical microphotographs in Fig.2 represent the cross sectional view of the center of A220 plate along MD direction. All specimens consist of five macro layers: two skin layers, two intermediate layers and one core layer. In the case of film gate, the fibers orient randomly inside the skin and core layers, and in the flow direction inside the intermediate layer. With side gate, the fiber orientation in the skin layer is random. In the intermediate layer, there are a few fibers oriented in the flow direction although the majority has random one. In the core layer, the fibers are oriented perpendicular to the flow direction. Variation in the fiber orientation due to injection speed does not appear in each layer. The intermediate layer at the low injection speed is thicker than that at the high injection speed.

Further, examination on polished planes in the skin, intermediate and core layers is performed based on the previous cross sectional observation to gain better understanding on fiber orientation. Because there is no considerable difference in fiber orientation due to high injection speed, only photographs of the low injection speed are shown.

The planar view of fiber orientation in each layer of A220 is shown in Fig.3. In the case of the film gate, a random fiber orientation in the skin layer is observed. The fibers orient in the flow direction inside the intermediate layer except for the area close to the gate and edge. On the other hand the fibers orient randomly inside the core layer. The fibers are locally oriented in the flow direction near the side edges, and perpendicular to the flow direction around the gate.

In the case of side gate, the random fiber orientation is observed in the skin layer just as with film gate. In the intermediate layer, the fibers align somewhat randomly. The fibers are locally aligned in the flow direction at the side edges of the intermediate layer. In the core layer, the fibers orient perpendicularly to the flow direction. The fiber orientation parallel to the flow direction along the side edges is also observed in the core and intermediate layers.

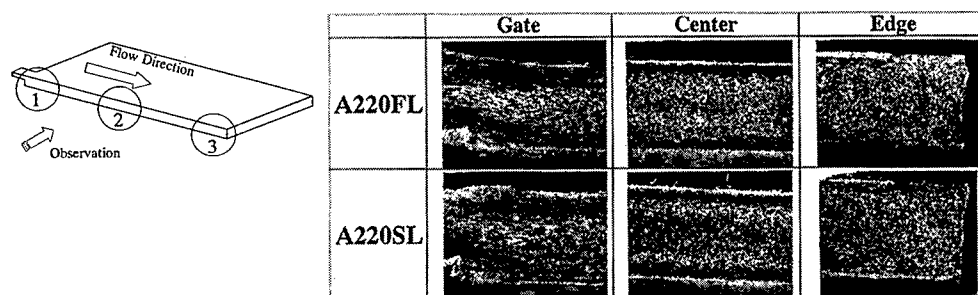


Fig.2 Optical microphotographs of the cross section at the center of plate A220 along the MD direction.

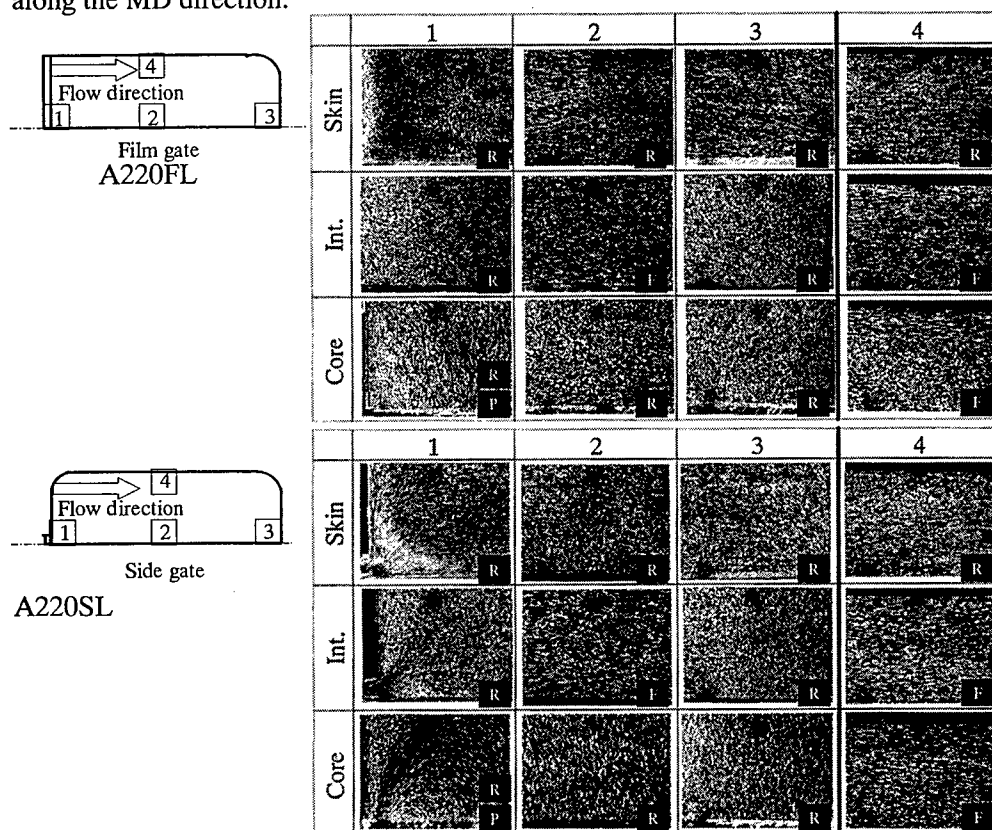


Fig.3 Planer view of fiber orientation of plain view in each layer of A220.

### 3.2 Bending Properties

Fig.4 show the relationship between bending properties and cutting position in A220. The MD specimens from the side edges exhibit higher bending moduli than the MD specimens in the center and width direction. Among the specimens in the center and the width direction, the bending moduli are similar. The bending moduli



of the specimens with the film gate are higher than those with side gate at any positions. As for the effect of injection speed, A220FL and A220SL specimens made under the low injection speed exhibit higher bending moduli than A220FH and A220SH made under high injection speed. On the other hand, in TD specimens, the bending moduli of the specimens obtained from the area around the gate are higher than those from around the edge regardless of the gate shape. The characteristics of bending modulus due to gate shape and injection speed are the opposite of those of MD specimens. For all specimens, the relationship between bending strengths and cutting position are similar to those of the bending moduli.

The fiber orientation in the intermediate layer contributes to the bending properties of MD specimens from all plates. With film gate, the fiber orientation parallel to the flow direction inside the intermediate layer lead to higher bending properties of MD specimens. The bending properties of MD specimens from the low injection speed are higher than those from high injection speed with both film and side gates because of the thicker intermediate layer at low injection speed. Similarly, in TD specimen, the fact that the fiber orientations in the core layer is perpendicular to the flow direction contributes to higher bending modulus and strength. The fiber orientation in the flow direction at the side edges of the intermediate and core layers contributed to high bending modulus and strength for the side edges of MD specimen. The fiber orientation in the core layer is perpendicular to the flow direction and results in high bending modulus and strength for TD specimens, near the gate.

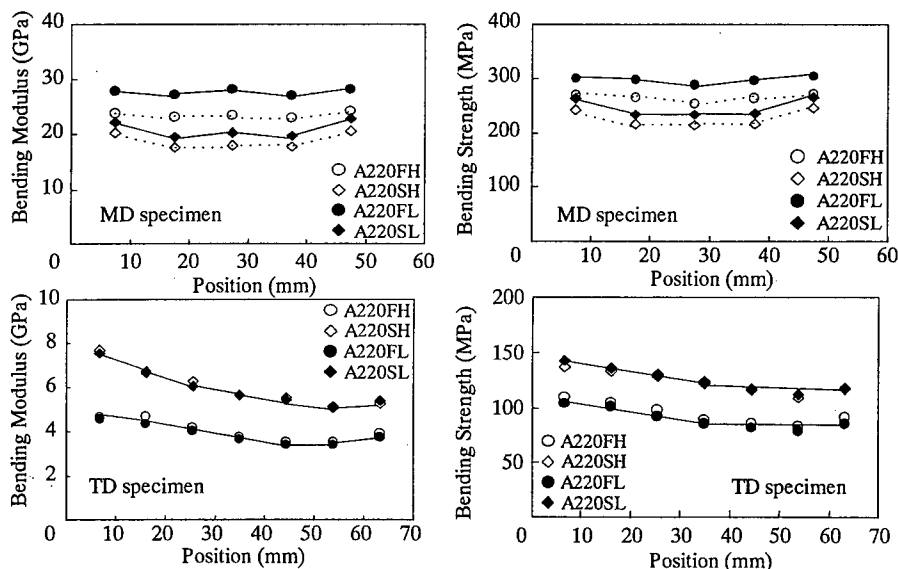


Fig.4 Relationship between bending properties and cutting position of the A220 specimen.

### 3.3 Fracture Aspects

Fig.5 and Fig.6 show the cross section of MD and TD specimens of A220 after bending test. The upper side is compressive side and the bottom side is tensile side.

In the specimen with the film gate, the fracture propagates at the interface between skin and intermediate layer. The fracture then reaches at the core layer through the intermediate layer. On the other hand, for side gate, the fracture propagates from the surface of tensile side to the intermediate layer, and passes to the thickness direction of the core layer. The fracture aspects were not influenced by the difference of cutting position in both film and side gate specimens.

In TD specimen with side gate, the fracture propagates in the thickness direction from skin layer to intermediate layer. After that, it grows along the interlayer between intermediate layer and core layer. In the film gate specimen, the fracture could not be observed at the interlayer between intermediate and core layer. However, at the edge of the specimen, the fracture occurs along thickness direction regardless of the gate shape. The fracture aspects are not influenced by the variation in injection speed in either MD or TD specimen.

The differences of fracture aspect with respect to the gate shape and cutting position are probably caused by the differences of modulus in each layer as in laminated composite.

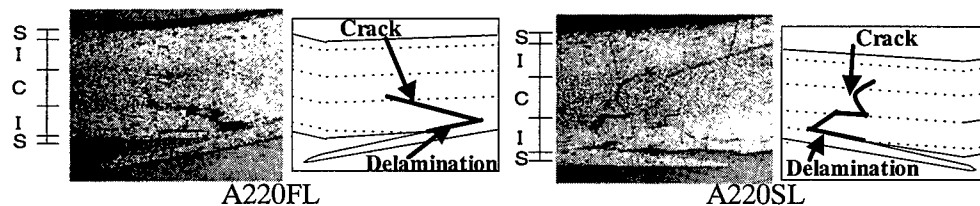


Fig.5 Fracture aspects of MD specimens of A220 after bending test.

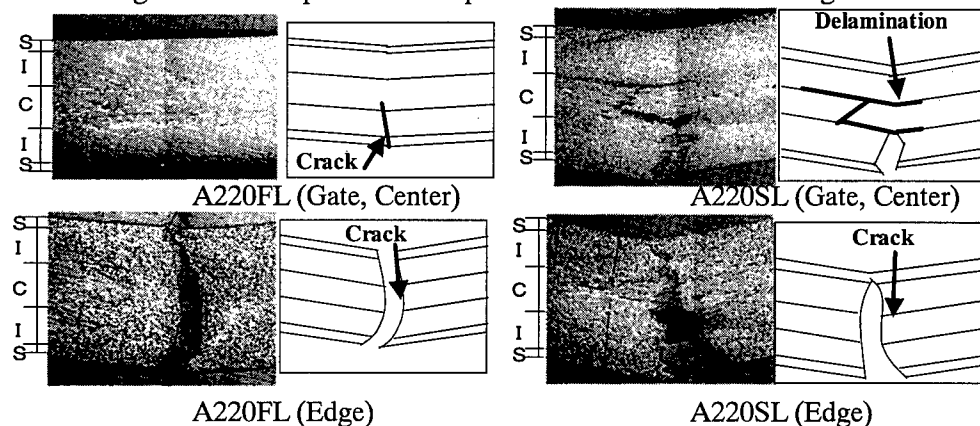


Fig.6 Fracture aspects of TD specimens of A220 after bending test.

#### 4. DISCUSSIONS

All injection molded plates consisted of five macro layers: two skin layers, two intermediate layers and one core layer. It is interesting to note that fiber orientation in each layer is changed by the gate shape of the plate mold. In the skin layer, fiber orientation is small, because resin is immediately solidified in the contact with the

mold. Therefore, the fibers are aligned randomly in the skin layer regardless of the gate shape. In the intermediate layer the fibers are aligned to the flow direction by shear force, but the resin flows in a diverging manner at the instance of side gate. The random fiber orientation in the intermediate layer observed in the close area of side gate is due to this flow behavior. In the core layer, the resin flow is divergent and the speed is high. These flow behaviors are dominant in small gate as well as in side gate, and lead to fiber orientation which is perpendicular to the flow direction. Therefore, the fibers in the core layer are aligned in perpendicularly to the flow direction in the side gate and randomly in the film gate.

The bending moduli in each cutting position of A220FL and A220SL are predicted by the laminate (sandwich) beam theory, since CF/LCP thin plate forms five layers of sandwich structure. In general, bending rigidity of the sandwich structure is presented by the following equation:

$$EI = \sum E_i (A_i z_{oi}^2 + I_{oi}) - z_0^2 \sum E_i A_i$$

Where  $EI$  is the Bending rigidity of laminated plate,  $E_i$ : Modulus of  $i$  layer,  $A_i$ : Cross section area of  $i$  layer,  $z_{oi}$ : Distance between any axis and neutral axis of  $i$  layer,  $I_{oi}$ : Second moment of area against neutral axis of  $i$  layer,  $z_0$ : Distance between any axis and neutral axis of laminated plate.

The modulus of each layer is measured by separating the specimen into each layer. The dynamic modulus of each layer is measured at 1 Hz by using a viscoelastometer DMS-210 (Seiko Electronic Co.). The samples at each cutting position are made by polishing to get the observed cross-sectional thickness of each layer. Fig.7 shows the relationship between theoretical and experimental bending moduli at each cutting position for each the A220 specimen. Theoretical and experimental moduli display similar characteristic. In the MD specimen, the experimental moduli are higher than the theoretical ones. In TD specimen, the opposite is true. The actual distribution of moduli for each layer is in the thickness direction due to the alignment of LCP and fiber. In the MD specimen, for example, the surface side in the intermediate layer possesses higher modulus than the core side and, the moduli for each layer are average values.

The theoretical moduli become close further to the experimental moduli by subdividing the layer. Laminate beam theory is suitable as a fundamental formula

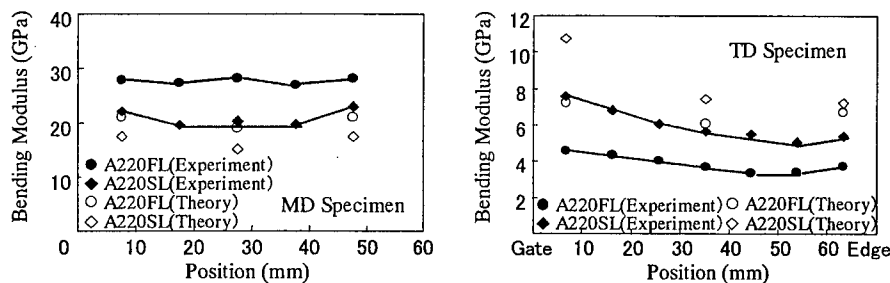


Fig.7 Relations between theoretical and experimental bending moduli of the each specimen and cutting position in the A220.

for predicting modulus in CF/LCP formed layer structure.

## 5. CONCLUSION

In this study, the effects of injection speed and gate shape of mold on the structure and bending properties of carbon fiber reinforced LCP injection molded plates have been investigated.

All specimens consisted of five macro layers: two skin layers, two intermediate layers and one core layer. The fiber orientation in each layer varies with the gate shape of the plate mold. The difference in fiber orientation affects the bending properties of the plate. The differences of bending properties and structures due to injection speed are not as marked as the effects of gate shape. The differences of fracture aspect due to the gate shape and cutting position are caused by the difference in modulus in each layer as in the laminated composite.

It is important to understand the relationship between fiber and polymer orientation and flow behavior of CF/LCP injection molded plate for the design of LCP products, and this area should be further clarified in the future.

Laminate beam theory is suitable as a fundamental formula for predicting modulus in CF/LCP formed multi layer structure.

## References

- 1) A.E. Zachariades and R.S. Porter, "High Modulus Polymers", (1987) Marcel Dekker Inc.
- 2) Z. Ophir and Y. Ide, Polym. Eng. Sci., **23**, 792 (1983).
- 3) E. Joseph, G.L. Wilkes, and D.G. Baird, Polym. Eng. Sci., **25**, 377 (1985).
- 4) G. Menges, T. Schacht, H. Ecker, and S. Ott, Inter. Polymer Processing, **2**, 77 (1987).
- 5) K. Engberg, O. Stromberg, and J. Martinsson, Polym. Eng. Sci., **34**, 1336 (1994).
- 6) S. Kenig, Polymer Composite, **7**, 50 (1986).
- 7) T. Weng, A. Hiltner, E. Bear, J. Mat. Sci., **21**, 744 (1986).
- 8) M.J. Folkers, D.A.M. Russell, Polymer, **21**, 1252 (1980).
- 9) P.F. Bright et al, J., Mat., Sci., **13**, 2497 (1978).
- 10) R.S. Bay and C.L. Tucker III, Polym. Compos., **13**, 332 (1992).
- 11) S. Kenig, B. Trattner and H. Anderson, Polym. Compos., **9**, 20 (1988).
- 12) D.G. Bird, S.S. Bafna, J.P. De Souza, and T. Sun, Polym. Compos., **14** (1993) 214.
- 13) S.H. Jang and B.S. Kim, Polym. Eng. Sci., **35** (1995) 528.
- 14) J.P. De Souza and D.G. Bird, Polym. Compos., **17** (1996) 578.
- 15) F. Baba and S. Etoh, Mol. Cryst. Liq. Cryst., **169**, 119 (1989).

## **Fabrication and Mechanical Properties of PP/PP Composites**

Takeo Kitayama, Kentaro Ishikura, Tatsuro Fukui and Hiroyuki Hamada

### **Abstract**

The interface structure of polypropylene(PP/PP) composites, consisting of homo-PP fibers and propylene-ethylene random copolymer matrix, was investigated. Generally, in the case of increasing the relative nucleus concentration on the fiber surface, the transcrystalline grows on interface instead of spherulitic growth. PP fibers which filled the nucleating agent were prepared in order to increase the relative nucleus concentration in this paper. As a result, it was found that the amount of fiber surface nucleation in PP/PP composite gradually increases with increasing of a nucleating agent, and transcrystalline grows on the PP fiber. The shear strength of PP/PP single-filament composites, consisting of homo-PP fibers with a nucleating agent and propylene-ethylene random copolymer matrix, were measured. The interfacial shear strength increased with increasing amounts of a nucleating agent.

### **Introduction**

In recent years, various studies on composites with excellent properties have been achieved. Adhesive properties of fiber-matrix interface especially have been subjects in composites, because the presence of interfaces influences mechanical properties of composites. For example, a combination between inorganic fibers and organic matrices make high performance composites such as CFRP and GFPP. However, adhesion between two materials is essentially not good due to completely different natures of both substances. The composites that consist of the same matters, thermoplastic materials, but different roles such as reinforcing fiber and matrix phase, do not require to pay any attention to its interface.

---

Takeo KITAYAMA: Plastics Technical Center, SUMITOMO CHEMICAL CO.,LTD, 10-12-Chome, Tsukahara, Takatsuki-City, Osaka, 569-1093, Japan .

Kentaro ISHIKURA, Tatsuro FUKUI, Hiroyuki HAMADA: Division of Advanced Fibro-Science, Kyoto Institute of Technology, Matsugasaki, Sakyo-ku, Kyoto 606-8585, Japan .

In this point of view, the thermoplastic materials of same kind in fiber and matrix were focused and evaluated. In thermoplastic composites the improvement in mechanical properties is due to the interface structures. Generally, in the case of increasing the relative nucleus concentration on the fiber surface, the transcrystalline grows on interface instead of spherulitic growth. However, the effects of the transcrystalline have not been clarified on the mechanical properties of composites, especially the PP/PP composite [1].

In this study, PP fibers which filled the nuclear agent were prepared by changing the relative nucleus concentration. The unidirectional PP fiber reinforced PP single-filament composites were fabricated by the aid of film stacking and press molding process. The effects of a nucleating agent on interfacial structures and properties of single-filament composites were discussed by using single-filament fragmentation tests [2].

## Experimental

Materials used were a homo-polypropylene fiber and a propylene-ethylene random copolymer matrix (Sumitomo Chemical Industry CO Ltd.). The material as nuclear agent was polyvinyl-cyclohexane (PVCH) filled in a buten-propylene random copolymer (1000p.p.m.) (Sumitomo Chemical Industry CO Ltd.).

In PP/PP composites, the molding temperature is important for strengthening adhesion and keeping the fiber shape because the reinforcement and matrix are of the same materials. DSC measurement was thus carried out to reinforcement and matrix respectively. According to result of DSC, the melting temperature of PP film was 135°C and that of PP fiber and PP fiber which filled a nuclear agent were 165°C (3.5wt%, 5.0wt%), so that 159°C was selected as molding.

Specimens of single-filament fragmentation test were fabricated by aid of film stacking and press molding process as shown in Figure 1. Tensile test was performed using an Autograph universal testing machine (type AG-500E) at room temperature. The test condition was 1 mm/min crosshead speed.

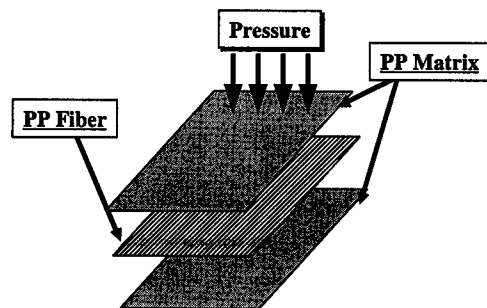


Figure 1 Film Stacking.

Single-filament fragmentation tests have been employed to evaluate interfacial shear strength. Figure 2 indicates the specimen shape of single-filament fragmentation test. In this technique a critical fiber length can be measured. When tensile strain is applied to the specimen, a number of fractures of embedded fibers occur. It is said that fiber is not cut in shorter when enough strain is applied. Then the fracture length is correlated to the critical fiber length. The fiber-matrix interfacial shear strength  $\tau_i$  was evaluated by the equation (1).

$$\tau_i = \frac{3D\sigma_f}{8\langle L \rangle} \quad (1)$$

where,  $\langle L \rangle$  is the average length of fiber in fracture,  $D$  is the diameter of fiber and  $\sigma_f$  is the tensile strength of fiber[3].

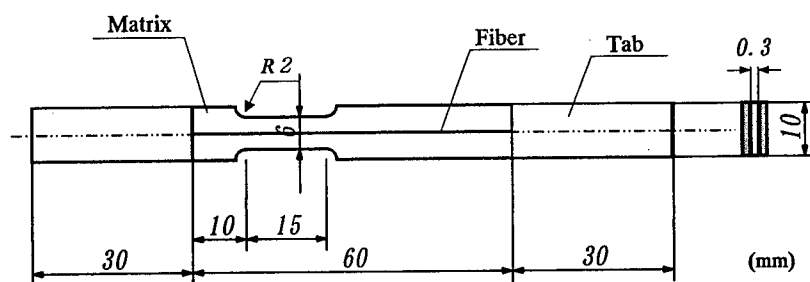


Figure 2 Specimen Shape of Single-filament Fragmentation Test.

## Results and discussion

Figure 3 shows the optical microscope photographs of specimens after single-filament fragmentation test. It is clear that a number of fractures of embedded fibers occurred. The critical fiber lengths were evaluated by averaging the fiber lengths.

Figure 4 presents the relationship between the fiber-matrix interfacial shear strength and the PVCH concentrations in fibers. The fiber-matrix interfacial shear strength increased with increasing concentration of PVCH in fibers. The adhesive properties of fiber-matrix interface may be improved by PP fibers added the nucleating agent.

In the PE/PE composite, it can be observed crystallization of the matrix generates at first on the fiber surface and then in the bulk. This crystallization behavior of the PE/PE composite is similar to that of the PP/PP composite. If the fiber surface has many nuclear agents which can grow matrix polymer crystallines, a transcrystalline layer on fiber surface is produced.



—  $\times 1000 \mu\text{m}$

—  $\times 1000 \mu\text{m}$

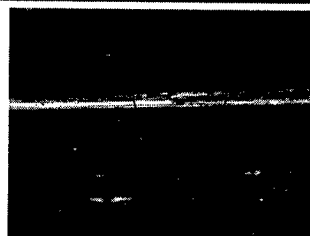
(a) PVCH 0 p.p.m.



—  $\times 1000 \mu\text{m}$

—  $\times 1000 \mu\text{m}$

(b) PVCH 35 p.p.m.



—  $\times 1000 \mu\text{m}$

—  $\times 1000 \mu\text{m}$

(c) PVCH 50 p.p.m.

Figure 3 Microphotograph of Specimen after Single-filament Specimen Fragmentation test.



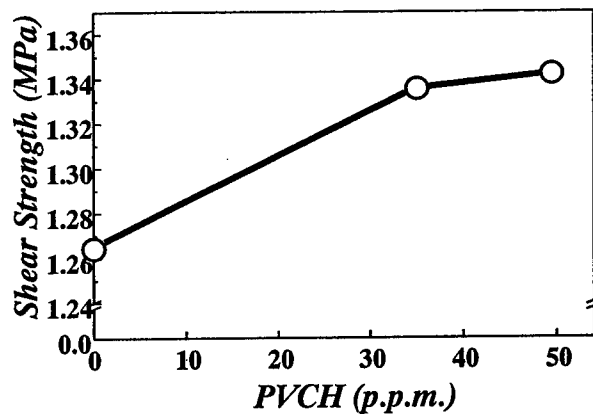
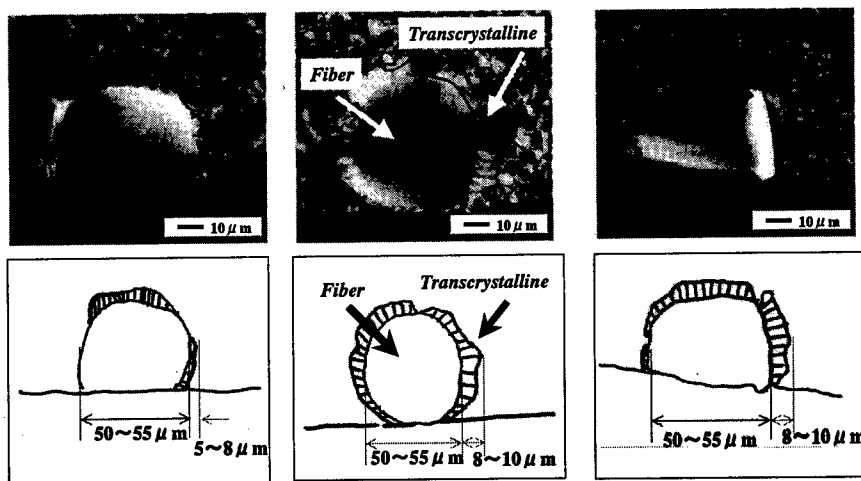


Figure 4 Shear Strength in Single-filament Fragmentation Test.

Then, the growth of transcrystalline on fiber surface was observed by a polarized light optical microscope. Figure 5 shows the optical micrographs of cross-sections of PP/PP composites which have fibers filled with PVCH as the nucleating agent.

When utilizing the fibers filled with PVCH of 35p.p.m. and 50p.p.m., the transcrystalline growth was definitely observed on the fiber surface, as compared with fibers which do not have PVCH. The thickness of transcrystalline layers in PP/PP composites with PVCH were about  $8\sim 10\mu\text{m}$ . On the other hand, in the case of utilizing the fibers without PVCH the thickness of transcrystalline layers was about  $5\sim 8\mu\text{m}$ . This result indicated that increasing the concentration of PVCH on fibers increased the extent of the transcrystalline layer.



(a) PVCH 0 p.p.m.

(b) PVCH 35 p.p.m.

(c) PVCH 50 p.p.m.

Figure 5 Optical Micrographs of Cross-sections for PP/PP Composites.

## Conclusions

In this study, a fiber with a nucleating agent, PVCH, was selected as reinforcement, and the fiber-matrix interfacial shear strength in single-filament fragmentation specimen and the mechanical properties of PP/PP composites were investigated. As a consequence, the good adhesion between a fiber with a nucleating agent and a matrix was realized by producing the transcrystalline layer in the interface of single-filament fragmentation specimen and recognized due to the fiber-matrix interfacial shear strength of single-filament fragmentation specimen. From this result, it is concluded the mechanical properties were affected by the presence of the transcrystalline layer.

## References

1. A.Gati and H.D.Wagner, 1996. "Stress Transfer Efficiency in Semicrystalline-Based Composites Comprising Transcrystalline Interlayers" *Macromolecules*, 30,3933-3935.
2. Devesh Tripathi, F.Chen and Frank R.Jones, 1996. "The effect of matrix yield strain on the data reduction technique of single-filament fragmentation test" *Composites, PartA*, 27A, 709-715.
3. M.Shiotani and A.Takahisa, 1995. "Evaluation of shear strength in fiber-matrix interface of composites" *Hyoumen*, Vol.33, No.12, 22(744)-40(762)

## **Thermal Shock Induced Damage in Si-Ti-C-O Fiber Bonded Ceramics**

Y.Kogo, M.Kamiya, H.Hatta, and T.Ishikawa

### **Abstract**

Thermal shock behavior of unidirectionally reinforced Si-Ti-C-O fiber bonded ceramics was experimentally examined. Water quench tests were carried out with various temperature differences ( $\Delta T$ ) up to 800K. Change in Young's modulus and electrical resistance were measured to detect microscopic damage in the materials. Macroscopic cracks were introduced with  $\Delta T$  of 600K, although no degradation was observed in Young's modulus. With larger  $\Delta T$ , large cracks were introduced accompanied by the degradation of Young's modulus. SEM observation revealed that microscopic damage near the surface occurred even when  $\Delta T$  was less than 600K. The microscopic damage might play an important role to release the thermal stresses induced by the thermal shock.

### **Introduction**

Various types of ceramic matrix composites (CMC) have been developed and studied for high temperature applications. Among them, Si-Ti-C-O fiber bonded ceramics (FBC) is one of the promising materials, which possess superior high temperature mechanical properties and long term durability at elevated temperature [1].

In actual operation conditions, the materials will be exposed to severe temperature changes, which will induce large thermal stresses. Because of this, knowledge of thermal shock resistance is indispensable for structural design. However, thermal shock behavior of the CMCs is generally complicated compared with monolithic ceramics [2-4], and is not fully understood yet. In this study, water quench tests were carried out on the unidirectionally reinforced (UD) FBC to investigate micro- and macroscopic damages induced by the thermal shock. Young's modulus before and after thermal shock tests were also measured to clarify the effect of the thermal shock induced

---

Y.Kogo, Department of Materials Science and Technology, Science University of Tokyo, 2641, Yamazaki, Noda, Chiba 278-8510, Japan

M.Kamiya, Graduate Student, Science University of Tokyo

H.Hatta, The Institute of Space and Astronautical Science, 3-1-1 Yoshinodai, Sagami-hara, Kanagawa 229-8510, Japan

T.Ishikawa, Ube Industries Ltd., 1978-5 Kogushi, Ube, Yamaguchi, 755-8633, Japan

damage on the mechanical properties of the UD FBC.

## Experimental Procedure

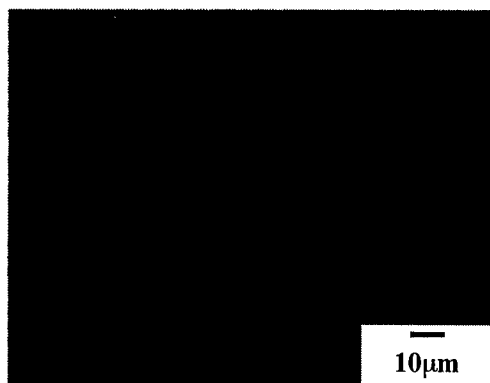
### Materials

Material used in this study was unidirectionally (UD) reinforced Si-Ti-C-O fiber bonded ceramics (FBC) manufactured by UBE Industries [5]. Continuous Si-Ti-C-O fiber was used as the starting material for the manufacturing of the FBC. The fiber was first heat treated in air to form an oxide layer on the fiber surface. The pre-oxidized Si-Ti-C-O fibers were hot-pressed to pack interstices by the oxide material on the fiber surface. A thin carbon layer was formed between the fiber and the oxide layer after the hot-pressing [1]. Typical optical micrographs of as-received UD FBC is shown in **Fig.1**. Fiber volume fraction was approximately 90%, which was much higher than those of other CMCs. The physical and mechanical properties of the UD FBC are listed in **Table I**.

The UD FBC plate was machined into rectangular bars, and the wedge made of the UD FBC was bonded to the tip of the specimen as shown in **Fig.2**. The wedge was necessary to avoid formation of thick air layers on the specimen surface when the specimen entered into the water. As already reported [6,7], a heat transfer rate at a specimen surface was increased by attaching a wedge due to change in the boiling condition on the surface. This resulted in more severe thermal shock condition compared with a specimen without a wedge.

### Thermal Shock Test

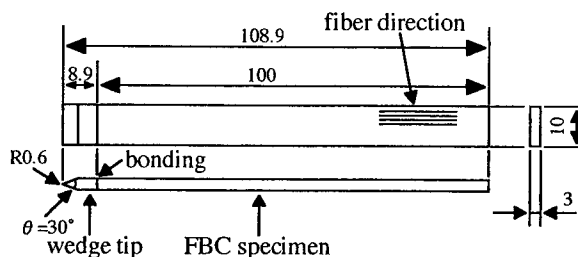
The apparatus used for the water quench tests is illustrated in **Fig.3**. The specimen was connected to a stainless steel pipe



**Fig.1** Cross-sectional view of as-received UD FBC.

**Table I** Material Properties

Tensile strength (MPa)	Young's modulus (GPa)	Thermal conductivity (W/mK)	CTE ( $\times 10^{-6}/K$ )	Density (g/cm <sup>3</sup> )
L: 450~550 T: 20	L: 135 T: 110	L: 3.08 T: 2.81	L: 3.2 T: 3.2	2.54



**Fig.2** Geometry of thermal shock specimen

(a support holder) and they were suspended by a stainless wire at the center of an infrared furnace. To avoid oxidation of the specimen during heating, the specimen was heated in an inert atmosphere. After keeping 15 min. at a given temperature (473 K ~ 800 K), the specimen was made to fall freely with the support holder and then stopped in the water. Both falling height and falling depth from the water surface were set to 600 mm following the Japanese standard for the thermal shock test of ceramics (*JIS-R1615*). **Figure 4** shows a specimen just entered into the water. Although thick air layers were formed on the side surfaces of the specimen, no air layer was observed on the top surface.

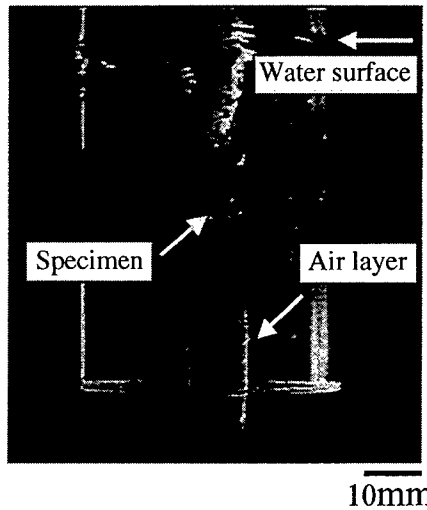
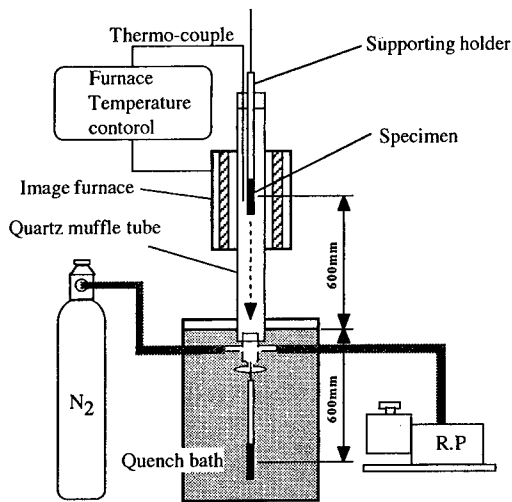


Fig.3 Experimental set-up for the water-quench thermal shock test

Fig.4 Specimen just fall into the water

In order to investigate macro- and microscopic damage induced in the UD FBCs, the dye penetrant test and the SEM observation were carried out on the surface of the thermally shocked specimens. Cross-sections were also observed to estimate depth of the damaged area. Young's modulus was measured by four-point flexure tests before and after the thermal shock test. As additional information for the damage induced in the UD FBC, electrical resistance was also measured before and after the thermal shock test.

Finite element analyses (FEA) were carried out to estimate thermal stresses induced in the FBC. Prior to the FEA, the boundary conditions were determined by experiments using rod-shaped silver specimens with and without the wedge as shown in **Fig.5**. A thermocouple was set in the silver specimens to measure the temperature

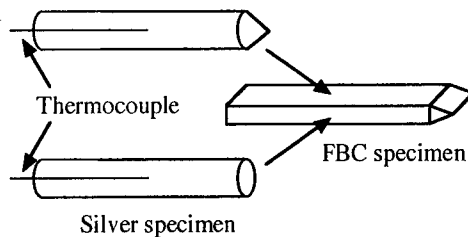


Fig.5 Silver specimens to determine boundary condition

change during the thermal shock test. The heat flow on each silver specimen surface was assumed to correspond to the side surface or the top surface of the FBC specimen. Because the temperature difference between the center and the surface of the silver specimen was less than 8% during the thermal shock test, the heat flow at the surface could be determined assuming uniform temperature distribution in the silver specimen.

## Results and Discussion

### Thermal Shock Damage

**Figure 6 (a)** shows a typical thermal shocked specimen ( $\Delta T=800\text{K}$ ). Two types of cracks along the fiber direction (**Type A** and **B** in **Fig.6 (b)**) were introduced in the UD FBC. **Type A** crack was first observed when  $\Delta T$  was 600K. With increasing  $\Delta T$ , the length of **Type A** crack was increased and **Type B** crack appeared on the side surface of the specimen. With these results, the critical temperature difference ( $\Delta T_c$ ) of the UD FBC could be determined as 600K.

Change in the longitudinal Young's modulus was measured by the four-point flexure tests as shown in **Fig.7**. Normalized electrical resistance is also shown in the figure. When  $\Delta T$  was lower than 600K, the Young's modulus after the thermal shock test was the same with that of the as-received

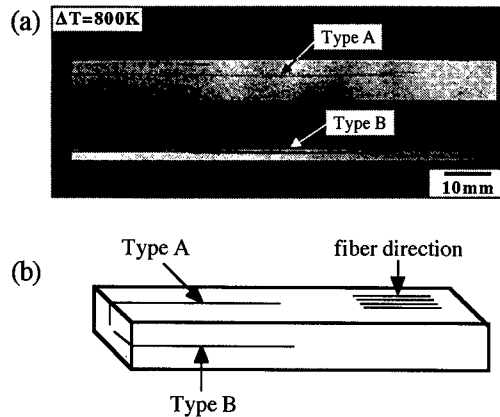


Fig.6 Cracks introduced by thermal shock  
(a) Typical crack observed,  
(b) Two types of crack in FBC

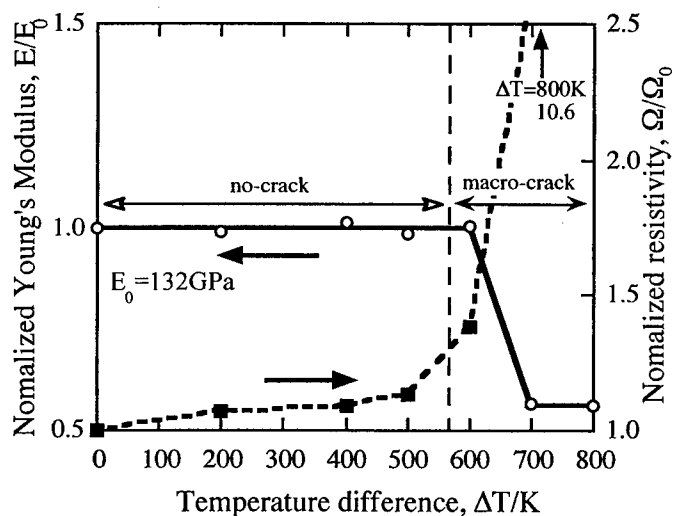


Fig.7 Change in Young's moduls and electrical resistance

specimen. However, when  $\Delta T$  was above 600K, the Young's modulus dramatically decreased with increasing  $\Delta T$ . This was due mainly to formation of *Type B* cracks in the UD FBC. The electrical resistance also changed drastically above 600K. At  $\Delta T$  of 800K, the electrical resistance showed ten times larger than that of as-received specimen. This results suggested that the electrical resistance be closely related to the damage induced in the UD FBC. If we pay attention to  $\Delta T$  lower than 600K, the electrical resistance gradually increased with increasing  $\Delta T$ , even though no macroscopic damages were observed in the UD FBC.

In order to examine microscopic damage in the specimen, the surface of the thermally shocked specimen was observed by SEM as shown in *Fig.8*. Compared with the as-received specimen, the specimen surface looks like rougher even when the  $\Delta T$  was lower than 600K. For the quantitative evaluation, surface roughness ( $R_{max}$ ) was measured as shown in *Fig.9*. Even when the  $\Delta T$  was 200K, the surface roughness was higher than that of the as-received specimen. This results suggests that fibers near the surface be broken away from the specimen surface. *Figure 10* shows the typical cross-sectional views of the as-received and the thermally shocked specimens. Even in the specimens subjected to the lower  $\Delta T$  than 600K, fiber spacing near the surface increased. This must be a microscopic damaged area induced by the thermal shock. *Figure 11* shows a microscopic damage area at a higher magnification. Microcracks were generated at the fiber/matrix interface.

The depth of microscopic damage area ( $td$ ) was measured at 20 arbitrary points in each specimen, and plotted against  $\Delta T$  as shown in *Fig.12*. The  $td$  increased monotonously with increasing  $\Delta T$ ,

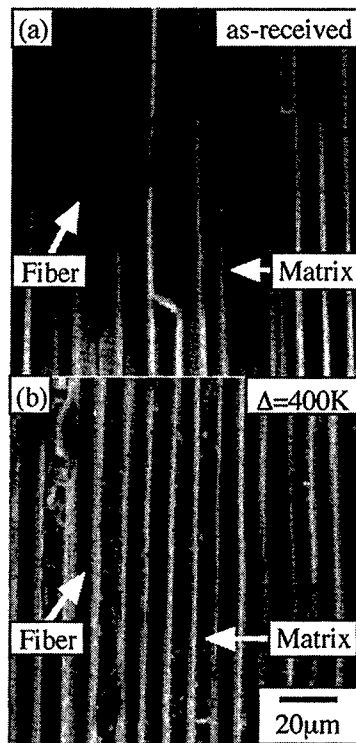


Fig.8 SEM of surface view of the UD FBC. (a) As-recieved, (b)  $\Delta T=400K$

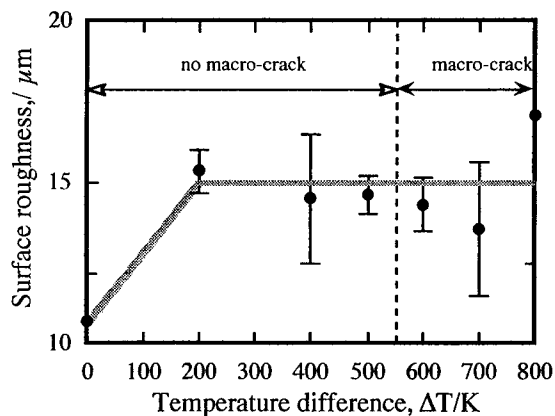


Fig.9 Surface roughness of the thermally shocked FBC.

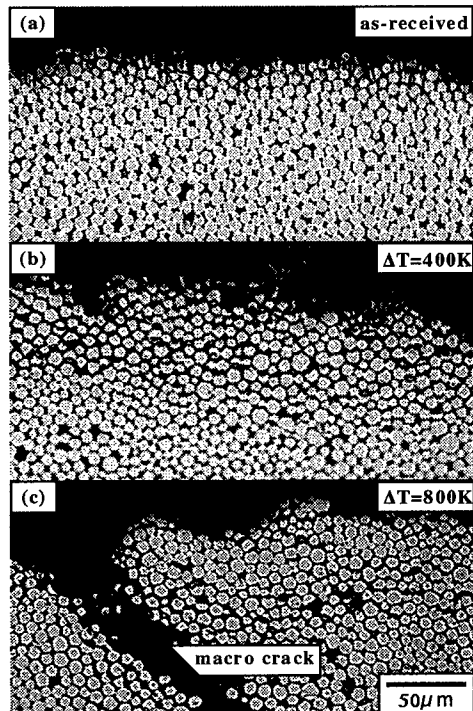


Fig.10 Typical optical micrographs of cross-sectional view of the UD FBC.  
(a) before test, (b)  $\Delta T=400K$ , (c)  $\Delta T=800K$

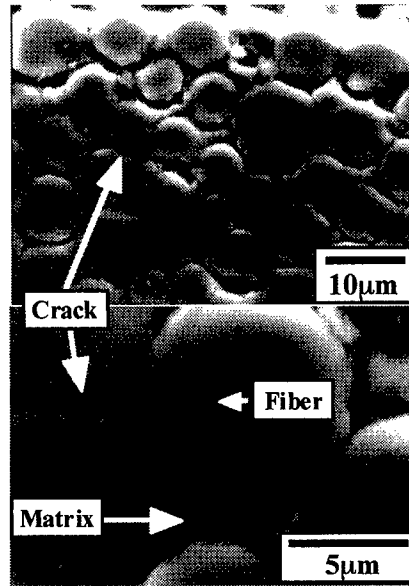


Fig.11 fiber-matrix interface view of  $\Delta T=400K$  thermal shocked the UD FBC.

and saturated at  $\Delta T_c$ . These observations suggested that the breakaway of the fibers from the specimen surface and/or delamination at the fiber/matrix interfaces near the surface occur due to the thermal shock even below the  $\Delta T_c$ . It was also expected that slight increase in the electrical resistance corresponded to formation of the microscopic damage in the UD FBC.

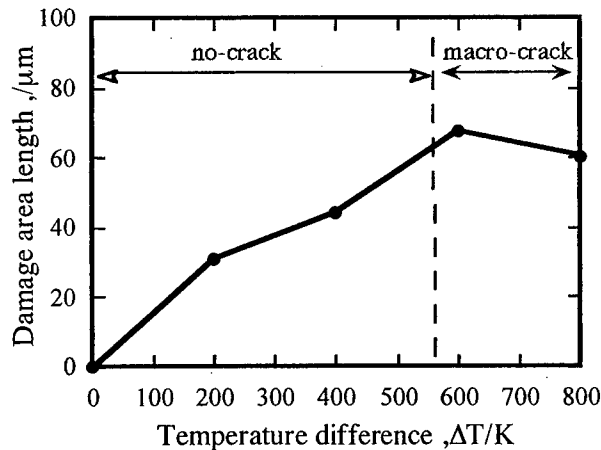


Fig.12 Depth of microscopic damage area



### Thermal Stress Induced by thermal shock

**Figure 13** shows the temperature change in the silver specimens with and without the wedge during the thermal shock test. In case of the specimen with the wedge, the temperature started to decrease when the specimen just entered into the water, and decreased rapidly till the specimen stopped in the water bath. On the other hand, the temperature of the specimen without the wedge was almost constant during falling in the water, and gradually decreased after the specimen stopped in the water bath. These results

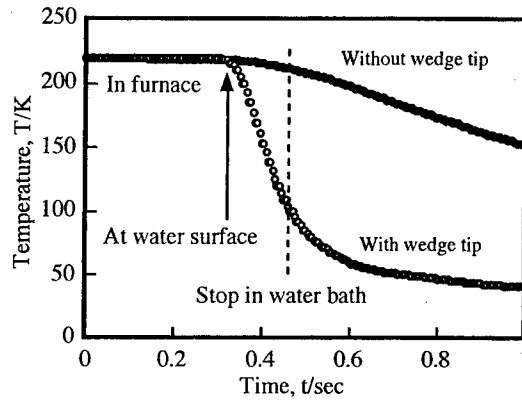


Fig.13 Temperature change in silver specimen during thermal shock test

indicated that the boundary condition of the side surface of the specimen can be assumed as a heat insulated condition and only top surface should be considered. The transient heat flow can be estimated and considered in the boundary condition of finite element modeling. Linear elastic two dimensional model was used assuming the plane strain condition. The cross section was modeled using 8 nodes isoparametric elements.

The calculated maximum thermal stress induced in the UD FBC is shown in **Fig.14**. Even at  $\Delta T$  of 200K, the maximum thermal stress was higher than the transverse tensile strength of the UD FBC. This results suggested that the thermal stresses be released in the UD FBC. It is expected that the microscopic damage observed near the surface of the UD FBC specimen play an important role to relax thermal stress. This must be an unique stress release mechanism to the UD FBCs.

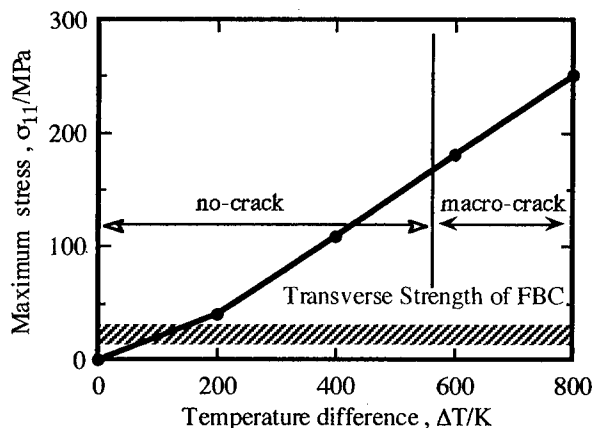


Fig.17 Maximum Stress Induced in the Specimen

## 5.SUMMARY

The thermal shock behavior of the unidirectionally reinforced Si-Ti-C-O fiber bonded ceramics was experimentally examined, and following results were obtained.

1. The critical temperature difference of the unidirectionally reinforced Si-Ti-C-O fiber bonded ceramics was estimated as 600K, which was higher than those of monolithic ceramics.
2. Even below the critical temperature difference, microscopic damage such as delamination of fiber/matrix interface and/or breakaway of fibers from the surface occurred in the unidirectionally reinforced Si-Ti-C-O fiber bonded ceramics. The microscopic damage was expected to release the thermal stresses induced in the material.

## REFERENCE

1. T.Ishikawa, S.Kajii, K.Matsunaga, T.Hogami, and Y.Kohtoku, 1995. "Structure and properties of Si-Ti-C-O fiber bonded ceramic material" : *J.Mater.Sci.*, **30** : 6218-6222.
2. Y.Kagawa, N.Kurosawa, and T.Kishi, 1993. "Thermal shock resistance of SiC fibre-reinforced borosilicate glass and lithium aluminosilicate matrix composites" : *ibid.*, **28** : 735-741.
3. H.Wang and R.N.Singh, 1994. "Thermal Shock Behavior of Ceramics and Ceramic Composites" : *Int. Mater. Rev.*, **39** : 228-244.
4. H.Wang, R.N.Singh, and R.A.Lowden, 1996. "Thermal Shock Behavior of Two-Dimensional Woven Fiber-Reinforced Ceramic Composites" : *J.Am.Ceram.Soc.*, **79** : 1783-1792.
5. K.Magtsunaga, T.Ishikawa, S.Kajii, T.Hogami and Y.Kohtoku, 1995. "Influence of Interfacial Carbon-Layer on Mechanical Properties of Si-Ti-C-O Fiber Bonded-Ceramic Material" : *J.Ceram.Soc.Japan*, **103** : 288-292. (in Japanese)
6. T.Sakuma, U.Iwata and H.Takaku, 1991. "Evaluation of Thermal Shock Resistance of Ceramics (1st Report, A Novel Quench Technique)" : *Trans.Japan Soc.Mech.Eng.A*, **57** : 2741-2746.
7. T.Sakuma, U.Iwata and H.Takaku, 1992. "Evaluation of Thermal Shock Resistance of Ceramics (4th Report, Transient Boiling Curves of Low Boiling Point Medium and Thermal Stress at Quenching)" : *ibid.*, **58** : 1424-1429.

## **Design of Musical Instrument Material Substitutes Using FRP Structures**

T.Matsubara, T.Nishiwaki and Z.Maekawa

### **Abstract**

Musical instrument material substitutes are designed by using FRP related structures. Because it is impossible to design musical instrument material substitutes by only FRP, we fabricate two types of adhesive structures and investigate these acoustic properties. One is the 2-layered structure, FRP/EVA foam. The other is the sandwich structure, FRP/Balsa/FRP. In the former, it is confirmed that acoustic properties can be controlled by changing the EVA foam position. In the latter, it is confirmed that musical instrument material substitutes can be designed by changing skin/core thickness.

### **Introduction**

Recently, the constant supply of wooden materials has been difficult as a result of serious environmental problems. The substitutes for wooden materials have been developed in various fields. However specific wooden materials, Sitka spruce, Spruce and Yezo spruce are still used as musical instrument materials. The musical instrument material is used as a production of sound, a resonance board and a sounding pipe, all the component produce a sound due to their vibration [1]. In other words, acoustic properties are related to vibration properties. In the previous studies[2]-[3], several researchers mainly investigated the vibration properties of various materials for the designing musical instrument material substitutes. The substitute with the equivalent property with wooden musical instrument materials has not been proposed yet. The design of musical instrument material substitutes has been required. Yano[4]-[6] designed a high quality musical instrument material substitute by using a Japan cedar and the chemical treatment. However the treatment needs a long period and high cost. Therefore a simple and effective designing method has been required.

FRP has been applied to various industrial fields, because of its superior specific mechanical properties. In this study, the required acoustic properties are first investigated by a vibration test of wooden musical instrument materials. The acoustic properties of substitute materials designed by FRP are proposed by using the above vibration test.

---

T.Matsubara and Z.Maekawa, Graduate Program of Advanced Fibro-Science in Graduate School, Kyoto Institute of Technology, Matsugasaki, Sakyo-ku, Kyoto 606-8585, Japan

T.Nishiwaki, ASICS corporation, Takatsukadai, Nishi-ku, Kobe 651-2271, Japan

## Specimen

The acoustic properties of musical instrument materials are investigated by the comparison between wooden musical instrument materials and wooden general-purpose materials. The test specimens used in this experiment were Sitka spruce, Spruce and Yezo spruce as wooden musical instrument materials. As comparison wooden general-purpose materials, Mahogany, Maple and Boxwood were also used. All the geometry of specimens was constant, the length, wide and thickness were 280, 70 and 2mm, respectively. The grain was arranged in the longitudinal direction.

## Experimental method

Acoustic properties are measured by the vibration test. In the vibration test, the center of specimen was impacted by an impulse hammer as an input data and out-plane acceleration was measured at the corner as an output data. Both the data were Fast Fourier Transformed, the transfer functions were obtained from dividing an output data by an input data. In this study, acoustic properties corresponded to 1st bending mode with the main curvature in the longitudinal direction were evaluated. The logarithmic decrement was calculated by the damping curve obtained from Reversed Fast Fourier Transformation of the transfer function near the 1st bending eigenfrequency. The dynamic modulus was calculated from the 1st bending frequency and the classical beam theory. The specific dynamic modulus was obtained from dividing the dynamic modulus by density. We focus on the logarithmic decrement and the specific dynamic modulus, because acoustic properties, the specific acoustic resistance and the acoustic transfer efficiency can be calculated by these properties.

## Experimental results

The specific dynamic modulus plotted against the logarithmic decrement for all the wooden materials is shown in Fig.1. Judging from Fig.1, it was confirmed that wooden musical instrument materials have the high specific dynamic moduli and the low logarithmic decrement.

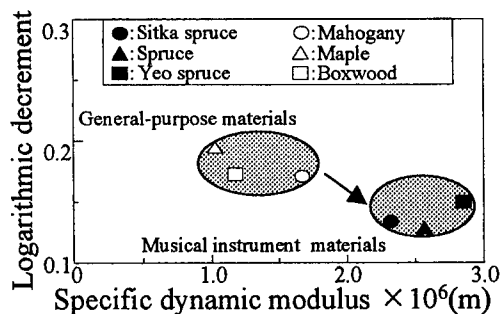


Figure 1 Comparison of vibration properties between musical instrument materials and general-purpose wooden materials

## Discussions

Before designing the 2-layered and sandwich structures, acoustic properties of unidirectional CFRP and GFRP laminates are first investigated. The CFRP and GFRP were fabricated by stacking T700/#2500epoxy and E-glass/Q111epoxy prepreg sheets, respectively. The fiber orientation angles of CFRP and GFRP were 0, 30, 45, 60 and 90 degree. Geometry of specimens were constantly 280mm×70mm×2mm. The specific dynamic moduli and the logarithmic decrement of both the plates with various fiber orientation angles were calculated by the vibration-testing machine. Both the results are listed in Table 1.

Judging from Table I, it was confirmed that the specific dynamic moduli decreased with increasing fiber orientation angles in both the plates. These results are proper because the specific dynamic moduli measured depend upon the fiber orientation angles. On the other hand, the logarithmic decrement increased with increasing the fiber orientation angles. This results indicate that the bending mode with large fiber orientation angles causes the large out-plane shear deformation of the matrix. Compared the results shown in Table I with those of wooden musical instrument materials, it was clear that the difference in both the properties were quite large. Judging from the above, the introduction of another material to FRP related structures are proposed.

Table I The comparison of the specific dynamic modulus and logarithmic decrement between CFRP and GFRP laminates

Specimen	Fiber orientation angle (degree)	Specific dynamic modulus $\times 10^6 (m)$	Logarithmic decrement
CFRP laminates	[0]	9.076	0.045
	[30]	1.620	0.082
	[45]	1.182	0.122
	[60]	0.621	0.143
	[90]	0.502	0.155
GFRP laminates	[0]	1.799	0.080
	[30]	0.593	0.129
	[45]	0.504	0.141
	[60]	0.500	0.147
	[90]	0.459	0.157
Wooden musical instrument materials	Sitka spruce	2.301	0.136
	Spruce	2.544	0.131
	Yezo spruce	2.828	0.152

For designing the 2-layered and sandwich structures, two types of components, EVA foam and Balsa were used. EVA foam is a foamed copolymer of ethylene and vinyl acetate, has low modulus. EVA foam used in this study had hardness 60 (SRIS-C). Balsa is the most lightweight wooden material. Before the applications of EVA foam and Balsa, these mechanical properties are measured. Geometry of

specimens were correctly 280mm×70mm×5mm. The specific dynamic moduli and the logarithmic decrement of EVA foam, Balsa and wooden musical instrument materials are listed in Table II. Judging from Table II, it was found that EVA foam and Balsa had the lower specific moduli and the higher logarithmic decrement, as compared with the wooden musical instrument materials.

Table II The comparison of the specific dynamic modulus and logarithmic decrement between Balsa, EVA foam and wooden musical instrument materials

Specimen		Specific dynamic modulus $\times 10^6 (m)$	Logarithmic decrement
Balsa		0.024	0.167
EVA foam		0.001	0.227
Wooden musical instrument materials	Sitka spruce	3.096	0.068
	Spruce	3.230	0.073
	Yezo spruce	3.096	0.096

As musical instrument material substitutes, we propose the 2-layered structures, CFRP/EVA foam. CFRP/EVA foam was adhered by using epoxy type adhesives on the market. The fiber orientation angles of CFRP adhered were 0, 45 and 90 degree. Geometry of 2-layered structures were constantly 280mm×70mm×1.6mm. Thickness of CFRP, EVA foam and adhesive layer were 1.0mm, 0.5mm and 0.1mm, respectively. As a comparison, geometry of wooden musical instrument materials were constantly 280mm×70mm×2.0mm. The results of the specific dynamic moduli and the logarithmic decrement of 2-layered structures with various fiber orientation angles are listed in Table III. Except for fiber orientation angle 0 degree, these 2-layered structures had the lower specific moduli and the higher logarithmic decrement, as compared with musical instrument materials. These results indicate that the application of EVA foam can control the acoustic properties.

Table III The comparison of the specific dynamic modulus and logarithmic decrement between CFRP/EVA foam with changing the fiber orientation angles

Fiber orientation angle (degree)		Specific dynamic modulus $\times 10^6 (m)$	Logarithmic decrement
CFRP/EVA	[0]	6.225	0.142
	[45]	0.768	0.294
	[90]	0.455	0.351

Musical instrument material substitutes are designed by changing the EVA foam position. Figure 2 shows test specimens with various EVA foam positions. The summation of area of EVA foam was constantly a half that of the whole specimen. Geometry of 2-layered structures were 280mm×70mm×1.6mm. Thickness of

CFRP, EVA foam and adhesives was same as the above. Figure 3 shows the specific dynamic modulus and the logarithmic decrement obtained from specimens shown in Fig.2. Judging from Fig.3, it was confirmed that all specimens had the higher specific dynamic moduli rather than wooden musical instrument. The specific dynamic modulus couldn't be controlled by the EVA foam position. These results are derived from that EVA foam stiffness is too low. On the other hand, it is found that the EVA foam position affected on the logarithmic decrement of the whole structure. Type II had the highest logarithmic decrement. These results are derived from that EVA foam with a large damping is located on the position with the largest amplitude in Type II. Judging from the above, it was confirmed that 2-layered structure composed of CFRP and EVA foam was not proper for designing the musical instrument materials.

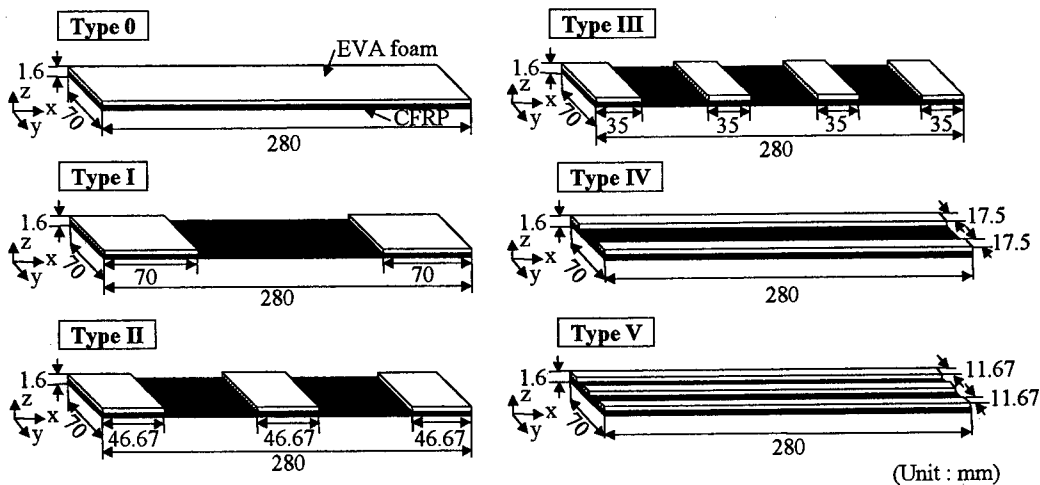


Figure 2 EVA foam position

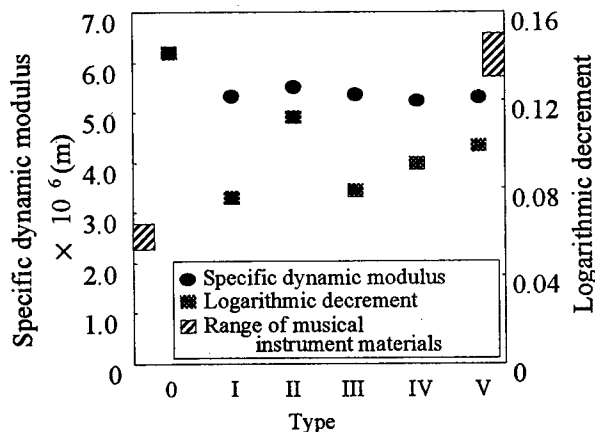


Figure 3 The comparison of specific dynamic moduli and logarithmic decrement between EVA foam position

For other musical instrument material substitutes, two types of sandwich structures are proposed. One is a sandwich structure composed of CFRP skins and balsa core. The other is a sandwich structure composed of GFRP skins and balsa core. Adhesive between FRP and Balsa was not used in the fabrication process. It is possible to adhere both by the matrix in FRP. In the sandwich structure used, thickness of skin and core were constantly 0.5mm and 3.0mm, respectively. The total thickness was 4.0mm. The fiber orientation angles of CFRP and GFRP skins were 0, 45 and 90 degree. Geometry of sandwich structures were constantly 280mm  $\times$  70mm  $\times$  4.0mm. Figure 4(a) shows the comparison of the specific dynamic moduli between sandwich structures and musical instrument materials. The hatched range in this figure denotes the range of wooden musical instrument materials. Judging from Fig.4(a), it was confirmed that the specific dynamic moduli of sandwich structures decreased with increasing the fiber orientation angles. Figure 4(b) shows the comparison of the logarithmic decrement between sandwich structures and musical instrument materials. The hatched range in this figure denotes the range of wooden musical instrument materials. Judging from Figure 4(b), it was confirmed that the logarithmic decrement also decreased with increasing the fiber orientation angles. These results are derived from the decrease in the bending stiffness and the increase in the shear deformation of matrix in CFRP with increasing the fiber orientation angles.

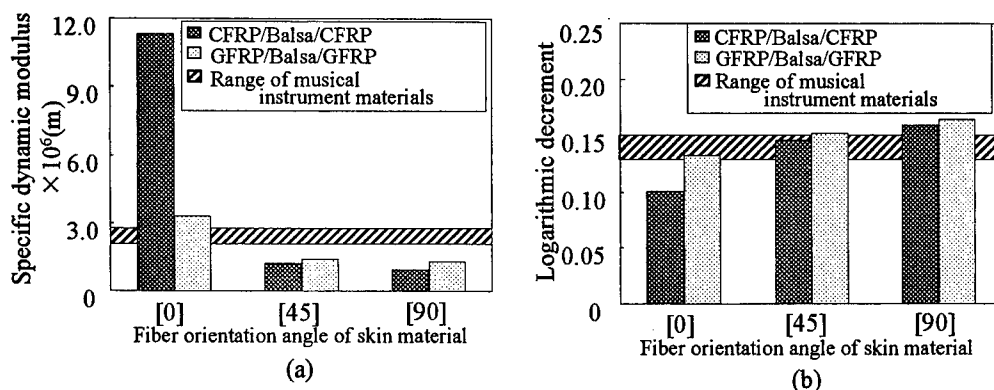


Figure 4 Comparison of specific dynamic modulus(a) and logarithmic decrement(b) between FRP/Balsa/FRP with changing the fiber orientation angles

With the constant skin thickness, 0.5mm, Balsa core thickness is changed. Influence of the core thickness on the acoustic properties is investigated. The fiber orientation angle of skin was 0 degree, thickness of the whole sandwich structures were 2mm, 3mm and 4mm, respectively. Skin and core thickness of sandwich structures was used 0.5/1.0/0.5, 0.5/2.0/0.5 and 0.5/3.0/0.5, respectively. Figure 5(a) shows the comparison of the specific dynamic modulus between sandwich structures and wooden musical instrument materials. As a comparison, geometry of wooden musical instrument materials were 280mm  $\times$  70mm  $\times$  2.0mm. The hatched



range in this figure denotes the range of wooden musical instrument materials. Judging from Figure 5(a), it was confirmed that sandwich structures CFRP/Balsa/CFRP had the higher specific dynamic moduli, as compared with the wooden musical instrument materials. The specific dynamic moduli of all sandwich structures GFRP/Balsa/GFRP was near to the wooden musical instrument materials. Figure 5(b) shows the comparison of the logarithmic decrement between sandwich structures and musical instrument materials. The logarithmic decrement of sandwich structures CFRP/Balsa/CFRP was the lower rather than wooden musical instrument materials. Judging from Figure 5(b), it was confirmed that musical instrument material substitutes could be designed by GFRP/Balsa/GFRP thickness 0.5/2.0/0.5.

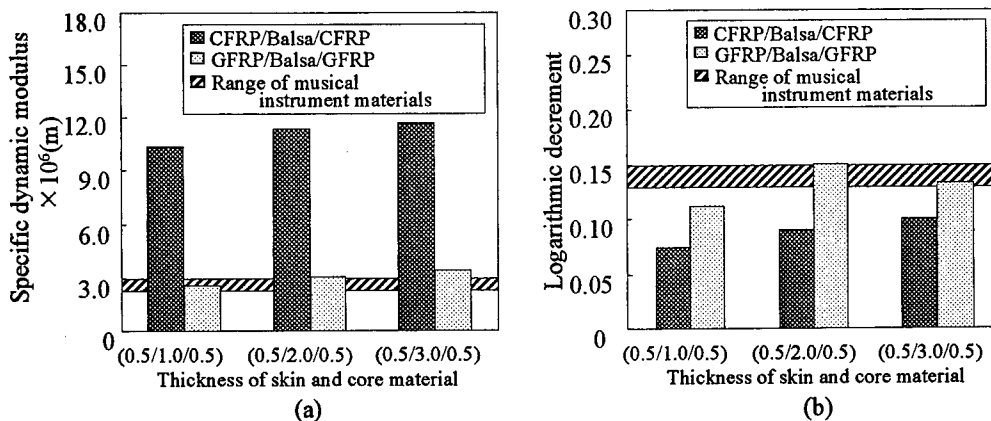


Figure 5 Comparison of specific dynamic modulus(a) and logarithmic decrement(b) between FRP/Balsa/FRP with changing core Balsa thickness

## Conclusions

For the designing of the musical instrument material substitute, some adhesive structures were proposed. First of all, the dynamic properties, specific dynamic modulus and logarithmic decrement of some wooden musical instrument materials were measured by the vibration testing system, and compared with other materials. Generally various acoustic properties can be calculated from the above parameters. It was found that the musical instrument materials had the higher dynamic modulus and the lower logarithmic decrement rather than another materials. From the testing results of unidirectional CFRP and GFRP could not have the same properties as the musical instrument material substitute. Next the 2-layered structures, CFRP/EVA foam was proposed. However 2-layered structures could not satisfy the above dynamic properties. Finally two types of the sandwich structures, CFRP/Balsa/CFRP and GFRP/Balsa/GFRP were proposed. In these structures, the skin/core thickness ratio has a great influence on the dynamic properties. By designing the ratio, it was confirmed that the GFRP/Balsa/GFRP could have the

same dynamic properties as the musical instrument material. These results indicate the sandwich structure is effective for designing substitutes.

### Reference

- 1.T.Okano, 1991. "Acoustic Properties of Wood." *Mokuzai Gakkaishi*, 37(11):991-998
- 2.R.Chandra, S.P.Singh and K.Gupta, 1999. "Damping studies in fiber-reinforced composites-a review." *Composite Structures*, 46:41-51
- 3.D.X.Lin, R.G.Ni and R.D.Adams, 1984. "Prediction and Measurement of the Vibrational Damping Parameters of Carbon and Glass Fiber-Reinforced Plastics Plates." *Journal of Composite Materials*, 18:132-152
- 4.H.Yano and K.Minato, 1992. "Improvement of the Acoustic and Hygroscopic Properties of Wood by a Chemical Treatment and Application to the Violin Parts." *Journal of Acoustical Society of America*, 92(3):1222-1227
- 5.H.Yano, K.Norimoto and R.W.Rowell, 1993. "Stabilization of Acoustical Properties of Wooden Musical Instruments by Acetylation." *Wood Fiber Science*, 25:395-403
- 6.H.Yano, K.Minato and H.Kajita, 1994. "Chemical Treatment of Wood for Musical Instruments." *Journal of Acoustical Society of America*, 96(6):3380-3391

## **Effects of matrix characteristics on mechanical properties in knitted composites**

A.Nakai, T.Osada, M.Inoda, N.Takeda and H.Hamada

### **Abstracts**

In this study, polyethylene reinforced knitted composites using two types of matrix resin with different modulus are investigated. Tensile testing of composites is performed, and the effects of matrix characteristics on mechanical properties in knitted composites are investigated. Moreover in order to clarify the effect of matrix characteristics on mechanical properties in detail, numerical analysis using finite element methods is performed. The experimental results were explained with analytical results with finite element model. Ratio of strength of composite to resin in experiments increased with decrease in elastic modulus of composite and increase in load shearing ratio of fiber bundle.

### **Introduction**

It is well known that knit fabrics have excellent flexibility, drapability, net-shape manufacturability and high productivity. Namely, knitted fabrics might be promising to be reinforcements of composites. The yarns of knits have a loop structure. The drapability is a direct consequence of the loops in the knit; the bent yarns can still be

---

A.Nakai and N.Takeda, The University of Tokyo, 4-6-1 Komaba, Meguro-ku, Tokyo 153-8904, Japan

T.Osada, M.Inoda and H.Hamada, Kyoto Institute of Technology, Matsugasaki, Sakyo-ku, Kyoto 606-8585, Japan

straightened before the yarn itself has to be extended. This allows the composites producer to drape complex double-curved shapes very easily.

Recently, the design methods to have expected functionally composites have developed such as composites which have flexible matrix or interphase. Such composite materials are expected to draw the above merits of knit fabrics in the form of composites. In this study, ultra high molecular weight polyethylene (UHMW-PE) reinforced knitted composites are investigated. Two types of matrix resin with different properties in modulus are used. Tensile testing of composites is performed, and the effects of matrix characteristics on mechanical properties in knitted composites are investigated. Moreover in order to clarify the effect of matrix characteristics on mechanical properties in detail, numerical analysis using finite element methods is performed.

## Materials and Experiments

Plain weft knitted fabric as shown in Fig.1 is used as reinforcements. Materials used in this study is UHMW-PE (DYNEEMA SK60 TOYOBO Co., Ltd.) as reinforcement and two types of matrix resin, one is vinyl ester (designated as VE) (RIPOXY R806, Showa High Polymer Co., Ltd.) the other is unsaturated polyester (designated as UP) (FK2000, Showa High Polymer Co, Ltd.). Figure 2 shows the load-displacement curves of these resins. As shown in Fig.2, VE has high modulus and UP is more flexible than VE. These PE/VE composites and PE/UP composites were called as "VE" and "UP" respectively.

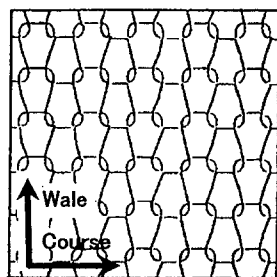


Figure 1 Schematic drawing of knitted structure

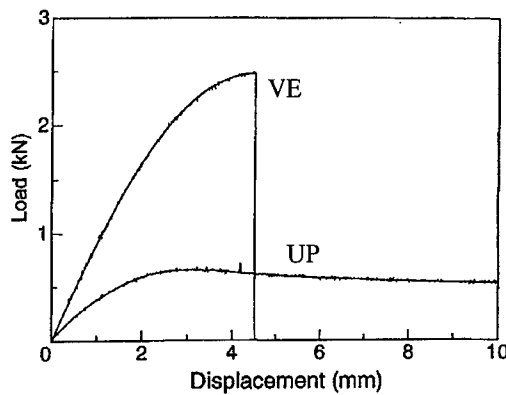


Figure 2 Load-displacement curves of these resins

The laminates with 3 plies of knitted fabric were prepared by hand, and were cured for 48 h at room temperature, followed by post cure for 3 h at. Dimensions of the specimen were 1 mm in thickness, 250 mm in length, and 25 mm in width. FRP end-tabs were placed on the specimen and the gage length was 150 mm. Specimens were cut in Wale, Course and 45 degree direction (designated as Wale, Course, 45 specimen, respectively), and tensile testing of these knitted composites was performed.

## Experimental Results

Figure 3 shows the stress-strain curves for VE specimens. Tensile modulus, strength and ultimate strain of Wale are higher than those of Course, and 45 specimen showed the middle properties. Figure 4 shows the stress-strain curves for UP specimens. In the case of UP specimen with flexible matrix, tensile modulus and strength of Wale are higher than those of Course, whereas ultimate strain of Course is two times as high as that of Wale. The strength of 45 specimen is highest in these UP specimens. Comparing UP and VE specimens, tensile strength of VE is twice as that of UP, however, strain of UP is much larger than VE. Most remarkable point is that the dependence of mechanical properties on loading direction is varied with matrix properties.

Table 1 shows the tensile strength of each specimen and the improvement ratio compared to each strength of matrix. In the case of VE specimen, the improvement ratio of Wale is smaller than 5 %, and regarding 45 and Course the strength of

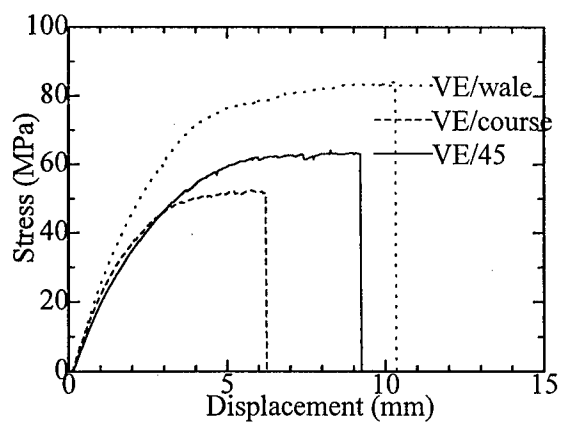


Figure 3 Stress-strain curves for VE specimens.

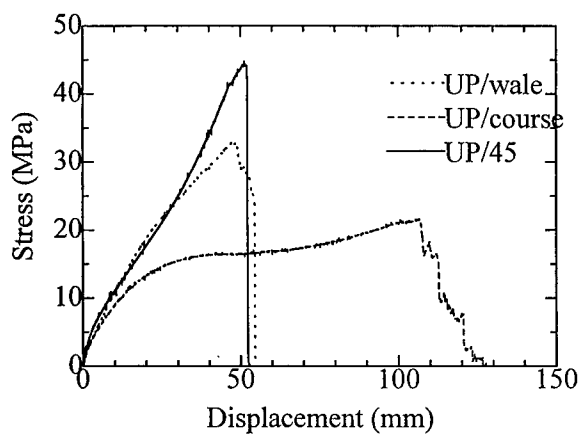


Figure 4 Stress-strain curves for UP specimens

Table 1 The tensile strength of each specimen and the improvement ratio compared to each strength of matrix

	VE (MPa)	Improvement ratio (%)	UP (MPa)	Improvement ratio (%)
Wale	80.7	4.3	32.1	104.5
45	63.5	-17.9	45.6	190.5
Course	52.4	-32.3	18.4	17.2

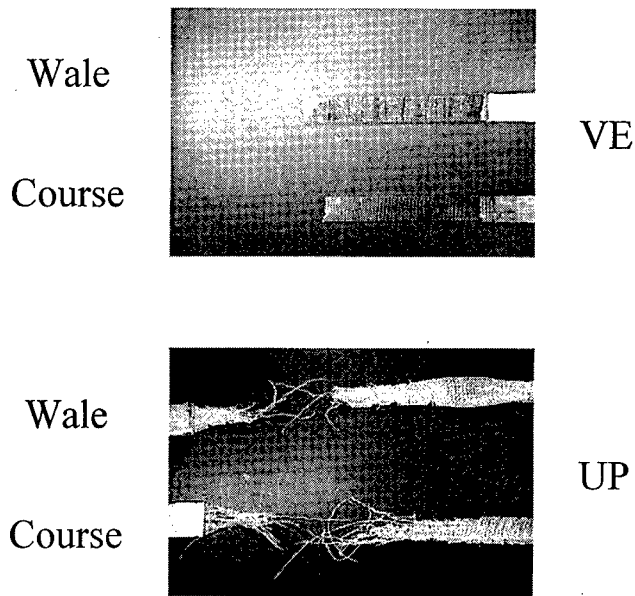


Figure 5 Fracture aspect of each specimen

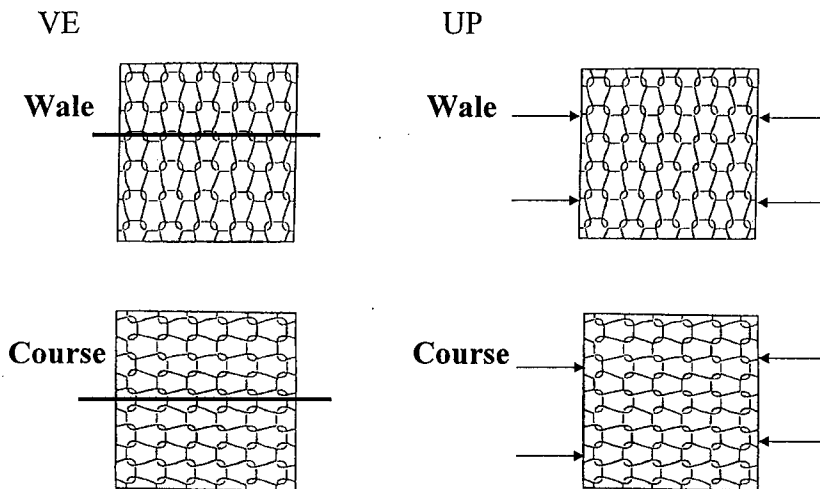


Figure 6 Schematic drawing of composites under tensile loading.

composite is smaller than that of matrix and the improvement ratio showed minus value. On the other hand, the improvement ratio of UP specimen is much larger than that of VE specimen, and regarding Wale and 45 the improvement ratio rise above 100 %.

Figure 5 shows fracture aspect of each specimen. Fracture of VE specimen

progressed with ductile manner. On the other hand, pull out of fiber bundles and deformation of knitted structure were observed in UP specimen. This is because of low modulus of the UP specimen. Figure 6 shows schematic drawing of composites under tensile loading. There are many cracks at loop intersections in VE/Wale, and these cracks grow along the loop, then final fracture occurs. In VE/Course initial crack occurs at matrix rich region within loops and then final fracture occurs. Concerning UP/Wale and UP/Course, crack occurs at side edge of specimen and because the resin has very low modulus, fiber bundles exhibit the high mechanical properties and pull out of fiber bundles occur after large deformation.

### Analysis

In order to investigate the effects of matrix characteristics on mechanical properties in knitted composites, numerical analysis by finite element method is performed. The continuity of fiber bundles and precise weaving structures of knitted fabric are represented by a finite element model with 3-D beam elements (Weaving structural

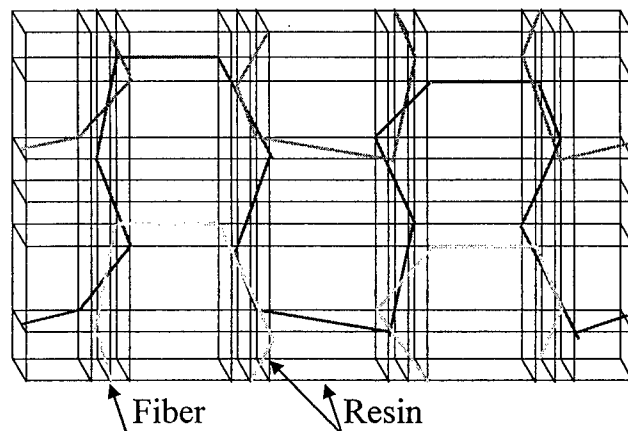


Figure 7 Finite element divisions for Weaving structural model

Table 2 Material constants.

	VE Modulus (GPa)	Poisson's ratio	UP Modulus (MPa)	Poisson's ratio
Fiber	76.63	0.350	75.15	0.350
Resin	4.09	0.385	37.76	0.466



model). Finite element divisions for Weaving structural model are shown in Fig.7. The textile composites are recognized as an aggregation of the resin impregnated fiber bundle and resin region. Resin existing between crossing fiber bundles is expressed as beam elements for considering the transmission of force at the crossing point between fiber bundles. The resin elements are also set up on both surface of the textile composite since the resin exists throughout at the surface of the textile. Table 2 shows the material constants used in the model. By changing the material constants of resins in the elastic model, the deformation state and tensile properties are investigated.

### Analytical Results and Discussion

Table 3 Analytical results

	<u>VE</u> Modulus (GPa)	shearing ratio	<u>UP</u> Modulus (GPa)	shearing ratio
Wale	52.9	51.9	9.93	73.2
Course	35.1	35.8	6.04	64.9

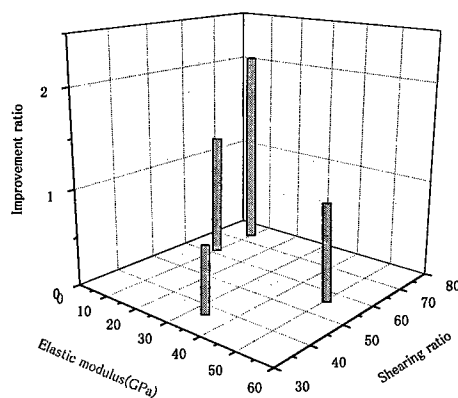


Figure 8 Relation between ratio of strength of composite to strength of resin in experiments and elastic modulus of composites, shearing ratio obtained by analytical model.

Table 3 shows the analytical results. Elastic modulus of Wale is higher than that of Course, depending on the knitted structure for both VE and UP specimens. The elastic modulus of VE is 6 times as high as that of UP specimen. Moreover, the shearing ratio of load by fiber bundle (designed as shearing ratio) was calculated as shown in Table 3; shearing ratio was obtained by dividing total load supported with fiber bundle element except resin element by the applied load to the model. The shearing ratio of Wale is higher than that of Course for both VE and UP, and the shearing ratio of UP is higher than that of VE for both Wale and Course. It is considered that the higher shearing ratio attributes to the above improvement ratio of strength.

The experimental results were arranged with analytical results. Figure 8 shows the relation between ratio of strength of composite to strength of resin in experiments and elastic modulus of composites, shearing ratio obtained by analytical model. From these results, ratio of strength of composite to resin increased with decrease in elastic modulus of composite and increase in shearing ratio. It is considered that the lower elastic modulus results in exhibition of deformability of knitted fabric and higher shearing ratio results in exhibition of high mechanical properties of fiber bundle.

## Conclusions

In this study, polyethylene reinforced knitted composites using two types of matrix resin with different modulus are investigated. Most remarkable point is that the dependence of mechanical properties on loading direction is varied with matrix properties. The experimental results were explained with analytical results with finite element model. Ratio of strength of composite to resin increased with decrease in elastic modulus of composite and increase in load shearing ratio of fiber bundle. It is considered that the lower elastic modulus results in exhibition of deformability of knitted fabric and higher shearing ratio results in exhibition of high mechanical properties of fiber bundle. Consequently, knitted fabric composites can be designed by combining the structure of knitted fabric and mechanical properties of constituent materials.

## **Effect of Pre-tensioned Fiber on Mechanical Properties of Plain Woven Glass Fabric Composite Materials**

T.Ota<sup>1</sup>, T.Matsuoka<sup>2</sup> & K.Sakaguchi<sup>2</sup>

### **ABSTRACT**

The effect of the pre-tensioned to warp/weft bundles in laminating, which was made of the plain weave glass fabric as reinforcement and the epoxy resin as matrix, was investigated. The influence on the bundle waviness was estimated by four point bending tests, tensile tests and compressive tests, focusing on the bundle buckling as the compressed waviness. As a result, it was found that each strength on pre-tensioned ratio ( $T_1/T_2$ ) 400/0 types could be increased with compared to those on 0/0 types and 800/0 and 800/800 types were decreased with compared to those on 400/0 types. Woven structural parameters relate to the bending strength, the tensile strength and the compressive strength. Stress-Strain curves were varied due to the magnitude of a stress concentration at crossing point of warp/weft fiber bundles, the waviness or the crimping on fiber bundles. And, it became clear that the waviness or the crimping on fiber bundles occurred a micro-buckling failure on the internal damage in bending tests and compressive tests, particularly.

### **INTRODUCTION**

It is well known that the material properties of fiber reinforced plastics composites (FRP) depend on the form of reinforcement. Woven textile composites form the waviness or the crimping in fiber bundle. This waviness and crimping produces the significant reduction in the strength and the stiffness under the compressive loading, particularly. The mechanical properties of fiber reinforced composite materials focusing on fiber waviness have been studied by many researchers [1-5]. For example, A.C.West et al. [2] investigated the effect on the axial yarn crimping in two-dimensional triaxially braided composite materials under static compressive loading. H.M.Hsiao et al. [3] investigated the effect of fiber waviness on the elastic properties of unidirectional and cross-ply composites. D.O.Adams et al. [4] determined experimentally that the layer waviness produces the significant compressive strength reductions in cross-ply composite laminates.

In this paper, the static four-point test, the tensile test and the compressive test are carried out in order to investigate the effect of pre-tensioned fiber on mechanical properties and internal damage of plain weave fabric composites materials.

---

<sup>1</sup> Graduate student, Doshisha University, 1-3 Miyakodani, Tatara, Kyo-tanabe, Kyoto 610-0321, Japan

<sup>2</sup> Department of Mechanical Engineering, Doshisha University, 1-3 Miyakodani, Tatara, Kyo-tanabe, Kyoto 610-0321, Japan

## EXPERIMENTAL

### Test specimens

A plain woven glass fabric (MS-253C : Asahi fiber glass ltd., Japan) is used as the reinforcement and epoxy resin (EPICLON 850 : Dainippon ink and chemicals Co.ltd., Japan) is used as the matrix. The specimens are fabricated by the hand-lay-up method. The laminated table shown in Figure 1 is prepared to make a lamination. During the curing process, the tensile force are able to be applied to warp/weft fiber bundles by means of the weights through the wire rope after chuck 1 and chuck 2 fixed to the plain weave glass fabric. The laminating conditions are determined by the pre-tensioned ratio  $T_1/T_2$  ( $T_1$  : Warp direction,  $T_2$  : Weft direction, unit : N) in warp/weft directions. The fiber weight fraction of the specimen is about  $33 \pm 2\%$ .

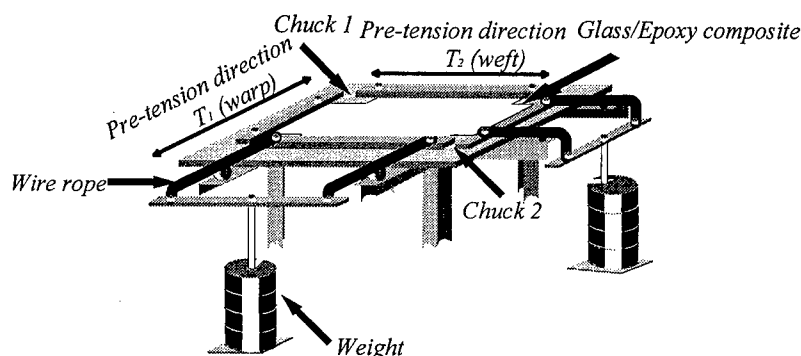


Figure 1 Schematic figure of laminated table.

### Four point bending test

Four point bending tests were performed with some test pieces obtained from the pre-tensioned ratio 0/0, 400/0, 800/0, 500/500 and 800/800 types. Four point bending tests with the upper span length of 30mm and the lower span length of 90mm are carried out at a static cross-head speed of 3.0mm/min at the room temperature with a screw-servo material test machine (Type 4467 : Instoron Inc. USA). Dimensions of the specimen are 15mm×120mm×3mm. The strains at upper and lower surfaces on the central position are measured by strain gages (Gage length : 5mm, Active-gage method).

### Tensile test

Tensile tests were performed with test pieces of the pre-tensioned ratio 0/0, 400/0, 800/0 and 800/800 types. Tensile tests are carried out at a static cross-head speed of 1.0mm/min at the room temperature with a screw-servo material test machine (Type 4467 : Instoron Inc. USA). The strain in the small deformation region was measured by a strain gage (Gage length : 5mm, Active-gage method), and the surface strain in the large deformation region was measured by the clip-gage type extensometer (Gage length : 25mm).

### Compressive test

Compressive tests were performed with test pieces under the pre-tension ratio 0/0, 400/0,

800/0 and 800/800 types. Compressive tests are carried out at a static cross-head speed of 1.0mm/min at the room temperature with a screw-servo material test machine (Type 4206 : Instoron Inc. USA) according to JIS K 7076-1991 standard. Dimensions of the specimen are 12.5mm×78mm×3mm. The longitudinal strain is measured by a strain gage (Gage length : 1mm).

## RESULT AND DISCUSSION

### *Change of woven structural parameter*

In the plain weave glass fabric, the woven structural parameters; the weaving angle, the aspect ratio and the inter fiber bundle distance, are defined in order to investigate the change of the structural parameters of pre-tensioned plain weave glass fabrics. The schematic figure of the structural parameters of plain weave fabrics are shown in Figure 2.

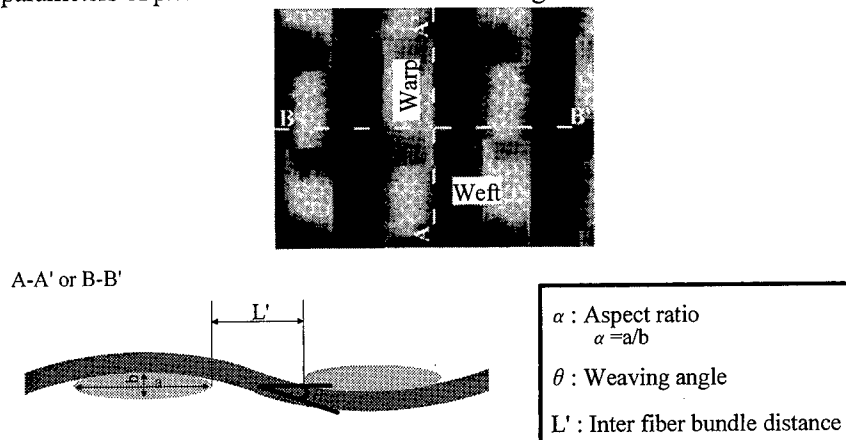


Figure 2 Structural parameters of plain woven glass fabric.

Figure 3 shows the relationship between the aspect ratio and the weaving angle in the cross section A-A'. The aspect ratio decreased by about 3.3(deg.) on the weaving angle with decreasing the weaving angle. When the pre-tension to be warp direction acts on plain woven fabric, the contact pressure in warp/weft bundles acts on the crossing point of warp/weft bundles [6]. Thus, it is considered that the result is a cause of decreasing the aspect ratio at a weft bundle. On the other hand, when the pre-tension to a warp direction overacts on a plain woven fabric, the contact pressure action

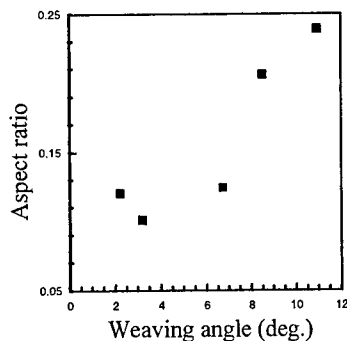


Figure 3 The relationship between aspect ratio and weaving angle.

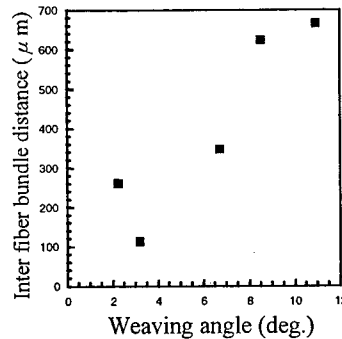


Figure 4 The relationship between inter fiber bundle distance and weaving angle.

at the crossing point of warp/weft bundles decreases. Thus, the increase of the aspect ratio, in the case of about 2.2(deg.) on the weaving angle, is considered to decrease the contact pressure in warp/weft bundles for the pre-tensioned fiber. The relationship between the inter fiber bundle distance and the weaving angle as shown in Figure 4 is also considered as same as the above mentioned reason.

### Bending properties

Figure 5 shows the relationship between the bending strength and the pre-tensioned ratio  $T_1/T_2$ . A peak value of bending strength is shown in the pre-tensioned ratio 400/0 types. Although the bending strength is increased by 400/0 types, the bending strength in 800/0, 500/500 and 800/800 types decreased. Figure 6 shows load-displacement curves in the each specimen. The load-displacement curves in 0/0, 500/500, 800/800 types showed the non-linear behavior, as the applied load is increased. On the other hand, the load-displacement curves in 400/0 types and 800/0 types are different from the above mentioned results, as the slope of curves aren't varied to the failure. Figure 7 shows the relationship between the bending moment and the facial strain, which are measured at upper and lower surfaces of the central position of the test specimen.

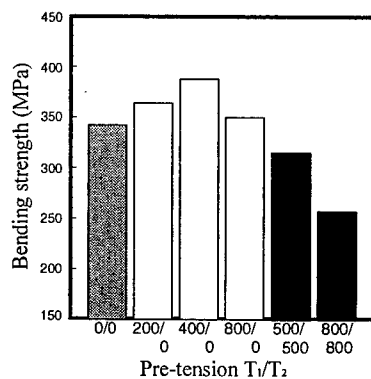


Figure 5 The relationship between the bending strength and the pre-tension in static bending test.

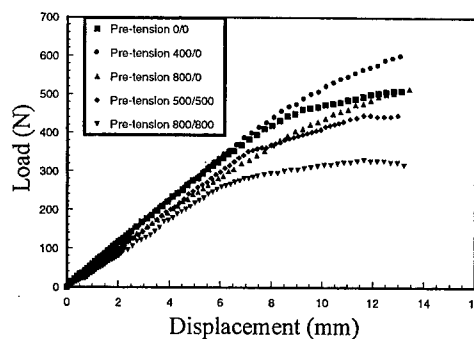


Figure 6 The relationship between the load and the displacement in static bending test.

The facial strains of compressive sides in 0/0 and 800/800 types are increased with increasing the applied load. Figure 8 shows damage states on compressive sides to the edge-wise direction of each specimen. Micro-buckling failures of warp bundle were appeared at 0/0 types, 500/500 types and

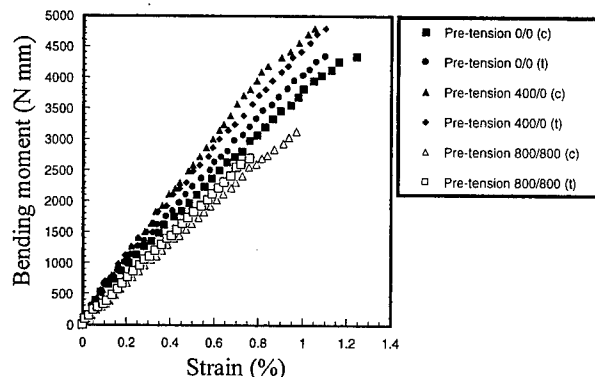


Figure 7 The relationship between bending moment and facial strain for pre-tension.

800/800 types. On the other hand, the interfacial failure and the debonding were appeared at 400/0 and 800/0 type specimens. It is clear that these results relate to non-linear behaviours of load-displacement curves.

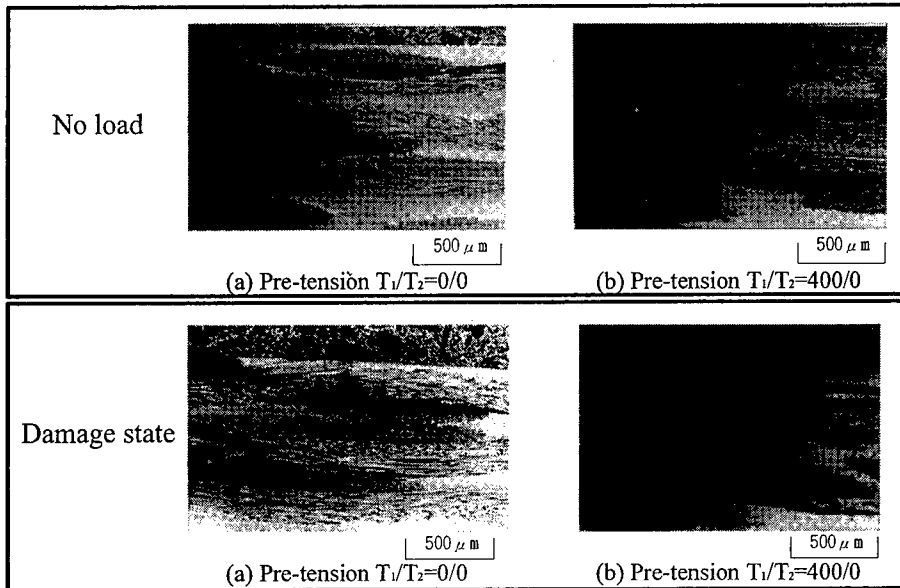


Figure 8 Damage states of composites in bending tests.

#### Tensile properties

Figure 9 shows the relationship between tensile strength, Young's modulus and laminating conditions. It is clear from these results that the tensile strength and the Young's modulus in 400/0 type increase in comparison with those in 0/0 type. On the other hand, the tensile strength and the Young's modulus in 800/0 type and 800/800 type specimens decrease than those in 400/0 type. Thus, it is found that the tensile strength and the Young's modulus are also able to be increased by the pre-tensioned fiber. The stress-strain curves in tensile tests for four types are shown in Figure 10. In tensile tests, the stress-strain behaviours of each specimen were different, in the particular failure strain. Figure 11 shows optical micrographs to the edge-wise direction on each specimen. Transverse cracks were appeared in 0/0, 800/0 and 800/800 type specimens, interfacial failures were observed in 400/0 type

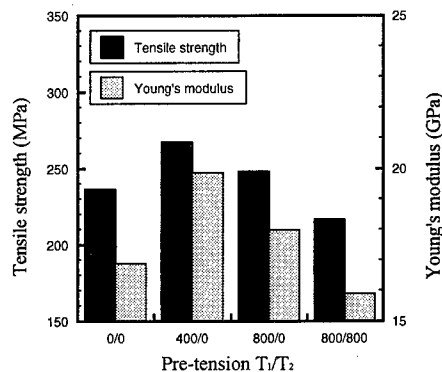


Figure 9 Tensile strength and Young's modulus versus pre-tension  $T_1/T_2$ .

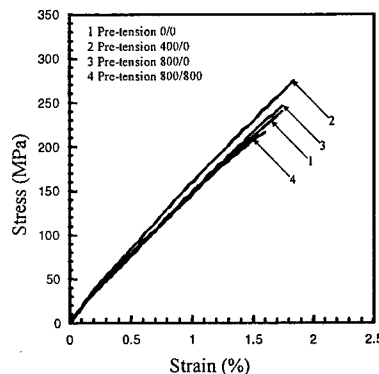


Figure 10 Stress-Strain curves of tensile tests.

specimen. The pre-tension as 400/0 type caused decreasing a stress concentration at crossing point of warp/weft fiber bundles, the waviness or the crimping on fiber bundles. Furthermore, the stress-strain curves are varied by the magnitude of a stress concentration at the crossing point of warp/weft fiber bundles.

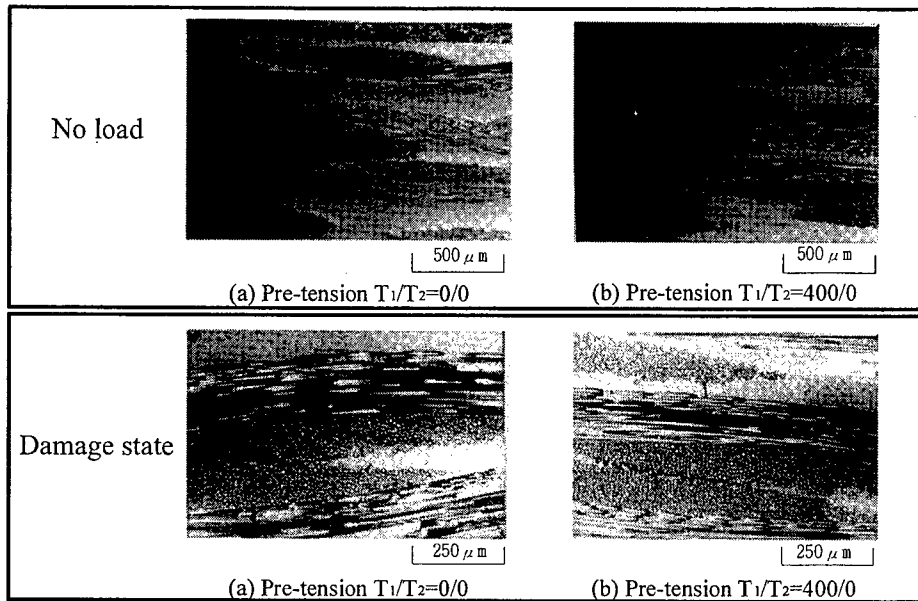


Figure 11 Damage states of composites in tensile tests.

#### Compressive properties

Figure 12 shows the relationship between the compressive strength and the compressive modulus and the laminating condition. The result shows that the compressive strength and the compressive modulus in 400/0 type increase in comparison with those of 0/0 type. On the other hand, the compressive strength and compressive modulus in 800/0 and 800/800 types decrease as compared to those in 400/0 type. The pre-tension to the warp bundle direction as 400/0 type is effective to improve the compressive strength and modulus. The stress-strain curves on the compressive tests for four types are shown in Figure 13. The stress-strain curves in 0/0 types and

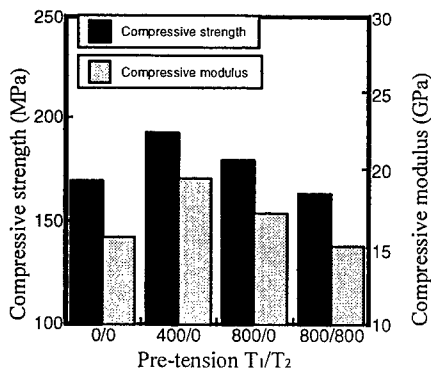


Figure 12 Compressive strength and compressive modulus v.s. pre-tension.

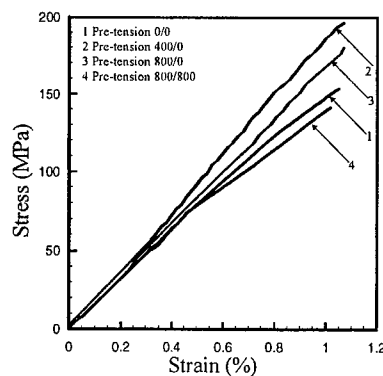


Figure 13 Stress-Strain curves in compressive tests.



800/800 types shows the non-linear behaviour. On the other hand, the stress-strain curves in 400/0 and 800/0 types are different from the above mentioned result, as the slope of curves have not been varied to the failure. This behaviour is almost similar to that on the bending test. Figure 14 shows optical micrographs to the edge-wise direction of each specimen. Micro-buckling failures in the warp bundle were observed in 0/0 types and 800/800 type specimens, a shear mode failure in warp bundle was appeared in 400/0 and 800/0 type specimens. When the fiber bundle forms the waviness or the crimping as 0/0 and 800/800 types, the damage is easy to show a micro-buckling failure, furthermore, the compressive strength and the modulus decrease.

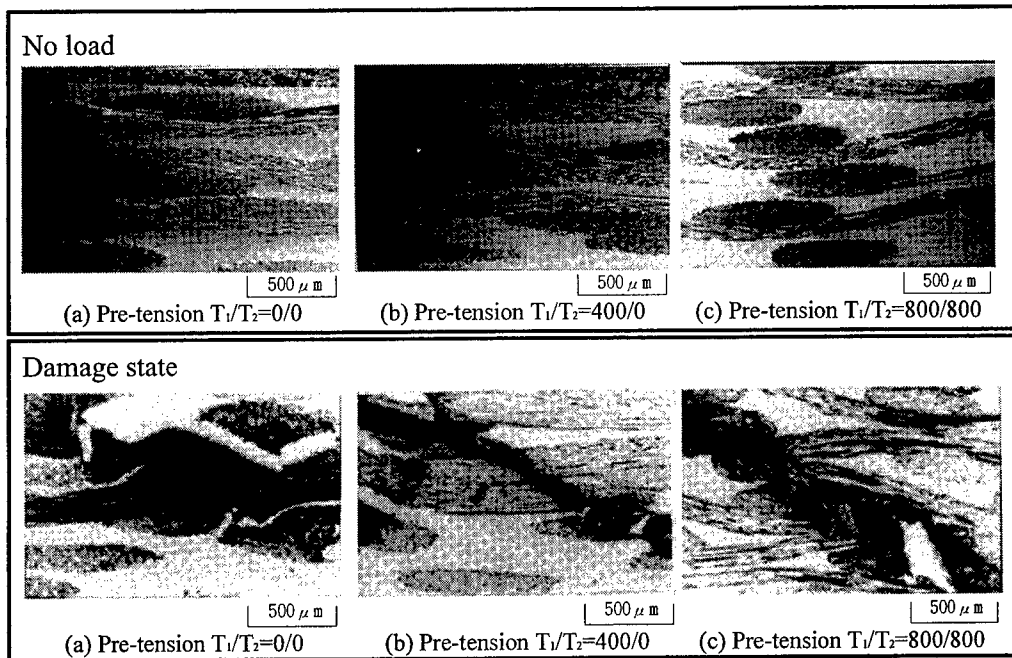


Figure 14 Damage states of composites in compressive tests.

## CONCLUSION

The effects of the pre-tension to warp/weft bundles in laminating on the strength properties of plain woven glass fabric composites were investigated. As a result, from the static bending, tensile and compressive tests, it is found each strength and modulus on the pre-tension ratio ( $T_1/T_2$ ) 400/0 type is able to increase with compared to that on 0/0 types, that on 800/0 types and 800/800 types are decreased with compared to that on 400/0 types. Stress-Strain curves are varied by the magnitude of a stress concentration at crossing point of warp/weft fiber bundles, the waviness or crimping on fiber bundle. And, the waviness or crimping on fiber bundle occurs micro-buckling failures on internal damages in bending tests and compressive tests, particularly. Each strength and modulus of the specimens on 800/0 and 800/800 types are decreased due to the fiber damage and low resin penetrating. Furthermore, it is clear from the results of 800/800 type that the internal damage occurs for a stress concentration increase at crossing points of warp/weft bundles with an increase of the contact pressure on each bundle.

## ACKNOWLEDGEMENT

The authors would like to express their special thanks to Dainippon Ink & Chemicals Co. Ltd., and Asahi Fiber glass Co. Ltd., for providing materials in this study. And, this work was supported by a grant to RCAST at Doshisha University from the Ministry of Education, Japan, and the aid of Doshisha University's Research Promotion Fund.

## REFERENCE

- [1] Jong-Won Lee, Charles E. Harris, "A Micromechanics Model for the Effective Young's Modulus of a Piecewise-Isotropic Laminate with Wavy Patterns", *Journal of Composite Materials*, Vol.22 (1988) 717-741
- [2] A.C.West, D.O.Adams ; "Axial Yarn Crimping Effects in Braided Composite Materials", *Journal of Composite Materials*, Vol.33 No.5 (1999) 402-419
- [3] H.M.Hsiao, I.M.Daniel ; "Elastic Properties of Composites with Fiber Waviness", *Composites, Part A* 27A (1996) 931-941
- [4] Daniel O'Hare Adams & Steven J. Bell ; "Compression Strength Reductions in Composite Laminates due to Multiple-Layer Waviness", *Comp. Sci. and Tech.*,53 (1995) 207-212
- [5] K.H.Leong, M.Nguyen, I.Herszberg ; "The Effect of Deforming Knitted Glass Fabrics on the Basis Composite Mechanical Properties", *Journal of Materials Sciences*, 34 (1999) 2377-2387
- [6] B.J.Souter, A.C.Long et al. ; "The Influence of Fabric Mechanics on Draping", *The Sixth International Conference Automated Composites*, (1999) 55-62

## **Eigenvalue Analysis Method for Honeycomb Sandwich Panels**

T.Shioda, T.Nishiwaki and Z.Maekawa

### **Abstract**

The honeycomb sandwich panel(HSP) is composed of facings and a honeycomb core has excellent specific properties. In case that the panel is applied to various structural components, the prediction of the mechanical properties of the panels is important. The finite element method is a powerful tool in this prediction. In this study, we propose a simple numerical modeling method which can consider the heterogeneity of the HSP. In the proposed modeling, facing, adhesive, layer and honeycomb core are independently represented by two kinds of finite elements, shell and beam elements, respectively. By using the proposed model, the eigenvibration analyses of the CFRP/aluminum honeycomb/CFRP sandwich panels are simulated. The validity of the proposed modeling method is checked by the comparison with experimental results.

### **Introduction**

Recently compound designing have been increasingly important methods. The sandwich panel is the most popular compound structure, because the fabrication is easy and the sandwich panel assembled different facing and core materials can have various mechanical properties. Especially it has been said that the HSP can have excellent mechanical properties, for example high specific modulus[1-2] and low damping, and so on[3-5]. In the process of designing the prediction is indispensable. The finite element method is an effective and powerful tool in this prediction. In the finite element method, a modeling of the honeycomb core will be an important key. Moreover facing, adhesive layer and core must be individually represented by the finite elements in order to check the influences of these components upon the whole mechanical behaviors.

In this study, a new numerical modeling method of CFRP/aluminum honeycomb/CFRP sandwich panel is proposed and eigenvibration analyses are performed. The validity of the proposed modeling method is checked by the comparison with experimental results. Moreover the influences of the geometric parameters in honeycomb core on the eigenfrequency are discussed.

T.Shioda and Z.Maekawa, Graduate Program of Advanced Fibro-Science in Graduate School, Kyoto Institute of Technology, Matsugasaki, Sakyo-ku, Kyoto 606-8585, Japan

T.Nishiwaki, ASICS Corporation, 6-2-1 Takatsukadai, Nishi-ku, Kobe, 651-2271, Japan

### Modeling method

The HSP is composed of two facings, honeycomb core and adhesive layers. Namely this panel has a heterogeneous property. In case that the mechanical behavior of the honeycomb panel, the modeling method of the heterogeneity is important[6-9]. In the proposed modeling, the heterogeneity is represented by the construction of two kinds of elements. Figure 1(a) shows the basic concept of this modeling method. At first the facings are modeled by shell elements. Then

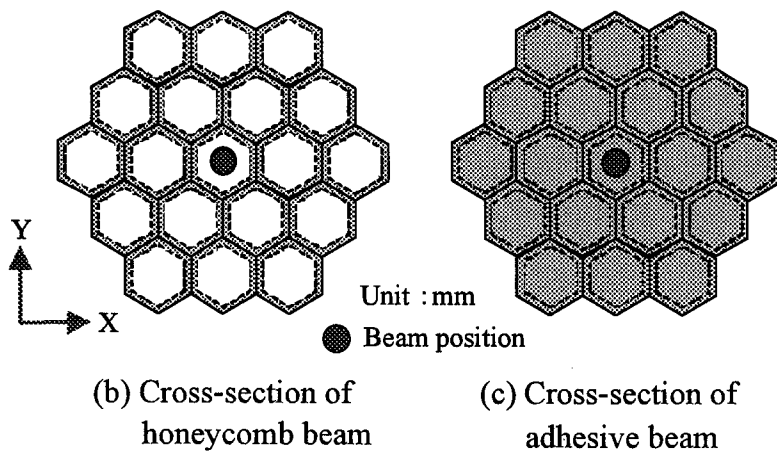
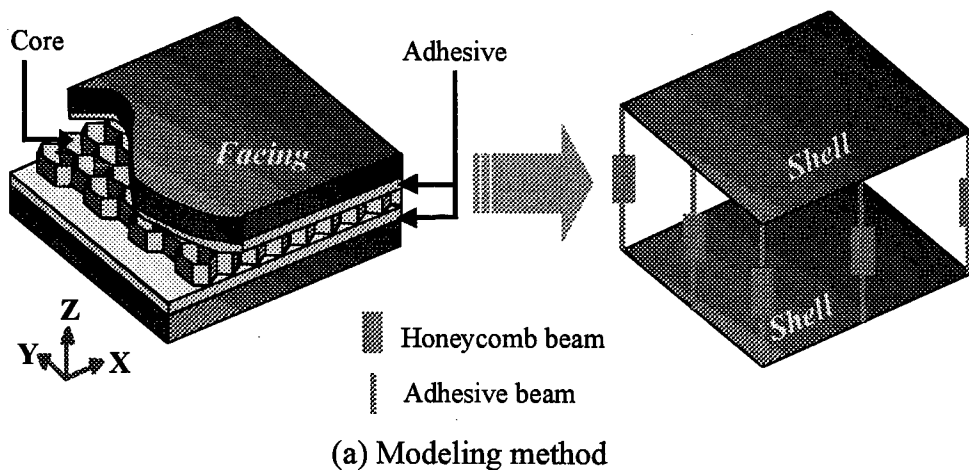


Figure 1 Basic concept for numerical modeling method.

adhesive layer and HC core are modeled by using two kinds of beam elements. The of the HSP are individually modeled. Honeycomb core has constant periodicity. Considering this periodicity, honeycomb core can be dispersed by beam elements.

In this modeling, 19 honeycombs cell is defined to be a cross-sectional area of beam element, as shown in Fig.1(b). Therefore, automatically facings must be modeled by using triangular shell elements. Similarly adhesive layer modeled by using beam elements with a hatched cross-sectional area, as shown in Fig.1(c). In this model, two layered shell elements corresponded to facings are connected by three beam elements in thickness direction. Figure 2 shows the beam element positions in the top view.

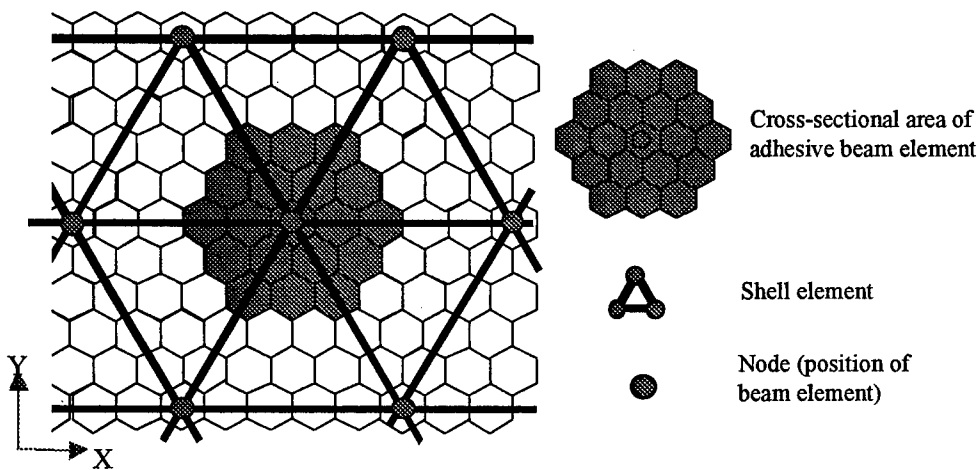


Figure 2 Cross-section of adhesive beam element

### Analytical procedure

Figure 3 shows the geometry of the HSP used in this study. The fiber arranges in X direction, the orientation angle  $\theta$  is 0. The core is an aluminum honeycomb, the height,  $h_c$ , wall thickness,  $t$  and cell size,  $l$  are 5mm, 0.0254mm and 3.14mm, respectively. The thickness of adhesive layer between the facing and core is constantly 0.25mm. The overall length of the panel is 180mm and the width is 135mm. Three types of thickness of the each facing, 0.5, 1.0 and 1.5mm are used. Figure 4 shows the finite element model used in this simulation. As already mentioned, 19 cells are modeled by one beam element corresponded to honeycomb core. Here X, Y and Z-axis show the longitudinal, width and thickness direction, respectively. By using this model, we performed the eigenvibration analyses under the free boundary condition, calculated eigenfrequencies corresponded to the 1st torsional mode and 1st bending mode with a main curvature in the longitudinal direction. On the other hand, we make an experiment in order to investigate the propriety of the proposed modeling method. The facings were supplied by Toray Industries Inc. and consisted of 'T-700' carbon fiber bonded in common epoxy resin '#2500'. The fiber volume fraction  $V_f$  are equal to 67% constantly.

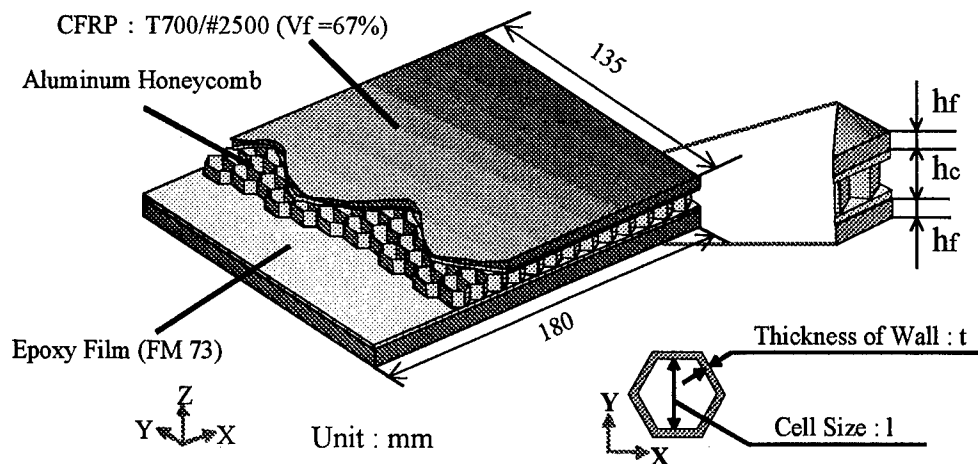


Figure 3 Geometry of the whole specimen

Aluminum honeycomb, AL1/8-5052-001 was supplied by SHOWA Aircraft Industry Co., Ltd. Adhesive layer was a toughened epoxy film, FM73 supplied by CYTEC FIBERITE Inc. In this experiment, the vibration testing system(AD3542, A&D Inc.) was used. The plate measured was suspended with a fine strings, this condition was equivalent with the free boundary condition in the analysis. A center of the plate was condition was impacted by an impact hammer and out-plane acceleration outputs were recorded by the accelerometer attached on the plate. From both the input and output, eigenfrequencies corresponded to the 1st torsion and 1st bending modes were calculated.

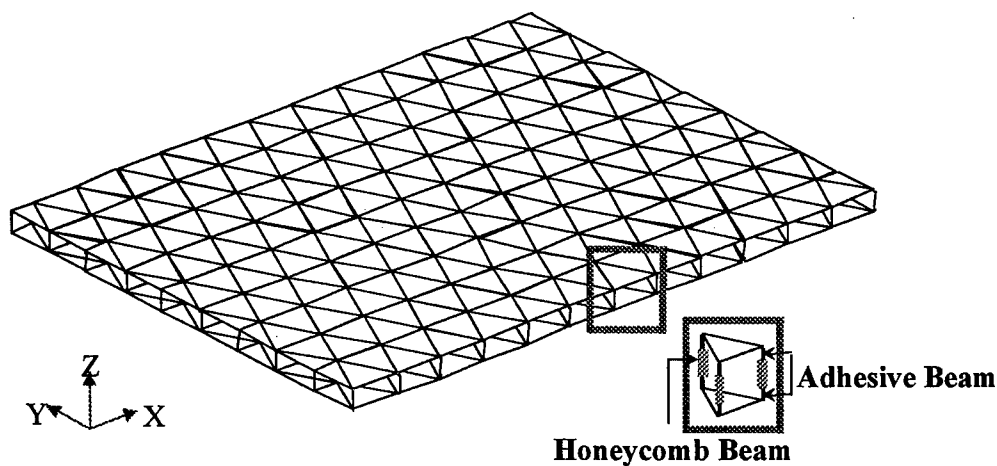


Figure 4 Numerical model used in this study

## Analytical results

Figure 5(a) and (b) shows the 1st torsion and 1st bending modes of the HSP with 1mm facings obtained from the analysis. In this analysis, it was found that the 1st torsional mode and 1st bending mode with the main curvature in the longitudinal direction, respectively. The thickness of facing cannot depend on this order. This result could be also obtained from the measurement. Table I shows the comparison of eigenfrequencies between analytical and experimental results. Judging from this table, it is confirmed that both the eigenfrequencies agree well. This indicates that the proposed model could predict the 1st torsion and 1st bending eigenfrequencies.

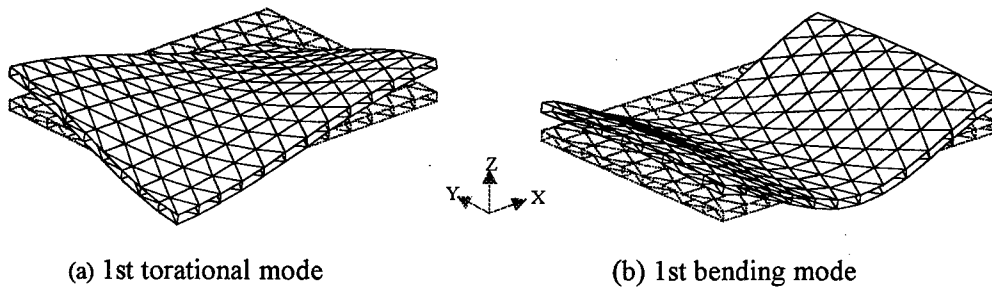


Figure 5 Eigenvibration mode shapes obtained from the proposed model

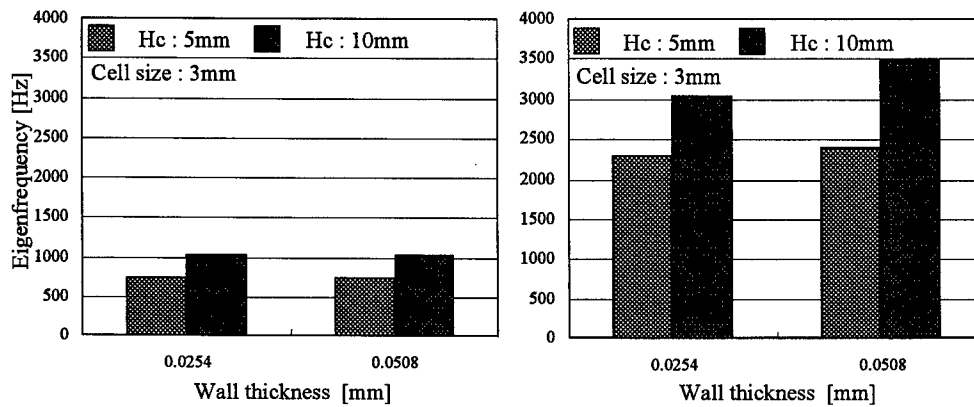
Table I Comparison of eigenfrequencies

Type	Sample	Thickness	Eigenfrequency[Hz]					
			1st torsional			1st bending		
			FEM	Exp	Error(%)	FEM	Exp	Error(%)
CF-0.5		0.5/5/0.5	736.93	766.98	3.92	1853.73	1874.70	1.12
CF-1.0	CF/ALHC/CF	1.0/5/1.0	558.08	584.57	4.53	1190.44	1239.69	3.97
CF-1.5		1.5/5/1.5	652.51	705.51	7.51	1274.40	1370.71	7.03

## Discussions

The HSP has various geometric parameters. Wall thickness, height and cell size representative. An influence of these parameters on the eigenvibration mode and the eigenfrequency are predicted by using the proposed model. The treating method is very easy. The changes of wall thickness and cell size can be represented by changing the moment of inertia and cross-sectional area. The change of height can be represented by changing beam length. At first, the influences of the wall thickness and core height are predicted by using the proposed model. The thickness of facing is constantly 1mm. The cell size is also fixed to be 3mm. Figure 6(a) and (b) shows the 1st torsional and 1st bending eigenfrequencies with changing the

core height and wall thickness, respectively. In case that the wall was changed from 0.0254mm to 0.0508mm, it was found that the increasing to ratio in both the eigenfrequencies was very small. On the other hand, in case that the core height was

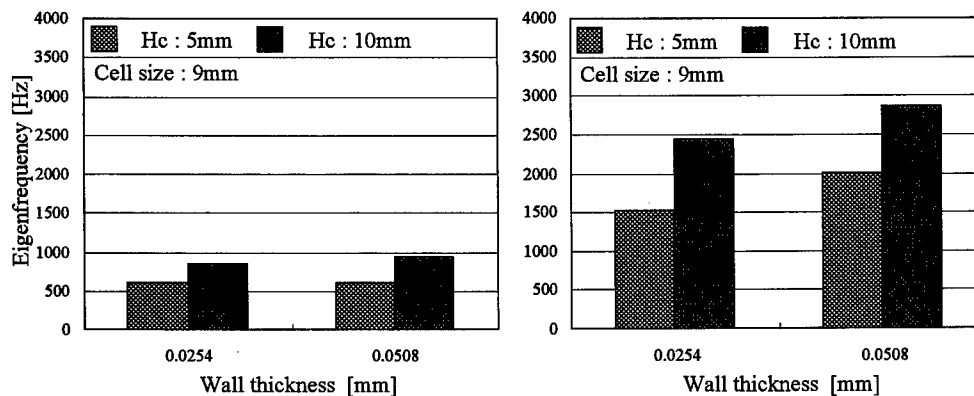


(a) 1st torsional eigenfrequencies

(b) 1st bending eigenfrequencies

Figure 6 Analytical results of both the eigenfrequencies in case of that cell size  $l=3\text{mm}$

changed from 5mm to 10mm, it was found that the increasing ratio corresponded to the torsional mode is smaller than that corresponded to the bending mode. This results indicates that the increasing the core thickness causes higher bending stiffness rather than torsional stiffness. The above tendencies are supported under the large cell size, 9mm as shown in Figure 7(a) and (b). Results shown in Figure 7 are



(a) 1st torsional eigenfrequencies

(b) 1st bending eigenfrequencies

Figure 7 Analytical results of both the eigenfrequencies in case of that cell size  $l=9\text{mm}$



predicted by using another proposed model. Namely, 7 honeycomb cores were modeled by one beam element in this model as shown in Figure 8. In order to check the effect of cell size, Figure 6 and 7 are compared. On the whole, eigenfrequencies of HSP with cell size of 3mm are larger than that with cell size of 9mm. When considered the cell size effect, it was clarified that the increasing cell size decreased both the torsional and bending stiffnesses. Solution time in each analysis is smaller than 37sec. on PC with 397MHz. It is said that the solution time is generally short as compared with that of the previous numerical model. This convenience will be a powerful design designing tool.

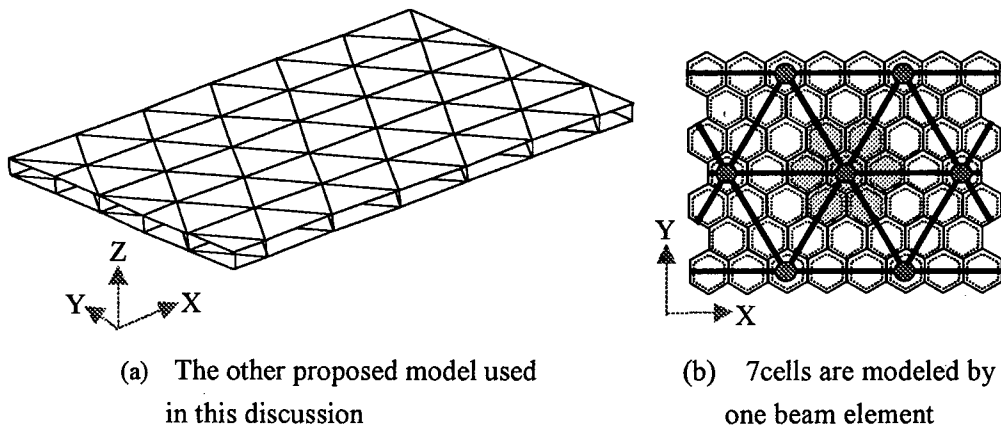


Figure 8 Eigenvibration mode shapes obtained from the finite element analysis

## Conclusions

In order to predict the mechanical properties of HSP, the new numerical model was proposed. The model constructed by the shell and two types of beam elements can consider the heterogeneity of the HSP. The eigenvibration mode and eigenfrequencies of the CFRP/aluminum honeycomb core/CFRP panels were simulated, compared with the experimental results. Therefore it was found that the vibration properties of CFRP/ALHC/CFRP panels could be accurately obtained in a short time. By using the proposed model, the influences of the geometric parameters in honeycomb core upon the eigenvibration properties were simulated. Therefore the influences of wall thickness, core height and cell size were individually clarified.

## References

1. R.B.Hall, 1996. "Performance Limits for Stiffness-Critical Graphitic Foam Structures. Part II:Comparisons of Foams, Foam-Core and Honeycomb-Core Sandwiches in Bending/Shear.", *Journal of Composite Materials*, **30**(17):1938-19

2. D.M.Cise & R.S.Lakes, 1997. "Moisture Ingression in Honeycomb Core Sandwich Panels: Directional Aspects.", *31*(22), 2249-2263
3. M.R.Maheri, R.D.Adams, 1994. "Steady-State Flexural Vibration Damping of Honeycomb Sandwich Beams.", *Composites Science and Technology*, *52*:333-3473.
4. M.Coni, B.Benchekchou & R.G.White, 1996 "The Structural Damping of Composite Beams with Tapered Boundaries.", *Composite Structures*, *35*:207-212
5. T.Lekszycki, N.Olhoff & J.J.Pedersen, 1992. "Modelling and Identification of Viscoelastic Properties of Vibrating Sandwich Beams.", *Composite Structures*, *22*:15-31
6. T.Nishiwaki, A.Yokoyama, Z.Maekawa & H.Hamada, 1995. "A New Numerical Modeling for Laminated Composites.", *Composite Structures*, *32*:641-647
7. T.Nishiwaki, A.Yokoyama, 1994. "A Quasi-Three-Dimensional Bending Analysis Method for Laminated Composites.", *J.JSCM*, *21*:15-20
8. T.Nishiwaki, A.Yokoyama, 1995. "A Quasi-Three-Dimensional Lateral Compressive Analysis Method for a Composite Cylinder Method for Laminated Composites.", *J.JSCM*, *21*:293-298
9. T.Nishiwaki, A.Yokoyama, Z.Maekawa & H.Hamada, 1995, "A Quasi-Three-Dimensional Elastic Wave Propagation Analysis for Laminated Composites.", *J.JSCM*, *32*:635-640

# **Development of CAE System**

## **Predicting Stiffness of SMC structure**

### **-Research on the Young's Modulus in Rib Part -**

T. Katayama, M. Shinohara, M. Hakotani, M. Toutani

#### **Abstract**

Sheet Moulding Compound (SMC) products have some ribs to improve stiffness of structures. So, because of the ribs, expected stiffness can't often be obtained. In these cases, while it is needed to change die design, it costs greatly to do so. There, CAE system predicting stiffness to improve efficiency of die design is needed.

The structure analysis is used in the stiffness prediction. Therefore, the prediction of Young's modulus is required. We aim to construct the method for the calculation of Young's modulus in rib part of SMC product. In this study the effect of the flow channel geometry and reinforced fiber length on a Young's modulus in rib part was investigated.

In the result we could show the effect of the flow channel geometry on fiber weight content and orientation in rib part. However, we couldn't show the effect of the reinforced fiber length.

#### **1. Introduction**

Sheet Moulding Compound (SMC) has been widely applied to industries such as automotive exterior parts and housing facilities for its excellent mechanical properties, relatively low cost and lightweight and good design possibilities.

Typical SMC products have some ribs in order to reduce weight of the structures without loss of stiffness. However, in these products, various problems such as sink mark, weld lines, warpage and heat cracks often occur. These problems are caused by complexity of fiber distribution and fiber orientation. In such cases, it is needed to change the design of the mould. However, it enormously costs to do so since the die for compression moulding of SMC, which must be able to endure the moulding in high temperature and high pressure,

---

T. Katayama Department of Mechanical Engineering, Doshisha University, Japan.

M. Shinohara Department of Mechanical Engineering, Maizuru National College of Tech, Japan.

M. Hakotani Research Lab. Takeda Chemical Industries, Ltd.

is very expensive. It needs more enormous time to change the design after making the die. So, CAE system is needed to improve the efficiency of mold design. And we are trying to

construct the CAE system to predict the stiffness of structure in SMC compression moulding.

In the past study the structure analysis is used in the stiffness prediction. Therefore, the prediction of a Young's modulus is required. Since material flow of SMC is complicated and unsteady, and that is more complicated especially in rib part, it is difficult to estimate the conditions of material flow, fiber distribution, fiber orientation and so on. So, it becomes effective to apply the database that is systematically arranged by these various factors.

The SMC structural member is divided into the flat plate part of which the material flow is not so complicated and the rib part of which the material flow is very complicated. Then we have predicted the Young's modulus of each part. We can predict Young's modulus in the flat plate part by the simulation (flow analysis, fiber orientation analysis) and database. In the rib part it is possible to predict Young's modulus according to the database that shows the relationship between Young's modulus and  $B/ts$  with the correlation with the flow<sup>1)</sup> (Here  $B/ts$  is the ratio between rib width  $B$  and material thickness  $ts$  as the material passes the rib in moulding process.). However the relationship between flow channel geometry and Young's modulus in the rib part is not clear. And the relationship between flow channel geometry and reinforced fiber length also is not clear because only fiber length which is 1 [inch] was an object.

In this paper we investigate the effect of flow channel geometry and reinforced fiber length on Young's modulus in rib part. Concretely we investigate fiber distribution, fiber orientation and Yong's modulus in rib part.

## 2. The basic research on Young's modulus in rib part

### 2.1 Moulding Method

Products were moulded by using the press machine for FRP compression moulding. There is a rib in the centre part of die. It is possible to change rib width  $B$  to 2, 3, 4, 5, 10, 20[mm] and rib height  $H$  to 10, 20, 30, 40[mm].

Products were moulded in the shape of a letter T such as Fig.1 on 100% charge pattern. Here, charge pattern presents the ratio of material area to the whole die area. Closing speed was set at 0.15[mm/s] and the die pressure at 5[MPa] to all shapes of the rib. The die temperature of the upper and lower die was maintained at 140[°C].

In this experiment, reinforced fiber length of the SMC material is 1,2/3[inch] ( $L=1,2/3$ [inch]). Contents of SMC are shown in Table 1.

Table I Contents of SMC

Resin	25.0 Wt%
Glass fibre	22.0 Wt%
CaCO <sub>3</sub>	53.0 Wt%

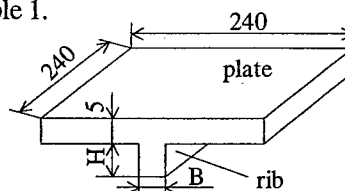


Figure 1 Shape of product

## 2.2 Material Flow and Fiber Orientation in Rib Part

The soft X-ray photographs were taken from the side of the rib on  $B=2, 3, 4, 5$  [mm]. The test pieces were cut off from the central part of rib to prevent the effect of the edge.

Fig.2 shows the soft X-ray photograph in case of  $H=30$ ,  $B=2$ [mm],  $L=1$ [inch]. From soft X-ray photographs, it is observed that the proportion of resin-rich part increases with the decrease of the rib width. It is considered that glass fibers were bound in rib upper part, and then the resin was pressed out into the rib lower, when the material flows into the rib part. When the orientation of glass fiber is noticed, it is proven that fibers relatively orientate in the longitudinal direction of rib part in the region over the resin-rich layer a little, and in the transverse direction of that in upper layer a little.



Figure 2 Soft X-ray Photograph ( $B=2, H=30, L=1$ )

## 2.3. Fiber weight content in rib part

### 2.3.1 Experimental Method

The test pieces were made by dividing into the height direction of the rib at every 5[mm] as shown in Fig.3 on  $B=2, 3, 4, 5$ [mm],  $H=30, 40$ [mm] and  $L=1, 2/3$ [inch], and the measuring of fiber weight content was carried out. In this experiment, the ratio  $B/t_s$  was used as the parameter that showed the geometry of die. Here, it is proven that  $B/t_s$  had the large correlation with material flow in the past research.

### 2.3.2 Results and Discussion

The relationship between fiber weight content and  $B/t_s$  in case of  $H=30$ [mm],  $L=1$ [inch] is shown in Fig.3. From these result, as  $B/t_s$  is larger to some extent, fiber weight content in each region is about a constant value which is the SMC raw material of 22[wt%] in all this experiment in moulding conditions. In the meantime, as  $B/t_s$  is smaller to some extent, fiber weight content grow lower in the lower layer of rib part in all conditions. However, it grows higher in the upper and middle layer. It is considered that the geled resin in the upper and middle layer was pressed out into the rib lower, when the matelial flows into the rib part.

## 2.4 Young's modulus in rib part

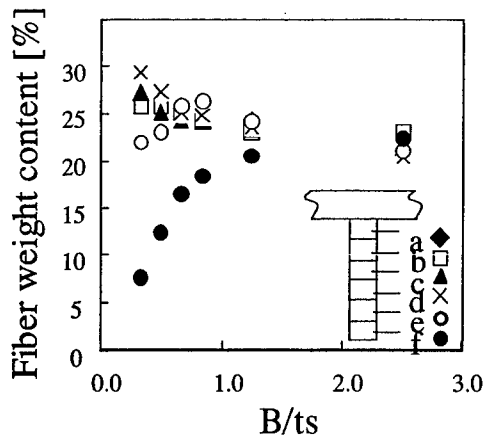


Figure 3 The relationship between B/ts and Fiber weight content (H=30, L=1)

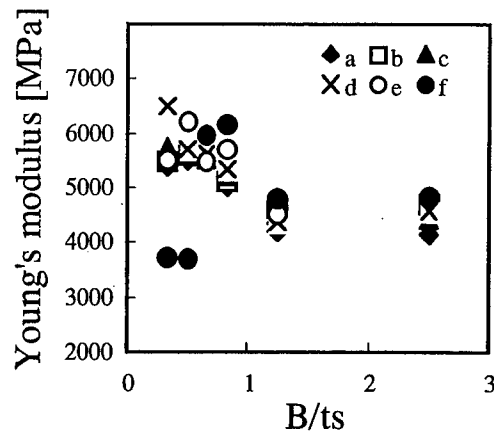


Figure 4 The relationship between B/ts Young's modulus (H=30, L=1)

#### 2.4.1 Experimental Method

The tensile test was carried out by the application of JIS K7054 by using INSTRON universal test machine of 4206 types. The test pieces were made by dividing into the height direction of the rib at every 5[mm] on B=2, 3, 4, 5[mm], H=10, 20, 30[mm] and L=1,2/3[inch] as shown in Fig.3. The test pieces were cut off from the central part of rib to prevent the effect of the edge. The tensile test was carried out in the longitudinal direction of the rib.

#### 2.4.2 Results and Discussion

The relationship between Young's modulus and B/ts in case of H=30, L=1[inch] is shown in Fig.4. In all conditions, as B/ts is larger to some extent, Young's modulus is about a constant value and Young's modulus in rib part is able to be express by using B/ts. However as B/ts is smaller to some extent, in each region the dispersion of Young's modulus occurs and the Young's modulus in rib part isn't able to be express by using B/ts. As an apparent tendency of the dispersion, it is mentioned that in the rib bottom the Young's modulus is extremely low in the effect of resin-rich.

### 3 The research on Young's modulus in rib part

In previous section the rib becomes heterogenous in all moulding conditions, as B/ts is smaller to some extent. But the heterogeneity is largely divided into two. They are resin-rich region and the other region. If there is a database that show how the size and Young's modulus of each region change by the moulding condition it is possible to predict a Young's modulus in the heterogeneous rib part. So the rib part is divided and the effect of the moulding condition on each region was investigated.

### 3.1 The method to divide the rib part

Resin-rich shows the region in which the fiber weight content is smaller than the other part of the product. It should be possible that Resin-rich region can be expressed by soft X-ray photograph and glass fiber weight content. However, it is impossible to express the correspondence of stiffness since factors such as the fiber orientation and so on complicatedly affect it each other.

So we defined that the region in which Young's modulus is under an appropriate Young's modulus<sup>1)</sup> as resin-rich is the resin-rich region. Its Young's modulus is 3700[MPa]. The test piece of 2, 4, 6 [mm] height from rib bottom is made and the tensile test was carried out. Therefore we defined the largest height under 3700[MPa] is the range  $H_R$  in which resin-rich influences.

Other region was divided equally for 2, because the Young's modulus differs in the upper and lower region a little in Fig.4. The following the upper area is called upper area and the lower area is called lower area.

### 3.2 The effect of moulding condition on resin-rich region

In previous section the Young's modulus in resin-rich region is defined 3700[MPa]. Therefore it is important that how  $H_R$  changes by the moulding condition.

The relationship between  $H_R$  and  $B/ts$  in case of  $H=30$ [mm],  $L=1, 2/3$ [inch] is shown in Fig.5. From the result, it is proven that  $H_R$  increases with the decrease of  $B/ts$  in case of each fiber length.  $H_R$  is almost same, as rib height is 30, 40[mm].

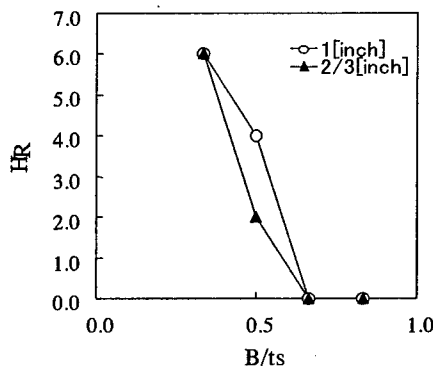


Figure 5 The relationship between  $B/ts$  and  $H_R$  ( $H=30$ )

### 3.3 The effect of moulding condition on the other region

The relationship between Young's modulus in the other region and  $B/ts$  in case of  $H=30$ ,  $L=1$ [inch] is shown in Fig.6. It is proven that Young's modulus in the other region increases with the decrease of  $B/ts$  in all conditions

The relationship between Young's modulus in the other region and  $H$  in case of

$L=1$ [inch] is shown in Fig.7. It is proven that the Young's modulus in the other region decrease, as the rib height increase from 30 to 40[mm].

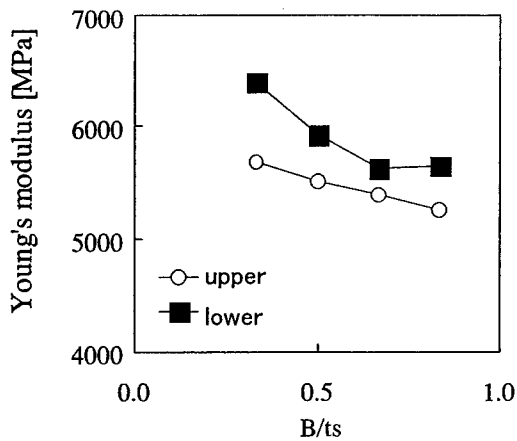


Figure 6 The relationship between  $B/ts$  and Young's modulus ( $H=30$ ,  $L=1$ )

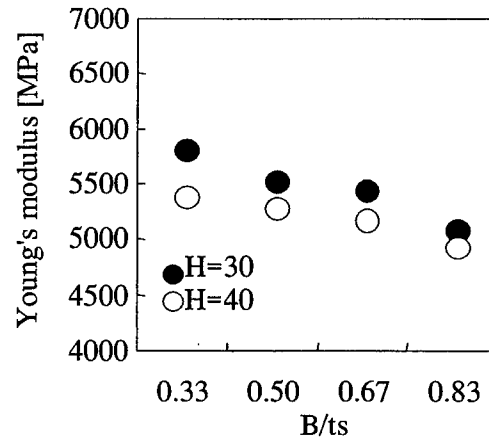


Figure 7 The relationship between  $B/ts$  and Young's modulus ( $L=1$ )

### 3.3.1 Research on fiber orientation in other region

From 3-3, it was proven that Young's modulus was affected by  $B/ts$  and rib height. As this reason, it is considered that the fiber orientation and fiber weight content changed by  $B/ts$  and rib height. So Fiber orientation in other region is investigated.

#### (a) Experimental Method

The rib width is very thin. Therefore the two-dimensional plane between rib height direction and longitudinal direction is investigated. However considering the rib width, the rib is divided width in 4 equally and each cross sections are investigated in one rib. And they were superimposed. To obtain the generous tendency, the fiber orientation in case of  $B=2,5$ [mm],  $H=30, 40$ [mm],  $L=1, 2/3$ [inch] was investigated.

#### (b) The fiber orientation characteristics

$0$ [rad.] shows the orientation in the longitudinal direction of rib part and  $+\pi/2, -\pi/2$  [rad.] shows respectively the orientation in upper and lower direction of rib height direction. By investigating the fiber orientation characteristics, it is proven that the as  $B/ts$  is smaller fiber orientation polarize the inflow direction which is approximate to  $+\pi/2, -\pi/2$  [rad.]. The fiber orientation distribution in case of  $H=30$ [mm],  $L=2/3$ [inch] is shown in Fig.8. As this reason, it is considered as rib width is smaller the velocity gradient of the inflow direction increases by the reduction flow and in the flow the fiber is turned in the



flow direction which is approximate to  $+\pi/2, -\pi/2$  [rad.].

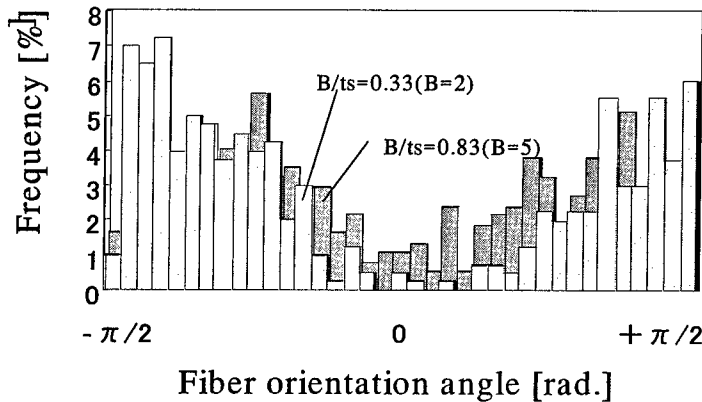


Figure 8 The orientation characterisutic (H=30, L=2/3)

Because the proportion of the longitudinal fiber is lower in Fig.8, Young's modulus seems to become lower, as rib width is smaller. However actually it don't so in Fig.6. As this reason, it is considered that fiber weight content influences Young's modulus. So fiber weight content in other region is investigated and the result is shown in the Fig.9. From the result, Fiber weight content is higher, as rib width is smaller. From these results, it is confirmed both fiber orientation and fiber weight content which are changed by rib width influences in Young's modulus in the heterogeneity rib.

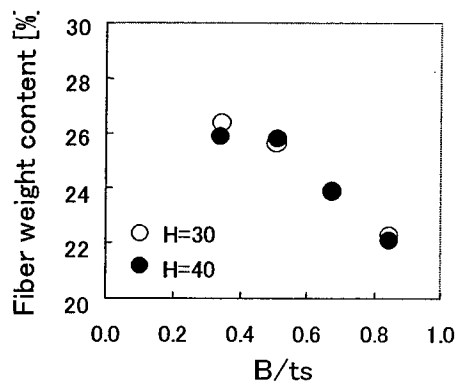


Figure 9 The relationship between B/ts and Fiber weight content (L=1)

By investigating the fiber orientation characteristics, it is proven that the proportion of the fiber orientation which is approximate to  $+\pi/2, -\pi/2$  [rad.] increases a little, as rib height increases. The fiber orientation distribution in case of H=30, 40[mm], L=2/3[inch] is shown in Fig10. As this reason, it is considered that as the rib height

increases the flow distance is lengthened and the fiber is turned in the inflow direction.

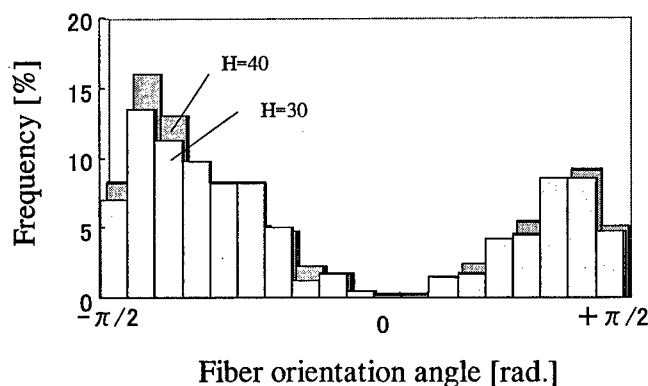


Figure 10 The orientation characteristic ( $B=2$ ,  $L=2/3$ )

From Fig.7, the Young's modulus in the other region decreases a little as rib height  $H$  increases. And from Fig.9 the fiber weight content in other region is almost same, even if the rib height changes. From these results, it is confirmed not fiber weight content but fiber orientation which are changed by rib height influences in Young's modulus in the heterogeneity rib

#### 4. Conclusion

- (1) The size of resin-rich region is largely affected by  $B/t_s$ . However it hardly is affected by rib height, fiber length.
- (2) Young's modulus in other region is affected by rib width and rib height. However we couldn't confirm the effect of the fiber length.

#### 5. References

1. T. Katayama, M. Shinohara, M. Hakotani, A.Kitade, "Development of CAE for predicting stiffness of SMC structure-Estimation of young's modulus in rib "part-"AMPT'99, VolumeII (B1) : 1063-1072

## **Elastoplastic shear-lag Monte Carlo Simulation for the single fiber composite test**

T. OKABE and N. TAKEDA

### **Abstract**

The present paper proposes a new approach to predict the number of fragments during the single fiber composite test. Elastoplastic shear-lag approach, which considers a nonlinear stress-strain curve of the matrix, has been developed to obtain the stress distribution of the fiber fragments. Non-linear finite element analysis was conducted to check the validity of the present approach. The present approach can also predict the debonding length near the fiber breaking point. The number of fragments was measured in the fragmentation test and compared with the prediction by the Monte Carlo Simulation with the present shear-lag approach.

### **Introduction**

The single fiber composite (SFC) test has been used to evaluate micro-damage and material properties of the composite. Many models [1,2] have been proposed, based on the Kelly and Tyson model [3] that the interfacial shear stress between fiber and matrix is assumed to be constant. However, since the interfacial shear stress depends on the properties of matrix which include Young's and shear modulus [4], the assumption for the interfacial shear stress is essential to understand the fragmentation process in SFC. Therefore, it is required that an analytical model which uses the valid interfacial shear stress should be developed. The present paper proposes a new shear-lag model which considers the elastoplasticity of the matrix. In addition, non-linear finite element analysis are conducted to check the validity of the present model. Based on the above analysis, the fragmentation process in the real SFC (Fiber: SiC Fiber (HI-NICALON<sup>TM</sup>), Matrix: Epoxy) is predicted by the Monte Carlo Simulation with the present shear-lag model and compared with the experimental results.

---

Department of Advanced Energy, Graduate School of Frontier Sciences, The University of Tokyo, c/o Komaba Open Laboratory (KOL), Takeda Lab. 4-6-1 Komaba, Meguro-ku, Tokyo 153-8904, Japan

### Elastoplastic shear-lag analysis with a finite difference method

A cylindrical model of half of a fragment, which includes matrix, interfacial shear region and fiber, is assumed as shown in Fig. 1. Matrix and interfacial shear region is assumed to follow the elastoplastic stress-strain curve as shown in Fig. 2. In addition, we assume that an interfacial shear region does not carry any axial load and follows the pure shear stress-strain curve of matrix. The model is divided into  $k$  elements and each node is called, in turn,  $i = 0, 1, \dots, k$  as shown in Fig. 1. The superscripts  $m$  and  $f$  denote matrix.  $E^e$  and  $E^p$  are Young's and plastic tangent modulus of matrix and interfacial shear region shown in Fig. 2 and  $G$  is the shear modulus of matrix and interfacial shear region. Radius of the fiber and interfacial shear region are  $r$  and  $r+d$ , respectively.

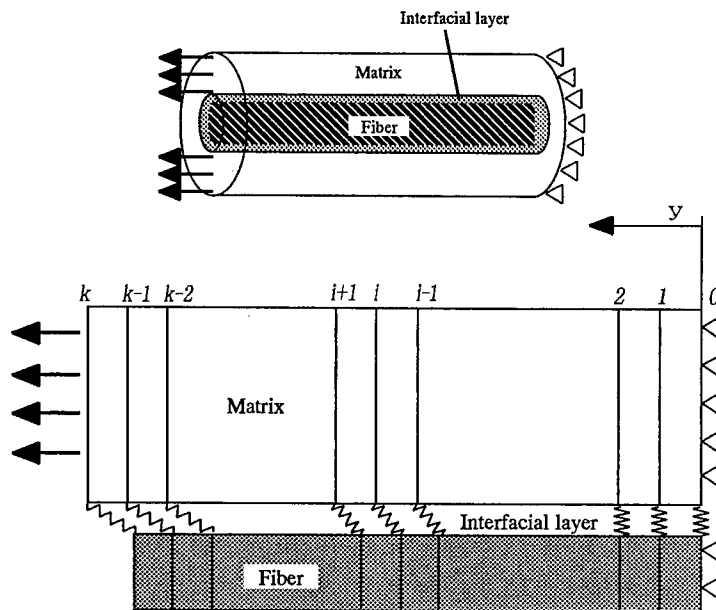


Figure 1 Schematics of analytical model

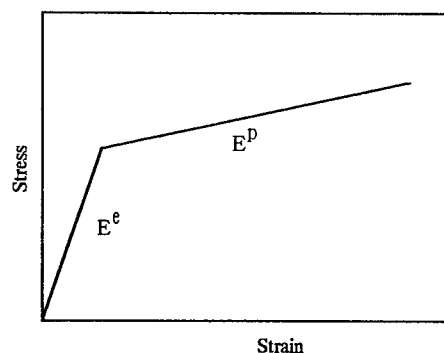


Figure 2 Schematic of stress-strain curve of matrix and interface

The shear-lag equations for fiber elements are divided into two regions as shown in Fig. 3. One is the region where the fiber stress is transferred by the elastic interfacial shear region. The other is the one where the fiber stress is transferred by the plastic interfacial shear region. The shear-lag equations for both regions are given by

$$\frac{d\sigma^f}{dy} = -\frac{2\tau}{r} \quad (1)$$

and  $\tau = G\gamma$  (Elastic interfacial shear region) (2)

or  $\tau = \left\{ \frac{2(E^e - E^p)}{E^e E^p} + \frac{1}{G} \right\}^{-1} \left\{ \gamma + \frac{2\sqrt{3}(E^e - E^p)}{3E^e E^p} \sigma_y \right\}$  (3)

$$= A(\gamma + B) \text{ (Plastic interfacial shear region)}$$

where  $\gamma$  is the shear strain and  $\sigma_y$  is the yield stress given by the Von-Mises relation.

The equation (3) is expressed with the Hencky relation.

The above equations can be approximately rewritten by the nodal displacements and given by

(Elastic interfacial shear region)

$$\left( \frac{2G}{rd} + \frac{2E^f}{\Delta y^2} \right) u_i^f = \frac{2G}{rd} u_i^m + \frac{E^f}{\Delta y^2} (u_{i-1}^f + u_{i+1}^f) \quad (4)$$

(Plastic interfacial shear region)

$$\left( \frac{2A}{rd} + \frac{2E^f}{\Delta y^2} \right) u_i^f = \frac{2A}{r} \left( \frac{u_i^m}{d} + B \right) + \frac{E^f}{\Delta y^2} (u_{i-1}^f + u_{i+1}^f) \quad (5)$$

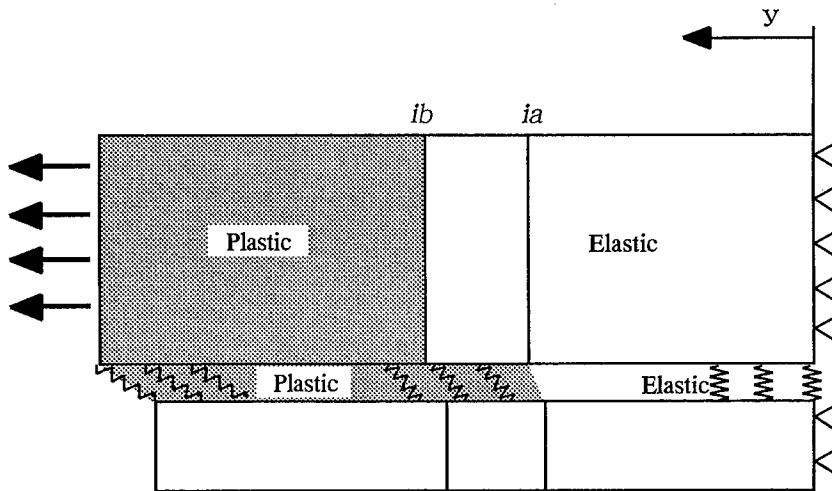


Figure 3 Schematics of elastic and plastic region

The shear-lag equations for matrix elements are divided into four regions. It is because matrix itself will be yielded at the higher strain. Thus it should be considered whether the interfacial shear region is elastic or plastic and matrix is elastic or plastic.

The shear-lag equation for matrix elements are given by

$$\frac{d\sigma^m}{dy} S^m = 2\pi(r+d)\tau \quad (6)$$

$$\tau = G\gamma \quad (\text{Elastic interfacial shear region}) \quad (7)$$

$$\tau = A(\gamma + B) \quad (\text{Plastic interfacial shear region}) \quad (8)$$

Where  $S^m$  is the area of matrix. Though matrix follows the elastoplastic stress-strain curve shown in Fig. 2, it is assumed that a strain hardening of matrix does not occur due to the interfacial shear strain. The above equations can be rewritten by the nodal displacements and given by

(matrix: Elastic, interface: Elastic)

$$\left( \frac{2\pi(r+d)G}{S^m d} + \frac{2E^e}{\Delta y^2} \right) u_i^m = \frac{2\pi(r+d)G}{S^m d} u_i^f + \frac{E^e}{\Delta y^2} (u_{i-1}^m + u_{i+1}^m) \quad (9)$$

(matrix: Elastic, interface: Plastic)

$$\left( \frac{2\pi(r+d)A}{S^m d} + \frac{2E^e}{\Delta y^2} \right) u_i^m = \frac{2\pi(r+d)}{S^m} A \left( \frac{u_i^f}{d} - B \right) + \frac{E^e}{\Delta y^2} (u_{i-1}^m + u_{i+1}^m) \quad (10)$$

(matrix: Plastic, interface: Elastic)

$$\left( \frac{2\pi(r+d)G}{S^m d} + \frac{2E^p}{\Delta y^2} \right) u_i^m = \frac{2\pi(r+d)G}{S^m d} u_i^f + \frac{E^p}{\Delta y^2} (u_{i-1}^m + u_{i+1}^m) \quad (11)$$

(matrix: Plastic, interface: Plastic)

$$\left( \frac{2\pi(r+d)A}{S^m d} + \frac{2E^p}{\Delta y^2} \right) u_i^m = \frac{2\pi(r+d)A}{S^m} \left( \frac{u_i^f}{d} - B \right) + \frac{E^p}{\Delta y^2} (u_{i-1}^m + u_{i+1}^m) \quad (12)$$

Next, the elastic-plastic boundary is explained. Interfacial shear region includes elastic and plastic regions. When a boundary node number between both regions is called as  $ia$ , the following condition should be satisfied

$$\frac{G}{d} (u_{ia-1}^m - u_{ia-1}^f) + \left\{ \frac{G}{d} (u_{ia-1}^m - u_{ia-1}^f) - \frac{G}{d} (u_{ia-2}^m - u_{ia-2}^f) \right\} \geq \tau_y \quad (13)$$

when  $\tau_y$  is the yield shear stress and is given by  $\tau_y = \sigma_y / \sqrt{3}$ .

As like an interfacial shear region, matrix also includes elastic and plastic regions. When a boundary node number between both regions is given as  $ib$ , the following condition should be satisfied

$$\frac{E^e(u_{ib-1}^m - u_{ib-2}^m)}{\Delta y} + \left\{ \frac{E^e(u_{ib-1}^m - u_{ib-2}^m)}{\Delta y} - \frac{E^e(u_{ib-2}^m - u_{ib-3}^m)}{\Delta y} \right\} \geq \sigma_y \quad (14)$$

Here, the shear-lag equation for a boundary node of matrix should be rewritten considering elastic and plastic constitutive equations and given by

$$\frac{1}{\Delta y} \left[ \left\{ E^p \left( \frac{u_{ib+1}^m - u_{ib}^m}{\Delta y} - \frac{\sigma_y}{E^m} \right) + \sigma_y \right\} - E^e \frac{u_{ib}^m - u_{ib-1}^m}{\Delta y} \right] = \frac{2\pi(r+d)}{S^m} A \left[ \left( \frac{u_{ib}^m - u_{ib}^f}{d} \right) + B \right] \quad (15)$$

The stress-displacement distribution should satisfy the following geometrical boundary condition. As shown in Fig. 1, a node number 0 of fiber and matrix is a fixed one and the following condition must be satisfied

$$u_0^m = u_0^f = 0 \quad (16)$$

$u_k^m$  must stands for the total displacement of the model and is given by

$$u_k^m = \frac{l}{2} (\epsilon^c + \alpha^c \Delta T) \quad (17)$$

where  $l$  is the fragment length,  $\epsilon^c$  is the whole strain of the model (i.e. strain of the tested composite),  $\alpha^c$  is the composite thermal expansion coefficient and  $\Delta T$  is a difference in tested and fabricated temperatures. The fiber stress is zero where the fiber is broken and  $u_k^f$  is given by

$$u_k^f = u_{k-1}^f \quad (18)$$

Equations (1)~(18) are in suitable forms to be solved with the Jacobi method. The displacements for fiber and matrix can be numerically obtained with the above method. The element stresses are given with the obtained displacements by

(Fiber)

$$\sigma^f = \frac{E^f(u_i^f - u_{i-1}^f)}{\Delta y} \quad (19)$$

(Matrix : Elastic)

$$\sigma^m = \frac{E^e(u_i^m - u_{i-1}^m)}{\Delta y} \quad (20)$$

(Matrix : Plastic)

$$\sigma^m = E^p \left( \frac{u_i^m - u_{i-1}^m}{\Delta y} - \varepsilon_y \right) + \sigma_y \quad (21)$$

(Interface : Elastic)

$$\tau = G \frac{u_i^m - u_i^f}{d} \quad (22)$$

(Interface : Plastic)

$$\tau = A \left( \frac{u_i^m - u_i^f}{d} + B \right) \quad (23)$$

### FEM calculation

In order to assert the validity of the present model, we conducted the FEM calculation. The FEM model and meshes are shown in Fig. 4. Based on the experiments, a short matrix crack, which is equal to the fiber radius, is assumed in the model. The present material properties (Fiber: SiC Fiber (HI-NICALON<sup>TM</sup>), Matrix: Epoxy) used for the calculation are shown in Table 1.

The calculated stress distribution are shown in Figs. 5 (a) and (b). The present model used  $\Delta T=0$  to compare with the FEM results. In the calculation,  $d=7\mu\text{m}$ , which is equal to the matrix crack size, was used. A good agreement was obtained between the elastoplastic shear-lag analysis and FEM results. The present model is found to be very useful approximate approach.

Table 1 Material properties

Material properties	Values
$E^f$ :	250(GPa)
$E^e$ :	2.476(GPa)
$E^p$ :	223.1(MPa)
$\nu$ (for both fiber and matrix):	0.2
$\sigma_y$ :	60.29(MPa)
$r$ :	7( $\mu\text{m}$ )
$d$ :	7( $\mu\text{m}$ )



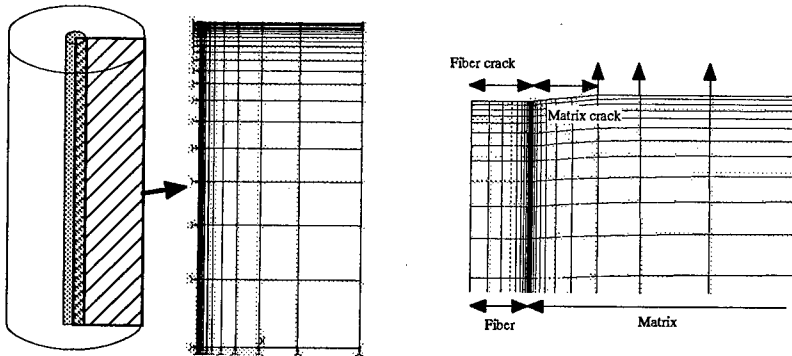


Fig. 4 Schematics of FEM model and meshes

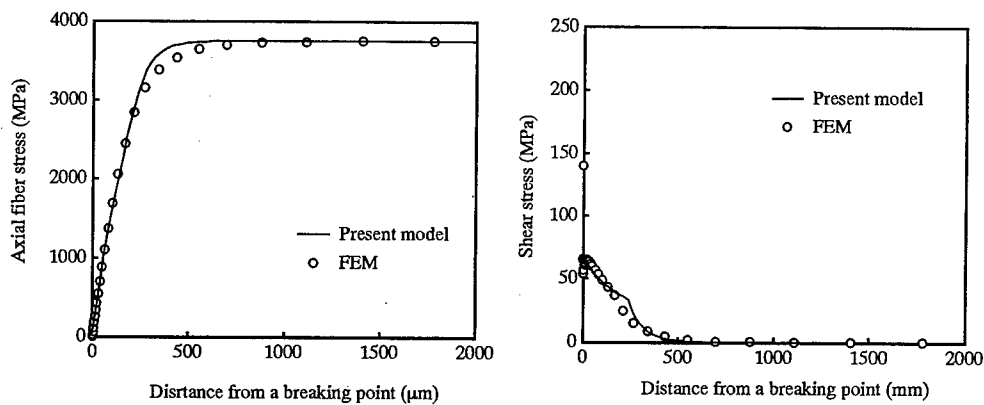


Figure 5 Stress distribution near a fiber breaking point; (a) Axial fiber stress distribution at  $\epsilon=1.5(\%)$ , (b) Shear stress distribution at  $\epsilon=1.5(\%)$

### Monte Carlo Simulation

Then, we conducted the Monte Carlo Simulation using the present shear-lag model. Following the classical approach [5], the continuous fiber in SFC is divided into small elements in the model. For each element, the strengths  $\sigma_s$  are given by

$$\sigma_s = \left( \frac{L_0}{\delta} \ln \frac{1}{1-R} \right)^{1/m} \sigma_0 \quad (24)$$

where  $R$  is a random number in the interval  $[0,1]$ ,  $\delta$  is a size of a unit element and  $m$  and  $\sigma_0$  are Weibull and scale parameters for a fiber length  $L_0=25\text{mm}$ . As the applied strain increases, it is judged whether the elements are broken by comparing each strength

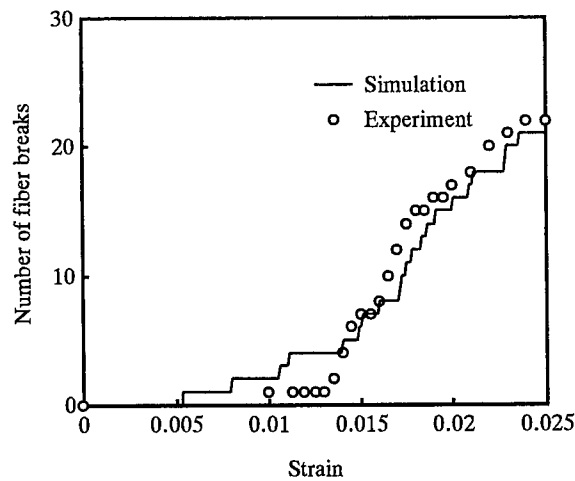


Figure 6 Simulation results with  $\sigma_0 = 1650$  MPa and  $m = 3.5$

with the stress distribution obtained from the shear-lag analysis. The simulation results are shown in Fig. 6. The simulation results with  $\sigma_0 = 1650$  MPa and  $m = 3.5$  are well fitted with the experimental results (SFC consists of SiC fiber (HI-NICALON<sup>TM</sup>) and Epoxy). Since our simulation is based on the valid stress distribution, it is believed that the simulation can accurately reproduce the fragmentation process in the SFC.

## Conclusion

The present paper proposed a new approach to predict the number of fragments during the single fiber composite test. A new elastoplastic shear-lag model had a good agreement with FEA results. The number of fragments can be well predicted by the Monte Carlo Simulation with the present shear-lag approach.

## Reference

- (1)W. A. Curtin : J. Mater. Sci., 26(1991), p.5239
- (2)C. Y. Hui, S. L. Phoenix, M. Ibnabdeljalil and R. L. Smith: J. Mech. Phys. Solids, (1995), p. 1551
- (3)A. Kelly and W. R. Tyson: J. Mech. Phys. Solids, (1995), p. 329
- (4)D. Tripathi, F. Chen and F. R. Jones: Proc. R. Soc. Lond. A,(1996), p. 621
- (5)K. P. Oh : J. Comp. Mater. 13(1979), p. 311

# Author Index

Abbott, R.,	87	Horide, A.,	669
Abe, T.,	363	Horizono, H.,	105
Ando, M.,	363	Hsu, D.K.,	409
Aoki, T.,	243	Hyer, M.W.,	57
Aoki, T.,	677, 687, 697, 705	Iarve, E.V.,	401
Aoki, Y.,	469	Ikueda, M.,	589
Aoki, Y.,	629	Inada, T.,	637
Asagumo, R.,	355, 603	Inai, R.,	383, 809
Baba, F.,	817	Inoda, M.,	847
Bakis, C.E.,	257	Inomata, K.,	613
Barton, Jr., O.,	521	Ishida, H.,	817
Beaumont, P.R.W.,	281	Ishikawa, T.,	133, 219, 227, 363, 677, 687, 697, 705, 761, 801
Biswas, K.K.,	589	Ishikawa, T.,	831
Byon, O-IL,	133, 629, 801	Ishikiriya, K.,	105
Chang, F.-K.,	75	Ishikura, K.,	825
Crasto, A.S.,	503	Ishimuro, Y.,	105
Davis, I.J.,	227, 373	Itabashi, M.,	563
Deng, Y.,	547	Ito, H.,	219
Fei, D.,	409	Ito, T.,	393
Fink, B.K.,	117	Itoh, M.,	363
Fujii, T.,	201, 209	Iwahori, Y.,	761
Fujii, T.,	375	Iwamoto, M.,	809
Fujii, Y.,	613	Izumiya, T.,	477
Fujimoto, S.,	273	Jiang, J.,	375
Fujita, A.,	817	Jilani, A.B.,	57
Fukuda, H.,	243, 785	Kageyama, K.,	159, 555
Fukuda, T.,	151, 167	Kameo, K.,	383, 715, 809
Fukui, T.,	349, 825	Kameyama, M.,	621
Fukunaga, H.,	201, 209	Kamiya, M.,	831
Fukunaga, H.,	273, 621	Kamiyama, T.,	281
Fuyama, N.,	201, 209	Karbhari, V.M.,	41
Gillespie, Jr., J.W.,	117	Kasano, H.,	485
Guceri, S.I.,	115	Kataoka, A.,	785
Hakotani, M.,	871	Katayama, T.,	871
Hamada, H.,	235, 349, 373, 383, 613, 715, 723, 729, 753, 793, 809, 817, 825, 847	Katoh, H.,	355, 603
Hamada, T.,	425	Katsuki, F.,	49
Hamaguchi, Y.,	355	Kawabata, S.,	581
Hara, E.,	133, 801	Kawada, H.,	315
Hatakeyama, T.,	97	Kawagoe, M.,	341
Hatta, H.,	235, 243, 831	Kawasaki, T.,	785
Hayashi, Y.,	677, 705	Kawasaki, Y.,	167
Hirose, Y.,	97	Kawata, K.,	563
Hitomi, T.,	243	Kedward, K.T.,	29
Hojo, M.,	185, 291	Kemmochi, K.,	737
Honda, T.,	193	Kido, A.,	581
Hong, C.S.,	77	Kikukawa, H.,	125

- |                    |                    |                    |                         |
|--------------------|--------------------|--------------------|-------------------------|
| Kim, H.-S.,        | 323                | Nakai, A.,         | 715, 723, 729, 753, 847 |
| Kim, H.J.,         | 117                | Nakai, H.,         | 49                      |
| Kim, R.Y.,         | 503                | Nakamura, H.,      | 331, 637                |
| Kim, T.D.,         | 661                | Nakamura, H.,      | 355                     |
| Kimpara, I.,       | 159, 555           | Nakanishi, Y.,     | 291                     |
| Kimura, H.,        | 563                | Naruse, H.,        | 159                     |
| Kitade, S.,        | 647                | Nishide, S.,       | 193                     |
| Kitagawa, K.,      | 613                | Nishii, N.,        | 769                     |
| Kitayama, T.,      | 825                | Nishiwaki, T.,     | 451, 839, 863           |
| Kobayashi, A.,     | 529                | Noda, M.,          | 23                      |
| Kobayashi, H.,     | 143, 331, 637      | Nojiri, T.,        | 251                     |
| Kobayashi, M.,     | 655                | Ochiai, S.,        | 185, 291                |
| Kobayashi, S.,     | 435                | Ochoa, O.O.,       | 513                     |
| Kogo, Y.,          | 235, 831           | Ogasawara, T.,     | 219, 227, 363           |
| Kondo, K.,         | 417                | Ogi, K.,           | 597                     |
| Kosaka, T.,        | 151, 167, 175      | Ogi, Y.,           | 621                     |
| Kosugi, K.,        | 97                 | Ogihara, S.,       | 435                     |
| Kumazawa, H.,      | 697, 705           | Oh, H.-S.,         | 299                     |
| Kunoo, K.,         | 477                | Ohki, T.,          | 729                     |
| Kuo, C.,           | 115                | Ohno, M.,          | 185                     |
| Loos, A.C.,        | 31                 | Okabe, T.,         | 879                     |
| Ma, Y.,            | 613                | Okabe, Y.,         | 175                     |
| Machida, K.,       | 477                | Okamoto, A.,       | 209                     |
| Maeda, M.,         | 613                | Okubo, K.,         | 375                     |
| Maekawa, S.,       | 97                 | Onita, T.,         | 451                     |
| Maekawa, Z.,       | 291, 451, 839, 863 | Ono, K.,           | 477                     |
| Majima, O.,        | 469                | Osada, T.,         | 715, 847                |
| Maruyama, K.,      | 49                 | Osaka, K.,         | 151, 167                |
| Matsubara, T.,     | 323                | Ota, T.,           | 855                     |
| Matsubara, T.,     | 839                | Ozaki, T.,         | 777                     |
| Matsuda, S.,       | 291                | Ozawa, T.,         | 777                     |
| Matsuoka, T.,      | 855                | Ozawa, Y.,         | 281                     |
| Matsushima, M.,    | 133, 801           | Pan, J.,           | 201, 209                |
| Mibayashi, H.,     | 745                | Park, J.W.,        | 77                      |
| Minnaar, K.,       | 461                | Park, S.W.,        | 461                     |
| Mistretta, J.P.,   | 503                | Pistor, C.,        | 115                     |
| Miyagawa, K.,      | 669                | Qiu, J.,           | 341                     |
| Miyanaga, T.,      | 281                | Rajapakse, Y.D.S., | 39                      |
| Miyano, Y.,        | 573                | Ryu, C.Y.,         | 77                      |
| Mizuno, H.,        | 105, 355           | Saafi, M.,         | 539                     |
| Mizuno, W.,        | 341                | Saito, H.,         | 383, 809                |
| Mollenhauer, D.H., | 401                | Saito, M.,         | 529                     |
| Morimoto, T.,      | 265, 687           | Sakaguchi, K.,     | 855                     |
| Morino, Y.,        | 687, 697, 705      | Sakai, A.,         | 603                     |
| Morita, H.,        | 647                | Sakai, S.,         | 655                     |
| Morita, M.,        | 341                | Sakamoto, A.,      | 23                      |
| Moriya, K.,        | 193                | Sana, T.,          | 97                      |
| Mouring, S.E.,     | 521                | Sanbongi, S.,      | 355                     |
| Muki, R.,          | 573                | Sando, M.,         | 151                     |
| Murakami, A.,      | 291                | Sasaki, G.,        | 201, 209                |
| Murase, S.,        | 761                | Sato, M.,          | 273, 281                |
| Murayama, H.,      | 159                | Sawada, T.,        | 185                     |
| Nagayasu, T.,      | 477                | Sawada, Y.,        | 235                     |
| Nakada, M.,        | 573                | Sekine, H.,        | 273, 281                |

Shevchencko, N.,	117	Uda, N.,	477
Shibuya, M.,	373	Ueda, T.,	723
Shibuya, Y.,	273	Uozumi, T.,	809
Shigei, T.,	235	Uyama, M.,	193
Shigenari, Y.,	669	Wakashima, K.,	393
Shimada, A.,	159	Wakayama, S.,	669
Shimamura, Y.,	143, 331, 637	Wang, W.X.,	323
Shimizu, R.,	655	Watanabe, K.,	185
Shimoda, T.,	687	Watanabe, N.,	219, 745, 769
Shimoi, T.,	863	Xia, M.,	737
Shimokawa, T.,	355, 603	Xiao, Y.,	443
Shimomura, T.,	49	Yamaguchi, K.,	555
Shinohara, M.,	871	Yamaguchi, Y.,	23, 105
Shiota, I.,	243	Yamashita, Y.,	581
Shirahata, H.,	273	Yarlagadda, S.,	117
Sierakowski, R.L.,	3	Yashiro, S.,	175
Simmons, D.K.,	521	Yokobori, Jr., A.T.,	281
Siron, O.,	425	Yokota, R.,	363
Smith, P.A.,	597	Yokozeke, T.,	677
Somiya, S.,	235, 251, 589	Yoshida, M.,	201, 209
Strait, S.J.,	257	Yunoki, N.,	193
Suemasu, H.,	469	Zhai, J.,	461
Suganuma, T.,	393	Zhou, M.,	461
Sugimoto, K.,	793		
Sugiyama, Y.,	105		
Susuki, I.,	443		
Suzuki, N.,	227		
Suzuki, S.,	669		
Tada, M.,	715		
Takahashi, K.,	647		
Takanashi, M.,	555		
Takao, Y.,	323		
Takayanagi, H.,	737		
Takeda, N.,	65, 175, 435, 715, 723, 729, 753, 847, 879		
Takeo, A.,	15		
Takeuchi, S.,	201		
Takiguchi, R.,	417		
Tamura, H.,	95, 97, 105, 125, 355		
Tanaka, A.,	669		
Tanaka, H.,	307		
Tanaka, K.,	307		
Tanaka, Y.,	143		
Tanigaki, E.,	817		
Tanimoto, T.,	493		
Tashiro, S.,	785		
Todoroki, A.,	143, 331, 637		
Toge, K.,	315		
Toutani, M.,	871		
Toutanji, H.,	539, 547		
Tressler, R.E.,	257		
Tsay, K.N.,	315		
Tsuda, H.,	425, 603		
Tsujioka, N.,	291		